

Published in Journals: Energies, International Journal of Environmental Research and Public Health, Processes, Buildings and Atmosphere

Topic Reprint

---

# Energy Efficiency, Environment and Health

Volume II

---

Edited by  
Roberto Alonso González Lezcano,  
Francesco Nocera and Rosa Giuseppina Caponetto

[www.mdpi.com/topics](http://www.mdpi.com/topics)



# **Energy Efficiency, Environment and Health—Volume II**



# Energy Efficiency, Environment and Health—Volume II

Editors

**Roberto Alonso González Lezcano**

**Francesco Nocera**

**Rosa Giuseppina Caponetto**

MDPI • Basel • Beijing • Wuhan • Barcelona • Belgrade • Manchester • Tokyo • Cluj • Tianjin



*Editors*

Roberto Alonso  
González Lezcano  
Departamento de  
Arquitectura y Diseño,  
Escuela Politécnica Superior,  
Universidad CEU San Pablo,  
Madrid, Spain

Francesco Nocera  
Department of Civil  
Engineering and Architecture,  
University of Catania,  
Catania, Italy

Rosa Giuseppina Caponetto  
Department of Civil  
Engineering and Architecture,  
University of Catania,  
Catania, Italy

*Editorial Office*

MDPI  
St. Alban-Anlage 66  
4052 Basel, Switzerland

This is a reprint of articles from the Topic published online in the open access journals *Energies* (ISSN 1996-1073), *International Journal of Environmental Research and Public Health* (ISSN 1660-4601), *Processes* (ISSN 2227-9717), *Buildings* (ISSN 2075-5309), and *Atmosphere* (ISSN 2073-4433) (available at: [https://www.mdpi.com/topics/energy\\_health](https://www.mdpi.com/topics/energy_health)).

For citation purposes, cite each article independently as indicated on the article page online and as indicated below:

LastName, A.A.; LastName, B.B.; LastName, C.C. Article Title. <i>Journal Name</i> <b>Year</b> , <i>Volume Number</i> , Page Range.
--

**Volume I**

ISBN 978-3-0365-8224-5 (Hbk)

ISBN 978-3-0365-8225-2 (PDF)

**Volume I-III**

ISBN 978-3-0365-8220-7 (Hbk)

ISBN 978-3-0365-8221-4 (PDF)

© 2023 by the authors. Articles in this book are Open Access and distributed under the Creative Commons Attribution (CC BY) license, which allows users to download, copy and build upon published articles, as long as the author and publisher are properly credited, which ensures maximum dissemination and a wider impact of our publications.

The book as a whole is distributed by MDPI under the terms and conditions of the Creative Commons license CC BY-NC-ND.

# Contents

<b>About the Editors</b> . . . . .	ix
<b>Haoran Yin, Chaonan Chen, Qingdong Dong, Pingping Zhang, Quantong Chen and Lianqi Zhu</b> Analysis of Spatial Heterogeneity and Influencing Factors of Ecological Environment Quality in China's North-South Transitional Zone Reprinted from: <i>Int. J. Environ. Res. Public Health</i> <b>2022</b> , <i>19</i> , 2236, doi:10.3390/ijerph19042236 . . .	1
<b>Xiaoxuan Wei, Meng Ye, Liang Yuan, Wei Bi and Weisheng Lu</b> Analyzing the Freight Characteristics and Carbon Emission of Construction Waste Hauling Trucks: Big Data Analytics of Hong Kong Reprinted from: <i>Int. J. Environ. Res. Public Health</i> <b>2022</b> , <i>19</i> , 2318, doi:10.3390/ijerph19042318 . . .	21
<b>Maria Cristina Morani, Mariana Simão, Ignac Gazur, Rui S. Santos, Armando Carravetta, Oreste Fecarotta and Helena M. Ramos</b> Pressure Drop and Energy Recovery with a New Centrifugal Micro-Turbine: Fundamentals and Application in a Real WDN Reprinted from: <i>Energies</i> <b>2022</b> , <i>15</i> , 1528, doi:10.3390/en15041528 . . . . .	43
<b>Ran Wang, Hao Lin, Jinhua Cheng, Zixi Xu, Haoying Feng and Yameng Tang</b> Optimizing the Water Ecological Environment of Mining Cities in the Yangtze River Economic Belt Using the Cloud Model, CV-TOPSIS, and Coupling Coordination Degree Reprinted from: <i>Int. J. Environ. Res. Public Health</i> <b>2022</b> , <i>19</i> , 2469, doi:10.3390/ijerph19042469 . . .	69
<b>Song Xin, Xiaozhen Zhu, Shangxiao Liu and Jianghui Guo</b> Research on Fault Tree Reconstruction Based on Contingency Reprinted from: <i>Processes</i> <b>2022</b> , <i>10</i> , 427, doi:10.3390/pr10020427 . . . . .	91
<b>Ling Yang, Qiang Ren, Shiji Ge, Zhiqiang Jiao, Wenhao Zhan, Runxiao Hou, et al.</b> Metal(loid)s Spatial Distribution, Accumulation, and Potential Health Risk Assessment in Soil-Wheat Systems near a Pb/Zn Smelter in Henan Province, Central China Reprinted from: <i>Int. J. Environ. Res. Public Health</i> <b>2022</b> , <i>19</i> , 2527, doi:10.3390/ijerph19052527 . . .	99
<b>Jianping Yang, Hong Xu, Fanyue Meng, Qingjie Guo, Tao He, Zequn Yang, et al.</b> A Molten-Salt Pyrolysis Synthesis Strategy toward Sulfur-Functionalized Carbon for Elemental Mercury Removal from Coal-Combustion Flue Gas Reprinted from: <i>Energies</i> <b>2022</b> , <i>15</i> , 1840, doi:10.3390/en15051840 . . . . .	111
<b>Alice Wistar, Marissa G. Hall, Maxime Berholz and Lindsey Smith Taillie</b> Designing Environmental Messages to Discourage Red Meat Consumption: An Online Experiment Reprinted from: <i>Int. J. Environ. Res. Public Health</i> <b>2022</b> , <i>19</i> , 2919, doi:10.3390/ijerph19052919 . . .	127
<b>Samanta A. Weber, Dirk Volta and Jürgen Kuck</b> Comparison of the Energetic Efficiency of Gas Separation Technologies Using the Physical Optimum by the Example of Oxygen Supply Options Reprinted from: <i>Energies</i> <b>2022</b> , <i>15</i> , 1855, doi:10.3390/en15051855 . . . . .	141
<b>Tian Wang, Hui Tu, Bo Min, Zuzheng Li, Xiaofang Li and Qingxiang You</b> The Mitigation Effect of Park Landscape on Thermal Environment in Shanghai City Based on Remote Sensing Retrieval Method Reprinted from: <i>Int. J. Environ. Res. Public Health</i> <b>2022</b> , <i>19</i> , 2949, doi:10.3390/ijerph19052949 . . .	163

<b>Rogger José Andrade-Cedeno, Jesús Alberto Pérez-Rodríguez, Carlos David Amaya-Jaramillo, Ciaddy Gina Rodríguez-Borges, Yolanda Eugenia Llosas-Albuerne and José David Barros-Enríquez</b> Numerical Study of Constant Pressure Systems with Variable Speed Electric Pumps Reprinted from: <i>Energies</i> <b>2022</b> , <i>15</i> , 1918, doi:10.3390/en15051918 . . . . .	187
<b>Michele Preziosi, Alessandro Federici and Roberto Merli</b> Evaluating the Impact of Public Information and Training Campaigns to Improve Energy Efficiency: Findings from the Italian Industry Reprinted from: <i>Energies</i> <b>2022</b> , <i>15</i> , 1931, doi:10.3390/en15051931 . . . . .	209
<b>Do-won Kim, Jeongwon Ock, Kyong-Whan Moon and Choong-Hee Park</b> Association between Heavy Metal Exposure and Dyslipidemia among Korean Adults: From the Korean National Environmental Health Survey, 2015–2017 Reprinted from: <i>Int. J. Environ. Res. Public Health</i> <b>2022</b> , <i>19</i> , 3181, doi:10.3390/ijerph19063181 . . .	223
<b>Yifan Yu, Jafar Ali, Yuesuo Yang, Peijing Kuang, Wenjing Zhang, Ying Lu and Yan Li</b> Synchronous Cr(VI) Remediation and Energy Production Using Microbial Fuel Cell from a Subsurface Environment: A Review Reprinted from: <i>Energies</i> <b>2022</b> , <i>15</i> , 1989, doi:10.3390/en15061989 . . . . .	235
<b>Silvia Ruggiero, Francesco Tariello and Giuseppe Peter Vanoli</b> Evaluation of Comfort Models Considering the Peculiarities of Hospitalization: Bedding, Clothing and Reduced Activity of Patients Reprinted from: <i>Buildings</i> <b>2022</b> , <i>12</i> , 343, doi:10.3390/buildings12030343 . . . . .	257
<b>Yajun Luan, Junzeng Xu, Jing Zhou, Haiyu Wang, Fengxiang Han, Kechun Wang and Yuping Lv</b> Migration and Removal of Labile Cadmium Contaminants in Paddy Soils by Electrokinetic Remediation without Changing Soil pH Reprinted from: <i>Int. J. Environ. Res. Public Health</i> <b>2022</b> , <i>19</i> , 3812, doi:10.3390/ijerph19073812 . . .	293
<b>Yu Cai, Haiyan Duan, Zhiqiang Luo, Zhiyuan Duan and Xian'en Wang</b> Dynamic Driving Mechanism of Dual Structural Effects on the Correlation between Economic Growth and CO <sub>2</sub> Emissions: Evidence from a Typical Transformation Region Reprinted from: <i>Int. J. Environ. Res. Public Health</i> <b>2022</b> , <i>19</i> , 3970, doi:10.3390/ijerph19073970 . . .	311
<b>João Andrade de Carvalho, Jr., André de Castro, Gutemberg Hespanha Brasil, Paulo Antonio de Souza, Jr. and Andrés Z. Mendiburu</b> CO <sub>2</sub> Emission Factors and Carbon Losses for Off-Road Mining Trucks Reprinted from: <i>Energies</i> <b>2022</b> , <i>15</i> , 2659, doi:10.3390/en15072659 . . . . .	329
<b>Jingyuan Li, Jinhua Cheng, Yang Wen, Jingyu Cheng, Zhong Ma, Peiqi Hu and Shurui Jiang</b> The Cause of China's Haze Pollution: City Level Evidence Based on the Extended STIRPAT Model Reprinted from: <i>Int. J. Environ. Res. Public Health</i> <b>2022</b> , <i>19</i> , 4597, doi:10.3390/ijerph19084597 . . .	347
<b>Tianzhen Li, Jun Xia, Chee Seong Chin and Pei Song</b> Investigation of the Thermal Performance of Lightweight Assembled Exterior Wall Panel (LAEWP) with Stud Connections Reprinted from: <i>Buildings</i> <b>2022</b> , <i>12</i> , 473, doi:10.3390/buildings12040473 . . . . .	365
<b>Hongjie Cao, Meina Li, Fengqin Qin, Yankun Xu, Li Zhang and Zhifeng Zhang</b> Economic Development, Fiscal Ecological Compensation, and Ecological Environment Quality Reprinted from: <i>Int. J. Environ. Res. Public Health</i> <b>2022</b> , <i>19</i> , 4725, doi:10.3390/ijerph19084725 . . .	379

<b>Z-John Liu, Minh-Hieu Le and Wen-Min Lu</b> An Innovation Perspective to Explore the Ecology and Social Welfare Efficiencies of Countries Reprinted from: <i>Int. J. Environ. Res. Public Health</i> <b>2022</b> , <i>19</i> , 5113, doi:10.3390/ijerph19095113 . . .	<b>399</b>
<b>Haiqian Ke, Bo Yang and Shangze Dai</b> Does Intensive Land Use Contribute to Energy Efficiency?—Evidence Based on a Spatial Durbin Model Reprinted from: <i>Int. J. Environ. Res. Public Health</i> <b>2022</b> , <i>19</i> , 5130, doi:10.3390/ijerph19095130 . . .	<b>417</b>
<b>Chen Wang, Liangcheng Yu, Yiyi Mo, Lincoln C. Wood and Carry Goon</b> Pareidolia in a Built Environment as a Complex Phenomenological Ambiguous Stimuli Reprinted from: <i>Int. J. Environ. Res. Public Health</i> <b>2022</b> , <i>19</i> , 5163, doi:10.3390/ijerph19095163 . . .	<b>435</b>
<b>Rundong Luo, Yan Li, Zhicheng Wang and Mengjiao Sun</b> Co-Movement between Carbon Prices and Energy Prices in Time and Frequency Domains: A Wavelet-Based Analysis for Beijing Carbon Emission Trading System Reprinted from: <i>Int. J. Environ. Res. Public Health</i> <b>2022</b> , <i>19</i> , 5217, doi:10.3390/ijerph19095217 . . .	<b>459</b>
<b>Chan-Hee Park, Eunhee Park, Hyun-Min Oh, Su-Jin Lee, Sun-Hee Park and Tae-Du Jung</b> Health-Related Quality of Life According to Sociodemographic Characteristics in the South Korean Population Reprinted from: <i>Int. J. Environ. Res. Public Health</i> <b>2022</b> , <i>19</i> , 5223, doi:10.3390/ijerph19095223 . . .	<b>475</b>
<b>Maolan Zhang, Guoming Zeng, Dong Liang, Yiran Xu, Yan Li, Xin Huang, et al.</b> An Analysis of the Colony Structure of Prokaryotes in the Jialing River Waters in Chongqing Reprinted from: <i>Int. J. Environ. Res. Public Health</i> <b>2022</b> , <i>19</i> , 5525, doi:10.3390/ijerph19095525 . . .	<b>485</b>
<b>Marcel Neberich, Nathalie Gerner, Carina Romodow, Johanna Freidl, Daniela Huber, Renate Weisböck-Erdheim, et al.</b> Positive Effects of Advanced Daylight Supply of Buildings on Schoolchildren—A Controlled, Single-Blinded, Longitudinal, Clinical Trial with Real Constructive Implementation Reprinted from: <i>Buildings</i> <b>2022</b> , <i>12</i> , 600, doi:10.3390/buildings12050600 . . . . .	<b>501</b>
<b>Weixiang Zhao and Yankun Xu</b> Public Expenditure and Green Total Factor Productivity: Evidence from Chinese Prefecture-Level Cities Reprinted from: <i>Int. J. Environ. Res. Public Health</i> <b>2022</b> , <i>19</i> , 5755, doi:10.3390/ijerph19095755 . . .	<b>521</b>
<b>Anandh Thankaswamy, Tao Xian, Yong-Feng Ma and Lian-Ping Wang</b> Sensitivity to Different Reanalysis Data on WRF Dynamic Downscaling for South China Sea Wind Resource Estimations Reprinted from: <i>Atmosphere</i> <b>2022</b> , <i>13</i> , 771, doi:10.3390/atmos13050771 . . . . .	<b>549</b>
<b>Xi Ouyang, Wen'e Qi, Donghui Song and Jianjun Zhou</b> Does Subjective Well-Being Promote Pro-Environmental Behaviors? Evidence from Rural Residents in China Reprinted from: <i>Int. J. Environ. Res. Public Health</i> <b>2022</b> , <i>19</i> , 5992, doi:10.3390/ijerph19105992 . . .	<b>573</b>
<b>Jelena Tihana, Aleksandrs Zajacs, Dmitrijs Ivancovs and Baiba Gaujena</b> Influence of Ventilation Operating Modes on Energy Efficiency Reprinted from: <i>Buildings</i> <b>2022</b> , <i>12</i> , 668, doi:10.3390/buildings12050668 . . . . .	<b>593</b>
<b>Wan-Jiun Chen, Jihn-Fa Jan, Chih-Hsin Chung and Shyue-Cherng Liaw</b> Resident Willingness to Pay for Ecosystem Services in Hillside Forests Reprinted from: <i>Int. J. Environ. Res. Public Health</i> <b>2022</b> , <i>19</i> , 6193, doi:10.3390/ijerph19106193 . . .	<b>605</b>





# About the Editors

## **Roberto Alonso González Lezcano**

Accredited as full professor by AQU Catalunya (March 2023). Extraordinary Doctorate Award. San Pablo CEU University Tenured Professor at the Department of Architecture and Design, the area of Building Systems, within the Institute of Technology of Universidad CEU San Pablo. Coordinator of the Mechanical Systems area. Professor Accredited by ANECA in the position of Tenured Professor. Two six-year research periods at CNEAI (last period 2016–2021). Coordinator of the post-graduate degree of Energy Efficiency and Mechanical Systems in Buildings and Coordinator of the Laboratory of Building Systems within Universidad CEU San Pablo. Member of the PhD Program in “Health Science and Technology” and the PhD Program “Composition, History and Techniques pertaining to Architecture and Urbanism”, where he is the Coordinator of the Construction, Innovation and Technology line and Coordinator of the complementary training program “Methodology of technical and statistical experimentation”. Ángel Herrera Award for the best research work in the areas of Architecture and Engineering for the year 2020/2021 in the XXV Edition of the Ángel Herrera Awards of the CEU San Pablo University. Coordinator of the Wind Energy Section within the master’s course in Renewable Energy of the Institute of Technology (Universidad CEU San Pablo).

Architecture and Solidarity Award (2019) of the 1st Housing Excellence Awards of the newspaper La Razón for the VEM Project financed by Airbus Defense and Space and developed at the CEU San Pablo University. Award won due to the VEM project developed with the AIRBUS company, 2015. Member of the Team Crew and Advisor of the Universidad Autónoma de Occidente and Universidad de San Buenaventura in the MIHOUSE Project team in the Solar Decathlon Latin American and Caribbean 2015.

## **Francesco Nocera**

Qualified as a Full Professor through the Italian National Scientific Qualification, sector 09/C2—Building Physics and Energy Systems in the year 2020. He is the author of more 200 research papers dealing with several research topics experimentally as well as numerically and analytically, including basic thermodynamics, thermo-fluid dynamics, heat transmission, lighting, acoustics, the rational use of energy, the use of renewable energy sources, buildings energy analysis, IEQ, UHI, and HVAC systems.

He was a postdoctoral researcher in Fluid Dynamics Modeling of Aeraulic Ducts, University of Catania (01-10-2007–31-10-2007) and gained a Ph.D. in Applied Environmental Physics, University di Palermo (01-10-2003–10-02-2006).

Scientist responsible for the Computer Laboratory at Special Didactic Structures of Architecture Siracusa (2010–) and responsible for the Energetic Sustainability and Environmental Control (SECA) Laboratory at Special Didactic Structures Architecture (2020–). Rector’s Delegate for the UN Sustainable Development Solutions Network (SDSN) (17-05-2018; 02-07-2019). Member of the Quality Management Board of the Architecture Degree Course, University of Catania (2018–2019) Member of the Joint Committee of the DICAR Department, the University of Catania (2020–). Secretary of Special Didactic Structure of Architecture, University of Catania (2020–2021). Visiting Professor at the University of Valladolid (2020) Scientific Responsible of Memorandum of understanding, cooperation agreement of general interest: CEU Cardenal Herrera University (Spain), Faculty of Urban Construction and Environmental Engineering of Chongqing University (China), Applied Science and Arts of Southern Switzerland University (SUPSI), Lega Ambiente, EURAC center.

Member of International Building Physics Association—IABP (2018). Member of the International Commission on Illumination (CIE)—UNI/CT 023/GL 02 Lighting of Work Places and Schools.

### **Rosa Giuseppina Caponetto**

Qualified as a Full Professor through the Italian National Scientific Qualification, sector 08/C1—Design and Technological Architecture Design, in the year 2022. Her main research topics are: materials and technologies for sustainable construction; the durability of building materials and components; the experimental assessment of building materials’ performance; self-build; knowledge of local building tradition and innovative scenarios; the assessment of buildings’ sustainability; and energy and seismic upgrading of existing buildings.

She is the scientific director of the LaTPrE laboratory, Laboratory of Building Production Technologies (University of Catania). She is a member of the “Smart Cities & Communities” National Laboratory by CINI (focus group: “ICT for Smart Energy & Smart Buildings”). She is the head of operations management and a member of the scientific committee of “MuRa”, Museum of Representation (University of Catania), as well as a member of the “Technical College for Building Consultancy” (University of Catania).

She is the co-inventor of the patent idea entitled “Anti-seismic construction system: technology and production process”. She has developed several research works in collaboration with national research institutes (e.g., CNR) and/or with some municipalities (cooperative agreements).

She has been involved in the following projects: the VVITA project “Modernizing Learning and Teaching for Architecture through Smart and Long-lasting Partnerships leading to sustainable and inclusive development strategies to Vitalize Heritage Villages through Innovative Technologies”, ERASMUS + KA2 program funded by the European Community (2016–2019), U.O Scientific Responsible; the EWAS project “An Early Warning System for cultural-heritage”, funded by the PNR program (2017–2022).



Article

# Analysis of Spatial Heterogeneity and Influencing Factors of Ecological Environment Quality in China's North-South Transitional Zone

Haoran Yin, Chaonan Chen, Qingdong Dong, Pingping Zhang, Quantong Chen and Lianqi Zhu \*

College of Geography and Environmental Science, Henan University, Kaifeng 475004, China; yjsyhr@163.com (H.Y.); 15736870141@163.com (C.C.); dongqd961103@126.com (Q.D.); zhangpp@henu.edu.cn (P.Z.); a13804817736@126.com (Q.C.)

\* Correspondence: lqzhu@henu.edu.cn

**Abstract:** The ecological environment is important for the natural disaster prevention of human society. The monitoring of ecological environment quality has far-reaching practical significance for the functional construction of ecosystem services and policy coordination. Based on Landsat 8 operational land image (OLI)/thermal infrared sensor (TIRS) remote sensing image data, this study selected the normalized vegetation (NDVI), tasseled cap transformation humidity (WI), bare soil (SI), construction index (NDSI), and land surface temperature (LST) indexes from the aspects of greenness, humidity, dryness, and heat. Using spatial principal component analysis (SPCA) and the remote sensing ecological index (RSEI) analyzed the spatial differentiation characteristics and influencing factors of the original remote sensing ecological index (RSEI<sub>0</sub>). The results showed that: (1) the overall RSEI average value of the Qinling-Daba Mountains in 2017 was 0.61, and the ecological environment quality was at a "Good" level. Greenness contributed the most to the comprehensive index of the area, and vegetation distribution had a significant impact on the ecological environment quality of the study area. Heat is a secondary impact, and it has an inhibitory effect on habitat quality; (2) the overall distribution of regional ecological environment quality was quite different, with the ecological environment quality level showing a decreasing trend from low to high altitude; RSEI<sub>0</sub> spatial heterogeneity at the optimal scale of 2 km was the largest, and the nugget effect was 88% which indicated a high degree of spatial variability, mainly affected by structural factors; (3) Slope, relief amplitude, elevation, the proportion of high-vegetation area, proportion of construction land area, and average population density significantly impact the spatial differentiation of RSEI<sub>0</sub>. The explanatory powers of slope and relief amplitude were 56.1% and 65.3%, respectively, which were the main factors affecting the spatial differentiation of the ecological environment quality in high undulation. The results can provide important scientific support for ecological environment construction and ecological restoration in the study area.

**Citation:** Yin, H.; Chen, C.; Dong, Q.; Zhang, P.; Chen, Q.; Zhu, L. Analysis of Spatial Heterogeneity and Influencing Factors of Ecological Environment Quality in China's North-South Transitional Zone. *Int. J. Environ. Res. Public Health* **2022**, *19*, 2236. <https://doi.org/10.3390/ijerph19042236>

Academic Editors: Roberto Alonso González Lezcano, Francesco Nocera and Rosa Giuseppina Caponetto

Received: 5 December 2021

Accepted: 3 February 2022

Published: 16 February 2022

**Publisher's Note:** MDPI stays neutral with regard to jurisdictional claims in published maps and institutional affiliations.



**Copyright:** © 2022 by the authors. Licensee MDPI, Basel, Switzerland. This article is an open access article distributed under the terms and conditions of the Creative Commons Attribution (CC BY) license (<https://creativecommons.org/licenses/by/4.0/>).

**Keywords:** China's North-South Transitional Zone; eco-environmental quality; remote sensing monitoring; regional policy coordination; climate change

## 1. Introduction

The ecological environment is a complex system formed by the interaction between natural and social factors. The ecological environment is a characteristic of the comprehensive performance of each element and its function, and it is also the resource and environmental basis for human survival and development [1]. No single environmental element can scientifically and objectively reflect the quality of the ecological environment [2,3]. Eco-environmental quality is one of the important types of ecosystem service functions, and maintaining the stability of its functions is crucial to ecological environmental protection and the integration of natural resources. In particular, the mountains, which characterize a unique geographical unit of the earth's land surface, have a fragile ecological environment

and are more sensitive to global changes. They are the “amplifiers” of global change signals. Changes in the quality of the mountain ecological environment have an important impact on the surrounding areas [4]. The potential factors affecting the ecological environment of mountainous areas are currently dominated by climate and topography. Their changes have varying degrees of impact on the quality of the ecological environment [5]. In addition, the mountain ecological environment is affected more by environmental problems such as soil erosion, forest degradation, and land desertification than other areas; the heterogeneity of the mountain itself and the negative interference by human beings have exacerbated the vulnerability of the ecological environment [6–8]. Therefore, studying the impact mechanism of mountain ecological and environment assessment is of great significance in constructing an ecological civilization and estimating the value of ecosystem services.

Satellite remote sensing technology has been widely used in ecological environment monitoring and environmental assessment in recent years, based on the high speed of remote sensing satellites and the macroscopic nature of real-time monitoring of the ground truth, and many scholars have used remote sensing indexes to assess the urban ecological environment [9–11], ecological demonstration area [12], aquatic environment [13], and terrestrial surface vegetation [14–16], and have obtained important theoretical results. However, the index selection is relatively single, mainly because the natural environment is a more complex ecological environment. The indicators selected for fragile areas lack scientific knowledge, and it is impossible to grasp the overall habitat quality from a macro perspective. Subsequently, the ecological environment evaluation index (EI) issued by the Ministry of Environmental Protection in 2006 has been widely used in China. Still, the determination of the weight value of the method and the setting and acquisition of the index is very simple [17], making it impossible to visualize the quality of the regional ecological environment. It cannot monitor the spatial change characteristics of the ecological environment any better [18]. Second, many studies are based on multi-angle evaluation methods, using comprehensive evaluation methods such as the fuzzy evaluation method and the analytic hierarchy process (AHP) to analyze the ecological environment and its quality standards; however, human subjectivity is strong, and it is widely used in research and cannot be sufficiently compared with regional differences. When studying the differences between regions, it is difficult to comprehensively evaluate the ecological environment quality using multiple composite factors [19,20]. Xu proposed a remote sensing technology-based regional, remote sensing ecological index (RSEI) in 2013 [11,21]. The calculation of this index is relatively convenient, and multiple environmental index factors are considered comprehensively, which can compensate for the suitability of the subjective analysis method for areas with more complex geographical environments. In recent years, it has been widely used by many scholars in the detection and evaluation of temporal and spatial changes in ecological environment quality [20,22–25]. However, systematic analysis of regional ecology research on the impact of environmental quality change and its driving factors is relatively scarce. The spatial differentiation characteristics of mountain ecological and environmental quality have rarely been studied. Therefore, the use of RSEI has important scientific and practical significance for research on the spatial difference of the mountain ecological environment quality at a mesoscale, which is conducive to an accurate understanding of the ecological environment problems in mountainous areas and for the better development of research.

The Qinling-Daba Mountains are the main components of China’s North-South Transitional Zone. The mountains are undulating and the vegetation coverage is relatively high. Abundant vegetation and water resources and diversified wild animal resources have created a complex ecological and geographical environment. As a natural barrier for ecological security in central China, an important ecological function area, its natural ecosystem is typicality and representativeness [26]. The quality of the ecological environment is critical. Current research is mostly based on areas such as southern Shaanxi [27], Taibai Mountain [28], and single administrative units [9], discussing the human factors of ecological environment degradation and the scientific nature of the regional ecological envi-

ronment quality index system, based on the research of land use ecological risk assessment. There is no specific discussion on the quality of the ecological environment based on the Qinling-Daba Mountains as a whole, which leads to relatively imprecise research on the ecological environment of the area. Therefore, it is impossible to look at the trend as a whole. In addition, the study found that the analysis of different scale features and the selection of indicators are very important [29], considering that the Qinling-Daba Mountains are mesoscale regional mountainous landforms, the vegetation coverage is moderate, and the distribution of water and heat is different according to the terrain gradients. For this reason, the normalized vegetation index, the tasseled cap transformation humidity index, the bare soil index, the man-made building index, and the surface temperature were selected as the main factors to explore the spatial distribution of ecological quality based on remote sensing data and its impact mechanism. Finally, whether Structural factors or random factors affect the quality of the ecological environment, and how the local characteristics of the region lead to this process. Whether the research in this area can supplement the shortcomings and deficiencies of other scholars, and how it is different from other studies, are worthy of exploration. Therefore, this study uses the Qinling-Daba Mountains as the research area, based on the 2017 Landsat 8 OLI/TIRS remote sensing images, and uses the special principal component analysis method to construct the regional RSEI to comprehensively evaluate the ecological environment quality of the Qinling-Daba Mountains, analyze the spatial pattern and differentiation characteristics of the ecological environment quality, and systematically explore the potential factors affecting ecological and environmental quality. This study can explore a set of comprehensive remote sensing monitoring methods to monitor ecological environment changes in the areas. It aims to provide theoretical guidance and decision support for managers regarding soil erosion control, disaster prevention, and ecological environment restoration in the area and promote the sustainable development of the regional ecological environment.

## 2. Materials and Methods

### 2.1. Study Area

The study areas range from 30°–36° N and 101°–114° E to the east of the Qinghai-Tibet Plateau in the west, the eastern plain in the east, the southern edge of the Loess Plateau, and the northern Sichuan Basin, with the Qinling and Daba Mountains as the main body. It is approximately 300 km from north to south, with a span of nearly 1000 km from east to west, a total area of approximately 300,000 km<sup>2</sup>, covering the six provinces of Sichuan, Henan, Gansu, Shaanxi, Chongqing, and Hubei. The terrain slopes from west to east (Figure 1). The climate is dominated by the subtropical monsoon climate, high vegetation coverage, and rich biodiversity. It is in the transition zone between subtropical and warm temperate zones [30]. Affected by geographical location and mountain topography, the special area has a unique ecological and geographic environment, and has become an important ecological function area in the country. The average net primary productivity (NPP) of vegetation refers to the remainder after deducting autotrophic respiration from the total amount of organic dry matter produced by photosynthesis in a unit of time and area. It represents the vegetation growth status. The average net primary productivity of the areas has increased annually, forming an ecological environment pattern made of a multi-dimensional zonal landscape [31].

### 2.2. Data Source and Processing

The remote sensing data in this study area were obtained from the OLI image of the geospatial data cloud Landsat 8, with a spatial resolution of 30 m, involving 26 images of the study area from March to August 2017. The cloud cover of the images was less than 5%, and they were concentrated in the spring and summer, without falling leaves. The seasons are similar to each other, which can avoid the influence of seasonal differences. The overall workflow is shown in Figure 2.

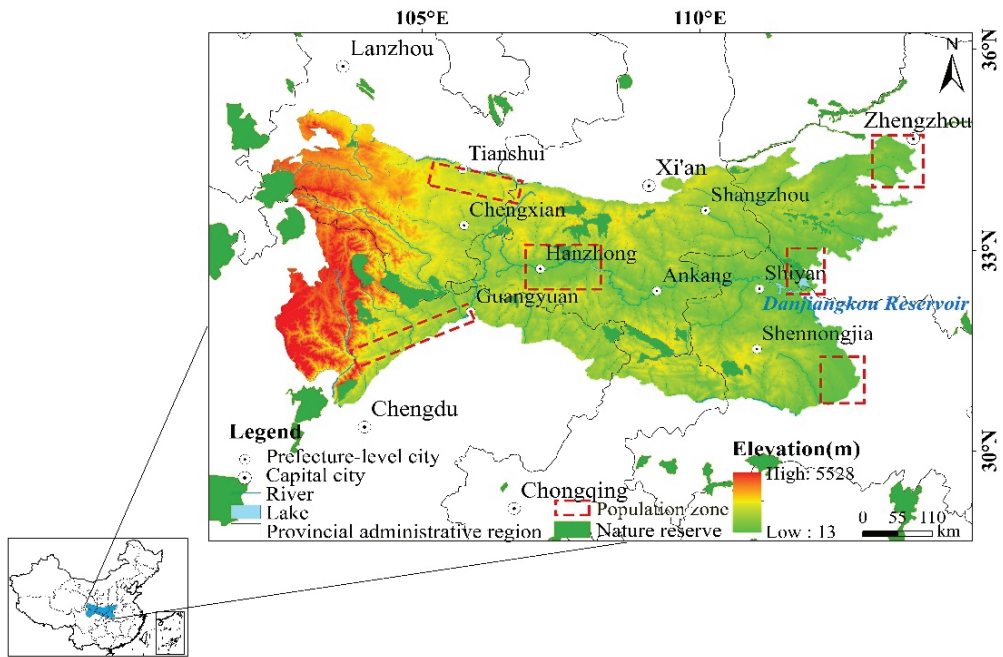


Figure 1. Geographical location of study area.

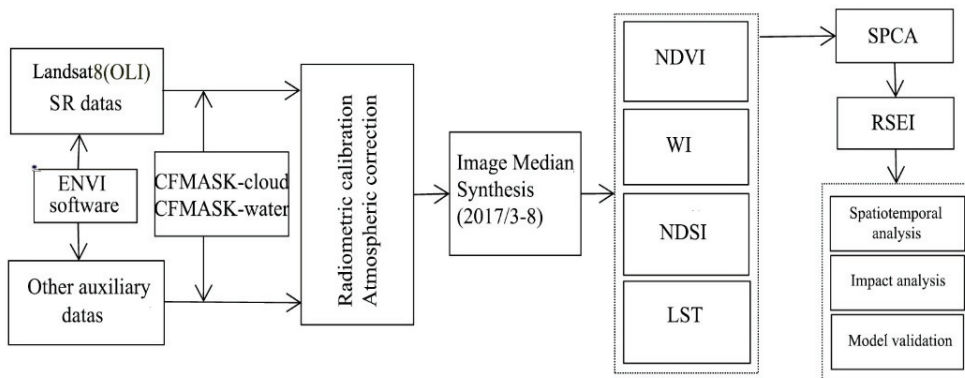
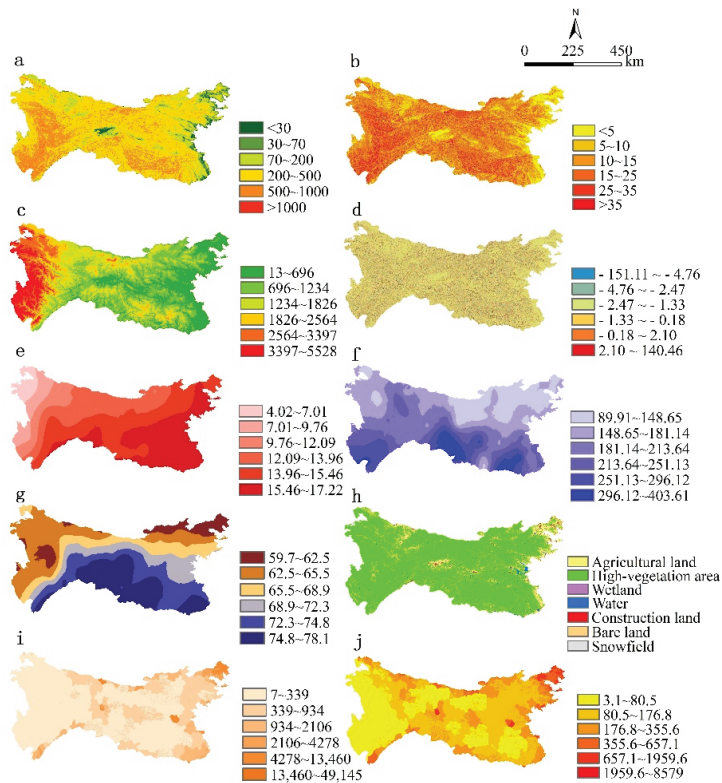


Figure 2. Technical roadmap. NDVI: normalized vegetation; WI: tasseled cap transformation humidity; NDSI: construction index; LST: land surface temperature; SPCA: spatial principal component analysis; RSEI: remote sensing ecological index.

The land cover data of the study area in 2017 comes from the FROM-GLC10 dataset developed by the Department of Earth System Science of Tsinghua University (<http://data.ess.tsinghua.edu.cn>) (accessed on 11 October 2020), with a spatial resolution of 10 m; the meteorological data is from China Meteorology. The daily value data of the Science Data Center (<http://data.cma.cn>) (accessed on 15 October 2020) are interpolated to obtain a raster dataset; the soil organic carbon data is in the Harmonized World Soil Database (HWSD) (<http://www.fao.org/land-water/en>) (accessed on 23 October 2020), the spatial resolution is 30 arc seconds, and the data of the entire study area is obtained by stitching and cutting; the soil erosion data of the study area are obtained according to previous studies [32]. The socio-economic data for 2017 is based on the 2015 annual average population and GDP,

and is replaced by raster data, both from the Resource and Environment Data Center of the Chinese Academy of Sciences (<http://www.resdc.cn>) (accessed on 25 May 2020), with a resolution of 1 km; the DEM data comes from NASA\_SRTM with a spatial resolution of 90 m. In the data set, the elevation, slope, and curvature-related data information are extracted. Combined with the actual situation of the study area, the average change-point method is used to extract the relief amplitude data of the areas. The input variables of the Geodetector are categorical, and the terrain relief amplitude is divided into six levels [33]: flat (<30 m), mesa (30–70 m), hills (70–200 m), small undulating mountains (200–500 m), medium undulating mountains (500–1000 m), and large undulating mountains (>1000 m). Other influencing variables are divided into six categories by the ArcGIS natural breakpoint method so that the results of the impact factors at all levels are comparable in the case of stratification. The results for each Geodetector category component are shown in Figure 3.



**Figure 3.** Distribution of each factor class of the Geodetector in Qinling-Daba Mountains. (a) Relief (m); (b) slope (°); (c) elevation (m); (d) curvature; (e) mean annual temperature (°C); (f) mean annual precipitation (mm); (g) mean annual relative humidity (%); (h) land use types; (i) mean annual GDP (yuan km<sup>-2</sup>); (j) Mean annual population density (person km<sup>-2</sup>).

### 2.3. Methodology

#### 2.3.1. Selection of Various Index Factors of RSEI

This study selected the normalized vegetation index, changing the constitution of the tasseled cap, Bare soil index, Construction Index, and Surface Temperature from the perspectives of vegetation, soil, human activities, and climate [13,21]. Combining the spatial principal component analysis (SPCA) to construct the RSEI of the study area, the spatial differentiation of the ecological environment quality of the Qinling-Daba Mountains was assessed (Table 1) [34].



**Table 1.** RSEI evaluation index and its calculation formula.

Index	Calculation Formula
Greenness	$NDVI = (NR - NIR) / (NR + NIR)$
Humidity	$WI = 0.1511B + 0.1973G + 0.3283NR + 0.3407NIR - 0.7117M_1 - 0.4559M_2$
Bare soil and construction	$NDSI = (SI + NDIBI) / 2$
	$SI = [(M_1 + NR) - (NIR + B)] / [(M_2 + NR) + (NIR + B)]$
	$NDIBI = \{2M_1 / (M_1 + NIR) [NIR / (NIR + NR) + G / (G + M_1)]\} / \{2M_2 / (M_2 + NIR) + [NIR / (NIR + NR) + G / (G + M_2)]\}$
Land surface temperature	$LST = T / [1 + (\lambda T / \rho) \ln \varepsilon] - 273$
	$T = B_2 / \ln (B_1 / H_t + 1)$
	$H_t = (L_t - \uparrow U - V (1 - \varepsilon) \downarrow D) / V_\varepsilon$

Note: B, G, NR, NIR, M<sub>1</sub>, M<sub>2</sub>, T, K, ρ, λ, ε, H<sub>t</sub>, B<sub>1</sub>, B<sub>2</sub>, L<sub>t</sub>, ↑U, ↓D, V represent the reflectance of the Landsat 8 remote sensing image in bands 2, 3, 4, 5, 6, and 7, the surface brightness temperature (K = 1.38 × 10<sup>-23</sup> J·K<sup>-1</sup>), ρ = 1.438 × 10<sup>-2</sup> M·K (M is the default constant parameter set by the platform), the center wavelength of the OLI thermal infrared band (λ = 11.45 μm), the surface emissivity image (ε), the radiation value of the pixel in thermal infrared 10 band at the sensor, the calibration parameters (B<sub>1</sub>, B<sub>2</sub>), the thermal infrared band radiance image (L<sub>t</sub>), upward radiance value and downward radiance value (↑U = 1.64 W/(m<sup>2</sup>·sr·μm), ↓D = 2.75 W/(m<sup>2</sup>·sr·μm)), atmospheric profile thermal infrared transmittance (V = 0.78).

In this study, the NDVI, closely related to the leaf area index, surface vegetation, and biomass, is widely used to study vegetation and environmental changes as the greenness index [35].

Second, based on OLI land imager data, this study uses the tasseled cap change correlation coefficient method [36], combined with Gram–Schmidt and Prueck correlation algorithms, to obtain the study area atmospheric reflectivity remote sensing data. Regarding the OLI coefficient of variation method, the calculation results show that the accuracy is relatively high, and it has good sorting properties for ground objects [37]. It reflects the abundance of moisture in the soil, water bodies, and vegetation in the study area.

Third, to better characterize the degree of “Dryness” of natural and anthropogenic land in the study area, this study uses the bare soil index [38] and the building index [39] to indicate the dryness components. It takes the average value of the indexes for the quantitative calculation, which represents the natural area of the region and the ecological degradation caused by human activities.

Finally, the temperature component in this study is derived from the ground radiation ratio and the ground surface temperature corrected by the black body image grayscale, which can better quantify the energy exchange parameters between the surface image and the atmosphere and more accurately reflect the surface temperature. Therefore, using the atmospheric correction method to retrieve land surface temperature [40]. ε is estimated based on the NDVI and vegetation coverage image according to the Landsat model [41]. T was calculated using the Landsat model manual and the latest revised calibration parameter method [42,43]. It should be noted that, before calculating the blackbody radiance value, it is necessary to perform radiometric calibration and surface emissivity correction and select the Landsat 8 calculation formula to invert the ground temperature. We referred to the previous improved single-channel algorithm (SC algorithm) to verify and check the ground surface temperature [44]. The last three parameters mentioned above can be queried through the NASA website (<http://atmcorr.gsfc.nasa.gov>) (accessed on 3 October 2020) to obtain atmospheric profile parameter information.

### 2.3.2. Construction of Comprehensive Index of Ecological Environment Quality Evaluation

In this study, the SPCA was used to couple the above four indicators to eliminate the high correlation between variables to reduce the inaccuracy of information caused by anthropogenic factors; the indicators were normalized through a unified dimension, and the initial study area was obtained. The initial RSEI<sub>0</sub> was normalized again to obtain the final comprehensive index RSEI.

Positive normalization processing formula:

$$N_i = \frac{M_i - I_{\min}}{I_{\max} - I_{\min}} \quad (1)$$

Reverse normalization processing formula:

$$N_i = \frac{I_{\max} - M_i}{I_{\max} - I_{\min}} \quad (2)$$

The initial RSEI<sub>0</sub> is obtained by principal component analysis:

$$RSEI_0 = PC_1[f(NDVI, WI, NDSI, LST)] \quad (3)$$

Then normalize RSEI<sub>0</sub>:

$$RSEI = \frac{RSEI_0 - RSEI_{0\min}}{RSEI_{0\max} - RSEI_{0\min}} \quad (4)$$

where  $M_i$  and  $N_i$  represent the pixel values of RSEI<sub>0</sub> before and after normalization, respectively;  $I_{\max}$  and  $I_{\min}$  represent the maximum and minimum values of the image, respectively, and  $PC_1$  represents the first principal component of the four indicators.

### 2.3.3. Spatial Heterogeneity Analysis Method of Ecological Environment Quality

Because natural and human factors have different degrees of impact on the environmental quality of mountainous areas, to distinguish the impact of structural factors and random factors on the ecological and environmental benefits of the areas and their structural degrees, this study uses a semi-variance function to analyze the degree of spatial differentiation and structural characteristics quantitatively. The image was gridded and sampled based on the optimal research scale of 2 km, and a 2 km scale spatial structure model was constructed. Based on whether the GS+9.0 conforms to the normal distribution and following the removal of a few sample points that do not meet the normal distribution, the square root conversion conforms to the normal distribution and meets the requirements of semi-variance function analysis. The semi-variance function formula is as follows:

$$F(h) = \frac{1}{2I(h)} \sum_{i=1}^{I(h)} [(W(C_i) - W(C_i + h))]^2 \quad (5)$$

where  $F(h)$  is the value of the semi-variance function with  $h$  as the distance,  $h$  is the sample point spacing,  $I(h)$  is the number of sample pairs divided by the distance point, and  $W(C_i)$  and  $W(C_i + h)$  are located in the range of  $C_i$  and  $C_i + h$  interval variables. The “Nugget effect” refers to the proportion of spatial autocorrelation heterogeneity at a scale. When  $C/C_0 + C < 0.25$ , the spatial correlation is weak, indicating that the spatial variation caused by the random part plays a major role, and the spatial heterogeneity is weak. When  $C/C_0 + C$  is between 0.25 and 0.75, the degree of correlation is moderate, and its spatial variability is determined by both random and structural factors. When  $C/C_0 + C > 0.75$ , the spatial correlation is very strong, and its spatial variability is mainly caused by structural factors, and the degree of spatial heterogeneity is relatively large [45–47].

By combining the above sorting results, this study uses the factor detection of Geodetector to analyze the influence of each geographical element on the ecological environment of the Qinling-Daba Mountains to further study the independent interpretation of the influencing factors of the ecological environment quality to obtain the main factors affecting the differentiation of the mountain ecological environment quality. The formula for the influence degree of mass spatial heterogeneity is as follows:

$$q = 1 - \frac{1}{D\alpha_i^2} \sum_{i=1}^n D\alpha_i^2 \quad (6)$$

where  $q$  is the degree of influence of each influencing factor on the spatial distribution of the area's ecological quality,  $q \in [0,1]$ ,  $D$  is the total number of samples in the study area,  $\alpha_i^2$  is the variance of the sub-regional ecological, environmental quality indicators,  $i = 1, 2, \dots, n$ ,  $i$  represents each secondary partition, and  $n$  represents the number of all partitions. The size of  $q$  reflects the degree of spatial heterogeneity of the ecological environment quality in the area. The larger the value of  $q$ , the stronger the heterogeneity within the spatial partition. The various factors of the partition have a greater impact on the spatial distribution of the ecological environment quality and vice versa. In particular, when  $q = 0$ , it indicates no spatial heterogeneity in the ecological environment quality of the study area; when  $q = 1$ , it indicates perfect spatial heterogeneity. Geodetectors can perform a significant test for the  $q$  value [48].

#### 2.3.4. Eco-Environmental Quality Index (EQI) Verification

To verify how scientific and accurate the value of RSEI is in this study, EQI is combined with possible influencing factors, and principal component analysis is used to couple and analyze multiple environmental indicators [49], as follows:

$$EQI = SPCA\{f(TEM, PRE, TI, LAND, SL, SOM, POP, GDP)\} \quad (7)$$

where TEM and PRE are the average annual temperature and annual precipitation in the study area, respectively, TI is the topographic index based on slope and altitude, LAND is the land use degree, SL is the soil erosion intensity, SOM is the soil organic matter content, and POP and GDP are the population density and total GDP, respectively.

### 3. Results

#### 3.1. Principal Component Analysis Results of RSEI Index in Qinling-Daba Mountains

To comprehensively study the quality of the ecological environment of the Qinling-Daba Mountains in 2017, according to the research classification standard of Xu Hanqiu [21], the RSEI is divided into excellent (0.8–1.0), good (0.6–0.8), middle (0.4–0.6), poor (0.2–0.4), and very poor (0–0.2).

Principal component analysis was performed using the ENVI software to obtain the covariance matrix and correlation coefficient matrix of each component. The eigenvalues and contribution rates are presented in Table 2. It shows that the cumulative contribution rate of  $PC_1$  has reached more than 85%, indicating that it has concentrated on the main characteristics of the four indicators, and the first principal component can be used to replace the four indicators. The overall RSEI average of the Qinling-Daba Mountains reached 0.61, and the overall ecological environment quality was at a "good" level. It can be seen from the  $PC_1$  load values of the four component indicators that the greenness NDVI and humidity WI are positive in the overall load, and the dryness NDSI and heat LST are negative. Consistent with the fact that greenness and humidity positively affect the quality of the ecological environment, dryness and heat negatively affect the environmental quality [24,50–52]; the load value of  $PC_2$ – $PC_4$  can be of different sizes and cannot represent the overall component well. Among the positive indicators, the average value of NDVI was 0.63, and its contribution to the indicator was 0.614. It has the largest contribution of all indicators, suggesting that vegetation plays a vital role in the quality and maintenance of the ecological environment of the area. Humidity is second only to greenness in the ecological environment of the Qinling-Daba Mountains. The load value of  $PC_1$  was relatively low, whereas  $PC_2$  was relatively large and negative. Such findings contrast the large wetland in the area located in the urban concentration area with the low humidity in the high-altitude zone; humidity is affected by terrain and is man-made. Among the negative indicators, heat has a large negative impact on the ecological environment quality of the overall study area, and loads of  $PC_1$  and  $PC_2$  are opposite, indicating that appropriate temperature and light have a positive effect on vegetation and biological growth. However, affected by geomorphic features and aspects, vegetation and soil moisture will evaporate faster, and the habitat benefit will gradually decline.

**Table 2.** Results of RSEI and its indicators.

Index	Mean	Standard Deviation	PC <sub>1</sub>	PC <sub>2</sub>	PC <sub>3</sub>	PC <sub>4</sub>	PC <sub>1</sub> Load Value
NDVI	0.63	0.27	0.614	0.133	0.427	0.654	0.614
WI	0.54	0.16	0.232	−0.971	0.233	0.048	0.232
NDSI	0.40	0.20	−0.521	−0.194	−0.826	0.094	−0.521
LST	0.58	0.29	−0.597	0.030	0.285	−0.749	−0.597
Eigenvalues	-	-	0.193	0.023	0.005	0.004	-
Eigenvalue	-	-	85.41	10.29	2.31	1.99	-
Contribution rate (%)	-	-	-	-	-	-	-
RSEI	0.61	0.10	-	-	-	-	-

**3.2. The Spatial Distribution Characteristics of RSEI in Qinling-Daba Mountain Area**

It can be seen from Figure 4 that the ecological environment quality of the Qinling-Daba Mountains in 2017 is significantly different: excellent areas are scattered in the Shennongjia forest area, western Henan Mountains, Taibai Mountain, and western high-altitude areas, covering Shennongjia, Taibai Mountain, Baotianman, Funiu Mountain nature reserves, and Lianhuashan in Gansu. They have good natural vegetation growth and high ecological environment quality. The poor areas are mainly distributed in the middle and low altitude areas in the northwestern part of the west. The central Hanzhong area, and the areas along the eastern line, with relatively concentrated areas, are generally located in the fringe areas of cities, such as Hanzhong City, Danjiangkou City, Shiyang City, Nanyang City, and other important urban areas.

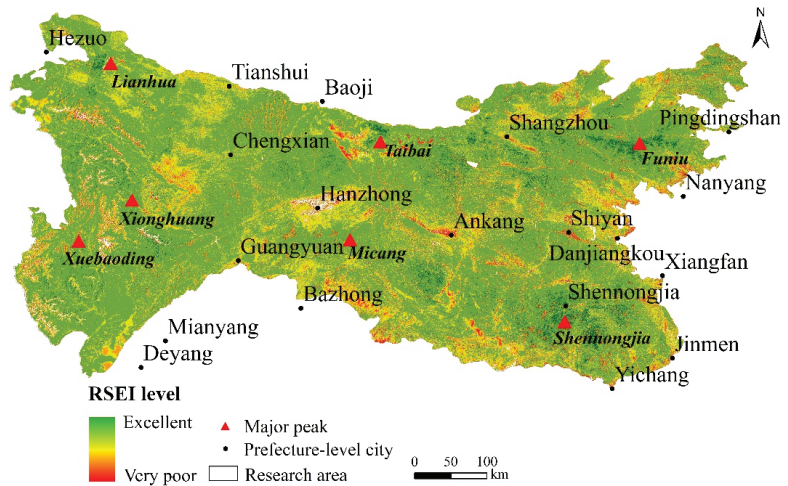


**Figure 4.** Spatial distribution of eco-environmental quality in Qinling-Daba Mountains by remote sensing.

Table 3 shows the area and proportion of each quality grade of the ecological environment in the study area (water area was not included). Among the various grades of the area ecological environment quality, good (0.6–0.8) and medium (0.4–0.6) are  $17.9 \times 10^4 \text{ km}^2$  (63.14%) and  $8.2 \times 10^4 \text{ km}^2$  (29.15%), respectively, occupying a large proportion. Poor (0.0–0.2), very poor (0.2–0.4), and excellent (0.8–1.0) are  $0.3 \times 10^4 \text{ km}^2$  (1.11%),  $1.3 \times 10^4 \text{ km}^2$  (4.54%), and  $0.58 \times 10^4 \text{ km}^2$  (2.06%), respectively, accounting for relatively less. The overall distribution characteristics are “small at both ends and big in the middle,” and the proportion of excellent-grade and poor-grade areas is relatively small. In contrast, the area of middle-grade areas is larger. According to the characteristics of the terrain, the ecological environment quality of the middle and high altitude (1000–4500 m) mountainous areas are mainly excellent-grade and middle-grade areas, and the low-altitude (<1000 m) areas are

mainly poor or very poor-level areas. The ecological environment quality level shows a decreasing trend from low to high altitude.

**Table 3.** Area and proportion of remote sensing eco-environmental quality.

RSEI Level	Area (km <sup>2</sup> )	Proportion (%)
Very poor (0~0.2)	3154.5	1.11
Poor (0.2~0.4)	12,851.15	4.54
Middle (0.4~0.6)	82,487.02	29.15
Good (0.6~0.8)	178,672.98	63.14
Excellent (0.8~1.0)	5832.89	2.06
Total	282,998.54	100.00

**3.3. The Spatial Differentiation Characteristics of RSEI<sub>0</sub> under Different Scale Effects**

It can be seen from Figure 5 that the Moran’s I shows a single-peak trend, first increasing sharply, before slowly decreasing, with the lowest value being 0.71; at the spatial scale of 1 × 1 km, 1.5 × 1.5 km, 2 × 2 km, 2.5 × 2.5 km, 3 × 3 km, 3.5 × 3.5 km, and 4 × 4 km, the values are 0.72, 0.75, 0.78, 0.76, 0.73, 0.72, and 0.71, respectively. The Z-score feature trend was similar to Moran’s I. All passed the significance test (Z-score > 1.96), indicating that RSEI<sub>0</sub> has a strong positive spatial correlation at various scales and the spatial heterogeneity is relatively large. Second, the mean and standard deviation of RSEI<sub>0</sub> under the seven scales did not change with the scale. The scale had a relatively small impact on the ecological and environmental benefits itself, thus avoiding the inequality of research objects at different spatial scales. The Moran’s I reach a maximum at 2 km of the grid, indicating that RSEI<sub>0</sub> has strong spatial aggregation and spatial heterogeneity at this scale. The spatial distribution characteristics of RSEI<sub>0</sub> are related to geographical locations so that RSEI<sub>0</sub> can study spatial structure characteristics and factor detection.

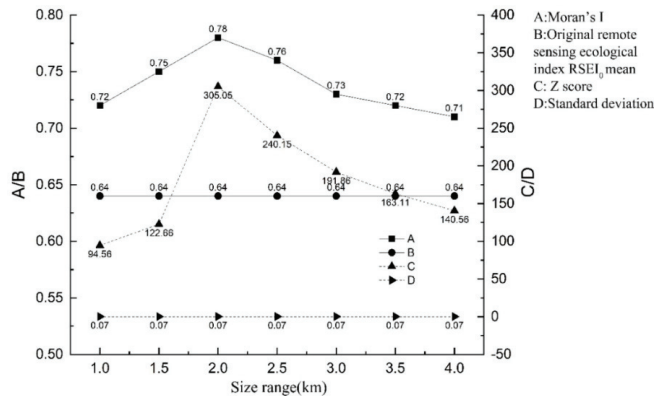


**Figure 5.** Spatial statistical characteristics of RSEI<sub>0</sub> in different scales of Qinling-Daba Mountains.

Table 4 shows that the optimal fitting theoretical model of RSEI<sub>0</sub> is the exponential model, the coefficient of determination (R-Square) is 0.80, the residual error (RSS) is  $2.3 \times 10^{-7}$ , and its nugget effect is 88%, indicating that a high degree of space heterogeneity is mainly affected by structural factors. Among them, the nugget value ( $C_0$ ) of RSEI<sub>0</sub> in the study area is relatively small ( $7.6 \times 10^{-4}$ ), indicating that factors affect the spatial distribution of ecological environment quality on a small sampling scale. At the same time, the nugget effect ( $C/C_0 + C$ ) exceeded 0.75, indicating that the spatial heterogeneity dominated by structural factors was relatively large, and the randomness was relatively small. Combined with the Geodetector analysis results, the detection factors of elevation, slope, and relief amplitude were 0.528, 0.561, and 0.653, respectively, all of which passed the two-tailed significance test, which has a greater impact than climate (0.256, 0.312, and

0.23) and socio-economic (0.002, 0.174, and 0.214) factors (from Section 3.4). Such findings are due to the vast mountainous area in the study area. Large topographical undulations account for more than 1/5 of the total area, and they are mostly distributed in man-made protected nature reserves and mountain hinterlands. Topographic factors have a significant impact on the quality of the ecological environment. On the best analysis scale, the spatial differentiation of ecological environment quality in different regions is equally large, but it is worth noting that this region is a concentrated area for poverty alleviation under many plains, where urbanization and economic development are relatively slow. Because of the impact of key local engineering constructions such as returning farmland to forests and water and soil conservation in the areas, the ecological environment of the middle and low altitude areas is better than other areas in China, but it is different from other research results such as plateau, arid, and agricultural and pastoral areas [53–56]. Differences and comparisons will be described in the discussion section.

**Table 4.** RSEI<sub>0</sub> Semi-variance function model and its results.

Model	C <sub>0</sub>	C <sub>0</sub> + C	C/C <sub>0</sub> + C	R-Square	RSS
Gaussian model	0.001	0.0063	83.9	0.74	$2.9 \times 10^{-7}$
Linear model	0.002	0.0071	71.0	0.34	$1.7 \times 10^{-7}$
Exponential model	0.00076	0.0064	88.0	0.80	$2.3 \times 10^{-7}$
Spherical model	0.00032	0.0060	94.9	0.74	$2.9 \times 10^{-7}$

### 3.4. Factors Influencing Spatial Heterogeneity of RSEI<sub>0</sub> in Qinling–Daba Mountains

In this study, the Pearson correlation analysis method was used to analyze the correlation between each variable. As shown in Table 5, the RSEI<sub>0</sub> in the study area positively correlates with the slope, relief amplitude, elevation, and curvature in the terrain factors, with correlation coefficients of 0.62, 0.56, 0.52, and 0.1, respectively. The slope has the largest contribution rate to the terrain factor, followed by relief amplitude and elevation, indicating that the greater the slope, the higher the elevation, and the greater the relief amplitude, the better the quality of the ecological environment. Conversely, the lower the elevation, the lower the quality of the ecological environment. Among climatic elements, RSEI<sub>0</sub> was negatively correlated with annual average temperature and annual precipitation, but positively correlated with relative humidity, consistent with the negative effect of heat on the quality of the ecological environment in the previous article (from Section 3.1). The annual precipitation correlation coefficient was 0.38, and that of the annual average relative humidity was 0.18. Although it is consistent with the PC<sub>1</sub> load value and the positive correlation with RSEI<sub>0</sub>, the precipitation and humidity index correlation are different. This difference is because the mask image was extracted from the water area, and the most important wetland areas were removed, so the correlation between humidity and RSEI<sub>0</sub> was weakened. Among the land use types, the correlation coefficients of the proportion of high-vegetation area, construction land, and agricultural land were 0.37, 0.33, and 0.09, respectively. Among them, only the proportion of high-vegetation areas had a high positive correlation with RSEI<sub>0</sub>. The ratio of construction land to agricultural land area is negatively correlated with the quality of the ecological environment, proving that the vegetation areas with higher altitudes mentioned above contribute to the quality of the ecological environment. At the same time, improving the ecological deterioration with high vegetation coverage has a positive effect on the quality of the ecological environment. The expansion of industrial agriculture in low-altitude areas has a restraining effect on the ecological environment of the study area. Among the socio-economic factors, the correlation coefficients between the population density and the average annual GDP are only 0.22 and 0.19, respectively. Both have a negative correlation with RSEI<sub>0</sub>, indicating that socio-economic development and human activities negatively affect the quality of the regional ecological environment. In summary, slope, elevation, relief amplitude, average annual precipitation, and high-vegetation land use types have a close spatial correlation with RSEI<sub>0</sub>, which affects the degree of spatial heterogeneity of the ecological environment quality.

**Table 5.** RSEI<sub>0</sub> and the correlation analysis result of each index factor.

Influencing Factor	Analytic Index	Correlation Coefficient	Correlation
Terrain factors	Elevation	0.52	+
	Slope	0.62	+
	Curvature	0.10	+
	Relief amplitude	0.56	+
Climatic factors	Average annual temperature	0.25	−
	Average annual precipitation	0.38	−
	Annual average relative humidity	0.18	+
Land use type	Proportion of high vegetation area	0.37	+
	Proportion of construction land area	0.33	−
	Proportion of agricultural land area	0.09	−
Socio-economic factors	Annual average GDP	0.19	−
	Population density	0.22	−

+: positive; −: negative.

The effect of the influencing factors mentioned above was analyzed by exploring the explanatory power of each influencing factor on the spatial variability of RSEI<sub>0</sub> in the Qinling-Daba Mountains based on geographic detectors. As shown in Table 6, slope, elevation, curvature, relief amplitude, annual average temperature, annual average precipitation, annual relative humidity, the proportion of high vegetation area, the proportion of construction land area, and population density affect the ecological environment quality of the study area. The impact of spatial differentiation is more significant, but its explanatory power is different. Among the terrain factors, the interpretation ability of topographic undulation was the highest, reaching 65.3%; the second was elevation and slope, which were 52.8% and 56.1%, respectively; the weakest interpretation ability was curvature, which was only 2.1%. Among the climatic factors, the interpretation ability of the spatial differentiation of annual average precipitation is higher (31.2%); the annual average temperature and relative humidity are second, only 25.6% and 23%, respectively. Among the land use types, high-vegetation areas accounted for a higher explanation ability (28.2%), followed by construction land (13.5%). Among the socio-economic indicators, the explanatory ability of population density was 21.4%. The spatial heterogeneity of the relief amplitude was relatively high, exceeding 60%. As shown in Figure 6, the average value of RSEI<sub>0</sub> in the area increases with the relief amplitude on flat land (<30 m), mesa (30–70 m), hills (70–200 m), and small relief mountains (200–500 m). However, the sharp increase began slowly after the medium-relief mountain area (500–1000 m). The change also quickly stabilized, indicating that the overall ecological quality can be quickly improved through adjustment and optimization measures in the medium and small relief mountain areas. The high relief mountain area needs to maintain the current good ecological environment by maintaining the water, soil, and vegetation. In summary, structural factors have a greater impact on the RSEI<sub>0</sub> of the Qinling-Daba Mountains. Among them, the spatial differentiation of relief amplitude has the highest interpretation ability. The influence of slope on RSEI<sub>0</sub> cannot be underestimated and is consistent with the results of the semi-variance function study. Such results show that the quality of the ecological environment in the study area is restricted by natural factors. The influence of social and economic factors is not enough to offset the changes in the regional mountain ecological environment. The relief amplitude and slope factors can be considered to improve the ecological environment quality of the entire region in the future.

Table 6. RSEI<sub>0</sub> detection results of various influencing factors.

Factor Types	Influencing Factor	Detection Index	(q Value)
Structural factors	Terrain factors	Elevation	0.528 **
		Slope	0.561 **
		Curvature	0.021 **
		Relief amplitude	0.653 **
	Climatic factors	Annual average temperature	0.256 **
		Annual average precipitation	0.312 **
Annual average relative humidity		0.230 **	
Randomness factors	Land use type	Proportion of high vegetation area	0.282 **
		Proportion of construction land area	0.135 **
		Proportion of agricultural land area	0.002
	Socio-economic factors	Annual average GDP	0.174
		Population density	0.214 **

\*\*  $p < 0.01$ .

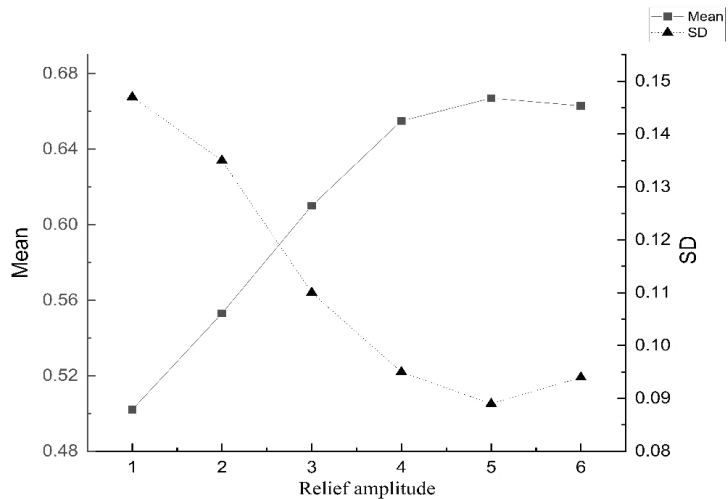


Figure 6. Distribution of mean value of RSEI<sub>0</sub> under different relief amplitudes.

#### 4. Discussion

##### 4.1. Verification of the Accuracy of the RSEI Comprehensive Method

This study uses RSEI's comprehensive analysis index to characterize the ecological environment quality of the Qinling-Daba Mountains and analyzes the spatial structure differentiation characteristics and its influencing factors. The advantage of using this method is that a comprehensive index can quantitatively analyze the objects referred to by the index through the linear transformation of the data itself. The transformation algorithm is not obtained by an artificially weighted calculation, which overcomes the subjectivity of artificial evaluation. Second, the whole area has the characteristics of "population gathering" and has different levels of human activities in the complex natural geographical environment [32]. The simple and superimposed ecological environment evaluation method cannot be visualized, and the weight of a single element is relatively large. The method proposed by the present study overcomes this drawback. The analysis results show that the average values of the humidity index, dryness index, and heat index are 0.07, 0.21, and 0.03, respectively, and are less than the comprehensive index RSEI. The greenness index with the highest contribution is 0.2, which is higher than that of RSEI. The correlation between the indexes is also very high. These values show that



this comprehensive index can better integrate the information of each index and is also more representative than any single index, and can adequately reflect the quality of the ecological environment in the area. The EQI also verified the overall spatial distribution trend [49], which is highly fit with RSEI. However, RSEI is better than the verification data in local details, indicating that this comprehensive indicator is suitable for detecting the Qinling-Daba Mountains' ecological environment (Figure 7).

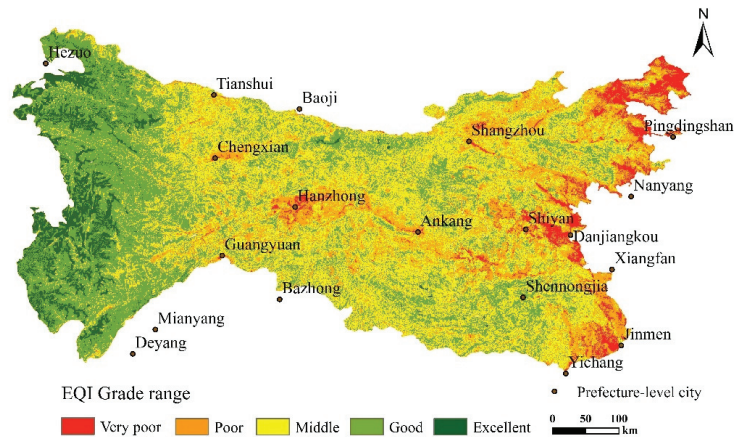


**Figure 7.** Spatial distribution of ecological environment quality index (EQI).

#### 4.2. The Rationality of the Selection of Indicators

In addition, the selection of indicators is scientific and reasonable, affecting the distribution of comprehensive indicators. The NDVI index selected for greenness in this study was due to the large differences in vertical relief in the Qinling-Daba Mountains areas, the longer plant growth seasons under different terrains, and the medium-level vegetation coverage that contributes to the ecological environment; therefore, the use of this index can reduce the detailed problem of special principal component analysis and is suitable for studying the mesoscale area [29,57]. The selection of humidity and heat indicators mainly consider the complexity of the areas' climate and the characteristics of the mountain elevation effect mechanism that led to a large difference in heat distribution between the mountain and the plain [58]. This selection is reflected by the differences in the internal and external environments of the mountains, resulting in huge differences in the distribution of humidity and heat, which indirectly affects the quality of the regional ecological environment through biological effects [59]. The selection of dryness includes unused natural wasteland and man-made construction land. Frequent human activities in low-altitude areas in the mountain area and the loss of natural wasteland in high-altitude areas strongly antagonistically affect ecological quality. This indicator takes natural and human factors into account and can be compared with the overall environmental quality, and comprehensively analyzes the spatial differences in ecological, environmental quality.

#### 4.3. Comparative Analysis and Suggestions on Influencing Factors

Structural factors have a more important impact on the ecological environment quality of the Qinling-Daba Mountains than random factors, especially the spatial interpretation of relief amplitude and slope, which can reflect the spatial differentiation of RSEI more than other factors. The change characteristics are mainly due to the diverse landform types of the area, and the complex geographic features make the spatial geographic differentiation huge [60]. Vegetation coverage is densely distributed in areas with large relief amplitudes and slopes due to fewer human activities; areas with lower undulations are subject to frequent human disturbances. The ecological environment is restricted by construction and agricultural land.

At the same time, we found that the explanatory power of the annual average precipitation was 31.2%. In comparison, the explanatory power of the agricultural land area was 0.2%, with a weak negative correlation, which is in accordance with similar studies [23,55]. In their results, the ecological environment of agricultural areas was relatively high, and the positive correlation was inconsistent. Such findings are due to intensive and unreasonable farming methods in the lowland plains of the area that hinder the development of the regional ecological environment. We also believe that there are various problems in the regional agricultural ecological environment, including soil pollution caused by chemicals such as pesticides, water pollution caused by breeding and domestic sewage, and backward energy utilization patterns that lead to energy waste and air pollution. In addition, the study time was selected as the spring and summer season, which is the farming season, when the vicinity of the original vegetation environment is affected by farming. These factors led to a weak negative correlation between the quality of the ecological environment and agricultural land.

On the other hand, the explanatory power of annual average temperature, annual average GDP, and population density are 25.6%, 17.4%, and 21.4%, respectively, and are negatively correlated with RSEI<sub>0</sub>, which is more consistent with the results of previous studies [52,61,62]. In view of this result, we all agree that the Qinling-Daba Mountains are one of the most sensitive areas to climate change. The climate varies greatly in some mountainous areas, and the temperature difference is more obvious. Abrupt climate change has a certain impact on the growth of vegetation in the transition zone, especially the increasing trend of extreme and high-temperature weather and the difference in water and heat evaporation caused by slope direction [63], combined with regional warming to reduce the quality of regional habitats to a certain extent. As far as socioeconomic indicators (annual average GDP, population density) are concerned, because the Qinling-Daba Mountains area is one area where the poor population is concentrated in China, various social and economic development indicators are relatively weak [64]. The lack of coordination between the natural ecological environment and economic development makes the ecological environment subject to less human disturbance. It maintains a virtuous cycle of the ecosystem in areas with relatively poor economic development [65–68].

At the same time, we also found that the low ecological, environmental quality areas are located near many cities; the expansion of local land scale, infiltration of human activities, unreasonable land planning, the pursuit of the formal economy, and other adverse social reactions have negatively affected the nearby ecological environment. The large areas are located in the transition zone from the northern subtropical to the warm temperate zone [31]. The ecological environment is relatively fragile and sensitive. Although the implementation of many environmental measures has effectively improved the resilience of the mountain ecological environment, the area is suffering in terms of special ecological environment construction. Therefore, we must coordinate the overall situation and pay more attention to the local, regional governance of mountain characteristics, water and soil, and man-made environments.

#### 4.4. Shortcomings and Prospects

The disadvantage of this study is that it does not fully explore the deeper index framework of the ecological environment. It only analyzes the quality of the ecological environment on the land surface system without considering the influence of water bodies and human ecological environment index factors. The time phase of remote sensing data does not reach a very high degree of closeness, and there is a certain error in the results of the analysis of RSEI. Moreover, climate change has an important impact on the quality of ecosystems and the ecological environment and should be considered in the future [69,70]. Limited by the number of data acquisitions, this study only studies the 2017 Qinling-Daba Mountains' RSEI and its influencing factors and has not carried out multi-dimensional studies on multiple years to reveal its temporal and spatial distribution characteristics. In the future, the quality of the ecological environment in different regions of the Qinling-Daba

Mountains will be studied on a long-term scale, including research on topography, extreme climate, atmospheric circulation, water body ecological environment, and human effects. The research is mainly based on high-precision spatial resolution remote sensing image data to explore the ecological status of different provinces and urban areas, and to reveal the impact mechanism of atmospheric changes and human activities on the quality of the ecological environment. Future work will continue to advance this research.

## 5. Conclusions

- (1) The overall RSEI average value of the Qinling-Daba Mountains reached 0.61, and the ecological environment quality was mostly above the middle level; the greenness contributed the most to the RSEI comprehensive index of the areas, indicating that vegetation coverage plays an important role in the improvement of the ecological environment quality of the areas. Heat has the second-highest contribution to the RSEI index of the area, and it has an inhibitory effect on improving the area's habitat quality.
- (2) The overall distribution of ecological environment quality in the study area in 2017 was quite different, with good and bad being distributed alternately from east to west; the ecological environment quality level decreased from low to high altitude. Low-value areas accounted for a relatively large area in low-altitude land, and high-value areas accounted for a relatively large area in high-altitude areas.
- (3) There are scale changes in the spatial clustering of  $RSEI_0$ . The degree of spatial heterogeneity is the most obvious at a scale of 2 km. The  $RSEI_0$  nugget effect is 88%, which is high spatial heterogeneity, mainly affected by structural factors such as slope, relief amplitude, elevation, curvature, annual average temperature, annual average precipitation, annual average relative humidity, the proportion of high-vegetation areas, proportion of construction land area, and average annual population density which have significant effects on the spatial differentiation of  $RSEI_0$ . Among them, slope and relief amplitude are the main factors affecting the spatial differentiation of the Qinling-Daba Mountains' ecological environment quality.

**Author Contributions:** H.Y.: Conceptualization, Writing—original draft. C.C.: Methodology, Writing—review. Q.D.: Data analysis. P.Z. and Q.C.: Software, Visualization. L.Z.: Validation, Supervision, Financial support. All authors have read and agreed to the published version of the manuscript.

**Funding:** The work presented in this paper was supported by the National Science and Technology Basic Resource Investigation Program of China (Grant No. 2017FY1009002), National Natural Science Foundation of China (Grant No. 41671090).

**Institutional Review Board Statement:** Not applicable.

**Informed Consent Statement:** Not applicable.

**Acknowledgments:** We thank the anonymous reviewers for their constructive comments on the earlier version of the manuscript and the staff of the editorial department for their hard work. We would like to thank our experts for English language editing.

**Conflicts of Interest:** The authors declare that they have no known competing financial interest or personal relationships that could have appeared to influence the work reported in this paper.

## References

1. Rastorgueff, P.A.; Bellan, S.D.; Bianchi, C.N. An ecosystem-based approach to evaluate the ecological quality of Mediterranean undersea caves. *Ecol. Ind.* **2015**, *54*, 137–152. [[CrossRef](#)]
2. Imhoff, M.L.; Zhang, P.; Wolfe, R.E.; Bounoua, L. Remote sensing of the urban heat island effect across biomes in the continental USA. *Remote Sens. Environ.* **2009**, *114*, 504–513. [[CrossRef](#)]
3. Zhao, Q.G.; Huang, G.Q.; Ma, Y.Q. Ecological environment and construction of ecological civilization in China. *Acta Ecol. Sin.* **2016**, *36*, 6328–6335. [[CrossRef](#)]
4. Colwell, R.K.; Brehm, G.; Cardelús, C.L.; Gilman, A.C.; Longino, J.T. Global warming, elevational range shifts, and lowland biotic attrition in the wet tropics. *Science* **2008**, *322*, 258–261. [[CrossRef](#)]

5. Li, T.T.; Ma, C.; Guo, Z.Z. RSEI model based long time series ecological quality assessment and analysis of influencing factors in Helan Mountains. *J. Ecol.* **2021**, *40*, 1154–1165. [[CrossRef](#)]
6. Wang, F.T.; Huang, C.S.; Chen, Z.H.; Bao, K. Distribution, ecological risk assessment, and bioavailability of cadmium in soil from Nansha, Pearl River Delta, China. *Int. J. Environ. Res. Public Health* **2019**, *16*, 3637. [[CrossRef](#)] [[PubMed](#)]
7. Wang, M.X.; Liao, G.K.; Li, Y.L. The relationship between environmental regulation, pollution and corporate environmental responsibility. *Int. J. Environ. Res. Public Health* **2021**, *18*, 8018. [[CrossRef](#)]
8. Zhu, L.Q.; Xu, L.M. Study on the impact of global change on terrestrial ecosystem. *Areal Res. Develop.* **2011**, *30*, 161–164. [[CrossRef](#)]
9. Wang, Y.H.; Li, J.Y. Evaluation of coupling and coordination between ecological environment quality and economic development level in contiguous destitute areas. *J. Appl. Ecol.* **2015**, *26*, 1519–1530. [[CrossRef](#)]
10. Wang, D.S.; Wang, X.L.; Lei, Z.Y. Ecological quality assessment of fuxin based on remote sensing ecological index. *Eco. Sci.* **2020**, *39*, 88–94. [[CrossRef](#)]
11. Xu, H.Q. Establishment and application of urban remote sensing ecological index. *Acta Ecol. Sin.* **2013**, *33*, 7853–7862. [[CrossRef](#)]
12. Sun, C.J.; Li, X.M.; Zhang, W.Q.; Chen, W.; Wang, J.R. Assessment of ecological security in poverty-stricken areas of Luliang Mountains based on remote sensing information. *Environ. Sci.* **2019**, *39*, 5352–5360. [[CrossRef](#)]
13. Ivits, E.; Cherlet, M.; Mehl, W.; Sommer, S. Estimating the ecological status and change of riparian zones in Andalusia assessed by multi-temporal AVHRR datasets. *Eco. Ind.* **2008**, *9*, 422–431. [[CrossRef](#)]
14. Jiang, C.L.; Wu, L.; Liu, D.; Wang, S.M. Remote sensing dynamic monitoring of eco-environmental quality in arid desert areas: A case study of Gurbantungut Desert. *J. Appl. Ecol.* **2019**, *30*, 877–883. [[CrossRef](#)]
15. Wen, L.T. Discussion on remote sensing monitoring of agrometeorological disasters. *Remote Sens.* **2020**, *9*, 38–41. [[CrossRef](#)]
16. Song, W.; Song, W.; Gu, H.H.; Li, F.P. Progress in the remote sensing monitoring of the ecological environment in mining areas. *Int. J. Environ. Res. Public Health* **2020**, *17*, 1846. [[CrossRef](#)]
17. Ministry of Environmental Protection of the People's Republic of China. *Technical Code for Assessment of Ecological and Environmental Conditions (In Operation)*; China Environmental Science Publishing House: Beijing, China, 2006.
18. Ye, Y.H.; Liang, Y.X.; Shen, Y.Q.; Xie, L.S. Some problems to be discussed in technical standard for assessment of ecological and environmental conditions (trial implementation). *Trop. Geo.* **2009**, *29*, 404–406. [[CrossRef](#)]
19. Liu, H.; Che, G.H.; Gao, C.J.; Zhao, Y.J. Change of ecological environment quality and its influencing factors in Hebei Province. *Eco. Sci.* **2016**, *35*, 89–97. [[CrossRef](#)]
20. Wang, H.J.; Bi, F.F.; Dong, Z.F. Performance evaluation of ecological compensation policy in Xin Anjiang River Basin based on AHP-fuzzy comprehensive evaluation method. *Acta Ecologica Sinica* **2020**, *40*, 7493–7506. [[CrossRef](#)]
21. Xu, H.Q. Remote sensing evaluation index of regional ecological environment change. *Environ. Sci.* **2013**, *33*, 889–897. [[CrossRef](#)]
22. Liao, W.H.; Jiang, W.G. Evaluation of the spatiotemporal variations in the eco-environmental quality in China based on the remote sensing ecological index. *Remote Sens.* **2020**, *12*, 2462. [[CrossRef](#)]
23. Wang, Y.; Zhao, Y.H.; Wu, J.S. Long-time dynamic monitoring of urban agglomeration ecological quality based on Google Earth Engine Cloud Computing: A case study of Guangdong-HongKong-MacaoGreaterBayArea. *Acta Ecol. Sin.* **2020**, *40*, 1–13. [[CrossRef](#)]
24. Zhou, L.M.; Wang, S.H. Remote sensing monitoring and assessment of spatial-temporal change of ecological environment in Hang Jin Banner, Inner Mongolia. *J. Appl. Ecol.* **2020**, *31*, 1999–2006. [[CrossRef](#)]
25. Zhu, D.; Chen, T.; Zhen, N.; Niu, R.Q. Monitoring the effects of open-pit mining on the eco-environment using a moving window-based remote sensing ecological index. *Environ. Sci. Pollut. Res. Int.* **2020**, *27*, 15716–15728. [[CrossRef](#)]
26. Liu, K.; Ma, N.X.; Xu, Y.L.; Sun, G.N. Protection and construction of ecological environment in Qinling Mountains. *Chin. J. Ecol.* **2004**, *23*, 157–160. [[CrossRef](#)]
27. Liu, Y.S.; Ni, S.X.; Jiang, J.J. Comprehensive evaluation of ecological environment quality in southern Shaanxi Mountain. *Mt. Res.* **1997**, *3*, 178–182.
28. Lang, G.D.; Guo, J.L. Study on the ecological environment quality of Taibai Mountain scenic area. *J. Northwest Univ.* **2001**, *5*, 431–433. [[CrossRef](#)]
29. Zhang, Y.Q.; Jiang, F.; Ji, M.D.; Jiang, H.S.; Wang, Z.Y. Evaluation of ecological environment at district and county level based on remote sensing index. *Arid. Zone Stud.* **2020**, *37*, 1598–1605. [[CrossRef](#)]
30. Zhao, F.; Zhang, B.; Zhu, L.; Yao, Y.; Cui, Y.; Liu, J. Spatial differentiation of vertical band spectral structure in Qinling-Daba Mountains and the problem of warm temperate zone-Subtropical boundary. *Acta Geogr. Sin.* **2019**, *74*, 889–901. [[CrossRef](#)]
31. Zhao, F.; Zhang, J.; Liu, S.; Wang, Z.; Wang, L.; Gu, H.; Li, W. NPP and its response to climate change in Qinling-Daba Mountains: A multi-dimensional zonal and warm temperate-subtropical boundary problem. *Acta Ecol. Sin.* **2021**, *41*, 1–12. [[CrossRef](#)]
32. Li, Y.H. *Research on Multi-Dimensional Changes of Soil Erosion in Qinling-Daba Mountains*; Henan University: Kaifeng, China, 2020. [[CrossRef](#)]
33. Liu, J.J.; Pan, Z.W.; Qin, F.; Gu, J.Y.; Zhu, M.Y.; Zhao, F. Land temperature estimation and mass elevation effect analysis of Qinling-Daba Mountains based on MODIS data. *Geo. Res.* **2020**, *39*, 735–748. [[CrossRef](#)]
34. Zhao, Y.L.; Zhang, L.J. Study on quantitative assessment method of fragile ecological environment. *Prog. Geogr.* **1998**, *18*, 3–5. [[CrossRef](#)]

35. Goward, S.N.; Xue, Y.K.; Czajkowski, K.P. Evaluating land surface moisture conditions from the remotely sensed temperature /vegetation index measurements: An exploration with the simplified simple biosphere model. *Remote Sens. Environ.* **2002**, *79*, 225–242. [\[CrossRef\]](#)
36. Todd, S.W.; Hoffer, R.M. Responses of spectral indices to variations in vegetation cover and soil background. *Photogramm. Eng. Remote Sens.* **1998**, *64*, 915–921.
37. Li, B.L.; Jing, C.P.; Yan, X.Y. Derivation of tassell-cap transformation of Landsat 8 land imager image. *Sci. Surv. Mapp.* **2016**, *41*, 102–107. [\[CrossRef\]](#)
38. Ashutosh, S.; Roy, P.S. Three decades of nationwide forest cover mapping using indian remote sensing satellite data: A success story of monitoring forests for conservation in india. *J. Indian Soc. Remote. Sens.* **2021**, *49*, 61–70. [\[CrossRef\]](#)
39. Xu, H.Q. A new index for delineating built-up land features in satellite imagery. *Int. J. Remote Sens.* **2008**, *29*, 4269–4276. [\[CrossRef\]](#)
40. Nichol, J. Remote sensing of urban heat islands by day and night. *Photogramm. Eng. Remote Sens.* **2005**, *71*, 613–622. [\[CrossRef\]](#)
41. Ding, F.; Xu, H.Q. Land surface temperature inversion algorithm and experimental analysis of TM thermal band image. *J. Geo-informa. Sci.* **2006**, *8*, 125–130, 135. [\[CrossRef\]](#)
42. Chander, G.; Markham, B.L.; Helder, D.L. Summary of current radiometric calibration coefficients for Landsat MSS, TM, ETM+ and EO-1 ALI sensors. *Remote Sens. Environ.* **2009**, *113*, 893–903. [\[CrossRef\]](#)
43. Williams, D. *Landsat 7 Science Data Users Handbook*; U.S. Geological Survey: Sacramento, CA, USA, 1998. [\[CrossRef\]](#)
44. Jimenez-Munoz, J.C.; Cristobal, J.; Sobrino, J.A.; Soria, G.; Ninyerola, M.; Pons, X. Revision of the single-channel algorithm for land surface temperature retrieval from Landsat Thermal-Infrared data. *IEEE Trans. Geofence Remote Sens.* **2009**, *47*, 339–349. [\[CrossRef\]](#)
45. Qi, Y.C.; Dong, Y.S.; Jin, Z.; Peng, Q.; Xiao, S.S.; Ya-ting, H.E. Spatial heterogeneity of soil nutrients and respiration in the decertified grasslands of inner mongolia, China. *Pedosphere* **2010**, *20*, 655–665. [\[CrossRef\]](#)
46. Wang, M.; Wang, J.; Meng, Z.; Cai, X.; Lv, S.; Wang, D.; Wu, Y. Heterogeneity of spatial distribution of Haloxylon ammo dendron population in the eastern margin of Badain Jaran Desert. *Acta Ecol. Sin.* **2016**, *36*, 4055–4063. [\[CrossRef\]](#)
47. Yan, L.; Zhou, G.; Zhang, F.; Sui, X.; Ping, X. Spatial heterogeneity dynamic analysis of vegetation coverage in desert steppe of Inner Mongolia. *Acta Ecol. Sin.* **2012**, *32*, 4017–4024. [\[CrossRef\]](#)
48. Wang, J.F.; Xu, C.D. GEO-DETECTOR: Principles and prospects. *Acta Geogr. Sin.* **2017**, *72*, 116–134. [\[CrossRef\]](#)
49. Fan, C.; Xia, B.C.; Qin, J.Q. A comprehensive evaluation model of county eco-environmental quality based on RS and GIS: Taking Huidong County as an example. *Chin. J. Ecol.* **2013**, *32*, 719–725. [\[CrossRef\]](#)
50. Liu, P.; Ren, C.Y.; Wang, Z.M.; Zhang, B.; Chen, L. Assessment of the eco-environmental quality in the Nanweng River nature reserve, Northeast China by remote sensing. *J. Appl. Ecol.* **2018**, *29*, 3347–3356. [\[CrossRef\]](#)
51. Wang, L.C.; Jiao, L.; Lai, F.B.; Zhang, N.M. Ecological change assessment of Manas Lake Wetland in Xinjiang based on remote sensing ecological index. *Acta Ecol. Sin.* **2019**, *39*, 2963–2972.
52. Wang, Y.; Wang, S.D. Analysis of dynamic change of ecological quality based on RSEI: A case study of Danjiang River (Henan Section). *Sci. Soil Water Conserv.* **2019**, *17*, 57–65. [\[CrossRef\]](#)
53. Gao, W.P.; Alimjiang, k.; Tursunayi, R.; Zhao, M. Spatio-temporal analysis of ecological and environmental benefits in Yizhou District. *Arid. Zone Res.* **2020**, *37*, 1057–1067. [\[CrossRef\]](#)
54. Li, F.L.; Chang, Q.R.; Shen, J.; Liu, J. Dynamic monitoring of ecological environment in some random place somewhere region by remote sensing: A case study of Fuxian County, Shaanxi Province. *J. Appl. Ecol.* **2015**, *26*, 3811–3817. [\[CrossRef\]](#)
55. Liu, T.; Bao, G.D.; Zhai, C.; Yang, J.; Zhang, D.W.; Lv, M.Y. Change of eco-environmental quality and its driving forces in ecologically fragile areas. *Jilin For. Sci. Technol.* **2020**, *49*, 18–25. [\[CrossRef\]](#)
56. Wang, J.; Liu, D.; Ma, J.; Cheng, Y.; Wang, L. Development of a large-scale remote sensing ecological index in arid areas and its application in the Aral Sea Basin. *J. Arid Land.* **2021**, *13*, 40–55. [\[CrossRef\]](#)
57. Li, F.M.; Yin, S.Y.; Yin, T.Y. Study on the spatial-temporal variation of extreme temperature in Qinling-Daba mountains and its adjacent regions from 1960 to 2017. *Proc. Natl. Sun Yat-Sen Univ.* **2020**, *272*, 86–98. [\[CrossRef\]](#)
58. Zhang, B.P.; Yao, Y.H. *Mass Elevation Effect Study*; China Environmental Science Publishing House: Beijing, China, 2015; pp. 45–93.
59. Cong, N.; Shen, M.; Yang, W.; Yang, Z.; Zhang, G.; Piao, S. Varying responses of vegetation activity to climate changes on the Tibetan Plateau grassland. *Int. J. Biometeorol.* **2017**, *61*, 1433–1444. [\[CrossRef\]](#) [\[PubMed\]](#)
60. Zhang, B.P. Ten scientific problems in the study of the north-south transition zone in China. *Progr. Geogr.* **2019**, *38*, 305–311. [\[CrossRef\]](#)
61. Yang, J.; Wu, T.; Pan, X.; Du, H.; Li, J.; Men, M.; Chen, Y. Ecological quality assessment of Xiongan New Area based on remote sensing ecological index. *J. Appl. Ecol.* **2019**, *30*, 277–284. [\[CrossRef\]](#)
62. Zhu, Q.; Guo, J.; Guo, X.; Xu, Z.; Ding, H.; Han, Y. Spatial differentiation of eco-environmental quality and its influencing factors in Poyang Lake region. *J. Appl. Ecol.* **2019**, *30*, 4108–4116. [\[CrossRef\]](#)
63. Li, J.; Feng, X.; Yin, J.; Chen, F. Change analysis of spring vegetation green-up date in Qinba Mountains under the support of spatiotemporal data cube. *J. Sens.* **2020**, *3*, 1–12. [\[CrossRef\]](#)
64. Jia, L.; Liu, Y.; Liu, J.; Li, J. Analysis on the causes of poverty in China's contiguous extreme poverty-stricken areas and its helping needs. *Hum. Geogr.* **2018**, *33*, 85–93. [\[CrossRef\]](#)
65. Ren, Q.R. Coupling analysis of coordinated development of eco-environment and socio-economic system in Gansu Province. *J. Ecol.* **2021**, *41*, 2944–2953. [\[CrossRef\]](#)

66. Zhu, W.; Zhang, J.; Cui, Y.; Zhu, L. Ecosystem carbon storage under different scenarios of land use change in Qihe catchment, China. *J. Geogr. Sci.* **2020**, *30*, 1507–1522. [[CrossRef](#)]
67. Zhang, J.; Zhu, W.; Zhu, L.; Cui, Y.; He, S.; Ren, H. Topographical relief characteristics and its impact on population and economy: A case study of the mountainous area in western Henan, China. *J. Geo. Sci.* **2019**, *29*, 598–612. [[CrossRef](#)]
68. Yin, H.; Zhang, P.; Dong, Q.; Chen, Q.; Zhu, L. Evaluation on climate comfortable degree for ecotourism along altitude gradient in Qinling-Daba Mountains areas, China. *J. Mt. Sci.* **2021**, *39*, 710–721. [[CrossRef](#)]
69. Schmidt, D.N. Determining climate change impacts on ecosystems: The role of palaeontology. *Palaeontology* **2018**, *61*, 1–12. [[CrossRef](#)]
70. Wang, L.; Chen, S.; Zhu, W.; Ren, H.; Zhang, L.; Zhu, L. Spatiotemporal variations of extreme precipitation and its potential driving factors in China's North-South Transition Zone during 1960–2017. *Atmos. Res.* **2021**, *252*, 105429. [[CrossRef](#)]





Article

# Analyzing the Freight Characteristics and Carbon Emission of Construction Waste Hauling Trucks: Big Data Analytics of Hong Kong

Xiaoxuan Wei <sup>1,2,\*</sup>, Meng Ye <sup>3</sup>, Liang Yuan <sup>2</sup>, Wei Bi <sup>2</sup> and Weisheng Lu <sup>2</sup>

- <sup>1</sup> School of Management Science and Real Estate, International Research Center for Sustainable Built Environment, Chongqing University, Chongqing 400045, China
- <sup>2</sup> Department of Real Estate and Construction, The University of Hong Kong, Pokfulam Rd, Hong Kong, China; u3007096@connect.hku.hk (L.Y.); biwei.226@gmail.com (W.B.); wilsonlu@hku.hk (W.L.)
- <sup>3</sup> School of Economics and Management, Southwest Jiaotong University, Chengdu 610000, China; mengye@swjtu.edu.cn
- \* Correspondence: weixx@cqu.edu.cn

**Abstract:** Unlike their counterparts that are used for container or municipal solid waste hauling, or their peers of taxis and other commercial vehicles, construction waste hauling trucks (CWHTs) are heterogeneous in that they transport construction waste from construction sites to designated disposal facilities. Depending on the intensity of the construction activities, there are many CWHTs in operation, imposing massive impacts on a region's transportation system and natural environment. However, such impacts have rarely been documented. This paper has analyzed CWHTs' freight characteristics and their carbon emission by harnessing a big dataset of 112,942 construction waste transport trips in Hong Kong in May 2015. It has been observed that CWHTs generate 4544 daily trips with 307.64 tons CO<sub>2</sub>-eq emitted on working days, and 553 daily trips emitting 28.78 tons CO<sub>2</sub>-eq on non-working days. Freight carbon emission has been found to be related to the vehicle type, transporting weight, and trip length, while the trip length is the most influential metric to carbon emission. This research contributes to the understanding of freight characteristics by exploiting a valuable big dataset and providing important benchmarking metrics for monitoring the effectiveness of policy interventions related to construction waste transportation planning and carbon emission.

**Citation:** Wei, X.; Ye, M.; Yuan, L.; Bi, W.; Lu, W. Analyzing the Freight Characteristics and Carbon Emission of Construction Waste Hauling Trucks: Big Data Analytics of Hong Kong. *Int. J. Environ. Res. Public Health* **2022**, *19*, 2318. <https://doi.org/10.3390/ijerph19042318>

Academic Editors: Roberto Alonso González Lezcano, Francesco Nocera and Rosa Giuseppina Caponetto

Received: 13 January 2022  
Accepted: 14 February 2022  
Published: 17 February 2022

**Publisher's Note:** MDPI stays neutral with regard to jurisdictional claims in published maps and institutional affiliations.



**Copyright:** © 2022 by the authors. Licensee MDPI, Basel, Switzerland. This article is an open access article distributed under the terms and conditions of the Creative Commons Attribution (CC BY) license (<https://creativecommons.org/licenses/by/4.0/>).

**Keywords:** freight characteristics; construction waste hauling trucks; carbon emission; big data

## 1. Introduction

By transporting goods, freights play a crucial role in a nation's economy. This is particularly true with the increase in e-commerce, logistics, and supply chains around the globe. As a heterogeneous group for the logistics, construction waste has been one of the heaviest and most voluminous waste streams produced globally under the fast-economic development and intensive urban renewal [1–3]. In 2018, 600 million tons of construction waste were generated in the US, which is more than twice the amount of generated municipal solid waste [4]. In 2016, 66.2 million tons of non-hazardous construction waste were generated in the UK [5]. In 2019, the generation of construction waste in Hong Kong doubled since 2008, hitting nearly 18 million tons per annum [6]. Owing to its non-combustible nature, construction waste normally ends up in disposal facilities, such as public fills or landfills [7,8]. A large number of construction waste hauling trucks (CWHTs) have been mobilized to transport such construction waste to various disposal facilities [9].

CWHTs thus play a pivotal role in the entire construction waste management system [10]. However, little is known about how they perform. In general, the freight performance is regarded as the metrics that are associated with freight characteristics of the trucks, which can be investigated by several dimensions, such as transporting weight, vehicle type,



trip length, trip time, and so forth, which can be exploited in order to better understand the current problems in transporting construction waste and support decision making. For example, the transporting weight for each trip is helpful in order to schedule trucks with suitable permitted gross vehicle weight. In reality, infrastructure systems are underutilized for most of the day, while overwhelmed during the peak hours [11]. A good knowledge of trip time can help planners to better cater for construction projects through improved design and use of facilities and infrastructure, and to arrange the transporting time. It is therefore essential to measure the CWHTs properly in order to provide a reference for the responsible parties (e.g., a shipment company, urban planners) to improve the efficiency of freight transportation. Without an understanding of the freight performance of CWHTs, the construction project may be delayed and cause economic loss.

In addition to the performance, freight transportation also causes significant negative environmental and social externalities for cities [12]. The transport sector has contributed to around 14% of total greenhouse gas emissions on average over the last ten years or so, with three-quarters from road transport [13]. Among the road transport emissions, 29.4% comes from freight movements [14]. As the backbone of urban road freight, CWHTs thus need to be closely scrutinized in terms of carbon emissions. It is commonly appreciated that freight carbon emission is related to freight performance. For example, trip length and transporting weight are important factors that influence the energy consumption for waste transportation, which can largely determine carbon emission in road transportation [15]. Moreover, similar to most hauling trucks, CWHTs are bulky and can easily cause road congestion, which is associated with frequent gear changing, resulting in increased carbon emission [16]. Investigating the relationship between CWHTs' freight performance and carbon emission can help to formulate appropriate emission reduction policies.

This paper probes into construction waste hauling trucks (CWHTs) as a heterogeneous freight group and analyzes their characteristics and carbon emission, intending to provide a departure point for planning, optimization, and implementation of freight transportation and carbon emission reduction policies. It does so by focusing on Hong Kong as a highly built-up city and exploiting a big dataset therein. The remainder of the paper is organized as follows. Section 2 provides a critical literature review on freight performance metrics and freight carbon emission. Section 3 introduces the construction waste disposals in Hong Kong. Section 4 describes the data and methods. Section 5 elaborates the analyses and findings of the freight performance and carbon emission of CWHTs. The discussion is presented in Section 6, followed by Section 7, which draws the conclusion and policy implication.

## 2. Literature Review

### 2.1. Freight Performance Metrics

Freight performance metrics are regarded as analytical and interpretive tools to assist policy-makers in tackling problems associated with freight transportation and developing optimal freight strategies [17]. Although the metrics that are used are hardly consistent, they can be divided into the following two categories: vehicle-related and trip-related [18]. While the former describes the characteristics of the trucks, the latter depicts the variables that are affiliated with a trip. Khan and Machemehl (2017) reveal that these two categories of metrics can help us to understand efficient tour chain strategies [19]. Table 1 summarizes the two categories of freight performance metrics identified in the literature.

**Table 1.** List of freight performance metrics.

Categories	Performance Metrics	Description	References
Vehicle-related	Vehicle type	Vehicles are normally classified into different types based on their load capacity as follows: light vehicles, medium vehicles, and heavy vehicles.	Combes and Leurent, 2013 [18], D'Este, 2007 [20], Khan and Machemehl, 2017 [19]
	Commodity type	The key commodities include building and construction materials, consumer goods, industrial inputs, and waste.	Beliën et al., 2014 [17], Combes and Leurent, 2013 [18], Errampalli et al., 2020 [21], Ruan et al., 2012 [22]
	Weight capacity	The weight of commodity carried for a trip.	Combes and Leurent, 2013 [18], D'Este, 2007 [20], Errampalli et al., 2020 [21]
	Permitted gross vehicle weight	The maximum permitted loading weight.	D'Este, 2007 [20], Lu, 2019 [23]
	Ownership of the vehicles	Ownership of the vehicles can be divided into private companies, government, and individuals.	Errampalli et al., 2020 [21]
Trip-related	Trip origin	Location of the trip origin.	Combes and Leurent, 2013 [18], Nuzzolo et al., 2020 [24]
	Trip destination	Location of the trip destination.	Akter, 2019 [25], Combes and Leurent, 2013 [18]
	Departure time	The time starting from the origin.	Akter, 2019 [25], Nuzzolo et al., 2020 [24], Ruan et al., 2012 [22]
	Arrival time	The time reaching the destination.	Akter, 2019 [25], Ruan et al., 2012 [22]
	Trip length	Distance traveled by the truck from the origin of the trip to the destination.	Combes and Leurent, 2013 [18], Khan and Machemehl, 2017 [19], Nuzzolo et al., 2020 [24]
	Trip time	Time taken to travel from the origin of the trip to the destination.	Akter, 2019 [25], FHWA, 2017 [26], Khan and Machemehl, 2017 [19], Nuzzolo et al., 2020 [24], Schrank et al., 2012 [27]
	Trip speed	The average speed of the trip between the origin and the destination.	FHWA, 2017 [26], Khan and Machemehl, 2017 [19]
	Number of stops	The number of stops for a trip.	Akter, 2019 [25], D'Este, 2007 [20], Nuzzolo et al., 2020 [24], Ruan et al., 2012 [22]
	Routing type	Variable, regular, fixed.	D'Este, 2007 [20]

Fourteen freight performance metrics are revealed in the literature with five vehicle-related metrics and nine trip-related metrics, which can describe the different freight activities. For example, Ehmke et al. (2012) examined the logistic trip duration to choose more reliable and efficient delivery tours [28]. Sulemana et al. (2019) examined the influencing factors of routing optimization for municipal solid waste collection with the respect to travel distance, travel time, and fuel consumption [29]. Comi et al. (2021) retrieved origin–destination (O–D) flows for light goods freight vehicles by delivery tour analysis [30]. Although the freight performance in terms of CWHTs is rarely explored, the literature can suggest the categories of freight performance metrics for this research (shown in Figure 1).

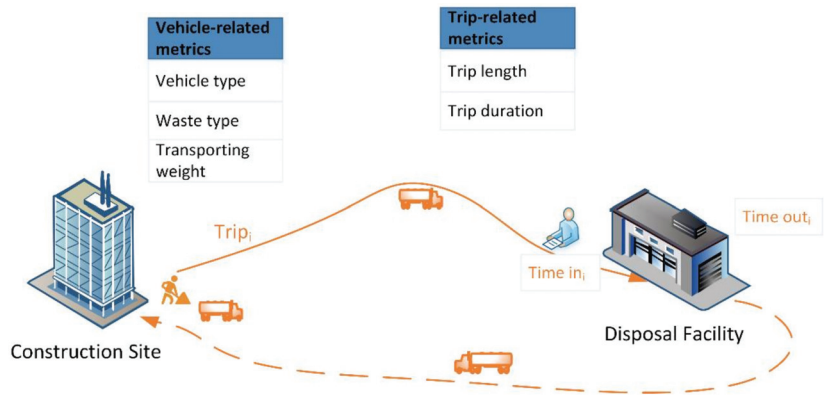


**Figure 1.** Freight performance metrics for construction waste hauling trucks.

While the vehicle-related category includes vehicle type, waste type, and transporting weight, the trip-related category consists of trip length and trip duration. Vehicle type describes the CWHTs' physical properties, including fuel type, permitted gross vehicle weight, unit energy consumption and so on. Waste type is the type of construction waste that is transported by CWHTs, which can be divided into inert waste (e.g., bricks, concrete, etc.) and non-inert waste (e.g., vegetation, timber, etc.) [31]. Transporting weight is the net weight of the construction waste transported by CWHTs. The trip length and trip duration are distance traveled and time consumed by the CWHTs from the construction site to the disposal facility, respectively.

## 2.2. Freight Carbon Emission

Many studies have focused on freight carbon emission. By estimating freight carbon emission of logistics sectors in Hong Kong, To (2015) found that land transport is more environmentally friendly than sea and air transport [32]. Lee (2011) found that 12% of the supply chain carbon emission comes from the stage of goods distribution [33]. Tian et al. (2014) examined different regions' freight carbon emission by various transport modes in China and found that highway freight plays a prominent role in the total carbon emission trajectory [34]. Some research proposes attention to alternative fuels with regards to their potential to reduce freight carbon emission, such as liquefied natural gas [35], or even all-electric trucks [36]. The freight carbon emission, however, is highly associated with a good freight transportation arrangement by considering the carbon emission efficiency [37], which requires an investigation of the freight performance metrics. For example, the choices of vehicle types are explored by Sim (2017), who found that the optimal weight of trucks will promote carbon emission reduction [38].

The following two kinds of methods have been applied for calculating freight carbon emission: "top-down" and "bottom-up" methods [39]. The "top-down" method apportions carbon emission to different sectors [40]. Ma et al. (2019), for example, adopted this method in order to decompose transportation carbon emission in different regions in China from 2007 to 2016, reporting that there are significant variations in the carbon emission of the eastern, central, and western regions of China [41]. Gilman et al. (2013) reported that carbon emission calculated by the "top-down" method is likely to be underestimated [42]. The "bottom-up" method, on the other hand, estimates carbon emission from fuel consumption, together with regional carbon emission factors. Hao et al. (2015) reflected that the major merit of this "bottom-up" method is its low data requirement to populate the model [43]. By using this method, Sun et al. (2017) calculated and obtained the carbon emission of urban traffic in Shanghai in 2014, using the number of vehicles, mileage, energy consumption structure, and carbon emission factors for different energy sources [44]. Lv et al. (2019)

found that the total amount of freight carbon emission in China increased from 3.73 Mt in 1988 to 96.41 Mt in 2016 [45].

### 2.3. Freight Data

The freight performance is usually measured by manually collected data and the private sector database. The most popular methods of collecting data manually include questionnaires [35], roadside surveys [18,46], and enumerations [21]. The private sector database also contributes to the measurement of freight performance, such as the data source from the university [47] and second-by-second GPS data gathered by a private company [48]. While manual data collection needs abundant manpower and material resources [49], the private sector data are inaccessible to the public. The public high-quality database is thus desired for measuring freight performance.

The public database can be exploited due to the rapid development of the Internet, Internet of Things (IoTs), cloud computing, wireless sensor, and other technologies, within which the truck Global Positioning System (GPS) data are widely employed. The integration of GPS with the emission monitoring sensor system can measure real-time emission concentration of vehicles [50]. For example, Akter (2019) explores the freight characteristics with the truck GPS data [25], and the data can also be converted into a freight database in order to investigate the freight characteristics of hauling trucks [51]. However, there are several challenges associated with the application of GPS data. Only a handful of vehicles in the traffic network may be equipped to record data via GPS and the quality of GPS data may be interfered with by various factors, such as tall buildings, tunnels, highway overpasses, etc. Moreover, GPS data fail to provide detailed information on individual trucks, such as commodity type, weight carried, and the type of truck [47].

By overcoming the drawbacks of GPS data, administrative record data provide another public database for the freight performance measurement. For example, Yang et al. (2021) exploited a high-quality dataset provided by the Southern California Association of Governments in the U.S. in order to determine transportation volume [52]. Nevertheless, the availability of high-quality and detailed data regarding construction waste freight movements is typically poor, which limits the research on the freight performance of CWHTs [53]. Inspired by the success of administrative record data in measuring freight performance, this paper aims to probe into the freight performance and carbon emission of CWHTs based on “waste transaction” big data in Hong Kong.

## 3. Construction Waste Disposals in Hong Kong

This research is conducted in the context of Hong Kong, where a huge quantity of construction waste is generated and transported from construction sites to disposal facilities, and most importantly, these data are recorded by the government, presenting a large set of high-quality structured data for measuring the freight performance of CWHTs. In order to effectively manage construction waste, the Hong Kong government has enacted the Construction Waste Disposal Charging Scheme since 2006. It mandates that all construction waste must be transported to government waste reception facilities (i.e., public fills, sorting facilities, and landfills) [54]. The Hong Kong Environment Protection Department (HKEPD) records each of the trucks delivering construction waste to the waste reception facilities. HKEPD (2020) reports that approximately 17.62 million tons of construction waste are generated, with 1.44 million tons disposed into landfills and 16.18 million tons received at public fills [6].

Table 2 summarizes construction waste disposal facilities and the types of accepted construction waste in Hong Kong. Consequently, different types of construction waste are expected to be transported to the designed disposal facilities. For example, inert materials, comprising mainly sand, bricks, and concrete, should be transported to public fills [55]. Based on the disposal facilities, the freight trips of CWHTs in Hong Kong can be categorized into the following three types: trips to public fills (TPF), trips to sorting facilities (TSF), and trips to landfill facilities (TLF).

**Table 2.** Government construction waste disposal facilities.

Facility Type	Existing Facilities	Abbreviation	Type of Accepted Construction Waste
Public fills	Chai Wan Public Fill Barging Point	CW-PFBP	Entirely inert construction waste
	Mui Wo Temporary Public Fill Reception Facility	MW-PFRF	
	Fill Bank at Tseung Kwan O Area 137	TKO137FB	
	Fill Bank at Tuen Mun Area 38	TM38-FB	
Sorting facilities	Sorting Facilities at Tseung Kwan O Area 137	TKO137SF	More than 50%, by weight, of inert construction waste
	Sorting Facilities at Tuen Mun Area 38	TM38-SF	
Landfill facilities	Northeast New Territories Landfill	NENT	Not more than 50%, by weight, of inert construction waste
	Southeast New Territories Landfill	SENT	
	West New Territories Landfill	WENT	

Source: “Hong Kong Green Organisation Certification Guidebook” for carbon reduction certificate. 2021. <https://www.hkgoc.gov.hk/en-hk/carbon-reduction-certificate.html>. Accessed on 13 February 2022.

Construction waste hauling trucks (CWHTs) for transporting construction waste must be registered at the HKEPD, with their plate numbers and permitted gross vehicle weight (PGVW) recorded. As the maximum gross weight assigned or determined concerning the vehicles, PGVW is always regarded as the basis for classifying CWHTs. By referring to the Hong Kong Transport Department vehicle class definition system, the registered CWHTs can be categorized into light trucks ( $0 < PGVW \leq 5.5$ ), medium trucks ( $5.5 < PGVW \leq 24$ ), and heavy trucks ( $24 < PGVW \leq 38$ ), examples of which are shown in Figure 2.



**Figure 2.** Illustrative schematic of truck classifications in Hong Kong.

#### 4. Data and Method

##### 4.1. Data Description

Data used for this research were obtained from the HKEPD, consisting of three inter-dependent datasets, including datasets of construction waste disposal records (Dataset 1), billing account (Dataset 2), and vehicle information (Dataset 3). An excerpt of the three datasets and their interdependency can be understood from Figure 3.

Dataset 1 describes construction waste disposal records by the waste disposal facilities, which records information on every load of construction waste, including the facility name, transaction date, vehicle number, account number, time-in, time-out, and net weight, etc. Detailed information on these parameters is available in Table 3. This leads to a database of more than one million transaction records in a single year, which is considered to be a full coverage of the waste generated from all of the construction sites in Hong Kong. This “transaction records” dataset is composed of more than 12.7 million construction waste transaction records, from 2011 to 2019.

Dataset 2 describes billing account information. Before using disposal facilities, the responsible party (e.g., the main contractor if the contract exceeds HKD 1 million, or an individual, such as a vehicle owner or a small contractor if the contract values less than HKD 1 million) is mandated to register a billing account in the HKEPD. Dataset 2 thus describes basic information of all of the construction projects including the account number, contract name, contract sum, site address, and the type of construction work, etc. Particularly, the site address in Dataset 2 is critical to identify the origins of construction waste hauling trucks fleet trips, and this dataset is linked with Dataset 1 through account number. Dataset 3 describes CWHTs with vehicle numbers and permitted gross vehicle weight (PGVW) recorded. There are more than 10,000 CWHTs traced.

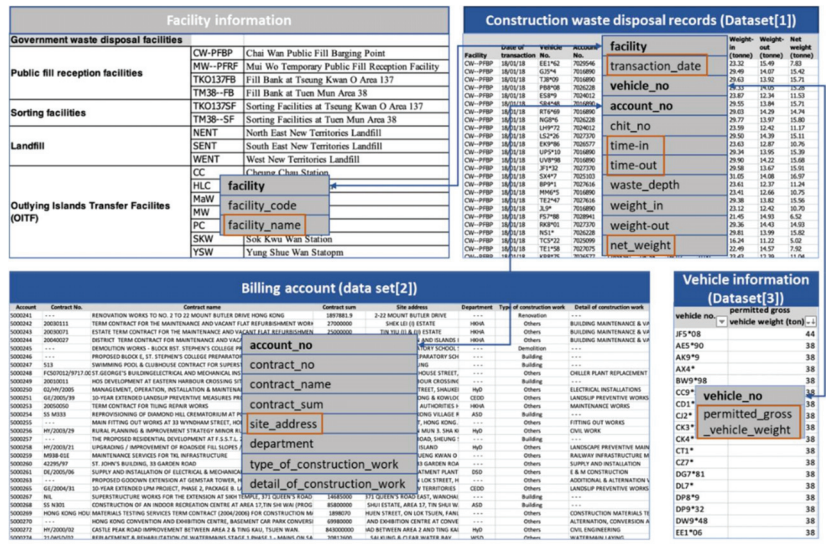


Figure 3. Three datasets and their interdependency.

Table 3. Details of construction waste disposal records.

Record	Description
Facility	The government waste disposal facilities for construction waste, as well as the destination of the construction waste hauling trucks for a trip.
Vehicle no	The license plate number of the trucks involved in transportation.
Transaction date	The date when the freight occurs.
Time-in	The time when the vehicle enters the facility, as well as the arrival time for a trip.
Time-out	The time when the vehicle exits the facility.
Net weight	The total weight of construction waste carried by hauling truck per trip.

The datasets cover more than 6 million transporting records of construction waste over the past five years and the number is increasing at the rate of 4000 records per day. A broad range of elements is involved in the datasets. Due to the three Vs (volume, velocity, and variety) characteristics, the dataset is qualified as big data. By mining the big data, it is anticipated that the freight performance of CWHs, as well as the related carbon emission in Hong Kong, can be measured.

#### 4.2. Research Design

To facilitate the understanding of our research design, Figure 4 illustrates the research framework, which includes data processing, freight performance metrics analyses, and freight carbon emission measurement.

##### 4.2.1. Data Processing

Two tasks were involved in the data processing. The first task was to match records and determine the origin–destination (O–D) pairs. A random month (May 2015) was chosen for this research with 113,025 transporting records shown in Dataset 1. The “facility” in Dataset 1 records the disposal facilities, which are the destinations of CWHs. By referring to the account number and vehicle number, the records can be linked to “site address” in Dataset 2, showing where CWHs load construction waste. Further to the names of O–D pairs, the geographical coordinates need to be further obtained for estimating the trip length and duration.

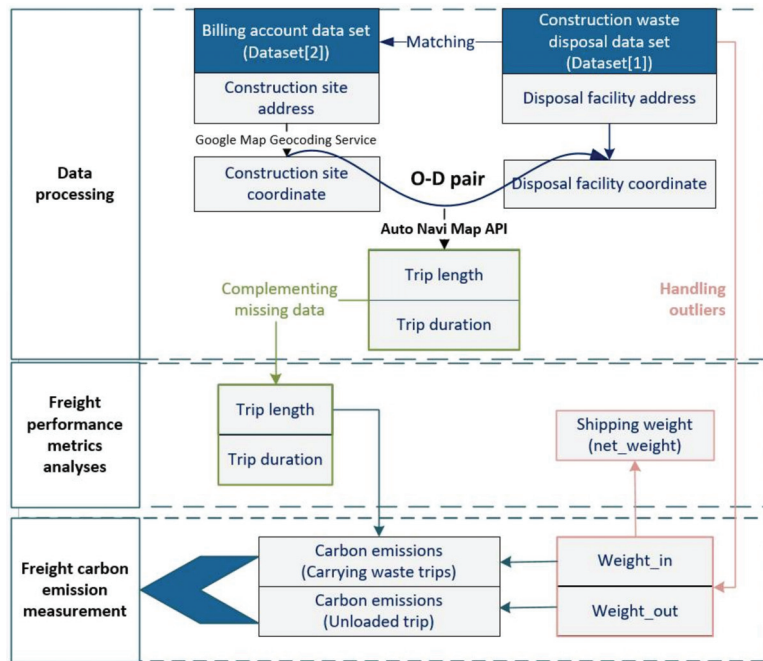


Figure 4. Research design.

By engaging Google Maps Geocoding Service, the longitude and latitude data for each construction site (the origin) and disposal facility (the destination) are geocoded. Based on this, the trip length and duration can be extracted by applying the Auto Navi Map Application Programming Interface (API) in Python. This step follows the following two assumptions: (a) the driving trajectory is along with the shortest route for each O–D pair; (b) trip durations for the same O–D pair are static without considering traffic congestion (e.g., on-peak and off-peak period) or infrastructure changes (e.g., ad hoc diversion). In this regard, each trip length is assumed to be the shortest travel distance from the construction site to the disposal facility, and the corresponding trip duration is calculated regardless of the actual traffic situation but with the free traffic flow state.

The other task was data cleansing. A total of 83 (0.07% of data) transporting records were recognized as outliers by considering “weight\_in” or “weight\_out” (e.g., “weight\_in” recorded with 3000.7 kg). These outliers were removed to ensure the appropriateness of further analyses. For the cases where site addresses were missing, the trip length and duration were complemented by using the mean value of trip length and duration of the corresponding freight trip type as well. This data processing was implemented in Matlab, which is an open-source statistical analytical software. Consequently, 112,942 effective transporting records in May 2015 were finalized for further analyses in this study.

#### 4.2.2. Freight Performance Metrics Analyses

The vehicle type, one of the vehicle-related freight performance metrics, was analyzed and summarized according to the freight trip types. Three kinds of trip-related freight performance metrics were further analyzed, including transporting weight, trip length, and trip duration. Transporting weight can be denoted by the “net\_weight”, which was calculated by using the differences between “weight\_in” and “weight\_out”. The trip-related freight performance metrics were further analyzed statistically by showing histograms and box charts based on the vehicle types and freight trip types.

#### 4.2.3. Freight Carbon Emission Measurement

Freight carbon emission was measured by multiplying the energy consumption by the carbon emission factor [56]. The first step is to estimate energy consumption, which is determined by multiplying the trip length and the according average energy consumption. The Electrical and Mechanical Services Department in Hong Kong has provided the reference for the average energy consumption based on the gross vehicle weight (GVW, including the weight of the vehicle and the construction waste), shown in Table 4. For example, if GVW is less than 2.5 tons, the average energy consumption for the freight is 10.2 L/100 km. The effectiveness of the data has been widely demonstrated for calculating carbon emission in previous studies. For example, Bi et al. [57] used average energy consumption based on gross vehicle weight to calculate the carbon emission of the construction waste transportation.

**Table 4.** Average energy consumption based on gross vehicle weight.

Gross Vehicle Weight (GVW)	Average Energy Consumption (L/100 km)
GVW ≤ 2.5 tons	10.2
2.5 tons < GVW ≤ 4 tons	12.2
4 tons < GVW ≤ 5.5 tons	18.6
5.5 tons < GVW ≤ 10 tons	31.9
10 tons < GVW ≤ 15 tons	34.3
15 tons < GVW ≤ 20 tons	44.3
20 tons < GVW ≤ 24 tons	54.1
24 tons < GVW ≤ 38 tons	61.1

Data source: <https://www.cleanair.hk/eng/index.htm>, accessed on 30 April 2021.

The daily trip-chaining patterns of CWHTs can be investigated and summarized with the finding that most (more than 60%) trips follow a single site-single facility pattern. CWHTs may take business from other nearby sites as well, but this would not cause significant differences. To simplify, we assume that each CWHT has a round trip between the construction site and the disposal facility, with one carrying waste and the other unloaded. Therefore, the GVWs for the fourth and return trips are different. Following the bottom-up approach for carbon emission calculation, the energy consumption for each CWHT can be estimated by utilizing the following equation:

$$E_i = e_i \times TL_i + e_i' \times TL_i \quad (1)$$

where  $E_i$  represents the energy consumption for the  $i$ th trip;  $e_i$  represents the average energy consumption based on GVW of the  $i$ th carrying-waste trip;  $e_i'$  represents the average energy consumption based on GVW of the  $i$ th unloaded trip; and  $TL_i$  denotes the on-way trip length for the  $i$ th trip.

The energy consumption can be further calculated into the freight carbon emission based on the carbon emission factor, which varies according to the carbon emission types. By referring to the HKEPD (2010), the three main types of carbon emission contain the emission of carbon dioxide (CO<sub>2</sub>), methane (CH<sub>4</sub>), and nitrous oxide (N<sub>2</sub>O), which can be examined by carbon dioxide equivalents (CO<sub>2</sub>-eq) [58]. Different types of carbon emission may lead to global warming to a different extent, which can be called the global warming potential (GWP). The freight carbon emission for each type of carbon emission can be calculated following Equation (2), as follows:

$$C_{ij} = \sum_i E_i \times F_j \times GWP_j \quad (2)$$

where  $C_{ij}$  represents the carbon emission for each trip and each type (in tons CO<sub>2</sub>-eq);  $E_i$  represents the energy consumption for the  $i$ th trip,  $F_j$  represents carbon emission factor for  $j$ th type of carbon emission,  $GWP_j$  represents global warming potential for  $j$ th type of carbon emission,  $i$  represents trips, and  $j$  stands for CO<sub>2</sub>, CH<sub>4</sub>, and N<sub>2</sub>O. According to the Carbon Reduction Certificate created by Hong Kong Green Organization Certification



(HKGOC, 2021), carbon emission factors for different types of CWHTs can be obtained (See Table 5) [59]. Additionally, IPCC (2006) defined the GWP for CO<sub>2</sub>, CH<sub>4</sub>, and N<sub>2</sub>O to be 1, 21, and 310, respectively [60]. As energy consumption is the same for the three types of carbon emission, the total freight carbon emission can be obtained by the following equation:

$$C_i = \sum_i E_i \times \sum_j (F_j \times GWP_j) \tag{3}$$

where  $C_i$  represents the carbon emission for each trip (in tons CO<sub>2</sub>-eq);  $\sum_j (F_j \times GWP_j)$  denotes the total transferring factor, which is determined by the vehicle types. As CWHTs in Hong Kong are diesel, the transferring factors for light, medium, and heavy CWHTs were calculated to be 2.78, 2.84, and 2.84, respectively, the detailed process can be seen in Table 5.

Table 5. Detailed parameters for calculating carbon emissions.

Vehicle Type	CO <sub>2</sub>		CH <sub>4</sub>		NO <sub>2</sub>		Transferring Factor
	Emission Factor (kg/L)	GWP	Emission Factor (kg/L)	GWP	Emission Factor (kg/L)	GWP	
Light CWHTs	2.614	1	$0.072 \times 10^{-3}$	21	$0.506 \times 10^{-3}$	310	2.78
Medium CWHTs			$0.145 \times 10^{-3}$		$0.072 \times 10^{-3}$		2.84
Heavy CWHTs			$0.145 \times 10^{-4}$		$0.072 \times 10^{-4}$		2.84

## 5. Data Analyses, Results, and Findings

### 5.1. Freight Performance

#### 5.1.1. Vehicle Type

Table 6 presents the different trucks that are used for freight trip types. The heavy trucks are mostly used for carrying waste, accounting for 56.05% of the total trips, particularly for the trips to public fills, i.e., 62.68% of the trips to TKO137FB and 68.98% of the trips to TM38—FB. The medium trucks are also frequently used (43.64%), while only 0.32% of trips are conducted by the light trucks. Most of the trips to landfill facilities (i.e., 87.97% to NENT and 72.87% to SENT), and the majority of the trips to sorting facilities (i.e., 90.97% to TKO137SE, and 83.72% to TM38—SF), use the medium trucks. This can imply that the amount of construction waste transported to public fills is large enough for the heavy trucks to load, while for trips to landfills and sorting facilities, medium trucks are enough.

#### 5.1.2. Transporting Weight

Transporting weight is considered to be a vital freight performance metric. Figure 5 illustrates the transporting weight of CWHTs in May 2015. It is noted from Figure 5a that the transporting weight for each trip ranges from 0 to 25 tons, with 15 to 17 tons occupying the highest probability. Figure 5b reports that the average transporting weight by the light trucks is 1.26 tons, while it is 6.96 tons for the medium trucks, and 15.27 tons for the heavy trucks. Drawn from the “weight\_out” data from Dataset 1, we can get the weight of the empty trucks. The average weights for the light, medium, and heavy trucks are 3.5, 13.4, and 14.5 tons, respectively. By adding the transporting weight and the truck weights, the average gross vehicle weights for the light, medium, and heavy trucks are 4.76, 20.36, and 29.77 tons, respectively. Compared with the maximum PGVW for each truck type, say, 5.5, 24, and 38 tons, it has been found that on average, the gross vehicle weights can reach 86.5% (4.76/5.5) of the maximum PGVW for the light trucks, 84.8% (20.36/24) for the medium trucks, and 78.3% (29.77/38) for the heavy trucks. This indicates a relatively high loading ratio for all of the truck types and that the medium trucks have higher utilization efficiency than the heavy trucks. Figure 5c shows the transporting weights for the different trip types. The average transporting weights for TLF, TSF, and TPF are 5.01 tons, 5.41 tons, and 13.95 tons, respectively. Compared with the trips to the landfill and sorting facilities,

the demands of transporting entirely inert construction waste to public fills are larger, evidenced by the high transporting weights per trip.

Table 6. Distribution of trips by vehicle types.

Freight Trip Type	Facility	Light Truck (0 < PGVW ≤ 5.5)	Medium Truck (5.5 < PGVW ≤ 24)	Heavy Truck (24 < PGVW ≤ 38)	Total Trips
TLF	NENT	14 (0.28%)	4468 (87.97%)	597 (11.75%)	5079
	SENT	76 (0.61%)	9061 (72.87%)	3297 (26.52%)	12,434
	WENT	5 (0.20%)	1174 (45.84%)	1382 (53.96%)	2561
TSF	TKO137SF	217 (3.28%)	6023 (90.97%)	381 (5.75%)	6621
	TM38-SF	24 (0.70%)	2890 (83.72%)	538 (15.59%)	3452
TPF	MW-PFRF	5 (0.42%)	1198 (99.58%)		1203
	TKO137FB	14 (0.03%)	16,427 (37.29%)	27,612 (62.68%)	44,053
	TM38-FB	1 (0.02%)	8042 (31.00%)	29,496 (68.98%)	37,539
<b>Total trips</b>		<b>356 (0.32%)</b>	<b>49,283 (43.64%)</b>	<b>63,303 (56.05%)</b>	<b>112,942</b>

TLF denotes the trips to landfill facilities; TPF denotes trips to public fills; TSF denotes trips to sorting facilities.

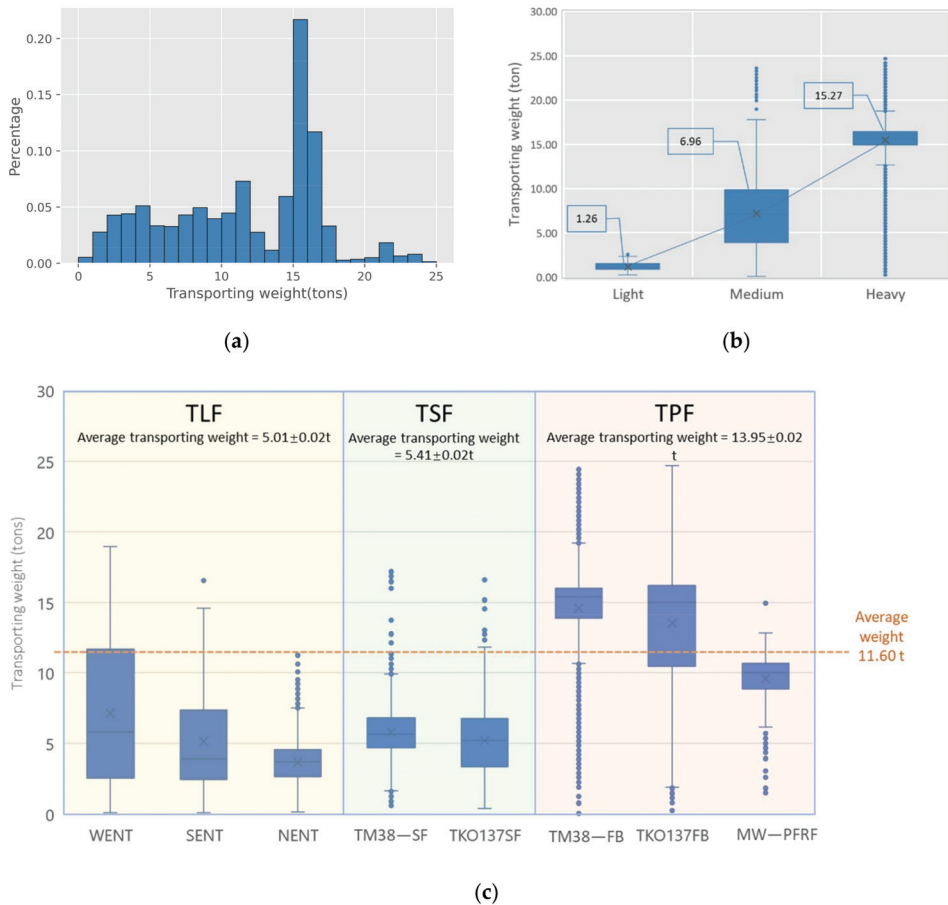
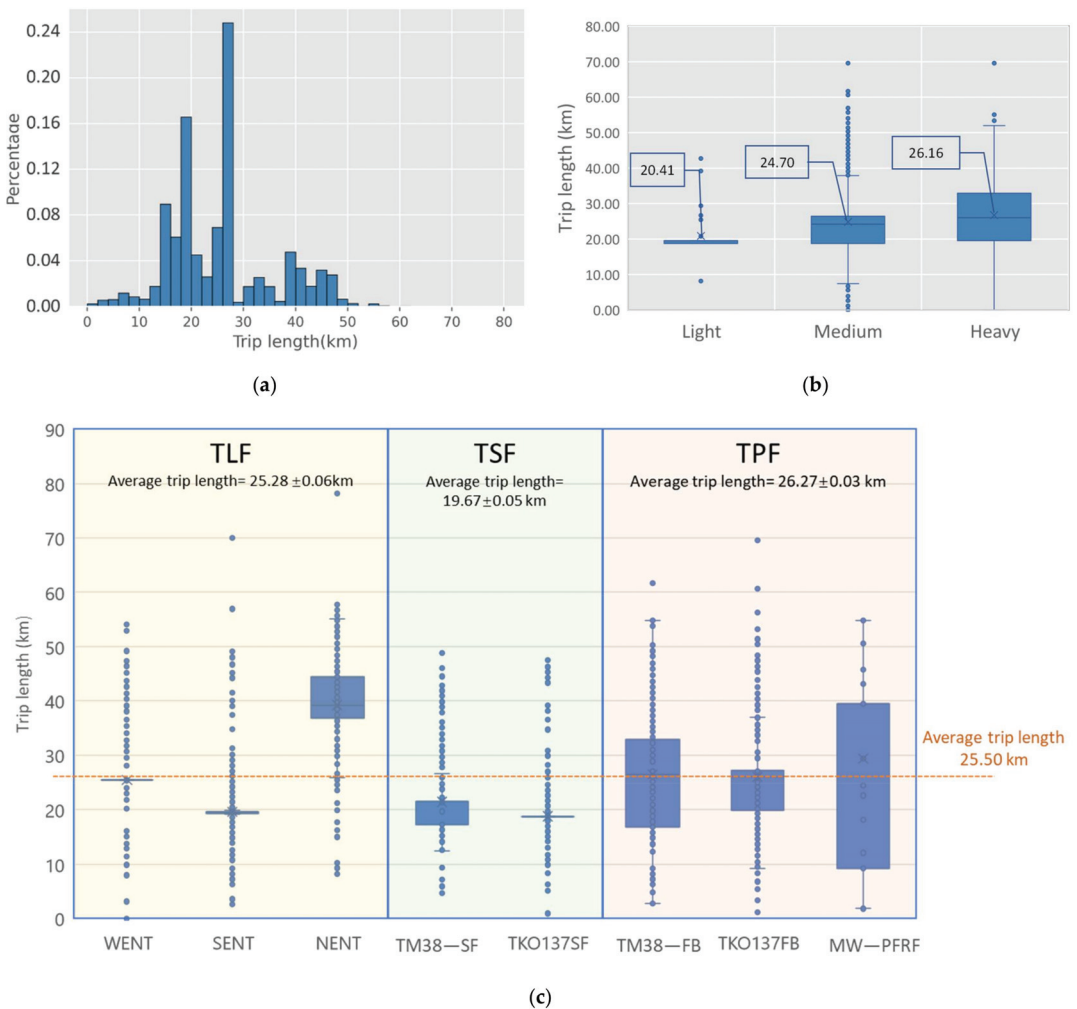


Figure 5. Transporting weight of CWHTs: (a) transporting weight histograms of CWHTs; (b) transporting weight distribution by vehicle types; (c) transporting weight distribution by freight trip types. Notes: Average transporting weight in (c) is presented as mean value ± SEM (standard error of the mean).

### 5.1.3. Trip Length

Figure 6 presents the trip length distributions of CWHTs. The trip length is about 26 km on average, with the longest trip length being about 80 km. Figure 6a presents a considerable proportion of the trip length within 30 km, with 24% of the trip length 26–28 km and 16% of 18–20 km, indicating that short or medium distance transportation is preferred, and it is likely that drivers will choose the nearby disposal facilities. It can be shown in Figure 6b that the average trip length for each vehicle type is almost the same, indicating that the vehicle type would not affect the trip length of CWHTs. Figure 6c shows the trip length for the different freight trip types. The average trip length for TSF is 19.67 km, which is shorter than that of the overall average trip length, while trip lengths for TPF are distributed around the average level. This indicates that most of the drivers are supposed to choose a disposal facility with a suitable trip length, which is to say, the trip length would be an important factor to be considered for the construction waste freight transportation.



**Figure 6.** Trip length of CWHTs: (a) trip length histograms of CWHTs; (b) trip length distribution by vehicle types; (c) trip length distribution by freight trip types. Notes: Average trip length in (c) is presented as mean ± SEM (standard error of the mean).

### 5.1.4. Trip Duration

The trip duration is highly related to the trip length. The average trip duration is 36.15 min, with the longest duration of 120 min. Figure 7a shows that most of the trip durations for CWHTs range from 30 to 40 min, accounting for 40% of the total trips. Similar to the trip length, Figure 7b shows that the average trip duration for each type of CWHT show no obvious differences, indicating no significant effects of the vehicle type on the trip duration. Figure 7c reveals that TLF takes the longest time on average with a mean of 44.28 min. While TSF takes 27.91 min, a shorter time than the overall average trip duration, trip durations for TPF are distributed around the average level, with the average duration of TPF 35.18 min.

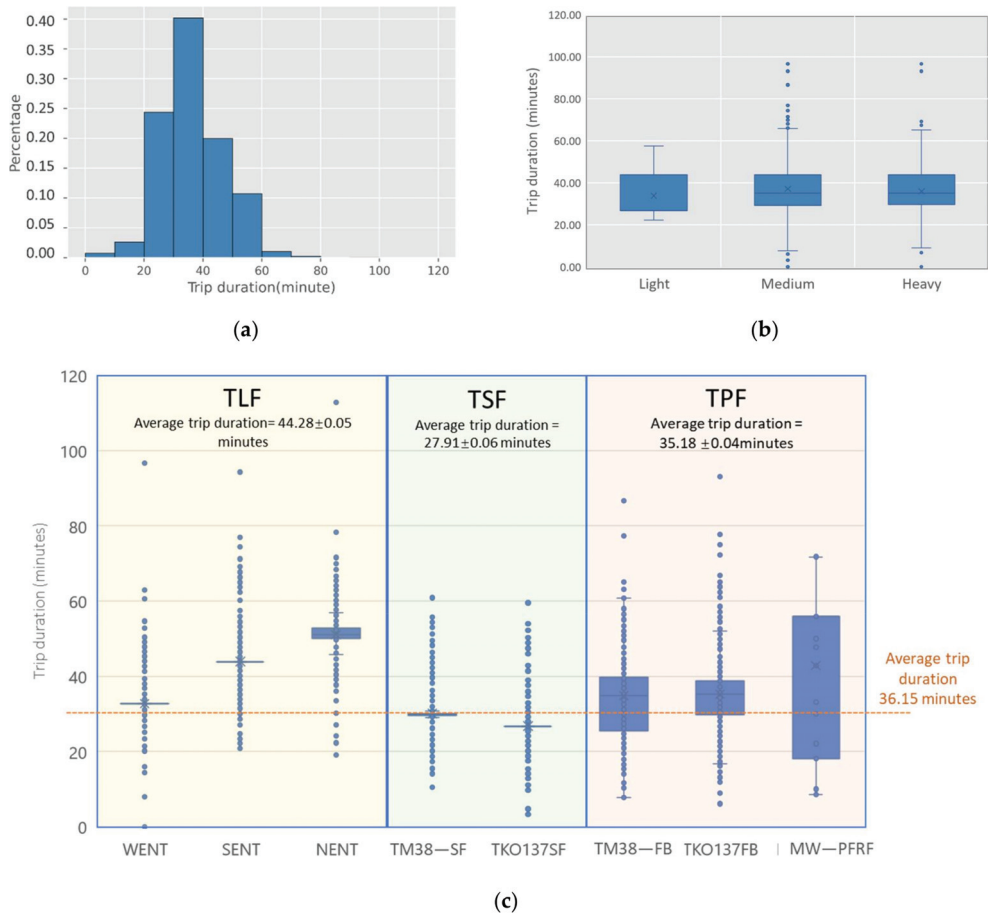


**Figure 7.** Trip duration of CWHTs: (a) trip duration histograms of CWHTs; (b) trip duration distribution by vehicle types; (c) trip duration distribution by freight trip types. Notes: Average trip duration in (c) is presented as mean ± SEM (standard error of the mean).

### 5.2. Carbon Emission Performance

Referring to Equations (1)–(3), the carbon emission generated from the construction waste transportation in May 2015 can be calculated and shown in Figure 8. On average, construction waste transportation contributes 67.16 kg CO<sub>2</sub>-eq emission for each trip. Most of the trips emit 40 to 80 kg CO<sub>2</sub>-eq, as shown in Figure 8a. Referring to Figure 8b, the average construction waste carbon emission produced by the light, medium, and heavy

trucks is 19.46, 61.21, and 72.06 kg CO<sub>2</sub>-eq, respectively, revealing that regardless of other factors, such as trip length, the heavier trucks seem to generate more carbon emission. Figure 8c shows that the average trip carbon emission of TLF, TSF, and TPF were 62.98, 46.44, and 70.69 kg CO<sub>2</sub>-eq, respectively. In particular, the trips to “NENT” generate the most carbon emission, with an average of 96.74 kg CO<sub>2</sub>-eq, due to its longest trip length. By considering the transporting weight and trip length, the trips to “NENT” are characterized with the lowest transporting weight but longest trip length, resulting in the lowest efficiency.

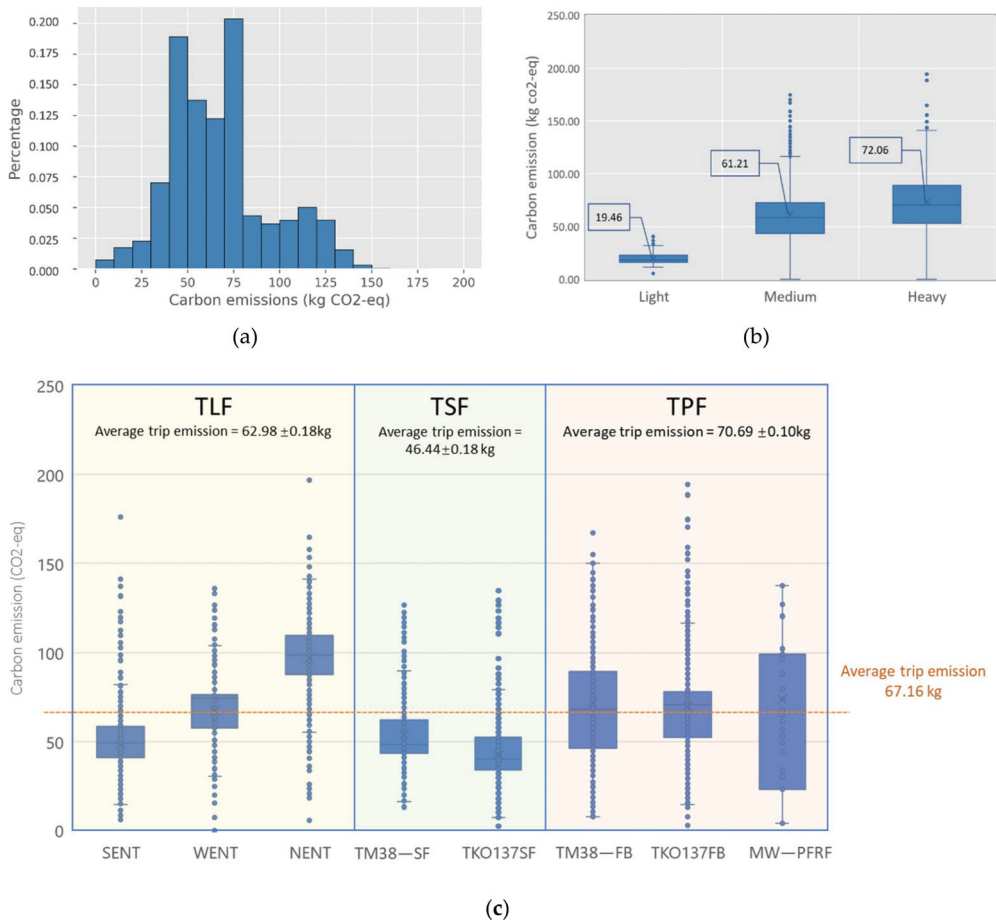


**Figure 8.** Carbon emission of CWHTs: (a) carbon emission histograms of CWHTs; (b) carbon emission distribution by vehicle types; (c) carbon emission distribution by freight trip types. Notes: Average trip emission in (c) is presented as mean ± SEM (standard error of the mean).

In order to better illustrate the carbon emission efficiency of construction waste transportation, we calculate the carbon emission for transporting one-ton construction waste, as shown in Table 7. In general, the larger the value of carbon emission for transporting one-ton construction waste, the lower the carbon emission efficiency. It shows that TPF has the highest carbon emission efficiency (5.07 kg CO<sub>2</sub>-eq/ton waste), followed by TSF (8.58 kg CO<sub>2</sub>-eq/ton waste) and TLF has the lowest (12.56 kg CO<sub>2</sub>-eq/ton waste). HKGOC (2021) shows that the carbon emission calculation needs to consider the vehicle type, the transporting weight, and the trip length of freight trips by CWHTs [59]. The TLF has low

carbon emission efficiency due to the following two reasons: (1) the long trip length to “NENT”, one of the landfill facilities; (2) the majority of TLF uses the medium and heavy trucks but just loads an average of 5.01 tons of transporting weights, leading to more trips and, thus, longer total trip length.

**Table 7.** Carbon emission efficiency of construction waste transportation.

Trip Type		TLF	TSF	TPF
Total transporting weight (ton)	a	100,694	54,504	1153,40
Total carbon emission (kg)	b	1,264,269	467,825	5,852,637
Carbon emission efficiency of construction waste transportation (kg CO <sub>2</sub> -eq/ton waste)	b/a	12.56	8.58	5.07

Notes: TLF = trips to landfill facilities, TSF = trips to sorting facilities, and TPF = trips to public fills.

5.3. Daily Freight Performance and Carbon Emission

Further to the analysis for one month, daily freight performance and carbon emission are explored in order to present the brief picture of construction waste freight transportation in one time dimension (a single day) and to illustrate the relationships among the metrics. For the daily analysis, working days and non-working days are analyzed separately. Table 8 shows the detailed daily freight performance and carbon emission for working days and non-working days.

**Table 8.** Daily freight performance and carbon emission.

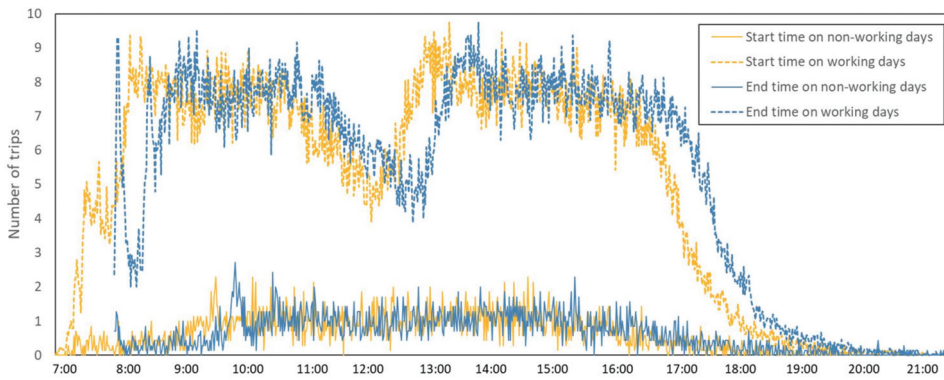
	Travel Types	TLF	TSF	TPF	Daily
Working days	Number of trips	763 (17%)	392 (9%)	3390 (74%)	4544
	Transporting weight (ton)	3704.06 (7%)	2135.67 (4%)	47,270.79 (89%)	53,110.52
	Trip length (km)	19,488.03 (17%)	7711.85 (6%)	89,510.99 (77%)	116,711.86
	Trip duration (h)	565.89 (20%)	182.40 (7%)	1997.82 (73%)	2746.11
	Carbon emission (ton CO <sub>2</sub> -eq)	48.45 (16%)	18.31 (6%)	240.87 (78%)	307.64
	Trip duration/Trip length (h/100 km)	2.90	2.37	2.23	2.35
Non-working days	Number of trips	252 (46%)	96 (17%)	205 (37%)	553
	Transporting weight (ton)	1685.34 (33%)	464.12 (9%)	2977.28 (58%)	5126.75
	Trip length (km)	5688.42 (50%)	1861.84 (16%)	3791.98 (34%)	11,342.24
	Trip duration (h)	176.35 (58%)	43.93 (14%)	85.91 (28%)	306.18
	Carbon emission (ton CO <sub>2</sub> -eq)	14.49 (50%)	4.05 (14%)	10.24 (36%)	28.78
	Trip duration/Trip length (h/100 km)	3.10	2.36	2.27	2.69

Notes: TLF represents trips to landfill facilities, TSF represents trips to sorting facilities, and TPF represents trips to public fills.

Table 8 shows that among the total of 4544 trips made per working day, the 3390 TPF accounts for the largest proportion (74%). It is followed by TLF, which accounts for 17% of the total daily trips and TSF accounts for only 9%. Accordingly, a total of 53,110.52 tons of construction waste are transported per working day, and about 90% of which are disposed into the public fills. The result implies that inert construction waste transportation is the most significant contributor to the freight movements on working days. Comparably, the freight performance of CWHs presents a significantly different situation on non-working days. Fewer trips are generated on non-working days, with an average of 553 daily trips and 5126.75 tons of daily transporting weights. The majority (46%) of freight trips are TLF on non-working days, followed by TPF (37%). This result is in line with the fact that two public fills (i.e., “MW—PFRF” and “TKO137FB”) are closed during non-working days.

The average daily carbon emission for the construction waste transportation by CWHTs is also shown in Table 8, which are 307.64 and 28.78 tons CO<sub>2</sub>-eq on working days and non-working days, respectively. On working days, TPF is the largest carbon emission contributor, accounting for 78%, followed by TLF (16%) and TSF (6%). During non-working days, carbon emissions produced by TLF, TSF, and TPF were 14.49, 4.05, and 10.24 tons CO<sub>2</sub>-eq, respectively. It has been found that the proportion of carbon emission for different freight trip types is highly consistent with the trip lengths, showing a highly related relationship between the trip length and carbon emission.

The analyses of daily performance and carbon emission can be further examined by time-of-day profiles. As plotted in Figure 9a, the line of the start time for the freight trips shows that freight trips of CWHTs start at 7:00 a.m. and continue until 10:00 p.m. Most of the CWHTs start freight trips for construction waste during 8:00–11:00 a.m. and 1:30–4:00 p.m., which seems to aggravate traffic congestion during the morning peak hours (7:00–9:00 a.m.). It is suggested to select the trip start time that would avoid the morning peak hours. The end time of the freight trips represents the time to enter the disposal facilities during 8:30–11:30 a.m. and 2:00–5:00 p.m. on working days. During those periods, the disposal facilities are suggested to improve efficiency in order to deal with the large amount of the CWHTs. On the contrary, the lines of start time and end time for CWHTs show a different view on non-working days. There are no obvious busy hours for CWHTs and the CWHTs transport construction waste during 10:00–16:00 on non-working days. Accordingly, the average freight carbon emission on both working and non-working days is shown by minutes in Figure 9b. We can see that the freight carbon emission is intensive during 8:30–11:00 a.m. and 1:30–5:00 p.m. on working days, but there is no obvious intensive period on non-working days. By dividing trip duration by trip length, it is interesting to find that it takes a longer time (2.69 h/100 km) on non-working days compared to that (2.35 h/100 km) on working days (shown in Table 8), although the traffic congestion is not that serious on non-working days.



(a)

Figure 9. Cont.

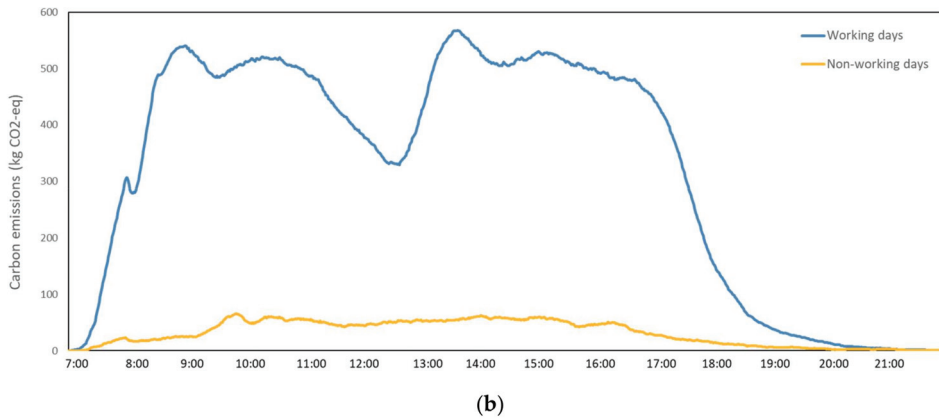


**Figure 9.** Time of day profiles of freight tips and carbon emission in Hong Kong: (a) Number of trips; (b) Carbon emission. Note: “end time” was described as the “time\_in” in the Dataset 1; “start time” was calculated as “end\_time” minus “trip duration”.

## 6. Discussion

This research takes advantage of an existing big dataset of construction waste transportation in order to understand the characteristics of freight performance and carbon emission of CWHTs in Hong Kong. When comparing the vehicles that are used for different types of trips, it was found that heavy trucks are mostly used for TPF, while other types of trips prefer to use medium trucks. This may be because of the high demands of transporting entirely inert waste to public fills, evidenced by the fact that the transporting weights of TPF occupy 89% of the total transporting weights per working day. The choices of vehicle types are supposed to be determined by the demands of transporting construction waste.

The trip length from construction sites to different facilities was calculated around 26 km on average, with a considerable proportion of the trip length within 30 km. This indicates that short- or medium-distance transportation is preferred by the CWHT drivers. By comparing the number of trips to the different disposal facilities and their locations, it can be found that facilities in the closer area, with a suitable trip length, are supposed to be chosen. The average trip length for each vehicle type is without obvious differences, indicating that the vehicle type would not affect the trip length.

By referring to the carbon emission calculation method provided by HKGOC (2021), the vehicle type, the transporting weight, and the trip length are supposed to affect the carbon emission of CWHTs freight transportation [59]. TPF uses heavy trucks with higher transporting weights, which are supposed to take more fuel and emit more carbon emission. However, the total trip length for transporting entirely inert waste to public fills would be reduced since the times of freight transportation would be less. Evidenced by the high carbon emission efficiency for TPF, trip length is supposed to be more important, compared to the transporting weight and the vehicle type, when calculating carbon emission. It is thus suggested that the trip length (trip length per trip as well as the total trip length) is a considerable metric to well coordinate freight transportation in terms of carbon emission. As opined by Yazdani (2021), carbon emission reduction can be achieved by optimizing the routing between the construction site and the disposal facilities.

The choices of vehicle types also matter to the carbon emission of CWHTs freight transportation. A relatively high loading ratio was found for all of the truck types, reaching around 80% on average. However, some types of trips still suffer a low loading ratio, for example, the majority of TLF uses the medium or heavy trucks but just loads an average of 5.01 tons of transporting weights. This leads to more trips and, thus, more carbon emission. It is thus suggested to choose suitable vehicle types based on the consideration of carbon emission. By involving the construction waste disposal charging scheme, the Hong Kong



government encourages on-site waste sorting [61]. For example, the public fills charge HKD 71 per ton to accept entirely inert construction waste, while sorting facilities charge HKD 175 per ton for more than 50%, by weight, of inert construction waste [58]. Accordingly, the demands of transporting different types of construction waste to different facilities need to be considered when choosing vehicle types.

The time-of-day profiles provide the start time of freight trips for CWHTs during 8:00–11:00 a.m. and 1:30–4:00 p.m. on working days, aggravating the traffic congestion during the morning peak hours (7:00–9:00 a.m.), and the end time of freight trips showing the busy time of disposal facilities during 8:30–11:00 a.m. and 1:30–5:00 p.m. on working days. On the contrary, there is no obvious intensive period on non-working days for all of the facilities. An interesting finding shows that the trips on non-working days take a longer time than those on working days, by calculating trip duration/trip length. This may be because the demands for transporting construction waste on working days are larger than those on non-working days, drivers are motivated by the transporting behavior. A dynamic pricing system can be proposed with different transporting fees in order to disperse the freight transportation of CWHTs, with consideration of time constraint or loading ratio. For example, higher transporting fees can be paid at off-peak hours, or non-working days, by considering the road network congestion in order to improve transportation efficiency and to reduce carbon emission caused by traffic congestions [62]; additionally, a low-load fee would be charged if the trucks come in with a relatively low loading ratio in order to improve the utilization efficiency and to reduce relevant carbon emission.

## 7. Conclusions and Implications

Based on the big datasets, this research analyzes the freight characteristics and carbon emission of construction waste hauling trucks (CWHTs) in Hong Kong. The results reveal the following: (a) average daily CWHTs' trip was 4544 on working days and 553 (trip to landfills accounts for the largest portion) on non-working days; (b) medium and heavy trucks are commonly used for transporting construction waste; (c) the majority of CWHTs' trips were short and medium trips, with a distance of less than 30 km, naturally drivers are inclined to choose the nearby disposal facilities; (d) the CWHTs in Hong Kong emitted 307.64 and 28.78 tons CO<sub>2</sub>-eq of carbon emission separately on working days and non-working days, and trips to landfill facilities have the lowest carbon emission efficiency; (e) busy time for CWHTs' trips and the disposal facilities are 8:00–11:00 a.m. and 1:30–4:00 a.m., and 8:30–11:00 a.m. and 1:30–5:00 p.m., respectively on working days, while there is no obvious intensive period on non-working days.

This research offers a comprehensive understanding of CWHTs freight characteristics and carbon emission performance. One implication of the research is that governments are suggested to propose a dynamic pricing system with different transporting fees in order to disperse the freight transportation of CWHTs. Higher transporting fees can be initiated for off-peak hours or non-working days in order to improve transportation efficiency; therefore, a low-load fee can be charged to deal with the low loading ratio of trucks. Another implication is that it provides important benchmarking metrics for monitoring the effectiveness of any policy interventions related to carbon emission. Freight carbon emission was found to be related to the vehicle type, transporting weight, and trip length, while trip length was the most considerable metric to carbon emission. The demands of transporting construction waste need to be monitored in order to choose suitable vehicle types and disposal facilities. It is vital to increase the loading ratio of the CWHTs and thus reduce the overall trip length. This study provides new insights for investigating freight characteristics and carbon emissions, which is significant reference material for other cities around the world.

This paper provides a springboard for further research. First, this research follows the assumption that the trip length and duration extracted are unrelated to the actual traffic situation, such as traffic congestion and infrastructure changes. Future research can make more accurate time-of-day profiles by considering the real-time traffic. Second, our research

implies the potential of a dynamic pricing system to disperse the freight transportation of CWHTs, but this system is yet to be further developed by considering the demands of transporting construction waste, the price sensitivity of CWHT drivers, and many other factors. Third, the method for optimizing construction waste collection routing can be extended to further study in order to improve the efficiency of waste transportation and reduce carbon emission.

**Author Contributions:** X.W.: Conceptualization, Methodology, Formal analysis, Writing—Original Draft, Writing—Review and Editing; M.Y.: Conceptualization, Investigation, Writing—Original Draft, Writing—Review and Editing; L.Y.: Methodology, Data Curation; W.B.: Data Curation; W.L.: Conceptualization, Writing—Review and Editing, Supervision. All authors have read and agreed to the published version of the manuscript.

**Funding:** This research is jointly supported by the Strategic Public Policy Research (SPR) (Project No.: S2018.A8.010.18S) Funding Schemes and the Environmental Conservation Fund (ECF) (Project No.: ECF Project 111/2019) of the Hong Kong SAR Government.

**Institutional Review Board Statement:** Not applicable.

**Informed Consent Statement:** Not applicable.

**Data Availability Statement:** Not applicable.

**Conflicts of Interest:** The authors declare no conflict of interest. The funders had no role in the design of the study; in the collection, analyses, or interpretation of data; in the writing of the manuscript, or in the decision to publish the results.

## References

1. Chen, J.; Su, Y.; Si, H.; Chen, J. Managerial Areas of Construction and Demolition Waste: A Scientometric Review. *Int. J. Environ. Res. Public Health* **2018**, *15*, 2350. [CrossRef]
2. Lu, W.S.; Lee, W.M.W.; Bao, Z.K.; Chi, B.; Webster, C. Cross-jurisdictional construction waste material trading: Learning from the smart grid. *J. Clean. Prod.* **2020**, *277*, 123352. [CrossRef]
3. Luo, J.; Chen, S.; Li, Q.; Liu, C.; Gao, S.; Zhang, J.; Guo, J. Influence of Graphene Oxide on the Mechanical Properties, Fracture Toughness, and Microhardness of Recycled Concrete. *Nanomaterials* **2019**, *9*, 325. [CrossRef] [PubMed]
4. USEPA. Advancing Sustainable Materials Management: 2018 Fact Sheet. Available online: [https://www.epa.gov/sites/default/files/2020-11/documents/2018\\_ff\\_fact\\_sheet.pdf](https://www.epa.gov/sites/default/files/2020-11/documents/2018_ff_fact_sheet.pdf) (accessed on 30 April 2021).
5. Defra UK Statistics on Waste. Available online: [https://assets.publishing.service.gov.uk/government/uploads/system/uploads/attachment\\_data/file/1002246/UK\\_stats\\_on\\_waste\\_statistical\\_notice\\_July2021\\_accessible\\_FINAL.pdf](https://assets.publishing.service.gov.uk/government/uploads/system/uploads/attachment_data/file/1002246/UK_stats_on_waste_statistical_notice_July2021_accessible_FINAL.pdf) (accessed on 30 April 2021).
6. HKEPD Monitoring of Solid Waste in Hong Kong, Waste Statistics for 2019. Available online: <https://www.wastereduction.gov.hk/sites/default/files/msw2019tc.pdf> (accessed on 30 April 2021).
7. Duan, H.; Li, J. Construction and demolition waste management: China's lessons. *Waste Manage. Res.* **2016**, *34*, 397–398. [CrossRef] [PubMed]
8. Lu, W.; Tam, V.W.Y. Construction waste management policies and their effectiveness in Hong Kong: A longitudinal review. *Renew. Sustain. Energy Rev.* **2013**, *23*, 214–223. [CrossRef]
9. Kim, Y.; Zhang, Y.; Park, W.; Cha, G.; Kim, J.; Hong, W. Analysis of Waste Generation Characteristics during New Apartment Construction—Considering the Construction Phase. *Int. J. Environ. Res. Public Health* **2019**, *16*, 3485. [CrossRef] [PubMed]
10. Akhtar, M.; Hannan, M.A.; Begum, R.A.; Basri, H.; Scavino, E. Backtracking search algorithm in CVRP models for efficient solid waste collection and route optimization. *Waste Manag.* **2017**, *61*, 117–128. [CrossRef] [PubMed]
11. Sánchez-Díaz, I.; Holguín-Veras, J.; Ban, X.J. A time-dependent freight tour synthesis model. *Transp. Res. Part B Methodol.* **2015**, *78*, 144–168. [CrossRef]
12. Cui, J.; Dodson, J.; Hall, P.V. Planning for Urban Freight Transport: An Overview. *Transp. Rev.* **2015**, *35*, 583–598. [CrossRef]
13. Kuramochi, T.; Elzen, M.G.J.D.; Peters, G. *Global Emissions Trends and G20 Status and Outlook*. UN Emissions Gap Report 2019; United Nations Environment Programme: Geneva, Switzerland, 2020.
14. Ritchie, H. Cars, Planes, Trains: Where Do CO<sub>2</sub> Emissions from Transport Come from? Available online: <https://ourworldindata.org/co2-emissions-from-transport> (accessed on 12 January 2022).
15. Wei, R.; Liu, C. Research on carbon emission reduction in road freight transportation sector based on regulation-compliant route optimization model and case study. *Sustain. Comput. Inform. Syst.* **2020**, *28*, 100408. [CrossRef]
16. Milton, K.; Grix, J. Public health policy and walking in England-analysis of the 2008 'policy window'. *BMC Public Health* **2015**, *15*, 614. [CrossRef]

17. Belien, J.; Boeck, L.D.; Ackere, J.V. Municipal Solid Waste Collection and Management Problems: A Literature Review. *Transp. Sci.* **2014**, *48*, 78–102. [CrossRef]
18. Combes, F.; Leurent, F. Improving road-side surveys for a better knowledge of road freight transport. *Eur. Transp. Res. Rev.* **2013**, *5*, 41–51. [CrossRef]
19. Khan, M.; Machemehl, R. Commercial vehicles time of day choice behavior in urban areas. *Transp. Res. Part A Policy Pract.* **2017**, *102*, 68–83. [CrossRef]
20. D'Este, G. Urban Freight Movement Modeling. In *Handbook of Transport Modelling*; David, A.H., Kenneth, J.B., Eds.; Emerald Group Publishing Limited: Bingley, UK, 2007; Volume 1, pp. 633–647.
21. Errampalli, M.; Kayitha, R.; Chalumuri, R.S.; Tavasszy, L.A.; Borst, J.; Chandra, S. Assessment of urban freight travel characteristics—A case study of Delhi. *Transp. Res. Procedia* **2020**, *48*, 467–485. [CrossRef]
22. Ruan, M.; Lin, J.J.; Kawamura, K. Modeling urban commercial vehicle daily tour chaining. *Transp. Res. Part E Logist. Transp. Rev.* **2012**, *48*, 1169–1184. [CrossRef]
23. Lu, W. Big data analytics to identify illegal construction waste dumping: A Hong Kong study. *Resour. Conserv. Recycl.* **2019**, *141*, 264–272. [CrossRef]
24. Nuzzolo, A.; Comi, A.; Polimeni, A. Urban Freight Vehicle Flows: An Analysis of Freight Delivery Patterns through Floating Car Data. *Transp. Res. Procedia* **2020**, *47*, 409–416. [CrossRef]
25. Akter, T. Truck Activity Pattern Classification Using Anonymous Mobile Sensor Data. Ph.D. Thesis, University of Arkansas, Fayetteville, NC, USA, 2019.
26. FHWA, F.H.A. Transportation Performance Measures. Available online: <https://www.fhwa.dot.gov/tpm/rule/freightmeas20042016.pdf>. (accessed on 30 April 2021).
27. Schrank, D.; Eisele, B.; Lomax, T. *TTI's 2012 Urban Mobility Report*; Texas Transportation Institute, Texas A&M University: College Station, TX, USA, 2012.
28. Ehmke, J.F.; Steinert, A.; Mattfeld, D.C. Advanced routing for city logistics service providers based on time-dependent travel times. *J. Comput. Sci.* **2012**, *3*, 193–205. [CrossRef]
29. Sulemana, A.; Emmanuel Amponsah, D.; Forkuo, E.K.; Sampson, O. Effect of optimal routing on travel distance, travel time and fuel consumption of waste collection trucks. *Manag. Environ. Qual.* **2019**, *30*, 803–832. [CrossRef]
30. Comi, A.; Nuzzolo, A.; Polimeni, A. Aggregate delivery tour modeling through AVM data: Experimental evidence for light goods vehicles. *Transp. Lett.* **2021**, *13*, 201–208. [CrossRef]
31. Cerminara, G.; Cossu, R. 1.2 - Waste Input to Landfills. In *Solid Waste Landfilling*; Cossu, R., Stegmann, R., Eds.; Elsevier: Amsterdam, The Netherlands, 2018; pp. 15–39.
32. To, W.M. Greenhouse gases emissions from the logistics sector: The case of Hong Kong, China. *J. Clean. Prod.* **2015**, *103*, 658–664. [CrossRef]
33. Lee, K. Integrating carbon footprint into supply chain management: The case of Hyundai Motor Company (HMC) in the automobile industry. *J. Clean. Prod.* **2011**, *19*, 1216–1223. [CrossRef]
34. Tian, Y.; Zhu, Q.; Lai, K.; Venus Lun, Y.H. Analysis of greenhouse gas emissions of freight transport sector in China. *J. Transp. Geogr.* **2014**, *40*, 43–52. [CrossRef]
35. Rodrigues Teixeira, A.C.; Machado, P.G.; Borges, R.R.; Felipe Brito, T.L.; dos Santos, E.M.; Mouette, D. The use of liquefied natural gas as an alternative fuel in freight transport—Evidence from a driver's point of view. *Energy Policy* **2021**, *149*, 112106. [CrossRef]
36. Talebian, H.; Herrera, O.E.; Tran, M.; Mérida, W. Electrification of road freight transport: Policy implications in British Columbia. *Energy Policy* **2018**, *115*, 109–118. [CrossRef]
37. Kellner, F. Allocating greenhouse gas emissions to shipments in road freight transportation: Suggestions for a global carbon accounting standard. *Energy Policy* **2016**, *98*, 565–575. [CrossRef]
38. Sim, J. The influence of new carbon emission abatement goals on the truck-freight transportation sector in South Korea. *J. Clean. Prod.* **2017**, *164*, 153–162. [CrossRef]
39. Van Vuuren, D.P.; Hoogwijk, M.; Barker, T.; Riahi, K.; Boeters, S.; Chateau, J.; Scriciecu, S.; van Vliet, J.; Masui, T.; Blok, K. Comparison of top-down and bottom-up estimates of sectoral and regional greenhouse gas emission reduction potentials. *Energy Policy* **2009**, *37*, 5125–5139. [CrossRef]
40. Omara, M.; Sullivan, M.R.; Li, X.; Subramanian, R.; Robinson, A.L.; Presto, A.A. Methane Emissions from Conventional and Unconventional Natural Gas Production Sites in the Marcellus Shale Basin. *Environ. Sci. Technol.* **2016**, *50*, 2099–2107. [CrossRef]
41. Ma, F.; Wang, Y.; Yuen, K.F.; Wang, W.; Li, X.; Liang, Y. The Evolution of the Spatial Association Effect of Carbon Emissions in Transportation: A Social Network Perspective. *Int. J. Environ. Res. Public Health* **2019**, *16*, 2154. [CrossRef] [PubMed]
42. Gilman, J.B.; Lerner, B.M.; Kuster, W.C.; de Gouw, J.A. Source signature of volatile organic compounds from oil and natural gas operations in northeastern Colorado. *Environ. Sci. Technol.* **2013**, *47*, 1297–1305. [CrossRef] [PubMed]
43. Hao, H.; Geng, Y.; Li, W.; Guo, B. Energy consumption and GHG emissions from China's freight transport sector: Scenarios through 2050. *Energy Policy* **2015**, *85*, 94–101. [CrossRef]
44. Sun, D.J.; Zhang, Y.; Xue, R.; Zhang, Y. Modeling carbon emissions from urban traffic system using mobile monitoring. *Sci. Total Environ.* **2017**, *599–600*, 944–951. [CrossRef] [PubMed]
45. Lv, Q.; Liu, H.; Yang, D.; Liu, H. Effects of urbanization on freight transport carbon emissions in China: Common characteristics and regional disparity. *J. Clean. Prod.* **2019**, *211*, 481–489. [CrossRef]

46. Alho, A.R.; You, L.; Lu, F.; Cheah, L.; Zhao, F.; Ben-Akiva, M. Next-generation freight vehicle surveys: Supplementing truck GPS tracking with a driver activity survey. In Proceedings of the 2018 21st International Conference on Intelligent Transportation Systems (ITSC), Maui, HI, USA, 4–7 November 2018; pp. 2974–2979.
47. Rashidi, T.H.; Roorda, M.J. A business establishment fleet ownership and composition model. *Transportation* **2018**, *45*, 971–987. [[CrossRef](#)]
48. Figenbaum, E. Can battery electric light commercial vehicles work for craftsmen and service enterprises? *Energy Policy* **2018**, *120*, 58–72. [[CrossRef](#)]
49. Venkadavarahan, M.; Raj, C.T.; Marisamynathan, S. Development of freight travel demand model with characteristics of vehicle tour activities. *Transp. Res. Interdiscip. Perspect.* **2020**, *8*, 100241. [[CrossRef](#)]
50. Sepasgozar, S.M.E.; Li, H.; Shirowzhan, S.; Tam, V.W.Y. Methods for monitoring construction off-road vehicle emissions: A critical review for identifying deficiencies and directions. *Environ. Sci. Pollut. R* **2019**, *26*, 15779–15794. [[CrossRef](#)]
51. Siripirote, T.; Sumalee, A.; Ho, H.W. Statistical estimation of freight activity analytics from Global Positioning System data of trucks. *Transp. Res. Part E Logist. Transp. Rev.* **2020**, *140*, 101986. [[CrossRef](#)]
52. Yang, W.H.; Wong, R.C.P.; Szeto, W.Y. Modeling the acceptance of taxi owners and drivers to operate premium electric taxis: Policy insights into improving taxi service quality and reducing air pollution. *Transp. Res. Part A Policy Pract.* **2018**, *118*, 581–593. [[CrossRef](#)]
53. Ambrosini, C.; Routhier, J.L. Objectives, Methods and Results of Surveys Carried out in the Field of Urban Freight Transport: An International Comparison. *Transp. Rev.* **2004**, *24*, 57–77. [[CrossRef](#)]
54. Yuan, H.; Lu, W.; Jianli Hao, J. The evolution of construction waste sorting on-site. *Renew. Sustain. Energy Rev.* **2013**, *20*, 483–490. [[CrossRef](#)]
55. Lu, W.; Yuan, H. Off-site sorting of construction waste: What can we learn from Hong Kong? *Resour. Conserv. Recycl.* **2012**, *69*, 100–108. [[CrossRef](#)]
56. Kang, P.; Song, G.; Xu, M.; Miller, T.R.; Wang, H.; Zhang, H.; Liu, G.; Zhou, Y.; Ren, J.; Zhong, R.; et al. Low-carbon pathways for the booming express delivery sector in China. *Nat. Commun.* **2021**, *12*, 450. [[CrossRef](#)] [[PubMed](#)]
57. Bi, W.; Lu, W.; Zhao, Z.; Webster, C.J. Combinatorial optimization of construction waste collection and transportation: A case study of Hong Kong. *Resour. Conserv. Recycl.* **2021**, *179*, 106043. [[CrossRef](#)]
58. HKEPD Construction Waste Disposal Charging Scheme. Available online: <https://www.epd.gov.hk/epd/misc/cdm/scheme.htm> (accessed on 20 April 2021).
59. Hong Kong Green Organisation Certification Guidebook for Carbon Reduction Certificate. 2021. Available online: <https://www.hkgoc.gov.hk/en-hk/carbon-reduction-certificate.html> (accessed on 27 August 2021).
60. Change, I. *2006 IPCC Guidelines for National Greenhouse Gas Inventories*; Institute for Global Environmental Strategies: Kanagawa, Japan, 2006.
61. Poon, C.S.; Yu, A.T.; Wong, A.; Yip, R. Quantifying the impact of construction waste charging scheme on construction waste management in Hong Kong. *J. Constr. Eng. Manag.* **2013**, *139*, 466–479. [[CrossRef](#)]
62. Khan, M.; Machemehl, R. Analyzing tour chaining patterns of urban commercial vehicles. *Transp. Res. Part A Policy Pract.* **2017**, *102*, 84–97. [[CrossRef](#)]



Article

# Pressure Drop and Energy Recovery with a New Centrifugal Micro-Turbine: Fundamentals and Application in a Real WDN

Maria Cristina Morani <sup>1</sup>, Mariana Simão <sup>2</sup>, Ignac Gazur <sup>3</sup>, Rui S. Santos <sup>4</sup>, Armando Carravetta <sup>1</sup>, Oreste Fecarotta <sup>1</sup> and Helena M. Ramos <sup>2,\*</sup>

<sup>1</sup> Department of Hydraulic, Geotechnical and Environmental Engineering, Università di Napoli Federico II, Via Claudio, 21, 80125 Napoli, Italy; mariacristina.morani@unina.it (M.C.M.); arcarrav@unina.it (A.C.); oreste.fecarotta@unina.it (O.F.)

<sup>2</sup> Civil Engineering Research and Innovation for Sustainability (CERIS), Instituto Superior Técnico, Department of Civil Engineering, Architecture and Georesources, University of Lisbon, 1049-001 Lisbon, Portugal; m.c.simao28@gmail.com

<sup>3</sup> IG Energy Ignac Gazur, Unipessoal, Lda, Rua Ferreira de Castro, Lote 46, Rio de Loba, 3505-570 Viseu, Portugal; ignac.gazur@gmail.com

<sup>4</sup> RSS Engenharia, Lda, Centro de Escritórios das Laranjeiras, Prç. Nuno Rodrigues dos Santos, 7, 1600-171 Lisboa, Portugal; rss@netcabo.pt

\* Correspondence: hramos.ist@gmail.com

**Abstract:** Water distribution networks need to improve system efficiency. Hydropower is a clean and renewable energy that has been among the key solutions to environmental issues for many decades. As the turbine is the core of hydropower plants, high attention is paid to creating new design solutions and increasing the performance of turbines in order to enhance energy efficiency of leakage by pressure control. Hence, design and performance analysis of a new turbine is a crucial aspect for addressing the efficiency of its application. In this study, computational fluid dynamics (CFD) modeling is coupled with experimental tests in order to investigate the optimal performance of a new centrifugal turbine. The behavior of the flow through the turbine runner is assessed by means of velocity profiles and pressure contours at all components of the machine under different operating conditions. Finally, the turbine geometry is scaled to a real water distribution network and an optimization procedure is performed with the aim of investigating the optimal location of both the designed new centrifugal micro-turbines (CMT) and pressure reducing valves (PRV) in order to control the excess of pressure and produce energy at the same time.

**Keywords:** centrifugal turbine; CFD models; experimental tests; dimensionless coefficients; optimal location; water distribution network

**Citation:** Morani, M.C.; Simão, M.; Gazur, I.; Santos, R.S.; Carravetta, A.; Fecarotta, O.; Ramos, H.M. Pressure Drop and Energy Recovery with a New Centrifugal Micro-Turbine: Fundamentals and Application in a Real WDN. *Energies* **2022**, *15*, 1528. <https://doi.org/10.3390/en15041528>

Academic Editors: Francesco Nocera, Roberto Alonso González Lezcano and Rosa Giuseppina Caponetto

Received: 30 December 2021

Accepted: 15 February 2022

Published: 18 February 2022

**Publisher's Note:** MDPI stays neutral with regard to jurisdictional claims in published maps and institutional affiliations.



**Copyright:** © 2022 by the authors. Licensee MDPI, Basel, Switzerland. This article is an open access article distributed under the terms and conditions of the Creative Commons Attribution (CC BY) license (<https://creativecommons.org/licenses/by/4.0/>).

## 1. Introduction

Hydropower is a well-advanced technology that convert the potential energy of water into electric energy [1–3] and contributes to about 50% of the all existing renewable energy sources [4,5]. It is reported that at least 16% of worldwide energy production results from the hydraulic power generation [6,7].

The turbine represents the core device of any hydropower plant, converting the hydraulic energy in mechanical energy of a rotating shaft [8], which is then converted into an electrical current by means of a generator. Turbines can operate under steady-state or transient operations in hydropower plants [9]: the angular frequency of the runner, as well as the discharge through the turbine, is constant in the former case and varies over time for transient operations [10]. Moreover, steady-states include both best efficiency point (BEP) conditions and off-design conditions, such as part load (PL), high load (HL), and full load (FL), whereas transient operations include start-stops and load variations [11,12]. The operation of a turbine is significantly complex and is characterized by high turbulence,

even in steady-state conditions [13]. When the runner is supplied by a constant angular frequency, between the trailing edge of the guide vane and leading edge of the runner blade an exchange of momentum occurs, known as a rotor-stator interaction [14,15], causing the propagation of a sound wave in all directions [16]. In addition, away from the BEP, the turbine is affected by a large variation in velocity and pressure, which can result in output power swings, as well as in mechanical vibrations that can damage the machine in the long term [17]. In transient conditions, the development of fatigue to the runner and wear and tear of the turbine components have also been observed [18] due to fluctuant pressure loadings and mechanical stresses varying in magnitude, direction and frequency [19]. A thorough analysis is therefore required to investigate the phenomena affecting the flow behavior within a turbine in order to improve the efficiency and power output with increased operational stability [20]. An improvement in performance of the turbine and its components definitely results in the improvement of overall hydropower plant efficiency [21]. Computational fluid dynamics (CFD) is a well-known reliable technique for performing a careful design [22,23] and simulation of hydraulic turbines [24,25]. A computational approach allows one to investigate minor details of flow, which cannot be caught by simple experiments [8,26]. A huge selection of studies based on CFD approaches to investigate design and behavior of turbomachines is available in the literature. Among the studies on turbines, Aghaei Tog et al. (2008) [27] showed an advanced turbulence model in CFD analysis of radial turbines and presented an accurate way to select turbulent parameters for FLUENT [28] users, applying this software as a complementary design tool for high-speed turbo-machinery components. Chen et al. (2008) [29] defined an advanced aerodynamic system to optimize blade design by the use of parametric modeling and optimization strategy modules. Biesinger et al. (2010) [30] used numerical techniques (i.e., phase-shift and time-inclining methods) to investigate unsteady flow phenomena for a more efficient future-generation turbine blade design. Wang et al. (2012) [31] investigated a novel design of a composite material axial water turbine, relying on a three-dimensional numerical flow analysis. The flow characteristics were investigated at different components of the turbine, and both the exact torque and power were analyzed at different rotating speeds. With reference to pumps as turbines (PATs), several studies investigated steady turbulent flows by CFD analysis [32–34], and other works have studied unsteady flow fields by means of a moving mesh technique in CFD codes [35,36].

The aim of this work is to investigate the optimal performance of a new centrifugal turbine by using both computational fluid dynamics modeling and experimental tests on a laboratory prototype. The experimental measurements in terms of flow rate, pressure-drop, torque and rotational speed allow one to assess the turbine behavior under different operating conditions. Such experimental tests have been crucial in performing a CFD analysis, providing the boundary conditions needed to properly model the reference turbine. Based on the CFD simulation in the whole flow passage, the analysis of three-dimensional steady flows is carried out under both design and off-design conditions. Pressure contours and pressure drops across the runner are provided to assess the entity of losses within the turbine components for different rotational speeds. Moreover, velocity profiles at the inlet and outlet of the runner are compared in order to analyze the behavior of the vanes in guiding the fluid exiting from the volute, as well as to quantify any slip phenomena at the outlet of the runner, which may occur owing to the limited number of blades. Moreover, the application of the turbine to a real case study network is presented. An optimization procedure is carried out to investigate the optimal scale design of the machine, as well as the optimal number and position of such designed turbines together with pressure reducing valves, in order to maximize both water and energy savings and minimize the investment costs. In this study, the optimization has been applied to a new mathematical model, including, in a comprehensive way, the optimization constraints, as well as turbine design formulations and the equations modeling the hydraulic behavior of the network.

## 2. Experimental Tests

Modeling the geometry of a centrifugal turbine involves defining the impeller and volute components. In this study the geometric modeling of the draft tube has also been considered, as it is one of the crucial components of a turbine. Performance tests have been carried out with reference to a centrifugal turbine prototype (Figure 1) in order to assess the hydraulic behavior profile under different operating conditions.

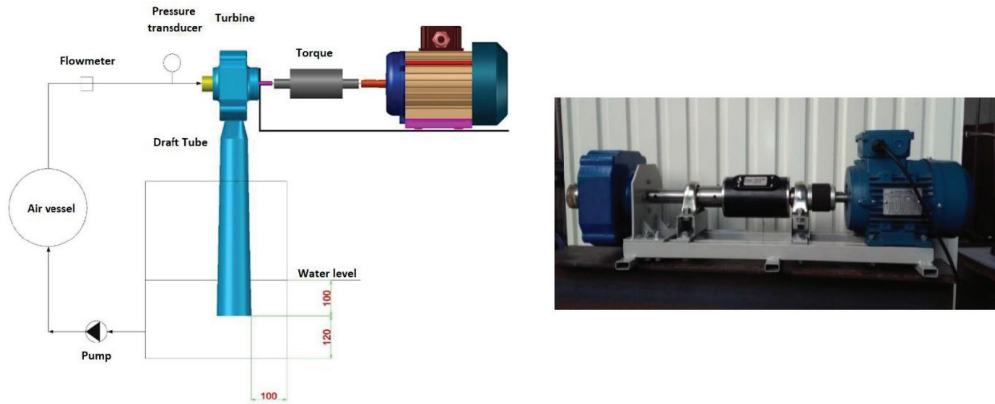


**Figure 1.** Experimental setup of the centrifugal turbine. Units: mm.

The experimental setup consists of a free surface reservoir, on the top of which a turbine is installed with a low-return suction tube. The setup is also equipped with an air vessel to control sudden pressure impulses, a flow-control circulation pump, and all required hydraulic and electrical components, such as a permanent magnet generator (or SEIG) and energy dissipation for flow control.

The turbine prototype is characterized by an intake external diameter of 46 mm (40 mm inside) and a shaft diameter of 12 mm (Figure 2). The turbine is installed on a rigid base and connected to a generator. A datum torque meter (model M425-S2-B) is installed between the turbine shaft and the electric brake.

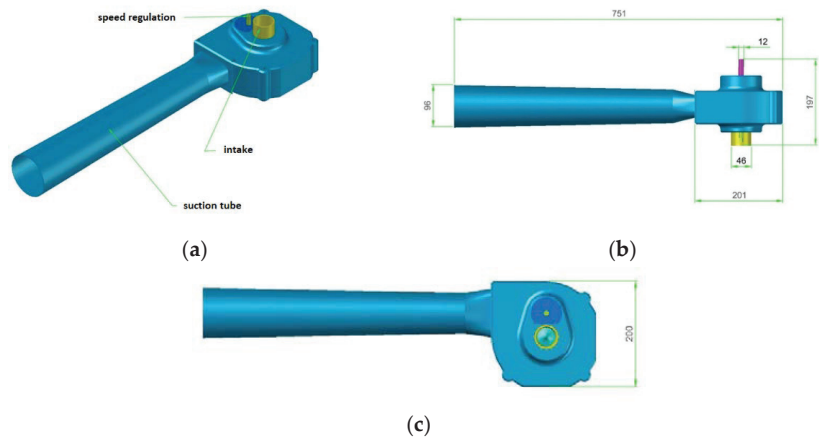


**Figure 2.** Turbine prototype: (a) description; (b,c) dimensions. Units: mm.

In the first stage of the tests, the turbine is experimented with variable pressure, flow and variable speed, keeping the opening guide vane at maximum to establish the performance points. The measured values are flow, pressure, torque and rotational speed.



During the tests, the flow was varied within the range of 19–46 L/s, whereas the head drop was kept as 32.8 m (3.17 bar). The measured torque range was 25–50 N·m., whereas the rotational speed varied between 750 and 1850 rpm. Finally, the power on the turbine shaft was between 2 and 10 kW. The experimental points are shown in Table 1.

**Table 1.** Experimental results of the turbine prototype.

D (mm)	150					
H (m)	32.8					
Q (L/s)	19.49	27.98	34.1	39.19	43.72	46.26
Q (%)	42	60	74	85	95	100
$\eta$ (%)	33	40	52	55	62	65
N (rpm)	767	1064	1489	1580	1792	1843
P (W)	2040	3590	5680	6930	8710	9690
V (m/s)	0.97	1.39	1.70	1.95	2.17	2.30
T (N m)	25.40	32.22	36.43	41.88	46.41	50.21
$P_h$ (W)	6265	8994	10,961	12,597	14,053	14,870

D—impeller diameter; H—head drop; Q—flow discharge;  $\eta$ —efficiency; N—rotational speed; P—mechanical power; V—flow velocity; T—torque;  $P_h$ —hydraulic power.

### 3. Numerical Model

#### 3.1. Turbine Geometry and Boundary Conditions

Providing a qualitative and quantitative prediction of fluid, CFD tools represent an important technological advance toward a detailed analysis of the flow behavior. CFD modeling allows one to study the behavior of both turbulent and laminar flows, as well as exchanges of energy, flow phases, vorticity and turbulence levels. Based on the experimental data provided as boundary conditions, as well as the virtual prototype of the turbine (Figure 1), a turbine modeling was performed with the aid of a CFD software for turbulent 3D flow and a design/drafting software. In particular, the software COMSOL Multiphysics [37] was selected for the CFD modeling in terms of geometry modification, mesh generation, calculation and results analysis, presenting accurate results for several fluid flow problems. COMSOL is a finite element method (FEM) software, relying on the mass conservation and the RANS (Reynolds-averaged Navier-Stokes) equations. FEM is a computational method according to which an object is divided into smaller elements. Each element is assigned to a set of characteristic equations, which are then solved as a set of simultaneous equations to investigate the behavior of the whole object [38]. The design of each machine component was, instead, performed by the software AutoCAD [39] and then imported by COMSOL to reproduce the physical problem and post-processing capabilities. The CFD approach was mainly intended to investigate the complex internal flows through all components of the machine at different operating conditions, which may be crucial to improve the performance of the machine at off-design conditions. The simulations were performed by using the  $k-\epsilon$  model for turbulent flows (with Reynolds number ranging between 20,850 and 209,000), assuming water as an incompressible fluid and the fluid regime as steady state. This model exhibits a good convergence rate and relatively low memory requirements. A crucial assumption on which the  $k-\epsilon$  model is based is that the Reynolds number is high enough. Moreover, such a model assumes that the turbulence is in equilibrium in boundary layers, which means that the production equals the dissipation. Being not always verified, such assumptions limit the accuracy of the model. Furthermore, in case of rotating flows, such a model often shows poor agreement with experimental data [40]. However, the flow close to the surface of the blade is turbulent; thus, the assumptions used to derive the  $k-\epsilon$  model are not valid there. The correction of the  $k-\epsilon$  model to better describe the flow in regions near the blades is not always desirable due to the significantly high resolution requirements. Analytical expressions, well known as wall functions, are instead preferred to describe the flow in the critical regions [41] and are used in this application. Wall functions ignore the flow field in the buffer region and analytically compute a nonzero fluid velocity [40–42]. When wall functions are used, the wall lift-off in

viscous units  $\delta_w^+$  has to be thoroughly verified to be below 30 in the whole region. In case of  $\delta_w^+$  greater than the threshold value, a finer boundary layer mesh is added.

All calculations were performed on an Intel 5, CPU 3.90 GHz, RAM 8 GB with four cores and threads running in parallel. The model uses a physics-controlled mesh, according to which the size attributes and operation sequences are automatically defined; thus, the mesh is automatically generated and adapted for the model's physics settings. Hence, once the geometric model was defined, the automatic mesh generation was performed by a careful selection of the related parameters, in order to achieve good precision results with an acceptable computational effort. The mesh near the surface of the blade was refined by an additional fine mesh to solve turbulence equations. Based on the assessment of the accuracy of the calculated maximum pressure, a mesh convergence analysis was tested by the use of a finer mesh and, thus, a greater number of degrees of freedom (DOF). In particular, local sizing and curvature size functions were used to obtain a sufficiently fine mesh to properly capture regions characterized by a rapid change in key variables, such as pressure and flow velocity. According to the mesh convergence analysis, for a mesh of approximately 150,000 DOF, the computed pressure value increased from 0.1 to 2.0 bar for a mesh of approximately 1,000,000 DOF, showing that 500,000 DOF provides the same precision as 1,000,000 DOF. Finally, the fluid domain was constructed with 280,056 tetrahedral components, with 85% of quality element. This number of elements is a compromise between the mesh quality as computed by the automatic mesh generator and the computational capacity. Nevertheless, as demonstrated in [43], the number of elements and their size ensure for limited error in the calculation of global parameters. The good agreement between calculation and experimental results in terms of global parameters, as shown below in Section 3.2, demonstrates the accuracy of the numerical solution.

The analyzed domain consists of an inlet, an outlet and two periodic interfaces. The boundary conditions at the inlet and outlet parts of the turbine were set according to the experimental measurements. In particular, the pressure value recorded by the pressure transducer located downstream of the draft tube was assumed as boundary condition at the outlet, whereas the flow discharge was considered as the the boundary condition at the inlet.

Hence, for each simulation, the rotation of the impeller was assumed as the rotational speeds achieved experimentally, and such a rotating domain was considered as a moving mesh. This definition regulates the spatial frame and applies to all interfaces of physics where domains rotate. Thus, in a rotating coordinate system in the inner domain, and in the outer one in fixed coordinates, these interfaces formulate the Navier-Stokes equations for incompressible fluids which are expressed in Equation (1) [44]:

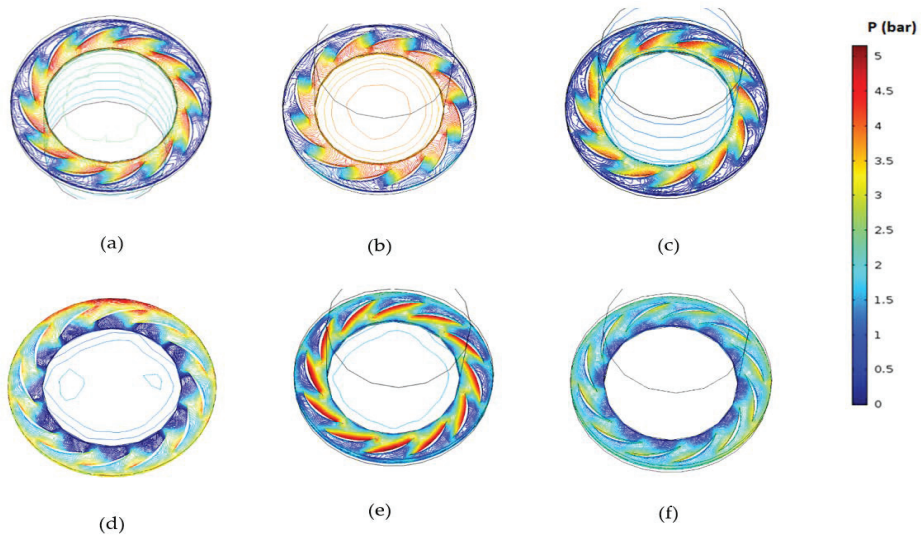
$$\begin{aligned} \nabla \cdot \mathbf{V} &= 0 \\ \rho \frac{\partial \mathbf{V}}{\partial t} + \rho \mathbf{V} \cdot \nabla (\mathbf{V}) &= -\nabla p + \nabla \cdot \left( \mu (\nabla \mathbf{V} + \nabla \mathbf{V}^T) \right) + \mathbf{F} \end{aligned} \quad (1)$$

where  $\mu$  is the dynamic viscosity,  $\rho$  the fluid density,  $p$  the pressure and  $\mathbf{F}$  is the external forces applied to the fluid. Non-rotating parts can be considered as fixed parts, which were coupled with the rotating parts by means of an identity pair set, that is, the fluid continuity boundary condition.

### 3.2. Numerical Results

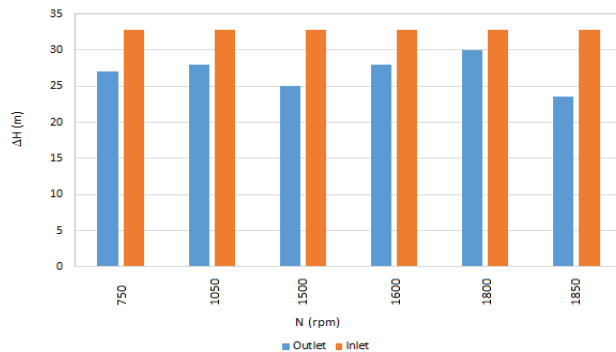
The design of a turbine impeller is generally based on given values of differential head, flow rate and rotating speed. This means that the specific speed is practically imposed. Hence, the novel geometry was designed to target the specific speed resulting from the experimental results. Thus, the turbine was simulated for different rotational speeds (varying between 700 and 1800 rpm), different flow values (ranging between 19 and 50 L/s), and keeping the head drop value at 32.8 m.

Figure 3 shows the total pressure contours across the runner of the turbine for different rotational speeds.



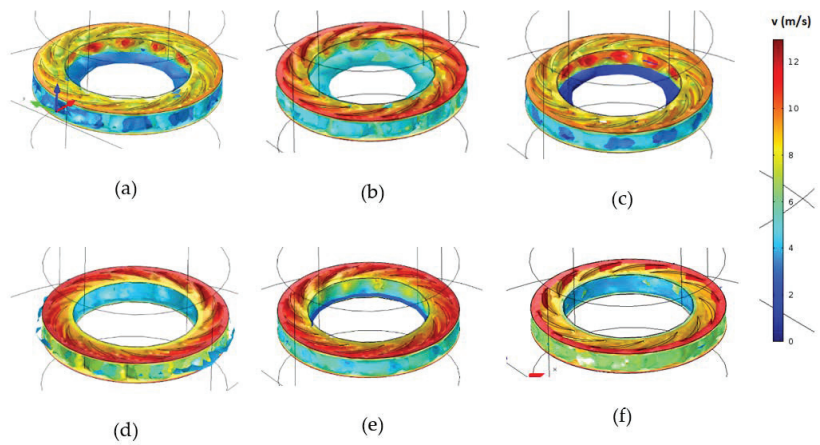
**Figure 3.** Pressure contours for different rotational speeds: (a)  $N = 750$  rpm; (b)  $N = 1050$  rpm; (c)  $N = 1500$  rpm; (d)  $N = 1600$  rpm; (e)  $N = 1800$  rpm; (f)  $N = 1850$  rpm.

Figure 4 shows the total pressure drop at the inlet and outlet rotor for different rotational speeds. According to this figure, such a difference in terms of pressure drop is quite small for most rotational speeds. Instead, a more significant difference is detected for a rotational speed equal to 1850 rpm.



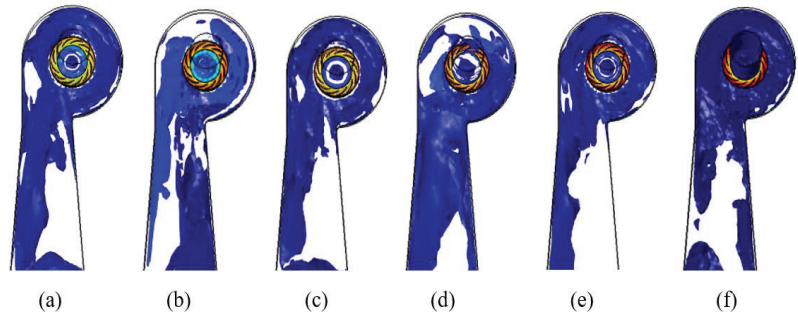
**Figure 4.** Comparison in terms of total pressure drop between inlet and outlet rotor.

A comparison of the flow velocity for different rotational speeds is presented in Figure 5. It is clearly shown that the geometry is more resistive to the flowrate for  $N < 1500$  rpm for a given range of the total pressure drop. This results in a higher change in absolute kinetic energy over the range of pressure differentials, causing a higher change in dynamic pressure.



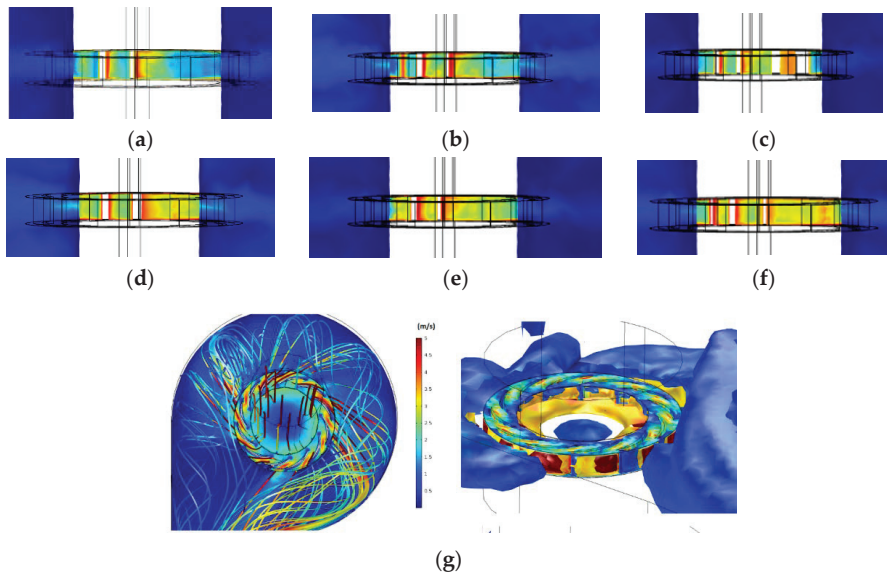
**Figure 5.** Velocity isosurfaces in the turbine runner for different rotational speeds: (a)  $N = 750$  rpm; (b)  $N = 1050$  rpm; (c)  $N = 1500$  rpm; (d)  $N = 1600$  rpm; (e)  $N = 1800$  rpm; (f)  $N = 1850$  rpm.

Figure 6 represents for each rotational speed the velocity isosurface at the first instant the turbine is crossed by flow and starts to rotate. According to Figure 6, the turbine response becomes faster by increasing the rotational speed. The fastest response is attained at a rotational speed at 1850 rpm.



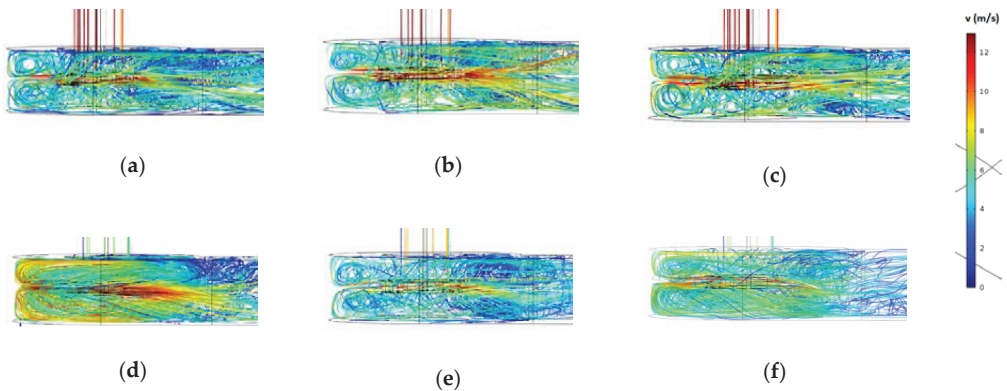
**Figure 6.** Velocity isosurface in the runner and draft tube for different rotational speeds with  $H = 32.8$  m: (a)  $N = 750$  rpm; (b)  $N = 1050$  rpm; (c)  $N = 1500$  rpm; (d)  $N = 1600$ ; (e)  $N = 1800$  rpm; (f)  $N = 1850$  rpm.

Figure 7 shows the velocity field at six operating points in a section plan of the turbine runner. The characteristics of the flow were analyzed in critical regions, such as near the hub and tip zones. With reference to Figure 7a, high flow acceleration is present from the leading to the trailing edge, but at 68% along the blade chord, a sudden increase in static pressure is observed, causing flow deceleration. Figure 7b,c shows almost the same conditions as in Figure 7a, with a sharper velocity magnitude near the trailing edges. Figure 7c–f shows some differences in terms of flow velocities, with higher values in the regions near the hub. The degree of flow deceleration is lower when compared with  $N < 1500$  rpm, inducing lower internal losses as well.



**Figure 7.** Velocity magnitude for  $H = 32.8\text{m}$  and different rotational speeds: (a)  $N = 750\text{ rpm}$ ; (b)  $N = 1050\text{ rpm}$ ; (c)  $N = 1500\text{ rpm}$ ; (d)  $N = 1600$ ; (e)  $N = 1800\text{ rpm}$ ; (f)  $N = 1850\text{ rpm}$ ; (g) general horizontal plan view.

Figure 8 presents the velocity streamlines between the runner and the guide vane. According to the streamline trend, it is clear that the fluid moves radially outward in the rotor boundary layer. With reference to Figure 9, the velocity contour shows that the maximum velocity reaches about  $12\text{ m/s}$  in the region close to the leading edge of the rotating blade, whereas the minimum velocity occurs close to the right side of the vane.



**Figure 8.** Velocity streamlines near the impeller for different rotational speeds: (a)  $N = 750\text{ rpm}$ ; (b)  $N = 1050\text{ rpm}$ ; (c)  $N = 1500\text{ rpm}$ ; (d)  $N = 1600$ ; (e)  $N = 1800\text{ rpm}$ ; (f)  $N = 1850\text{ rpm}$ .

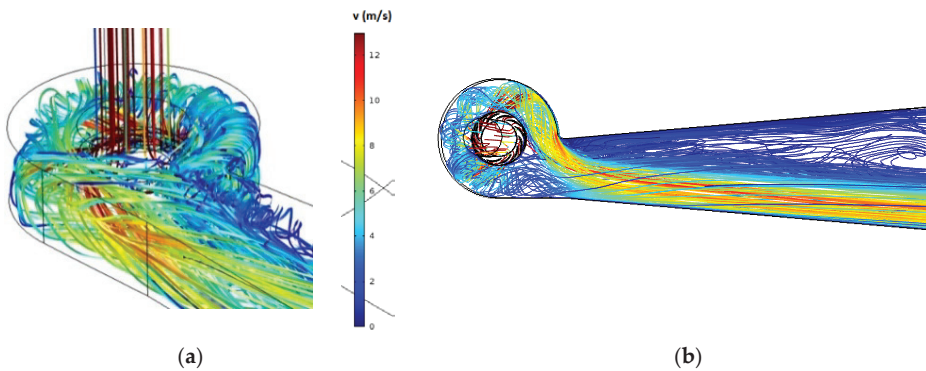


**Figure 9.** Detail of velocity streamlines with reference to the top view (a) and bottom view (b) of the guide vane ( $N = 1500$  rpm).

Dimensional analysis is a useful and powerful tool to analyze complex problems and solve different technical/physical problems. Thus, non-dimensional hydraulic feature terms of the machine were described in accordance with the geometric and kinetic resemblance principles:

$$\psi = \frac{gH}{N^2 D^2} \quad (2)$$

$$\varphi = \frac{Q}{ND^3} \quad (3)$$

$$\tau = \frac{T}{\rho N^2 D^5} \quad (4)$$

Non-dimensional quantities defined by Equations (2)–(4) represent the head coefficient, the flow coefficient and the torque coefficient of the centrifugal turbine, respectively.

Figure 10 shows the comparison between experimental measurements and numerical results. Scale effects, due to design parameters not perfectly adherent to real parameters, lead to a deviation between the prototype and the numerical model. In addition, since the Reynolds number of the model is typically higher than the prototype, losses of friction resulting from the CFD analysis are larger than the prototype. In addition, the model efficiency is generally greater because of the viscous effects associated with vortex or eddy effects. The maximum efficiency of the tested is attained as 65% for a value of the flow coefficient as about 0.45.

According to Figure 10, the comparison between CFD and experimental tests predicted that CFD results are slightly higher than the experimental results.

Based on experimental results and affinity laws, the following relationships were obtained:

$$\varphi = q_T \alpha \sqrt{\psi} \quad (5)$$

$$N = \frac{n_T}{D} \sqrt{gH} \quad (6)$$

$$\eta = 1 - (0.4) \left( \frac{75}{1000 D} \right)^{0.25} \left( \frac{5}{H} \right)^{0.1} \quad (7)$$

where  $q_T$  and  $n_T$  are experimental coefficients equal to 0.141 and 22.76, respectively, whereas  $\alpha$  is the runner thickness.

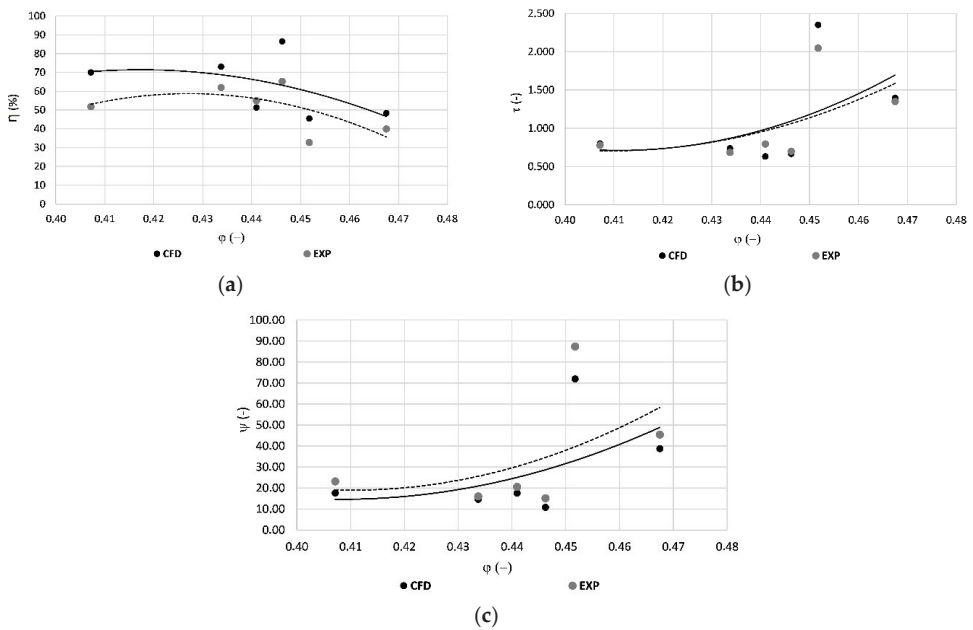


**Figure 10.** Comparison between experimental measurements and numerical results. (a) Efficiency vs. flow rate coefficient; (b) torque coefficient vs. flow rate coefficient; (c) head coefficient vs flow rate coefficient.

#### 4. Application to the Water Distribution Network (WDN) of Funchal City—Madeira, Portugal

Once the design and performance of the novel turbine were investigated by experiments and CFD analyses, an application to a real case study network was then considered. The case study concerns the water distribution network supplying Funchal city in the Madeira region (PT) (Figure 11). Such a network consists of a number of links ( $l$ ) and nodes ( $n$ ) as 2844 and 2801, respectively, and it is supplied by five reservoirs, whose water levels were assumed as constant. The total flowrate supplied by the reservoirs is 300 L/s. Out of five reservoirs, two are located at 360 and 400 m.a.s.l., whereas the elevation of the remaining three reservoirs is approximately 250 m.a.s.l. The network layout is presented in Figure 11. According to the current configuration of the network, several pressure reducing valves (PRVs) and throttle control valves (TCVs) are installed with the aim of controlling the pressure in the whole network. Moreover, further valves are present in order to close some links and determine a kind of district area of the network.

Due to the large topographical variability, a significant energy potential is available. Hence, the installation of one or more turbines could allow for a large production of energy, as well as a large water savings due to the reduction of the overall pressure. Nevertheless, in the links where the flow is significantly low, the energy production is low as well, and installing a valve instead of a turbine could be a more viable solution. Hence, in this study, the optimal location of turbines and valves was simultaneously investigated. An optimization procedure is implemented with reference to the daily average flow condition, with the aim of searching for the best scale design for turbines and, simultaneously, the best number and location of turbines and valves in order to maximize both water and energy savings, and minimize the investment cost.



**Figure 11.** Funchal network layout.

#### 4.1. The Optimization Procedure

In this study, the optimization problem was coupled with the hydraulic resolution of the network in one single mathematical model. Instead of using a hydraulic external solver (e.g., EPANET) to compute flow through links and pressure at nodes, the hydraulic behavior of the network is modeled within the optimization procedure by means of the mass continuity equations at the nodes and momentum balance equations along the pipes. The mathematical model will therefore consist of both linear and non-linear inequalities constraining the optimization problem, as well as non-linear equations modeling the hydraulic resolution of the network. With regard to the variables of the optimization, these are both binary (i.e., the installation of a device within a branch of the network) and continuous (i.e., pressure in the nodes, the discharges within the pipes, head loss within the devices). The resulting mathematical model is therefore a mixed integer non-linear programming (i.e., MINLP). Due to the non-convexity of some constraints, among the existing MINLP solvers, the Solving Constraint Integer Programs (SCIP) [45] was chosen to perform the optimization, since it is a robust global optimization solver, suitable for general MINLP problems—no matter if the optimization problem is convex or non-convex. SCIP relies on spatial branch-and-bound algorithm with linear relaxation, various heuristics, and bound-tightening procedures. This solver can handle only differentiable functions; hence, it cannot perform the optimization in the presence of absolute values, if/sign function, etc. Morani et al. (2021) [46,47] found proper formulations of both variables and constraints in a general optimal location problem, avoiding the use of any non-differentiable functions within the mathematical model. Most of these formulations will be used in this study and presented later on.

##### 4.1.1. The Variables

The location of a general device within a water network consisting of  $l$  links and  $n$  nodes is represented by a binary variable (i.e.,  $I_k^T$  and  $I_k^V$  for turbine and valve, respectively) assuming a value of 1 if the device is installed and 0 otherwise. As previously highlighted, since the hydraulic behavior of the network is modeled within the optimization procedure, flow through links ( $Q_k$ ) and head at nodes ( $H_i$ ) are continuous variables of the optimization problem. With regard to  $H_i$ , it is constrained between a lower and an upper bound, as follows:

$$\frac{P_{\min}}{\gamma} \leq H_i - z_i \leq \frac{P_{\max}}{\gamma} \quad (8)$$



where  $p_{\min}$  and  $p_{\max}$  represent the minimum and maximum pressure values allowable at each node,  $z_i$  the elevation of the  $i$ -th ( $i = 1 \dots n$ ) node, and  $\gamma$  the specific weight of water.

When the node is a reservoir ( $r$ ), the head  $H_i(t)$  is a boundary condition, and the variable is given by the discharge  $q_r$ , which flows into or out of the reservoir itself. Regarding the discharge ( $Q_k$ ) flowing through the  $k$ -th ( $k = 1 \dots l$ ) link, it is expressed according to Morani et al. (2021) [46], as follows:

$$0 \leq q_k^+ \leq Q_{\max} \zeta_k \tag{9}$$

$$0 \leq q_k^- \leq Q_{\max} (1 - \zeta_k) \tag{10}$$

where  $q_k^+$  and  $q_k^-$  are, respectively, the positive and negative parts of the discharge, and  $Q_{\max}$  is the upper bound. With regard to  $\zeta_k$ , it is a binary variable modeling the direction of the flow within a branch, and it is equal to 1 if the discharge flows according to the direction of the pipe  $k$  (i.e., the flow is given by the only positive component  $q_k^+$ ) and 0 if otherwise (i.e., the flow is given by the only negative component  $q_k^-$ ).

The head loss within the device ( $H_k^T$  and  $H_k^V$  for turbine and valve, respectively) is a further continuous variable of the optimization problem. As presented in Morani et al. (2021) [46], these variables can also be split into their positive and negative components, as follows:

$$0 \leq H_k^{T+} \leq H_{k \max} \zeta_k \tag{11}$$

$$0 \leq H_k^{V+} \leq H_{k \max} \zeta_k \tag{12}$$

$$0 \leq H_k^{T-} \leq H_{k \max} (1 - \zeta_k) \tag{13}$$

$$0 \leq H_k^{V-} \leq H_{k \max} (1 - \zeta_k) \tag{14}$$

where  $H_{k \max}$  is the maximum value of head loss achievable within the devices.

Further variables of the problem are related to the design of the turbines. The machine presented in the previous sections is a small-scale prototype; hence, its diameter ( $D$ ) should be properly scaled to be suitable for such a real application. Such a diameter represents a further variable of the optimization problem and has is bounded as:

$$D \geq D_{\min} I_k^T \tag{15}$$

$$D \leq D_{\max} I_k^T \tag{16}$$

where  $D_{\min}$  and  $D_{\max}$  represent the lower and upper bound, respectively, of the variable  $D$  in the case of turbine installation (i.e.,  $I_k^T = 1$ ).

A further design variable of the optimization problem is represented by the impeller thickness ( $\alpha$ ). As the diameter  $D$ ,  $\alpha$  is constrained as:

$$\alpha \geq \alpha_{\min} I_k^T \tag{17}$$

$$\alpha \leq \alpha_{\max} I_k^T \tag{18}$$

where  $\alpha_{\min}$  and  $\alpha_{\max}$  represent the lower and upper bound, respectively, of the variable  $\alpha$  in the presence of a turbine (i.e.,  $I_k^T = 1$ ).

#### 4.1.2. Non-Linear Constraints

Most of the non-linearities in the optimization problem are given by the equations modeling the turbine design. In addition to the diameter ( $D$ ), the installed turbine should also be characterized in terms of flow ( $Q_T$ ), efficiency ( $\eta_T$ ) and producible power ( $P_T$ ). With regard to the flow through the turbine, it can be obtained from Equation (5), as follows:

$$Q_T = q_T D^2 \alpha \sqrt{g (H_k^{T+} + H_k^{T-})} \tag{19}$$

In order to set  $Q_T$  as the total discharge flowing through the  $k$ -th pipe if the turbine is installed, the following constraint was defined:

$$Q_T = (q_k^+ + q_k^-) I_k^T \tag{20}$$

According to Equation (20), when the turbine is not installed in the  $k$ -th pipe (i.e.,  $I_k^T = 0$ ), the  $Q_T$  is forced to be equal to 0.

The turbine efficiency can be expressed according to Equation (7) as a function of  $(H_k^{T+} + H_k^{T-})$ :

$$\eta = 1 - (0.4) \left( \frac{75}{1000 D} \right)^{0.25} \left( \frac{5}{H_k^{T+} + H_k^{T-}} \right)^{0.1} \tag{21}$$

The producible power is hence given by the following expression:

$$P_T = \gamma \left( H_k^{T+} + H_k^{T-} \right) Q_T \eta \eta_G \tag{22}$$

where  $\eta_G$  is the generator efficiency, assumed equal to 90%.

As constraints (19)–(22) are written with reference to each link of the network, the total number of such constraints is equal to  $4l$ .

Further non-linearities are represented by the hydraulic equations modeling the resolution of the network, such as the mass continuity equations within the nodes, and momentum balance equations along the links.

Given a node  $i$  ( $i = 1 \dots n$ ), the mass continuity equation can be expressed as follows:

$$\sum_{k \in K_i} (q_k^+ + q_k^-)^{in} - \sum_{k \in K_i} (q_k^+ + q_k^-)^{out} - f_i (H_i - z_i)^\beta = q_i^d \tag{23}$$

where  $(q_k^+ + q_k^-)$  is the total discharge in the  $k$ -th link belonging to set  $K_i$  of links approaching the node  $i$ , and the superscripts in and out indicate whether the discharge flows into or out of the  $i$ -th node, respectively. The term  $f_i (H_i - z_i)^\beta$  represents the amount of leaked water at the  $i$ -th node, which will be better defined in Section 4.1.4. As the constraint (23) was written for each node  $i$  ( $i = 1 \dots n$ ), the number of mass continuity equations can be accounted for as  $n$ .

Given a link  $k$  ( $k = 1 \dots l$ ), the momentum balance equation is given by the following expression:

$$H_i - H_j - r_k L_k - (H_k^{T+} - H_k^{T-}) - (H_k^{V+} - H_k^{V-}) = 0 \tag{24}$$

where  $H_i$  and  $H_j$  are the head at the initial ( $i$ -th) and final ( $j$ -th) node of the  $k$ -th link, and  $r_k L_k$  is the head loss due to the resistance along the  $k$ -th pipe presenting a length  $L_k$ . The unit head loss  $r_k$  was calculated by the Hazen Williams formula:

$$r_k = \frac{10.67}{C_k^{1.852}} \frac{[(q_k^+)^{1.852} - (q_k^-)^{1.852}]}{D_k^{4.8704}} \tag{25}$$

where  $C_k$  and  $D_k$  are the roughness coefficient and the diameter of the  $k$ -th pipe, respectively. As constraint (24) is expressed for each link  $k$  ( $k = 1 \dots l$ ), the total number of such constraints can be accounted for as  $l$ .

### 4.1.3. Linear Constraints

Some linear constraints were used and were already presented in Section 4.1.1 (see Equations (9)–(14)) to define the variables of the problem. An additional set of  $l$  linear constraints (i.e., one for each link  $k$ ) was defined in order to avoid the installation of both turbine and valve within a same link:

$$I_k^T + I_k^V \leq 1 \tag{26}$$

Finally, further linear constraints were introduced in order to push the head loss within the devices to be equal to 0 if the device is not installed, and to be bounded otherwise.

$$H_k^{T+} + H_k^{T-} \leq H_{k \max} I_k^T \quad (27)$$

$$H_k^{V+} + H_k^{V-} \leq H_{k \max} I_k^V \quad (28)$$

As constraints (27) and (28) defined for each link  $k$  of the network, the total number of such devices is equal to  $4l$ .

#### 4.1.4. The Objective Function

As already highlighted, the aim of the optimization is to search for the best design and location of both turbines and valves, in order to maximize both the energy and water savings and minimize the investment cost. As in Morani et al. (2021) [46,48], the objective function that can be suitable for such an optimization problem is the net present value (NPV) of the investment, whose expression is given in Equation (29).

$$NPV = \sum_{k=1}^l \left( -c_k^T I_k^T - c_k^V I_k^V \right) + \sum_{y=1}^Y \frac{E_y^P + W_y^S}{(1+\lambda)^y} \quad (29)$$

In Equation (29) the terms  $c_k^T I_k^T$  and  $c_k^V I_k^V$  represent, respectively, the total cost of turbines and valves occurring only at the beginning of the investment, whereas  $E_y^P$  and  $W_y^S$  are the annual inflow cash due, respectively, to the energy production and reduction of leaked water. Moreover,  $Y$  is the total number of  $y$  years, assumed as 10 years, and  $\lambda$  is the discount rate (set as 5%). In order to evaluate the annual income resulting from the energy production, an energy unit selling price equal to 0.1 €/kWh was assumed. With regard to the cost of the valve, the model cost suggested by Garcia et al. (2019) [49] was adopted, according to which the total cost of PRVs is dependent on pipe diameter (Figure 12):

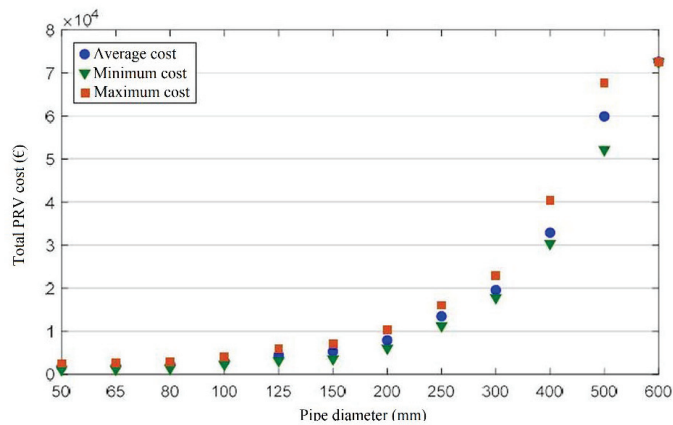


**Figure 12.** Total PRV cost depending on pipe diameter according to Garcia et al. (2019) [49].

With reference to the total cost of the turbines, since the analyzed turbine is a prototype, a function to properly model its cost is not actually available. Hence, in this study, the cost models of both a traditional turbine and a pump as turbine (PAT) (Figure 13) were alternatively used to carry out the optimization, since the effective cost model of the novel turbine is likely to comprise these two cost models. Among all the models presented in Figure 13, in this study the costs of the devices were evaluated according to the interpolations of experimental points presented by the authors in [50] (i.e., black dots for turbine unit costs and grey dots for PAT unit costs).

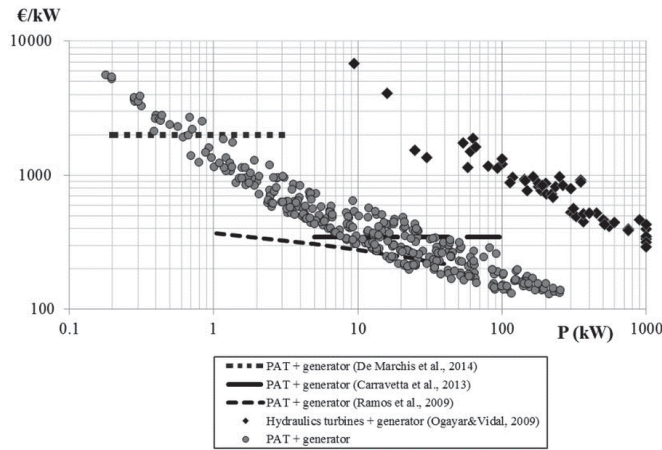


**Figure 13.** Unit cost per rated power of PATs and conventional turbines coupled to generators [50], compared to other literature cost models [51–54].

With regard to the annual income due to water saving ( $W_y^s$ ) in Equation (29), it was evaluated as the difference between the total volume of water leaked without and in presence of devices within the network [46,48]:

$$W_y^s = c_w \left( Q_l^0 \Delta t_d - Q_l^s \right) \tag{30}$$

The water unit cost  $c_w$  was fixed as  $0.3 \text{ €}/\text{m}^3$ , as representative of the analyzed case study area. According to the formulation proposed by Araujo et al. (2006) [55], the total leaked discharge in the network  $Q_l$  can be evaluated as the sum of the discharge leaked in all single nodes:

$$Q_l = \sum_{i=1}^n q_i^l = \sum_{i=1}^n f_i (H_i - z_i)^\beta \tag{31}$$

where  $\beta$  is an exponent depending on both the material and the shape of the orifice [56], which was set equal to 1.18, according to Araujo et al. (2006) [48,55]. With regard to  $f_i$ , it represents a leakage coefficient whose expression is following presented:

$$f_i = c \sum_{j=1}^{K_i} 0.5 L_{i,j} \tag{32}$$

where  $c$  is a coefficient equal to  $0.00001 \text{ L/s m}^{1+\beta}$  [48,55] and  $K_i$  is the set of nodes linked to the  $i$ -th node by a pipe with length as  $L_{i,j}$ .

#### 4.1.5. The Mathematical Model

The combination of all variables, objective function and linear/non-linear constraints presented in the previous sections results in the mathematical model in Equation (33).

Regarding the model in Equation (33),  $H_{k \text{ max}}$ , that is the upper bound of the variables head losses within the devices, was set as 200 m;  $p_{\text{min}}$  and  $p_{\text{max}}$  were set as 25 m and 150 m, respectively. Regarding the bounds of the impeller diameter of the turbines, the lower bound  $D_{\text{min}}$  was set as 50 mm, whereas the upper bound  $D_{\text{max}}$  varies for each pipe  $k$  and is equal to four times the diameter of the pipe itself. Finally, the upper bound of the variable discharges, which is  $Q_{\text{max}}$ , was set as 500 L/s, whereas  $\alpha_{\text{min}}$  and  $\alpha_{\text{max}}$  were assumed equal at 10% and 200%, respectively.

As in Morani et al. (2021) [46], two small feasibility tolerances ( $tol_k^H$ ,  $tol_i^Q$ ) were introduced within the momentum balance equation and mass continuity equation, respectively, in order to push the solver to achieve a solution. Such tolerances are small quantities ( $tol_k^H = 0.01$  m and  $tol_i^Q = 0.005$  L/s) and can be considered as acceptable as all other uncertainties affecting the accuracy of the problem (e.g., evaluation of end-used demands, use of Hazen Williams formula).

$$\begin{aligned}
 & \text{maximize} \\
 & I_k^T, I_k^V, \zeta_k \\
 & H_k^{T+}, H_k^{T-}, H_k^{V+}, H_k^{V-} \\
 & q_k^+, q_k^-, H_i, D, \alpha,
 \end{aligned}
 \quad
 \begin{aligned}
 NPV = & \sum_{k=1}^I \left( -c_k^T I_k^T - c_k^V I_k^V \right) + \sum_{y=1}^Y \frac{E_y^E + W_y^S}{(1+\lambda)^y} \\
 -tol_i^Q \leq & \sum_{k \in K_i} (q_k^+ + q_k^-)^{in} - \sum_{k \in K_i} (q_k^+ + q_k^-)^{out} - f_i P_i^\beta - q_i^d \leq tol_i^Q \\
 -tol_k^H \leq & H_i - H_j - r_k L_k - (H_k^{T+} - H_k^{T-}) - (H_k^{V+} - H_k^{V-}) \leq tol_k^H \\
 & 0 \leq q_k^+ \leq Q_{max} \zeta_k \\
 & 0 \leq q_k^- \leq Q_{max} (1 - \zeta_k) \\
 & 0 \leq H_k^{T+} \leq H_k \max \zeta_k \\
 & 0 \leq H_k^{T-} \leq H_k \max (1 - \zeta_k) \\
 & 0 \leq H_k^{V+} \leq H_k \max \zeta_k \\
 & 0 \leq H_k^{V-} \leq H_k \max (1 - \zeta_k) \\
 & D \geq D_{min} I_k^T \\
 & D \leq D_{max} I_k^T \\
 & \alpha \geq \alpha_{min} I_k^T \\
 & \alpha \leq \alpha_{max} I_k^T
 \end{aligned}
 \tag{33}$$

$$\begin{aligned}
 & \text{subject to} \\
 & Q_T = q_T D^2 \alpha \sqrt{g \left( H_k^{T+} + H_k^{T-} \right)} \\
 & \eta = 1 - (0.4) \left( \frac{75}{1000 D} \right)^{0.25} \left( \frac{5}{H_k^{T+} + H_k^{T-}} \right)^{0.1} \\
 & P_T = \gamma \left( H_k^{T+} + H_k^{T-} \right) Q_T \eta \eta_G \\
 & \frac{P_{min}}{\gamma} \leq (H_i - z_i) \leq \frac{P_{max}}{\gamma} \\
 & H_k^{T+} + H_k^{T-} \leq H_k \max I_k^T \\
 & H_k^{V+} + H_k^{V-} \leq H_k \max I_k^V \\
 & Q_T = (q_k^+ + q_k^-) I_k^T \\
 & I_k^T + I_k^V \leq 1 \\
 & 0 \leq I_k^T \leq 1 \\
 & 0 \leq I_k^V \leq 1 \\
 & 0 \leq \zeta_k \leq 1 \\
 & (I_k^T, I_k^V, \zeta_k) \in \mathbb{Z} \quad (H_k^{T+}, H_k^{T-}, H_k^{V+}, H_k^{V-}) \in \mathbb{R}, \\
 & (q_k^+, q_k^-, Q_T, P_T, \eta_T, D, \alpha) \in \mathbb{R} \\
 & \forall i, j = 1 \dots n, \quad \forall k = 1 \dots l
 \end{aligned}$$

The total number of variables amounts to 42,617, whereas the sum of both linear and non-linear constraints is accounted for as 51,149.

#### 4.2. Optimization Results

Table 2 shows the results of the optimization obtained by using the cost models presented in Section 4.1.4. In Table 2, (I) and (II) refer to results obtained when a traditional

turbine and a PAT cost model, respectively, are employed to evaluate the cost of the installed turbines.

**Table 2.** Results of the optimization procedure using two different literature cost models.

	NPV (€)	N° Turbines (-)	N° Valves (-)	Av. Power (kW)	Water Saving (m <sup>3</sup> /day)	Invest. Cost (€)
(I) <sup>1</sup>	7,169,083	5	4	68	8507	482,298
(II) <sup>1</sup>	11,942,920	6	1	65	13,673	55,786

<sup>1</sup> (I): traditional turbine + generator cost model; (II) PAT + generator cost model.

When the turbine cost is evaluated according to the traditional turbine cost model (see (I)), the optimization solver installs a number of turbines and valves as 5 and 4, respectively, with an investment cost of EUR 482,298.

The resulting average produced power was accounted for as 68 kW, and the amount of water saved per day is equal to 8507 m<sup>3</sup>. When the literature PAT cost model is, instead, employed to evaluate the cost of the installed turbines (see (II)), the solver selects more turbines than valves (i.e., 6 against 1—Figure 14), since the installation of valves could not be convenient compared to turbines, especially where the pipe diameters are large. However, compared to the results in case (I), the increased value of NPV in case (II) (i.e., EUR 11,942,920) is due to the larger water savings, which is equal to 13,673 m<sup>3</sup> per day, and smaller investment costs (EUR 55,786). Regarding the power production, it is quite similar between the two cases, obtaining around 65 kW.

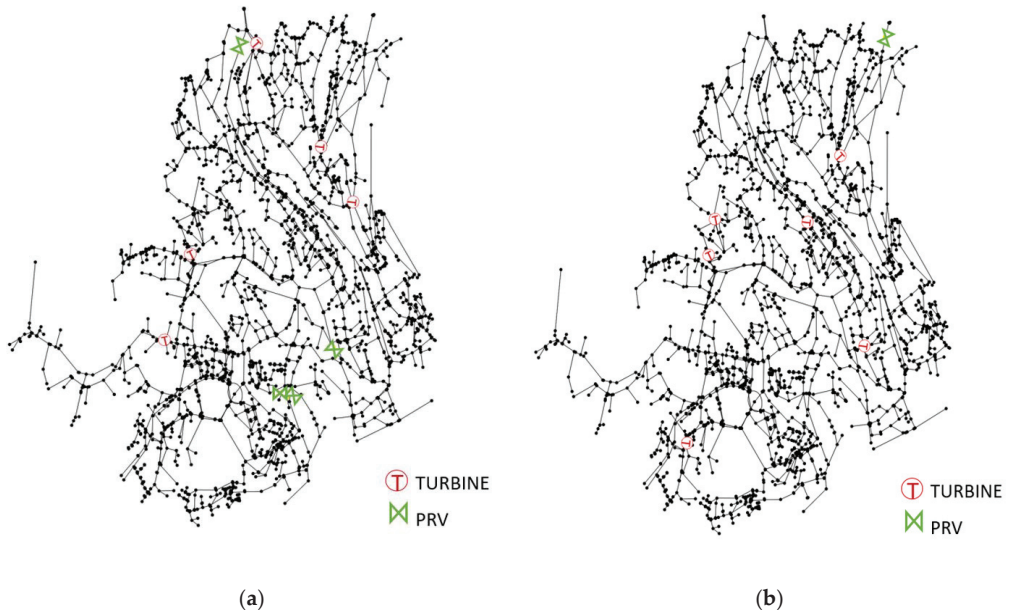


**Figure 14.** Device positions within the case study WDN according to the results in (I) (a) and (II) (b).

The turbines are installed in both the cases in the middle region of the network, whereas the valves are installed in the peripheral area, where the water saving potential is large but the recoverable energy is contained.

Tables 3 and 4 show the results in terms of turbine geometry and operating conditions at BEP for case (I) and case (II), respectively. With reference to N, it is the rotational speed resulting from the optimal diameter (D) and head drop ( $H_T$ ) according to Equation (6).

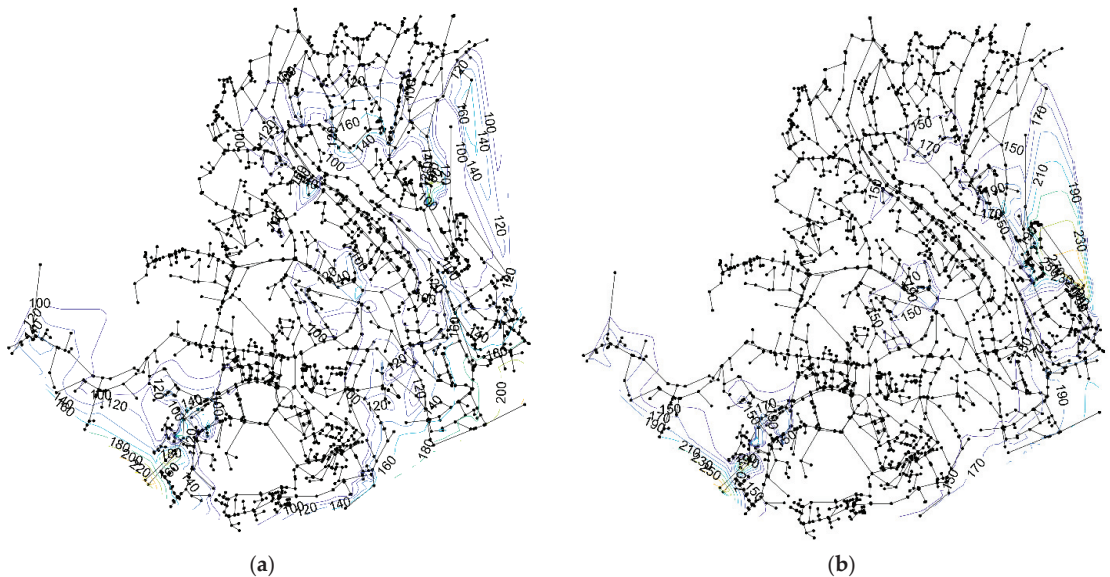
**Table 3.** Turbine geometry resulting from case (I).

	D (mm)	H <sub>T</sub> (m)	Q <sub>T</sub> (L/s)	N (rpm)	η <sub>T</sub> (%)
Link 89	187	52	11	2748	75
Link 795	540	50	91	933	81
Link 1358	500	5	25	319	75
Link 1375	940	13.5	144	278	80
Link 2485	165	161	15	5480	77

**Table 4.** Turbine geometry resulting from case (II).

	D (mm)	H <sub>T</sub> (m)	Q <sub>T</sub> (L/s)	N (rpm)	η <sub>T</sub> (%)
Link 8	685	5.95	51	254	77
Link 14	70	50	1.6	7200	68
Link 108	170	119	14	4573	76
Link 1241	535	41.5	82	858	80
Link 1242	747	11.5	84	323	79
Link 2485	220	122.5	24	3585	78

Figure 15a shows the pressure contour plots according to case (I) when devices are installed within the network: the installation results in a significant reduction in the overall excess pressure when compared with the scenario without installed devices (Figure 15b). The same is valid for case (II), whose pressure contour plot is presented in Appendix A (Figure A1).

**Figure 15.** Pressure contour plot when devices are installed (a) and without performing any pressure control strategy (b) for case (I).

The produced power, as well as the head drop within the installed devices, for case (I) is shown in Figure 16a,b, respectively. According to Figure 16b, the reduction in head resulting from the device installation is significant, even reaching a value of 160 m. The same figure for case (II) is presented in Appendix A (Figure A2).

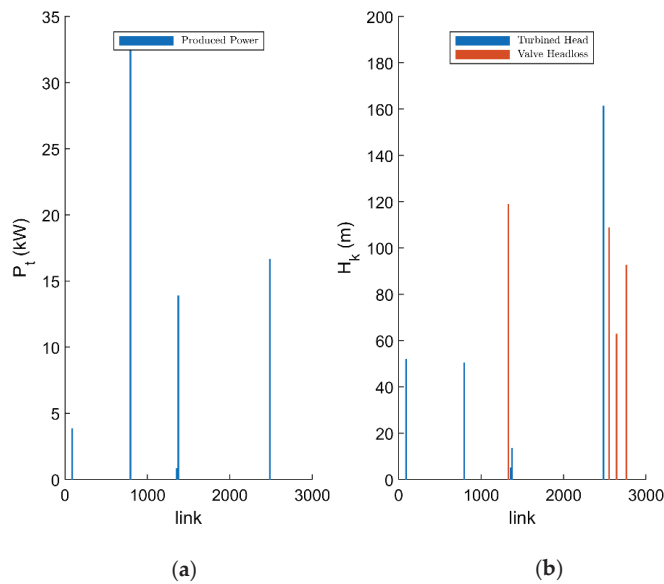


**Figure 16.** Produced power of the installed turbines (a) and head drop within the devices (b) resulting from case (I).

## 5. Conclusions

In this paper a new centrifugal micro-turbine (CMT) was investigated in terms of performance and design. Based on a CFD modeling coupled with experimental tests on a turbine prototype, the unstable phenomena affecting the turbine components during its operation have been investigated in detail. In particular, the velocity and pressure profiles within turbine components were presented for different operating conditions. According to the results, the difference in terms of pressure drop at inlet and outlet of the rotor is significantly small, except for rotational speeds greater than 1850 rpm. According to the velocity profiles at the runners, high flow acceleration was detected from the leading edge to the trailing edge, followed by a significant flow deceleration due to an increase in static pressure. Moreover, the degree of flow deceleration was lower for high rotational speeds, at which the internal losses were therefore lower. A maximum velocity value of 12 m/s was detected in the region close to the leading edge of the rotating blade, whereas the minimum velocity of around 1 m/s is presented at the right side of the vane. However, the validation of the CFD numerical simulation was proven by a good agreement with experimental data in terms of global parameters. Based on affinity laws and the experimental tests, some relationships were obtained to design the centrifugal turbine at its best efficiency point. Finally, based on this new centrifugal micro-turbine design, a real water distribution network (WDN), in the Funchal system, was assumed as the case study and an optimization procedure was carried out in order to search for an optimal scale design of turbines, as well as an optimal location of such designed turbines together with pressure reducing valves (PRV), in order to maximize the energy production and minimize the leakage water volume. Due to the lack of information about the purchase cost of such a new centrifugal turbine, two different literature cost models were assumed to evaluate the investment cost: the effective solution will definitely comprise the two obtained solutions. According to the results, the use of a PAT cost model pushes the solver to install more turbines than valves. Moreover, compared to the solution resulting from the use of a traditional turbine cost model, when the turbine cost is evaluated according to a literature PAT cost model, the resulting water savings is large (i.e., 13,673 m<sup>3</sup> per day against 8507 m<sup>3</sup> per day) and the investment cost is significantly more confined (EUR 55,786 against EUR 482,298), where



the power production has been accounted for at around 65 kW. However, in both analyzed cases, the turbines are installed in the middle part of the network, where the available energy is significant, whereas the valves are mainly located in the peripheral area where valves represent a more viable solution due to the limited available potential energy.

**Author Contributions:** Conceptualization, H.M.R., M.S. and M.C.M.; methodology, H.M.R., I.G., R.S.S., O.F. and A.C.; validation, I.G., M.S. and M.C.M.; formal analysis, H.M.R., O.F. and A.C.; investigation, I.G., H.M.R. and A.C.; resources, R.S.S., M.S. and M.C.M.; writing—original draft preparation, M.S. and M.C.M.; writing—review and editing, H.M.R., O.F. and A.C.; supervision, H.M.R. and A.C.; funding acquisition, H.M.R. and A.C. All authors have read and agreed to the published version of the manuscript.

**Funding:** This research is supported by the project REDAWN (Reducing Energy Dependency in Atlantic Area Water Networks) EAPA\_198/2016 from INTERREG ATLANTIC AREA PROGRAMME 2014–2020.

**Institutional Review Board Statement:** Not applicable.

**Informed Consent Statement:** Not applicable.

**Data Availability Statement:** Not applicable.

**Acknowledgments:** The authors want to thank the project REDAWN (Reducing Energy Dependency in Atlantic Area Water Networks) EAPA\_198/2016 from INTERREG ATLANTIC AREA PROGRAMME 2014–2020 and CERIS (CEHIDRO-IST).

**Conflicts of Interest:** The authors declare no conflict of interest.

### List of Symbols

$\alpha$	Runner thickness
$\alpha_{\max}$	Maximum runner thickness
$\alpha_{\min}$	Minimum runner thickness
$\beta$	Leakage exponent
$\gamma$	Fluid specific weight
$\delta_w^+$	Wall lift-off
$\zeta_k$	Binary variable of flow direction through the k-th link
$\lambda$	Discount rate
$\eta$	Turbine efficiency
$\mu$	Flow viscosity
$\rho$	Flow density
$\tau$	Non-dimensional torque
$\varphi$	Non-dimensional discharge
$\psi$	Non-dimensional head drop
$C_k$	Roughness coefficient of the k-th link
$c_k^T$	Total cost of turbine
$c_k^V$	Total cost of valve
$c_w$	Water unit cost
$D$	Turbine diameter
$D_k$	Diameter of the k-th pipe
$D_{\max}$	Maximum turbine diameter
$D_{\min}$	Minimum turbine diameter
$E_y^P$	Energy income
$F$	External force
$f_i$	Leakage coefficient at the i-th node
$g$	Gravity acceleration
$H$	Head drop
$H_i$	Head at i-th node

$H_k^{\max}$	Maximum head drop within the devices
$H_k^T$	Head drop within turbine
$H_k^{T+}$	Positive component of head drop within turbine
$H_k^{T-}$	Negative component of head drop within turbine
$H_k^V$	Head drop within valve
$H_k^{V+}$	Positive component of head drop within valve
$H_k^{V-}$	Negative component of head drop within valve
$I_k^T$	Binary variable for turbine location
$I_k^V$	Binary variable for valve location
$i, j$	Indices for nodes
$K_i$	Set of nodes linked to the $i$ -th node
$k$	Index for links
$L_{i,j}$	Length of pipe connecting nodes $i$ and $j$
$L_k$	Length of the $k$ -th link
$l$	Number of links
$N$	Rotational speed
NPV	Net present value
$n$	Number of nodes
$n_T$	Experimental coefficient
$P_h$	Hydraulic power
$P_T$	Produced power
$p$	Pressure
$P_{\max}$	Maximum allowable pressure
$P_{\min}$	Minimum allowable pressure
$Q$	Experimental discharge
$Q_l$	Total leaked discharge
$Q_T$	Discharge through the turbine
$Q_k$	Discharge through the $k$ -th link
$Q_{\max}$	Maximum discharge through the $k$ -th link
$q_i^d$	Demand of the $i$ -th node
$q_i^l$	Leaked discharge at the $i$ -th node
$q_k^+$	Positive component of discharge through $k$ -th link
$q_k^-$	Negative component of discharge through $k$ -th link
$q_T$	Experimental coefficient
$r_k$	Resistance term at the $k$ -th link
$T$	Torque
$V$	Flow velocity
$W_y^s$	Water saving
$Y$	Number of years
$y$	Index for years
$z$	Node elevation

Appendix A

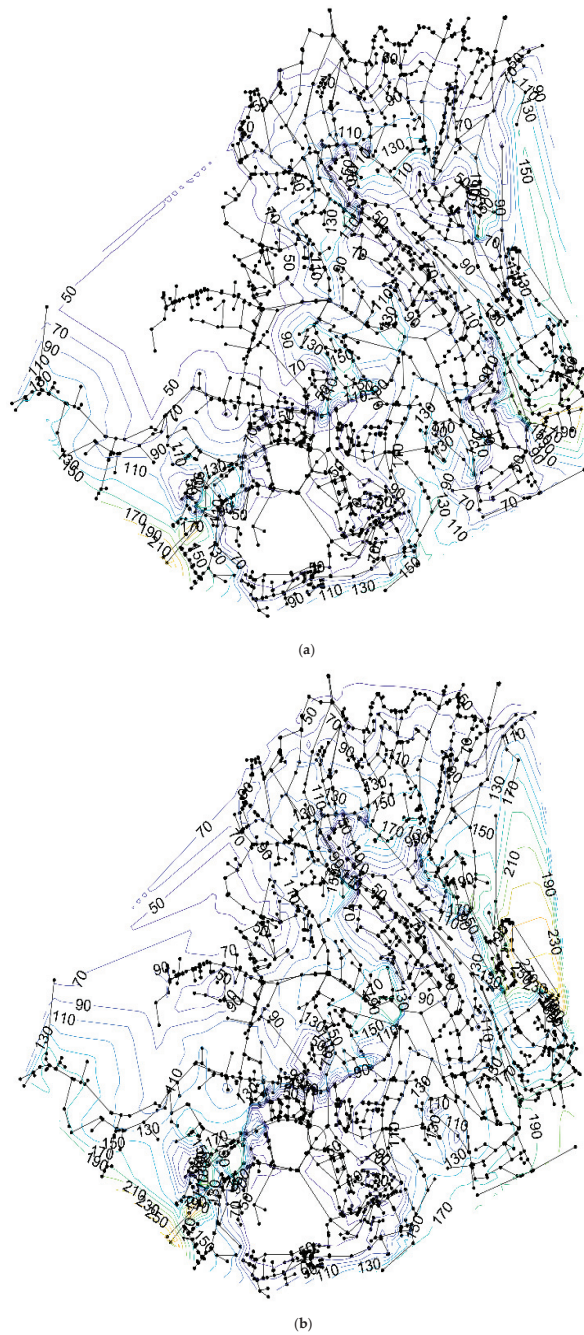


**Figure A1.** Pressure contour plot when devices (CMT and PRV) are installed (a) and without performing any pressure control strategy (b) for case (II).

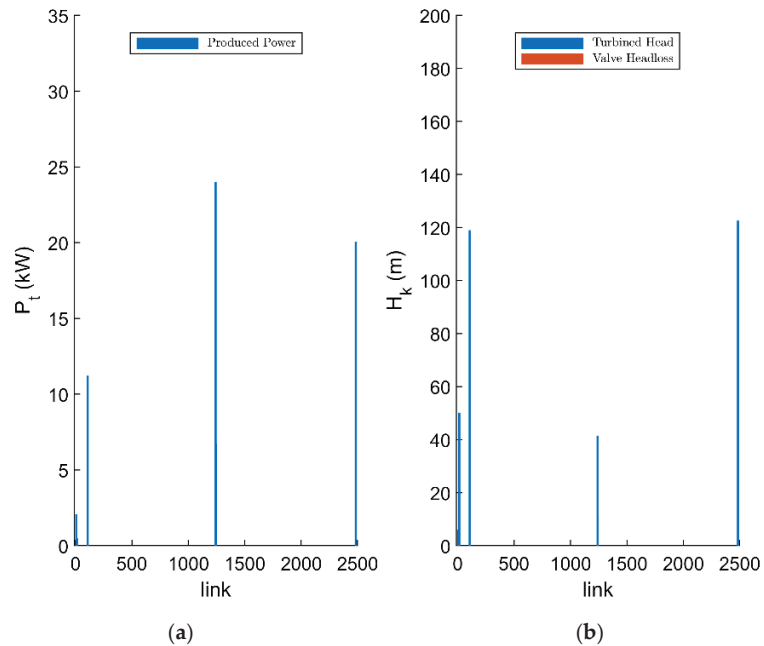


**Figure A2.** Produced power of the installed turbines (a) and head drop within the devices (b) resulting from case (II).

## References

- Zhu, D.; Tao, R.; Xiao, R.; Pan, L. Solving the runner blade crack problem for a Francis hydro-turbine operating under condition-complexity. *Renew. Energy* **2020**, *149*, 298–320. [\[CrossRef\]](#)
- Morani, M.C.; Carravetta, A.; Del Giudice, G.; McNabola, A.; Fecarotta, O. A Comparison of Energy Recovery by PATs against Direct Variable Speed Pumping in Water Distribution Networks. *Fluids* **2018**, *3*, 41. [\[CrossRef\]](#)
- Carravetta, A.; Del Giudice, G.; Fecarotta, O.; Gallagher, J.; Morani, M.C.; Ramos, H.M. The Potential Energy, Economic & Environmental Impacts of Hydro Power Pressure Reduction on the Water-Energy-Food Nexus. *J. Water Resour. Plan. Manag.* **2022**, accepted.
- Pasche, S.; Gallaire, F.; Avellan, F. Origin of the synchronous pressure fluctuations in the draft tube of Francis turbines operating at part load conditions. *J. Fluids Struct.* **2019**, *86*, 13–33. [\[CrossRef\]](#)
- Morani, M.C.; Carravetta, A.; Fecarotta, O.; McNabola, A. Energy transfer from the freshwater to the wastewater network using a PAT-equipped turbopump. *Water* **2020**, *12*, 38. [\[CrossRef\]](#)
- Thapa, B.S.; Dahlhaug, O.G.; Thapa, B. Flow measurements around guide vanes of Francis turbine: A PIV approach. *Renew. Energy* **2018**, *126*, 177–188. [\[CrossRef\]](#)
- Gautam, S.; Neopane, H.P.; Acharya, N.; Chitrakar, S.; Thapa, B.S.; Zhu, B. Sediment erosion in low specific speed francis turbines: A case study on effects and causes. *Wear* **2020**, *442–443*, 203152. [\[CrossRef\]](#)
- Tiwari, G.; Kumar, J.; Prasad, V.; Patel, V.K. Utility of CFD in the design and performance analysis of hydraulic turbines—A review. *Energy Rep.* **2020**, *6*, 2410–2429. [\[CrossRef\]](#)
- Trivedi, C.; Gandhi, B.; Michel, C.J. Effect of transients on Francis turbine runner life: A review. *J. Hydraul. Res.* **2013**, *51*, 121–132. [\[CrossRef\]](#)
- Goyal, R.; Gandhi, B.K. Review of hydrodynamics instabilities in Francis turbine during off-design and transient operations. *Renew. Energy* **2018**, *116*, 697–709. [\[CrossRef\]](#)
- Nicolet, C. Hydroacoustic modelling and numerical simulation of unsteady operation of hydroelectric systems. *Ec. Polytech. Fédérale Lausanne* **2017**. [\[CrossRef\]](#)
- Goyal, R.; Trivedi, C.; Gandhi, B.K.; Cervantes, M. Numerical Simulation and Validation of a High Head Model Francis Turbine at Part Load Operating Condition. *J. Inst. Eng. (India) Ser. C* **2018**, *99*, 557–570. [\[CrossRef\]](#)
- Bergan, C.; Goyal, R.; Cervantes, M.J.; Dahlhaug, O.G. Experimental Investigation of a High Head Model Francis Turbine During Steady-State Operation at Off-Design Conditions. In *IOP Conference Series: Earth and Environmental Science*; IOP Publishing: Bristol, UK, 2016.
- Trivedi, C.; Cervantes, M.J.; Gandhi, B.K.; Dahlhaug, O.G. Experimental and numerical studies for a high head Francis turbine at several operating points. *J. Fluids Eng. Trans. ASME* **2013**, *135*, 111102. [\[CrossRef\]](#)

15. Zhang, F.; Lowys, P.; Houdeline, J.; Guo, X.; Hong, P.; Laurant, Y. Pump-turbine Rotor-Stator Interaction Induced Vibration: Problem Resolution and Experience. In *IOP Conference Series: Earth and Environmental Science*; IOP Publishing: Bristol, UK, 2021.
16. Keck, H.; Sick, M. Thirty years of numerical flow simulation in hydraulic turbomachines. *Acta Mech.* **2008**, *201*, 211–229. [[CrossRef](#)]
17. Favrel, A.; Junior, J.G.P.; Landry, C.; Müller, A.; Yamaishi, K.; Avellan, F. Dynamic modal analysis during reduced scale model tests of hydraulic turbines for hydro-acoustic characterization of cavitation flows. *Mech. Syst. Signal Process.* **2019**, *117*, 81–96. [[CrossRef](#)]
18. Scarlett, G.T.; Viola, I.M. Unsteady hydrodynamics of tidal turbine blades. *Renew. Energy* **2020**, *146*, 843–855. [[CrossRef](#)]
19. Luna-Ramírez, A.; Campos-Amezcuca, A.; Dorantes-Gómez, O.; Mazur-Czerwicz, Z.; Muñoz-Quezada, R. Failure analysis of runner blades in a Francis hydraulic turbine—Case study. *Eng. Fail. Anal.* **2016**, *59*, 314–325. [[CrossRef](#)]
20. Khare, R.; Prasad, V.; Kumar, S. Cfd Approach for Flow Characteristics of Hydraulic Francis Turbine. *Int. J. Eng. Sci.* **2010**, *2*, 3824–3831.
21. Tiwari, G.; Prasad, V.; Shukla, S.; Patel, V.K. Hydrodynamic analysis of a low head prototype Francis turbine for establishing an optimum operating regime using CFD. *J. Mech. Eng. Sci.* **2020**, *14*, 6625–6641. [[CrossRef](#)]
22. Kerikous, E.; Thévenin, D. Optimal shape of thick blades for a hydraulic Savonius turbine. *Renew. Energy* **2019**, *134*, 629–638. [[CrossRef](#)]
23. Ma, Z.; Zhu, B.; Rao, C.; Shanguan, Y. Comprehensive Hydraulic Improvement and Parametric Analysis of a Francis Turbine Runner. *Energies* **2019**, *12*, 307. [[CrossRef](#)]
24. Pérez, L.C.A.; Acosta, M.J.A.; Yepes, C.A.P. CFD simulation data of a pico-hydro turbine. *Data Brief* **2020**, *33*, 106596. [[CrossRef](#)] [[PubMed](#)]
25. Chen, J.; Engeda, A. Standard module hydraulic technology: A novel geometrical design methodology and analysis for a low-head hydraulic turbine system, Part I: General design methodology and basic geometry considerations. *Energy* **2020**, *196*, 117151. [[CrossRef](#)]
26. Bai, B.; Zhang, L.; Guo, T.; Liu, C. Analysis of Dynamic Characteristics of the Main Shaft System in a Hydro-turbine Based on ANSYS. *Procedia Eng.* **2012**, *31*, 654–658. [[CrossRef](#)]
27. Tog, R.A.; Tousi, A.; Tourani, A. Comparison of turbulence methods in CFD analysis of compressible flows in radial turbomachines. *Aircr. Eng. Aerosp. Technol.* **2008**, *80*, 657–665.
28. Fluent, A. *Ansys Fluent Theory Guide*; ANSYS Inc.: Canonsburg, PA, USA, 2013.
29. Chen, B.; Yuan, X. Advanced Aerodynamic Optimization System for Turbomachinery. *J. Turbomach.* **2008**, *130*, 021005. [[CrossRef](#)]
30. Biesinger, T.; Cornelius, C.; Rube, C.; Braune, A.; Campregher, R.; Godin, P.G.; Schmid, G.; Zori, L. Unsteady CFD Methods in a Commercial Solver for Turbomachinery Applications. In Proceedings of the ASME Turbo Expo 2010: Power for Land, Sea, and Air, Glasgow, UK, 14–18 June 2010; pp. 2441–2452.
31. Wang, J.-F.; Piechna, J.; Müller, N. A Novel Design of Composite Water Turbine Using CFD. *J. Hydrodyn.* **2012**, *24*, 11–16. [[CrossRef](#)]
32. González, J.; Oro, J.M.F.; Argüelles-Díaz, K.M.; Santolaria, C. Flow analysis for a double suction centrifugal machine in the pump and turbine operation modes. *Int. J. Numer. Methods Fluids* **2009**, *61*, 220–236. [[CrossRef](#)]
33. Bogdanović-Jovanović, J.B.; Milenković, D.R.; Svrkota, D.M.; Bogdanović, B.; Spasić, Z.T. Pumps used as turbines: Power recovery, energy efficiency, CFD analysis. *Therm. Sci.* **2014**, *18*, 1029–1040. [[CrossRef](#)]
34. Fecarotta, O.; Messa, G.V.; Pugliese, F. Numerical assessment of the vulnerability to impact erosion of a pump as turbine in a water supply system. *J. Hydroinformatics* **2020**, *22*, 691–712.
35. Morros, C.S.; Oro, J.M.F.; Díaz, K.M.A. Numerical modelling and flow analysis of a centrifugal pump running as a turbine: Unsteady flow structures and its effects on the global performance. *Int. J. Numer. Methods Fluids* **2011**, *65*, 542–562. [[CrossRef](#)]
36. Barrio, R.M.; Fernández, J.; Blanco, E.F.; Parrondo, J.L.; Marcos, A. Performance characteristics and internal flow patterns in a reverse-running pump–turbine. *Proc. Inst. Mech. Eng. Part C J. Mech. Eng. Sci.* **2011**, *226*, 695–708. [[CrossRef](#)]
37. Dickinson, E.; Ekström, H.; Fontes, E. COMSOL Multiphysics. *Electrochem. Commun.* **2014**, *40*, 71–74. [[CrossRef](#)]
38. Georgescu, A.-M.; Georgescu, S.-C.; Bernad, S.I.; Cosoiu, C.I. Comsol Multiphysics versus Fluent: 2D Numerical Simulation of the Stationary Flow around a Blade of the Achard Turbine. *Sci. Bull. Politeh. Univ. Timis. Trans. Mech.* **2007**, *52*, 13–21.
39. AutoCAD Basics. In Construction Detailing for Interior Design. 2020. Available online: <https://www.autodesk.it> (accessed on 25 December 2021).
40. Simão, M.; Mora-Rodriguez, J.; Ramos, H. Computational dynamic models and experiments in the fluid–structure interaction of pipe systems. *Can. J. Civ. Eng.* **2016**, *43*, 60–72. [[CrossRef](#)]
41. Speziale, C.G. On nonlinear K-1 and K-ε models of turbulence. *J. Fluid Mech.* **1987**, *178*, 459–475. [[CrossRef](#)]
42. Gresho, P. Incompressible Fluid Dynamics: Some Fundamental Formulation Issues. *Annu. Rev. Fluid Mech.* **1991**, *23*, 413–453. [[CrossRef](#)]
43. Simão, M.; Besharat, M.; Carravetta, A.; Ramos, H.M. Flow Velocity Distribution Towards Flowmeter Accuracy: CFD, UDV, and Field Tests. *Water* **2018**, *10*, 1807. [[CrossRef](#)]
44. Yang, J.; Preidikman, S.; Balaras, E. A Strong Coupling Scheme for Fluid-Structure Interaction Problems in Viscous Incompressible Flows. In Proceedings of the International Conference on Computational Methods for Coupled Problems in Science and Engineering, Santorini Island, Greece, 25–28 May 2005.
45. Vigerske, S.; Gleixner, A. SCIP: Global optimization of mixed-integer nonlinear programs in a branch-and-cut framework. *Optim. Methods Softw.* **2018**, *33*, 563–593. [[CrossRef](#)]
46. Morani, M.C.; Carravetta, A.; D’ambrosio, C.; Fecarotta, O. A new mixed integer non-linear programming model for optimal PAT and PRV location in water distribution networks. *Urban Water J.* **2021**, *18*, 394–409. [[CrossRef](#)]
47. Morani, M.C.; Carravetta, A.; D’ambrosio, C.; Fecarotta, O. A New Preliminary Model to Optimize PATs Location in a Water Distribution Network. *Environ. Sci. Proc.* **2020**, *2*, 57. [[CrossRef](#)]

48. Fecarotta, O.; McNabola, A. Optimal Location of Pump as Turbines (PATs) in Water Distribution Networks to Recover Energy and Reduce Leakage. *Water Resour. Manag.* **2017**, *31*, 5043–5059. [[CrossRef](#)]
49. García, J.M.; Salcedo, C.; Saldarriaga, J. Minimization of Water Losses in WDS through the Optimal Location of Valves and Turbines: A Comparison between Methodologies. In Proceedings of the World Environmental and Water Resources Congress 2019: Hydraulics, Waterways, and Water Distribution Systems Analysis—Selected Papers from the World Environmental and Water Resources Congress 2019, Pittsburgh, PA, USA, 19–23 May 2019. [[CrossRef](#)]
50. Novara, D.; Carravetta, A.; McNabola, A.; Ramos, H.M. Cost Model for Pumps as Turbines in Run-of-River and In-Pipe Microhydropower Applications. *J. Water Resour. Plan. Manag.* **2019**, *145*, 04019012. [[CrossRef](#)]
51. De Marchis, M.; Fontanazza, C.M.; Freni, G.; Messineo, A.; Milici, B.; Napoli, E.; Notaro, V.; Puleo, V.; Scopa, A. Energy recovery in water distribution networks. Implementation of pumps as turbine in a dynamic numerical model. *Procedia Eng.* **2014**, *70*, 439–448. [[CrossRef](#)]
52. Carravetta, A.; Del Giudice, G.; Fecarotta, O.; Ramos, H. PAT Design Strategy for Energy Recovery in Water Distribution Networks by Electrical Regulation. *Energies* **2013**, *6*, 411–424. [[CrossRef](#)]
53. Ramos, H.M.; Borga, A.; Simão, M. New design solutions for low-power energy production in water pipe systems. *Water Sci. Eng.* **2009**, *2*, 69–84.
54. Ogayar, B.; Vidal, P.G. Cost determination of the electro-mechanical equipment of a small hydro-power plant. *Renew. Energy* **2009**, *34*, 6–13. [[CrossRef](#)]
55. Araujo, L.S.; Ramos, H.M.; Coelho, S.T. Pressure Control for Leakage Minimisation in Water Distribution Systems Management. *Water Resour. Manag.* **2006**, *20*, 133–149. [[CrossRef](#)]
56. Greyvenstein, B.; Van Zyl, J.E. An experimental investigation into the pressure—Leakage relationship of some failed water pipes. *J. Water Supply Res. Technol. Aqua* **2007**, *56*, 117–124. [[CrossRef](#)]





Article

# Optimizing the Water Ecological Environment of Mining Cities in the Yangtze River Economic Belt Using the Cloud Model, CV-TOPSIS, and Coupling Coordination Degree

Ran Wang <sup>1,2</sup>, Hao Lin <sup>2</sup>, Jinhua Cheng <sup>1,2,\*</sup>, Zixi Xu <sup>2</sup>, Haoying Feng <sup>2</sup> and Yameng Tang <sup>2</sup>

<sup>1</sup> School of Economic & Management, China University of Geosciences, Wuhan 430074, China; wangran2cug@163.com

<sup>2</sup> Research Center of Resource and Environmental Economics, China University of Geosciences, Wuhan 430074, China; linhao2020@126.com (H.L.); xuzixi163@163.com (Z.X.); haoyingfeng@cug.edu.cn (H.F.); tangyameng0413@163.com (Y.T.)

\* Correspondence: chengjinhua100@126.com; Tel.: +86-139-7112-8538

**Abstract:** The Yangtze River Economic Belt (YREB) is the core region for the security of mineral resources in China and is a strategic water source containing rich water resources. Coordinating the security of mineral resources and water resources in the YREB is a key problem. Establishing and optimizing the water ecological environment (WEE) is crucial for addressing this problem in mining cities, which are the main bases for the supply of mineral resources. This study applies the cloud model, CV-TOPSIS, the standard deviation ellipse, and the coupling coordination degree model to evaluate the WEE and the coordinated development state, and to optimize the WEE. The results show that: (1) the WEE of mining cities in the YREB is generally good; (2) the protection of WEE in most mining cities has achieved significant results recently, and the results in the downstream are more remarkable than those in the mid-upstream; (3) the coordinated development of WEE in regenerative mining cities is better than that of mature and declining cities; and (4) most mining cities still belong to the lagging type of water environment (heavy metal pollution has been better treated and the threat of water ecological security caused by heavy metal pollution is low). This study suggests improvements to the sewer system, promotes WEE management in the mid-upstream, and propels the transformational development of mature and declining mining cities in advance.

**Keywords:** Yangtze river economic belt; mining city; water ecological environment; cloud model; CV-TOPSIS; coupling coordination degree model

**Citation:** Wang, R.; Lin, H.; Cheng, J.; Xu, Z.; Feng, H.; Tang, Y. Optimizing the Water Ecological Environment of Mining Cities in the Yangtze River Economic Belt Using the Cloud Model, CV-TOPSIS, and Coupling Coordination Degree. *Int. J. Environ. Res. Public Health* **2022**, *19*, 2469. <https://doi.org/10.3390/ijerph19042469>

Academic Editors: Roberto Alonso González Lezcano, Francesco Nocera, Rosa Giuseppina Caponetto and Paul B. Tchounwou

Received: 23 November 2021

Accepted: 14 February 2022

Published: 21 February 2022

**Publisher's Note:** MDPI stays neutral with regard to jurisdictional claims in published maps and institutional affiliations.



**Copyright:** © 2022 by the authors. Licensee MDPI, Basel, Switzerland. This article is an open access article distributed under the terms and conditions of the Creative Commons Attribution (CC BY) license (<https://creativecommons.org/licenses/by/4.0/>).

## 1. Introduction

The Yangtze River Economic Belt (YREB) has become a major national strategic development area in China. The YREB accounts for more than 40% of the population and gross domestic product (GDP), and approximately 40% of total imports and exports in China. The YREB, which integrates mountains, rivers, forests, farmland, and lakes, has a prominent position in the ecological environment, and is an important ecological treasure-house in China. Additionally, it is a strategic and extremely rich water resource, and an important ecological safety barrier area, with soil and water conservation, and flood regulation and storage.

The report of the 19th Party Congress proposed a coordinated regional development strategy for “grasping great protection and not engaging in great development” to promote the development of the YREB [1]. The ecological environment of the YREB can only be optimized, and cannot be allowed to deteriorate. Water ecological environment (WEE) protection has become an overarching strategic issue with regard to the sustainable development of the YREB. However, due to the influence of the traditional economic development path [2], WEE in the YREB remains severe [3].



Meanwhile, the YREB is rich in mineral resources, and the exploitation and utilization of these resources are of great significance to the security of China's mineral resources. Copper, tungsten, tin, and antimony account for 65.9%, 86.15%, 71.45%, and 88.06%, respectively, of the strategic production of metallic ore in the YREB in 2016. Compared with the reserve ratio, their mining intensity is relatively high, especially antimony; the mining intensity of iron, aluminum, and gold is moderate (Figure 1).

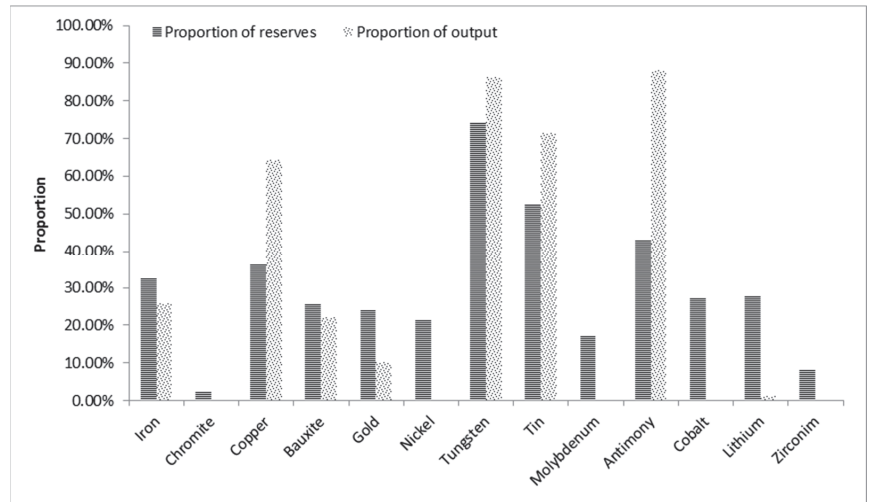


**Figure 1.** Proportion of reserves and output of strategic metal minerals in the YREB in 2016.

There are 98 mining cities in the YREB, which are faced with prominent environmental problems [4]. The quality of the aquatic environment of mining cities in the YREB is related to their own healthy economic and social development, and has a vital impact on the entire Yangtze River basin and the country. Mining cities should take the lead in “grasping great protection and not engaging in great development”. Therefore, evaluating and optimizing the WEE of mining cities in the YREB is crucial to achieve high-quality development.

The contribution of this study is mainly reflected in three aspects. First, an index system for water ecological environment is constructed, which conforms to the characteristics of mining cities in the YREB. Second, CV-TOPSIS, cloud model, a standard deviation ellipse model, and a coupling coordination model are used to evaluate and optimize WEE in mining cities in the YREB. Third, the diverse characteristics of WEE in mining cities are analyzed from different timescales, spaces, and stages. The findings of this study are important for the protection of WEE and economic development of mining cities in the YREB, while providing an informative reference for policy makers.

## 2. Literature Review

Existing related research mainly focuses on evaluating the water environment and the ecological environment quality. Research on the water environment quality is relatively mature, including the evaluation of key indices and a comprehensive index [5,6]. The water environment comprises spaces surrounding people or surrounding water bodies, and it can directly or indirectly affect human life and development [7]. Dos et al. (2018) selected the concentration of pollutants, such as chemical oxygen demand (COD) and ammonia nitrogen ( $\text{NH}_4\text{-N}$ ), as the key indices for evaluating water environmental quality [8]. Avila et al. (2018) regarded the quantity of *Escherichia coli* as an indicator of fresh water quality, and believed that the growth in the quantity of *Escherichia coli* increases the risk of disease [9]. Li et al. (2011) explored the water environment quality using the proportion of water quality sections in the basin, such as the proportion of water above class III (inclusive), and inferior

class V water quality [10]. The calculation of a composite index based on the construction of an index system has also been applied in many studies [11–13], and pollutants, such as COD, NH<sub>4</sub>-N, DO, and TN, have been considered in the literature [14–16].

With the introduction of the “five-in-one” strategy for ecological civilization, environmental protection has been raised to unprecedented heights. Recently, studies on ecological and environmental protection have increased significantly [17,18], including studies related to WEE protection. Water ecosystems support a wide range of organisms, including bacteria, fungi, algae, plants, invertebrates, and fish [19]. Zuo et al. (2021) selected total water resources per capita, waste water discharge per 10,000 yuan of GDP, sewage treatment rate, and other indicators for constructing China’s provincial ecological civilization evaluation index system [20]. Liu et al. (2018) selected total water resources per capita, waste water discharge, and other indicators for building an ecological environment assessment system [21]. Li et al. (2021) selected industrial wastewater emissions per CNY 100 million GDP, industrial SO<sub>2</sub> emissions per CNY 100 million GDP, and smoke and dust emissions per CNY 100 million GDP as the indicators for environmental evaluation [22].

The development of mining cities in the YREB has attracted attention in many studies [23–27], including sustainable development of the WEE. Li et al. (2016) studied the distribution characteristics of heavy metal pollution in a copper mining area of Yalong River through field sampling surveys, combing with GIS and remote sensing technology [28]. Zhang et al. (2011) and Dong et al. (2014) regarded the tributaries of the Yangtze River as the research subjects for evaluating heavy metal pollution [29,30]. Chen et al. (2021) considered Huainan city, which is one of the mining cities in YREB, as the research subject for evaluating the genesis and dominant processes of groundwater salinization [31].

The coupling coordination degree model has been used in various fields of ecological civilization construction [32–35]. Additionally, some scholars have chosen one aspect of the system to study. Li et al. (2021) and Yang et al. (2020) assessed the coupling and coordinated development state of the rural production–living–ecological function by considering the territorial space system as the research subject [10,36]. Zuo et al. (2021) evaluated the coordinated development state of the economy, society, and nature in the ecological civilization system [20]. Dong and Li (2021) evaluated the coupling coordination degree of “up-mid-downstream” of China’s wind power industry chain [37]. Therefore, this study analyzes the coordinated development of the WEE system of mining cities in the YREB by referring to the coupling coordination degree model. Additionally, the TOPSIS model is used.

The TOPSIS model selects a limited number of evaluation indicators based on the characteristics of the evaluation object. Subsequently, it chooses the ideal value for each indicator before calculating the distance between each solution and the ideal value. This allows it to determine the best solution by considering the strengths and weaknesses of each evaluation object [38–40]. Similar to TOPSIS, stable preference ordering towards ideal solutions (SPOTISs) and the characteristic object method (COMET) use reference objects to determine preferences for any alternatives. They mainly focus on being resistant to the rank reversal phenomenon [41,42]. The main advantage of the TOPSIS algorithm over other methods is that it makes full use of raw data. Additionally, its results accurately reflect the gaps between the various assessment options. Furthermore, the simpler data handling and ease of computational processing of TOPSIS makes it widely applicable [43–45]. Consequently, the model has been used extensively used in assessing river health [46–48].

Throughout the existing literature, the evaluation of the water environment has increasingly attracted the attention of scholars, and some research focusing on WEE protection of the provinces and cities in the YREB exists. However, the focus on protecting WEE of mining cities in the YREB is insufficient, especially the different characteristics of WEEs. Based on this, the main innovation points of this study include: (1) constructing a unique index system for evaluating WEEs for mining cities in the YREB; (2) analyzing the diverse characteristics of WEEs of mining cities in diverse times, spaces, and stages; and (3) analyzing the coordinated development state in WEE systems.

### 3. Study Area and Method

#### 3.1. Study Area

Mining cities are those established near to or within regions rich in mineral resources, and have ore mining, processing, and/or smelting as the main industry [49]. Based on the ideas of distribution pattern, occurrence characteristics, and the development stage, combined with the principle of data accessibility, 19 mining cities were selected as the study areas (Figure 2). The names, regions, development stages, and codes of each mining city are shown in Table 1. The first letter, M or D, denotes mid-upstream or downstream, the second letter, M, D, or R, denotes mature, declining and regenerative, and the third letter (for example, A, B, and C) denotes the ordinal.

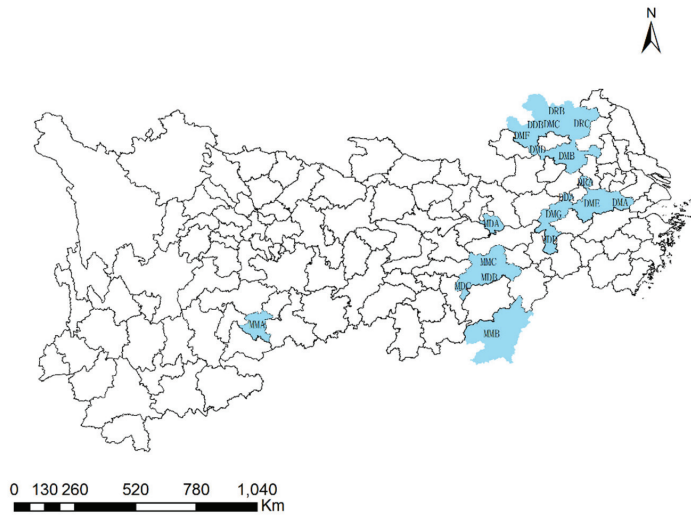


Figure 2. Study areas.

Table 1. List of study areas.

Scope	City	Stage	Code
Mid-upstream	Anshun	Mature	MMA
	Ganzhou	Mature	MMB
	Yichun	Mature	MMC
	Huangshi	Declining	MDA
	Xinyu	Declining	MDB
	Pingxiang	Declining	MDC
	Jingdezhen	Declining	MDD
Downstream	Huzhou	Mature	DMA
	Chuzhou	Mature	DMB
	Suzhou	Mature	DMC
	Huainan	Mature	DMD
	Yicheng	Mature	DME
	Haozhou	Mature	DMF
	Chizhou	Mature	DMG
	Tongling	Declining	DDA
	Huaibei	Declining	DDB
	Maanshan	Regenerative	DRA
	Xuzhou	Regenerative	DRB
	Suqian	Regenerative	DRC

The specific selection criteria were based on the following ideas: (1) prefecture-level cities were considered for the site selection. There are 44 mining cities at prefecture level in YREB, and about 50% (19) of the total mining cities were selected based on the accessibility of data. (2) Focus was placed on non-growing mining cities that were not growing with reference to their development stages. Growing mining cities are in the rising stage of resource development, and the impacts of mineral resource development on the WEE have not been highlighted. In contrast, mature, declining, and regenerating mining cities face greater problems of ecological environment and economic transformation. Hence, the present study mainly focused on such mature mining cities.

### 3.2. Research Framework

For achieving a better WEE of mining cities in the YREB, this study attempted to answer the following three questions: (1) what is the level of WEE systems of mining cities in the YREB? (2) What are the temporal and spatial distribution characteristics of WEE systems of mining cities in the YREB? (3) What is the coordinated development state of WEE systems of mining cities in the YREB? Therefore, based on the problem-oriented background, the cloud model, coefficient of variation (CV)-TOPSIS, the standard deviational ellipse (SDE) model, and the coupling coordination degree model are used to answer these questions. The research framework is shown in Figure 3.

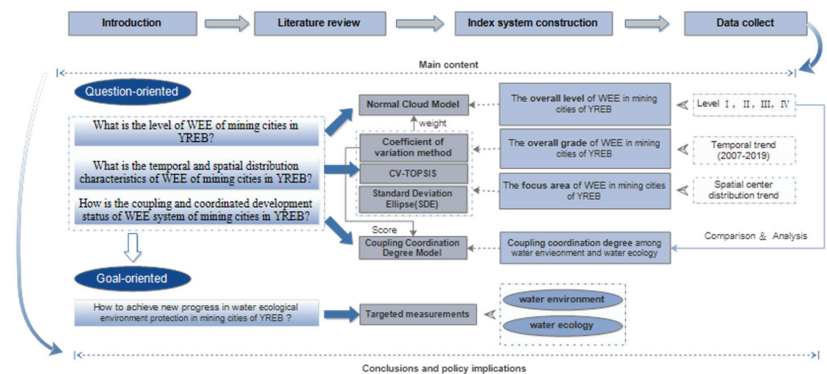


Figure 3. Research framework.

### 3.3. Construction of an Index System

In April 2018, the Chinese President convened a symposium to promote the development of the YREB, stressing the need to solidly promote the control of water pollution, the restoration of water ecology, and the protection of water resources. In 2020, academician Wang Jinnan proposed “five-water integration” of water resources, water environment, water ecology, water disasters, and water regulation. Whether it is the “three waters” or “five waters”, the top priorities are given to water resources, water environment, and water ecology. The YREB is very rich in water resources and, hence, the present study focuses on the WEE protection, which includes both water environment and water ecology. Water environment focuses on indicators of discharge of a water pollutant and its management, and water ecology focuses on indicators that are more likely to have a negative impact on aquatic plants and animals.

The wastewater discharge of various mines in YREB has a great impact on WEEs in the river basin. Our research group summarized the impact factors of mineral resources development on the WEEs of each province and city in the YREB, based on the investigation. It can be observed that surface water and groundwater pollution in mining cities is relatively serious, especially the latter (Table 2). Water sources and reservoirs are polluted to varying degrees, and aquatic life and human settlements are facing great challenges. There were mining agglomerations in mining cities that discharged the sewage directly into the Yangtze

River. For example, Dongchuan district, which is located in the mining city of Yunnan Province, connected a sewage pipe to the Yangtze River; Huidong County of Liangshan Yi Autonomous Prefecture, which is in the mining city of Sichuan Province, fed the wastewater of mineral separation into the tail water of a power plant and dumped it into the Jinsha River. These behaviors polluted the water body and threatened the water environment of the Yangtze River.

**Table 2.** Identification of water pollution impact factors in provinces (cities), YREB.

Province	Surface Water Pollution	Groundwater Pollution	Water Source and Reservoir Pollution
Guizhou	▲☆◇	▲★◆	▲★◆
Yunnan	▲★◇	▲★◇	-
Sichuan	△☆◇	▲★◇	-
Chongqing	△☆◇	▲★◆	▲☆◇
Hunan	▲☆◇	▲★◆	▲★◇
Hubei	▲☆◇	▲★◆	▲★◇
Jiangxi	-	-	-
Anhui	▲☆◇	▲★◆	▲★◇
Zhejiang	△☆◇	△☆◆	△☆◇
Jiangsu	▲☆◇	▲★◆	▲★◇
Shanghai	▲☆◇	△☆◆	△☆◇

(Degree of impact: ▲ remarkable, △ slight; aging of impact: ★ long term, ☆ short term; category of impact: ◆ irreversible, ◇ reversible).

Water pollution in mining cities has a strong negative impact on the quantity and quality of aquatic animals and plants [50,51]. The group incidents and safety problems of agricultural products, such as cadmium rice and heavy metal vegetables, caused by heavy metal pollution are increasing annually, threatening the safety of aquatic organisms and anthropogenic settlements. For example, cadmium rice appeared in Hunan, Jiangxi, Guangdong, and Guangxi, and there were 161 batches of unqualified food in Guangxi. In 2016, the heavy metal emissions from non-ferrous metal mining and dressing in the YREB totaled 323.87 kg, among which cadmium, plumbum, and arsenic amounted to 22.27 kg, 47.32 kg, and 253.36 kg, respectively, accounting for 6.97%, 14.61%, and 78.22% of the heavy metal emissions, respectively (Figure 4).

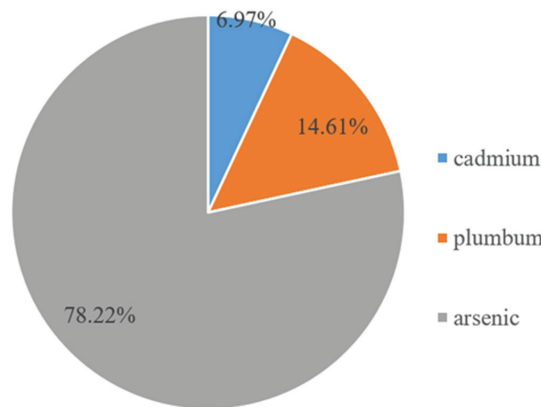


**Figure 4.** Proportion of heavy metal pollution in the YREB.

The construction of the index system is the core of WEE quality evaluation [52]. Based on the above considerations and combined with the principles of scientific, operability, and authoritative of data sources, the index system for evaluating the WEE of mining cities in the YREB can be constructed from two aspects: water environment and ecology. Given

the impact of industrial development in mining cities, indices of water environment dimension are selected from the discharge of industrial wastewater, industrial sulfur dioxide, industrial (tobacco) dust, industrial COD, and ammonia nitrogen. China is promoting new infrastructures, and the length of sewage pipelines is considered as a part of the infrastructure for water environmental management. Given the particularity of mineral resources development and utilization in mining cities, the emphasis of the water ecology dimension is placed on the heavy metal pollution that affects the safety of aquatic organisms and humans; thus, the indicators of discharge of mercury, cadmium, plumbum, and arsenic were selected. The indicators and their attributes are shown in Table 3.

Table 3. Evaluation index system of the WEE system.

Dimensionality	Indicator	Attribute	Weight
Water environment	Discharge of industrial wastewater (10 kt)	-	0.120789
	Discharge of industrial sulfur dioxide (t)	-	0.107262
	Length of sewage pipelines (km)	+	0.226373
	Discharge of industrial (tobacco) dust (t)	-	0.108185
	Discharge of industrial COD (t)	-	0.09297
	Discharge of industrial ammonia nitrogen (t)	-	0.068896
Water ecology	Discharge of mercury (mg/t)	-	0.067365
	Discharge of cadmium (g/t)	-	0.067581
	Discharge of plumbum (g/t)	-	0.068432
	Discharge of arsenic (g/t)	-	0.072146

### 3.4. Cloud Model

The cloud model is a decision-making method that can establish the transformation between qualitative and quantitative concepts. Additionally, it can reflect the randomness and fuzziness of comprehensive evaluation [53]. The cloud model has been previously used for risk assessments [54] and disaster assessments [55]. Considering the characteristics of the evaluation of WEE systems, the cloud model can be applied. This method reflects the qualitative concept quantitatively by cloud digital features (Ex, En, He). Ex is the expected value of the evaluation results; En is entropy reflecting the fuzzy degree of the evaluation results; and He is hyper-entropy reflecting the discreteness of entropy. This method uses the reverse cloud generator to convert accurate values into cloud model parameters and uses the forward cloud generator to convert cloud parameters into cloud droplets, and finally forms a cloud chart [56]. The following steps should be used to draw the cloud chart using Python software.

Build the standard cloud:

$$\begin{cases} Ex_0 = \frac{Q_{min} + Q_{max}}{2} \\ En_0 = \frac{Q_{max} - Q_{min}}{2} \\ He_0 = b \end{cases}, \tag{1}$$

$$Ex_j^o = \frac{\sqrt{\sum_{j=1}^n (U_{ij} - U_j^o)^2}}{\sqrt{\sum_{j=1}^n (U_{ij} - U_j^o)^2} + \sqrt{\sum_{j=1}^n (U_{ij} - U_j^*)^2}}, \tag{2}$$

$Q_{max}$ ,  $Q_{min}$  represent the upper and lower limits of the evaluation interval, respectively;  $(U_j^o, Ex_j^o)$  represent the cloud droplets; and b is a constant that represents the standard value of super entropy. The value of b is 0.001 [57].

Calculate the indicator cloud parameters:

$$\left\{ \begin{array}{l} \bar{X}_j = \frac{1}{k} \sum_{i=1}^k x_{ij} \\ S_j^2 = \frac{1}{k-1} \sum_{i=1}^k (x_{ij} - \bar{X}_j)^2 \\ Ex_j = \bar{X}_j \\ En_j = \sqrt{\frac{\pi}{2}} \cdot \frac{1}{k} \sum_{i=1}^k |x_{ij} - \bar{X}_j| \\ He_j = \sqrt{|S_j^2 - En_j^2|} \end{array} \right. \quad (3)$$

$X_{ij}$  is sample data;  $\bar{X}_j$  is sample mean;  $S_j^2$  is the sample variance;  $Ex_j$  is the expected value;  $En_j$  is entropy; and  $He_j$  is hyper-entropy.

Calculate the comprehensive cloud parameters:

$$\left\{ \begin{array}{l} Ex = \sum_{j=1}^n Ex_j z_j \\ En = \sqrt{\sum_{j=1}^n En_j^2 z_j} \\ He = \sum_{j=1}^n He_j z_j \end{array} \right. \quad (4)$$

where  $Z_j$  represents the weight of the index combination obtained by the coefficient of variation (CV) method.  $Ex$  is the expected value of the comprehensive cloud parameters;  $En$  is entropy; and  $He$  is hyper-entropy.

Cloud models are relatively new tools for studying uncertain knowledge and converting qualitative concepts and quantitative dates [58]. As the fuzzy cloud model evaluations can effectively evaluate WEE systems, the present study applied the method to the evaluation of WEE systems, and the specific classification standard is shown in Table 4.

**Table 4.** Standard for classification of WEE systems.

Level	Interval Partition	Standard Cloud Parameter	Description
1	[0, 0.25)	(0.125, 0.0736, 0.001)	Bad
2	[0.25, 0.5)	(0.375, 0.0736, 0.001)	Normal
3	[0.5, 0.75)	(0.625, 0.0736, 0.001)	Good
4	[0.75, 1)	(0.875, 0.0736, 0.001)	Very Good

The three numbers in the standard cloud parameters are ( $Ex, En, He$ ) where  $Ex$  is the expected value of the evaluation results;  $En$  is the entropy reflects the fuzzy degree of the evaluation results; and  $He$  is the hyper-entropy that reflects the discreteness of entropy. The value of  $He$  is 0.001 refers to the reference. For example, for level 1, 0.125 is the expected value, 0.0736 is the entropy, and 0.001 is the hyper-entropy.

### 3.5. Standard Deviation Ellipse Model

The SDE model analyzes the distribution characteristics of discrete point data using a rotated ellipse with a long axis, to denote the main orientation of a discrete data [59]. SDE can elucidate the center of gravity shift tendencies in an area using a standard planar coordinate system ( $X, Y$ ) with any discrete point having the coordinates ( $x_i, y_i$ ). The long half axis of the ellipse represents the direction of data distribution, and the short half axis represents the range of data distribution. The larger the value difference between the long and short half axes, the more obvious the data directionality. In contrast, the closer the long and short half axes are, the less obvious the directivity. The short half axis indicates the range of data distribution. The shorter the short half axis, the more obvious the centripetal force is. In contrast, the longer the short semi axis, the greater the degree of dispersion of the data. The SDE model has been previously used for ecological environment assessment [60] and environmental management [61].

The SDE model reflects the spatial distribution characteristics of WEE quality from multiple angles. SDE was selected for this study because it reveals changes in the spatial distribution range of WEE quality through the comparative areas of the standard elliptical difference. The calculation formula is as follows:

Ellipse center coordinates:

$$SDE_x = \sqrt{\frac{\sum_{i=1}^n (x_i - \bar{X})^2}{n}}, \tag{5}$$

$$SDE_y = \sqrt{\frac{\sum_{i=1}^n (y_i - \bar{Y})^2}{n}}, \tag{6}$$

$x_i$  and  $y_i$  are the spatial position coordinate of each feature, and  $X$  and  $Y$  are the arithmetic mean center.

Direction of ellipse:

$$\tan \theta = \frac{A + B}{C}, \tag{7}$$

$$A = \sum_{i=1}^n \tilde{x}_i^2 - \sum_{i=1}^n \tilde{y}_i^2, \tag{8}$$

$$B = \sqrt{\left(\sum_{i=1}^n \tilde{x}_i^2 - \sum_{i=1}^n \tilde{y}_i^2\right)^2 + 4\left(\sum_{i=1}^n \tilde{x}_i \tilde{y}_i\right)^2}, \tag{9}$$

$$C = 2 \sum_{i=1}^n \tilde{x}_i \tilde{y}_i, \tag{10}$$

where  $\theta$  represents the azimuth of the ellipse,  $\tilde{x}_i$  and  $\tilde{y}_i$  are the difference between the mean center, and  $X$  and  $Y$ .

Length of XY axis:

$$\sigma_x = \sqrt{2} \sqrt{\frac{\sum_{i=1}^n (\tilde{x}_i \cos \theta - \tilde{y}_i \sin \theta)^2}{n}}, \tag{11}$$

$$\sigma_y = \sqrt{2} \sqrt{\frac{\sum_{i=1}^n (\tilde{x}_i \cos \theta + \tilde{y}_i \sin \theta)^2}{n}}, \tag{12}$$

$\sigma_x$  and  $\sigma_y$  represent the standard deviation along the  $x$  and  $y$  axes, respectively.

### 3.6. Coupling Coordination Degree Model

The coupling coordination degree model can be used to evaluate the coupling and coordination state of water ecology and the water environment, and to identify the short board factors. On the basis of data standardization, CV-TOPSIS and the coupling coordination degree model are used for calculations. The specific steps include:

1. Data standardization and weight calculation. The range method is used to standardize the data, and the coefficient of variation method is used to calculate the weight of each index (Table 3).
2. The CV-TOPSIS method is used to calculate the comprehensive evaluation value.

Calculation specification matrix:

$$Z_{ij} = \frac{y_{ij}}{\sqrt{\sum_{i=1}^n y_{ij}^2}}, \tag{13}$$

Calculate the weighted gauge matrix:

$$U_{ij} = w_i \cdot z_{ij}, \tag{14}$$



Calculate the distance between each scheme and the ideal solution as the evaluation value:

$$C_i^* = \frac{\sqrt{\sum_{j=1}^n (U_{ij} - U_j^0)^2}}{\sqrt{\sum_{j=1}^n (U_{ij} - U_j^0)^2 + \sum_{j=1}^n (U_{ij} - U_j^*)^2}} \tag{15}$$

where the ideal solution is:  $U_j^* = \max(U_1, U_2 \dots, U_j)$ ; the negative ideal solution is:  $U_j^0 = \min(U_1, U_2 \dots, U_j)$ .

3. Calculation of coupling coordination degree.

$$B_i = \left\{ \frac{EN_i^* \times EC_i^*}{[(EN_i^* + EC_i^*)/2]^2} \right\}^{\frac{1}{2}}, \tag{16}$$

where  $EN_i^*$ ,  $EC_i^*$  are the evaluation value of the water environment and water ecosystem calculated by the weighted TOPSIS method.

Calculate coupling co scheduling:

$$D^i = \sqrt{B_i \times (\alpha EN_i^* + \beta EC_i^*)}, \tag{17}$$

where “ $\alpha$ ” and “ $\beta$ ” represent the importance of the water environment and water ecology, which are equally important in WEE protection. Therefore,  $\alpha$  and  $\beta$  are defined as 0.5 and 0.5, respectively, in this study. The classification standard of reference [62] and the classification of coupling coordination degree of the WEE are shown in Table 5.

**Table 5.** Classification of coupling coordination degree of the WEE.

Range	Grade
(0, 0.4]	Unbalanced
(0.4, 0.5]	Basic balanced
(0.5, 0.8]	Moderate coordination
(0.8, 1]	High coordination

### 3.7. Data Sources

The data were collected from 2007 to 2019. The data of indicators of the water environment dimension are mainly obtained from China’s urban statistical yearbook, provincial and municipal statistical yearbooks, and a small part of environmental data are obtained through investigation and interpolation. The data of indicators of water ecological dimension are mainly calculated by referring to The Manual on the Production and Emission Coefficient of Industrial Pollution Sources in the First China Pollution Source Survey. The mining volume of main metal mineral resources in mineral resources of mining cities are mainly obtained through the China Mining Yearbook and the mineral resources development and utilization database of the Ministry of Natural Resources, and the heavy metal emission coefficient of the mineral resources is obtained through The Manual on the Production and Emission Coefficient of Industrial Pollution Sources in the First China Pollution Source Survey.

## 4. Results

### 4.1. WEE Assessment

Based on the cloud model theory, the cloud model parameters Ex, En, and He are calculated and determined. Figure 5 shows that the WEE index and water environment are generally suitable, and the water ecology is highly suitable in mining cities in the YREB in 2019. The He of the water ecology dimension is the largest (0.161), indicating that its uncertainty is higher than that of the water environment dimension. It can be observed

that the overall level of water ecology of mining cities in the YREB is better than that of water environment, but the former takes greater fluctuation risk than the latter. Therefore, we should improve the water environment quality of most mining cities and pay attention to the water ecological safety of some key mining cities.

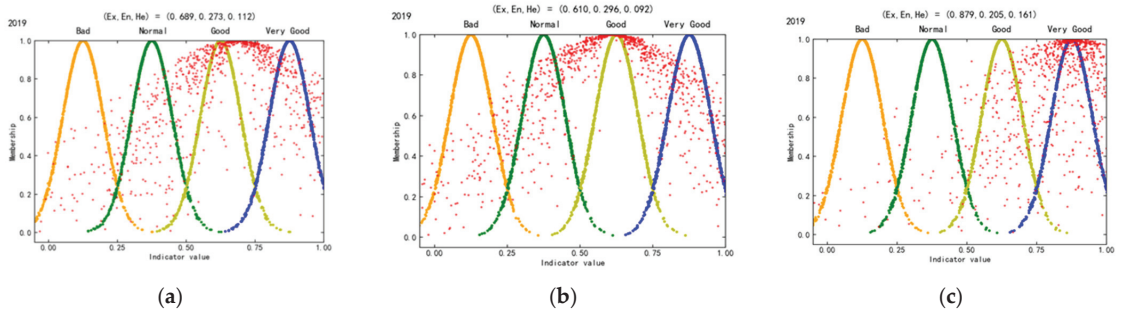


**Figure 5.** WEE cloud maps in mining cities in the YREB. (a) WEE index. (b) Water environment. (c) Water ecology.

The WEE of the mid-upstream and downstream mining cities is acceptable (Figure 6). Ex (0.71) of downstream mining cities is greater than that of mid-upstream mining cities (0.641), indicating that the WEE of the former is slightly better than that of the latter. Similarly, He (0.128) of downstream mining cities is greater than that of mid-upstream mining cities (0.122), which indicates that the WEE fluctuation risk of downstream mining cities is greater.

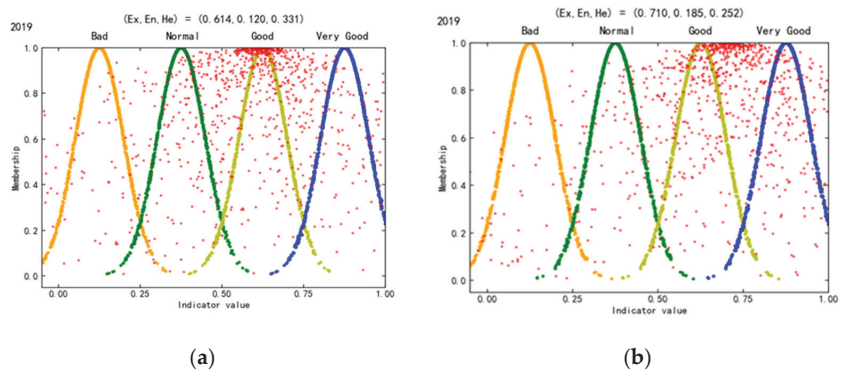


**Figure 6.** WEE cloud maps in mid-upstream and downstream mining cities in the YREB. (a) Mid-upstream mining cities. (b) Downstream mining cities.

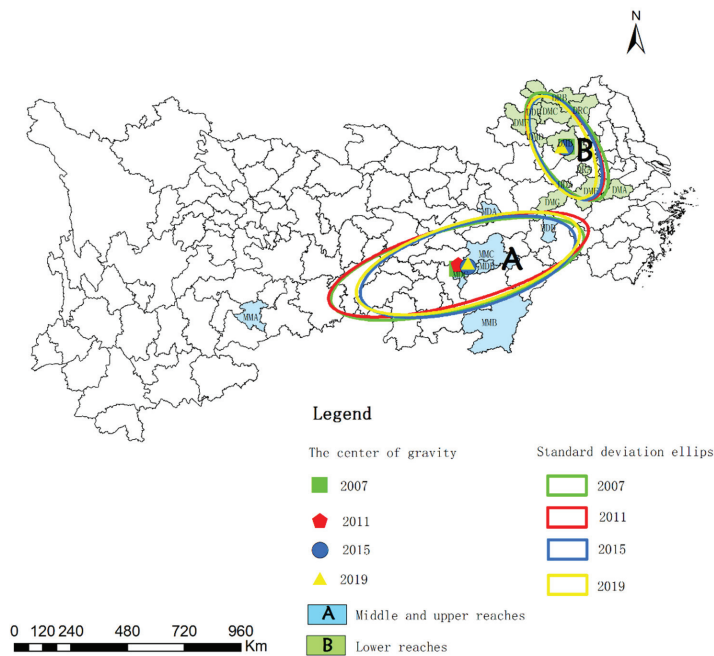
4.2. Temporal and Spatial Distribution Characteristics of the WEE

Table 6 and Figure 7 show the standard deviation ellipse of the WEE of mining cities in different regions. From the center of gravity transfer perspective, the center of gravity of the WEE of mid-upstream mining cities is transferred from MDC to MMC from 2007 to 2019, and the center of gravity of the WEE moved 0.04° longitudinally and 0.2° latitudinally. The center of gravity of the WEE of downstream mining cities has always been DMB, and the center of gravity of the WEE has moved 0.19° longitudinally and 0.02° latitudinally. Considering the coverage, MDC and MDB are the main areas of the WEE of mid-upstream mining cities, and DMB, DMC, and DRA are the main areas of the WEE of downstream mining cities. From 2007 to 2019, the length of the long semi axle in mid-upstream and downstream mining cities decreased from 4.98 km to 4.42 km, and from 2.35 km to 2.12 km,

respectively. The length of the short semi axle in mid-upstream mining cities increased from 1.54 km to 1.57 km, and decreased from 1.10 km to 1.02 km in downstream mining cities. This indicates that the WEE of mid-upstream mining cities is shrinking in the main direction and expanding in the secondary direction, while the WEE of downstream mining cities is shrinking in the main and secondary directions. The long and short axis ratios of downstream mining cities is significantly higher than those in the mid-upstream, indicating that the WEE quality of downstream mining cities is better. The standard deviation ellipse azimuth is used to reflect the main trend direction of spatial distribution. The ellipse azimuth of mid-upstream mining cities is expanded from 75.01° to 73.32°, and the ellipse azimuth of downstream mining cities is expanded from 146.85° to 153.23°. The ellipse axis shows a clockwise rotation trend.

**Table 6.** Standard deviation ellipse parameters of the WEE of mining cities in different regions.

Region	Year	2007	2011	2015	2019
Mid-upstream	Key City Center	MDC 113.77° E, 27.75° N	MDC 113.81° E, 27.91° N	MMC 114.17° E, 27.83° N	MMC 114.17° E, 27.95° N
	Elliptical area/km <sup>2</sup>	24.08	23.73	21.46	21.74
	Length of long half shaft/km	4.98	5.14	4.24	4.42
	Length of short half shaft/km	1.54	1.47	1.61	1.57
	Long and short axis ratio	0.31	0.29	0.38	0.36
	Rotation	75.01	74	74.06	73.32
Downstream	Key City Center	DMB 117.94° E, 32.41° N	DMB 117.88° E, 32.36° N	DMB 117.89° E, 32.37° N	DMB 117.75° E, 32.39° N
	Elliptical area/km <sup>2</sup>	8.14	7.59	7.28	6.82
	Length of long half shaft/km	2.35	2.21	2.17	2.12
	Length of short half shaft/km	1.1	1.09	1.07	1.02
	Long and short axis ratio	0.47	0.49	0.49	0.48
	Rotation	146.85	149.06	151.83	153.23



**Figure 7.** Standard deviation ellipse of the WEE of mining cities in different regions.

Table 7 and Figure 8 show the standard deviation ellipse of the WEE in mining cities at different stages. From 2007 to 2019, the center of gravity of the WEE in mature, declining, and renewable mining cities changes little, and the change of the longitude and latitude is not evident. In mature cities, the lengths of the long and short semi axes are shortened from 5.70 km to 5.03 km, and 2.67 km to 2.52 km, respectively. There is little change in the declining mining cities. In regenerative mining cities, the length of long semi axle is expanded from 1.77 km to 1.92 km, with shortening from 0.26 km to 0.22 km considering length of the short semi axle. It indicates that the WEE of mature mining cities is shrinking in the main and secondary directions, while renewable mining cities are expanding in the main direction and shrinking in the secondary trend direction. It can be seen that the long-short axis ratio of mature mining cities is greater than that of the declining and regenerative, indicating that the WEE of mature mining cities is better. The standard deviation ellipse azimuth is used to reflect the main trend direction of spatial distribution. The ellipse azimuth of mature and declining mining cities are reduced from 59.80° to 53.43°, and 28.49° to 28.43°, respectively, but that of the regenerative mining cities is expanded from 160.13° to 161.99°. The elliptical axis of mature and declining mining cities rotate counterclockwise, and the elliptical axis of regenerative mining cities shows a clockwise rotation trend.

**Table 7.** Standard deviation ellipse parameters of the WEE of mining cities in different stages of the YREB.

Stage	Year	2007	2011	2015	2019
Mature	Center	116.53° E, 30.70° N	116.33° E, 30.79° N	116.24° E, 30.33° N	116.52° E, 30.94° N
	Elliptical area/km <sup>2</sup>	47.79	47.27	46.79	39.76
	Length of long half shaft/km	5.7	5.86	5.54	5.03
	Length of short half shaft/km	2.67	2.57	2.69	2.52
	Long and short axis ratio	0.47	0.44	0.49	0.5
	Rotation	59.8	59.93	54.97	53.43
Declining	Center	115.81° E, 29.72° N	115.94° E, 29.81° N	115.68° E, 29.56° N	115.88° E, 29.90° N
	Elliptical area/km <sup>2</sup>	14.11	14.38	13.34	14.59
	Length of long half shaft/km	3.36	3.26	3.27	3.36
	Length of short half shaft/km	1.34	1.4	1.3	1.38
	Long and short axis ratio	0.4	0.43	0.4	0.41
	Rotation	28.49	29.78	29.77	28.43
Regenerative	Center	118.11° E, 33.42° N	118.23° E, 33.11° N	118.26° E, 33.03° N	118.22° E, 33.02° N
	Elliptical area/km <sup>2</sup>	2.58	2.64	2.62	2.56
	Length of long half shaft/km	1.77	1.86	1.87	1.92
	Length of short half shaft/km	0.46	0.45	0.45	0.42
	Long and short axis ratio	0.26	0.24	0.24	0.22
	Rotation	160.13	162.53	163.05	161.99

Figure 9 shows the WEE index of mining cities in 2007, 2011, 2015, and 2019. From the perspective of time change, the WEE index of many mining cities shows an upward trend, and the WEE index is the largest in 2015 or 2019. In terms of the spatial distribution, most mid-upstream mining cities had the highest WEE index in 2015, accounting for approximately 71.43%; 50% of the downstream mining cities have the highest WEE index in 2019. Among them, the mid-upstream mining cities with the highest WEE index in 2015 accounted for 62.5%. It can be seen that the WEE quality of most mining cities has been continuously optimized over the past five years. The WEE quality of downstream mining cities is better than that of mid-upstream mining cities in 2019, and improved extensively than that in 2007. The three mining cities with the largest increase in the WEE index in 2019 compared with 2007 are DME (126.38%), DMB (126.78%), and DRA (99.56%). Simultaneously, according to the development stage types of mining cities with the highest WEE index, the WEE index of mature mining cities is the highest. The above results further verify the results of the standard deviation ellipse.

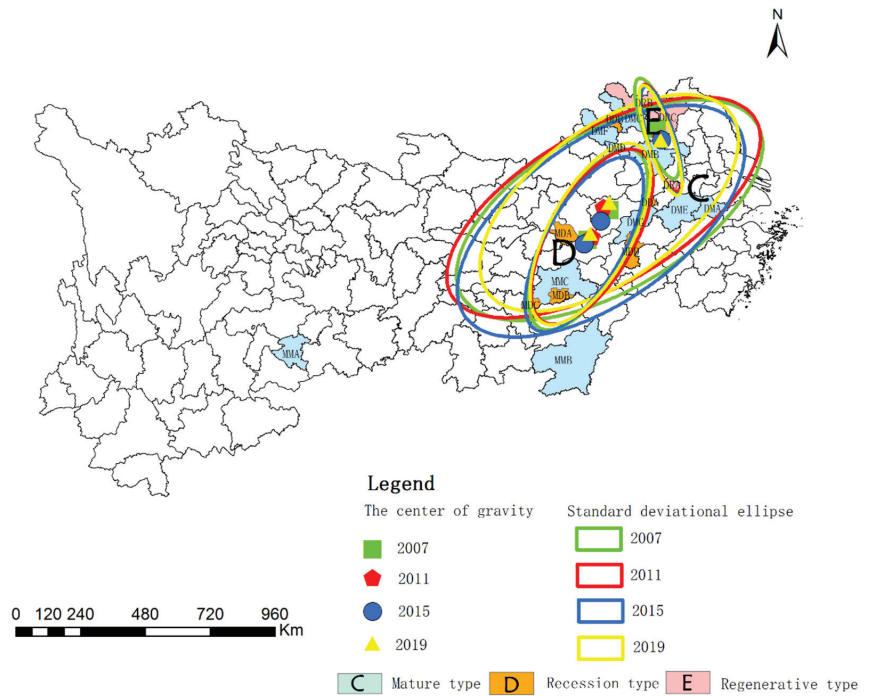


Figure 8. Standard deviation ellipse of the WEE of mining cities in different stages.

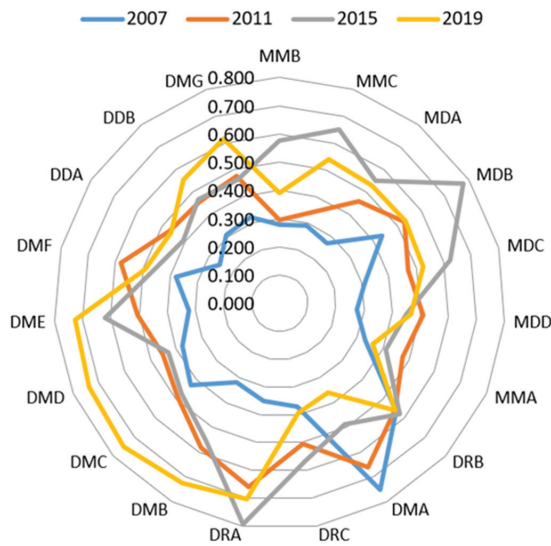
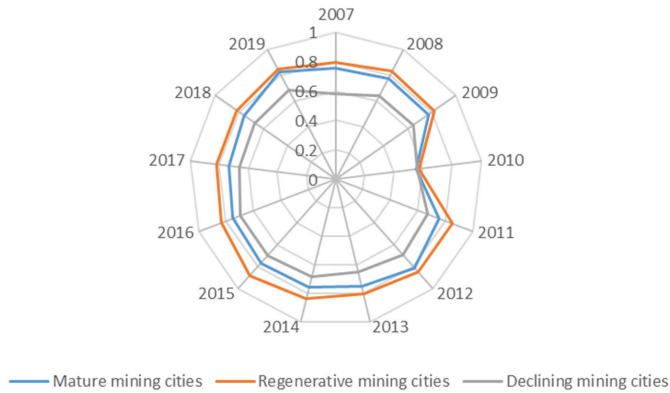


Figure 9. WEE index of mining cities in 2007, 2011, 2015, and 2019.

#### 4.3. Coupling Coordination Degree

Generally speaking, the coupling coordinated development between the water environment and water ecology in mature and renewable mining cities is in a well-coordinated development state in the initial stage, and the trend of coupling coordination is basically

balanced (Figure 10). From 2015 to 2019, the overall level of water environment and water ecology coupling coordination degree of renewable mining cities is higher than that of mature mining cities. The average value range of the coupling coordination degree of renewable mining cities is [0.7501, 0.9228], and the average value range of mature mining cities is [0.6644, 0.8238]. The water environment and water ecology of declining mining cities fluctuates frequently, and the average value range of the coupling coordination degree in past five years is [0.0602, 0.8758] (Figure 11).



**Figure 10.** Average value of the coupling coordination degree in different types of mining cities from 2007 to 2019.

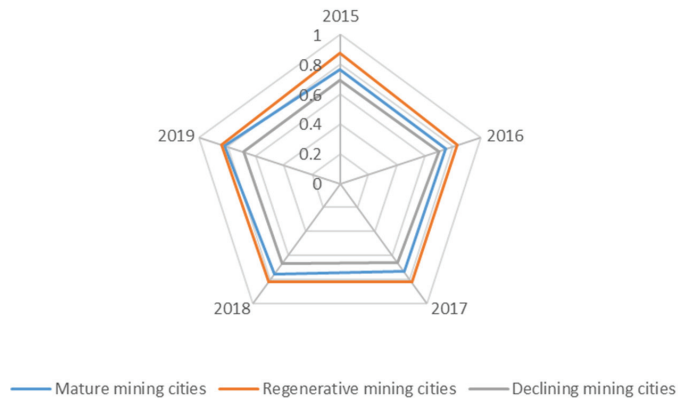


**Figure 11.** Average value of the coupling coordination degree in different types of mining cities from 2015 to 2019.

The coupling coordination degree of mining cities is shown in Figure 12. The average coupling coordination degree of DMF reaches 0.795, the highest among the mature mining cities. In 2008, the coupling coordination degree of DMF reaches 0.8182, achieving a good coordination stage and maintaining a stable trend compared with other mature mining cities. The coupling coordination degree of MDB and MDC are higher than those in declining mining cities. However, the coupling coordination degree in DDA is lower than 0.4, which demonstrates the unbalanced of WEE. MDA, MDD, and DDB are in moderate coordination. The coupling coordination degree of DRA is higher than DRB and DRC. The average coupling coordination degree of DRB is higher than 0.8, which is in a high coordination. The coupling coordination degree between DRA and DRB increased slightly, and the average coupling coordination degree of DRC reaches 0.7649, which is in a moderate coordination.

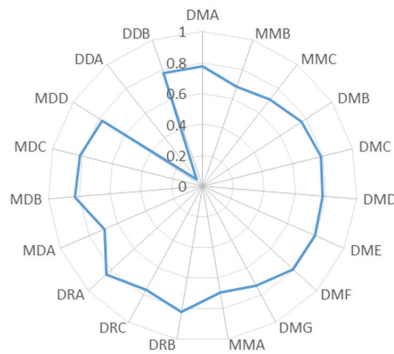


**Figure 12.** Average value of the coupling coordination degree of each mining city from 2007 to 2019.

Most mining cities still belong to a lagging water environment. Table 8 shows that 17 mining cities belong to a water environment lag type, accounting for 89.5%, and 2 belong to a water ecology lag type, accounting for 10.5%.

**Table 8.** Lag types of water environment and water ecology coordinated development of mining cities in the YREB in 2019.

Lag Type	Quantity	Mining Cities
Water environment	17	MMA, MMB, MMC, MDB, MDC, MDD, DMA, DMB, DMC, DMD, DME, DMF, DMG, DDB, DRA, DRB, DRC
Water ecology	2	MDA, DDA

### 5. Discussion

The WEE of mining cities in the YREB is generally good, but there is still room for improvement. Efforts should be made to improve the construction of sewage pipelines in mining cities for optimizing the quality of the water environment. According to the weight data, the indicator of length of sewage pipeline accounts for the highest proportion in the index system of the WEE, which is in line with China’s saying that “black odor is in the water, the root is on the shore, the key is the outlet, and the core is the pipe network.” Optimizing the construction of sewage pipelines in mining cities under the background of China’s new infrastructure is one of the starting points for improving the quality of the WEE. Conversely, mining cities that fall behind in the construction of water ecological civilization should be the point of focused. This also indicates the necessity of analyzing spatial distribution characteristics for locating these mining cities.

Compared with 2007, WEE protection in most mining cities has achieved remarkable results. This agrees with the findings of Yang (2019) that the ecological quality in most regions of the Yangtze River Basin has remained the same or increased [63], and of Zhou (2021) and Deng (2021) that the emissions of water pollutants COD and NH<sub>3</sub>-N in the YREB have been decreasing year by year [64,65]. In November 2012, the construction of ecological civilization was evidently proposed in the 18th National Congress of the Communist Party of China, and then The Water Pollution Prevention and Control Action Plan, The Ecological Environment Protection Plan of YREB, The Outline of The Regional Integration Development Plan of The Yangtze River Delta, The Yangtze River Water Protection Law, and other documents were intensively issued, which indicates the direction for WEE protection of mining cities in the YREB. This also reflects the advantage of the party and government leaders of the Communist Party of China in “concentrating on major events” [66], and “joint protection and no large-scale development” of the YREB has been implemented. The

WEE quality of mature mining cities in the downstream is better than that of other types of mining cities in 2019, and the maturity has made greater progress than that in 2007, which is consistent with the fact that nonferrous and ferrous metals in the mid-upstream of the YREB play an important role in local economic and social development and a positive role in China's resource protection. In addition, mature mining cities in the downstream have achieved remarkable results during the construction of sewage pipelines.

The coordinated development of water environment and water ecology in regenerative mining cities is better than that in mature and declining mining cities. Transformation is the only way for China's mining cities for achieving sustainable development [67]. Both mature and declining mining cities are facing transformation, and regenerative mining cities have basically completed economic transformation. Developing mining cities into tourist destinations has been adopted by many cities [68], such as regenerative mining cities Lijiang City and Shangri-La County. The transformation of mining cities is often planned after they enter a recession [69], i.e., most mature and declining mining cities plan the economic transformation late, and mining development remains their focus. Therefore, the focus should be on coordinated development of water environment and water ecology in regenerative mining cities.

Most mining cities still belong to the lagging type of water environment. Heavy metal pollution has been well treated, and the threat to water ecological security caused by heavy metal pollution is low. Huang (2020) also mentioned that the pollution of Cd, Pb, As, Cu, and Zn in the YREB have been reduced [70], and Yan (2021) noted that heavy metal pollution in surface water in the YREB has decreased in recent years [71]. These studies all confirm our conclusion. Heavy metals are toxic, persistent, and bio-aggregative. Aquatic ecosystems have attracted much attention worldwide because of their heavy metal pollution [72,73]. In The 12th Five Year Plan for Comprehensive Prevention and Control of Heavy Metal Pollution, China defined 138 key protection areas and 4452 key prevention and control enterprises to tackle heavy metal pollution by classification and zoning. The comprehensive assessment results of the implementation of the above plan show that in 2015, the total discharge of major heavy metal pollutants in China decreased by 27.6% compared with 2007, and less than 3 heavy metal-related environmental emergencies occurred annually from 2012 to 2015 [74].

## 6. Conclusions and Recommendations

Based on the above research, the following conclusions were drawn: (1) the WEE of mining cities in the YREB is generally good, but efforts should be made to improve the construction of sewage pipelines in mining cities, and attention should be paid to mining cities that lag in constructing ecological water civilization. (2) Recently, remarkable results have been achieved in WEE protection of most mining cities. The WEE quality of mature mining cities in the downstream is better than that of other types of mining cities in 2019, which is greater than that in 2007. (3) The coordinated development of water environment and water ecology in regenerative mining cities is better than that in the mature and declining cities. (4) Most mining cities still belong to the lagging type of water environment. Heavy metal pollution has been well treated, and the threat to water ecological security caused by heavy metal pollution is low.

To solve the WEE problems existing in the development of mineral resources, "joint protection and no large-scale development" should be followed, and the relationship between development and the bottom line should be coordinated. The specific recommendations are as follows.

- (1) Improve the sewage pipe network system of mining cities. The improvement of urban and rural drainage pipe network construction should be accelerated to establish 100% coverage and collection of sewage pipe network in city proper as soon as possible. WEE protection awareness of rural residents should be improved by public service advertising. Both the treatment of rural domestic sewage and the toilet revolution



and the treatment of livestock and poultry manure should be promoted scientifically and reasonably.

- (2) Promote the treatment of the WEE in the mid-upstream mining cities further. The mid-upstream in the YREB has the most mines and is rich in strategic metal minerals. While developing strategic metal minerals and ensuring the safety of China's resources, a strict environmental protection system should be implemented. For 306 key mining agglomeration areas in the YREB, the discharge of wastewater and solid waste from various activities should be strictly controlled for ensuring that the discharge of various pollutants meets the discharge standards, and curbing the water environment pollution in mining areas and parks. Ecological compensation for the ecological functional areas in the mid-upstream should be increased to alleviate the economic and social pressure of WEE treatment.
- (3) The transformational development of mature and declining mining cities should be arranged in advance. The efficiency of resource development and utilization and industrial technology should be improved in mature mining cities, and the resource industrial chain should be extended for cultivating resource deep-processing industrial clusters and build leading enterprises. Meanwhile, the adjustment and upgrading of resource processing industrial structure should be accelerated, and the formation of corresponding pillar alternative industries should be promoted. In declining mining cities, the problem of urban internal dual structure and left over by history, such as accelerating the comprehensive treatment of hidden dangers of geological disasters, should be solved. With China's policy support, the development of alternative industries should be vigorously supported to constantly enhance their sustainable development capacity.

There are limitations to the analysis performed in this study. In establishing the water ecological indicator system, the quantities of fish, shrimp, and microorganisms are more informative indicators of the water quality. However, this data is rarely available owing to the degree of work involved in determining the numbers of these aquatic organisms. Therefore, mercury, cadmium, lead, and arsenic emissions were used as the indicators of water quality from a different perspective. In future studies, we will focus on the biological accounting of aquatic organisms, as well as explore the means to improve the water environment while assessing the impact of various policies on this specific environment.

**Author Contributions:** Conceptualization, R.W. and J.C.; methodology, R.W. and J.C.; software, H.L.; validation, R.W. and J.C.; formal analysis, H.L.; investigation, Z.X. and H.F.; data curation, H.L.; writing—original draft preparation, R.W. and H.L.; writing—review and editing, H.L., Z.X. and Y.T.; visualization, R.W. and H.F.; supervision, J.C.; project administration, J.C. All authors have read and agreed to the published version of the manuscript.

**Funding:** This research was funded by the Major Projects of National Natural Science Foundation of China, grant number 71991482; the Ministry of Education Philosophy and Social Sciences Fund, grant number 19YJZH168, and the Fundamental Research Funds for the Central Universities, China University of Geosciences (Wuhan).

**Institutional Review Board Statement:** Not applicable.

**Informed Consent Statement:** Not applicable.

**Data Availability Statement:** The data presented in this study are available in China's urban statistical yearbook, provincial and municipal statistical yearbooks, The Manual on the Production and Emission Coefficient of Industrial Pollution Sources in the First China Pollution Source Survey.

**Acknowledgments:** The authors gratefully acknowledge support from the Major Projects of National Natural Science Foundation of China (71991482), the Ministry of Education Philosophy and Social Sciences Fund (19YJZH168), and the Fundamental Research Funds for the Central Universities, China University of Geosciences (Wuhan).

**Conflicts of Interest:** The authors declare no conflict of interest.

## References

1. Xi Jinping, Delivered at the 19th National Congress of the Communist Party of China. Available online: <http://cpc.people.com.cn/n1/2017/1028/c64094-29613660.html> (accessed on 28 October 2017).
2. Varol, M. Use of water quality index and multivariate statistical methods for the evaluation of water quality of a stream affected by multiple stressors: A case study. *J. Environ. Pollut.* **2020**, *266*, 115417. [[CrossRef](#)]
3. Ministry of Environmental Protection; National Development and Reform Commission; Ministry of Water Resources; Ministry of Ecological Environment of the People's Republic of China. Ecological Environment Protection Planning of the Yangtze River Economic Belt. 2017. Available online: [https://www.zhb.gov.cn/gkml/hbb/qt/201707/t20170718\\_418074.htm](https://www.zhb.gov.cn/gkml/hbb/qt/201707/t20170718_418074.htm) (accessed on 18 July 2017).
4. Bridge, G. Contested Terrain: Mining and the Environment. *J. Annu. Rev. Environ. Resour.* **2004**, *21*, 205–295. [[CrossRef](#)]
5. Zhang, J.; Liu, C.L. Riverine composition and estuarine geochemistry of particulate metals in China—Weathering features, anthropogenic impact and chemical fluxes. *J. Estuar. Coast. Shelf Sci.* **2002**, *54*, 1051–1070. [[CrossRef](#)]
6. Birch, G.F.; Chang, C.H.; Lee, J.H.; Churchill, L.J. The use of vintage surficial sediment data and sedimentary cores to determine past and future trends in estuarine metal contamination (Sydney estuary, Australia). *J. Sci. Total Environ.* **2013**, *454*, 542–561. [[CrossRef](#)] [[PubMed](#)]
7. Zou, S.R.; Du, S.X.; Song, M.; Li, M.X. How Polluting Industries React to Ambient Water Quality: Seven River Basins in China. *J. Water* **2021**, *13*, 1232. [[CrossRef](#)]
8. Dos Santos, E.S.; Lopes, P.P.P.; da Silva Pereira, H.H.; de Oliveira Nascimento, O.; Rennie, C.D.; O'Reilly, L.D.S.L.; da Cunha, A.C. The impact of channel capture on estuarine hydro-morphodynamics and water quality in the Amazon delta. *J. Sci. Total Environ.* **2018**, *624*, 887–899. [[CrossRef](#)] [[PubMed](#)]
9. Avila, R.; Horn, B.; Moriarty, E.; Hodson, R.; Moltchanova, E. Evaluating statistical model performance in water quality prediction. *J. Environ. Manag.* **2018**, *206*, 910. [[CrossRef](#)]
10. Li, M.; Zhang, J.; Luo, H.; Liang, N.; Yu, Y.; Sun, Y. Correlation analysis between China's chemical oxygen demand emission reduction and changes in water environment quality during the Eleventh Five Year Plan. *J. Ecol. Environ.* **2011**, *20*, 463–467. [[CrossRef](#)]
11. Wei, X.; Wang, J.; Wu, S.; Xin, X.; Wang, Z.; Liu, W. Comprehensive evaluation model for water environment carrying capacity based on VPOSRM framework: A case study in Wuhan, China. *J. Sustain. Cities Soc.* **2019**, *50*, 101640. [[CrossRef](#)]
12. Zhang, Y.; Yue, Q.; Wang, T.; Zhu, Y.; Li, Y. Evaluation and early warning of water environment carrying capacity in Liaoning province based on control unit: A case study in Zhaosutai River Tieling City control unit. *J. Ecol. Indic.* **2021**, *124*, 107392. [[CrossRef](#)]
13. Duan, T.T.; Feng, J.S.; Zhou, Y.Q.; Chang, X.; Li, Y.X. Systematic evaluation of management measure effects on the water environment based on the DPSIR-Tapio decoupling model: A case study in the Chaohu Lake watershed, China. *J. Sci. Total Environ.* **2021**, *801*, 149528. [[CrossRef](#)] [[PubMed](#)]
14. Simeonov, V.; Stratis, J.A.; Samara, C.; Zachariadis, G.; Voutsas, D.; Anthemidis, A.; Sofoniou, M.; Kouimtzis, T. Assessment of the surface water quality in Northern Greece. *J. Water Res.* **2003**, *37*, 4119–4124. [[CrossRef](#)]
15. Wan, R.; Meng, F.; Su, E.; Fu, W.; Wang, Q. Development of a classification scheme for evaluating water quality in marine environment receiving treated municipal effluent by an integrated biomarker approach in *Meretrix meretrix*. *J. Ecol. Environ.* **2018**, *93*, 697–703. [[CrossRef](#)]
16. Ji, X.L.; Wang, X.; Yang, G.P. A water quality assessment model for Suya Lake Reservoir. *J. Water Supply Dec.* **2020**, *20*, 3715–3721. [[CrossRef](#)]
17. Xing, L.; Xue, M.; Hu, M. Dynamic simulation and assessment of the coupling coordination degree of the economy–resource–environment system: Case of Wuhan City in China. *J. Environ. Manag.* **2019**, *230*, 474–487. [[CrossRef](#)]
18. Yang, C.; Zeng, W.; Yang, X. Coupling coordination evaluation and sustainable development pattern of geo-ecological environment and urbanization in Chongqing municipality, China. *J. Sustain. Cities Soc.* **2020**, *61*, 102271. [[CrossRef](#)]
19. Kavka, P. Spatial Delimitation of Small Headwater Catchments and Their Classification in Terms of Runoff Risks. *J. Water* **2021**, *13*, 3458. [[CrossRef](#)]
20. Zuo, Z.; Guo, H.; Cheng, J.; Li, Y. How to achieve new progress in ecological civilization construction?—Based on cloud model and coupling coordination degree model. *J. Ecol. Indic.* **2021**, *127*, 107789. [[CrossRef](#)]
21. Liu, N.; Liu, C.; Xia, Y.; Da, B. Examining the coordination between urbanization and eco-environment using coupling and spatial analyses: A case study in China. *J. Ecol. Indic.* **2018**, *93*, 1163–1175. [[CrossRef](#)]
22. Li, W.; Wang, Y.; Xie, S.; Cheng, X. Coupling coordination analysis and spatiotemporal heterogeneity between urbanization and ecosystem health in Chongqing municipality, China. *J. Sci. Total Environ.* **2021**, *791*, 148311. [[CrossRef](#)]
23. Wang, R.; Cheng, J.; Zhu, Y.; Xiong, W. Research on diversity of mineral resources carrying capacity in Chinese mining cities. *J. Resour. Policy* **2016**, *47*, 108–114. [[CrossRef](#)]
24. Zeng, L.; Wang, B.; Fan, L.; Wu, J. Analyzing sustainability of Chinese mining cities using an association rule mining approach. *J. Resour. Policy* **2016**, *49*, 394–404. [[CrossRef](#)]
25. Tai, X.; Xiao, W.; Tang, Y. A quantitative assessment of vulnerability using social-economic-natural compound ecosystem framework in coal mining cities. *J. Clean. Prod.* **2020**, *258*, 120969. [[CrossRef](#)]
26. Zhou, M.; Li, X.; Zhang, M.; Liu, B.; Zhang, Y.; Gao, Y.; Ullah, H.; Peng, L.; He, A.; Yu, H. Water quality in worldwide coal mining city: A scenario in water chemistry and health risks exploration. *J. Geochem. Explor.* **2020**, *213*, 106513. [[CrossRef](#)]

27. Xi, X.; Wang, S.; Yao, L.; Zhang, Y.; Niu, R.; Zhou, Y. Evaluation on geological environment carrying capacity of mining city—A case study in Huangshi City, Hubei Province, China. *Int. J. Appl. Earth Obs. Geoinf.* **2021**, *102*, 102410. [[CrossRef](#)]
28. Li, X.; Li, Y.; Lu, Z. Study on distribution characteristics of heavy metal pollution in mineral resources development—Taking a copper mine area in Yalong river flow area as an example. *J. Miner. Prot. Util.* **2016**, *1*, 56–63. [[CrossRef](#)]
29. Zhang, C.; Qiao, Q.; Piper, J.D.; Huang, B. Assessment of heavy metal pollution from a Fe-smelting plant in urban river sediments using environmental magnetic and geochemical methods. *J. Environ. Pollut.* **2011**, *159*, 3057–3070. [[CrossRef](#)]
30. Dong, C.; Zhang, W.; Ma, H.; Feng, H.; Lu, H.; Dong, Y.; Yu, L. A magnetic record of heavy metal pollution in the Yangtze River subaqueous delta. *J. Sci. Total Environ.* **2014**, *368*, 476–477. [[CrossRef](#)]
31. Chen, X.; Jiang, C.; Zheng, L.; Zhang, L.; Fu, X.; Chen, S.; Chen, Y.; Hu, J. Evaluating the genesis and dominant processes of groundwater salinization by using hydrochemistry and multiple isotopes in a mining city. *J. Environ. Pollut.* **2021**, *283*, 117381. [[CrossRef](#)]
32. Cui, D.; Chen, X.; Xue, Y.; Li, R.; Zeng, W. An integrated approach to investigate the relationship of coupling coordination between social economy and water environment on urban scale—A case study of Kunming. *J. Environ. Manag.* **2019**, *234*, 189–199. [[CrossRef](#)]
33. Tian, Y.; Zhou, D.; Jiang, G. Conflict or Coordination? Multiscale assessment of the spatio-temporal coupling relationship between urbanization and ecosystem services: The case of the Jingjinji Region, China. *J. Ecol. Indic.* **2020**, *117*, 106543. [[CrossRef](#)]
34. Li, J.; Sun, W.; Li, M.; Meng, L. Coupling Coordination Degree of Production, Living and Ecological Spaces and its Influencing Factors in the Yellow River Basin. *J. Clean. Prod.* **2021**, *298*, 126803. [[CrossRef](#)]
35. Ariken, M.; Zhang, F.; Chan, N.; Kung, H. Corrigendum to “Coupling coordination analysis and spatio-temporal heterogeneity between urbanization and eco-environment along the Silk Road Economic Belt in China”. *J. Ecol. Indic.* **2020**, *121*, 107014. [[CrossRef](#)]
36. Yang, Y.; Bao, W.; Liu, Y. Coupling coordination analysis of rural production-living-ecological space in the Beijing-Tianjin-Hebei region. *J. Ecol. Indic.* **2020**, *117*, 106512. [[CrossRef](#)]
37. Dong, F.; Li, W. Research on the coupling coordination degree of “upstream-midstream-downstream” of China’s wind power industry chain. *J. Clean. Prod.* **2021**, *283*, 124633. [[CrossRef](#)]
38. Yeh, C.H. The selection of multiattribute decision making methods for scholarship student selection. *J. Int. J. Sel. Assess.* **2003**, *11*, 289–296. [[CrossRef](#)]
39. Chen, P. Effects of normalization on the entropy-based topsis method. *J. Expert Syst. Appl.* **2019**, *136*, 34–41. [[CrossRef](#)]
40. Sun, W.; Li, D.; Liu, P. A decision-making method for sponge city design based on grey correlation degree and topsis method. *J. Interdiscip. Math.* **2018**, *21*, 1031–1042. [[CrossRef](#)]
41. Sałabun, W.; Ziemia, P.; Wątróbski, J. The rank reversals paradox in management decisions: The comparison of the ahp and comet methods. In Proceedings of the International Conference on Intelligent Decision Technologies, Puerto de la Cruz, Spain, 15–17 June 2016; Springer: Cham, Switzerland, 2016; pp. 181–191. [[CrossRef](#)]
42. Dezert, J.; Tchamova, A.; Han, D.; Tacnet, J.M. The SPOTIS rank reversal free method for multi-criteria decision-making support. In Proceedings of the IEEE 23rd International Conference on Information Fusion (FUSION), Rustenburg, South Africa, 6–9 July 2020; IEEE: Piscataway, NJ, USA, 2020; pp. 1–8. [[CrossRef](#)]
43. Leng, L.; Mao, X.; Jia, H.; Xu, T.; Chen, A.S.; Yin, D.; Fu, G. Performance assessment of coupled green-grey-blue systems for Sponge City construction. *J. Sci. Total Environ.* **2020**, *728*, 138608. [[CrossRef](#)]
44. Zeng, J.; Lin, G.; Huang, G. Evaluation of the cost-effectiveness of Green Infrastructure in climate change scenarios using TOPSIS. *J. Urban For. Urban Green.* **2021**, *64*, 127287. [[CrossRef](#)]
45. Long, R.; Li, H.; Wu, M.; Li, W. Dynamic evaluation of the green development level of China’s coal-resource-based cities using the TOPSIS method. *J. Resour. Policy* **2021**, *74*, 102415. [[CrossRef](#)]
46. Lin, S.S.; Shen, S.L.; Zhou, A.; Xu, Y.S. Approach based on TOPSIS and Monte Carlo simulation methods to evaluate lake eutrophication levels. *J. Water Res.* **2020**, *187*, 116437. [[CrossRef](#)] [[PubMed](#)]
47. Lin, S.S.; Shen, S.L.; Zhang, N.; Zhou, A. Method for lake eutrophication levels evaluation: TOPSIS-MCS. *J. MethodsX* **2021**, *8*, 101311. [[CrossRef](#)] [[PubMed](#)]
48. Yang, T.; Zhang, Q.; Wan, X.; Li, X.; Wang, Y.; Wang, W. Comprehensive ecological risk assessment for semi-arid basin based on conceptual model of risk response and improved TOPSIS model—a case study of Wei River Basin, China. *J. Sci. Total Environ.* **2020**, *719*, 137502. [[CrossRef](#)] [[PubMed](#)]
49. Yang, Y. Expansion and evolution of a typical resource-based mining city in transition using the Google Earth engine: A case study of Datong, China. *J. Remote Sens.* **2021**, *13*, 4045. [[CrossRef](#)]
50. Camp, B.L.M.; Nel, V.; Mphambukeli, T. A thriving coal mining city in crisis? The governance and spatial planning challenges at Witbank, South Africa. *Land Use Policy* **2017**, *62*, 223–231. [[CrossRef](#)]
51. Peng, K.; Luo, C.; Lou, L.; Li, X.; Shen, Z. Bioaccumulation of heavy metals by the aquatic plants *Potamogeton pectinatus* L. and *Potamogeton malaianus* Miq. and their potential use for contamination indicators and in wastewater treatment. *Sci. Total Environ.* **2008**, *392*, 22–29. [[CrossRef](#)]
52. Salehpour Jam, A.; Mosaffaie, J.; Sarfaraz, F.; Shadfar, S.; Akhtari, R. GIS-based landslide susceptibility mapping using hybrid MCDM models. *J. Nat. Hazards* **2021**, *108*, 1025–1046. [[CrossRef](#)]

53. Li, D.; Cheung, D.; Shi, X.; Ng, V. Uncertainty reasoning based on cloud models in controllers. *J. Comput. Math. Appl.* **1998**, *35*, 99–123. [CrossRef]
54. Wang, J.; Zhai, T.; Lin, Y.; Kong, X.; He, T. Spatial imbalance and changes in supply and demand of ecosystem services in China. *J. Sci. Total Environ.* **2019**, *657*, 781–791. [CrossRef]
55. Liu, D.; Wang, D.; Wu, J.; Wang, Y.; Wang, L.; Zou, X.; Chen, Y.; Chen, X. A risk assessment method based on RBF artificial neural network-cloud model for urban water hazard. *J. Intell. Fuzzy Syst.* **2014**, *27*, 2409–2416. [CrossRef]
56. Li, D.; Liu, C.Y.; Liu, L.Y. Study on the universality of the normal cloud model. *J. Eng. Sci.* **2004**, *6*, 28–34.
57. Liu, Y.; Chen, H.Y.; Wang, X.J. Research on green renovations of existing public buildings based on a cloud model. *J. Build. Eng.* **2021**, *34*, 101930. [CrossRef]
58. Min, C.; Wen, G.; Li, B.; Zhao, X. Comprehensive evaluation of offshore oilfield development plans based on grey clustering analysis with cloud model. *J. Math. Probl. Eng.* **2018**, *2018*, 4020753. [CrossRef]
59. Hou, M.; Deng, Y.; Yao, S. Spatial Agglomeration Pattern and Driving Factors of Grain Production in China since the Reform and Opening Up. *J. Land* **2021**, *10*, 10. [CrossRef]
60. Tao, F.; Hu, Y.; Tang, G.; Zhou, T. Long-term evolution of the suhi footprint and urban expansion based on a temperature attenuation curve in the Yangtze river delta urban agglomeration. *J. Sustain.* **2021**, *13*, 8530. [CrossRef]
61. Ren, S.; Song, C.; Ye, S.; Cheng, C.; Gao, P. The spatiotemporal variation in heavy metals in China's farmland soil over the past 20 years: A meta-analysis. *J. Sci. Total Environ.* **2022**, *806*, 150322. [CrossRef] [PubMed]
62. Xu, S.; He, W.; Shen, J.; Degefu, D.M.; Yuan, L.; Kong, Y. Coupling and Coordination Degrees of the Core Water-Energy-Food Nexus in China. *Int. J. Environ. Res.* **2019**, *16*, 1648. [CrossRef]
63. Yang, X.; Meng, F.; Fu, P.; Zhang, Y.; Liu, Y. Spatiotemporal change and driving factors of the Eco-Environment quality in the Yangtze River Basin from 2001 to 2019. *J. Ecol. Indic.* **2021**, *131*, 108214. [CrossRef]
64. Zhou, K.; Wu, J.; Liu, H. Spatiotemporal variations and determinants of water pollutant discharge in the Yangtze River Economic Belt, China: A spatial econometric analysis. *J. Environ. Pollut.* **2021**, *271*, 116320. [CrossRef]
65. Deng, C.; Li, H.; Peng, D.; Liu, L.; Zhu, Q.; Li, C. Modelling the coupling evolution of the water environment and social economic system using PSO-SVM in the Yangtze River Economic Belt, China. *J. Ecol. Indic.* **2021**, *129*, 108012. [CrossRef]
66. Wang, R.; Jia, T.; Qi, R.; Cheng, J.; Zhang, K.; Wang, E.; Wang, X. Differentiated impact of politics- and science-oriented education on pro-environmental behavior: A case study of Chinese university students. *J. Sustain.* **2021**, *13*, 616. [CrossRef]
67. Jiao, W.; Zhang, X.; Li, C.; Guo, J. Sustainable transition of mining cities in China: Literature review and policy analysis. *J. Resour. Policy* **2021**, *74*, 101867. [CrossRef]
68. Armis, R.; Kanegae, H. The attractiveness of a post-mining city as a tourist destination from the perspective of visitors: A study of Sawahlunto old coal mining town in Indonesia. *J. Asia-Pac. J. Reg. Sci.* **2020**, *4*, 443–461. [CrossRef]
69. He, S.Y.; Lee, J.; Zhou, T.; Wu, D. Shrinking cities and resource-based economy: The economic restructuring in China's mining cities. *J. Cities* **2017**, *60*, 75–83. [CrossRef]
70. Huang, Z.; Liu, C.; Zhao, X.; Dong, J.; Zheng, B. Risk assessment of heavy metals in the surface sediment at the drinking water source of the Xiangjiang River in South China. *J. Environ. Sci. Eur.* **2020**, *32*, 23. [CrossRef]
71. Yan, J.; Qu, Z.; Li, F.; Li, H. Heavy metals in the water environment of Yangtze River Economic Belt: Status, fuzzy environmental risk assessment and management. *J. Urban Clim.* **2021**, *40*, 100981. [CrossRef]
72. Hulscher, T.; Mol, G.; Lüers, F. Release of metals from polluted sediments in a shallow lake: Quantifying resuspension. *J. Hydrobiol.* **1992**, *235–236*, 97–105. [CrossRef]
73. Thomas, K.V.; Bijlsma, L.; Castiglioni, S.; Covaci, A.; Emke, E.; Grabic, R.; Hernández, F.; Karolak, S.; Kasprzyk-Hordern, B.; Lindberg, R.H.; et al. Heavy metal pollution in reservoirs in the hilly area of southern China: Distribution, source apportionment and health risk assessment. *J. Sci. Total Environ.* **2018**, *634*, 158–169. [CrossRef]
74. Former Ministry of Environmental Protection of China. 12th Five Year Plan for Comprehensive Prevention and Control of Heavy Metal Pollution. 2016. Available online: [http://www.gov.cn/xinwen/2016-11/30/content\\_5140517.htm](http://www.gov.cn/xinwen/2016-11/30/content_5140517.htm) (accessed on 30 November 2016).



## Article

# Research on Fault Tree Reconstruction Based on Contingency

Song Xin <sup>1,2,3</sup>, Xiaozhen Zhu <sup>1,2</sup>, Shangxiao Liu <sup>1,2,\*</sup> and Jianghui Guo <sup>1,2</sup>

- <sup>1</sup> College of Safety and Environmental Engineering, Shandong University of Science and Technology, Qingdao 266590, China; xinsong@sdust.edu.cn (S.X.); zxz19971227@163.com (X.Z.); gjh199609@126.com (J.G.)  
<sup>2</sup> State Key Laboratory of Mining Disaster Prevention and Control Co-Founded by Shandong Province and the Ministry of Science and Technology, Shandong University of Science and Technology, Qingdao 266590, China  
<sup>3</sup> College of Transportation, Shandong University of Science and Technology, Qingdao 266590, China  
\* Correspondence: liushangxiao\_24@163.com

**Abstract:** The fault tree analysis (FTA) method is an important analysis method for safety system engineering. Traditional accident analysis theory agrees that basic events lead to top events, but it does not fully consider that the accident process is accidental, and the calculation results exaggerate the probability of accident occurrence. This paper selects typical collision accidents, analyzes the shortcomings of the existing fault tree, indicates that there is a contingency in the accident process, constructs a probability fault tree based on the traditional fault tree, and puts forward concepts of “probability AND gate” and “probability OR gate”. In addition, based on the traditional quantitative analysis method of fault trees, calculations of the occurrence probability, probability importance coefficient, and critical importance coefficient of top events are modified, and the modified quantitative calculation is applied to accident cases.

**Keywords:** fault tree reconstruction; contingency; probability AND gate; probability OR gate

**Citation:** Xin, S.; Zhu, X.; Liu, S.; Guo, J. Research on Fault Tree Reconstruction Based on Contingency. *Processes* **2022**, *10*, 427. <https://doi.org/10.3390/pr10020427>

Academic Editors: Roberto Alonso González Lezcano, Francesco Nocera, Rosa Giuseppina Caponetto and Hector Budman

Received: 3 January 2022

Accepted: 16 February 2022

Published: 21 February 2022

**Publisher’s Note:** MDPI stays neutral with regard to jurisdictional claims in published maps and institutional affiliations.



**Copyright:** © 2022 by the authors. Licensee MDPI, Basel, Switzerland. This article is an open access article distributed under the terms and conditions of the Creative Commons Attribution (CC BY) license (<https://creativecommons.org/licenses/by/4.0/>).

## 1. Introduction

The causal analysis of accidents is a common method for identifying and analyzing the causes of accidents and preventing or controlling them. However, both the causal model and the causal analysis method have some shortcomings [1–4]. Using fault tree analysis, we can analyze the optimization decision, accident prediction, and accident investigation processing of the entire system, as well as discuss system safety [5,6]. Fault tree analysis is the quantitative analysis of a fault tree, that is, quantification of the top-event probability as the core goal and accurate expression of the accident risk degree with data [7].

According to the existing fault tree analysis method and the event-causal chain, basic cause events lead to intermediate events and then to top events. The theoretical description of a series of events leading to accidents according to a specific causal relationship is too simplistic [8,9], and different from reality.

Wang et al. [10] believe that if the nonquantifiable judgment of failure probability is insufficient, the logical relationship between all events cannot be measured. Their research results indicate that fault tree analysis cannot essentially deal with the dynamic process of accidents. Therefore, a new event tree analysis method including probability basic events was proposed. Hua et al. [11] considered the accidental explosion of dangerous goods in Tianjin Port, China, as the research object and systematically analyzed the causes of the accident based on fault tree analysis. Their results showed that the basic events of the fault tree should be introduced into the probability model, which should then be used to quantitatively analyze and judge various top events. Zhu et al. [12] reported that in fault tree analysis, with the extension of time, the impact of basic events on top events changes, that is, the probability of basic events changes with time. However, their research did not consider the contingency in the accident chain, which leads to a change in the impact of basic events on top events.

Many studies have recommended different methods of dealing with uncertainty in FTA, including, but not limited to, fuzzy set theory [13] and the Bayesian network [14]. Mohammad Yazdi [15] reviewed the uncertainty treatment in risk assessment based on fault tree analysis (FTA) in the past decade and found that the research on uncertainty treatment in qualitative and quantitative risk assessment is a developing field. Because the logical relationship of the fault tree is artificially determined, the contingency in the process of transferring basic events to top events in the fault tree is ignored.

In response to the above problem, this paper considers the chance nature of accidents to analyze and explain the existing problems of a typical fault tree. Based on this, the concepts of the probability AND gate and the probability OR gate are proposed, the fault tree is modified, the concept of a probability fault tree is proposed, and the quantitative calculation method is improved. This theory is helpful to produce a more reasonable risk assessment of fault tree analysis.

**2. Analysis of the Construction Process of a Probability Accident Tree**

*2.1. Problems in the Existing Fault Tree*

To analyze problems in the existing fault tree, this section selects typical traffic accidents for collision accident analysis and combined with the accident contingency, analyzes accident occurrence and development, identifies the possible problems, and lays the foundation for the transformation of the fault tree (Figure 1).

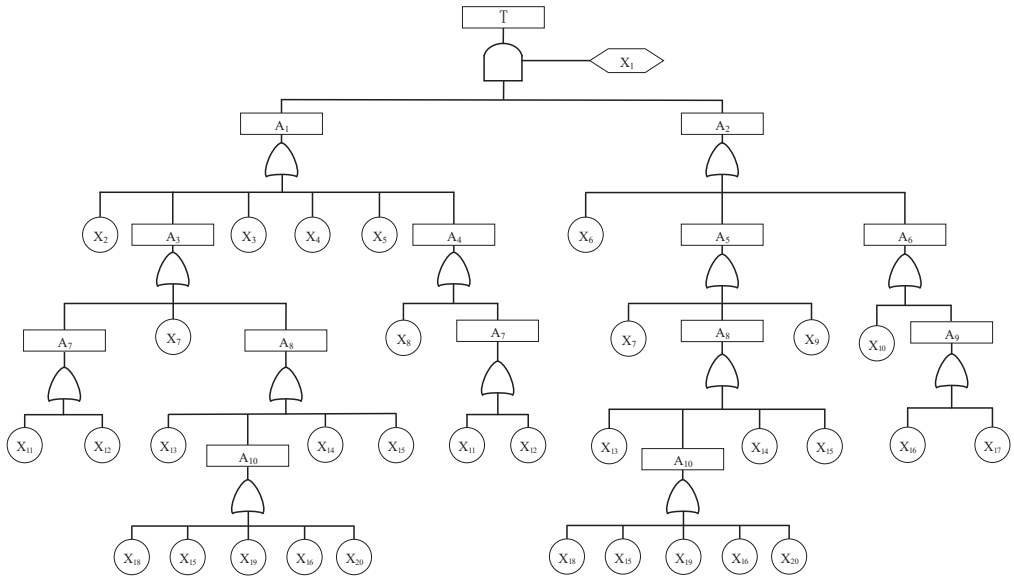


**Figure 1.** Fault tree of a collision accident.

In order to facilitate the subsequent analysis of the evolutionary fault tree, each event is generally marked with a word symbol. The top event is represented by T, and the intermediate event is represented by A, which is distinguished from the basic event X in the fault tree, as shown in Table 1.

According to the existing collision fault tree and event chain, during accident occurrence and development, the basic events or a combination of basic events leads to the occurrence of the accident layer by layer; that is, previous conditions inevitably lead to the occurrence of subsequent events, such as poor road traffic conditions leading to fatigue driving, which, in turn, leads to inattention, incorrect judgment, insufficient longitudinal distance, and too fast a speed, which further leads to collisions.

**Table 1.** Fault tree accident type and symbol comparison [16].

Symbol	Event Name	Symbol	Event Name	Symbol	Event Name
T	Collision accident	X1	Inability to dodge	X12	Poor lighting for driving at night
A1	Insufficient vertical spacing	X2	Illegal turn	X13	Bad mood
A2	Speed too fast	X3	Violation of giving way to an oncoming vehicle	X14	Drive after drinking
A3	Misjudgment	X4	Overtaking in violation of regulations	X15	Poor health
A4	Observation error	X5	Illegal parking	X16	Poor road traffic conditions
A5	Operation error	X6	Pursuit of stimulation	X17	Bad brake performance or too much wear
A6	Braking problem	X7	Lack of knowledge and experience	X18	Lack of sleep
A7	Poor sight	X8	Not enough sight distance	X19	Driving too long
A8	Inattention	X9	Limited driving skills	X20	Poor temperature ventilation
A9	Poor braking	X10	Brake failure		
A10	Fatigue driving	X11	Impact of rain, snow, and fog		

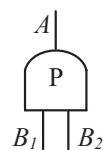
Previous studies have found that there is a certain contingency in this chain of events, and the occurrence of accidents is not inevitable. For example, poor road traffic conditions do not necessarily cause fatigue driving, and a poor mood does not necessarily lead to a lack of concentration. For knowledge-level experience, insufficiency does not necessarily cause judgment errors. Therefore, the accident tree has certain loopholes; it ignores the contingency of the event itself and the event chain in the transmission process, that is, the probability of the AND gate or the OR gate. The description of the causality in accident development is too absolute, and it is believed that an accident is the inevitable result of the causal transmission of various factors. Therefore, the existing accident tree should be improved so that accidents can be fully understood.

## 2.2. Fault Tree Reconstruction

Analysis of typical collision accidents shows that there is a contingency in accident occurrence and development, that is, in event tree construction, which was not considered by the traditional AND and OR gates. To fully understand accidents, the concepts of the probability AND gate, probability OR gate, and probability fault tree are proposed.

### 2.2.1. Probability AND Gate

The probability AND gate mean that when input events,  $B_1$  and  $B_2$ , occur simultaneously, output event  $A$  may not necessarily occur. Based on the input events,  $B_1$  and  $B_2$ , occurring simultaneously, there may be chance events that prevent output event  $A$  from occurring. Therefore, there is a probability that when input events,  $B_1$  and  $B_2$ , occur simultaneously, output event  $A$  occurs. Namely,  $A = B_1 \cap B_2 \cap B_{12}$ , or  $A = B_1 \cdot B_2 \cdot B_{12}$ . This is also true if multiple input events exist, such as  $A = B_1 \cdot B_2 \cdot \dots \cdot B_n \cdot B_{12\dots n}$ . The probability AND gate symbol is shown in Figure 2.

**Figure 2.** Probability AND gate symbol.

### 2.2.2. Probability OR Gate

The probability OR gate means that at least one of the input events,  $B_1$  and  $B_2$ , occurs and output event  $A$  does not necessarily occur. Based on at least one of the input events,  $B_1$  and  $B_2$ , there may be chance events that prevent output event  $A$  from occurring. Therefore, there is a probability that when at least one of the input events,  $B_1$  and  $B_2$ , occurs, output event  $A$  will occur. Namely,  $A = B_1 B_{m1} \cup B_2 B_{m2}$ , or  $A = B_1 B_{m1} + B_2 B_{m2}$ . This is also true for multiple input events. The probability OR gate symbol is shown in Figure 3.



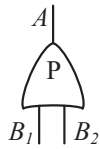


**Figure 3.** Probability OR gate symbol.

### 2.2.3. Probability Accident Tree

Through an analysis of the probability AND and probability OR gates, the probability accident tree was constructed, as shown in Figure 4. Probability fault trees reflect that there is a specific chance of occurrence of the top event. Therefore, the probability AND and probability OR gates are used to connect basic events, intermediate events, and top events.

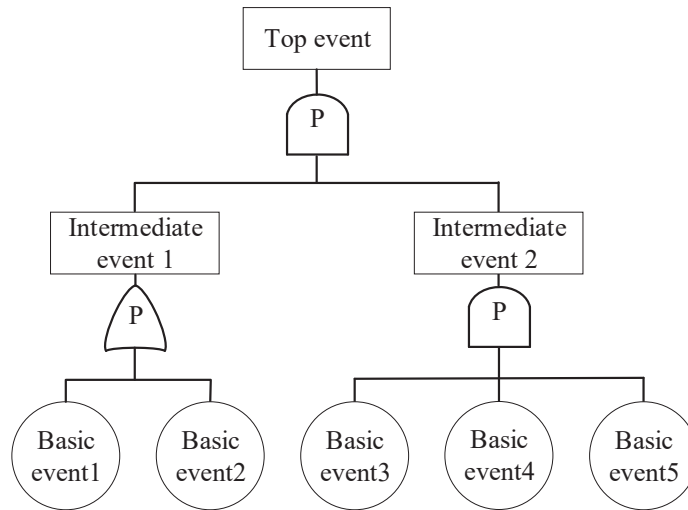


**Figure 4.** Schematic diagram of probability accident tree.

When at least one of basic events 1 and 2 occurs, it does not necessarily lead to the occurrence of intermediate event 1. There is a probability  $q_{m_r}$  that when at least one of basic events 1 and 2 occurs, intermediate event 1 occurs. That is, there is a probability  $\bar{q}_{m_r}$  that when at least one of the basic events 1 and 2 occurs, intermediate event 1 does not occur. If basic event 1 inevitably leads to intermediate event 1,  $q_{m_r} = 1$  and  $\bar{q}_{m_r} = 0$ .

## 3. Improvement of the Quantitative Calculation Method of Fault Trees

Quantitative analysis of the accident tree is mainly based on the occurrence probability of each basic event, calculation of the top event's occurrence probability, and probability and the critical importance of each basic event [17]. The concept of the probability AND and probability OR gates is introduced after the above modification of the accident tree; therefore, the corresponding quantitative analysis method of the accident tree also needs to be improved.

### 3.1. Improvement of the Quantitative Calculation Method

The calculation of the top event's occurrence probability is the basis of the fault tree's quantitative analysis [18], and the improved method for calculating the top event's occurrence probability considers the contingency in the transmission process of the event chain; thus, the resulting probability of the accident is closer to reality.

The probability product of events connected by the probability AND gate is

$$q_A = q_j \prod_{i=1}^n q_i \tag{1}$$

where

$$\prod_{i=1}^n q_i = q_1 q_2 \cdots q_n \tag{2}$$

and

$$q_j = 1 - \bar{q}_j \tag{3}$$

In this formula,  $q_j$  is the occurrence probability of the  $i$ -th basic event,  $q_A$  is the probability of AND gate events,  $n$  is the number of input events,  $q_j$  is the probability that the occurrence of the basic event leads to the occurrence of an AND gate event,  $\bar{q}_j$  is the probability that the occurrence of the basic event does not lead to the occurrence of an AND gate event, and  $\prod$  is a mathematical operation symbol that indicates the product of the probabilities.

The sum of the probabilities of events connected by a probability OR gate is

$$q_o = \coprod_{i=1, m=1}^n q_i q_m = 1 - \prod_{i=1, m=1}^n (1 - q_i q_m) \tag{4}$$

where

$$q_m = 1 - \bar{q}_m \tag{5}$$

In this formula,  $q_o$  is the probability of OR gate events,  $q_m$  is the probability that the occurrence of the basic event leads to the occurrence of an OR gate event,  $\bar{q}_m$  is the probability that the occurrence of the basic event does not lead to the occurrence of an OR gate event, and  $\coprod$  is a mathematical operation symbol that indicates the sum of the probabilities.

The minimum cut set is used to calculate the occurrence probability of the top events, and there are no repeated events.

$$g = \prod_{r=1}^k (q_{j_r} \prod_{x_i \in k_r, j=1}^k q_i) q_{m_r} = 1 - \prod_{i=1}^n \left( 1 - q_m q_j \prod_{x_i \in k_r} q_i \right) \tag{6}$$

In this formula,  $x_i$  is the  $i$ -th basic event,  $k_r$  is the  $r$ -th minimum cut set,  $k$  is the number of minimum cut sets,  $x_i \in k_r$  is the  $i$ -th basic event belonging to the  $r$ -th minimum cut set,  $q_{j_r}$  is the probability of the occurrence of  $k_r$  caused by the occurrence of the basic event, and,  $q_{m_r}$  is the probability that the occurrence of  $k_r$  leads to an accident.

If there are repeated events in the minimum cut set, the occurrence probability of the top event is

$$g = \sum_{r=1}^k q_{j_r} q_{m_r} \prod_{x_i \in k_r} q_i - \sum_{1 \leq r < s \leq k} q_{j_r} q_{j_s} q_{m_r} q_{m_s} \prod_{x_i \in k_r \cup k_s} q_i + \cdots + (-1)^{k-1} \prod_{r=1, x_i \in k_r}^k q_i q_{j_r} q_{m_r} \tag{7}$$

In this formula,  $r, s$  is the sequence number of the smallest cut set.

The occurrence probability of the event at the top of the accident tree has been modified above; therefore, the probability importance and critical importance of the corresponding basic events should also be modified and studied. Among these, Equations (8) and (9), the probabilistic importance coefficient and the critical importance coefficient, remain unchanged. However, if the top event's probability changes, then the magnitudes of the probabilistic and critical importance coefficients also change accordingly.

$$I_g(i) = \frac{\partial g}{\partial q_i} \quad (8)$$

In this formula,  $I_g(i)$  is the probability importance coefficient of a basic event  $x_i$ .

$$CI_g(i) = \frac{q_i}{g} I_g(i) \quad (9)$$

In this formula,  $CI_g(i)$  is the critical importance coefficient of a basic event  $x_i$ .

### 3.2. Application of the Probability Fault Tree

With the development of the urban economy, the number of high-rise buildings in cities is gradually increasing. At the same time, fires in these high-rise buildings have become the focus of firefighting. This section describes the construction of a probability accident tree and draws a probability accident tree by analyzing fire accidents in the college and university dormitories [19]. The occurrence probability of each basic event in the probability accident tree is recorded in Table 2 [20].

**Table 2.** Probability accident tree accident event type and occurrence probability of basic events.

Symbol	Event Name	Probability Value	Symbol	Event Name	Probability Value
T	Dormitory fire accident		A6	Open fire source	
A1	On fire		A7	Electric fire source	
A2	Out of control		A8	Firefighting facilities not working	
A3	Fire source		A9	Line	
A4	Combustible		A10	Electrical appliances	
A5	Rescue not timely				
X1	Smoking	0.02	X13	Clothes, quilt	0.02
X2	Alcohol stove	0.05	X14	Textbook, desk	0.03
X3	Burning mosquito repellent incense	0.02	X15	Other flammable materials	0.02
X4	Thunder	0.03	X16	Alarm system not working	0.05
X5	Connecting wires without permission	0.05	X17	Not found in time	0.03
X6	Wires short-circuited	0.02	X18	At a loss	0.03
X7	Line aging	0.03	X19	Fire extinguishers in short supply	0.05
X8	Use of illegal electrical appliances	0.06	X20	Insufficient input in fire hydrants	0.01
X9	Use of inferior electrical appliances	0.05	X21	Unreasonable configuration of the automatic sprinkler system	0.02
X10	Use of an electric heater	0.03	X22	Lack of knowledge of how to use a fire extinguisher	0.03
X11	Use of an electric blanket	0.03	X23	Insufficient water supply for fire hydrants	0.03
X12	Use of hand warmers	0.02	X24	Failure of the automatic sprinkler system	0.02

By simplifying the fault tree shown in Figure 5 and using the calculation for the probability of the event at the top of the fault tree in the early stage, we calculated the probability of fire in the dormitory as 0.98%.

Considering the uncertainty that exists in the accident process, the occurrence of a specific basic event does not necessarily lead to an intermediate event. The existence of the probability of occasionality allows the occurrence of a basic event without the occurrence of an intermediate event regardless of the size of that probability; using the revised fault tree quantitative calculation method, the calculated probability of a college dormitory fire is always  $\leq 0.98\%$ .

These results show that the accident probability obtained through the quantitative analysis of the original accident tree does not consider the contingency. We believe that a specific basic event would inevitably lead to intermediate events, thus leading to accidents. Therefore, the accident probability obtained was extremely high. In reality, contingencies exist in the occurrence of accidents, especially for a single accident, in which the contingency is more obvious. Therefore, the modified quantitative calculation method for accident trees has practical theoretical value.

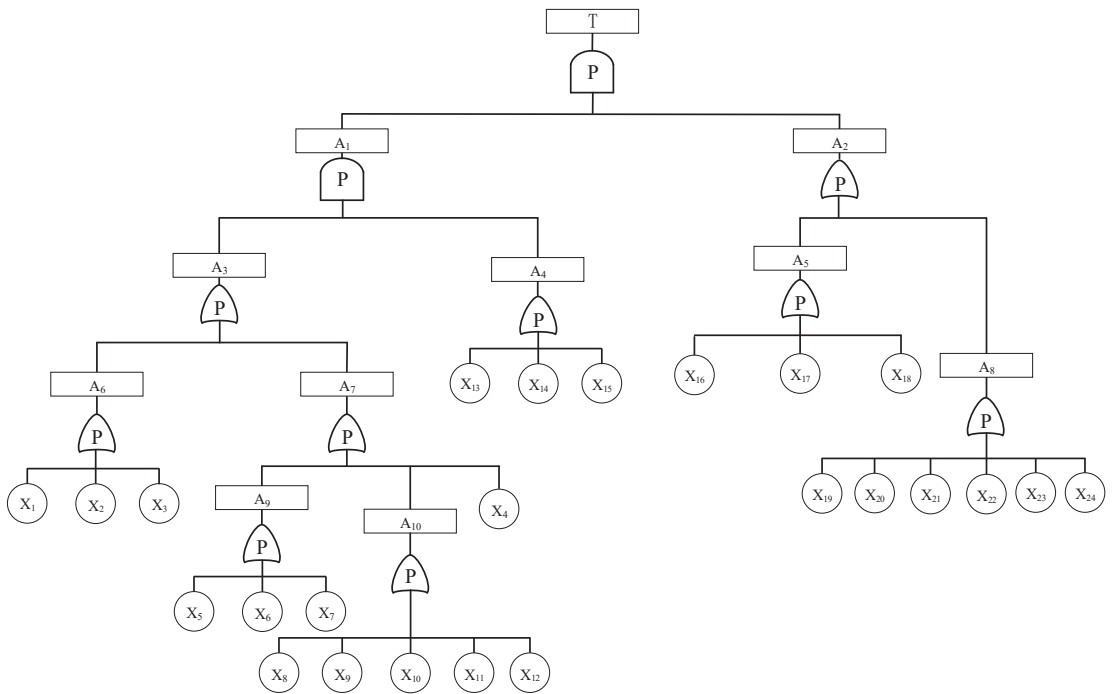


**Figure 5.** Fire accident tree diagram of a college dormitory.

#### 4. Conclusions

- (1) Through the analysis of typical collision accidents, the shortcomings of the existing FTA are analyzed, and the concept of a probabilistic FTA is innovatively proposed to enrich accident tree analysis. The concepts of probability AND and OR gates are presented and applied to the accident tree.
- (2) The quantitative calculation method of traditional FTA essentially exaggerates the probability of an accident. Therefore, the traditional FTA has been reformed and the probability accident tree is compiled, and the quantitative calculation method of probability FTA is proposed.
- (3) The proposal of probabilistic FTA has important practical significance and theoretical value for guiding safety management. It provides a new idea for the study of top event probability in traditional FTA.

**Author Contributions:** S.X. and S.L. presided over the main work and wrote the thesis; X.Z. completed the basic theoretical research; J.G. completed the data processing and analysis; they all provided insightful suggestions and revised the thesis. All authors have read and agreed to the published version of the manuscript.

**Funding:** This work has been funded by the National Natural Science Foundation of China, grant numbers 51774197.

**Institutional Review Board Statement:** This study was abandoned for ethical review and approval.

**Informed Consent Statement:** Informed consent was obtained from all subjects involved in the study.

**Data Availability Statement:** The study did not report any data.

**Conflicts of Interest:** The authors declare no conflict of interest.

## References

- Xin, S.; Zhang, L.; Jin, X.; Zhang, Q. Reconstruction of the Fault Tree Based on Accident Evolution. *Process Saf. Environ. Prot.* **2019**, *121*, 307–311. [[CrossRef](#)]
- Li, W.; Zhang, L.; Liang, W. An Accident Causation Analysis and Taxonomy (ACAT) Model of Complex Industrial System from both System Safety and Control Theory Perspectives. *Saf. Sci.* **2017**, *92*, 94–103. [[CrossRef](#)]
- Liu, P.; Yang, L.; Gao, Z.; Li, S.; Gao, Y. Fault Tree Analysis Combined with Quantitative Analysis for High-Speed Railway Accidents. *Saf. Sci.* **2015**, *79*, 344–357. [[CrossRef](#)]
- Lippiello, D.; Degan, G.A.; Pinzari, M. A Novel Fault Tree Analysis Approach to Investigate Uncommon Accidents in Quarries: A Case Study. *Int. J. Saf. Secur. Eng.* **2018**, *8*, 451–462. [[CrossRef](#)]
- Chen, Y.Q.; Li, S.G.; He, X. Fault Tree Analysis of “Mistakes, Forgetfulness, and Negligence” Accidents in ATC. *Appl. Mech. Mater.* **2011**, *1280*, 924–929. [[CrossRef](#)]
- Jafari, M.J.; Pouyakian, M.; Khanteymoori, A.; Hanifi, S.M. Reliability Evaluation of Fire Alarm Systems Using Dynamic Bayesian Networks and Fuzzy Fault Tree Analysis. *J. Loss Prev. Process Ind.* **2020**, *67*, 104229. [[CrossRef](#)]
- Lee, W.S.; Grosh, D.L.; Tillman, F.A.; Lie, C.H. Fault Tree Analysis, Methods, and Applications-A Review. *IEEE Trans. Reliab.* **2009**, *R-34*, 194–203. [[CrossRef](#)]
- Khan, F.I.; Iqbal, A.; Ramesh, N.; Abbasi, S.A. SCAP: A New Methodology for Safety Management Based on Feedback from Credible Accident-Probabilistic Fault Tree Analysis System. *J. Hazard. Mater.* **2001**, *87*, 23–56. [[CrossRef](#)]
- Nicolae, F.; Cotorcea, A.; Ristea, M.; Atodiresei, D. Human Reliability Using the Fault Tree Analysis. A Case Study of a Military Accident Investigation. *Int. Conf. Knowl.-Based Organ.* **2016**, *22*, 215–219. [[CrossRef](#)]
- Wang, W.; Jiang, X.; Xia, S.; Cao, Q. Incident Tree Model and Incident Tree Analysis Method for Quantified Risk Assessment: An In-Depth Accident Study in Traffic Operation. *Saf. Sci.* **2010**, *48*, 1248–1262. [[CrossRef](#)]
- Hua, W.; Chen, J.; Qin, Q.; Wan, Z.; Song, L. Causation Analysis and Governance Strategy for Hazardous Cargo Accidents at Ports: Case Study of Tianjin Port’s Hazardous Cargo Explosion Accident. *Mar. Pollut. Bull.* **2021**, *30*, 542–555. [[CrossRef](#)] [[PubMed](#)]
- Zhu, C.; Tang, S.; Li, Z.; Fang, X. Dynamic Study of Critical Factors of Explosion Accident in Laboratory Based on FTA. *Saf. Sci.* **2020**, *130*, 104877. [[CrossRef](#)]
- Jafarian, E.; Rezvani, M.A. Application of fuzzy fault tree analysis for evaluation of railway safety risks: An evaluation of root causes for passenger train derailment. *Proc. Inst. Mech. Eng. Part F J. Rail Rapid Transit.* **2012**, *226*, 14–25. [[CrossRef](#)]
- Chu, Z.; Yang, Z.; Peng, M.; Sun, W. *Research of Security Analysis Based on Subjective Bayesian Networks*; IEEE: Piscataway, NJ, USA, 2011.
- My, A.; Skb, C.; Mw, B. Uncertainty handling in fault tree based risk assessment: State of the art and future perspectives. *Process Saf. Environ. Prot.* **2019**, *131*, 89–104.
- Cao, Q. *Safety System Engineering*; China Coal Industry Press: Beijing, China, 2010.
- Khare, V.; Nema, S.; Baredar, P. Reliability analysis of hybrid renewable energy system by fault tree analysis. *Energy Environ.* **2019**, *30*, 542–555. [[CrossRef](#)]
- Cho, B.H.; Yum, B.; Kim, S. Calculation of Top Event Probability of Fault Tree using BDD. *J. Korea Inst. Inf. Commun. Eng.* **2016**, *20*, 654–662. [[CrossRef](#)]
- Fei, P.; Nali, S. Fire Hazard Analysis of Student Dormitory in a University Based on Accident Tree. *J. Jilin Univ. Chem. Technol.* **2019**, *36*, 46–50.
- Zhang, X. Exploration and Prevention of University Student Dormitory Fire Laws Based on Accident Tree Analysis. *Smart City* **2019**, *5*, 3.



Article

# Metal(loid)s Spatial Distribution, Accumulation, and Potential Health Risk Assessment in Soil-Wheat Systems near a Pb/Zn Smelter in Henan Province, Central China

Ling Yang <sup>1,2,†</sup>, Qiang Ren <sup>2,†</sup>, Shiji Ge <sup>2</sup>, Zhiqiang Jiao <sup>3</sup>, Wenhao Zhan <sup>4</sup>, Runxiao Hou <sup>3</sup>, Xinling Ruan <sup>1,2,3</sup>, Yanfang Pan <sup>1,2,\*</sup> and Yangyang Wang <sup>1,2,3,\*</sup>

<sup>1</sup> National Demonstration Center for Environmental and Planning, College of Geography and Environmental Science, Henan University, Kaifeng 475004, China; yangling0606@163.com (L.Y.); 0412420xx@163.com (X.R.)

<sup>2</sup> Key Laboratory of Geospatial Technology for the Middle and Lower Yellow River Regions, Henan University, Ministry of Education, Kaifeng 475004, China; 1610131137@vip.henu.edu.cn (Q.R.); GSGe@henu.edu.cn (S.G.)

<sup>3</sup> Henan Engineering Research Center for Control and Remediation of Soil Heavy Metal Pollution, Henan University, Kaifeng 475004, China; ZQJiao@henu.edu.cn (Z.J.); hou20010423@163.com (R.H.)

<sup>4</sup> National Key Laboratory of Human Factors Engineering, China Astronaut Research and Training Center, Beijing 100094, China; zhanwenhao2005@126.com

\* Correspondence: panyanfang@henu.edu.cn (Y.P.); wangyangyangxyz@163.com (Y.W.)

† These authors contributed equally to this work.

**Abstract:** To understand the influence of Pb/Zn smelter on surrounding environment, 110 soil and 62 wheat grain samples (62 paired samples) were collected nearby a Pb/Zn smelter in Jiaozuo City, Henan Province, China. The content and spatial distribution of metal(loid)s in the soil-wheat system, and the potential health risk via consumption of wheat grains were determined. Results showed that the average content of Pb, Cd, As, Cu, Zn, and Ni in soil were 129.16, 4.28, 17.95, 20.43, 79.36, and 9.42 mg/kg, respectively. The content of Cd in almost all soil samples (99.1%) exceeded the national limitation of China (0.6 mg/kg). Spatial distribution analysis indicated that atmospheric deposition might be the main pollution source of Pb, Cd, As, and Zn in soil. In addition, the average content of Pb, Cd, As, Cu, Zn, and Ni in wheat grain were 0.62, 0.35, 0.10, 3.7, 35.77, and 0.15 mg/kg, respectively, with the average Pb and Cd content exceeding the national limitation of China. The average bioaccumulation factor of these metal(loid)s followed the following order: Zn (0.507) > Cu (0.239) > Cd (0.134) > Ni (0.024) > Pb (0.007) > As (0.006). Health risk assessment indicated that the average noncarcinogenic risk of children (6.78) was much higher than that of adults (2.83), and the carcinogenic risk of almost all wheat grain is higher than the acceptable range, with an average value of  $2.43 \times 10^{-2}$ . These results indicated that humans who regularly consume these wheat grains might have a serious risk of noncarcinogenic and carcinogenic diseases.

**Keywords:** health risk assessment; metal(loid)s; soil; spatial distribution; wheat

**Citation:** Yang, L.; Ren, Q.; Ge, S.; Jiao, Z.; Zhan, W.; Hou, R.; Ruan, X.; Pan, Y.; Wang, Y. Metal(loid)s Spatial Distribution, Accumulation, and Potential Health Risk Assessment in Soil-Wheat Systems near a Pb/Zn Smelter in Henan Province, Central China. *Int. J. Environ. Res. Public Health* **2022**, *19*, 2527. <https://doi.org/10.3390/ijerph19052527>

Academic Editors: Roberto Alonso González Lezcano, Francesco Nocera and Rosa Giuseppina Caponetto

Received: 24 January 2022

Accepted: 20 February 2022

Published: 22 February 2022

**Publisher's Note:** MDPI stays neutral with regard to jurisdictional claims in published maps and institutional affiliations.



**Copyright:** © 2022 by the authors. Licensee MDPI, Basel, Switzerland. This article is an open access article distributed under the terms and conditions of the Creative Commons Attribution (CC BY) license (<https://creativecommons.org/licenses/by/4.0/>).

## 1. Introduction

Rapid urbanization, agricultural modernization, and industrialization in the last few decades have resulted in a large amount of metal(loid)s released into the environment [1]. As the primary environmental reservoir and storage bank of metal(loid)s, soil accumulates most of the released metal(loid)s and is severely contaminated in some areas [2,3]. Based on the national survey of China in 2014, more than 10% of the farmland was contaminated with metal(loid)s [4,5], which was more serious in other developing countries. Metal(loid)s are toxic, nondegradable, and pose a serious risk to human health through the food chain bioaccumulation, which gained great attention worldwide [6]. A main pollution source of metal(loid)s is the nonferrous smelting and processing industry (NSPI), which can discharge metal(loid)s through the wastewater, atmospheric deposition, and solid waste [7,8]. Therefore, a study on the pollution status of metal(loid)s in the soil around

these enterprises can provide an important guide for the safe use of land resources and control of human behavior.

Great attention has been given to the impact of NSPI on the surrounding soil in recent years [9–12]. Shen et al. [13] reported that the topsoil in the smelter area was highly contaminated by metals, and Cd and Zn mainly exist in mobile fractions, which can migrate even to a depth of 80 cm. A similar result has also been reported by Aminiyan et al. [9], indicating that copper smelter results in the surrounding soil were severely contaminated with metal(loid)s (As, Cd, Cr, Cu, Pb, and Zn), and these metal(loid)s were dramatically mobile and available. The metal(loid)s discharged by NSPI may be more active than that of other pollution sources, which may enter into the food chain easily and threaten the health of the ecosystem [14,15]. However, the attention given to the migration of metal(loid)s in the soil-crop system around NSPI is not enough.

The accumulation and translocation of metal(loid)s in a soil-maize system around a zinc-smelting area (southwest of China) has been reported by Duan et al. [16]. Their results indicated that targeted metal(loid)s in soil were significantly higher than the background values but had no potential noncarcinogenic risk for local maize consumers (adults and children), which may mainly attribute to the weak metal(loid)s accumulation capacity of maize [17]. In contrast, the metal(loid)s content in vegetables, rice grain, and fish around a large Cu-smelter all exceeded the maximum permissible level of food in China [18]. In addition, the metal(loid)s contamination in soil-crop systems around the NSPI has also been reported in several other countries [19,20]. However, there is little information about the migration of metal(loid)s in the soil-wheat system around the NSPI in China.

Henan province, located in the central-eastern region of China, is a major wheat-producing province, which contributes more than 27% of the total wheat production in China [21]. At the same time, NSPI is very developed in Henan province, especially for Pb/Zn smelting, which may result in metal(loid)s contamination in surrounding farmland [22,23]. In addition, wheat is generally considered a potential accumulator of metal(loid)s [17,24]. The wheat planted close to the smelter may accumulate various metal(loid)s and cause great risk to wheat consumers. Therefore, it is urgent to understand to what extent these metal(loid)s accumulated in soils and wheat grain around the NSPI. This study aimed to investigate: (1) the content and spatial distribution of metal(loid)s (Pb, Cd, As, Cu, Zn, and Ni) in the soil around a Pb/Zn smelter in Henan province; (2) the accumulation of these metal(loid)s in wheat grains; and (3) the potential health risk of these metal(loid)s to local wheat consumers.

## 2. Materials and Methods

### 2.1. Study Area and Samples Collection

The study area (around Dongfang Gold Lead Co., Ltd.: Jiaozuo, China) was located in the northwest of Henan province (Jiaozuo city), Huanghuai Plain, China (33°19′17.61″ N, 113°02′17″ E) (Figure 1). The climate of Jiaozuo City is a typical continental monsoon climate with four clearly distinct seasons. The annual average temperature and the annual precipitation are 14.9 °C and 603.5 mm. The soil in the study area was classified as Luvisol [25]. Jiaozuo is rich in mineral resources, including coal, bauxite, and pyrite. Sufficient energy supply promoted the rapid development of the nonferrous smelting industry, such as Pb/Zn smelter and aluminum smelting. Dongfang Gold Lead Co., Ltd. is one of the Pb/Zn smelting enterprises established in 2003; their main products are electrolytic lead, silver, gold, zinc oxide, copper, and other nonferrous metals. Due to inadequate environmental management, the company discharged a large amount of pollutants into the surrounding environment and was closed by the local government in 2014. After that, wheat and other crops were planted very close to the smelter by local farmers.

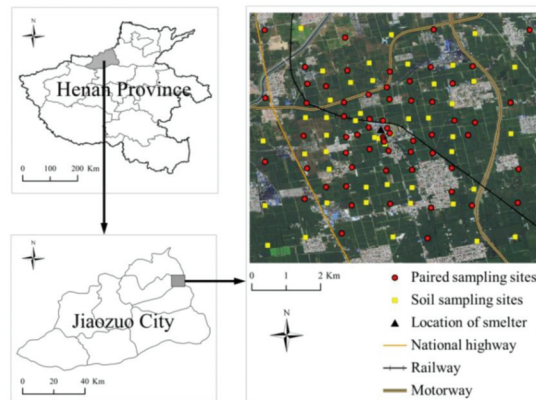


**Figure 1.** The study area and sampling sites.

One hundred and ten soil and 62 wheat grain samples (62 paired samples) were collected around 36 km<sup>2</sup> of Dongfang Gold Lead Co., Ltd. Approximately 500 g of surface soil samples (0–25 cm) were collected from each site, and soil was sampled from five individual locations at each site to minimize the heterogeneity. The collected soil samples were stored in polyethylene bags at room temperature, transported to the laboratory, air-dried and crushed (1 mm and 150 µm) for soil properties (pH, cation exchange capacity (CEC), organic matter content (OM), and total nitrogen (TN)) and metal(loid)s content detection. At the same time, 62 corresponding wheat ears samples (each location providing 30 wheat ears totaling 150 wheat ears per site) were collected and husked manually to obtain wheat grain. The wheat grains were washed with deionized water and dried to constant weight at 70 °C, then crushed into a fine powder with a stainless steel crusher (2 mm) for further analysis.

## 2.2. Chemical Analysis

The pH of the soil was determined by a pH meter (PHSJ-3F, INESA, Shanghai, China) with a soil-to-water ratio of 1:2.5 (*w/v*). Sodium acetate exchange and flame photometer (FP6410, INESA, Shanghai, China) were used to determine the CEC of these soil samples. OM content was determined by potassium dichromate oxidation and ferrous sulfate volumetric method (NY/T 1121.6-2006). TN was determined by an automatic Kjeldahl nitrogen analyzer (NKB3000, Hanon, Shanghai, China). The contents of metals (Pb, Cd, Cu, Zn, and Ni) in soil and wheat grain were measured by inductively coupled plasma mass spectrometry (ICP-MS, Thermo Fisher X2, Waltham, MA, USA) after digestion with an acid mixture [26]. For soil, 0.1 g of soil samples were digested in Teflon vessels with an acid mixture of HNO<sub>3</sub> (9 mL)-HF (3 mL)-HClO<sub>4</sub> (1.5 mL) at 180 °C until the solution became transparent, then transferred to a 50 mL volumetric flask and constant to volume with nitric acid (5%, *w/w*). For wheat grain, 0.5 g of wheat powder were digested with an acid mixture of HNO<sub>3</sub> (12 mL)-HClO<sub>4</sub> (2 mL) at 160 °C until the solution became transparent, then transferred to a 100 mL volumetric flask and constant to volume with nitric acid (5%, *w/w*). Arsenic (As) content in soil and wheat grain was determined by atomic fluorescence spectroscopy (AFS-3100, Haiguang Corp., Beijing, China) according to the description of Yu et al. [27].

## 2.3. Bioaccumulation Factor

Bioaccumulation factor (BF) was used to determine the transfer of metal(loid)s from soil to wheat grain. The BF was calculated based on the following Equation [26]:

$$BF = \frac{C_{wheat}}{C_{soil}} \quad (1)$$



where  $C_{wheat}$  represents the metal(loid)s content in wheat grain (mg/kg),  $C_{soil}$  represents the metal(loid)s content in the corresponding soil sample (mg/kg).  $C_{wheat}$  and  $C_{soil}$  used for the  $BF$  calculation were the 62 paired samples, which were collected from the same point with the same coordinates.

#### 2.4. Potential Health Risk Assessment

The noncarcinogenic risk of metal(loid)s to local residents via wheat consumption was assessed using the target hazard quotient ( $HQ$ ) and hazard index ( $HI$ ) according to the description of Liu et al. [28], which calculated by the following Equations:

$$EDI = \frac{C_i \times IR \times EF \times ED}{BW \times AT} \quad (2)$$

$$HQ = \frac{EDI}{RfD} \quad (3)$$

$$HI = \sum_{i=1}^n HQ_i \quad (4)$$

where estimated daily intake ( $EDI$ ) is the average daily dose of the considered element via food ingestion (mg/kg/day);  $C_i$  is the content of considered metal(loid)s in wheat grain (mg/kg); intake reference ( $IR$ ) is the daily intake of wheat grain, 94.47 and 172.87 g/day for children and adults, respectively [29];  $EF$  is the exposure frequency (days/year), 365 days/year for both children and adults;  $ED$  is the exposure duration (year), 12 and 70 years are assumed for children and adults, respectively [30];  $BW$  is the average body weight of wheat consumers (kg), 15 and 63.5 kg for children and adults, respectively [29];  $AT$  is the average time of metal(loid)s exposure (day), calculated by 365 days/year  $\times$   $ED$ ;  $RfD$  is the reference dose (mg/kg/day), 0.0035, 0.001, 0.0003, 0.04, 0.3 and 0.02 mg/kg/day for Pb, Cd, As, Cu, Zn, and Ni, respectively [28]. The value of  $HQ$  or  $HI$  higher than 1 was assumed to have adverse effects on human health.

The cancer risk ( $CR$ ) was used to determine the probability of an individual developing cancer disease due to exposure to a carcinogenic substance [31]. If there are multiple carcinogenic substances, the  $CR$  of each substance is added together. The  $CR$  is calculated by the following Equation:

$$CR = EDI \times SF \quad (5)$$

where  $SF$  is the cancer slope factor, the  $SFs$  for Cd, As, Pb and Ni were 6.1, 1.5, 0.0085, and 0.84 mg/kg/day, respectively [29,32]. If the value of  $CR < 10^{-4}$ , it is assumed that the cancer risk for wheat consumers is in an acceptable range.

#### 2.5. Quality control and Quality Assurance

The standard reference materials (GBW07413 for soil and GBW10011 for wheat grain) were used for quality assurance and quality control. The recoveries of considered elements were between 96.7% and 106.2%. The detection limit and practical limit were 0.009 ug/L and 0.03 ug/L for Pb, 0.0005 ug/L and 0.0017 ug/L for Cd, 0.009 ug/L and 0.03 ug/L for Cu, 0.15 ug/L and 0.5 ug/L for Zn, 0.009 ug/L and 0.03 ug/L for Ni, and 0.017 ug/L and 0.053 ug/L for As, respectively.

#### 2.6. Statistical Analysis

All data are presented as the means  $\pm$  standard deviations. The spatial distribution of metal(loid)s in soil was created by ArcGIS 10.6 software (ESRI, Redlands, USA). The Spearman correlation analysis was conducted by SPSS (ver. 25.0)(IBM, NY, USA). The box plot was drawn by origin 8.5 (OriginLab, Northampton, MD, USA).

### 3. Results and Discussion

#### 3.1. Metal(loid)s Content and Selected Properties of Soil

The contents of metal(loid)s in these soil samples are ranging from 12.04 to 2259.20 mg/kg for Pb, 0.54 to 64.89 mg/kg for Cd, 5.91 to 102.31 mg/kg for As, 5.00 to 87.93 mg/kg for Cu, 27.71 to 480.47 mg/kg for Zn, and 0.25 to 20.90 mg/kg for Ni, with the average contents of 129.16, 4.28, 17.95, 20.43, 79.36 and 9.42 mg/kg, respectively (Table 1). The average contents of these metal(loid)s are all much higher than that of the local background value (except for Ni) and lower than the national limitation of China (except for Cd).

**Table 1.** Descriptive statistic of metal(loid)s and selected soil properties ( $n = 110$ ).

	pH	OM (g/kg)	CEC (cmol/kg)	TN (g/kg)	Pb (mg/kg)	Cd (mg/kg)	As (mg/kg)	Cu (mg/kg)	Zn (mg/kg)	Ni (mg/kg)
Min	8.13	2.30	12.46	0.02	12.04	0.54	5.91	5.00	27.71	0.25
Max	9.07	63.20	32.31	0.93	2259.20	64.89	102.31	87.93	480.47	20.90
Average	8.57	25.48	23.17	0.22	129.16	4.28	17.95	20.43	79.36	9.42
SD	0.16	8.15	4.58	0.14	296.40	8.72	10.43	14.83	50.60	4.03
CV (%)	1.9	31.97	19.77	63.97	229.47	203.74	58.13	72.56	63.76	42.77
Background value *	-	-	-	-	22.30	0.07	9.8	20.00	62.50	27.40
Risk screening values **	-	-	-	-	170	0.6	25	100	300	190

\* China National Environmental Monitoring Centre. Background values of soil elements in China. China Environmental Science Press [M]. Beijing, China. \*\* The risk screening values are cited from the national standard of China (GB 15618-2018). SD: standard deviation; CV: coefficient of variation; OM: organic matter content; CEC: cation exchange capacity; TN: total nitrogen content.

The average content of Cd in soil (4.28 mg/kg) exceeded the national limitation of China (0.6 mg/kg, GB 15618-2018) more than six times. The minimum Cd content (0.54 mg/kg) was close to the national limitation. In addition, more than 99.1% of these soil samples with Cd content exceeded the national limitation. The number of soil samples with Pb, As, and Zn contents higher than the national limitation just occupied 13.6%, 8.2%, and 0.9% of the total soil samples. Therefore, Cd is the most polluted metal in the study area, followed by Pb, As, and Zn. In addition, previous studies reported that Cd could be accumulated by wheat more easily than other crops [17,33]; the high content of Cd in soil may result in serious pollution of wheat grain planted in the study area.

The coefficient of variation (CV) of Pb and Cd in soil was higher than 200%, and the CVs of As, Cu, and Zn in the soil also exceeded 50%, indicating that these metal(loid)s differed greatly among different soil samples and mainly caused by anthropogenic activities [34]. This result is similar to many previous reports [17,35,36]. The study area of the present study is 36 km<sup>2</sup>, and just part of these soil samples was dramatically influenced by the Pb/Zn smelter, which may be the main reason for the high CV value.

The pH, OM, CEC, and TN of these soil samples ranged from 8.13 to 9.07, 2.30 to 63.20 g/kg, 12.46 to 32.31 cmol/kg, and 0.02 to 0.93 g/kg, respectively. The soil in the study area is alkaline, with an average pH of 8.57. Most previous studies have indicated that higher pH can reduce the activity of metals but increase the activity of As in soil [37,38]. Therefore, the risk of As contamination in wheat grain should be paid more attention to. The average OM content was 25.48 g/kg, which belongs to the moderate scale (20–30 g/kg) [39]. The CVs of pH, OM, and CEC were lower than 32%, indicating anthropogenic activities have little influence on these soil properties. The CV value of TN was 63.97%, which may be attributed to the different land-use types and fertilization patterns [40].

#### 3.2. Spatial Distribution of Metal(loid)s

The spatial distribution of these metal(loid)s in soil is shown in Figure 2. The distribution of Pb, Cd, As, and Zn are similar, and their contents decreased gradually with the

increase of the distance far from the smelter. Field research indicated that there was no sewage irrigation and inappropriate disposal of the smelting solid waste in the study area in the past. Therefore, atmospheric deposition may be attributed to the main source for Pb, Cd, As, and Zn contamination in the soil near the smelter. In addition, the distribution of Pb, Cd, As, and Zn in the study area is oval from northeast to southwest, which is consistent with the local dominant wind direction (southwest wind) [41,42].

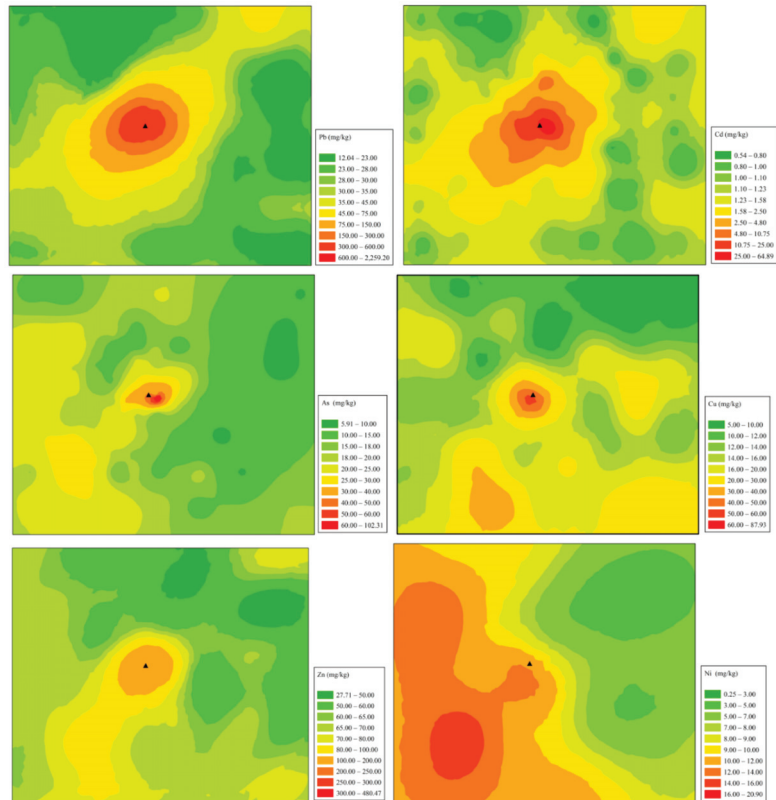


**Figure 2.** Spatial distribution of metal(loid)s in soil around the Pb/Zn smelter. ▲ Represents the location of the smelter.

The content of Ni in soil was distributed in the band, which may mainly be caused by the highway (S233). Previous studies indicated that highways could cause metal(loid)s accumulation along with the soil, which is consistent with our present studies [43]. Besides the central area (very close to the smelter), there is still a high-value area of Cu in the southeast of the study area, which coincides with the position of a piggery. As a trace element of livestock, the average content of Cu in pig feeds reached 200–300 mg/kg [44,45], and most of this Cu can be excreted by urine and manure [46]. More importantly, pig manure has been widely used as organic fertilizers by farmers in China, which resulted in the accumulation of Cu in the soil near the piggery.

### 3.3. Metal(loid)s Content in Wheat Grain

The contents of metal(loid)s in wheat grain are ranging from 0.001 to 10.75 mg/kg for Pb, 0.04 to 1.73 mg/kg for Cd, 0.03 to 0.67 mg/kg for As, 1.55 to 5.7 mg/kg for Cu, 21.32 to 54.81 mg/kg for Zn, and 0.001 to 0.48 mg/kg for Ni, respectively (Table 2). The average contents of Cd and Pb in wheat grain are 0.35 and 0.62 mg/kg, which all exceeded

the national limitation of China (0.1 mg/kg for Cd and 0.5 mg/kg for Pb, GB 2762-2017). The International Agency for Research on Cancer has classified Cd and Pb as Group I and Group II carcinogens, respectively, which can cause detrimental effects on the reproductive, immune system, nervous and cardiovascular [47,48]. Therefore, the high content of Cd and Pb in wheat grain may cause serious health risks to local residents via wheat consumption.

**Table 2.** Descriptive statistic of metal(loid)s in wheat grain ( $n = 62$ ).

	Pb (mg/kg)	Cd (mg/kg)	As (mg/kg)	Cu (mg/kg)	Zn (mg/kg)	Ni (mg/kg)
Min	0.001	0.04	0.03	1.55	21.32	0.001
Max	10.75	1.73	0.67	5.70	54.81	0.48
Average	0.62	0.35	0.11	3.70	35.77	0.15
SD	1.55	0.43	0.10	0.92	7.34	0.12
CV (%)	249.50	125.12	90.80	24.76	20.53	75.96
National limits	0.5 *	0.1 <sup>†</sup>	0.5 *	10 **	50 **	-

\* National standard of China on the maximum residue limits of pollutants in food (GB 2762-2017); \*\* Limits by Ministry of Agriculture of China (NY 861-2004); <sup>†</sup> represent no limitation in the standard.

In fact, the content of Pb and Cd in soil exceeded the national limitation of China, occupying 13.6% and 99.1% of the total soil samples, respectively. Whereas, the proportions of Pb and Cd content in wheat grain exceeded the national limitation of China were 22.58% and 62.90%. Correlation analysis indicated that the correlation between the metal(loid)s content in wheat grain and soil properties was not significant (Table 3). In addition, metal(loid)s content in wheat grain (except for Cu) was significantly positively correlated with soil Pb and Cd. Furthermore, the wheat grain Pb content also positively correlated with soil As ( $p = 0.01$ ) and Zn ( $p = 0.01$ ), the wheat grain Cd content also positively correlated with soil As ( $p = 0.05$ ), Cu ( $p = 0.01$ ) and Zn ( $p = 0.01$ ), the wheat grain As and Zn content also positively correlated with soil Cu ( $p = 0.01$ ) and Zn ( $p = 0.05$ ) (Table 3). These results may imply that the metal(loid)s contents in wheat grain are mainly dependent on their total contents in soil and the influence of other factors (fraction of metals in soil, soil OM content, and soil pH) on the accumulation of metals in wheat grains is nonsignificant. This result is inconsistent with previous studies [49,50].

**Table 3.** Correlation analysis between metal(loid)s content in wheat grain with its content in soil and soil properties ( $n = 62$ ).

	W-Pb	W-Cd	W-As	W-Cu	W-Zn	W-Ni
pH	-0.042	0.151	-0.095	-0.208	-0.016	-0.160
TN	-0.162	0.085	-0.003	-0.029	-0.057	-0.040
OM	-0.192	0.041	0.039	0.000	-0.100	-0.069
CEC	-0.037	0.136	-0.094	-0.211	0.071	0.066
S-Pb	0.810 **	0.631 **	0.452 **	-0.063	0.550 **	0.315 *
S-Cd	0.824 **	0.607 **	0.397 **	-0.018	0.534 **	0.295 *
S-As	0.416 **	0.263 *	0.069	0.143	0.168	-0.004
S-Cu	0.234	0.419 **	0.345 **	0.064	0.416 **	0.081
S-Zn	0.511 **	0.379 **	0.313 *	-0.100	0.319 *	0.138
S-Ni	0.135	0.192	-0.206	-0.150	0.125	-0.132

\* significance level of 0.05; \*\* significance level of 0.01; TN: total nitrogen content; OM: organic matter content; CEC: cation exchange capacity; W-: the content of metal(loid)s in wheat grain; S-: the content of metal(loid)s in soil.

Although As content in part of the soil samples exceeded the national limitation of China, just one wheat grain sample with As content higher than 0.5 mg/kg, indicating that the activity of As in soil is low even the soil pH is alkaline. The average contents of Cu and Zn in wheat grain were 3.70 and 35.77 mg/kg, respectively (Table 2), which are lower than the national limitation of China (NY 861-2004). In addition, Cu and Zn are essential

trace elements for humans [51]; a small amount of Cu and Zn intake by wheat may have a positive effect on human health. The average Ni content in wheat grain is 0.15 mg/kg, but its content in wheat grain was not limited in China. Previous reports have indicated that Ni is toxic and carcinogenic [51], the neglect of Ni in the national standards of China may be harmful to human health, which should be given more attention.

### 3.4. Bioaccumulation of Metal(loid)s in Wheat Grain

The BF values of these metal(loid)s ranged from 0.001 to 0.050 for Pb, 0.010 to 0.787 for Cd, 0.006 to 0.022 for As, 0.239 to 0.890 for Cu, 0.507 to 0.973 for Zn, and 0.024 to 0.115 for Ni, respectively, with the average BF value decreased in the following order: Zn > Cu > Cd > Ni > Pb > As (Figure 3). Due to the high toxicity of Cd, most of the previous reports emphasized that Cd can be accumulated in wheat grain easier than other metals [17,30], and just a few attentions paid to the BF value of Cu and Zn in wheat.

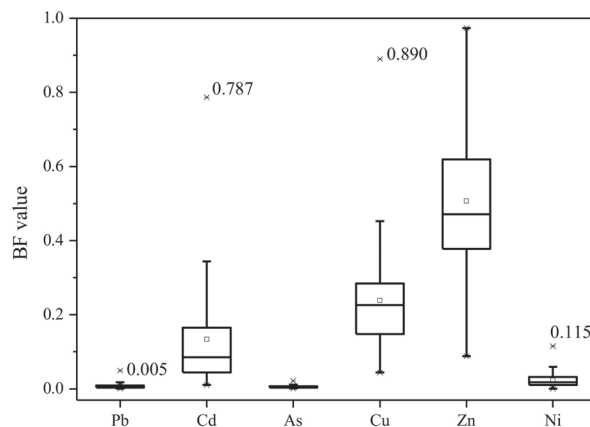


**Figure 3.** Bioaccumulation factor of metal(loid)s in wheat grain ( $n = 62$ ).

The average BF values of Cu and Zn were 0.239 and 0.507, respectively, which are much higher than that of other metal(loid)s considered in the present study. Similar results have been reported in many previous studies [29,52]. Fortunately, Cu and Zn are essential trace elements for the metabolism of plants and mammals; the high BF value of Cu and Zn in wheat may be important for the health of mammals [53]. The average BF value of Cd was 0.134, which is much higher than that of Pb (0.007), As (0.006), and Ni (0.024). Previous reports indicated that the accumulation capacity of wheat to Cd might be the highest among various toxic metals [29,54], which are consistent well with the present study.

### 3.5. Potential Health Risk Assessment

The potential noncarcinogenic diseases risk index (HI) of metal(loid)s for local wheat consumers are shown in Figure 4a. The HI by intake of wheat grain ranged from 0.99 to 9.30 for adults and 2.35 to 22.19 for children, with an average HI of 2.83 and 6.75, respectively. The HI values of all wheat samples are higher than the acceptable range ( $HI < 1$ ) for both adults and children (except for one wheat sample with HI of 0.99), which indicates that local residents had a high risk of noncarcinogenic diseases due to the intake of metal(loid)s contaminated wheat [55,56]. Furthermore, part of the wheat samples with the  $HQ_{Cd}$  (19 and 29 for adults and children),  $HQ_{As}$  (20 and 54 for adults and children),  $HQ_{Pb}$  (5 for children), and  $HQ_{Zn}$  (6 for children) were higher than 1 (Table 4). Cd and As exposure was the main contributor of HI, with the average contribution higher than 63% for both adults and children.

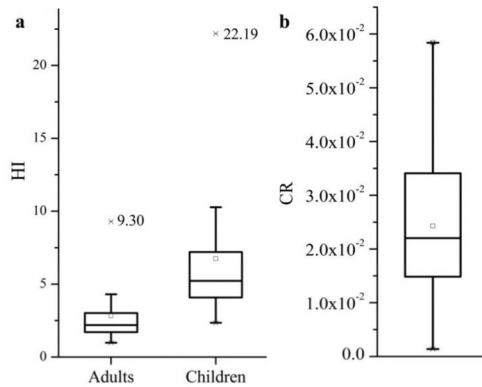


**Figure 4.** Potential health risk assessment of metal(loid)s for local wheat consumers. (a): noncarcinogenic risk assessment; (b): carcinogenic risk assessment.

**Table 4.** Number of the HQ higher or lower than 1 for individual element in adults and children.

	Adults		Children	
	HQ>1	HQ<1	HQ>1	HQ<1
Pb	0	62	5	57
Cd	19	43	29	33
As	20	42	54	8
Cu	0	62	0	62
Zn	0	62	6	56
Ni	0	62	0	62

The minimum and maximum CR values calculated based on Equation (5) are  $1.39 \times 10^{-3}$  and  $5.84 \times 10^{-2}$ , respectively (Figure 4b). The CR values of all wheat samples are much higher than the acceptable range recommended by EPA ( $1.0 \times 10^{-4}$ ) [26], indicating local wheat consumers are at serious risk of carcinogenic diseases. In addition, the minimum CR value of Cd, As, and Ni were  $6.0 \times 10^{-3}$ ,  $4.5 \times 10^{-4}$ , and  $2.4 \times 10^{-2}$ , respectively, which all exceeded the acceptable range ( $1.0 \times 10^{-4}$ ). The sensitivity of human organs to different metal(loid)s is different [57], and the excessively multi-metal(loid)s exposure may result in various carcinogenic diseases to local wheat consumers.

In fact, studies regard to the influence of anthropogenic activities on metal(loid)s accumulation in wheat grain and related potential health risks have been carried out in many previous reports [28,29,31,56]. The long-term application of phosphorus fertilizer or nitrogen fertilizer increased the accumulation of metal(loid)s in wheat grain and the related potential health to humans, but their HI and CR values are still within the acceptable range [29,31]. However, sewage irrigation and artisanal mining can result in excessive accumulation of metal(loid)s in wheat and generate a serious threat to human health [56,58], which are consistent with our present studies. In addition, the Pb/Zn smelter result in serious metal(loid)s contamination in more than 36 km<sup>2</sup> of both farmland soil and wheat in the present study. These results suggested that more attention should be paid to land use planning, which can reduce their influence on agricultural production and food safety.

This section may be divided into subheadings. It should provide a concise and precise description of the experimental results, their interpretation, as well as the experimental conclusions that can be drawn.

#### 4. Conclusions

In conclusion, Pb/Zn smelting results in the surrounding soil being seriously contaminated with metal(loid)s, especially for Cd. The distribution of these metal(loid)s differ greatly and may be caused by a different source. The accumulation capacity of Cu and Zn

was much higher than other elements, but their content in wheat grain was all within the national limitation of China, whereas the average contents of Pb and Cd in wheat grain exceeded the national limitation of China. The accumulation of metal(loid)s in wheat grain generated serious health risks (both noncarcinogenic and carcinogenic risk) to local wheat consumers. These results suggested that more reasonable land-use planning should be established to reduce the impact of Pb/Zn smelting on the surrounding environment.

**Author Contributions:** Conceptualization and writing—original draft preparation, L.Y. and X.R.; data curation, Q.R. and R.H.; investigation, S.G. and Z.J.; supervision, W.Z.; writing—review and editing, Y.P.; methodology, Y.W. All authors have read and agreed to the published version of the manuscript.

**Funding:** This research was funded by a grant from the National Natural Science Foundation of China (41902251); Program for Innovative Research Team (in Science and Technology) in University of Henan Province (21IRTSTHN008); Science and Technology Development Project of Henan Province, China (212102310503); China Postdoctoral Science Foundation Funded Project (2020M682284), Open Funding Project of National Key Laboratory of Human Factors Engineering (SYFD062007).

**Institutional Review Board Statement:** Not applicable.

**Informed Consent Statement:** Not applicable.

**Data Availability Statement:** Not applicable.

**Conflicts of Interest:** The authors declare no conflict of interest.

## References

1. Wan, M.; Hu, W.; Wang, H.; Tian, K.; Huang, B. Comprehensive assessment of heavy metal risk in soil—Crop systems along the Yangtze River in Nanjing, Southeast China. *Sci. Total Environ.* **2021**, *780*, 146567. [[CrossRef](#)] [[PubMed](#)]
2. Ma, X.; Ren, Q.; Zhan, W.; Zheng, K.; Chen, R.; Wang, Y. Simultaneous stabilization of Pb, Cd, Cu, Zn and Ni in contaminated sediment using modified biochar. *J. Soils. Sediments.* **2022**, *22*, 392–402. [[CrossRef](#)]
3. Quan, S.X.; Yan, B.; Yang, F.; Li, N.; Xiao, X.; Fu, J. Spatial distribution of heavy metal contamination in soils near a primitive e-waste recycling site. *Environ. Sci. Pollut. Res.* **2015**, *22*, 1290–1298. [[CrossRef](#)]
4. Li, X.; Zhu, W.; Meng, G.; Guo, R.; Wang, Y. Phytoremediation of alkaline soils co-contaminated with cadmium and tetracycline antibiotics using the ornamental hyperaccumulators *Mirabilis jalapa* L. and *Tagetes patula* L. *Environ. Sci. Pollut. Res.* **2020**, *27*, 14175–14183. [[CrossRef](#)] [[PubMed](#)]
5. Wang, Y.; Liu, Y.; Zhan, W.; Zheng, K.; Wang, J.; Zhang, C.; Chen, R. Stabilization of heavy metal-contaminated soils by biochar: Challenges and recommendations. *Sci. Total Environ.* **2020**, *729*, 139060. [[CrossRef](#)] [[PubMed](#)]
6. Kukusamude, C.; Sricharoen, P.; Limchoowong, N.; Kingsri, S. Heavy metals and probabilistic risk assessment via rice consumption in Thailand. *Food Chem.* **2021**, *334*, 127402. [[CrossRef](#)]
7. Sungur, A.; Vural, A.; Gundogdu, A.; Soylyak, M. Effect of antimonite mineralization area on heavy metal contents and geochemical fractions of agricultural soils in Gumushane Province, Turkey. *Catena* **2020**, *184*, 104255. [[CrossRef](#)]
8. Xing, W.; Zheng, Y.; Scheckel, K.G.; Luo, Y.; Li, L. Spatial distribution of smelter emission heavy metals on farmland soil. *Environ. Monit. Assess.* **2019**, *191*, 115. [[CrossRef](#)]
9. Aminiyan, M.M.; Rahman, M.M.; Rodriguez-Seijo, A.; Begloo, R.; Cheraghi, M.; Aminiyan, F. Elucidating of potentially toxic elements contamination in topsoils around a copper smelter: Spatial distribution, partitioning and risk estimation. *Environ. Geochem. Health* **2021**, 1–17. [[CrossRef](#)]
10. Ghayoraneh, M.; Qishlaqi, A. Concentration, distribution and speciation of toxic metals in soils along a transect around a Zn/Pb smelter in the northwest of Iran. *J. Geochem. Explor.* **2017**, *180*, 1–14. [[CrossRef](#)]
11. Sajin, R.; Aliu, M.; Stafilov, T.; Alijagic, J. Heavy metal contamination of topsoil around a lead and zinc smelter in Kosovska Mitrovica/Mitrovic, Kosovo/Kosov. *J. Geochem. Explor.* **2013**, *134*, 1–16. [[CrossRef](#)]
12. Xu, D.; Fu, R.; Liu, H.; Guo, X. Current knowledge from heavy metal pollution in Chinese smelter contaminated soils, health risk implications and associated remediation progress in recent decades: A critical review. *J. Clean. Prod.* **2021**, *286*, 124989. [[CrossRef](#)]
13. Shen, F.; Liao, R.; Ali, A.; Mahar, A.; Guo, D.; Li, R.; Sun, X.; Awasthi, M.; Wang, Q.; Zhang, Z. Spatial distribution and risk assessment of heavy metals in soil near a Pb/Zn smelter in Feng County, China. *Ecotoxicol. Environ. Saf.* **2017**, *139*, 254–262. [[CrossRef](#)]
14. Valente, J.; Valente, A.; Duraes, L. Assessment of heavy metal pollution from anthropogenic activities and remediation strategies: A review. *J. Environ. Manag.* **2019**, *246*, 101–118. [[CrossRef](#)]
15. Wang, Y.; Zheng, K.; Zhan, W.; Huang, L.; Liu, Y.; Li, T.; Yang, Z.; Liao, Q.; Chen, R.; Zhang, C.; et al. Highly effective stabilization of Cd and Cu in two different soils and improvement of soil properties by multiple-modified biochar. *Ecotoxicol. Environ. Saf.* **2021**, *207*, 111294. [[CrossRef](#)]

16. Duan, Z.; Luo, Y.; Wu, Y.; Wang, J.; Cai, X.; Wen, J.; Xu, J. Heavy metals accumulation and risk assessment in a soil-maize (*Zea mays* L.) system around a zinc-smelting area in southwest China. *Environ. Geochem. Health* **2021**, *43*, 4875–4889. [[CrossRef](#)]
17. Wang, Y.; Li, F.; Song, J.; Xiao, R.; Luo, L.; Yang, Z.; Chai, L. Stabilization of Cd-, Pb-, Cu- and Zn-contaminated calcareous agricultural soil using red mud: A field experiment. *Environ. Geochem. Health* **2018**, *40*, 2143–2153. [[CrossRef](#)]
18. Cai, L.; Wang, Q.; Luo, J.; Chen, L.; Zhu, R.; Wang, S.; Tang, C. Heavy metal contamination and health risk assessment for children near a large Cu-smelter in central China. *Sci. Total Environ.* **2018**, *650*, 725–733. [[CrossRef](#)]
19. Chen, C.; Hu, H.; Li, X.; Zheng, Z.; Wang, Z.; Wang, X.; Zheng, P.; Cui, F.; Li, G.; Wang, Y.; et al. Rapid Detection of Anti-SARS-CoV-2 antibody Using a Selenium Nanoparticle-based Lateral Flow Immunoassay. *IEEE. T. Nanobiosci.* **2022**, *21*, 37–43. [[CrossRef](#)]
20. Islam, A.; Akber, A.; Rahman, B.; Rahman, A.; Haque, M.; Islam, A. Trace elements in rice grain and agricultural soils: Assessment of health risk of inhabitants near a former secondary lead smelter in Khulna, Bangladesh. *Environ. Geochem. Health* **2019**, *41*, 2521–2532. [[CrossRef](#)]
21. Feng, J.; Li, X.; Zhao, J.; Sun, J. Distribution, transfer, and health risks of polycyclic aromatic hydrocarbons (PAHs) in soil-wheat systems of Henan Province, a typical agriculture province of China. *Environ. Sci. Pollut. Res.* **2017**, *24*, 18195–18203. [[CrossRef](#)] [[PubMed](#)]
22. Obiri-Nyarko, F.; Duah, A.A.; Karikari, A.Y.; Agyekum, W.; Manu, E.; Tagoe, R. Assessment of heavy metal contamination in soils at the Kpone landfill site, Ghana: Implication for ecological and health risk assessment. *Chemosphere* **2021**, *282*, 131007. [[CrossRef](#)] [[PubMed](#)]
23. Wei, X.; Zhou, Y.; Jiang, Y.; Tsang, D.; Zhang, C.; Liu, J.; Zhou, Y.; Yin, M.; Wang, J.; Shen, N.; et al. Health risks of metal(loid)s in maize (*Zea mays* L.) in an artisanal zinc smelting zone and source fingerprinting by lead isotope. *Sci. Total Environ.* **2020**, *742*, 140321. [[CrossRef](#)] [[PubMed](#)]
24. Douay, F.; Roussel, H.; Pruvot, C.; Waterlot, C. Impact of a smelter closedown on metal contents of wheat cultivated in the neighbourhood. *Environ. Sci. Pollut. Res.* **2008**, *15*, 162–169. [[CrossRef](#)]
25. IUSS Working Group WRB. *World Reference Base for Soil Resources 2014, Update 2015 International Soil Classification System for Naming Soils and Creating Legends for Soil Maps*; World Soil Resources Reports No. 106; FAO: Rome, Italy, 2015.
26. Yang, L.; Ren, Q.; Zheng, K.; Jiao, Z.; Ruan, X.; Wang, Y. Migration of heavy metals in the soil-grape system and potential health risk assessment. *Sci. Total Environ.* **2022**, *806*, 150646. [[CrossRef](#)]
27. Yu, Z.; Qiu, W.; Wang, F.; Lei, M.; Wang, D.; Song, Z. Effects of manganese oxide-modified biochar composites on arsenic speciation and accumulation in an indica rice (*Oryza sativa* L.) cultivar. *Chemosphere* **2017**, *168*, 341–349. [[CrossRef](#)]
28. Liu, Y.; Cui, J.; Peng, Y.; Li, Y.; Yao, D.; Yang, J.; He, Y. Atmospheric deposition of hazardous elements and its accumulation in both soil and grain of winter wheat in a lead-zinc smelter contaminated area, Central China. *Sci. Total Environ.* **2020**, *707*, 135789. [[CrossRef](#)]
29. Chen, X.X.; Liu, Y.M.; Zhao, Q.Y.; Cao, W.; Chen, X.; Zou, C. Health risk assessment associated with heavy metal accumulation in wheat after long-term phosphorus fertilizer application. *Environ. Pollut.* **2020**, *262*, 114348. [[CrossRef](#)]
30. Huang, M.; Zhou, S.; Bo, S.; Zhao, Q. Heavy metals in wheat grain: Assessment of potential health risk for inhabitants in Kunshan, China. *Sci. Total Environ.* **2008**, *405*, 54–61. [[CrossRef](#)]
31. Zhang, Y.; Yin, C.; Cao, S.; Cheng, L.; Wu, G.; Guo, J. Heavy metal accumulation and health risk assessment in soil-wheat system under different nitrogen levels. *Sci. Total Environ.* **2018**, *622–623*, 1499–1508. [[CrossRef](#)]
32. Antoniadis, V.; Shaheen, S.M.; Levizou, E.; Shahid, M.; Niazi, N.K.; Vithanage, M.; Ok, Y.; Bolan, N.; Rinklebe, J. A critical prospective analysis of the potential toxicity of trace element regulation limits in soils worldwide: Are they protective concerning health risk assessment?—A review. *Environ. Int.* **2019**, *127*, 819–847. [[CrossRef](#)]
33. Skiba, E.; Kobylička, J.; Wolf, W.M. Influence of 2,4-D and MCPA herbicides on uptake and translocation of heavy metals in wheat (*Triticum aestivum* L.). *Environ. Pollut.* **2017**, *220*, 882–890. [[CrossRef](#)]
34. Douay, F.; Pelfrène, A.; Planque, J.; Fourrier, H.; Richard, A.; Roussel, H.; Girondelot, B. Assessment of potential health risk for inhabitants living near a former lead smelter. Part 1: Metal concentrations in soils, agricultural crops, and homegrown vegetables. *Environ. Monit. Assess.* **2013**, *185*, 3665–3680. [[CrossRef](#)]
35. Li, P.; Lin, C.; Cheng, H.; Duan, X.; Lei, K. Contamination and health risks of soil heavy metals around a lead/zinc smelter in southwestern China. *Ecotoxicol. Environ. Saf.* **2015**, *113*, 391–399. [[CrossRef](#)]
36. Yun, S.; Baveye, P.; Kim, D.; Kang, D.; Lee, S.; Kong, M.; Park, C.; Kim, H.; Son, J.; Yu, C. Analysis of metal(loid)s contamination and their continuous input in soils around a zinc smelter: Development of methodology and a case study in South Korea. *Environ. Pollut.* **2018**, *238*, 140–149. [[CrossRef](#)]
37. Beesley, L.; Moreno-Jimenez, E.; Gomez-Eyles, J.L. Effects of biochar and greenwaste compost amendments on mobility, bioavailability and toxicity of inorganic and organic contaminants in a multi-element polluted soil. *Environ. Pollut.* **2010**, *158*, 2282–2287. [[CrossRef](#)]
38. Vithanage, M.; Herath, I.; Joseph, S.; Bundschuh, J.; Bolan, N.; Ok, Y.; Kirkham, M.; Rinklebe, J. Interaction of arsenic with biochar in soil and water: A critical review. *Carbon* **2017**, *113*, 219–230. [[CrossRef](#)]
39. Zhang, G.; Bai, J.; Xi, M.; Zhao, Q.; Lu, Q.; Jia, J. Soil quality assessment of coastal wetlands in the Yellow River Delta of China based on the minimum data set. *Ecol. Indic.* **2016**, *66*, 458–466. [[CrossRef](#)]



40. Duan, L.; Li, Z.; Xie, H.; Li, Z.; Zhang, L.; Zhou, Q. Large-scale spatial variability of eight soil chemical properties within paddy fields. *Catena* **2020**, *188*, 104350. [[CrossRef](#)]
41. Zhu, M.; Liu, D.; Tang, W.; Chi, Q.; Zhao, X.; Xu, S.; Ye, S.; Wang, Y.; Cui, Y.; Zhou, S. Exploring the ecological climate effects based on five land use types: A case study of the Huang-Huai-Hai River Basin in China. *Land* **2022**, *11*, 265. [[CrossRef](#)]
42. Chen, W.; Meng, H.; Song, H.; Zheng, H. Progress in dust modelling, global dust budgets, and soil organic carbon dynamics. *Land* **2022**, *11*, 176. [[CrossRef](#)]
43. Zhi, Y.; Wang, Z.; Ma, Z.; Wang, Z.; Deng, Z.; Li, H. The speciation and bioavailability of heavy metals pollutants in soil along highway in Erdos. *Act. Eco. Sinica*. **2007**, *27*, 2030–2039. [[CrossRef](#)]
44. Pan, X.; Han, Z.; Ben, W. Heavy Metal Contents in Pig Manure and Pig Feeds from Intensive Pig Farms in Shandong Province, China. *J. Agro-Environ. Sci.* **2013**, *32*, 160–165. [[CrossRef](#)]
45. Wang, H.; Dong, Y.; Yang, Y.; Toor, G.; Zhang, X. Changes in heavy metal contents in animal feeds and manures in an intensive animal production region of China. *J. Environ. Sci.* **2013**, *25*, 2435–2442. [[CrossRef](#)]
46. Nicholson, F.A.; Chambers, B.J.; Williams, J.R.; Unwin, R. Heavy metal contents of livestock feeds and animal manures in England and Wales. *Bioresource. Technol.* **1999**, *70*, 23–31. [[CrossRef](#)]
47. Turner, A.; Kearl, E.R.; Solman, K.R. Lead and other toxic metals in playground paints from South West England. *Sci. Total Environ.* **2016**, *544*, 460–466. [[CrossRef](#)]
48. Yang, X.R.; Wang, C.R.; Huang, Y.C.; Liu, B.; Liu, Z.; Huang, Y.; Cheng, L.; Huang, Y.; Zhang, C. Foliar application of the sulfhydryl compound 2,3-dimercaptosuccinic acid inhibits cadmium, lead, and arsenic accumulation in rice grains by promoting heavy metal immobilization in flag leaves. *Environ. Pollut.* **2021**, *285*, 117355. [[CrossRef](#)]
49. Baize, D.; Bellanger, L.; Tomassone, R. Relationships between concentrations of trace metals in wheat grains and soil. *Agron. Sustain. Dev.* **2009**, *29*, 297–312. [[CrossRef](#)]
50. Bhatti, S.S.; Sambyal, V.; Singh, J.; Nagpal, A. Analysis of soil characteristics of different land uses and metal bioaccumulation in wheat grown around rivers: Possible human health risk assessment. *Environ. Dev. Sustain.* **2017**, *19*, 571–588. [[CrossRef](#)]
51. Jagodic, J.; Rovcanin, B.; Paunovic, I.; Jovanovic, M.; Gavrovic-Jankulovic, M.; Manojlovic, D.; Stojisavljevic, A. The first insight into the trace element status of human adrenal gland accompanied by elemental alterations in adrenal adenomas. *J. Trace. Elem. Med. Bio.* **2021**, *63*, 126658. [[CrossRef](#)]
52. Bermudez, G.M.A.; Jasan, R.; Pla, R.; Pignata, M. Heavy metal and trace element concentrations in wheat grains: Assessment of potential non-carcinogenic health hazard through their consumption. *J. Hazard. Mater.* **2011**, *193*, 264–271. [[CrossRef](#)]
53. Ishfaq, M.; Wakeel, A.; Shahzad, M.N.; Kiran, A.; Li, X. Severity of zinc and iron malnutrition linked to low intake through a staple crop: A case study in east-central Pakistan. *Environ. Geochem. Health* **2021**, *43*, 4219–4233. [[CrossRef](#)]
54. Wang, Y.; Xu, Y.; Sun, G.; Liang, X.; Sun, Y.; Wang, L.; Huang, Q. Comparative effects of *Tagetes patula* L. extraction, mercapto-palygorskite immobilisation, and the combination thereof on Cd accumulation by wheat in Cd-contaminated soil. *Ecotoxicol. Environ. Saf.* **2021**, *224*, 112639. [[CrossRef](#)]
55. Rezapour, S.; Atashpaz, B.; Moghaddam, S.; Kalavrouziotis, I.; Damalas, C. Cadmium accumulation, translocation factor, and health risk potential in a wastewater-irrigated soil-wheat (*Triticum aestivum* L.) system. *Chemosphere* **2019**, *231*, 579–587. [[CrossRef](#)]
56. Xiao, R.; Wang, S.; Li, R.; Wang, J.; Zhang, Z. Soil heavy metal contamination and health risks associated with artisanal gold mining in Tongguan, Shaanxi, China. *Ecotoxicol. Environ. Saf.* **2017**, *141*, 17–24. [[CrossRef](#)]
57. Magrone, T.; Russo, M.A.; Jirillo, E. Impact of Heavy Metals on Host Cells: Special Focus on Nickel-Mediated Pathologies and Novel Interventional Approaches. *Endocr. Metab. Immune.* **2020**, *20*, 1041–1058. [[CrossRef](#)]
58. Lei, L.; Liang, D.; Yu, D.; Chen, Y.; Song, W.; Li, J. Human health risk assessment of heavy metals in the irrigated area of Jinghui, Shaanxi, China, in terms of wheat flour consumption. *Environ. Monit. Assess.* **2015**, *187*, 647. [[CrossRef](#)]

## Article

# A Molten-Salt Pyrolysis Synthesis Strategy toward Sulfur-Functionalized Carbon for Elemental Mercury Removal from Coal-Combustion Flue Gas

Jianping Yang<sup>1</sup>, Hong Xu<sup>1</sup>, Fanyue Meng<sup>1</sup>, Qingjie Guo<sup>2</sup>, Tao He<sup>3</sup>, Zequn Yang<sup>1</sup>, Wenqi Qu<sup>1</sup> and Hailong Li<sup>1,\*</sup>

- <sup>1</sup> School of Energy Science and Engineering, Central South University, Changsha 410083, China; jpyang@csu.edu.cn (J.Y.); xh18@foxmail.com (H.X.); mfy19941029@163.com (F.M.); zequn\_yang@hotmail.com (Z.Y.); wenqiqu1984@163.com (W.Q.)
- <sup>2</sup> State Key Laboratory of High-Efficiency Utilization of Coal and Green Chemical Engineering, Ningxia University, Yinchuan 750021, China; qingjie\_guo@nxu.edu.cn
- <sup>3</sup> Shandong Shiheng Thermal Power Co., Ltd., Taian 271600, China; hthetao1988@163.com
- \* Correspondence: hailongli18@gmail.com; Tel.: +86-18670016725; Fax: +86-731-88879863

**Abstract:** The emission of mercury from coal combustion has caused consequential hazards to the ecosystem. The key challenge to abating the mercury emission is to explore highly efficient adsorbents. Herein, sulfur-functionalized carbon (S-C) was synthesized by using a molten-salt pyrolysis strategy and employed for the removal of elemental mercury from coal-combustion flue gas. An ideal pore structure, which was favorable for the internal diffusion of the Hg<sup>0</sup> molecule in carbon, was obtained by using a SiO<sub>2</sub> hard template and adjusting the HF etching time. The as-prepared S-C with an HF etching time of 10 h possessed a saturation Hg<sup>0</sup> adsorption capacity of 89.90 mg·g<sup>-1</sup>, far exceeding that of the commercial sulfur-loaded activated carbons (S/C). The S-C can be applied at a wide temperature range of 25–125 °C, far exceeding that of commercial S/C. The influence of flue gas components, such as SO<sub>2</sub>, NO, and H<sub>2</sub>O, on the Hg<sup>0</sup> adsorption performance of S-C was insignificant, indicating a good applicability in real-world applications. The mechanism of the Hg<sup>0</sup> removal by S-C was proposed, i.e., the reduced components, including sulfur thiophene, sulfoxide, and C-S, displayed a high affinity toward Hg<sup>0</sup>, which could guarantee the stable immobilization of Hg<sup>0</sup> as HgS in the adsorbent. Thus, the molten-salt pyrolysis strategy has a broad prospect in the application of one-pot carbonization and functionalization sulfur-containing organic precursors as efficient adsorbents for Hg<sup>0</sup>.

**Keywords:** mercury; adsorption; carbon; molten salt; coal combustion

**Citation:** Yang, J.; Xu, H.; Meng, F.; Guo, Q.; He, T.; Yang, Z.; Qu, W.; Li, H. A Molten-Salt Pyrolysis Synthesis Strategy toward Sulfur-Functionalized Carbon for Elemental Mercury Removal from Coal-Combustion Flue Gas. *Energies* **2022**, *15*, 1840. <https://doi.org/10.3390/en15051840>

Academic Editors: Roberto Alonso González Lezcano, Francesco Nocera and Rosa Giuseppina Caponetto

Received: 29 January 2022

Accepted: 27 February 2022

Published: 2 March 2022

**Publisher's Note:** MDPI stays neutral with regard to jurisdictional claims in published maps and institutional affiliations.



**Copyright:** © 2022 by the authors. Licensee MDPI, Basel, Switzerland. This article is an open access article distributed under the terms and conditions of the Creative Commons Attribution (CC BY) license (<https://creativecommons.org/licenses/by/4.0/>).

## 1. Introduction

The excessive emission of mercury from industrial activities has caused consequential hazards to the ecosystem and human health [1–3]. Coal combustion is one of the largest industrial sources of mercury emission. The mercury emitted from typical coal-combustion flue gas generally existed in three forms, i.e., elemental mercury (Hg<sup>0</sup>), oxidized mercury (Hg<sup>2+</sup>), and particulate bound mercury (Hg<sup>P</sup>) [4–8]. The Hg<sup>P</sup> can be captured by using particulate matter control devices, while the Hg<sup>2+</sup> can be removed by using wet flue-gas scrubbers due to Hg<sup>2+</sup>'s water solubility [9–12]. However, Hg<sup>0</sup> is difficult to remove owing to its water insolubility and high volatility [13–15]. As a consequence, Hg<sup>0</sup> is the primary species of mercury discharged into the atmosphere from coal-combustion flue gases. The highly efficient removal of Hg<sup>0</sup> is a key challenge to reducing mercury pollution from coal-fired power plants.

Activated carbons (ACs) are the most widely researched and skilled mercury adsorbents for coal-fired power plants [16–21]. However, ACs were generally limited by

adsorption kinetics and equilibrium capacities, hence causing large consumptions of ACs during  $\text{Hg}^0$  removal [22,23]. Moreover, the weak binding affinity of ACs toward mercury induced leaching risks of mercury when the ACs were dumped in landfills together with fly ashes [24,25]. Thus, active components that can accommodate  $\text{Hg}^0$  were generally introduced to the ACs to improve the  $\text{Hg}^0$  adsorption capacity. In nature, the mercury was tied to sulfides owing to its sulphophile affinity [26,27]. Inspired by this natural law, sulfur was widely employed to modify the  $\text{Hg}^0$  adsorption capacity of ACs [28,29]. This strategy was relatively simple, cheap, and effective, but was still found to suffer from drawbacks [30,31]. The most significant one is that the sulfur was not actually anchored to the carbon surface during the impregnation process, hence affecting the activity, abundance, and accessibility of the sulfur groups during  $\text{Hg}^0$  removals [32]. The impregnation method for introducing sulfur would plug the pores of ACs. As a result, the efficient diffusion of  $\text{Hg}^0$  on the sulfur-modified ACs would be limited [33]. In addition, the anchoring of sulfur on ACs was not firm, hence causing leaching risks of sulfur as well as mercury adsorption products when ACs were disposed of in landfills [32,34]. Therefore, a new strategy is urgently undergoing exploration to overcome the disadvantages associated with sulfur-impregnated ACs [35,36].

Traditionally, the sulfur-functionalized carbon materials were prepared by using two steps, i.e., the carbonization of natural products (e.g., cellulose, chitin, starch, alginic acid, and chitosan) as well as some synthetic polymers (e.g., poly-acrylonitrile, polyaniline, and phenolic resins) first and then introducing sulfur onto carbons by using an impregnation method [37–40]. A one-pot carbonization and functionalization step, which could guarantee the uniform distribution and firm fixation of sulfur functionality on the carbon matrix, was required. Very recently, a simple approach via the carbonization of small organic molecules with the assistance of transition metals was reported to prepare a series of functional carbon materials [37]. This approach was realized via the pyrolysis of a mixture of small organic molecules and transition-metal salts in a conventional tubular furnace, hence avoiding the barriers to large-scale production, such as complicated equipment and harsh conditions. The salts would act as a heat-transfer medium and provide an oxygen-free environment for pyrolysis [41]. Moreover, the salts catalyze the formation of a thermally stable intermediate polymerization structure, avoiding the direct sublimation of small organic molecules during heating [37,38]. More attractive, template-like  $\text{SiO}_2$  could be mixed into the precursors and hence adopted to adjust the porosity of carbons. This strategy is commonly available and easy to use to control the surface sulfur functionalities, porosities, and morphologies of carbons.

In this work, porous sulfur-functionalized carbons were prepared and employed for  $\text{Hg}^0$  removal from coal-fired flue gas. The removal performance of sulfur-functionalized carbon (S-C) on  $\text{Hg}^0$  was studied and compared with that of commercial sulfur-loaded ACs (S/C). The  $\text{Hg}^0$  removal performances of S-C and S/C under various adsorption temperatures and flue gas conditions were studied. The excellent adsorption mechanism of  $\text{Hg}^0$  by S-C was further investigated. This work not only provides a promising trap for highly efficient  $\text{Hg}^0$  sequestration from coal-fired power plants but also illustrates a versatile platform for preparing functional carbon materials by using a one-pot carbonization and functionalization organic precursor.

## 2. Experimental Section

### 2.1. Sample Preparation

S-C was prepared by using a molten-salt pyrolysis strategy [38]. Two grams of 2,2-bithiophene and 2.0 g of  $\text{SiO}_2$  were added into 150 mL of tetrahydrofuran and stirred at room temperature for 6 h. The mixture was then dried and then ground to a powder. After that, the powder was placed into a rail boat and covered with 5.0 g of  $\text{Co}(\text{NO}_3)_2 \cdot 6\text{H}_2\text{O}$ , which was heated at 800 °C for 2 h. Then, the  $\text{SiO}_2$  was removed by using 10% HF solution. To obtain different porosity of S-C, the sample was etched by using HF for different times (0, 24, 48 and 56 h). After drying at 105 °C for 10 h, the S-C was finally obtained.

## 2.2. Sample Characterization

The morphology of the sample was studied by using a scanning electronic microscope (SEM, FEI F50, New York, NY, USA). Transmission electron microscope (TEM, EOL JEM 2100F, microscope Tokyo, Japan) and high-resolution TEM (HRTEM) were used to study the morphology and structure of sample. The valence states of samples were characterized by using X-ray photoelectron spectroscopy (XPS, Thermo ESCALAB 250Xi, New York, NY, USA).

## 2.3. Hg<sup>0</sup> Adsorption Activity Tests

The Hg<sup>0</sup> adsorption activity test was measured on a fixed-bed reactor [42,43]. The adsorbent was placed in a quartz reactor, reaction temperature of which was controlled by using a tube furnace. The flue gas was composed of N<sub>2</sub>, O<sub>2</sub>, SO<sub>2</sub>, NO, and H<sub>2</sub>O, with the total flow rate of 1 L·min<sup>-1</sup>. Hg<sup>0</sup> was provided by a mercury permeation tube placed in a constant temperature water bath, delivering Hg<sup>0</sup> by using N<sub>2</sub> to ensure a stable concentration of 65 µg·m<sup>-3</sup>. The concentration of Hg<sup>0</sup> was monitored by using an online mercury analyzer (RA-915M, Lumex, Tianjin, China). The Hg<sup>0</sup> adsorption capability was calculated by using the following equations:

$$Q = \frac{1}{m} \int_{t_1}^{t_2} (C_{in} - C_{out}) \times f \times dt \quad (1)$$

where  $C_{in}$  (µg·m<sup>-3</sup>) and  $C_{out}$  (µg·m<sup>-3</sup>) represent the inlet and outlet concentrations of Hg<sup>0</sup>,  $Q$  (µg·g<sup>-1</sup>) is the Hg<sup>0</sup> adsorption capacity,  $m$  (g) is the sample amount,  $f$  (m<sup>3</sup>·h<sup>-1</sup>) is the gas flow rate, and  $t$  (h) is the reaction time.

## 3. Description of Sorption Kinetic Models

### 3.1. Pseudo-First-Order Model

This model is described as follows [44]:

$$\frac{dq_t}{dt} = k_1(q_e - q_t) \quad (2)$$

Based on the initial conditions, i.e.,  $t = 0$   $q_t = 0$ , Equation (2) is revised as:

$$q_t = q_e(1 - e^{-k_1 t}) \quad (3)$$

where  $q_t$  and  $q_e$  represent the adsorbed mercury amount at any time  $t$  and equilibrium time (µg·g<sup>-1</sup>).  $k_1$  represents the rate constant (min<sup>-1</sup>).

### 3.2. Pseudo-Second-Order Model

This model is described as follows [45]:

$$\frac{dq_t}{dt} = k_2(q_e - q_t)^2 \quad (4)$$

On the basis of initial conditions, i.e.,  $t = 0$  and  $q_t = 0$ , Equation (4) is modified as:

$$q_t = \frac{t}{\frac{1}{k_2 q_e^2} + \frac{1}{q_e} t} \quad (5)$$

where  $k_2$  represents the rate constant (µg/(cm<sup>3</sup>·min)).

### 3.3. Elovich Model

This model is described as follows [46]:

$$\frac{dq_t}{dt} = \alpha \exp(-\beta q_t) \quad (6)$$

where  $\alpha$  represents the initial rate and  $\beta$  is related to surface coverage and activation energy. If  $t$  is much larger than  $t_0$ , this equation is modified as follows:

$$q_t = \frac{1}{\beta} \ln(\alpha\beta) + \left(\frac{1}{\beta}\right) \ln t \quad (7)$$

### 3.4. Intra-Particle Diffusion Model

This model is described by the following formula [47]:

$$q_t = k_{id}t^{0.5} + C \quad (8)$$

where  $k_{id}$  represents the diffusion rate constant within the particle and  $C$  is a constant, which is related to the boundary layer.

## 4. Results and Discussion

### 4.1. Preparation and Characterization of Samples

The S-C was prepared by using the molten  $\text{Co}(\text{NO}_3)_2 \cdot 6\text{H}_2\text{O}$ -assisted carbonization of sulfur-containing small organic molecule precursors.  $\text{SiO}_2$  nanoparticles were adopted as hard templates, followed by an HF etching step to remove the  $\text{SiO}_2$  template. The porosity of S-C was adjusted by using the HF etching time (shown in Figure 1). As listed in Table 1, the HF etching step will generate mesopores on the S-C. The S-C with HF etching for 10 h possessed the largest BET surface area of  $318.5 \text{ m}^2 \cdot \text{g}^{-1}$ , with an average pore size of 7.31 nm and total pore volume of  $0.58 \text{ cm}^3 \cdot \text{g}^{-1}$ . Pore size affects the internal mass transfer process of  $\text{Hg}^0$  on adsorbents, thus affecting the removal rate of  $\text{Hg}^0$ . As shown in Figure 2a, the  $\text{N}_2$  absorption–desorption isotherms for S-C belonged to a typical II isotherm, indicating that the porosity of S-C was very limited. The S-C after the HF etching step presented a typical IV isotherm with a negligible absorption at lower pressures but significant absorption at higher pressures ( $p/p^0 = 0.2\text{--}1.0$ ). This indicates that S-C is composed of mesopores or macropores rather than micropores. The pore distribution curves shown in Figure 2b demonstrate that the pore size of the S-C was in the range of 2–10 nm. The mesoporous structure in the range of 2–50 nm is beneficial for  $\text{Hg}^0$ 's diffusion to the inner surface of an adsorbent [48]. Thus, the pore structure of S-C is favorable for  $\text{Hg}^0$  adsorption.

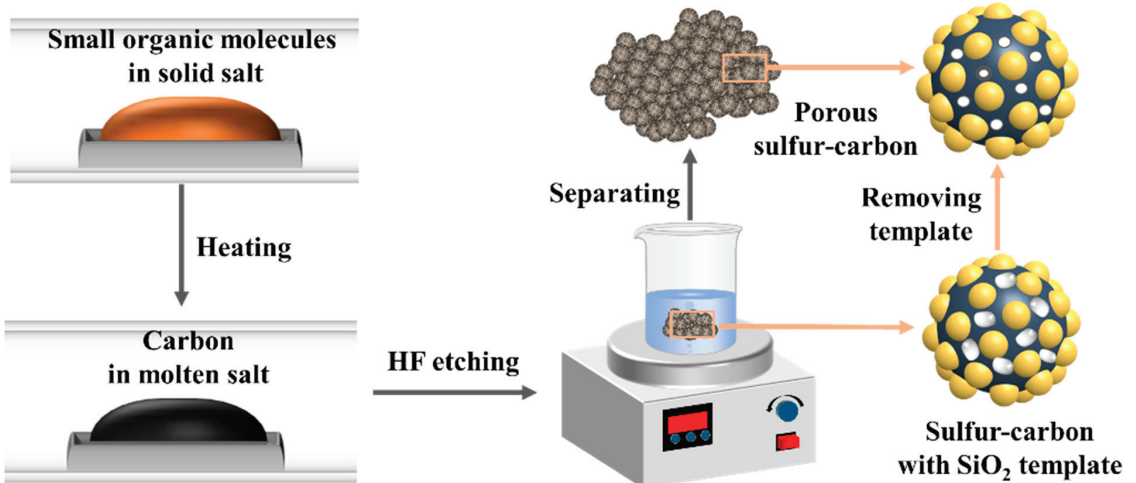


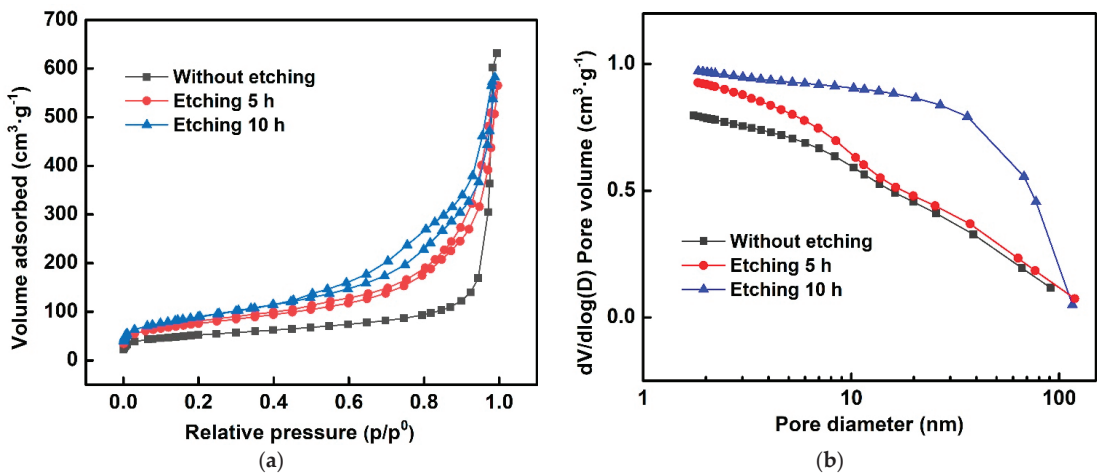
Figure 1. Schematic illustration of the synthesis process for S-C.

Figure 3 shows the morphologies of S-Cs with different HF etching times. These images display the high-solution local microscopies of individual particles, in which the

sizes of individual particles are in the range of 100–200 mesh. As shown, the morphology of S-C was significant dependent on the HF etching time. The S-C without HF etching displayed a dense surface, and there were negligible pores observed on the S-C surface. After etching with HF, abundant pores were generated on the S-C surface, and more pores were generated with the extension of the HF etching time from 5 to 10 h. Thus, the SiO<sub>2</sub> was embedded in the carbon structure as a template, which could be removed by using the HF solution to induce the formation of a porous structure. However, upon reaching a higher HF etching time, the resultant carbon framework collapsed, which might have affected the internal diffusion of mercury. Therefore, a SiO<sub>2</sub> template was used to achieve the adjustable preparation of porous carbons.

**Table 1.** Pore structure parameters of various S-Cs with different HF etching times.

HF Etching Time (h)	Total Surface Area (m <sup>2</sup> ·g <sup>-1</sup> )	Surface Area of Micropores (m <sup>2</sup> ·g <sup>-1</sup> )	Pore Volume (cm <sup>3</sup> ·g <sup>-1</sup> )	Pore Diameter (nm)
0	180.92	143.33	0.29	6.32
5	267.66	263.68	0.50	7.43
10	318.50	335.88	0.58	7.31



**Figure 2.** (a) N<sub>2</sub> adsorption–desorption isotherms and (b) pore size distributions of S-C.

The surface-functional groups of S-C were studied by using FTIR. As shown in Figure 4, there were four main peaks on the FTIR spectra, which could be assigned to the C-OH (3392 and 615 cm<sup>-1</sup>) and aromatic C = C (1626 and 1100 cm<sup>-1</sup>) [49]. Figure 5 shows the XPS spectra for S-C. As shown in Figure 5a, the spectra for high-resolution C 1s spectra could be divided into three peaks at 284.8, 286.0, and 288.8 eV, assigned to the characteristic peaks of C = C, C-O, and C = O [30]. Figure 5b shows the O 1s spectra for C-S, in which the peaks at 531.5, 532.3, and 533.3 eV are regarded as C-OH, C-O, and O-H [31]. Figure 5c shows the S spectra for S-C. The sulfur on the S-C existed in four forms. The two peaks at 164.2 and 165.3 eV corresponded to S 2p<sub>3/2</sub> and S 2p<sub>1/2</sub> for thiophenic sulfur (i.e., -C-S<sub>x</sub>-C-, x = 1-2), the small peak at 169.1 eV could be assigned to sulfoxide [50], the peak at 166.2 eV could be assigned to C-S, while the peaks at 167.2 and 170.3 eV could be assigned to sulfate [51,52].

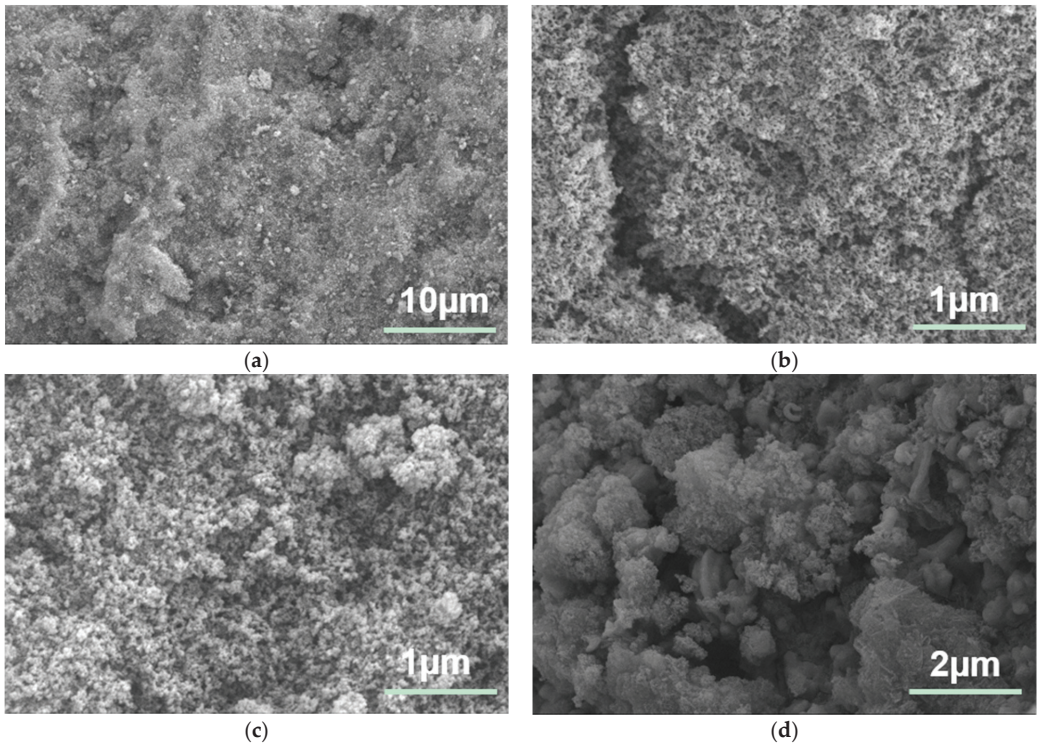


Figure 3. SEM images of S-C with HF etchings for (a) 0 h, (b) 5 h, (c) 10 h, and (d) 20 h.

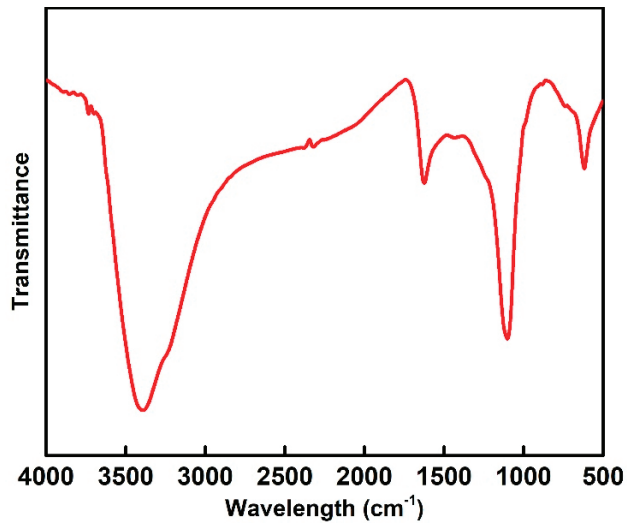


Figure 4. FTIR spectra of the synthetic S-C sample.

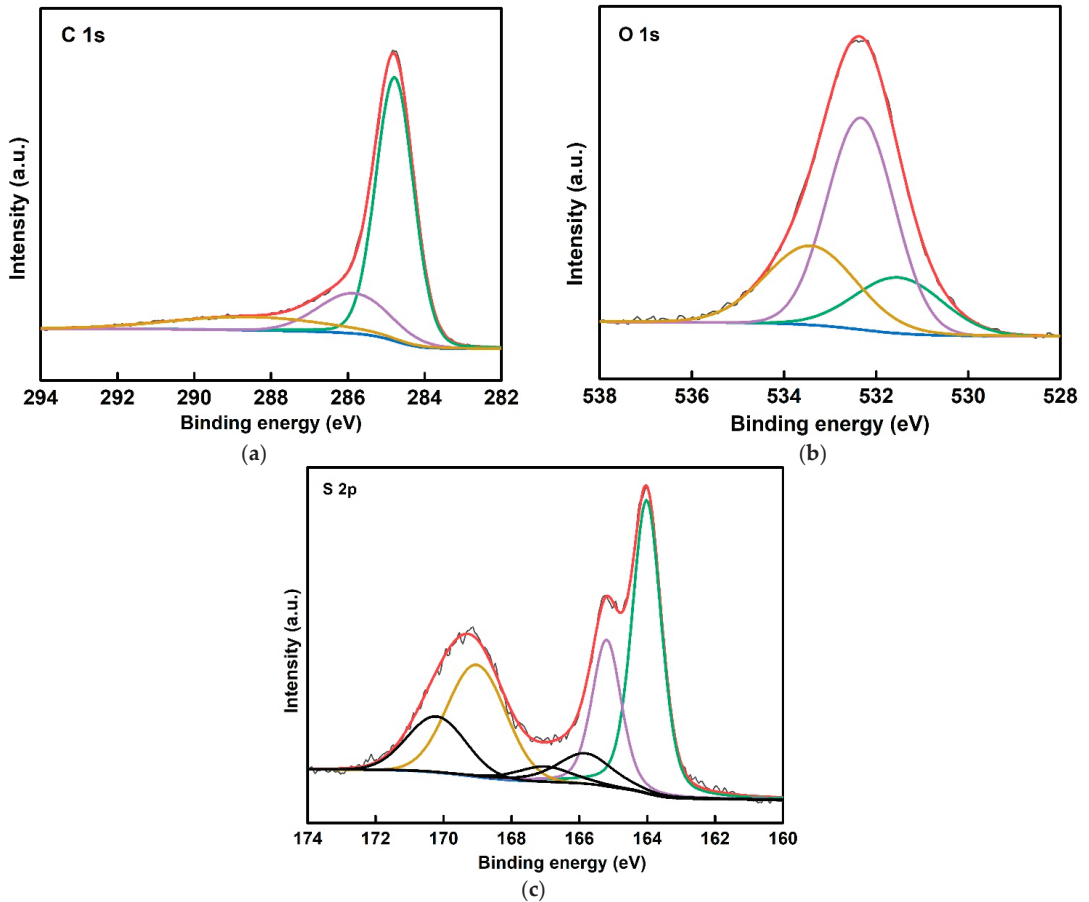


Figure 5. XPS spectra of S-C for (a) C 1s, (b) O 1s, and (c) S 2p.

#### 4.2. $\text{Hg}^0$ Adsorption Capacity Tests

Figure 6 shows the  $\text{Hg}^0$  adsorption performances of S-Cs with various HF etching times. As shown, the normalized-outlet  $\text{Hg}^0$  concentration of S-C without etching climbed dramatically to above 0.90. Thus, the S-C without etching has a poor  $\text{Hg}^0$  adsorption performance, and the removal rate of  $\text{Hg}^0$  is only below 10%. However, after the HF etching, the S-C displayed far superior  $\text{Hg}^0$  removal performances. The HF etching times played significant roles in the  $\text{Hg}^0$  adsorption of S-C. After etching for 5 h, the concentration of  $\text{Hg}^0$  at the normalized outlet remained below 0.2. With the extension of the etching time to 10 h, the  $\text{Hg}^0$  adsorption performance of S-C can be further improved. However, a too-long etching time resulted in a decrease in  $\text{Hg}^0$  adsorption performance. This is attributed to the fact that HF etching can remove the  $\text{SiO}_2$  template to generate abundant pores on S-C, which allows for accessible mercury molecule transportation. As a result, the sulfur in S-C can be accessible sufficiently for binding mercury. However, the excessive etching will result in the collapse of the framework of carbons, hence the weakening of the  $\text{Hg}^0$  adsorption on S-C.



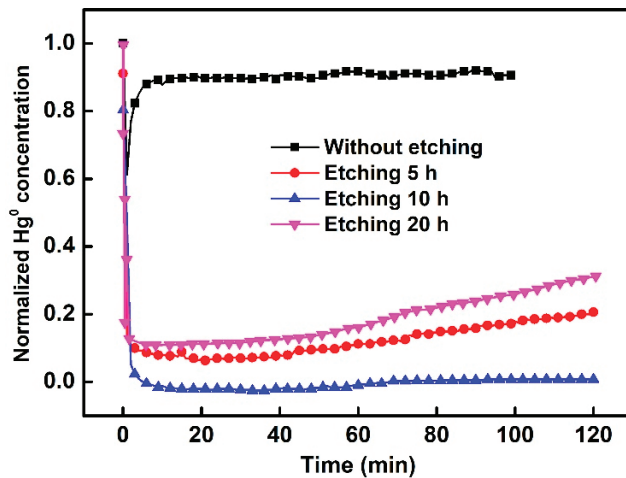


Figure 6.  $\text{Hg}^0$  removal performances of S-C with different etching times.

The saturated adsorption capacity of an adsorbent is an important index to use to evaluate the adsorption performances of materials, so it is necessary to study the change in S-C adsorption capacity with time. The curve of  $\text{Hg}^0$  adsorption capacity changing over time is shown in Figure 7. When the reaction duration was 1200 min, the adsorption capacity of  $\text{Hg}^0$  exceeded 50% and reached  $45.39 \text{ mg}\cdot\text{g}^{-1}$ . In addition, it can be seen from the figure that the adsorption rate increases first and then decreases with time, and the slope is zero when the adsorption is saturated. Adsorption kinetic models can be adopted to investigate the process of  $\text{Hg}^0$  adsorption and the dominant controlling factors. The pseudo-first-order-based kinetic model is the most common adsorption kinetic model.  $\ln(q_e - q_t)$  is used to plot  $t$ , and the adsorption mechanism conforms to the pseudo-first-order model if a straight line can be obtained. The pseudo-second-order model is based on the assumption that the adsorption rate is controlled by the chemisorption mechanism. Elovich describes a series of reaction mechanism processes, which are suitable for processes with large activation energy changes in reactions and for complex heterogeneous diffusion processes. The intra-particle diffusion model is commonly used to analyze the control steps in the reaction. Generally, the material adsorption process is divided into two processes: adsorbent surface adsorption and slow pore diffusion. If the fitting result fails to reach the origin, it indicates that the internal diffusion of the material is not the only step to controlling the adsorption process. As shown in Figure 8, the pseudo-first-order model was closest to the adsorption process of  $\text{Hg}^0$  on S-C, with an extremely high correlation coefficient ( $R^2 = 0.9982$ ). The saturation adsorption capacity of S-C was simulated as  $89.90 \text{ mg}\cdot\text{g}^{-1}$ . When the molar ratio of  $\text{Hg}:\text{S}$  is 1:1, it is equivalent to 55% of the sulfur accessibility in  $\text{Hg}^0$  adsorption. For comparison, the  $\text{Hg}^0$  saturation adsorption capacity of a sulfur-loaded commercial activated carbon (S/C) was also investigated. It should be noted that the S/C possessed a higher sulfur content and surface area compared with S-C. However, the saturation adsorption capacity of S/C was less than  $1 \text{ mg}\cdot\text{g}^{-1}$ , which was much lower compared with its theoretical adsorption capacity of  $352.1 \text{ mg}\cdot\text{g}^{-1}$ . Thus, most of the sulfur in S/C was not adopted sufficiently for binding mercury, although it possessed a higher surface area. It fully shows that the key to  $\text{Hg}^0$  adsorption improvements lies in the high dispersion of active sulfur species [53]. Thus, the molten-salt pyrolysis synthesis strategy toward sulfur-functionalized carbon would be more superior compared with other traditional methods, such as impregnation when significantly dispersing the active components (i.e., sulfur).

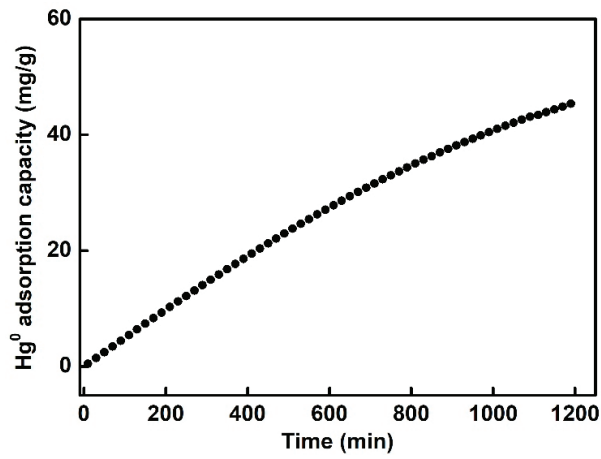


Figure 7.  $\text{Hg}^0$  adsorption-capacity curve for S-AC as a function of time.

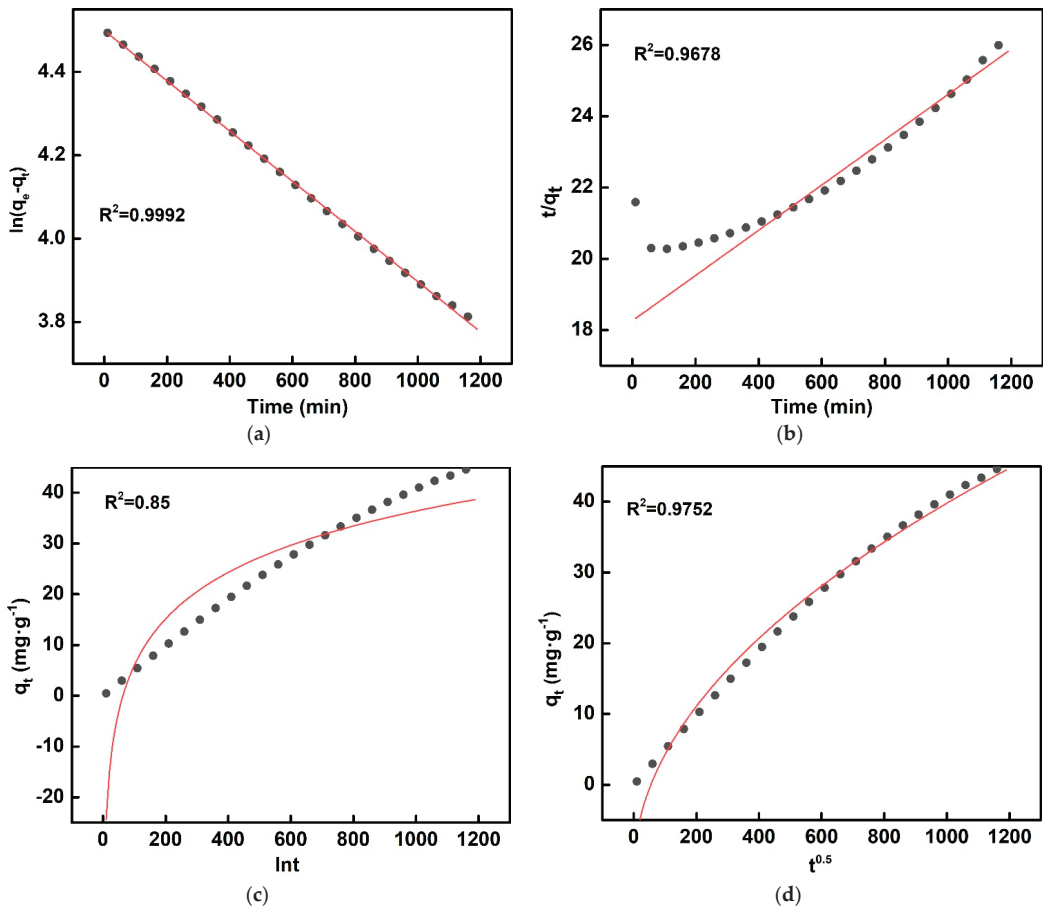


Figure 8.  $\text{Hg}^0$  adsorption behaviors of S-C simulated by the (a) pseudo-first-order, (b) pseudo-second-order, (c) Elovich, and (d) intra-particle diffusion models.

#### 4.3. Impact of Operation Conditions on $\text{Hg}^0$ Adsorption Capacity

An excellent adsorbent should have a good stability at various conditions. Figure 9 shows the influence of temperature on the  $\text{Hg}^0$  adsorption capacities of S-C and S/C. The normalized-outlet  $\text{Hg}^0$  concentration when passing through the S-C was maintained below 0.05 in a wide reaction temperature range of 25–125 °C. This suggests that an above 95%  $\text{Hg}^0$  adsorption efficiency was obtained; even the sorbent dosage was as low as 5 mg. This wide temperature range proves that the S-C can be applied flexibly at different scenes for  $\text{Hg}^0$  removal. In contrast, the S/C exhibited significantly different  $\text{Hg}^0$  adsorption capacities under various temperatures, in which relatively limited  $\text{Hg}^0$  adsorption capacities were obtained at low temperatures. Even at the optimum reaction temperature and the same amount of adsorbent, the concentration of  $\text{Hg}^0$  at the normalized outlet is still higher than 0.15, much higher than S-C. Depending on the preferred temperature range, setting the S/C upstream of the ESP is the ideal application in which the  $\text{Hg}^0$  adsorption capacity of S-C might be affected by various flue gas components, such as high concentrations of fly ash,  $\text{SO}_2$ , and  $\text{NO}_2$ .

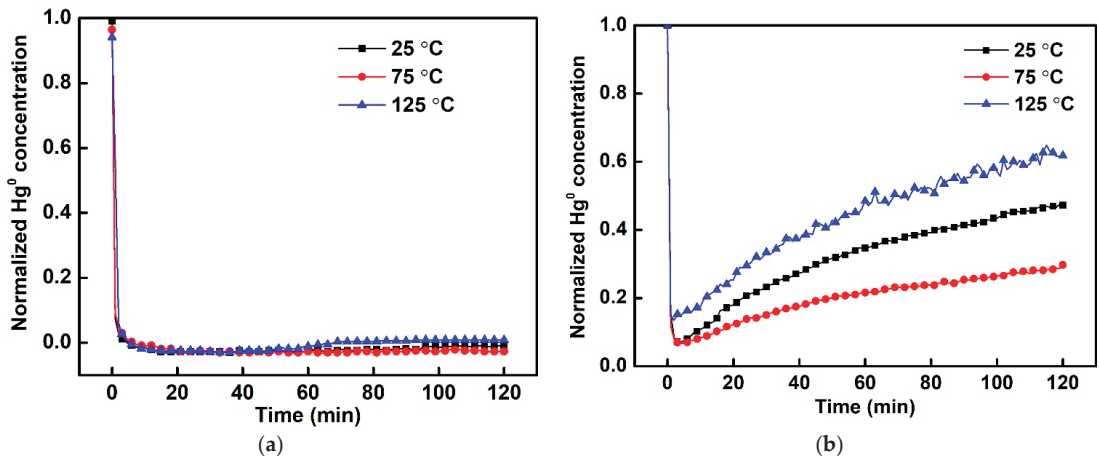
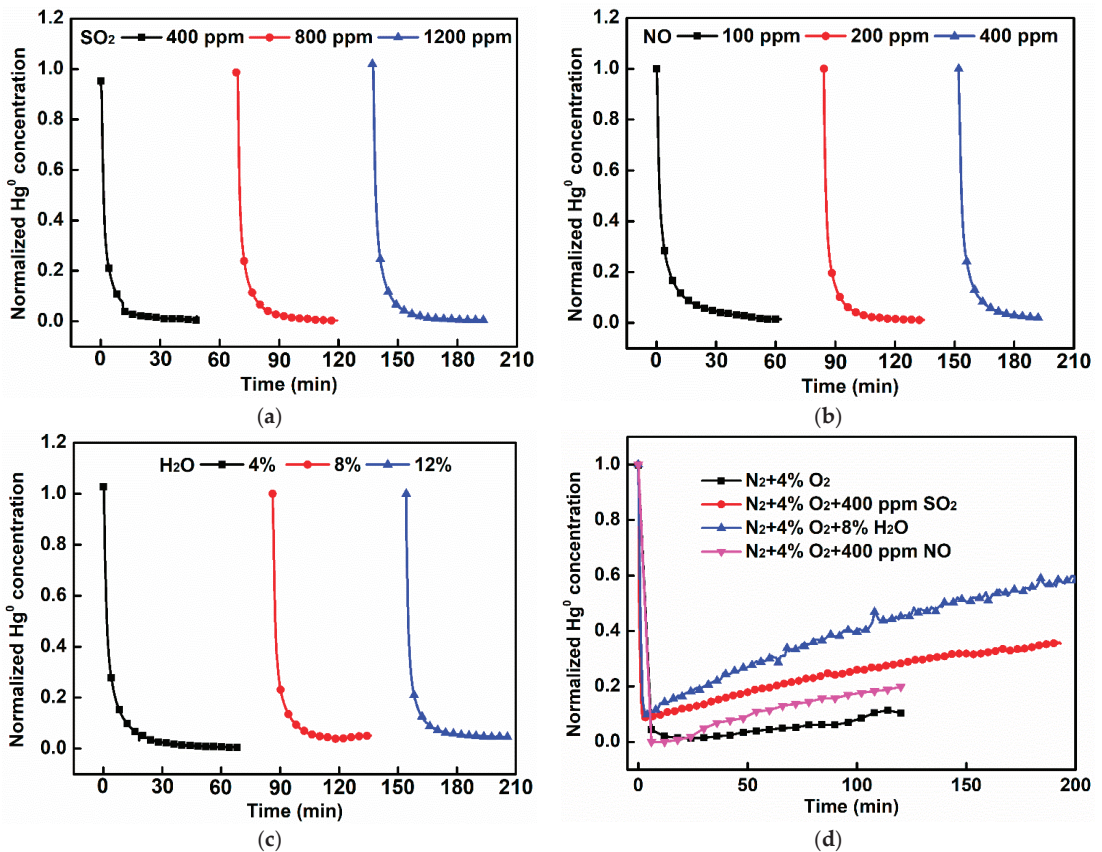


Figure 9.  $\text{Hg}^0$  removal performances of (a) S-C and (b) S/C under different temperatures.

According to previous studies,  $\text{SO}_2$  and  $\text{H}_2\text{O}$  generally compete with  $\text{Hg}^0$  for adsorption sites, hence exhibiting inhibitive effects on the  $\text{Hg}^0$  removal over carbonaceous sorbents [54,55]. However, the S-C exhibited an excellent resistance to these detrimental flue gas components. Figure 10a–c show that, in the presence of  $\text{SO}_2$ ,  $\text{H}_2\text{O}$ , as well as  $\text{NO}$ , the  $\text{Hg}^0$  removal performance was very similar to that under a pure  $\text{N}_2$  atmosphere. Even adding 1200 ppm of  $\text{SO}_2$ , 12%  $\text{H}_2\text{O}$ , or 400 ppm of  $\text{NO}$ , the normalized-outlet  $\text{Hg}^0$  concentration was kept at less than 0.05. As a direct comparison, the adsorption performance of S/C for  $\text{Hg}^0$  was investigated. As shown in Figure 10d, the  $\text{SO}_2$ ,  $\text{H}_2\text{O}$ , and  $\text{NO}$  significantly weakened the adsorption capacity of S/C. These results could fully demonstrate the excellent resistance of S-C to the detrimental impacts of flue gas impurities compared with commercial activated carbon, which would facilitate the real-world applications.



**Figure 10.** Effects of (a) SO<sub>2</sub>, (b) NO, and (c) H<sub>2</sub>O on the Hg<sup>0</sup> removal performances of S-Cs and (d) effects of flue gas components on the Hg<sup>0</sup> removal performances of S/Cs.

#### 4.4. Reaction Mechanism

To study the mechanism of a Hg<sup>0</sup> removal on S-C, the valence states of elements on spent S-C after adsorbing mercury were investigated by using XPS. Figure 11a shows that there is no significant change in the spectral binding energy of C 1s for the spent adsorbent, indicating that C did not participate in the Hg<sup>0</sup> adsorption [56]. Figure 11b shows the O 1s spectra for the spent adsorbent. The spectra of O 1s can be divided into four separate corresponding peaks: C = O, C-O-C, COOH, and H<sub>2</sub>O at 531.3, 532.5, 533.8, and 536.1 eV, respectively [57]. After the Hg<sup>0</sup> adsorption, part of the C-O groups changed to C = O, and H<sub>2</sub>O was generated on the adsorbent surface, which may have been caused by a charge imbalance after binding Hg<sup>0</sup>. Figure 11c shows the S 2p for the spent adsorbent, including only two peaks: C-S at 163.94 eV and thiophene at 165.22 eV [58]. The transformations of sulfur species on the spent adsorbent indicate that sulfur played a crucial role in the Hg<sup>0</sup> removal. The absolute content of thiophene and C-S decreased after adsorbing Hg<sup>0</sup>, especially the peaks for sulfoxide, which disappeared compared with the fresh adsorbent. This variation indicates that thiophene (i.e., -C-S<sub>x</sub>-C-, x = 1-2), sulfoxide, and C-S were beneficial to improving the Hg<sup>0</sup> removal capacity. This is in line with a previous study [59], i.e., findings that the sulfur in sulfide existing in a low state as well as the reducing sulfur (such as thiosulfone) had a high affinity with the Hg<sup>0</sup> atom. Electrons around the sulfur atom were easy to combine with Hg<sup>0</sup>, which was conducive to the removal of mercury. Figure 11d shows that the two peaks of Hg 4f corresponded to the peaks of 103 and 107

eV of HgS [60], further demonstrating that the sulfur in the adsorbent was active for binding Hg<sup>0</sup>.

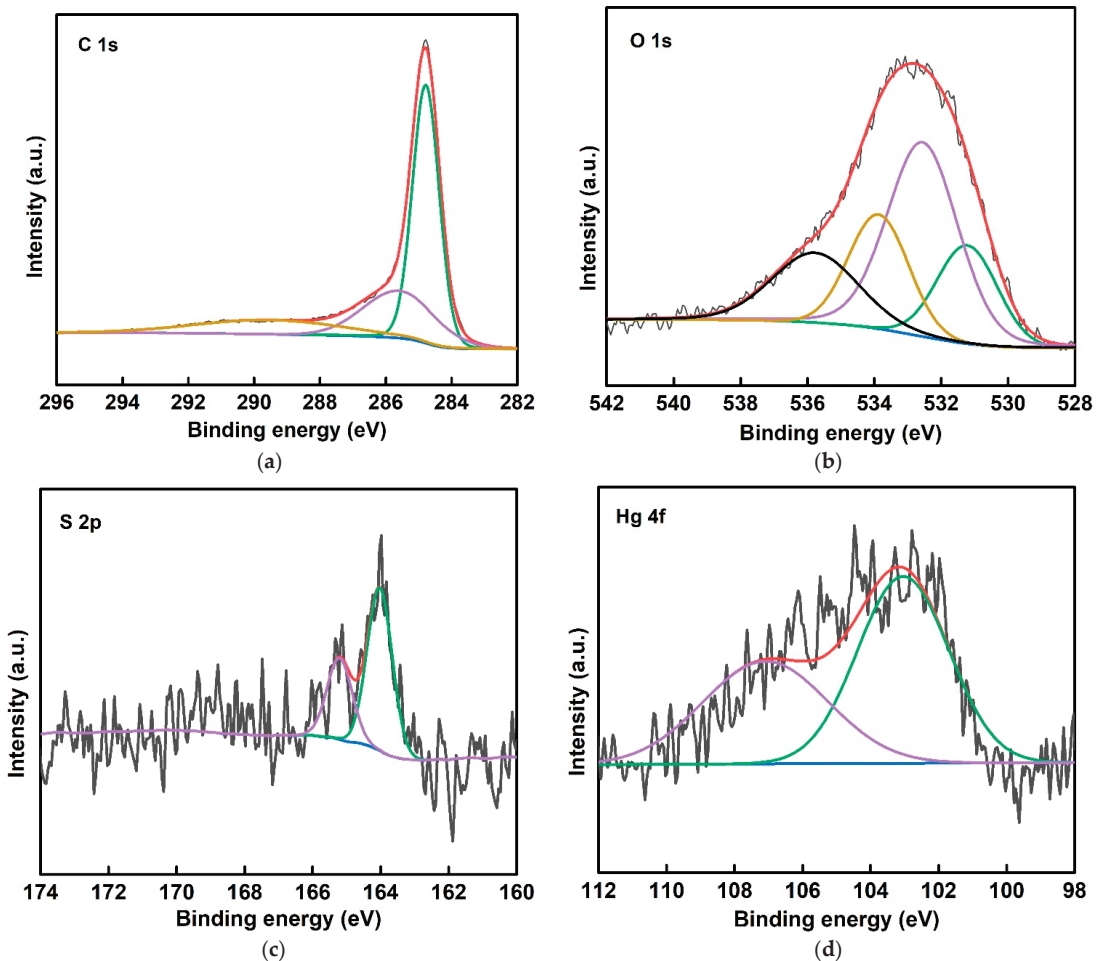


Figure 11. (a) C 1s, (b) O 1s, (c) S 2p, and (d) Hg 4f spectra of spent S-C.

## 5. Conclusions

Sulfur-functionalized carbon (S-C) derived from a molten-salt pyrolysis strategy was employed for a Hg<sup>0</sup> removal. Abundant pores could be generated by using a SiO<sub>2</sub> hard template and a subsequent HF etching step. The HF etching time significantly affected the Hg<sup>0</sup> removal performances of S-Cs. With an HF etching time of 10 h, the S-C presented the best Hg<sup>0</sup> removal performance, the saturation Hg<sup>0</sup>-adsorption capacity of which reached 89.90 mg·g<sup>-1</sup>. This value far exceeded that of the commercial sulfur-loaded activated carbon (S/C), which was specialized for Hg<sup>0</sup> removals. The S-C displayed a good applicability at 25–125 °C, while the S/C could be adopted around only 125 °C since the Hg<sup>0</sup> adsorption performances decreased when deviating from this temperature. The SO<sub>2</sub>, NO, and H<sub>2</sub>O had negligible adverse effects on Hg<sup>0</sup> adsorption over S-C. The good Hg<sup>0</sup> removal performance of S-C was ascribed to the existence of reduced sulfurs, such as thiophene, sulfoxide, and C-S, which have high affinities toward Hg<sup>0</sup>, and the fact that gaseous Hg<sup>0</sup> was converted into HgS after the adsorption. These results indicate that molten-salt pyrolysis

can simultaneously achieve the carbonization and functionalization of sulfur-containing organic precursors and is an ideal method for preparing carbonaceous adsorbents for Hg<sup>0</sup> removal.

**Author Contributions:** Conceptualization, J.Y.; Writing—original draft, J.Y.; Formal analysis, J.Y.; Investigation, H.X.; Writing—review & editing, H.X.; Software, F.M. and W.Q.; Methodology, F.M.; Supervision, Q.G.; Validation, Q.G., T.H. and Z.Y.; Data curation, T.H. and W.Q.; Visualization, Z.Y.; Resources, H.L.; Project administration, H.L. All authors have read and agreed to the published version of the manuscript.

**Funding:** This research received no external funding.

**Institutional Review Board Statement:** Not applicable.

**Informed Consent Statement:** Not applicable.

**Data Availability Statement:** No data was reported.

**Acknowledgments:** This project was supported by the National Natural Science Foundation of China (51906260), the Natural Science Foundation of Hunan Province, China (2021JJ30851), the Postgraduate Scientific Research Innovation Project of Hunan Province (CX20210098), the Foundation of State Key Laboratory of High-efficiency Utilization of Coal and Green Chemical Engineering (Grant No. 2022-K09 and 2022-K52), and the Key Research and Development Program of Sichuan Province (2021YFG0117).

**Conflicts of Interest:** The authors declare no conflict of interest.

## References

- Landrigan, P.J.; Wright, R.O.; Birnbaum, L.S. Mercury toxicity in children. *Science* **2013**, *342*, 1447. [[CrossRef](#)] [[PubMed](#)]
- Richardson, J.B.; Moore, L. A tale of three cities: Mercury in urban deciduous foliage and soils across land-uses in Poughkeepsie NY, Hartford CT, and Springfield MA USA. *Sci. Total Environ.* **2020**, *715*, 136869. [[CrossRef](#)] [[PubMed](#)]
- Li, M.; Yang, H.E.; Lu, H.; Wu, T.; Zhou, D.; Liu, Y. Investigation into the Classification of Tight Sandstone Reservoirs via Imbibition Characteristics. *Energies* **2018**, *11*, 2619. [[CrossRef](#)]
- Masoomi, I.; Kamata, H.; Yukimura, A.; Ohtsubo, K.; Schmid, M.O.; Scheffknecht, G. Investigation on the behavior of mercury across the flue gas treatment of coal combustion power plants using a lab-scale firing system. *Fuel Process. Technol.* **2020**, *201*, 106340. [[CrossRef](#)]
- Lee, S.S.; Wilcox, J. Behavior of mercury emitted from the combustion of coal and dried sewage sludge: The effect of unburned carbon, Cl, Cu and Fe. *Fuel* **2017**, *203*, 749–756. [[CrossRef](#)]
- Yang, S.; Liu, C.; Wang, P.; Yi, H.; Shen, F.; Liu, H. Co<sub>9</sub>S<sub>8</sub> nanoparticles-embedded porous carbon: A highly efficient sorbent for mercury capture from nonferrous smelting flue gas. *J. Hazard. Mater.* **2021**, *412*, 124970. [[CrossRef](#)]
- Fernández-Miranda, N.; Rodríguez, E.; Lopez-Anton, M.; García, R.; Martínez-Tarazona, M. A New Approach for Retaining Mercury in Energy Generation Processes: Regenerable Carbonaceous Sorbents. *Energies* **2017**, *10*, 1311. [[CrossRef](#)]
- Mei, J.; Liao, Y.; Qin, R.; Sun, P.; Wang, C.; Ma, Y.; Qu, Z.; Yan, N.; Yang, S. Acceleration of Hg<sup>0</sup> adsorption onto natural sphalerite by Cu<sup>2+</sup> activation during flotation: Mechanism and applications in Hg<sup>0</sup> recovery. *Environ. Sci. Technol.* **2020**, *54*, 7687–7696. [[CrossRef](#)]
- Yu, M.Y.; Luo, G.Q.; Sun, R.Z.; Zou, R.J.; Li, X.; Yao, H. A mechanism study on effects of bromide ion on mercury re-emission in WFGD slurry. *Chem. Eng. J.* **2021**, *406*, 127010. [[CrossRef](#)]
- Zhang, Y.; Yang, J.; Yu, X.; Sun, P.; Zhao, Y.; Zhang, J.; Chen, G.; Yao, H.; Zheng, C. Migration and emission characteristics of Hg in coal-fired power plant of China with ultra low emission air pollution control devices. *Fuel Process. Technol.* **2017**, *158*, 272–280. [[CrossRef](#)]
- Wen, M.; Wu, Q.; Li, G.; Wang, S.; Li, Z.; Tang, Y.; Xu, L.; Liu, T. Impact of ultra-low emission technology retrofit on the mercury emissions and cross-media transfer in coal-fired power plants. *J. Hazard. Mater.* **2020**, *396*, 122729. [[CrossRef](#)] [[PubMed](#)]
- Zhang, X.; Cui, L.; Li, Y.; Zhao, Y.; Dong, Y.; Cao, S. Adsorption and oxidation of mercury by montmorillonite powder modified with different copper compounds. *Energy Fuels* **2019**, *33*, 7852–7860. [[CrossRef](#)]
- Heidel, B.; Klein, B. Reemission of elemental mercury and mercury halides in wet flue gas desulfurization. *Int. J. Coal. Geol.* **2017**, *170*, 28–34. [[CrossRef](#)]
- Jia, T.; Ji, Z.; Wu, J.; Zhao, X.; Wang, F.; Xiao, Y.; Qi, X.; He, P.; Li, F. Nanosized ZnIn<sub>2</sub>S<sub>4</sub> supported on facet-engineered CeO<sub>2</sub> nanorods for efficient gaseous elemental mercury immobilization. *J. Hazard. Mater.* **2021**, *419*, 126436. [[CrossRef](#)] [[PubMed](#)]
- Xu, H.; Qu, Z.; Zong, C.; Quan, F.; Mei, J.; Yan, N. Catalytic oxidation and adsorption of Hg<sup>0</sup> over low-temperature NH<sub>3</sub>-SCR LaMnO<sub>3</sub> perovskite oxide from flue gas. *Appl. Catal. B* **2016**, *186*, 30–40. [[CrossRef](#)]

16. Choi, S.; Lee, S.S. Mercury adsorption characteristics of Cl-impregnated activated carbons in simulated flue gases. *Fuel* **2021**, *299*, 120822. [[CrossRef](#)]
17. Dastgheib, S.A.; Mock, J.; Ilangovan, T. Evaluation of modified activated carbons for mercury reemission control during neutralization of a simulated wastewater from the direct contact cooler of a pressurized oxy-combustion process. *Ind. Eng. Chem. Res.* **2021**, *60*, 947–954. [[CrossRef](#)]
18. Huang, T.F.; Duan, Y.F.; Luo, Z.K.; Zhao, S.L.; Geng, X.Z.; Xu, Y.F.; Huang, Y.J.; Wei, H.Q.; Ren, S.J.; Wang, H.; et al. Influence of flue gas conditions on mercury removal by activated carbon injection in a pilot-scale circulating fluidized bed combustion system. *Ind. Eng. Chem. Res.* **2019**, *58*, 15553–15561. [[CrossRef](#)]
19. Zhao, W.M.; Geng, X.Z.; Lu, J.C.; Duan, Y.F.; Liu, S.; Hu, P.; Xu, Y.F.; Huang, Y.J.; Tao, J.; Gu, X.B. Mercury removal performance of brominated biomass activated carbon injection in simulated and coal-fired flue gas. *Fuel* **2021**, *285*, 119131. [[CrossRef](#)]
20. Liu, D.J.; Li, B.; Liu, Y.X.; Wu, J. Copper sulfide-loaded boron nitride nanosheets for elemental mercury removal from simulated flue gas. *Energy Fuel* **2021**, *35*, 2234–2242. [[CrossRef](#)]
21. Park, J.; Lee, S.S. Adsorption of mercury by activated carbon prepared from dried sewage sludge in simulated flue gas. *J. Air Waste Manag. Assoc.* **2018**, *68*, 1077–1084. [[CrossRef](#)] [[PubMed](#)]
22. Yang, Z.; Li, H.; Liao, C.; Zhao, J.; Feng, S.; Li, P.; Liu, X.; Yang, J.; Shih, K. Magnetic rattle-type Fe<sub>3</sub>O<sub>4</sub>@CuS nanoparticles as recyclable sorbents for mercury capture from coal combustion flue gas. *ACS Appl. Nano Mater.* **2018**, *1*, 4726–4736. [[CrossRef](#)]
23. Oliveira, L.C.A.; Rios, R.V.R.A.; Fabris, J.D.; Garg, V.; Sapag, K.; Lago, R.M. Activated carbon/iron oxide magnetic composites for the adsorption of contaminants in water. *Carbon* **2002**, *40*, 2177–2183. [[CrossRef](#)]
24. Padak, B.; Wilcox, J. Understanding mercury binding on activated carbon. *Carbon* **2009**, *47*, 2855–2864. [[CrossRef](#)]
25. Li, H.; Zhu, L.; Wang, J.; Li, L.; Shih, K. Development of nano-sulfide sorbent for efficient removal of elemental mercury from coal combustion flue gas. *Environ. Sci. Technol.* **2016**, *50*, 9551–9557. [[CrossRef](#)] [[PubMed](#)]
26. Qiao, G.; Liu, L.; Hao, X.; Zheng, J.; Liu, W.; Gao, J.; Zhang, C.C.; Wang, Q. Signal transduction from small particles: Sulfur nanodots featuring mercury sensing, cell entry mechanism and in vitro tracking performance. *Chem. Eng. J.* **2020**, *382*, 122907. [[CrossRef](#)]
27. Zhao, L.; Wu, Y.-W.; Han, J.; Wang, H.-X.; Liu, D.-J.; Lu, Q.; Yang, Y.-P. Density Functional Theory Study on Mechanism of Mercury Removal by CeO<sub>2</sub> Modified Activated Carbon. *Energies* **2018**, *11*, 2872. [[CrossRef](#)]
28. Manceau, A.; Merkulova, M.; Murdzek, M.; Batanova, V.; Baran, R.; Glatzel, P.; Saikia, B.K.; Paktunc, D.; Leticariu, L. Chemical Forms of Mercury in Pyrite: Implications for Predicting Mercury Releases in Acid Mine Drainage Settings. *Environ. Sci. Technol.* **2018**, *52*, 10286–10296. [[CrossRef](#)]
29. Deng, J.; Li, M.; Wang, Y. Biomass-derived carbon: Synthesis and applications in energy storage and conversion. *Green Chem.* **2016**, *18*, 4824–4854. [[CrossRef](#)]
30. Wang, W.; Lu, Y.C.; Huang, H.; Wang, A.J.; Chen, J.R.; Feng, J.J. Solvent-free synthesis of sulfur- and nitrogen-co-doped fluorescent carbon nanoparticles from glutathione for highly selective and sensitive detection of mercury(II) ions. *Sens. Actuators B Chem.* **2014**, *202*, 741–747. [[CrossRef](#)]
31. Ma, J.; Zhou, B.; Zhang, H.; Zhang, W. Fe/S modified sludge-based biochar for tetracycline removal from water. *Powd. Technol.* **2020**, *364*, 889–900. [[CrossRef](#)]
32. Shin, Y.; Fryxell, G.E.; Um, W.; Parker, K.; Mattigod, S.V.; Skaggs, R. Sulfur-Functionalized Mesoporous Carbon. *Adv. Funct. Mater.* **2007**, *17*, 2897–2901. [[CrossRef](#)]
33. Marczak-Grzesik, M.; Budzyn, S.; Tora, B.; Szufa, S.; Kogut, K.; Burmistrz, P. Low-cost organic adsorbents for elemental mercury removal from lignite flue gas. *Energies* **2021**, *14*, 2174. [[CrossRef](#)]
34. Gwenzi, W.; Chaukura, N.; Wenga, T.; Mtisi, M. Biochars as media for air pollution control systems: Contaminant removal, applications and future research directions. *Sci. Total Environ.* **2021**, *753*, 142249. [[CrossRef](#)]
35. Shen, B.; Li, G.; Wang, F.; Wang, Y.; He, C.; Zhang, M.; Singh, S. Elemental mercury removal by the modified bio-char from medicinal residues. *Chem. Eng. J.* **2015**, *272*, 28–37. [[CrossRef](#)]
36. Li, G.; Wang, S.; Wang, F.; Wu, Q.; Tang, Y.; Shen, B. Role of inherent active constituents on mercury adsorption capacity of chars from four solid wastes. *Chem. Eng. J.* **2017**, *307*, 544–552. [[CrossRef](#)]
37. Wang, L.; Chen, M.X.; Yan, Q.Q.; Xu, S.L.; Chu, S.Q.; Chen, P.; Lin, Y.; Liang, H.W. A sulfur-tethering synthesis strategy toward high-loading atomically dispersed noble metal catalysts. *Sci. Adv.* **2019**, *5*, 6322. [[CrossRef](#)]
38. Wu, Z.Y.; Xu, S.L.; Yan, Q.Q.; Chen, Z.Q.; Ding, Y.W.; Li, C.; Liang, H.W.; Yu, S.H. Transition metal-assisted carbonization of small organic molecules toward functional carbon materials. *Sci. Adv.* **2018**, *4*, 0788. [[CrossRef](#)]
39. Xu, Y.; Luo, G.; Zhang, Q.; Li, Z.; Zhang, S.; Cui, W. Cost-effective sulfurized sorbents derived from one-step pyrolysis of wood and scrap tire for elemental mercury removal from flue gas. *Fuel* **2021**, *285*, 119221. [[CrossRef](#)]
40. Shen, B.; Liu, Z.; Xu, H.; Wang, F. Enhancing the absorption of elemental mercury using hydrogen peroxide modified bamboo carbons. *Fuel* **2019**, *235*, 878–885. [[CrossRef](#)]
41. Yang, J.; Xu, H.; Zhao, Y.; Li, H.; Zhang, J. Mercury Removal from Flue Gas by Noncarbon Sorbents. *Energy Fuel* **2021**, *35*, 3581–3610. [[CrossRef](#)]
42. Yang, J.; Li, Q.; Zu, H.; Yang, Z.; Qu, W.; Li, M.; Li, H. Surface-engineered sponge decorated with copper selenide for highly efficient gas-phase mercury immobilization. *Environ. Sci. Technol.* **2020**, *54*, 16195–16203. [[CrossRef](#)] [[PubMed](#)]

43. Yang, Z.; Yang, J.; Li, H.; Qu, W.; Leng, L.; Zhao, J.; Feng, Y.; Xu, Z.; Liu, H.; Shih, K. Advances in magnetically recyclable remediators for elemental mercury degradation in coal combustion flue gas. *J. Mater. Chem. A* **2020**, *8*, 18624–18650. [[CrossRef](#)]
44. Yang, J.; Zhao, Y.; Ma, S.; Zhu, B.; Zhang, J.; Zheng, C. Mercury removal by magnetic biochar derived from simultaneous activation and magnetization of sawdust. *Environ. Sci. Technol.* **2016**, *50*, 12040–12047. [[CrossRef](#)]
45. Revellame, E.D.; Fortela, D.L.; Sharp, W.; Hernandez, R.; Zappi, M.E. Adsorption kinetic modeling using pseudo-first order and pseudo-second order rate laws: A review. *Cleaner Eng. Technol.* **2020**, *1*, 100032. [[CrossRef](#)]
46. Pichler, C.; Lackner, R. Post-peak decelerating reaction of Portland cement: Monitoring by heat flow calorimetry, modelling by Elovich-Landsberg model and reaction-order model. *Constr. Build. Mater.* **2020**, *231*, 117107. [[CrossRef](#)]
47. Cabooter, D.; Song, H.; Makey, D.; Sadriaj, D.; Dittmann, M.; Stoll, D.; Desmet, G. Measurement and modelling of the intra-particle diffusion and b-term in reversed-phase liquid chromatography. *J. Chromatogr. A* **2021**, *1637*, 461852. [[CrossRef](#)]
48. Yang, J.; Li, Q.; Zhu, W.; Qu, W.; Li, M.; Xu, Z.; Yang, Z.; Liu, H.; Li, H. Recyclable chalcopyrite sorbent for mercury removal from coal combustion flue gas. *Fuel* **2021**, *290*, 120049. [[CrossRef](#)]
49. Cheng, F.; Zhou, P.; Huo, X.; Liu, Y.; Liu, Y.; Zhang, Y. Enhancement of bisphenol A degradation by accelerating the Fe(III)/Fe(II) cycle in graphene oxide modified Fe(III)/peroxymonosulfate system under visible light irradiation. *J. Colloid Interf. Sci.* **2020**, *580*, 1021. [[CrossRef](#)]
50. Feng, P.; Wang, W.; Wang, K.; Cheng, S.; Jiang, K. A high-performance carbon with sulfur doped between interlayers and its sodium storage mechanism as anode material for sodium ion batteries. *J. Alloys Compd.* **2019**, *795*, 223–232. [[CrossRef](#)]
51. Yu, H.; Qian, C.; Ren, H.; Chen, M.; Tang, D.; Wu, H.; Lv, R. Enhanced catalytic properties of bimetallic sulfides with the assistance of graphene oxide for accelerating triiodide reduction in dye-sensitized solar cells. *Sol. Energy* **2020**, *207*, 1037–1044. [[CrossRef](#)]
52. Wen, X.; Zhao, Z.; Zhai, S.; Wang, X.; Li, Y. Stable nitrogen and sulfur co-doped carbon dots for selective folate sensing, in vivo imaging and drug delivery. *Diam. Relat. Mater.* **2020**, *105*, 107791. [[CrossRef](#)]
53. Asasian, N.; Kaghazchi, T.; Faramarzi, A.; Hakimi-Siboni, A.; Asadi-Kesheh, R.; Kavand, M.; Mohtashami, S.-A. Enhanced mercury adsorption capacity by sulfurization of activated carbon with SO<sub>2</sub> in a bubbling fluidized bed reactor. *J. Taiwan Inst. Chem. E.* **2014**, *45*, 1588–1596. [[CrossRef](#)]
54. Guo, Y.; Niu, J.; Zhang, H.; Cheng, F.; Wu, H.; Jin, D. Enhanced SO<sub>2</sub> and Rhodamine B Removal by Blending Coke-Making Waste Benzene Residue (BR) for Pelletized Activated Coke (PAC) Production and Mechanisms. *Energy Fuel* **2019**, *33*, 5173–5181. [[CrossRef](#)]
55. Liu, H.; Xie, X.; Chen, H.; Yang, S.; Liu, C.; Liu, Z.; Yang, Z.; Li, Q.; Yan, X. SO<sub>2</sub> promoted ultrafine nano-sulfur dispersion for efficient and stable removal of gaseous elemental mercury. *Fuel* **2020**, *261*, 116367. [[CrossRef](#)]
56. Zhou, M.; Xie, X.; Liu, Q.; Zhang, M.; Peng, C.; Li, F.; Liu, Q.; Song, Y.; Wu, J.; Qiao, Z. Spherical In<sub>2</sub>S<sub>3</sub> anchored on g-C<sub>3</sub>N<sub>4</sub> nanosheets for efficient elemental mercury removal in the wide temperature range. *Chem. Eng. J.* **2022**, *430*, 132857. [[CrossRef](#)]
57. Alegre, C.; Sebastián, D.; Lázaro, M.J. Carbon xerogels electrochemical oxidation and correlation with their physico-chemical properties. *Carbon* **2019**, *144*, 382–394. [[CrossRef](#)]
58. Hsu, C.J.; Chiou, H.J.; Chen, Y.H.; Lin, K.S.; Rood, M.J.; Hsi, H.C. Mercury adsorption and re-emission inhibition from actual WFGD wastewater using sulfur-containing activated carbon. *Environ. Res.* **2019**, *168*, 319–328. [[CrossRef](#)]
59. Zhao, S.; Luo, H.; Ma, A.; Sun, Z.; Zheng, R. Experimental study on mercury removal from coal-fired flue gas by sulfur modified biomass coke with mechanochemical method. *Fuel* **2022**, *309*, 122201. [[CrossRef](#)]
60. Yang, Q.; Yang, Z.; Li, H.; Zhao, J.; Yang, J.; Qu, W.; Shih, K. Selenide functionalized natural mineral sulfides as efficient sorbents for elemental mercury capture from coal combustion flue gas. *Chem. Eng. J.* **2020**, *398*, 125611. [[CrossRef](#)]







Article

# Designing Environmental Messages to Discourage Red Meat Consumption: An Online Experiment

Alice Wistar <sup>1</sup>, Marissa G. Hall <sup>2,3,4</sup>, Maxime Bercholz <sup>4</sup> and Lindsey Smith Taillie <sup>4,5,\*</sup>

<sup>1</sup> Program in Global Health and Health Policy, Center for Health and Wellbeing, Princeton School of Public and International Affairs, Princeton University, Princeton, NJ 08544, USA; alicewistar@gmail.com

<sup>2</sup> Department of Health Behavior, Gillings School of Global Public Health, University of North Carolina at Chapel Hill, Chapel Hill, NC 27599, USA; mghall@unc.edu

<sup>3</sup> Lineberger Comprehensive Cancer Center, University of North Carolina at Chapel Hill, Chapel Hill, NC 27599, USA

<sup>4</sup> Carolina Population Center, University of North Carolina at Chapel Hill, Chapel Hill, NC 27516, USA; bercholz@email.unc.edu

<sup>5</sup> Department of Nutrition, Gillings School of Global Public Health, University of North Carolina at Chapel Hill, Chapel Hill, NC 27599, USA

\* Correspondence: taillie@unc.edu

**Abstract:** Reducing red meat consumption in high-consuming countries is critical for mitigating climate change and preventing chronic disease. This study tested the effectiveness of messages conveying the worsening or reduction of environmental harms at discouraging red meat consumption. 1078 U.S. adults viewed seven messages in an online survey highlighting the reduction or worsening of environmental harms associated with eating red meat (between-subjects factor) and rated the messages on how much they discouraged them from wanting to buy beef. Each message highlighted a different environmental harm: deforestation, climate change, water shortages, biodiversity loss, carbon footprint, greenhouse gas emissions, or environment (within-subjects factor). No statistically significant difference was found between the reduction and worsening of environmental harms conditions for most topics, though the worsening of harms frame slightly outperformed the reduction of harms frame for the ‘environment’ topic. ‘Environment’ was also the message topic that elicited the strongest response from participants overall. Latino participants, those with more than a high school degree, and those who consume beef once a week or less rated messages as more effective than non-Latino participants, those who completed high school or less, and those who consumed beef more than once a week. Future research should explore the effect of messages on behavioral outcomes.

**Keywords:** vegetarianism; goal framing; emphasis framing; sustainability; meat consumption; environmental behavior; health communication

**Citation:** Wistar, A.; Hall, M.G.; Bercholz, M.; Taillie, L.S. Designing Environmental Messages to Discourage Red Meat Consumption: An Online Experiment. *Int. J. Environ. Res. Public Health* **2022**, *19*, 2919. <https://doi.org/10.3390/ijerph19052919>

Academic Editors: Roberto Alonso González Lezcano, Francesco Nocera and Rosa Giuseppina Caponetto

Received: 10 February 2022

Accepted: 28 February 2022

Published: 2 March 2022

**Publisher’s Note:** MDPI stays neutral with regard to jurisdictional claims in published maps and institutional affiliations.



**Copyright:** © 2022 by the authors. Licensee MDPI, Basel, Switzerland. This article is an open access article distributed under the terms and conditions of the Creative Commons Attribution (CC BY) license (<https://creativecommons.org/licenses/by/4.0/>).

## 1. Introduction

Reducing red meat consumption in countries with high levels of consumption was identified by the 2019 EAT-Lancet commission as a strategy that would benefit both the environment and human health [1]. Recent meta-analyses show the associations between red meat (beef, lamb, pork, and other mammalian meat) and colorectal cancer [2–4], type II diabetes [5], stroke [6], coronary heart disease [6], heart failure [6], obesity [7], and all-cause mortality [8,9]. Because of these relationships, organizations including the American Cancer Society recommend limiting red meat consumption in favor of poultry, fish, or plant-based proteins [10,11]. Substituting whole, plant-based foods such as nuts, legumes, and whole grains for red meat is associated with a lower risk of type II diabetes [12,13] and mortality risk [14] and can lead to an increase in life expectancy [15]. One meta-analysis concluded that reducing or eliminating consumption of red or processed meat would also reduce the risk of stroke, coronary heart disease, and heart failure [6].

In addition, livestock contributes 14.5% of all anthropogenic GHG emissions [16], beef alone representing 41% of these emissions [16], and is the single most significant source of methane emissions [17]. Livestock also uses 30% of the planet's ice-free terrestrial surface [18] and is a leading cause of biodiversity loss [16–19], deforestation [16–18,20,21], aquifer depletion and water shortages [17,22], eutrophication [23], terrestrial acidification [23], and land degradation and pollution [16,17,19,24].

In the U.S., where beef consumption is the second highest in the world [25] and where beef accounts for nearly half of land-use and GHG emissions associated with diets [26,27], reducing red meat consumption could yield significant environmental benefits [19,26–34]. An analysis from the World Resources Institute showed that reducing beef consumption to the world average level in regions such as the U.S. where beef consumption is above average could spare 300 million hectares of pasture [27], an area nearly the size of India. More recent research shows that annual agricultural production emissions of high-income countries' diets could be reduced by 61% if their populations adopted the EAT-Lancet planetary health diet [35], which limits red meat consumption to 98 g per week [36]. A gradual phase out of all of animal agriculture, while unlikely, could achieve half of the net GHG emission reductions necessary to limit global warming to 2 °C above preindustrial levels, a goal set at the Paris Agreement, with the phasing out of beef accounting for 47% of those GHG reductions [37]. Indeed, limiting global temperature rises to 2 °C above preindustrial levels is not possible without GHG reductions from the food system [38]. Other specific environmental benefits of diets lower in red meat include reduced clearing of agricultural land [39], global water consumption [22], extinction risk for mammals and birds [39], terrestrial acidification [23], and eutrophication [23].

Given high levels of red meat consumption in the U.S., one challenge relates to identifying effective strategies to reduce consumption. Messaging has been an effective strategy to change health behaviors such as smoking [40], sugar-sweetened beverage (SSB) consumption [41], and alcohol use [42]. Although most public health messages about food have focused on individual health outcomes, messages that focus on the environment are promising. Considering that public awareness and concern around the threats of climate change are increasing [43], particularly among young people [44], environmental messaging may further increase awareness about red meat's environmental harms. In an online experiment with 590 German adults, Cordts et al. (2014) found that providing information about meat's environmental harms increased participants' intention to reduce their meat consumption in the future [45]. Thus, environmental messaging may also help change meat consumption behaviors. Yet, relatively little is understood about the types of messages that are most effective at discouraging red meat consumption.

Message framing, or the particular way in which information is communicated and emphasized, is an important tool used to maximize the impact of messages on individuals' thoughts and behaviors. Though little research explores framing in the context of meat reduction messaging strategies specifically, message framing has been shown to alter individuals' behavioral intentions and attitudes on environmental issues more broadly [46,47].

There are numerous types of message framing. Goal framing is one such type that involves emphasizing either the advantages of engaging in a target behavior (e.g., composting can help the environment) or the disadvantages of not engaging in a target behavior (e.g., not composting can hurt the environment) [48]. Prior research suggests that negatively framed messages are more effective than positively framed messages due to a negativity bias wherein individuals tend to dislike losses more than equivalent gains [49–51]. A recent systematic review of 61 studies finds that emphasizing the negative outcomes of an environmentally relevant decision is more likely to prompt a change in behavior and intentions to change behavior, whereas emphasizing the positive outcomes of an environmentally relevant decision is more likely to change attitudes towards the specified behavior [52]. Indeed, additional research conducted in the U.K., Iran, and Australia, found that messages highlighting the positive consequences of engaging in climate change mitigation activities were more effective at changing attitudes towards participating in

pro-environmental behaviors than messages emphasizing the negative consequences of not engaging in climate change mitigation activities [53–55]. Thus, for promoting actual engagement in pro-environmental behaviors, existing research suggests that highlighting negative consequences tends to be more effective, although there is still no clear consensus. To our knowledge, no research has explored whether emphasizing positive or negative outcomes is more effective at discouraging red meat consumption specifically.

A separate type of message framing, emphasis framing, is focused on emphasizing a specific aspect or feature of a given issue (e.g., portraying climate change as an environmental issue versus a public health issue) [46]. A recent meta-analysis found that framing climate change as an opportunity for economic growth, an environmental hazard, or a moral issue modestly altered individuals' support for climate policy and intentions to engage in environmental behaviors [46]. It is currently unknown, however, whether emphasizing specific topics within the environmental frame at large (e.g., water shortages, biodiversity loss) affects individuals' intentions to participate in pro-climate behaviors such as reducing red meat consumption.

In addition, little is currently known about which audiences will be most responsive to meat-reduction focused messages. While existing messaging studies in high-income countries show that being female [56–61] and eating meat less regularly [56–58] tend to be consistent predictors of willingness to eat less meat, there is limited and inconsistent evidence regarding the effects of other demographic characteristics such as age, education, ethnicity, and income level [62].

The primary objective of this research is to explore the efficacy of goal framing for discouraging red meat purchases by experimentally testing whether messages that convey the worsening of environmental harms or the reduction of environmental harms are perceived as more effective at discouraging beef purchases. Perceived message effectiveness is a predictor of longer-term behavior change [63] and is a widely-used measure in initial testing of messages because it tends to be sensitive to small differences between similar messages [64–68]. Given the paucity of research on goal framing for messages focused on discouraging red meat consumption, this was an exploratory study and as such, we did not have an a priori hypothesis about which type of message would elicit higher effectiveness. As secondary goals, this study explores whether PME varies between seven different environmental topics (emphasis frames) or based on demographic characteristics.

## 2. Materials and Methods

### 2.1. Sample

Survey participants ( $n = 1088$ ) were recruited through convenience sampling in October 2019 using CloudResearch Prime Panels as part of an experiment that tested the impact of sugar-sweetened beverage (SSB) warnings on SSB purchasing behavior and reactions among Latino and non-Latino parents. Prime Panels used purposive sampling to recruit half Latino and half non-Latino participants.

Utilizing online panels to recruit convenience samples has been found to generate experimental findings comparable to those from representative samples [69,70]. Inclusion criteria included residing in the U.S., being 18 or older, and having at least one child between 2 and 12. The latter criterion was included because the primary experiment focused on reactions to sugar-sweetened beverage warnings among parents. Participants received incentives in cash, gift cards, or rewards points from Prime Panels. The University of North Carolina (UNC) Institutional Review Board approved this study (IRB #19-0277).

### 2.2. Messages

Message topics were chosen based on a high level of peer-reviewed and scientific organizations' (including the Intergovernmental Panel on Climate Change) evidence on the environmental harms of beef consumption and production. For each of the seven topics, message text was then developed to either highlight that purchasing beef can *worsen* environmental harms ("worsening harms" goal frame) or that purchasing less beef can

reduce environmental harms (“reducing harms” goal frame). Message topics (the emphasis frames) were the within-subjects factor (Table 1). Participants were randomized to see messages in either the worsening harms or reducing harms frame (between-subjects factor).

**Table 1.** Text of Environmental Messages Tested in an Online Study of U.S. Adults ( $n = 1078$ ).

Frame 1: Worsening of Environmental Harms	Frame 2: Reduction of Environmental Harms
Buying beef can . . .	Buying less beef can . . .
increase your carbon footprint	reduce your carbon footprint
increase greenhouse gas emissions	reduce greenhouse gas emissions
contribute to water shortages	reduce water shortages
hurt the environment	help the environment
worsen climate change	help mitigate climate change
contribute to biodiversity loss	reduce biodiversity loss
contribute to deforestation	reduce deforestation

### 2.3. Procedures

This experiment was conducted online using Qualtrics and employed a mixed between-within design. After completing informed consent, eligible participants first answered a series of questions about SSB warnings and SSB consumption. Participants then responded to one question about their beef consumption frequency before viewing seven randomly ordered messages about different environmental harms. For each of these seven messages, participants answered the same question about how much the message discouraged them from wanting to buy beef. Finally, participants answered several demographic questions.

### 2.4. Measures

Beef consumption frequency was measured using a modified NHANES item: “Thinking about the last month, how often did you typically consume beef (including steak, ground beef, or other types of beef)?” Response options included Never, Once a month, 2–3 times a month, Once a week, 2–6 times a week, Once a day, or More than once a day [71]. Discouragement from buying beef was measured using one item from the UNC PME Scale [72]: “How much does each statement discourage you from wanting to buy beef?” Response options were: not at all (coded as 1); a little bit (2); somewhat (3); quite a bit (4); and a great deal (5). PME is a common measure used in health-related message development and testing and has been found to predict behavioral change [73].

### 2.5. Analysis

Statistical analyses were conducted in Stata/SE 16.1 using two-tailed tests and a significance level of 0.05 (StataCorp LLC, College Station, TX, USA). A multilevel mixed-effects linear model with random intercepts at the respondent level was estimated to test for differences in PME between goal framing conditions (worsening of environmental harms vs. reduction of environmental harms) and message topics (climate change, deforestation, etc.). The dependent variable was PME and the independent variables were dummy variables for the worsening of harms framing condition (relative to reduction of harms) and for six of the seven message topics (relative to carbon footprint), and interactions between the worsening of harms framing condition dummy and each of the six message topic dummies. Using the model estimates, we then estimated the mean PME by framing condition on average over the seven message topics, and the difference in these means (the average framing effect). Similarly, we estimated the mean PME by message topic on average over the two framing conditions, and all pairwise differences in those means. To test whether the framing effect differed by message topic, we carried out a Wald test of joint significance of the coefficients on the interaction terms, with joint significance indicating that the framing effect did differ by message topic, i.e., was not homogenous across message topics. In further analyses, we estimated the average framing effect for each message topic separately. Results using a

multilevel mixed-effects ordered logit model did not differ in any meaningful way with respect to the direction of findings and statistical significance.

To explore predictors of PME, PME was averaged over all seven topics and regressed using ordinary least squares (OLS) on categories of age, beef consumption frequency, education level, income level, Latino ethnicity, and gender. Demographic characteristics were categorized as follows—age: 18–29, 30–39, or over 39 years old; beef consumption frequency: eats beef more than once a week or less than once a week; education level: more than high school or less than high school; Latino ethnicity: yes or no; gender: man, woman, or transgender; and income level: less than \$35,000, between \$35,000 and \$74,999, or \$75,000 and above. These categorizations were chosen to create the most equal split between categories. Where an equal split was not possible in two categories (e.g., age and income level), three categories were created and two regression coefficients were reported.

### 3. Results

#### 3.1. Demographic Characteristics

Participants' mean age was 35.3 years (Table 2). More than half (58.3%) identified as female and approximately half (47.7%) were Latino, had a college degree or higher (52.5%), and had an annual household income of less than \$50,000 (46.5%). Regarding beef consumption, most (65.0%) participants ate beef once a week or more.

**Table 2.** Descriptive Statistics of Sociodemographic Characteristics, Beef Consumption, and Language Preference of Participants in an Online Study of U.S. Adults ( $n = 1078$ ).

Age * (Years), Mean and SD	<i>n</i> or Mean	% or SD
	35.3	7.4
Education level †, <i>n</i> and %		
High school diploma ‡ or less	512	47.5
4 year college degree or more	566	52.5
Income level, <i>n</i> and %		
Less than \$25,000	213	19.8
\$25,000 to \$49,999	288	26.7
\$50,000 to \$74,999	202	18.7
\$75,000 to \$99,999	157	14.6
\$100,000 or more	218	20.2
Latino ethnicity, <i>n</i> and %		
Non-Latino	564	52.3
Latino	514	47.7
Gender, <i>n</i> and %		
Male	445	41.3
Female	628	58.3
Transgender	5	0.5
Beef consumption †, <i>n</i> and %		
Less than once a week	377	34.9
Once a week or more	701	65.0
Survey language, <i>n</i> and %		
English	924	85.7
Spanish	154	14.3

\* Three incorrect age entries were treated as missing values. † Demographic data for these categories were initially collected using the following categories but were dichotomized to avoid small cells by treatment status and increase power by reducing the number of categories. For education, these categories were: less than high school or U.S. equivalent, high school or U.S. equivalent, 4 year college degree, and graduate degree or more. For beef consumption, these categories were: never, once a month, 2–3 times a month, once a week, 2–6 times a week, once a day, and more than once a day. ‡ Or U.S. equivalent (GED).

### 3.2. Message Framing Conditions

The messages for both the worsening harms and reducing harms frames are shown in Table 1. The mean PME was 2.80 (95% CI 2.70, 2.91) in the reducing harms framing condition and 2.89 (95% CI 2.78, 2.99) in the worsening harms framing condition. Although this difference was not statistically significant ( $p = 0.277$ ), it is notable that PME was on average higher in the worsening of harms frame than in the reduction of harms frame for all message topics (Figure 1). Figure 1 shows the mean PME for both messaging frames across each environmental message topic.

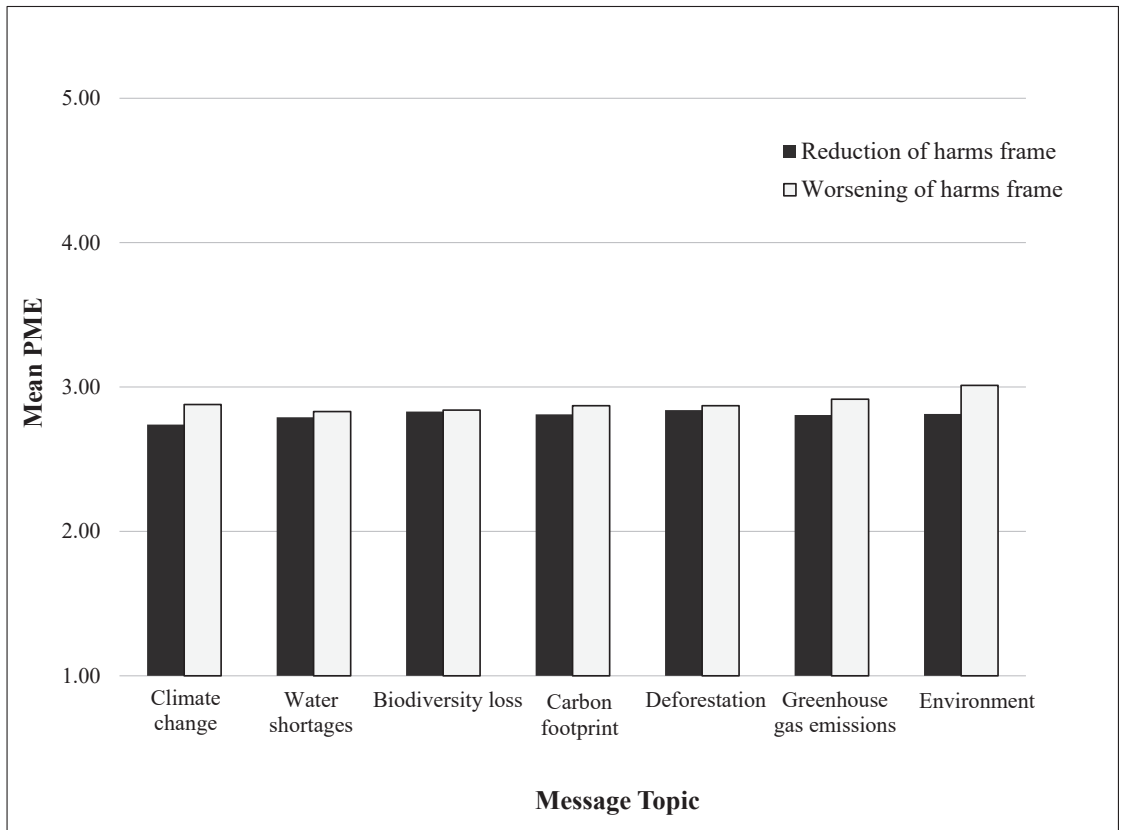


**Figure 1.** Perceived Message Effectiveness by Message Topic and Framing Condition in an Online Study of U.S. Adults ( $n = 1078$ ).

The coefficients on the interactions between the worsening of harms frame dummy and the message topic dummies were jointly statistically significant ( $p = 0.004$ ), rejecting the hypothesis of a homogenous framing effect across message topics. This result was driven by the mean PME difference between frames on ‘environment’ messages: 3.01 for the message ‘buying beef can hurt the environment’ vs. 2.81 for the message ‘buying less beef can help the environment’ ( $p = 0.017$ ), while it was not statistically different from zero for the other message topics.

Mean PME ratings by message topic are displayed in Figure 2, and ranged from 2.81 (climate change, water shortages) to 2.91 (environment). The ‘environment’ message elicited statistically higher PME ( $p < 0.05$ ) than all topics except GHG emissions. All other comparisons between topics were not statistically significant. Figure 2 shows the mean PME, averaged across both message frames, for each environmental message topic.

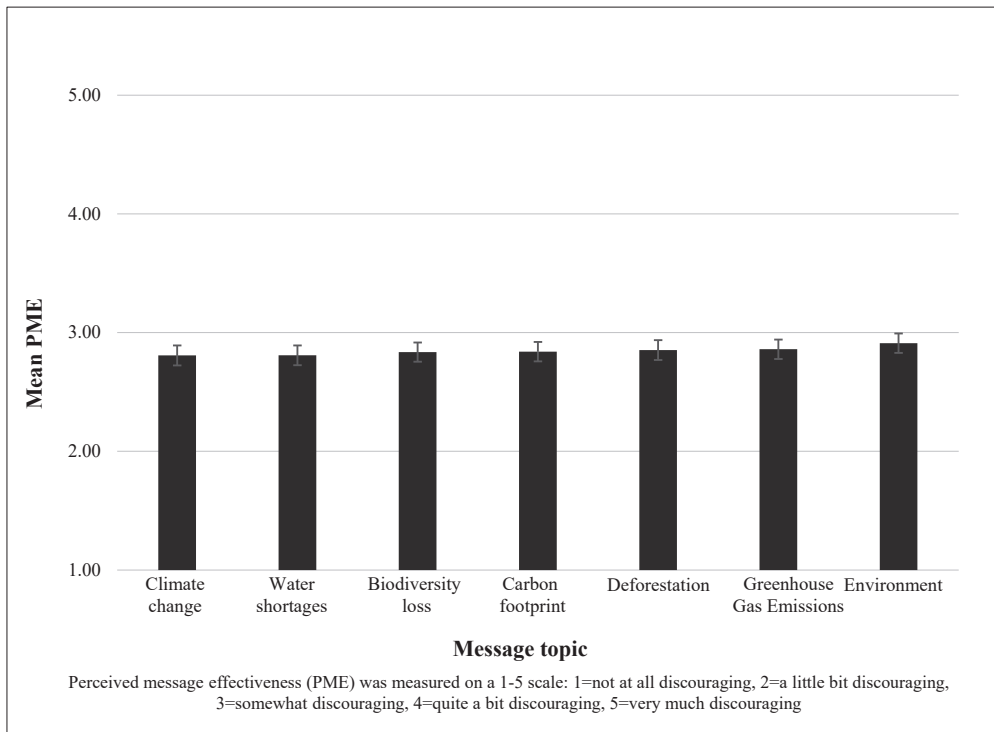


**Figure 2.** Perceived Message Effectiveness by Message Topic in an Online Study of U.S. Adults ( $n = 1078$ ).

3.3. Demographic Predictors of PME

The results of the OLS regression of average PME (averaged over the seven questions) on demographic characteristics are presented in Table 3.

Messages elicited lower PME among participants aged 40 years and older compared to participants aged 18–29 ( $b = -0.10, p < 0.05$ ). Messages also elicited lower PME among participants who consumed beef more than once a week compared to those who consumed beef once a week or less ( $b = -0.10, p < 0.01$ ). Participants who had completed more than a high school degree had higher PME ratings than participants who had completed high school or less ( $b = 0.10, p < 0.01$ ). Messages also elicited higher PME among Latino participants compared to non-Latino participants ( $b = 0.09, p < 0.01$ ).

**Table 3.** Results of Ordinary Least Squares Regression of Perceived Message Effectiveness on Demographic Covariates in an Online Study of U.S. Adults ( $n = 1078$ ).

	Coefficient	p Value	95% CI	Standardized Coefficient
Aged over 39 (vs. between 18 and 29)	-0.28 *	0.013	-0.49, -0.06	-0.10
Aged between 30 and 39 (vs. between 18 and 29)	-0.06	0.507	-0.25, 0.12	-0.03
Eats beef more than once a week (vs. once a week or less)	-0.26 ***	0.001	-0.41, -0.11	-0.10
More than high school (vs. high school or less)	0.24 **	0.005	0.08, 0.41	0.10
Latino ethnicity (vs. non Latino ethnicity)	0.21 **	0.005	0.07, 0.36	0.09
Male (vs. female) †	0.06	0.455	-0.10, 0.21	0.02
Income between \$35,000 and \$74,999 (vs. less than \$35,000)	-0.02	0.842	-0.20, 0.17	-0.01
Income of \$75,000 or more (vs. less than \$35,000)	0.19	0.068	-0.01, 0.40	0.07

\*  $p < 0.05$ , \*\*  $p < 0.01$ , \*\*\*  $p < 0.001$ . † We do not report the coefficient for transgender (relative to female, the reference gender category) due to small cell size ( $n = 5$ ).



#### 4. Discussion

This study adds to the limited literature on environmental messages aimed at reducing beef consumption. This study found no statistically significant differences in PME between messages that highlighted the worsening or reduction of environmental harms. However, the pattern of results suggested that PME tended to be higher for messages that focused on worsening environmental harms compared to reducing environmental harms, although these differences were small. The exception was the message that emphasized that purchasing beef can “hurt the environment,” which elicited greater PME than the message emphasizing that purchasing less beef can “help the environment.” The message topic that elicited the strongest response from participants was the one that included the ‘environment’ topic and messages overall elicited the highest PMEs among participants that were Latino, less than 30 years old, ate beef once a week or less, and had a college or advanced degree.

The finding that the message frames describing either the worsening or reduction of environmental harms were equally discouraging is in contrast to existing research that has explored the impacts of goal framing in environmental messages. In a systematic review of 61 studies that investigated the use of goal framing to promote pro-environmental behaviors and attitudes, only 6 found that the effect of emphasizing negative or positive outcomes did not differ, whereas 30 studies found that emphasizing negative outcomes was more effective and 18 studies found that emphasizing positive outcomes was more effective [52]. Numerous other studies have also found that either highlighting positive consequences [53–55,74] or negative consequences [75,76] of a decision is more effective at promoting participation in environmentally friendly behaviors. Differences in the message content could help explain the contrast in findings, this being the first study to explore goal framing to discourage beef purchases specifically. Overall, the result that the two message frames equally discouraged beef purchasing across most topics suggests that multiple framing strategies may be effective for campaigns and other initiatives aimed at generating awareness about the environmental harms of red meat.

The message that included the ‘environment’ topic elicited greater discouragement than all other topic but ‘greenhouse gas emissions’ although the difference was small in magnitude. These findings suggest that employing a more general, straightforward term like ‘the environment’ is more persuasive for people who are less familiar with specific environmental harms like deforestation and water shortages. Further, the ‘environment’ is an overarching term that encompasses the specific harms. Thus, it may seem more important or salient to consumers compared to more specific harms.

The interaction of framing (reducing harms and worsening harms) with topic was driven by differences in framing with the ‘environment’ message topic. This topic had higher PME ratings when the message focused on the worsening of environmental harms as opposed to the reduction of environmental harms. This result is consistent with environmental communications research which has found that highlighting negative outcomes is more effective at promoting participation in pro-climate behaviors than highlighting positive outcomes [52] and supports the notion of a negativity bias wherein individuals dislike losses more than equivalent gains [49–51]. This finding is also consistent with SSB research, which has generally found that messages emphasizing the negative consequences (e.g., graphic warning labels) of SSB consumption are more effective than health-promoting logos at getting consumers to select lower sugar products [77–79]. We did not see this pattern among any other message topic besides the environment. Given that the awareness of environmental harms of red meat is low [62,80], the lack of variation in PME ratings across framing conditions for the other environmental topics could be due to participants having less baseline knowledge about those specific environmental harms, whereas helping or hurting the environment was easier to understand and interpret across frames. Future research should further explore the use of the term “environment” in messages aimed at reducing red meat purchasing and consumption.

This experiment is the first that has tested the differences between Latino adults and non-Latino adults in messages related to reducing beef purchasing. Considering U.S. Latino populations consume the highest level of unprocessed red meat [81] compared to other ethnic groups, this demographic is important to assess. The finding that Latino adults rated messages as more discouraging compared to non-Latino adults is consistent with other research about Latino adults and the environment in general: Latino adults in the U.S. are more likely than non-Latino white adults to believe climate change is a problem that is human caused [82,83] and personally affecting them [82–86]. Considering a recent report found that individuals that were convinced global warming is happening, human caused, and an urgent threat were more willing to adopt a more plant-based diet [80], it is possible that Latino participants in our sample were more discouraged from buying red meat because of their stronger pro-environmental views and belief in human-caused climate change. Qualitative research could help further elucidate these relationships.

Our other findings examining the association between sociodemographic characteristics and PME ratings of the messages were consistent with previous literature. For example, the finding that participants below 30 years of age had higher PME ratings on average is consistent with research that has found that young people are more likely to know about the environmental harms of meat [87] and to eat less meat for environmental reasons [88]. People aged between 41 and 60, in contrast, are more likely to reduce meat consumption because of health concerns [88], suggesting that they may be less persuaded by environmental arguments to purchase less meat.

The result that participants that eat beef once a week or less were more discouraged by the messages compared to more regular beef consumers is consistent with prior research that has found that more frequent meat-eaters are less willing to reduce their meat consumption [56–58]. This finding also builds on research showing that reactance or resistance to persuasive messages may be more pronounced among those with higher engagement with the target behavior [89]. This difference could be due to more regular meat-eaters' greater preference for meat [90], enjoyment of meat [91], or belief that eating meat is a natural and normal human behavior [91]. This finding also supports the notion of a 'meat paradox,' wherein more regular meat-eaters resist information about the harms of meat consumption because they are in conflict to their values or behavior [91,92]. Regular beef-eaters in our sample may have minimized the potential benefits of purchasing less beef instead of accepting personal responsibility, lowering PME. Belief that consuming meat is necessary for maintaining good health has also been identified as a persistent barrier for meat reduction among individuals from the U.S. and U.K. [91,93,94] despite research showing that balanced vegetarian diets are nutritionally adequate and healthful [95] and research documenting the significant health benefits that can result from adhering to diets higher in plant-based foods and lower in animal-based foods [96]. Red meat can also be culturally symbolic, representing strength and masculinity [97]. Combined, these factors may amplify resistance among frequent meat-eaters to purchase less meat.

Participants who had completed more than a high school degree had higher PME ratings than participants who had completed high school or less. Few studies have explored the effect of education on willingness to reduce meat purchases or consumption. Our findings are consistent with a nationally representative Dutch study that found that as education level increased, participants were more willing to eat meatless meals [97]. This finding complements other research that has found that having greater awareness of the environmental toll of meat increases willingness to eat less meat [62]. It may be that participants in our study with a higher education level were more discouraged from buying beef due to their greater knowledge of meat's environmental harms. However, we did not assess this knowledge of harms in our study. This relationship warrants further exploration.

Despite sizable research that has indicated that being female is a predictor of willingness to eat less meat [62], we observed no relationship between gender and PME in our study. Income level also had no effect on participants' PME ratings.

Strengths of this study include that it was the first study to our knowledge to experimentally test perceived effectiveness of different environmental messages aimed at reducing red meat consumption and that it involved a large sample of U.S. adults. Additionally, the sample was approximately half Latino, which allowed a large enough sample to explore the association between Latino ethnicity and responsiveness to environmentally themed messages to reduce meat purchases.

Limitations of this study include that the messages were displayed and assessed in an online survey, and as such consumption and behavioral outcomes were not assessed. Moreover, the design, while allowing us to compare two types of goal frames, precluded the ability to compare messages to a control. We also did not evaluate participants' engagement level in other pro-environmental behaviors or emotional responses to the messages, both of which have been shown to influence which goal frame is more impactful at promoting pro-environmental behaviors [48,49] and could have helped explain why both goal frames performed similarly in this study. Finally, we did not assess participants' baseline views on or knowledge of meat consumption and its effect on the environment, which would have helped to better contextualize the PME ratings overall. Future research should examine these types of messages in more detail (e.g., using qualitative methods) and test how they affect consumers' purchases of red meat in real-world settings.

## 5. Conclusions

Reducing beef consumption in the U.S. is critical for promoting human and planetary health. This study is one of the first that has explored the impact of goal or emphasis framing on messages aimed at reducing red meat consumption. We found that messages emphasizing that purchasing less beef *reduces* environmental harms performed similarly to messages emphasizing that purchasing beef *worsens* environmental harms. There were few differences between specific environmental topics (e.g., water shortages and greenhouse gas emissions), though the message focusing on 'the environment' at large elicited the greatest response from survey participants overall and seems promising for future messaging studies. To build on this finding, additional research should assess whether the term 'environment' is more familiar or understandable to consumers than more specific environmental harms. We also recommend directly testing the effectiveness of emphasis frames spanning across multiple topics (e.g., health and environment) to determine which frame overall is best at discouraging red meat consumption.

Populations that were over 39 years old, ate beef more than once a week, had a high school education or less, and were non-Latino were less responsive to the messages overall. Collectively, these findings suggest that to maximize the effectiveness of messages to reduce red meat consumption, employing different messaging tactics for different demographics may be a winning strategy. To assess this, future research should test the effectiveness of these messages across other subpopulations and explore how these messages affect consumers' purchases of red meat in real-world settings.

**Author Contributions:** A.W. led the conceptualization and design of this study with support from L.S.T. and M.G.H.; A.W. led initial manuscript preparation with support and contribution from L.S.T. and M.G.H.; M.B. led data analysis and contributed to manuscript preparation; L.S.T. and M.G.H. oversaw data collection and provided feedback and editing on drafts. All authors have read and agreed to the published version of the manuscript.

**Funding:** This work was funded through a grant from the Wellcome Trust, grant id # 216042/Z/19/Z. Grant # K01HL147713 from the National Heart, Lung, and Blood Institute of the NIH supported M.G.H.'s time on this paper. The content is solely the responsibility of the authors and does not necessarily represent the official views of the NIH. We are grateful to the Carolina Population Center and its NIH Center grant (P2C HD050924) for general support. The survey data used in this study were supported by a grant from Healthy Eating Research, a national program of the Robert Wood Johnson Foundation. The views expressed here do not necessarily reflect the views of the Foundation.

**Institutional Review Board Statement:** This study was conducted in accordance with the Declaration of Helsinki, and all procedures involving study participants were approved by the University of North Carolina Institutional Review Board (IRB #19-0277).

**Informed Consent Statement:** Informed consent was obtained from all subjects involved in this study; after reading an online consent form, participants consented prior to starting the survey by clicking an agreement button at its beginning.

**Data Availability Statement:** Data will be shared upon request; those requesting access will be added to the UNC IRB before receiving data.

**Acknowledgments:** The authors thank Isabella Higgins for her logistical support in this study. The authors also thank Christina Chauvenet her for contributions.

**Conflicts of Interest:** The authors declare no conflict of interest.

## References

1. Willett, W.; Rockström, J.; Loken, B.; Springmann, M.; Lang, T.; Vermeulen, S.; Garnett, T.; Tilman, D.; DeClerck, F.; Wood, A.; et al. Food in the Anthropocene: The EAT-Lancet Commission on healthy diets from sustainable food systems. *Lancet* **2019**, *393*, 447–492. [CrossRef]
2. Carr, P.; Walter, V.; Brenner, H.; Hoffmeister, M. Meat subtypes and their association with colorectal cancer: Systematic review and meta-analysis. *Int. J. Cancer* **2016**, *138*, 293–302. [CrossRef] [PubMed]
3. Sandhu, M.S.; White, I.R.; McPherson, K. Systematic Review of the Prospective Cohort Studies on Meat Consumption and Colorectal Cancer Risk: A Meta-Analytical Approach. *Cancer Epidemiol. Biomark. Prev.* **2001**, *10*, 439–446.
4. Collins, K. Reducing Colorectal Cancer Risk by Cutting Red Meat. American Institute for Cancer Research. 2019. Available online: <https://www.aicr.org/resources/blog/reducing-colorectal-cancer-risk-by-cutting-red-meat/> (accessed on 5 March 2020).
5. Aune, D.; Ursin, G.; Veierød, M.B. Meat consumption and the risk of type 2 diabetes: A systematic review and meta-analysis of cohort studies. *Diabetologia* **2009**, *52*, 2277–2287. [CrossRef] [PubMed]
6. Bechthold, A.; Boeing, H.; Schwedhelm, C.; Hoffmann, G.; Knüppel, S.; Iqbal, K.; De Henauw, S.; Michels, N.; Devleeschauwer, B.; Schlesinger, S.; et al. Food groups and risk of coronary heart disease, stroke and heart failure: A systematic review and dose-response meta-analysis of prospective studies. *Crit. Rev. Food Sci. Nutr.* **2019**, *59*, 1071–1090. [CrossRef] [PubMed]
7. Rouhani, M.H.; Salehi-Abargouei, A.; Surkan, P.J.; Azadbakht, L.J.O.R. Is there a relationship between red or processed meat intake and obesity? A systematic review and meta-analysis of observational studies. *Obes. Rev.* **2014**, *15*, 740–748. [CrossRef] [PubMed]
8. Larsson, S.C.; Orsini, N. Red Meat and Processed Meat Consumption and All-Cause Mortality: A Meta-Analysis. *Am. J. Epidemiol.* **2014**, *179*, 282–289. [CrossRef]
9. Etemadi, A.; Sinha, R.; Ward, M.H.; Graubard, B.I.; Inoue-Choi, M.; Dawsey, S.M.; Abnet, C.C. Mortality from Different Causes Associated with Meat, Heme Iron, Nitrates, and Nitrites in the NIH-AARP Diet and Health Study: Population Based Cohort Study. *BMJ* **2017**, *357*, j1957. [CrossRef]
10. Rock, C.L.; Thomson, C.; Gansler, T.; Gapstur, S.M.; McCullough, M.L.; Patel, A.V.; Bandrews, K.S.; Bandera, E.V.; Spees, C.K.; Robien, K.; et al. American Cancer Society guideline for diet and physical activity for cancer prevention. *CA A Cancer J. Clin.* **2020**, *70*, 245–271. [CrossRef]
11. American Diabetes Association. Protein. Available online: <https://www.diabetes.org/healthy-living/recipes-nutrition/eating-well/protein> (accessed on 12 December 2020).
12. Pan, A.; Sun, Q.; Bernstein, A.M.; Schulze, M.B.; E Manson, J.; Willett, W.C.; Hu, F.B. Red meat consumption and risk of type 2 diabetes: 3 cohorts of US adults and an updated meta-analysis. *Am. J. Clin. Nutr.* **2011**, *94*, 1088–1096. [CrossRef]
13. Ibsen, D.B.; Steur, M.; Imamura, F. Replacement of Red and Processed Meat With Other Food Sources of Protein and the Risk of Type 2 Diabetes in European Populations: The EPIC-InterAct Study. *Diabetes Care* **2020**, *43*, 2660–2667. [CrossRef] [PubMed]
14. Harvard Health. Cutting Red Meat for a Longer Life. 2012. Available online: <https://www.health.harvard.edu/staying-healthy/cutting-red-meat-for-a-longer-life> (accessed on 15 December 2020).
15. Fadnes, L.T.; Økland, J.-M.; Haaland, A.; Johansson, K.A. Estimating impact of food choices on life expectancy: A modeling study. *PLOS Med.* **2022**, *19*, e1003889. [CrossRef] [PubMed]
16. Gerber, P.J.; Steinfeld, H.; Henderson, B. *Tackling Climate Change Through Livestock: A Global Assessment of Emissions and Mitigation Opportunities*; Food and Agriculture Organization of the United Nations: Rome, Italy, 2013.
17. Godfray, H.C.J.; Aveyard, P.; Garnett, T. Meat consumption, health, and the environment. *Science* **2018**, *361*, eaam5324. [CrossRef]
18. Steinfeld, H.; Gerber, P.; Wassenaar, T.; Castel, V.; Rosales, M.; de Haan, C. *Livestock's Long Shadow: Environmental Issues and Options*; Food and Agriculture Organization of the United Nations: Rome, Italy, 2006.
19. Machovina, B.; Feeley, K.J.; Ripple, W.J. Biodiversity conservation: The key is reducing meat consumption. *Sci. Total Environ.* **2015**, *536*, 419–431. [CrossRef] [PubMed]
20. Beznier-Kerr, R.; McGuire, K.L.; Nigh, R.; Rocheleau, D.; Soluri, J.; Perfecto, I.; Hemming, D. Effects of industrial agriculture on climate change and the mitigation potential of small-scale agro-ecological farms. *CAB Rev.* **2011**, *6*, 1–18.

21. Asner, G. Measuring Carbon Emissions from Tropical Deforestation: An Overview. Environmental Defense Fund. 2009. Available online: [https://www.edf.org/sites/default/files/10333\\_Measuring\\_Carbon\\_Emissions\\_from\\_Tropical\\_Deforestation-An\\_Overview.pdf](https://www.edf.org/sites/default/files/10333_Measuring_Carbon_Emissions_from_Tropical_Deforestation-An_Overview.pdf) (accessed on 12 February 2020).
22. Chai, B.C.; van der Voort, J.R.; Grofelnik, K.; Eliasdottir, H.G.; Klöss, I.; Perez-Cueto, F.J. Which Diet Has the Least Environmental Impact on Our Planet? A Systematic Review of Vegan, Vegetarian and Omnivorous Diets. *Sustainability* **2019**, *11*, 4110. [CrossRef]
23. Poore, J.; Nemecek, T. Reducing food's environmental impacts through producers and consumers. *Science* **2018**, *360*, 987–992. [CrossRef]
24. Aiking, H.; de Boer, J. The next protein transition. *Trends Food Sci. Technol.* **2020**, *105*, 515–522. [CrossRef]
25. OECD Meat Consumption (Indicator). Available online: <https://data.oecd.org/agroutput/meat-consumption.htm> (accessed on 10 April 2020).
26. Searchinger, T.; Waite, R.; Hanson, C.; Ranganathan, J.; Dumas, P.; Matthews, E.; Klirs, C. *Creating a Sustainable Food Future: A Menu of 50 Solutions to Feed Nearly 10 Billion People by 2050*; World Resources Institute: Washington, DC, USA, 2019.
27. Ranganathan, J.; Vennard, D.; Waite, R.; Lipinski, B.; Searchinger, T.; Dumas, P. Shifting Diets for a Sustainable Food Future. 2016. Available online: <https://www.wri.org/research/shifting-diets-sustainable-food-future> (accessed on 27 January 2022).
28. Garnett, T. *Cooking Up a Storm: Food, Greenhouse Gas Emissions and our Changing Climate*; Center for Environmental Strategy, University of Surrey: Food Climate Research Network: Guildford, UK, 2008.
29. Eshel, G.; Shepon, A.; Makov, T.; Milo, R. Land, irrigation water, greenhouse gas, and reactive nitrogen burdens of meat, eggs, and dairy production in the United States. *Proc. Natl. Acad. Sci. USA* **2014**, *111*, 11996–12001. [CrossRef]
30. Shukla, P.R.; Skea, J.; Calvo Buendia, E.; Masson-Delmotte, V.; Pörtner, H.-O.; Roberts, D.C.; Zhai, P.; Slade, R.; Connors, S.; van Diemen, R.; et al. Summary for Policymakers. In *Climate Change and Land: An IPCC Special Report on Climate Change, Desertification, Land Degradation, Sustainable Land Management, Food Security, and Greenhouse Gas Fluxes in Terrestrial Ecosystems*; Intergovernmental Panel on Climate Change: Geneva, Switzerland, 2019.
31. Rockström, J.; Stordalen, G.A.; Horton, R. Acting in the Anthropocene: The EAT–Lancet Commission. *Lancet* **2016**, *38*, 2364–2365. [CrossRef]
32. McMichael, A.J.; Powles, J.W.; Butler, C.D.; Uauy, R. Food, livestock production, energy, climate change, and health. *Lancet* **2007**, *370*, 1253–1263. [CrossRef]
33. Hedenus, F.; Wirsenius, S.; Johansson, D.J.A. The importance of reduced meat and dairy consumption for meeting stringent climate change targets. *Clim. Chang.* **2014**, *124*, 79–91. [CrossRef]
34. Hallström, E.; Carlsson-Kanyama, A.; Börjesson, P. Environmental impact of dietary change: A systematic review. *J. Clean Prod.* **2015**, *91*, 1–11. [CrossRef]
35. Sun, Z.; Scherer, L.; Tukker, A.; Spawn-Lee, S.A.; Bruckner, M.; Gibbs, H.K.; Behrens, P. Dietary change in high-income nations alone can lead to substantial double climate dividend. *Nat. Food* **2022**, *3*, 29–37. [CrossRef]
36. EAT. EAT–Lancet Commission Brief for Everyone. Available online: <https://eatforum.org/lancet-commission/eatinghealthilyandsustainable/> (accessed on 25 January 2022).
37. Eisen, M.B.; Brown, P.O. Rapid global phaseout of animal agriculture has the potential to stabilize greenhouse gas levels for 30 years and offset 68 percent of CO<sub>2</sub> emissions this century. *PLoS Climate* **2020**, *1*, e0000010. [CrossRef]
38. Clark, M.A.; Domingo, N.G.; Colgan, K.; Thakrar, S.K.; Tilman, D.; Lynch, J.; Hill, J.D. Global food system emissions could preclude achieving the 1.5° and 2 °C climate change targets. *Science* **2020**, *370*, 705–708. [CrossRef]
39. Tilman, D.; Clark, M.; Williams, D.R.; Kimmel, K.; Polasky, S.; Packer, C. Future threats to biodiversity and pathways to their prevention. *Nature* **2017**, *546*, 73–81. [CrossRef]
40. Noar, S.M.; Hall, M.G.; Francis, D.B.; Ribisl, K.M.; Pepper, J.K.; Brewer, N.T. Pictorial cigarette pack warnings: A meta-analysis of experimental studies. *Tob. Control* **2016**, *25*, 341–354. [CrossRef]
41. Grummon, A.H.; Hall, M.G. Sugary drink warnings: A meta-analysis of experimental studies. *PLoS Med.* **2020**, *17*, e1003120. [CrossRef]
42. Clarke, N.; Pechey, E.; Kosıte, D.; König, L.M.; Mantzari, E.; Blackwell, A.K.; Marteau, T.; Hollands, G. Impact of health warning labels on selection and consumption of food and alcohol products: Systematic review with meta-analysis. *Health Psychol. Rev.* **2020**, *15*, 430–453. [CrossRef]
43. Leiserowitz, A.; Maibach, E.; Rosenthal, S.; Kotcher, J.; Bergquist, P.; Ballew, M.; Goldberg, M.; Gustafson, A.; Wang, X. *Climate Change in the American Mind: April 2020*; Yale University and George Mason University, Yale Program on Climate Change Communication: New Haven, CT, USA, 2020.
44. Ballew, M.; Marlon, J.; Kotcher, J.; Maibach, E.; Rosenthal, S.; Bergquist, P.; Leiserowitz, A. *Young Adults, Across Party Lines, Are More Willing to Take Climate Action*; Yale University and George Mason University, Yale Program on Climate Change Communication: New Haven, CT, USA, 2020.
45. Cordts, A.; Nitzko, S.; Spiller, A. Consumer Response to Negative Information on Meat Consumption in Germany. *Int. Food Agribus. Manag. Rev.* **2014**, *17*, 83–106.
46. Li, N.; Su, L.Y.F. Message Framing and Climate Change Communication: A Meta-Analytical Review. *J. Appl. Commun.* **2018**. [CrossRef]
47. Nisbet, M.C. Communicating Climate Change: Why Frames Matter for Public Engagement. *Environ. Sci. Policy* **2009**, *51*, 12–23. [CrossRef]

48. Van de Velde, L.; Verbeke, W.; Popp, M.; Van Huylenbroeck, G. The importance of message framing for providing information about sustainability and environmental aspects of energy. *Energy Policy* **2010**, *38*, 5541–5549. [CrossRef]
49. Cheng, T.; Woon, D.K.; Lynes, J.K. The Use of Message Framing in the Promotion of Environmentally Sustainable Behaviors. *Soc. Mar. Q.* **2011**, *17*, 48–62. [CrossRef]
50. Kahneman, D.D.; Tversky, A. Prospect Theory: An Analysis of Decision under Risk. *Econometrica* **1979**, *47*, 263–291. [CrossRef]
51. Meyerowitz, B.E.; Chaiken, S. The effect of message framing on breast self-examination attitudes, intentions, and behavior. *J. Pers. Soc. Psychol.* **1987**, *52*, 500–510. [CrossRef]
52. Homar, A.R.; Cvelbar, L.K. The effects of framing on environmental decisions: A systematic literature review. *Ecol. Econ.* **2021**, *183*, 106950. [CrossRef]
53. Hurlstone, M.J.; Lewandowsky, S.; Newell, B.; Sewell, B. The Effect of Framing and Normative Messages in Building Support for Climate Policies. *PLoS ONE* **2014**, *9*, e114335. [CrossRef]
54. Mir, H.M.; Behrang, K.; Isaai, M.T.; Nejat, P. The impact of outcome framing and psychological distance of air pollution consequences on transportation mode choice. *Transp. Res. Part D Transp. Environ.* **2016**, *46*, 328–338. [CrossRef]
55. Spence, A.; Pidgeon, N. Framing and communicating climate change: The effects of distance and outcome frame manipulations. *Glob. Environ. Chang.* **2010**, *20*, 656–667. [CrossRef]
56. De Boer, J.; de Witt, A.; Aiking, H. Help the climate, change your diet: A cross-sectional study on how to involve consumers in a transition to a low-carbon society. *Appetite* **2016**, *98*, 19–27. [CrossRef] [PubMed]
57. De Boer, J.; Schösler, H.; Aiking, H. “Meatless days” or “less but better”? Exploring strategies to adapt Western meat consumption to health and sustainability challenges. *Appetite* **2014**, *76*, 120–128. [CrossRef] [PubMed]
58. De Groeve, B.; Bleys, B. Less Meat Initiatives at Ghent University: Assessing the Support among Students and How to Increase It. *Sustainability* **2017**, *9*, 1550. [CrossRef]
59. Schösler, H.; de Boer, J.; Boersema, J.J.; Aiking, H. Meat and masculinity among young Chinese, Turkish and Dutch adults in the Netherlands. *Appetite* **2015**, *89*, 152–159. [CrossRef]
60. Tobler, C.; Visschers, V.H.M.; Siegrist, M. Eating green. Consumers’ willingness to adopt ecological food consumption behaviors. *Appetite* **2011**, *57*, 674–682. [CrossRef]
61. Verain, M.C.D.; Dagevos, H.; Antonides, G. Sustainable food consumption. Product choice or curtailment? *Appetite* **2015**, *91*, 375–384. [CrossRef]
62. Sanchez-Sabate, R.; Sabaté, J. Consumer Attitudes Towards Environmental Concerns of Meat Consumption: A Systematic Review. *Int. J. Environ. Res. Public Health* **2019**, *16*, 1220. [CrossRef]
63. Baig, S.A.; Noar, S.M.; Gottfredson, N.C.; Lazard, A.J.; Ribisl, K.M.; Brewer, N.T. Incremental criterion validity of message perceptions and effects perceptions in the context of anti-smoking messages. *J. Behav. Med.* **2021**, *44*, 74–83. [CrossRef]
64. Grummon, A.H.; Hall, M.G.; Taillie, L.S.; Brewer, N.T. How should sugar-sweetened beverage health warnings be designed? A randomized experiment. *Prev. Med.* **2019**, *121*, 158–166. [CrossRef]
65. Hall, M.G.; Lazard, A.J.; Grummon, A.H.; Higgins, I.C.; Bercholz, M.; Richter, A.P.C.; Taillie, L.S. Designing warnings for sugary drinks: A randomized experiment with Latino parents and non-Latino parents. *Prev. Med.* **2021**, *148*, 106562. [CrossRef]
66. Hall, M.G.; Grummon, A.H.; Lazard, A.J.; Maynard, O.M.; Taillie, L.S. Reactions to graphic and text health warnings for cigarettes, sugar-sweetened beverages, and alcohol: An online randomized experiment of US adults. *Prev. Med.* **2020**, *137*, 106120. [CrossRef] [PubMed]
67. Taillie, L.S.; Chauvenet, C.; Grummon, A.H.; Hall, M.G.; Waterlander, W.; Prestemon, C.E.; Jaacks, L.M. Testing front-of-package warnings to discourage red meat consumption: A randomized experiment with US meat consumers. *Int. J. Behav. Nutr. Phys. Act.* **2021**, *18*, 1–13. [CrossRef] [PubMed]
68. Taillie, L.S.; Hall, M.G.; Gómez, L.F.; Higgins, I.; Bercholz, M.; Murukutla, N.; Mora-Plazas, M. Designing an Effective Front-of-Package Warning Label for Food and Drinks High in Added Sugar, Sodium, or Saturated Fat in Colombia: An Online Experiment. *Nutrients* **2020**, *12*, 3124. [CrossRef] [PubMed]
69. Crump, M.J.C.; McDonnell, J.V.; Gureckis, T.M. Evaluating Amazon’s Mechanical Turk as a Tool for Experimental Behavioral Research. *PLoS ONE* **2013**, *8*, e54710. [CrossRef]
70. Pauszek, J.R.; Szybel, P.; Gibson, B.S. Evaluating Amazon’s Mechanical Turk for psychological research on the symbolic control of attention. *Behav. Res.* **2017**, *49*, 1969–1983. [CrossRef]
71. Centers for Disease Control and Prevention. *National Center for Health Statistics (2009–2010) National Health and Nutrition Dietary Screener Questionnaire*; U.S. Department of Health and Human Services, Centers for Disease Control and Prevention: Hyattsville, MD, USA, 2019. Available online: <https://epi.grants.cancer.gov/diet/shortreg/instruments/dsq-in-nhanes-09-10-interviewer-administered-english-version.pdf> (accessed on 4 August 2019).
72. Baig, S.A.; Noar, S.M.; Gottfredson, N.C.; Boynton, M.H.; Ribisl, K.M.; Brewer, N.T. UNC Perceived Message Effectiveness: Validation of a Brief Scale. *Ann. Behav. Med.* **2018**, *53*, 732–742. [CrossRef]
73. Noar, S.M.; Barker, J.; Bell, T.; Yzer, M. Does Perceived Message Effectiveness Predict the Actual Effectiveness of Tobacco Education Messages? A Systematic Review and Meta-Analysis. *Health Commun.* **2020**, *35*, 148–157. [CrossRef]
74. Kim, S.B.; Kim, D.Y. The Effects of Message Framing and Source Credibility on Green Messages in Hotels. *Cornell. Hosp. Q.* **2014**, *55*, 64–75. [CrossRef]

75. Davis, J.J. The Effects of Message Framing on Response to Environmental Communications. *J. Mass. Commun. Q.* **1995**, *72*, 285–299. [CrossRef]
76. Blose, J.E.; Mack, R.W.; Pitts, R.E. The Influence of Message Framing on Hotel Guests' Linen-Reuse Intentions. *Cornell. Hosp. Q.* **2015**, *56*, 145–154. [CrossRef]
77. De Alcantara, M.; Ares, G.; de Castro, I.P.L.; Deliza, R. Gain vs. loss-framing for reducing sugar consumption: Insights from a choice experiment with six product categories. *Food Res. Int.* **2020**, *136*, 109458. [CrossRef] [PubMed]
78. Rosenblatt, D.H.; Bode, S.; Dixon, H.; Murawski, C.; Summerell, P.; Ng, A.; Wakefield, M. Health warnings promote healthier dietary decision making: Effects of positive versus negative message framing and graphic versus text-based warnings. *Appetite* **2018**, *127*, 280–288. [CrossRef] [PubMed]
79. Vidal, G.; Machín, L.; Aschemann-Witzel, J.; Ares, G. Does message framing matter for promoting the use of nutritional warnings in decision making? *Public Health Nutr.* **2019**, *22*, 3025–3034. [CrossRef]
80. Leiserowitz, A.; Ballew, M.; Rosenthal, S. *Climate Change and the American Diet*; Yale University and Earth Day Network, Yale Program on Climate Change Communication: New Haven, CT, USA, 2020.
81. Zeng, L.; Ruan, M.; Liu, J.; Wilde, P.; Naumova, E.N.; Mozaffarian, D.; Zhang, F.F. Trends in Processed Meat, Unprocessed Red Meat, Poultry, and Fish Consumption in the United States, 1999–2016. *J. Acad. Nutr. Diet.* **2019**, *119*, 1085–1098. [CrossRef] [PubMed]
82. Ballew, M.T.; Goldberg, M.H.; Rosenthal, S.A.; Cutler, M.J.; Leiserowitz, A. Climate Change Activism Among Latino and White Americans. *Front. Commun.* **2019**, *3*, 375–384. [CrossRef]
83. Leiserowitz, A.; Cutler, M.; Rosenthal, S. *Climate Change in the Latino Mind*; Yale University, Yale Program on Climate Change Communication: New Haven, CT, USA, 2017.
84. The New York Times, Stanford University, Resources for the Future. Global Warming National Poll. 2015. Available online: <https://s3.amazonaws.com/s3.documentcloud.org/documents/1658128/global-warming-hispanics-poll.pdf> (accessed on 11 March 2020).
85. Environmental Defense Fund. Latinos Communities and Climate Change: Why we Care and What We Can Do. Available online: [https://www.edf.org/sites/default/files/content/latinos\\_and\\_climate\\_change\\_factsheet\\_0317\\_refresh.pdf](https://www.edf.org/sites/default/files/content/latinos_and_climate_change_factsheet_0317_refresh.pdf) (accessed on 10 March 2020).
86. Vargas, E.D. Latinos and Climate Change. Latino Decisions. 2020. Available online: <https://latinodecisions.com/wp-content/uploads/2020/02/CA-TX-LD-Poll-Final-Slide-Deck.pdf> (accessed on 10 March 2020).
87. Dibb, S.; Fitzpatrick, I. Let's Talk about Meat: Changing Dietary Behavior for the 21st Century. Eating Better. 2014. Available online: <https://www.eating-better.org/uploads/Documents/LetsTalkAboutMeat.pdf> (accessed on 9 February 2020).
88. Pribis, P.; Pencak, R.C.; Grajales, T. Beliefs and Attitudes toward Vegetarian Lifestyle across Generations. *Nutrients* **2010**, *2*, 523–531. [CrossRef] [PubMed]
89. Hall, M.G.; Sheeran, P.; Noar, S.M.; Ribisl, K.M.; Bach, L.E.; Brewer, N.T. Reactance to Health Warnings Scale: Development and Validation. *Ann. Behav. Med.* **2016**, *50*, 736–750. [CrossRef]
90. Graça, J.; Oliveira, A.; Calheiros, M.M. Meat, beyond the plate. Data-driven hypotheses for understanding consumer willingness to adopt a more plant-based diet. *Appetite* **2015**, *90*, 80–90. [CrossRef]
91. Piazza, J.; Ruby, M.B.; Loughnan, S.; Luong, M.; Kulik, J.; Watkins, H.M.; Seigerman, M. Rationalizing meat consumption. The 4Ns. *Appetite* **2015**, *91*, 114–128. [CrossRef] [PubMed]
92. Stoll-Kleemann, S.; Schmidt, U.J. Reducing meat consumption in developed and transition countries to counter climate change and biodiversity loss: A review of influence factors. *Reg. Environ. Change* **2017**, *17*, 1261–1277. [CrossRef]
93. Campbell, J.; Macdiarmid, J.I.; Douglas, F. Young people's perception of the environmental impact of food and their willingness to eat less meat for the sake of the environment: A qualitative study. *Proc. Nutr. Soc.* **2016**, *75*, E224. [CrossRef]
94. Macdiarmid, J.I.; Douglas, F.; Campbell, J. Eating like there's no tomorrow: Public awareness of the environmental impact of food and reluctance to eat less meat as part of a sustainable diet. *Appetite* **2016**, *96*, 487–493. [CrossRef] [PubMed]
95. Craig, W.J.; Mangels, A.R. Position of the American Dietetic Association: Vegetarian diets. *J. Am. Diet. Assoc.* **2009**, *109*, 1266–1282.
96. Kim, H.; Caulfield, L.E.; Garcia-Larsen, V.; Steffen, L.M.; Coresh, J.; Rebholz, C.M. Plant-Based Diets Are Associated With a Lower Risk of Incident Cardiovascular Disease, Cardiovascular Disease Mortality, and All-Cause Mortality in a General Population of Middle-Aged Adults. *J. Am. Heart Assoc.* **2019**, *8*, 16. [CrossRef]
97. De Boer, J.; Schösler, H.; Boersema, J.J. Climate change and meat eating: An inconvenient couple? *J. Environ. Psychol.* **2013**, *33*, 1–8. [CrossRef]

Article

# Comparison of the Energetic Efficiency of Gas Separation Technologies Using the Physical Optimum by the Example of Oxygen Supply Options

Samanta A. Weber <sup>1,\*</sup>, Dirk Volta <sup>1</sup> and Jürgen Kuck <sup>2</sup>

<sup>1</sup> Department of Energy and Biotechnology, Flensburg University of Applied Sciences (FUAS), 24943 Flensburg, Germany; dirk.volta@hs-flensburg.de

<sup>2</sup> Faculty of Utilities Supply Technology, Ostfalia University of Applied Sciences, 38302 Wolfenbüttel, Germany; j.kuck@ostfalia.de

\* Correspondence: samanta.weber@hs-flensburg.de

**Abstract:** This study applies the Physical Optimum (*PhO*) as a reference value to rate the efficiency of two technical options for the oxygen supply of a hospital. The systematic comparison of the alternative processes using the *PhO* as a benchmark for the minimum input (exergy in this case) required to run a process with a certain benefit allows to determine the potential for optimization of each technology. Differences are analyzed by visualizing the losses of each individual production step in a process as well as by the resulting overall energy demand, including the primary energy. Possible alternatives are purchasing liquid oxygen from a cryogenic process or the production by means of Pressure Swing Adsorption (PSA) on site. The cryogenic production shows a lower exergy demand even though it also has a higher potential for optimization. Yet, the total losses, significantly impacted by the unavoidable transportation, sum up, resulting in the conclusion that the PSA is the preferable option overall, considering energy aspects. Finally, additional criteria such as economic, legal, and structural consequences of the respective choices are briefly outlined.

**Keywords:** physical optimum; *PhO*; energy efficiency; gas separation; medical oxygen; exergy

**Citation:** Weber, S.A.; Volta, D.; Kuck, J. Comparison of the Energetic Efficiency of Gas Separation Technologies Using the Physical Optimum by the Example of Oxygen Supply Options. *Energies* **2022**, *15*, 1855. <https://doi.org/10.3390/en15051855>

Academic Editor: Roberto Alonso González Lezcano

Received: 10 January 2022

Accepted: 1 March 2022

Published: 2 March 2022

**Publisher's Note:** MDPI stays neutral with regard to jurisdictional claims in published maps and institutional affiliations.



**Copyright:** © 2022 by the authors. Licensee MDPI, Basel, Switzerland. This article is an open access article distributed under the terms and conditions of the Creative Commons Attribution (CC BY) license (<https://creativecommons.org/licenses/by/4.0/>).

## 1. Introduction

The Covid pandemic has recently set a public focus on the relevance of a reliable oxygen supply for medical purposes. Yet, while medical care must be guaranteed, clinics also have to operate economically. Efficiency measures are an option to reduce energy costs. This work aims at analyzing the technical strategy of producing the medical oxygen for a hospital currently in the planning phase in order to point out the more efficient option. Using the method of the Physical Optimum (*PhO*), saving potentials are outlined precisely referencing a theoretical ideal process to classify the efficiency of a real existing process.

Volta [1] gives the definition of the *PhO* in his dissertation for the first time. Keichel [2] edits the definition in his dissertation expanding particular aspects. The VDI 4663 [3] is mainly based on the findings of these works. Wenzel [4] compares the *PhO* to other methods for process evaluation such as the exergy method. Kerpen [5] analyzes differences between the *PhO* and the exergy evaluation pointing out the advantages of each method. Volta and Weber [6] additionally explain the integration of the state variable exergy into the evaluation with the *PhO*.

This study gives a practical example of the application of the *PhO*. Unlike other methods for process evaluation, the *PhO* distinguishes between avoidable and unavoidable losses. This study explains the relevance of this distinction. A general ultimate value for air separation is defined with the process independent  $PhO_{ind}$ . Furthermore, the *PhO* of a specific process, which includes further unavoidable losses in this case, enables the process evaluation. The study aims to outline the advantage of an ultimate reference value for the



evaluation of a process as well as the comparison of different technologies, respectively, processes with the same benefit.

## 2. Materials and Methods

The standard VDI 4663 [3] describes the purpose of the *PhO*. In the following section, this method is explained. Furthermore, information on the production of medical oxygen is provided.

### 2.1. The Physical Optimum

The *PhO* serves as a benchmark for processes. From thermodynamics, two kinds of efficiency are known: energy efficiency, also known as first law efficiency, and exergetic efficiency or second law efficiency. Energy efficiency is the ratio between the useful energy output of an energy conversion process and the energy input, while exergetic efficiency is the ratio between the useful exergy output and the exergy input. Exergy efficiency may only become unity in case of a completely reversible process.

The shortcomings of the concept of energy efficiency are well known: energy efficiency does not account for the value of the respective input and output energies, and therefore a simple heating boiler yields a higher energy efficiency than a sophisticated combined cycle power plant. On the other hand, exergetic efficiency of many processes have very poor values, suggesting high improvement potentials, which very often are simply impossible to realize with a given process.

In order to provide operational practitioners with a tool that gives them a realistic benchmark and to distinguish between unavoidable losses ( $U$ ) and avoidable losses ( $\Delta\Omega$ ), with respect to a given process, the *PhO* concept was developed. The *PhO* gives the ideal state of a given process, which does not have to be reversible in thermodynamic terms. To determine it, firstly, a process is chosen. Secondly, an ideal version of this process is defined, for thermal processes meaning in particular operation with temperature differences of zero within the process, wherever possible.

The differences from the exergetic efficiency are obvious: neither a combustion process, a common part of industrial processes, can ever be thermodynamically reversible, nor a heat-exchanger with different capacitance currents on both sides, even if it is operated in counterflow.

The well-known Betz factor in the use of wind energy may serve as another example. Both the energetic and the exergetic efficiency of a wind turbine are  $16/27$  in the best case, i.e., with a deceleration of the wind speed to  $1/3$  of the speed of the free inflow. The *PhO* factor, on the other hand, would be related to this value and could assume the value “one” for a completely loss-free turbine with swirl-free outflow.

The *PhO* is a calculated, theoretical value [3] 5. Two different processes can have different *PhOs*, even if the benefit is the same in both cases [3]. There are two different perspectives for the application of the *PhO*. In this case, the demand perspective was chosen because the output (the consumed amount of oxygen) is definite, while the consumption perspective focuses on a definite input. For the demand perspective ( $B$ ), the *PhO* factor can be calculated to estimate the efficiency of a process as given in Equation (1) [3]. No value smaller than one can be reached [3], so the closer the value is to one, the more efficient the process.

$$F_{PhO}^B = \frac{\text{real demand}}{\text{ideal demand}} \geq 1 \quad (1)$$

In the ideal case, the demand can be limited to the unavoidable losses  $U$ . In the real case, further losses  $\Delta\Omega$  cause a higher demand. Only the latter are the subject of process optimization.

The exception for which the efficiency gives the avoidable losses  $\Delta\Omega$  only, is a process with a limit value of 100% ( $\eta_{ideal} \rightarrow 1$ ), for which no unavoidable losses occur in the ideal case. For any case showing an ideal efficiency of less than one  $\eta_{ideal} < 1$  or even more than

one  $\eta_{ideal} > 1$  (e.g., heat pumps), the *PhO* gives a higher degree of detail concerning the losses, focusing  $\Delta\Omega$ .

Unlike other efficiency indicators, for the *PhO* the Equation (1) is generally valid. The result does not depend on the process. For example, Lucia and Grisolia [7] recently introduced the concept of the “unavailability percentage”. For this concept, the amount of energy not convertible into exergy is calculated. The smaller the value, the higher the efficiency [7]. However, a limit value is not considered. Therefore, one application could be highly efficient showing an unavailability percentage of 60% (e.g., wind turbines) while another shows a value of 1% (electric motor). The minimum value of the unavailability percentage could change with technical development. The approach is therefore more suitable for experts in the field, because the results need a skilled interpretation.

Another characteristic of the *PhO*, however, is the ultimate definition showing avoidable losses in a *PhO* factor exceeding the value of one for any application. The *PhO* is therefore a user-oriented method enabling a wide range of applicants to present their results to others, also laypersons, in an understandable way.

## 2.2. Application of the $PhO_{ind}$

This section introduces the ideal gas separation by reversible isothermal partial compression, which defines the minimum amount of energy necessary ( $PhO_{ind}$ ). In this study, the value for the  $PhO_{ind}$  is calculated as the process independent theoretical minimum needed to separate oxygen from air.

For energetic processes, the minimum demand often equals the minimum amount of exergy needed. In gas separation, the reversible isothermal partial compression of the components describes the ideal process causing the minimal demand of exergy [8] (p. 307). The amount of exergy that is calculated to separate the components equals the exergy of the pure components in relation to the mixture (both at ambient state). The principle of reversible isothermal partial compression as an ideal standard cycle for air separation is described below. The value of the  $PhO_{ind}$  is calculated for this application. Additionally, the utilization of the  $PhO_{ind}$  in general is explained using the example of the removal of  $CO_2$  from the atmosphere.

### 2.2.1. Energy Demand of Air Separation by Reversible Isothermal Partial Compression

Air shall be considered as consisting of  $r_{O_2} = 21\%$  oxygen and  $r_{N_2} = 79\%$  nitrogen (volume fraction). Ideal gas behavior is assumed, meaning that the partial pressure of each component equals the ambient pressure multiplied with this fraction. The database for the material properties is CoolProp [9]. To separate the mixture, the partial pressure of each component is increased by reversible isothermal compression until the partial pressure equals the ambient pressure. The input of specific work can be calculated according to Equation (2). The property values and results are given in Table 1. The product would be the components (pure oxygen and nitrogen only for this analysis) at ambient state.

$$w_{i,ith}^{rev} = h_2 - h_1 - T \times (s_2 - s_1) \quad (2)$$

**Table 1.** Property values and results of the rev. isothermal partial compression for oxygen generation at 293.15 K (Database: [9]).

Substance	State	$p_i$ In Pa	$s$ In J/(kg K)	$h$ In J/kg	$\rho$ In kg/m <sup>3</sup>	$w_{i,ith,i}^{rev}$ In J/kg <sub>i</sub>	$\zeta_i$ In kg <sub>i</sub> /kg <sub>air</sub>	$w_{i,ith,i,air}^{rev}$ In J/kg <sub>air</sub>
O <sub>2</sub>	1	21,278	6798	266,618	0.279	118,832	0.23	27,331
	2	101,325	6392	266,414				
N <sub>2</sub>	1	80,047	6888	304,110	0.920	20,505	0.77	15,789
	2	101,325	6818	304,060				
Air							1	43,120

Figure 1 shows the volume fraction of the components before and after reversible isothermal partial compression, as well as the resulting energy demand.

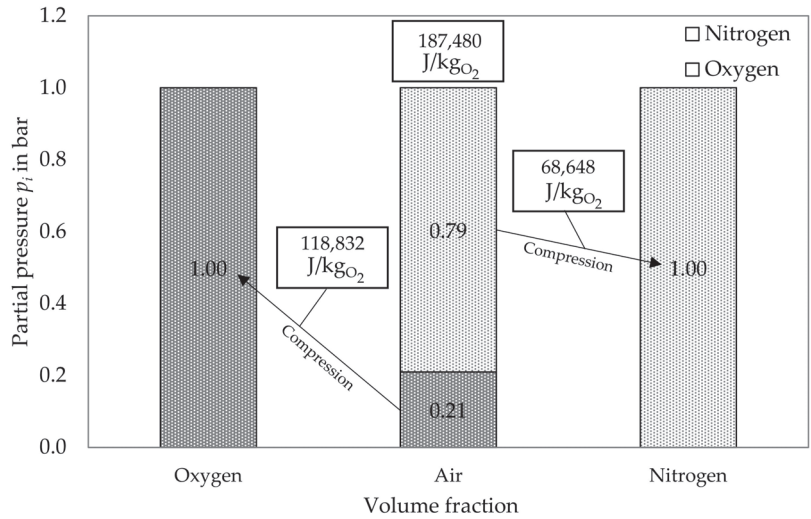


Figure 1. Reversible isothermal partial compression for air separation: energy consumption.

To produce one kilogram of oxygen, a higher amount of air, depending on  $\zeta_{O_2}$ , has to be separated, as given in Equation (3).

$$w_{i,ith,O_2}^{rev} = \frac{w_{i,ith,sum,air12}^{rev}}{\zeta_{O_2}} = \frac{w_{i,ith,sum,air12}^{rev} \frac{\rho_{O_2}}{\rho_{air}}}{\frac{\rho_{O_2}}{\rho_{O_2} + \rho_{N_2}}} = \frac{w_{i,ith,sum,air12}^{rev}}{\frac{\rho_{O_2}}{\rho_{O_2} + \rho_{N_2}}} = \frac{43,120 \frac{J}{kg_{air}}}{\frac{0.279 \frac{m^3}{m^3}}{(0.279+0.920) \frac{kg_{air}}{m^3}}} = \frac{43,120 \frac{J}{kg_{air}}}{0.23 \frac{kg_{O_2}}{kg_{air}}} = 187,480 \frac{J}{kg_{O_2}} \quad (3)$$

Further, taking into account the standard density ( $1.429 \text{ kg/m}^3_{n,O_2}$ ), the necessary amount of energy to produce one standard cubic meter of oxygen results in  $0.0744 \text{ kWh/m}^3_{n,O_2}$ , as shown in Equation (4).

$$w_{i,ith,O_2}^{rev} \times \rho_{n,O_2} = 187,480 \frac{J}{kg_{O_2}} \times 1.429 \frac{kg_{O_2}}{m^3_{n,O_2}} = 0.0744 \frac{kWh}{m^3_{n,O_2}} \quad (4)$$

The specific energy demand for oxygen generation with reversible isothermal partial compression over the initial partial pressure of the oxygen is given in Figure 2. The energy demand is significantly higher for lower concentrations of oxygen in the initial mixture. For a concentration of 100% oxygen, the demand logically equals zero. As an example, which could gain in importance in the future due to an increase in hydrogen production, the waste gas of electrolysis with a concentration of about 99.99% oxygen is illustrated. This method is not investigated any further in this study, because it has not yet been considered for the oxygen production for medical purposes.

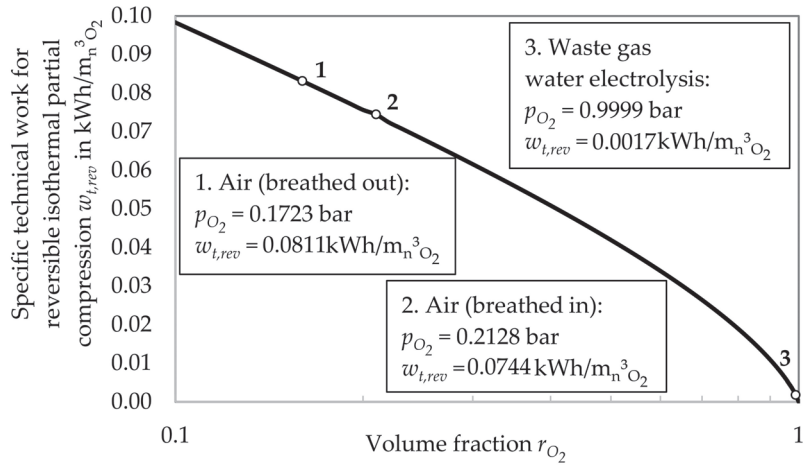


Figure 2. Energy demand for oxygen generation with rev. isothermal partial compression over  $r_{O_2}$ .

2.2.2. Process Evaluation with the  $PhO_{ind}$  by the Example of  $CO_2$  Removal

As explained, the  $PhO_{ind}$  is defined for a certain application scenario with a specific benefit. Apart from the function of the  $PhO_{ind}$  to compare different processes with the same benefit, the  $PhO_{ind}$  allows for a quick evaluation of any application based on the same principle. Another example for gas separation would be the technological approach to split off  $CO_2$  from the mixture in the atmosphere to reduce the  $CO_2$  content (so-called “negative emissions”). Table 2 lists the values for the  $CO_2$  removal from air in the same manner as for the oxygen production in Table 1. The concentration of  $CO_2$  in air is currently about  $r_{CO_2} = 400$  ppm [10].

Table 2. Property values and results of the reversible isothermal partial compression for  $CO_2$  removal at 293.15 K (Database: [9]).

Substance	State	$p_i$	$s$	$h$	$\rho$	$w_{t,ith,i}^{rev}$	$\zeta_i$	$w_{t,ith,i,air}^{rev}$
		In Pa	In J/(kg K)	In J/kg	In kg/m <sup>3</sup>	In J/kg <sub>i</sub>	In kg <sub>i</sub> /kg <sub>air</sub>	In J/kg <sub>air</sub>
CO <sub>2</sub>	1	41	4203	502,573	0.0007318	433,025	0.0607%	263
	2	101,325	2722	501,599				
Rest (Air)	1	101,284	3864	419,405	1.2040932	34	99.9393%	34
	2	101,325	3863	419,405				
Air							1.00	297

Again, the minimum amount of energy can be calculated as given in Equation (5).

$$\frac{w_{t,ith,air,sum12}^{rev}}{\zeta_{CO_2}} = \frac{297 \frac{J}{kg_{air}}}{0.000607 \frac{kg_{CO_2}}{kg_{air}}} = 0.1357 \frac{kWh}{kg_{CO_2}} \quad (5)$$

(with  $\rho_{n,CO_2} = 1.977 \frac{kg_{CO_2}}{m_n^3} \rightarrow 0.2682 \frac{kWh}{m_n^3}$ )

No value smaller than this can be reached in any process, neither real nor ideal, no matter which technology is chosen. The result allows to roughly evaluate the potential for an implementation of the technology in question. In Germany, 754,112 thousand tons of  $CO_2$  was emitted in 2018 [11]. This equals an amount of 102 TWh/a of exergy input, which would have been necessary to compensate the emission for the  $PhO_{ind}$ , for which no losses occur at all. As this is the model with the highest degree of idealization possible, the

real demand would highly exceed this value. In 2018, the electric energy consumption in Germany was 513 TWh [12] (p. 20). Thus, if the overall efficiency of the CO<sub>2</sub> separation and storage process was about 20%, the electric demand of Germany would already be doubled for this concept. To avoid further CO<sub>2</sub> emissions, the electric production would have to be based exclusively on renewable sources.

The approach is more realistic for an intake gas mixture with a higher concentration of CO<sub>2</sub>. Figure 3 shows the energy demand for CO<sub>2</sub> removal with reversible isothermal partial compression over the volume fraction  $r_{CO_2}$ . As realistic examples, the separation of CO<sub>2</sub> from exhaust gas of a natural gas combustion and of a wood pellet fired boiler both working with an air ratio  $\lambda$  of 1.5 are added. In both cases, as the gas would be cooled down to ambient temperature before separating the CO<sub>2</sub>, thus losing its water content due to condensation. Therefore, the remaining components are treated as dry air to simplify the calculation.

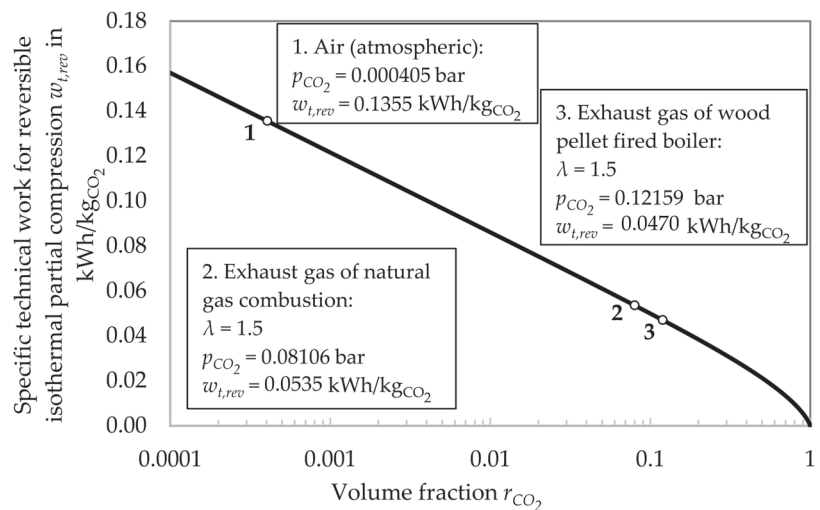


**Figure 3.** Energy demand for CO<sub>2</sub> removal with rev. isothermal partial compression over  $r_{CO_2}$ .

The example illustrates the application of the  $PhO_{ind}$ . By determining the minimum input, the feasibility of the method can be evaluated. To conclude, the  $PhO_{ind}$  is suitable for the evaluation of a technical application in general. The comparison of two processes with the same benefit is a special case of this approach.

### 2.3. Legal Requirements of Oxygen Production for Medical Purposes

“Pure oxygen” contains at least 99.5% of O<sub>2</sub> [13] (p. 466). Only cryogenic processes reach concentrations that high [13] (p. 466). Meanwhile the ‘Oxygenium 93 per centum’ (O<sub>2</sub> 93) has been registered in the European Pharmacopoeia. Using O<sub>2</sub> 93 as an alternative to O<sub>2</sub> 100 is possible [13] (p. 466). For O<sub>2</sub> 93, PSA continuously produces a product with a ratio of 90 to 96% oxygen [13] (p. 466). From a medical point of view, no objections have been raised against O<sub>2</sub> 93 [13] (p. 472). On the other hand, technical devices such as the calibration and measurement units would need to be modified. This results in the necessity of adjusting the operating license, as liability and responsibility are otherwise transferred to the operator, namely the hospital [13] (p. 470). On the technical side, these modifications are feasible [13] (p. 472). This work analyses the energetic aspects.

## 3. Results

In comparison to the  $PhO_{ind}$ , even under ideal conditions, the two methods in question for supplying the hospital show further unavoidable losses ( $PhO_{ind} + U = PhO$ ). Thus, the

$PhO$  for a specific process can differ from the ultimate theoretical minimum  $PhO_{ind}$ , in this case mainly because the final thermodynamic state of the oxygen varies between the different processes (liquid for the cryogenic process, gaseous, and pressurized after PSA). For each case, the ideal and real processes are analyzed in order to highlight the more efficient option. The  $PhO$  for a specific process gives the potential for optimization of this particular process, whereas the  $PhO_{ind}$  allows to compare two different processes (under ideal or real conditions) with the same benefit. The difference is explained by the examples for separation processes below.

### 3.1. Oxygen Extraction with Cryogenic Processes

The distillation of cryogenically liquefied gases enables the separation of gas components. Firstly, the  $PhO$  of liquefaction processes is described. The expense is the input exergy in form of electric energy per unit of produced oxygen. Secondly, a real plant is analyzed to compare the actual demand to the ideal process. The exergy of gaseous oxygen is the potential a pure gas ( $O_2$ ) shows in comparison to a mixture (air). When the oxygen is extracted in liquid state, additional exergy is stored in the liquefied gas due to a temperature below ambient state. Therefore, the input must be higher than for gaseous oxygen. In general, the cryogenic production is favorable for high production rates, while the less efficient methods like PSA are advantageous for lower demand [14] (pp. 123–124). Ebrahimi concludes that a cryogenic Air Separation Unit (in this case, the common two-column design) is economically feasible for an oxygen production rate of 9 kg/s, or higher [15] (p. 1316). For the regarded hospital, the average demand is about 0.004 kg/s. Thus, a cryogenic production on site is not feasible. Liquid oxygen is only an option if produced externally.

#### 3.1.1. Ideal Process of Oxygen Liquefaction (Definition of the $PhO_{cryo}$ )

Figure 4 shows the process for the ideal liquefaction of a real gas. In the cryogenic liquefaction machine, the aim is the removal of, firstly, sensible and, subsequently, latent heat from the gas in ambient state (state 1) leading to the complete liquefaction (state 3) [16] (p. 324).

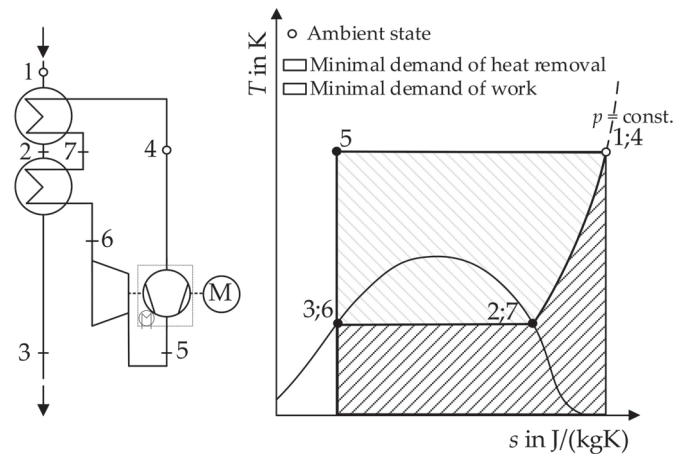


**Figure 4.** Flow chart and  $T$ - $s$ -diagram of the ideal gas liquefaction, emulated from [16] (p. 326).

The mass flow of the gas in the chiller cycle equals the outer mass flow of the gas intended to be liquefied [16] (p. 324). The compression (state 4 to state 5) is isothermal in the ideal case. The compressed gas subsequently passes the isentropic expansion machine, reaching the boiling point curve (state 6) on the same isobar as state 1. In two ideal heat-

exchangers, the heat transfer from the outer mass flow to the mass flow in the cycle results in the complete liquefaction of the outer flow (state 1, 2, and 3) while the gas in the cycle reaches ambient state again (state 6, 7, and 4) [16] (p. 324).

The minimal specific work necessary to run the process is the input for the compression reduced by the amount, which is recovered by the expansion machine. Furthermore, it has to be taken into account that  $h_3 = h_6$ ,  $h_1 = h_4$ , and  $s_5 = s_3$  [16] (p. 326), resulting in Equation (6).

$$w_{min,liqu} = w_{compression,ith} - |w_{expansion,isen}| = \frac{((h_5 - h_4) - T_1 \times (s_5 - s_4)) - (h_5 - h_6)}{(h_3 - h_1) - T_1 \times (s_3 - s_1)} = \tag{6}$$

Therefore, the minimum amount of work for the liquefaction depends on state 1 and state 3 [16] (p. 326) only and equals the amount of exergy of the liquefied oxygen in relation to pure oxygen at ambient state (state 1). Table 3 lists the state variables necessary for the calculation based on [9].

**Table 3.** State variables for oxygen liquefaction.

State	<i>h</i> in (J/kg)	<i>s</i> in (J/(kg K))	<i>T</i> in K	<i>p</i> in Pa
1 (amb.)	266,414	6392	293.15	101,325
3	−133,368	2942	90.19	101,325

The specific work for the liquefaction of one standard cubic meter of oxygen can be determined, resulting in 0.2433 kWh/m<sup>3</sup><sub>n,O<sub>2</sub></sub>. Summarizing, the production of liquid oxygen demands at least the sum of the work for the reversible isothermal partial compression and the subsequent liquefaction, adding up to the *PhO* of 0.3178 kWh/m<sup>3</sup><sub>n,O<sub>2</sub></sub> for this process. No cryogenic air separation site producing liquefied oxygen can reach lower values. Thus, this value is a reference to evaluate the efficiency of real processes. As mentioned before, the minimum energetic expense necessary equals the exergy of the product.

### 3.1.2. Energetic Analysis of the Cryogenic Oxygen Production

Generally, for the real demand of the production of gaseous oxygen, literature provides a value of 0.35 kWh/m<sup>3</sup><sub>n,O<sub>2</sub></sub> [17] (p. 63), [18] (p. 277), while the demand for liquid oxygen is estimated to be 0.86 kWh/m<sup>3</sup><sub>n,O<sub>2</sub></sub> [18] (p. 277). The data given by an exergetic analysis of an oxygen production plant, outlining the minimum necessary input as well as the losses of the production process [17] (p. 63), is used to evaluate the process in comparison to the *PhO* in Figure 5.

Firstly, only the production process of gaseous oxygen is analyzed. The *PhO<sub>ind</sub>* is shown on the right. To the left, the unavoidable losses of each step add up to the actual demand. The additional demand for the liquefaction in the physically optimal and real case follow. This leads to the conclusion, that the necessity of liquefying the oxygen for transportation causes nearly 60% of the energy demand. Additionally, the *PhO* factor, which outlines the overall efficiency, can be calculated as shown in Equation (7).

$$F_{PhO,cryo}^B = \frac{EE_{el}}{PhO_{cryo}} = \frac{EE_{el}}{PhO_{ind}+U} = \frac{0.86 \frac{kWh}{m^3_{n,O_2}}}{(0.07+0.24) \frac{kWh}{m^3_{n,O_2}}} = \frac{0.86 \frac{kWh}{m^3_{n,O_2}}}{0.31 \frac{kWh}{m^3_{n,O_2}}} = 2.77 \tag{7}$$

$$F_{PhO,cryo,ind}^B = \frac{EE_{el}}{PhO_{ind}} = \frac{0.86 \frac{kWh}{m^3_{n,O_2}}}{0.07 \frac{kWh}{m^3_{n,O_2}}} = 12.3$$

1. For the liquefied oxygen ( $F_{PhO,cryo}^B$ ), the *PhO* is the sum of the demand for separation and for liquefaction ( $PhO_{ind} + U = PhO_{cryo}$ ). The *PhO* factor puts the real demand of electric end energy ( $EE_{el}$ ) in relation to  $PhO_{cryo}$  and results in 2.77; and

- It is also possible to compare the overall demand  $EE_{el}$  to the  $PhO_{ind}$ , resulting in a  $PhO$  factor ( $F_{PhO,cryo,ind}^B$ ) of 12.3. So, over 12 times the amount of the ultimate optimum is consumed for the cryogenic production.

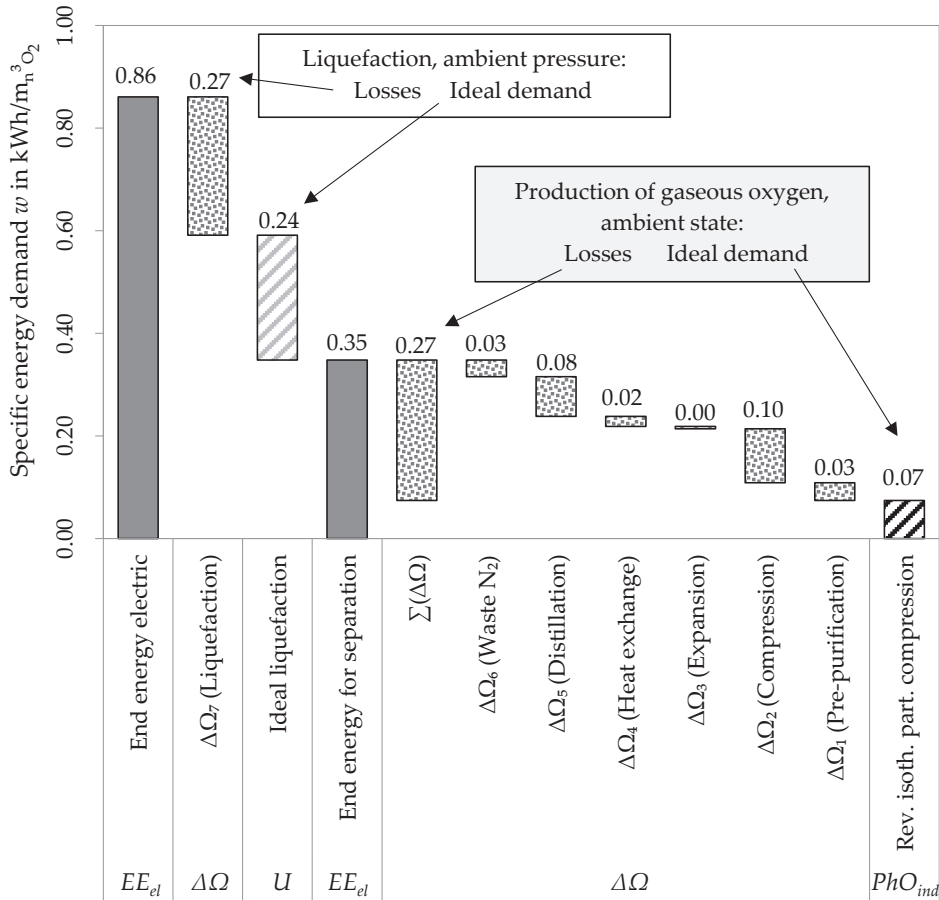


Figure 5. Evaluation of the cryogenic air separation process with the  $PhO$  method.

This example highlights the importance of defining the  $PhO$  in a suitable way. For the evaluation of a specific process, the  $PhO$  describes the efficiency. The value of 2.77 on the one hand gives the potential for optimization of the cryogenic liquefaction and separation process. This value can therefore function as the starting point for the optimization process. To determine effective efficiency measures, a detailed analysis of the losses with regard to their share of the overall losses should be done as given in Figure 5. The avoidable losses are highest for the liquefaction, compression, and distillation. These steps of the process should therefore be addressed first in the optimization process. Using the  $PhO$ , the conclusion can be drawn that the major part of the energy input for liquefaction is an unavoidable loss for this process. To lower this specific input, the process must be changed (see PSA as an option below). If this is impossible, the losses for this step must be accepted as a fixed with no potential for improvement. Therefore, the essential characteristic of the  $PhO$ , the distinction between avoidable and unavoidable losses, facilitates the optimization process and enables it to be strategically directed.



The value of 12.3 on the other hand gives the potential for optimization of any conceivable air separation process. The process independent  $PhO_{ind}$  is applicable, but does not necessarily (if  $PhO_{ind} \neq PhO$ ) outline the avoidable losses of a specific process. The  $PhO_{ind}$  is defined for a process with a specific benefit without giving further information on the technology. Thus, the  $PhO_{ind}$  is more general, yet it can be over-idealized to outline the avoidable losses only. In this case, if the process is evaluated using  $PhO_{ind}$ , losses, which are actually unavoidable for the given process, are indicated as avoidable ones. Nevertheless, the  $PhO_{ind}$  is suitable for process comparison as shown below.

Furthermore, the transport of the liquefied oxygen from the plant to the hospital is considered. Table 4 lists relevant values to calculate the energy input for the transportation taking the primary energy into account as well. For Diesel, properties of “ultra-light” heating oil are used. The exemplary hospital is sited in a remote area, so the distance is comparatively high. In this case, the end energy consumption for the transport almost equals the input for production.

**Table 4.** Relevant values of the transport of liquid oxygen to the hospital.

Quantity	Value and Unit
Distance to production site (real example)	548 km
Diesel consumption of lorry (assumption)	25 L Diesel/100 km (9.4 mpg)
Average scope of delivery	1822 m <sup>3</sup> <sub>n,O<sub>2</sub></sub> /transport
Gross calorific value Diesel [8] (p. 417)	45.9 MJ/kg
Density Diesel at 15 °C	845 kg/m <sup>3</sup>
End energy consumption transportation	0.8099 kWh/m <sup>3</sup> <sub>n,O<sub>2</sub></sub>
Primary energy factor Diesel (PE <sub>Diesel</sub> ) [19] (p. 9)	1.1
Primary energy consumption transportation	0.8909 kWh/m <sup>3</sup> <sub>n,O<sub>2</sub></sub>

Figure 6 shows the influence of the distance by a comparison of the primary and end energy consumption for the production and transport of the liquid oxygen as a function of the distance to the production site. The distance for which the amounts are equal is indicated in both cases. For electric energy in Germany, the primary energy factor is assumed to be 1.9 [19] (p. 9). Considering, that the lorry has to go both directions and that it is likely to be empty on the way back, the distances could be halved for a conservative analysis. The significance of the transport would be almost doubled (an empty lorry probably shows lower consumption). This aspect was not considered in the figure, but outlines the significance of PSA for the reduction of energy consumption.

### 3.2. Oxygen Generation with Pressure Swing Adsorption (PSA)

An alternative to the cryogenic extraction of oxygen is the application of Pressure Swing Adsorption (PSA). Firstly, the physical principles are briefly explained. Secondly, the physically optimal process is defined. A comparison to the real process follows.

Figure 7 illustrates the principle of the PSA. Adsorption isotherms for the equilibrium load an adsorbent can hold of a specific substance are plotted against the partial pressure of this substance [20] (p. 4). For a higher partial pressure, the amount, which can be adsorbed at a certain temperature, increases. The adsorption process therefore demands an increased pressure, the adsorption pressure  $p_A$  [20] (p. 4). The equilibrium load under these conditions is called adsorption load. To regenerate the adsorbent, the pressure is lowered to desorption pressure  $p_D$  [20] (p. 4). The load difference between adsorption and desorption equals the amount of substance which can be removed in every adsorption cycle [20] (p. 4).

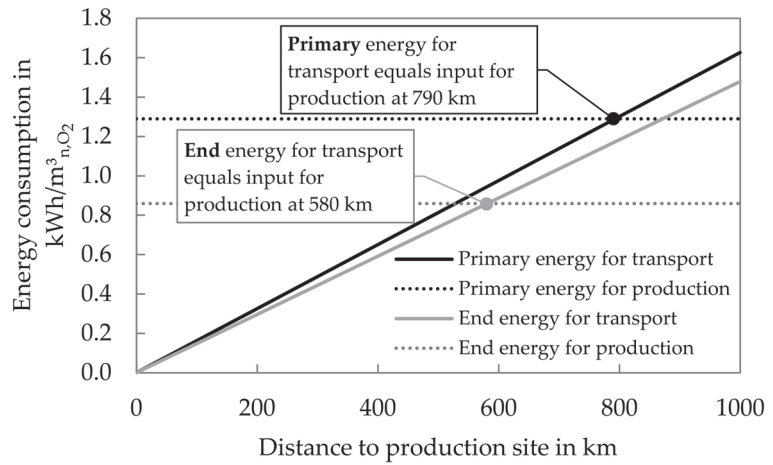


Figure 6. Comparison of energy consumption for transport and production of liquid O<sub>2</sub>.

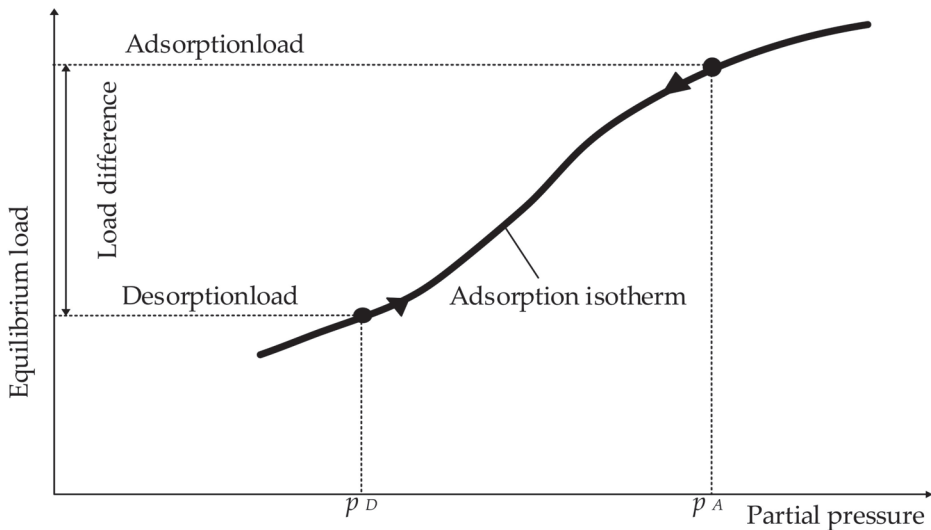


Figure 7. Adsorption and regeneration by pressure swing, emulated from [20] (p. 5).

### 3.2.1. Ideal Process of the PSA (Definition of the PhO<sub>PSA</sub>)

In hospitals, although a high product purity is vital, the mole fraction of the oxygen does not have to be 100% (see Section 2.3). For the ideal process no safety margin is necessary, so the fraction of 90% oxygen required by law is sufficient. Generally, the yield  $Y$ , given by the fraction of O<sub>2</sub> flow in the product and the feed O<sub>2</sub> flow as given in (8), determines the energetic efficiency of the process [21] (p. 126).

$$Y = \frac{\dot{n}_{O_2}^{Prod}}{\dot{n}_{O_2}^{Feed}} \quad (8)$$

With decreasing  $Y$ , the amount of air to be compressed increases, causing a higher demand of energy. An increased product purity is only achievable at the expense of a lower

$Y$ . The reason is mainly the increase of the recirculation of product for rinsing the adsorbent (rinsing losses,  $RL$ ) [21] (p. 121). Furthermore, the amount of product extracted when the pressure is lowered for desorption (pressure-relieving losses,  $PL$ ) lowers  $Y$  [21] (p. 126). As the regeneration of an adsorbent of limited capacity is unavoidable, these losses influence the determination of the  $PhO$ .  $PL$  and  $RL$  are defined by the amount of oxygen that is emitted unused to the environment during regeneration [21] (p. 126) in relation to the feed  $O_2$  flow as given in (9).

$$RL = \frac{\dot{n}_{O_2}^{-RL}}{\dot{n}_{O_2}^{-Feed}} \quad PL = \frac{\dot{n}_{O_2}^{-PL}}{\dot{n}_{O_2}^{-Feed}} \quad (9)$$

In this case,  $p_A$  is 6 bars. For the isothermal compression, the energy demand reaches its minimum and again equals the exergetic content of the compressed air. A study [21], analyzing the improvement of fuel cell efficiency by means of oxygen supply via air separation with PSA, determines an optimal process. For this,  $Y$  is given over the product purity as shown in Figure 8.

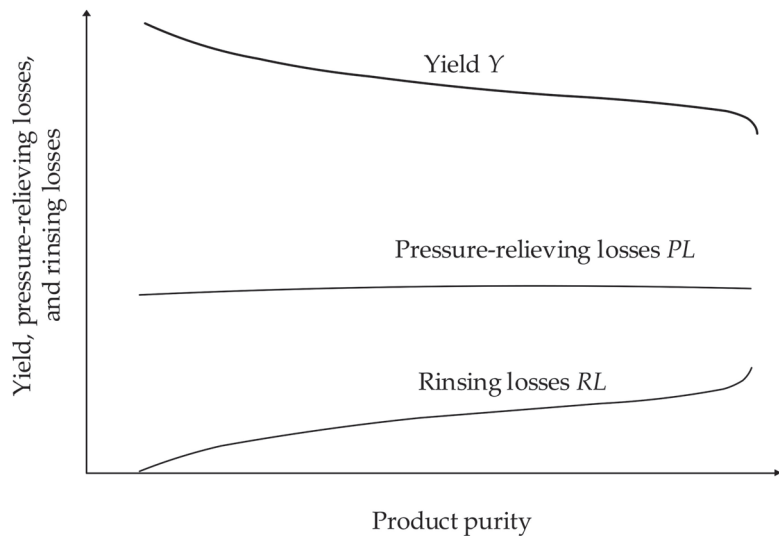


**Figure 8.** Qualitative development of  $Y$ ,  $PL$ , and  $RL$  over the product purity, emulated from [21] (p. 127).

Under ideal conditions, a  $Y$  of 60.3% is reached for a product purity of 90% [21] (p. 129). Table 5 contains the process conditions and results. The minimum input of energy, which is the  $PhO$  for the PSA process, results in  $0.4291 \text{ kWh/m}^3_{n,O_2}$ . The necessary expense of exergy exceeds the exergy in the product by the losses due to the limited  $Y$ .  $Y$  therefore represents an unavoidable exergetic loss equalling the exergy which exits the process with the loss flow of product. Therefore, in contrast to the ideal cryogenic process, the minimum exergy input exceeds the exergy content of the product.

**Table 5.** Process conditions and energy demand of the ideal Pressure Swing Adsorption.

Quantity	Value and Unit
Demand for isothermal compression of dry air (1 to 6 bar, 20 °C)	0.2587 kWh/m <sup>3</sup> <sub>n,O<sub>2</sub></sub>
Ideal yield (only $RL$ , $PL$ considered)	60.3%
Specific energy demand including $RL$ , $PL$	0.4291 kWh/m <sup>3</sup> <sub>n,O<sub>2</sub></sub>

### 3.2.2. Energetic Analysis of the Oxygen Production with PSA

As given in literature, applications for oxygen enrichment using PSA consume about  $0.9 \text{ kWh/m}_n^3\text{O}_2$  of electric energy [22] (p. 76). Establishing an exact model in order to simulate the PSA exceeds the aim of this work. Thus, the results of [21] are used for the evaluation, mainly focusing on the reasons for the losses, which are explained briefly.

In order to evaluate the effect of the losses, the impact on  $Y$  must be specified. If the total energy demand is defined, the additional demand caused by a specific loss can be calculated as given in (10) by the resulting decrease of  $Y$ .

$$w_{t,overall} = \frac{w_{t,ideal}}{Y_{overall}} \quad (10)$$

Reference is a purity of 90%. Firstly, the influence of limited kinetics, namely, the resistance against mass transfer, inhibits oxygen transportation [21] (p. 133). The study concludes that  $Y$  reaches 57% taking limited kinetics into account [21] (p. 135).

Secondly, as in every flow process, friction causes pressure losses. The decisive factor is the diameter of the pellets in the bulk material as well as the flow velocity [21] (p. 135). Considering the pressure losses for this application,  $Y$  reaches about 56% [21] (p. 135).

Thirdly, the reaction heat causes an increase of temperature for adsorption and a decrease for desorption processes [21] (p. 141). The heat transfer in the direction of flow causes a change in temperature in following layers before the load changes [21] (p. 143), lowering  $Y$  to 50% [21] (p. 145).

For the value of  $0.9 \text{ kWh/m}_n^3\text{O}_2$  [22] (p. 76), as stated in literature, the amount of energy for air compression and treatment can be calculated, accounting for the losses of this step in the process. In total, the  $PhO$  factor in relation to the reversible isothermal partial compression ( $F_{PhO,PSA,total}^B$ ) and in relation to the  $PhO$  of the PSA process ( $F_{PhO,PSA}^B$ ) can be determined as given in (11).

$$F_{PhO,PSA}^B = \frac{EE_{el}}{PhO_{PSA}} = \frac{0.9 \frac{\text{kWh}}{\text{m}_n^3\text{O}_2}}{0.4291 \frac{\text{kWh}}{\text{m}_n^3\text{O}_2}} = 2.09$$

$$F_{PhO,PSA,ind}^B = \frac{EE_{el}}{PhO_{ind}} = \frac{0.9 \frac{\text{kWh}}{\text{m}_n^3\text{O}_2}}{0.0744 \frac{\text{kWh}}{\text{m}_n^3\text{O}_2}} = 12.86 \quad (11)$$

Again, the  $PhO$  factor for the PSA describes the amount of avoidable losses for this specific process. The PSA shows less potential for optimization ( $F_{PhO,PSA}^B$ ) than the cryogenic process ( $F_{PhO,l}^B = 2.77$ ). It is closer to the ideal reference and, thus, the more efficient process.

Figure 9 shows the PSA process, including the  $PhO$  and  $PhO_{ind}$  as well as the occurring losses. In contrast to the cryogenic option, the hospital itself can intervene to carry out optimization measures. Whereas the PSA itself only accounts for a limited share of the avoidable losses, the compression significantly increases the energy demand. This, however, is a process step which can be influenced by the operator. For example, an improved cooling of the process would lead to a lower demand and can increase the exergetic benefit at the same time if a heat recovery is implemented. However, the input of  $0.26 \text{ kWh/m}_n^3\text{O}_2$  is a fixed value. No optimization measure can lower this input any further. After a reduction of the input, the new consumption should be compared to this value again. If the  $PhO$  factor for the compression approaches the value one, further measures are not purposeful any more. Again, the distinction between avoidable and unavoidable losses enables a more strategical orientation of the optimization measures.

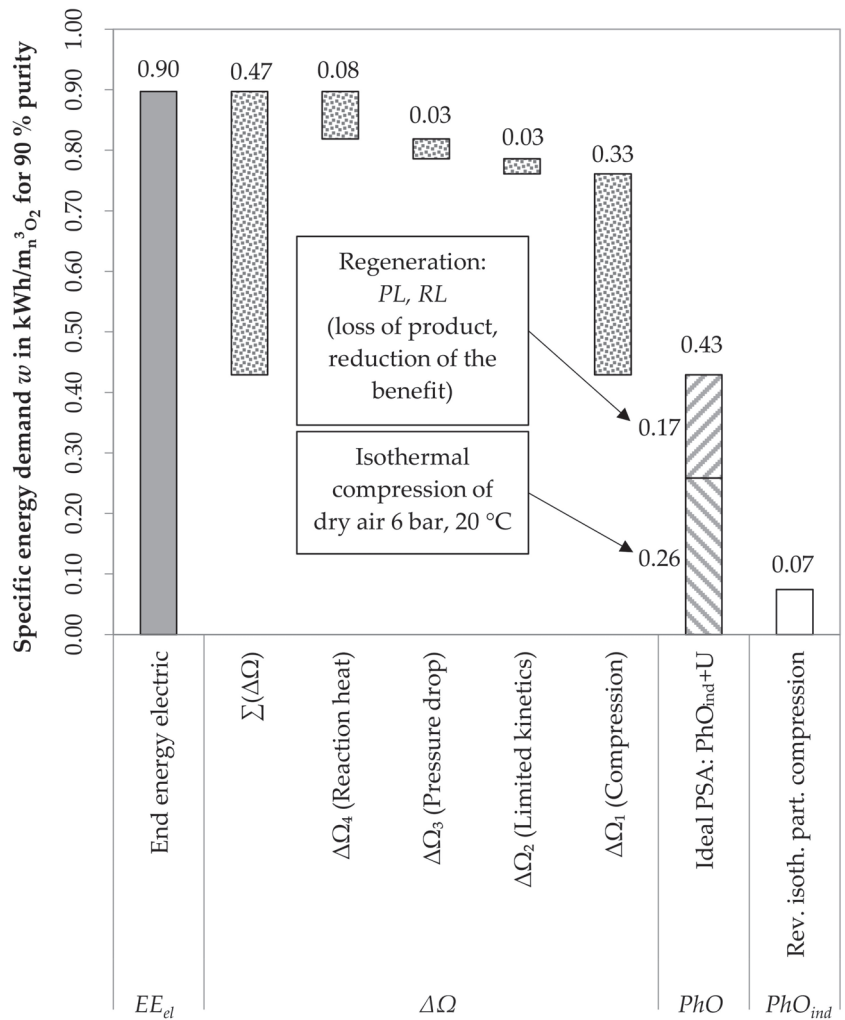


Figure 9. Evaluation of the oxygen purification using PSA with the *PhO* method.

Yet, overall, a higher amount of energy is consumed in comparison to the cryogenic process, as shown by  $F_{PhO,PSA,total}^B$ , which exceeds the value for the cryogenic production ( $F_{PhO,cryo,ind}^B = 12.29$ ). As said before, the  $PhO_{ind}$  should be used for process comparison.

### 3.3. Comparison of the Production Methods

The cryogenic oxygen production is compared to the PSA process in the following section. Primary energy consumption as well as the necessary transport for the cryogenic production are taken into account in addition to the results already given. Figure 10 shows the respective *PhO* as well as the total losses for each option. With the  $PhO_{ind}$ , both options are compared directly.

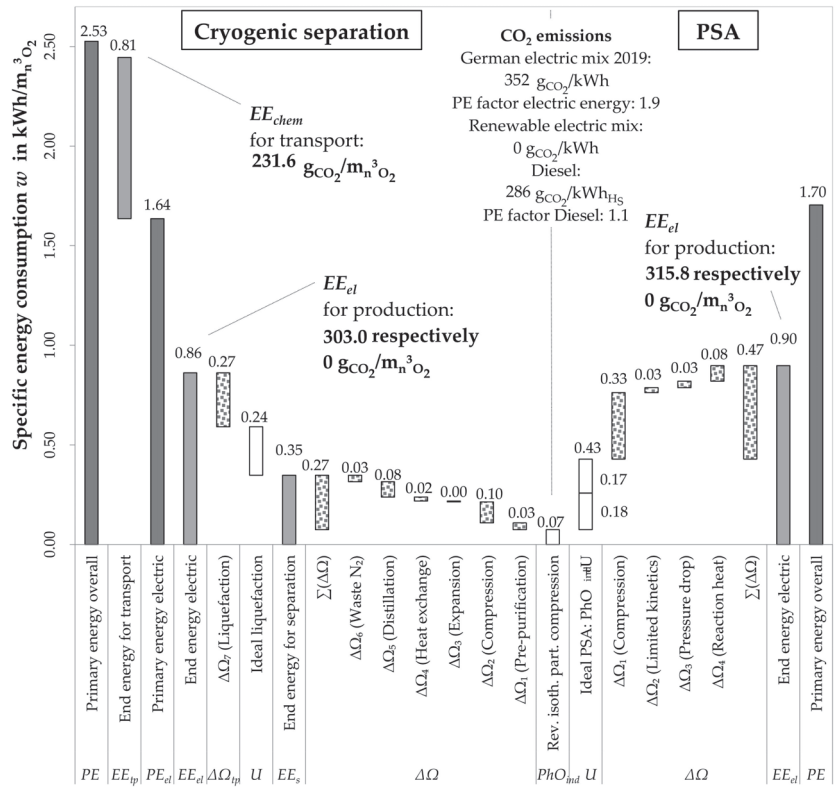


Figure 10. Comparison of the oxygen production processes with PhO method.

Centered, the  $PhO_{ind}$  gives the ultimate minimum energy demand. To the left and right, the unavoidable losses  $U$  and the avoidable losses  $\Delta\Omega$  sum up to the real demand.

Comparing the  $PhOs$  for the production of gaseous oxygen, a surplus of  $0.36 \text{ kWh/m}^3_{n,O_2}$  is consumed using PSA. Furthermore, the purity of the product is lower in this case. In theory, the cryogenic option is more efficient, because the unavoidable losses are higher for PSA. The real energy consumption, for which the losses are considered additionally, is lower as well for cryogenic production.

Figure 11 shows the more common analysis with an energy-flow diagram enabling an illustration of the inner process back-coupling of the expansion machine for the cryogenic process. Eventual balancing differences in Figure 11 are due to rounding imprecision.

Comparing the  $PhOs$  for liquefied oxygen and the gaseous product of PSA, the advantage of cryogenic production is lowered to  $0.12 \text{ kWh/m}^3_{n,O_2}$ . The real demand for the cryogenic production ( $0.86 \text{ kWh/m}^3_{n,O_2}$ ) is a little lower than production with PSA ( $0.9 \text{ kWh/m}^3_{n,O_2}$ ).

Considering the primary energy factors and including the transport for the cryogenic option, the result is in favor of the PSA. For delivering, additional primary energy is used. Thus, the demand for cryogenic production exceeds that of PSA over  $0.82 \text{ kWh/m}^3_{n,O_2}$ , respectively 49%. In this case (due to a long distance to the production plant), PSA is preferable.

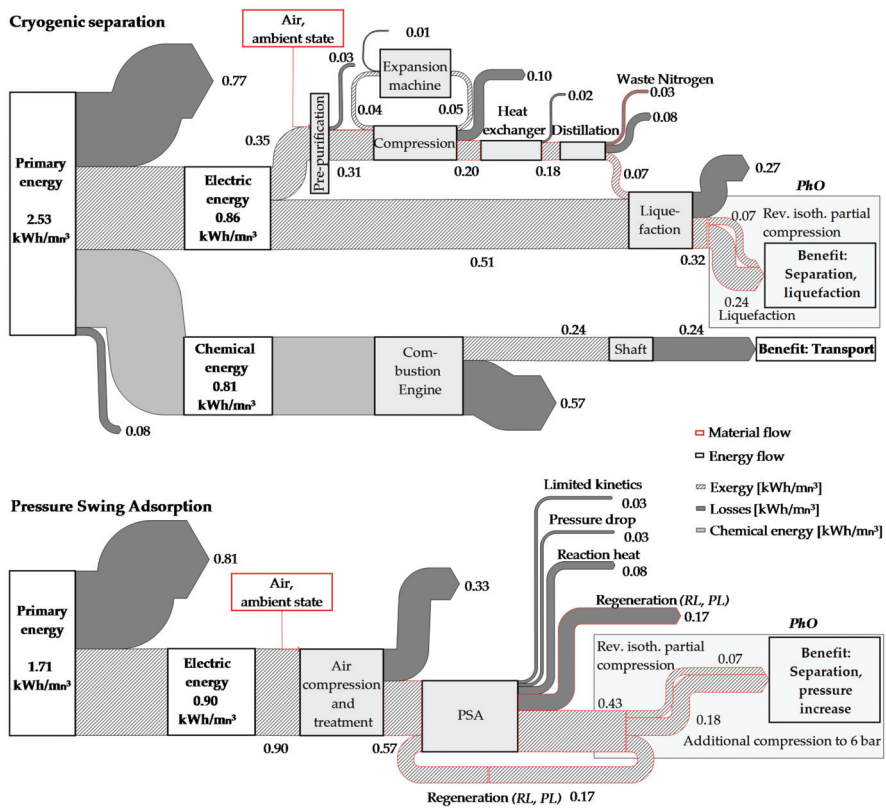


Figure 11. Comparison of oxygen production options with energy-flow diagrams.

To sum up, the cryogenic process theoretically has a lower demand of energy for production. However, it is the less efficient process. In total, with significant influence of the transport, PSA uses less energy.

Additionally, the specific CO<sub>2</sub> emissions are determined. Firstly, regarding the German electric mix with 352 g<sub>CO<sub>2</sub></sub>/kWh [23], and including the transport (for cryogenic only: Diesel 285 g<sub>CO<sub>2</sub></sub>/kWh [8] (p. 538), [24] (p. 35)), 215 g<sub>CO<sub>2</sub></sub>/m<sup>3</sup><sub>n,O<sub>2</sub></sub> can be avoided. If renewable energies are used, the CO<sub>2</sub> emissions are considered as zero. However, it is currently unlikely, due to economic reasons, that an industrial company would use renewable energies exclusively. Especially, changing the fuel for the transport is, momentarily, unrealistic. Thus, the PSA is again preferable under the aspect of CO<sub>2</sub> emissions. Overall, the conclusion is, that in this case, with respect to energetic aspects, the PSA is advantageous.

Additionally, the running costs of liquid oxygen and the PSA are compared in Tables 6 and 7. For the liquid oxygen, the actual values of the hospital are given. For the PSA, the investment has been assumed to be 40,000 € with a payback period of 10 years. Maintenance costs were considered to be identical for both options. Only the adsorption itself is a process uncommon for a hospital. Therefore, the size of the compression unit would change, but the personnel and spare parts do not depend on the implementation of the adsorber. It is therefore assumed that an external company charges the same amount for monthly maintenance of the adsorber as is charged for the liquid oxygen.

**Table 6.** Running costs for liquid oxygen.

Matter of Expense	Costs
Costs per standard cubic metre of oxygen	0.2346 €/m <sup>3</sup> O <sub>2</sub>
GGVSEB liquid	25 €/Delivery
Road toll	25 €/Delivery
Monthly rent oxygen tank MEDSt	160 €/Month
22-000201 Telemetriesystem LOX	20 €/Month
Monthly maintenance	25 €/Month
Annual costs oxygen only	31,606 €/a
Annual overall costs	36,666 €/a
Specific overall costs	0.2722 €/m <sup>3</sup> O <sub>2</sub>

**Table 7.** Running costs for oxygen from PSA.

Matter of Expense	Costs
Annual electricity demand	121,359 kWh/a
Specific electricity costs	17.15 €/kWh
Investment (payback period 10 years)	40,000 €
Monthly maintenance	25 €/Month
Annual overall costs	25,113 €/a
Specific overall costs	0.1864 €/m <sup>3</sup> O <sub>2</sub>

The comparison results in an advantage for the PSA for the running costs as well as for the energetic evaluation.

#### 4. Discussion

The results presented here are based on exemplary data found in literature. For the application of the *PhO*, actual measured data would give a more realistic evaluation. Since the hospital has not been built yet, the data could not be collected. Therefore, certain simplifications, as well as assumptions, are made, resulting in the typical uncertainty of predictions. In the following section, the methods used in this study are discussed. Moreover, aspects influencing the decision process for one of the options are explained.

Firstly, certain simplifications are made. For example, additional losses would occur in reality, which are not quantified in this study. The storage of liquid oxygen causes boil-off losses. As the heat flow from the environment to the liquid oxygen cannot be avoided completely, a particular amount of oxygen evaporates, which is usually blown off periodically to reduce pressure.

The boil-off losses do not occur for compressed oxygen. This, again, is an advantage of PSA. Furthermore, the cryogenic oxygen plant produces in large scales. For a smaller plant, the losses would increase due to scale effects. A study [25] concludes, that for a production flow of only 350 m<sup>3</sup>/h of oxygen, the power intake of a PSA plant can be lower than for a cryogenic plant [25] (p. 1378). Therefore, the PSA is preferable for small-scale production.

Another relevant simplification is the assumption of a stationary process. In the actual case, the demand for oxygen can be a very dynamic variable. Over daytime, the oxygen supply is increased, for example, for operations taking place. During the night, only the clients constantly in need of a surplus of oxygen cause a demand. Therefore, either the production of the PSA would have to meet the exact demand or a storage would be obligatory to buffer the changes. For the cryogenic option in the hospital, the only limitation is the maximum heat transfer in the evaporator limiting the amount of oxygen which can be fed to the system. The dynamic behavior as well as the resulting losses are not analyzed in this study and therefore a potential aspect of further investigation.

Furthermore, the coupling of the potential oxygen processes with other applications in the hospital is not considered. As shown, the evaporation of liquid oxygen causes a demand for heat. It is also possible to interpret this as a potential for cooling applications. The exergy



of the liquefied oxygen might be integrated into the supply system to contribute to the demand for refrigeration in the building. For the PSA, the waste heat of the compression is a potential source for heating purposes. By process coupling, the advantages of the options could be increased, resulting in a more detailed evaluation of the efficiency.

Besides, the study used for the evaluation of PSA refers to the application of PSA as a method to purify oxygen for the more efficient operation of fuel cells. As the common method to realize the oxygen supply is the purchase of liquefied oxygen, the data specification in literature for the application of PSA is not sufficient. The possible degree to which the results deviate would have to be examined more closely. To ensure the accuracy of the results, the value for the end energy consumption taken from literature is used to calculate backwards the energy demand for the compression and conditioning of the air. As the calculated value complies with the expected value, only the percentage distribution of the losses would possibly differ for the production of medical oxygen. Yet, more accurate data would refine the results.

In addition, there are further options for the production of oxygen. The current debate about the integration of hydrogen into the energy supply chain outlines the possibility of using the waste oxygen, which is generated as a by-product in electrolysis. As an additional field of research, this option could be compared to the two methods analyzed in this study.

Lastly, a prioritization within the relevant aspects is necessary for the hospital's decision process. One of the key issues in this study is the impact of the supply options on the climate. A good example is the purchase of strictly renewable electric energy. The CO<sub>2</sub> emissions are immediately reduced to zero, while the energy costs exceed those of the general electric mix in the grid.

An economical evaluation would ideally supplement the study, as this factor is highly significant for the hospital as a business enterprise. The given comparison is simplified. For example, the installation space should be considered. The PSA is economically advantageous if the savings in comparison to the purchase of liquid oxygen justify the additional costs. An adequate economic feasibility study demonstrates the practicability of the technological option. The oxygen demand is substantial in this case. Scale effects increase not only the efficiency of the process, the payback time is lowered as well. Future energy prices as the main influence on the costs of the oxygen should be taken into account. Thus, the main question is which aspect is prioritized. For the external cryogenic production, no effective influence can be exercised on the purchase of the energy. In addition to the emissions of the production, the transport is unavoidable. For the in-house production with PSA, the decision lies with the hospital operators. It can be taken leaning to either economical or climate advantages.

Additional factors, namely an emergency reserve argue against the PSA. The liquid oxygen can easily be stored in capacities sufficient for a month of supply. For the PSA, an oxygen reserve could be realized by the storage in pressure cylinders, but not an amount sufficient for a month. Furthermore, for the case of a blackout, the emergency generator must be dimensioned to also maintain the oxygen supply. Therefore, other supply units are influenced as well. A redundant PSA installation should also be considered. On the other hand, problems in the supply chain are less likely for PSA, because the transport is not necessary.

It is shown that the distance of the hospital from the production plant of the liquid oxygen is the decisive factor that categorizes the PSA as advantageous. The long distance is the reason for the liquefaction as well as the necessity of storage. For a hospital closer to the production site, the picture might change. The significance of the distance and the method of transport must therefore be highlighted. Especially for a hospital in a remote location, the comparison should be performed. A direct transfer of the results to another hospital is not possible without verification of the data.

Furthermore, legal consequences as given in Section 2.3 cause an increased effort for the quality management and a risk of liability. This study outlines the more efficient option in terms of energetic aspects only. Yet, the decision must take all the consequences such as

the named into account. For another hospital, the individual conditions of the site must be considered. Table 8 contains the presented results and further criteria leading to a decision.

**Table 8.** Comparison of options for medical oxygen supply.

Criteria		Cryogenic		PSA		
End energy consumption	+/-	Lower energy demand for production, liquefaction and transport necessary	++	Continuous savings		
Primary energy consumption	-	No influence on source of energy, additional demand for transport	+	In case of electric energy from renewable sources, almost equivalent to end energy		
CO <sub>2</sub> emissions	+/-	Powered by electric energy (emission avoidable by simple means) avoidance of emissions from transport currently expensive	+	Powered by electric energy only (emission avoidable by simple means)		
Process coupling	-	None	+	Heat recovery in compression unit		
Running costs	-	Additional	+	Savings		
Further economic aspects	++	Standard method, maintenance and repairs by external company, predictability of costs	-	Custom solution, increased investment, additional installation space, staff training, hospital carries financial risks		
Legal framework	++	O <sub>2</sub> 100: Supplier charged with quality control and liability	-	O <sub>2</sub> 93: Liability with operator, hospital pharmacy carries responsibility		
Further technical aspects	+	Standard method	-	Modifications of applications necessary (calibration, etc.)		
Emergency management	+	One month of reserve	-	In case of power failure, supply by emergency power system, little experience		
++	Significant advantage	+/-	Advantages and disadvantages	-	Significant	Quantified
+	Advantage			-		Qualified

## 5. Conclusions

By the application of the *PhO*, it is shown that the cryogenic production method depicts more potential for optimization, although it uses less energy in comparison to PSA.

The concept of the *PhO* is to define an ultimate reference value for process evaluation in order to distinguish between avoidable and unavoidable losses. This study gives an example for the application of the *PhO* to a real industrial process, namely, the production of oxygen for medical purposes. Comparing the process independent  $PhO_{ind}$  and the *PhO* of a specific process, the particularities of the method are outlined. The application enables a detailed analysis of losses to determine relevant options for efficiency measures. The more general  $PhO_{ind}$  allows to compare different processes with the same benefit, while the *PhO* of a specific process defines the potential for optimization, i.e., the avoidable losses.

The *PhO* method enables a process evaluation which allows to integrate a wide range of boundary conditions. An analysis of losses is the key to process efficiency. The goal of reaching 100% renewable energy supply can only be reached by significantly increasing energy efficiency. The *PhO* is a user-oriented method contributing to resource efficiency by the concept of reducing the input of a process to the unavoidable minimum amount.

**Author Contributions:** Conceptualization, S.A.W. and D.V.; methodology, S.A.W., D.V. and J.K.; software, S.A.W.; validation, S.A.W., D.V. and J.K.; formal analysis, S.A.W. and D.V.; investigation, S.A.W. and D.V.; resources, D.V.; data curation, S.A.W.; writing—original draft preparation, S.A.W.; writing—review and editing, S.A.W., D.V. and J.K.; visualization, S.A.W. and D.V.; supervision, S.A.W. and D.V.; project administration, D.V.; funding acquisition, D.V. All authors have read and agreed to the published version of the manuscript.

**Funding:** This research was funded by the Evangelical Lutheran Deaconess Hospital Flensburg and the Society for Energy and Climate Protection Schleswig-Holstein (Gesellschaft für Energie und Klimaschutz Schleswig-Holstein GmbH, EKSH), grant number 8/12-40. We acknowledge financial support by Land Schleswig-Holstein within the funding program Open Access-Publikationsfonds.

**Institutional Review Board Statement:** Not applicable.

**Informed Consent Statement:** Not applicable.

**Data Availability Statement:** No new data were created or analyzed in this study. Data sharing is not applicable to this article.

**Acknowledgments:** The authors gratefully acknowledge the support of the proofreaders, in particular, for language support.

**Conflicts of Interest:** The authors declare no conflict of interest.

## Nomenclature

### Roman Symbols

Symbol	Unit	Description
$B$	e.g., kWh/kg	Demand
$F_{PhO}^B$		$PhO$ factor, based on demand
$h$	J/kg	Specific enthalpy
$p_i$	Pa	Partial pressure
$PL$		Pressure-relieving losses
$r_i$		Volume fraction
$RL$		Rinsing losses
$s$	J/(kg × K)	Specific entropy
$T$	K	Temperature
$U$	e.g., kWh/kg	Unavoidable losses
$w$	J/kg	Specific work
$Y$		Yield

### Greek Symbols

$\lambda$		Air ratio
$\Delta\Omega$	e.g., kWh/kg	Avoidable losses

### Sub- and Superscript

Symbol	Description
$A$	Adsorption
$chem$	Chemical
$cryo$	Cryogenic
$D$	Desorption
$el$	Electric
$Feed$	Feed flow
$ind$	Process independent
$isen$	Isentropic
$ith$	Isothermal
$liqu$	Liquefied
$min$	Minimum
$n$	Standard
$PhO$	Physical optimum
$PL$	Pressure-relieving losses

<i>Prod</i>	Product flow
<i>PSA</i>	Pressure swing adsorption
<i>rev</i>	reversible
<i>RL</i>	Rinsing losses
<i>s</i>	Separation
<i>t</i>	Technical

## References

- Volta, D. Das Physikalische Optimum als Basis von Systematiken zur Steigerung der Energie- und Stoffeffizienz von Produktionsprozessen. Ph.D. Thesis, TU Clausthal, Clausthal-Zellerfeld, Germany, December 2014.
- Keichel, C. Methode der Grenzwertorientierten Bewertung—Energie- und Ressourceneffizienz von Gesamtbetriebsweisen. Ph.D. Thesis, TU Clausthal, Clausthal-Zellerfeld, Germany, April 2017.
- VDI. *Fachbereich Energietechnik 4663, Blatt 1: Bewertung von Energie- und Stoffeffizienz—Methodische Anwendung des Physikalischen Optimums*; Verein Deutscher Ingenieure: Düsseldorf, Germany, 2019.
- Wenzel, P.; Radgen, P.; Westermeyer, J. Comparing Exergy Analysis and Physical Optimum Method Regarding an Induction Furnace. *Energies* **2021**, *14*, 1621. [[CrossRef](#)]
- Kerpen, L.; Schmidt, A.; Sankol, B. Differentiating the Physical Optimum from the Exergetic Evaluation of a Methane Combustion Process. *Energies* **2021**, *14*, 3419. [[CrossRef](#)]
- Volta, D.; Weber, S.A. The Physical Optimum as an Ideal Reference Value for Balancing Thermodynamic Processes Integrating the Exergetic Evaluation by the Example of Heat Supply. *Energies* **2021**, *14*, 4426. [[CrossRef](#)]
- Lucia, U.; Grisolia, G. Unavailability percentage as energy planning and economic choice parameter. *Renew. Sustain. Energy Rev.* **2017**, *75*, 197–204. [[CrossRef](#)]
- Cerbe, G.; Wilhelms, G. *Technische Thermodynamik—Theoretische Grundlagen und Praktische Anwendungen*, 17th ed.; Carl Hanser Verlag: Munich, Germany, 2017; pp. 319–538.
- Bell, I.; The CoolProp Team. CoolProp. Available online: [//www.coolprop.org/](http://www.coolprop.org/) (accessed on 9 January 2022).
- Umweltbundesamt Kohlendioxid-Konzentration in der Atmosphäre (Monatsmittel). (Schauinsland, Zugspitze), NOAA Global Monitoring Division and Scripps Institution of Oceanography (Mauna Loa, Hawaii), World Meteorological Organization, WDCGG (World Trend). Available online: [https://www.umweltbundesamt.de/sites/default/files/medien/384/bilder/dateien/2\\_abb\\_kohlendioxid-konz\\_2021-05-26.pdf](https://www.umweltbundesamt.de/sites/default/files/medien/384/bilder/dateien/2_abb_kohlendioxid-konz_2021-05-26.pdf) (accessed on 28 July 2021).
- Umweltbundesamt Nationale Treibhausgas-Inventare 1990 bis 2019 (Stand 12/2020) sowie Vorjahresschätzung (VJS) für das Jahr 2020. Available online: [https://www.umweltbundesamt.de/sites/default/files/medien/384/bilder/dateien/3\\_tab\\_emi-direkt-indirekt-thg\\_2021.pdf](https://www.umweltbundesamt.de/sites/default/files/medien/384/bilder/dateien/3_tab_emi-direkt-indirekt-thg_2021.pdf) (accessed on 14 October 2021).
- AG Energiebilanzen e.V. *Auswertungstabellen zur Energiebilanz Deutschland—Daten für die Jahre von 1990 bis 2018—Stand: März 2020 (endgültige Ergebnisse bis 2018)*; AG Energiebilanzen e.V.: Bergheim, Germany, 2020; p. 20.
- Prien, T.; Meineke, I.; Züchner, K.; Rathgeber, J. Sauerstoff 93—Eine neue Option auch für deutsche Krankenhäuser. *Anästhesiol. und Intensivmed.* **2013**, *54*, 466–472.
- Smith, A.R.; Klosek, J. A review of air separation technologies and their integration with energy conversion processes. *Fuel Processing Technol.* **2001**, *70*, 115–134. Available online: <https://www.sciencedirect.com/science/article/pii/S037838200100131X> (accessed on 9 November 2021). [[CrossRef](#)]
- Ebrahimi, A.; Meratizaman, M.; Reyhani, H.A.; Pourali, O.; Amidpour, M. Energetic, exergetic and economic assessment of oxygen production from two columns cryogenic air separation unit. *Energy* **2015**, *90*, 1298–1316. Available online: <https://www.sciencedirect.com/science/article/pii/S0360544215008397> (accessed on 9 November 2021). [[CrossRef](#)]
- Maurer, T. *Kältetechnik für Ingenieure*, 1st ed.; VDE Verlag GmbH: Berlin, Germany, 2016; pp. 324–326.
- Fu, C.; Gundersen, T. Using exergy analysis to reduce power consumption in air separation units for oxy-combustion processes. *Energy* **2012**, *44*, 60–68. [[CrossRef](#)]
- Blesl, M.; Kessler, A. *Energieeffizienz in der Industrie*, 2nd ed.; Springer: Berlin/Heidelberg, Germany, 2018; p. 277.
- Peht, M.; Mellwig, P.; Blöhmer, S.; Hertle, H.; Nast, M.; von Oehsen, A.; Lempik, J.; Langreder, N.; Thamling, N.; Hermelink, A.; et al. *7-03-17 Untersuchung zu Primärenergiefaktoren—Endbericht—Leistung gemäß Rahmenvertrag zur Beratung der Abteilung II des BMWi*; Bundesministerium für Wirtschaft (BMWi): Berlin/Heidelberg, Germany, 2018; p. 9.
- Linde Group: Hydrogen Recovery by Pressure Swing Adsorption. Available online: [https://www.linde-engineering.com/en/images/HA\\_H\\_1\\_1\\_e\\_09\\_150dpi\\_NB\\_tcm19-6130.pdf](https://www.linde-engineering.com/en/images/HA_H_1_1_e_09_150dpi_NB_tcm19-6130.pdf) (accessed on 6 July 2021).
- Lengerer, W. *Sauerstoffanreicherung durch Druckwechseladsorption für Membran-Brennstoffzellensysteme*, 1st ed.; Logos Verlag Berlin GmbH: Berlin, Germany, 2008; pp. 121–145.
- Kriegel, R. *Energiebedarf von Sauerstoff-Membrananlagen und Technologievergleich*. Fraunhofer; IKTS Annual Report; Fraunhofer-Institut für Keramische Technologien und Systeme IKTS: Dresden, Germany, 2013; pp. 76–77.
- Stadtwerke Flensburg GmbH. *Stadtwerke Flensburg Strommix-SWFL-2019*; Stadtwerke Flensburg GmbH: Flensburg, Germany, 2020; Available online: [https://www.stadtwerke-flensburg.de/fileadmin/user\\_upload/Strommix-SWFL-2019.pdf](https://www.stadtwerke-flensburg.de/fileadmin/user_upload/Strommix-SWFL-2019.pdf) (accessed on 6 July 2021).

24. Juhrich, K. *CO<sub>2</sub>-Emissionsfaktoren für Fossile Brennstoffe*; Umweltbundesamt, Fachgebiet Emissionssituation (I 2.6): Dessau-Roßlau, Germany, 2016; p. 35.
25. Banaszekiewicz, T.; Chorowski, M.; Gizicki, W. Comparative analysis of cryogenic and PTSA technologies for systems of oxygen production. *AIP Conf. Proc.* **2014**, *1573*, 1373–1378.



Article

# The Mitigation Effect of Park Landscape on Thermal Environment in Shanghai City Based on Remote Sensing Retrieval Method

Tian Wang <sup>1,\*</sup>, Hui Tu <sup>1,\*</sup>, Bo Min <sup>1</sup>, Zuzheng Li <sup>2</sup>, Xiaofang Li <sup>1</sup> and Qingxiang You <sup>1</sup>

- <sup>1</sup> Key Laboratory of Software Technology Research and Application of Changzhou City, Department of Computer Information and Engineering, Changzhou Institute of Technology, Changzhou 213032, China; minb45@126.com (B.M.); lixf@czu.cn (X.L.); youqx@czu.cn (Q.Y.)  
<sup>2</sup> State Key Laboratory of Urban and Regional Ecology, Research Center for Eco-Environmental Sciences, Chinese Academy of Sciences, Beijing 100085, China; zuzhengli@rceres.ac.cn  
\* Correspondence: wangtian@czu.cn (T.W.); th2509105144@126.com (H.T.)

**Abstract:** The mitigation effects of park green space on Urban Heat Island (UHI) have been extensively documented. However, the relative effects of the configuration of park components on land surface temperature (LST) inside the park and indicators (i.e., park cooling intensity and distance) surrounding the park is largely unknown. Therefore, the main objective of this study is to explore the quantitative impacts of configuration and morphology features under different urban park scales on the cooling effect. In this study, based on Landsat-8 OLI/TIRS images on 3 August 2015 and 16 August 2020 during summer daytime, the LSTs of Shanghai City were retrieved by atmospheric correction method. Then, the relationships of park landscape features with LSTs in the park and typical indicators representing cooling efficiency of 24 parks on different grades were analyzed. The results showed that the average temperature in urban parks was, respectively, 1.46 °C and 1.66 °C lower than that in the main city of Shanghai in 2015 and 2020, suggesting that urban parks form cold islands in the city. The landscape metrics of park area (PA), park perimeter (PP), green area (GA) and water area (WA), were key characteristics that strong negatively affect the internal park LSTs. However, the park perimeter-to-area ratio (PPAR) had a significant positive power correlation with the park LSTs. Buffer zone analysis showed that LST cools down by about 0.67 °C when the distance from the park increases by 100 m. The Maximum Cooling Distance (MCD) for 2015 and 2020 had a significant correlation with PA, PC, PPAR, GA and WA, and increased sharply within the park area of 20 ha. However, the medium park group had the largest Maximum Cooling Intensity (MCI) in both periods, followed by the small park group. There could be a trade-off relationship between the MCD and MCI in urban parks, which is worth pondering to research. This study could be of great significance for planning and constructing park landscapes, alleviating Urban Heat Island effect and improving urban livability.

**Citation:** Wang, T.; Tu, H.; Min, B.; Li, Z.; Li, X.; You, Q. The Mitigation Effect of Park Landscape on Thermal Environment in Shanghai City Based on Remote Sensing Retrieval Method. *Int. J. Environ. Res. Public Health* **2022**, *19*, 2949. <https://doi.org/10.3390/ijerph19052949>

Academic Editors: Roberto Alonso González Lezcano, Francesco Nocera and Rosa Giuseppina Caponetto

Received: 16 January 2022  
Accepted: 28 February 2022  
Published: 3 March 2022

**Publisher's Note:** MDPI stays neutral with regard to jurisdictional claims in published maps and institutional affiliations.

**Keywords:** Urban Heat Island; park landscape; remote sensing inversion; land surface temperature; Maximum Cooling Distance and intensity; Shanghai City



**Copyright:** © 2022 by the authors. Licensee MDPI, Basel, Switzerland. This article is an open access article distributed under the terms and conditions of the Creative Commons Attribution (CC BY) license (<https://creativecommons.org/licenses/by/4.0/>).

## 1. Introduction

According to the report from Intergovernmental Panel Climate Change (IPCC), over the past century global warming has been recognized as a profound universal problem and the increase is likely to happen faster than was predicted [1,2]. Furthermore, more than half of the world's population lives in urban areas and this value is set to increase to 66% by 2050 [3], which would aggravate the Urban Heat Island effect (UHI). The UHI phenomenon refers to the fact that when a city grows to a certain scale, the temperature in the urban area is significantly higher than that in the non-urban areas [4], and this has been observed worldwide [5–7]. The increased impervious surface cover instead of

evaporative vegetation surfaces and anthropogenic heat releases have been proven to be the main reasons for the UHI [8]. Overheating conditions in cities can increase urban energy consumption, raise pollution levels and may even affect the habitability of cities and potentially lead to increases in morbidity and mortality [9–11]. This grim situation has brought challenges to the sustainable development of cities. There are several strategies to alleviate Urban Heat Island effect in cities, such as increasing urban vegetation, using cool pavements and proper urban planning [12–14]. Among these cooling measures, the photosynthesis and transpiration of park green space can play a critical role in cooling and humidifying, carbon fixation and oxygen release. Urban parks, an essential component of urban green infrastructure, which not only are cold and wet islands in cities, but can influence its vicinity areas [13,15–18], are of great significance to mitigate the “Urban Heat Island” (UHI). Therefore, how to make good use of the limited urban parks and obtain the maximum ecological benefit under a high-density metropolitan area is a topic worthy of study.

Intensive studies have been conducted to assess the UHI effect for hundreds of cities around the world [7,12,13]. Land surface temperature (LST) is a crucial indicator of one component of the UHI known as the surface UHI [14,15]. Compared with in situ air temperature measurement, remote sensing provides not only the detailed information of land use/land cover, but also the LST observation with more uniform and accurate sampling [4,16]. It avoids inconsistency in data collection processes, sensor types, and other meteorological factors [17]. In recent years, the rapid development of thermal infrared remote sensing technique has greatly promoted the diversification of remote sensing inversion methods for obtaining LST, such as Linear spectral mixture analysis (LSMA) model [18,19], single channel algorithm [20], atmospheric correction or radiative transfer method [21–23] and split-window algorithm [24,25]. In recent years, passive microwave (PMW) satellites have developed rapidly because of their ability to penetrate clouds, although PMW data suffer from lower spatial resolution and LST retrieval accuracy compared with thermal infrared data [26]. Landsat 8 Thermal Infrared Sensor (TIRS) is the new, stable thermal infrared sensor for the Landsat project, carrying two thermal infrared bands, which provides a great benefit to the LST inversion. For example, Yu et al. (2014) [27] compared three different methods for LST retrieval from TIRS, and found that the LST inverted from the radiative transfer equation-based approach using Landsat 8 TIRS has the highest accuracy a Root Mean Square Error (RMSE) lower than 1 K. Considering that the surface UHI is more pronounced during daytime and in summer [17], this paper selects the years of 2015 and 2020 (the key period of the 13th five-year plan) to reflect the impacts of the urbanization-associated green space on urban LST at typically the same period, which has seldom been reported by other studies in Shanghai, China.

Several previous studies have found that the average LST of urban parks was 1–2 °C, and sometimes even 4–8 °C, cooler than their urban surroundings, generating a “cooling island” [7,28,29]. The spatial scope of scholars’ research about UHI mitigation effects of urban parks is generally from (1) the relationship of the urban green space landscape spatial configuration and land surface temperature (LST) [30–33], and (2) the microclimate in the parks and the impacts of their structure factors on the thermal environment of the surrounding areas [34–36]. Furthermore, when studying the cooling effect of the park on surrounding environment, some scholars adopted the designated buffer zone distance to calculate the average temperature around the parks and compared it with its internal temperature using remote sensing image data [28,37,38], or analyzed the impact of specific parks on the surrounding microclimate based on the field meteorological observation data [39–42]. However, the park cooling effect has mainly been characterized by a single indicator of park cooling intensity (PCI) and limited datasets (e.g., using one image or in a year), and the study of multiple parks seldom consider the impact differences of various grades of parks on the cooling effect. According to the research results of many scholars, urban parks have a significant cooling effect on urban local thermal environment with the main factors including green space, water body, impermeable layers and other park

landscape composition parameters as well as park patch morphology. As we have known, the relationship between park area, shape and park cooling island is complex [43]. Zhu et al. (2021) [29] found that only parks larger than a threshold size (20 ha) would provide a larger cooling effect with the increase in park size, through a study in Jinan, China. Jaganmohan et al. (2016) [44] suggested that a number of small green spaces distributed in a city might have a stronger cooling effect than a few larger green spaces [29]. As for the shape, Cao et al. (2010) [16] quantified the cool island intensity of 92 urban parks in Nagoya, Japan, and indicated that the formation of PCI being negative affected by complex shape and fostered by shrubs and trees. In the research of Chang et al. (2007) [45], the authors thought that parks with complex shapes provided stronger cooling island effects. The above studies, with some different conclusions, suggest that the effect of configuration of park components on relative indicators (i.e., park cooling intensity and distance) is still uncertain.

Shanghai is a megacity with a subtropical monsoon climate that has undergone rapid urbanization in the last few decades. The total population has reached 24.87 million in 2021 [46], and the proportion people living of urban areas, with the highest population urbanization rate in China, reaching more than 88% [47]. Such vast urbanization has exacerbated UHI effect in Shanghai. Therefore, how to scientifically configure the landscape elements and improve ecological service function of urban parks, especially their cooling effect, has become an urgent problem that need to be solved. Previous studies about effects of urban green space on thermal environment were reported in Shanghai, which mainly concentrated on the relationship between LST and green space pattern combined with landscape metrics from the urban landscape scale [48–50], the cooling effects of specific park features (e.g., park size), single landscape elements (e.g., water body) or single park type (e.g., pocket parks) [51–53] and thermal comfort and space use in a specific park by meteorological measurements [40]. However, a clear understanding of the composition and morphological characteristics under different scale levels of urban parks and their quantitative impact on the LST inside and in the surrounding of the parks in a time-series analyses, is still a lacking. This research can reveal the differences in the cooling capacity of park green space with different morphological characteristics over two critical years.

In view of this, based on landsat-8 OLI/TIRS remote sensing images of Shanghai in 2015 and 2020, land surface temperature was retrieved by atmospheric correction method to investigate the mitigation impacts of urban park landscapes on the thermal environment. Additionally, a total of 24 parks were selected in Shanghai City, China. The purposes of this research are to explore: (1) What kind of correlations exist between landscape composition and patch morphology of parks with LST and which are the key influencing indicators; (2) How about the Maximum Cooling Distances (MCD) and maximum cooling intensities (MCI) of parks on four different park scales? (3) Are there significant differences in heat release effects among parks of different scales and does the significance change with the development of urbanization? The results could provide some decision-making bases and references for planning and constructing Shanghai parks and alleviating Urban Heat Island effect in a hot summer, humid, subtropical large metropolis.

The paper is organized as follows. Following the description of the study area, the methodology of LST retrieval algorithm, extraction of park landscape features, buffer zone setting and data processing flow are presented in Section 2. The results, discussion and conclusions are presented in Sections 3–5, respectively.

## 2. Materials and Methods

### 2.1. Description of the Study Area

This study was conducted in Shanghai (30°40′–31°53′ N, 120°52′–122°12′ E), covering an area of 6340.5 km<sup>2</sup>, which is located in the central point of the north and south coast of China, where the Yangtze River and the Huangpu River meet the sea (Figure 1). It is part of the Yangtze Delta alluvial plain, with an average elevation of about 4 m and a maximum elevation of 103.4 m. According to the Köppen–Geiger climate classification, this city has a typical subtropical monsoon climate characterized by being humid and having



a hot summer [54], with average annual temperature of 18.4 °C, annual precipitation of 1042.6 mm and 129 days of precipitation per year. As the famous water town in Jiangnan, Shanghai has a water area of 697 km<sup>2</sup>, equivalent to 11% of its total area. The zonal vegetation consists evergreen broad-leaved forest and evergreen deciduous broad-leaved mixed forest, and the non-zonal vegetation is dominated by intertidal vegetation and aquatic vegetation. Within the total area, green space covers 1242.95 km<sup>2</sup>, and the per capita area of park green space is 8.6 m<sup>2</sup> [46]. Since the 1990s, rapid economic growth of Shanghai was accompanied by enormous urbanization in both scope and degree [55]. Currently, it is one of the four municipalities directly under the Central Government in China, belonging to the Yangtze River Delta economic circle, with a large population and developed economy and trade. It is one of China's important foreign trade cities, known as the “magic capital”.

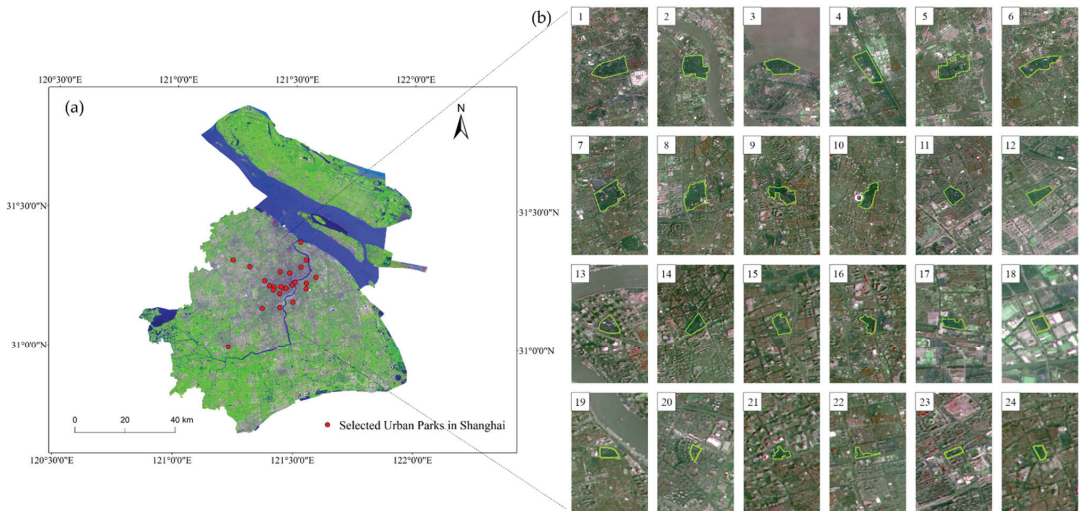


**Figure 1.** (a) The space distribution of selected urban parks in Shanghai. (b) The geometric features of the selected 24 parks and their surrounding environment. Natural true colors with RGB composition of band 4, 3 and 2, are fused with panchromatic band (band 8) to form an image base map with 15 m spatial resolution.

In the study, 24 parks in Shanghai, which have been completed and not significantly altered in the last 15 years, were selected as objects. According to Figure 1, the selected parks are mainly concentrated in the center of Shanghai City and their geometric characteristics are diverse. Location information and vector maps of the parks, water system, green spaces and road network in the study area were precisely extracted from Amap by Python crawler module. Referring to the study by Cheng X et al. (2015) [51] and taking into account reality, the parks were classified into four classes in terms of their sizes, as follows: super large (>50 ha), large (10–50 ha), medium (4–10 ha), and small (<4 ha). There are at least five parks in each grade (Table 1). The rules for demarcating the parks' boundaries are: (1) The sidewalks and buildings in the parks were included in the park. (2) The water body within the boundaries of the parks was included in the scope of the parks, with the water body outside the boundaries excluded from the scope of the parks. (3) The traffic lines through the park were also included in the parks. This means that the vector maps of the parks were closed irregular patterns.

**Table 1.** Statistical description of 24 Urban Parks in Shanghai.

Park Group	Park Name	Park Area (ha)	Area Percentage (%)	Green Coverage (%)	Fuction	Predominant Tree Species and Main Biological Feature
Super large (>50 ha)	Century park	143.1380	0.1156	78.36	Integrated park	<i>Ginkgo biloba</i> L. (deciduous)
	GongQing forest park	127.0630	0.1026	85.08	Specialized park	<i>Ginkgo biloba</i> L.(deciduous + evergreen)
	Binjiang forest park	111.8870	0.0904	95.84	Specialized park	<i>Acer buergerianum</i> (deciduous)
	Minhang sports park	86.1472	0.0696	86.14	Integrated park	<i>Ginkgo biloba</i> L. (deciduous + evergreen)
	Shanghai botanical garden	77.9539	0.0630	72.43	Specialized park	<i>Cinnamomum camphora</i> (evergreen + deciduous)
	Daninyujinxiang park	58.0379	0.0469	79.37	Integrated park	<i>Ginkgo biloba</i> L. (deciduous + evergreen)
Large (10–50 ha)	Huangxing park	39.7864	0.0321	72.67	Integrated park	<i>Ginkgo biloba</i> L. (deciduous)
	Changfeng park	35.8347	0.0289	58.86	Integrated park	<i>Osmanthus fragrans</i> (evergreen)
	Zhongshan park	20.7742	0.0168	87.38	Integrated park	<i>Platycladus orientalis</i> (evergreen)
	Luxun park	20.2863	0.0164	78.32	Historic Garden	<i>Acer palmatum</i> (deciduous + evergreen)
	Jinqiao park	10.2522	0.0083	81.46	Community park	<i>Cedrus deodara</i> ( evergreen + deciduous)
	Medium (4–10 ha)	Guyi garden	9.5335	0.0077	88.83	Historic Garden
Lujiazui central green		9.2272	0.0075	83.47	Integrated park	<i>Magnolia denudata</i> (deciduous + evergreen)
Xujiahui park		9.0939	0.0073	92.24	Integrated park	<i>Ginkgo biloba</i> L. (deciduous)
Fuxing park		6.7610	0.0055	88.65	Historic Garden	<i>Platanus hispanica</i> (deciduous)
Tianshan park		5.7487	0.0046	65.83	Integrated park	<i>Pterocarya stenoptera</i> (deciduous + evergreen)
Zuibaichi park		4.7679	0.0039	96.81	Historic Garden	<i>Pseudolarix amabilis</i> (deciduous + evergreen)
Small (<4 ha)	Gushu park	4.2421	0.0034	88.29	Community park	<i>Ginkgo biloba</i> L. (deciduous)
	Gucheng park	3.7272	0.0030	89.73	Community park	<i>Osmanthus fragrans</i> (evergreen)
	Xianghe park	3.0011	0.0024	83.04	Community park	<i>Cinnamomum contractum</i> (evergreen)
	Jing'an park	2.7355	0.0022	77.84	Integrated park	<i>Platanus hispanica</i> (deciduous)
	Shangnan park	2.6522	0.0021	91.88	Community park	<i>Salix babylonica</i> L. (deciduous + evergreen)
	Jingnan park	2.5440	0.0021	95.03	Community park	<i>Magnolia grandiflora</i> (evergreen + deciduous)
Xiangyang park	2.1324	0.0017	87.76	Community park	<i>Prunus serrulata</i> (deciduous + evergreen)	

Notes: Area percentage = Percentage of the area of each park in the built-up area of Shanghai. Green coverage = Percentage of the trees or grass area in each park divided by park area. Function of each park came from the “Guiding opinions of Shanghai on the implementation of classified and hierarchical management of urban parks” jointly released by Shanghai Landscape and City Appearance Administrative Bureau and Forestry Bureau. The tree species types and main biological feature were retrieved from Baidu Encyclopedia. Because of the length of the table, the table only lists the dominant tree species in the park. The order of parks in Table 1 is consistent with that in Figure 1b.

## 2.2. Data Sources

The remote sensing data used in this study come from two periods of Landsat-8 OLI/TIRS satellite image data, two scenes of data at about 10:24 a.m. (UTC/GMT+08:00) on 3 August 2015 (path: 118, row: 38; path: 118, row: 39) and two scenes of data at about 10:25 a.m. on 16 August 2020 (path: 118, row: 38; path: 118, row: 39), which are obtained from Geospatial Data Cloud platform of Computer Network Information Center, Chinese Academy of Sciences (<http://www.gscloud.cn/search> (accessed on 15 May 2021)), and imported into ENVI 5.2 software for processing to obtain two periods of land surface temperature data in Shanghai. The maximum arbitrary land cloud cover threshold adopted in this study to ensure image reliability was less than 0.28%. Landsat-8 was successfully launched by NASA on February 11, 2013. It provides global coverage every 16 days and carries two sensors—OLI Land Imager and TIRS Thermal Infrared Sensor. Landsat-8 is basically consistent with Landsat 1-7 in terms of spatial resolution and spectral characteristics. The satellite

has a total of 11 bands. Band 1–7 and 9–11 have a spatial resolution of 30 m, and band 8 is a panchromatic band with a resolution of 15 m (<https://earthobservatory.nasa.gov/> (accessed on 26 August 2021)).

### 2.3. Data Processing and Analysis Methods

#### 2.3.1. Land Surface Temperature Retrieval Algorithm

A previous study result has shown that the accuracy of retrieved LST based on atmospheric profile measurement is 0.6 °C, by the radiative transfer equation [56]. Therefore, this study adopted an atmospheric correction method to retrieve the land surface temperature of Shanghai in two periods [27,57]. According to the radiation transmission theory of electromagnetic wave, the thermal infrared radiation brightness value received by the satellite sensor consists of three parts: blackbody radiation brightness, atmospheric downward radiation brightness and atmospheric upward radiation brightness [27]. Its equation, which is the radiative transfer equation (RTE), is as follows:

$$L_{\lambda} = [\varepsilon B(T_s) + (1 - \varepsilon)L \downarrow] \tau + L \uparrow \quad (1)$$

where  $L_{\lambda}$  is the radiance registered in the at-sensor of the thermal band ( $\text{W}\cdot\text{m}^{-2}\cdot\text{sr}^{-1}\cdot\mu\text{m}^{-1}$ ),  $B$  is the blackbody radiance ( $\text{W}\cdot\text{m}^{-2}\cdot\text{sr}^{-1}\cdot\mu\text{m}^{-1}$ ),  $T_s$  is the land surface temperature,  $L \downarrow$  is the downwelling path radiance,  $L \uparrow$  is the upwelling path radiance,  $\tau$  is the atmospheric transmittance, and  $\varepsilon$  is the land surface emissivity.

The equation for  $B(T_s)$  is as follows:

$$B(T_s) = \frac{[L_{\lambda} - L \uparrow - \tau(1 - \varepsilon)L \downarrow]}{\tau\varepsilon} \quad (2)$$

Finally,  $T_s$  can be calculated from the inversion of Planck's law, as follows:

$$T_s = \frac{K_2}{\ln\left(\frac{K_1}{B(T_s)} + 1\right)} \quad (3)$$

For the number 10 band  $K_1$  of Landsat 8, a constant of 774.89 ( $\text{watt}/(\text{m}^2\cdot\text{srad}\cdot\mu\text{m})$ ) was applied, and for  $K_2$ , a constant of 1321.08 K (Kelvin) was applied [36]. The value of  $\varepsilon$  was determined using the equation based on the NDVI threshold proposed by Sobrino et al. 2004 [56].

ENVI 5.2 software was first applied to interpret Landsat-8 OLI/TIRS images to obtain the land surface temperature of Shanghai in two periods. The experimental procedure for retrieving LST is shown in Figure 2.

For result validation, the multi-point verification method in Figure 2 represents verification of the LST values with the daily temperature data (i.e., the air temperature on 3 August 2015 and 16 August 2020 in this study) of multiple meteorological stations at the corresponding location. If the temperature trend of the retrieved results coordinates with meteorological station, the precision can be validated [50]. Hence, the corresponding temperature of five meteorological stations in Shanghai (including Pudong, Baoshan, Chongming, Hongqiao and Minhang) were used for validation (<https://www.ncei.noaa.gov/maps/daily/> (accessed on 10 December 2021)). The comparison between retrieved LSTs and the data from meteorological stations are shown in Figure A1. It is clearly indicated that the trend of the curves of the retrieved LST and the air temperature from five meteorological stations were the same in 2015 and 2020. Additionally, the retrieved LST showed a larger temperature difference, which is consistent with the characteristic between the air and land surface temperature [50]. In suburban areas such as Chongming District, there are more green spaces and bodies of water with fewer buildings, resulting in its low surface temperature, which in 2015 was lower than the air temperature. After comparison and verification, the overall accuracy can meet the requirements of application.

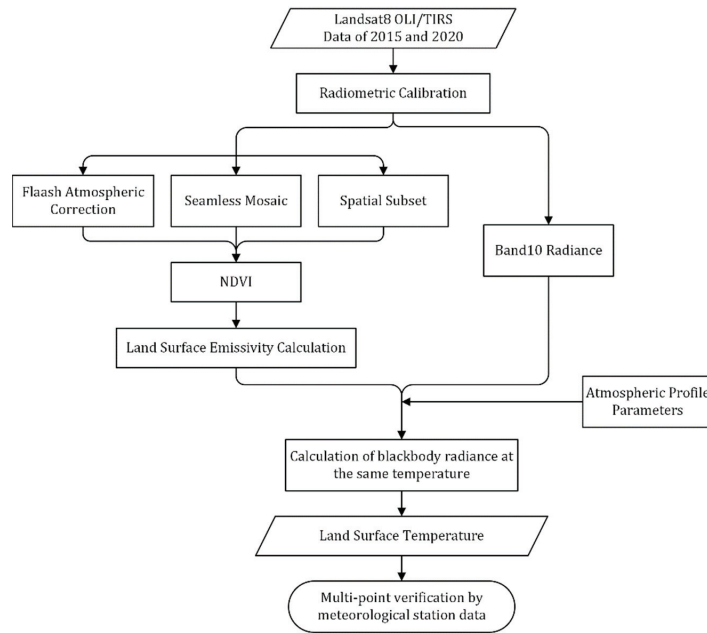


**Figure 2.** Diagram of land surface temperature retrieval process.

### 2.3.2. Temperature Division Method

In the study, natural breaks (Jenks) were taken as the temperature division method. Natural Breaks classes are based on natural groupings inherent in the data. Class breaks are identified that best group similar values and that maximize the differences between classes [58]. The features are divided into classes whose boundaries are set where there are relatively big differences in the data values. The Jenks optimization method, also called the Jenks natural breaks classification method, is a data classification method designed to determine the best arrangement of values into different classes. This is achieved by seeking to minimize each class's average deviation from the class mean, while maximizing each class's deviation from the means of the other groups. In other words, the method seeks to reduce the variance within classes and maximize the variance between classes. Natural breaks (Jenks), the classification method provided by ArcGIS, is the most commonly used and robust classification method. Chen J et al. (2013) [58] concluded that natural breaks (Jenks) method is of good adaptability and high accuracy on the geographical environment unit division.

### 2.3.3. Features Extraction of Park Landscape and Buffer Zone Analysis

The cooling effect of parks on surrounding thermal environment was analyzed from the aspects of park plaque morphology and landscape composition in the study. Landscape composition represents the size of different landscape types in the park. Plaque morphology is also known as landscape shape indicator, which usually calculates the deviation between a patch shape and a circle or square with the same area to measure the complexity of its shape. The selected indicators of quantitative analysis of park landscape are shown in Table 2 [32,35,59].

**Table 2.** Landscape Metrics of Shanghai’s Park and calculation method.

Classification	Landscape Metrics and Abbreviation	Calculation
Landscape composition	Green area (ha), GA	GA = green area of park
	Water area (ha), WA	WA = water area of park
	Proportion of impermeable layers (%), PIL	PIL = $A_i/PA \times 100\%$ ; $A_i$ = area of impermeable layers (PA-GA-WA)
Plaque morphology	Park area (ha), PA	PA = area of park
	Park perimeter (m), PP	PP = perimeter of park
	Park perimeter-to-area ratio (%), PPAR	PPAR = $PP/PA \times 100\%$
	Park fractal dimension, PFD	$D = 2 \times \ln(PP/4)/\ln(PA)$ [59]

Specifically, the vector maps of 24 parks, water systems, green spaces and road networks in the study area were precisely extracted from Amap by Python crawler module. Then, the basic metrics of the parks, such as the area and perimeter of parks, green spaces and water bodies were calculated by the “computational geometry” tool of the attribute table in each vector graph through ArcGIS 10.2 software. Subsequently, the indices of proportion of impermeable layers (PIL), park perimeter-to-area ratio (PPAR) and park fractal dimension (PFD), were calculated by “Field Calculator” tool based on the above attribute table, according to the formulas in Table 2.

The method of buffer zone is used to explore the cooling range and intensity of the park to its surrounding environment [29]. As the selected temperature retrieval images are from Landsat-8 OLI/TIRS with an initial spatial resolution of 100 m in the thermal infrared band, multiple graded buffers were generated outwards at this interval based on park boundaries. Some studies have reported that the range of the park cooling effect is usually around 10 s to 1000 s of meters, without exceeding 1.5 times of the width of the parks [45,60]. Therefore, 1.5 times the width of the park was set as the outermost boundary of the buffer zone in this study. Then, the cooling space was identified around each park to exclude larger areas of green space, water bodies and other influencing factors from the buffer zone, in order to homogenize the surface coverage of the analysis area as much as possible, so as to better analyze the mechanism of the park’s effect on the general urban substrate. Finally, the shapefile of each park and its buffer zone were spatially overlaid with the LST raster layers of the two phases separately to extract the average LST in the corresponding region.

The cooling effect of a park on LST can be measured in several ways [51]. Theoretically, a park’s cooling effect decreases with the distance from the edge of the park. For each park, there is an empirical relationship between the cooling intensity and the distance to the park edge. However, the cooling intensity is influenced by the surrounding environment, and may fluctuate with the distance and eventually reaches equilibrium with its surroundings; therefore, there may be several peaks on the fitness curve of the cooling intensity to the distance from the edge of the park [51]. So, we selected the cubic polynomial fitting to calculate the distance corresponding to the first peak of the cooling intensity as the MCD value [29]. In this study, two indicators were devised to quantify the cooling effect. The first is the Maximum Cooling Intensity (MCI) which was used as the indicator to quantify the cooling effect of the park according to Cheng X et al. (2015) [51]. It was calculated using equation:

$$MCI = T_H - T_L \quad (4)$$

where:  $T_H$  = the temperature at the first peak of the cubic polynomial fit curve,  $T_L$  = the temperature at a distance of zero from the park boundary of the cubic polynomial fit curve.

Another indicator is the Maximum Cooling Distance (MCD) which was defined as the largest distance where the Maximum Cooling Intensity (MCI) occurs. The maps of buffer analysis were produced using GIS software Arcmap 10.2 (Esri, Redlands, CA, USA).

#### 2.4. Statistical Analysis

First, Pearson's correlation analysis was utilized to assess the relationship between the mean LSTs inside and outside of the parks and each park landscape metrics. Subsequently, one way analysis of variance (ANOVA) was used to explore the significant differences between the cooling effects of different levels of parks on the surrounding thermal environment. The statistical analyses were conducted by SPSS 18.0 software. Additionally, SigmaPlot 13.0 was used as a supplementary statistical regression analysis and for mapping.

### 3. Results

#### 3.1. Land Surface Temperature Features of Shanghai and the Parks in 2015 and 2020

The Landsat-8 OLI/TIRS images in 2015 and 2020 were interpreted to obtain the results of land surface temperature in Shanghai (Figure 3) by atmospheric correction method, taking advantage of natural breaks (Jenks) to divide the temperature into five grades (Table 3). From the angle of space, there was some difference in the distributions of Shanghai's temperature between two periods of 3 August 2015 and 16 August 2020. The low-temperature zones of two periods were mainly distributed in the Yangtze River region and some areas near the East China Sea. The middle-low-temperature zones were mostly scattered in Chongming Island, the Huangpu River region in the northeast of the city as well as areas with dense water systems in the south and southeast of Shanghai. The middle-high- and high-temperature zones were mainly in the middle of Shanghai, where intensive commercial and residential districts exist. Additionally, the middle-temperature zones were primarily distributed around the surrounding zones of middle-high temperature and high temperature, and in Chongming Island and Changxing Island. From the angle of time, the overall average LST of Shanghai in 2020 (32.65 °C) was higher than that in 2015 (31.18 °C) by 1.47 °C. In addition, the highest and lowest LST in 2020 were 48.48 and 26.19 °C, respectively, 5.05 and 3.72 °C higher than that in 2015. It indicated that rapid urbanization has led to a significant increase in urban surface temperature.

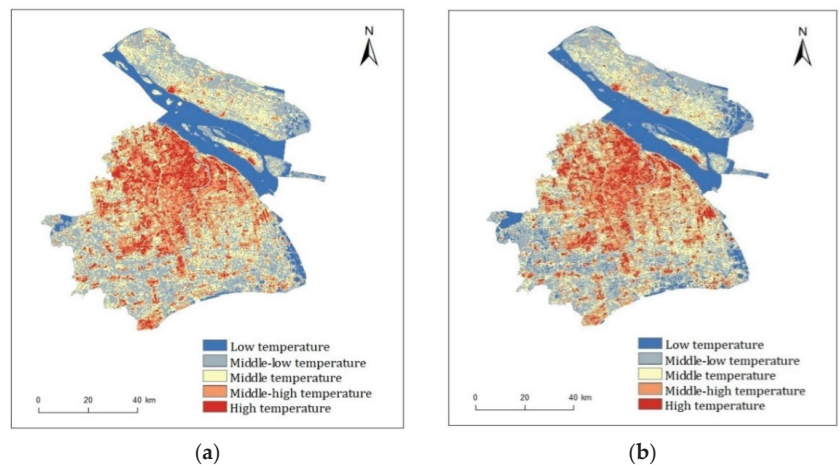


**Figure 3.** Land surface temperature derived from Landsat-8 OLI/TIRS images for the study area on 3 August 2015 (a) and 16 August 2020 (b), separately. Additionally, the temperature unit is centigrade.

**Table 3.** Classification of Land Surface Temperature in Shanghai.

Classification	Temperature Range in 2015 (°C)	Temperature Range in 2020 (°C)
Low temperature	<28.71	<30.03
Middle–low temperature	28.71–30.60	30.03–32.05
Middle temperature	30.60–32.25	32.05–34.06
Middle–high temperature	32.25–34.06	34.06–36.24
High temperature	>34.06	>36.24

In order to further compare the differences in LST and cooling capacity among these parks, the LST of the 24 parks and MCI in 2015 and 2020 are shown in Figure 4. It can be seen that there were evident differences among the LST inside the parks. The average LST and MCI of parks in 2020 were 1.73 and 0.53 °C higher than in 2015, respectively. The cooling effect of parks showed a certain fluctuation trend with the general increase in LST. For example, park 18 (Gushu park) had a relatively high LST (34.02 °C) and the strongest MCI (6.02 °C) in 2020. Park 3 (Binjiang forest park) had the lowest LST in 2015 (30.48 °C) and 2020 (31.84 °C), while its MCI scores were lower than the average temperature level. This suggested that the low LST inside the park did not imply a corresponding strong MCI. The cooling effect of the park is likely to be affected by other characteristics of the parks and the surrounding environment.

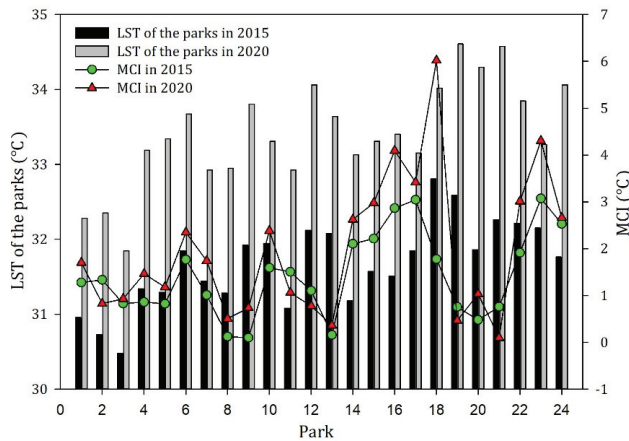


**Figure 4.** The LST inside the 24 parks and their MCIs in 2015 and 2020.

**3.2. Correlation of Park Landscape Features with Land Surface Temperature within the Parks**

To explore the quantitative relationship between the park landscape features and the mean land surface temperature within the parks, the quantitative indicators, such as park area, park perimeter, areas of different landscape elements and other metrics, were selected to analyze the correlation with the mean LST within the parks (Table 4). Additionally, the statistical regression analysis is shown as Figure 5. From the analyses, there are results as follows: (1) The park area showed a significant negative polynomial correlation with the mean LST within the parks in 2015 ( $r = -0.716, p < 0.01$ ), and also with that in 2020 ( $r = -0.719, p < 0.01$ ). (2) The park perimeter had a significant negative power correlation with the mean LST within the parks in 2015 ( $r = -0.690, p < 0.01$ ) and 2020 ( $r = -0.677, p < 0.01$ ). (3) The park perimeter-to-area ratio had a significant positive power correlation with the mean LST within the parks in 2015 ( $r = 0.632, p < 0.01$ ), and also in 2020 ( $r = 0.640, p < 0.01$ ). (4) The park fractal dimension exhibited an insignificant positive polynomial correlation with the mean LST within the parks in 2015 ( $r = 0.182,$

$R^2 = 0.4763$ ) and 2020 ( $r = 0.192$ ,  $R^2 = 0.4636$ ); the correlation is not significant. (5) There was a significant negative exponential correlation of the green area to the mean LST within the parks in 2015 ( $r = -0.722$ ,  $p < 0.01$ ) and 2020 ( $r = -0.729$ ,  $p < 0.01$ ). (6) The water area showed a significant negative polynomial correlation with the mean LST within the parks in 2015 ( $r = -0.498$ ,  $p < 0.05$ ) and with that of 2020 ( $r = -0.532$ ,  $p < 0.05$ ). (7) There was an insignificant negative polynomial correlation of the proportion of impermeable layers with the mean LST within the parks in 2015 ( $r = 0.312$ ,  $p > 0.05$ ), however, there was a significant positive polynomial correlation with that of 2020 ( $r = 0.536$ ,  $p < 0.01$ ).

**Table 4.** Pearson correlation coefficients of park landscape metrics with mean LST within the parks.

Landscape Metrics	In 2015		In 2020	
	Pearson Correlation	Sig.	Pearson Correlation	Sig.
PA	-0.716 **	0.000	-0.719 **	0.000
PP	-0.690 **	0.000	-0.677 **	0.000
PPAR	0.632 **	0.001	0.640 **	0.001
PFD	0.182	0.394	0.192	0.370
GA	-0.722 **	0.000	-0.729 **	0.000
WA	-0.498 *	0.013	-0.532 **	0.007
PIL	0.312	0.138	0.536 **	0.007

Notes: \* Correlation is significant at the 0.05 level (two-tailed). \*\* Correlation is significant at the 0.01 level (two-tailed). PA = park area, PP = park perimeter, PPAR = park perimeter-to-area ratio, PFD = park fractal dimension, GA = green area, WA = water area, PIL = proportion of impermeable layers (the same below).

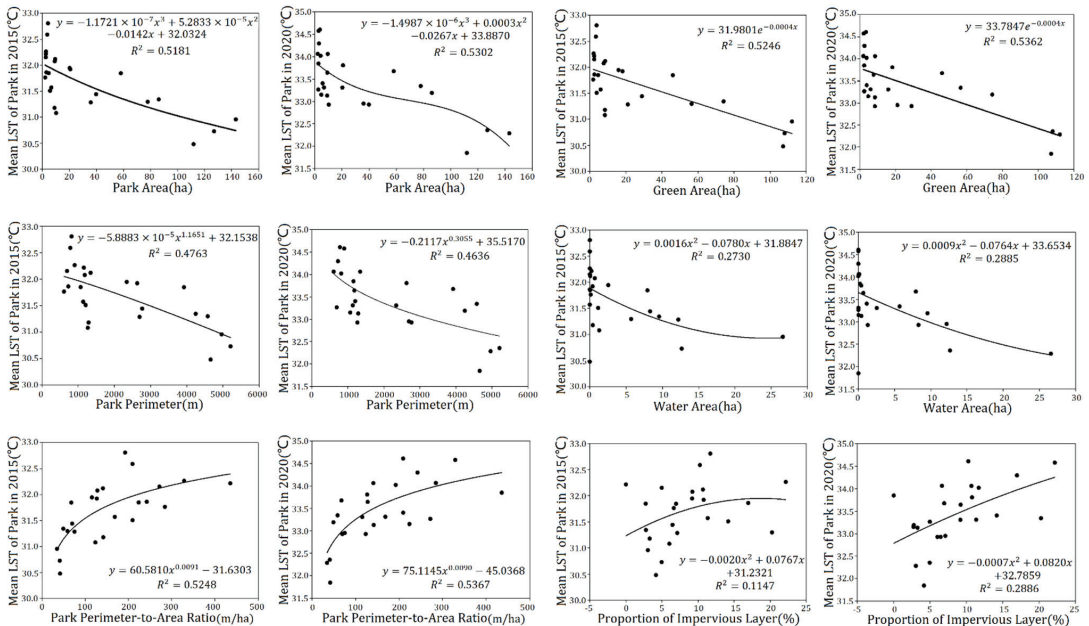


**Figure 5.** Regression analysis of park landscape metrics with mean LSTs in the parks. Note: LST = land surface temperature (the same below).

The above correlation analysis shows that PA, PP, GA, and WA are important characteristics that negatively affect the internal LST of the park. However, the more complex the shape of the park (PPAR), the higher LST inside the parks.



### 3.3. Correlation between Park Cooling Effect and Landscape Metrics

The size and landscape composition of the public parks have an impact on the Maximum Cooling Distance and the Maximum Cooling Intensity. In the study, the buffer zones of the 24 parks were established at an interval of 100 m, with 1.5 times of the width of every park, after excluding interference space such as water bodies and impermeable layers of large size, as the area of buffer zones (Figure 6).

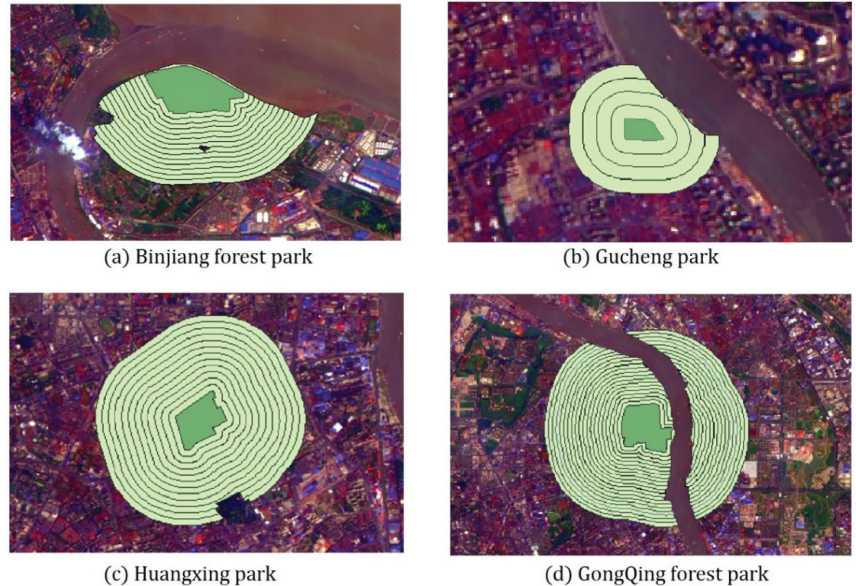


**Figure 6.** Four examples of parks' buffer zones.

Two indicators of Maximum Cooling Distance (MCD) and Maximum Cooling Intensity (MCI) were devised to measure the park cooling effects on surrounding thermal environment. The Maximum Cooling Distances and the maximum cooling intensities of the 24 parks in 2015 and 2020 (Table 5) have been obtained by cubic polynomial fitting ( $R^2 > 0.54$ ) between cooling distances and cooling intensities for the 24 urban parks in Shanghai. In 2015, the MCD exhibited large variations from 197.30 m recorded in Shangnan Park to 1041.71 m observed in Binjiang Forest Park, with a difference of 844.41 m. While the MCI was largest in Jingnan Park and smallest in Zhongshan Park, with a difference of 2.98 °C. In 2020, the MCD was also largest in Binjiang Forest Park at 1016.19 m and smallest in Gushu Park at 201.60 m, with a difference of 814.59 m; the MCI was greatest in Gushu Park and lowest in Jing'an Park, with a difference of 5.92 °C. Notably, the Gushu Park had the smallest MCD but the strongest MCI.

Then, the correlation analysis (Table 6) of park landscape metrics with Maximum Cooling Distance and Maximum Cooling Intensity was conducted. It can be seen that the MCD for 2015 and 2020, had a significant correlation with PA, PC, PPAR, GA and WA, while the MCI of two periods had no significant correlation with any of the seven park landscape metrics. Furthermore, different from other metrics, PPAR were negatively and significantly correlated with MCD and positively correlated with the MCI both in these two years. This result implies that the more complex the shape of the park boundary, the smaller the cooling distance, but the stronger the cooling intensity. Thus, the MCD for 2015 and 2020 were fitted (Figure 7) to PA, PC, PPAR, GA and WA for further exploration.

**Table 5.** Maximum Cooling Distance and Maximum Cooling Intensity of the 24 parks in Shanghai.

Park Grade	Park Name	In 2015		In 2020	
		MCD (m)	MCI (°C)	MCD (m)	MCI (°C)
Super large parks (≥ 50 ha)	Century park	706.9506	1.2782	762.3386	1.7007
	GongQing forest park	795.7450	1.3335	570.4900	0.8273
	Binjiang forest park	1041.7070	0.8286	1016.1858	0.9299
	Minhang sports park	522.2678	0.8592	861.2296	1.4615
	Shanghai botanical garden	634.6422	0.8223	539.7231	1.1805
	Daninyujinxiang park	585.0422	1.7656	568.6326	2.3472
Large parks (10–50 ha)	Huangxing park	554.9581	1.0104	633.7859	1.7390
	Changfeng park	881.0605	0.1235	881.0605	0.5083
	Zhongshan park	412.2149	0.0986	799.8771	0.7355
	Luxun park	381.2560	1.5903	365.7999	2.3829
	Jinqiao park	472.2197	1.5060	502.9135	1.0606
Medium parks (4–10 ha)	Guyi garden	252.9480	1.1000	217.5562	0.7764
	Lujiazui central green	510.3497	0.1572	527.7217	0.3621
	Xujiahui park	393.4313	2.1042	328.3025	2.6251
	Fuxing park	304.8691	2.2150	283.3706	2.9778
	Tianshan park	441.1852	2.8666	273.8877	4.0943
	Zuibaichi park	260.5534	3.0442	291.7883	3.4186
Small parks (≤ 4 ha)	Gushu park	284.7108	1.7763	201.6045	6.0184
	Gucheng park	353.0546	0.7561	338.6038	0.4656
	Xianghe park	347.0739	0.4785	339.1409	1.0331
	Jing'an park	316.6093	0.7609	316.6093	0.0988
	Shangnan park	197.3022	1.9122	203.9789	3.0141
	Jingnan park	218.6293	3.0756	225.7952	4.3050
Xiangyang park	248.9833	2.5277	248.9833	2.6617	

Notes: MCD = Maximum Cooling Distance, MCI = Maximum Cooling Intensity (the same below).

**Table 6.** Pearson correlation coefficients of park landscape metrics with MCD and MCI.

Landscape Metrics	In 2015				In 2020			
	MCD		MCI		MCD		MCI	
	Pearson Correlation	Sig.	Pearson Correlation	Sig.	Pearson Correlation	Sig.	Pearson Correlation	Sig.
PA	0.792 **	0.000	−0.267	0.207	0.715 **	0.000	−0.292	0.166
PP	0.805 **	0.000	−0.335	0.109	0.769 **	0.000	−0.330	0.116
PPAR	−0.757 **	0.000	0.392	0.059	−0.733 **	0.000	0.330	0.115
PFD	−0.220	0.303	0.094	0.663	−0.128	0.551	0.053	0.807
GA	0.790 **	0.000	−0.254	0.232	0.715 **	0.000	−0.287	0.173
WA	0.575 **	0.003	−0.215	0.313	0.549 **	0.006	−0.203	0.341
PIL	−0.148	0.490	−0.298	0.157	−0.234	0.272	−0.194	0.365

Note: \*\* Correlation is significant at the 0.01 level (two-tailed).

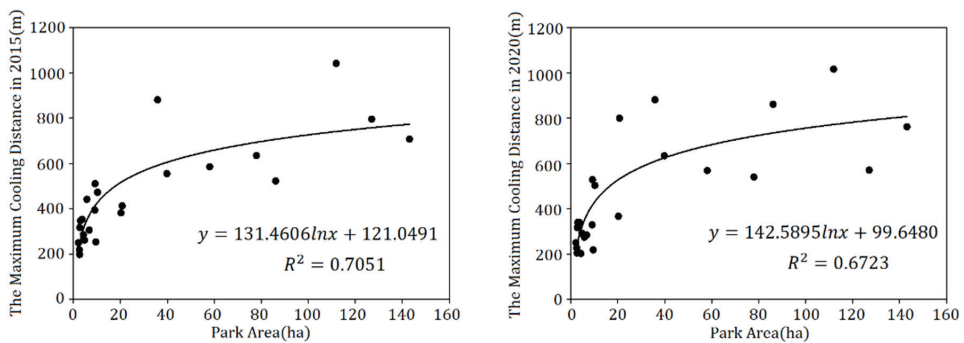


**Figure 7.** Cont.

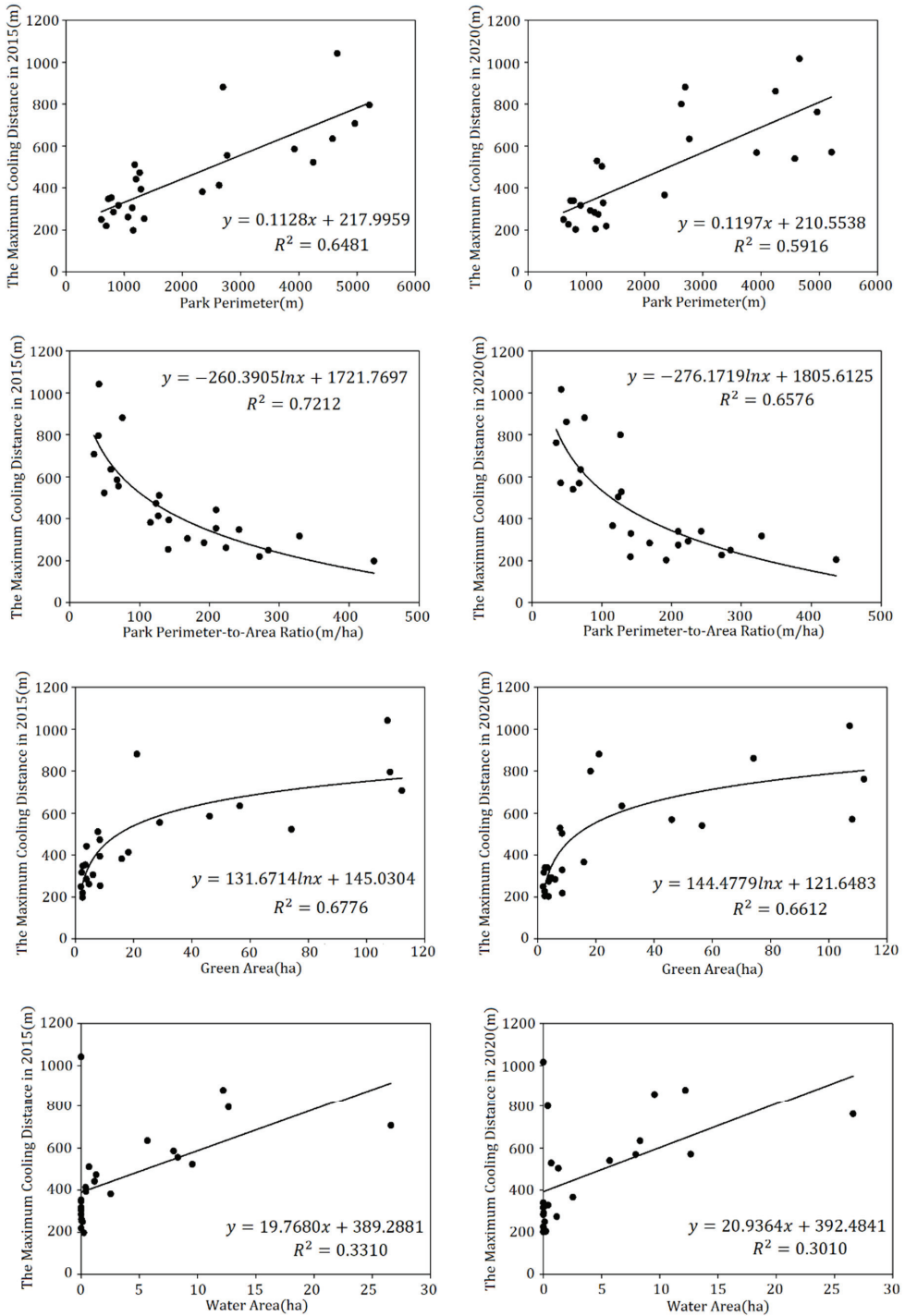


Figure 7. Correlation of park landscape metrics of PA, PP, PPAR, GA, WA with MCD for 2015 and 2020.

3.4. One Way ANOVA of the Influence of Different Park Groups on the Cooling Effect Indicators

To further explore the impact of the park on the surrounding thermal environment, the additional study was conducted in six super large parks (>50 ha), five large parks (10–50 ha), seven medium parks (5–10 ha) and six small parks (<4 ha), in terms of the relationships between park size group and the two cooling effect indicators of Maximum Cooling Distance (MCD) and Maximum Cooling Intensity (MCI). The mean MCD of different park groups in both 2015 and 2020 decreased with park class, while there was no significant linear correlation between the mean MCI and park class in 2015 and 2020, with the medium park group having the largest cooling intensity in both two periods, followed by the small park group. It was also evident that the difference between the mean MCD of different park groups in 2015 and in 2020 was generally small, while the mean MCI of different park groups in 2020 was significantly higher than that in 2015 (Figure 8).

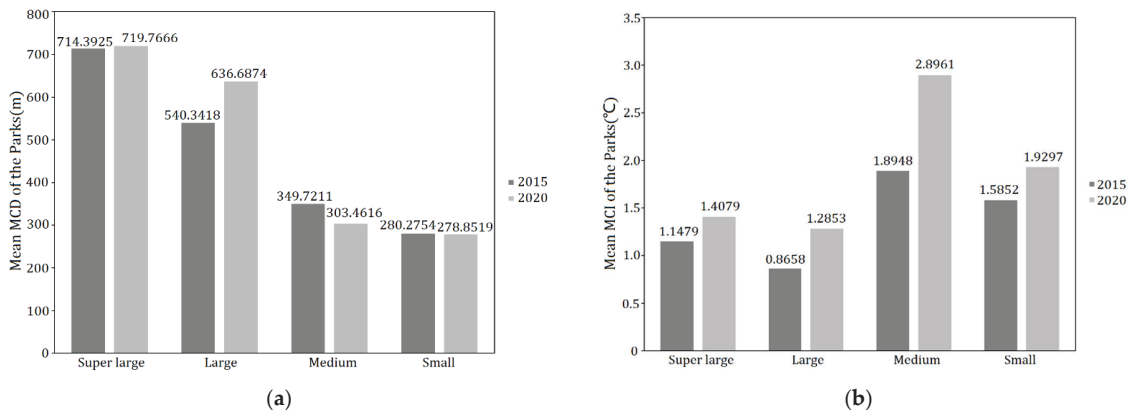


Figure 8. Mean MCD (a) and MCI (b) of different park groups in 2015 and 2020.

Then, analysis of variance (ANOVA) on the mean MCD and MCI at different park classes was further performed. According to the test of homogeneity of variances by SPSS, the significance values (Sig.) of MCD and MCI of two periods (2015 and 2020) were greater than 0.05, which meant that, the variance meets the requirement of homogeneity, after which the analysis of variance (ANOVA) could be performed. Referring to ANOVA (Table 7), the significance values (Sig.) of MCI in 2015 and 2020 were greater than 0.05, while the significance values (Sig.) of MCD were less than 0.01 in both periods. In other words, both in 2015 and 2020, the difference between the MCI of the four park groups was not significant and not statistically significant, while the opposite was true for the MCD of the parks of the four park groups, where the difference was statistically significant.

Table 7. ANOVA results of MCI and MCD among park green spaces of different scales.

		Sum of Squares	Mean Square	F	Sig.
MCI in 2015	Between Groups	3.721	1.240	1.687	0.202
	Within Groups	14.705	0.735		
	Total	18.426			
MCI in 2020	Between Groups	10.241	3.414	1.704	0.198
	Within Groups	40.061	2.003		
	Total	50.301			

Table 7. Cont.

		Sum of Squares	Mean Square	F	Sig.
MCD in 2015	Between Groups	699,250.864	233,083.621	11.130	0.000
	Within Groups	418,854.943	20,942.747		
	Total	1,118,105.807			
MCD in 2020	Between Groups	926,578.689	308,859.563	13.640	0.000
	Within Groups	452,884.738	22,644.237		
	Total	1,379,463.427			

However, as the ANOVA was only able to determine whether the control variables had a significant effect on the observed variables, the next step was to conduct a multiple comparison test using the Least Significant Difference (LSD) method to further determine the exact degree of variation in MCD across the different park groups. As can be seen from the results (Figure 9), with consistency in 2015 and 2020, there was significant difference in MCD between super large and large park groups, as well as medium and small park groups, while the differences between super large and large park group and between medium and small park group were not significant. The LSD result suggested that the ability of parks of more than 10 hectares (the boundary value between large- and medium-sized parks) to affect the cooling distance was significantly enhanced.

To further assess the effects of the potential differences between the groups, the landscape metrics data were also applied to the one-way ANOVA (Figure 10). The significant difference law of PP and PPAR was similar to that of MCD, while PA and GA values represented significant differences between super large parks and other types. Among the seven landscape characteristic metrics, the differences in five metrics among four park groups were significant, except for PFD and PIL.

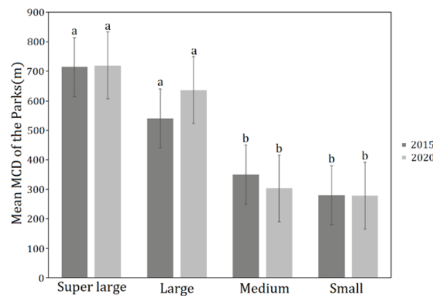
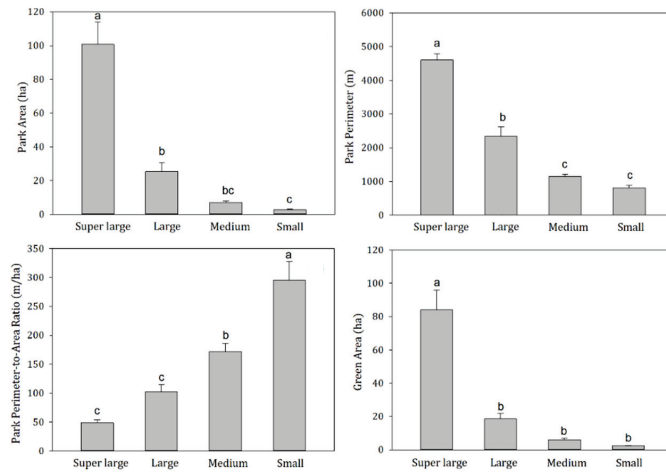


Figure 9. Differences in mean MCD of the parks in two periods for different park groups. Bars and line error represent mean ± standard deviation (S.D.). Lowercase letters indicate significant differences ( $p < 0.05$ ) among park groups (the same below).



**Figure 10.** Differences in main landscape metrics (PA, PP, PPAR, GA) among different park groups.

## 4. Discussion

### 4.1. Influence of Park Landscape Characteristics on Local Surface Temperature

As an important part of the urban landscape, the park landscape not only provides recreational areas for the surrounding residents, but also to a certain extent regulates the regional climate. The cooling effect of green spaces inside the urban park is a phenomenon that has been widely studied and validated in various regions and cities [39,42,61]. In this study, we investigated and analyzed the distribution pattern of thermal environment inside and outside the urban park through a remote sensing retrieval method. The results indicate that green spaces in parks form obvious cold islands in the city, and whether from the morphological characteristics or the composition of patches, there are key factors affecting the cooling effect. Therefore, it is important to plan the construction of urban parks in a city like Shanghai where the urban area is an expensive space. Numerous studies have shown that a park's patchy morphology and its internal landscape metrics have a significant cooling effect on the local thermal environment [29,51]. This study found that in 2015, the average temperature of the 24 parks was 31.68 °C, 1.46 °C lower than that in the main urban area of Shanghai (33.14 °C) in that year; in 2020, the average temperature of the 24 parks was 33.42 °C, 1.66 °C lower than that in the main urban area of Shanghai (35.08 °C) in that year. This temperature difference is consistent with the conclusion drawn by Bowler et al. (2010) [62], in which the meta-analysis of data from different studies suggested that, on average, an urban park would be around 1 °C cooler than a non-green site.

This study also found that the park's patch morphology and configuration characteristics had an impact on the thermal environment of the park. The negative relationship of mean LST of two periods to park area suggests that the LST of a park decreases with increasing park area, as well as the park perimeter. The park perimeter-to-area ratio (PPAR) had a significant positive correlation with the mean park LST ( $r = 0.63, p < 0.01$ ). Additionally, the greater the PPAR, the relatively more complex the shape of the park, the easier it is to exchange material energy within the park, and the higher the mean LST of the park. However, Zhu et al. (2021) [29] found that the correlation coefficient between them was  $-0.39$  ( $p < 0.01$ ), indicating that parks with irregular shapes could have lower LSTs. This might be attributable to the differences in the range of PPAR of the parks and different climate backgrounds.

From the perspective of the park's landscape composition, the negative exponential relationship of mean LST in two periods to green area suggests that the mean LST of the park decreases as the green area increases. The results of the exponential fit of the mean LST to the green area for both periods are approximately linear, and the calculation shows

that for every 50-ha increase in the green space area within the park in 2015, the average park temperature decreased by approximately 0.63 °C, and for every 50-ha increase in the green space area within the park in 2020, the average park temperature decreased by approximately 0.66 °C. Therefore, when planning the internal landscape composition of urban parks, the size of the green space area should be fully considered and the green space area inside the parks should be increased as much as possible. This is because vegetation can reduce the LST through evapotranspiration and shadows, which has been proven by several studies [37,41,50].

In addition to this, the water area within the park also plays an important role in reducing the mean LST. The high specific heat capacity of the water body and the fact that evaporation from the water body can absorb some of the heat from the air results in the mean LST of the park decreasing as the water area increases [52]. The effect on temperature is relatively significant as the water area increases from 0 to 20 ha. At the same time, considering that Shanghai is a densely populated and fast-growing metropolis, its park landscape area is limited, so from the perspective of urban park landscape planning, it is more reasonable to consider the actual situation of the water body for providing greater cooling benefits. However, the results of the study show that the proportion of the impervious layer in the park had no significant effect on the mean LST of the park in 2015. Several parks selected in this study, such as Binjiang Forest Park and Jingnan Park, are surrounded by wide rivers and/or large green space (green space coverage rate exceeds 90%, shown in Table A1), which has a cooling effect on the parks and could have some impact on the results.

#### 4.2. Influence of Park Landscape Characteristics on the Surrounding Thermal Environment

The scale of any cooling effect beyond the boundary of the green area is particularly important for the likely public health consequences of park greening, as park green space may not be directly accessible to all who might benefit during high temperatures [62]. Therefore, the key influencing factors and laws of the scale and intensity of cooling effect have been examined by scholars. The results reported in this paper showed that the landscape metrics of park area (PA), park perimeter (PP), park perimeter-to-area ratio (PPAR), green area (GA), water area (WA), as the critical influencing factors, influence the cooling effect of the park on the surrounding thermal environment. This result coincides with the findings of other scholars [29,37,51]. However, the effects of the park landscape features on the cooling indicator MCD were significant, while the effect on MCI was not. MCI is an indicator of temperature difference that depends not only on the LST of the park, but also on the land surface temperature around the park (Figure 3). Shanghai is located at the confluence of the Yangtze and Huangpu rivers, with a low and flat topography and a dense network of water. Many parks in Shanghai are surrounded by dense fine water flows, but in this study, buffer zones of parks did not eliminate these fine streams or some of the smaller green areas, which may have caused a slightly lower calculated surface temperature in the buffer zone than in reality.

From the plaque morphology of the park, the Maximum Cooling Distance (MCD) in 2015 ( $R^2 = 0.70$ ) and 2020 ( $R^2 = 0.67$ ) of park increased logarithmically and sharply within the park area of 20 ha but eventually reached an asymptote. After the park area exceeded the threshold (about 20–40 ha), the cooling distance tends to be gentle with the increase in the park area. Combined with the results of the MCI of the park groups, the cooling intensity of medium- (4–10 ha) and small-scale parks (<4 ha) is evidently higher than that of the super large and large group (Figure 8b). This result is in agreement with that of a previous study, in which super large parks with areas exceeding 30 ha on average were not more efficient than small parks less than 3 ha when measured by mean ratio of cooling area to park size [51]. Additionally, the Maximum Cooling Distance of the park increases linearly with increasing park perimeter. The larger the park area and the greater the park perimeter, the greater the Maximum Cooling Distance and the more significant the cooling effect of the park. In addition, the PPAR and the park's Maximum Cooling Distance (MCD)

had a negative logarithmic relationship (in 2015:  $R^2 = 0.72$ , in 2020:  $R^2 = 0.66$ ). The smaller the PPAR, the simpler the park shape, and the more pronounced the cooling effect distance of the park on the surrounding environment. When planning and building urban parks it is necessary to take into account controlling the park PPAR from 0 to 100 to achieve a better cooling effect of park. Analyzed in terms of the park's landscape composition, MCD of the park increased logarithmically with park green area and linearly with the park's water area. According to the fitting results of the two periods (Figure 7), the degree of impact of the green area on the park surroundings increased sharply from 0 to 20 ha. When the vegetation area reached a certain threshold, the degree of impact tended to increase smoothly. For every 10-ha increase in the area of park water bodies, the cooling distance of park increased by 197.68 m in 2015 and 209.36 m in 2020. Transpiration from the green space and evaporation from the water body can absorb heat from the land surface and produce water vapor, which then generates wind under the action of the horizontal pressure gradient force at the land surface, resulting in a more efficient exchange of material and energy in the horizontal direction, thus mitigating the sharp rise in temperature around the park. In the planning of urban parks in metropolitan cities such as Shanghai, compared with the difficult control of water area, the proportion of green space in the parks should be maximized and the proportion of impermeable layers should be controlled while taking into account aesthetics.

#### 4.3. Influence of Different Park Size Groups on the Cooling Effect Indicators

Cheng X et al., 2015, concluded that park size can explain nearly 73% of the variance in cooling distance; therefore, park size is the main factor that influences the cooling effect on land surface temperature [51]. Our results showed that the cooling distance of most parks in the study were limited within 600 m. Only a few very large parks have cooling distance over 800 m. The Maximum Cooling Distance varied significantly under different park size grades. The mean MCD values for the super large and large park groups are much larger than for medium and small ones. This is consistent with the findings of other scholars that park size does have a significant effect on the cooling effect of parks [16,37,44]. Whereas the values of mean MCD of the super large and large park groups in 2020 were larger than that in 2015, those of small and medium park group had instead shrunk slightly. With urban temperatures rising year by year, it is clear that small (<4 ha) and medium (4–10 ha) park groups have less scope for cooling influence than super large (>50 ha) and large (10–50 ha) park groups. Therefore, more large parks can be considered in large cities with a dense water network such as Shanghai, and water systems should be included in or adjacent to parks as much as possible, so that the cooling effect of parks and these water systems interact with each other to achieve a stronger cooling island effect. However, the cooling intensity of medium and small parks with less than 10 hectares should not be ignored. On the contrary, it needs to be fully utilized, especially in metropolises such as Shanghai.

#### 4.4. Limitations

Land surface temperature (LST) has been widely used to describe the cooling effect of green spaces on Urban Heat Islands [16,25,55]. When using LST data rather than air temperature to study the cooling effect of parks, the intensity of cold islands is often overestimated because LST responds to direct solar radiation reaching the land surface [16]. However, remotely sensed land surface temperature data can provide more detailed spatial information and data, and they are easier to manipulate than obtaining air temperature data. Subsequent studies may consider comparing multiple inversion algorithms or using high-resolution image data combined with weather station data for calibration, etc., to make the temperature data more accurate and reliable.

According to available studies, the intensity of cold islands in the park varies during the day and night [7,45], as well as seasonally [16,63,64]. Nevertheless, only two days of Landsat-8 OLI/TIRS data during summer daytime for two periods (3 August 2015, 16 August 2020) were selected for this paper, due to the limitation of data acquisition



quality and article length. The time difference between days may also induce slight errors for the comparison of LSTs between years. Although it can reflect the changes in cooling effect in different years during typical summer daytime to a certain extent, it can neither reflect the changes in cooling effect in the park by day and night, nor the changes in cooling effect by season. The amount of data should be further increased appropriately to analyze changes in the cooling effect of the park landscape. In addition, although this paper excluded larger areas of green space and water space within buffer zones, it is not precise enough to consider the effect of fine water flows and small areas of greenfield vegetation around the park on land surface temperatures. Additionally, considering that the condition of LST and configuration of greenspace may be scale dependent, a study across spatial scales should be carried out to better understand the impact mechanism of public parks on the thermal environment.

## 5. Conclusions

Understanding the effects of structure and configuration characteristics in park landscape on inside-park LST and cooling efficiency in the buffer zone is important for designing effective strategies to mitigate the amplitude of UHI. In this study, Landsat-8 OLI/TIRS images in hot-summer daytime of 2015 and 2020 representing the rapid urbanization process were interpreted, from which the LSTs were retrieved. Based on that, the relationships between park landscape features with LSTs inside the park and two cooling efficiency indicators representing change in their surrounding thermal environment were studied. We found that the average LST of urban parks was 31.68 °C in 2015 and 33.42 °C in 2020, which was 1.46 and 1.66 °C lower than that of the main urban area of Shanghai, respectively. Therefore, public parks have been performing the service functions of regulating the local thermal environment of the city. For the two indicators of MCD and MCI, the MCD results exhibited large variations ranging from 197.30 m to 1041.71 m and MCI ranges from 0.10 °C to 6.02 °C in 24 parks. The cooling distance and intensity of most parks in the study were concentrated within 600 m and 3 °C.

In terms of the park's plaque morphology and configuration, the landscape metrics of PA, PP, GA and WA, were important characteristics that negatively affected the internal LST of the parks. However, the park PPAR had a significant positive power correlation with the park LST data. Subsequently, the MCD for 2015 and 2020 had a significant correlation with PA, PC, PPAR, GA and WA, while the MCI of two periods had no significant correlation with any of the seven park landscape metrics. Not surprisingly, larger parks had a longer cooling distance and the MCD increased logarithmically and sharply within the park area of 20 ha. However, the medium park group had the largest cooling intensity in both periods, followed by the small park group. Therefore, the cooling intensity of medium and small parks with less than 10 hectares should be fully utilized, especially in metropolises such as Shanghai with expensive space. This result also indicated that the more complex the shape of the park boundary, the smaller the cooling distance but the stronger the cooling intensity. Therefore, whether there is a trade-off relationship between the Maximum Cooling Distance and intensity of urban parks is worth pondering and continuing to research. Additionally, the original water systems should be included in or adjacent to parks as far as possible, so that the cooling effects of both can be superimposed on each other to produce a stronger cooling effect. The limitation of this paper is that the seasonal and diurnal changes in LST were not studied. At the same time, extracting the characteristics of the park combined with higher resolution images should be considered in the future. For future research we will also carry out multi-scale and multi-region comparison studies to advance our understanding of the trade-off relationship between the cooling distance and intensity of urban parks in order to maximizing the cooling effects.

**Author Contributions:** Conceptualization, T.W., H.T.; methodology, T.W., H.T., B.M.; software, H.T., B.M., Z.L.; validation, H.T., B.M.; formal analysis, T.W., X.L.; investigation, T.W., H.T., B.M.; resources, H.T., B.M., X.L.; data curation, H.T.; writing—original draft preparation, H.T., T.W.; writing—review and editing, T.W., H.T., X.L.; visualization, Z.L.; supervision, Z.L., Q.Y.; project administration, T.W., Q.Y.; funding acquisition, T.W. All authors have read and agreed to the published version of the manuscript.

**Funding:** This research was funded by the National Natural Science Foundation of China (Grant No. 31800392), the Research Fund Project of Changzhou Institute of Technology (YN1782).

**Conflicts of Interest:** The authors declare no conflict of interest.

**Appendix A**

**Table A1.** Multiple Comparisons of MCD among park green spaces of different scales.

Dependent Variable	(I) Park Group	(J) Park Group	Mean Difference (I–J)	Std. Error	Sig.	95% Confidence Interval	
						Lower Bound	Upper Bound
MCD in 2015	Super large	Large	174.0506	87.6299	0.061	-0.8009	1.3652
		Medium	364.6714 *	80.5126	0.000	-1.7420	0.2482
		Small	434.1170 *	83.5518	0.000	-1.4699	0.5954
	Large	Super large	-174.0506	87.6299	0.061	-1.3652	0.8009
		Medium	190.6208 *	84.7370	0.036	-2.0763	0.0183
		Small	260.0664 *	87.6299	0.008	-1.8025	0.3637
	Medium	Super large	-364.6714 *	80.5126	0.000	-0.2482	1.7420
		Large	-190.6208 *	84.7370	0.036	-0.0183	2.0763
		Small	69.4456	80.5126	0.399	-0.6855	1.3047
	Small	Super large	-434.1170 *	83.5518	0.000	-0.5954	1.4699
		Large	-260.0664 *	87.6299	0.008	-0.3637	1.8025
		Medium	-69.4456	80.5126	0.399	-1.3047	0.6855
MCD in 2020	Super large	Large	83.0792	91.1201	0.373	-1.6651	1.9103
		Medium	416.3050 *	83.7193	0.000	-3.1307	0.1542
		Small	440.9147 *	86.8796	0.000	-2.2263	1.1826
	Large	Super large	-83.0792	91.1201	0.373	-1.9103	1.6651
		Medium	333.2257 *	88.1120	0.001	-3.3395	0.1178
		Small	357.8355 *	91.1201	0.001	-2.4321	1.1432
	Medium	Super large	-416.3049 *	83.7193	0.000	-0.1542	3.1307
		Large	-333.2257 *	88.1120	0.001	-0.1178	3.3395
		Small	24.6097	83.7193	0.772	-0.6761	2.6089
	Small	Super large	-440.9147 *	86.8796	0.000	-1.1826	2.2263
		Large	-357.8355 *	91.1201	0.001	-1.1432	2.4321
		Medium	-24.6097	83.7193	0.772	-2.6089	0.6761

Note: \* The mean Difference between the park groups is significant at the 0.05 level.

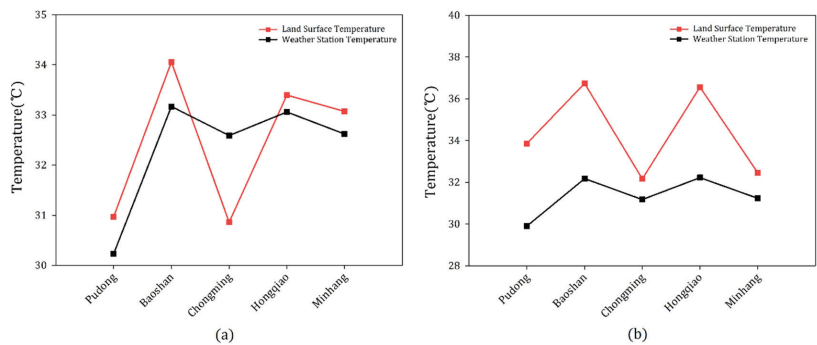


**Figure A1.** Comparison and verification of the air temperature and the LSTs in Shanghai on 3 August 2015 (a) and 16 August 2020 (b), respectively.

## References

1. Cubasch, U.; Wuebbles, D.; Chen, D.; Facchini, M.C.; Frame, D.; Mahowald, N.; Winther, J.G. Introduction. In *Climate Change 2013: The Physical Science Basis. Contribution of Working Group I to the Fifth Assessment Report of the Intergovernmental Panel on Climate Change*; Stocker, T.F., Qin, D., Plattner, G.-K., Tignor, M., Allen, S.K., Boschung, J., Nauels, A., Xia, Y., Bex, V., Midgley, P.M., Eds.; Cambridge University Press: Cambridge, UK; New York, NY, USA, 2013.
2. Brysse, K.; Oreskes, N.; O'Reilly, J.; Oppenheimer, M. Climate change prediction: Erring on the side of least drama? *Glob. Environ. Chang.* **2013**, *23*, 327–337. [[CrossRef](#)]
3. DESA. *World Urbanization Prospects: The 2014 Revision*; United Nations Department of Economics and Social Affairs, Population Division: New York, NY, USA, 2015; Volume 41.
4. Stewart, I.D. A systematic review and scientific critique of methodology in modern Urban Heat Island literature. *Int. J. Climatol.* **2011**, *31*, 200–217. [[CrossRef](#)]
5. Clinton, N.; Gong, P. MODIS detected surface Urban Heat Islands and sinks: Global locations and controls. *Remote Sens. Environ.* **2013**, *134*, 294–304. [[CrossRef](#)]
6. Li, X.; Zhou, Y.; Asrar, G.R.; Imhoff, M.; Li, X. The surface Urban Heat Island response to urban expansion: A panel analysis for the conterminous United States. *Sci. Total Environ.* **2017**, *605–606*, 426–435. [[CrossRef](#)]
7. Peng, S.; Piao, S.; Ciais, P.; Friedlingstein, P.; Ottle, C.; Breon, F.-M.; Nan, H.; Zhou, L.; Myneni, R.B. Surface Urban Heat Island across 419 global big cities. *Environ. Sci. Technol.* **2012**, *46*, 696–703. [[CrossRef](#)]
8. Memon, R.A.; Leung, D.Y.; Chunho, L. A review on the generation, determination and mitigation of Urban Heat Island. *J. Environ. Sci.* **2008**, *20*, 120–128.
9. Basu, R.; Samet, J.M. Relation between Elevated Ambient Temperature and Mortality: A Review of the Epidemiologic Evidence. *Epidemiol. Rev.* **2002**, *24*, 190–202. [[CrossRef](#)]
10. Wong, L.P.; Alias, H.; Aghamohammadi, N.; Aghazadeh, S.; Nik Sulaiman, N.M. Urban Heat Island experience, control measures and health impact: A survey among working community in the city of Kuala Lumpur. *Sustain. Cities Soc.* **2017**, *35*, 660–668. [[CrossRef](#)]
11. Wu, Z.; Zhang, Y. Spatial Variation of Urban Thermal Environment and Its Relation to Green Space Patterns: Implication to Sustainable Landscape Planning. *Sustainability* **2018**, *10*, 2249. [[CrossRef](#)]
12. Santamouris, M. Analyzing the heat island magnitude and characteristics in one hundred Asian and Australian cities and regions. *Sci. Total Environ.* **2015**, *512–513*, 582–598. [[CrossRef](#)]
13. Morabito, M.; Crisci, A.; Guerri, G.; Messeri, A.; Congedo, L.; Munafo, M. Surface Urban Heat Islands in Italian metropolitan cities: Tree cover and impervious surface influences. *Sci. Total Environ.* **2021**, *751*, 142334. [[CrossRef](#)] [[PubMed](#)]
14. Voogt, J.A.; Oke, T.R. Thermal remote sensing of urban climates. *Remote Sens. Environ.* **2003**, *86*, 370–384. [[CrossRef](#)]
15. Zhou, D.; Xiao, J.; Bonafoni, S.; Berger, C.; Deilami, K.; Zhou, Y.; Frolking, S.; Yao, R.; Qiao, Z.; Sobrino, J. Satellite Remote Sensing of Surface Urban Heat Islands: Progress, Challenges, and Perspectives. *Remote Sens.* **2018**, *11*, 48. [[CrossRef](#)]
16. Cao, X.; Onishi, A.; Chen, J.; Imura, H. Quantifying the cool island intensity of urban parks using ASTER and IKONOS data. *Landscape Urban Plan.* **2010**, *96*, 224–231. [[CrossRef](#)]
17. Chakraborty, T.; Lee, X. A Simplified Urban-Extent Algorithm to Characterize Surface Urban Heat Islands on a Global Scale and Examine Vegetation Control on Their Spatiotemporal Variability. *Int. J. Appl. Earth Obs. Geoinf.* **2019**, *74*, 269–280. [[CrossRef](#)]
18. Feizizadeh, B.; Blaschke, T. Examining Urban Heat Island Relations to Land Use and Air Pollution: Multiple Endmember Spectral Mixture Analysis for Thermal Remote Sensing. *IEEE J-Stars* **2013**, *6*, 1749–1756. [[CrossRef](#)]
19. Mayes, M.T.; Mustard, J.F.; Melillo, J.M. Forest cover change in Miombo Woodlands: Modeling land cover of African dry tropical forests with linear spectral mixture analysis. *Remote Sens. Environ.* **2015**, *165*, 203–215. [[CrossRef](#)]
20. Cristóbal, J.; Jiménez-Muñoz, J.; Prakash, A.; Mattar, C.; Skoković, D.; Sobrino, J. An Improved Single-Channel Method to Retrieve Land Surface Temperature from the Landsat-8 Thermal Band. *Remote Sens.* **2018**, *10*, 431. [[CrossRef](#)]
21. Gilabert, M.A.; Conese, C.; Maselli, F. An atmospheric correction method for the automatic retrieval of surface reflectances from TM images. *Int. J. Remote Sens.* **1994**, *15*, 2065–2086. [[CrossRef](#)]
22. Bokaie, M.; Zarkesh, M.K.; Arasteh, P.D.; Hosseini, A. Assessment of Urban Heat Island based on the relationship between land surface temperature and Land Use / Land Cover in Tehran. *Sustain. Cities Soc.* **2016**, *23*, 94–104. [[CrossRef](#)]
23. Guerri, G.; Crisci, A.; Messeri, A.; Congedo, L.; Munafo, M.; Morabito, M. Thermal Summer Diurnal Hot-Spot Analysis: The Role of Local Urban Features Layers. *Remote Sens.* **2021**, *13*, 538. [[CrossRef](#)]
24. Ou, S.C.; Chen, Y.; Liou, K.N.; Cosh, M.; Brutsaert, W. Satellite remote sensing of land surface temperatures: Application of the atmospheric correction method and split-window technique to data of ARM-SGP site. *Int. J. Remote Sens.* **2002**, *23*, 5177–5192. [[CrossRef](#)]
25. Dwivedi, A.; Khire, M.V. Application of split-window algorithm to study Urban Heat Island effect in Mumbai through land surface temperature approach. *Sustain. Cities Soc.* **2018**, *41*, 865–877. [[CrossRef](#)]
26. Duan, S.; Han, X.; Huang, C.; Li, Z.; Wu, H.; Qian, Y.; Gao, M.; Leng, P. Land Surface Temperature Retrieval from Passive Microwave Satellite Observations: State-of-the-Art and Future Directions. *Remote Sens.* **2020**, *12*, 2573. [[CrossRef](#)]
27. Yu, X.; Guo, X.; Wu, Z. Land Surface Temperature Retrieval from Landsat 8 TIRS—Comparison between Radiative Transfer Equation-Based Method, Split Window Algorithm and Single Channel Method. *Remote Sens.* **2014**, *6*, 9829–9852. [[CrossRef](#)]

28. Chen, X.; Su, Y.; Li, D.; Huang, G.; Chen, W.; Chen, S. Study on the cooling effects of urban parks on surrounding environments using Landsat TM data: A case study in Guangzhou, southern China. *Int. J. Remote Sens.* **2012**, *33*, 5889–5914. [[CrossRef](#)]
29. Zhu, W.; Sun, J.; Yang, C.; Liu, M.; Xu, X.; Ji, C. How to Measure the Urban Park Cooling Island? *A Perspective of Absolute and Relative Indicators Using Remote Sensing and Buffer Analysis.* *Remote Sens.* **2021**, *13*, 3154.
30. Masoudi, M.; Tan, P.Y. Multi-year comparison of the effects of spatial pattern of urban green spaces on urban land surface temperature. *Landscape Urban Plan.* **2019**, *184*, 44–58. [[CrossRef](#)]
31. Sun, R.; Chen, L. Effects of green space dynamics on Urban Heat Islands: Mitigation and diversification. *Ecosyst. Serv.* **2017**, *23*, 38–46. [[CrossRef](#)]
32. Ren, Z.; Zheng, H.; He, X.; Zhang, D.; Yu, X. Estimation of the Relationship Between Urban Vegetation Configuration and Land Surface Temperature with Remote Sensing. *J. Indian Soc. Remote* **2014**, *43*, 89–100.
33. Willie, Y.A.; Pillay, R.; Zhou, L.; Orimoloye, I.R. Monitoring spatial pattern of land surface thermal characteristics and urban growth: A case study of King Williams using remote sensing and GIS. *Earth Sci. Inform.* **2019**, *12*, 447–464. [[CrossRef](#)]
34. Lee, S.; Lee, K.; Jin, W.; Song, H. Effect of an urban park on air temperature differences in a central business district area. *Landscape Ecol. Eng.* **2009**, *5*, 183–191. [[CrossRef](#)]
35. Li, Y.; Fan, S.; Li, K.; Zhang, Y.; Dong, L. Microclimate in an urban park and its influencing factors: A case study of Tiantan Park in Beijing, China. *Urban Ecosyst.* **2020**, *24*, 767–778. [[CrossRef](#)]
36. Qaid, A.; Bin Lamit, H.; Ossen, D.R.; Raja Shahminan, R.N. Urban Heat Island and thermal comfort conditions at micro-climate scale in a tropical planned city. *Energy Build.* **2016**, *133*, 577–595. [[CrossRef](#)]
37. Chibuike, E.M.; Ibukun, A.O.; Abbas, A.; Kunda, J.J. Assessment of green parks cooling effect on Abuja urban microclimate using geospatial techniques. *Remote Sens. Appl.* **2018**, *11*, 11–21. [[CrossRef](#)]
38. Leonie, K.; Joy, A.; Andreas, R. Satellite-based investigation on the surface cooling effects of urban parks and their range—A case study for north rhine-westphalia, germany. *Erdkunde* **2021**, *75*, 209–223.
39. Yan, H.; Wu, F.; Dong, L. Influence of a large urban park on the local urban thermal environment. *Sci. Total Environ.* **2018**, 622–623, 882–891. [[CrossRef](#)]
40. Chen, L.; Wen, Y.; Zhang, L.; Xiang, W. Studies of thermal comfort and space use in an urban park square in cool and cold seasons in Shanghai. *Build. Environ.* **2015**, *94*, 644–653. [[CrossRef](#)]
41. Aram, F.; Solgi, E.; Higuera García, E.; Mosavi, A.; Várkonyi-Kóczy, A.R. The Cooling Effect of Large-Scale Urban Parks on Surrounding Area Thermal Comfort. *Energies* **2019**, *12*, 3904. [[CrossRef](#)]
42. Karimi, A.; Sanaieian, H.; Farhadi, H.; Norouziyan-Maleki, S. Evaluation of the thermal indices and thermal comfort improvement by different vegetation species and materials in a medium-sized urban park. *Energy Rep.* **2020**, *6*, 1670–1684. [[CrossRef](#)]
43. Chen, A.; Yao, X.A.; Sun, R.; Chen, L. Effect of urban green patterns on surface urban cool islands and its seasonal variations. *Urban For. Urban Green.* **2014**, *13*, 646–654. [[CrossRef](#)]
44. Jaganmohan, M.; Knapp, S.; Buchmann, C.M.; Schwarz, N. The Bigger, the Better? *The Influence of Urban Green Space Design on Cooling Effects for Residential Areas.* *J. Environ. Qual.* **2016**, *45*, 134–145. [[PubMed](#)]
45. Chang, C.; Li, M.; Chang, S. A preliminary study on the local cool-island intensity of Taipei city parks. *Landscape Urban Plan.* **2007**, *80*, 386–395. [[CrossRef](#)]
46. Shanghai Municipal Bureau Statistics. Shanghai Statistical Yearbook 2021 [WWW Document]. Available online: <http://tj.sh.gov.cn/tjgb/20210517/cc22f48611f24627bc5ee2ae96ca56d4.html> (accessed on 10 February 2022).
47. National Bureau of Statistics of China (Beijing). *Beijing Statistical Yearbook 2017*; China Statistics Press: Beijing, China, 2018.
48. Yue, W.; Xu, J.; Tan, W.; Xu, L. The relationship between land surface temperature and NDVI with remote sensing: Application to Shanghai Landsat 7 ETM+ data. *Int. J. Remote Sens.* **2007**, *28*, 3205–3226. [[CrossRef](#)]
49. Zhou, W.; Cao, F. Effects of changing spatial extent on the relationship between urban forest patterns and land surface temperature. *Ecol. Indic.* **2020**, *109*, 105778. [[CrossRef](#)]
50. Du, H.; Cai, Y.; Zhou, F.; Jiang, H.; Jiang, W.; Xu, Y. Urban blue-green space planning based on thermal environment simulation: A case study of Shanghai, China. *Ecol. Indic.* **2019**, *106*, 105501. [[CrossRef](#)]
51. Cheng, X.; Wei, B.; Chen, G. Influence of park size and its surrounding urban landscape patterns on the park cooling effect. *J. Urban Plan. Dev.* **2015**, *141*, A4014002. [[CrossRef](#)]
52. Du, H.; Song, X.; Jiang, H.; Kan, Z.; Wang, Z.; Cai, Y. Research on the cooling island effects of water body: A case study of Shanghai, China. *Ecol. Indic.* **2016**, *67*, 31–38. [[CrossRef](#)]
53. Wu, C.; Li, J.; Wang, C.; Song, C.; Haase, D.; Breuste, J.; Finka, M. Estimating the Cooling Effect of Pocket Green Space in High Density Urban Areas in Shanghai, China. *Front. Environ. Sci.* **2021**, *9*, 181. [[CrossRef](#)]
54. Rubel, F.; Kottke, M. Observed and projected climate shifts 1901–2100 depicted by world maps of the Köppen-Geiger climate classification. *Meteorol. Z.* **2010**, *19*, 135–141. [[CrossRef](#)]
55. Li, J.; Wang, X.; Wang, X.; Ma, W.; Zhang, H. Remote sensing evaluation of Urban Heat Island and its spatial pattern of the Shanghai metropolitan area, China. *Ecol. Complex.* **2009**, *6*, 413–420. [[CrossRef](#)]
56. Sobrino, J.A.; Jiménez-Muñoz, J.C.; Paolini, L. Land surface temperature retrieval from LANDSAT TM 5. *Remote Sens. Environ.* **2004**, *90*, 434–440. [[CrossRef](#)]

57. Kim, D.; Yu, J.; Yoon, J.; Jeon, S.; Son, S. Comparison of Accuracy of Surface Temperature Images from Unmanned Aerial Vehicle and Satellite for Precise Thermal Environment Monitoring of Urban Parks Using In Situ Data. *Remote Sens.* **2021**, *13*, 1977. [[CrossRef](#)]
58. Chen, J.; Yang, S.T.; Li, H.W.; Zhang, B.; Lv, J.R. Research on Geographical Environment Unit Division Based on the Method of Natural Breaks (Jenks). *Int. Arch. Photogramm. Remote Sens. Spat. Inf. Sci.* **2013**, *XL-4/W3*, 47–50. [[CrossRef](#)]
59. Wu, S.; Yang, H.; Luo, P.; Luo, C.; Li, H.; Liu, M.; Ruan, Y.; Zhang, S.; Xiang, P.; Jia, H.; et al. The effects of the cooling efficiency of urban wetlands in an inland megacity: A case study of Chengdu, Southwest China. *Build. Environ.* **2021**, *204*, 108128. [[CrossRef](#)]
60. Jauregui, E. Influence of a large urban park on temperature and convective precipitation in a tropical city. *Energ. Build.* **1990**, *15*, 457–463. [[CrossRef](#)]
61. Farhadi, H.; Faizi, M.; Sanaieian, H. Mitigating the Urban Heat Island in a residential area in Tehran: Investigating the role of vegetation, materials, and orientation of buildings. *Sustain. Cities Soc.* **2019**, *46*, 101448. [[CrossRef](#)]
62. Bowler, D.E.; Buyung-Ali, L.; Knight, T.M.; Pullin, A.S. Urban greening to cool towns and cities: A systematic review of the empirical evidence. *Landsc. Urban Plan.* **2010**, *97*, 147–155. [[CrossRef](#)]
63. Zhou, W.; Qian, Y.; Li, X.; Li, W.; Han, L. Relationships between land cover and the surface Urban Heat Island: Seasonal variability and effects of spatial and thematic resolution of land cover data on predicting land surface temperatures. *Landsc. Ecol.* **2013**, *29*, 153–167. [[CrossRef](#)]
64. Li, J.; Song, C.; Cao, L.; Zhu, F.; Meng, X.; Wu, J. Impacts of landscape structure on surface Urban Heat Islands: A case study of Shanghai, China. *Remote Sens. Environ.* **2011**, *115*, 3249–3263. [[CrossRef](#)]

## Article

# Numerical Study of Constant Pressure Systems with Variable Speed Electric Pumps

Rogger José Andrade-Cedeno <sup>1,\*</sup>, Jesús Alberto Pérez-Rodríguez <sup>1</sup>, Carlos David Amaya-Jaramillo <sup>2</sup>,  
Ciaddy Gina Rodríguez-Borges <sup>3</sup>, Yolanda Eugenia Llosas-Albuerne <sup>1</sup> and José David Barros-Enríquez <sup>4</sup>

<sup>1</sup> Departamento de Electricidad, Facultad de Ciencias Matemáticas, Físicas y Químicas, Universidad Técnica de Manabí, Portoviejo 130150, Ecuador; [jesus.perez@utm.edu.ec](mailto:jesus.perez@utm.edu.ec) (J.A.P.-R.); [yolanda.llosas@utm.edu.ec](mailto:yolanda.llosas@utm.edu.ec) (Y.E.L.-A.)

<sup>2</sup> Departamento de Electricidad, Facultad de Ciencias de la Ingeniería, Universidad Técnica Estatal de Quevedo, Quevedo 120550, Ecuador; [camaya@uteq.edu.ec](mailto:camaya@uteq.edu.ec)

<sup>3</sup> Departamento de Ingeniería Industrial, Facultad de Ciencias Matemáticas, Físicas y Químicas, Universidad Técnica de Manabí, Portoviejo 130150, Ecuador; [ciaddy.rodriguez@utm.edu.ec](mailto:ciaddy.rodriguez@utm.edu.ec)

<sup>4</sup> Departamento de Diseño, Facultad de Ciencias de la Industria y Producción, Universidad Técnica Estatal de Quevedo, Quevedo 120550, Ecuador; [josedavid985@gmail.com](mailto:josedavid985@gmail.com)

\* Correspondence: [rogger.andrade@gmail.com](mailto:rogger.andrade@gmail.com)

**Abstract:** This work focuses on the modeling and simulation of constant pressure systems based on variable speed pumps, with the aim of studying and evaluating their performance from a multidisciplinary approach. Using the physical models of the Simscape library, from MATLAB/Simulink R2019b, two study cases are assembled consisting of: piping system, a hydropneumatic tank, centrifugal pumps with an induction motor, variable speed drives, and a control system. Case one is comprised of one pump at a fixed speed and another at variable speed, and case two with both pumps at variable speed. For the parameterization of the models, data from manufacturers and process requirements are used. The different stages of the control system are integrated and configured; these are constant V/f control, slip compensation, space vector modulation (SVM,) and pressure controller. The dynamic response of the system, power saving, transient current at startup, and harmonic distortion are evaluated. The results showed that both cases kept the pressure constant in the face of variable flow demand and smoothed out the current during startup. Case two saved more energy (between 28 and 49%) but generated more harmonic distortion. In addition, both cases have better performance compared with traditional fixed-speed technologies.

**Keywords:** constant pressure system; pumping system; centrifugal pump; induction motor; variable speed drive; control system; energy efficiency; harmonic distortion; modeling and simulation

**Citation:** Andrade-Cedeno, R.J.; Pérez-Rodríguez, J.A.; Amaya-Jaramillo, C.D.; Rodríguez-Borges, C.G.; Llosas-Albuerne, Y.E.; Barros-Enríquez, J.D. Numerical Study of Constant Pressure Systems with Variable Speed Electric Pumps. *Energies* **2022**, *15*, 1918. <https://doi.org/10.3390/en15051918>

Academic Editors: Roberto Alonso González Lezcano, Francesco Nocera and Rosa Giuseppina Caponetto

Received: 3 February 2022

Accepted: 3 March 2022

Published: 6 March 2022

**Publisher's Note:** MDPI stays neutral with regard to jurisdictional claims in published maps and institutional affiliations.



**Copyright:** © 2022 by the authors. Licensee MDPI, Basel, Switzerland. This article is an open access article distributed under the terms and conditions of the Creative Commons Attribution (CC BY) license (<https://creativecommons.org/licenses/by/4.0/>).

## 1. Introduction

At an industrial, commercial, and residential level, applications with pumps, compressors, fans, and others driven by electric motors represent 53% of total energy consumption, and there are new technologies that have the potential to reduce this electricity demand by between 20 to 30% [1]. In pumping applications with variable flow demand, the implementation of variable-frequency drives adapted to electric motors should be evaluated because of the potential energy savings that can be achieved and improvements in the overall performance of the system [2–5]. In these applications, the scalar control strategy with a constant V/f ratio is the most feasible, mainly because of its simplicity and low-cost implementation [6–8]. There are several studies where scalar control with a constant V/f ratio was simulated for the speed control of an induction motor; for example, in an open loop with voltage and slip compensation to improve the performance in low frequencies [9], and adding a PID controller for automatic regulation in a closed loop to eliminate the speed position error [8,10,11]. The performances of the control system in the open and

close loop were also compared, concluding that the close loop system presents a better performance [12–15]. For the particular case of centrifugal pumps driven by an induction motor with variable speed requirements, computer simulations have also been developed. For example, Lysenko and Simakov [16] simulated V/f scalar control in an open loop on an electric centrifugal pump, studying the dynamic response of the current, torque, speed, flow, and pressure in order to analyze and coordinate different modes of operation. An ideal source of DC voltage was used at the input of the inverter, even though the grid is normally AC. Furthermore, voltage waves and harmonic distortion were not studied. Abdelwanis and Selim [17] simulated the V/f control in a closed loop without a sensor (sensorless), that is, the axis speed was estimated from stator voltage and current, and the speed error correction was performed using a PID controller. They compared the harmonic distortion with and without the PID controller, finding improvements when operating with the PID controller. Gevorkov et al. [18] simulated a constant pressure pumping system by adding a feedback controller for automatic pressure regulation. They compared the P controller with the PI controller and showed that the second case performed better, reducing oscillation and position error. Arun Shankar et al. [19] conducted mixed simulation and real experimentation studies, where a cascade constant pressure system was implemented with pumps in parallel and a variable frequency drive. The algorithm implemented allowed the system to operate more efficiently, achieving energy savings between 15% and 45%. No electrical analysis, such as current transient or harmonic distortion, was performed in this study. Oshurbekov et al. [20] compared two configurations: a single pump at variable speed and two pumps of lower power in parallel with one pump at a fixed speed and another at variable speed. The results showed that the second case was more efficient, with energy savings of 29.8%. The analysis of electrical variables, such as current and voltage waveform, was not part of the scope of this study.

In this research, the modeling, simulation, and numerical study of two cases is carried out using MATLAB/Simulink R2019b, with the aim of developing a constant pressure system in a pumping station with variable flow demand, made up of two parallel centrifugal pumps driven by an induction motor. In case one, there is a fixed speed pump through a direct connection to the electrical grid and another variable speed pump. In case two, both pumps operate at variable speeds. Variable speed is achieved using a variable frequency drive governed by scalar control with a constant V/f ratio and slip compensation, in conjunction with space vector modulation (SVM). The automatic pressure control is achieved with a PI controller. These two case studies are compared with the base case (both pumps at fixed speed), performing analysis of the dynamic response of the control system, evaluating the power consumption and savings, startup current transients, and harmonic distortion. This research is of scientific relevance because of its multidisciplinary approach methodology, with potential for application in industry, commerce, buildings, and agriculture, in addition to containing topics of interest in pumping system optimization, energy efficiency, and energy quality.

## 2. Materials and Methods

Figure 1 shows the methodology used and the aims of each stage. It begins with the study of the mathematical methods that govern the components of a pumping system in order to conceptualize models and systems. In the hydraulic and mechanical area: centrifugal pump theory, parallel pumping, affinity laws, piping systems, Darcy equation, Haaland equation, gas-charged accumulator. For the electrical and electronic part: the model of the induction motor in state space, the operability of the variable speed drive, the scalar control with constant V/f ratio, the space vector modulation (SVM), the control system, and the PI controller.

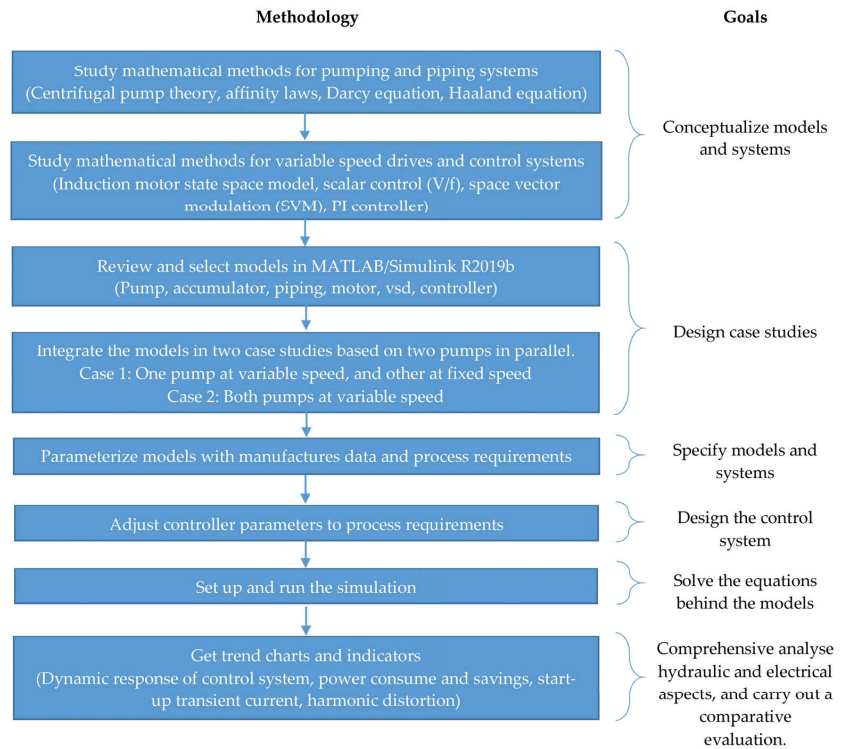


**Figure 1.** Flow diagram of methodology.

Using the MATALAB/Simulink R2019b Simscape library, the blocks are reviewed, selected, and integrated to form two case studies, as described in Section 2.3. The models are parameterized using data from manufacturers and process requirements. Then all the stages of the control system are adjusted to meet the process requirements; these are: PI slip compensator, V/f scalar control, space vector modulation (SVM), and PI pressure controller. The simulation is run to solve the mathematical models, data and trend graphs are obtained for the subsequent analysis and evaluation. Finally, a comprehensive analysis of the hydraulic and electrical aspects of each case study is carried out, evaluating the dynamic response of the control system, power consumption and savings, starting transient current, and harmonic distortion. Based on these results, the case studies are compared to determine which one has the best performance. The novelty of this methodology lies in the use of Simscape physical models and the multidisciplinary analysis of the results. In other studies, linearized and approximate models are used, and the analysis is partial depending on the discipline (purely hydraulic or electric).

### 2.1. Capacity Regulation Methods in Centrifugal Pumps

Typical methods to regulate the capacity of a pumping system are on-off control, control valve, and speed variation. On-off control is justified for applications where there are tanks or reservoirs and where such precise control is not required. When demand flow adjustment is required, a control valve or variable speed drive should be used [21]. Flow regulation with a control valve can be seen in the laboratory work developed by [22], where a PID algorithm was implemented on a control valve placed in the discharge of a centrifugal pump operating at a fixed speed. The results showed a good performance of the flow control system, but the study did not delve into the performance of the centrifugal pump. However, fixed speed operation with a control valve can waste energy, while variable



speed operation can increase energy efficiency [23]. When a centrifugal pump operates at a variable speed, it is important to monitor its efficiency curve to determine its performance based on the flow it delivers. This curve defines the efficiency “from the cable to the water”, that is to say, the total efficiency, which considers the mechanical losses in the pump as well as the electrical losses in the motor and the variable speed drive [24]. Figure 2a shows the characteristic curves of a variable speed centrifugal pump, which is the preferred choice for operating in a region where the required flow remains controlled at best possible efficiency.

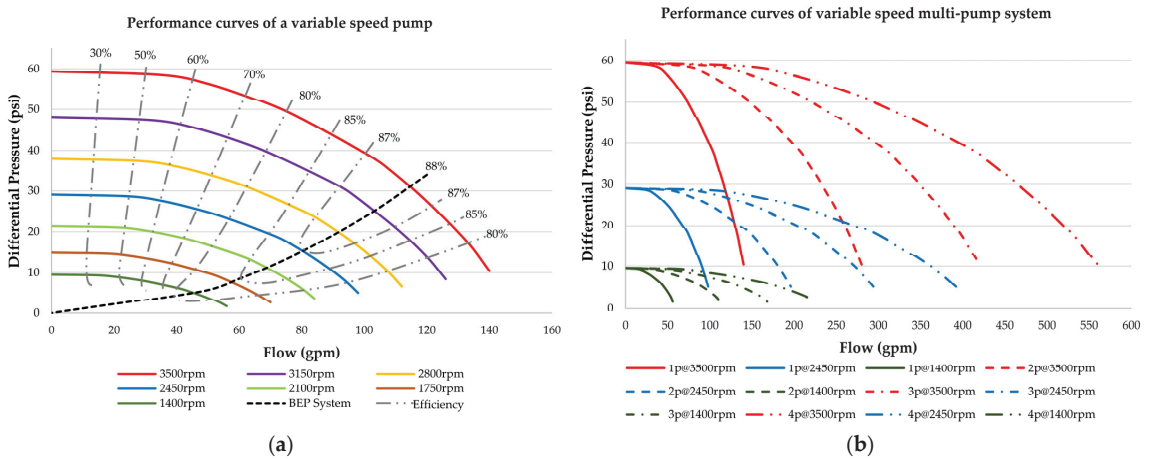


**Figure 2.** Performance curves in centrifugal pumps with speed variation: (a) in a single pump; (b) in a system of multiple pumps in parallel.

An alternative to using a single pump in an application with variable demand is to use several smaller capacity pumps connected in parallel since the multiple variations in the demand of the system prevent a single pump from operating constantly, close to the best efficiency point (BEP). Operating a centrifugal pump too far from the BEP to either the right or left of the curve can put equipment at risk from adverse effects such as cavitation, vibration, impeller damage, recirculation in suction, or unloading, and reduced life of seals and bearings [21,24]. These damages can be minimized by maintaining the operating flow in the Preferred Operating Region (POR). The POR is the range of flow rates on both sides of the BEP, where the operational reliability and hydraulic efficiency of the pump are not substantially degraded, so operating the pump within the POR generally results in lower energy consumption, higher reliability, and less impact on the useful life of the equipment. Most centrifugal pumps have a POR between 70–120% of the BEP [25].

Figure 2b shows the performance curves of a multipump system at variable speeds for different speeds. Variation in speed allows greater flexibility in operation and provides better performance for the system. In the study developed by Ahmed et al. [26], two configurations of multiple pump systems are presented: the first with a single pump at a variable speed, and the second where all the pumps operate at variable speed. The diagrams of both configurations can be seen in Figure 3.

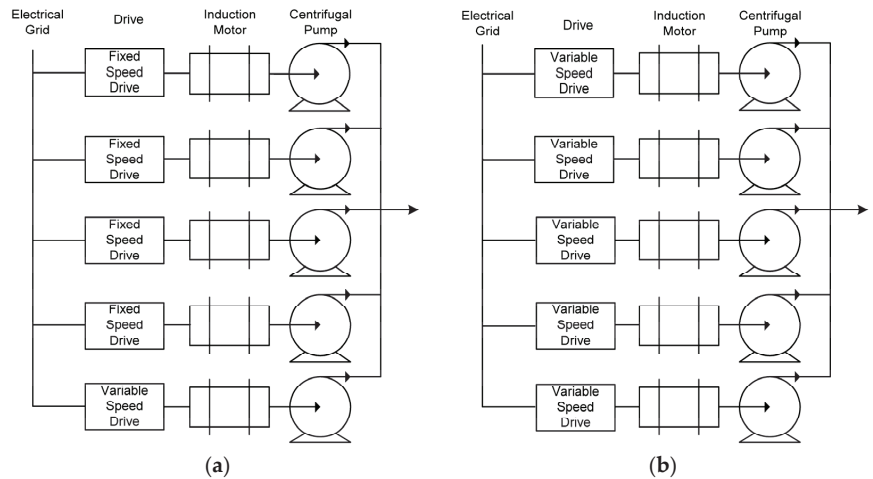


**Figure 3.** System of multiple pumps in parallel: (a) with a single pump at variable speed; (b) with all pumps at variable speed.

## 2.2. Electrical Power and Control System

There are different types of motors to drive pumps, but the induction motor is one of the most widely used because of the advantages it presents compared with other electric machines [11,14,27,28]. The accelerated advance of microprocessor systems and power electronics has made it possible to position variable speed drives as the main technology for motion control in applications driven by induction motors [10,29]. These types of equipment reduce the input energy to the motor when it is not operating at full load, which allows energy savings and operational improvements in systems that previously used motors without any type of speed control.

As concerns control techniques, there are two broad categories used by variable speed drives: scalar control and vector control. The most widely used scalar control technique is voltage-frequency (V/f) control, and vector control includes oriented field control and direct torque control [28–30]. Scalar control is less precise and presents a limited response in torque compared with other control techniques; it is simple to implement, it presents lower losses in switching, reduced computational processing, and a lower cost of implementation [4,11,12,14,30]. Some of the most common applications driven by the variable speed drive induction motor are pumps, compressors, fans, and small machines that operate at high speeds, but also, these types of applications require a strategy of simple control and moderate precision, so the V/f control is the most feasible in these cases [6–8].

Automatic process controllers can also help improve the performance of electromechanical systems. The implementation of better monitoring, control, and optimization strategies improves the energy performance directly through the reduction of waste (very frequently associated with undue oscillations in the process) and indirectly through better maintenance practices [31]. The most widely used automatic process controller is the PID controller, present in more than 95% of control loops, constituting an important tool for improving productivity, quality, and energy efficiency [32]. Research conducted by Gomes et al. [33] on energy efficiency in industrial processes and PID controllers demonstrates how an adequate control strategy together with a correct controller adjustment procedure can contribute to saving energy consumption.

## 2.3. Study Cases for Modeling and Simulation

Figure 4 shows the two cases to be modeled, simulated, and studied, which are made up of two pumps connected in parallel supplying flow and pressure to a water network (system) where there is a variable demand for flow and constant pressure needs to be

maintained. When there are low flow rates, both cases operate with a single pump at variable speed. However, it is necessary to operate the two pumps in parallel if the flow increases; in this scenario, case one operates with one pump at a fixed speed and the other at a variable speed, and case two operates with both pumps at variable speed. In the discharge head of each pumping group, there is an ideal pressure sensor (simulating a manometer or pressure transducer) and an ideal flow sensor (simulating a flow meter). The models of the hydraulic, mechanical, electrical, and control components were obtained from Simulink’s Simscape library in the R2019b version of MATLAB. These models are detailed below.

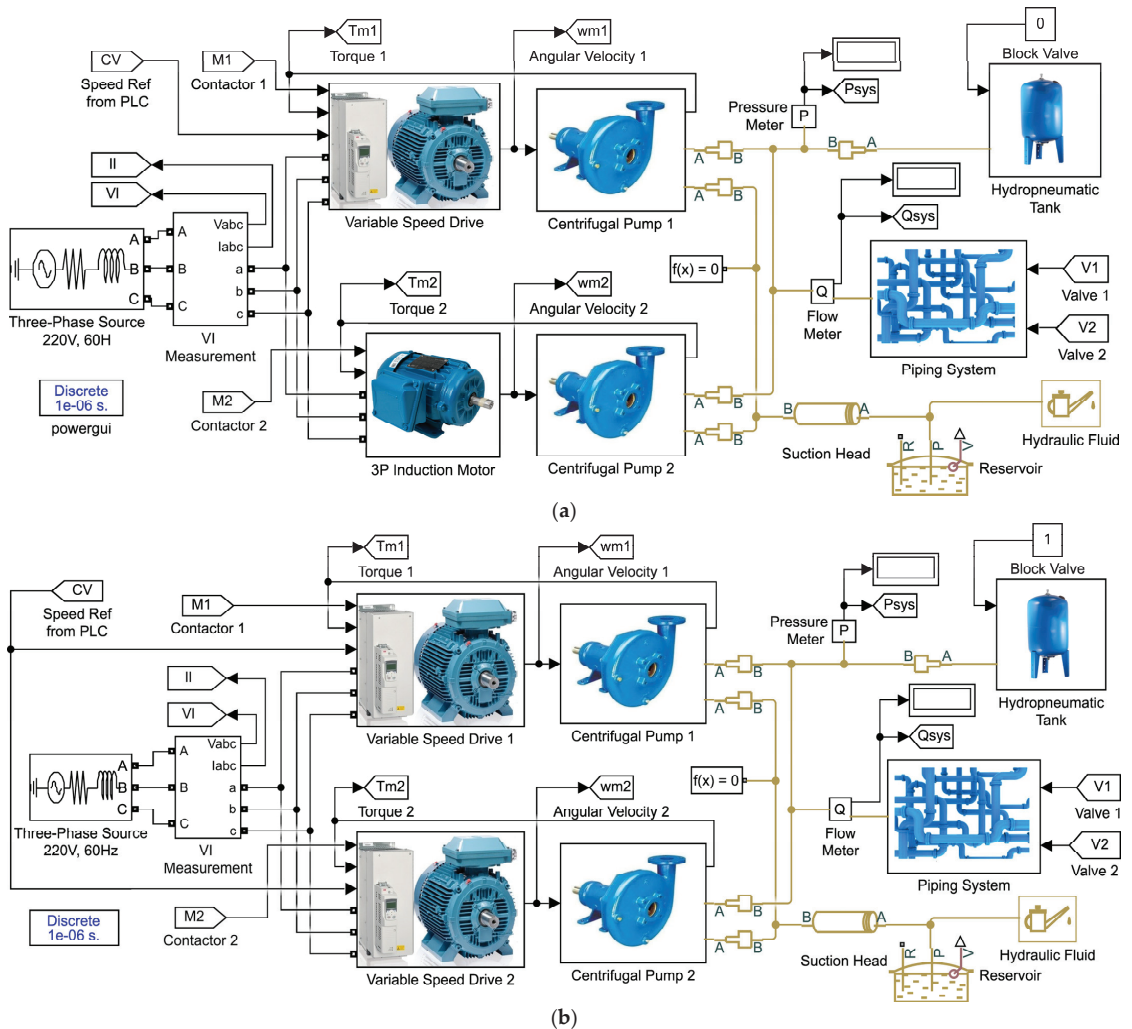


**Figure 4.** Case studies modeled in Simulink: (a) Case one: only one pump at variable speed. (b) Case two: both pumps at variable speed.

### 2.3.1. Pumping System Model

Figure 5 shows the pumping system model, where the centrifugal pump is the main component. The pump has a mechanical and hydraulic component.

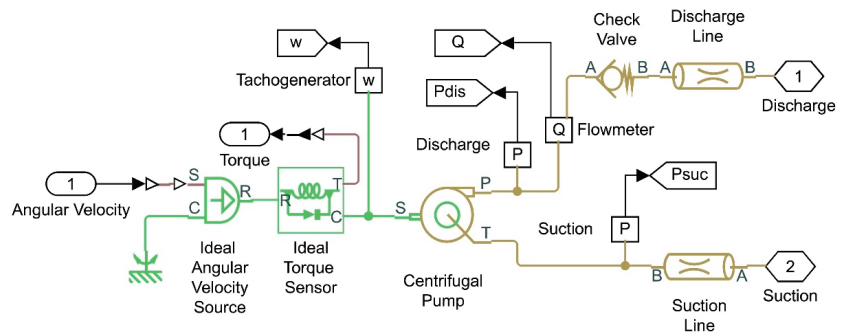


Figure 5. Pump train model developed in Simulink.

The mechanical component corresponds to an ideal source of angular velocity (from the induction motor) and an ideal torque load (towards the induction motor). The hydraulic component comprises a suction pipe and a discharge pipe. In addition, a check valve is installed in the discharge to isolate the pump when it goes out of operation. An ideal pressure sensor is connected to both sides, simulating a manometer or pressure transducer, and an ideal flow sensor is also used at the discharge, simulating a flow meter. The centrifugal pump is parameterized with the performance curve obtained from the datasheet provided by the manufacturer.

The characterization of the centrifugal pump is carried out using two one-dimensional search tables: (i) differential pressure vs. flow and (ii) brake power vs. flow—both at nominal angular velocity and flow density. To obtain the parameters at another angular velocity, the laws of affinity are used [34]. Equations (1)–(9) describe the complete model.

$$q_{nom} = q \frac{\omega_{nom}}{\omega} \tag{1}$$

$$p = p_{nom} \left( \frac{\omega}{\omega_{nom}} \right)^2 \frac{\rho}{\rho_{nom}} \tag{2}$$

$$P_{hyd\_nom} = p_{nom} q_{nom} \tag{3}$$

$$P_{hyd} = P_{hyd\_nom} \left( \frac{\omega}{\omega_{nom}} \right)^3 \frac{\rho}{\rho_{nom}} \tag{4}$$

$$P_{hyd0} = p_{E} q_{nom} \left( \frac{\omega}{\omega_{nom}} \right)^3 \tag{5}$$

$$P_{fr} = (T_0 + k_p p) \omega \tag{6}$$

$$P_{mec} = P_{hyd0} + P_{fr} \tag{7}$$

$$T = \frac{P_{mec}}{\omega} \tag{8}$$

$$\eta = \frac{P_{hyd}}{P_{mec}} \tag{9}$$

### 2.3.2. Hydropneumatic Tank Model

Figure 6 shows the model of the hydropneumatic tank, consisting of an accumulator tank with precharged gas, a connection pipe between the tank and the water network, and a blocking valve. The accumulator tank comprises a chamber with precharged gas and a chamber with fluid, which is connected to a hydraulic system. The process is mathematically modeled with Equations (10)–(15) [35].

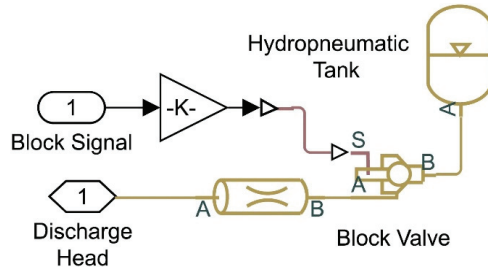


Figure 6. Hydropneumatic tank model developed in Simulink.

$$(p_G + p_A)(V_T - V_F)^k = (p_{pr} + p_A)V_T^k \tag{10}$$

$$p_F = p_G + p_{TD} \tag{11}$$

$$p_{TD} = \begin{cases} K_S(V_F - V_C) + K_d q_F^+(V_F - V_C) & \text{if } V_F \geq V_C \\ K_S V_F - K_d q_F^- V_F & \text{if } V_F \leq 0 \\ 0 & \text{opposite case} \end{cases} \tag{12}$$

$$q_F^+ = \begin{cases} q_F & \text{if } q_F \geq 0 \\ 0 & \text{opposite case} \end{cases} \tag{13}$$

$$q_F^- = \begin{cases} q_F & \text{if } q_F \leq 0 \\ 0 & \text{opposite case} \end{cases} \tag{14}$$

$$q_F = \frac{dV_F}{dt} \tag{15}$$

At  $t = 0$ , the initial condition is  $V_F = V_i$ , where  $V_i$  is a parameter that can be entered initially.

### 2.3.3. Piping System Model

The water network, or piping system, is shown in Figure 7.

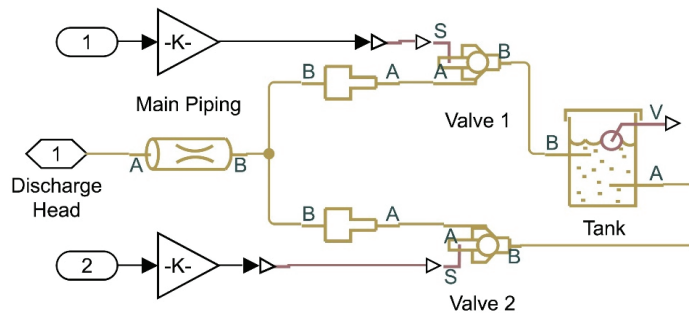


Figure 7. Model of the piping system developed in Simulink.

In this model, there is the main pipeline, consumption valves that simulate the variable flow demand, and a discharge tank. The pipe is modeled with a circular cross section, taking into consideration only the resistive property of the pipe. The Darcy equation is used to calculate the pressure loss due to the friction, and the Haaland approximation is used to calculate the friction factor in the turbulent regime. In the transition of regimens,

from laminar to turbulent, the friction factor is determined by linear interpolation. As a result, the section of pipe is modeled according to Equations (16)–(18) [36].

$$p = f \frac{(L + L_{eq})}{D_H} \frac{\rho}{2A^2} q \cdot |q| \tag{16}$$

$$f = \left\{ \begin{array}{ll} K_s / R_e & \text{if } Re \leq Re_L \\ f_L + \frac{f_T - f_L}{Re_T - Re_L} (Re - Re_L) & \text{if } Re_L \leq Re < Re_T \\ \frac{1}{\left( -1.8 \log_{10} \left( \frac{6.9}{Re} + \left( \frac{r/D_H}{3.7} \right)^{1.11} \right) \right)^2} & \text{if } Re \geq Re_T \end{array} \right\} \tag{17}$$

$$Re = \frac{q \cdot D_H}{A \cdot v} \tag{18}$$

### 2.3.4. Induction Motor Model

To simulate the induction motor, the asynchronous machine model is used. This block makes it possible to model three-phase induction motors of the winding rotor, squirrel cage, or double squirrel cage type. The stator and rotor windings are “Y” connected with internal neutral. The electrical component of the machine is represented by a six-order state-space model (for double squirrel cage machine) or a fourth-order state-space model (for single squirrel cage machine), and the mechanical part is modeled by a second-order system [37]. In Figure 8, the equivalent circuit of the electrical system of the asynchronous double cage machine is shown under the reference frame  $dq$ . The electrical system is governed by Equations (19)–(34).

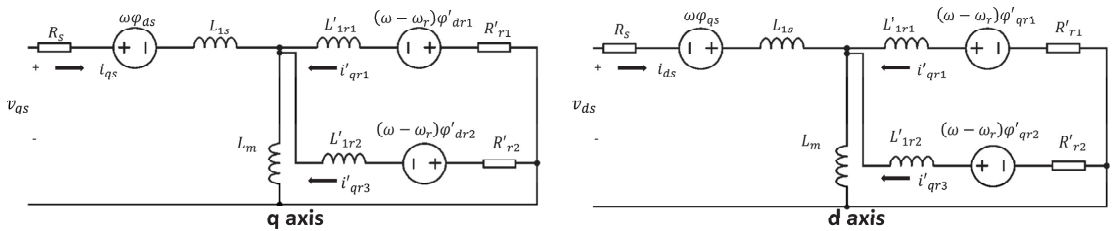


Figure 8. Equivalent circuit for double cage induction machine.

$$V_{qs} = R_s i_{qs} + d\varphi_{qs}/dt + \omega \varphi_{ds} \tag{19}$$

$$V_{ds} = R_s i_{ds} + d\varphi_{ds}/dt - \omega \varphi_{qs} \tag{20}$$

$$0 = R'_{r1} i'_{qr} + d\varphi'_{qr1}/dt + (\omega - \omega_r) \varphi'_{dr1} \tag{21}$$

$$0 = R'_{r1} i'_{dr1} + d\varphi'_{dr1}/dt - (\omega - \omega_r) \varphi'_{qr1} \tag{22}$$

$$0 = R'_{r2} i'_{qr2} + d\varphi'_{qr2}/dt + (\omega - \omega_r) \varphi'_{dr2} \tag{23}$$

$$0 = R'_{r2} i'_{dr2} + d\varphi'_{dr2}/dt - (\omega - \omega_r) \varphi'_{qr2} \tag{24}$$

$$T_e = 1.5p(\varphi_{ds} i_{qs} - \varphi_{qs} i_{ds}) \tag{25}$$

$$\varphi_{qs} = L_s i_{qs} + L_m i'_{qr} \tag{26}$$

$$\varphi_{ds} = L_s i_{ds} + L_m i'_{dr} \tag{27}$$

$$\varphi'_{qr1} = L'_{r1} i'_{qr1} + L_m i_{qs} \tag{28}$$

$$\varphi'_{dr1} = L'_{r1} i'_{dr1} + L_m i_{ds} \tag{29}$$

$$\varphi'_{qr2} = L'_{r2} i'_{qr2} + L_m i_{qs} \tag{30}$$

$$\phi'_{dr2} = L'_{r2}i'_{dr2} + L_m i_{ds} \tag{31}$$

$$L_s = L_{lS} + L_m \tag{32}$$

$$L'_{r1} = L'_{lr1} + L_m \tag{33}$$

$$L'_{r2} = L'_{lr2} + L_m \tag{34}$$

Equations (35) and (36) apply to the mechanical component.

$$\frac{d}{dt}\omega_m = \frac{1}{2H}(T_e - F\omega_m - T_m) \tag{35}$$

$$\frac{d}{dt}\theta_m = \omega_m \tag{36}$$

The induction motor is used in two connections: with a direct connection to the grid (frequency and nominal speed) and with a connection to a variable speed drive (frequency and variable speed). Figure 9a shows the model of the induction motor with a direct connection to the grid, and in Figure 9b is the model for a variable speed drive made up of an induction motor and a frequency inverter.

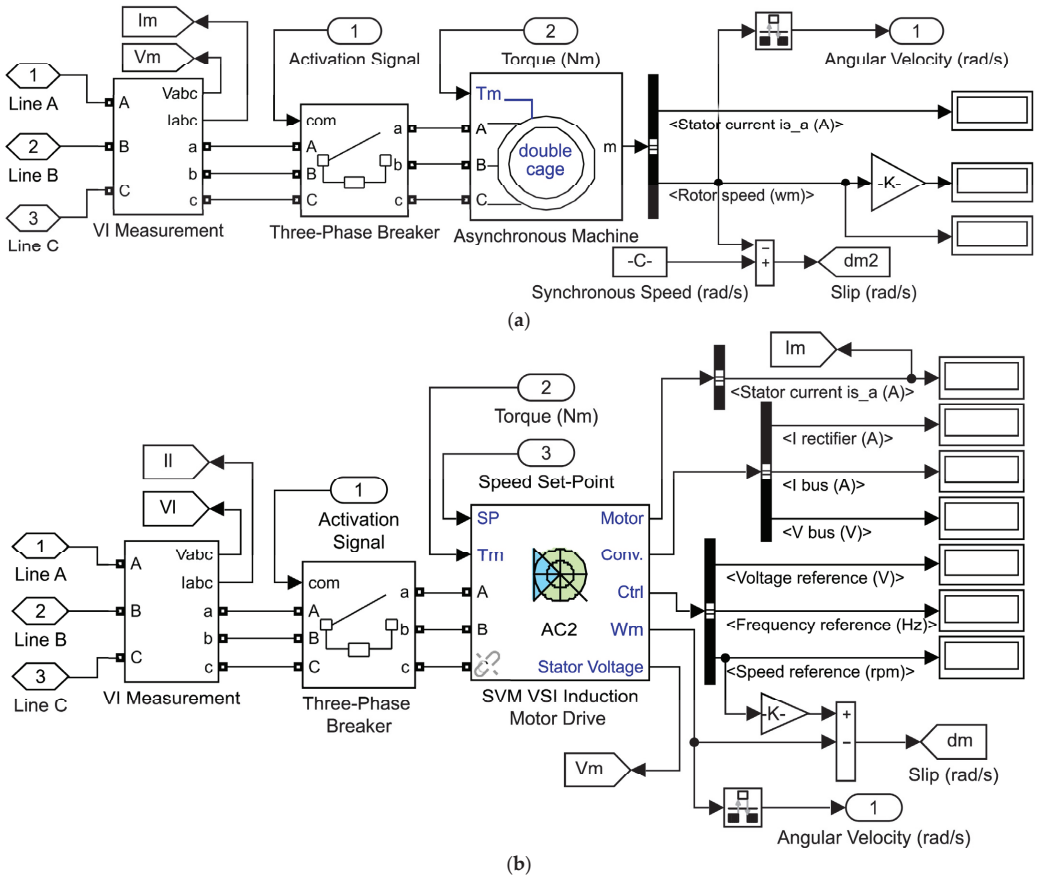


**Figure 9.** Simulink models of the three-phase induction motor with its drives and meters: (a) with a direct connection to the grid at nominal speed; (b) with variable speed drive.

### 2.3.5. Variable Speed Drive Model

The variable speed drive is modeled with the block Drive AC2 “Space Vector PWM VSI Induction Motor Drive”, which contains an asynchronous and a PWM-VSI variable frequency drive. The asynchronous machine is configured as a three-phase induction motor, and its variable frequency converter is made up of a three-phase rectifier, DC link, three-phase inverter, and control system, as seen in Figure 10a. Both the inverter and the rectifier of the block AC2 are based on the Universal Bridge, which allows the modeling and simulation of static converters using forcibly switched devices (GTO, IGBT, MOSFET) and naturally switched power electronic devices (diodes or thyristors) connected in a bridge configuration [38]. In this work, a rectifier made up of power diodes and an inverter based on IGBTs were selected.

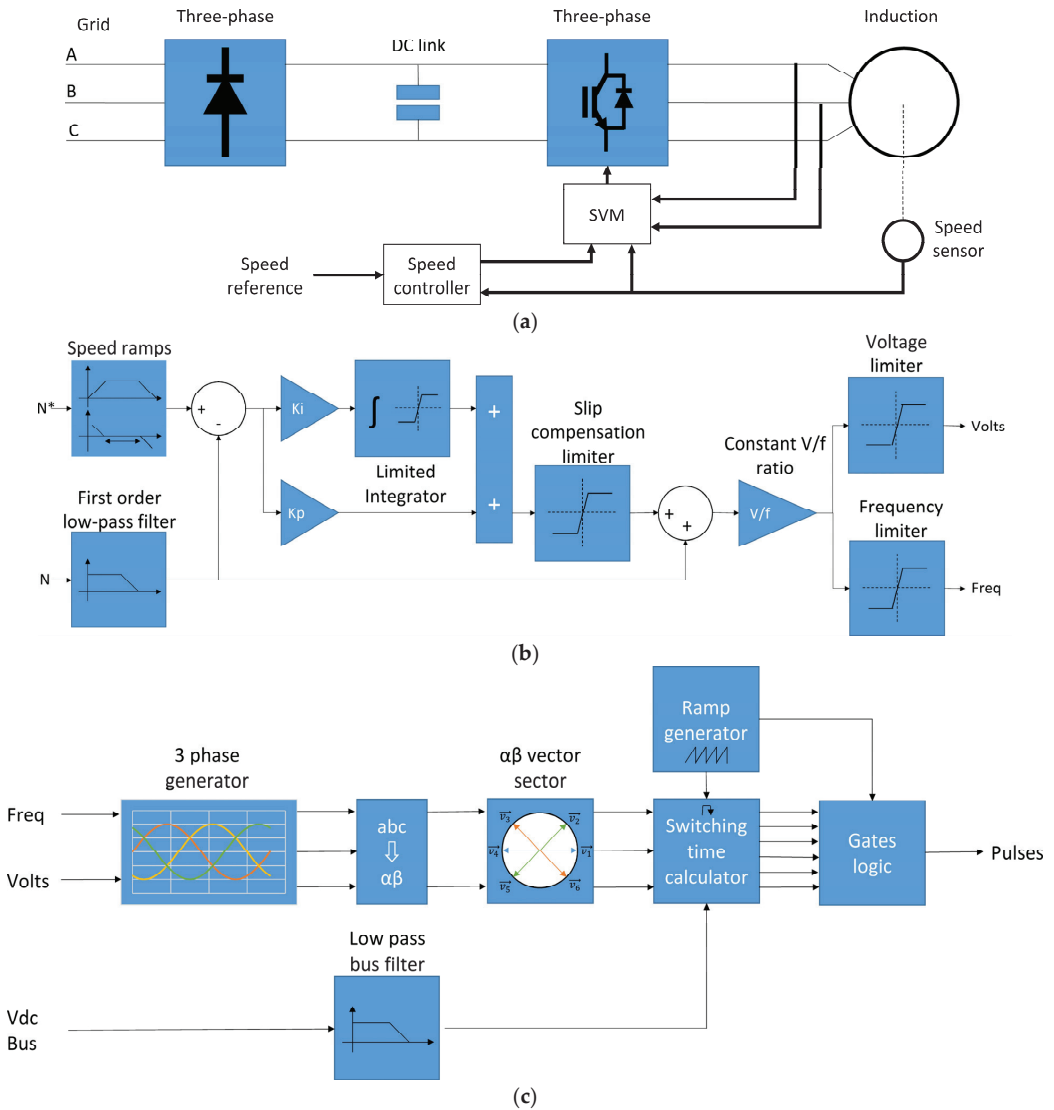


**Figure 10.** Block diagram of the Drive AC2 model in Simulink: (a) general power and control system diagram; (b) speed controller; (c) space vector modulation (SVM).



Regarding the speed controller, the Drive AC2 has a closed loop speed control, made up of the classic V/f scalar control plus a slip compensator. Figure 10b shows the block diagram of the speed controller, which is fed back with a tachogenerator connected to the motor shaft. The slip compensator, based on a PI controller, corrects the speed error in the motor. The constant V/f ratio block allows the fundamental component of the voltage to the motor to have the desired amplitude and frequency. This is why it provides the voltage and frequency reference to the PWM generator [39]. Figure 10c shows the block diagram of the PWM generator based on space vector modulation (SVM), whose mission is to generate the control pulses for the IGBTs [39].

### 2.3.6. Process Control System

Figure 11 shows the block diagram of the pumping process control system. It has a PI pressure controller as an external loop and a slip compensator as an internal loop. Feedback for each control loop is achieved with a pressure transmitter and a tachometer, respectively. In practice, variable speed drives contain a PLC that provides digital inputs and outputs to connect discrete signals, analog inputs to receive sensor signals, analog outputs to control actuators, blocks to program PID algorithms, and specialized macros for pump control.

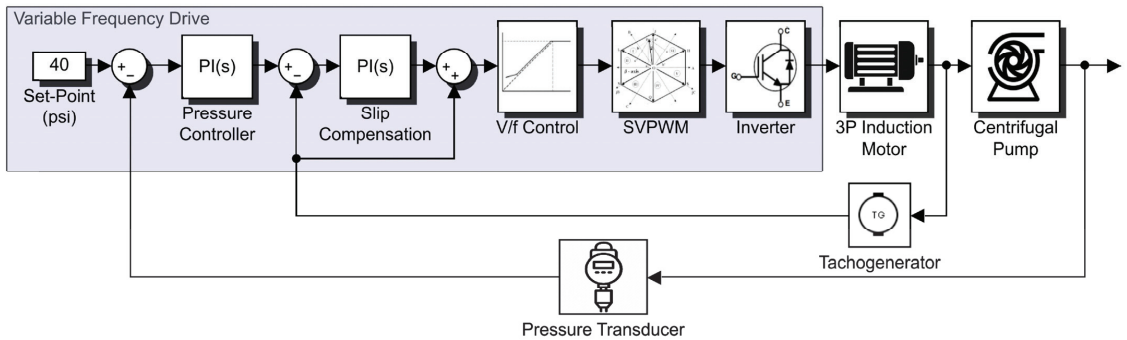


Figure 11. Block diagram of the pumping process control system.

The mathematical representation of the PID control algorithm is presented in Equations (37) and (38).

$$u(t) = K_p \left( e(t) + \frac{1}{T_i} \int_0^t e(t) dt + T_d \frac{de(t)}{dt} \right) \quad (37)$$

$$K_i = \frac{K_c}{T_i} \quad K_d = K_c \cdot T_d \quad (38)$$

The controller parameters  $K_p$ ,  $T_i$ , and  $T_d$ , can be determined by applying various analytical or experimental techniques [40].

### 3. Results and Discussion

For the simulations, 120 gpm @ 35 m and 3500 rpm was considered, with a three-phase induction motor of 5 HP, 220 Vac, 60 Hz, and two poles. The study cases were contrasted with each other and with the base case. The base case consisted of operating the pumps at a fixed speed through a direct connection to the electrical grid, requiring a hydropneumatic tank and an on-off control with hysteresis. For the base case, a hydropneumatic tank of 80 gal was considered. To reduce the on/off frequency of the pump, the capacity of the hydropneumatic tank must be increased, or the hysteresis band must be widened, which can make the application more expensive and affect the quality of the service because of low pressures. When upgrading the traditional on-off control for a regulatory control with variable speed drive, certain advantages and disadvantages were observed, which are detailed below.

### 3.1. Dynamic Response

Two tests were carried out to study the dynamic response:

- Test 1: In low flow conditions with a pump operating at variable speed. This operation was the same in both study cases;
- Test 2: In high flow conditions with two pumps operating in parallel. In case one, one pump operated at a fixed speed and the other at variable speed, and in case two, both pumps were at variable speed.

In both tests, the pressure set point was set at 40 psi, and the acceleration/deceleration ramps of the variable speed drive were set at 3600 rpm/s. The hydropneumatic tank capacity was reduced to 10 gal, which is an 87.5% reduction from the base case. The system responses were for step-type disturbances produced by sudden changes in the consumption valve. These disturbances were ideal and sufficiently drastic since, in a real system, every valve has a response time, even those of the quick opening type.

The results of test 1 are presented in Figure 12, where the dynamic response of the pressure, flow, and slip is shown, under three scenarios: with slip compensation and a hydropneumatic tank (Figure 12a), no-slip compensation (Figure 12b), and without the hydropneumatic tank (Figure 12c). As can be seen, in the three scenarios, it was possible to keep the pressure constant at 40 psi in view of the variable flow demand. When it was operated with a hydropneumatic tank (Figures 11b and 12a), the pressure overshoot did not exceed 10% of the set point; when the tank was removed (Figure 12c), the overshoot exceeded 50%. This shows that it is not advisable to completely eliminate this element since it contributes to the damping of pressure transients due to sudden changes in demand and prevention of water hammer [41], in addition to improving the energy efficiency of the system when operating at low flow rates [42]. The action of the slip compensator is also observed. In Figure 12a, slip compensation is active, while in Figure 12b, it is inactive. As observed, a slight improvement in the transient response is achieved (Figure 12a), but this improvement was not representative.

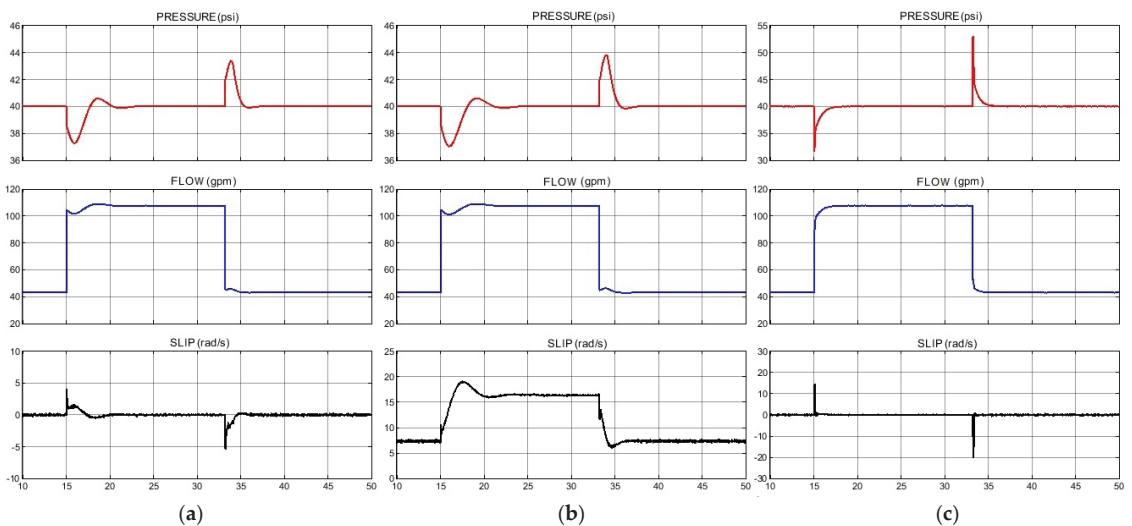


**Figure 12.** Comparison of the dynamic response under three different conditions: (a) with slip compensation and hydropneumatic tank; (b) without slip compensation; (c) without hydropneumatic tank.

In Figure 13, the results of test 2 are presented, where the dynamic response of several hydraulic and mechanical variables of interest is observed. Figure 13a shows the results

of the first case study, and Figure 13b the second case study. In both cases, very similar transient responses are observed for pressure and flow rate, and in a steady state, there were practically no differences. The dynamic response of the flow rate, total dynamic head, suction pressure, discharge pressure, angular velocity, and mechanical torque of each pump train is also appreciated. It is noticeable that in the pumps that operated at variable speeds, the angular speed and the mechanical torque increased and decreased with the flow demand. This action is what produces power savings.

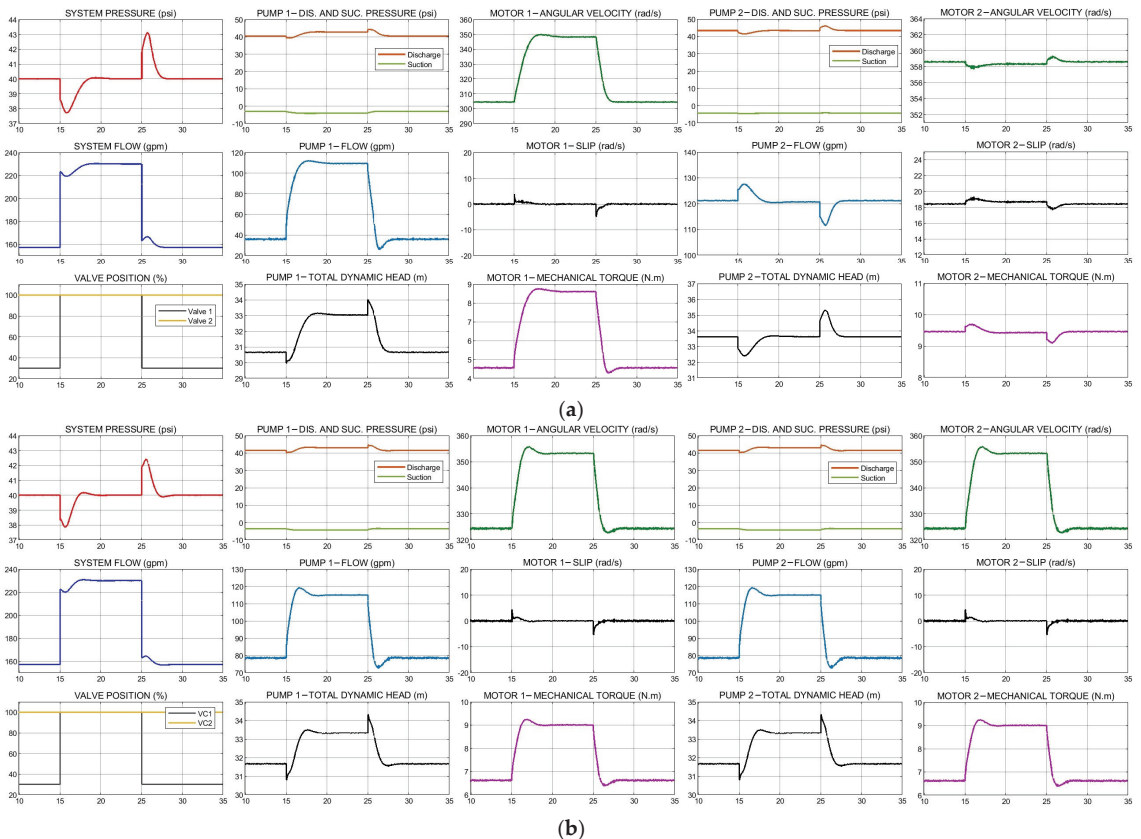


**Figure 13.** Dynamic response of the different hydraulic and mechanical variables of interest for a set point of 40 psi: (a) case study 1: a single pump at variable speed; (b) case study 2: both pumps at variable speed.

### 3.2. Starting Current and Harmonic Distortion

Figure 14 shows the waveforms of the currents and voltages during the induction motor starting process. Figure 14a corresponds to the direct start that occurred in the base case, through a direct connection to the electrical grid, a process that lasted approximately 200 ms (12 cycles). It is observed that the starting current was approximately 8.5 times the steady state current. On the other hand, Figure 14b shows the starting process through the acceleration ramp of 3600 rpm/s provided by the variable speed. In this second case, it is observed that the starting current did not exceed three times the current in steady state (Figure 14b), therefore this transient current was reduced by 64.7% compared with the base case (Figure 14a). The frequency inverter smooths the starting and stopping (Figure 14b) which prevents some unwanted electrical, mechanical, and hydraulic effects produced in

sudden starts and stops, such as water hammer and pressure peaks [43], vibrations in the pipes [44], voltage drops in the motor and the electrical grid [45], or mechanical stress that reduces the useful life of the motor [46].

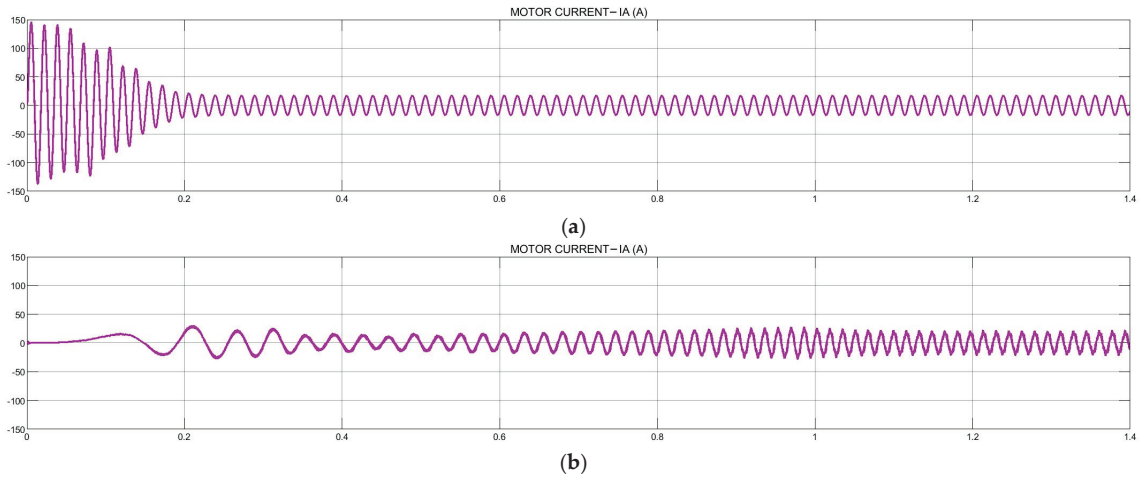


**Figure 14.** Currents and voltages during starting: (a) starting by direct connection to the grid; (b) starting by variable speed drive with 3600 rpm/s ramp.

When a pump operates at variable speed, the waveforms of the voltages and currents at the input and output of the drive are as shown in Figure 15a. The line voltage and current waveforms, for cases one and two, are presented in Figure 15b,c, respectively. For these simulations, a short-circuit power of the source of 450 kVA and a ratio  $X/R = 10$  were considered. Distortions in current and voltage waveform are observed, which can be evaluated with a THD indicator.

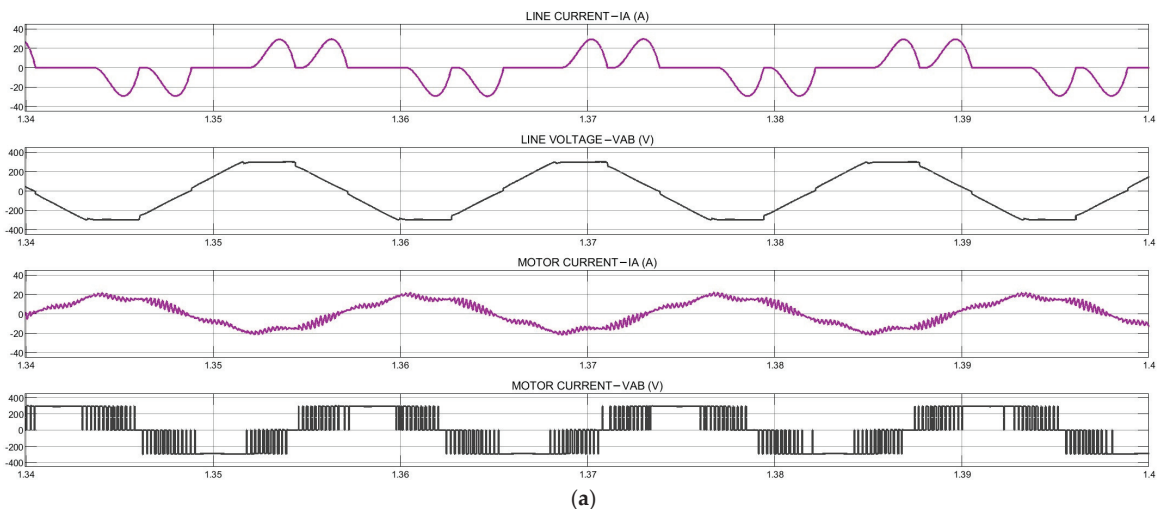


**Figure 15.** Cont.

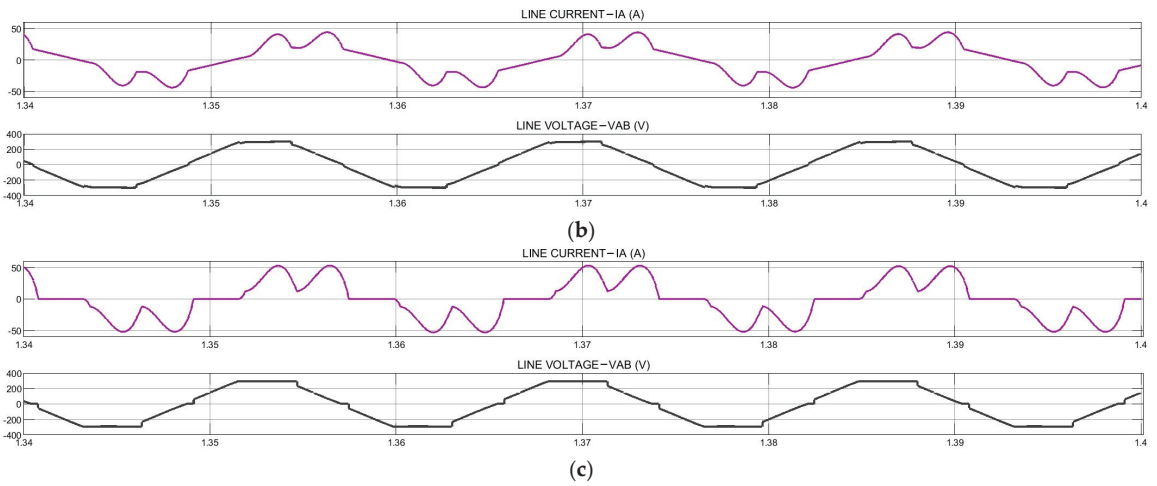


**Figure 15.** Steady-state currents and voltages: (a) Motor with variable speed drive; (b) case 1: one pump with a variable speed drive and the other with a direct connection to the grid; (c) case 2: both pumps with variable speed drive. The three scenarios at nominal speeds. The short circuit power of the source is 450 kVA, and the X/R ratio is 10.

Table 1 presents a summary of the total harmonic distortion (THD), an indicator that can be obtained using the Fast Fourier Transform (FFT), a tool that is part of Simulink’s specialized “powergui” block.

**Table 1.** Total Harmonic Distortion (THD).

Study Case	Pumps Running	Waveform	Current		Voltage	
			Line	Motor	Line	Motor
1, 2	1	Figure 15a	79.00	35.17	4.93	57.5
1	2	Figure 15b	33.87	-	4.30	-
2	2	Figure 15c	47.47	-	7.08	-

Values are in %.

The noncontrolled rectifier bridge was responsible for the harmonic distortion on the line side, and the inverter IGBT bridge produced the motor side harmonic distortion. Harmonic pollution generates various unwanted effects on the electrical grid and the loads connected to it [47–49] and also damages the induction motor [50,51]. However, the switching of power semiconductors also produces the reflected wave phenomenon, although this was not observed in the simulation. The reflected wave is amplified if the distance between the frequency inverter and the motor increases, generating overvoltages harmful to the conductors and the induction motor and also damaging overcurrents for the frequency inverter [52,53]. The harmonic distortion and reflected wave can be mitigated by implementing filters [49,53].

### 3.3. Power Saving

Table 2 shows the mechanical power required for the base case and the two study cases and also shows the percentage of mechanical power savings of the two study cases with respect to the base case. Eight operating scenarios defined by the opening percentage of consumption valves one and two were evaluated. With the torque and angular velocity data, the mechanical power was calculated using Equation (8).

**Table 2.** Power consumption and savings for various operating scenarios.

Scenarios			Total Mechanical Power			Savings Compared to the Base Case	
Valve 1 %	Valve 2 %	Pumps Running	Base Case kW	Case 1 kW	Case 2 kW	Case 1 %	Case 2 %
100	100	2	6.75	6.55	6.70	3.07	0.83
75	100	2	6.57	5.76	5.83	12.32	11.28
50	100	2	6.33	5.29	5.06	16.40	20.07
25	100	2	6.04	4.84	4.33	19.95	28.29
0	100	1	3.47	3.72	3.72	7.43	7.43
0	75	1	3.23	2.72	2.72	15.77	15.77
0	50	1	2.88	1.92	1.92	33.41	33.41
0	25	1	2.37	1.25	1.25	47.23	47.23

In high-demand scenarios (two pumps in parallel), the mechanical power was reduced to 19.95% for case one and 28.29% for case two. With decreasing demand, both cases operate with a single pump at variable speed, and mechanical power savings of up to 47.23% were obtained compared with the base case at a fixed speed. This analysis did not consider the losses of the motor or the frequency inverter, since under nominal conditions, electric motors are more efficient than pumps, and frequency inverters more efficient than motors; However, the efficiency of the motor can change with variations in load torque and speed [54–56]. The efficiency of the electrical system with a variable speed drive can be reduced by up to 8% with respect to the efficiency of the system with direct connection to the grid, but this reduction is not significant in relation to the energy savings achieved [56].

### 3.4. Investment Costs

CAPEX is higher in solutions with variable speed drive compared with traditional solutions at a fixed speed. However, the improvement in performance allows savings during the operation and maintenance of the system that increase profitability considering the entire life cycle.

### 3.5. Evaluation of the Case Studies

Table 3 presents, as a summary, the evaluation criteria of the cases studied.

**Table 3.** Evaluation summary of the cases studied.

Evaluation Criteria	Study Case		
	Base Case: Fixed Speed Pumps	Case 1: One Variable Speed Pump	Case 2: Both Pumps at Variable Speed
Pressure Control	At 40 psi $\pm$ hysteresis	Constant at 40 psi	Constant at 40 psi
Hydropneumatic tank capacity	80 gallons	10 gallons	10 gallons
Starting Current	Up to 8.5 times nominal	Up to 3 times the nominal	Up to 3 times the nominal
Harmonic Content	No harmonics	> THD	$\gg$ THD
Save Energy	There are no savings	Up to 47.23% savings in low flow rates	Up to 47.23% savings in low flow rates
		Up to 19.95% savings in high flow rates	Up to 28.29% savings in high flow rates
Investment Costs	Less	Intermediate	Higher

Table 3 shows that both studied cases develop a better performance compared with the base case in terms of process quality and energy efficiency. In addition, both cases affect the quality of the electrical energy because of the harmonic pollution they produce and require a higher CAPEX compared with the base case.

#### 4. Conclusions

In this research, two cases were studied to achieve a constant pressure system in a pumping station consisting of two centrifugal pumps in parallel, powered by electricity, and subjected to variable flow demand. The analysis was numerical in nature with modeling and simulation of systems carried out in MATLAB/Simulink R2019b. In the first case, one pump was operated at a fixed speed and the other at a variable speed, while in the second case, both pumps operated at a variable speed. These case studies were compared with each other and also compared with the base case where both pumps operated at a fixed speed. The results showed that with variable speed drives, it is possible to have a pressure regulating control system, achieving constant pressure in the face of variable flow demands, which is not achieved in the base case. In addition, variable speed drives smooth the current during acceleration and deceleration, leading to energy savings during startup and preventing unwanted electrical, mechanical, and hydraulic problems that are generated in sudden starts and stops (base case). Both study cases managed to reduce the required power by up to 47% compared with the base case. The second case obtained first place in energy efficiency by considering a variable speed drive in each pump. The harmonic distortion produced by frequency inverters was observed both on the line side and on the motor side. The harmonic distortion on the line side was higher in the second case, having two frequency inverters in parallel. This phenomenon can produce serious problems in the electrical grid, third-party equipment connected to the grid, and in induction motors, but it can be treated by implementing filters. The developed model is useful to study other control strategies that allow raising the degree of quality and efficiency of the pumping system, as well as harmonic filtering systems to improve the quality of energy.

**Author Contributions:** Conceptualization, R.J.A.-C. and J.A.P.-R.; methodology, C.D.A.-J. and C.G.R.-B.; software, R.J.A.-C.; validation, C.G.R.-B. and J.D.B.-E.; formal analysis, R.J.A.-C., J.A.P.-R., Y.E.L.-A. and C.D.A.-J.; investigation, R.J.A.-C.; resources, J.D.B.-E.; data curation, C.G.R.-B.; writing—original draft preparation, C.D.A.-J. and R.J.A.-C.; writing—review and editing, J.A.P.-R.; visualization, J.D.B.-E.; supervision, Y.E.L.-A. All authors have read and agreed to the published version of the manuscript.

**Funding:** This research received no external funding.

**Institutional Review Board Statement:** Not applicable.

**Informed Consent Statement:** Not applicable.

**Data Availability Statement:** Not applicable.

**Conflicts of Interest:** The authors declare no conflict of interest.

#### Abbreviations and Symbols

$q_{nom}$	Nominal flow rate of the pump
$q$	Arbitrary flow rate
$\omega_{nom}$	Nominal angular velocity of the pump
$\omega$	Arbitrary angular velocity
$\rho_{nom}$	Density of the fluid at nominal values
$\rho$	Density of the fluid at arbitrary values
$p_{nom}$	Differential pressure at nominal flow rate
$p$	Differential pressure at arbitrary flow rate
$P_{hyd\_nom}$	Hydraulic power at nominal conditions
$P_{hyd}$	Hydraulic power at arbitrary conditions
$P_{hyd0}$	Theoretical hydraulic power
$p_E$	Euler pressure
$P_{fr}$	Power of friction losses
$T_0$	Constant torque on the impeller shaft
$k_p$	Torque-pressure relationship

$P_{mec}$	Brake horsepower
$T$	Braking torque
$\eta$	Centrifugal pump efficiency
$V_T$	Total volume of the accumulator
$V_F$	Volume of the fluid in the accumulator
$V_i$	Initial volume of fluid in the accumulator
$V_C$	Total capacity of the fluid chamber
$V_d$	Dead volume of the gas chamber
$p_F$	Gauge pressure of the fluid in the fluid chamber
$p_{pr}$	Gauge pressure in the gas chamber when de fluid chamber is full
$p_A$	Atmospheric pressure
$p_G$	Pressure of the gas in the gas chamber
$p_{TD}$	Contact pressure of the hard stop
$K_r$	Stiffness coefficient of the hard stop
$K_a$	Damping coefficient of the hard stop
$k$	Specific heat ratio (adiabatic index)
$q_F$	Flow rate inside the accumulator
$p$	Pressure lost along the pipe
$q_p$	Flow rate in the pipe
$Re$	Reynolds number
$Re_L$	Maximum Reynolds number in laminar flow
$Re_T$	Minimum Reynolds number in turbulent flow
$K_s$	Form factor characterizing the pipe section
$f_L$	Friction factor at the laminar edge
$f_T$	Friction factor at turbulent edge
$A$	Cross-sectional area of the pipe
$D_H$	Diameter of the hydraulic pipe
$L$	Geometric length of the pipe
$L_{eq}$	Total equivalent length by local resistances
$r$	Height of the roughness on the internal surface of the pipe
$\nu$	Kinematic viscosity of the fluid
$R_s, L_{1s}$	Stator leakage resistance and inductance
$L_m$	Magnetization inductance
$L_s$	Total inductance of the stator
$V_{qs}, i_{qs}$	Stator voltage and current, referred to the $q$ axis
$V_{ds}, i_{ds}$	Stator voltage and current, referred to the $d$ axis
$\phi_{qs}, \phi_{ds}$	Stator fluxes referred to the $q$ axis and the $d$ axis
$R'_{r1}, L'_{lr1}$	Leakage resistance and inductance of rotor cage 1
$R'_{r2}, L'_{lr2}$	Leakage resistance and inductance of rotor cage 2
$L'_{r1}, L'_{r2}$	Total inductance of cage 1 and 2 of the rotor
$i'_{qr1}, i'_{qr2}$	Current of cage 1 and 2 of the rotor, referred to $q$ axis
$i'_{dr1}, i'_{dr2}$	Current of cage 1 and 2 of the rotor, referred to $d$ axis
$\phi'_{qr1}, \phi'_{dr1}$	Fluxes of the rotor cage 1 referred to $q$ y and $d$ axes
$\phi'_{qr2}, \phi'_{dr2}$	Fluxes of the rotor cage 2 referred to $q$ y and $d$ axes
$\omega_m$	Angular velocity of the rotor
$\theta_m$	Angular position of the rotor
$p$	Number of pole pairs
$\omega_r$	Electrical angular velocity ( $\omega_m * p$ )
$\theta_r$	Angular position of the electric motor ( $\theta_m * p$ )
$T_e$	Electromagnetic torque
$T_m$	Mechanical torque on the shaft
$J$	Coefficient of inertia of the rotor/load assembly
$H$	Inertia constant of the rotor/load set
$F$	Viscosity coefficient of friction of the rotor/load assembly
$N$	Speed set point in rpm
$N^*$	Speed feedback in rpm
$u(t)$	Control signal
$e(t)$	Control error



$K_p$	Proportional gain
$T_i$	Integral time
$T_d$	Derivative time
BEP	Best efficiency point
PI	Proportional and integral
PID	Proportional, integral and derivative
PLC	Programmable logic controller
POR	Preferred operating region
PWM	Pulse with modulation
SVM	Space vector modulation
THD	Total harmonic distortion
V/f	Voltage/frequency ratio
VSI	Voltage source inverter
VSD	Variable speed drive

## References

1. Werkhoven, M.V.; Werle, R.; Brunner, C.U. *Policy Guidelines for Motor Driven Units. Part 2: Recommendations for Aligning Standards and Regulations for Pumps, Fans and Compressors*; 4E Electric Motor Systems Annex: Zurich, Switzerland, 2018. Available online: [https://www.iea-4e.org/wp-content/uploads/publications/2018/05/PGMdu\\_Final\\_250418.pdf](https://www.iea-4e.org/wp-content/uploads/publications/2018/05/PGMdu_Final_250418.pdf) (accessed on 14 October 2021).
2. Rakibuzzaman, M.; Kim, K.; Kim, H.-H.; Suh, S.-H. Energy saving rates for a multistage centrifugal pump with variable speed drive. *J. Power Technol.* **2017**, *97*, 163–168.
3. Shankar, V.K.A.; Umashankar, S.; Paramasivam, S.; Norbert, H. Real time simulation of Variable Speed Parallel Pumping system. *Energy Procedia* **2017**, *142*, 2102–2108. [[CrossRef](#)]
4. Arun Shankar, V.K.; Umashankar, S.; Paramasivam, S.; Hanigovszki, N. A comprehensive review on energy efficiency enhancement initiatives in centrifugal pumping system. *Appl. Energy* **2016**, *181*, 495–513. [[CrossRef](#)]
5. Andrade-Cedeno, R. Gestión Energética de una Estación de Bombeo mediante el uso del Control Estadístico de Procesos. Estudio de Caso: Acueducto “La Esperanza”—Refinería del Pacífico. *Rev. Politécnica* **2018**, *40*, 7–18.
6. Arun Shankar, V.K.; Umashankar, S.; Padmanaban, S.; Bhaskar, M.S.; Almakles, D. Investigation for Performances Comparison PI, Adaptive PI, Fuzzy Speed Control Induction Motor for Centrifugal Pumping Application. In Proceedings of the 2019 IEEE 13th International Conference on Compatibility, Power Electronics and Power Engineering (CPE-POWERENG), Sonderborg, Denmark, 23–25 April 2019; pp. 1–6. [[CrossRef](#)]
7. Boldea, I.; Moldovan, A.; Tutelea, L. Scalar V/f and I-f control of AC motor drives: An overview. In Proceedings of the 2015 Intl Aegean Conference on Electrical Machines & Power Electronics (ACEMP), 2015 Intl Conference on Optimization of Electrical & Electronic Equipment (OPTIM) & 2015 Intl Symposium on Advanced Electromechanical Motion Systems (ELECTROMOTION), Side, Turkey, 2–4 September 2015; pp. 8–17.
8. Elan, S.; Aishwarya, A. Simulation & Development of Inverter Fed Three Phase Induction Motor Using V/f Control Strategy. *Int. J. Emerg. Technol. Adv. Eng.* **2014**, *4*, 151–156.
9. Zhang, Z.; Liu, Y.; Bazzi, A.M. An improved high-performance open-loop V/f control method for induction machines. In Proceedings of the 2017 IEEE Applied Power Electronics Conference and Exposition (APEC), Tampa, FL, USA, 26–30 March 2017; pp. 615–619. [[CrossRef](#)]
10. Chitra, A.; Sultana, W.R.; Vanishree, J.; Sreejith, S.; Jose, S.; Pulickan, A.J. Performance Comparison of Multilevel Inverter Topologies for Closed Loop v/f Controlled Induction Motor Drive. *Energy Procedia* **2017**, *117*, 958–965. [[CrossRef](#)]
11. Nasser, A.; Szemes, P.T. Speed Control of Three Phase Induction Motor Using Scalar Method and PID Controller. *Recent Innov. Mechatron. (RIIM)* **2018**, *5*, 1–5. [[CrossRef](#)]
12. Behera, P.K.; Behera, M.K.; Sahoo, A.K. Speed Control of Induction Motor using Scalar Control Technique. *IJCA Proc. Int. Conf. Emerg. Trends Comput. Commun. ETCC* **2014**, *1*, 37–39.
13. Hartono, H.; Sudjoko, R.I.; Iswahyudi, P. Speed Control of Three Phase Induction Motor Using Universal Bridge and PID Controller. *J. Phys. Conf. Ser.* **2019**, *1381*, 1–8. [[CrossRef](#)]
14. Moreano Peña, J.; Vásquez Díaz, E. Implementation of V/f scalar control for speed regulation of a three-phase induction motor. In Proceedings of the 2016 IEEE ANDESCON, Arequipa, Peru, 19–21 October 2016; pp. 1–4. [[CrossRef](#)]
15. Andrade-Cedeno, R.; Perez-Rodriguez, J.A. Análisis del control V/f con SVM en un accionamiento de velocidad variable. *Dominios De La Cienc.* **2021**, *7*, 38–62.
16. Lysenko, O.A.; Simakov, A.V. The Pump Hydraulic Load Effect Determination on the Parameters of an Frequency-Controlled Asynchronous Electric Drive. In Proceedings of the XIII International Scientific and Technical Conference “Dynamics of Systems, Mechanisms and Machines” (Dynamics), Omsk, Russia, 5–7 November 2019; pp. 1–6. [[CrossRef](#)]
17. Abdelwanis, M.I.; Selim, F. A sensorless six-phase induction motor driving a centrifugal pump system. In Proceedings of the 2017 Nineteenth International Middle East Power Systems Conference (MEPCON), Cairo, Egypt, 19–21 December 2017; pp. 242–247. [[CrossRef](#)]

18. Gevorkov, L.; Vodovozov, V.; Raud, Z. Simulation study of the pressure control system for a centrifugal pump. In Proceedings of the 2016 57th International Scientific Conference on Power and Electrical Engineering of Riga Technical University (RTUCON), Riga, Latvia, 13–14 October 2016; pp. 1–5. [\[CrossRef\]](#)
19. Arun Shankar, V.K.; Umashankar, S.; Paramasivam, S.; Hanigovszki, N. An Energy Efficient Control Algorithm for Parallel Pumping Industrial Motor Drives System. In Proceedings of the 2018 IEEE International Conference on Power Electronics, Drives and Energy Systems (PEDES), Chennai, India, 23–25 April 2019; pp. 1–6. [\[CrossRef\]](#)
20. Oshurbekov, S.; Kazakbaev, V.; Prakht, V.; Dmitrievskii, V.; Gevorkov, L. Energy Consumption Comparison of a Single Variable-Speed Pump and a System of Two Pumps: Variable-Speed and Fixed-Speed. *Appl. Sci.* **2020**, *10*, 8820. [\[CrossRef\]](#)
21. Viholainen, J. Energy-efficient control strategies for variable speed driven parallel pumping systems based on pump operation point monitoring with frequency converters. Ph.D. Thesis, Lappeenranta University of Technology, Lappeenranta, Finlandia, 2014.
22. Andrade-Cedeño, R. Módulo didáctico para controlar nivel y caudal de agua, mediante sistema SCADA, PLC y algoritmo PID. *RIEMAT* **2019**, *4*, 50–62. [\[CrossRef\]](#)
23. Sarbu, I.; Valea, E.S. Energy Savings Potential for Pumping Water in District Heating Stations. *Sustainability* **2015**, *7*, 5705–5719. [\[CrossRef\]](#)
24. Al-Ani, D.S. Energy Optimization Strategy for System-Operational Problems. Ph.D. Thesis, McMaster University, Hamilton, ON, Canada, 2012.
25. ANSI; Hydraulic Institute. *Rotodynamic (Centrifugal and Vertical) Pumps—Guideline for Allowable Operating Region (ANSI/HI 9.6.3-2017)*; Hydraulic Institute: Parsippany, NJ, USA, 2017.
26. Ahmed, A.; Moharam, B.; Rashad, E. Power Saving of Multi Pump-Motor Systems Using Variable Speed Drives. In Proceedings of the 2018 Twentieth International Middle East Power Systems Conference (MEPCON), Cairo, Egypt, 18–20 December 2018; pp. 839–844. [\[CrossRef\]](#)
27. Bharti, R.; Kumar, M.; Prasad, B.M. V/F Control of Three Phase Induction Motor. In Proceedings of the 2019 International Conference on Vision Towards Emerging Trends in Communication and Networking (ViTECoN), Vellore, India, 30–31 March 2019; pp. 1–4. [\[CrossRef\]](#)
28. Anjum, F.; Sharma, N. Speed Control of Induction Motor using Hybrid PID Fuzzy Controller. *Int. Res. J. Eng. Technol. (IRJET)* **2018**, *5*, 576–580.
29. Aranz, R.; García, F.J.; Miguel, L.J. Métodos de control de motores de inducción: Síntesis de la situación actual. *Rev. Iberoam. De Automática E Inf. Ind. RIAI* **2016**, *13*, 381–392. [\[CrossRef\]](#)
30. Pati, S.; Patnaik, M.; Panda, A. Comparative performance analysis of fuzzy PI, PD and PID controllers used in a scalar controlled induction motor drive. In Proceedings of the 2014 International Conference on Circuits, Power and Computing Technologies [ICCPCT-2014], Nagercoil, India, 20–21 March 2014; pp. 910–915. [\[CrossRef\]](#)
31. Bonavita, N. How process automation can increase energy efficiency. In *Hydrocarbon Processing*; Gulf Energy Information: Genoa, Italy, 2013; pp. 71–75. Available online: <https://library.e.abb.com/public/953141f99f2f77985257b810060bb17/Hydrocarbon%20Processing%20June%202013%20Energy%20Efficiency.pdf> (accessed on 3 December 2021).
32. Likins, M. PID tuning improves process efficiency. In *Control Engineering*; CFE Media and Technology: Downers Grove, IL, USA, 2013. Available online: <https://www.controleng.com/articles/pid-tuning-improves-process-efficiency/> (accessed on 10 December 2021).
33. Gomes, F.J.; Queiroz, F.P.; Lopes, I.F.; Coelho, A.A.R. Energy Savings in Industrial Processes: A Case Study of Strategies and Tuning Procedures for PI and PID Controllers. *IFAC Proc. Vol.* **2012**, *45*, 607–612. [\[CrossRef\]](#)
34. MathWorks Help Center. Centrifugal Pump with Choice of Parameterization Options. Available online: <https://la.mathworks.com/help/physmod/hydro/ref/centrifugalpump.html> (accessed on 12 January 2022).
35. MathWorks Help Center. Hydraulic Accumulator with Gas as Compressible Medium. Available online: <https://la.mathworks.com/help/physmod/hydro/ref/gaschargedaccumulator.html> (accessed on 12 January 2022).
36. MathWorks Help Center. Hydraulic Resistive Tube. Available online: <https://la.mathworks.com/help/physmod/simscape/ref/hydraulicresistivetube.html> (accessed on 12 January 2022).
37. MathWorks Help Center. Transformadas de Clarke y Park. Available online: <https://la.mathworks.com/solutions/power-electronics-control/clarke-and-park-transforms.html> (accessed on 12 January 2022).
38. MathWorks Help Center. Universal Bridge. Available online: <https://la.mathworks.com/help/physmod/sps/powersys/ref/universalbridge.html> (accessed on 12 January 2022).
39. MathWorks Help Center. Space Vector PWM VSI Induction Motor Drive. Available online: <https://la.mathworks.com/help/physmod/sps/powersys/ref/spacevectorpwmvsiinductionmotordrive.html> (accessed on 12 January 2022).
40. Ogata, K. *Ingeniería de Control Moderna*; Pearson Educación S.A.: Madrid, Spain, 2010.
41. Latchoomun, L.; Sockalingum, T.; Poullé, K.V.; King, R.T.F.A.; Busawon, K.K.; Barbot, J.P. Design of a Water Pressure Boosting System for Pressure-Driven Demand in a Distribution Network. In Proceedings of the 2018 5th International Symposium on Environment-Friendly Energies and Applications (EFEA), Rome, Italy, 24–26 September 2018; pp. 1–6. [\[CrossRef\]](#)
42. Khayatzaadeh, F.; Ghafouri, J. Dynamical modeling of frequency controlled variable speed parallel multistage centrifugal pumps. *Arch. Mech. Eng.* **2015**, *62*, 347–361. [\[CrossRef\]](#)
43. Greenwood, S. Soft starter benefits in pump control. *World Pumps* **2015**, *2015*, 24–27. [\[CrossRef\]](#)

44. Lale, D.; Oršulić, M.; Palunko, I. Modelling and soft-start control of measurement and transport line. In Proceedings of the 2020 International Conference on Smart Systems and Technologies (SST), Osijek, Croatia, 14–16 October 2020; pp. 59–64. [\[CrossRef\]](#)
45. Matanov, N. Study of the impact of induction motors starting on the supply voltage. In Proceedings of the 2019 16th Conference on Electrical Machines, Drives and Power Systems (ELMA), Varna, Bulgaria, 6–8 June 2019; pp. 1–5. [\[CrossRef\]](#)
46. Habyarimana, M.; Dorrell, D.G. Methods to reduce the starting current of an induction motor. In Proceedings of the 2017 IEEE International Conference on Power, Control, Signals and Instrumentation Engineering (ICPC-SI), Chennai, India, 21–22 September 2017; pp. 34–38. [\[CrossRef\]](#)
47. Zare, F.; Soltani, H.; Kumar, D.; Davari, P.; Delpino, H.A.M.; Blaabjerg, F. Harmonic Emissions of Three-Phase Diode Rectifiers in Distribution Networks. *IEEE Access* **2017**, *5*, 2819–2833. [\[CrossRef\]](#)
48. Srividhya, J.P.; Sivakumar, D.; Shanmathi, T. A Review on causes, effects, and detection techniques of harmonics in the power system. In Proceedings of the 2016 International Conference on Computation of Power, Energy Information and Communication (ICCPEIC), Melmaruvathur, India, 20–21 April 2016; pp. 680–686. [\[CrossRef\]](#)
49. Kalair, A.; Abas, N.; Kalair, A.R.; Saleem, Z.; Khan, N. Review of harmonic analysis, modeling and mitigation techniques. *Renew. Sustain. Energy Rev.* **2017**, *78*, 1152–1187. [\[CrossRef\]](#)
50. Beleiu, H.G.; Maier, V.; Pavel, S.G.; Birou, I.; Pică, C.S.; Dărab, P.C. Harmonics Consequences on Drive Systems with Induction Motor. *Appl. Sci.* **2020**, *10*, 1528. [\[CrossRef\]](#)
51. Zhang, D.; An, R.; Wu, T. Effect of voltage unbalance and distortion on the loss characteristics of three-phase cage induction motor. *IET Electr. Power Appl.* **2018**, *12*, 264–270. [\[CrossRef\]](#)
52. Narayanasamy, B.; Sathyanarayanan, A.S.; Deshpande, A.; Luo, F. Impact of cable and motor loads on wide bandgap device switching and reflected wave phenomenon in motor drives. In Proceedings of the 2017 IEEE Applied Power Electronics Conference and Exposition (APEC), Tampa, FL, USA, 26–30 March 2017; pp. 931–937. [\[CrossRef\]](#)
53. Narayanasamy, B.; Sathyanarayanan, A.S.; Luo, F.; Chen, C. Reflected Wave Phenomenon in SiC Motor Drives: Consequences, Boundaries, and Mitigation. *IEEE Trans. Power Electron.* **2020**, *35*, 10629–10642. [\[CrossRef\]](#)
54. Lozanov, Y.; Tzvetkova, S.; Petleshkov, A. Study of the effectiveness of a variable frequency drive of an induction motor. In Proceedings of the 2019 11th Electrical Engineering Faculty Conference (BulEF), Varna, Bulgaria, 11–14 September 2019; pp. 1–6. [\[CrossRef\]](#)
55. Agamloh, E.; Cavagnino, A.; Vaschetto, S. Induction Machine Efficiency at Variable Frequencies. In Proceedings of the 2019 IEEE Energy Conversion Congress and Exposition (ECCE), Baltimore, MD, USA, 29 September–3 October 2019; pp. 1655–1662. [\[CrossRef\]](#)
56. Burt, C.; Piao, X.; Gaudi, F.; Busch, B.; Taufik, N.F. Electric Motor Efficiency under Variable Frequencies and Loads. *J. Irrig. Drain. Eng.-ASCE* **2008**, *134*, 129–136. [\[CrossRef\]](#)

## Article

# Evaluating the Impact of Public Information and Training Campaigns to Improve Energy Efficiency: Findings from the Italian Industry

Michele Preziosi <sup>1</sup>, Alessandro Federici <sup>1</sup> and Roberto Merli <sup>2,\*</sup>

<sup>1</sup> Energy Efficiency Department, ENEA (Italian National Agency for New Technologies, Energy and Sustainable Economic Development), Lungotevere Thaon di Revel, 76, 00196 Roma, Italy;

michele.preziosi@enea.it (M.P.); alessandro.federici@enea.it (A.F.)

<sup>2</sup> Department of Business Studies, Roma Tre University, Via Silvio D'Amico 77, 00145 Roma, Italy

\* Correspondence: roberto.merli@uniroma3.it

**Abstract:** Energy efficiency is a pillar for the energy system transition and for reaching the Sustainable Development Goals. In the light of the “energy efficiency first!” principle, European member states enforce policies to spread energy saving throughout the whole energy chain involving both citizens and industries. In this context, information and training campaigns arise as valuable support tools to disseminate energy efficiency and, therefore, for reducing energy consumption. Although various studies have evaluated the impact of information campaigns targeted to citizens, there is a lack of investigations that assess the impact of campaigns dedicated to industry sectors. This study discusses the results of a survey targeted at energy-intensive Italian companies, with a sample of 300 responses. Starting from the analysis of drivers that trigger the implementation of energy efficiency measures, the paper proposes an approach to evaluate the amount of energy savings linked to the Italian information and training program targeted to industries carried out by the Italian Energy Efficiency Agency. Results show that although information campaigns are not a crucial driver for companies, they are recognized as a factor that contributes to the implementation of energy efficiency practices. Findings show that roughly 1.4% of energy savings noted by interviewed companies to the Italian Energy Efficiency Agency are a direct effect of the information and training program. This outcome has significant implications, especially for decision-makers, giving evidence of the efficacy of information campaigns on industries, which have great potential for the transition to low carbon production systems.

**Citation:** Preziosi, M.; Federici, A.; Merli, R. Evaluating the Impact of Public Information and Training Campaigns to Improve Energy Efficiency: Findings from the Italian Industry. *Energies* **2022**, *15*, 1931. <https://doi.org/10.3390/en15051931>

Academic Editors: Roberto Alonso González Lezcano, Francesco Nocera and Rosa Giuseppina Caponetto

Received: 9 February 2022

Accepted: 27 February 2022

Published: 7 March 2022

**Publisher's Note:** MDPI stays neutral with regard to jurisdictional claims in published maps and institutional affiliations.



**Copyright:** © 2022 by the authors. Licensee MDPI, Basel, Switzerland. This article is an open access article distributed under the terms and conditions of the Creative Commons Attribution (CC BY) license (<https://creativecommons.org/licenses/by/4.0/>).

**Keywords:** information and training campaign; energy savings assessment; energy efficiency policy; industry; industrial energy efficiency

## 1. Introduction

Among the main global challenges to be tackled over the coming decades, energy represents one of the major issues to ensure a sustainable economy and society. The United Nations 2030 Agenda for Sustainable Development underlines the importance of guaranteeing to all “access to affordable, reliable, sustainable and modern energy” with a dedicated Sustainable Development Goal [1]. A shift toward a more sustainable energy system is also necessary to meet the ambitious climate goals of the Paris Agreement of keeping a global temperature rise this century well below 2 °C above pre-industrial levels and to pursue efforts to limit the temperature increase even further to 1.5 °C [2].

Decarbonization arises as a strategic priority for all sectors, from industry [3] to urban areas [4], with the goal of reaching nearly zero emissions by 2050 [5,6]. This process requires the engagement of all levels of society, embracing a wide range of stakeholders who may have and require different approaches for the implementation of deep decarbonization [7]. To achieve a zero-emission economy, inter-organizational cooperation is needed as well as

cross-border partnerships, especially among European Union member states [8]. Currently, the development of knowledge and technologies has paved the way to a possible decarbonization without undermining the ability of the economic system to grow and prosper through the improvement of energy efficiency and a zero-emission clean energy supply replacing fossil fuels. However, this transition to low-carbon technologies is a great policy challenge, as the measures implemented must maintain their cost-effectiveness [9]. In this race to a net-zero carbon economy, together with the diffusion of renewable energy sources, energy efficiency has a crucial role [10], representing the first goal for the energy transition and a crucial pillar for reaching Sustainable Development Goals [11]. To respond to this global challenge, the European Union has launched the Clean Energy for all Europeans package, a comprehensive assessment of its energy policy framework. In order to achieve the 2050 long-term climate neutrality strategy, the package sets ambitious energy and climate target for 2030 with a reduction of energy use of at least 32.5%. It also introduces the principle of “energy efficiency first!”, identifying energy efficiency as the key objective of the European Union.

Indeed, energy savings are the most accessible way of saving money for consumers and reducing greenhouse gases emissions [12,13]. Moderation of energy demand should be achieved throughout the whole energy chain, involving both citizens and companies. According to the European Union Directive on Energy Efficiency (Directive 2012/27/EU), member states should play an active role in informing and engaging households and businesses in adopting technical and behavioral energy savings measures [14,15]. Considering this aspect, information and training campaigns arise as an enabling factor available to the member states for the dissemination of energy efficiency awareness and, therefore, for the achievement of European energy savings targets. These programs may contribute to mitigate the energy efficiency gap [16], as awareness campaigns contribute to reduce the issue of imperfect information in markets, guiding interested parties to a more efficient allocation of energy efficiency actions and investments [17–19]. Also in the industry sector, information and training campaigns can be considered as a supportive policy measure, promoting and stimulating a favorable environment for the implementation of energy saving practices, helping to improve industry’s access to information that is considered a relevant barrier to energy efficiency measures [20,21].

Previous experiences have pointed out that one of the most critical aspects for industry is the ability to identify efficiency measures that are both energy-efficient and cost-effective [22]. A cost-effective energy efficiency measure is defined as an investment that lowers the use of energy and is considered cost-effective according to the company’s investment criteria [23]. This issue is known as the efficiency gap and is a relevant barrier toward the process of decarbonization of the sector. This is often due to a lack of knowledge and information and represents a major market failure to implement cost-effective energy-saving practices [22]. The European Green Paper on Energy Efficiency (COM (2005) 265 final) underlines that information and training are two under-used tools that provide clear information on how to make cost-effective energy savings and can be effective in changing perceptions and encouraging industry action. Authors over the years have debated over the effectiveness of information and training campaigns: whereas some consider them as not effective, others argue that if properly delivered they can be effective and actively reduce the efficiency gap [18,24]. For instance, Thollander [23] highlights that information and training campaigns help to reduce market failures or market imperfections, reducing the risk that industry does not take the most cost-effective energy-saving measures, compromising the sector’s potential to actively participate in the process of decarbonization [25].

Once the information campaigns have been implemented, the next crucial step is the evaluation of their efficacy in terms of their impact on energy savings. Nevertheless, for national institutions, a punctual assessment of the reduction of energy uses ascribable to information campaigns still remains a big challenge [26]. Although various studies evaluated the impact of information campaigns targeted to citizens, there is a lack of

investigations that assess the impact of campaigns dedicated to non-residential sectors, e.g., [27,28]. Thus, the aim of this work is to illustrate the approach that the Italian national authorities have adopted to assess and quantify the energy savings resulting from the implementation of the national information and training program dedicated to industries. Through a survey dedicated to those companies, identified as the target of the Italian program, the study has two main purposes. The first is to quantify energy savings achieved by industries as an effect of the information and training campaign carried out by the public competent authorities to support the implementation of energy savings practices. The second purpose relates to the identification of the main drivers that led industries to realize energy efficiency interventions, in order to evaluate if the information campaign plays a significant role in activating those drivers.

The paper is structured as follows: first, it introduces the regulatory and the national context with respect to the information and training campaigns for energy efficiency. Next, it explores previous investigations that analyzed the drivers and enabling factors behind the implementation of energy efficiency measures in industry, trying to identify if information campaigns have played a significant role. Once presented the context and findings from previous studies, the survey was developed to evaluate the results is described. The presentation of the results and their discussion follows. Finally, limitations of the study and future lines of research are illustrated.

## 2. European and National Context

The European Union framework on energy efficiency is drawn by Directive 2012/27 (EED) and its recast by Directive 2018/2002 that set up new energy savings targets to be accomplished by 2030. According to the EED, instead of energy efficiency obligation schemes, member states may implement alternative policy measures to achieve their targets. These alternative measures include training and information campaigns that can positively contribute to the diffusion of technologies, techniques, or behaviors for the reduction of energy consumption (Art.7 EED). Article 17 (information and training) stresses the importance of member states in ensuring that information on energy efficiency is disseminated to all relevant stakeholders. Given the great energy-saving potential of information in spreading energy efficiency, the Directive also underlines the importance of public institutions in supporting firms in the implementation of energy efficiency measures by providing technical assistance and targeted information (EED whereas clause n.41).

Italy adopted the prescriptions of the EED with the National Decree n.104/2012. Specifically, Article 13 assigns to the Italian Agency for Energy Efficiency the implementation of a three-year information and training program with the aim of promoting the efficient use of energy among both households and companies. With respect to the latter category, the goals are to support and encourage the implementation of energy audits and then, through subsequent interventions, the diffusion of energy-efficient technologies and awareness on energy efficiency measures in the industry. The program was carried out between 2015 and 2019, and primary activities related to the establishment of permanent technical panels of experts with the main industrial associations; the organization of seminars and conferences; the formulation of standardized reporting models for energy audit data processing; and the preparation of sectoral guidelines for energy audits and energy efficiency interventions [29].

According to the legislative framework of the European Union, member states shall deliver a National Energy Efficiency Action Plan (NEEAP). Additionally, annually member states shall publish a progress report of all energy efficiency improvement measures that deliver energy savings [15]. Some member states over the last several years have reported in the NEEAPs and in the annual progress reports the measures implemented through information and training campaigns [30]. Those measures mainly target citizens' behaviors, whereas fewer efforts have been addressed to improve companies' awareness of energy efficiency. According to the European Joint Research Centre, a critical aspect that member states should further develop is related to the assessment of the efficacy of these measures implemented by member states. In fact, it remains still a challenge establishing a common

and shared framework to evaluate the impact of information and training campaigns in terms of energy saved from citizens and from companies [26].

### 3. Energy Conservation Drivers in the Industry: Analysis of the Literature

Industry barriers to the implementation of energy efficiency measures have been extensively analyzed mainly through surveys and case studies from a variety of perspectives such as financial/economic, organizational, and behavioral [31–33]. In general, the analysis and categorization of barriers is a result of the theoretical approach followed to investigate the phenomenon, for instance, the behavioral perspective relies on theories like the transaction cost economy and the economic perspective of the neoclassic theories [34]. Barriers have been studied also on the basis of their internal or external origin [35].

Other scholars differentiate between barriers dealing with the technical system and technological regime, and the socio-technical regime [36]. A multi-level categorization in micro-meso-macro barriers was proposed as well [37]. Given the industry process-related peculiarities, on several occasions scholars analyzed barriers from a specific industry perspective [25,38–42] or based on firm size [13,32,43–45]. These different analysis points reflect the peculiarities of the various industrial processes, also determining barriers whose level of intensity varies significantly depending on the sector under analysis.

Whereas barriers to energy efficiency practices have been widely studied, less research has been carried out on the driving forces behind energy-saving practices in the industry [31,32]. According to Cagno and Trianni [32], drivers for energy efficiency practices adoption were “factors facilitating the adoption of both energy-efficient technologies and practices, thus going beyond the view of investments and including the promotion of an energy-efficient culture and awareness”. Over the years authors have classified drivers into several categories, adapting them to the aim of the study and the context in which the investigations were conducted [38]. Thus, studies differ in relation to the theoretical approach, the industry sector, and the country in which the analysis was conducted.

Most studies identified in the review of the literature investigated energy-intensive sectors. The Swedish foundry industry was investigated by Rohdin et al. [42]. According to the results of that study, the most powerful drivers for energy savings were people with real ambitions and companies’ long-term strategies. A study conducted in 2013 analyzed driving forces for energy efficiency in 65 foundry industries in six European countries [25]. In that case, the most important forces to drive energy-saving practices related to financial aspects (rising energy prices and beneficial loans) and to organizational factors, such as companies’ environmental profile and long-term strategies. The Swedish iron and steel sector was studied by Brunke et al. [38]. Authors found out that the top management commitment was ranked as the highest, followed by the opportunity to reduce operational costs. Again in the Swedish context, Thollander and Ottosson [41] analyzed driving forces in the pulp and paper industry. The main drivers were cost reduction resulting from a reduced energy consumption, ambition, and companies’ long-term strategy for sustainability. Considering energy-intensive sectors, the Belgian cement sector was investigated by Venmans [39]. Starting from a selection of 53 energy efficiency projects, companies identified increasing energy prices as the main motivation that triggers energy efficiency measures, followed by the top-management commitment and the sustainable image of the companies in relation to customers. Hasanbeigi et al. [22] investigated drivers in the Thai cement industry. Results showed that reducing energy-related costs was the most significant force. Together, in second place, both improvement of product quality and enhancing staff health and safety were considered relevant drivers.

Another part of the literature studied energy-saving drivers in the manufacturing industries. Through a multiple case-study approach, Cagno and Trianni [32] investigated 71 Italian manufacturing small and medium enterprises (SMEs). The most meaningful drivers for implementing energy-saving measures were the allowances of public funding, external pressures, and long-term benefits. In contrast, increasing internal competencies and responding to customers’ requirements were not considered as important forces.

A similar analysis was conducted in Italy targeting 222 Italian manufacturing SMEs in 2016 [13]. In order of importance, economic and regulatory aspects (both internal and external) were the most significant. In the Netherlands, Cagno et al. [46] investigated manufacturing companies participating in the Dutch voluntary agreements for energy efficiency. Companies ranked first long-term strategy, clarity of information, and cost reduction from the reduced energy use as the crucial forces for interventions, whereas technological appeal and education and training programs were the least relevant.

Considering the Asian continent, a study was conducted in Korea [47] and one in Japan [48]. According to results, determinant factors for companies to practice energy-saving activities were in both cases internal, related to individual business strategies and energy savings motivation. Companies revealed that a major driver might be the promotion of energy efficiency in SMEs through government subsidies.

Other authors have tried to analyze energy efficiency drivers for industries with a theory-based approach, in several cases extending the scope of the institutional theory [31,47–49]. In China, 299 manufacturing companies were surveyed on the drivers and barriers about energy efficiency practices. According to results, coercive drivers did not significantly motivate companies, whereas normative and mimetic drivers had a positive influence on energy-saving practices implementation [49]. Zhang et al. [50] developed a conceptual model to better understand the formation of companies' energy savings practices integrating Institutional Theory. Findings showed that managers' environmental concern was significant in linking companies' energy-saving practices and the external pressure for energy conservation. Specifically, market-based tools (normative and mimetic pressure) were more effective than coercive pressure to drive companies toward energy use reduction. Similarly, Zhang et al. [31], starting from the institutional theory, showed that top management significantly linked external pressure and companies' energy efficiency practices. Results from the Chinese companies highlighted that coercive, mimetic, and normative pressure were important drivers for energy-saving measures implementation.

Taking into account energy efficiency drivers linked to information campaigns, Cagno et al. [46] found out that education and training programs were not considered by Netherlands' SMEs as relevant drivers, as none of the companies evaluated them as important or very important. In the Italian context, training and informative drivers were also evaluated to have low power [13].

#### 4. Aim of Study, Research Process, and Data Collection

##### 4.1. Aim and Scope of the Investigation

The analysis of the literature has shown, in the context of energy efficiency measures in the industry, that there is no consensus on the approach to evaluating if and to what extent the information and training campaigns are effective in stimulating the implementation of measures to reduce energy consumption. A starting point is to understand and recognize the most effective drivers for energy efficiency that are crucial for the information campaigns to deliver an effective message that could stimulate companies' action toward energy use reduction. Additionally, from the literature it has emerged that an approach to evaluate the significance of the energy savings arising from campaigns carried out by third-party institutions is still not available. From the analysis, two main research questions arise. The first one relates to the drivers that push industries to implement energy efficiency measures and the role of information and training campaigns. The second concerns the evaluation of the energy savings that can be attributed to the activities carried out by the institutions aimed at increasing awareness of possible applicable energy efficiency measures.

RQ1: What are the main drivers for the implementation of energy efficiency measures in the industry?

RQ2: How much energy savings achieved by industry is attributable to information and training activities carried out by third-party institutions?



#### 4.2. Research Process

According to the Art.7 of Italian National Decree 104/2012, companies subject to mandatory energy audit requirements should notify the Italian Energy Efficiency Agency on the energy savings achieved each year, additional to those that already benefited from the White Certificates scheme (energy efficiency obligation scheme) or other incentive mechanisms. Therefore, this specific group of companies was employed for the subsequent analysis. The companies' communications of energy savings are the baseline to estimate energy savings during the years (2015–2019) in which the Italian information and training program was conducted.

In order to answer the research questions, the first step was to identify the energy savings communicated by the selected group of companies. Next, through a survey targeted at the same companies, drivers for energy-saving measures implementation were evaluated to estimate the amount of energy savings that can be linked to the Italian information and training campaign.

The questionnaire is organized into three main parts. To obtain a clear picture of the responding population, in the first part of the questionnaire companies were asked to indicate their main economic activity according to The European Classification of Economic Activities (NACE rev.2—Regulation (EC) n.1893/2006). Given that the main goal of information campaign is to stimulate companies to take action, the section explores what the most relevant drivers are for the implementation of energy efficiency measures.

The second part of the questionnaire aims to identify (1) how much of the energy savings are due to measures implemented to comply with the legislation and to remedy design errors and (2) how much savings are due to interventions for which state incentives have been obtained (see Figure 1, STEP 1). In the view of the annual report to the European Commission about EDD article 7, the identification of these groups is necessary to avoid double counting when evaluating the savings obtained by the country through several energy efficiency policies.

Once we identified the companies that did not implement interventions for (1) and (2), we selected from the questionnaire responses those companies that considered the increased awareness on energy efficiency had played a significant role in the decision to implement energy reduction measures (STEP 2). The final part explores the significance of awareness factors for implementing energy efficiency measures and companies' evaluation of the importance of acquiring information and training to stimulate the energy efficiency interventions. In particular, the percentage of companies that considered the information and training activities carried out by the Italian Energy Efficiency Agency as "very important" in the decision to carry out energy efficiency interventions was considered. In more detail, companies were asked to indicate the relevance of the list of awareness factors in contributing to a greater awareness of energy efficiency and, thus, implementing energy efficiency measures. The awareness factors identified are external consultants; internal energy manager; mandatory energy audit; technical discussion tables organized by the Italian Energy Efficiency Agency; Italian Energy Efficiency Agency Road Show; Italian Energy Efficiency Agency commentary in meeting and seminars; Italian Energy Efficiency Agency interviews on TV/Web (STEP 3).

Once we identified this percentage of companies, the final step of the process was to multiply the obtained percentage for the energy savings communicated. The result gave a quantification of the energy savings directly associated with the information and training campaign carried out by Italian Energy Efficiency Agency (STEP 4).

Finally, the quantified energy savings associated with the information and training program was considered to be the 20% of the energy savings declared by this percentage of companies (correction factor). This choice was because, although the information campaign is considered to be very important for energy efficiency interventions, there are the other four awareness factors that simultaneously contribute to this choice (STEP 5).

Figure 1 summarizes the evaluation process used to quantify the energy savings directly associated with the information campaign carried out by the Italian Energy Efficiency Agency.

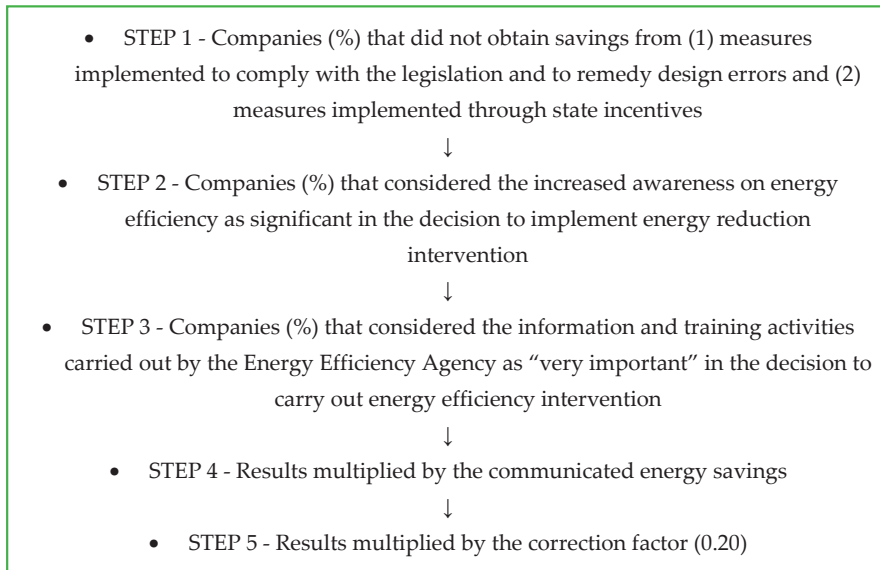


**Figure 1.** Evaluation process of energy savings from the Italian information and training programme in industry.

#### 4.3. Data Collection

As described in Section 5.1, data on the additional energy savings were collected through the communications made by companies according to Art.7 of National Decree 2004/2012. This list of companies was then used to send the email invitation to participate in the survey. Respondents are those who have responsibility for energy management for the selected companies (the selected companies are among those subject to mandatory energy audits) and who are responsible for communicating to relevant authorities the additional energy savings. Therefore, the interviewees are individuals fully aware of the energy-related processes within the target companies and have the role of supporting business strategies for more efficient energy management. The survey consisted of a questionnaire with multiple-choice questions with a Likert scale ranging from 1 to 4, with 1 corresponding to not important and four to very important. We decided not to have a mid-point or neutral score on the scale to stimulate a definite answer by respondents and, thus, to reduce uncertainty [51]. The investigation was carried out with an online survey tool. Eventually, 300 responses to the questionnaire were collected, with a response rate of 38.02% (the questionnaire was submitted to 789 companies).

## 5. Results

The section presents the main output of the survey. In addition to the analysis of the main sectors of activity of respondents' companies and drivers for energy-saving measures, the section illustrates the results following the process as described in Figure 1.

### 5.1. Sector of Activities

To contextualize and have a better viewpoint of respondent companies, they were asked to indicate their main economic activity following the NACE classification of economic activities. The main activity sectors are provided in Table 1. Only those sectors with

more than five responses are displayed, representing 78% of the respondents. Two sectors represent each over 10% of the total, namely “Manufacture of rubber and plastics” (12.2%) and “Manufacture of machinery and equipment” (10.8%). Other representative sectors with a share over 5% are “Manufacture of fabricated metal products, except machinery and equipment” (8.0%), “Manufacture of food products” (6.3%), “Manufacture of basic metals” (6.3%), and “Manufacture of chemicals and chemical products” (5.6%).

**Table 1.** NACE economic activities of respondents with a share of more than five companies.

NACE Code	Description	Number of Companies	Percent of Total
22	Manufacture of rubber and plastic products	35	11.7
28	Manufacture of machinery and equipment n.e.c	31	10.3
25	Manufacture of fabricated metal products, except machinery and equipment	23	7.7
10	Manufacture of food products	18	6.0
24	Manufacture of basic metals	18	6.0
20	Manufacture of chemicals and chemical products	16	5.3
23	Manufacture of other non-metallic mineral products	14	4.7
17	Manufacture of paper and paper products	12	4.0
13	Manufacture of textiles	10	3.3
27	Manufacture of electrical equipment	10	3.3
21	Manufacture of basic pharmaceutical products and pharmaceutical preparations	8	2.7
52	Warehousing and support activities for transportation	7	2.3
46	Wholesale trade, except of motor vehicles and motorcycles	6	2.0
47	Retail trade, except of motor vehicles and motorcycles	6	2.0
26	Manufacture of computer, Electronic, and optical products	5	1.7
30	Manufacture of other transport equipment	5	1.7
32	Other manufacturing	5	1.7
36	Water collection, treatment and supply	5	1.7
	Other sectors of activities	66	22.0

### 5.2. Drivers for Energy Efficiency Measures Implementation

Next, the questionnaire investigates companies’ perceptions with respect to the drivers for energy efficiency. Companies were asked to indicate the importance of four categories of drivers for the implementation of energy efficiency measures. Respondents evaluated the potential saving in operating costs as the most important reason for enforcing measures, which was considered “very important” by roughly 70% of companies and “important” by 23.9% of them. In addition, the opportunity of improving the relationship with customer and supply chain partners is considered as a significant driver for investing in energy efficiency; over 60% of companies considered this driver as “very important” (20.82%) or “important” (40.27%). Similarly, actions implemented as part of the Corporate Social Responsibility strategy are considered as relevant in roughly 58% of cases (“very important” 19.45%; “important” 38.23%). In contrast, the chance to obtain public incentives from energy efficiency interventions is irrelevant for the majority of companies. Almost half of respondents (43%) state that public incentives are “not important”, and 33.45% consider this driver as “slightly important”. Only in 3.75% of cases is this driver is “very important”. Figure 2 shows companies’ evaluation for each driver category.

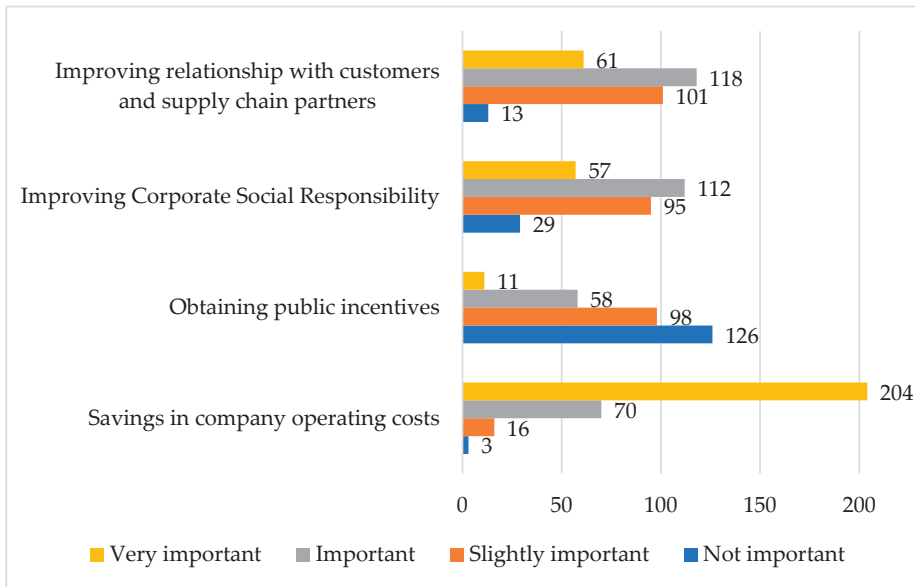


**Figure 2.** Companies' evaluation of the drivers for implementing energy efficiency measures.

### 5.3. Evaluation of Information Campaign Impact

Results of the survey show that 190 companies (63.33%) declared that they did not obtain energy savings from measures implemented to comply with the legislation and to remedy design errors or through state incentives (STEP 1). STEP 2 identified those companies that considered the information and training activities carried out by the National Energy Efficiency Agency (Italian National Energy Efficiency Agency: on behalf of the Ministry of Economic Development, the role of National Energy Efficiency Agency is assigned to ENEA (Italian National Agency for New Technologies, Energy and Sustainable Economic Development). <https://www.enea.it/en> (accessed 30 May 2021)) as “very important” in the decision to carry out energy efficiency interventions. This group consisted of 36 companies (12.00%). Next, STEP 3 showed that 93.67% (281) of respondents consider the increased awareness of energy efficiency as significant in the decision to implement energy reduction intervention. Table 2 summarizes the results of the first three steps of the evaluation process.

**Table 2.** Number of companies and associated percentage on the total of respondents identified in the first three steps (STEP 1–STEP 2–STEP 3) of the evaluation process.

Step of the Evaluation Process		Number of Companies	Percentage on the Total Respondents
STEP 1	Companies that did not obtain savings from (1) measures implemented to comply with the legislation and to remedy design errors and (2) measures implemented through state incentives	190	63.33%
STEP 2	Companies that considered the increased awareness on energy efficiency as significant in the decision to implement energy reduction intervention	281	93.67%
STEP 3	Companies that considered the information and training activities carried out by the National Energy Efficiency Agency as “very important” in the decision to carry out energy efficiency interventions	36	12.00%

Figure 3 illustrates how companies have evaluated the factors that contribute to stimulating their decision to apply energy-saving measures. The most significant factor is a consequence of the companies' obligation to perform the energy audit (“important”

or “very important” for 65.33% of the sample), followed by the influence of the external consultants (“important” or “very important” for 52.66% of the sample) and the internal energy manager (“important” or “very important” for 42.33% of the sample). Even though the information and training activities carried out by the public competent body were considered less powerful, respondents have recognized the role of the activities proposed by the National Energy Efficiency Agency in disseminating the energy efficiency culture.

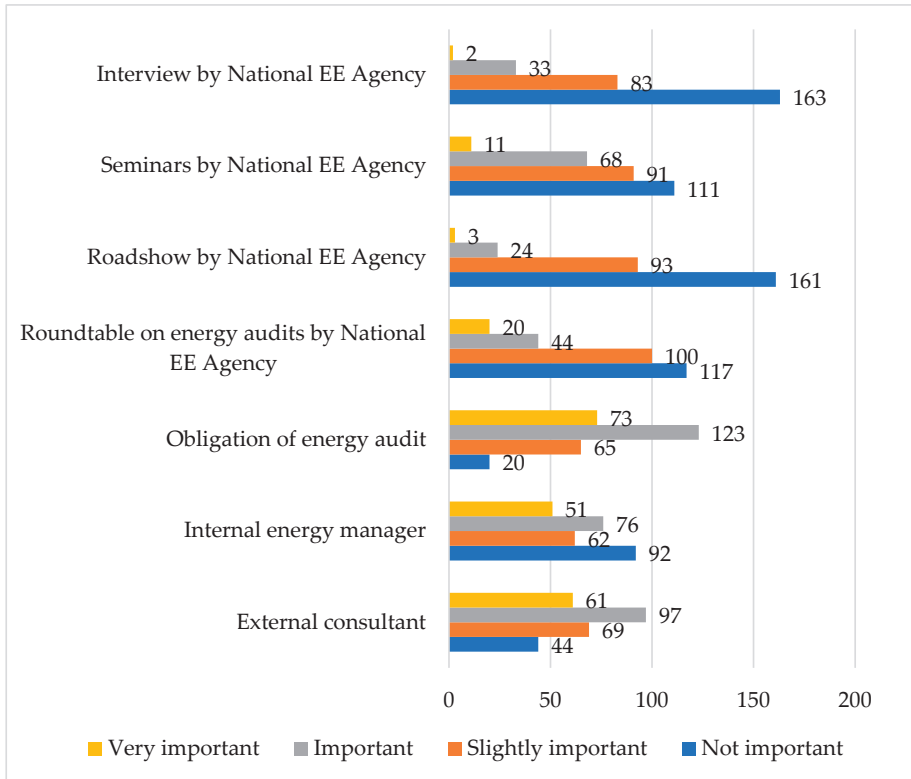


**Figure 3.** Importance of factors in contributing to the decision to implement energy efficiency measures.

Table 3 illustrates the energy savings communicated by companies to the Italian competent authority in 2015, 2016, 2017, 2018, 2019 and the cumulative savings for the same years.

**Table 3.** For the years 2015–2019, energy savings (ktoe) communicated to the Italian competent authority by companies’ subject to energy audit obligation.

Year	Energy Savings (ktoe)					Total
	2015	2016	2017	2018	2019	
2015	1046	1046	1046	1046	1046	5230
2016		790	790	790	790	3160
2017			1482	1482	1482	4446
2018				314	314	628
2019					431	431
						Cumulative savings
						13,896

Step 4 was to multiply the additional savings communicated by companies by the percentages obtained in Steps 1–2–3, and by the correction factor of 0.2 (STEP 5) (Table 4).

**Table 4.** Final energy savings (ktoe) for the years 2015–2019 associated with the information and training program carried out by the National Energy Efficiency Agency.

Energy Savings (ktoe)						
Year	2015	2016	2017	2018	2019	Total
2015	14.89	14.89	14.89	14.89	14.89	74.46
2016		11.25	11.25	11.25	11.25	44.99
2017			21.10	21.10	21.10	63.30
2018				4.47	4.47	8.94
2019					6.14	6.14
Cumulative savings						197.83

Eventually, the process has allowed quantifying the amount of energy savings that can be directly linked to the positive influence of the information campaign. Specifically, the cumulative savings for the period 2015–2019 amount to 197.83 ktoe.

## 6. Discussion and Conclusions

The first research question the study has tried to answer is related to the identification of drivers and factors that push companies to implement energy-saving measures. Results of the survey show that the reduction of energy use and the subsequent monetary savings is by far the most powerful force that pushes companies to invest in energy efficiency. Findings are consistent with other studies that identify energy-saving practices to be highly linked with companies' financial aspects and the reduction of operational costs [22,25,32,38,39,41]. Similar findings have been also identified in the Italian context, where the economic drivers were identified with the highest relevance by companies together with companies' long-term strategy [13]. In contrast, results do not confirm the findings by Suk et al. [47], and Cagno and Trianni [32] that identified access to public funding as one of the main drivers for energy efficiency measures. The study also corroborates previous findings that showed that the long-term strategy for sustainability is a significant driver for energy-saving practices [25,32,39,41,42]. Interviewed companies recognize that increasing the awareness of energy efficiency is significant in the decision to implement energy reduction intervention. This result corroborates other studies that highlight the importance of information for disseminating energy efficiency culture in industries [52]. Nevertheless, when specifically considering the information and training campaign in comparison with other driving factors, companies do not evaluate them as a key factor in the decision to put into practice energy-saving activities. This result is in line with other studies in which information campaigns are not considered a top-ranking driver for companies [13,47] (Figures 2 and 3).

Considering the second research question "How much energy savings achieved by industry is attributable to information and training activities carried out by third-party institutions?", the study tries to reduce the gap identified in the literature. The process presented in the paper has allowed us to quantify the amount of energy savings that can be considered as the outcome of the information and training campaign targeted to Italian companies. Specifically, the cumulative savings for the period 2015–2019 amount to 197.83 ktoe, corresponding to the 1.42% of the energy savings communicated by companies that are subject to the obligation to notify energy savings to the national authority. Due to the lack of literature on this specific field of research Rivas et al. [26], it has not been possible to compare findings with other previous studies. However, companies recognize the role of the Italian information and training program carried out by the National Energy Efficiency Agency. Nevertheless, vocational training emerges as especially crucial to remove barriers

affecting companies' awareness of energy efficiency [13]. In the study of Suk et al. [47] information and training support for energy-saving practices and providing information for the implementation of an internal energy management system was recognized as of significant importance for Korean companies. Even the survey conducted by Liu et al. [52] highlighted that employees' training would improve companies' willingness to implement energy-saving measures, suggesting that the Chinese government should organize energy efficiency information and training for companies.

The approach described and the associated results have significant implications both for practitioners and scholars. For the national authorities in charge of developing information and training campaigns, it represents a support for the decision-making process. It provides a way to evaluate the effects of the public investment made to spread the energy efficiency culture to the most energy-intensive industries. Additionally, it supports national authorities in considering how information and training programs directly contribute to the country's target in terms of reduction of energy consumption, especially for EU member states that have binding targets with at least 32.5% of improvement in energy efficiency at 2030 [14]. Findings of the research are also valuable to the academic world, as they pave the way toward a possible approach to assess energy savings deriving from this specific policy measure.

However, the evaluation process has some limitations. In order to isolate and calculate those energy savings directly linked to information and training programs, it has been necessary to make some assumptions to simplify the evaluation process directly connecting the answer from the questionnaire to the energy savings communicated by the companies. Another aspect not considered in the present study is the evaluation of the cost-effectiveness of the information and training campaign. When assessing the effectiveness of the campaign, it would be useful and significant to include an assessment of the return on the investment made by the Italian public authorities. This could be developed by comparing the financial capital invested in the campaign with the monetary value of the energy savings associated with the energy efficiency measures adopted by the target industries and induced by the campaign itself. Another drawback relates to the scope of the survey, which addresses a small sample size and a convenient sample choice. The survey was addressed only to companies that are bound to notify the national authority of the energy savings made, not considering all the companies that had taken part in the information and training activities carried out during the 2015–2019 period.

The evolution of the impact of information and training campaigns remains a challenge for both scholars and practitioners. Although several authors have successfully approximated the energy savings from campaigns targeted to citizens, the effects of campaigns on companies still remain relatively unexplored. Therefore, both practitioners and academics should approach the assessment of energy savings deriving from information and training campaigns targeted to energy-intensive industries, which still maintain a great potential to contribute to the energy transition required for a sustainable society [5] and to reach the Paris Agreement objectives [53]. A further step of the investigation may assess cost-benefits of energy efficiency information and training campaigns, to evaluate if the ratio between the expenditure incurred and energy saved is better or worse than other policy instruments set to reduce energy consumption.

**Author Contributions:** Conceptualization, M.P., A.F. and R.M.; data curation, M.P. and A.F.; formal analysis, M.P.; investigation, M.P.; methodology, M.P. and R.M.; project administration, M.P.; supervision, A.F. and R.M.; validation, M.P.; writing—original draft, M.P.; writing—review and editing, A.F. and R.M. All authors have read and agreed to the published version of the manuscript.

**Funding:** This research received no external funding.

**Institutional Review Board Statement:** Not applicable.

**Acknowledgments:** The authors would like to thank Marcello Salvio (ENEA) for making possible delivering the survey to the companies and Silvia Ferrari (ENEA) for the support in the design of the questionnaire.

**Conflicts of Interest:** The authors declare no conflict of interest.

## References

1. United Nations. *Transforming Our World: The 2030 Agenda for Sustainable Development*; United Nations: New York, NY, USA, 2015.
2. United Nations. *Report of the Conference of the Parties on its Twenty-First Session, Held in Paris from 30 November to 13 December 2015*; United Nations: New York, NY, USA, 2016.
3. Griffin, P.W.; Hammond, G.P.; Norman, J.B. Industrial energy use and carbon emissions reduction in the chemicals sector: A UK perspective. *Appl. Energy* **2018**, *227*, 587–602. [CrossRef]
4. Drożdż, W.; Kinelski, G.; Czarnecka, M.; Wójcik-Jurkiewicz, M.; Maroušková, A.; Zych, G. Determinants of decarbonization—How to realize sustainable and low carbon cities? *Energies* **2021**, *14*, 2640. [CrossRef]
5. Åhman, M.; Nilsson, L.J.; Johansson, B. Global climate policy and deep decarbonization of energy-intensive industries. *Clim. Policy* **2017**, *17*, 634–649. [CrossRef]
6. Rockström, J.; Gaffney, O.; Rogelj, J.; Meinshausen, M.; Nakicenovic, N.; Schellnhuber, H.J. A roadmap for rapid decarbonization. *Science* **2017**, *355*, 1269–1271. [CrossRef] [PubMed]
7. Bataille, C.; Waisman, H.; Colombier, M.; Segafredo, L.; Williams, J.; Jotzo, F. The need for national deep decarbonization pathways for effective climate policy. *Clim. Policy* **2016**, *16*, 7–26. [CrossRef]
8. Kurowska-Pysz, J.; Szczepańska-Woszczyna, K. The analysis of the determinants of sustainable cross-border cooperation and recommendations on its harmonization. *Sustainability* **2017**, *9*, 2226. [CrossRef]
9. Wójcik-Jurkiewicz, M.; Czarnecka, M.; Kinelski, G.; Sadowska, B.; Bilińska-Reformat, K. Determinants of decarbonisation in the transformation of the energy sector: The case of Poland. *Energies* **2021**, *14*, 1217. [CrossRef]
10. European Commission. COM(2018) 773 Final. *A European Strategic Long-Term Vision for a Prosperous, Modern, Competitive and Climate Neutral Economy*; European Commission: Brussels, Belgium, 2018.
11. International Energy Agency. *Energy Efficiency Market Report 2019*; International Energy Agency: Paris, France, 2019.
12. European Commission. *Clean Energy for All Europeans*; European Commission: Brussels, Belgium, 2019.
13. Trianni, A.; Cagno, E.; Farné, S. Barriers, drivers and decision-making process for industrial energy efficiency: A broad study among manufacturing small and medium-sized enterprises. *Appl. Energy* **2016**, *162*, 1537–1551. [CrossRef]
14. European Parliament DIRECTIVE (EU) 2018/2002 on Energy Efficiency. *Off. J. Eur. Union* **2018**, *L 328/210*. Available online: <https://eur-lex.europa.eu/legal-content/EN/TXT/PDF/?uri=CELEX:32018L2002&from=EN> (accessed on 2 February 2022).
15. European Parliament DIRECTIVE (EU) 2012/27 on Energy Efficiency. *Off. J. Eur. Union* **2012**, *L 315/1*. Available online: <https://eur-lex.europa.eu/legal-content/EN/TXT/PDF/?uri=CELEX:32012L0027&from=EN> (accessed on 2 January 2022).
16. Jaffe, A.B.; Stavins, R.N. The energy-efficiency gap What does it mean? *Energy Policy* **1994**, *22*, 804–810. [CrossRef]
17. Asensio, O.I.; Delmas, M.A. The dynamics of behavior change: Evidence from energy conservation. *J. Econ. Behav. Organ.* **2016**, *126*, 196–212. [CrossRef]
18. Linares, P.; Labandeira, X. Energy efficiency: Economics and policy. *J. Econ. Surv.* **2010**, *24*, 573–592. [CrossRef]
19. Trianni, A.; Cagno, E.; Worrell, E. Innovation and adoption of energy efficient technologies: An exploratory analysis of Italian primary metal manufacturing SMEs. *Energy Policy* **2013**, *61*, 430–440. [CrossRef]
20. Tanaka, K. Review of policies and measures for energy efficiency in industry sector. *Energy Policy* **2011**, *39*, 6532–6550. [CrossRef]
21. Abadie, L.M.; Ortiz, R.A.; Galarraga, I. Determinants of energy efficiency investments in the US. *Energy Policy* **2012**, *45*, 551–566. [CrossRef]
22. Hasanbeigi, A.; Menke, C.; du Pont, P. Barriers to energy efficiency improvement and decision-making behavior in Thai industry. *Energy Effic.* **2010**, *3*, 33–52. [CrossRef]
23. Thollander, P. *Towards Increased Energy Efficiency in Swedish Industry- Barriers, Driving Forces & Policies*; Linköping Institute of Technology: Linköping, Sweden, 2008; ISBN 9789173937931.
24. Grycan, W. Legislative support for improving sustainable and smart electricity consumption in polish residential sector. *J. Clean. Prod.* **2020**, *266*, 121995. [CrossRef]
25. Thollander, P.; Backlund, S.; Trianni, A.; Cagno, E. Beyond barriers—A case study on driving forces for improved energy efficiency in the foundry industries in Finland, France, Germany, Italy, Poland, Spain, and Sweden. *Appl. Energy* **2013**, *111*, 636–643. [CrossRef]
26. Rivas, S.; Cuniberti, B.; Bertoldi, P. *Effective Information Measures to Promote Energy Use Reduction in EU Member States. Analysis of Information, Empowerment and Training Measures in Member States National Energy Efficiency Action Plans*; Joint Research Centre: Brussels, Belgium, 2016.
27. Delmas, M.A.; Fischlein, M.; Asensio, O.I. Information strategies and energy conservation behavior: A meta-analysis of experimental studies from 1975 to 2012. *Energy Policy* **2013**, *61*, 729–739. [CrossRef]
28. Trotta, G. Factors affecting energy-saving behaviours and energy efficiency investments in British households. *Energy Policy* **2018**, *114*, 529–539. [CrossRef]
29. ENEA Italian Information and Training Programme (PIF). Available online: <http://italiainclassea.enea.it/programma/> (accessed on 2 February 2022).



30. European Commission National Action Plans and Annual Progress Reports. Available online: [https://ec.europa.eu/energy/topics/energy-efficiency/targets-directive-and-rules/national-energy-efficiency-action-plans\\_en?redir=1#demo](https://ec.europa.eu/energy/topics/energy-efficiency/targets-directive-and-rules/national-energy-efficiency-action-plans_en?redir=1#demo) (accessed on 8 January 2020).
31. Zhang, Y.; Wei, Y.; Zhou, G. Promoting firms' energy-saving behavior: The role of institutional pressures, top management support and financial slack. *Energy Policy* **2018**, *115*, 230–238. [[CrossRef](#)]
32. Cagno, E.; Trianni, A. Exploring drivers for energy efficiency within small- and medium-sized enterprises: First evidences from Italian manufacturing enterprises. *Appl. Energy* **2013**, *104*, 276–285. [[CrossRef](#)]
33. Sorrell, S.; Schleich, J.; Scott, S.; O'Malley, E.; Trace, F.; Boede, U.; Ostrertrag, K.; Radgen, P. *Reducing Barriers to Energy Efficiency in Public and Private Organizations*; University of Sussex: Sussex, UK, 2000.
34. König, W. Energy efficiency in industrial organizations—A cultural-institutional framework of decision making. *Energy Res. Soc. Sci.* **2020**, *60*, 101314. [[CrossRef](#)]
35. Cagno, E.; Worrell, E.; Trianni, A.; Pugliese, G. A novel approach for barriers to industrial energy efficiency. *Renew. Sustain. Energy Rev.* **2013**, *19*, 290–308. [[CrossRef](#)]
36. Thollander, P.; Palm, J.; Rohdin, P. *Categorizing Barriers to Energy Efficiency: An Interdisciplinary Perspective*; Palm, J., Ed.; InTech: Rijeka, Croatia, 2010; ISBN 978-953-307-137-4.
37. Sudhakara Reddy, B. Barriers and drivers to energy efficiency—A new taxonomical approach. *Energy Convers. Manag.* **2013**, *74*, 403–416. [[CrossRef](#)]
38. Brunke, J.C.; Johansson, M.; Thollander, P. Empirical investigation of barriers and drivers to the adoption of energy conservation measures, energy management practices and energy services in the Swedish iron and steel industry. *J. Clean. Prod.* **2014**, *84*, 509–525. [[CrossRef](#)]
39. Venmans, F. Triggers and barriers to energy efficiency measures in the ceramic, cement and lime sectors. *J. Clean. Prod.* **2014**, *69*, 133–142. [[CrossRef](#)]
40. Ren, T. Barriers and drivers for process innovation in the petrochemical industry: A case study. *J. Eng. Technol. Manag.* **2009**, *26*, 285–304. [[CrossRef](#)]
41. Thollander, P.; Ottosson, M. An energy efficient Swedish pulp and paper industry—Exploring barriers to and driving forces for cost-effective energy efficiency investments. *Energy Effic.* **2008**, *1*, 21–34. [[CrossRef](#)]
42. Rohdin, P.; Thollander, P.; Solding, P. Barriers to and drivers for energy efficiency in the Swedish foundry industry. *Energy Policy* **2007**, *35*, 672–677. [[CrossRef](#)]
43. Trianni, A.; Cagno, E. Dealing with barriers to energy efficiency and SMEs: Some empirical evidences. *Energy* **2012**, *37*, 494–504. [[CrossRef](#)]
44. Henriques, J.; Catarino, J. Motivating towards energy efficiency in small and medium enterprises. *J. Clean. Prod.* **2016**, *139*, 42–50. [[CrossRef](#)]
45. Thollander, P.; Danestig, M.; Rohdin, P. Energy policies for increased industrial energy efficiency: Evaluation of a local energy programme for manufacturing SMEs. *Energy Policy* **2007**, *35*, 5774–5783. [[CrossRef](#)]
46. Cagno, E.; Trianni, A.; Abeelen, C.; Worrell, E.; Miggiano, F. Barriers and drivers for energy efficiency: Different perspectives from an exploratory study in the Netherlands. *Energy Convers. Manag.* **2015**, *102*, 26–38. [[CrossRef](#)]
47. Suk, S.; Liu, X.; Sudo, K. A survey study of energy saving activities of industrial companies in the Republic of Korea. *J. Clean. Prod.* **2013**, *41*, 301–311. [[CrossRef](#)]
48. Liu, X.; Yamamoto, R.; Suk, S. A survey analysis of energy saving activities of industrial companies in Hyogo, Japan. *J. Clean. Prod.* **2014**, *66*, 288–300. [[CrossRef](#)]
49. Zhu, Q.; Geng, Y. Drivers and barriers of extended supply chain practices for energy saving and emission reduction among Chinese manufacturers. *J. Clean. Prod.* **2013**, *40*, 6–12. [[CrossRef](#)]
50. Zhang, B.; Wang, Z.; Lai, K. Mediating effect of managers' environmental concern: Bridge between external pressures and firms' practices of energy conservation in China. *J. Environ. Psychol.* **2015**, *43*, 203–215. [[CrossRef](#)]
51. Garland, R. The Mid-Point on a Rating Scale: Is It Desirable? *Mark. Bull* **1991**, *1*, 66–70.
52. Liu, X.; Niu, D.; Bao, C.; Suk, S.; Shishime, T. A survey study of energy saving activities of industrial companies in Taicang, China. *J. Clean. Prod.* **2012**, *26*, 79–89. [[CrossRef](#)]
53. Bataille, C.; Åhman, M.; Neuhoﬀ, K.; Nilsson, L.J.; Fishedick, M.; Lechtenböhmer, S.; Solano-Rodriquez, B.; Denis-Ryan, A.; Stiebert, S.; Waisman, H.; et al. A review of technology and policy deep decarbonization pathway options for making energy-intensive industry production consistent with the Paris Agreement. *J. Clean. Prod.* **2018**, *187*, 960–973. [[CrossRef](#)]



Article

# Association between Heavy Metal Exposure and Dyslipidemia among Korean Adults: From the Korean National Environmental Health Survey, 2015–2017

Do-won Kim <sup>1,2,†</sup>, Jeongwon Ock <sup>1,†</sup>, Kyong-Whan Moon <sup>2,\*</sup> and Choong-Hee Park <sup>1,\*</sup>

- <sup>1</sup> Environmental Health Research Division, National Institute of Environmental Research, Ministry of Environment, Incheon 22689, Korea; done35005@gmail.com (D.-w.K.); ockjeongwon@korea.kr (J.O.)  
<sup>2</sup> BK21 FOUR R & E Center for Learning Health System, Department of Health and Environmental Science, Korea University, Seoul 02841, Korea  
\* Correspondence: kwmoon@korea.ac.kr (K.-W.M.); whoispch@korea.kr (C.-H.P.); Tel.: +82-02-3290-5692 (K.-W.M.); +82-32-560-7126 (C.-H.P.); Fax: +82-32-568-2035 (C.-H.P.)  
† These authors contributed equally to this work.

**Abstract:** Cardiovascular disease (CVD) is a leading cause of death in Korea. Dyslipidemia, characterized by the presence of abnormal lipid levels, has been suggested as an early diagnostic and preventable factor for CVD. Recent studies have shown that exposure to lead (Pb), cadmium (Cd), and mercury (Hg) affects lipid metabolism. This study aimed to verify the association between heavy metal concentrations and serum lipid profiles in the general population. A representative sample of 2591 Korean adults from the Korean National Environmental Health Survey (2015–2017) was analyzed. The associations between heavy metals [Blood Pb (BPb), blood Hg (BHg), urinary Hg (UHg), urinary Cd (UCd)] and serum lipid profiles [total cholesterol (TC), triglyceride (TG), low-density lipoprotein cholesterol (LDL-C), non-low level of high-density lipoprotein cholesterol (Non-HDL-C)] were assessed using regression analysis. After adjusting for demographic and socioeconomic factors, the proportional changes in serum lipid levels were significantly associated with increases in BPb, BHg, and UHg levels ( $p$  for trend < 0.05). Overall, BPb, BHg, and Uhg levels positively correlated with dyslipidemia, whereas UCd levels did not show a significant association. Our results suggest that heavy metal exposure, at low levels, may contribute to an increased prevalence of dyslipidemia in Korean adults.

**Keywords:** heavy metals; serum lipid profiles; dyslipidemia; KoNEHS

**Citation:** Kim, D.-w.; Ock, J.; Moon, K.-W.; Park, C.-H. Association between Heavy Metal Exposure and Dyslipidemia among Korean Adults: From the Korean National Environmental Health Survey, 2015–2017. *Int. J. Environ. Res. Public Health* **2022**, *19*, 3181. <https://doi.org/10.3390/ijerph19063181>

Academic Editors: Roberto Alonso González Lezcano, Francesco Nocera and Rosa Giuseppina Caponetto

Received: 24 January 2022

Accepted: 3 March 2022

Published: 8 March 2022

**Publisher's Note:** MDPI stays neutral with regard to jurisdictional claims in published maps and institutional affiliations.



**Copyright:** © 2022 by the authors. Licensee MDPI, Basel, Switzerland. This article is an open access article distributed under the terms and conditions of the Creative Commons Attribution (CC BY) license (<https://creativecommons.org/licenses/by/4.0/>).

## 1. Introduction

Hypertension, hyperglycemia, and dyslipidemia are observed in individuals with metabolic syndrome [1]. Dyslipidemia is an important risk factor of cardiovascular disease (CVD) which is one of the diseases with high mortality worldwide [2]. In particular, dyslipidemia causes lipid accumulation in the arterial wall, which reduces blood flow to the heart, leading to CVD [3–5]. The prevalence of dyslipidemia is 53% and 45% in the United States and Canada [2,6] respectively. In Korea, the prevalence has increased from 34.1% in 2010–2013 to 36.5% in 2013–2015 [7,8]. Dyslipidemia is characterized by an imbalance of lipid levels in the blood, and it is caused by excessive entry of lipoproteins into the bloodstream or impaired ability to remove them [9–11].

Dyslipidemia is generally defined as elevated total cholesterol (TC), triglyceride (TG), low-density lipoprotein cholesterol (LDL-C), and a low level of non-high-density lipoprotein cholesterol (Non-HDL-C) [12–14]. Lifestyle features, such as dietary habits, lack of exercise, and alcohol consumption are commonly known risk factors for dyslipidemia [15]; however, several recent epidemiological studies suggest that abnormal lipid metabolism is associated with environmental chemical exposure [16–19]. Heavy metals, such as lead

(Pb), cadmium (Cd), and mercury (Hg), are released into the environment by natural and anthropogenic sources [20,21]. Human anthropogenic activities (e.g., agricultural, household, and industrial activities) have increased exposure to heavy metals through respiratory and dietary intake [22]. Environmental exposure to heavy metals occurs through breathing contaminated air, eating plants, and drinking water from contaminated soil or groundwater [23].

Heavy metals can accumulate in various tissues and exhibit toxic effects on intracellular metabolic processes (DNA damage, oxidative proteolysis, etc.) [24]. As a result, heavy metal exposure can cause various diseases [25]. Oxidative stress is one of the most important consequences of heavy metal exposure [26]. In particular, the production of hydroxyl ( $\bullet\text{OH}$ ) and peroxynitrite ( $\text{ONOO}^-$ ), which are involved in oxidative stress, are known to cause lipid imbalance and CVD [27,28]. In conclusion, heavy metal exposure may affect an increase in cholesterol, triglyceride, and lipoprotein content [28]. According to previous studies, Xu et al. (2021) reported significant increases in TC, Non-HDL-C, and LDL-C levels with Pb exposure in the US adult population [29]. A significant association has been proposed between Cd-exposed Korean adults and an increased risk of dyslipidemia [30]. Participants with above-average Hg concentrations were reported to have a higher risk of dyslipidemia than those who did not [31]. However, heavy metal toxicity depends on several factors, including the age, gender, genetics, and nutritional status of the exposed individual [32]. As heavy metal concentrations in Korea are higher than those in developed countries [33], low levels of chronic heavy metal exposure remain a public health concern. In addition, only a few studies have been conducted to investigate the association between heavy metal exposure and dyslipidemia in Koreans. Therefore, it is necessary to confirm the effect of heavy metals on the serum lipid profile of a representative adult sample of Korea. In the present study, we investigated blood and urine heavy metals (Pb, Cd, Hg), as well as serum lipid profiles (0, TG, LDL-C, non-HDL-C) provided in the Korea National Environmental Health Survey (KoNEHS) 2015–2017.

## 2. Methods

### 2.1. Study Population

The KoNEHS is a cross-sectional survey conducted every 3 years since 2009. The survey was designed to estimate and monitor exposure to various environmental pollutants in a representative Korean adult population. We analyzed the association between heavy metal exposure and serum lipid profile using data from 2015 to 2017, provided by KoNEHS. The national survey consists of a questionnaire, a physical examination, and the collection and analysis of biological samples, including a total of 26 chemicals and 16 clinical trial samples. Through a survey of trained investigators, six categories of information were obtained, including demographic and socioeconomic questions. Biological samples were collected by medical technicians and nurses under the supervision of a physician. In KoNEHS cycle 3, urine and blood samples were collected from a total of 3787 adults, aged 19 years and older. The following participants were excluded from the study (Figure 1): those who self-reported taking medications for hypertension or hyperlipidemia ( $n = 997$ ), those who were not tested for heavy metals or serum lipid profiles ( $n = 34$ ), and those with TG levels above 400 mg/dL ( $n = 151$ ), according to the Friedewald's equation, used to calculate LDL-C levels. Participants without urine creatinine concentration information, as well as demographic and socio-economic information used as covariates ( $n = 14$ ), were also excluded. Therefore, a total of 2591 participants were used for the analysis. This study was approved by the Research Ethics Committee of the National Institute of Environmental Research [34].

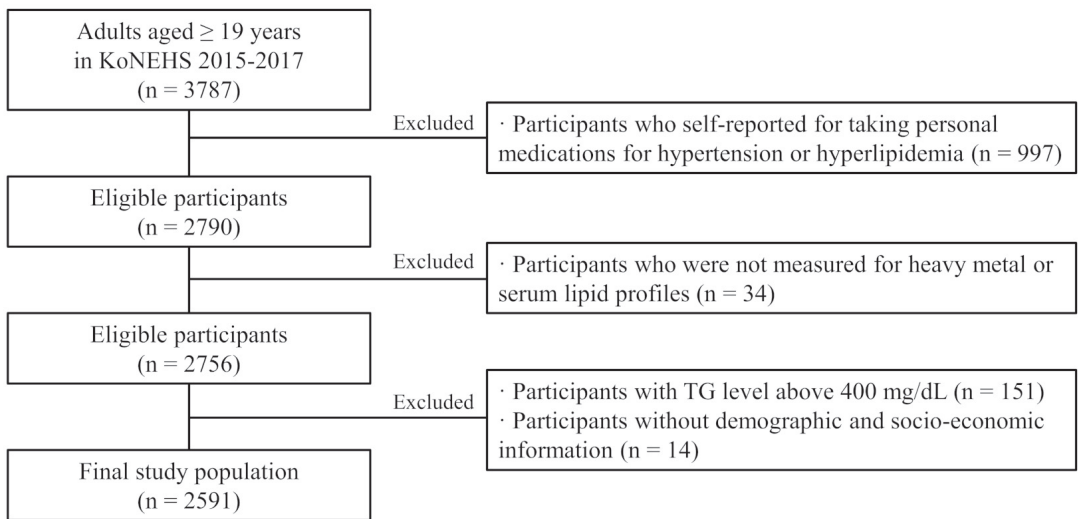


**Figure 1.** Participant flow chart of Korea National Environmental Health Survey (KoNEHS) 2015–2017 data available in this study.

## 2.2. Measurement of Heavy Metals

KoNEHS analyzed three heavy metals, including Pb, Cd, and Hg. Among these, Pb and total Hg were analyzed in blood, while Hg and Cd were analyzed in spot urine. Blood samples and spot urine samples were collected using a blood collection vessel (VACCU-TAINER Royal blue cap) and a sterile urine collection vessel (sample cup), respectively. The samples were maintained at 2–6 °C, using an ice box, and refrigerated at –20 °C for future analysis. Blood Pb (BPb) and urine Cd (UCd) were analyzed using graphite furnace-atomic absorption spectroscopy (AAAnalyst-800, Perkin Elmer) at wavelengths of 283.3 and 228.8 nm, respectively. Mercury concentrations in blood (BHg) and urine (UHg) were analyzed at wavelengths of 254.65 and 253.7 nm, respectively, using a gold amalgamation direct mercury analyzer (DMA-80, Milestone). The limits of detection (LOD) of heavy metals (Pb, Cd, and Hg) were 0.3 µg/dL, 0.1 µg/L, and 0.05 µg/L, respectively [35]. Values below the LOD of Pb, Cd, and Hg were substituted with the square root of the LOD. The quality control procedure was conducted using the standardized protocol procedure of the National Academy of Environmental Sciences.

## 2.3. Measurement of Serum Lipid Profile

KoNEHS collected total cholesterol (TC), Triglyceride (TG), and high-density lipoprotein cholesterol (HDL) from serum samples. Whole blood samples were collected in serum separation tubes (SST). The samples were mixed by inversion, held for 30 min, and then, centrifuged at 3500 RPM (revolutions per minute). TC, TG, and HDL-C levels were analyzed using an automated analyzer (ADVIA 1800; Siemens Medical Solutions, Ann Arbor, MI, USA) at 505/694, 505/694, and 596 nm wavelengths, respectively. The limits of detection (LOD) for TC, HDL-C, and TG were 10.0, 5.0, 10.0 mg/dL, respectively [36]. Values below the LOD of TC, HDL-C, and TG were replaced with the square root of the LOD.

## 2.4. Evaluation of Serum Lipid Profile

Dyslipidemia was defined as the presence of one or more of the following: TC ≥ 200 mg/dL, TG ≥ 150 mg/dL, LDL-C ≥ 130 mg/dL, and non-HDL-C ≥ 160 mg/dL [12,37]. In this study, LDL-C and non-HDL-C levels were obtained using indirect methods. LDL-C was calculated as  $TC - HDL(C) - [TG/5]$  using Friedewald's formula [38]. Owing to a limitation of the formula, TG values greater than 400 mg/dL were treated as missing

values [39,40]. This is because TG levels above 400 mg/dL may be underestimated, owing to a decrease in the TC: TG ratio of very low-density lipoprotein cholesterol (VLDL-C) [38]. Non-HDL-C was calculated as TC – HDL(C) [41]. Indirectly estimated non-HDL-C levels may be a better indicator of atherosclerotic lipoprotein particles than HDL-C levels [42,43]. KoNEHS samples could be used since fasting conditions are not required for lipid analysis.

### 2.5. Covariates

Covariates were chosen based on the associations between serum lipid profiles, according to the following characteristics provided in previous epidemiological studies [22,44]: age (19–39, 40–59, and 60 years or older); sex (Male, female); body mass index (BMI) calculated by dividing body weight (kg) by the square of height, and then, divided into categories of underweight (<18.5), normal (18.5–23), overweight (23–25), and obese (>25), according to the criteria of the Korean Society for the Study of Obesity (KOSSO); household income [low < 840; medium, 840–4220; high  $\geq$  4220 US dollars]; education ( $\leq$ middle school; high school;  $\geq$ college); smoking status (non-smoker, former smoker, current smoker); alcohol consumption [non-drinkers, light drinkers (twice a month), heavy drinker (once a week to almost daily)]; physical activity (none, moderate, and rarely).

### 2.6. Statistical Analysis

Stratum and cluster weights were applied to the regression model to consider a two-step proportional stratified sample design for KoNEHS data. For the analysis, differential probabilities of selection, non-response, and sample weights were applied. Serum lipid profiles were normally distributed and calculated as the arithmetic mean. The heavy metal concentrations did not follow a normal distribution, and the geometric means was calculated by log-transformation. Student's *t*-test and analysis of variance (ANOVA) were used to analyze statistical differences between different groups for continuous variables. Heavy metal concentrations were divided into quartiles, and serum lipid profiles were used as continuous variables. The mean change in serum lipid profile concentration by heavy metal concentration was analyzed using multiple linear regression analysis. For multivariate logistic regression, serum lipid profiles were divided into two groups, based on cholesterol levels (dyslipidemia or non-dyslipidemia by cholesterol levels) and the odds ratio [OR, 95% confidence interval (CI)] of dyslipidemia by heavy metal concentration. A value of  $p < 0.05$  was considered as statistically significant in all analyses. Statistical analysis was performed using the Statistical Analysis System (SAS) 9.4 software.

### 2.7. Sensitivity Analysis

First, as a limitation of the use of the LDL-C estimation formula, exclusion of participants with TG  $\geq$  400, may have confounded the results of other serum lipid profiles. Therefore, we performed an additional sensitivity analysis, for OR, of serum lipid profiles (TC, TG, and non-HDL-C) by heavy metal concentration in 2742 participants, including TG  $\geq$  400. Second, after further adjustment for heavy metal-related occupations for high exposure, the association between heavy metal exposure and serum lipid profile was analyzed. This analysis was performed on 74 participants involved in occupations related to heavy metals among 2951 participants with occupational data. Third, since non-occupational Hg exposure is primarily due to seafood consumption, we further adjusted for the high seafood dietary group. The high seafood consumption group was calculated by the sum of the frequency of consuming one or more of the five items (large fish and tuna, crustaceans, shellfish, and other seafood) at least once a week. Therefore, 1627 participants were classified into the high seafood dietary group, and the remaining 964 participants constituted the other group.

### 3. Results

#### Demographic Characteristics and Serum Lipid Profiles

The weighted arithmetic means (AM) of TC, TG, LDL-C, and non-HDL-C were 185.70 (0.97), 145.42 (2.17), 99.10 (0.87), and 128.18 (0.97) mg/dL, respectively (Table 1). Serum lipid profile levels were significantly higher in male than in female, and they significantly increased with age and BMI ( $p < 0.001$ ). In participants with low household income, TG significantly increased ( $p < 0.05$ ). Participants with low education levels had higher serum lipid profile levels ( $p < 0.05$ ). Participants who smoked had significantly higher lipid levels than those who did not ( $p < 0.05$ ). TG was significantly linked with drinking status ( $p < 0.05$ ). In terms of physical activity, only TG was significantly lower in the group, with hardly any physical activity compared with the reference group ( $p < 0.05$ ).

**Table 1.** Arithmetic means (mg/dL) of serum lipid profiles (mg/dL) in participants ( $n = 2591$ ) by demographic characteristics.

	<i>n</i> (%)	TC (mg/dL (SE))		TG (mg/dL (SE))		LDL-C (mg/dL (SE))		Non-HDL-C (mg/dL (SE))		
<b>Total</b>	2591	(100)	185.70	(0.97)	145.42	(2.17)	99.10	(0.87)	185.70	(0.97)
<b>Sex</b>										
Male	1111	(49.4)	182.52	(1.67)	145.45	(3.08)	95.00	(1.51)	128.48	(1.63)
Female	1480	(50.6)	182.58	(1.11)	110.71	(1.98)	93.86	(0.97)	119.03	(1.12)
<i>p</i> -value			<0.001		<0.001		0.249		<0.001	
<b>Age group (years)</b>										
19–39	766	(29.56)	175.58	(1.54)	116.95	(3.11)	88.32	(1.41)	115.55	(1.51)
40–59	1152	(44.46)	190.12	(1.20)	134.35	(2.34)	100.57	(0.99)	131.07	(1.14)
≥60	673	(25.97)	183.13	(2.06)	137.16	(3.53)	96.81	(1.83)	128.63	(2.07)
<i>p</i> -value			<0.001		<0.001		<0.001		<0.001	
<b>BMI (kg/m<sup>2</sup>)</b>										
<18.5	82	(3.92)	174.05	(5.25)	95.39	(6.33)	89.15	(3.62)	108.23	(4.01)
18.5–22.9	944	(39.0)	177.41	(1.33)	115.01	(2.82)	91.84	(1.11)	114.84	(1.25)
23.0–25.0	677	(25.9)	191.55	(1.95)	154.45	(3.47)	104.59	(1.92)	135.48	(2.03)
>25	888	(31.8)	192.36	(1.75)	180.91	(4.00)	104.61	(1.56)	140.80	(1.64)
<i>p</i> -value			<0.001		<0.001		<0.001		<0.001	
<b>Household income (US\$/month)</b>										
Low (840)	332	(12.81)	180.64	(3.08)	139.78	(5.73)	94.08	(2.75)	126.74	(2.97)
Middle (840–4220)	1777	(68.58)	181.64	(1.09)	124.58	(2.23)	94.05	(1.01)	122.59	(1.08)
High (≥4220)	482	(18.60)	185.86	(2.02)	129.04	(4.42)	95.64	(1.78)	125.65	(1.98)
<i>p</i> -value			0.063		0.006		0.729		0.103	
<b>Education levels</b>										
≤Middle school	641	(24.74)	187.29	(1.69)	135.53	(2.99)	99.84	(1.60)	131.36	(1.60)
High school	847	(32.69)	184.23	(1.47)	130.27	(3.16)	96.52	(1.19)	126.35	(1.40)
≥College	1103	(42.57)	180.52	(1.37)	122.76	(2.66)	92.05	(1.31)	120.35	(1.32)
<i>p</i> -value			0.001		0.025		<0.001		<0.001	
<b>Smoking status</b>										
Never	1694	(65.38)	181.05	(1.05)	116.05	(2.03)	93.44	(0.92)	120.01	(1.06)
Former	455	(17.56)	187.55	(2.11)	149.54	(4.36)	99.08	(1.81)	133.42	(1.93)
Current	442	(17.06)	183.27	(2.15)	145.87	(5.08)	93.81	(1.88)	127.41	(2.21)
<i>p</i> -value			0.002		<0.001		0.001		<0.001	

Table 1. Cont.

	<i>n</i> (%)	TC (mg/dL (SE))	TG (mg/dL (SE))	LDL-C (mg/dL (SE))	Non-HDL-C (mg/dL (SE))
<b>Drinking status</b>					
Never	783 (30.22)	182.08 (1.57)	123.99 (4.23)	95.32 (1.44)	123.86 (1.69)
Light	889 (34.31)	180.61 (1.78)	118.92 (3.07)	95.37 (1.48)	122.64 (1.77)
Heavy	919 (35.47)	184.57 (1.42)	135.69 (3.51)	93.06 (1.40)	124.31 (1.40)
<i>p</i> -value		0.118	<0.001	0.099	0.760
<b>Physical activity</b>					
None	1458 (56.27)	182.55 (1.21)	126.51 (2.32)	94.40 (1.11)	123.51 (1.27)
Moderate	204 (7.87)	184.92 (3.00)	138.31 (7.15)	93.85 (2.86)	125.82 (3.57)
Hardly	929 (35.85)	182.08 (1.70)	124.70 (3.00)	94.58 (1.48)	123.31 (1.65)
<i>p</i> -value		0.631	0.014	0.856	0.575

*p*-values are calculated based on survey *t*-test for binominal groups (sex) and based on Wald F-test for categorical groups (age groups, BMI, household income, education levels, smoking status, drinking status, and physical activity); Abbreviations: SE, standard error; TC, total cholesterol; TG, triglyceride; LDL, low-density lipoprotein cholesterol; HDL-C, high density lipoprotein cholesterol; Non-HDL, non-high density lipoprotein cholesterol.

Table 2 shows the comparison of heavy metal concentrations in the non-dyslipidemia and the dyslipidemia group. Concentrations of BPb in the elevated lipid profile group of TC, TG, LDL-C, and Non-HDL-C were significantly higher than that in the non-dyslipidemia group ( $p < 0.05$ ). BHg concentrations were significantly higher in the dyslipidemia group of TC, TG, LDL-C, and Non-HDL-C than that in the non-dyslipidemia group ( $p < 0.05$ ). UHg concentrations were significantly higher in the dyslipidemia group of LDL-C and Non-HDL-C than that in the non-dyslipidemia group ( $p < 0.05$ ). The UCd concentrations were significantly higher in the dyslipidemia group of LDL-C and Non-HDL-C than that in the non-dyslipidemia group ( $p < 0.05$ ).

**Table 2.** Geometric means of heavy metal concentrations, according to the dyslipidemia or non-dyslipidemia group ( $n = 2591$ ).

	<i>n</i>	BPb ( $\mu\text{g/dL}$ (95% CIs))	BHg ( $\mu\text{g/L}$ (95% CIs)) <sup>a</sup>	UHg ( $\mu\text{g/L}$ (95% CIs)) <sup>a</sup>	UCd ( $\mu\text{g/L}$ (95% CIs))
<b>TC (mg/dL)</b>					
<200	1703	1.50 (1.46, 1.55)	2.56 (2.41, 2.71)	0.38 (0.36, 0.41)	0.39 (0.36, 0.42)
$\geq 200$	888	1.64 (1.57, 1.71)*	3.06 (2.89, 3.24)*	0.42 (0.39, 0.45)	0.43 (0.39, 0.47)
<b>TG (mg/dL)</b>					
<150	2254	1.45 (1.40, 1.50)	2.53 (2.38, 2.68)	0.39 (0.36, 0.41)	0.38 (0.35, 0.42)
$\geq 150$	337	1.72 (1.65, 1.79)*	3.02 (2.85, 3.20)*	0.40 (0.38, 0.43)	0.43 (0.39, 0.47)
<b>LDL-C (mg/dL)</b>					
<160	2168	1.52 (1.47, 1.56)	2.62 (2.48, 2.76)	0.38 (0.36, 0.40)	0.39 (0.36, 0.42)
$\geq 160$	423	1.72 (1.63, 1.83)*	3.32 (3.10, 3.56)*	0.46 (0.41, 0.51)*	0.48 (0.43, 0.53)*
<b>Non-HDL-C (mg/dL)</b>					
<130	2091	1.51 (1.46, 1.55)	2.61 (2.48, 2.76)	0.38 (0.36, 0.40)	0.39 (0.36, 0.42)
$\geq 130$	500	1.76 (1.67, 1.86)*	3.20 (2.97, 3.45)*	0.45 (0.41, 0.50)*	0.45 (0.40, 0.50)*

<sup>a</sup> Total mercury, \* *p*-value < 0.05. Abbreviations: CI, confidence interval; BPb, blood lead; BHg, blood mercury; UHg, urinary mercury; UCd, urinary cadmium; TC, total cholesterol; Non-HDL, non-high density lipoprotein cholesterol; TG, triglyceride; LDL, low-density lipoprotein cholesterol.

Table 3 presents the adjusted ORs (95% CIs) for dyslipidemia by heavy metals. BPb and BHg concentrations showed significant associations with a higher risk of dyslipidemia (all  $p < 0.05$ ). For BPb, the ORs of the upper quartiles of elevated TC, LDL-C, and non-HDL-C compared with the OR of the lowest quartile were 1.49 (95% CI: 1.07–2.08;  $p = 0.084$ ), 1.57 (95% CI: 1.02–2.40;  $p = 0.041$ ), 1.71 (95% CI: 1.09–2.68;  $p = 0.049$ ), respectively. Compared with the OR in the lowest quartile of BHg, the OR of elevated TC in the 4th quartile was 1.72 (95% CI: 1.21–2.44;  $p = 0.016$ ), and ORs for elevated LDL-C for the 2nd, 3rd, and 4th quartiles, compared with the OR of the 1st quartile, were 1.63 (95% CI: 1.08–2.45), 1.77

(95% CI:1.17–2.68), and 2.21 (95% CI:1.49–3.28), respectively ( $p$  for trend < 0.05). There are no significant associations between Uhg, UCd, and dyslipidemia. Additionally, we examined the association between heavy metals and serum lipid profiles for including  $TG \geq 400$ . The results were similar to those obtained, with the exclusion of  $TG \geq 400$  (Supplementary Materials, Table S1). After adjustment for heavy metal-related occupations or the high seafood dietary group, the results were consistent with those obtained with the non-adjustment models (Supplementary Materials, Tables S2 and S3).

**Table 3.** Multivariate logistic regression of serum lipid profiles by heavy metal concentrations in participants ( $n = 2591$ ).

		$\beta$ (95% CI) of Serum Lipid Levels							
		$n$	Elevated TC ( $\geq 200$ mg/dL)	Elevated TG ( $\geq 150$ mg/dL)	Elevated LDL-C ( $\geq 130$ mg/dL)	Elevated Non-HDL-C ( $\geq 160$ mg/dL)			
<b>BPb (<math>\mu\text{g/dL}</math>)</b>									
Q1	(0.37–1.21)	651	Reference	Reference	Reference	Reference			
Q2	(1.21–1.65)	644	1.05 (0.76, 1.45)	1.11 (0.77, 1.62)	0.96 (0.59, 1.53)	1.03 (0.66, 1.60)			
Q3	(1.65–2.23)	647	1.14 (0.87, 1.50)	1.13 (0.78, 1.65)	1.24 (0.84, 1.84)	1.27 (0.84, 1.92)			
Q4	(2.23–20.58)	649	1.49 (1.07, 2.08) *	1.43 (0.98, 2.08)	1.57 (1.02, 2.40) *	1.71 (1.09, 2.68) *			
$p$ for trend			0.084	0.249	0.041	0.049			
<b>BHg (<math>\mu\text{g/L}</math>)<sup>a</sup></b>									
Q1	(0.33–1.85)	647	Reference	Reference	Reference	Reference			
Q2	(1.86–2.77)	648	1.17 (0.86, 1.59)	1.23 (0.81, 1.56)	1.63 (1.08, 2.45) *	1.20 (0.80, 1.79)			
Q3	(2.77–4.30)	649	1.21 (0.87, 1.68)	1.00 (0.73, 1.37)	1.77 (1.17, 2.68) *	1.02 (0.64, 1.64)			
Q4	(4.30–60.60)	647	1.72 (1.21, 2.44) *	0.86 (0.59, 1.24)	2.21 (1.49, 3.28) *	1.52 (1.01, 2.28) *			
$p$ for trend			0.016	0.478	0.012	0.011			
<b>UHg (<math>\mu\text{g/L}</math>)<sup>a</sup></b>									
Q1	(0.10–0.23)	655	Reference	Reference	Reference	Reference			
Q2	(0.24–0.35)	641	0.87 (0.64, 1.18)	0.95 (0.66, 1.36)	0.89 (0.55, 1.44)	0.79 (0.51, 1.20)			
Q3	(0.36–0.64)	648	1.19 (0.85, 1.66)	1.10 (0.74, 1.62)	1.36 (0.88, 2.11)	1.32 (0.86, 2.02)			
Q4	(0.65–8.70)	647	1.32 (0.88, 1.96)	0.77 (0.52, 1.15)	1.55 (0.98, 2.45)	1.37 (0.89, 2.10)			
$p$ for trend			0.154	0.185	0.055	0.037			
<b>UCd (<math>\mu\text{g/L}</math>)</b>									
Q1	(0.05–0.22)	688	Reference	Reference	Reference	Reference			
Q2	(0.22–0.45)	607	1.00 (0.70, 1.43)	1.18 (0.88, 1.58)	0.84 (0.58, 1.22)	1.16 (0.65, 2.06)			
Q3	(0.45–0.87)	648	0.78 (0.56, 1.09)	1.06 (0.74, 1.52)	0.61 (0.39, 0.94)	1.72 (0.95, 3.11)			
Q4	(0.87–16.82)	648	0.86 (0.59, 1.24)	1.14 (0.83, 1.56)	0.85 (0.56, 1.29)	1.58 (0.83, 2.99)			
$p$ for trend			0.396	0.657	0.661	0.172			

<sup>a</sup> Total mercury, \*  $p$ -value < 0.05, Abbreviations: CI, confidence interval; BPb, blood lead; BHg, blood mercury; UHg, urinary mercury; UCd, urinary cadmium; TC, total cholesterol; Non-HDL, non-high density lipoprotein cholesterol; TG, triglyceride; LDL, low-density lipoprotein cholesterol.

Figure 2 presents the estimated associations between serum lipid profiles and heavy metal concentrations using multiple linear regression analysis. After multivariable adjustment, BPb, BHg, and UHg in the upper quartiles had higher TC, TG, LDL-C, and non-HDL-C levels than those in the lowest quartile. There is evidence of dose-response relationships between: BPb and TC, LDL-C, and non-HDL-C; BHg and TC and Non-HDL-C; UHg and TC, LDL-C, and Non-HDL-C ( $p$  for trend < 0.05). We did not observe dose-response relationships between the UCd concentrations and serum lipid profiles.



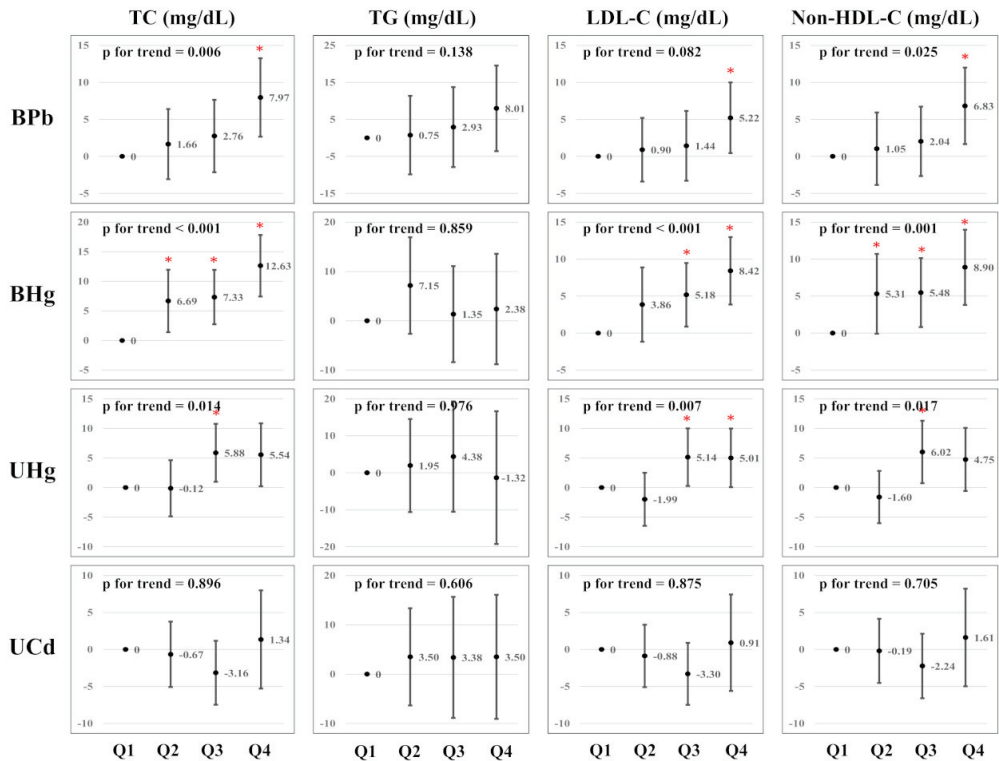


**Figure 2.** Multiple linear regression analysis of serum lipid profile by heavy metal concentrations ( $n = 2591$ ). Asterisks (\*) indicate significance level ( $<0.05$ ).

#### 4. Discussion

In a representative sample of Korean adults, using KoNEHS 2015–2017, we examined the association between heavy metal exposure and serum lipid profiles. After adjusting for all covariates in multivariate regression analysis, it was observed that there was a positive association between high BPb, BHg, UHg, and serum lipid profiles, including TC, LDL-C, and non-HDL-C. In addition, high BPb and BHg were observed to be significantly associated with dyslipidemia in logistic regression analysis.

The Ministry of Environment has been involved in ongoing efforts to reduce environmental exposure to heavy metals since 1988 [45]. According to data from the KoNEHS (2009–2017), the concentration of heavy metals in Korean adults is decreasing, but it is still higher than that found in the adults of developed countries [33]. The Korean geography (island/coastal country) may influence high heavy metal concentrations, owing to the culture of high seafood consumption [39]. Seafood consumption has been reported as one of the main sources of heavy metal exposure in the general population [46]. In addition, soil and groundwater contamination, caused by abandoned mines in Korea, is a serious social problem [47]. The traditional Asian food culture, which frequently consumes grains and herbal medicines grown in contaminated soil, is supported by the high concentration of heavy metals in Korea [48].

Previous epidemiological studies have suggested an association between dyslipidemia and heavy metal exposure. According to a study using the National Health and Nutrition Examination Survey (NHANES), the ORs for TC, non-HDL-C, and LDL-C were 1.88, 1.59, and 1.68 times higher in the highest BPb quartile ( $>1.90 \mu\text{g/dL}$ ) than that in the lowest quartile ( $\leq 0.76 \mu\text{g/dL}$ ), respectively [29]. Another study found that TC and LDL-C levels

were 1.5–2.0 and 1.6–2.4 times higher ( $p < 0.001$ ) in the occupational Pb exposure group (27.00–48.90  $\mu\text{g}/\text{dL}$  for BPb) than in the control group (15.78  $\mu\text{g}/\text{dL}$  for BPb), whereas TG and HDL-C levels did not show a significant association ( $p < 0.05$ ) [49]. Furthermore, a study using the KoNEHS observed that BHg concentrations are significantly higher in the hyperlipidemia group (4.03 and 2.83  $\mu\text{g}/\text{L}$  for male and female) than that in the non-hyperlipidemia group (3.48 and 2.69  $\mu\text{g}/\text{L}$  of male and female), and individuals with higher BHg concentrations have a 11% higher risk of hyperlipidemia [50]. Significant increases in TC, HDL-C, and LDL-C levels are reported with increasing BHg concentrations in Korean adults, based on the KoNEHS [40,51].

The toxic mechanism of lipid metabolism by heavy metal exposure is not yet completely understood, but it is generally associated with oxidative stress. Oxidative stress is caused by an imbalance between the antioxidant defense system and the free radical production system [24]. Heavy metal binds to sulfhydryl protein groups and depletes glutathione, leading to oxidative stress through reactive oxygen species (ROS) generation [52]. Oxidative stress activates several protein phosphorylation pathways, including phosphatidylinositol 3-kinase (PI3K) and MAPK, c-Jun N terminal kinase (JNK), and stress-activated protein kinase (SAPK) [53]. This activity is involved in the apoptotic process of pancreatic  $\beta$ -cells responsible for insulin production, which plays a major role in glycemic homeostasis, leading to insulin resistance [20,54]. This condition can lead to endothelial dysfunction through decreased vasodilator production and increased vasoconstrictor production [55]. Animal studies have demonstrated that heavy metal exposure impairs glucose metabolism by pancreatic  $\beta$ -cell damage. In vitro and in vivo studies have proved that chronic exposure to Pb affects the pancreas and disrupts glucose homeostasis [56,57]. Exposure to Hg induces ROS production, impaired insulin secretion, and apoptosis of  $\beta$ -cell-derived HIT-T15 cells [58,59].

In our study, UCd concentrations were not significantly associated with elevated serum lipid levels. According to a previous study, a positive correlation was observed between BCd concentrations and HDL-C risk in Korean adults [30]. In addition, an increased prevalence of high TC, TG, and LDL-C, as well as low HDL-C, with increasing BCd concentrations was observed in Chinese occupationally exposed to Cd [60]. In contrast, several studies using NHANES data have shown no significant association between UCd or BCd levels and metabolic syndrome risk [61,62], which is consistent with our study findings. These conflicting results might be due to differences in individual participant characteristics, exposure levels, sampling bias, size, and covariate settings [29]. Some kinds of biosamples (i.e., urine or blood) might affect the associations because UCd serves as a biomarker of long-term cadmium exposure, and BCd serves as a biomarker of recent cadmium exposure, [63,64].

Our study has several limitations that warrant discussion. First, it is a cross-sectional observational study based on a single measurement. Thus, it cannot indicate the exact causal relationship of the observed association. Second, since heavy metals in blood reflect relatively recent exposure, there is a limit to explaining the burden on the body due to long-term exposure. Third, although this study focused on Pb, Cd, and Hg exposure, these may be accompanied by potential exposure to other metals.

However, our study has several notable advantages. First, we used individual blood or urine heavy metal concentrations to account for heavy metal exposure levels, and we observed the association with serum lipid profiles. Second, we used three types (Pb, Cd, and Hg) of heavy metal biomarkers to provide the opportunity to observe different associations between each heavy metal exposure and serum lipid profiles. Third, our results can be interpreted as the results of the national population because we used data from KoNEHS, a large representative sample of Korean adults. The results of our study provide epidemiological evidence for an association with dyslipidemia and current heavy metal exposure levels in Koreans.

## 5. Conclusions

We assessed the association between heavy metal exposure and dyslipidemia using data from a nationally representative adult population in Korea. Our findings showed a positive association between BPb, BHg, and UHg concentrations and serum lipid profiles. In addition, BPb and BHg concentrations were positively associated with a prevalence of dyslipidemia. These results support evidence that heavy metal exposure may be an important risk factor for abnormal lipid metabolism. Results from this study, in conjunction with others, strengthen the concern on heavy metal effects at low-level when evaluating heavy metal regulations concerning adverse health effects. However, further studies are needed to elucidate the mechanisms supporting the association between heavy metal exposure and dyslipidemia in the general population.

**Supplementary Materials:** The following supporting information can be downloaded at: <https://www.mdpi.com/article/10.3390/ijerph19063181/s1>, Table S1: Multivariate logistic regression of serum lipid profiles by heavy metal concentrations including TG  $\geq$  400 in participants ( $n = 2742$ ); Table S2: High seafood dietary group-adjusted OR (95% CIs) of serum lipid profiles by heavy metal concentrations in participants ( $n = 2591$ ); Table S3: Heavy metals related occupation-adjusted OR (95% CIs) of serum lipid profiles by heavy metal concentrations in participants ( $n = 2591$ ).

**Author Contributions:** Conceptualization, D.-w.K. and J.O.; methodology, D.-w.K. and J.O.; software, D.-w.K. and J.O.; formal analysis, D.-w.K. and J.O.; writing—original draft preparation, D.-w.K. and J.O.; writing—review and editing, D.-w.K., J.O., K.-W.M. and C.-H.P. All authors have read and agreed to the published version of the manuscript.

**Funding:** This survey was supported by a grant from the National Institute of Environmental Research funded by the Ministry of Environment (MOE) of Korea (NIER-2017-01-01-001).

**Institutional Review Board Statement:** Ethical review and approval were waived for this study, due to existing information, data, documents, and records.

**Informed Consent Statement:** Not applicable.

**Data Availability Statement:** This study used data from the Second Korean National Environmental Health Survey (KoNEHS) which was conducted by the Ministry of Environment, National Institute of Environmental Research. The data presented in this study are available on request from the corresponding authors. The data are not publicly available due to protect personal information.

**Conflicts of Interest:** The authors declare no conflict of interest.

## References

1. Pitsavos, C.; Panagiotakos, D.; Weinem, M.; Stefanadis, C. Diet, exercise and the metabolic syndrome. *Rev. Diabet. Stud.* **2006**, *3*, 118. [[CrossRef](#)] [[PubMed](#)]
2. Tóth, P.P.; Potter, D.; Ming, E.E. Prevalence of lipid abnormalities in the united states: The national health and nutrition examination survey 2003–2006. *J. Clin. Lipidol.* **2012**, *6*, 325–330. [[CrossRef](#)] [[PubMed](#)]
3. Srikanth, S.; Deedwania, P. Management of dyslipidemia in patients with hypertension, diabetes, and metabolic syndrome. *Curr. Hypertens. Rep.* **2016**, *18*, 1–10. [[CrossRef](#)]
4. Pires, A.; Sena, C.; Seiça, R. Dyslipidemia and cardiovascular changes in children. *Curr. Opin. Cardiol.* **2016**, *31*, 95–100. [[CrossRef](#)] [[PubMed](#)]
5. Koba, S.; Hirano, T. Dyslipidemia and atherosclerosis. *Nihon Rinsho. Jpn. J. Clin. Med.* **2011**, *69*, 138–143.
6. Asghari, S.; Aref-Eshghi, E.; Godwin, M.; Duke, P.; Williamson, T.; Mahdavian, M. Single and mixed dyslipidaemia in Canadian primary care settings: Findings from the Canadian primary care sentinel surveillance network database. *BMJ Open* **2015**, *5*, e007954. [[CrossRef](#)]
7. Jang, S.; Lee, J. Prevalence and management of dyslipidemia among Korean adults: KNHANES 2010–2012. *J. Korea Acad.-Ind. Coop. Soc.* **2015**, *16*, 7978–7989.
8. Jeon, M.Y.; Choi, W.H.; Seo, Y.M. Risk factors of dyslipidemia and related factors of medication adherence in Korea adults: KNHANES 2013–2015. *J. Korean Biol. Nurs. Sci.* **2017**, *19*, 131–140.
9. Knopp, R.H.; LaRosa, J.C.; Burkman, R.T., Jr. Contraception and dyslipidemia. *Am. J. Obstet. Gynecol.* **1993**, *168*, 1994–2005. [[CrossRef](#)]
10. Carmena, R. Type 2 diabetes, dyslipidemia, and vascular risk: Rationale and evidence for correcting the lipid imbalance. *Am. Heart J.* **2005**, *150*, 859–870. [[CrossRef](#)]

11. Packard, C.J.; Boren, J.; Taskinen, M.-R. Causes and consequences of hypertriglyceridemia. *Front. Endocrinol.* **2020**, *11*, 252. [[CrossRef](#)] [[PubMed](#)]
12. National Cholesterol Education Program (NCEP). Third Report of the National Cholesterol Education Program (NCEP) Expert Panel on Detection, Evaluation, and Treatment of High Blood Cholesterol In Adults (Adult Treatment Panel III)—The Program. *Circulation* **2002**, *106*, 3143–3421. [[CrossRef](#)]
13. Jacobson, T.A.; Ito, M.K.; Maki, K.C.; Orringer, C.E.; Bays, H.E.; Jones, P.H.; McKenney, J.M.; Grundy, S.M.; Gill, E.A.; Wild, R.A. National Lipid Association recommendations for patient-centered management of dyslipidemia: Part 1—Executive summary. *J. Clin. Lipidol.* **2014**, *8*, 473–488. [[CrossRef](#)] [[PubMed](#)]
14. Hedayatnia, M.; Asadi, Z.; Zare-Feyzabadi, R.; Yaghoobi-Khorasani, M.; Ghazizadeh, H.; Ghaffarian-Zirak, R.; Nosrati-Tirkani, A.; Mohammadi-Bajgiran, M.; Rohban, M.; Sadabadi, F. Dyslipidemia and cardiovascular disease risk among the MASHAD study population. *Lipids Health Dis.* **2020**, *19*, 1–11. [[CrossRef](#)]
15. Mozaffarian, D.; Benjamin, E.J.; Go, A.S.; Arnett, D.K.; Blaha, M.J.; Cushman, M.; Das, S.R.; De Ferranti, S.; Després, J.-P.; Fullerton, H.J. Heart disease and stroke statistics—2016 update: A report from the American Heart Association. *Circulation* **2016**, *133*, e38–e360. [[CrossRef](#)]
16. Feng, H.; Ha, F.; Hu, G.; Wu, Y.; Yu, S.; Ji, Z.; Feng, W.; Wang, T.; Jia, G. Concentration of chromium in whole blood and erythrocytes showed different relationships with serum apolipoprotein levels in Cr (VI) exposed subjects. *J. Trace Elem. Med. Biol.* **2018**, *50*, 384–392. [[CrossRef](#)]
17. Mendrick, D.L.; Diehl, A.M.; Topor, L.S.; Dietert, R.R.; Will, Y.; La Merrill, M.A.; Bouret, S.; Varma, V.; Hastings, K.L.; Schug, T.T. Metabolic syndrome and associated diseases: From the bench to the clinic. *Toxicol. Sci.* **2018**, *162*, 36–42. [[CrossRef](#)]
18. Zhao, L.; Zhu, Y.; Chen, Z.; Xu, H.; Zhou, J.; Tang, S.; Xu, Z.; Kong, F.; Li, X.; Zhang, Y. Cardiopulmonary effects induced by occupational exposure to titanium dioxide nanoparticles. *Nanotoxicology* **2018**, *12*, 169–184. [[CrossRef](#)]
19. Cho, H.W.; Kim, S.-H.; Park, M.J. An association of blood mercury levels and hypercholesterolemia among Korean adolescents. *Sci. Total Environ.* **2020**, *709*, 135965. [[CrossRef](#)]
20. Chen, Y.; Wang, J.; Gao, W.; Sun, X.; Xu, S. Comprehensive analysis of heavy metals in soils from Baoshan District, Shanghai: A heavily industrialized area in China. *Environ. Earth Sci.* **2012**, *67*, 2331–2343. [[CrossRef](#)]
21. Mahurpawar, M. Effects of heavy metals on human health. *Int. J. Res.-Granthaalayah* **2015**, *3*, 1–7. [[CrossRef](#)]
22. Zhang, Y.; Tian, Y.; Shen, M.; Zeng, G. Heavy metals in soils and sediments from Dongting Lake in China: Occurrence, sources, and spatial distribution by multivariate statistical analysis. *Environ. Sci. Pollut. Res.* **2018**, *25*, 13687–13696. [[CrossRef](#)] [[PubMed](#)]
23. Kaur, R.; Sharma, S.; Kaur, H. Heavy metals toxicity and the environment. *J. Pharmacogn. Phytochem. SP1* **2019**, 247–249. [[CrossRef](#)]
24. Fatema, K.; Shoily, S.S.; Ahsan, T.; Haidar, Z.; Sumit, A.F.; Sajib, A.A. Effects of arsenic and heavy metals on metabolic pathways in cells of human origin: Similarities and differences. *Toxicol. Rep.* **2021**, *8*, 1109–1120. [[CrossRef](#)] [[PubMed](#)]
25. Fu, Z.; Xi, S. The effects of heavy metals on human metabolism. *Toxicol. Mech. Methods* **2020**, *30*, 167–176. [[CrossRef](#)] [[PubMed](#)]
26. Ercal, N.; Gurer-Orhan, H.; Aykin-Burns, N. Toxic metals and oxidative stress part I: Mechanisms involved in metal-induced oxidative damage. *Curr. Top. Med. Chem.* **2001**, *1*, 529–539. [[CrossRef](#)]
27. Navas-Acien, A.; Guallar, E.; Silbergeld, E.K.; Rothenberg, S.J. Lead exposure and cardiovascular disease—A systematic review. *Environ. Health Perspect.* **2007**, *115*, 472–482. [[CrossRef](#)]
28. Poreba, R.; Gać, P.; Poreba, M.; Andrzejak, R. Environmental and occupational exposure to lead as a potential risk factor for cardiovascular disease. *Environ. Toxicol. Pharmacol.* **2011**, *31*, 267–277. [[CrossRef](#)]
29. Xu, H.; Mao, Y.; Xu, B.; Hu, Y. Low-level environmental lead and cadmium exposures and dyslipidemia in adults: Findings from the NHANES 2005–2016. *J. Trace Elem. Med. Biol.* **2021**, *63*, 126651. [[CrossRef](#)]
30. Kim, K. Blood cadmium concentration and lipid profile in Korean adults. *Environ. Res.* **2012**, *112*, 225–229. [[CrossRef](#)]
31. Park, K.; Seo, E. Toenail mercury and dyslipidemia: Interaction with selenium. *J. Trace Elem. Med. Biol.* **2017**, *39*, 43–49. [[CrossRef](#)] [[PubMed](#)]
32. Tchounwou, P.B.; Yedjou, C.G.; Patlolla, A.K.; Sutton, D.J. Heavy metal toxicity and the environment. *Mol. Clin. Environ. Toxicol.* **2012**, *101*, 133–164.
33. Kim, D.-W.; Ock, J.; Moon, K.-W.; Park, C.-H. Association between Pb, Cd, and Hg exposure and liver injury among Korean adults. *Int. J. Environ. Res. Public Health* **2021**, *18*, 6783. [[CrossRef](#)] [[PubMed](#)]
34. NIER. *Guidebook of the National Institute of Environmental Research*; NIER: Incheon, Korea, 2019.
35. NIER. *Analysis Manual of the National Institute of Environmental Research (Heavy Metals)*; NIER: Incheon, Korea, 2018.
36. NIER. *Clinical Analysis Manual of the National Institute of Environmental Research*; NIER: Incheon, Korea, 2019.
37. Ma, C.; Schupp, C.; Armstrong, E.; Armstrong, A. Psoriasis and dyslipidemia: A population-based study analyzing the National Health and Nutrition Examination Survey (NHANES). *J. Eur. Acad. Dermatol. Venereol.* **2014**, *28*, 1109–1112. [[CrossRef](#)]
38. Friedewald, W.T.; Levy, R.I.; Fredrickson, D.S. Estimation of the concentration of low-density lipoprotein cholesterol in plasma, without use of the preparative ultracentrifuge. *Clin. Chem.* **1972**, *18*, 499–502. [[CrossRef](#)]
39. Choi, H.; Shim, J.-S.; Lee, M.H.; Yoon, Y.M.; Choi, D.P.; Kim, H.C. Comparison of formulas for calculating low-density lipoprotein cholesterol in general population and high-risk patients with cardiovascular disease. *Korean Circ. J.* **2016**, *46*, 688–698. [[CrossRef](#)]
40. Sohn, S.H.; Heo, H.C.; Jo, S.; Park, C.; Sakong, J. The association between mercury concentrations and lipid profiles in the Korean National Environmental Health Survey (KoNEHS) cycle 3. *Ann. Occup. Environ. Med.* **2020**, *32*, e19. [[CrossRef](#)]
41. Virani, S.S. Non-HDL cholesterol as a metric of good quality of care: Opportunities and challenges. *Tex. Heart Inst. J.* **2011**, *38*, 160.

42. Havel, R.J.; Rapaport, E. Management of primary hyperlipidemia. *N. Engl. J. Med.* **1995**, *332*, 1491–1498. [[CrossRef](#)]
43. Rana, J.S.; Boekholdt, S.M.; Kastelein, J.J.; Shah, P.K. The role of non-HDL cholesterol in risk stratification for coronary artery disease. *Curr. Atheroscler. Rep.* **2012**, *14*, 130–134. [[CrossRef](#)]
44. Ni, W.-Q.; Liu, X.-L.; Zhuo, Z.-P.; Yuan, X.-L.; Song, J.-P.; Chi, H.-S.; Xu, J. Serum lipids and associated factors of dyslipidemia in the adult population in Shenzhen. *Lipids Health Dis.* **2015**, *14*, 1–11. [[CrossRef](#)] [[PubMed](#)]
45. Oh, S.-E.; Kim, G.B.; Hwang, S.H.; Ha, M.; Lee, K.-M. Longitudinal trends of blood lead levels before and after leaded gasoline regulation in Korea. *Environ. Health Toxicol.* **2017**, *32*, e2017019. [[CrossRef](#)] [[PubMed](#)]
46. Castro-González, M.; Méndez-Armenta, M. Heavy metals: Implications associated to fish consumption. *Environ. Toxicol. Pharmacol.* **2008**, *26*, 263–271. [[CrossRef](#)] [[PubMed](#)]
47. Ok, Y.S.; Usman, A.R.; Lee, S.S.; Abd El-Azeem, S.A.; Choi, B.; Hashimoto, Y.; Yang, J.E. Effects of rapeseed residue on lead and cadmium availability and uptake by rice plants in heavy metal contaminated paddy soil. *Chemosphere* **2011**, *85*, 677–682. [[CrossRef](#)]
48. Park, S.; Lee, B.-K. Strong positive association of traditional Asian-style diets with blood cadmium and lead levels in the Korean adult population. *Int. J. Environ. Health Res.* **2013**, *23*, 531–543. [[CrossRef](#)]
49. Ademuyiwa, O.; Ugbaja, R.N.; Idumebor, F.; Adebawo, O. Plasma lipid profiles and risk of cardiovascular disease in occupational lead exposure in Abeokuta, Nigeria. *Lipids Health Dis.* **2005**, *4*, 1–7. [[CrossRef](#)]
50. Lee, S.; Cho, S.-R.; Jeong, I.; Park, J.B.; Shin, M.-Y.; Kim, S.; Kim, J.H. Mercury exposure and associations with hyperlipidemia and elevated liver enzymes: A nationwide cross-sectional survey. *Toxics* **2020**, *8*, 47. [[CrossRef](#)]
51. Cho, Y.M. Fish consumption, mercury exposure, and the risk of cholesterol profiles: Findings from the Korea National Health and Nutrition Examination Survey 2010–2011. *Environ. Health Toxicol.* **2017**, *32*, e2017014. [[CrossRef](#)]
52. Liu, J.; Qu, W.; Kadiiska, M.B. Role of oxidative stress in cadmium toxicity and carcinogenesis. *Toxicol. Appl. Pharmacol.* **2009**, *238*, 209–214. [[CrossRef](#)]
53. Matsuoka, M.; Igisu, H. Effects of heavy metals on mitogen-activated protein kinase pathways. *Environ. Health Prev. Med.* **2002**, *6*, 210–217. [[CrossRef](#)]
54. Newsholme, P.; Keane, K.N.; Carlessi, R.; Cruzat, V. Oxidative stress pathways in pancreatic  $\beta$ -cells and insulin-sensitive cells and tissues: Importance to cell metabolism, function, and dysfunction. *Am. J. Physiol.-Cell Physiol.* **2019**, *317*, C420–C433. [[CrossRef](#)] [[PubMed](#)]
55. Rask-Madsen, C.; King, G.L. Mechanisms of disease: Endothelial dysfunction in insulin resistance and diabetes. *Nat. Clin. Pract. Endocrinol. Metab.* **2007**, *3*, 46–56. [[CrossRef](#)] [[PubMed](#)]
56. Mostafalou, S.; Baeri, M.; Bahadar, H.; Soltany-Rezaee-Rad, M.; Gholami, M.; Abdollahi, M. Molecular mechanisms involved in lead induced disruption of hepatic and pancreatic glucose metabolism. *Environ. Toxicol. Pharmacol.* **2015**, *39*, 16–26. [[CrossRef](#)] [[PubMed](#)]
57. Tyrrell, J.B.; Hafida, S.; Stemmer, P.; Adhami, A.; Leff, T. Lead (Pb) exposure promotes diabetes in obese rodents. *J. Trace Elem. Med. Biol.* **2017**, *39*, 221–226. [[CrossRef](#)]
58. Chen, Y.W.; Huang, C.F.; Yang, C.Y.; Yen, C.C.; Tsai, K.S.; Liu, S.H. Inorganic mercury causes pancreatic  $\beta$ -cell death via the oxidative stress-induced apoptotic and necrotic pathways. *Toxicol. Appl. Pharmacol.* **2010**, *243*, 323–331. [[CrossRef](#)]
59. Schumacher, L.; Abbott, L.C. Effects of methyl mercury exposure on pancreatic beta cell development and function. *J. Appl. Toxicol.* **2017**, *37*, 4–12. [[CrossRef](#)]
60. Zhou, Z.; Lu, Y.-h.; Pi, H.-f.; Gao, P.; Li, M.; Zhang, L.; Pei, L.-p.; Mei, X.; Liu, L.; Zhao, Q. Cadmium exposure is associated with the prevalence of dyslipidemia. *Cell. Physiol. Biochem.* **2016**, *40*, 633–643. [[CrossRef](#)]
61. Lee, B.-K.; Kim, Y. Association of blood cadmium level with metabolic syndrome after adjustment for confounding by serum ferritin and other factors: 2008–2012 Korean National Health and Nutrition Examination Survey. *Biol. Trace Elem. Res.* **2016**, *171*, 6–16. [[CrossRef](#)]
62. Noor, N.; Zong, G.; Seely, E.W.; Weisskopf, M.; James-Todd, T. Urinary cadmium concentrations and metabolic syndrome in US adults: The National Health and Nutrition Examination Survey 2001–2014. *Environ. Int.* **2018**, *121*, 349–356. [[CrossRef](#)]
63. Järup, L.; Åkesson, A. Current status of cadmium as an environmental health problem. *Toxicol. Appl. Pharmacol.* **2009**, *238*, 201–208. [[CrossRef](#)]
64. Lin, J.; Zhang, F.; Lei, Y. Dietary intake and urinary level of cadmium and breast cancer risk: A meta-analysis. *Cancer Epidemiol.* **2016**, *42*, 101–107. [[CrossRef](#)] [[PubMed](#)]

# Synchronous Cr(VI) Remediation and Energy Production Using Microbial Fuel Cell from a Subsurface Environment: A Review

Yifan Yu <sup>1,2</sup>, Jafar Ali <sup>1,2</sup>, Yuesuo Yang <sup>1,2,\*</sup>, Peijing Kuang <sup>3,\*</sup>, Wenjing Zhang <sup>1,2</sup>, Ying Lu <sup>1,2</sup> and Yan Li <sup>1,2</sup>

<sup>1</sup> Key Laboratory of Groundwater Resources and Environment, Jilin University, Ministry of Education, Changchun 130021, China; yuyf19@mails.jlu.edu.cn (Y.Y.); jafaraliqau@gmail.com (J.A.); zhwenjing@jlu.edu.cn (W.Z.); luying819@jlu.edu.cn (Y.L.); liyanhjgc@jlu.edu.cn (Y.L.)

<sup>2</sup> Jilin Provincial Key Laboratory of Water Resources and Environment, Jilin University, Changchun 130021, China

<sup>3</sup> College of Environment and Resources, Dalian Minzu University, Dalian 116600, China

\* Correspondence: yangyuesuo@jlu.edu.cn (Y.Y.); kuangpeijing@dlmu.edu.cn (P.K.)

**Abstract:** Applying microbial fuel cell (MFC) technology for eco-remediation of Cr(VI) pollution from a subsurface environment has great scientific value and practical significance due to its promising advantages of pollutant remediation and renewable energy generation. The aim of the current review is to summarize the migration characteristics of Cr(VI) in a subsurface soil/water environment and investigate the factors affecting the MFC performance for synchronous Cr(VI) remediation and power generation, and sequentially highlight diverse challenges of MFC technology for in situ remediation of subsurface groundwater and soils. The critical review put forward that Cr(VI) removal efficiency and energy production of MFC can be improved by enhancing the adjustability of cathode pH, setting potential, modifying electrode, and incorporating other technologies into MFC. It was recommended that designing typical large-scale, long-term continuous flow MFC systems, adding electron shuttle media or constructing artificial electron according to actual groundwater/soil and Cr(VI) pollution characteristics, site geology, and the hydrogeology condition (hydrochemical conditions, colloid type, and medium) are essential to overcome the limitations of the small size of the laboratory experiments and improve the application of technology to in situ Cr(VI) remediation. This review provided reference and ideas for future research of MFC-mediated onsite Cr(VI) remediation.

**Keywords:** microbial fuel cell; hexavalent chromium; subsurface environment; remediation; energy production

**Citation:** Yu, Y.; Ali, J.; Yang, Y.; Kuang, P.; Zhang, W.; Lu, Y.; Li, Y. Synchronous Cr(VI) Remediation and Energy Production Using Microbial Fuel Cell from a Subsurface Environment: A Review. *Energies* **2022**, *15*, 1989. <https://doi.org/10.3390/en15061989>

Academic Editor: Attilio Converti

Received: 1 February 2022

Accepted: 2 March 2022

Published: 9 March 2022

**Publisher's Note:** MDPI stays neutral with regard to jurisdictional claims in published maps and institutional affiliations.



**Copyright:** © 2022 by the authors. Licensee MDPI, Basel, Switzerland. This article is an open access article distributed under the terms and conditions of the Creative Commons Attribution (CC BY) license (<https://creativecommons.org/licenses/by/4.0/>).

## 1. Introduction

The existence of hexavalent chromium Cr(VI) in waste water and soil has caused serious environmental and health issues. Occurrences of Cr(VI) in the environment can be distinguished in two major sources, i.e., natural sources and man-made sources. Natural sources are mainly the weathering of bedrocks due to water-rock interactions [1], while man-made sources are the legacy of human activities. As one of the most widely used metals in the industry, Cr has been released from leather tanning, electroplating, paint manufacturing, and some other industries [2]. Due to its non-biodegradability, Cr(VI) can remain persistent in the environment for a long time and accumulate in the food chain through contaminated subsurface environments, which eventually threaten human health as well as the environment and ecology [3]. Therefore, the United States Environmental Protection Agency (US EPA) stipulated that the maximum limit of Cr (VI) concentration in drinking water and discharged wastewater cannot exceed 0.05 mg/L and 0.5 mg/L, respectively [4]. Thus, the effective removal of Cr(VI) from the subsurface environment has attracted extensive attention from both eco-environmental regulators and academia worldwide. Compared with other valence states of Cr, Cr(VI) and Cr(III) are relatively stable, and Cr(III) generally exists as precipitates in the environment [5] with lower toxicity

and mobility than Cr(VI). It remains an indispensable trace element for some functional cells Cr(III) participates in the glucose/oil metabolism in the organism [6]. Hence, converting Cr(VI) to Cr(III) is a reliable way to remediate Cr(VI) pollution in the environment. Considering the nature of subsurface and linkages between Cr(VI) and drinking water sources, the in situ biological/ecological remediation of Cr(VI) remains crucial.

At present, Cr(VI) remediation strategies including solidification [7], stabilization [8], phytoremediation [9], bioremediation [10], elution [11,12], and electric remediation [13] are widely studied. These traditional remediation methods have some disadvantages relating to higher energy consumption and costs, as well as incomplete removal of pollutants. The introduction of chemical reagents can also cause secondary pollution and excessive sludge formation. Thus, the application of these previous technologies has been severely limited. Compared with the above conventional remediation methods, the unique advantage of simultaneously generating electricity and Cr(VI) removal in microbial fuel cell (MFC) technology has attracted the attention of many researchers [14]. Research on MFC to generate electricity can be traced back to the beginning of the 20th century, however Logan [15] firstly used MFC in water pollution treatment and successfully achieved the removal of organic pollutants and energy production. The system had a removal efficiency of 60% for COD and a power density of 26 mW/m<sup>2</sup> [15]. Similarly, a large number of studies have shown that MFC can also effectively remove heavy metal pollution in the subsurface environment. Among them, the remediation of Cr(VI) has received widespread attention. Tandukar et al. [16] first applied the dual-chamber MFC for the remediation of Cr(VI) polluted wastewater. The complete removal of Cr(VI) was achieved after operating 300 h and the maximum power reached 55.5 mW/m<sup>2</sup>, where Cr(VI) existed in the form of Cr(OH)<sub>3</sub> precipitates. Microbes decomposed the inorganic and organic components in the anode and generated electrons transferred to the cathode through the external circuit, which reduced the Cr(VI) into Cr(III) and generated electricity. These findings proved that MFC can effectively remove Cr(VI) and produce energy through bioelectrochemical reduction [16]. Thus it is essential to develop MFC as a method of ecological remediation of Cr(VI) in subsurface environments.

Bioelectrochemical active bacteria, such as *Aeromonas*, *Pseudomonas*, and *Thiomonas*, metabolize substrate in the anode to generate electrons that are transferred to the cathode through the external circuit, thus promoting the cathodic reduction of the target electron receptor [17]. Sindhuja et al. [18] found that when cow dung was used as the main component of the anode in MFC, *Geobacter Metallofordii* became the dominant population and Cr(VI) was completely reduced after 10 days. Moreover, researchers have found that abiotic electrodes can effectively reduce the operating cost of Cr(VI) pollution remediation technology. Gupta et al. used transition metal aluminum (Al)/Nickel (Ni) and carbon nanofibers to prepare electrodes with high conductivity and the enhanced catalytic reduction of Cr(VI) [19]. Some studies have shown that when the  $\alpha$ -Fe<sub>2</sub>O<sub>3</sub> modified polyaniline nanocomposite electrode was utilized as a cathode, the power density of the MFC system increased by 1.75 times [20]. At the same time, electrode potential also had a significant impact on the Cr(VI) reduction process. Huang et al. [21] found that the reduction performance of Cr(VI) and electricity generation efficiency can be effectively improved when the potential of the biological cathode is set at −300 mV. Therefore, an optimized design of MFC electrodes for Cr(VI) contaminated sites is the core issue in both the scientific and engineering field.

Cr(VI) pollution is a typical and intractable pollution problem for the subsurface environment. Subsurface environmental conditions also affect Cr(VI) reduction and power generation in the MFC system. Results show that acidic conditions are more conducive to the reduction of Cr(VI) in MFC. Li et al. [22] found that the removal efficiency of Cr(VI) reach up to 99.5% under the pH condition of 2, and the power generation was 1600 mW/m<sup>2</sup>. Huang et al. [23] found that when pH conditions changed from alkaline (pH = 8.0) to weak acidic (pH = 5.0), the reduction efficiency of Cr(VI) increased from 21.2% to 27.3%, and the electricity generation efficiency was also increased from 6.0% to 89.8%.

Similarly, the temperature can directly influence the performance of MFC by encouraging the growth of the anodic community at optimized conditions. It was suggested that the temperature range of 25–30 °C in the system was the most suitable for the growth and metabolism of most microorganisms, and a high Cr(VI) removal efficiency was achieved at the same time [24]. Oxygen (O<sub>2</sub>) is an essential element for the growth and metabolism of aerobic microorganisms, however it has a negative impact on anaerobic microorganisms in MFC. In the cathode region, O<sub>2</sub> and Cr(VI) form a competitive relationship to inhibit the reduction of Cr(VI) [25]. However, some heterotrophic microorganisms can decompose part of organic matter in the presence of O<sub>2</sub> and improve the reduction efficiency of Cr(VI) in the cathode chamber [9]. Therefore, oxygen content can affect the growth activity of microorganisms and thus, have a non-directional effect on the remediation efficiency of Cr(VI) pollution. Therefore, it is necessary to carry out targeted research in different characteristic environmental conditions of the sites, to ensure the effective application of MFC at Cr(VI) contaminated soil and groundwater.

In summary, remediation of Cr(VI) using MFC has been tackled in a few studies that produced some preliminary achievement. However, there is still a lack of systematic, in-depth analysis and comprehensive effort based upon current experience on Cr(VI) remediation for subsurface environments using MFC. The effective mechanism of different influencing factors on remediation efficiency, and the practical application of MFC in different contaminated sites are still timely needed. Considering the demand for efficient and cost-effective eco-remediation technology for Cr(VI) polluted water and soil under the worldwide commitment to the overall aims of peak carbon dioxide emissions and carbon neutrality, this paper systematically reviewed the state-of-art experience of using MFC for eco-remediation of Cr(VI) pollution and the dominant factors influencing the MFC performance on Cr(VI) removal, based upon a review summary of the migration and transformation of Cr(VI) in a subsurface environment. From the understanding of the above critical reviews, a few points of scientific research gaps and potential focuses for engineering problems in the field of eco-remediation of Cr(VI) contaminated subsurface environment by MFC were proposed and possible future research direction toward innovative technology were prospected. It is anticipated that the current review will effectively promote the research and development of efficient and cost-effective technologies for increased practical applications of MFC-mediated remediation for synchronous Cr(VI) cleanup and new energy production for contaminated lands.

## 2. Characteristics of Cr(VI) and the Law of Migration and Transformation

In the 21st century, Cr is the most abundant element in the earth's crust, with an average content of about 100 mg/kg in rocks [26]. Cr usually exists in the form of trivalent or hexavalent. Cr(OH)<sub>3</sub> and minerals containing Cr(III) widely exist in soil and show a strong complexation ability and low solubility [27] while, Cr(VI) has the feature of high solubility, high mobility, high toxicity, significant genotoxicity, and carcinogenesis [28]. Many studies have revealed that inducing free radical generation and leading to DNA damage might be the carcinogenic mechanism of Cr(VI) [29]. The morphology of Cr(VI) is also related to the pH of the solution. When the pH is between 2 and 6, Cr(VI) mainly exists as HCrO<sub>4</sub><sup>−</sup> and Cr<sub>2</sub>O<sub>7</sub><sup>2−</sup> ions, while that exists in the form of CrO<sub>4</sub><sup>2−</sup> when pH is higher than 6 [30]. The toxicity of Cr(VI) is about 100 times higher than that of Cr(III), so the reduction of Cr(VI) to Cr(III) and immobilization of Cr(VI) are common methods for the remediation of Cr(VI) contamination.

The biogeochemical cycle of Cr(VI) is determined by its chemical redox transformation, adsorption and desorption, dissolution, and precipitation [31]. When Cr(VI) enters into the soil and water, the adsorption effect of soil particles in the infiltration process can inhibit the migration of Cr(VI), and the metal oxides such as Fe(III) in soil and media show a good adsorption capacity for Cr(VI) [32]. After entering the groundwater environment, Cr(VI) can be naturally reduced by Fe(II), minerals containing Fe(II), sulfur, organic compounds, and anaerobic and aerobic microorganisms, and then achieve the immobilization



of Cr(VI) [33–35]. The detoxification mechanism of Cr(VI) by microorganisms mainly includes the following four aspects [36]: (1) Cr(VI) directly gains electrons by consuming biodegradable organic matter; (2) adsorption of Cr(VI) by microbial extracellular polymeric substances (EPS); (3) in microbial cells, Cr(VI) penetrates the cell membrane and enters into the cytoplasm, where Cr(VI) is reduced by chromate reductase, or binds to metallothionein and accumulates in the cell; and (4) Cr(VI) is reduced through the redox medium of microbial exogenous nutrients. Some reasons, including the fluidity of water, the presence of colloid in groundwater, the negatively charged characteristics of soil particles, and the existence of other competitive anions, result in the reducing adsorption rate of Cr(VI) and the higher mobility of Cr(VI) [37–39]. Based on a large amount of data, the migration and transformation rules and transfer paths of Cr(VI) in a subsurface environment are summarized as follows, as shown in the conceptual model in Figure 1.

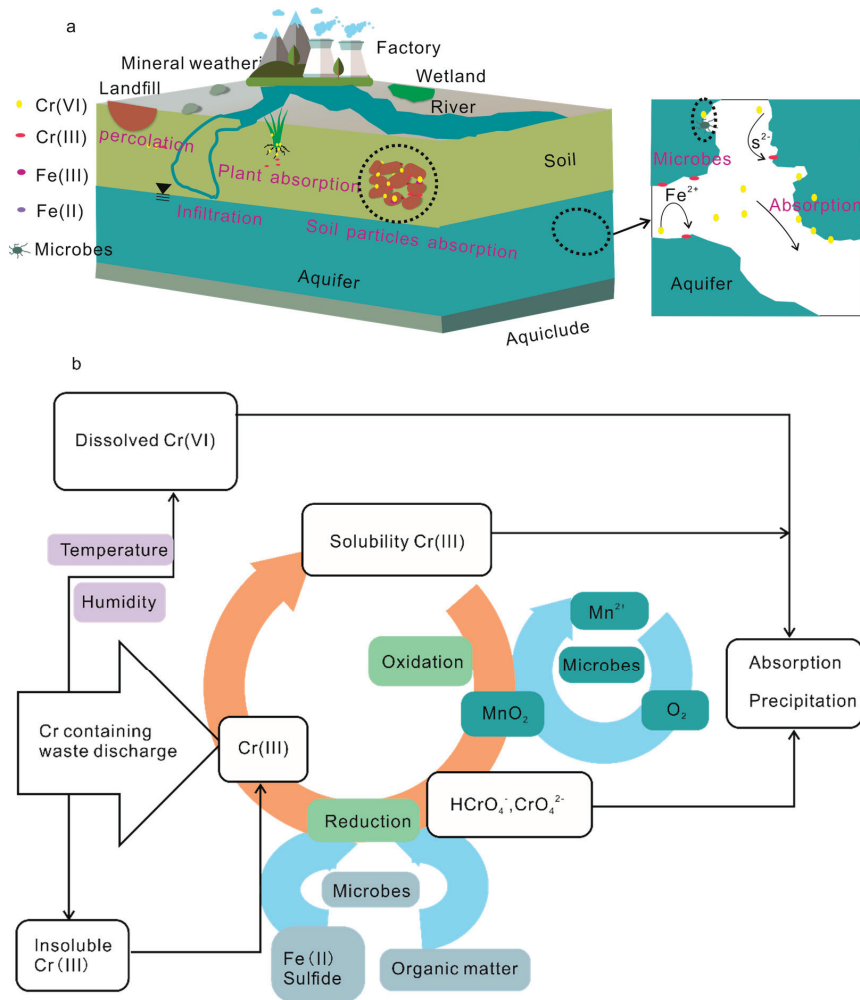


**Figure 1.** Conceptual model of Cr(VI) migration and transformation: (a) 3D diagram and ecological effects, and (b) pathways of transformation in a subsurface environment.

### 3. Mechanism of Cr(VI) Reduction and Synchronous Energy Productivity in MFC

#### 3.1. Bioelectrochemical Reduction of Cr(VI)

Bioelectrochemical reduction of Cr(VI) using MFC has been proven to be a feasible approach. For the first time, Wang et al. [40] used synthetic wastewater containing Cr(VI) as a catholyte electron acceptor and anaerobic microorganisms as an anode biocatalyst. In 150 h, Cr(VI) with an initial concentration of 200 mg/L was completely removed, and the maximum power density produced was 150 mW/m<sup>2</sup>. Aiyer et al. [41] found that Cr(VI) was reduced at the cathode by obtaining electrons using a two-compartment MFC, with the highest reduction rate compared with Cu(II) and V(IV) under the same concentration. Some studies have shown that more than 60% of Cr(VI) can be directly reduced by obtaining electrons at the cathode [42], which proves that bioelectrochemical reduction is the key process of Cr(VI) removal by MFC. The study found that some microorganisms evolved over billions of years to complete the electron transfer by exchanging electrons with insoluble minerals or related natural extracellular electron receptors [43]. This outstanding feature promotes the development of MFCs. The extracellular transport of electrons to electrodes takes place in three different ways, including a direct way (within nanowire and redox active proteins) and indirect way (by electron mediator), which is illustrated in Figure 2 [44]. In the bioelectrochemical reduction of Cr(VI), the interaction between the abiotic cathode and biological cathode determines the mode and routes of electron transfer, which has been widely studied [45]. The most important characteristic of abiotic cathodes is the conduction of electrons that are produced from the oxidation of organic matter by anodic microorganisms through the electrode surface [46], which achieved the conversion from chemical energy to electric energy as well as the simultaneous removal of Cr(VI). By summarizing previous results, we draw the abiotic cathode mechanism in Figure 3a [16,42,47]. However, the traditional MFC with abiotic cathode has some problems such as difficult chemical regeneration, demand for platinum and other precious metals catalysts, as well as a high cost. The results show that a biological cathode can overcome these defects due to microorganisms participating in the cathode reactive process [48]. Moreover, the accumulated bacteria can promote electron transfer and decrease the charge transfer resistance [49], along with increasing reduction efficiency. Biological cathode uses microorganisms as the catalyst to transfer electrons towards the electron acceptor through an external circuit [21] and By summarizing previous results, its mechanism is shown in Figure 3b [16,42,47]. Tandukar et al. [16] used a biological cathode MFC for the first time for Cr(VI) remediation. They found that the removal rate of Cr(VI) was significantly increased in the presence of microorganisms in the cathode, hence proving that the catalytic action of cathodic microorganisms for effective Cr(VI) reduction in MFC. Studies have also shown that bacillus cathode can significantly improve the reduction performance of Cr(VI) in both autotrophic and heterotrophic environments [47].

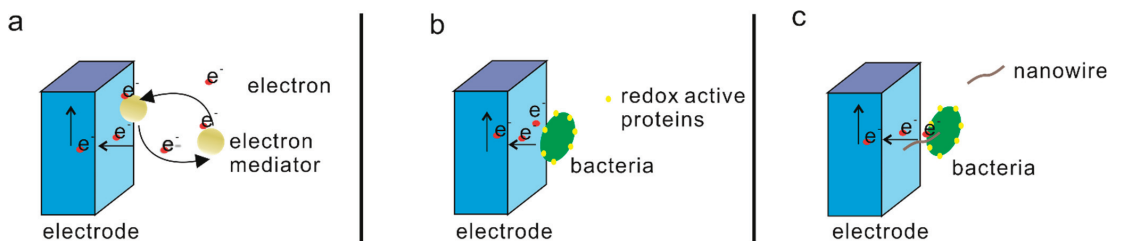


**Figure 2.** Three ways of electron reaching the electrode: (a) indirect electron transport by electron mediator; (b) direct electron transport within redox active proteins; and (c) direct electron transport within nanowire.

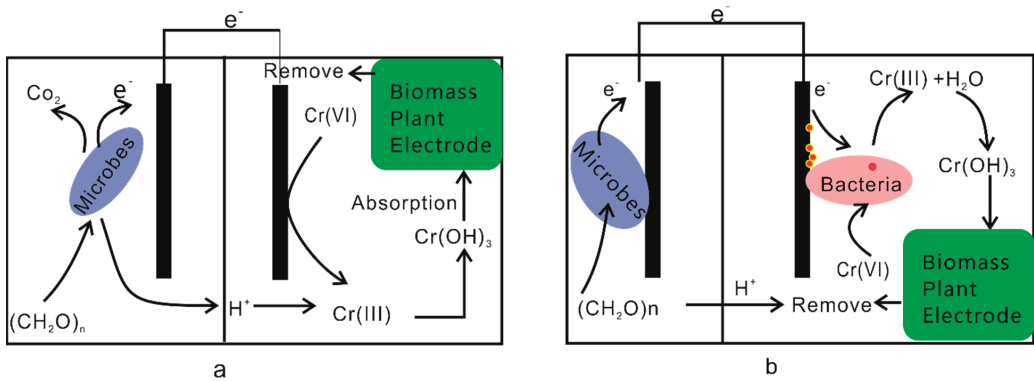


**Figure 3.** Electron transfer process and reaction principle in the Cr(VI) reduction process: (a) abiotic cathode bioelectrochemical process and (b) biocathode bioelectrochemical process.

### 3.2. Other Reduction Mechanisms of Cr in MFC

Due to the presence of other substances and organisms in the MFC system, the bioelectrochemical reduction of Cr(VI) is not the only mechanism involved. Adsorption by electrodes and bacteria could also be the alternate pathways for Cr removal in the cathode chamber [42]. Wu et al [47]. used a graphite carbon stick as an abiotic MFC cathode to reduce Cr(VI), and found that Cr(VI) was reduced to Cr(III). Finally, part of Cr(III) was adsorbed on a graphite carbon stick cathode after reaction. Habiul et al. [42,50] found that the absorption by plants *Pennisetum* and reed could remove approximately 13% to 23% of Cr(VI) in the system by comparing MFC without a plant. In addition, the removal rate of Cr(VI) in a plant-microbial fuel cell (PMFC) system with *Pennsylvania* was higher than that in a *Phragmites communis* PMFC system because transport factors in plants absorbed Cr(VI) and then transferred it to stems, leaves, and the entire plant [51].

### 3.3. Energy Conversion

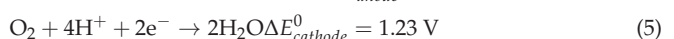
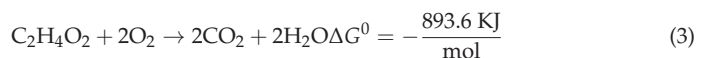
MFC can be regarded as a primary battery. The Gibbs free energy is negative in the MFC redox reaction, so the reaction can be carried out spontaneously and the electromotive force can be converted into battery voltage ( $\Delta E^0$ ).  $\Delta E^0$  is shown in Equation (1). The potential difference between the anode and cathode ( $\Delta E_{Cell}^0$ ) determines whether the system can generate electricity (Equation (2)). Negative free energy and positive electromotive force determine that MFCs can undergo redox reactions and generate electrical energy [52].

$$\Delta E^0 = - \left[ \sum v_i \Delta G_p^0 - \sum v_i \Delta G_r^0 \right] / nF = - \frac{\Delta G}{nF} \quad (1)$$

$$\Delta E_{Cell}^0 = \Delta E_{cathode}^0 - \Delta E_{anode}^0 \quad (2)$$

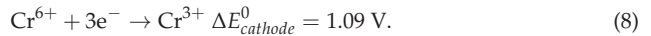
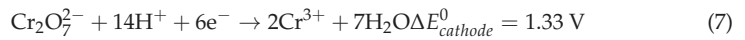
where the  $\Delta G$  value represents the free energies (J/mol) ( $\Delta G_p^0$  represents the free energies of products and  $\Delta G_r^0$  represents the free energy of reactants),  $F$  is Faraday's constant (96,485.3 C/mol), and  $v$  represents stoichiometry factors of the redox reaction.

For instance, MFCs can treat acidic wastewater and generate spontaneous electricity due to two major mechanisms: (1) The Gibbs free energy of the reaction being negative and (2) the electromotive force being positive [53,54]:



$$\Delta G^0 = -893.6 \text{ KJ/mol} < 0 \Delta E_{anode}^0 - \Delta E_{cathode}^0 = 1.52 \text{ V} > 0. \quad (6)$$

The reaction of Cr(VI) is described as follows: [55].



During the process of Cr(VI) removal, microorganisms also play an important role in the bioelectricity generation of the MFC system, which directly affects the electron transfer rate and power generation [56]. Microorganisms can obtain all the sources of energy and carbon from the oxidation of complex organic matter and use it for cell growth, for which the chemically inactive substrate is converted into a form that can be used for electrochemical oxidation, thus converting the chemical energy into electrical energy. During the oxidation of respiratory substrates, the released electrons are transmitted through the respiratory chain and transferred to externally available terminal electron receptors. The higher the redox potential of terminal electron receptors, the more energy that can be obtained by microorganisms [57]. Theoretically, MFC has the potential to produce unlimited electricity as long as the production conditions for anode-associated microorganisms remain favorable [43]. Cr(VI) has a higher oxidation potential (1.33 V) than other heavy metals and is a better oxidant than oxygen (1.23 V) [58], which can generate more power in the MFC system [41]. Therefore, when Cr(VI) is used as the target pollutant, it has certain advantages in pollution remediation and synchronous electricity generation for MFC. Preliminary studies show that the maximum power generation of Cr(VI) removal using MFC is 1600 mW/m<sup>2</sup>. Owing to the optimization of process parameters and influencing factors, the power generation of the system is expected to be further improved in the future [59]. It is also predicted that Cr(VI)-contaminated wastewater can replace the commercially available catholyte, thus making MFC technology more sustainable and cost effective for practical applications.

#### 4. Factors Influencing the Cr(VI) Remediation in MFC

##### 4.1. Electrode Position and Potential

The electrode position in bioelectrochemical systems has a significant effect on the remediation potential of MFC. Zhou et al. [60] constructed MFC with different electrode positions to evaluate the performance of MFC on remediation and electricity generation. When the electrode distance was 2 cm, the internal resistance was low and conductivity was high. The maximum power density and Cr(VI) removal rate were 535.4 mW/m<sup>2</sup> and 0.91 g/m<sup>3</sup> h, respectively. Mu and his coworkers investigated the effect of the electrode gap on the Cr(VI) removal performance of wetland MFC. It was observed that as the electrode spacing increased from 5 cm to 15 cm, the output voltage decreased and resistance was increased, and the results showed that the maximum power was obtained when the electrode distance is 10 cm. Although the electrode spacing of 5 cm had the minimum resistance to make the MFC system obtain higher power in theory, it would cause oxygen diffusion into the anode region, thus disturbing the anaerobic conditions where some electrons will be directly utilized by anodic microorganisms without passing through the external circuit [61]. The role of the electrode potential is also crucial for lowering the startup time and improving the performance of MFC. When the electrode potential was set around −300 mV in Cr(VI) remediation, the startup time was reduced by 19 days. Meanwhile, the reduction rate of Cr(VI) was increased up to 19.7 mg/L d and the maximum power density reached up to 6.4 W/m<sup>3</sup> [21]. It could be inferred that setting the electrode potential can provide an appropriate condition for microbial adaptation, which may enhance the electrochemical interaction between microorganisms and electrodes, and sequentially improve current generation [62]. According to the existing literature, the limitation of the electrode location may affect the onsite remediation of Cr(VI) contaminated water. Therefore, this huge technological gap needs to be explored further for the development of basic research and technological breakthroughs.

#### 4.2. Electrode Materials

Electrode material types and exposed surface area determine the microbial abundance and carrier of electron transfer thereby, playing a pivotal role in MFC operation. At present, the most commonly used electrode materials are traditional carbon materials, such as carbon cloth, graphite, etc. To further improve the performance, modification and optimization of electrode materials have received continuous attention. Li and his coworkers [63] prepared polypyrrole/sludge carbon electrodes by an electropolymerization loading method and used it as the MFC cathode. The maximum output power and Cr(VI) reduction rate of MFC was 760.7 mW/m<sup>2</sup> and 2.16 g/m<sup>3</sup> h, respectively, which were 2.79 and 1.51 times that of carbon cloth electrodes (272.5 mW/m<sup>2</sup> and 1.43 g/m<sup>3</sup> h). The electrochemical analysis found that polypyrrole/sludge carbon electrodes had a low charge transfer resistance. As an electron shuttler, pyrrole can reduce the internal resistance of electron transfer in the system and then significantly improve the power generation and Cr(VI) removal rate of MFC. Studies found that the maximum power density of graphene electrode MFC was 5.7 times that of graphite felt electrode. At the same time, the graphene electrode also effectively improved the reduction efficiency of Cr(VI), and the removal rate of Cr(VI) reached 100% within 48 h with the initial concentration of Cr at 40 mg/L. In contrast, the removal efficiency of Cr(VI) using graphite felt electrode was only 58.3%. Compared with graphite felt, graphene electrode has higher conductivity and microbial attachment sites to enhance the electron transfer rate, thus the MFC with graphene electrode has a higher Cr(VI) reduction rate and high power density [64]. Ali and his coworkers [65] found that the MFC with FeS@rGO nanocomposites (MFC-FeS@rGO) exhibited a 100% Cr(VI) removal efficiency for the concentration of 15 mg/L and also acquired a high reduction rate of 1.43 mg/L which was due to the high conductivity and low internal resistance of MFC-FeS@rGO [66]. Meanwhile, the FeS@rGO nanocomposite provided a larger electroactive surface area to improve the electron transfer. [21].

The combination of light and MFC to improve the reduction rate of Cr(VI) and the electrode material has also been proved to be one of the important factors that affect photoelectric combination technology. When using natural molybdenite as raw material, TiO<sub>2</sub> nanocomposites modified with MoS<sub>2</sub> nanosheets could be prepared by a liquid phase stripping method combined with in situ hydrolysis. These materials were also first used as photocathodes for the reduction of Cr(VI) in MFC. Under visible light irradiation, the removal efficiency of Cr(VI) with the initial concentration of 20 mg/L reached 99.57% within 8 h. This could be due to the introduction of MoS<sub>2</sub> nanosheets as a cocatalyst that can expand the absorption of visible light, which can contribute to electron migration and increase the active site, thus promoting more electrons to participate in the Cr(VI) reduction process [67]. Ren et al. [68] designed silicon solar cells and constructed a dual-anode MFC system using a one-dimensional TiO<sub>2</sub>/Fe<sub>2</sub>O<sub>3</sub> photoanode and conventional biological anode. The maximum power density was 638.3 mW/m<sup>2</sup>, almost 7.6 times that of ordinary MFC (84.2 mW/m<sup>2</sup>). The removal efficiency of Cr(VI) at the concentration of 50 ppm was 90.9% within 13.5 h. The dual-anode MFC achieved efficient microbial oxidation and photocatalysis and enhanced the transfer of electrons to the external circuit. The electrons were driven by the built-in electric field in the silicon solar cell, during which the potential barrier of the system is simultaneously decomposed. The output power and Cr(VI) reduction efficiency was significantly improved. In conclusion, electrode modification and optimization can enhance the electron transfer rate and improve the Cr(VI) reduction efficiency. To compare the performance of different electrodes, the remediation and energy production effects of different electrode materials were shown in Table 1

**Table 1.** Effect of different electrode materials on Cr(VI) remediation and energy generation.

Electrode Materials	Cr(VI) Removal Rate (%)	Energy (mW/m <sup>2</sup> )	Operation Time (h)	Initial Concentration	Features	References
Polypyrrole/sludge carbon electrodes	0.50 g/m <sup>3</sup> h	760.7	1200	25 mg/L	A low charge transfer resistance	[63]
Graphene electrode	100%	163.8	48	40 mg/L	Higher conductivity and microbial attachment sites	[64]
FeS@rGO nanocomposites	100%	154	25	15 mg/L	More electroactive surface area	[66]
TiO <sub>2</sub> nanocomposites modified with MoS <sub>2</sub> nanosheets	99.57	140	8	20 mg/L	More absorption of visible light	[67]
1-D TiO <sub>2</sub> /Fe <sub>2</sub> O <sub>3</sub> photoanode	90.9	6383	13.5	50 ppm	More electrons to the external circuit.	[68]

#### 4.3. Environmental Conditions of the Anode Chamber

Temperature is an important operating parameter for MFC. Yu et al. [69] found that *Escherichia coli* in the anodic area had the highest electrical activity at 37 °C compared with the other two MFCs working at 20 °C and 45 °C. Studies on MFC have shown that microorganisms play the best role at temperatures between 25–30 °C, while no obvious current was generated at temperatures below 15 °C, even if the start time is as long as a week [70]. Another limiting condition for the remediation of Cr(VI) is the oxygen content in the MFC system. Generally, anodes must maintain the anaerobic conditions. Otherwise, microorganisms oxidize organic matter by electron transfer via oxygen reduction rather than Cr reduction in the presence of oxygen. As the facultative anaerobes, *Ochrobactrum* sp. YC211 had a better capacity to remove Cr(VI) under anaerobic conditions than in aerobic conditions with more biological power generation using the MFC system. The maximum power density and Cr(VI) removal efficiency was 445 mW/m<sup>2</sup> and 97.2%, respectively. Removing Cr(VI) by *Ochrobactrum* sp. YC211 mainly occurred in the soluble part of cells during the anaerobic process, which could be considered as an enzymatic reaction [71]. However, studies have shown that strain KN400 can oxidize substrates and transfer electrons in the presence of oxygen at the anode, and the bioelectricity generation is comparable to that of anaerobic fuel cells [72]. In the PMFC system, photosynthesis of the plant generates oxygen through the roots and releases oxygen into the solution. However, in the presence of oxygen, some electrons released by bacteria are directly used for oxygen reduction, resulting in the decreased reduction rate of Cr(VI) [73]. Therefore, MFC possesses a better potential for Cr(VI) remediation in an anaerobic groundwater environment in a certain depth, which provides positive and optimistic support for in situ remediation of Cr(VI) using MFC-related technologies. In order to more intuitively compare the effects of different bacteria in MFC systems under different conditions, we summarized the remediation effect and energy production of Cr(VI) under different microbial species and environmental conditions in Table 2.

During the operation of the MFC system, substrates provide energy for microorganisms, and the remediation efficiency and productivity of MFC are also largely related to the composition of substrates and the extent of substrates utilization by microorganisms. Substrates that are easier to decompose by microorganisms can improve the activity of microorganisms and the rate of electrons production [74]. At present, many studies have investigated the effects of different substrates on the contaminants removal rate and electricity production. Tandukar et al. [16] took acetate as the substrate and found the complete removal of Cr(VI) with an initial concentration of 80 mg/L in 300 h, with the maximum power density reaching 55.5 mW/m<sup>2</sup>. Some researchers also used glucose as an MFC substrate to remove Cr(VI), and the maximum power density was 6.67 W/m<sup>3</sup> [75]. In addition, substrate formulations that can be better utilized by microorganisms also attract more attention. Wu et al. [76] used 0.31 g/L NH<sub>4</sub>Cl, 2.452 g/L NaH<sub>2</sub>PO<sub>4</sub>·H<sub>2</sub>O, 4.576 g/L Na<sub>2</sub>HPO<sub>4</sub>, 0.13 g/L KCl, and 1 g/L C<sub>6</sub>H<sub>12</sub>O<sub>6</sub>·H<sub>2</sub>O as substrates, and the removal rate of

Cr(VI) at the initial concentration of 20 mg/L reached 79.3%, 24 h later. Another study reported that the maximum power density of MFC with a specific substrate formulation in the anode chamber ( $\text{KH}_2\text{PO}_4$  4.4 g/L,  $\text{K}_2\text{HPO}_4$  3.4 g/L,  $\text{NH}_4\text{Cl}$  1.3 g/L,  $\text{NaCl}$  0.5 g/L, acetic acid 1.0 g/L,  $\text{CaCl}_2$  0.0146 g/L,  $\text{NaHCO}_3$  1.0 g/L, yeast extract 0.375 g/L, peptone 0.375 g/L) could reach 89.3  $\text{mW}/\text{m}^2$ , and the removal rate of 4 mg/L Cr(VI) was 95% after 456 h for a reaction in MFC [77].

On the other hand, the hydrogeochemical background value of the contaminated site can affect the pollution remediation process. Most studies currently regard COD as the organic background field of Cr(VI) polluted water. Mu et al.'s study showed that the efficiency of Cr(VI) removal increased from 74.2% to 90.7% when the COD concentration in the anode area increased from 100 mg/L to 500 mg/L, and then gradually decreased with the further increase of the COD concentration. When the COD concentration reached 700 mg/L, the Cr(VI) removal rate decreased to 84.0% [61]. Microorganisms oxidize organic matter as their nutrient source and sequentially generate electrons. A higher substrate content contributes to the generation of higher electrical energy [78]. However, when the concentration of organic matter is too high, too much organic matter may lead to the accumulation of organic acids in bacterial cells, thus inhibiting the activity of microorganisms. Accumulating too much organic matter in the system is not conducive to the transfer of electrons and reduces the power generation as well [79].

**Table 2.** Removal rate and energy production of Cr(VI) under different bacteria type and environmental.

Bacteria Type	Cr initial Concentration	pH	Anode Inoculum	Temperature	Operation Time	Cr Removal Rate	Energy	Reference
Anaerobic sludge	50 mg/L	2	-	-	16 h	40%	141 $\mu\text{v}$	[80]
Proteobacteria	19 mg/L	7	sodium acetate	-	16 h light, 8 h dark	99%	-	[42]
Proteobacteria	200 mg/kg	6.86	-	-	100 d	90%	23.83 $\text{mW}/\text{m}^2$	[81]
Anaerobic sludge	1000 mg/kg	7	3.32 g/L, $\text{NaH}_2\text{PO}_4 \cdot 2\text{H}_2\text{O}$ ; 10.32 g/L, $\text{Na}_2\text{HPO}_4 \cdot 12\text{H}_2\text{O}$ ; 2.0 g/L, $\text{CH}_3\text{COONa}$ ; 0.31 g/L $\text{NH}_4\text{Cl}$ ; 0.13 g/L $\text{KCl}$ ; 0.2 g/L $\text{MgSO}_4 \cdot 7\text{H}_2\text{O}$ ; 15 mg/L $\text{CaCl}_2$ ; 20 mg/L $\text{MnSO}_4 \cdot \text{H}_2\text{O}$ and 12.5 mL of trace elements solution. 1 g/L, $\text{CH}_3\text{COONa}$ ; 0.31 g/L, $\text{NH}_4\text{Cl}$ ;	-	16 d	62.70%	200 $\text{mA}/\text{m}^2$	[82]
Anaerobic sludge	1 g/L	7	5.38 g/L, $\text{NaH}_2\text{PO}_4 \cdot \text{H}_2\text{O}$ ; 8.66 g/L, $\text{Na}_2\text{HPO}_4$ ; 0.13/L, $\text{KCl}$ ; vitamin solution (12.5 mL) and trace mineral solution	-	8 d	80%	140 $\text{mW}/\text{m}^2$	[41]
Anaerobic sludge	100 mg/L	2	$\text{CH}_3\text{COONa}$	-	10 h	99%	1.4 $\text{W}/\text{m}^2$	[83]
Anaerobic sludge	20 mg/L	2	-	33 °C	18 h	99.57%	140 $\text{mW}/\text{m}^2$	[84]
<i>Trichococcus pasteurii</i>	80 mg/L	7	0.78 g/L, $\text{KCl}$ ; 0.58 g/L, $\text{NaCl}$ ; 0.68 g/L, $\text{KH}_2\text{PO}_4$ ; 0.8 g/L, $\text{K}_2\text{HPO}_4$ ; 0.1 g/L, $\text{MgSO}_4 \cdot 7\text{H}_2\text{O}$ ; 0.28 g/L, $\text{NH}_4\text{Cl}$ ; 0.1 g/L, $\text{CaCl}_2 \cdot 2\text{H}_2\text{O}$ .	22–24 °C	25 d	-	5.5 $\text{mW}/\text{m}^2$	[16]
Anaerobic sludge	40 mg/L	5	-	22–50 °C	5 h	100%	7.2 $\text{W}/\text{m}^3$	[23]
$\gamma$ - <i>Proteobacteria</i>	20 mg/L	7	0.3 g/L, $\text{NH}_4\text{Cl}$ ; 2.452 g/L, $\text{NaH}_2\text{PO}_4 \cdot \text{H}_2\text{O}$ ; 4.576 g/L, $\text{Na}_2\text{HPO}_4$ ; 0.13 g/L, $\text{KCl}$ ; 1 g/L $\text{C}_6\text{H}_{12}\text{O}_6 \cdot \text{H}_2\text{O}$	25 °C	30 d	79.30%	9.5 $\text{mW}/\text{m}^2$	[76]
Anaerobic sludge	60 mg/L	6.5	-	-	3 d	93.4%	414.4 $\text{mW}/\text{m}^3$	[61]

#### 4.4. Role of Cathode Conditions in Cr(VI) Remediation

The concentration of Cr(VI) and the MFC performance is heavily interrelated, as a high concentration of contaminants up to a certain range will lead to high electricity generation [42]. However, many high concentrations are far from the concentrations of real wastewater or contaminated soils. Therefore, MFC studies could be exploratory for the in situ remediation of Cr(VI) in soils and waters. It has been reported that Cr(VI) can

be completely removed when the concentration of Cr(VI) was 20 mg/L in constructed wetland-microbial fuel cell (CW-MFC). When the Cr(VI) concentration in the influent increased to 60 mg/L, the removal efficiency of Cr(VI) was still above 90%, and then gradually decreased to 74.3% when the Cr(VI) concentration was further increased to 100 mg/L [61]. It can be seen that when the concentration of Cr(VI) is too high, Cr(VI) is toxic to cathodic microorganisms, which will inhibit the activity of microorganisms and hinder electricity generation. As mentioned above, chromium has different forms in different pH environments, and relevant studies have shown that the pH condition of the cathode is an important environmental factor affecting MFC performance. A higher concentration of Cr(VI) can be reduced when the pH value of the cathode is 2, indicating that the acidic environment favors Cr(VI) reduction [22]. Huang et al. also confirmed the pH dependence of the Cr(VI) reduction process. Compared with pH = 7, the reduction rate and power generation of Cr(VI) increased by 27.3% and 61.8%, respectively, in acidic conditions with the pH value of 5, and the reduction rate and power generation of Cr(VI) decreased by 21.2% and 6.0%, respectively, at alkaline pH = 8. The reason is that the microorganism's catalysis increases the potential as pH decreases. On the other hand, in terms of chemical reactions on the basis of Equations (7) and (8), the reduction reaction of Cr(VI) is more easily carried out under acidic conditions [23].

#### 4.5. Soil Properties and Media Types

Compared with the surface water environment, the vadose zone and soil involved in groundwater are more complex with multi-phase environmental media, and the environmental conditions of Cr(VI) contaminated soil would significantly affect the removal outcome of MFC. Although acidic conditions promote Cr(VI) reduction, it has been found that the ubiquitous red soil has a lower rate of Cr(VI) removal under the acidic condition due to the existence of more electron receptors (such as Fe(III)) in red soil. These electron receptors compete with Cr(VI) to inhibit the remediation of Cr(VI) [82]. Meanwhile, there is more clay in red soil, which is the inherent adsorbent [85], and its presence prevents Cr(VI) migration to the cathode surface. Another reason is that the clay soil with a smaller particle size has a lower removal rate of Cr(VI). The particle size of the soil medium would affect its pore size distribution. Wang et al. found that the larger the particle size of soil medium, the higher the relative abundance of electrochemically active bacteria, and the better the electricity generation and pollutant removal ability [86]. Mu et al. [61] successfully used the CW-MFC system to remove Cr(VI) from polluted water. The system was composed of a gravel layer (3 cm thick), bottom layer (14 cm thick), anode layer (8 cm thick), intermediate layer, cathode layer (8 cm thick), and top layer from bottom to top. The gravel layer (gravel with a diameter of 4.6 mm) was used to improve the distribution of wastewater in the system. The bottom, middle, and top layers were filled with volcanic slag with a diameter of 35 mm. The anode and cathode were made of granular activated carbon and 12-mesh stainless steel mesh (thickness: 4 cm, diameter: 16.9 cm). The stainless-steel net acted as an electron collector. The removal rate of Cr(VI) with the initial concentration of 60 mg/L reached 93% in the CW-MFC system, and the maximum power density was 458.2 mW/m<sup>2</sup>. Due to the different electronic supply capacities of different soils and media, the remediation performance and electricity generation capacity will be significantly different. Yan et al. [84] showed that when quartz sand and pyrite were used as CW-MFC fillers, the pyrite filler with microbial activity showed a higher capacity for supplying electrons, while quartz sand anode filler could hardly give electrons. The results showed that the pyrite filler group had a better remediation ability. Therefore, the ability of soil and medium for giving and transporting electrons is critical to the efficiency of Cr(VI) reduction and productivity in MFC. However, the remediation of groundwater using MFC is rarely studied. It is urgent to study the types of aquifer media and the influence of groundwater flow fields on the MFC system, which is also a key research point to determine whether MFC technologies can be suitable for the environmentally friendly remediation of groundwater and soil environment.



### 5. Effect of MFC Design on Cr(VI) Soil and Water Pollution Remediation

Subsurface environments have their unique attributes and vary from site to site. Meanwhile, sediment and wetland environments are also complex. Therefore, people have researched different directions on MFC remediation technologies in different sites. Figure 4 is drawn by summarizing previous research results [42,68,80,87]. This figure shows some experimental device conceptual models for the study of remediating Cr(VI) pollution in a subsurface environment by MFC. Table 3 lists the effects of Cr(VI) remediation and energy recovery in the subsurface environment. This table comprehensively summarizes the application of MFC in a subsurface environment, which can provide a reference for future researchers.

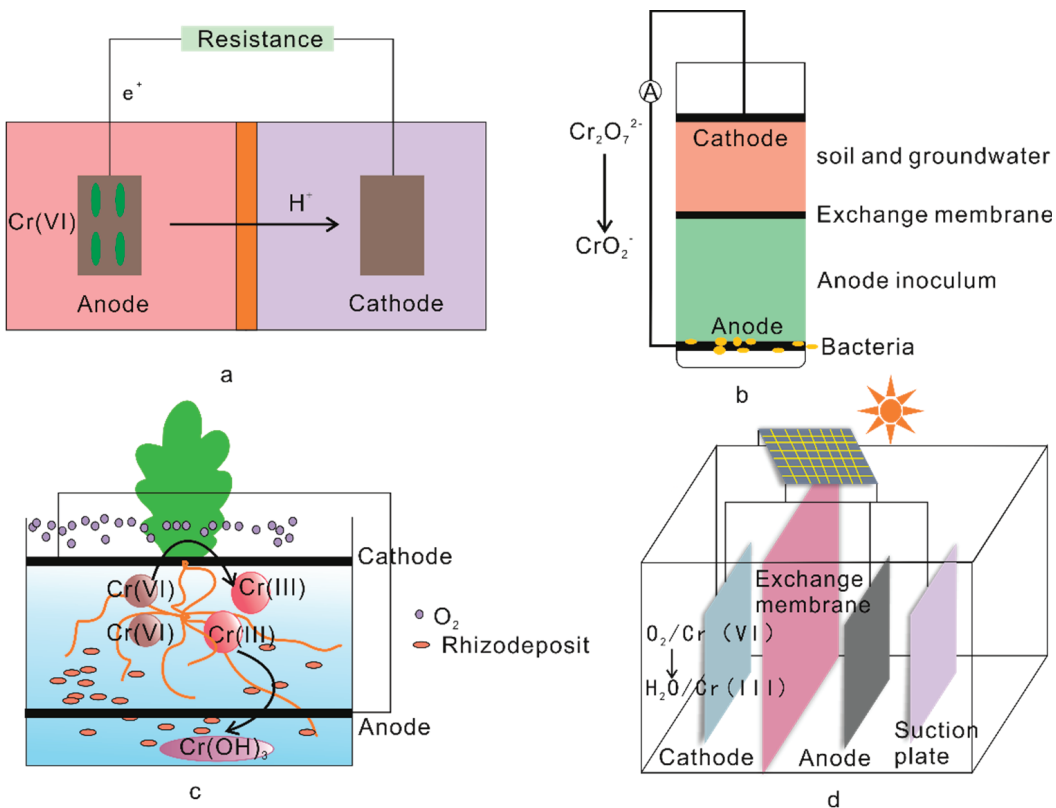


**Figure 4.** Models of an MFC device for treating Cr(VI) in a subsurface environment: (a) removal of Cr(VI) from wastewater by conventional MFC (adapted from Li (2018)); (b) the MFC for Cr(VI) treatment in groundwater and soil (adapted from Zhang (2019)); (c) plant-enhanced MFC for Cr(VI) removal from soil and water (adapted from Habibul (2016)); (d) photoanode MFC for Cr(VI) removal from wastewater (adapted from Ren (2018)).

**Table 3.** Removal rate of Cr(VI) and energy production in different MFC designing types.

MFC Type	Cr Initial Concentration	Operation Time	Cr Removal Rate	Energy	Reference
Absorption MFC	50 mg/L	16 h	40%	141 $\mu$ v	[80]
Plant MFC	19 mg/L	16 h light, 8 h dark	99%	-	[42]
Plant MFC	200 mg/kg	100 d	90%	23.83 mW/m <sup>2</sup>	[81]
Plant MFC	1000 mg/kg	16 d	62.70%	200 mA/m <sup>2</sup>	[82]
Dual MFC	1 g/L	8 d	80%	140 mW/m <sup>2</sup>	[41]
Dual MFC	100 mg/L	10 h	99%	1.4 W/m <sup>2</sup>	[83]
Photoelectric anode MFC	20 mg/L	18 h	99.57%	140 mW/m <sup>2</sup>	[67]
Photoelectric anode MFC	50 ppm	13.5 h	90.90%	1302 mw/m <sup>2</sup>	[68]
Dual MFC	10 mg/L	11 h	100%	535.4 mW/m <sup>2</sup>	[60]
Cu(III) dual MFC	11.36 g/L	8 h	51.64%	1235.53 mW/m <sup>2</sup>	[88]
Biological cathode MFC	80 mg/L	25 d	-	5.5 mW/m <sup>2</sup>	[16]
Biological cathode MFC	40 mg/L	5 h	100%	7.2 W/m <sup>3</sup>	[23]
Biological cathode MFC	20 mg/L	30 d	79.30%	9.5 mW/m <sup>2</sup>	[76]
Biological cathode MFC	0.4 mmol/L	48 h	99.97%	6.8 W/m <sup>3</sup>	[48]
Wetland MFC	60 mg/L	3 d	93.4%	414.4 mW/m <sup>3</sup>	[61]
Wetland MFC	300 $\mu$ g/g	70 d	68%	1.06 W/m <sup>3</sup>	[89]
Photoelectrode MFC	9 mg/L	2.5 d	90%	-	[90]

Note: “-” means no available data.

### 5.1. Soil and Groundwater Pollution

Plant microbial fuel cells (PMFC) have been widely used for the remediation of Cr(VI) pollution in soil. The advantage of PMFC is that it is a coupling system that can produce organic matter and energy by itself. The characteristics of soil are also favorable to MFC operation. Soil with more nutrients has higher microbial biodiversity and more species that are conducive to organic matter degradation and electron transfer [91,92]. Habibul and his coworkers [42] constructed a PMFC for the remediation of Cr contamination in soil. The device consists of a plexiglass cylinder anode chamber (diameter of 110 mm, height of 170 mm, and working volume of 1 L) filled with 300 g of graphite particles as an anode, and the distance between cathode with the anode was 10 cm. Ryegrass was chosen as MFC plants with fast growth, large biomass, and dense rhizosphere. Ryegrass released secretions into the rhizosphere through photosynthesis, increasing microbial activity, thus improving the electron transfer efficiency and enhancing the bioelectrochemical reduction process. In addition, plant absorption, electrode adsorption, and direct reduction of Cr(VI) by cathodic bacteria play a synergistic role with bioelectrochemical reduction to increase the removal efficiency to 90%. Wang and his coworkers [81] constructed a single PMFC with a soil moisture content of 60% and ctypha planted in the system. Finally, 90% of Cr(VI) was removed and the maximum power was 23.83 mW/m<sup>2</sup>. The study found that both soil type and applied resistance would affect the Cr(VI) removal process. Wang et al. [82] found that the Cr(VI) removal efficiency of fluvo-aquic soil were 99.1% and 64.3% with the resistance of 100  $\Omega$  and 1000  $\Omega$ , respectively, while the Cr(VI) removal efficiency were 62.7% and 50.4% for red clay with a resistance of 100  $\Omega$  and 1000  $\Omega$ , and finally the maximum power density of this system was 200 mA/m<sup>2</sup>. This result implies that low external resistance can improve remediation efficiency, and the soil medium type also has an important influence on the remediation. In addition, the researchers further improved Cr removal efficiency by adding different adsorption materials into the system. Zhang et al. [80] selected leaves, shell powder, and pine sawdust as the adsorption materials to investigate their adsorption ability for Cr. Finally, leaves with a better adsorption ability were selected as the adsorption material setting above the anode to isolate the contaminated soil from the anode. After running 16 h, the removal efficiency of Cr(VI) in the subsurface reached 96%. Chen et al. [93] built a sandbox to construct a two-compartment MFC and to study its performance in simulating a groundwater environment and found that MFC could be used for the remediation of actual groundwater environmental pollution. Lin et al. [94]

assembled a tubular MFC and inserted it into groundwater remediation well to achieve toluene removal and power generation under extreme matrix conditions, which became one of the effective reference methods for remediation of Cr(VI) pollution in groundwater. MFC systems have diverse applications for in situ remediation of groundwater contaminants, therefore future research directions must target pollutants of soil and water which are difficult to treat in conventional treatment methods.

### 5.2. Sediment and Wetland Pollution

Metals can be preserved in sediment easily [95], so remediation of sediment is particularly important. Wetlands have special rhizosphere bacteria and rhizosphere enzymes, and thus have a higher microbial activity for catalytic oxidation and reduction [96]. Sediment MFC can be applied to the field of organic high flux, such as deep river downstream. These areas can provide anaerobic conditions for the MFC and organic matter [97]. Therefore, integrating MFC with sediment and wetland has great potential in the field of environmental remediation. Razavi et al [89]. used CW-MFC to remove Cr from contaminated sediments, in which the maximum power density and Cr removal rate were  $1.06 \text{ W/m}^3$  and 68%, respectively. The results revealed that MFC technology has a high possibility to remediate Cr-contaminated sediments. He et al. [90] modified and used  $\text{ZnIn}_2\text{S}_4\text{-AgAgCl/GO}$  and  $\text{ZnIn}_2\text{S}_4\text{-RGO/MnO}_2$  photoelectrode (PFC) to effectively remove Cr(VI) in sand and gravel sediments. Under the light, the photocatalyst was deposited on the photoelectrode to generate electrons, which can be used for the current generation and pollutant remediation. Protons entered the cathode chamber through the proton exchange membrane (PEM) to react with electrons and Cr(VI) ions in the cathode chamber. Cr(VI) acted as an electron acceptor and then was reduced to Cr(III) or further removal by the precipitation reaction. Mu et al. [61], used CW-MFC to treat Cr(VI) polluted water and generate power synchronously. Studies show that plants play an important role in the CW-MFC system. The carbon source of this system comes from a plant root exudate. More importantly, plant fibrous roots with a large specific surface area provides a large number of attachment sites for microorganisms. When electrode spacing was 10 cm, the concentration of Cr (VI) and COD in the influent were 60 mg/L and 500 mg/L, the highest power density was  $458 \text{ mW/m}^3$ , and the removal rates of Cr (VI) and COD reached the highest. The results show that the larger surface area and higher biomass are beneficial to power generation [98]. Detailed studies on the removal of Cr(III) formed by Cr(VI) reduction have also been carried out. Hua et al. [99] found that adding citric acid to the cathode could be complex with Cr(III) in the cathode sediments, significantly improving the removal efficiency of Cr(VI) and Cr(III) in the sediments.

## 6. Challenges of MFC Remediation of Cr(VI) Contaminated Sites

### 6.1. Applicability of MFC System

At present, the majority of the research on MFC treatment of Cr(VI) pollution mainly focuses on laboratory-scale/pilot-scale experiments, which have mostly used a synthetic solution as the matrix, and the reactor volume is generally less than 1 L. Thus, a small electrode size and decent experimental conditions would easily achieve a higher performance level [100]. Therefore, there is still a long way to go for the practical application of MFC. Compared with the direct reduction of Cr(VI) by microorganisms, MFC has a higher power density and higher tolerance to the Cr(VI) concentration [22]. Proton exchange membranes play an important role in maintaining the anaerobic conditions and migrating protons into the cathode chamber [101]. In addition, the presence of the proton exchange membrane (PEM) avoided the attachment between microorganisms and Cr(VI) under certain conditions, so the MFC system can adapt to the environmental conditions with a higher Cr(VI) concentration. However, PEM should be cleaned every 6 to 7 months to avoid biological fouling, which makes the MFC system more laborious [102,103]. Therefore, PEM fouling is the main limiting factor for the development of MFC for the site and long-term application [104]. In addition, biofouling of cathode clogging, catalyst inactivation, and bacterial biofilm overgrowth would reduce the electrode conductive area [105], thus affecting the

removal of Cr(VI) and electricity generation. It has been reported that Cr(III) products, such as  $\text{Cr}(\text{OH})_3$  and  $\text{Cr}_2\text{O}_3$ , formed by Cr(VI) reduction will be adsorbed on the electrode surface to form a non-conductive covering layer [16]. The presence of coating would lead to the invalidation of MFC electrodes, and the cleaning and replacement of electrodes would be very costly. In addition, subsurface environments have characteristics of a porous structure, due to the electron transfer rate of the porous system being lower than that of the water-soluble system, the internal resistance of the system is greatly increased, so the electron transfer rate in the MFC system would be reduced [106]. Therefore, it is of great significance to improve the applicability of the MFC system to remove Cr(VI).

### 6.2. Characteristic of Site Specific Cr(VI) Pollution Remediation

Owing to various features, such as high solubility, high fluidity, and easy migration of Cr(VI) in the subsurface environment remediation present some challenges [107]. A study of the surface subsurface contaminated sites with Cr(VI) showed that Cr(VI) was not easily adsorbed when penetrating aquifers consisting of silt, clay, and silty clay layers from top to bottom, however it migrated with groundwater. Compared with the Cr(VI) pollution level (766–10711.4 mg/kg), the maximum adsorption capacity of Cr(VI) in the clay layer was only 1.2 mg/kg, indicating that the Cr(VI) adsorption capacity was very low. Moreover, in the case of rainwater leaching, Cr(VI) adsorbed on the aquifer was desorbed and released into the groundwater [108], thus making in situ remediation a difficult task. After converting Cr(VI) into Cr(III), the pollution risk still exists in the environment. Fortunately, previous studies have shown that if two-dual compartment MFC were connected, the negative influence of Cr(VI) and Cr(III) on the system performance could be simultaneously removed. Cr(VI)-MFC could reduce Cr(VI) and generate electrical energy that could be supplied to Cr(III)-MFC. It was found that Cr(III) could be effectively reduced by keeping the concentration ratio of Cr(VI) to Cr(III) at 2:1. After 10 h of reaction, the removal efficiency of Cr(III) by Cr(III)-MFC increased from 58% to 82%, and Cr(III) was reduced to metal ion Cr [83]. For the contaminated site scale, after the reduction of Cr(VI) to Cr(III), there would be problems such as an unstable state, being easy to react with oxygen, manganese dioxide, and other oxidants existing and resulting in the yellowing phenomenon [109]. Studies have shown that the process of soil microorganisms reducing oxidized manganese could promote the yellowing of Cr [110] and cause secondary pollution. The repulsion between the negatively-charged cathode and the negatively-charged  $\text{Cr}_2\text{O}_7^{2-}$  results in a slow reduction rate of Cr(VI) during the treatment process [29]. It has been pointed out that the material with reversible redox reaction can effectively eliminate the electric repulsion between the negatively-charged cathode and  $\text{Cr}_2\text{O}_7^{2-}$  or  $\text{CrO}_4^{2-}$  anions [29]. Li et al. used Cu(II) as the electronic shuttling medium of MFC to effectively improve the performance of bioelectricity generation and accelerate Cr(VI) reduction. Meanwhile, they found that in the presence of Cu(II), the power density and Cr(VI) reduction rate were 1235.5 mW/m<sup>2</sup> and 1.19 g/m<sup>3</sup> h, which is 1.44 times and 1.17 times of the MFC system without Cu(II) [88]. Therefore, under the background of site pollution, it is of great significance to study the Cr(VI) pollution process, and conversion mechanisms of various valence forms and for the successful application of MFC site remediation.

### 6.3. Complex Site Environmental Conditions

Groundwater temperature in Northern China is usually kept at 6.5–9.5 °C, while that in Northwest China is kept at 9–12 °C. The groundwater pH in Southern China is generally lower than that in Northern China. The harsh groundwater environment will limit the growth of microorganisms [93]. It was also suggested that the removal process of Cr(VI) is pH dependent. The neutral environment at the anode is encouraging to the generation of the electron from microbial oxidation of substrates and the acidic environment at the cathode is conducive to the reduction of Cr(VI), while the precipitation of Cr(III) is more likely to occur in a neutral environment [111]. Generally speaking, the pH of untreated Cr slag heap is 8.5–13.0 [112], while the pH of industrial chromium-containing wastewater is

between 0.42 and 0.79 [113]. The excessive acid or alkali environment is not conducive to the growth of anode microorganisms. Studies have shown that during sediment purification, the pH of the anodic chamber solution decreases gradually with each batch cycle. This phenomenon is related to the properties of soil and sediment, which inhibit the migration of H<sup>+</sup> in pore water. The accumulation of H<sup>+</sup> in the anode chamber would form an acidic environment [114]. Then the acidic environment would inhibit the activity of electroactive bacteria and affects the electron transfer, resulting in the decreasing power production during the last days of each batch cycle [115]. In addition, the biological reduction effect is negatively correlated with the Cr(VI) concentration, and excessive Cr(VI) inhibits the reduction process due to its high toxicity [116]. Literature has shown that when the Cr(VI) concentration exceeds 200 mg/L, the metabolic activities of microorganisms in the soil can be severely inhibited, resulting in the failure of a complete reduction of Cr(VI) and also affecting the generation of bioelectric energy [117]. As a strong oxidant, Cr(VI) causes oxidative stress to plant tissues in PMFC. Under continuous exposure to Cr(VI), the level of antioxidant enzymes in plants decreases, which seriously damages the activity of root tip cells, also resulting in the decrease in cell viability and affecting the secretion of organic matter in plant root [118], finally affecting the operation of PMFC. When different nutrients such as nitrate enter into the subsurface environment, organics will directly participate in the denitrification process rather than power generation [119], thus affecting the reduction of Cr(VI). Natural colloid exists widely in a subsurface environment and they would adsorb, carry, and migrate pollutants in a subsurface [39]. In addition, studies have shown that humic acid colloid in acidic soil could directly reduce Cr(VI) due to functional groups of humic acid, such as phenolic hydroxyl groups, which can provide additional electrons to reduce Cr(VI) through a hydrogen transfer mechanism, affecting the migration of Cr(VI) in the subsurface [120]. Conclusively, migration of Cr(VI) in groundwater and soil as well as the influence of organic substances poses diverse challenges for Cr(VI) removal by MFC in a complex site environment. These problems must be resolved to implement MFC technology with sustainable treatments.

## 7. Summary and Conclusive Remarks

With the continuous consumption of fossil fuels and increasingly prominent environmental problems, governments all over the world are actively advocating and realizing the carbon dioxide issue and related fossil energy management strategy. Energy transition with carbon peak as the environmental goal and carbon neutrality has been established within timeframes. The MFC technology has shown its unique advantages over other technologies under its dual functions of eco-remediation and bioenergy generation. Cr(VI)-contaminated sites with distinct groundwater and soil environment problems have become major ecological and environmental issues for many countries. The diverse potential of MFC and revised ones for the ecological remediation of a Cr(VI)-contaminated subsurface environment has been substantiated. Thus, the importance of developing and optimizing this innovative technology is self-evident. Through the characterization of Cr(VI) and its migration and transformation, this manuscript concluded that when Cr(VI) enters soil and groundwater, the changing morphology and properties of Cr(VI) after complex chemical and physical reactions provide interesting inspiration for the application of MFC in site remediation. By summarizing the mechanism of Cr(VI) remediation, energy conversion as well as influencing and restricting factors for the removal process in MFC, the key methods to improve the operation efficiency were put forward. Much effort was made on the remediation of Cr(VI) pollution in soil and groundwater by MFC, and some good progress was achieved. However, the applicability of the MFC system, the characterization of the Cr(VI) pollution site, and complex environmental conditions could limit the operating of Cr(VI) remediation with MFC if the professional investigation are not good enough. Based on the above comprehensive review of scientific and technological progress, it can be suggested that further enhancement in sustainability and technological applications for the eco-remediation of Cr (VI)-contaminated sites is a prerequisite for field applications. A

better understanding and in-depth improvement of these targets in the MFC research can be achieved in the following aspects:

1. It is suggested to improve the pH adjustability of the cathode to realize simultaneous immobilization of Cr(III) during Cr(VI) remediation so that long-term operation can be sustained in various harsh environmental conditions.
2. The MFC electrode may be modified wisely to avoid secondary pollution along with enhanced electron transfer capabilities for high power generation catering for subsurface environments.
3. MFC possesses the unique advantages of clean/green eco-remediation, however it may pose the problem of low energy productivity for an actual subsurface environment. We should not be limited to the sole use of MFC, but rather integrate other electrochemical technologies, e.g., a bioelectrochemical reactor (BER), with MFC, thus the application range and advantages of MFC can be expanded.
4. Designing large-scale and continuous flow MFC reactors according to the actual characteristics of a subsurface pollution, distribution, and migration of Cr(VI) in groundwater and the type of soil and medium, as well as the geological and hydrogeological conditions of the sites will optimize the Cr(VI) removal potential for the actual applications and help to overcome the limitations of small-scale laboratory experiments.
5. Oxidized Cr-contaminated water, biofouling of cathode clogging, catalyst inactivation, bacterial biofilm overgrowth, non-conductive covering layer forming, and PEM fouling can affect the long-term stability of the MFC operation, which need further study.
6. For soil with high clay content, low permeability, low electrical conductivity, and water-saturated porous media, in situ reaction zones with microbial activity can be constructed or electron transport channels can be constructed artificially to improve the capacity for better electron migration in the system.
7. Natural colloidal components in the subsurface environment can adsorb and carry pollutants, as well as dramatically influence the electron movement as their electrical proper-ties, which make them interact with the electric field formed by MFC. It is essential to explore the influence of colloid on remediation and productivity efficiencies of MFC and directly improve the applicability and operation efficiency of MFC under different site conditions.
8. With the continuous improvement and optimization of MFC technology, MFC systems have diverse applications for in situ remediation of groundwater contaminants, therefore future research directions must target pollutants in soil and water that are difficult to treat in conventional treatment methods.

**Author Contributions:** Conceptualization, Y.Y. (Yifan Yu), Y.Y. (Yuesuo Yang) and P.K.; methodology, Y.Y. (Yuesuo Yang) and P.K.; software, Y.Y. (Yifan Yu); validation, Y.Y. (Yuesuo Yang), P.K. and J.A.; formal analysis, Y.Y. (Yifan Yu); investigation, W.Z. and Y.L. (Yan Li); resources, Y.Y. (Yuesuo Yang) and P.K.; writing—original draft preparation, Y.Y. (Yifan Yu); writing—review and editing, Y.Y. (Yuesuo Yang), P.K. and J.A.; visualization, Y.Y. (Yuesuo Yang) and P.K.; supervision, J.A. and Y.L. (Ying Lu); funding acquisition, Y.Y. (Yuesuo Yang) and P.K. All authors have read and agreed to the published version of the manuscript.

**Funding:** This article was sponsored by the following funds: National Key Research and Development Program of China (2019YFC1804801), NSFC (42107071), and Program of Attracting Talents for Discipline Innovation in Chinese Universities (B16020).

**Institutional Review Board Statement:** Not applicable.

**Informed Consent Statement:** Not applicable.

**Data Availability Statement:** Not applicable.

**Conflicts of Interest:** The authors declare no conflict of interest.

## References

- Raddatz, A.L.; Johnson, T.M.; McLing, T.L. Cr Stable Isotopes in Snake River Plain Aquifer Groundwater: Evidence for Natural Reduction of Dissolved Cr(VI). *Environ. Sci. Technol.* **2011**, *45*, 502–507. [[CrossRef](#)] [[PubMed](#)]
- Bachate, S.P.; Nandre, V.S.; Ghatpande, N.S.; Kodam, K.M. Simultaneous reduction of Cr(VI) and oxidation of As(III) by *Bacillus firmus* TE7 isolated from tannery effluent. *Chemosphere* **2013**, *90*, 2273–2278. [[CrossRef](#)] [[PubMed](#)]
- Li, Y.; Jin, Z.; Li, T.; Xiu, Z. One-step synthesis and characterization of core-shell Fe@SiO<sub>2</sub> nanocomposite for Cr (VI) reduction. *Sci. Total Environ.* **2012**, *421–422*, 260–266. [[CrossRef](#)] [[PubMed](#)]
- Baral, A.; Engelken, R.D. Chromium-based regulations and greening in metal finishing industries in the USA. *Environ. Sci. Policy* **2002**, *5*, 121–133. [[CrossRef](#)]
- Lovley, D.R. Dissimilatory Metal Reduction. *Annu. Rev. Microbiol.* **1993**, *47*, 263–290. [[CrossRef](#)]
- Anderson, R.A. Essentiality of chromium in humans. *Sci. Total Environ.* **1989**, *86*, 75–81. [[CrossRef](#)]
- Tantawy, M.A.; El-Roudi, A.M.; Salem, A.A. Immobilization of Cr(VI) in bagasse ash blended cement pastes. *Constr. Build. Mater.* **2012**, *30*, 218–223. [[CrossRef](#)]
- Dong, H.; Deng, J.; Xie, Y.; Zhang, C.; Jiang, Z.; Cheng, Y.; Hou, K.; Zeng, G. Stabilization of nanoscale zero-valent iron (nZVI) with modified biochar for Cr(VI) removal from aqueous solution. *J. Hazard. Mater.* **2017**, *332*, 79–86. [[CrossRef](#)]
- Behera, M.; Jana, P.S.; Ghangrekar, M.M. Performance evaluation of low cost microbial fuel cell fabricated using earthen pot with biotic and abiotic cathode. *Bioresour. Technol.* **2010**, *101*, 1183–1189. [[CrossRef](#)]
- Dhal, B.; Thatoi, H.N.; Das, N.N.; Pandey, B.D. Chemical and microbial remediation of hexavalent chromium from contaminated soil and mining/metallurgical solid waste: A review. *J. Hazard. Mater.* **2013**, *250–251*, 272–291. [[CrossRef](#)]
- Peters, R.W. Chelant extraction of heavy metals from contaminated soils. *J. Hazard. Mater.* **1999**, *66*, 151–210. [[CrossRef](#)]
- Wasay, S.A.B.S.; Tokunaga, S. Organic acids for the in situ remediation of soils polluted by heavy metals: Soil flushing in columns. *Water Air Soil Pollut.* **2001**, *127*, 310–314. [[CrossRef](#)]
- Fu, R.; Wen, D.; Xia, X.; Zhang, W.; Gu, Y. Electrokinetic remediation of chromium (Cr)-contaminated soil with citric acid (CA) and polyaspartic acid (PASP) as electrolytes. *Chem. Eng. J.* **2017**, *316*, 601–608. [[CrossRef](#)]
- Jafar, A.; Aaqib, S.; Lei, W.; Muhammad, R.H.; Shahi, M.; Gang, P.J.E. Electro-Microbiology as a Promising Approach Towards Renewable Energy and Environmental Sustainability. *Energies* **2018**, *11*, 1822.
- Liu, H.; Ramnarayan, R.; Logan, B.E. Production of electricity during wastewater treatment using a single chamber microbial fuel cell. *Environ. Sci. Technol.* **2004**, *38*, 2281–2285. [[CrossRef](#)]
- Tandukar, M.; Huber, S.J.; Onodera, T.; Pavlostathis, S.G. Biological chromium(VI) reduction in the cathode of a microbial fuel cell. *Environ. Sci. Technol.* **2009**, *43*, 8159–8165. [[CrossRef](#)]
- Huang, L.; Logan, B.E. Electricity generation and treatment of paper recycling wastewater using a microbial fuel cell. *Appl. Microbiol. Biotechnol.* **2008**, *80*, 349–355. [[CrossRef](#)]
- Sindhuja, M.; Harinipriya, S.; Bala, A.C.; Ray, A.K. Environmentally available biowastes as substrate in microbial fuel cell for efficient chromium reduction. *J. Hazard. Mater.* **2018**, *355*, 197–205. [[CrossRef](#)]
- Gupta, S.; Yadav, A.; Verma, N. Simultaneous Cr(VI) reduction and bioelectricity generation using microbial fuel cell based on alumina-nickel nanoparticles-dispersed carbon nanofiber electrode. *Chem. Eng. J.* **2017**, *307*, 729–738. [[CrossRef](#)]
- Li, M.; Zhou, S.  $\alpha$ -Fe<sub>2</sub>O<sub>3</sub>/polyaniline nanocomposites as an effective catalyst for improving the electrochemical performance of microbial fuel cell. *Chem. Eng. J.* **2018**, *339*, 539–546. [[CrossRef](#)]
- Huang, L.; Chai, X.; Chen, G.; Logan, B.E. Effect of set potential on hexavalent chromium reduction and electricity generation from biocathode microbial fuel cells. *Environ. Sci. Technol.* **2011**, *45*, 5025–5031. [[CrossRef](#)] [[PubMed](#)]
- Li, Z.; Zhang, X.; Lei, L. Electricity production during the treatment of real electroplating wastewater containing Cr<sup>6+</sup> using microbial fuel cell. *Process Biochem.* **2008**, *43*, 1352–1358. [[CrossRef](#)]
- Huang, L.; Chai, X.; Cheng, S.; Chen, G. Evaluation of carbon-based materials in tubular biocathode microbial fuel cells in terms of hexavalent chromium reduction and electricity generation. *Chem. Eng. J.* **2011**, *166*, 652–661. [[CrossRef](#)]
- Tee, P.-F.; Abdullah, M.O.; Tan, I.A.W.; Amin, M.A.M.; Nolasco-Hipolito, C.; Bujang, K. Effects of temperature on wastewater treatment in an affordable microbial fuel cell-adsorption hybrid system. *J. Environ. Chem. Eng.* **2017**, *5*, 178–188. [[CrossRef](#)]
- Kumar, R.; Singh, L.; Zularisam, A.W.; Hai, F.I. Microbial fuel cell is emerging as a versatile technology: A review on its possible applications, challenges and strategies to improve the performances. *Int. J. Energy Res.* **2018**, *42*, 369–394. [[CrossRef](#)]
- Sarkar, B.; Naidu, R.; Krishnamurti, G.S.; Megharaj, M. Manganese(II)-catalyzed and clay-minerals-mediated reduction of chromium(VI) by citrate. *Environ. Sci. Technol.* **2013**, *47*, 13629–13636. [[CrossRef](#)]
- Watenphul, A.; Schmidt, C.; Jahn, S. Cr(III) solubility in aqueous fluids at high pressures and temperatures. *Geochim. Cosmochim. Acta* **2014**, *126*, 212–227. [[CrossRef](#)]
- Dai, R.; Yu, C.; Liu, J.; Lan, Y.; Deng, B. Photo-Oxidation of Cr(III)–Citrate Complexes Forms Harmful Cr(VI). *Environ. Sci. Technol.* **2010**, *44*, 6959–6964. [[CrossRef](#)]
- Wang, Q.; Huang, L.; Pan, Y.; Quan, X.; Li Puma, G. Impact of Fe(III) as an effective electron-shuttle mediator for enhanced Cr(VI) reduction in microbial fuel cells: Reduction of diffusional resistances and cathode overpotentials. *J. Hazard. Mater.* **2017**, *321*, 896–906. [[CrossRef](#)]
- Saha, R.; Nandi, R.; Saha, B. Sources and toxicity of hexavalent chromium. *J. Coord. Chem.* **2011**, *64*, 1782–1806. [[CrossRef](#)]

31. Pradhan, D.; Sukla, L.B.; Sawyer, M.; Rahman, P.K.S.M. Recent bioreduction of hexavalent chromium in wastewater treatment: A review. *J. Ind. Eng. Chem.* **2017**, *55*, 1–20. [[CrossRef](#)]
32. Mayes, M.A.; Larsen, P.M.J.I.L.; Brooks, S.C.; Fendorf, S.E. Multispecies transport of metal-ETDA complexes and chromate through undisturbed columns of weathered, fractured sapolite. *J. Contam. Hydrol.* **2000**, *45*, 243–265. [[CrossRef](#)]
33. Viamajala, S.; Peyton, B.M.; Apel, W.A.; Petersen, J.N. Chromate reduction in shewanella oneidensis MR-1 Is an inducible process associated with anaerobic growth. *Biotechnol. Prog.* **2002**, *18*, 290–295. [[CrossRef](#)] [[PubMed](#)]
34. Horton, R.N.; Apel, W.A.; Thompson, V.S.; Sheridan, P.P. Low temperature reduction of hexavalent chromium by a microbial enrichment consortium and a novel strain of *Arthrobacter aurescens*. *BMC Microbiol.* **2006**, *6*, 5. [[CrossRef](#)] [[PubMed](#)]
35. Eary, L.E.; Rai, D. Kinetics of chromate reduction by ferrous ions derived from hematite and biotite at 25 degrees C. *Am. J. Sci.* **1989**, *289*, 180–213. [[CrossRef](#)]
36. He, C.; Gu, L.; Xu, Z.; He, H.; Fu, G.; Han, F.; Huang, B.; Pan, X. Cleaning chromium pollution in aquatic environments by bioremediation, photocatalytic remediation, electrochemical remediation and coupled remediation systems. *Environ. Chem. Lett.* **2020**, *18*, 561–576. [[CrossRef](#)]
37. Zachara, J.M.; Girwin, D.C.; Schmidt, R.L.C.T.R. Chromate adsorption on amorphous iron oxyhydroxide in the presence of major groundwater ions. *Environ. Sci. Technol.* **1987**, *21*, 589–594. [[CrossRef](#)]
38. Kantar, C.; Cetin, Z.; Demiray, H. In situ stabilization of chromium(VI) in polluted soils using organic ligands: The role of galacturonic, glucuronic and alginic acids. *J. Hazard. Mater.* **2008**, *159*, 287–293. [[CrossRef](#)]
39. Wang, Y. Research progress of colloid and pollutant co-migration in soil and groundwater. *J. Chem. Ind.* **2017**, *68*, 24–36.
40. Wang, G.; Huang, L.; Zhang, Y. Cathodic reduction of hexavalent chromium [Cr(VI)] coupled with electricity generation in microbial fuel cells. *Biotechnol. Lett.* **2008**, *30*, 1959–1966. [[CrossRef](#)]
41. Aiyer, K.S. Recovery of chromium, copper and vanadium combined with electricity generation in two-chambered microbial fuel cells. *FEMS Microbiol. Lett.* **2020**, *367*, 15. [[CrossRef](#)] [[PubMed](#)]
42. Habibul, N.; Hu, Y.; Wang, Y.K.; Chen, W.; Yu, H.Q.; Sheng, G.P. Bioelectrochemical Chromium(VI) Removal in Plant-Microbial Fuel Cells. *Environ. Sci. Technol.* **2016**, *50*, 3882–3889. [[CrossRef](#)] [[PubMed](#)]
43. Lovley, D.R. Bug juice: Harvesting electricity with microorganisms. *Nat. Rev. Microbiol.* **2006**, *4*, 497–508. [[CrossRef](#)] [[PubMed](#)]
44. Kumar, A.; Katuri, K.; Lens, P.; Leech, D. Does bioelectrochemical cell configuration and anode potential affect biofilm response? *Biochem. Soc. Trans.* **2012**, *40*, 1308–1314. [[CrossRef](#)] [[PubMed](#)]
45. Nevin, K.P.; Richter, H.; Covalla, S.F.; Johnson, J.P.; Woodard, T.L.; Orloff, A.L.; Jia, H.; Zhang, M.; Lovley, D.R. Power output and coulombic efficiencies from biofilms of *Geobacter sulfurreducens* comparable to mixed community microbial fuel cells. *Environ. Microbiol.* **2008**, *10*, 2505–2514. [[CrossRef](#)]
46. Sun, D.Y.L.B.; Yun, H.; Wang, A.J. Degradation of chloramphenicol by bioanodes and biocathodes. *Environ. Sci.* **2015**, *36*, 1353–1358.
47. Wu, X.; Ren, X.; Owens, G.; Brunetti, G.; Zhou, J.; Yong, X.; Wei, P.; Jia, H. A facultative electroactive chromium(VI)-reducing bacterium aerobically isolated from a biocathode microbial fuel cell. *Front. Microbiol.* **2018**, *9*, 2883. [[CrossRef](#)]
48. Mao, Y.P.C.L.; Zhang, Y.H.; Hou, H.P.; Huang, G.T.; Liu, Y.D. Biological cathode microbial fuel cell. *Prog. Chem.* **2009**, *21*, 1673–1688.
49. Qiu, R.; Zhang, B.; Li, J.; Lv, Q.; Wang, S.; Gu, Q. Enhanced vanadium (V) reduction and bioelectricity generation in microbial fuel cells with biocathode. *Journal of Power Sources* **2017**, *359*, 379–383. [[CrossRef](#)]
50. Guan, C.Y.; Tseng, Y.H.; Tsang, D.C.W.; Hu, A.; Yu, C.P. Wetland plant microbial fuel cells for remediation of hexavalent chromium contaminated soils and electricity production. *J. Hazard. Mater.* **2019**, *365*, 137–145. [[CrossRef](#)]
51. Babu, A.G.; Kim, J.D.; Oh, B.T. Enhancement of heavy metal phytoremediation by *Alnus firma* with endophytic *Bacillus thuringiensis* GDB-1. *J. Hazard. Mater.* **2013**, *250–251*, 477–483. [[CrossRef](#)] [[PubMed](#)]
52. Harnisch, F.; Schröder, U. ChemInform Abstract: From MFC to MXC: Chemical and Biological Cathodes and Their Potential for Microbial Bioelectrochemical Systems. *Chem. Soc. Rev.* **2010**, *39*, 4433–4448. [[CrossRef](#)] [[PubMed](#)]
53. Gude, V.G. Wastewater treatment in microbial fuel cells—An overview. *J. Clean. Prod.* **2016**, *122*, 287–307. [[CrossRef](#)]
54. Rozendal, R.A.; Hamelers, H.V.M.; Rabaey, K.; Keller, J.; Buisman, C.J.N. Towards practical implementation of bioelectrochemical wastewater treatment. *Trends Biotechnol.* **2008**, *26*, 450–459. [[CrossRef](#)] [[PubMed](#)]
55. Aarthy, M.; Rajesh, T.; Thirunavoukkarasu, M. Critical review on microbial fuel cells for concomitant reduction of hexavalent chromium and bioelectricity generation. *J. Chem. Technol. Biotechnol.* **2020**, *95*, 1298–1307. [[CrossRef](#)]
56. Venkata Mohan, S.; Velvizhi, G.; Annie Modestra, J.; Srikanth, S. Microbial fuel cell: Critical factors regulating bio-catalyzed electrochemical process and recent advancements. *Renew. Sustain. Energy Rev.* **2014**, *40*, 779–797. [[CrossRef](#)]
57. Schroder, U. Anodic electron transfer mechanisms in microbial fuel cells and their energy efficiency. *Phys. Chem. Chem. Phys.* **2007**, *9*, 2619–2629. [[CrossRef](#)]
58. Pandit, S.; Sengupta, A.; Kale, S.; Das, D. Performance of electron acceptors in catholyte of a two-chambered microbial fuel cell using anion exchange membrane. *Bioresour. Technol.* **2011**, *102*, 2736–2744. [[CrossRef](#)]
59. Uddin, M.J.; Jeong, Y.-K.; Lee, W. Microbial fuel cells for bioelectricity generation through reduction of hexavalent chromium in wastewater: A review. *Int. J. Hydrogen Energy* **2021**, *46*, 11458–11481. [[CrossRef](#)]
60. Zhou, J.; Li, M.; Zhou, W.; Hu, J.; Long, Y.; Tsang, Y.F.; Zhou, S. Efficacy of electrode position in microbial fuel cell for simultaneous Cr(VI) reduction and bioelectricity production. *Sci. Total Environ.* **2020**, *748*, 141425. [[CrossRef](#)]



61. Mu, C.; Wang, L.; Wang, L. Performance of lab-scale microbial fuel cell coupled with unplanted constructed wetland for hexavalent chromium removal and electricity production. *Environ. Sci. Pollut. Res.* **2020**, *27*, 25140–25148. [[CrossRef](#)] [[PubMed](#)]
62. Yi, H.; Nevin, K.P.; Kim, B.C.; Franks, A.E.; Klimes, A.; Tender, L.M.; Lovley, D.R. Selection of a variant of *Geobacter sulfurreducens* with enhanced capacity for current production in microbial fuel cells. *Biosens. Bioelectron.* **2009**, *24*, 3498–3503. [[CrossRef](#)] [[PubMed](#)]
63. Li, M.; Zhou, J.; Bi, Y.-G.; Zhou, S.-Q.; Mo, C.-H. Polypyrrole/sewage sludge carbon as low-cost and high-effective catalyst for enhancing hexavalent chromium reduction and bio-power generation in dual chamber microbial fuel cells. *Sep. Purif. Technol.* **2021**, *256*, 117805. [[CrossRef](#)]
64. Song, T.-S.; Jin, Y.; Bao, J.; Kang, D.; Xie, J. Graphene/biofilm composites for enhancement of hexavalent chromium reduction and electricity production in a biocathode microbial fuel cell. *J. Hazard. Mater.* **2016**, *317*, 73–80. [[CrossRef](#)] [[PubMed](#)]
65. Ali, J.; Wang, L.; Waseem, H.; Djellabi, R.; Oladoja, N.A.; Pan, G. FeS@rGO nanocomposites as electrocatalysts for enhanced chromium removal and clean energy generation by microbial fuel cell. *Chem. Eng. J.* **2020**, *384*, 123335. [[CrossRef](#)]
66. Ali, J.; Wang, L.; Waseem, H.; Sharif, H.M.A.; Djellabi, R.; Zhang, C.; Pan, G. Bioelectrochemical recovery of silver from wastewater with sustainable power generation and its reuse for biofouling mitigation. *J. Clean. Prod.* **2019**, *235*, 1425–1437. [[CrossRef](#)]
67. Shan, Y.; Cui, J.; Liu, Y.; Zhao, W. TiO<sub>2</sub> anchored on MoS<sub>2</sub> nanosheets based on molybdenite exfoliation as an efficient cathode for enhanced Cr(VI) reduction in microbial fuel cell. *Environ. Res.* **2020**, *190*, 110010. [[CrossRef](#)]
68. Ren, G.; Sun, Y.; Lu, A.; Li, Y.; Ding, H. Boosting electricity generation and Cr(VI) reduction based on a novel silicon solar cell coupled double-anode (photoanode/bioanode) microbial fuel cell. *J. Power Sources* **2018**, *408*, 46–50. [[CrossRef](#)]
69. Zhao, Y.L.P.; Wang, X.B. Effect of temperature on electrochemical performance of microbial fuel cells. *Coal Convers.* **2012**, *35*, 4.
70. Aghababaie, M.; Farhadian, M.; Jeihanipour, A.; Biria, D. Effective factors on the performance of microbial fuel cells in wastewater treatment—A review. *Environ. Technol. Rev.* **2015**, *4*, 71–89. [[CrossRef](#)]
71. Chen, C.Y.; Cheng, C.Y.; Chen, C.K.; Hsieh, M.C.; Lin, S.T.; Ho, K.Y.; Li, J.W.; Lin, C.P.; Chung, Y.C. Hexavalent chromium removal and bioelectricity generation by *Ochrobactrum* sp. YC211 under different oxygen conditions. *J. Environ. Sci. Health A Toxic Hazard. Subst. Environ. Eng.* **2016**, *51*, 502–508. [[CrossRef](#)] [[PubMed](#)]
72. Nevin, K.P.; Zhang, P.; Franks, A.E.; Woodard, T.L.; Lovley, D.R. Anaerobes unleashed: Aerobic fuel cells of *Geobacter sulfurreducens*. *J. Power Sources* **2011**, *196*, 7514–7518. [[CrossRef](#)]
73. Helder, M.; Strik, D.P.B.T.B.; Timmers, R.A.; Raes, S.M.T.; Hamelers, H.V.M.; Buisman, C.J.N. Resilience of roof-top Plant-Microbial Fuel Cells during Dutch winter. *Biomass Bioenergy* **2013**, *51*, 1–7. [[CrossRef](#)]
74. Cao, L.; Ma, Y.; Deng, D.; Jiang, H.; Wang, J.; Liu, Y. Electricity production of microbial fuel cells by degrading cellulose coupling with Cr(VI) removal. *J. Hazard. Mater.* **2020**, *391*, 122184. [[CrossRef](#)]
75. Amutha, R.; Josiah, J.J.M.; Adriel Jebin, J.; Jagannathan, P.; Berchmans, S. Chromium hexacyanoferrate as a cathode material in microbial fuel cells. *J. Appl. Electrochem.* **2010**, *40*, 1985–1990. [[CrossRef](#)]
76. Wu, X.; Zhu, X.; Song, T.; Zhang, L.; Jia, H.; Wei, P. Effect of acclimatization on hexavalent chromium reduction in a biocathode microbial fuel cell. *Bioresour. Technol.* **2015**, *180*, 185–191. [[CrossRef](#)]
77. Sophia, A.C.; Saikant, S. Reduction of chromium(VI) with energy recovery using microbial fuel cell technology. *J. Water Process Eng.* **2016**, *11*, 39–45. [[CrossRef](#)]
78. Xu, F.; Ouyang, D.-L.; Rene, E.R.; Ng, H.Y.; Guo, L.-L.; Zhu, Y.-J.; Zhou, L.-L.; Yuan, Q.; Miao, M.-S.; Wang, Q.; et al. Electricity production enhancement in a constructed wetland-microbial fuel cell system for treating saline wastewater. *Bioresour. Technol.* **2019**, *288*, 121462. [[CrossRef](#)]
79. He, C.S.; Mu, Z.X.; Yang, H.Y.; Wang, Y.Z.; Mu, Y.; Yu, H.Q. Electron acceptors for energy generation in microbial fuel cells fed with wastewaters: A mini-review. *Chemosphere* **2015**, *140*, 12–17. [[CrossRef](#)]
80. Zhang, T.; Hu, L.; Zhang, M.; Jiang, M.; Fiedler, H.; Bai, W.; Wang, X.; Zhang, D.; Li, Z. Cr(VI) removal from soils and groundwater using an integrated adsorption and microbial fuel cell (A-MFC) technology. *Environ. Pollut.* **2019**, *252*, 1399–1405. [[CrossRef](#)]
81. Wang, J.S.Q.; Yng, Y. Remediation of Cr(VI) contaminated wetland soil by plant microbial fuel cells and its mechanism. *J. Environ. Sci.* **2019**, *39*, 518–526.
82. Wang, C.; Deng, H.; Zhao, F. The remediation of chromium (VI)-contaminated soils using microbial fuel cells. *Soil Sediment Contam. Int. J.* **2016**, *25*, 1–12. [[CrossRef](#)]
83. Fang, L.; Jin, C.; Chansoo, C. Simultaneous removal and/or recovery of Cr(VI) and Cr(III) using a double mfc technique. *Environ. Eng. Manag. J.* **2019**, *18*, 235–242.
84. Yan, J.; Hu, X.; He, Q.; Qin, H.; Yi, D.; Lv, D.; Cheng, C.; Zhao, Y.; Chen, Y. Simultaneous enhancement of treatment performance and energy recovery using pyrite as anodic filling material in constructed wetland coupled with microbial fuel cells. *Water Res.* **2021**, *201*, 117333. [[CrossRef](#)]
85. Reddy, K.R.; Parupudi, U.S.; Devulapalli, S.N. Effects of soil composition on the removal of chromium by electrokinetics. *J. Hazard. Mater.* **1997**, *55*, 135–138. [[CrossRef](#)]
86. Wang, J.; Song, X.; Wang, Y.; Bai, J.; Bai, H.; Yan, D.; Cao, Y.; Li, Y.; Yu, Z.; Dong, G. Bioelectricity generation, contaminant removal and bacterial community distribution as affected by substrate material size and aquatic macrophyte in constructed wetland-microbial fuel cell. *Bioresour. Technol.* **2017**, *245*, 372–378. [[CrossRef](#)]
87. Li, M.; Zhou, S.; Xu, Y.; Liu, Z.; Ma, F.; Zhi, L.; Zhou, X. Simultaneous Cr(VI) reduction and bioelectricity generation in a dual chamber microbial fuel cell. *Chem. Eng. J.* **2018**, *334*, 1621–1629. [[CrossRef](#)]

88. Li, M.; Zhou, S. Efficacy of Cu(II) as an electron-shuttle mediator for improved bioelectricity generation and Cr(VI) reduction in microbial fuel cells. *Bioresour. Technol.* **2019**, *273*, 122–129. [\[CrossRef\]](#)
89. Razavia, M.; Ebrahimib, Y.K.A. Electrokinetic and Sediment Remediation in Microbial Fuel Cell. *Int. J. Eng.* **2019**, *32*, 489–494.
90. He, R.; Liu, L.; Shi, P.; Nie, C. Environmental decontamination using photocatalytic fuel cells and photoelectrocatalysis-microbial fuel cells. *J. Chem. Technol. Biotechnol.* **2018**, *93*, 3336–3346. [\[CrossRef\]](#)
91. Li, W.W.; Yu, H.Q. Stimulating sediment bioremediation with benthic microbial fuel cells. *Biotechnol. Adv. Int. Rev. J.* **2015**, *33*, 1–12. [\[CrossRef\]](#)
92. Song, N.; Jiang, H.-L. Effects of initial sediment properties on start-up times for sediment microbial fuel cells. *Int. J. Hydrogen Energy* **2018**, *43*, 10082–10093. [\[CrossRef\]](#)
93. Chen, S.; Chen, W.; Wang, X.; Ding, Y.; Zhao, D.; Wang, J. Treating simulated nitrate pollution groundwater with different pH by microbial Fuel Cell. *Pol. J. Environ. Stud.* **2020**, *29*, 4007–4016. [\[CrossRef\]](#)
94. Lin, C.; Chen, J.; Zhao, J.; Liu, S.; Lin, L. Enhancement of power generation with concomitant removal of toluene from artificial groundwater using a mini microbial fuel cell with a packed-composite anode. *J. Hazard. Mater.* **2020**, *387*, 121717. [\[CrossRef\]](#) [\[PubMed\]](#)
95. Hosono, T.; Su, C.-C.; Delinom, R.; Umezawa, Y.; Toyota, T.; Kaneko, S.; Taniguchi, M. Decline in heavy metal contamination in marine sediments in Jakarta Bay, Indonesia due to increasing environmental regulations. *Estuar. Coast. Shelf Sci.* **2011**, *92*, 297–306. [\[CrossRef\]](#)
96. Wang, L.L.X.; Wang, L. Research progress of wetland type biofuel cell CW-MFC. *J. Environ. Eng.* **2018**, *36*, 73–76.
97. Franks, A.E.; Nevin, K.P. Microbial Fuel Cells, A Current Review. *Energies* **2010**, *3*, 899–919. [\[CrossRef\]](#)
98. Oodally, A.; Gulamhussein, M.; Randall, D.G. Investigating the performance of constructed wetland microbial fuel cells using three indigenous South African wetland plants. *J. Water Process Eng.* **2019**, *32*, 100930. [\[CrossRef\]](#)
99. Jiang, H.; Liu, G.; He, S.; Guo, J. Effects of complexes and pH buffer solution in electrokinetic oxidation treatment on sediments chromium removal. *Wuhan Univ. J. Nat. Sci.* **2018**, *23*, 265–269. [\[CrossRef\]](#)
100. Rossi, R.; Jones, D.; Myung, J.; Zikmund, E.; Yang, W.; Gallego, Y.A.; Pant, D.; Evans, P.J.; Page, M.A.; Crokek, D.M.; et al. Evaluating a multi-panel air cathode through electrochemical and biotic tests. *Water Res.* **2019**, *148*, 51–59. [\[CrossRef\]](#)
101. Du, Z.; Li, H.; Gu, T. A state of the art review on microbial fuel cells: A promising technology for wastewater treatment and bioenergy. *Biotechnol. Adv.* **2007**, *25*, 464–482. [\[CrossRef\]](#) [\[PubMed\]](#)
102. Tang, X.; Guo, K.; Li, H.; Du, Z.; Tian, J. Microfiltration membrane performance in two-chamber microbial fuel cells. *Biochem. Eng. J.* **2010**, *52*, 194–198. [\[CrossRef\]](#)
103. Ezziat, L.; Elabed, A.; Ibsouda, S.; El Abed, S. Challenges of microbial fuel cell architecture on heavy metal recovery and removal from wastewater. *Front. Energy Res.* **2019**, *7*, 1. [\[CrossRef\]](#)
104. Xu, J.; Sheng, G.-P.; Luo, H.-W.; Li, W.-W.; Wang, L.-F.; Yu, H.-Q. Fouling of proton exchange membrane (PEM) deteriorates the performance of microbial fuel cell. *Water Res.* **2012**, *46*, 1817–1824. [\[CrossRef\]](#)
105. Slate, A.J.; Whitehead, K.A.; Brownson, D.A.C.; Banks, C.E. Microbial fuel cells: An overview of current technology. *Renew. Sustain. Energy Rev.* **2019**, *101*, 60–81. [\[CrossRef\]](#)
106. Doherty, L.; Zhao, X.; Zhao, Y.; Wang, W. The effects of electrode spacing and flow direction on the performance of microbial fuel cell-constructed wetland. *Ecol. Eng.* **2015**, *79*, 8–14. [\[CrossRef\]](#)
107. Lyu, H.; Zhao, H.; Tang, J.; Gong, Y.; Huang, Y.; Wu, Q.; Gao, B. Immobilization of hexavalent chromium in contaminated soils using biochar supported nanoscale iron sulfide composite. *Chemosphere* **2018**, *194*, 360–369. [\[CrossRef\]](#)
108. Liu, Y.; Li, Y.; Hu, Y.; Mostofa, K.M.G.; Li, S.; Liu, Z. Adsorption characteristics and transport behavior of Cr(VI) in shallow aquifers surrounding a chromium ore processing residue (COPR) dumpsite. *J. Chem.* **2019**, *2019*, 1–10. [\[CrossRef\]](#)
109. Liu, W.; Li, J.; Zheng, J.; Song, Y.; Shi, Z.; Lin, Z.; Chai, L. Different pathways for Cr(III) oxidation: Implications for Cr(VI) reoccurrence in reduced chromite ore processing residue. *Environ. Sci. Technol.* **2020**, *54*, 11971–11979. [\[CrossRef\]](#)
110. He, J.-Z.; Meng, Y.-T.; Zheng, Y.-M.; Zhang, L.-M. Cr(III) oxidation coupled with Mn(II) bacterial oxidation in the environment. *J. Soils Sediments* **2009**, *10*, 767–773. [\[CrossRef\]](#)
111. Zhang, H.; Xu, W.; Wu, Z.; Zhou, M.; Jin, T. Removal of Cr(VI) with cogeneration of electricity by an alkaline fuel cell reactor. *J. Phys. Chem. C* **2013**, *117*, 14479–14484. [\[CrossRef\]](#)
112. Geelhoed, J.S.; Meeussen, J.C.L.; Roe, M.J.; Hillier, S.; Thomas, R.P.; Farmer, J.G.; Paterson, E. Chromium remediation or release? effect of Iron(II) sulfate addition on chromium(VI) leaching from columns of chromite ore processing residue. *Environ. Sci. Technol.* **2003**, *37*, 3206–3213. [\[CrossRef\]](#) [\[PubMed\]](#)
113. Bankole, M.T.; Abdulkareem, A.S.; Mohammed, I.A.; Ochigbo, S.S.; Tijani, J.O.; Abubakre, O.K.; Roos, W.D. Selected heavy metals removal from electroplating wastewater by purified and polyhydroxybutyrate functionalized carbon nanotubes adsorbents. *Sci. Rep.* **2019**, *9*, 4475. [\[CrossRef\]](#) [\[PubMed\]](#)
114. Al-Hamdan, A.Z.; Reddy, K.R. Transient behavior of heavy metals in soils during electrokinetic remediation. *Chemosphere* **2008**, *71*, 860–871. [\[CrossRef\]](#) [\[PubMed\]](#)
115. Habibal, N.; Hu, Y.; Sheng, G.P. Microbial fuel cell driving electrokinetic remediation of toxic metal contaminated soils. *J. Hazard. Mater.* **2016**, *318*, 9–14. [\[CrossRef\]](#)
116. Zhao, R.W.B.; Cai, Q.T.; Li, X.X.; Min, L.I.; Dong, H.; Guo, D.B.; Wang, J. Bioremediation of hexavalent chromium pollution by *Sporosarcina saromensis* M52 isolated from offshore sediments in Xiamen. *Bioremediat. Environ. Sci.* **2016**, *29*, 127–136.

117. Jeyasingh, J.; Philip, L. Bioremediation of chromium contaminated soil: Optimization of operating parameters under laboratory conditions. *J. Hazard. Mater.* **2005**, *118*, 113–120. [[CrossRef](#)]
118. Zeng, F.; Wu, X.; Qiu, B.; Wu, F.; Jiang, L.; Zhang, G. Physiological and proteomic alterations in rice (*Oryza sativa* L.) seedlings under hexavalent chromium stress. *Planta* **2014**, *240*, 291–308. [[CrossRef](#)]
119. Helder, M.; Strik, D.P.; Hamelers, H.V.; Kuijken, R.C.; Buisman, C.J. New plant-growth medium for increased power output of the Plant-Microbial Fuel Cell. *Bioresour. Technol.* **2012**, *104*, 417–423. [[CrossRef](#)]
120. Zhang, J.; Yin, H.; Wang, H.; Xu, L.; Samuel, B.; Chang, J.; Liu, F.; Chen, H. Molecular structure-reactivity correlations of humic acid and humin fractions from a typical black soil for hexavalent chromium reduction. *Sci. Total Environ.* **2019**, *651*, 2975–2984. [[CrossRef](#)]

## Article

# Evaluation of Comfort Models Considering the Peculiarities of Hospitalization: Bedding, Clothing and Reduced Activity of Patients

Silvia Ruggiero <sup>1</sup>, Francesco Tariello <sup>2,\*</sup> and Giuseppe Peter Vanoli <sup>3</sup><sup>1</sup> DING—Department of Engineering, University of Sannio, 82100 Benevento, Italy; sruggiero@unisannio.it<sup>2</sup> Department of Agricultural, Environment and Food Sciences, University of Molise, 86100 Campobasso, Italy<sup>3</sup> Department of Medicine and Health Sciences—Vincenzo Tiberio, University of Molise, 86100 Campobasso, Italy; giuseppe.vanoli@unimol.it

\* Correspondence: francesco.tariello@unimol.it

**Abstract:** The study of thermo-hygrometric comfort in hospitals involves several factors: the presence of different subjects: patients, operators, visitors; different conditions of hospitalization: patients bedridden or out of bed; psychological aspects and therapeutic treatments. In this paper, the analysis focuses on patients in ordinary hospitalization rooms of a hospital located in southern Italy. Different room orientations, several characteristics, and specific factors concerning hospitalized patients' conditions that significantly influence the comfort indices have been considered. In total, 41 scenarios have been defined and analyzed by means of two comfort models: static and adaptive. The study aims to investigate the application of these models to the complex environment of hospitals, finding strengths and weaknesses, which also results in a re-definition of the HVAC system operation. Results show that patient position (in bed or out), clothing type, and level of coverage in the bed can make the same microclimatic condition more suitable for one scenario over another. Furthermore, room exposure has an effect on the comfort of the indoor temperature. The seasonal analyses highlight that during summer, for all scenarios considering bedridden patients, more than 50% of the PMV calculated values are out of the comfort zone. In winter, the indoor conditions are good for bedridden patients with a cover level of 67% during the nighttime (almost 100% PMV values in comfort zone), while during the daytime, they are more suitable for a 48% coverage level if the patient is in bed or if they are walking (lower than 10% dissatisfied).

**Keywords:** patients' thermal comfort; healthcare facilities; PMV index; adaptive approach; nosocomial environmental conditions; clothing thermal resistance

**Citation:** Ruggiero, S.; Tariello, F.; Vanoli, G.P. Evaluation of Comfort Models Considering the Peculiarities of Hospitalization: Bedding, Clothing and Reduced Activity of Patients.

*Buildings* **2022**, *12*, 343. <https://doi.org/10.3390/buildings12030343>

Academic Editors: Roberto Alonso González Lezcano, Francesco Nocera and Rosa Giuseppina Caponetto

Received: 21 January 2022

Accepted: 8 March 2022

Published: 11 March 2022

**Publisher's Note:** MDPI stays neutral with regard to jurisdictional claims in published maps and institutional affiliations.



**Copyright:** © 2022 by the authors. Licensee MDPI, Basel, Switzerland. This article is an open access article distributed under the terms and conditions of the Creative Commons Attribution (CC BY) license (<https://creativecommons.org/licenses/by/4.0/>).

## 1. Introduction

In the last period, in which the World Health Organization (WHO) declared the COVID-19 pandemic, the essential role of hospitals has been accentuated. Comfort within healthcare facilities is essential for successful care both from the point of view of the patients—who receive treatments and benefit from optimal surrounding conditions (microclimate conditions) to increase their effectiveness—and from the point of view of the medical staff that administer the treatments. The PMV (predicted mean vote), after more than 50 years (it was introduced by Fanger in 1970 [1]), is still used in numerous studies concerning comfort in healthcare facilities.

The PMV index consists of a six-parameter model (four objective parameters: air temperature, relative humidity, air speed, and average radiant temperature; and two subjective ones: clothing and degree of activity), which expresses the comfort or discomfort condition on a scale of seven values, from −3 very cold to +3 very hot. Standards commonly adopted in Europe and the United States to assess comfort in buildings, including UNI EN ISO 7730 [2] and ASHRAE 55 [3], are based on PMV.

A recent literature review paper in 2020 [4] identified 62 works consistent with the four research questions concerning thermal comfort in the health sector. Twenty-four of these works are based on the evaluation of the PMV index; even if it was initially introduced for a moderate indoor environment and for people with normal no-compromised health conditions, it was widely applied to the nosocomial theaters. Historically, this index is the most used in studies relating to comfort in environments with different intended uses: schools, offices, industries, etc. Moreover, in the health sector, there are studies concerning different structures, mainly hospitals, but also elderly centers [5,6].

Healthcare facilities are air-conditioned buildings (in some cases only heated) with exclusive requirements connected to medical treatments, indoor air quality, and disease diffusion control, which is aimed to avoid pathogen transport [7]. Thermal comfort in a context with a variety of occupants, staff, visitors, and patients, who have specific needs and sensations on the basis of their problems, is intrinsically difficult to make for everyone simultaneously [8]. Furthermore, in hospitals, attention must be paid to hygiene, bacteria, and virus proliferation [9]. The combination of temperature and humidity affects the diffusion and survival of bacteria and viruses [10]. Their resistance generally depends on micro-climate environmental conditions differently from species to species.

An overview of the most recent papers treating thermo-hygrometric comfort in hospitals is reported here below. Hospitals are among the most complex types of buildings, gathering different functions, operating 24 h a day, 365 days a year, and hosting different wards and room types, e.g., emergency rooms, operating rooms, long- and short-stay rooms, laboratories, clean rooms, isolation rooms. Each of these rooms requires different climatic conditions because the comfort needs of the patients who occupy them are different. The study of comfort sometimes follows a broader approach by connecting, for example, to energy retrofittings [11,12]—hospitals are energy-intensive structures—or in some cases, comfort is linked to Indoor Air Quality or, more generally, to Indoor Environmental Quality [13–15]. In a paper by Wu et al. [16], thermo-hygrometric comfort was also correlated with acoustic comfort. The study analyzed data obtained from 18 Chinese hospitals in the Northern cold region. It was observed that the temperatures recorded in the rooms were on average higher than those established in the project, while the relative humidity was lower. Of the 220 patients (110 male and 110 female) interviewed, 87% said that the environment was comfortable or very comfortable. Between the three analyzed factors, temperature appeared to be the factor with the most influence on comfort; meanwhile, the acoustic aspects were less relevant, and the variation in relative humidity was insignificant. Patients demonstrated comfort sensations for temperatures between 26 °C and 28 °C and a relative humidity of 40%. With higher temperature levels, patients accepted noisier environments but were more susceptible to sounds.

In the work of Aloitabi and Lo [17], 522 patients agreed to participate in the research carried out in two hospitals of Saudi Arabia: a state-of-the-art private hospital and a public, specialist one. In the first structure, patients with specific pathologies of the cardiology and oncology wards were considered; in the second, the patients had different pathologies and were hospitalized in the surgery and medical wards. The thermal sensation vote (TSV) expressed by patients was between  $-1$  and  $+1$  in 72% and 67% of the answers, respectively, in the two hospitals indicated above; about 70% of patients said they were in a comfortable condition. The analysis of relative humidity showed that in almost all cases, it was less than 60% and, on average, less than 40% in all 18 rooms considered; it also did not seem to be related to temperature. The analysis of the data collected leads to the conclusion that patients perceive warmer conditions during their hospitalization period and that this perception is not attributable to the change in temperature at a certain time of day, nor to the change in relative humidity.

The air-conditioning of hospitals is complicated due to conflicting needs. From the data collected in situ and reported in [17], it can be observed that: in the surgery ward, the trend of the temperatures chosen in the different rooms were approximately the same, and the most recurrent values were between 22.2 °C and 23.9 °C; in the medical ward,

the temperature trend showed two more frequent values; in the oncology rooms, the desired temperatures were, on average, higher than in the other wards; for cardiology, the most recurrent values were less than 22 °C. From this situation, the Authors of the research derived that it is not possible to uniquely define a comfort zone for temperatures that vary too much, and it is necessary to modify the conventional model of the PMV. However, the same Authors say that the PMV index has, in some cases, proved to be adequate for a nosocomial setting [18], while in some others, it has not, as it overestimates or underestimates thermal sensations [19–22].

Alotaibi et al. [19] considered opinions about the thermo-hygrometric conditions of 120 patients of the surgical and medical wards of the International Medical Centre in Jeddah, Saudi Arabia. Data collected during the summer were compared with the PMV of field measurements (carried out from 11:00 to 16:00) when no doctors or visitors stayed with patients. The mean value for the PMV was about  $-0.5$ , whereas the mean TSV was  $0.32$ , highlighting a significant discrepancy between the two distributions. The Fanger's model underestimates the real patients' sensations due to the light clothes used and the reduced metabolic rate. The temperatures for which the PMV and TSV are equal to zero can be extrapolated from the analyses and are equal to about 25.5 °C and 22.5 °C, respectively. Furthermore, Azizpour et al. [20] confirmed that patients in large-scale hospitals in hot-humid areas would prefer cooler environmental temperatures with respect to the neutral temperature.

In [21], the applicability of the PMV model in the hospital setting and the suitability of the standard conditions for the tropical conditions of Bangkok were verified. The analyses were carried out by collecting experimental data in two hospitals involving a total of 928 occupants (451 patients, 331 visitors, and 146 staff members). The medical staff expressed a sensation of cold while, on the basis of the PMV (which is equal to 1), the indoor environment was slightly warm. On the other hand, the most common vote among visitors and patients was zero. The temperature ranges that determine less than 20% dissatisfied are: 21.8 °C–27.9 °C for patients, 22 °C–27.1 °C for visitors, and 24.1 °C–25.6 °C for medical staff; however, according to the Thai standard, the comfort range should be 20 °C–25 °C. By considering the obtained results, it emerges that the PMV model is not suitable for hospitals, especially far-from-neutrality temperatures, or for the staff. Patients accept a wider range of conditions due to their diseases and low expectations.

From the data collected in eight hospital wards located in a central region of Italy, del Ferraro et al. [22] compared the PMV and the judgments of 30 patients and 19 medical staff operators. Furthermore, the Authors studied the effect of age and gender on thermal sensation and verified that the PMV index is able to take these effects into account through parametric and non-parametric tests. The TSV distribution of patients was concentrated around zero, whereas that of staff was shifted towards warm. The distribution of patients' answers was tight, even if age differences were considered. The PMV index was not a good predictor of patients' sensation regarding the indoor climate; it is better for medical staff and more adequately represents male responses than females'. Furthermore, the best correlation appeared with the data of staff under 65 years.

Angelova and Velichkova [23] highlighted, throughout their assessment of PMV-PPD (predicted percentage of dissatisfied) indices, the different comfort sensations of doctors and patients in an operating room. They compared alternative clothes and climatic conditions and observed that a condition does not exist that can simultaneously satisfy all of the main occupants of the operating theatre. The lowest percentage dissatisfied (48% of patients and 44% of doctors) took place at 28 °C and a relative humidity of 30%, but this condition causes thermal stress for surgeons.

To overcome the lack of a regulatory framework relating to comfort and air quality in building environments on Madagascar Island, an experimental and subjective study was presented in [24]. Five large hospitals, naturally ventilated, were analyzed. A total of 400 people were involved in the surveys and interviews during both the rainy and dry seasons. The approach followed in this study was based on both PMV and adaptive

comfort, taking into account the influence of gender, clothing, activities, mind state, and control strategies of the occupants. By comparing the responses of males and females regarding thermal satisfaction, thermal preference, and thermal comfort, no obvious results were observed in both types of buildings considered. From the statistical analysis, it could be seen that at 26.41 °C, an equal number of people would like a warmer and colder environment; for this reason, it was assumed to be the preferred temperature. According to the adaptive approach, when the outdoor temperature varies between 20.3 °C and 29.5 °C, the corresponding indoor comfort temperature is in the range of 23.4 °C–26.8 °C, and a good linear interpolation of the data appears. The neutral operating temperature varies between males and females, with the former being 24.2 °C, and the latter, 23.65 °C. In hospitals, there is a percentage of dissatisfaction lower than 10% in the temperature range 22.4 °C–25.3 °C, but 99% of hospitalized patients find the indoor microclimate comfortable.

The work of Derks et al. [25] complained of a limited number of studies concerning nurses' comfort and was developed to reduce this gap. The data were collected in two wards of a hospital in The Netherlands during the summer and autumn period of 2016 to verify the perception of the microclimate during the working hours and the impact it has on the performance of the caretakers. The thermo-hygrometric conditions currently maintained in the wards are slightly unacceptable by the nurses and, in part, affect their performance; therefore, it is assumed that there is a need to maintain different climatic conditions in the different areas of the hospitals. The results show that the correlation between temperature and the TSV or thermal acceptance vote is linear even if the link with TSV is less marked; this means that as the temperature increases, the nurses tend to express that the sensation is unacceptably warm. With respect to work performance, most of the answers revealed obstructive conditions to adequately carrying out the required tasks.

Khalid et al. [26] evaluated the existing comfort conditions and preferences of patients and visitors in Malaysian hospitals. In particular, the responses of 305 patients and 84 visitors were collected in 3 hospitals in Kuala Lumpur (wards of medicine, surgery, maternity, and pediatrics). The data collected showed that 65% of patients and 55% of visitors fell within the range (−1, +1). Over half of the visitors and patients voted in the negative part of the scale, and their mean votes were −1.1 and −0.9, respectively. The judgment relative to humidity was very often (in more than 60% of cases) in the neutrality interval and was symmetrically distributed around zero. Air movement was acceptable for 86% of the occupants if the operating temperature remained between 22 °C and 28 °C. From the analysis of the data, it was further observed that the parameter that most affects thermal preference, overall comfort, and judgment of air quality of the patients is their state of health. State of health was more influential than age, gender, or hospitalization days.

The thermal responses of the body (temperature regulation, vasoconstriction, and vasodilatation), metabolic rate, and clothing can be significantly altered in hospitalized people with respect to healthy ones due to: the pharmacological treatments they are subject to, the diseases they have, the expectation about the surgical operation they are going to receive, and the place where they spend most of the day (patients lay in bed). In [27], the PMV model has been adapted and improved to take into account peculiarities of the inpatients' stay in the healthcare facilities. Modified equations for the metabolism and the clothing thermal resistance have been introduced in the standard model. Experimental data validation confirmed an excellent correspondence between numerical results and in-bed patient responses during the winter period (5% difference). By solving the modified model, typical comfort charts (operative–wet bulb temperature) have also been elaborated on for general hospitals wards.

A dilemma emerging from thermal comfort studies in health facilities is that the use of common thermal comfort indices, conventionally applied in other buildings, is not always suitable to represent and understand patients' behaviors and needs that are conditioned by the disease level, the state of health, medical aspects, therapeutic treatments, and further potential factors [17].

However, PMV is the index most often used for the assessment of comfort in the hospital setting, and it can provide an appropriate representation of patients' comfort status if suitably modified. In most papers, only temperature and humidity are measured (PMV depends on four objective variables), and often, PMV is applied over its validation range. Therefore, the aim of this paper is to evaluate whether thermo-hygrometric conditions conventionally maintained in patients' rooms of a hospital in southern Italy can be considered adequate by applying the standard comfort model of PMV, taking into account the modified thermal insulation of clothes, bed staying, and a reduced metabolic rate. A multitude of combinations is evaluated, considering different patient positions (in bed and out of bed), different types of clothing, and alternative solutions for bedding. The thermal resistance considered is calculated as the sum of clothing and bed resistance. For both terms, different configurations (different percentages of cover, alternative types of beddings, and clothes) are considered. For the metabolic rate, three possible levels are established (sleeping patients, laying/sitting patients, standing/walking patients).

These evaluations are carried out over four standard days, one per season, and simulated data is also statistically treated for the four entire seasons, considering patients without acute medical conditions. Furthermore, the adaptive model of ASHRAE Standard 55 is also assessed.

## 2. Case Study

The building chosen for this study was the "Ferdinando Veneziale" Hospital. It is located in the city of Isernia, an Italian backcountry, characterized by 1866 Heating Degrees-Day (baseline 20 °C). According to the Köppen climate classification, Isernia has a hot-summer Mediterranean climate (Csa).

The hospital was built between 1976 and 1986, but over the years, it has undergone several renovations, expansions, and maintenance works. The building, with a gross volume of about 88,000 m<sup>3</sup>, has an articulated geometry, arranged on 2 underground and 6 aboveground floors. The main facade is along the east-west direction (Figure 1).

An in-depth energy audit of the building in question was presented in a previous study [28]. In situ surveys, interviews, and measurements were used for characterizing the envelope-HVAC system.

The opaque building envelope is composed of two main types of walls: one made by masonry and one by prefabricated concrete panels. The thickness of both walls is 0.50 m overall, with an average thermal transmittance of 1.58 W/m<sup>2</sup>K. The horizontal elements of the basement floor are made of concrete beams, joists, and hollow bricks without insulating layers; the roof has the same structure, but with the presence of a light insulating layer. The U-value is ≈ 1.80 W/m<sup>2</sup>K and ≈ 0.70 W/m<sup>2</sup>K for the basement floor and roof, respectively. The transparent envelope has an incidence on the wall of about 16%. It is made of a single clear glass and metallic frame with an overall window thermal transmittance ( $U_W$ ) of 4.15 W/m<sup>2</sup>K.

The composition of the HVAC system includes heating systems with radiators in hospital wards, all-air systems for all surgery blocks and rooms, and a mixed air/water HVAC system, given by the combination of radiators and air handling units in corridors, ambulatories, and offices. The heating system is composed of two centralized boilers, also used for providing DHW, with a total thermal capacity of 7000 kW and nominal efficiency of 96%. Moreover, 11 air handling units are installed. For the cooling service, there are autonomous split systems installed in a few rooms and two water-cooled chillers (cooling capacity of 1860 kW each). The heating period goes from 1 November to 15 April with a continuous operating schedule (24 h) at the set-point temperature of 20 °C. The cooling period was assumed to be between 1 May to 30 September (10 h every day) at the set-point temperature of 26 °C. This is the real heating/cooling schedule used in the building, obtained by consulting the technical/maintenance office. Finally, as a lighting system, fluorescent lamps were used.



Further information regarding other dimensions and geometrical peculiarities, as well as the HVAC system and its real operation, are shown in Table 1.

**Table 1.** Main characteristics of the whole building.

Main Building's Dimensions and Geometry					
Total building area: 27,342.80 m <sup>2</sup>			Gross roof area: 8200.97 m <sup>2</sup>		
Maximum height: 18.87 m			Total volume: 88,100.38 m <sup>3</sup>		
Net conditioned building area: 24,474.15 m <sup>2</sup>			Conditioned volume: 78,821.25 m <sup>3</sup>		
Building envelope					
External wall U = 1.58 W/m <sup>2</sup> K		Basement floor U = 1.80 W/m <sup>2</sup> K		Window U = 4.15 W/m <sup>2</sup> K	
Internal wall U = 1.81 W/m <sup>2</sup> K		Roof U = 0.70 W/m <sup>2</sup> K		Solar factor: 0.86	
Heat transfer area of external walls, roof, and fenestration of the examined building					
	Total	North	East	South	West
Gross wall area [m <sup>2</sup> ]	10,673.43	3282.67	1971.24	3460.47	1959.05
Window opening area [m <sup>2</sup> ]	1529.61	486.56	305.77	459.50	277.78
Above ground window-wall ratio [%]	16.02	17.80	16.94	13.93	16.22
HVAC system and operation					
Heating service	2 boilers		Total thermal capacity: 7000 kW		Nominal efficiency of 96%
DHW service	4 thermal storages				Total capacity: 5000 L
Cooling service	2 water-cooled chillers				Total cooling capacity: 3720 kW.
Ventilation service	11 air handling units (not equipped with heat recovery systems) with liquid water humidifiers				
Operation	Heating period	1 November–15 April	24 h	Set-point temperature: 20 °C	
	Cooling period	1 May–30 September	10 h (9:00–19:00)	Set-point temperature: 26 °C	



**Figure 1.** “Ferdinando Veneziale” Hospital main entrance.

These data were the starting point in the creation of the numerical model of the hospital in the EnergyPlus engine (developed by U.S. Department of Energy’s (DOE) Building Technologies Office (BTO), Washington, DC, USA) [29] by means of its graphical interface DesignBuilder (developed by DesignBuilder Software Ltd., Gloucester, UK) [30]. In this paper, the transient heat transfer through the building was solved by using Conduction Transfer Function algorithms (CTF), while the time steps for the running of the simulations “Number of time-steps per hour” was set equal to 6.

The developed numerical model (Figure 2a) was calibrated by comparing the simulation outputs to the measured energy data (referring to the nine available years). Figure 2b shows the monthly comparison between the real gas consumption and the results of the dynamic energy simulation, as well as the calculated errors (EER<sub>month</sub>). Moreover, the values of other calibration indexes are also shown, such as the error in the annual energy consumption (EER<sub>average,year</sub>), the mean bias error (MBE), and the coefficient of variation of the root mean squared error CV(RMSE<sub>month</sub>). It can be seen that all data were within the threshold range defined by the most accredited and tightened guideline: the Measurement

and Verification [31]. Electricity was done with the same evaluation, with an  $ERR_{\text{average,year}}$  equal to 7.0%. Therefore, the numerical model developed could be considered as calibrated. It should be stressed that a calibrated model that faithfully describes the energy requests of the real building also simulates its thermal behavior and, therefore, the real indoor microclimate; as was shown by Bellia et al. [32] in a case study located in the same climate zone, and using the same software, as the present one. Calibrating the numerical model according to natural gas consumption and electricity demand, the hourly air temperature profile is comparable with the measured one, with the hourly error always  $<30\%$  (limit value for hourly data according to [31]). On the basis of this observation, it can be concluded that the model is suitable for patient comfort investigation.

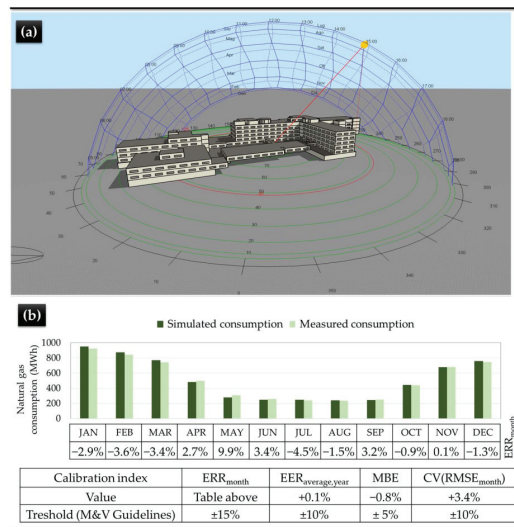


**Figure 2.** Numerical model developed (a); comparison between monthly real consumptions and energy simulation results (b).

### 3. Methodological Approach

#### 3.1. Analyzed Thermal Zones

The hospital ward under investigation was the surgery, located on the second floor of the building. The ward offers services both in ordinary hospitalization and in day-surgery and outpatient. For ordinary hospitalization, there are a total of 11 rooms. The analyzed zone has a very regular geometry oriented along the east-west direction, as shown in Figure 3a. The two chosen rooms, called “Room A” and “Room B”, are on opposite exposures and are separated by an internal corridor (Figure 3b). In detail, the two rooms have the same intended use (ordinary hospitalization), similar geometric characteristics, and approximately  $33 \text{ m}^2$  of floor area (including bathrooms). Similar radiator positions and ventilation duct distributions are also present, as depicted in Figure 3c. The rooms each have a single external vertical wall, with the same percentage of window area. The thermo-physical characteristics of the opaque building envelope are detailed in Table 2, where  $t$  is the thickness,  $\lambda$  is the thermal conductivity,  $\rho$  is the density,  $c_p$  is the specific heat,  $R$  is the thermal resistance, and  $U$  is the thermal conductance. The only difference between the two rooms is the orientation of the external walls: Room A has the facade facing south, while Room B is facing north.

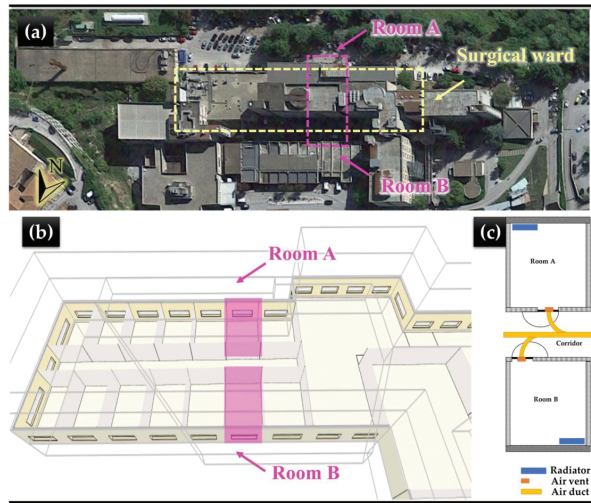


**Figure 3.** View from top of the hospital (a); view of analyzed rooms (b); HVAC units/ventilation ducts distribution in the rooms (c).

**Table 2.** Thermo-physical characteristics of opaque building envelope.

	$t$ (m)	$\lambda$ (W/mK)	$\rho$ (kg/m <sup>3</sup> )	$c_p$ (kJ/kgK)	$R$ (m <sup>2</sup> K/W)	Total $t$ (m)	$U$ (W/m <sup>2</sup> K)
External wall							
Cement plaster	0.01	0.72	1760	840		0.50	1.58
Brick reinforced	0.48	1.10	1920	840			
Gypsum plastering	0.01	0.80	1300	840			
Internal wall							
Gypsum plastering	0.01	0.80	1300	840		0.10	1.81
Hollow brick		0.30	800	1000			
Gypsum plastering	0.01	0.80	1300	840			
Internal floor slab							
Flooring	0.02	1.0	1200	1000		0.34	1.80
Concrete screed	0.05	1.06	2000	1000			
Concrete slab	0.05	1.6	2300	1000			
Brick and concrete block	0.22				0.218		
Lime and gypsum plaster	0.02	0.7	1400	1000			

### 3.2. Patients' Clothing and Activities

In order to define the thermal resistance of the clothing, different combinations of clothing have been hypothesized, as compatible as possible to staying in the ward. As shown by the literary review above, the metabolic rate and clothing resistance for hospitalized people could be altered by temperature regulation, vasoconstriction, and vasodilatation. Taking these aspects into account, suitable data were used. In detail, in the cases of bedridden patients, for greater accuracy of the evaluations, the resistance of the whole bed-patient system was considered, as defined by Lin and Deng [33]. The calculation of this thermal resistance included:

- Conventional mattress;
- Cover mattress;
- Cotton sheets;
- Polyester quilt.

Different body coverage rates in bed have been taken into account, as defined by [19], and shown in Figure 4. In addition, long or short pajamas with or without dressing gowns were also considered. Thus, all scenarios defined are reported in Table 3.

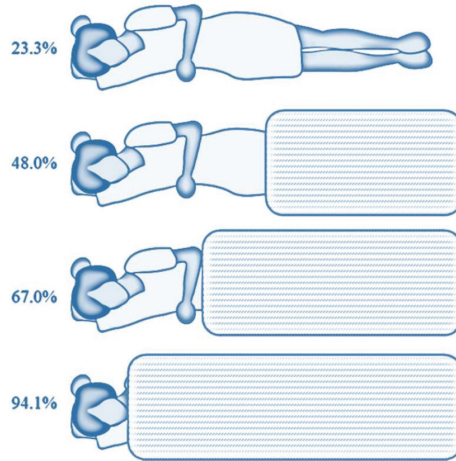


Figure 4. Coverage rates for patients in bed.

Table 3. Clothing and activity scenarios for patients.

Scenario	Activity	Clothing	Coverage	Clothing Insulation $I_{cl}$ (clo)	Metabolic Rate $M$ (met)
1	bedridden/asleep	underwear + long pajamas	94.1% with quilt	4.56	0.7
2	bedridden/asleep	underwear + long pajamas	67.0% with quilt	2.88	0.7
3	bedridden/asleep	underwear + long pajamas	48.0% with quilt	2.15	0.7
4	bedridden/asleep	underwear + long pajamas	23.3% with quilt	1.57	0.7
5	bedridden/asleep	underwear + short pajamas	94.0% with quilt	4.34	0.7
6	bedridden/asleep	underwear + short pajamas	67.0% with quilt	2.62	0.7
7	bedridden/asleep	underwear + short pajamas	48.0% with quilt	1.65	0.7
8	bedridden/asleep	underwear + short pajamas	23.3% with quilt	1.38	0.7
9	bedridden/asleep	underwear + long pajamas	94.1% with bed sheet	2.56	0.7
10	bedridden/asleep	underwear + long pajamas	67.0% with bed sheet	2.18	0.7
11	bedridden/asleep	underwear + long pajamas	48.0% with bed sheet	1.82	0.7
12	bedridden/asleep	underwear + long pajamas	23.3% with bed sheet	1.57	0.7
13	bedridden/asleep	underwear + short pajamas	94.1% with bed sheet	2.40	0.7
14	bedridden/asleep	underwear + short pajamas	67.0% with bed sheet	1.80	0.7
15	bedridden/asleep	underwear + short pajamas	48.0% with bed sheet	1.43	0.7
16	bedridden/asleep	underwear + short pajamas	23.3% with bed sheet	1.38	0.7
17	bedridden/awake	underwear + long pajamas	94.1% with quilt	4.56	0.8
18	bedridden/awake	underwear + long pajamas	67.0% with quilt	2.88	0.8
19	bedridden/awake	underwear + long pajamas	48.0% with quilt	2.15	0.8
20	bedridden/awake	underwear + long pajamas	23.3% with quilt	1.57	0.8
21	bedridden/awake	underwear + short pajamas	94.1% with quilt	4.34	0.8
22	bedridden/awake	underwear + short pajamas	67.0% with quilt	2.62	0.8
23	bedridden/awake	underwear + short pajamas	48.0% with quilt	1.65	0.8
24	bedridden/awake	underwear + short pajamas	23.3% with quilt	1.38	0.8
25	bedridden/awake	underwear + long pajamas	94.1% with bed sheet	2.56	0.8
26	bedridden/awake	underwear + long pajamas	67.0% with bed sheet	2.18	0.8

Table 3. Cont.

Scenario	Activity	Clothing	Coverage	Clothing Insulation $I_{cl}$ (clo)	Metabolic Rate $M$ (met)
27	bedridden/awake	underwear + long pajamas	48.0% with bed sheet	1.82	0.8
28	bedridden/awake	underwear + long pajamas	23.3% with bed sheet	1.57	0.8
29	bedridden/awake	underwear + short pajamas	94.1% with bed sheet	2.40	0.8
30	bedridden/awake	underwear + short pajamas	67.0% with bed sheet	1.80	0.8
31	bedridden/awake	underwear + short pajamas	48.0% with bed sheet	1.43	0.8
32	bedridden/awake	underwear + short pajamas	23.3% with bed sheet	1.38	0.8
33	bedridden/awake	underwear + long pajamas + dressing gown	-	1.07	0.8
34	bedridden/awake	underwear+ short pajamas+ dressing gown	-	0.92	0.8
35	sitting/awake	underwear+ short pajamas	-	0.46	1.0
36	sitting/awake	underwear+ long pajamas+ dressing gown	-	1.07	1.0
37	sitting/awake	underwear+ short pajamas+ dressing gown	-	0.92	1.0
38	standing/awake	underwear + long pajamas	-	0.92	1.2
39	standing/awake	underwear + short pajamas	-	0.46	1.2
40	standing/awake	underwear+ long pajamas+ dressing gown	-	1.07	1.2
41	standing/awake	underwear+ short pajamas + dressing gown	-	0.92	1.2

The parametric analyses developed with respect to patients' clothing, bedding types, and percentage of body coverage can help in considering the variation of bed-patient system thermal resistance that is usually not a static parameter.

### 3.3. Comfort Indices Calculation

For the evaluation of the static comfort, namely for the calculation of the PMV and PPD, the prescriptions of the ISO 7730 standard [2] were followed. The hourly values of dry-bulb air temperature,  $T_a$  ( $^{\circ}\text{C}$ ), average radiant temperature,  $T_r$  ( $^{\circ}\text{C}$ ), air relative humidity,  $R.H.$  (%), were carried out from the simulations over one year. These values, combined with clothing insulation  $I_{cl}$  ( $\text{m}^2\text{ }^{\circ}\text{C}/\text{W}$ ) and metabolic rate  $M$  ( $\text{W}/\text{m}^2$ ) (Table 3), were defined as follows.

- $T_{cl}$ : surface temperature of the dressed body ( $^{\circ}\text{C}$ ):

$$T_{cl} = 35.7 - 0.0028(M - W) - I_{cl}\{3.96 \times 10^{-8}[(T_{cl} + 273)^4 - (T_r + 273)^4] + f_{cl}h_c(T_{cl} - T_a)\} \quad (1)$$

- $h_c$ : convective heat transfer coefficient ( $\text{W}/\text{m}^2\text{ }^{\circ}\text{C}$ ):

$$\begin{cases} h_c = 2.38|T_{cl} - T_a|^{0.25} & \text{if } 2.38|T_{cl} - T_a|^{0.25} > 12.1\sqrt{v_{ar}} \\ h_c = 12.1\sqrt{v_{ar}} & \text{if } 2.38|T_{cl} - T_a|^{0.25} < 12.1\sqrt{v_{ar}} \end{cases} \quad (2)$$

- $f_{cl}$ : clothing area coefficient (-):

$$\begin{cases} f_{cl} = 1.00 + 1.29I_{cl} & \text{if } I_{cl} \leq 0.078 \text{ m}^2\text{ }^{\circ}\text{C}/\text{W} \\ f_{cl} = 1.05 + 0.645I_{cl} & \text{if } I_{cl} \geq 0.078 \text{ m}^2\text{ }^{\circ}\text{C}/\text{W} \end{cases} \quad (3)$$

- $v_{ar}$ : relative air speed (m/s):

$$v_{ar} = v_a + 0.005(M - 58.15) \quad (4)$$

- $p_a$ : partial pressure of the air vapor (Pa):

$$p_a = 10 R.H. e^{\frac{(16.6536 - 4030.183)}{(T_a + 235)}} \quad (5)$$

where  $W$  is the external work ( $\text{W}/\text{m}^2$ ) that is assumed equal to zero for the activities considered.

Once these quantities are known, it is possible to calculate the *PMV* (-) and the *PDD* (%) through Equations (6) and (7).

$$PMV = (0.303e^{-0.036M} + 0.028) \times \{(M - W) - 3.05 \times 10^{-3}[5733 - 6.99(M - W) - p_a] - 0.42[(M - W) - 58.15] - 1.7 \times 10^{-5}M(5867 - p_a) - 0.0014M(34 - T_a) - 3.96 \times 10^{-8}f_{cl}[(T_{cl} + 273)^4 - (T_r + 273)^4] - f_{cl}h_c(T_{cl} - T_a)\} \quad (6)$$

$$PDD = 100 - 95e^{-(0.03353PMV^4 - 0.2179PMV^2)} \quad (7)$$

Similarly, for the assessment of adaptive comfort, the prescriptions of the ASHRAE-55 standard [3] were followed. In particular, the hourly value of the operative temperature  $T_o$  (°C) for the rooms under examination, over the whole observation period, was determined from the simulations. In order to define the lower ( $T_{low\ limit}$ ) and upper ( $T_{up\ limit}$ ) limit values (°C) of the aforesaid temperature, Equations (8) and (9) were used. This is because the hospital could be considered a fully mechanically-controlled (FMC) building, so the equations proposed by the standard for correlating the outdoor air temperature and indoor limit values were not suitable. The proper model, developed for “HVAC buildings”, was used, as shown in [34]. These temperature limits define the area where <10% of people were dissatisfied with the microclimate.

$$T_{up\ limit} = 0.11T_{pma} + 23.95 \quad (8)$$

$$T_{low\ limit} = 0.11T_{pma} + 18.95 \quad (9)$$

where  $T_{pma}$  is the average value of the outdoor air temperature of the 30 days preceding the one in question.

### 3.4. Analyzed Periods and Boundary Conditions

The simulations were carried out by using the hourly climate file of Isernia.

The weather file showed a minimum outdoor dry-bulb temperature of  $-5.9$  °C (on 12 January) and a maximum of  $35.3$  °C (on 19 August). The average monthly outdoor air temperature is shown in Figure 5a. The average temperature was above  $18.0$  °C during the hottest months (June–September) and ranged from  $5$  °C to  $15$  °C in the colder months. The relative humidity was greater than 70% for 75% of the hours over the year, with an average annual value of 80%. The prevalent direction of the wind was south-north, and the maximum wind speed was greater than 8.0 m/s and occurred in March.

In order to analyze the results, the season periods were organized as follows: summer period from 15 June to 15 September; spring from 16 April to 14 June; autumn period from 16 September to 31 October; and winter from 1 November to 15 April. Among them, four days were chosen as a reference for their season, since they appeared to be representative of the period:

- 10 February, reference in winter;
- 15 May, reference in spring;
- 15 July, reference in summer;
- 10 October, reference day of autumn period.

These reference days were chosen after analyzing all available days, taking into consideration the days with outdoor parameter trends similar to the median trend of the season. Moreover, the chosen references are similar to those used in another paper [35]; furthermore, the approach for showing results is similar to that carried out in an analogous climate study.

The hourly trend of the main climatic parameters for the aforementioned days are depicted in Figure 5b (outdoor dry-bulb temperature), Figure 5c (relative humidity), and Figure 5d (global solar radiation on horizontal plane).

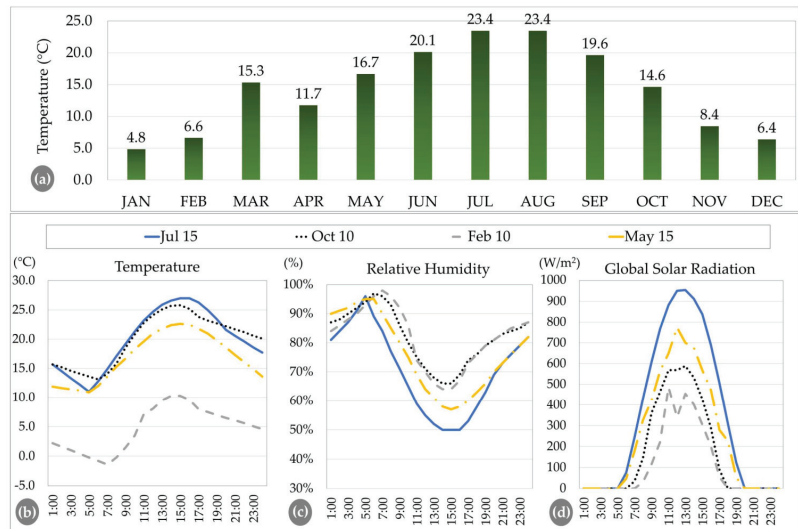


**Figure 5.** Average monthly outdoor air temperature (a); average hourly outdoor air temperature (b); relative humidity (c); and global solar radiation on horizontal surface (d).

Considering the methodological approach applied to the case study, the results could be representative of most southern Italian hospitals built in the late seventies since the climate boundary conditions and the HVAC-envelope system are similar. For instance, the hospital in Naples [12] is characterized by similar stratigraphy and thermal transmittance values (e.g., the external walls are made of hollow bricks and air gaps with an overall thermal transmittance of  $1.3 \text{ W/m}^2\text{K}$ ) with various HVAC typology systems for different served areas, as in the case study of the present paper. Similar characteristics in terms of the whole building could be found in other hospitals constructed in the same period in Europe [36]. However, it should be stressed that there are very few datasets available for the climatic zone regarding the hospitals building typology, as declared by Carnieletto et al. in a recent paper of 2021 [37]. On the other hand, the limitation on the results regards first, the type of patients; indeed, they are bedridden partially healthy patients in the surgery department, but it does not refer to very sensitive or fragile patients with special requirements like handicapped, sick, very young children, or elderly persons. Moreover, the thermal comfort was evaluated by means of two different accredited models [2,3] without considering the localized discomfort.

#### 4. Results

In this section, the results obtained from the application of the comfort model, traditional or adaptive, are proposed for the rooms under investigation.

##### 4.1. Daily Analysis

The scenarios shown in Table 3 differ by level of activity (or metabolic rate); therefore, they are not suitable for all hours of the day. For example, scenarios with a patient out of bed are unlikely during night hours. A further difference among the scenarios concerns the type of clothing adopted by the patient; this shows that not all scenarios are appropriate for all four days (or season) analyzed, i.e., a patient out of bed with only short pajamas in the winter period is implausible. Table 4 shows which periods of the day and which representative days the various scenarios were considered. By way of example, Scenario 1 considered the typical winter and autumn day during night hours, from 7:00 pm to 6:00 am; meanwhile, Scenarios 2 to 8 evaluated only the autumn period during nighttime. Again, on the basis of the data reported in Table 4, Scenario 39 is representative of a condition that

is good in the summer and autumn periods (and so in corresponding representative days) during the daytime.

**Table 4.** Summary of daily calculation scenarios.

Day	Day		Night	
	Scenario	Time Slot	Scenario	Time Slot
15 May	25–32	7:00–18:00	9–16	19:00–6:00
	36–38; 40–41	9:00–20:00		
15 July	25–32	7:00–18:00	9–16	19:00–6:00
	35–41	9:00–20:00		
10 October	17–24	7:00–18:00	1–8	19:00–6:00
	35–41	9:00–20:00		
10 February	17–20	7:00–18:00	1	19:00–6:00
	36; 40	9:00–20:00		

For the Fanger model, the hourly values of PMV are shown for all configurations and both rooms by means of radar charts and histograms. For a better understanding, we always highlight the comfort zone (green areas). For the adaptive model, the hourly trend of operative temperature is depicted, for both rooms, always highlighting the limit values (red lines).

#### 4.1.1. Spring Day (15 May)

First of all, the conditions of the bedridden patient, asleep or awake, were analyzed for all hours of the day. Figure 6 reports the case of a patient with long or short pajamas and with different coverage rates. On the radial axis, the PMV is shown; on the circular axis, the hours are shown. The latter refers to ante meridiem (AM) or post meridiem (PM), depending on the label. The comfort zone,  $-0.5 < \text{PMV} < 0.5$ , is depicted in green. The scenario considered for a given hour of the day refers to Table 4. For instance, considering the label “AM–coverage 23.3%” for the long pajamas case refers from 12:00 to 6:00 a.m. in Scenario 12 (bedridden/asleep) and from 7:00 to 11:00 a.m. in Scenario 28 (bedridden/awake). Analyzing the long pajamas case, only the 94.1% coverage from 12:00 to 6:00 p.m. showed a  $\text{PMV} > +0.5$ . On the other hand, in the same hours, all coverage percentages  $\leq 67.0\%$  resulted in a  $\text{PMV} \leq -0.5$ . From 7:00 to 11:00 p.m., only the 23.3% coverage showed a PMV ranging from  $-0.6$  to  $-0.9$ . The short pajamas case highlights more scenarios below the lower comfort limit, while only the 94.1% bed sheet coverage rate from 12:00 to 6:00 p.m. achieved a PMV greater than the upper limit ( $+0.5$ ). In general, the PMV values passing from room B (north-facing) to A (south-facing) increased  $\sim +0.1$ .

In Figure 7, the PMV histograms are shown together with operative temperature ( $T_o$ ) and relative humidity (RH) trends for the day and nighttime. During the nighttime, the mean values of micro-climate parameters were:

- For room B,  $T_o \approx 22.0$  °C and  $\text{RH} \approx 62\%$ ;
- For room A,  $T_o \approx 22.4$  °C and  $\text{RH} \approx 61\%$ .

Until 23:00,  $T_o$  was constant, around 23 °C, and then decreased by  $\sim 1$  °C, and remained constant until 6:00. After the decrease of  $T_o$ , the cold sensation increased for both long (9–12) and short pajama (13–16) scenarios. For the PMV, the further away from the comfort zone, the lower the coverage levels were. In order to stay in the comfort zone all night long, the short or long pajamas had to be combined with the maximum coverage percentage of the bedsheet. The aforementioned reduction of  $T_o$  determined that the long pajama with 67.0% coverage was not suitable.



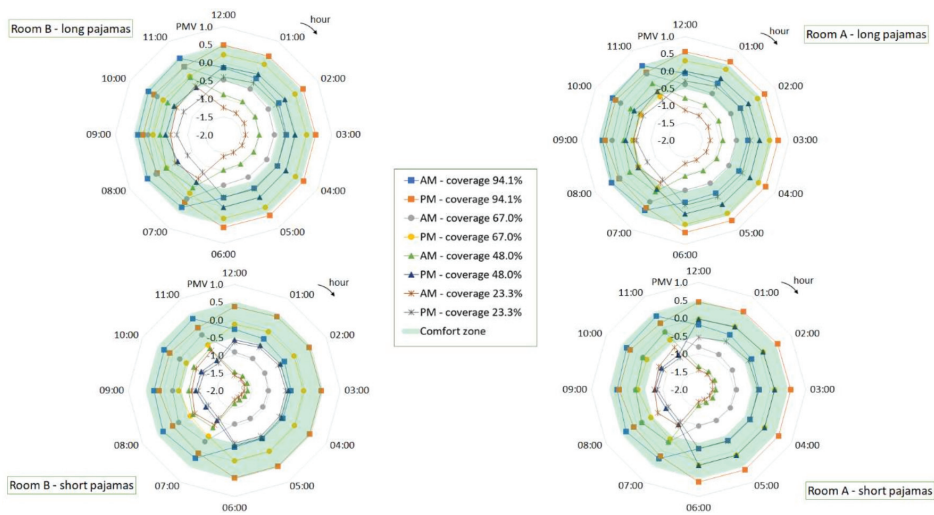


**Figure 6.** Hourly PMV of bedridden patients: different coverage rates and clothing on the spring day.

Regarding the daytime charts, the mean  $T_o$  was 23.0 °C in room A and 22.6 °C in room B, with an almost constant trend. The mean RH was 61% and 62% for room A and room B, respectively. During the day, the conditions were more favorable with respect to the nighttime, both for the long pajamas scenarios (25–28) and the short pajamas scenarios (29–32). Considering the long pajamas scenarios in room B, the thermo-hygrometric conditions were not acceptable for a coverage of 94.1% (scenario 25) when the  $T_o$  was  $\geq 23.0$  °C, from 14:00 to 18:00; and when the coverage was 23.3% with a  $T_o < 22$  °C, at 7:00. In the short pajamas scenarios, in room B, when  $T_o$  was  $< 23.0$  °C (from 7:00 to 15:00) and there was a lower coverage percentage of bedsheet, the PMV was  $< -0.5$ . In room A, the cool feeling discomfort (from 7:00 to 12:00 in scenarios 31 and 32) and the warm feeling discomfort (from 12:00 to 18:00 in scenarios 25 and 29) were more pronounced with respect to room B.

Finally, the results for the out-of-bed patient during the daytime are shown in Figure 8. In both rooms A and B, the only discomfort condition (“slightly cool”) was given by Scenario 37, in which the patient was sitting and wearing short pajamas in combination with a dressing gown.

For the same typical spring day, an analysis of the adaptive model was conducted. With the hourly data of the weather file used for the simulations, the daily outdoor air temperatures were calculated, and the  $T_{pma}$  was equal to 12.3 °C. Figure 9 shows the results. The upper and lower limits were 25.3 °C and 20.3 °C, respectively. It can be noted that the inner  $T_o$  during 24 h was always between the upper and lower limit both for room A and B.  $T_o$  varied in the range 21.4–23.7 °C for room A and 21.1–23.3 °C for room B. Contrary to the static comfort model, in this case for all hours of the day, the patient was in comfort conditions, but the adaptive model did not consider the patient’s hospitalization conditions in any way.

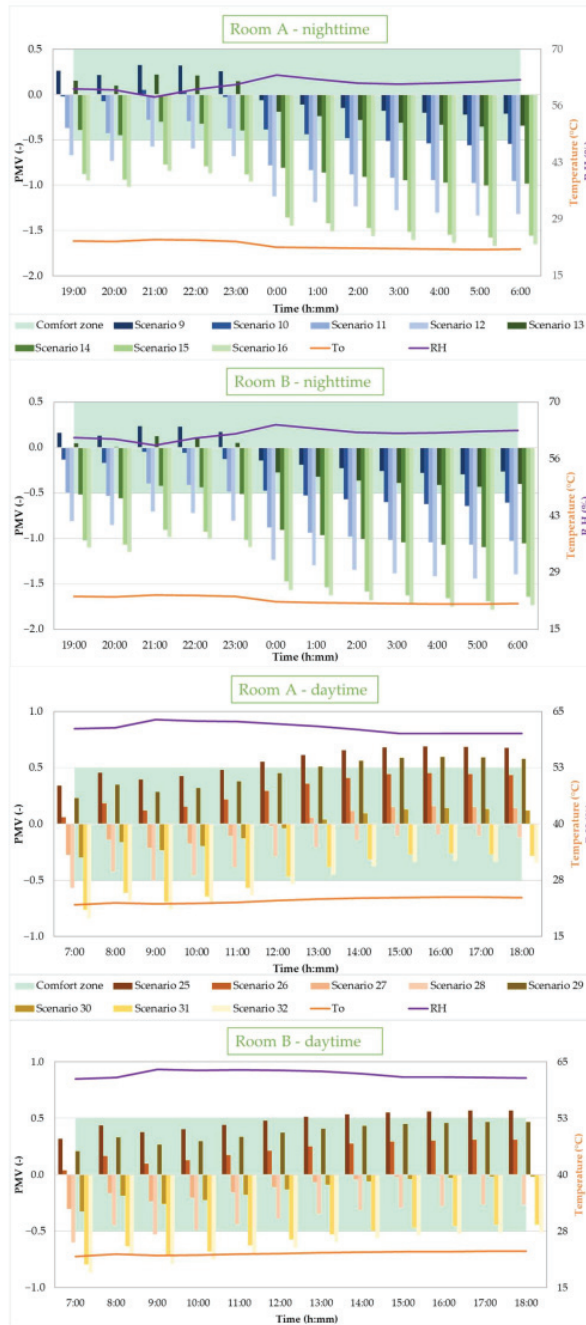


Figure 7. Hourly operative temperature, relative humidity, and PMV in rooms A and B with a bedridden patient: different scenarios in the spring day.

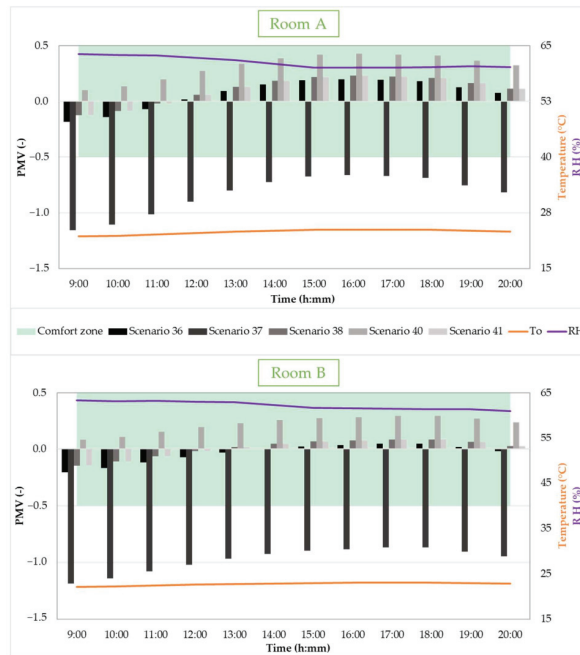


Figure 8. Hourly operative temperature, relative humidity, and PMV in rooms A and B with an out-of-bed patient: different scenarios in the spring day.

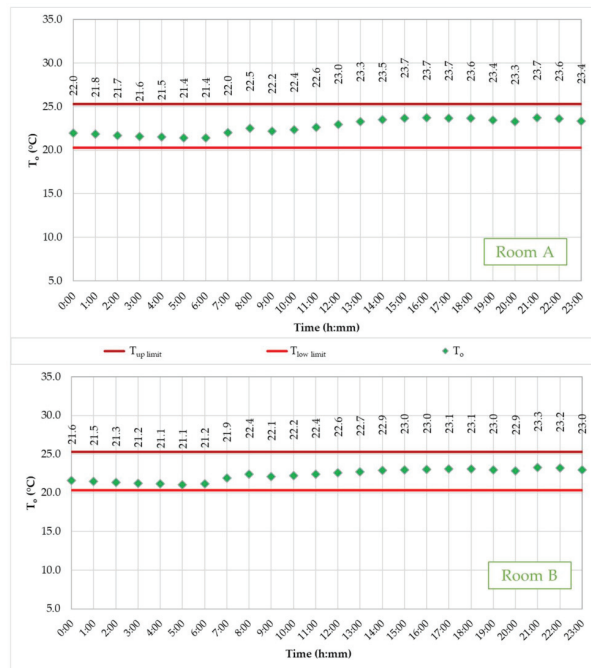
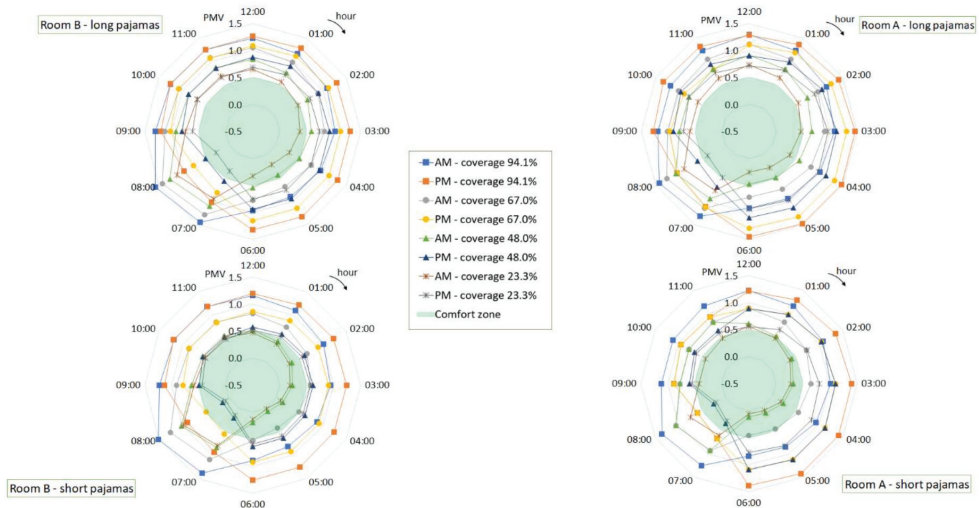


Figure 9. Hourly operative temperature for the spring day.

#### 4.1.2. Summer Day (15 July)

The reference summer day in Figure 10 shows the hourly PMV of the bedridden patient, asleep or awake, for the scenarios with long and short pajamas. For almost all scenarios with long pajamas (in room A or B), there was a PMV greater than +0.5: the discomfort was expressed as “slightly warm” or “warm” environment, according to the Fanger scale. Only in the few hours with 23.3% of coverage was there a PMV lower than 0.5, from 2:00 a.m. to 6:00 a.m. and from 7:00 p.m. to 8:00 p.m. Regarding the patient with short pajamas, the comfortable condition was reached only with the 23.3% or 48.0% coverage during the night hours.



**Figure 10.** Hourly PMV of bedridden patient: different coverage rate and clothing in the summer day.

In more detail, in Figure 11, it can be seen that during the night,  $T_o$ , starting from 26.4 °C in room B and 26.8 °C in room A, underwent a slight increase (about +1.0 °C) after 20:00, when the air conditioning system was switched off, and then decreased again after midnight. The mean value of  $T_o$  was 27.0 °C in room B and 27.2 °C in room A. Furthermore, RH had a tendency to decrease over the observation period, passing from 61–62% to 52–53%. The increase in  $T_o$  resulted in a corresponding increase in the PMV. In the scenarios with coverage percentages of 94.1% and 67.0% for both long and short pajama cases (Scenario 9–10 and 13–14), the PMV was higher than +0.5. Similarly, the scenarios with a lower coverage rate, when paired with long pajamas (Scenario 11 and 12), showed a PPD greater than 10%. Meanwhile, combinations with a low percentage of coverage in the case of short pajamas (Scenario 15 and 16) were within the comfort zone, for all night hours in room B and for the periods 19:00–20:00 and 1:00–6:00 in room A. Considering the midnight time, passing from room A (warmer) to B (colder), the PMV values decreased (nearing thermal neutrality) approximately:

- –5% in Scenario 9 and –5% in Scenario 13;
- –6% in Scenario 10 and –9% in Scenario 14;
- –8% in Scenario 11 and –15% in Scenario 15;
- –12% in Scenario 12 and –16% in Scenario 16.

The most marked percentage variations occurred in the cases with low coverage rates. This trend could also be seen in the other night hours. The patient with low coverage percentage found comfort conditions easier when the microclimate parameters changed in summer.

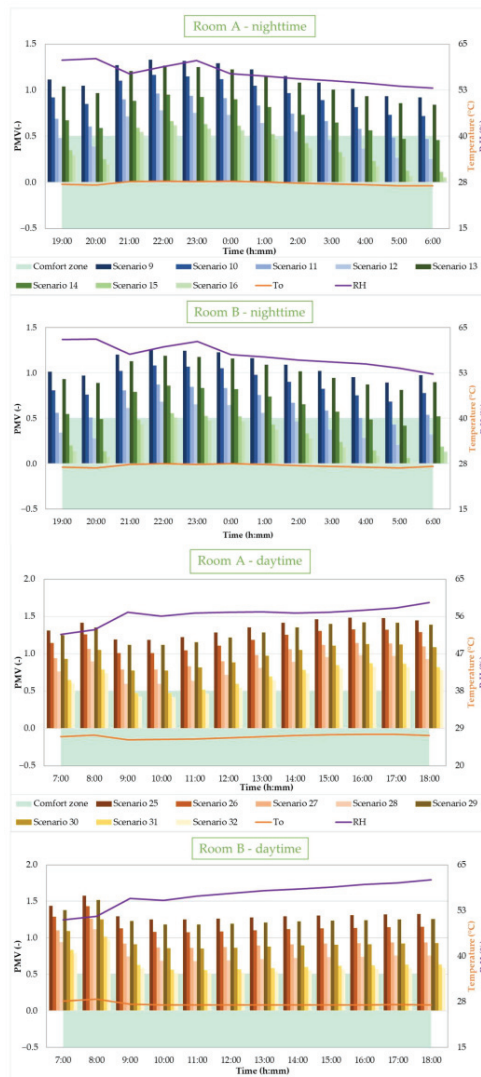


**Figure 11.** Hourly operative temperature, relative humidity, and PMV in rooms A and B with a bedridden patient: different scenarios in the summer day.

Regarding the daytime long pajama cases (Scenarios 25–28), despite the fact that after 8:00 in the morning, the HVAC systems are on, with  $T_o \approx 26.5$  °C and  $T_a \approx 25.1$  °C, the sensation was always between “slightly warm” to “warm”, in both rooms. This highlights the inadequacy of the long pajamas for indoor microclimatic conditions in summer. The situation was improved in the case of short pajamas (scenarios 29–32), but the PMV was greater than +0.5 for each level of coverage. The increase of RH during the morning (from 52% to 59% in room A and from 51% to 61% in room B) did not play a positive role with respect to these judgments.

In cases where the patient was out of bed (Figure 12), the application of the Fanger model suggested that positive judgments regarding the microclimate occurred where the person wore only short pajamas, both in standing and sitting situations (Scenarios 35, 37, and 39). Moreover, in this case, the PMV values in room A were greater than the ones in

room B starting from midday: the difference was most marked when the body was more uncovered. For instance, at 15:00, the percentage difference between the PMV in rooms A and B were:

- −14% in Scenario 40;
- −17% in Scenarios 36, 38, and 41;
- −44% in Scenario 37;
- −51% in Scenario 39;
- −94% in Scenario 35.

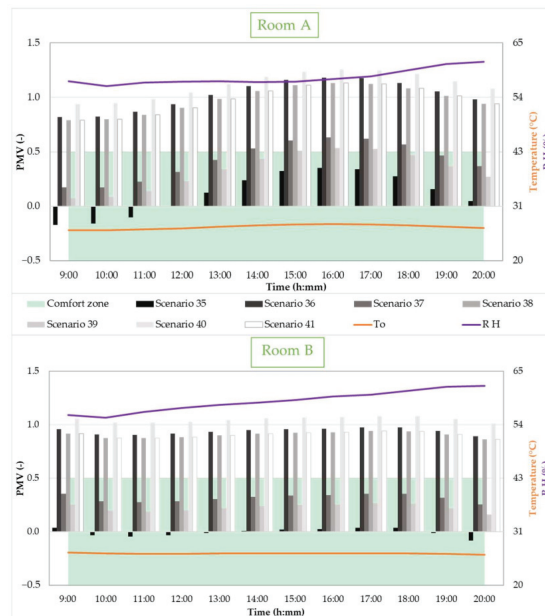


**Figure 12.** Hourly operative temperature, relative humidity, and PMV in rooms A and B with an out-of-bed patient: different scenarios in the summer day.

Analyzing the application of the adaptive comfort model on 15 July (Figure 13) confirmed that the  $T_o$  is equal or greater than the upper limit for most hours of the day in both rooms A and B. This demonstrates that the situation of discomfort persisted. For the day taken into account,  $T_{low\ limit} = 21.4\ ^\circ\text{C}$  and  $T_{up\ limit} = 26.4\ ^\circ\text{C}$ . Despite room B reaching a peak of  $T_o$  ( $28.2\ ^\circ\text{C}$ ) at 8:00, the sum of the hourly differences between indoor  $T_o$  and its upper limit, for the whole day, was  $13.6\ ^\circ\text{C}$  and  $18.5\ ^\circ\text{C}$  in room B and room A, respectively. This shows that the room in which there are greater discomfort conditions is the one facing south (room A).

#### 4.1.3. Autumn Day (10 October)

Applying the Fanger model for the typical autumn day, the obtained results are shown in Figures 14–16.

In Figure 14, showing a bedridden patient, the coverage level of 94.1% was in combination with long pajamas only. It is evident that, in both rooms, with both the short and long pajamas, there was a situation of discomfort tending to “hot”. In room B, with a long pajama, the “neutral” condition could be reached with 23.3% in the morning hours; with a short pajama, the “neutral” condition could be reached with 23.3% and 48.0%, during the same hours. On the other hand, in room A, comfort conditions were hardly ever reached, both with long and short pajamas, for any coverage rate.



Figure 13. Hourly operative temperature for the summer day.

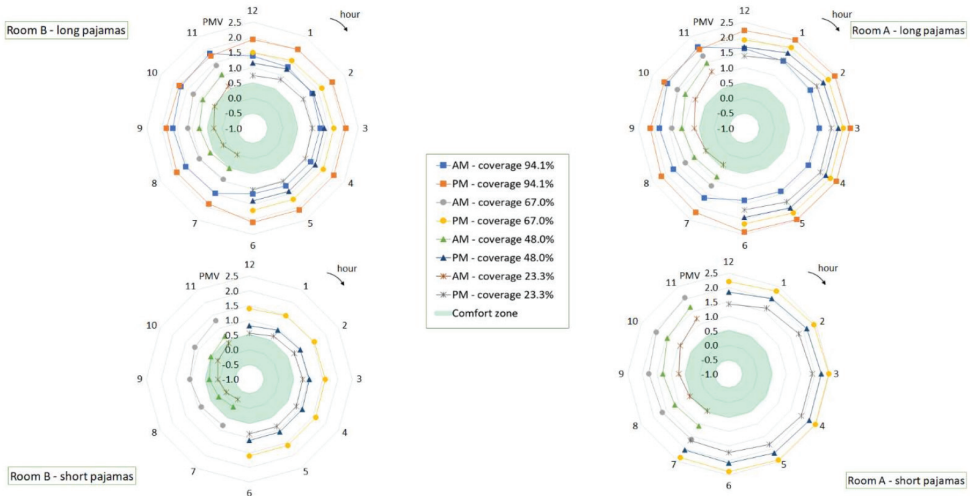
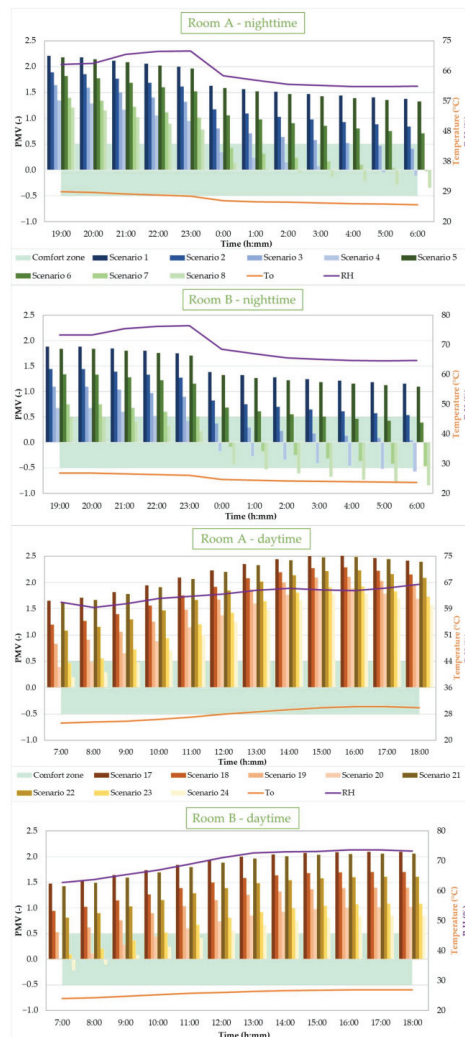


Figure 14. Hourly PMV of bedridden patient: different coverage rate and clothing in the autumn day.

Considering the trend of  $T_o$  and RH in Figure 15, it can be seen that during the night, in the early hours (19:00–23:00),  $T_o$  was around 27.0 °C in room B and 29.0 °C in room A, with an RH ranging 75–77% in room B and 68–72% in room A. This implies that any combination of clothing and cover in the early hours of the night is highly unacceptable, resulting in a perception going from “slightly warm” to “warm”, especially in south exposed rooms (room A). After 23:00, there was a progressive decrease in RH and  $T_o$ ; therefore, the PMV decreased, but the thermal discomfort sensation persisted if the level of coverage was 67.0%

or more, in room A, and 94.1% in room B, with short or long pajamas. At the same time, the situation of maximum uncovering with short pajamas (Scenario 8 in room B) became critical in the opposite direction: “slightly cool” sensation. Scenarios 7 and 8, over the 12-hour nighttime of the autumn day, showed a great variation of thermal sensation, from “slightly warm” to “slightly cool”.

Analyzing the daytime results for the bedridden patient (Figure 15), the RH ranged 63–73% and 60–67%, in room B and A, respectively, while the  $T_o$  varied between 24 °C and 27 °C in room B and between 25 °C and 30 °C in room A. In this time period, only in the early hours with minimum coverage rates (Scenarios 20 and 23) was there a situation of comfort, both with long and short pajamas. In all other cases, there was always a PMV greater than +0.5 and, therefore, a “slightly warm” to “warm” sensation. This trend was linked to the fact that the  $T_o$  and RH progressively increased during the day.



**Figure 15.** Hourly operative temperature, relative humidity, and PMV in rooms A and B with a bedridden patient: different scenarios in the autumn day.



In the case describing the patient out of bed in room A, for all scenarios and most hours, PMV values were  $> +0.5$  (Figure 16); only the combination involving short pajamas (Scenarios 35, 37, and 29) until 10:00 were within the comfortable range. In room B, the PMV values were reduced by 1–1.5 compared to room A. Over the day, Scenario 35 (sitting patient with short pajama) showed a PMV going from  $-0.6$  to  $+0.3$ .

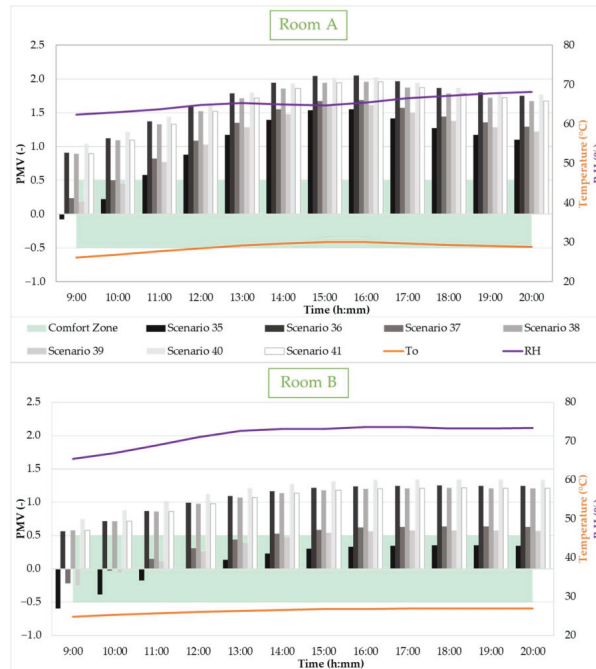


**Figure 16.** Hourly operative temperature, relative humidity, and PMV in rooms A and B with an out-of-bed patient: different scenarios in the autumn day.

Regarding the adaptive model (Figure 17) for the autumn day, the  $T_{low\ limit}$  was equal to  $20.9\text{ }^{\circ}\text{C}$ , and  $T_{up\ limit}$  was equal to  $25.9\text{ }^{\circ}\text{C}$ . The mean value of  $T_o$  over the whole day was  $25.5\text{ }^{\circ}\text{C}$  in room B and  $27.6\text{ }^{\circ}\text{C}$  in room A. Until midday in both rooms, the conditions were inside or on the upper limit. In the other hours of the day,  $T_o$  values were greater than the limit value. This behavior was more marked in room A. In room B, for 12 h, the  $T_o$  was greater than  $T_{up\ limit}$ , with a sum of differences of  $8.7\text{ }^{\circ}\text{C}$ . In room A, there were 18 h in which  $T_o$  was greater than  $T_{up\ limit}$ , with a sum of differences of  $42.7\text{ }^{\circ}\text{C}$ .

The results show a strong difference in thermos-hygro-metric conditions between the two analyzed rooms.

#### 4.1.4. Winter Day (10 February)

For the reference winter day, the results of the application of the Fanger model are shown in Figures 18–20.

In order to evaluate the PMV in the nighttime slot, only the scenarios with long pajamas were taken into account since, in this period, it is rather unlikely to wear short pajamas. In Figure 18, it can be seen that the 94.1% coverage rate fell within the satisfaction range from 7:00 to 11:00 pm. For the daytime slot, on the other hand, the 94.1% coverage rate determined a feeling closely to “slightly warm” in both rooms, while 67.0% was the optimal percentage of coverage in both rooms, in addition to 48.0% in room A.



Figure 17. Hourly operative temperature for the autumn day.

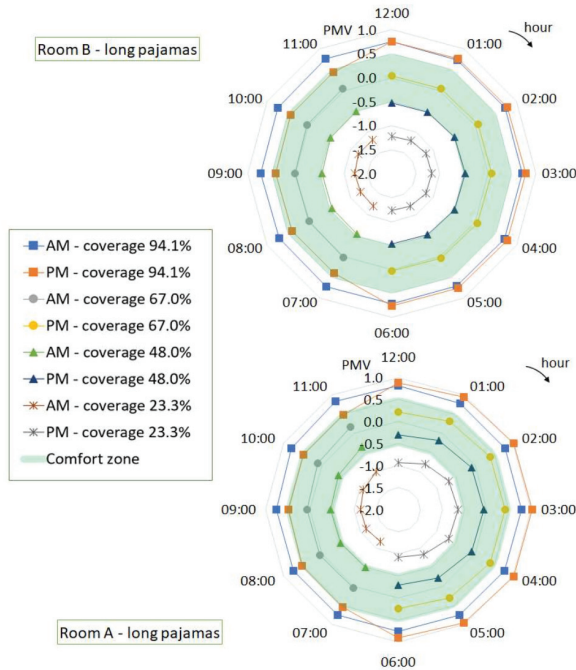


Figure 18. Hourly PMV of bedridden patient: different coverage rate in the winter day.

In more detail, by analyzing Figure 19, it can be seen that during the night, with a constant  $T_o$  around 20 °C and 21 °C in room B and room A, respectively, and an RH decreasing from 45% to 35% approximately, a neutral thermal sensation was guaranteed. Indeed, in room A, the PMV values were from +0.5 to +0.4, while in room B, they were +0.4 on average.

During the daytime, the  $T_o$  was constant at the same night values, with a small increase around 14:00 (+1 °C) in room A, while the RH from the 35% nighttime value progressively increased up to approximately 45%. In both rooms, the most critical conditions, “slightly warm” and “slightly cool”, were achieved by using the maximum and minimum coverage rate (Scenario 17 and Scenario 20, respectively) when the patient was in bed. Meanwhile, 48% and 67% coverage rates turned out to be optimal for the thermo-hygrometric comfort of the bedridden patient in the daytime.

Regarding the out-of-bed conditions (Figure 20), Scenarios 36 (sitting) and 40 (standing) demonstrated that the indoor microclimate could be evaluated as “slightly cool” all day long by the seated patient in room B.

In this case, the adaptive model could not be applied since the  $T_{pma}$  was lower than 10.3 °C; therefore, it was outside the range of applicability.

#### 4.2. Seasonal Results

Following the line defined to show the previous daily results, in these subsections, the results are presented on a seasonal basis. Regarding the assessment of the PMV, all calculated hourly values for the whole season period and for each type of scenario were taken into account. Table 5 summarizes the scenarios used and the relative periods. Since there are a large number of data, for a better presentation, statistical box-plot graphs were developed for the statistic parameters, always highlighting the comfort zone in green. For the adaptive analysis, the operative temperature with different colors in different seasons is plotted, always fixing the limits values as red lines.

**Table 5.** Summary of seasonal calculation scenarios.

Season	Reference Period	Scenario	
		Night (19:00–6:00)	Day (7:00–18:00)
Spring	16 April–14 June	9–16	25–32; 36–38; 40–41
Summer	15 June–15 September	9–16	25–32; 36–41
Autumn	16 September–31 October	1–8	17–24; 35–41
Winter	1 November–15 April	1–4	17–20; 36; 40

In order to better manage and represent the high number of data, the results of the PMV are shown with a statistical approach by means of “box and whiskers plots”. In this representation, the “x” identifies the mean value of the distribution; the line inside the box, the median; the lower limit of the box, the first quartile ( $Q_1$ ); and the upper limit, the third quartile ( $Q_3$ ). Finally, the two whiskers are equal to the minimum and the maximum values of the distribution, excluding any outliers.

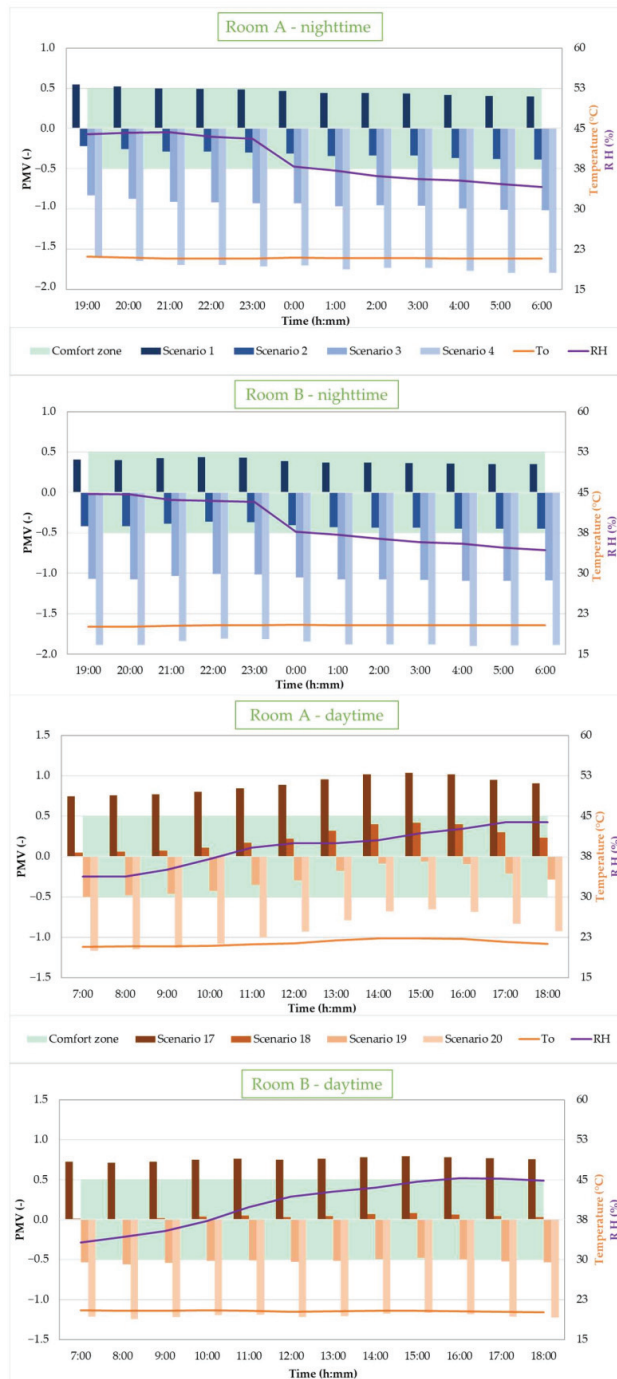


**Figure 19.** Hourly operative temperature, relative humidity, and PMV in rooms A and B with a bedridden patient: different scenarios in the winter day.

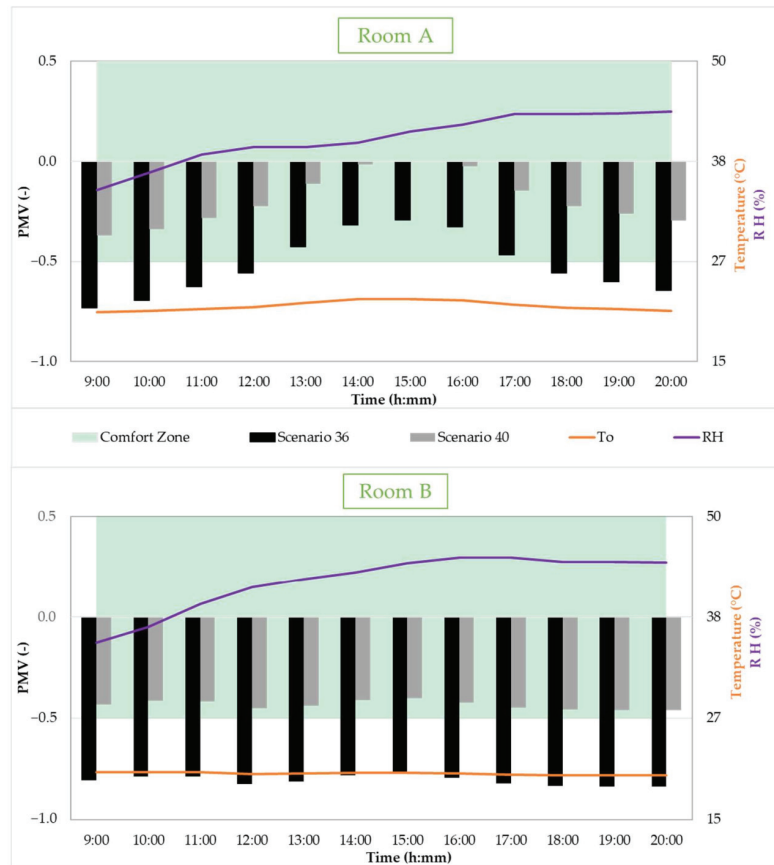


**Figure 20.** Hourly operative temperature, relative humidity, and PMV in rooms A and B with an out-of-bed patient: different scenarios in the winter day.

#### 4.2.1. Spring (16 April–14 June)

Figure 21 depicts the box and whiskers graphs for rooms A and B for all scenarios analyzed. In particular, Scenarios 9–16 refer to night hours (19:00–6:00) with a bedridden patient, while Scenarios 25–32; 36–38; 40–41 refer to daily hours (7:00–18:00) with the patient bedridden or out of bed. The statistic parameters depicted in Figure 21 were evaluated on the basis of the hourly values assumed by the independent variables during the entire spring period and taking into account the limits in the use of the scenarios during each day, as reported above.

In the case of scenarios with long pajamas during the nighttime (Scenarios 9–12), the values of the mean PMV for the coverage rate (94.1% to 67.0%) were inside the comfort range ( $\pm 0.5$ ), in room B. Meanwhile, for room A, this was true for 48.0% of the coverage rate. The interquartile range (IQR) increased with the decrease of coverage rate:

- 0.9 in room B and 0.7 in room A for Scenario 9;
- 0.9 in room B and 0.9 in room A for Scenario 10;
- 1.0 in room B and 1.0 in room A for Scenario 11;
- 1.7 in room B and 1.4 in room A for Scenario 12.

This means that when the clothing thermal resistance is lower, the PMV distribution is wider. The same trend could also be seen for the other scenarios in the same figure. Among the analyzed scenarios (9–12), for the north-facing room (room B), the scenario for which

50% of observations were inside the comfort range was Scenario 9, while in the south-facing one (room A), it was Scenario 10.

In the scenarios describing bedridden patients with short pajamas during the nighttime in both rooms (Scenarios 13–16), Scenario 13 had the best distribution with a null mean equal to the median. Scenarios 15 and 16 were characterized by 50% of the PMV values lower than  $-0.5$ .

In the daytime, the distributions had an IQR lower than the ones during the nighttime. For bedridden patients, null values of the mean and median, with 50% of data inside the comfort range, were achieved by long pajamas with 48.0% of bedsheets (Scenario 27) or short pajamas with a 67.0% rate (Scenario 30), both in rooms A and B.

For the scenarios out of bed, the comfort was achieved with heavy clothing: long pajamas in Scenarios 36 and 38 and short pajamas with a dressing gown in Scenario 41.

In general, for scenarios with bedridden patients, high levels of coverage (94.1% and 67.0%) showed a reduced PMV variation in mean, median,  $Q_1$ , and  $Q_3$  of  $\sim 0.1$ , passing from room B to room A. This value was  $\sim 0.2$  for the configuration with low coverage levels of 48.0% and 23.3%. The IQR had similar values for the same scenario in the two rooms.

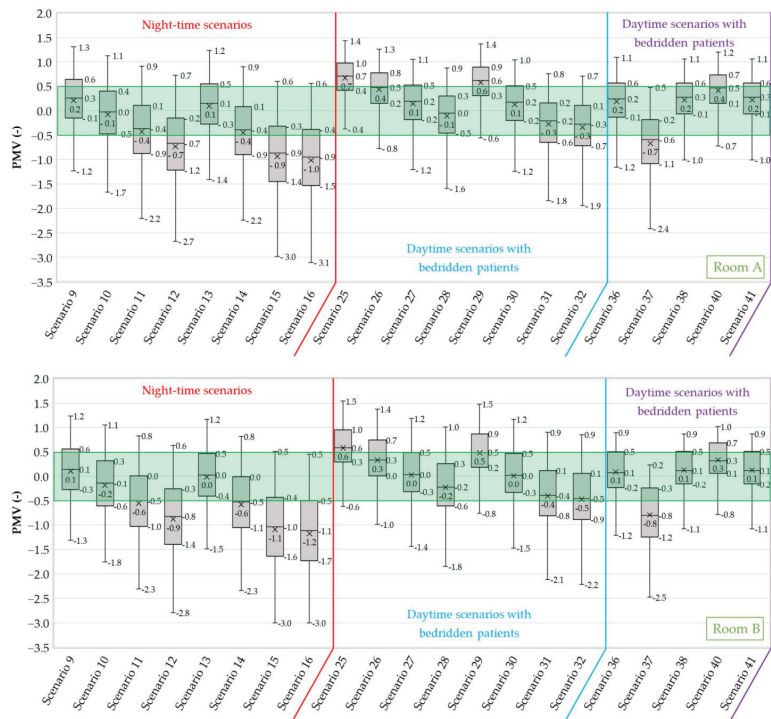


**Figure 21.** PMV distributions of the different scenarios in spring period.

In Figure 22, the results of the adaptive comfort model are shown.  $T_{pma}$  is the average outdoor temperature calculated with the mean daily temperatures of the 30 days preceding the one in question. The points are the  $T_o$  values for each hour, referring to different seasons. For instance, in spring, the results are shown by green points ( $T_o$  spring). It can be seen that for most of the observed hours, the  $T_o$  values during the spring period were within the limit imposed by the legislation. Only in some cases were the values outside the minimum and maximum range: their percentages are reported in Table 6. The comparison between the conditions in rooms B and A showed double the points above the  $T_{up}$  limit and half of the points below the limit  $T_{low}$  limit in the south exposed room (room A) with respect to the

north exposed room (room B). Data concerning the summer period ( $T_{O \text{ summer}}$ ) followed a wavy pattern; this trend is the result of the combination of the outdoor conditions, the building thermal response, and HVAC operation.

#### 4.2.2. Summer (15 June–15 September)

In the summer period, the mean value of  $T_o$  over the whole period was  $26.3 \text{ }^\circ\text{C}$ , and the RH was 65%. They were within the limits suggested by ISO 7730:  $T_o \approx 24.5 \text{ }^\circ\text{C} \pm 1.5 \text{ }^\circ\text{C}$  and RH 30–70%.



**Figure 22.** Adaptive model in spring, summer, and autumn periods.

**Table 6.** Percentage of data out of adaptive model bounds.

Season	Observation over $T_{up \text{ limit}}$		Observation under $T_{low \text{ limit}}$	
	Room B	Room A	Room B	Room A
Spring	6.6%	13.8%	11.5%	6.5%
Summer	80.2%	87.1%	-	-
Autumn	7.8%	25.7%	6.2%	0.6%

In Figure 23, the box and whiskers graph for the summer period is reported. In regard to the nighttime scenarios (9–16), the distributions were nearly symmetrical for both rooms, and the median decreased with the decrease of bedsheets percentage of coverage. Moreover, the IQR was almost the same in room B as in room A. It is noted that more than 50% of all scenarios were greater than  $PMV = +0.5$ . Only the conditions of short pajamas and minimum percentage of bedsheets coverage showed a mean and median inside the comfort range for room B and slightly higher than  $+0.5$  for room A.

Considering the daytime, for each scenario with a bedridden patient (scenarios 25–32), more than 50% of the data described an uncomfortable thermal sensation, between “slightly warm” to “warm”. Furthermore, in this case, the median values of PMV decreased with the decrease of bedsheets coverage. In the case of the patient sitting or standing up, in room

B, only Scenario 39 had 50% of the data inside the comfort zone. The same scenario in room A showed a  $Q_1$  inside the comfort zone.

Unlike nighttime conditions, all daytime scenarios (25–32 and 36–41) in room A had wider distributions than in room B. They had almost the same minimum and  $Q_1$  values, but higher maximum and  $Q_3$  values, and a difference of about 0.3 between the two rooms. During the daytime in summer, the contribution of solar radiation to the inner microclimatic conditions was strongly felt in the southern exposure room.

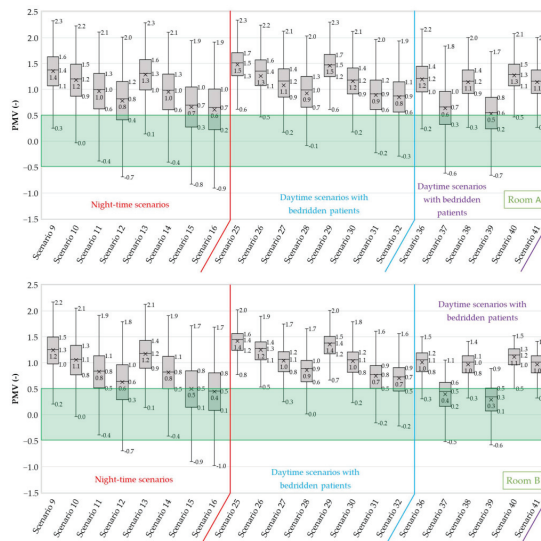


**Figure 23.** PMV distributions of the different scenarios in summer period.

Figure 22 is in accordance with the results of the PMV, as most of the  $T_{o, \text{summer}}$  values fell over the  $T_{\text{up}}$  limit. Specifically, this situation occurred in more than 80% of the hours for both rooms (Table 6).

#### 4.2.3. Autumn (16 September–31 October)

The box and whiskers graphs for the autumn season are shown in Figure 24. During the night hours (scenarios 1–8), there were no comfortable conditions both for long or short pajamas if the maximum coverage level was used (Scenarios 1 and 5). On the other hand, the best distribution in the case of long pajamas was given by Scenario 3, both for rooms B and A; for short pajamas, it was Scenario 7 in room A and Scenario 6 in room B.

Regarding the daytime hours in which the patient was bedridden (Scenarios 17–24), satisfactory judgments regarding the internal microclimate were observed with minimum levels of coverage and long pajamas (Scenario 20) and medium levels of coverage and short pajamas (Scenario 23). For these distributions, in room B, more than 50% of data were inside the comfort range, while in room A, the  $Q_3$  was greater than  $PMV = +0.5$ .

Finally, in the cases in which the patient was out of bed, the conditions for reaching the comfort zone were opposite in the south-facing room compared to the north-facing one. In room A, it was preferable to wear long pajamas (Scenarios 36 and 38). In room B, the comfort zone reached more than 50% of observations if a short pajama, with or without a dressing gown, was used (Scenarios 37 and 39).

As already observed in the previous time periods, the IQR of each scenario distribution increased with the decrease of coverage rate in autumn.



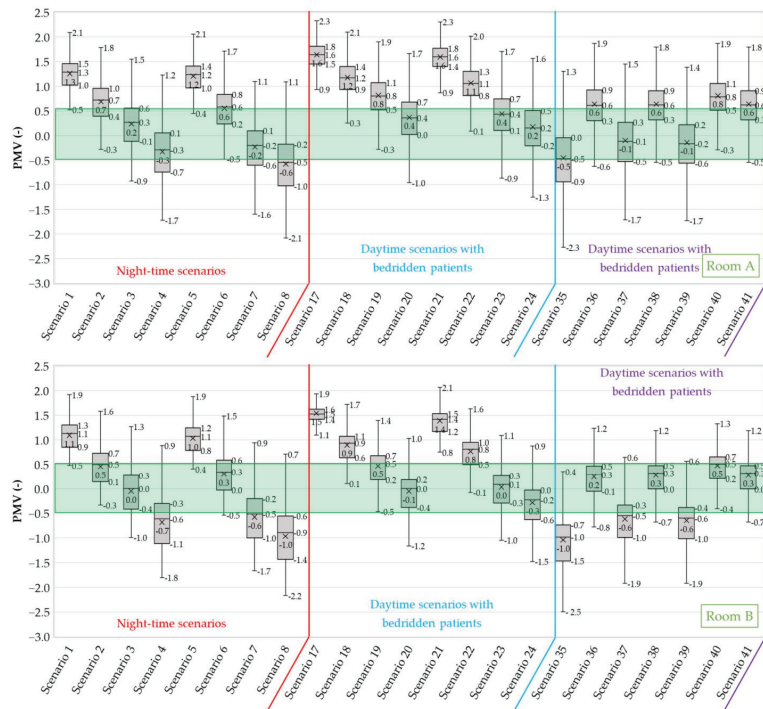


**Figure 24.** PMV distributions of the different scenarios in autumn period.

Considering the adaptive model applied to the autumn season, in Figure 22, the results are indicated by blue points ( $T_{o \text{ autumn}}$ ). In this case, the difference between the hygro-thermal conditions in the two rooms is evident. The percentage of  $T_{o \text{ autumn}}$  greater than  $T_{up \text{ limit}}$  passes from 8% in room B to 26% in room A (Table 6).

#### 4.2.4. Winter (1 November–15 April)

In this period, the HVAC system was turned on. The average value of indoor  $T_o$  was 20.5 °C, and RH was 50% in both rooms. Both are within the limits suggested by ISO 7730 for light activity, basically sedentary in winter:  $T_o \approx 22 \text{ °C} \pm 2 \text{ °C}$  and RH 30–70%. The box and whiskers graph in Figure 25 shows there was a lower IQR than all of the previous periods, with little total dispersed distributions: 0.5–1.2 in room B and 0.8–1.9 in room A. During the nighttime, the quilt with 67.0% of coverage and the long pajamas allowed the total PMV distribution inside the comfort range  $\pm 0.5$  in both rooms. Meanwhile, the coverage rate lower than 67.0% had a thermal sensation of “slightly cool” or “cool”.

During the day hours, when the patient was bedridden, Scenarios 18 and 19 were suitable. Furthermore, Scenario 40 (patient out of bed with the long pajamas and dressing gown) had the total distribution inside the comfort range, in room B, and the maximum value ( $PMV = 1.0$ ) in room A.

In this case, like the daily analysis, it was not possible to make a comparison with the adaptive model as the average daily outdoor temperatures were, in most cases, less than 10.3 °C, and therefore, below the limit of capability of the adaptive model.

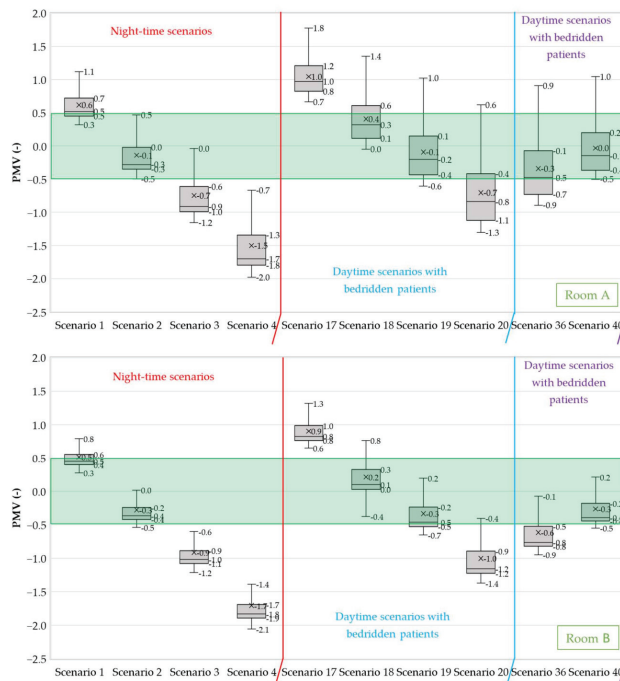


Figure 25. PMV distributions of the different scenarios in winter period.

## 5. Discussion

In this section, the Authors attempt to analyze the critical issues that appeared in the application of static or adaptive comfort models in hospitals.

First of all, it has been observed that when the HVAC system is turned on, in winter (1 November–15 April) and in summer (15 June–15 September), the indoor thermo-hygrometric parameters are stable and are within the limits suggested by ISO 7730 for light activity, basically sedentary. Therefore, the analyzed results in this paper could be considered representative of the thermo-hygrometric conditions of other hospitals designed following the international comfort standard. During the intermediate period (spring and autumn), the free-floating conditions have been presented and discussed.

In the winter period, the level of coverage greatly affected the perception of thermal comfort: if the right combination of quilt coverage and clothing is adopted, for all the hours of the analyzed period, the bedridden patient could be in the comfort range. It is not always true if the room is south facing due to the greater contribution of solar radiation that shows hours with a “slightly warm” sensation. It can also be deduced that if the internal conditions are those suitable for bedridden patients, a patient sitting out of bed is not in comfortable conditions.

Regarding the summer period, from both daily and seasonal results, various observations can be made. The first one is that in a hospital, the temperature range values conventionally adopted for a light activity, basically sedentary (such as residences or offices) patient, do not guarantee a dissatisfied percentage less than 10% in the case of bedridden patients. The additional resistance of the bed (always present) and the possible cover sheet determines the need to further reduce the indoor temperatures, despite the condition of the patient at rest, therefore, with a low metabolic level. For more than 50% of the observations in each scenario, the bedridden patient feels discomfort conditions during the daytime in summer, between “slightly warm” to “warm”. Therefore, during the summer, plant operation may need to be rescheduled, for instance, by using two levels of set-points, one

for day and one for nighttime. Confirming this, it has been observed that in cases where the patient is out of bed, on the basis of the Fanger model, a positive judgment was attributed to the microclimate.

In the intermediate period, with the HVAC turned off, the indoor microclimate conditions were floating, so the judgments against it were widely dispersed and could go from “slightly warm” to “slightly cold” for the same scenario. Furthermore, different sensations towards the microclimate could be achieved if the orientation of the room varied, with the same window area and same clothing insulation level.

Considering the differences between the two models, first of all, it should be emphasized that in the static model, both the metabolic rate and thermal resistance of the clothing were accurately assessed, while the adaptive comfort model was based on ranges already defined for these factors. During the summer period, the analysis of the adaptive model was in accordance with the results of the static model, suggesting that the indoor set-point of the air temperature must be redefined (reducing) in order to make the indoor environment more comfortable.

On the other hand, during the intermediate periods, the application of the two models leads to discordant results. For instance, in spring, the static model achieved thermal neutrality for 100% of the hours of the analyzed period by varying the insulation of clothing or the level of coverage when the patient is in bed. Meanwhile, according to the adaptive model, about 20% of the total hours showed uncomfortable conditions. The fundamental limit of the adaptive model was not considering clothing resistances as high as in the case of a bedridden patient. Similar conclusions could be written for the autumn period, characterized by a greater number of discomfort hours, above all in the south-facing room (27%).

Finally, it should be emphasized that the patient in a surgery ward, in addition to being confined to bed, is not able to modify the conditions of the context that surrounds them; consequently, the application of the static model was more appropriate. The evaluation of the PMV allowed us to take into account the type of clothing, the influence of the bed, and the metabolic rate, but it is completely detached from external climatic conditions. The analysis with an adaptive approach can provide discordant results with respect to the static model.

## 6. Conclusions and Future Developments

In this paper, the thermo-hygrometric conditions in ordinary hospitalization rooms of a surgery ward of the “Ferdinando Veneziale” Hospital are presented. The analysis was carried out by means of a calibrated energy numerical model in the EnergyPlus engine. Different characteristics and specific factors of the hospitalized patient that significantly influence the comfort indices were taken into account. In total, 41 scenarios were defined and analyzed by means of two comfort models: static and adaptive.

The first distinction must be made between periods with HVAC systems on and off. When the HVAC is on, in winter and in summer, the indoor thermo-hygrometric parameters are stable and within the limits suggested by ISO 7730 for light activity, basically sedentary. Thus, the analyzed results in this paper could be considered as representative of the thermo-hygrometric conditions of other hospitals designed following the international comfort standard. During the intermediate period, the free-floating conditions of the results could be representative of other hospital wards in a Mediterranean climate.

The main results could be summarized as follows.

During the winter period:

- If the patient is bedridden, long pajamas with 67.0% quilt coverage can achieve neutral sensation for all hours of the days in which HVACs are turned on.
- An increase of PMV ( $\approx +0.1$ ) has been observed in the south-facing room with respect to the north-facing one.
- Thanks to the bed thermal insulation and different coverages, the conditions suggested by ISO 7730 for light activity in wintertime (operative temperature  $\approx 22\text{ °C} \pm 2\text{ °C}$

and relative humidity 30–70%) seem appropriate for a bedridden patient in a surgery ward. Only during some hours (lower than 25% of the total period) was a thermal sensation of “slightly warm” observed in the room most exposed to solar radiation.

In summer:

- The thermal insulation of the bed system is a pejorative factor that, however, cannot be eliminated.
- The patient with a low coverage rate of bedsheets could create comfortable conditions more easily.
- For each possible combination of clothing-bed covering during the daytime, there were more than 50% of hours that had a thermal sensation between “slightly warm” and “warm”.
- The analysis of the adaptive model for the summer season was in accordance with the results of the static model (more than 80% of the hours are greater than the upper limit of 90% of the acceptability category).
- The microclimate conditions suggested by ISO 7730 ( $T_o \approx 24.5 \text{ }^\circ\text{C} \pm 1.5 \text{ }^\circ\text{C}$  and RH 30–70%) were not suitable for the hospital environment.

During autumn and spring:

- The thermal sensation with the same clothing-bed covering toward the microclimate can vary greatly within the same day, between “slightly warm” to “slightly cool”.
- In the cases in which the patient is out of bed, the optimal clothing-bed covering conditions are opposite in the south-facing room compared to the north-facing one. In south rooms, it is preferable to wear long pajamas, while, in north rooms, the thermohygro-metric comfort is reached in short pajamas, with or without a dressing gown.
- The application of the two models led to discordant results. For instance, in spring, if a static model is used, the variation of clothing or the level of bed coverage could be successful in achieving thermal neutrality. While according to the adaptive model, about 20% of the total hours are in not comfortable conditions. The fundamental limit of the adaptive model is not to consider clothing resistances as high as in the case of a bedridden patient.
- Similar conclusions could be written for the autumn period, characterized by a greater number of discomfort hours, above all, in the south-facing room (27%).

The results of the analysis carried out confirm that the heterogeneity of conditions that can occur inside a hospital room in terms of patient behavior (out of bed or in bed with different degrees of coverage) and clothing make it difficult to apply the usual comfort models.

Thanks to the large number of analyzed scenarios, this study could be the starting point for defining a standard of the thermal environmental conditions tailored to a hospital. A monitoring plan that includes in-field measurements and questionnaires has been defined and will be put in place after the COVID-19 pandemic. The questionnaires will be administered differently to patients and managers, and they will regard: general information on the state of the people (behavior and preferences) and judgments about air temperature, relative humidity, air speed, and its quality. At the same time, in some representative rooms, microclimate control units will monitor the same parameters. In this way, more information about the state of patients, pre or post-operative, and their pathologies, drug intake, and physical conditions will be involved in the study. Moreover, it could also be studied whether the use of common thermal comfort indices, conventionally applied in other buildings, are suitable to represent and understand patient comfort in hospitals.

**Author Contributions:** Conceptualization, S.R., F.T. and G.P.V.; methodology, S.R., F.T. and G.P.V.; software, S.R., F.T. and G.P.V.; validation, S.R., F.T. and G.P.V.; writing—original draft preparation, S.R., F.T. and G.P.V.; writing—review and editing, S.R., F.T. and G.P.V.; supervision, S.R., F.T. and G.P.V.; All authors have read and agreed to the published version of the manuscript.

**Funding:** The authors gratefully would like to thank the financial support from the “PRIN 2017-SUSTAIN/ABLE–Simultaneous Structural And energetic reNovAtion of Buildings through innovative solutions–MIUR, DD N. 240 DEL 14.02.2019, CUP F84I19001170001”.

**Institutional Review Board Statement:** Not applicable.

**Informed Consent Statement:** Not applicable.

**Conflicts of Interest:** The authors declare no conflict of interest.

## References

1. Fanger, P.O. *Thermal Comfort. Analysis and Applications in Environmental Engineering*; McGraw-Hill: New York, NY, USA, 1970.
2. ISO 7730; Ergonomics of the Thermal Environment—Analytical Determination and Interpretation of Thermal Comfort Using Calculation of the PMV and PPD Indices and Local Thermal Comfort Criteria. International Organization for Standardization: Geneva, Switzerland, 2006.
3. ASHRAE 55/2020; Thermal Environmental Conditions for Human Occupancy. ASHRAE: Atlanta, GA, USA, 2020.
4. Da Conceição Pereira, P.F.; Broday, E.E.; de Paula Xavier, A.A. Thermal Comfort Applied in Hospital Environments: A literature Review. *Appl. Sci.* **2020**, *10*, 7030. [CrossRef]
5. Mui, K.W.; Wong, L.T.; Fong, K.N.K.; Wong, W.W.Y. Evaluation of indoor environment quality of elderly centres of Hong Kong. *Int. J. Hous. Sci. Appl.* **2008**, *32*, 121–131.
6. Tartarini, F.; Cooper, P.; Fleming, R. Thermal perceptions, preferences and adaptive behaviours of occupants of nursing homes. *Build. Environ.* **2018**, *132*, 57–69. [CrossRef]
7. ASHRAE. *HVAC Design Manual for Hospitals and Clinics*, 2nd ed.; ASHRAE: Tullie Circle Atlanta, GA, USA, 2013.
8. Li, J.; Shu, Y.; Chen, N.; Wang, F.; Li, H. ‘Re-socialisation’ in isolated spaces: A case study on the social organisation of Fangcang shelter hospital patients under extreme spatial conditions. *Indoor Built Environ.* **2020**, 1–14. Available online: <https://journals.sagepub.com/doi/full/10.1177/1420326X20973745> (accessed on 20 January 2022). [CrossRef]
9. Khodakarami, J.; Nasrollahi, N. Thermal comfort in hospitals—A literature review. *Renew. Sust. Energy Rev.* **2012**, *16*, 4071–4077. [CrossRef]
10. Feng, Z.; Wei, F.; Li, H.; Yu, C.W. Evaluation of indoor disinfection technologies for airborne disease control in hospital. *Indoor Built Environ.* **2021**, *30*, 727–731. [CrossRef]
11. Gaspari, J.; Fabbri, K.; Gabrielli, L. A study on parametric design application to hospital retrofitting for improving energy savings and comfort conditions. *Buildings* **2019**, *9*, 220. [CrossRef]
12. Ascione, F.; Bianco, N.; de Masi, R.F.; Vanoli, G.P. Rehabilitation of the building envelope of hospitals: Achievable energy savings and microclimatic control on varying the HVAC systems in Mediterranean climates. *Energy Build.* **2013**, *60*, 125–138. [CrossRef]
13. King, M.F.; Noakes, C.J.; Sleigh, P.A. Modeling environmental contamination in hospital single- and four-bed rooms. *Indoor Air* **2015**, *25*, 694–707. [CrossRef]
14. De Giuli, V.; Zecchin, R.; Salmaso, L.; Corain, L.; de Carli, M. Measured and perceived indoor environmental quality: Padua Hospital case study. *Build. Environ.* **2013**, *59*, 211–226. [CrossRef]
15. Mahmood, F.J.; Tayib, A.Y. Healing environment correlated with patients’ psychological comfort: Post-occupancy evaluation of general hospitals. *Indoor Built Environ.* **2019**, *30*, 180–194. [CrossRef]
16. Wu, Y.; Meng, Q.; Li, L.; Mu, J. Interaction between sound and thermal influences on patient comfort in the hospitals of China’s Northern heating region. *Appl. Sci.* **2019**, *9*, 5551. [CrossRef]
17. Alotaibi, B.S.; Lo, S. Thermal environment perceptions from a longitudinal study of indoor temperature profiles in inpatient wards. *Buildings* **2020**, *10*, 136. [CrossRef]
18. Verheyen, J.; Theys, N.; Allonsius, L.; Descamps, F. Thermal comfort of patients: Objective and subjective measurements in patient rooms of a Belgian healthcare facility. *Build. Environ.* **2011**, *46*, 1195–1204. [CrossRef]
19. Alotaibi, B.S.; Lo, S.; Southwood, E.; Coley, D. Evaluating the suitability of standard thermal comfort approaches for hospital patients in air-conditioned environments in hot climates. *Build. Environ.* **2020**, *169*, 106561. [CrossRef]
20. Azizpour, F.; Moghimi, S.; Lim, C.H.; Mat, S.; Salleh, E.; Sopian, K. A thermal comfort investigation of a facility department of a hospital in hot-humid climate: Correlation between objective and subjective measurements. *Indoor Built Environ.* **2012**, *22*, 836–845. [CrossRef]
21. Sattayakorn, S.; Ichinose, M.; Sasaki, R. Clarifying thermal comfort of healthcare occupants in tropical region: A case of indoor environment in Thai hospitals. *Energy Build.* **2017**, *149*, 45–57. [CrossRef]
22. Del Ferraro, S.; Iavicoli, S.; Russo, S.; Molinaro, V. A field study on thermal comfort in an Italian hospital considering differences in gender and age. *Appl. Ergon.* **2015**, *50*, 177–184. [CrossRef]
23. Angelova, R.A.; Velichkova, R. Thermophysiological comfort of surgeons and patient in an operating room based on PMV-PPD and PHS indexes. *Appl. Sci.* **2020**, *10*, 1801. [CrossRef]
24. Nematchoua, M.K.; Ricciardi, P.; Reiter, S.; Asadi, S.; Demers, C.M.H. Thermal comfort and comparison of some parameters coming from hospitals and shopping centers under natural ventilation: The case of Madagascar Island. *J. Build. Eng.* **2017**, *13*, 196–206. [CrossRef]

25. Derks, M.T.H.; Mishra, A.K.; Loomans, M.G.L.C.; Kort, H.S.M. Understanding thermal comfort perception of nurses in a hospital ward work environment. *Build. Environ.* **2018**, *140*, 119–127. [[CrossRef](#)]
26. Khalid, W.; Zaki, S.A.; Rijal, H.B.; Yakub, F. Investigation of comfort temperature and thermal adaptation for patients and visitors in Malaysian hospitals. *Energy Build.* **2019**, *183*, 484–499. [[CrossRef](#)]
27. Zhang, H.; Xie, X.; Hong, S.; Lv, H. Impact of metabolism and the clothing thermal resistance on inpatient thermal comfort. *Energy Built Environ.* **2021**, *2*, 223–232. [[CrossRef](#)]
28. De Masi, R.F.; Ascione, F.; Sosto, G.; Vanoli, G.P. Cost-effective energy refurbishment of health care facilities in heating dominated climates of Italian backcountry. The case study of the Hospital Veneziale of Isernia. *Am. J. Eng. Appl. Sci.* **2017**, *10*, 756–768. [[CrossRef](#)]
29. *Energy Plus Simulation Software*; Version 8.1.0; U.S. Department of Energy’s (DOE) Building Technologies Office (BTO): Washington, DC, USA, 2016.
30. *Design Builder*, version.4.7; Design Builder Software Ltd.: Gloucester, UK, 2016.
31. U.S. Department of Energy Federal Energy Management Program. *M&V Guidelines: Measurement and Verification for Performance-Based Contracts Version 4.0*; U.S. Department of Energy Federal Energy Management Program: Washington, DC, USA, 2015.
32. Bellia, L.; Borrelli, M.; de Masi, R.F.; Ruggiero, S.; Vanoli, G.P. University building: Energy diagnosis and refurbishment design with cost-optimal approach. Discussion about the effect of numerical modelling assumptions. *J. Build. Eng.* **2018**, *18*, 1–18. [[CrossRef](#)]
33. Lin, Z.; Deng, S. A study on the thermal comfort in sleeping environments in the subtropics—Developing a thermal comfort model for sleeping environments. *Build. Environ.* **2008**, *43*, 70–81. [[CrossRef](#)]
34. Ferrari, S.; Zanotto, V. Adaptive comfort: Analysis and application of the main indices. *Build. Environ.* **2012**, *49*, 25–32. [[CrossRef](#)]
35. De Masi, R.F.; Ruggiero, S.; Tariello, F.; Vanoli, G.P. Passive envelope solutions to aid design of sustainable livestock buildings in Mediterranean climate. *J. Clean. Prod.* **2021**, *311*, 127444. [[CrossRef](#)]
36. Prada, M.; Prada, I.F.; Cristea, M.; Popescu, M.E.; Bungău, C.; Aleya, L.; Bungău, C.C. New solutions to reduce greenhouse gas emissions through energy efficiency of buildings of special importance—Hospitals. *Sci. Total Environ.* **2020**, *718*, 137446. [[CrossRef](#)]
37. Carnieletto, L.; Ferrando, M.; Teso, L.; Sun, K.; Zhang, W.; Causone, F.; Romagnoni, P.; Zarrella, A.; Hong, T. Italian prototype building models for urban scale building performance simulation. *Build. Environ.* **2021**, *192*, 107590. [[CrossRef](#)]





Article

# Migration and Removal of Labile Cadmium Contaminants in Paddy Soils by Electrokinetic Remediation without Changing Soil pH

Yajun Luan <sup>1,2</sup>, Junzeng Xu <sup>1,2,\*</sup>, Jing Zhou <sup>1,2</sup>, Haiyu Wang <sup>1,2</sup>, Fengxiang Han <sup>3</sup>, Kechun Wang <sup>1,2</sup> and Yuping Lv <sup>4</sup>

<sup>1</sup> State Key Laboratory of Hydrology-Water Resources and Hydraulic Engineering, Hohai University, Nanjing 210098, China; luan450705@163.com (Y.L.); rohana0218@163.com (J.Z.); haiyuwang@163.com (H.W.); kechunw101@hhu.edu.cn (K.W.)

<sup>2</sup> College of Agricultural Science and Engineering, Hohai University, Nanjing 210098, China

<sup>3</sup> Department of Chemistry and Biochemistry, Jackson State University, Jackson, MS 39217, USA; fengxiang.han@jsums.edu

<sup>4</sup> College of Hydraulic Science and Engineering, Yangzhou University, Yangzhou 225009, China; lvyupingsun@126.com

\* Correspondence: xjz481@hhu.edu.cn

**Abstract:** Electrokinetic remediation (EKR) is a viable, advanced cleaning strategy that can permanently reduce the toxicity of soil contaminants. However, EKR is prone to causing changes in soil pH. The negative impacts must be minimized if field-scale application is to be realized. In this study, EKR with polarity reversal was used to avoid soil pH polarization and to clean up cadmium (Cd)-contaminated paddy soils. Results showed that Cd desorbed from oxidizable and residual fractions to labile and easily available parts. Soil moisture content above 0.35 g g<sup>-1</sup> was conducive to achieving the desirable Cd-migration rate. The exchangeable Cd phase eventually migrated from both ends of that soil compartment towards the intermediate. Moreover, the addition of citric acid at the concentration of 0.1 mol L<sup>-1</sup> was an effective enhancement strategy. The methodology enriched Cd contaminants to specific sites. The technology can be used for electrokinetic-assisted phytoremediation during the rice growing period. Hyperaccumulator is planted in the intermediate area to remove the Cd contaminants. On the other hand, Cd removal is achieved in the region close to the electrodes. The present study provides a theoretical basis for in situ remediation. It has a wider significance for field-scale application.

**Citation:** Luan, Y.; Xu, J.; Zhou, J.; Wang, H.; Han, F.; Wang, K.; Lv, Y. Migration and Removal of Labile Cadmium Contaminants in Paddy Soils by Electrokinetic Remediation without Changing Soil pH. *Int. J. Environ. Res. Public Health* **2022**, *19*, 3812. <https://doi.org/10.3390/ijerph19073812>

Academic Editors: Roberto Alonso González Lezcano, Francesco Nocera and Rosa Giuseppina Caponetto

Received: 28 February 2022

Accepted: 22 March 2022

Published: 23 March 2022

**Publisher's Note:** MDPI stays neutral with regard to jurisdictional claims in published maps and institutional affiliations.



**Copyright:** © 2022 by the authors. Licensee MDPI, Basel, Switzerland. This article is an open access article distributed under the terms and conditions of the Creative Commons Attribution (CC BY) license (<https://creativecommons.org/licenses/by/4.0/>).

**Keywords:** paddy soils; cadmium; electrokinetic remediation; polarity reversal; soil pH

## 1. Introduction

Heavy metal pollution in agricultural soils has become a worldwide threat to human health and safe food production. It has attracted wide attention [1]. Heavy metal contamination in agricultural ecosystems originates from anthropogenic activities, such as fertilization and irrigation, and tends to accumulate over time [2,3]. Moreover, long-term fertilization or acid rain can reduce soil pH, which activates heavy metals in soil and increases its bioavailability, thereby posing threats to human health [4]. Thus, decontamination of contaminated soil and reduction in metal contaminants in grains are urgent demands.

Several remediation solutions have been developed to clean polluted soil and ensure grain security, including screening of low-accumulation cultivars [5,6], reducing the bioavailability of heavy metals in soils [7,8], and removing pollutants from soils through electrokinetic extraction, phytoremediation, bioremediation, or soil washing [9,10]. In situ chemical immobilization is a technique that has been widely considered by researchers [11]. However, this technique does not achieve the removal of contaminants from soil. Long-term stability of heavy metals in soils cannot be guaranteed. External influences, such as acid rain, can reactivate heavy metals. Thus, in situ contaminant removal or extraction



remediation is more favorable. Removing pollutants from soils is a promising soil-cleaning strategy that permanently reduces the toxicity of soil contaminants and minimizes their entry into crops. Among them, electrokinetic remediation (EKR) is a viable and advanced technology that uses a direct current (DC) electric field to mobilize polluted ions towards the opposite-charged electrode. This technology has been widely used due to its high efficiency, and has achieved favorable results [12,13]. However, one of the disadvantages is that EKR is prone to cause changes in the physical and chemical properties of soil [14]. The negative impacts caused by EKR must be minimized if field-scale application is to be realized.

During EKR process, the electrolysis of water leads to the division of soil areas into acidic zone ( $\text{H}_2\text{O} - 2\text{e}^- \rightarrow 2\text{H}^+ + 1/2\text{O}_2$ ) and alkaline zone ( $2\text{H}_2\text{O} + 2\text{e}^- \rightarrow 2\text{OH}^- + \text{H}_2$ ). The hydrogen ( $\text{H}^+$ ) ions from the oxidation of water make it easier to desorb metal cations from the soil surface. The hydroxyl ( $\text{OH}^-$ ) ions produced in the alkaline zone have a negative effect on metal transportation [10]. This raised two problems: soil acidification in the acidic zone and focusing precipitation in the alkaline zone. Soil acidification in the acidic zone disrupts the soil nutrient cycle. Low soil pH near the anode negatively affects plant growth [15–17]. Considering that the land would continue to be used for growing crops after remediation, soil acidification is one of the disadvantages that limits the practical application of EKR technology [18]. On the other hand, with the increase in soil pH in the alkaline area, the solubility of heavy metals decreases, and the migration of metal ions is limited [19]. Various methods have been developed to solve the focusing phenomenon during the EKR process. For example, using the appropriate conditioning solutions ( $\text{HNO}_3$ ,  $\text{HCl}$  et al.) at the cathode can help to control the pH, increasing the exchangeable fraction of metals and indicating better performance for pollutant removal [20,21]. By using ion exchange membranes, the influx of  $\text{H}^+$  and  $\text{OH}^-$  ions into soil can be impeded, this showed good results in preventing a wild pH variation and precipitation with metal ions in soil in [22]. These methodologies have shown good results in decreasing soil pH and improving metal solubility in the alkaline zone. However, chemical additives are not environmentally acceptable, and extra materials could be costly. Therefore, the EKR technology faces challenges in green and sustainable development, which requires more environmentally friendly and cost-effective methods for contaminated soil remediation [23,24].

Various biodegradable chelates have been found to combine with several kinds of heavy metals, and increase ion solubility, without requiring changes in soil pH [25,26]. Among these biodegradable chelates, low-molecular-weight organic acids, such as citric acid, oxalic acid, and acetic acid, are environmentally friendly for soil remediation, owing to their buffering, biodegradability, chelating, and complexing actions. Previous studies have shown that the supplied chloride ions from electrolyte would combine with heavy metals as a complexing agent, and then these metal complexes can increase the removal efficiency [27]. Other studies have also shown that citric acid can efficiently remove metals in electrokinetic remediation. Citric acid acts as a buffer substance, which quickly neutralizes the  $\text{OH}^-$  produced in the cathode. As a chelating agent, citric acid has also shown high removal efficiency for harbor sediments and electroplating sludge [28]. Many studies have proven that citric acid can efficiently remove metals in electrokinetic remediation. It helps to desorb metals and transfer them from the solid phase to the liquid phase [29,30]. Using citric acid could effectively improve the removal rate of the metals in the contaminated soil [31].

Periodic reversal of polarity during the EKR process is another effective method to avoid changes in soil pH. Metals were redissolved by the polarity exchange technique. Both the pH adjustment of the soil system and the control of the direction of contaminant migration could be achieved without additional costs. The application of this technique showed a removal of 72% of the initial manganese in 7.6 d in [32]. In field experiments, EKR with the polarity reversal operation could partially resolve the adverse effects of EKR on soil pH and remove chromium more efficiently [33]. Mao et al. [34] found that EKR enhanced with an electrode polarity inversion strategy was an effective technique for lead

decontamination from a low-permeability matrix. The electrode reversal was conducted for around 48 h to avoid pH polarization and Pb precipitation.

Soil moisture content is critical in achieving effective removal of the pollutants under EKR. Electric current and pollutants removal efficiency are positively correlated to soil moisture content. After a 72 h EKR experiment, it was found that the removal rate of total chromium was 14.4% with a soil moisture of  $0.20 \text{ g g}^{-1}$ , and the removal rate was 67.3% with a soil moisture of  $0.40 \text{ g g}^{-1}$  [35]. The moisture of the kaolinite specimen in the electrokinetic cell was adjusted from  $0.40 \text{ g g}^{-1}$  to  $0.60 \text{ g g}^{-1}$ . The increase in the moisture content clearly favored the electromigration of manganese towards the cathode. The increase in the moisture content up to  $0.60 \text{ g g}^{-1}$  resulted in over 90% manganese removal [36]. On the other hand, as an efficient water-saving irrigation model, controlled irrigation (CI) is widely used in China [37,38]. There is almost no water layer during the growth period of rice under CI. The soil gravimetric water content mostly ranges from  $0.29 \text{ g g}^{-1}$  to  $0.42 \text{ g g}^{-1}$ , which is near the soil moisture condition that has an efficient removal efficiency under EKR treatment [39,40]. Thus, placing the electrodes directly into the moist soil to obtain optimum performance in contaminated paddy soils under alternate wetting and drying (AWD) moisture conditions deserves further consideration. It was expected to guide the potential application for in situ remediation in paddy fields under CI irrigation.

Electrokinetic remediation as an in situ cleaning technology has attracted significant attention from researchers. The challenge of pH control has greatly limited the field application of EKR technology in Cd-contaminated paddy soils. In the present research, cadmium (Cd) was selected as the target toxic metal, which has been listed as a priority pollutant in soil contamination monitoring, with an over-standard rate of 7.0% according to the National Soil Pollution Survey Bulletin of China in 2014 [41,42]. The Cd-contaminated soil was taken from local paddy fields. Laboratory experiments were performed by inserting the electrodes vertically into the moist soils to drive the electromigration of heavy metals. A cycle progress of pulsed electric fields (10 h ON/14 h OFF) was conducted [43,44]. Three different voltage intensities were set to investigate the changes in electric current, soil pH, Cd fractions, and the migration rates of soil Cd. The objectives were as follows: (1) to study the mobilization and redistribution of Cd in soils under EKR with polarity reversal, and to explore the feasibility of mobilizing Cd in a specific area; (2) to study the effect of citric acid on the migration rate of Cd. The significance of this study lies in providing theoretical support for an innovative, in situ electrokinetic remediation, and in its exploration of a scientific approach to remove Cd from soils and hence reduce Cd content in rice.

## 2. Materials and Methods

### 2.1. Site Description

The experiment was conducted in 2020 at Kunshan Experiment Station ( $31^{\circ}15'50'' \text{ N}$ ;  $120^{\circ}57'43'' \text{ E}$ ), Eastern China. The soil texture was sandy clay, in which sand accounted for 41.20%, silt accounted for 51.92%, and clay accounted for 6.88%. The saturated soil moisture content was  $0.403 \text{ g g}^{-1}$ . Soil pH was 7.41, soil bulk density was  $1.30 \text{ g cm}^{-3}$ , and the soil organic matter content was  $25.82 \text{ g kg}^{-1}$ . The Cd concentration was  $0.793 \text{ mg kg}^{-1}$ . According to Environmental Quality Standard for Soils in China (GB15618-2018), the Cd concentration was higher than the risk screening value ( $0.6 \text{ mg kg}^{-1}$  for paddy fields, with soil pH ranging from 6.5 to 7.5), indicating an ecological risk [45].

### 2.2. Electrokinetic Experiment Setup

The EKR experimental diagram is shown in Figure 1. The experimental apparatus comprised three parts: the soil compartment, the graphite electrodes, and the DC power supply with an ammeter (DC power supply 305, Mestek, Shenzhen, China). The dimensions of the soil compartment were  $40 \text{ cm} \times 29 \text{ cm} \times 20 \text{ cm}$  (L  $\times$  B  $\times$  H). The soil used in the experiments was taken from the 0–20 cm soil layer of local paddy fields. After air-drying and crushing, the coarse fragments in the soil were removed with a 4 mm sieve. Then, the

soil was packed into pots at a depth of 15 cm, with the bulk density of  $1.3 \text{ g cm}^{-3}$ . Plate graphite electrodes ( $L \times H \times T$ :  $40 \text{ cm} \times 18 \text{ cm} \times 1 \text{ cm}$ ) were used for the anode and cathode, respectively. Two graphite electrodes were inserted vertically into the contaminated soils at a net distance of 27 cm.

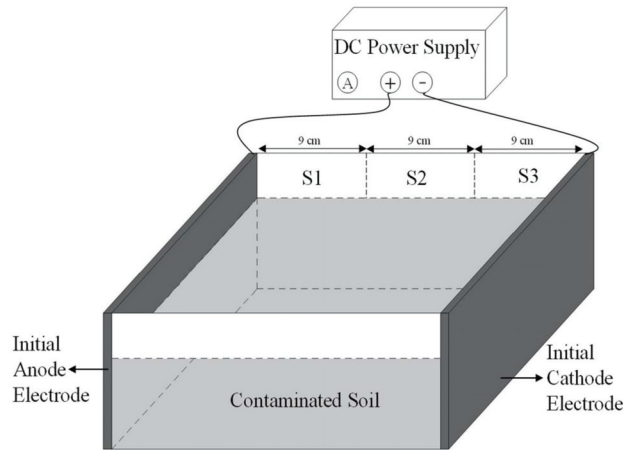


**Figure 1.** The electrokinetic remediation experiment diagram.

Table 1 summarizes the details of the experimental conditions. The experiment adopted the power supply of 1.0 V/cm, 0.8 V/cm, and 0.5 V/cm, namely EKR 1.0, EKR 0.8, and EKR 0.5, respectively. Each treatment was repeated three times. To match the soil moisture conditions of paddy fields under CI irrigation, soil gravimetric moisture content was controlled between  $0.310 \text{ g g}^{-1}$  and  $0.403 \text{ g g}^{-1}$ . EKR experiments were run for two AWD cycles over 14 days. A cycle progress of pulsed electric fields (10 h ON/14 h OFF) was conducted in this research. One cycle was the sum of time with electric field in “ON” + “OFF”, that was 24 h. In total, there were 14 periodic cycles. The polarity reversal was operated after one cycle. A total of 14 reversal operations were performed in this study. As shown in Figure 1, the soil was sectioned into three equal parts, labeled as S1, S2, and S3, between the anode and the cathode. Soil samples were taken from each section using a 1 cm diameter U-shaped shovel, and were used to analyze soil pH and Cd concentration. Three soil samples were taken from each soil section, mixed well, and used for measuring. Soils were sampled when the pulsed system was off. The sampling times were 34 h, 130 h, 226 h, 274 h, and 322 h during the EKR process.

**Table 1.** Summary of experimental conditions.

Treatment	Voltage Gradient ( $\text{V cm}^{-1}$ )	Duration (d)	Periodic Power/Day	Polarity Reversal Frequency (h)	Soil Moisture Alternate Wetting and Drying (AWD) Cycles
EKR 1.0	1.0	14	10 h ON/14 h OFF	24	Two AWD cycles
EKR 0.8	0.8				
EKR 0.5	0.5				
EKR <sup>C</sup> 1.0	1.0	6	10 h ON/14 h OFF	24	One AWD cycle
EKR <sup>C</sup> 0.8	0.8				
EKR <sup>C</sup> 0.5	0.5				

### 2.3. Citric Acid Preacidification Enhancement Experiment

Citric acid is a biodegradable organic acid, which is safe for the environment. In this study, it was used to enhance the removal of heavy metals. Other conditions were the same

as other EKR experiments, except that we added citric acid into the contaminated soils before the experiments started. After filling the air-dried soil into the soil compartment, citric acid was added into the soils at a concentration of  $0.1 \text{ mol L}^{-1}$  so that the moisture content reached  $0.3 \text{ g g}^{-1}$ . After that, the soil was saturated with deionized water. The concentration has been determined to preacidify the soil and enhance the electroosmotic flow [46,47]. The preacidified soil was equilibrated for 24 h before the DC system was powered on. The citric acid enhancement experiments (EKRC) were run for 1 AWD cycle over 6 d (Table 1). At the end of the EKRC experiment, soil samples were taken from different sections to analyze soil pH and Cd concentrations.

#### 2.4. Analysis and Calculation

The soil moisture content was calculated by weight loss after heating in an oven for 8 h at  $105 \text{ }^\circ\text{C}$  [48]. The soil pH was measured using the pH meter (Mettler-Toledo, Zurich, Switzerland) by preparing slurries with a soil to water ratio of 1:2.5 [49]. The current was measured using the ammeter.

Metal speciation in the soil was determined through a sequential extraction method according to the procedure recommended by the Standards, Measurements, and Testing (former BCR) Program of the European Commission [50,51]. The metals were divided into exchangeable fraction (F1-Cd), reducible fraction (F2-Cd), and oxidizable fraction (F3-Cd). The residual (F4-Cd) was considered as the mineral non-extractable form. The metals ions concentration in the supernatant collected in different steps of the sequential extraction was filtered through a  $0.45 \text{ }\mu\text{m}$  membrane and analyzed by inductively coupled plasma optical emission spectrometry (ICP-OES, Thermo Scientific, Waltham, MA, USA).

The Cd migration rate,  $\eta$ , was calculated as follows:

$$\eta = \frac{C_t - C_0}{C_0} \times 100\% \quad (1)$$

where  $C_t$  was the Cd concentration at time, and  $C_0$  was the initial Cd concentration.

The electrical energy consumption per unit mass ( $E_U$ ) was calculated as follows:

$$E_U = \frac{1}{m} \int_0^t UI dt \quad (2)$$

where  $E_U$  was the electrical energy consumption per unit mass ( $\text{kWh kg}^{-1}$ ),  $m$  was the mass of migrated Cd (kg),  $U$  was the voltage between the electrodes (V),  $I$  was the electric current (A), and  $t$  was the power-on time (h).

#### 2.5. Statistical Analysis

One-way ANOVA and the least significant difference (LSD) test for analysis with a significance level of  $p < 0.05$  were used. Statistical analyses were performed using SPSS Statistics 24.

### 3. Results

#### 3.1. Electric Current, Soil Moisture Content, and Soil pH Variation

The electric current and soil moisture content at different voltage gradients during the EKR process are shown in Figure 2. The electric current was proportional to the voltage gradient (Figure 2a). The soil moisture content was similar among different treatments. The lower the voltage gradient, the slightly smaller the gravimetric moisture content (Figure 2b). The electric current was also proportional to the soil moisture content. The higher the gravimetric moisture content, the greater the current intensity. The current variation ranges were 206–311 mA, 128–244 mA, and 30–149 mA at different voltage gradients from 0 to 144 h, respectively, and were 159–302 mA, 125–241 mA, and 65–147 mA from 144 to 322 h. The electric current decreased significantly from 106 h to 154 h, as well as from 250 h to 322 h. Correspondingly, the soil gravimetric moisture content ranged from  $0.321 \text{ g g}^{-1}$  to

0.345 g g<sup>-1</sup>, and from 0.314 g g<sup>-1</sup> to 0.357 g g<sup>-1</sup> for those two time periods. Generally, the smaller the current, the lower the migration rate of Cd ions in the soil. Therefore, it can be assumed that, when the soil gravimetric moisture content was higher than 0.35 g g<sup>-1</sup>, the electric current was higher, and the metal ions could have a desirable migration efficiency, which was more favorable for the remediation of contaminated soil.

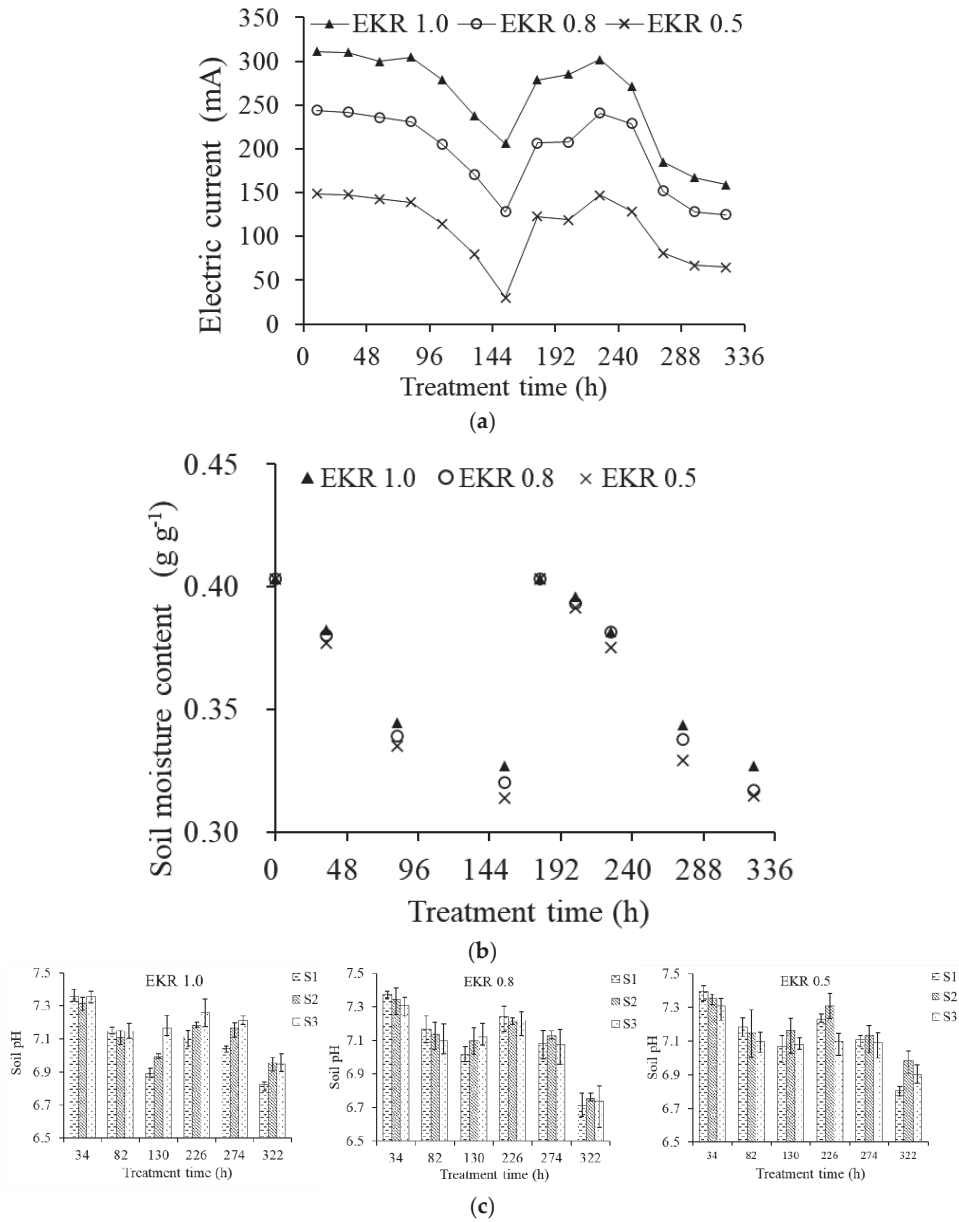


**Figure 2.** Electric current (a), soil moisture content variation (b), and soil pH in different soil sections (c) during the electrokinetic remediation process.

The soil pH was initially 7.41 and decreased gradually along with the reduction in soil moisture (Figure 2c). At 226 h, soil pH increased slightly due to the increase in soil

moisture after irrigation. After 226 h, the pH continued to decrease. At the end of EKR process, soil pH of S1, S2, and S3 soil sections decreased by 0.59, 0.45, and 0.46 pH units, respectively, for EKR 1.0; the soil pH of S1, S2, and S3 soil sections decreased by 0.70, 0.65, and 0.67 pH units, respectively, for EKR 0.8; and the soil pH of S1, S2, and S3 soil sections decreased by 0.61, 0.43, and 0.51 pH units, respectively, for EKR 0.5. There were no significant differences in soil pH among the treatments. Generally, soil pH ranged from 6.71 to 7.41, basically maintained in the neutral. The soil itself possessed a certain buffer ability of protons. During the EKR process, the electrolysis of water released  $H^+$  and  $OH^-$  at the anode and cathode surface, respectively.  $H^+$  and  $OH^-$  produced by electrolysis reactions could be directly neutralized after the polarity reversal operation. The acidification effect on the soil was minimized, and the formation of alkaline environment was also avoided, which could reduce the precipitation of Cd.

### 3.2. Migration and Redistribution of Cd during EKR process

Figure 3 showed the migration and redistribution of Cd concentrations in different fractions during the EKR process. Taking EKR 1.0 as an example, the concentrations of F1-Cd in S1 and S3 sections decreased by 15.07% and 11.86%, respectively. The concentration of F1-Cd in S2 section increased by 60.64%. The concentrations of F2-Cd increased by 59.58%, 36.32%, and 34.80%, respectively, in different soil sections. The concentrations of F3-Cd decreased by 54.46%, 58.25%, and 35.99%, respectively, in different soil sections. The concentrations of F4-Cd decreased by 50.84%, 33.22%, and 51.91%, respectively, in different soil sections. Similar results were also observed for EKR 0.8 and EKR 0.5 treatments. Finally, for all three treatments, the concentrations of F1-Cd decreased in the S1 and S3 sections, and increased in the S2 section. The concentrations of F2-Cd increased in all three sections. The concentrations of F3-Cd and F4-Cd decreased in all three sections. The magnitude of the change in Cd concentrations decreased with the decrease in voltage gradient.

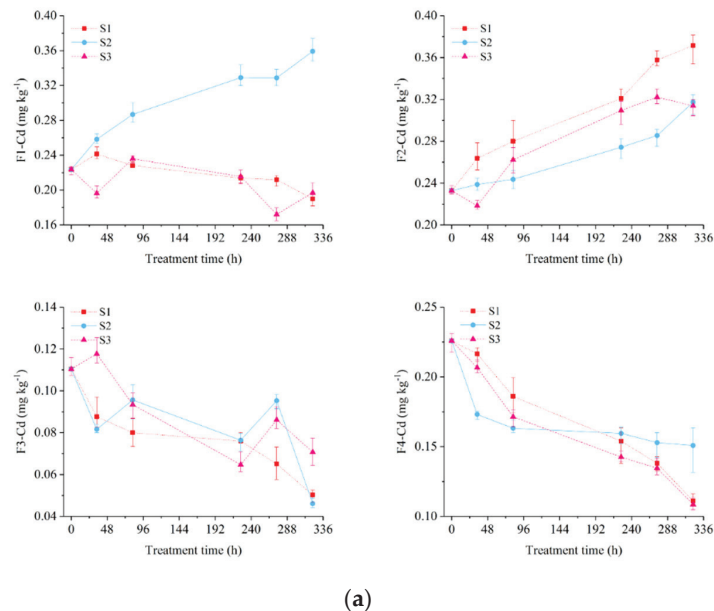
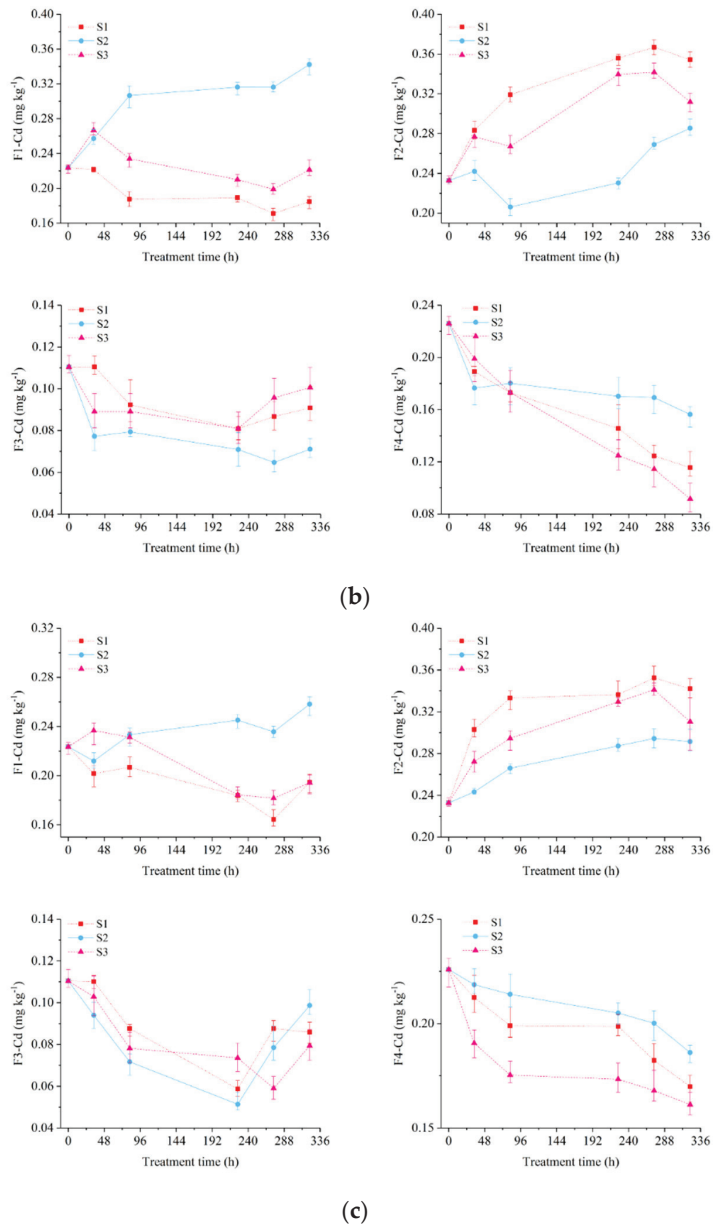


Figure 3. Cont.



**Figure 3.** Variation of Cd fraction concentration at EKR 1.0 (a), EKR 0.8 (b), and EKR 0.5 (c), respectively. F1-Cd, F2-Cd, F3-Cd, and F4-Cd were the exchangeable fraction, reducible fraction, oxidizable fraction, and residual, respectively.

At different voltage gradients, the variation of F3-Cd content during EKR process was irregular, which may be related to the change in soluble organic carbon caused by the change in soil moisture [52]. The concentrations of F4-Cd gradually decreased. The removal rates of F3-Cd and F4-Cd near the electrodes were higher than those in the middle soil section. Correspondingly, the increases in F2-Cd near the electrodes were higher than that in the middle soil section. It indicated that electrolysis reactions led to the transformation of

soil Cd from stable state to the labile state under EKR treatment. The concentration of F1-Cd decreased in the S1 and S3 sections, while it increased in the S2 section. This confirmed the promoting effect of repeating polarity reversal on the migration of F1-Cd towards the S2 section. The results showed that soil Cd desorbed from oxidizable and residual fractions to the exchangeable and reducible fractions under EKR technology. Polarity reversal significantly promoted the enrichment of exchangeable Cd in the middle soil section.

### 3.3. Speciation of Heavy Metals in the Soil

The mobility and bioavailability of heavy metals were related to their chemical forms in the soils. The exchangeable, reducible, oxidizable, and residual fractions of Cd in the initial soil were 28.20%, 29.37%, 13.93%, and 28.50%, respectively. Traditionally, the exchangeable and reducible fractions (F1-Cd and F2-Cd) were considered as the labile and easily available parts in soil [53]. Metals found in these two fractions were considered as the electromigration-accessible phases [54]. In this study, the electromigration-accessible phase of Cd was 57.57%. Therefore, Cd was expected to migrate efficiently during EKR process.

Figure 4 showed Cd fractions of different soil sections at the end of EKR process. Figures in the graph indicated the changes in different fractions of Cd compared with the initial one. The “+” indicates the increases in the percentages, and the “−” indicates the decreases in the percentages. At the end of EKR process, the F2-Cd fractions increased, and the F3-Cd and F4-Cd fractions decreased in different soil sections at different voltage gradients. The F1-Cd fractions slightly decreased in the S1 section, and significantly increased in the S2 section at different voltage gradient. However, the variations of F1-Cd did not show a consistent pattern in S3 section. The results of heavy metals speciation analysis contributed to the understanding of the mechanisms of EKR with polarity reversal. It indicated that the oxidizable and residual phases were desorbed from the soil, and were dissolved to the reducible and exchangeable phases. Finally, the exchangeable phases were gathered in the S2 section by repeating the polarity reversal operations.

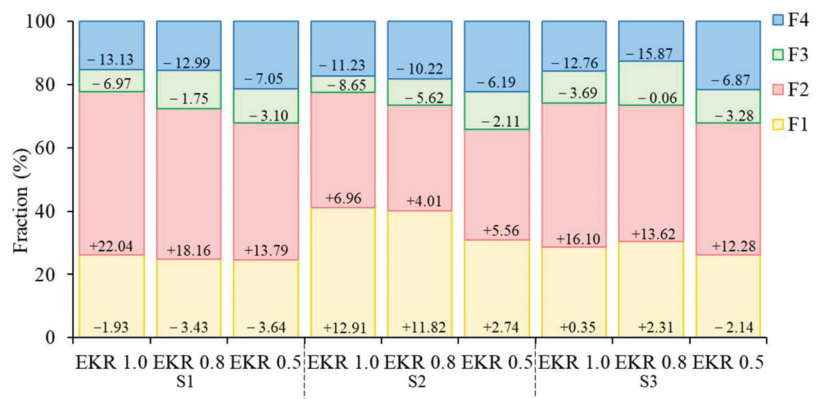


**Figure 4.** Cd fractions (%) at the end of EKR process. Figures in the graph indicated the variations of different fractions of Cd compared to the initial one. “+” indicates increase in the percentage, and “−” indicates the decrease in the percentage. EKR indicates electrokinetic remediation. F1-Cd, F2-Cd, F3-Cd, and F4-Cd indicate the exchangeable fraction, reducible fraction, oxidizable fraction, and residual, respectively.

### 3.4. Changes in Total Cd during EKR process

Figure 5 showed changes in total Cd concentration during EKR process. In general, the mobilization and transformation of Cd seemed to be similar at different voltage gradients. It was obvious that Cd contaminants in the soil migrated from the S1 and S3 sections to the S2 section. At 34 h, Cd contents in the S1 and S3 sections were higher than the initial values. Cd content showed a slight increase from 274 h to 322 h under the EKR



0.5 treatment. The phenomena may be related to the different lengths of the path for Cd migration under different soil moistures. Uneven sampling caused by the U-shaped shovel—instead of sampling whole soil sections—may be another reason. Generally, the slopes of the lines from 96 h to 226 h were smaller compared with the other time periods, indicating more moderate variations in Cd concentrations. It was related to the lower soil moisture content and smaller electric current during this time period. The moisture content decreased along with time until it dropped to  $0.301 \text{ g g}^{-1}$ . Then, the soil was irrigated to saturation at 154 h (Figure 2). In Figure 5, the slopes of the lines continued to increase after 226 h. The variation of Cd concentrations had a negative relationship with the soil moisture content. At lower soil moisture content, the current decreased, and the migration and transformation efficiency of the Cd contaminants was reduced. The above results further indicated that, when the soil gravimetric moisture content was higher than about  $0.35 \text{ g g}^{-1}$  (Figure 2), the current was higher, and the metal ions could have a desirable migration efficiency. Briefly, when applying the EKR technology with polarity reversal operation in paddy fields under CI, soil gravimetric moisture content should be kept higher than  $0.35 \text{ g g}^{-1}$ , or should be powered when the moisture content was above  $0.35 \text{ g g}^{-1}$  to achieve a reasonable performance.

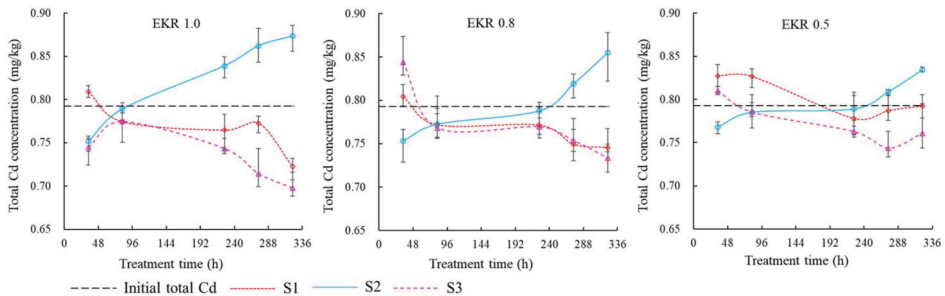


**Figure 5.** Total Cd concentration variation under different voltage gradients.

Cd contaminants eventually gathered in the S2 section. The total Cd contents increased by 10.19%, 7.85%, and 5.27%, respectively, for EKR 1.0, EKR 0.8, and EKR 0.5. Repeated polarity reversal operation at a higher voltage gradient could effectively mobilize the contaminants towards the S2 section. At the end of EKR experiment, in the S1 and S3 sections, the total Cd decreased by 8.83% and 12.93%, respectively, for EKR 1.0; the total Cd decreased by 5.97% and 8.51%, respectively, for EKR 0.8; the total Cd decreased by 0.04% and 5.96%, respectively, for EKR 0.5. The removal of Cd contaminants was asymmetric between the S1 and S3 soil sections. In previous studies, the lower pH formed by the acid front promoted the dissolution of heavy metals. It was essential for the efficient remediation of contaminated soil [50]. In this study, due to the neutral soil pH, the migration rate of Cd contaminants was at a low degree even at higher voltages. After 14 d of remediation, the Cd contents in all three soil sections were higher than the risk screening value of  $0.6 \text{ mg kg}^{-1}$ .

### 3.5. Citric Acid Preacidification Enhancement EKR Technology

In order to improve the migration rate, citric acid was added into the contaminated soils as an enhancement solution. The citric acid preacidification enhancement experiment was carried out over 6 d. Table 2 illustrated the current intensity, total Cd concentration, and soil pH variation after EKR<sup>C</sup> experiments. The current intensity gradually decreased as the soil became dry. Compared with the results in Figure 2a, citric acid resulted in a significant increase in current intensity. Soil pH ranged from 6.19 to 6.65 following citric acid preacidification. The soil with citric acid was slightly acidic. It was related to the buffering capacity of soil and biodegradability of citric acid. There were no significant differences in soil pH among treatments. This was consistent with the results in Figure 2.

The electromigration of heavy metal ions in soil between anode and cathode was the key process investigated in this study. Compared with the EKR experiment, citric acid had a significant contribution to the migration of Cd in the EKR<sup>C</sup> experiment. As can be seen in Table 2, polarity reversal also significantly promoted the enrichment of F1-Cd in S2 section, while soil Cd was gathered in the middle soil section.

**Table 2.** The current intensity, soil pH, and total Cd concentration after the citric acid preacidification enhancement experiment.

Soil Section	Treatment	Intensity Variation (mA)	Final pH	Final F1-Cd Concentration (mg kg <sup>-1</sup> )	Final Total Cd Concentration (mg kg <sup>-1</sup> )
S1	EKR <sup>C</sup> 1.0	459~807	6.25 ± 0.065 ab	0.195 ± 0.022 a	0.597 ± 0.015 c
	EKR <sup>C</sup> 0.8		6.19 ± 0.040 b	0.183 ± 0.012 a	0.662 ± 0.015 b
	EKR <sup>C</sup> 0.5		6.33 ± 0.035 a	0.180 ± 0.014 a	0.724 ± 0.011 a
S2	EKR <sup>C</sup> 1.0	368~647	6.50 ± 0.050 a	0.490 ± 0.019 a	1.151 ± 0.020 a
	EKR <sup>C</sup> 0.8		6.51 ± 0.080 a	0.421 ± 0.019 b	1.048 ± 0.011 b
	EKR <sup>C</sup> 0.5		6.65 ± 0.140 a	0.332 ± 0.012 c	0.960 ± 0.018 c
S3	EKR <sup>C</sup> 1.0	241~426	6.21 ± 0.087 a	0.196 ± 0.009 a	0.582 ± 0.010 b
	EKR <sup>C</sup> 0.8		6.34 ± 0.087 a	0.192 ± 0.015 a	0.643 ± 0.018 a
	EKR <sup>C</sup> 0.5		6.21 ± 0.070 a	0.194 ± 0.022 a	0.667 ± 0.016 a

Note: Different letters represent significant differences among treatments at the  $p < 0.05$  level ( $n = 3$ ).

According to Equation (1), the total Cd increased by 45.16%, 32.24%, and 21.10%, respectively, for EKR 1.0, EKR 0.8, and EKR 0.5. At the end of EKR experiment, in S1 and S3 sections, the total Cd decreased by 24.70% and 26.61%, respectively, for EKR 1.0; decreased by 16.45% and 18.93%, respectively, for EKR 0.8; and decreased by 8.64% and 15.80%, respectively, for EKR 0.5. The results evidenced that citric acid enhancement experiment significantly improved the migration of metals in a shorter time. The total Cd migration in the S1 and S2 sections was almost 2.5 times higher than that in the unenhanced EKR experiments (except for S3 section under EKR 0.5 treatment). Total Cd migration in the S2 section was almost four times higher than that in the unenhanced EKR experiments. The solubility and mobility of Cd ions were greatly enhanced following the EKR<sup>C</sup> progress. With a higher voltage gradient, the migration rate of Cd increased significantly. At the end of the EKR<sup>C</sup> experiment, the Cd concentrations in the S1 and S3 sections were lower than 0.6 mg kg<sup>-1</sup> at 1.0 V/cm voltage gradient, which met the requirements of the Chinese soil environmental quality standards.

The increase in Cd in S2 section was used as the target to analyze the electrical energy consumption per unit mass (Table 3). The energy consumption of EKR<sup>C</sup> 1.0 was 0.400 kWh kg<sup>-1</sup>, of EKR<sup>C</sup> 0.8 was 0.360 kWh kg<sup>-1</sup>, and of EKR<sup>C</sup> 0.5 was 0.230 kWh kg<sup>-1</sup>. In general, low voltage or electric current led to low energy consumption. However, the operating time was an important parameter, as it significantly influences decontamination efficiency and energy consumption. The shorter the operation time, the smaller the energy consumption [55]. Although EKR<sup>C</sup> 0.5 had the lowest energy consumption, the migration rate was too low to achieve the remediation of contaminated soil. Thus, the voltage gradient of 0.5 V/cm was not recommended as a solution. The energy consumption of EKR<sup>C</sup> 1.0 was slightly higher than that of EKR<sup>C</sup> 0.8. The results were generally satisfactory regarding the migration efficiency and the energy consumption at the two voltage gradients. In the future, the voltage gradient chosen for in situ remediation will depend on the distance between the anode and the cathode. For the larger distance between the electrode plates, the lower voltage gradient of 0.8 V/cm can be recommended for safety reasons [56]. If the distance between the electrode plates is around 27 cm, then the voltage gradient of 1.0 V/cm can be applied for the shorter time and the higher efficiency of remediation.

**Table 3.** The electrical energy consumption per unit mass ( $E_U$ ) for EKRC<sup>C</sup> experiment.

Treatment	the Mass of Increased Cd in S2 Section (kg)	$E_U$ (kWh kg <sup>-1</sup> )
EKR <sup>C</sup> 1.0	$2.51 \times 10^{-3}$	0.400
EKR <sup>C</sup> 0.8	$1.79 \times 10^{-3}$	0.360
EKR <sup>C</sup> 0.5	$1.17 \times 10^{-3}$	0.230

#### 4. Discussion

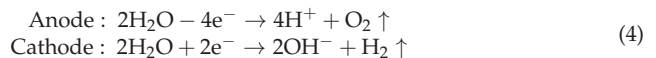
##### 4.1. Mechanisms and Functions of EKR with Polarity Reversal

The transport mechanisms of heavy metal pollutants between the electrodes include electromigration, electroosmosis, and electrophoresis, coupled with electrolysis reactions [57]. Electromigration is the movement of charged ions in soil under the pulsed electric fields. It is the dominant transport mechanism of inorganic contaminants. Metal cations move toward the cathode and anions toward the anode. The electromigration velocity ( $V_{em}$ ) is related to the electric gradient ( $E$ ), ionic valence ( $z$ ), the velocity of ionic mobility ( $u_i$ ), and the Ferrari constant ( $F$ ).

$$V_{em} = u_i z F E \quad (3)$$

Electroosmosis is the movement of soil pore fluid under the pulsed electric fields. Soil pore liquid carried out movement relative to the charged soil surface, and its movement direction is the same as the cation migration. Electrophoresis is the movement of charged particles or colloids under the pulsed electric fields. It has little effect on the movement of inorganic contaminants, and can be negligible in the EKR process.

During the EKR process, the electrolysis of water is an important reaction. As shown in Equation (4), the oxidation of water releases  $H^+$  ions at the anode zone, which contributes to desorb heavy metals from the soil. The reduction reaction of water releases  $OH^-$  ions at the cathode zone, which leads to the precipitation of heavy metals.



An electric field with polarity reversal was applied in this study. The anode and cathode were continuously exchanged during the EKR process. The  $H^+$  ions produced by electrolysis of water contributed to the desorption of Cd from the soil surface and released them into the soil liquid phase as free-moving ions, which increased the number of mobile ions in the EKR system. The ions were constantly migrating through the transport mechanisms of electromigration and electroosmosis. Cd ions showed reciprocal motion between cathode and anode. They migrated and accumulated in the S2 section. The Cd migration rate decreased with decreasing voltage gradient. On the other hand, the electric field with polarity reversal avoided the enrichment of  $H^+$  and  $OH^-$  ions in the soil, so that the soil zeta potential was not reduced, which facilitated the electroosmosis. The electrolysis of water was more intense, and the electroosmotic flow was higher, near the electrodes. On the contrary, the electrolysis of water was weaker in the S2 section away from the electrodes. Driven by transport mechanisms of electroosmotic, Cd ions advance from the area around the electrodes toward the S2 section. As shown in Figure 6, an electric field with polarity reversal helped to control the migration direction of Cd, thus allowing Cd to migrate directionally to specific areas.

##### 4.2. Effects of Soil Moisture on Electrokinetic Remediation

The thermal effect, as the energy losses accompanying the work carried out by electrical energy, is the most common mechanism. Ho et al. found that thermal effect due to temperature rise was not significant in bench-scale studies (less than 1 m in length) [58]. However, in field plot experiments, the voltage gradient more than 1 V/cm led to con-

siderable rise in the soil temperature which may not be neglected [59]. Saline–sodic soils were associated with high pH > 8.2. These properties made considerable rise in the soil temperature which may not be neglected during EKR process [60]. In this study, the differences in soil moisture contents among different voltage gradients were negligible (Figure 2). It meant that the higher voltage gradient did not have significant impact on the soil temperature and moisture. The reasons were mainly due to the bench-scale study and the neutral soil pH.

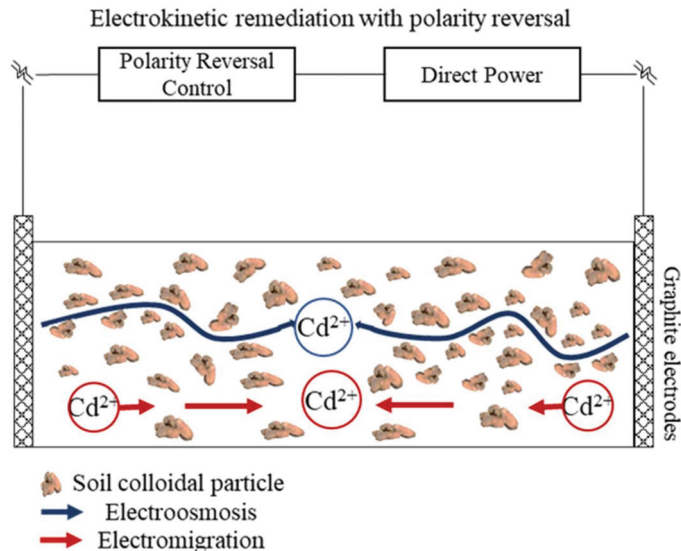


**Figure 6.** Transport mechanisms of Cd contaminants in the soil under EKR with polarity reversal.

It was found that high soil moisture could increase the current density to accelerate Cd contaminants migration. The lower limit of soil moisture for EKR was  $0.35 \text{ g g}^{-1}$ . Previous EKR studies have also indicated that the soil moisture influenced the dissolution rate and migration efficient of soil-mobilized Cd. Higher soil moisture enhanced the dissolved contaminant transport by ionic migration and electroosmosis, and hence improved removal efficiency [60]. Soil moisture complementation improved the diffusion and migration of Cd [61]. It can be assumed that higher soil moisture strengthened the current density, and had a positive effect on Cd migration.

#### 4.3. In Situ Electrokinetic-Assisted Phytoremediation Technology

EKR technology has been developed for remediating contaminated soil. In majority cases, it was proposed that the electrodes inserted into the electrolyte solutions, attached to the contaminated soils. Thus, the pollutants can be removed from the cathode [43,62]. However, setting up electrolyte cells for field applications can increase costs and operational difficulties. In this study, the electrodes were inserted vertically into the soils. EKR with polarity reversal was applied to achieve the migration and redistribution of Cd in the contaminated soil between the electrode plates. Before reversing the polarity, the S1 section was the anode where the oxidation of water produced  $\text{H}^+$  ions. After reversing the polarity, the former cathode (S3 section) would be the new anode, and Cd ions would migrate towards the new cathode. It had limited adverse effects on soil pH. The purpose of this study was to drive the enrichment of Cd contaminants to specific sites. The electromigration was the major mechanisms driving the movement of metals. Thus, EKR with polarity reversal were not limited to a single soil. It was also acceptable for both saturated and unsaturated soils and may have a wider significance.

Based on the above results, an innovative electrokinetic-assisted phytoremediation technology can be proposed. Phytoremediation was limited in practical applications due to its low efficiency. The pulsed electric fields could enhance the desorption of heavy metal contaminants from soil, and significantly improve the remediation efficiency. In recent years, the electrokinetic-assisted phytoremediation technology has been developed. By applying DC electric field, heavy metals were redistributed from anode to cathode in the soil. There was an enhancement of metal hyperaccumulator uptake near the cathode [63–65]. As mentioned in this study, the exchangeable phase of Cd was significantly enriched in the intermediate, where the hyperaccumulator could be planted to absorb the exchangeable Cd. A large number of hyperaccumulator species are available, such as lantana plant, sedum plumbizincicola, bulrush, and so on [6,66]. Based on the above, we can put forward a scheme of Cd-contaminated soil remediation during rice production process (Figure 7). The combined remediation technology can be conducted in paddy fields under CI irrigation [39]. As can be seen in Figure 7, in the field-scale application, the rice crop is planted near the electrodes, and hyperaccumulator is planted between two rows of rice plants. Before planting the rice, citric acid is added evenly into the surface soils at a concentration of  $0.1 \text{ mol L}^{-1}$  to improve metal solubility. EKR technology with polarity reversal should be conducted at soil gravimetric moisture content ranging from  $0.35 \text{ g g}^{-1}$  to full saturation to obtain a more desirable efficiency. The pulsed electric fields mimic the use of solar energy as a power source. The remediation was obtained during daytime and stopped through the nighttime. When using solar energy as a power source, the power-up circuit controller is used to boost the output voltage of the solar cell to meet the needs of the field experiments. The programmable logic controller can be programmed to automatically control pulsed electric fields and polarity reversal operations. The electrokinetic remediation runs in the daytime and stops at nighttime. The redistribution of Cd contaminants in soil can be expected. Cd contaminants migrate towards the soil section that between two rows of rice plants, where hyperaccumulator plants will take up more Cd contaminants. On the other hand, the removal of Cd and the low toxicity of the residue was achieved in soils close to the electrodes. Soil sections close to the electrodes were suitable for rice growth to avoid absorbing too much Cd contaminants.

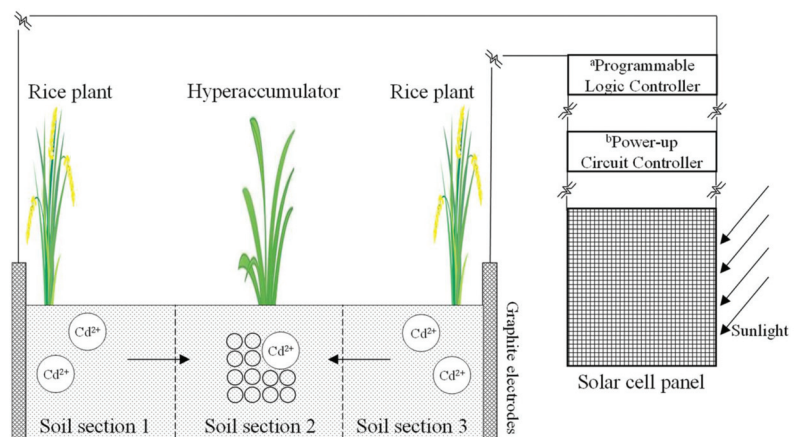


**Figure 7.** The electrokinetic-assisted phytoremediation technology of Cd-contaminated soil remediation during rice production process. <sup>a</sup> Programmable logic controller: with the functions of timing control and action sequence control, it can be programmed to automatically control pulsed electric fields and polarity exchanging operation. <sup>b</sup> Power-up circuit controller: boosting the output voltage of solar cell to meet the needs of field experiments.

Electrokinetic-assisted phytoremediation is a promising technology for soil environmental remediation. The significance of this study was to provide a theoretical basis. The combined remediation technology can be conducted during the rice production process. The methodology ensures the synchronization of purification of contaminated soil and safe production of rice crops. Briefly, the results of this paper provided strong theoretical supports for in situ electrokinetic remediation. It may offer a safe and cost-effective decontamination technique for Cd-contaminated soil. In the future, scaling up the EKR technique with polarity reversal, for field-scale applications, deserves further exploration.

## 5. Conclusions

The results showed that the application of electric fields with polarity reversal caused the migration of Cd contaminants from both ends of the soil compartment toward the intermediary section. In particular, the exchangeable phase of Cd was gathered in the middle area. Power should be supplied at a moisture content above  $0.35 \text{ g g}^{-1}$  to achieve reasonable performance. Preacidification of the soil with citric acid is an advisable enhancement strategy. The migration rate of Cd was proportional to voltage gradient. The application of citric acid at the voltage gradient of  $1.0 \text{ V/cm}$  or  $0.8 \text{ V/cm}$  appeared to be an advisable solution. The results provided strong theoretical supports for in situ electrokinetic remediation. The strategy is suitable to the remediation of mild-Cd-contaminated soil in paddy fields under control irrigation. Rice crop is planted near the electrodes to minimize the Cd contamination in grains. A hyperaccumulator can be planted between two rows of rice to absorb Cd contaminants. The proposed method provides a safe and cost-effective decontamination technique.

**Author Contributions:** Conceptualization, Y.L. (Yajun Luan) and J.X.; formal analysis, Y.L.; funding acquisition, J.X.; investigation, Y.L., J.Z. and K.W.; methodology, Y.L. (Yajun Luan) and J.X.; validation, J.X.; writing—original draft preparation, Y.L. (Yajun Luan) and H.W.; writing—review and editing, J.X., F.H. and Y.L. (Yuping Lv). All authors have read and agreed to the published version of the manuscript.

**Funding:** The research was financially supported by Jiangsu Provincial Key Research and Development Program (SBE2019310516).

**Institutional Review Board Statement:** Not applicable.

**Informed Consent Statement:** Not applicable.

**Data Availability Statement:** The datasets are available from the corresponding author on reasonable request.

**Conflicts of Interest:** We declare that we do not have any commercial or associative interest that represents a conflict of interest in connection with the work submitted.

## References

1. Tabelin, C.B.; Igarashi, T.; Villacorte-Tabelin, M.; Park, I.; Mopiso, E.; Ito, M.; Hiroyoshi, N. Arsenic, selenium, boron, lead, cadmium, copper, and zinc in naturally contaminated rocks: A review of their sources, modes of enrichment, mechanisms of release, and mitigation strategies. *Sci. Total Environ.* **2018**, *645*, 1522–1553. [[CrossRef](#)] [[PubMed](#)]
2. Cai, L.M.; Xu, Z.C.; Ren, M.Z.; Guo, Q.W.; Hu, X.B.; Hu, G.C.; Wan, H.F.; Peng, P.G. Source identification of eight hazardous heavy metals in agricultural soils of Huizhou, Guangdong Province, China. *Ecotox. Environ. Safte.* **2011**, *78*, 2–8. [[CrossRef](#)]
3. Rai, P.K.; Lee, S.S.; Zhang, M.; Tsang, Y.F.; Kim, K.H. Heavy metals in food crops: Health risks, fate, mechanisms, and management. *Environ. Int.* **2019**, *125*, 365–385. [[CrossRef](#)] [[PubMed](#)]
4. Oliva, S.R.; Espinosa, A.F. Monitoring of heavy metals in topsoils, atmospheric particles and plant leaves to identify possible contamination sources. *Microchem. J.* **2007**, *86*, 131–139. [[CrossRef](#)]
5. Tefera, W.; Tang, L.; Lu, L.L.; Xie, R.H.; Seifu, W.; Tian, S.K. Rice cultivars significantly mitigate cadmium accumulation in grains and its bioaccessibility and toxicity in human HL-7702 cells. *Environ. Pollut.* **2020**, *272*, 116020. [[CrossRef](#)]
6. Hussain, B.; Ashraf, M.N.; Shafeeq, R.; Abbas, A.; Li, J.M.; Farooq, M. Cadmium stress in paddy fields: Effects of soil conditions and remediation strategies. *Sci. Total Environ.* **2021**, *754*, 142188. [[CrossRef](#)]
7. Komárek, M.; Vaněk, A.; Ettler, V. Chemical stabilization of metals and arsenic in contaminated soils using oxides—A review. *Environ. Pollut.* **2013**, *172*, 9–22. [[CrossRef](#)]

8. Liu, L.W.; Li, W.; Song, W.P.; Guo, M.X. Remediation techniques for heavy metal-contaminated soils: Principles and applicability. *Sci. Total Environ.* **2018**, *633*, 206–219. [[CrossRef](#)]
9. Tang, J.; Qiu, Z.P.; Tang, H.J.; Wang, H.Y.; Sima, W.P.; Liang, C.; Li, Z.H.; Wan, S.; Dong, J.W. Coupled with EDDS and approaching anode technique enhanced electrokinetic remediation removal heavy metal from sludge. *Environ. Pollut.* **2020**, *272*, 115975. [[CrossRef](#)]
10. Wang, Y.C.; Han, Z.J.; Li, A.; Cui, C.W. Enhanced electrokinetic remediation of heavy metals contaminated soil by biodegradable complexing agents. *Environ. Pollut.* **2021**, *283*, 117111. [[CrossRef](#)]
11. Guo, F.Y.; Ding, C.F.; Zhou, Z.G.; Han, F.X.; Tang, R.G.; Huang, G.X.; Wang, X.X. Assessment of the immobilization effectiveness of several amendments on a cadmium-contaminated soil using *Eisenia fetida*. *Ecotox. Environ. Saf.* **2019**, *189*, 109948. [[CrossRef](#)] [[PubMed](#)]
12. Huang, T.; Liu, L.F.; Zhou, L.L.; Zhang, S.W. Electrokinetic removal of chromium from chromite ore-processing residue using graphite particle-supported nanoscale zero-valent iron as the three-dimensional electrode. *Chem. Eng. J.* **2018**, *350*, 1022–1034. [[CrossRef](#)]
13. Alka, S.; Shahir, S.; Ibrahim, N.; Ndejiko, M.J.; Vo, D.-V.N.; Manan, F.A. Arsenic Removal Technologies And Future Trends: A Mini Review. *J. Clean Prod.* **2020**, *278*, 123805. [[CrossRef](#)]
14. Giannis, A.; Gidarakos, E.; Skouta, A. Transport of cadmium and assessment of phytotoxicity after electrokinetic remediation. *J. Environ. Manag.* **2008**, *86*, 535–544. [[CrossRef](#)]
15. Kochian, L.V.; Hoekenga, O.A.; Pineros, M.A. How do crop plants tolerate acid soils? Mechanisms of aluminum tolerance and phosphorous efficiency. *Annu. Rev. Plant Biol.* **2004**, *55*, 459–493. [[CrossRef](#)]
16. Sojka, R.E.; Bjorneberg, D.L.; Entry, J.A.; Lentz, R.D.; Orts, W.J. Polyacrylamide in agriculture and environmental land management. *Adv. Agron.* **2007**, *92*, 75–162. [[CrossRef](#)]
17. Page, K.L.; Dalal, R.C.; Wehr, J.B.; Dang, Y.P.; Kopittke, P.M.; Kirchoff, G.; Fujinuma, R.; Menzies, N.W. Management of the major chemical soil constraints affecting yields in the grain growing region of Queensland and New South Wales. Australia—a review. *Soil Res.* **2018**, *56*, 765–779. [[CrossRef](#)]
18. Batty, L.C.; Dolan, C. The Potential Use of Phytoremediation for Sites with Mixed Organic and Inorganic Contamination. *Crit. Rev. Environ. Sci. Technol.* **2013**, *43*, 217–259. [[CrossRef](#)]
19. Saichek, R.E.; Reddy, K.R. Effect of pH control at the anode for the electrokinetic removal of phenanthrene from kaolin soil. *Chemosphere* **2003**, *51*, 273–287. [[CrossRef](#)]
20. Zhou, D.M.; Deng, C.F.; Cang, L. Electrokinetic remediation of a Cu contaminated red soil by conditioning catholyte pH with different enhancing chemical reagents. *Chemosphere* **2004**, *56*, 265–273. [[CrossRef](#)]
21. Zhou, D.M.; Deng, C.F.; Alshawabkeh, A.N.; Cang, L. Effects of catholyte conditioning on electrokinetic extraction of copper from mine tailings. *Environ. Int.* **2005**, *31*, 885–890. [[CrossRef](#)] [[PubMed](#)]
22. Souilah, O.; Akretche, D.E.; Cameselle, C. Electroremediation of contaminated soil by heavy metals using ion exchange fibers. *Electrochim. Acta* **2012**, *86*, 138–141. [[CrossRef](#)]
23. Huang, W.Y.; Hung, W.; Vu, C.T.; Chen, W.T.; Lai, J.W.; Lin, C. Green and sustainable remediation (GSR) evaluation: Framework, standards, and tool. A case study in Taiwan. *Environ. Sci. Pollut. Res.* **2016**, *23*, 21712–21725. [[CrossRef](#)] [[PubMed](#)]
24. Gidudu, B.; Chirwa, E.M.N. The combined application of a high voltage, low electrode spacing, and biosurfactants enhances the bio-electrokinetic remediation of petroleum contaminated soil. *J. Clean Prod.* **2020**, *276*, 122745. [[CrossRef](#)]
25. Rozas, F.; Castellote, M. Selecting enhancing solutions for electrokinetic remediation of dredged sediments polluted with fuel. *J. Environ. Manag.* **2015**, *151*, 153–159. [[CrossRef](#)] [[PubMed](#)]
26. Asadollahfardi, G.; Sarmadi, M.S.; Rezaee, M.; Khodadadi-Darban, A.; Yazdani, M.; Paz-Garcia, J.M. Comparison of different extracting agents for the recovery of Pb and Zn through electrokinetic remediation of mine tailings. *J. Environ. Manag.* **2021**, *279*, 111728. [[CrossRef](#)]
27. Kim, K.J.; Kim, D.H.; Yoo, J.C.; Baek, K. Electrokinetic extraction of heavy metals from dredged marine sediment. *Sep. Purif. Technol.* **2011**, *79*, 164–169. [[CrossRef](#)]
28. Wu, J.; Zhang, J.; Xiao, C. Focus on factors affecting pH, flow of Cr and transformation between Cr(VI) and Cr(III) in the soil with different electrolytes. *Electrochim. Acta* **2016**, *211*, 652–662. [[CrossRef](#)]
29. Zhang, Y.J.; Chu, G.H.; Dong, P.; Xiao, J.; Meng, Q.; Baumgartel, M.; Hao, T. Enhanced electrokinetic remediation of lead- and cadmium-contaminated paddy soil by composite electrolyte of sodium chloride and citric acid. *J. Soils Sediments* **2017**, *18*, 1915–1924. [[CrossRef](#)]
30. Xie, N.; Chen, Z.; Wang, H.M.; You, C.F. Activated carbon coupled with citric acid in enhancing the remediation of Pb-contaminated soil by electrokinetic method. *J. Clean Prod.* **2021**, *308*, 127433. [[CrossRef](#)]
31. Nasiri, A.; Jamshidi-Zanjani, A.; Darban, A.K. Application of enhanced electrokinetic approach to remediate Cr-contaminated soil: Effect of chelating agents and permeable reactive barrier. *Environ. Pollut.* **2020**, *266*, 115197. [[CrossRef](#)] [[PubMed](#)]
32. Pazos, M.; Sanroman, M.A.; Cameselle, C. Improvement in electrokinetic remediation of heavy metal spiked kaolin with the polarity exchange technique. *Chemosphere* **2006**, *62*, 817–822. [[CrossRef](#)] [[PubMed](#)]
33. Zhou, M.; Xu, J.M.; Zhu, S.F.; Wang, Y.J.; Gao, H. Exchange electrode-electrokinetic remediation of Cr-contaminated soil using solar energy. *Sep. Purif. Technol.* **2018**, *190*, 297–306. [[CrossRef](#)]

34. Mao, X.Y.; Shao, X.H.; Zhang, Z.Y. Pilot-scale electro-kinetic remediation of lead polluted field sediments: Model designation, numerical simulation, and feasibility evaluation. *Environ. Sci Eur.* **2019**, *31*, 25. [[CrossRef](#)]
35. Xu, Y.F.; Xu, X.J.; Hou, H.T.; Zhang, J.; Zhang, D.Y.; Qian, G.R. Moisture content-affected electrokinetic remediation of Cr(VI)-contaminated clay by a hydrocalumite barrier. *Environ. Sci. Pollut. Res.* **2015**, *23*, 6517–6523. [[CrossRef](#)] [[PubMed](#)]
36. Cameselle, C.; Gouveia, S.; Cabo, A. Analysis and Optimization of Mn Removal from Contaminated Solid Matrixes by Electrokinetic Remediation. *Int. J. Environ. Res. Public Health* **2020**, *17*, 1820. [[CrossRef](#)] [[PubMed](#)]
37. Liu, X.Y.; Yang, S.H.; Xu, J.Z.; Zhang, J.G.; Liu, J.T. Effects of soil heat storage and phase shift correction on energy balance closure of paddy fields. *Atmosfera* **2017**, *30*, 39–52. [[CrossRef](#)]
38. Wu, M.Y.; Cao, X.C.; Guo, X.P.; Xiao, J.F.; Ren, J. Assessment of grey water footprint in paddy rice cultivation: Effects of field water management policies. *J. Clean Prod.* **2021**, *313*, 127876. [[CrossRef](#)]
39. Chen, P.; Nie, T.Z.; Chen, S.H.; Zhang, Z.X.; Qi, Z.J.; Liu, W.N. Recovery efficiency and loss of 15N-labelled urea in a rice-soil system under water saving irrigation in the Songnen Plain of Northeast China. *Agric. Water Manag.* **2019**, *222*, 139–153. [[CrossRef](#)]
40. Wei, Q.; Liu, J.T.; Peng, Y.H.; Xu, J.Z.; Liao, L.X.; Yang, S.H. Storing and removing nitrogen in drainage from paddy field by using aquatic crops wetland. *Paddy Water Environ.* **2020**, *18*, 587–594. [[CrossRef](#)]
41. Liu, X.M.; Zhong, L.B.; Meng, J.; Wang, F.; Zhang, J.J.; Zhi, Y.Y.; Zeng, L.Z.; Tang, X.J.; Xu, J.M. A multi-medium chain modeling approach to estimate the cumulative effects of cadmium pollution on human health. *Environ. Pollut.* **2018**, *239*, 308–317. [[CrossRef](#)] [[PubMed](#)]
42. Wang, F.; Guan, Q.; Tian, J.; Lin, J.; Yang, Y.; Yang, L.; Pan, N. Contamination characteristics, source apportionment, and health risk assessment of heavy metals in agricultural soil in the Hexi Corridor. *Catena* **2020**, *191*, 104573. [[CrossRef](#)]
43. Hansen, H.K.; Rojo, A. Testing pulsed electric fields in electroremediation of copper mine tailings. *Electrochim. Acta* **2007**, *52*, 3399–3405. [[CrossRef](#)]
44. Wang, Y.C.; Li, A.; Cui, C.W. Remediation of heavy metal-contaminated soils by electrokinetic technology: Mechanisms and applicability. *Chemosphere* **2020**, *265*, 129071. [[CrossRef](#)]
45. He, S.Y.; Yang, X.; He, Z.L.; Baligar, V.C. Morphological and Physiological Responses of Plants to Cadmium Toxicity: A Review. *Pedosphere* **2017**, *27*, 421–438. [[CrossRef](#)]
46. Cameselle, C.; Pena, A. Enhanced electromigration and electro-osmosis for the remediation of an agricultural soil contaminated with multiple heavy metals. *Process Saf. Environ. Protect.* **2016**, *104*, 209–217. [[CrossRef](#)]
47. Meng, F.S.; Xue, H.; Wang, Y.Y.; Zheng, B.H.; Wang, J.L. Citric-acid preacidification enhanced electrokinetic remediation for removal of chromium from chromium-residue-contaminated soil. *Environ. Technol.* **2017**, *39*, 356–362. [[CrossRef](#)]
48. Laurent, J.P.; Ruelle, P.; Delage, L.; Zairi, A.; Nouna, B.B.; Adjmi, T. Monitoring soil water content profiles with a commercial TDR system. *Vadose Zone J.* **2005**, *4*, 1030–1036. [[CrossRef](#)]
49. Baek, K.; Kim, D.H.; Park, S.W.; Ryu, B.G.; Bajargal, T.; Yang, J.S. Electrolyte conditioning-enhanced electrokinetic remediation of arsenic-contaminated mine tailing. *J. Hazard. Mater.* **2009**, *161*, 457–462. [[CrossRef](#)]
50. Iannelli, R.; Masi, M.; Ceccarini, A.; Ostuni, M.B.; Lageman, R.; Muntoni, A.; Spiga, D.; Poletti, A.; Marini, A.; Pomi, R. Electrokinetic remediation of metal-polluted marine sediments: Experimental investigation for plant design. *Electrochim. Acta* **2015**, *181*, 146–159. [[CrossRef](#)]
51. Fernández-Ondoño, E.; Bacchetta, G.; Lallena, A.M.; Navarro, F.B.; Ortiz, I.; Jiménez, M.N. Use of BCR sequential extraction procedures for soils and plant metal transfer predictions in contaminated mine tailings in Sardinia. *J. Geochem. Explor.* **2017**, *172*, 133–141. [[CrossRef](#)]
52. Janowska, B.; Szymanski, K.; Sidelko, R.; Siebielska, I.; Walendzik, B. Assessment of mobility and bioavailability of mercury compounds in sewage sludge and composts. *Environ. Res.* **2017**, *156*, 394–403. [[CrossRef](#)] [[PubMed](#)]
53. Luo, X.S.; Yu, S.; Li, X.D. The mobility, bioavailability, and human bioaccessibility of trace metals in urban soils of Hong Kong. *Appl. Geochem.* **2012**, *27*, 995–1004. [[CrossRef](#)]
54. Kirkelund, G.M.; Ottosen, L.M.; Villumsen, A. Investigations of Cu, Pb and Zn partitioning by sequential extraction in harbour sediments after electro-dialytic remediation. *Chemosphere* **2010**, *79*, 997–1002. [[CrossRef](#)]
55. Krcmar, D.; Varga, N.; Prica, M.; Cveticanin, L.; Zukovic, M.; Dalmacija, B.; Corba, Z. Application of hexagonal two dimensional electrokinetic system on the nickel contaminated sediment and modelling the transport behavior of nickel during electrokinetic treatment. *Sep. Purif. Technol.* **2018**, *192*, 253–261. [[CrossRef](#)]
56. Zhuang, Y.F. Large scale soft ground consolidation using electrokinetic geosynthetics. *Geotext. Geomembr.* **2021**, *49*, 757–770. [[CrossRef](#)]
57. Wen, D.; Fu, R.; Li, Q. Removal of inorganic contaminants in soil by electrokinetic remediation technologies: A review. *J. Hazard. Mater.* **2020**, *401*, 123345. [[CrossRef](#)]
58. Ho, S.V.; Athmer, C.J.; Sheridan, P.W.; Shapiro, A.P. Scale-up aspects of the Lasagna process for in situ soil decontamination. *J. Hazard. Mater.* **1997**, *55*, 39–60. [[CrossRef](#)]
59. Tang, X.; Li, Q.; Wang, Z.; Hu, Y.; Hu, Y.; Li, R. In situ electrokinetic isolation of cadmium from paddy soil through pore water drainage: Effects of voltage gradient and soil moisture. *Chem. Eng. J.* **2018**, *337*, 210–219. [[CrossRef](#)]
60. Lukman, S.; Essa, M.H.; Mu'azu, N.D.; Bukhari, A. Coupled electrokinetics-adsorption technique for simultaneous removal of heavy metals and organics from saline-sodic soil. *Sci. World J.* **2013**, *2013*, 346910. [[CrossRef](#)]



61. Cherifi, M.; Hazourli, S.; Ziati, M. Initial water content and temperature effects on electrokinetic removal of aluminium in drinking water sludge. *Phys. Procedia* **2009**, *2*, 1021–1030. [[CrossRef](#)]
62. Luo, J.; Cai, L.M.; Qi, S.H.; Wu, J.; Gu, X.W.S. The interactive effects between chelator and electric fields on the leaching risk of metals and the phytoremediation efficiency of *Eucalyptus globulus*. *J. Clean Prod.* **2018**, *202*, 830–837. [[CrossRef](#)]
63. Sarwar, N.; Imran, M.; Shaheen, M.R.; Ishaque, W.; Kamran, M.A.; Matloob, A.; Rehim, W.; Hussain, S. Phytoremediation strategies for soils contaminated with heavy metals: Modifications and future perspectives. *Chemosphere* **2017**, *171*, 710–721. [[CrossRef](#)] [[PubMed](#)]
64. Sánchez, V.; López-Bellido, F.J.; Cañizares, P.; Rodríguez, L. Can electrochemistry enhance the removal of organic pollutants by phytoremediation? *J. Environ. Manag.* **2018**, *225*, 280–287. [[CrossRef](#)]
65. Wan, Y.A.; Huang, Q.Q.; Wang, Q.; Yu, Y.; Su, D.C.; Qiao, Y.H.; Li, H.F. Accumulation and bioavailability of heavy metals in an acid soil and their uptake by paddy rice under continuous application of chicken and swine manure. *J. Hazard. Mater.* **2020**, *384*, 121293. [[CrossRef](#)]
66. He, L.P.; Liu, D.; Lin, J.J.; Yu, Z.G.; Yang, X.X.; Fu, C.; Zheng, X.L.; Zhao, Q.H. Total nitrogen and pH-controlled chemical speciation, bioavailability and ecological risk from Cd, Cr, Cu, Pb and Zn in the water level-fluctuating zone sediments of the Three Gorges Reservoir. *Chem. Speciation Bioavail.* **2017**, *29*, 89–96. [[CrossRef](#)]



Article

# Dynamic Driving Mechanism of Dual Structural Effects on the Correlation between Economic Growth and CO<sub>2</sub> Emissions: Evidence from a Typical Transformation Region

Yu Cai <sup>1,2,†</sup>, Haiyan Duan <sup>1,\*,†</sup>, Zhiqiang Luo <sup>3</sup>, Zhiyuan Duan <sup>1,\*</sup> and Xian'en Wang <sup>1</sup>

<sup>1</sup> College of New Energy and Environment, Jilin University, Changchun 130012, China; cai.yu@sljg.mee.gov.cn (Y.C.); wxen@jlu.edu.cn (X.W.)

<sup>2</sup> Songliao River Basin Ecology and Environment Administration, Ministry of Ecology and Environment, Changchun 130021, China

<sup>3</sup> Energy and Food Integrated Administrative Enforcement Detachment of Jinan City, Jinan 250000, China; mathilde9007@163.com

\* Correspondence: duanhy1980@jlu.edu.cn (H.D.); duanzy18@mails.jlu.edu.cn (Z.D.)

† These authors contributed equally to this work.

**Abstract:** How will the dual structural effects, represented by industrial structure and energy structure, affect the future correlation between economic growth and CO<sub>2</sub> emissions? Taking Jilin Province as an example, this study explores the dynamic driving mechanism of dual structural effects on the correlation between economic growth and CO<sub>2</sub> emissions by innovatively building an integrated simulation model from 1995 to 2015 and setting different scenarios from 2016 to 2050. Correspondingly, the concept of marginal utility and the method of variance decomposition analysis are introduced to reveal the mechanism. The results show that the energy structure is different while the industrial structure tends to be similar when CO<sub>2</sub> emissions reach the peak under different scenarios. The slower the dual structure adjustment, the more significant the upward trend appears before the peak. The contribution of the dual structural effects to CO<sub>2</sub> emissions caused by unit GDP growth is basically the same in peak year. With the transformation of socio-economy, the positive driving effect of the industrial structure will gradually weaken, while the negative driving effect of the energy structure will gradually increase. The methods and results presented can provide insights into sensible trade-offs of CO<sub>2</sub> emissions and economic growth in different countries/regions during structural transitions.

**Citation:** Cai, Y.; Duan, H.; Luo, Z.; Duan, Z.; Wang, X. Dynamic Driving Mechanism of Dual Structural Effects on the Correlation between Economic Growth and CO<sub>2</sub> Emissions: Evidence from a Typical Transformation Region. *Int. J. Environ. Res. Public Health* **2022**, *19*, 3970. <https://doi.org/10.3390/ijerph19073970>

Academic Editors: Roberto Alonso González Lezcano, Francesco Nocera and Rosa Giuseppina Caponetto

Received: 15 January 2022

Accepted: 23 March 2022

Published: 26 March 2022

**Publisher's Note:** MDPI stays neutral with regard to jurisdictional claims in published maps and institutional affiliations.



**Copyright:** © 2022 by the authors. Licensee MDPI, Basel, Switzerland. This article is an open access article distributed under the terms and conditions of the Creative Commons Attribution (CC BY) license (<https://creativecommons.org/licenses/by/4.0/>).

**Keywords:** driving mechanism; CO<sub>2</sub> emissions; economic growth; dual structural effects; marginal utility; transformation region

## 1. Introduction

While the development of industrialization and urbanization has promoted the development of economic globalization, it has also exacerbated the climate change crisis caused by the increase in CO<sub>2</sub> emissions that stem largely from energy consumption. In the global context of tackling climate change, how to effectively suppress CO<sub>2</sub> emissions while promoting economic growth has become a challenge that most countries are facing in the development process. The Paris Agreement, which entered into force in 2016, is a legally binding global emission reduction agreement that plans the global climate governance pattern after 2020. Different countries and regions have accordingly proposed specific action plans for CO<sub>2</sub> emission reduction based on the principle of common but differentiated responsibilities, in order to achieve the pursuit of economic development and emission reduction synergistically.

In recent years, research on the relationship between economic growth and CO<sub>2</sub> emissions has been increasing drastically. In terms of research methods, the related literature

can be classified into four categories. The first category explores the contribution of the influencing factors of CO<sub>2</sub> emissions including economic scale through decomposition models. Since the logarithmic mean Divisia index (LMDI) method has the advantages of path independence and provides perfect decomposition results without residual terms [1], it has been widely adopted in the decomposition analysis regarding CO<sub>2</sub> emissions, and most studies have demonstrated that economic growth is the main contributor to the increase in CO<sub>2</sub> emissions. For example, Ma et al. [2] took advantage of the LMDI method to quantify the driving factors of CO<sub>2</sub> emissions in China from 2005 to 2016, showing that rapid economic growth is the most important reason for the increase in CO<sub>2</sub> emissions. Du et al. [3] identified the drivers of changes in energy-related CO<sub>2</sub> emissions of high-energy intensive industries in China during 1986–2013 based on the LMDI method, verifying that the expansion of economic scale was the leading force explaining why CO<sub>2</sub> emissions increased. In addition, Dong et al. [4] and Wang et al. [5] also confirmed that economic output was the dominantly positive driving factor of CO<sub>2</sub> emissions by using the LMDI model.

The second category is the quantitative or qualitative analysis of the impacts of the factors including economic growth on CO<sub>2</sub> emissions through econometrics and statistical models. Quantitative analysis models mainly reflect the influence degree and influence direction through fitting model coefficients, including the stochastic impacts by regression on population, affluence and technology (STIRPAT) model [3,6,7], the vector autoregressive (VAR) model [8,9], the autoregressive distributed lag (ARDL) model [10,11], the generalized method of moments (GMM) model [12,13], etc. For example, Li et al. [6] used the STIRPAT model to investigate the effect of the rationalization and upgrading of manufacturing structure on CO<sub>2</sub> emissions in China, and the simulation coefficients show that the greater the ratio of industrial output to GDP, the weaker the restricting effect of resource dependence on the emissions reduction of manufacturing structure. The qualitative analysis models such as the vector error correction model (VECM) and Granger causality analysis mainly explain the relationship between economic growth and CO<sub>2</sub> emissions by judging the causal relationship. Jian et al. [14] applied VECM to investigate the long-term equilibrium and short-term causality relationship among influencing factors and CO<sub>2</sub> emissions, and the results show the long-term cointegration relationship between them. Mirza et al. [15] used VECM to explore the existence of Grangers' long run, short run and strong causalities between economic growth, energy consumption and CO<sub>2</sub> emissions for Pakistan.

The third category investigates the relationship between economic growth and CO<sub>2</sub> emissions based on the EKC model. Compared with other methods that qualitatively determine the causality between variables or quantitatively determine the degree of impact by calculating model coefficients, the EKC proposed by Grossman and Krueger can better reflect the dynamic relationship between economic growth and CO<sub>2</sub> emissions at different stages of economic development [16]. The results of some studies conform to the EKC hypothesis characterized by an inverted U-shape [5,17,18], while others do not, showing an N-shaped [19–21] or even M-shaped, curve [22]. In general, the reasons leading to this phenomenon lie in three aspects. The first reason is the difference in the study objects and corresponding time series data. Most of these studies showed that the relationship between economic growth and CO<sub>2</sub> emissions in underdeveloped regions does not meet the EKC hypothesis compared with developed regions [23,24]. Besides, specific time periods parallel specific socioeconomic conditions, leading to different results even for the same research object [5,8]. The second reason stems from whether gross domestic product (GDP), as an independent variable, is quadratic or cubic when building the model [25,26]. The last reason derives mainly from different methods for estimating the coefficients of the model, among which FMOLS, DOLS and ARDL have been most commonly used [27–29].

The fourth category detects the decoupling relationship between economic growth and CO<sub>2</sub> emissions based on the Tapio decoupling model. The determination of the decoupling relationship is achieved by calculating the decoupling elasticity, which can be specifically expressed as strong decoupling, weak decoupling, expansive coupling, negative decoupling, strong negative decoupling and so on [30]. Wu et al. [31] conducted a Tapio

decoupling analysis of economic growth and CO<sub>2</sub> emissions with reference to 30 Chinese provinces from 2001 to 2015, finding that there is a strong decoupling relation between GDP and CO<sub>2</sub> emissions. Taking Beijing and Shanghai from 2005 to 2015 as examples, Wang et al. [32] used decoupling analysis to explore the relationship between sectoral economic output and carbon emissions. Both cities experienced weak decoupling in construction, expansive negative decoupling in transport and expansive coupling in trade.

In terms of research object, it can be basically divided into developed or developing countries or regions from the perspective of development level. Among them, the discussions with regard to developed countries have not been frequently seen, and most of the related studies aim to verify that economic growth and CO<sub>2</sub> emissions are in line with the EKC hypothesis [33,34]. Conversely, more empirical studies with developing countries as targets, especially China, have been extensively conducted. In terms of research content, it involves sector perspectives such as construction sector [35,36], transportation sector [37], manufacture sector [38], etc., or sub-region perspectives such as Beijing [39,40], Shanghai [41] and other provincial regions.

There are two deficiencies in the reviewed studies. The first one is the lack of explanation of what causes the dynamic changes in the correlation between economic growth and CO<sub>2</sub> emissions. As discussed above, the majority of the studies only quantified the impact of economic growth as one of the influencing factors on CO<sub>2</sub> emissions, or analyzed the correlation between economic growth on CO<sub>2</sub> emissions from the perspective of EKC hypothesis and decoupling status. Very few studies explored what factors drive the formation of the correlation, especially with a focus on the dynamic impacts of structural effects on the correlation. As mentioned by Grossman and Krueger [42], structural effects, including the effects of both industrial structure and energy structure, have important impacts on economic growth and CO<sub>2</sub> emissions. They are indispensable factors to conduct a comprehensive analysis of the driving mechanism of CO<sub>2</sub> emissions.

The second deficiency is the lack of research on the traditional industrial regions, which refer to those whose industrial structure is dominated by traditional industrial sectors (such as steel, machinery or electricity). These regions are currently undergoing industrialization, but in a desperate need for transformation in the pattern of economic development from the originally traditional industrial mode to a modern development mode. The structural characteristics of such regions are generally reflected in two aspects. The industrial structure has begun to transit from high-energy-consuming and high-emitting traditional industries toward service and emerging industries, but the main driving force of economic development is still traditional industries. The energy structure has begun to transit from coal to oil, gas and renewable energy, but it is still dominated by coal consumption, with relatively lower energy efficiency. Many countries and regions in the world have experienced this transformation stage, such as the Ruhr area in Germany, the central part of the United Kingdom, and the Great Lakes area in the northeast of the United States. More developing regions are now undergoing such a stage. On the one hand, different from developed regions, such regions generally face the dual pressures of CO<sub>2</sub> emission reduction while promoting high-quality economic growth. On the other hand, CO<sub>2</sub> emission reduction practices in such regions play a critical role in reducing global CO<sub>2</sub> emissions due to their large emission reduction potential.

Therefore, there are some questions that have not yet been thoroughly discussed in previous studies, especially for the large number of traditional industrial regions experiencing transformation in the world represented by China, that is, how will the dual structural effects, represented by industrial structure and energy structure, affect the future correlation between economic growth and CO<sub>2</sub> emissions? To what extent should industrial structure and energy structure be adjusted to make CO<sub>2</sub> emissions decouple from GDP growth? In-depth research on these issues is conducive to providing a path reference for carbon emission reduction in these regions while ensuring stable economic development.

To fill the gaps, this study selects Jilin Province, a typical transformation region in the Northeast China as the empirical target. First, we built an integrated simulation model

based on the evolution of various factors from 1995 to 2015. The indicator CO<sub>2</sub> emission intensity (CEI) (CO<sub>2</sub> emissions per unit GDP) functions as a bridge connecting economic growth and CO<sub>2</sub> emissions, on which basis we decomposed CEI into multiple factors through the Kaya identity and transformed the simulation model to contain only structural effects by the dynamic ordinary least squares (DOLS) method. Secondly, we simulated the correlation between economic growth and CO<sub>2</sub> emissions, and the peaking pathways of CO<sub>2</sub> emissions in four different scenarios were set according to different development patterns from 2016 to 2050. Finally, through introducing the concepts of marginal utility and total utility, we took advantage of variance decomposition analysis (VDA) based on the VAR model to explore the impacts of dual structural effects on the correlation between economic growth and CO<sub>2</sub> emissions. The methods and results of the study are expected to provide reference for coordinating economic growth and CO<sub>2</sub> emissions in the underdeveloped countries/regions undergoing structural transformation, especially in the context of CO<sub>2</sub> emission reduction globally.

## 2. Methods

### 2.1. Integrated Simulation Model

In this study, an integrated simulation model is built based on the interaction among the socioeconomic, industrial, energy and emission variables, as shown in Figure 1.

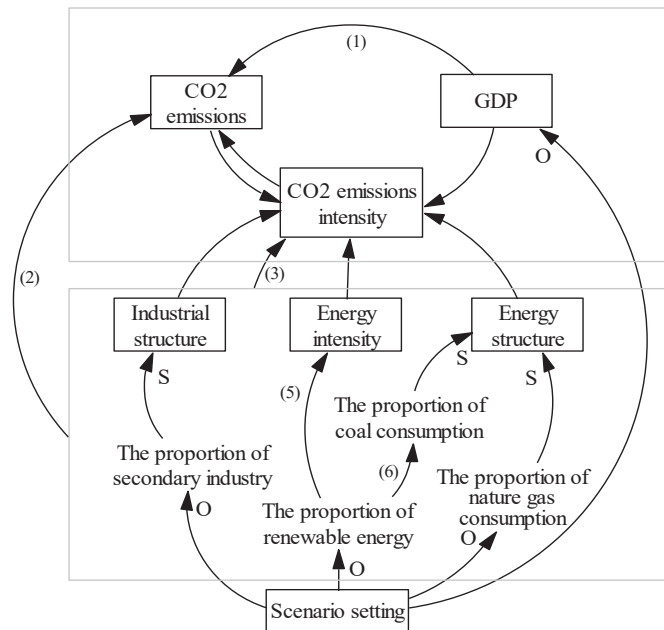


**Figure 1.** Integrated simulation modelling framework. (The numbers in the figure are consistent with the corresponding equations in the main context. Arrows without letters represent quantitative relationships; arrows with “S” represent representational relationships; arrows with “O” represent coverage relationships.)

This study uses a quadratic expression derived from the EKC modelling framework to analyze the correlation between economic growth represented by *GDP* and CO<sub>2</sub> emissions [16], as expressed in Equation (1).

$$\ln CO_2 = \alpha_0 + \alpha_1 \ln GDP_{it} + \alpha_2 \ln GDP_{it}^2 + \lambda_{it} \tag{1}$$

The prediction of CO<sub>2</sub> emissions is innovatively based on the combination of GDP and CEI. The prediction of the latter is based on the Kaya identity [43], which is built incorporating the influencing factors including industrial structure (IS) and energy structure (ES). By expanding the Kaya identity, CO<sub>2</sub> emissions can be expressed as Equation (2).

$$CO_2 = \sum_{ij} CO_{2,ij} = \sum_{ij} GDP \frac{GDP_i}{GDP} \frac{E_i}{GDP_i} \frac{E_{ij}}{E_i} \frac{CO_{2,ij}}{E_{ij}} = \sum_{ij} GDP \cdot IS_i \cdot EI_i \cdot ES_{ij} \cdot f_{ij} \quad (2)$$

where *E* denotes total energy consumption, *i* denotes the type of industry (primary industry, secondary industry or tertiary industry), *j* denotes the type of fossil energy (coal, oil or natural gas), *IS* denotes industrial structure of a region (the proportion of an industry's added value in GDP), *FEI* denotes fossil energy intensity of an industry (fossil energy consumed by unit added value of an industry), *ES* denotes energy structure of an industry (the proportion of a type of fossil energy in total energy consumption), and *f* denotes CO<sub>2</sub> emission coefficient (CO<sub>2</sub> emissions of unit fossil energy consumption).

By transforming Equation (2), CEI can be expressed as:

$$CI = \frac{CO_2}{GDP} = \sum_{ij} \frac{GDP_i}{GDP} \frac{E_i}{GDP_i} \frac{E_{ij}}{E_i} \frac{CO_{2,ij}}{E_{ij}} = \sum_{ij} IS_i \cdot EI_i \cdot M_{ij} \cdot U_{ij} \quad (3)$$

According to Equation (3), CEI is closely related to industrial structure, FEI and energy structure. Since the primary industry represented by agriculture may remain stable without dramatic changes in the long run according to the national policy, the proportion of secondary industry's added value in GDP (*SI*) is used to characterize industrial structure. The proportions of coal consumption (CC) and natural gas consumption (NG) in total energy consumption are used to characterize energy structure. Equation (3) can be extended after the logarithmization processing as Equation (4):

$$\ln CI = a \ln SI + b \ln EI + c \ln CC + d \ln NG + e \quad (4)$$

Based on the assumption that the use of renewable energy will effectively reduce FEI and coal consumption, the relationship between the proportion of renewable energy (RN) and FEI or CC is expressed as Equations (5) and (6), based on which Equation (4) can be further expressed as Equation (7).

$$\ln EI = m \ln RN + \delta_1 \quad (5)$$

$$\ln CC = n \ln RN + \delta_2 \quad (6)$$

$$\ln CI = a' \ln SI + b' \ln RN + c' \ln NG + \lambda \quad (7)$$

where *a*, *b*, *c*, *d*, *m*, *n*, *a'*, *b'* and *c'* are fitting parameters, and *e*, *δ*<sub>1</sub>, *δ*<sub>2</sub> and *λ* are error terms.

Attributed to the capability of eliminating the endogeneity in regression and the sequence correlation in error terms [44], the dynamic ordinary least squares (DOLS) method is used for parameter estimation.

## 2.2. Marginal Utility, Total Utility and Variance Decomposition Analysis

In order to quantitatively analyze the impacts of structural effects on the correlation between GDP and CO<sub>2</sub> emissions, the concepts of marginal utility (MU) and total utility (TU) in economics are introduced [45], as shown in Equation (8).

$$MU = f(TU) = \Delta TU / \Delta Q \quad (8)$$

In the field of economics, MU refers to the degree of satisfaction per unit consumption of an item, Q refers to the amount of consumption and TU refers to total degree of satisfaction from the consumption of a certain number of items. Generally speaking, MU follows

the law of gradual decrease, meaning that the first unit of consumption of a good or service yields more utility than the second and subsequent units, with a continuous reduction for greater amounts of consumption [46]. As illustrated in Figure 2, *MU* goes from positive to 0, and then to negative. Correspondingly, when *MU* > 0, *TU* goes up. When *MU* = 0, *TU* reaches the maximum value, that is, the turning point. When *MU* < 0, *TU* goes down.

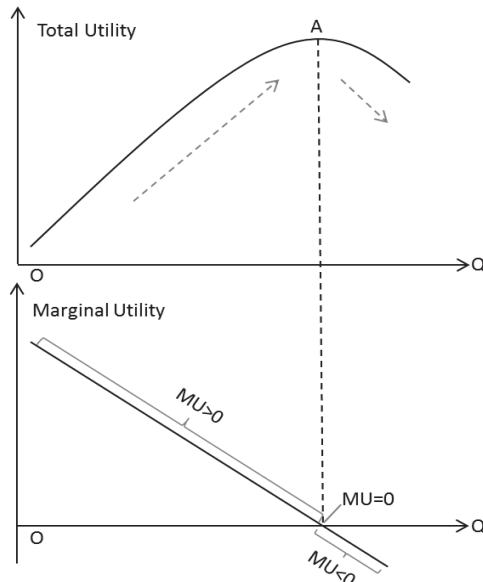


**Figure 2.** Marginal utility and total utility.

Due to the similarity with Equation (1) in the inverted U-shaped trend, *TU* can be used to reflect the trend in CO<sub>2</sub> emissions in the process of economic development. “CO<sub>2</sub> emissions caused by unit GDP growth” (denoted by CUG, the same below) herein can be analogized to *MU*.

Based on this, the exploration of the influence of structural effects on the correlation between GDP and CO<sub>2</sub> emissions reveals the contributions of industrial structure and energy structure to the changes in CUG, a perspective that has rarely been discussed before. We use VDA, which is based on the VAR model in econometrics, to quantify the contributions. The VAR model is an unstructured model containing multiple equations to estimate the dynamic relationship between all endogenous variables [8]. The principle is to take each endogenous variable in the system as the lag value of all endogenous variables, so as to extend the single variable autoregressive model to a VAR model composed of multivariate time series variables, as shown in Equations (9) and (10).

$$Y_t = A_0 + A_1 Y_{t-1} + \dots + A_p Y_{t-p} + \delta_t \tag{9}$$

$$Y_t = \{\ln CO_{2,t}, \ln IS_t, \ln RN_t, \ln NG_t\} \tag{10}$$

where  $Y_t$  is the time series of each variable;  $A_0, A_1, \dots, A_p$  are  $n$  order coefficient matrix;  $\delta_t$  is the error term.

The premise of the stability of the VAR model is that the inverse roots of the AR characteristic polynomial is less than 1. On this basis, VDA can be carried out. VDA further evaluates the importance of different influencing factors by analyzing the contribution of each factor to the changes in endogenous variables. Therefore, VDA provides information about the relative importance of each random disturbance that affects the variables in the VAR model, which can explain the contribution of each influencing factor to the change of

the dependent variables. This method can effectively explore the contribution of structural effects to changes in CUG. EViews 7.2 was employed to simulate the relevant results.

### 3. Data and Scenario Settings

#### 3.1. Study Area

Jilin Province, located in the Northeast China, is a typical traditional industrial region. In the process of China's industrial development, as the base of heavy industry, Jilin made a significant contribution to the country's industrialization from the 1950s to the 1970s. However, with the upgrading of China's industrial structure and the acceleration of modernization, Jilin has gradually been falling behind the eastern coastal regions. In addition, the adjustment of industrial structure and energy structure in Jilin has been sluggish in recent years. Meanwhile, the economic development level of Jilin has dropped below the national average level in recent years, ranking out of the top 20 in 31 provincial regions of China with even negative economic growth in 2019. What is more, Jilin has been listed as one of China's 16 relatively high-carbon regions since 2010. Under the double pressures of economic growth and CO<sub>2</sub> emissions reduction, the government has also proposed relevant plans for structural adjustment.

#### 3.2. Data Source

This study employs the panel data of Jilin Province for the period 1995–2015 for parameter fitting. The data on GDP, fossil fuels consumption and the proportion of renewable energy come from the Jilin Province Statistical Yearbook [47]. The amount of CO<sub>2</sub> emissions is calculated according to the National Greenhouse Gas Inventories published in the IPCC Guidelines [48], combined with the data on fossil fuel consumption. The descriptive statistics of the variables are presented in Table 1.

**Table 1.** The descriptive statistics of the variables.

Variable	Observation	Standard Error	Max	Mean	Min
CO <sub>2</sub> (Mt)	21	50.36	222.10	144.76	86.78
GDP (billion yuan)	21	456	1406	564	114
CEI (t/thousand yuan)	21	20.13	85.54	38.60	14.04
SI (%)	21	5.61	53.41	45.04	37.14
FEI (tce/thousand yuan)	21	8.18	34.77	15.69	5.71
CC (%)	21	9.92	78.70	68.55	53.00
NG (%)	21	1.13	3.70	1.94	0.50
RN (%)	21	1.04	6.48	5.06	3.23

#### 3.3. Scenario Setting

Scenario setting allows for adjusting the current development direction in a targeted manner based on foreseeable future development paths. In this study, we set four scenarios namely S1, S2, S3 and S4, each of which represented a different future development pattern. There were obvious hierarchical differences among four scenarios. Specifically, the settings for S1–S4 referred to the historical development trend of Jilin, the future development plan of Jilin, the average development level of China and the average development level of developed countries, respectively. The scenario setting was finally reflected in the parameter setting of the influencing factors involving SI, RN, NG and GDP, as shown in Table 2.



**Table 2.** Descriptions of the scenarios.

Scenario	Characteristic	Variables			
		SI	RN	GDP	NG
S1	Continuation of the historical development trajectory	Continuation of the historical annual change rate of $-0.6\%$	Continuation of the historical annual change rate of $4.3\%$	Continuation of the historical annual change rate of $6.9\%$ from 2016 to 2020	
S2	Reaching an ideal development state as in the future planning.	A certain degree of adjustment at an annual change rate of $-1\%$	A certain degree of adjustment at an annual change rate of $4.8\%$	Annual change rate of $6.5\%$ from 2016 to 2020	Annual change rate of $4.8\%$ from 2016 to 2050, reaching $18\%$ in 2050
S3	Basically in sync with the average level of China	In-depth adjustment with an annual change rate of $-1.4\%$	In-depth adjustment with an annual change rate of $5.2\%$	Annual change rate of $6.2\%$ from 2016 to 2020	
S4	Basically reaching the level of the developed countries	More in-depth adjustment with an annual change rate of $-1.8\%$ , lower than $30\%$ in 2050	More in-depth adjustment with an annual change rate of $5.6\%$ , more than $40\%$ in 2050	Annual change rate of $6.0\%$ from 2016 to 2020	

Among them, *SI* and *RN* were set based on the historical trends and related local plan [49] and national plan [50]. *GDP* was projected based on the historical trends and national planning, with the annual growth rate decreasing by  $0.5\%$  every five years [51]. Two reasons account for why the same parameter was set for *NG* in the four scenarios. On the one hand, *NG* in Jilin is very small, and the annual change is not significant, only increasing from  $1\%$  in 1995 to  $3\%$  in 2015. On the other hand, the future planning for *NG* in Jilin is not very optimistic, reaching a maximum of  $18\%$  by 2050 [52], far lower than the expectation for *RN*. Considering the limitations of natural gas development and to highlight the contribution of renewable energy, the variable control method was used to fix *NG*. By combining the settings for the three variables (*NG*, *IS* and *RN*), the results of *CEI* during 2016–2050 in the four scenarios can be obtained. The details of the above prediction results are displayed in Table 3.

**Table 3.** Settings for variables in four scenarios during 2016–2050.

Variable	Scenario	2020	2025	2030	2035	2040	2045	2050
<i>SI</i> (%)	S1	48.34	46.91	45.52	44.17	42.86	41.59	40.36
	S2	47.38	45.06	42.85	40.75	38.75	36.85	35.05
	S3	46.43	43.27	40.32	37.58	35.02	32.64	30.42
	S4	45.49	41.54	37.94	34.64	31.64	28.89	26.38
<i>RN</i> (%)	S1	8.50	11.37	15.14	19.79	23.62	26.46	27.95
	S2	8.91	12.79	17.93	23.77	28.10	31.48	33.58
	S3	9.29	13.84	20.05	26.21	31.58	36.08	38.87
	S4	9.73	15.25	22.40	29.98	36.47	41.26	44.45
<i>GDP</i> (billion yuan)	S1	1963	2677	3566	4638	5892	7203	8679
	S2	1927	2578	3370	4301	5360	6521	7745
	S3	1900	2518	3260	4122	5087	6130	7211
	S4	1882	2495	3184	3970	4828	5734	6647
<i>NG</i> (%)	S1–S4	4.42	5.59	7.07	8.94	11.30	14.29	18.06
<i>CEI</i> (t/thousand yuan)	S1	11.84	9.76	8.05	6.63	5.47	4.51	3.71
	S2	11.45	9.13	7.28	5.81	4.63	3.69	2.94
	S3	11.11	8.60	6.65	5.15	3.98	3.08	2.38
	S4	10.78	8.09	6.07	4.56	3.42	2.57	1.93

### 4. Results

#### 4.1. Correlation between Economic Growth and CO<sub>2</sub> Emissions under Dual Structural Effects

In order to ensure the stability and accuracy of the estimation results, we conducted an Augmented Dickey–Fuller (ADF) unit root test and a Johansen co-integration test on the time series variables for 1995–2015. The results demonstrate that the stationarity requirements of the time series variables could be met and a long-term stable equilibrium relationship between the variables exists. The parameter estimation results for Equations (4)–(6) are presented in Table 4. The t-statistic follows a normal distribution, and the corresponding coefficient is significant at the confidence level of 1%. Based on this, the coefficients  $\alpha'$ ,  $b'$ ,  $c'$  and the error term  $\lambda$  in Equation (7) that only includes the representation of industrial structure and energy structure can be finally obtained as 0.91,  $-0.62$ ,  $-0.15$  and  $-1.84$ , respectively.

**Table 4.** Parameter estimation results for Equations (4)–(6).

Parameter	Coefficient	T-statistics	Probability	Adjusted R <sup>2</sup>
<i>a</i>	0.9121 ***	3.7908	0.0016	
<i>b</i>	0.3387 ***	1.2684	0.0000	
<i>c</i>	0.8670 ***	3.5843	0.0026	0.9625
<i>d</i>	$-0.1494$ ***	$-2.9451$	0.0044	
<i>e</i>	$-6.5402$ ***	$-22.8653$	0.0000	
<i>m</i>	$-0.9302$ ***	$-12.9450$	0.0000	
$\delta_1$	1.2181 ***	271.8653	0.0000	0.9998
<i>n</i>	$-0.3525$ ***	$-4.4893$	0.0002	
$\delta_2$	4.9235 ***	19.5926	0.0000	0.9356

Note: \*\*\* indicates significance at the 1% level.

Based on the quantitative relationships among the variables, we inputted the parameters set in the four scenarios into the integrated simulation model and estimated the corresponding CO<sub>2</sub> emissions. Combining GDP set in the scenarios, we analyzed the correlation between GDP and CO<sub>2</sub> emissions from 2016 to 2050 based on Equation (1) by using DOLS. The results of the parameters are presented in Table 5.

**Table 5.** Parameter estimation results for Equation (1).

Variable	Scenario			
	S1	S2	S3	S4
lnGDP	3.56 ***	4.00 ***	4.40 ***	4.79 ***
lnGDP <sup>2</sup>	$-0.16$ ***	$-0.19$ ***	$-0.21$ ***	$-0.24$ ***
$\lambda$	$-9.47$ ***	$-11.16$ ***	$-12.70$ ***	$-14.24$ ***
Adjusted R <sup>2</sup>	0.9968	0.9808	0.9803	0.9943

Note: \*\*\* indicates significance at the 1% level.

We used the framework of the EKC model to quantify the relationship between GDP and CO<sub>2</sub> emissions, as it more intuitively shows the dynamic nonlinear relationship between two variables, which is more conducive to analyzing the impacts of structural effects along with the change of the relationship. The four scenarios reflect different evolution pathways of the correlation between GDP and CO<sub>2</sub> emissions. As depicted in Figure 3, there is a turning point in the scenario, which means that GDP and CO<sub>2</sub> emissions can be decoupled, that is, along with GDP growth, CO<sub>2</sub> emissions can change from increasing to decreasing. However, it can be observed that the state at which the turning point appears in each scenario is significantly different. The faster GDP grows, the larger CO<sub>2</sub> emissions, and the later the corresponding turning point appears. Specifically, in S1, the GDP at the turning point is 6683 billion yuan, with 292 Mt CO<sub>2</sub> emissions correspondingly. The CO<sub>2</sub> emissions slightly decline after reaching the turning point.

Different changing trends in CO<sub>2</sub> emissions after the turning point appear, reflecting different levels of decoupling between GDP and CO<sub>2</sub> emissions. The GDP in S2, S3 and S4 at the turning point is 4229, 3089 and 2410 billion yuan, respectively, with corresponding CO<sub>2</sub> emissions amounting to 248, 225 and 211 Mt, respectively.

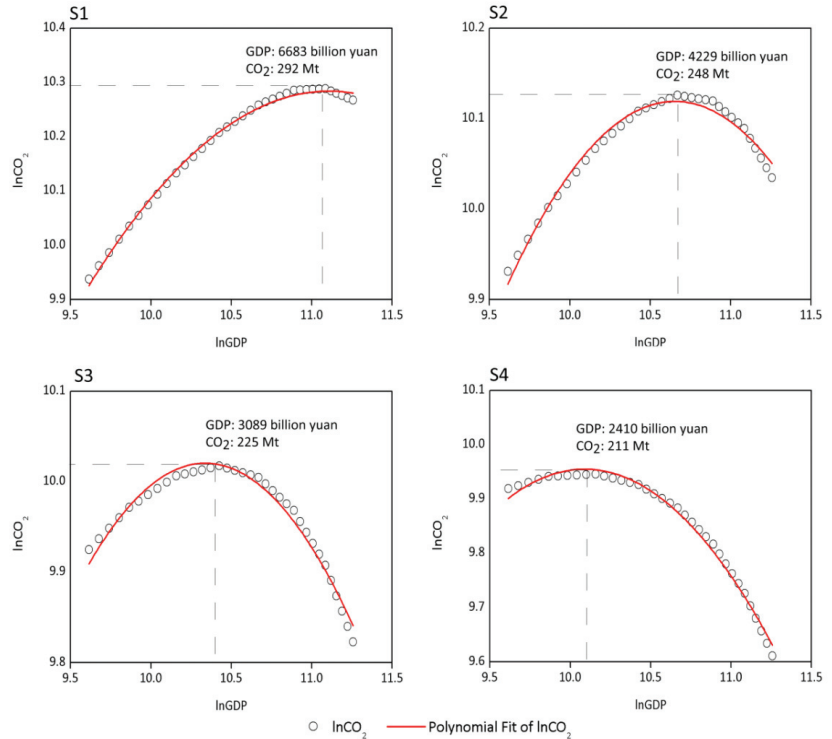


**Figure 3.** The correlation between GDP and CO<sub>2</sub> emissions during 2016–2050 in four scenarios.

The different results at the turning points are induced by different levels of the influencing factors. The results of *CEI* and corresponding *NG*, *RN*, *SI*, *CC* and *FEI* at the turning point are displayed in Table 6. The *CEI* in the four scenarios is 4.51, 5.81, 6.65 and 8.09 t/thousand yuan, respectively. Natural gas accounts for 14.29%, 8.94%, 7.07% and 5.59% in total energy consumption. Renewable energy accounts for 22.98%, 16.60%, 13.90% and 11.21% in total energy consumption. There are no insignificant changes in industrial structure in the four scenarios, with *SI* ranging within 40–42%. It can be observed from the states of the variables at the turning point that *NG*, *RN* and *CC* all decrease from S1 to S4. The *CEI* and *FEI* increase from S1 to S4. Therefore, S1 is a better scenario in terms of a higher proportion of clean energy and lower *FEI* and CO<sub>2</sub> emission intensity. However, if CO<sub>2</sub> emissions are combined within the whole economic development process (see Figure 3), the scenarios cannot be simply judged according to the states of the variables, as the four turning points appear at different economic development stages. The turning point in S1 appears in 2043, while in 2035, 2029 and 2025 in S2, S3 and S4, respectively. Accordingly, structural adjustment and economic development are in S1 for a longer time compared with other scenarios. In terms of the impacts of structural effects on the changing trend in the correlation between GDP and CO<sub>2</sub> emissions, the slower the adjustment of energy structure and industrial structure is, the more significant the growth trend in GDP will be before the turning point, resulting in significant differences in GDP and CO<sub>2</sub> emissions at the turning point. Specifically, in the four scenarios, the annual average growth rate of *RN* before the turning point is 4.3%, 4.8%, 5.2% and 5.6%, while the average annual

growth rate of *SI* is -0.6%, -1%, -1.4%, and -1.8%. Correspondingly, the difference in GDP between the base year and turning point-year is 5180, 2731, 1596 and 919 billion yuan, and the changes in CO<sub>2</sub> emissions are 84, 42, 21 and 9 Mt.

**Table 6.** Values of the variables at the turning point in four scenarios.

Variable	Scenario			
	S1	S2	S3	S4
CEI (t/10 <sup>3</sup> yuan)	4.51	5.81	6.65	8.09
NG (%)	14.29	8.94	7.07	5.59
RN (%)	22.98	16.60	13.90	11.21
SI (%)	41.59	40.75	40.32	41.54
CC (%)	45.73	51.25	54.53	58.80
FEI (tce/10 <sup>3</sup> yuan)	1.84	2.48	2.93	3.58

4.2. CO<sub>2</sub> Emission Peak under Dual Structural Effects

In addition to exploring the correlation between GDP and CO<sub>2</sub> emissions, considering the importance of CO<sub>2</sub> emission peak for absolute emission reductions, the impacts of structural effects in peaking CO<sub>2</sub> emissions were also analyzed. The trends in CO<sub>2</sub> emission in different scenarios from 2016 to 2050 were delineated in Figure 4. It can be found that the peak of CO<sub>2</sub> emissions is also a turning point, but it is different from the turning point of EKC. The turning point of EKC represents the decoupling of GDP and CO<sub>2</sub> emissions, that is, CUG begins to decline, which means a relative reduction in CO<sub>2</sub> emissions, while the peak turning point means the absolute reduction in CO<sub>2</sub> emissions. Specifically, the peaking time of CO<sub>2</sub> emissions in S1–S4 is 2043, 2035, 2030 and 2023, respectively, with corresponding peaking amount as 325, 250, 217, and 203 Mt. Compared with S1, the peaking time in S2–S4 is 8, 13 and 20 years earlier, with corresponding peaking amount 75, 108 and 122 Mt smaller, respectively. The scale effect represented by GDP and the structural effects characterized by industrial structure and energy structure collectively determine the pathways towards CO<sub>2</sub> emission peak. When CO<sub>2</sub> emissions in the four scenarios reach the peak, the corresponding GDP is 6685, 4301, 3260 and 2241 billion yuan; *SI* is 42.09%, 40.75%, 40.32% and 43.08%; *RN* is 34.14%, 25.54%, 20.98% and 15.14%, respectively.

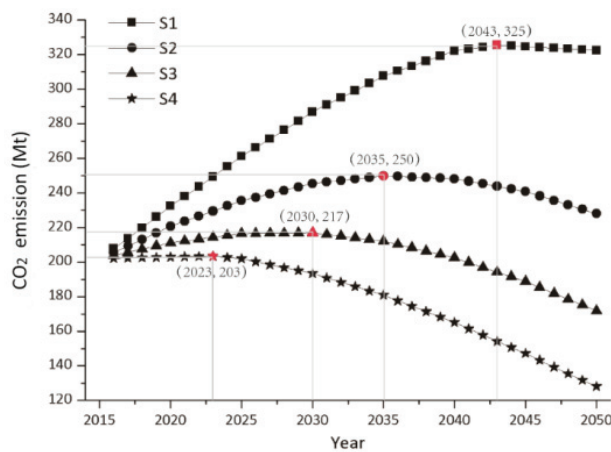


**Figure 4.** CO<sub>2</sub> emissions trend and emissions peak in different scenarios from 2016 to 2050.

There is a positive correlation between GDP and CO<sub>2</sub> emissions before the peak, showing an increasing trend, with the opposite conditions after reaching the turning point. When GDP growth rate is greater than the decrease rate in CEI, CO<sub>2</sub> emissions show

an upward trend; when GDP growth rate is smaller than the decrease rate of CEI, CO<sub>2</sub> emissions show a downward trend. Therefore, in order to reach peak CO<sub>2</sub> emissions as soon as possible, it is necessary to promote the decrease in CEI while controlling the economic growth rate to some extent. The dual structural effects characterized by industrial structure and energy structure are the main factors affecting CEI. Specifically, the increase in RN and NG and the decrease in SI are conducive to the decrease in CEI, thereby promoting the advancement of the peaking time and the reduction in the peaking emission amount.

4.3. Contributions of Structural Effects to the Correlation between Economic Growth and CO<sub>2</sub> Emissions

According to the above analysis, the EKC model can effectively explore the non-linear relationship between GDP and CO<sub>2</sub> emissions, but cannot clarify in detail how structural effects drive the evolution of the correlation between GDP and CO<sub>2</sub> emissions. Therefore, we further introduced the concepts of TU and MU to deal with this. Referring to the principle of MU, we employed VDA based on the VAR model to quantify the dynamic impacts of structural effects on CUG.

The contributions of CIS and CES to CUG in the four scenarios are illustrated in Table 7. It can be observed that the change in industrial structure (CIS) has a positive effect on CUG and the change in energy structure (CES) a negative effect on CUG. The average contribution of CES becomes enhanced (e.g., -5.56%, -6.48%, -7.69% and -8.56% during 2016–2020 and -9.34%, -11.01%, -12.93% and -14.32% during 2046–2050). The average contribution of CIS becomes weakened (e.g., 38.44%, 37.43%, 36.67% and 35.64% during 2016–2020 and 30.46%, 29.03%, 27.31% and 25.38% during 2046–2050). Industrialization is an important reason for the increase in CO<sub>2</sub> emissions while promoting economic growth. With the optimization of the industrial structure, traditional industries characterized by high energy consumption and high emissions will gradually be replaced by emerging industries characterized by low carbon. Therefore, the positive contribution of CIS on CUG gradually weakened. In this process, the replacement of fossil energy by clean energy also directly led to a significant decline in the growth rate of CO<sub>2</sub> emissions. The higher the proportion of clean energy, the more significant the negative contribution of CES to CUG.

Table 7. Contributions of structural effects (CES and CIS) to CUG (%).

Year	CIS				CES			
	S1	S2	S3	S4	S1	S2	S3	S4
2016–2020	38.44	37.43	36.67	35.64	-5.56	-6.48	-7.69	-8.56
2021–2025	37.21	35.85	34.37	33.01	-6.11	-6.99	-8.25	-9.38
2026–2030	36.28	34.21	31.98	31.18	-6.44	-7.74	-8.87	-10.24
2031–2035	35.13	32.97	30.92	28.77	-7.07	-8.16	-9.73	-11.24
2036–2040	33.24	31.33	29.03	27.01	-7.86	-9.48	-10.57	-12.49
2041–2045	32.45	30.15	28.01	26.12	-8.66	-10.06	-11.96	-13.45
2046–2050	30.46	29.03	27.31	25.38	-9.34	-11.01	-12.93	-14.32
Average	32.45	32.97	31.98	33.01	-8.66	-8.16	-8.87	-9.38

As the stability and co-integration of the time series variables have been verified, the VAR model was constructed directly and a stationarity test was performed for the model. The inverse roots of the AR characteristic polynomial in the four scenarios were all less than 1, indicating that the VAR model is a stationary system and the VDA could be conducted on this basis.

When the turning point appears, the overall average contributions of CIS and CES are 23.79%, 24.81%, 23.11% and 23.63%, respectively, in the four scenarios. Although the turning points corresponding to different development patterns occur at different times, the contributions of structural effects are similar in the four scenarios (around 23–24%). This verifies that the decoupling between CO<sub>2</sub> emissions and GDP can be achieved only when the collective impacts of industrial structure and energy structure have been adjusted to a certain level.

(1) When the decoupling between GDP and CO<sub>2</sub> emissions has not occurred, this means that CO<sub>2</sub> emissions will continue to increase with GDP growth. However, there are two different states at this stage. One is that CO<sub>2</sub> emissions are accelerating with GDP growth, indicating that the traditional development mode is still continuing. The other is that with further GDP growth, the increased rate of CO<sub>2</sub> emissions is gradually decreasing, indicating that structural optimization has begun. However, this optimization only results in relative reductions in CO<sub>2</sub> emissions and has not yet resulted in absolute reductions, which is a typical performance in the early stage of transformation. (2) When decoupling has occurred, this indicates that industrial structure and energy structure have been adjusted to a certain extent. At this time, it is approximately in the middle stage of transformation, where the GDP growth rate is slowing down, the tertiary industry is replacing the secondary industry to occupy a dominant position and the share of coal consumption in total energy consumption is declining. (3) With further decoupling of GDP and CO<sub>2</sub> emissions, the transformation region will eventually enter the late stage of transformation. Different from the previous states, under adequate support of technologies and investment, the space for the optimization of energy structure can be larger than that for industrial structure. Although the contribution of CIS to CUG is higher than that of CES during 2016–2050, this situation may be reversed. As can be observed from Table 7, the contribution of CIS to CUG in the four scenarios changes by 20.76%, 22.44%, 25.53% and 28.79% from 2016 to 2050, while that of CES changes by 67.99%, 69.91%, 68.14% and 67.29%. It can be concluded that CES has greater potential for CO<sub>2</sub> emission reduction in the future.

## 5. Discussion and Policy Implications

Jilin Province is a typical transformation region implementing a dual adjustment of both industrial structure and energy structure. In this study, an integrated simulation model is built based on the interactions among the socioeconomic, industrial, energy and CO<sub>2</sub> emission variables in Jilin from 1995 to 2015, using CEI as a bridge connecting GDP and CO<sub>2</sub> emissions. There is an inverted U-shaped dynamic correlation between GDP and CO<sub>2</sub> emissions. The turning points appearing in the four scenarios indicate that CO<sub>2</sub> emissions can decouple from GDP in Jilin once it has undergone sufficient development. However, the states at the turning points in the four scenarios differ significantly. The slower the adjustment of energy structure and industrial structure is, the more significant the upward trend appears before the turning point; furthermore, the slower the decrease in CEI is, the later CO<sub>2</sub> emissions decouple from GDP.

The turning point of the correlation between economic growth and CO<sub>2</sub> emissions reflects the beginning of relative emissions reduction, while the CO<sub>2</sub> emission peak is the beginning of absolute emissions reduction. The reduction in CO<sub>2</sub> emission intensity is the main representation of relative emissions reduction, which is reflected in the gradual slowdown of the increase in CO<sub>2</sub> emissions before the emission peak. GDP drives the increase in CO<sub>2</sub> emissions, while CEI suppresses the increase in CO<sub>2</sub> emissions. Only when the reduction rate of CEI is greater than GDP growth rate can CO<sub>2</sub> emissions change from rising to falling, thereby forming the peak. Lower GDP growth rate and greater decrease in CEI caused by more aggressive adjustment of energy structure and industrial structure results in an earlier arrival of the emission peak, which is similar to the findings of Du et al. [35] and Shuai et al. [53].

In order to explore the dynamic influence mechanism of structural effects on the correlation between GDP and CO<sub>2</sub> emissions, CO<sub>2</sub> emissions and CUG were analogized to TU and MU in the process of economic development. CIS and CES have opposite effects on CUG with different intensities of influence. When the turning point occurs, *SI* in the four scenarios is similar (about 41%), while *RN* in the four scenarios is distinct (37%, 26%, 21% and 17%, respectively). Even if the levels of GDP and CO<sub>2</sub> emissions in the four scenarios are different, also with differences in energy structure, the industrial structure tends to be similar, which is also in line with the socio-economic development characteristics of developed countries that have peaked CO<sub>2</sub> emissions in their peak years [54]. With

regard to the contribution to CUG, industrial structure and energy structure each makes similar contributions in the four scenarios. With the development of emerging industries and the optimization of energy utilization models, the positive contribution of CIS on CUG will gradually weaken while the negative contribution of CES to CUG will gradually increase. Although the turning points corresponding to different scenarios occur at different times, the contributions of structural effects to CUG are almost similar, which shows that structural adjustment plays a relatively fixed and irreplaceable role in the process of peaking CO<sub>2</sub> emissions.

Based on the findings, the following policy implications are proposed. As a traditional industrial region that is undergoing transformation in terms of both industrial structure and energy structure, Jilin should strive to coordinate the relationship between economic growth and CO<sub>2</sub> emission reduction. CEI is an important link to measure the relationship between economic growth and CO<sub>2</sub> emissions. Currently, the CEI in Jilin Province is relatively high, which still has a large potential for emission reduction. Structural adjustment is the key to realizing the transformation of economic development mode in Jilin Province.

The adjustment of industrial structure is the prerequisite for development. As one of the typical representatives of the heavy industrial base, under the impact of emerging industries such as information technology at home and abroad, Jilin has gradually lost its previous development advantages. The industrial mode characterized by high energy consumption, high emissions and low added value cannot provide an impetus for the sustainable development of economy and society. At the same time, due to the limitations of geographical location and resource endowment, emerging industries and service industries with high added value and low energy consumption have not been effectively developed, which causes the lag of regional development [55]. Therefore, Jilin Province should reduce energy-intensive industries while eliminating backward production capacity, and vigorously develop technology-intensive and capital-intensive industries.

The adjustment of energy structure is the guarantee of industrial transformation. In accordance with the characteristics of high energy consumption and high emissions of traditional industries, fossil energy consumption accounts for more than 90% of total energy consumption in Jilin Province, of which coal consumption accounts for more than 65%, which obviously does not meet the development requirements of a low-carbon economy. In order to meet the development needs of emerging industries and the requirements of CO<sub>2</sub> emission reduction, according to the simulation results, the energy structure adjustment of Jilin Province should be carried out in two steps. The first step is to gradually replace some coal energy consumption with oil and natural gas. However, considering the shortage of fossil energy, the second step is to continuously increase the proportion of renewable energy consumption in order to gradually replace fossil energy consumption.

Taking Jilin Province as an example, this study reveals the correlation between economic growth and CO<sub>2</sub> emissions under dual structural effects attributed to the Kaya identity of CEI. Owing to scenario analysis, the dynamic impacts of structural effects can be explored. However, the setting of the scenarios is based on the local development status and future planning. It is impossible to ensure the universal applicability for the transformation regions. Although each factor for future development is set as far as possible from the perspective of rationality and feasibility, there are still uncertainties, especially considering the periodicity of policy implementation. We used a five-year interval as a unit of parameter setting, which may induce deviations compared with the actual development situation. In addition, due to the lack of relevant planning, this study did not introduce technological factors into the simulation model, without further exploring the impacts of technological effects on the correlation between economic growth and CO<sub>2</sub> emissions. In the future, we will further improve our research in the following two respects. The first is to expand the scope of the research and take other transformation regions as targets, so as to make the research more widely representative. The second is to continuously update the scenario settings according to the actual development situation to ensure the accuracy of the prediction results.

## 6. Conclusions

This study aims to unravel the dynamic driving mechanism of dual structural effect on the correlation between economic growth and CO<sub>2</sub> emissions in a typical transformation region represented by Jilin province. We built an integrated simulation model to cover the interrelationships among the variables, and the prediction of CO<sub>2</sub> emissions was based on the combination of GDP and CO<sub>2</sub> emission intensity. The determination of the latter was based on the Kaya identity which is built incorporating the structural factors including industrial structure and energy structure. In order to quantitatively analyze the influence of structural effects on CUG, the concepts of marginal utility and total utility were introduced, and VDA based on the VAR model was employed to quantify the effects. The specific conclusions derived from the present study can be listed as follows:

(1) In terms of the impacts of structural effects on the changing trend in the correlation between GDP and CO<sub>2</sub> emissions, the slower the adjustment of energy structure and industrial structure is, the more significant the growth trend in GDP will be before the turning point, resulting in significant differences in GDP and CO<sub>2</sub> emissions at the turning point. The slower decrease in CEI is, the later CO<sub>2</sub> emissions decouple from GDP.

(2) Lower GDP growth rate and greater decrease in CEI caused by more aggressive adjustment of energy structure and industrial structure results in earlier arrival of the emission peak. The faster GDP grows, the larger CO<sub>2</sub> emissions, and the later the corresponding turning point appears.

(3) Even under different socio-economic development modes, when CO<sub>2</sub> emissions peak, the energy structure is different while the industrial structure tends to be similar. Meanwhile, the contribution of the dual structural effects to CUG is basically the same (around 23–24%). The change in industrial structure has a positive driving effect on CUG, while the change in energy structure has a negative driving effect. With the transformation of the socio-economy, the positive driving effect of the industrial structure will gradually weaken, while the negative driving effect of the energy structure will increase.

**Author Contributions:** Conceptualization, methodology, formal analysis, writing—original draft preparation, Z.D.; writing—review and editing, supervision, Y.C. and H.D.; data curation, Z.L. and X.W. All authors have read and agreed to the published version of the manuscript.

**Funding:** This research was funded by the National Natural Science Foundation of China (No. 41801199, No. 71773034, No. 71704157) and 111 Project of Jilin University (NO. B16020).

**Institutional Review Board Statement:** Not applicable.

**Informed Consent Statement:** Not applicable.

**Data Availability Statement:** The data presented in this study are available upon request from the corresponding author.

**Conflicts of Interest:** The authors declare no conflict of interest.

## Abbreviations

Abbreviation	Term
CEI	CO <sub>2</sub> emission intensity
VDA	Variance decomposition analysis
CIS	The change in industrial structure
CES	The change in energy structure
CUG	CO <sub>2</sub> emissions caused by unit GDP growth
MU	Marginal utility
TU	Total utility
RN	The proportion of renewable energy



## References

1. Ang, B.W. Decomposition analysis for policymaking in energy: Which is the preferred method? *Energy Policy* **2004**, *32*, 1131–1139. [[CrossRef](#)]
2. Ma, X.; Wang, C.; Dong, B.; Gu, G.; Chen, R.; Li, Y. Carbon emissions from energy consumption in China: Its measurement and driving factors. *Sci. Total Environ.* **2018**, *648*, 1411–1420. [[CrossRef](#)] [[PubMed](#)]
3. Du, W.; Xia, X. How does urbanization affect GHG emissions? A cross-country panel threshold data analysis. *Appl. Energy* **2018**, *229*, 872–883. [[CrossRef](#)]
4. Dong, K.; Jiang, H.; Sun, R.; Dong, X. Driving forces and mitigation potential of global CO<sub>2</sub> emissions from 1980 through 2030: Evidence from countries with different income levels. *Sci. Total Environ.* **2019**, *649*, 335–343. [[CrossRef](#)]
5. Wang, Y.; Zhang, C.; Lu, A.T.; Li, L.; He, Y.M.; Tojo, J.J.; Zhun, X.D. A disaggregated analysis of the environmental Kuznets curve for industrial CO<sub>2</sub> emissions in China. *Appl. Energy* **2017**, *190*, 172–180. [[CrossRef](#)]
6. Li, Z.; Shao, S.; Shi, X.P.; Sun, Y.P.; Zhang, X. Structural transformation of manufacturing, natural resource dependence, and carbon emissions reduction: Evidence of a threshold effect from China. *J. Clean. Prod.* **2019**, *206*, 920–927. [[CrossRef](#)]
7. Underwood, A.; Fremstad, A. Does sharing backfire? A decomposition of household and urban economies in CO<sub>2</sub> emissions. *Energy Policy* **2018**, *123*, 404–413. [[CrossRef](#)]
8. Zhang, Y.; Zhang, S.F. The impacts of GDP, trade structure, exchange rate and FDI inflows on China's carbon emissions. *Energy Policy* **2018**, *120*, 347–353. [[CrossRef](#)]
9. Lin, B.Q.; Zhu, J.P. Energy and carbon intensity in China during the urbanization and industrialization process: A panel VAR approach. *J. Clean. Prod.* **2017**, *168*, 780–790. [[CrossRef](#)]
10. Chen, X.; Shuai, C.; Wu, Y.; Zhang, Y. Analysis on the carbon emission peaks of China's industrial, building, transport, and agricultural sectors. *Sci. Total Environ.* **2019**, *709*, 135768. [[CrossRef](#)]
11. Chukwuemeka, N.; Cosmas, I. An econometric analysis of the macroeconomic determinants of carbon dioxide emissions in Nigeria. *Sci. Total Environ.* **2019**, *675*, 313–324. [[CrossRef](#)]
12. Hanif, I.; Aziz, B.; Chaudhry, I.S. Carbon Emissions across the Spectrum of Renewable and Nonrenewable Energy Use in Developing Economies of Asia. *Renew. Energy* **2019**, *143*, 586–595. [[CrossRef](#)]
13. Ganda, F. The impact of innovation and technology investments on carbon emissions in selected organisation for economic Co-operation and development countries. *J. Clean. Prod.* **2019**, *217*, 469–483. [[CrossRef](#)]
14. Jian, J.; Fan, X.; He, P.; Xiong, H. The Effects of Energy Consumption, Economic Growth and Financial Development on CO<sub>2</sub> Emissions in China: A VECM Approach. *Sustainability* **2019**, *11*, 4850. [[CrossRef](#)]
15. Mirza, F.M.; Kanwal, A. Energy consumption, carbon emissions and economic growth in Pakistan: Dynamic causality analysis. *Renew. Sustain. Energy Rev.* **2017**, *72*, 1233–1240. [[CrossRef](#)]
16. Dinda, S. Environmental Kuznets curve hypothesis: A survey. *Ecol. Econ.* **2004**, *49*, 431–455. [[CrossRef](#)]
17. Pao, H.; Chen, C. Decoupling strategies: CO<sub>2</sub> emissions, energy resources, and economic growth in the Group of Twenty. *J. Clean. Prod.* **2019**, *206*, 907–919. [[CrossRef](#)]
18. Sharif, A.; Raza, S.A.; Ozturk, I.; Afshan, S. The dynamic relationship of renewable and nonrenewable energy consumption with carbon emission: A global study with the application of heterogeneous panel estimations. *Renew. Energy* **2019**, *133*, 685–691. [[CrossRef](#)]
19. Baek, J. Environmental Kuznets curve for CO<sub>2</sub> emissions: The case of Arctic countries. *Energy Econ.* **2015**, *50*, 13–17. [[CrossRef](#)]
20. Pérez-Suárez, R.; López-Menéndez, A.J. Growing green? Forecasting CO<sub>2</sub> emissions with environmental Kuznets curves and logistic growth models. *Environ. Sci. Technol.* **2015**, *54*, 428–437. [[CrossRef](#)]
21. Özokcu, S.; Özdemir, Ö. Economic growth, energy, and environmental Kuznets curve. *Renew. Sustain. Energy Rev.* **2017**, *72*, 639–647. [[CrossRef](#)]
22. Yang, G.; Sun, T.; Wang, J. Modeling the nexus between carbon dioxide emissions and economic growth. *Energy Policy* **2015**, *86*, 104–117. [[CrossRef](#)]
23. Abid, M. Does economic, financial and institutional developments matter for environmental quality? a comparative analysis of eu and mea countries. *J. Environ. Manag.* **2017**, *188*, 183–194. [[CrossRef](#)] [[PubMed](#)]
24. Al-Mulali, U.; Ozturk, I.; Solarin, S.A. Investigating the environmental Kuznets curve hypothesis in seven regions: The role of renewable energy. *Ecol. Indic.* **2016**, *67*, 267–282. [[CrossRef](#)]
25. Kais, S.; Sami, H. An econometric study of the impact of economic growth and energy use on carbon emissions: Panel data evidence from fifty eight countries. *Renew. Sustain. Energy Rev.* **2016**, *59*, 1101–1110. [[CrossRef](#)]
26. Bilgili, F.; Koçak, E.; Bulut, Ü. The dynamic impact of renewable energy consumption on CO<sub>2</sub> emissions: A revisited Environmental Kuznets Curve approach. *Renew. Sustain. Energy Rev.* **2016**, *54*, 838–845. [[CrossRef](#)]
27. Dogan, E.; Turkekul, B. CO<sub>2</sub> emissions, real output, energy consumption, trade, urbanization and financial development: Testing the EKC hypothesis for the USA. *Environ. Sci. Pollut. Res.* **2016**, *23*, 1203–1213. [[CrossRef](#)]
28. Dong, K.; Sun, R.; Hochman, G. Impact of natural gas consumption on CO<sub>2</sub> emissions: Panel data evidence from China's provinces. *J. Clean. Prod.* **2017**, *162*, 400–410. [[CrossRef](#)]
29. Nasir, M.A.; Duc Huynh, T.L.; Xuan Tram, H.T. Role of financial development, economic growth & foreign direct investment in driving climate change: A case of emerging asean. *J. Environ. Manag.* **2019**, *242*, 131–141. [[CrossRef](#)]

30. Wang, C.; Wood, J.; Geng, X.; Wang, Y. Transportation CO<sub>2</sub> emission decoupling: Empirical evidence from countries along the belt and road. *J. Clean. Prod.* **2020**, *263*, 121450. [[CrossRef](#)]
31. Wu, Y.; Tam, V.W.Y.; Shuai, C.; Shen, L.; Zhang, Y.; Liao, S. Decoupling China's economic growth from carbon emissions: Empirical studies from 30 Chinese provinces (2001–2015). *Sci. Total Environ.* **2019**, *656*, 576–588. [[CrossRef](#)] [[PubMed](#)]
32. Wang, Q.; Jiang, R. Is China's economic growth decoupled from carbon emissions? *J. Clean. Prod.* **2019**, *225*, 1194–1208. [[CrossRef](#)]
33. Churchill, S.A.; Inekwe, J.; Ivanovski, K.; Smyth, R. The environmental Kuznets curve in the OECD: 1870–2014. *Energy Econ.* **2018**, *75*, 389–399. [[CrossRef](#)]
34. Kasman, A.; Duman, Y. CO<sub>2</sub> emissions, economic growth, energy consumption, trade and urbanization in new EU member and candidate countries: A panel data analysis. *Econ. Model.* **2015**, *44*, 97–103. [[CrossRef](#)]
35. Du, Q.; Zhou, J.; Pan, T.; Sun, Q. Relationship of carbon emissions and economic growth in China's construction industry. *J. Clean. Prod.* **2019**, *220*, 99–109. [[CrossRef](#)]
36. Wu, Y.; Chau, K.W.; Lu, W.; Shen, L.; Shuai, C. Decoupling relationship between economic output and carbon emission in the Chinese construction industry. *Environ. Impact Assess. Rev.* **2018**, *71*, 60–69. [[CrossRef](#)]
37. Feng, C.; Sun, L.; Xia, S. A temporal-spatial decomposition analysis of China's transport carbon dioxide emissions from technology and efficiency perspectives. *J. Clean. Prod.* **2020**, *263*, 121545. [[CrossRef](#)]
38. Li, X.; Xu, H.; Tol, R.; Ang, B.; Bachmeier, L.; Sadorsky, P. The Energy-conservation and Emission-reduction Paths of Industrial sectors: Evidence from China's 35 industrial sectors. *Energy Econ.* **2020**, *86*, 104628. [[CrossRef](#)]
39. Li, J.S.; Zhou, H.W.; Meng, J.; Yang, Q.; Chen, B.; Zhang, Y. Carbon emissions and their drivers for a typical urban economy from multiple perspectives: A case analysis for Beijing city. *Appl. Energy* **2018**, *226*, 1076–1086. [[CrossRef](#)]
40. Shen, L.; Wu, Y.; Lou, Y.; Zeng, D.; Shuai, C. What drives the carbon emission in the Chinese cities?—A case of pilot low carbon city of Beijing. *J. Clean. Prod.* **2018**, *174*, 343–354. [[CrossRef](#)]
41. Gu, S.; Fu, B.; Thriveni, T.; Fujita, T.; Ahn, J.W. Coupled LMDI and system dynamics model for estimating urban CO<sub>2</sub> emission mitigation potential in Shanghai, China. *J. Clean. Prod.* **2019**, *240*, 118034. [[CrossRef](#)]
42. Grossman, G.M.; Krueger, A.B. Environmental impacts of a North American free trade agreement. *CEPR Discussion Papers* **1992**, *8*, 223–250. [[CrossRef](#)]
43. Kaya, Y. *Impact of Carbon Dioxide Emission Control on GNP Growth: Interpretation of Proposed Scenarios*; IPCC Energy and Industry Subgroup, Response Strategies Working Group: Paris, France, 1989.
44. Mansson, K.; Kibria, B.M.; Shukur, G. On the estimation of the CO<sub>2</sub> emission, economic growth and energy consumption nexus using dynamic OLS in the presence of multicollinearity. *Sustainability* **2018**, *10*, 1315. [[CrossRef](#)]
45. Jevons, W.S. *The Theory of Political Economy*; Macmillan: London, UK, 1888; p. 52.
46. Geels, F.; Schwanen, T.; Sorrell, S. Reducing energy demand through low carbon innovation: A sociotechnical transitions perspective and thirteen research debates. *Energy Res. Soc. Sci.* **2018**, *40*, 23–35. [[CrossRef](#)]
47. Jilin Provincial Bureau of Statistics. *Jilin Province Statistical Yearbook*; China Statistics Press: Beijing, China, 2017. Available online: <http://tj.jl.gov.cn/tjsj/tjnj/2017/ml/indexc.htm> (accessed on 12 June 2020).
48. Intergovernmental Panel on Climate Change. IPCC Guidelines for National Greenhouse Gas Inventories, Intergovernmental Panel on Climate Change 2006. 2006. Available online: <http://www.ipcc-nggip.iges.or.jp/public/2006gl/chinese/index.html> (accessed on 12 June 2020).
49. Jilin Provincial Energy Bureau. *The 13th Five-Year Plan for Energy Development in Jilin Province*; Energy Administration of Jilin Province: Changchun, China, 2016. Available online: <http://nyj.jl.gov.cn> (accessed on 13 June 2020).
50. National Energy Administration of China. *The 13th Five-Year Energy Plan*; Energy Administration of China: Beijing, China, 2016. Available online: <http://www.nea.gov.cn> (accessed on 13 June 2020).
51. National Development and Reform Commission. *The National 13th Five-Year Plan*; National Development and Reform Commission: Beijing, China, 2016. Available online: <http://www.ndrc.gov.cn> (accessed on 14 June 2020).
52. CNPC Economics and Technology Research Institute. *World and China Energy Outlook 2050*; CNPC Economics and Technology Research Institute: Beijing, China, 2017; Available online: <http://etri.cnpc.com.cn> (accessed on 14 June 2020).
53. Shuai, C.; Chen, X.; Wu, Y.; Tan, Y.; Zhang, Y.; Shen, L. Identifying the key impact factors of carbon emission in China: Results from a largely expanded pool of potential impact factors. *J. Clean. Prod.* **2018**, *175*, 612–623. [[CrossRef](#)]
54. Dong, F.; Wang, Y.; Su, B.; Hua, Y.; Zhang, Y. The process of peak CO<sub>2</sub> emissions in developed economies: A perspective of industrialization and urbanization. *Resour. Conserv. Recycl.* **2019**, *141*, 61–75. [[CrossRef](#)]
55. Duan, Z.; Wang, X.; Dong, X.; Duan, H. Peaking industrial energy-related CO<sub>2</sub> emissions in typical transformation region: Paths and mechanism. *Sustainability* **2020**, *12*, 791. [[CrossRef](#)]



Article

# CO<sub>2</sub> Emission Factors and Carbon Losses for Off-Road Mining Trucks

João Andrade de Carvalho, Jr.<sup>1,2,\*</sup>, André de Castro<sup>3</sup>, Gutemberg Hespanha Brasil<sup>4</sup>, Paulo Antonio de Souza, Jr.<sup>5</sup> and Andrés Z. Mendiburu<sup>2,6</sup>

<sup>1</sup> Campus of Guaratinguetá, São Paulo State University, Guaratinguetá, CEP 12516-410, Brazil

<sup>2</sup> International Research Group for Energy Sustainability (IRGES), Porto Alegre, CEP 90040-060, Brazil; andresmendiburu@ufrgs.br

<sup>3</sup> Heatech—Technology for Energy Efficiency, São José dos Campos, CEP 12233-360, Brazil; andredecastro@gmail.com

<sup>4</sup> Graduate Program of Economics, Federal University of Espírito Santo, Vitória, CEP 29075-910, Brazil; ghbrasil@terra.com.br

<sup>5</sup> School of Information and Communication Technology, Griffith University, Gold Coast, QLD 4111, Australia; paulo.desouza@griffith.edu.au

<sup>6</sup> Department of Mechanical Engineering, Federal University of Rio Grande do Sul, Porto Alegre, CEP 90040-060, Brazil

\* Correspondence: ja.carvalho@unesp.br; Tel.: +55-12-312-328-38

**Abstract:** There are myriad questions that remain to be answered in greenhouse gas (GHG) emissions trading. This article addresses carbon dioxide (CO<sub>2</sub>) emission factors and carbon losses from heavy equipment that is used to transport ores. Differences occurred between the Intergovernmental Panel for Climate Change (IPCC) emission factor and those that were obtained by considering incomplete combustion and on-site exhaust concentration measurements. Emissions from four off-road vehicles were analyzed. They operated at idle (loading, unloading, and queuing) and in motion (front and rear, loaded and unloaded). The results show that the average CO<sub>2</sub> emission factors can be as low as 64.8% of the IPCC standard value for diesel fuel. On the other hand, carbon losses can be up to 33.5% and energy losses up to 25.5%. To the best of the authors' knowledge, the method that was developed here is innovative, simple, useful, and easily applicable in determining CO<sub>2</sub> emission factors and fuel losses for heavy machinery.

**Keywords:** CO<sub>2</sub> emission rates; carbon losses; heavy duty equipment

**Citation:** de Carvalho, J.A., Jr.; de Castro, A.; Brasil, G.H.; de Souza, P.A., Jr.; Mendiburu, A.Z. CO<sub>2</sub> Emission Factors and Carbon Losses for Off-Road Mining Trucks. *Energies* **2022**, *15*, 2659. <https://doi.org/10.3390/en15072659>

Academic Editors: Huichao Chen and Devinder Mahajan

Received: 8 February 2022

Accepted: 26 March 2022

Published: 5 April 2022

**Publisher's Note:** MDPI stays neutral with regard to jurisdictional claims in published maps and institutional affiliations.



**Copyright:** © 2022 by the authors. Licensee MDPI, Basel, Switzerland. This article is an open access article distributed under the terms and conditions of the Creative Commons Attribution (CC BY) license (<https://creativecommons.org/licenses/by/4.0/>).

## 1. Introduction

The Kyoto Protocol was launched in 1997 and set limits and timetables for greenhouse gas (GHG) emissions when a group of developed countries committed to reduce their emissions by an average of 5.2% over the period 2008–2012, from 1990 levels [1,2]. The Protocol also provided spatial flexibility through the Kyoto mechanisms, which allowed countries to trade their assigned emission rates, resulting in the International Emissions Trading (IET) system. Together with quantified reduction commitments, these mechanisms form an international system of GHG permits.

In addition to these measures, alternative markets have been created (such as the Chicago Climate Exchange, CCX) as well as voluntary targets that are implemented by companies without mandatory targets. There are also other initiatives, such as zero-emission services and the neutralization of certain emissions from industrial facilities.

Several studies have been conducted to analyze this emerging carbon market. It was estimated that the European trading scheme would turn over more than \$1 billion annually starting in 2010 [3]. To date, the European emissions trading system still needs improvement to make the carbon market efficient as a mitigation measure [4]. In 2020, the

carbon market reached a record and grew by 20%; the value of transactions reached US\$272 billion [5].

The rapid economic growth in China must also be considered. It has been argued that the country's development is threatened by energy shortages and increasing pollution [6]. Polygeneration and clean coal technologies can help clean China's air, but they will not be sufficient in the short term to limit the country's growing greenhouse gas emissions. The rapid growth of China's emissions [7] and the conflicting policies that China is using to meet its 2020 reduction target have been discussed [8]. In 1980, China released 400,000 metric tons of carbon (C) as carbon dioxide (CO<sub>2</sub>), a level that is equivalent to 31% of the United States. In 2004, China's emissions increased to 1,300,000 tons of C, which was 81% of the United States' emissions. Based on the available data, it was estimated in 2008 that China's emissions now exceed those of the United States [9], which is indeed true. GHG emissions from China's heavy industry are related to industrial structure, fixed asset investment, and historical emissions [10]; the results also suggest that energy efficiency is a key factor in reducing GHG emissions.

Gerlagh and Lise [11] considered the effect of carbon taxes on technological change and developed an economical partial equilibrium model for energy supply and demand, with capital and labor as production factors. They concluded that only with induced technological change will carbon taxes substantially accelerate the substitution of fossil fuel by carbon-free energy; otherwise, there will be a modest effect on emissions.

Transaction costs diminish the attractiveness of the Kyoto Protocol compared to domestic abatement options [12]; the argument was that project-based mechanisms are likely to incur significant costs for baseline development, verification, and certification. Nagase [13] developed a theory of "carbon-money exchange", in which carbon and money are exchanged similar to foreign currencies. He claimed that this exchange could automatically curb global warming and deforestation and replace the onerous costs of carbon trading. The International Standardization Organization published ISO 14064 [14] with the goal of supporting greenhouse gas emissions standardization and verification. This standard is divided into the following sections:

- a. ISO 14064-1: This section presents the details of the principles and requirements for designing, developing, managing, and reporting greenhouse gas inventories. It also includes the procedures that are used to determine GHG emission limits, quantify, reduce, and improve GHG emissions management. Guidance on GHG inventory quality, internal auditing, and organizational responsibilities for verification activities are also part of this section.
- b. ISO 14064-2: This section focuses on projects that aim to reduce greenhouse gas emissions and improve their removal. It details the principles that are used to establish project baselines and quantify and report project performance.
- c. ISO 14064-3: This section provides the principles that are used to verify inventories and project performances.

The relationship between economic development and carbon dioxide emissions in a small open economy was studied [15]. The conclusion was that emission projections that were derived from a single country specification—the country in the study was Austria—support the view that significant policy changes are needed in the implementation of the Kyoto Protocol.

Canada's iron, gold, and potash mining sectors offer scope for the introduction of new technologies that would reduce greenhouse gas emissions [16]. The introduction of 15 technologies would result in a reduction of 21 million metric tons of carbon dioxide equivalents (CO<sub>2eq</sub>) by 2050. It was also demonstrated that the marginal cost of reducing GHG emissions is negative, implying that the industry would also realize long-term cost savings if the proposed changes were implemented.

There are numerous questions that remain to be answered in GHG emissions trading. GHG inventories must be comparable between countries and time series must reflect the actual changes in emissions [17]. Fuels may have different compositions and general

combustion characteristics from one place to another, and a standard value for emission factors may not be representative of what happens in the process. Therefore, it is very important to develop methods that accurately determine these emission factors, especially in the transportation sector.

Emissions from diesel vehicles can be reduced by a dual-fuel configuration [18]; oxymethylene dimethyl ethers in dual-fuel mode with diesel have the potential to reduce CO<sub>2</sub> and NO<sub>x</sub> emissions. A life-cycle analysis-based study compared emissions from heavy-duty vehicles that were operating on pure diesel and on blends of diesel and liquefied natural gas [19]. The results showed that the blends have the potential to reduce greenhouse gas emissions by 8.0%.

The extensive use of diesel-powered heavy-duty engines has resulted in significant greenhouse gas pollution in the Beijing-Tianjin-Hebei-Shandong regions of China [20], and it has been proposed to replace this fleet with heavy-duty trucks that are powered by hydrogen fuel cells. In 2015, the greenhouse gas emissions from heavy-duty vehicles in the Beijing-Tianjin-Hebei region were  $5.12 \times 10^6$  ton-CO<sub>2eq</sub> [21].

The CO<sub>2</sub> emissions from cars in Europe [22] and China [23] have been studied. The CO<sub>2</sub> emissions from trucks have also been the subject of interest. Truck fleet regulation for a future zero-emissions market in Europe has been discussed [24]. In Germany, 99.7% of heavy trucks run on diesel fuel [25]. Heavy-duty trucks are responsible for 20% of greenhouse gas emissions from the transportation sector in the United States [26]. Therefore, the study of greenhouse gas emissions from vehicles remains an interesting topic.

There may be discrepancies between official and real CO<sub>2</sub> emission rates [27]. This is the focus of this article, which presents a novel method for determining GHG rates that take into account the presence of carbon monoxide (CO), unburned hydrocarbons (C<sub>m</sub>H<sub>n</sub>) or (UHC), and particulate matter (PM) in exhaust gases. The method is based on the principles of Ostwald, who produced his well-known diagram in the early 20th century [28].

The experimental study by Clairotte et al. [29] from 2009 to 2019 showed that heavy-duty vehicles generate up to 9 g/km CO<sub>2eq</sub> from CH<sub>4</sub> emissions and 32 g/km CO<sub>2eq</sub> from N<sub>2</sub>O emissions. Liu and Tan [30] emphasized the importance of real-world measurements to improve the emission factors of heavy-duty vehicles and the suitability of portable emission measurement systems (PEMS) to perform such measurements. In their work, Wang et al. [31] used a PEMS to estimate the emission factors of heavy-duty diesel engines by measuring NO<sub>x</sub> and CO. The relative errors were within 20%.

While most of the available models are based on a multiple linear regression approach [27,31–34] or a moving average ratio [31], this article presents an estimation model that uses basic combustion theory to determine emission factors and energy that is lost as particulates. Real emissions were collected and used to develop the model. It is important to note that the PEMS equipment that was used in other works [30,31,35] can be used together with the method that was developed in the present work. Moreover, due to the remarkable decrease in CO<sub>2</sub> emissions associated with the COVID-19 pandemic [36], various strategies and opportunities have been triggered [37]. For example, electric propulsion for ocean shipping [38] and integrated renewable energy sources for smart cities [39], among other strategies.

The study was conducted using heavy-duty, off-road ore hauling trucks that run on diesel fuel and are among the main CO<sub>2</sub> emitters from mining equipment. Off-road trucks are designed to be the most robust mining equipment. They are available in different weight classes and can carry 25 to 400 tons of material. These trucks meet production targets for transporting heavy loads at a low cost of ownership.

## 2. Procedure

### 2.1. Emission Measurements

Figure 1a shows a photograph of a heavy-duty truck that is similar to the vehicles that were examined in this study. Its tires are 3.6 m in diameter, and it can carry 220 tons of ore. The employee standing in the truck gives a clear idea of its size.

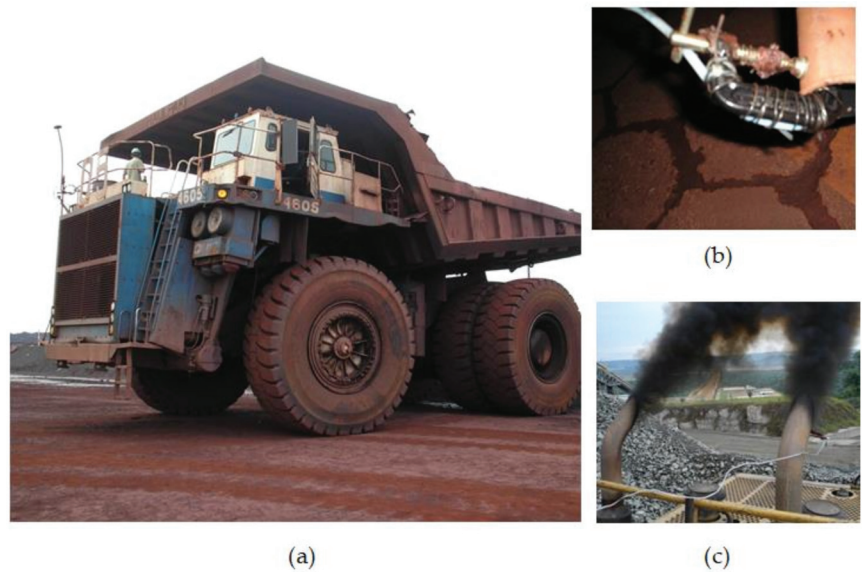


**Figure 1.** Photographs of: (a) an off-road truck for transporting iron ore, (b) the gas sampling nozzle, (c) a set of two exhaust pipes. Source: the authors.

A total of four trucks were investigated in this study, and they were designated #1 (Komatsu 830, Carajás), #2 (Komatsu 830, Carajás), #3 (Caterpillar 793C, Carajás), and #4 (Caterpillar 793C, Sossego). The Carajás mine is located in the state of Pará and the Sossego mine in the state of Minas Gerais, both in Brazil, and they belong to the Vale mining company.

Concentration measurements of the exhaust components were made by sampling the exhaust pipes of the trucks and determining the gas composition with a portable analyzer. The sampling was performed using a Teflon hose to avoid contamination or charring of the samples. This tubing contained a series of filters to remove large particles (greater than 100  $\mu\text{m}$ ) and moisture to prevent overloading of the analyzer's filter system and to reduce the pressure drop in the instrument. The sampling tip was placed a few centimeters inside the exhaust pipe near the center of the circular section, as shown in Figure 1b. Figure 1c shows a case of particulate emissions from the exhaust pipe of a truck.

The device that was used to measure the gas composition was a portable multifunctional gas analyzer model Greenline 8000 from the company Eurotron, which performs continuous measurements. It determines the concentrations of oxygen ( $\text{O}_2$ ), CO, and nitric oxide (NO) based on electrical signals that are emitted by electrochemical cells. It uses a nondispersive infrared (NDIR) system to analyze  $\text{CO}_2$  and UHC. This instrument can also be used to measure the supply temperature and differential pressure, ambient temperature, and relative humidity. Its operating characteristics are summarized in Table 1. Concentrations of  $\text{CO}_2$ ,  $\text{O}_2$ , CO, NO, and UHC were determined on a dry basis. The data were collected at 10-s intervals. Despite the amounts of particulates, the concentrations of CO and UHC were negligible in terms of mass balance. For the four trucks whose emissions were measured in this work, Table 2 presents the number of points for which the ratio CO/ $\text{CO}_2$  concentrations were below 3%, 2%, and 1%, respectively. The average UHC volume concentration was 210 ppm for truck #1; this average was lower for the other trucks and was neglected in the carbon balance for all of them. The procedure considered the absence of sulfur in the diesel fuel.

**Table 1.** Operational characteristics of the Greenline 8000 gas analyzer.

Parameter	Sensor Type	Limits	Resolution	Maximum Response Time (s)
O <sub>2</sub>	Electrochemical	0–25.0%	0.1%	20
CO	Electrochemical	0–20,000 ppm	1 ppm	40
CO <sub>2</sub>	NDIR	0–20.00%	0.01%	15
NO	Electrochemical	0–4000 ppm	1 ppm	40
C <sub>x</sub> H <sub>y</sub>	NDIR	0–50,000 ppm	1 ppm	15
T <sub>amb</sub>	Pt100	–10–100 °C	0.1 °C	
T <sub>comb gases</sub>	Thermocouple	0–1000 °C	0.1 °C	
Pressure	Bridge	±150.00 hPa	0.01 hPa	

**Table 2.** The number of points for which the ratio CO/CO<sub>2</sub> concentrations were below 3%, 2%, and 1%.

	Truck #1	Truck #2	Truck #3	Truck #4	Total	% of Total
# of points	457	347	417	635	1856	100.0%
Below 3%	456	347	412	622	1837	99.0%
Below 2%	452	346	397	618	1813	97.7%
Below 1%	431	329	305	509	1574	84.8%

The analyzer did not possess the capability of determining gases that were derived from sulfur. Some small amounts of the compound (<0.2%) could be expected. Sulfur could be expected to react completely to SO<sub>2</sub> and be accounted for in the procedure.

The mean volume concentrations of CO and NO were 650 and 280 ppm, respectively, for Truck #1. Although these concentrations are negligible, they were used to correct for the concentrations of CO<sub>2</sub> and O<sub>2</sub>, as described in the following section.

## 2.2. Diesel Formulation

No data were available on the formulation of the diesel fuel that was used in the heavy-duty engines. In addition, it was not possible to determine the exact composition of the diesel fuel that was used in the field. The concentrations of the exhaust components, determined by the Vale [40] locomotive mechanical workshop in Vitória, in the Brazilian state of Espírito Santo, were used to evaluate the composition of the diesel fuel and, consequently, the carbon content and the CO<sub>2</sub> emission factor. The data are presented in Table 3. Each data point is the average result of four measurements.

**Table 3.** Concentrations of locomotive flue gas components [40].

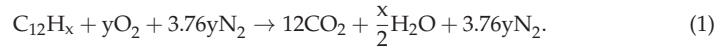
[CO <sub>2</sub> ] (%)	[O <sub>2</sub> ] (%)	[CO] (%)	[SO <sub>2</sub> ] (ppm)	[NO <sub>x</sub> ] (p.p.m)	[CO <sub>2</sub> ] <sub>corr</sub> (%)	[O <sub>2</sub> ] <sub>corr</sub> (%)
7.0	11.0	0.08	15.8	447	7.1	10.9
6.6	11.7	0.05	18.5	487	6.7	11.6
6.1	12.3	0.04	24.8	478	6.2	12.2
6.0	12.4	0.02	27.8	408	6.0	12.3
5.8	12.8	0.03	21.8	443	5.8	12.7
5.5	13.2	0.03	10.8	432	5.5	13.1
5.2	13.5	0.01	22.0	257	5.2	13.5
3.5	15.8	0.01	13.5	133	3.5	15.8
1.1	19.0	0.01	12.5	44	1.1	19.0

The CO<sub>2</sub> concentration was corrected with CO concentration by taking  $[CO_2]_{corr} = [CO_2] + [CO]$ , and the O<sub>2</sub> concentration was corrected with CO and NO<sub>x</sub> (assumed to be NO) concentrations by taking  $[O_2]_{corr} = [O_2] - [CO]/2 - 2[NO]/10,000$ , where [CO] and [NO] are in % and ppm, respectively. These corrections imply that complete combustion of CO and NO can be assumed.

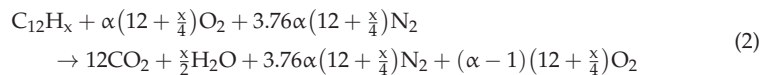


Note that NO is present in hundredths of a ppm in the combustion products, while NO<sub>2</sub> is present in a tenths of a ppm [41]. Therefore, assuming that all NO<sub>x</sub> is present as NO does not lead to significant differences.

If a generic formula C<sub>12</sub>H<sub>x</sub> is used for the diesel fuel, its stoichiometric combustion reaction takes the form shown in Equation (1).



where y is obtained by the oxygen balance, that is,  $y = 12 + x/4$ . Thus, the combustion reaction for a normalized generic excess of air,  $\alpha$ , can be represented by Equation (2).



Then, the theoretical percent concentrations of CO<sub>2</sub> and O<sub>2</sub>, in dry basis, in the absence of CO, are shown in Equations (3) and (4).

It can be easily demonstrated that the [CO<sub>2</sub>]<sub>D</sub> vs. [O<sub>2</sub>]<sub>D</sub> line is also a straight line for any C<sub>c</sub>H<sub>h</sub>N<sub>n</sub>S<sub>s</sub>O<sub>o</sub> type fuel if sulfur is considered to react to SO<sub>2</sub>, the above corrections for CO and NO are applied, and combustion air is above stoichiometry.

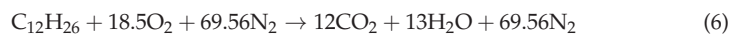
$$[CO_2]_D = \frac{12x}{12 + (4.76\alpha - 1)(12 + \frac{x}{4})} 100\% \quad (3)$$

$$[O_2]_D = \frac{(\alpha - 1)(12 + \frac{x}{4})}{12 + (4.76\alpha - 1)(12 + \frac{x}{4})} 100\% \quad (4)$$

Isolating  $\alpha$  from Equations (3) and (4), a descending straight-line relating [O<sub>2</sub>]<sub>D</sub> and [CO<sub>2</sub>]<sub>D</sub> is obtained:

$$[O_2]_D = \frac{1200 - (57.12 + 0.94x)[CO_2]_D}{57.12} \quad (5)$$

The value of x in Equations (3) and (4) was adjusted to fit the data of Table 3. The result is  $x = 26$ , as shown in Figure 2. The stoichiometric combustion reaction for a fuel with a molecule C<sub>12</sub>H<sub>26</sub> is given in Equation (6).



and its CO<sub>2</sub> emission factor, for complete combustion, in terms of kg/kg is obtained as shown in Equation (7).

$$EF_{\text{diesel}} = \frac{12 \times 44}{12 \times 12 + 26} = 3.106 \frac{\text{kg CO}_2}{\text{kg diesel}} \quad (7)$$

The concentrations of gases that are produced by the combustion of a diesel fuel that is obtained from a gas station in the city of Cachoeira Paulista, São Paulo State, Brazil, were measured [42]. Using the same procedure as here, the formula C<sub>12</sub>H<sub>21.15</sub> was determined. The corresponding emission factor for complete combustion was 2.9% higher, with a value of EF<sub>diesel</sub> = 3.197 kg – CO<sub>2</sub>/kg-diesel.

In Brazil, the density of diesel fuel ranges from 0.82 kg/L (light diesel) to 0.88 kg/L (heavy diesel) [43]. This gives an average density of 0.85 kg/L, and using the EF that is given in [42], the emission factor in kg/L is 2.717 kgCO<sub>2</sub>/L of fuel. This value, with a deviation of 0.48%, compares very favorably with the value of 2.730 kgCO<sub>2</sub>/L of fuel that is given by ECC Canada [44].

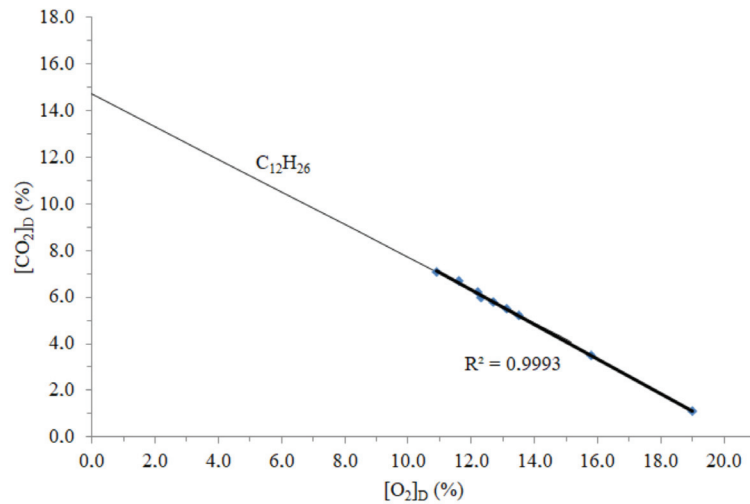


**Figure 2.** The CO<sub>2</sub> concentration as a function of O<sub>2</sub> concentration, both on a dry basis, for diesel fuel combustion in locomotives. Experimental data source: [40].

The combustion of diesel fuel in heavy machinery in mining operations produces a significant amount of particulate matter [see Figure 1b] which must be considered when calculating the actual emission factor for the activity. The particulate matter is not directly quantifiable but can be accounted for by measuring the concentrations of product gases that are generated by the equipment.

### 2.3. Fuel Losses to Particles

The engine does not operate under the same conditions during the different maneuvers that are required during the tasks that the truck has to perform. In addition, trucks have different ages and maintenance schedules that can affect their performance.

The losses can be estimated if it is assumed that the engine only partially consumes the heavy diesel compounds and forms the dark smoke, which consists of a large amount of carbon. Consider a diesel fuel with the general formula C<sub>12</sub>H<sub>a</sub>, which releases particulates during combustion. If we consider the effective combustion of a lighter diesel fuel (C<sub>12</sub>H<sub>b</sub>) as a result of the emission of particles, the balance of hydrogen atoms leads to:

$$C_{12}H_a = \frac{a}{b}(C_{12}H_b + yC) \quad (8)$$

with  $b > a$ , being  $y$  the number of moles of carbon per mole of C<sub>12</sub>H<sub>b</sub>. For carbon, the balance leads to:

$$y = 12 \left( \frac{b}{a} - 1 \right) \quad (9)$$

The carbon loss is, then:

$$C(\%) = \frac{144(1 - \frac{a}{b})}{144 + a} 100\% \quad (10)$$

It is clear that the carbon loss given by Equation (10) cannot be determined by the ratio  $a/b$  alone, i.e., the value of “ $a$ ” is necessary for the analysis. This value was assumed to be 26, as determined with the data from the laboratory of the locomotives.

Assuming a diesel fuel with a calorific value of 43 MJ/kg [17] and that the calorific value of carbon is 32.76 MJ/kg, the percentage of the fuel's calorific value that is lost as soot particles is:

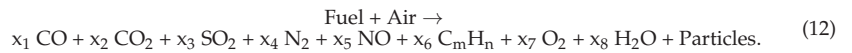
$$\text{Energy loss (\%)} = 0.762 \frac{144(1 - \frac{a}{b})}{144 + a} 100\% \quad (11)$$

It should be mentioned that this method does not determine the overall energy efficiency of the device. This depends on many other parameters than only carbon loss as particles. Moreover, it was assumed that the carbon loss occurs only in the form of carbon particles, which is confirmed by the conditions that were observed during the field measurements.

#### 2.4. Fuel Losses to Carbon Monoxide and Unburned Hydrocarbons

Other losses may be considered, e.g., to CO and UHC if they occur in non-negligible concentrations. For UHC, the assumption can be made that it is CH<sub>4</sub>, since this is the main compound of the UHC mixture.

The following formula can be established for a general chemical reaction between fuel and air:



Instruments that measure the concentrations of gas constituents usually report the values as a dry basis. Water interferes with most detection systems of analytical instruments. On a dry basis (subscript D) is the molar fraction of each gaseous combustion product:

$$[X]_{i,D} = \frac{x_i}{\sum_1^7 x_i} \quad (13)$$

These molar fractions are important when determining the mass flow rate of carbon in each of the combustion products, as shown in the following. Particles do not interfere with concentrations of gas components.

It is necessary to determine the concentrations of CO<sub>2</sub>, CO, C<sub>m</sub>H<sub>n</sub>, and particles in the combustion gases, and the carbon content of such particles.

Applying a mass balance, the mass flow rate of carbon that is emitted as CO<sub>2</sub>,  $\dot{m}_{C,CO_2}$ , through the several stacks and as fugitive emissions, is:

$$\dot{m}_{C,CO_2} = \dot{m}_{C,fuel} - \dot{m}_{C,CO} - \dot{m}_{C,part} - \dot{m}_{C,C_mH_n}, \quad (14)$$

where  $\dot{m}_{C,fuel}$  is the mass flow rate of carbon that enters the truck with the diesel fuel,  $\dot{m}_{C,CO}$  is the mass flow rate of carbon that is emitted as CO,  $\dot{m}_{C,part}$  is the mass flow rate of carbon that is emitted in the particulate material, and  $\dot{m}_{C,C_mH_n}$  is the mass flow rate of carbon that is emitted as unburned gaseous hydrocarbons C<sub>m</sub>H<sub>n</sub>.

The mass flow rate of carbon in the inlet of the equipment is  $\dot{m}_{C,fuel} = Y_{C,fuel} \dot{m}_{fuel}$ , where  $Y_{C,fuel}$  is the total carbon content in  $\dot{m}_{fuel}$ .

The mass flow ratios of carbon that are emitted CO<sub>2</sub>, to CO and C<sub>m</sub>H<sub>n</sub> species, are related by the concentrations of such gases, in a dry basis, in the combustion products, as shown in

$$\dot{m}_{C,x_i} = m \frac{x_i}{x_1} \dot{m}_{C,CO_2} = m \frac{[X]_{i,D}}{[CO_2]_D} \dot{m}_{C,CO_2} \quad (15)$$

where  $m = 1$  for CO. Thus, the relationship between the mass flow rates of carbon as CO and as CO<sub>2</sub> is  $[CO]_D/[CO_2]_D$ . For CH<sub>4</sub>, the relationship is  $[CH_4]_D/[CO_2]_D$ . These represent the losses to CO and CH<sub>4</sub>, respectively, on the assumption that their volume concentrations can be measured.

In the case of the particulate material emission, to obtain  $\dot{m}_{C,part}$  as function of  $\dot{m}_{C,CO_2}$ , it is necessary to determine the concentration of particulate material that is emitted by the

equipment through its several exhaust tubes and the carbon content of each of the respective samples. This requires adequate equipment and careful procedures, as described in the EPA Method number 5, and is impractical with heavy trucks performing different maneuvers. The term  $\dot{m}_{C,part}$  is obtained from the procedure outlined in the previous subsection.

Therefore, with the previous considerations, Equation (14) leads to the following for the mass flow rate of emitted  $CO_2$ :

$$\dot{m}_{CO_2} = \frac{44}{12} \frac{Y_{C,fuel} \dot{m}_{fuel}}{1 + \frac{[CO]_D}{[CO_2]_D} + \frac{m[C_mH_n]_D}{[CO_2]_D} + \frac{\dot{m}_{part}}{\dot{m}_{CO_2}}} \quad (16)$$

where the factor 44/12 corresponds to the relative mass of carbon dioxide to the mass of carbon in a carbon dioxide molecule.

### 3. Results and Discussion

#### 3.1. Time Concentrations, Carbon and Energy Losses, and Emission Factors

Figure 3 shows the time variation of the  $O_2$  and  $CO_2$  concentration for all the trucks. It includes operation in idle (during loading, unloading, and waiting in line), and when in movement (with and without load).

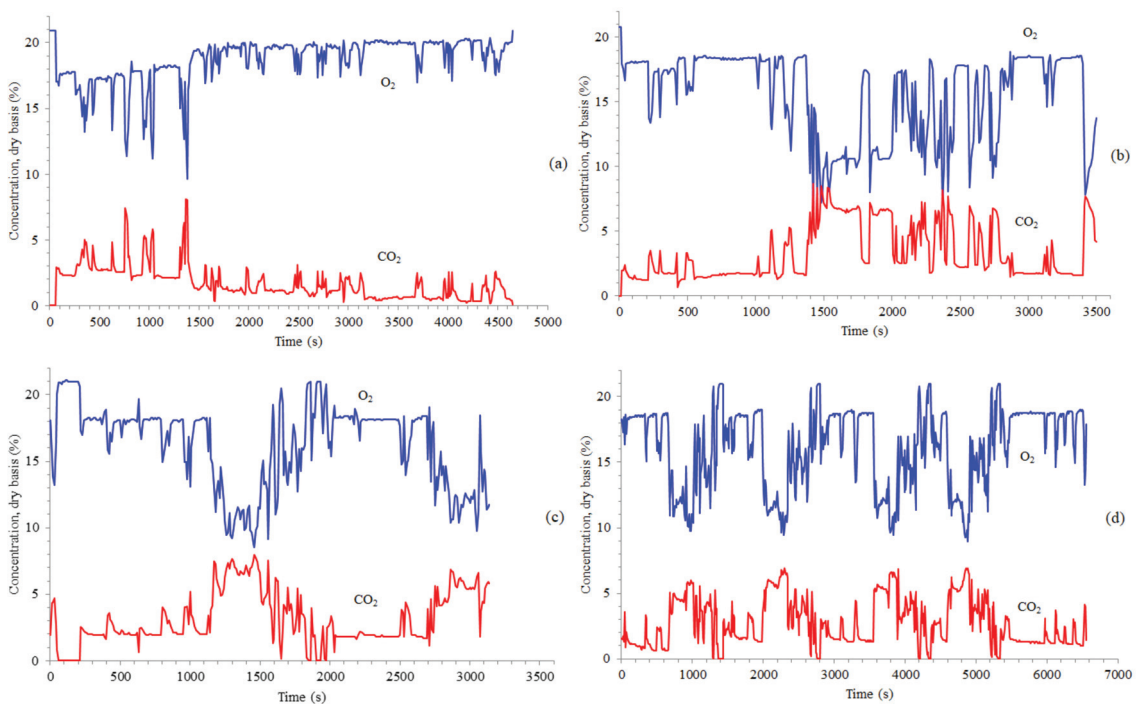


**Figure 3.** The  $O_2$  and  $CO_2$  concentrations as functions of time for all trucks: #1 (a), #2 (b), #3 (c), and #4 (d).

As expected, the  $O_2$  and  $CO_2$  concentration data are consistent with each other, that is, a decrease in the  $O_2$  concentration goes together with an increase in the  $CO_2$  concentration, and vice versa. While Trucks #1, #2, and #3 performed operations that did not repeat (with #1 in idle for a long period), Truck #4 performed four similar tasks, as shown in Figure 3d by the peaks. The correlations between the measured instantaneous  $O_2$  and  $CO_2$  concentrations will be examined below.

The CO<sub>2</sub> concentration was plotted as function of the O<sub>2</sub> concentration for each data point. The value of  $x$  was allowed to fluctuate and the dependence between the CO<sub>2</sub> and O<sub>2</sub> concentrations, given by Equations (3) and (4), was fit to the experimental values. Figure 4 shows the results of such procedure for all trucks. The values of  $x$  that give the best match against the experimental data, whose linear fit was plotted in a bold straight line, are shown in the figure. They were  $x = 26$  for #1,  $x = 37.5$  for #2,  $x = 37.5$  for #3, and  $x = 43$  for #4. The R<sup>2</sup> coefficient was higher than 0.94 in all cases.

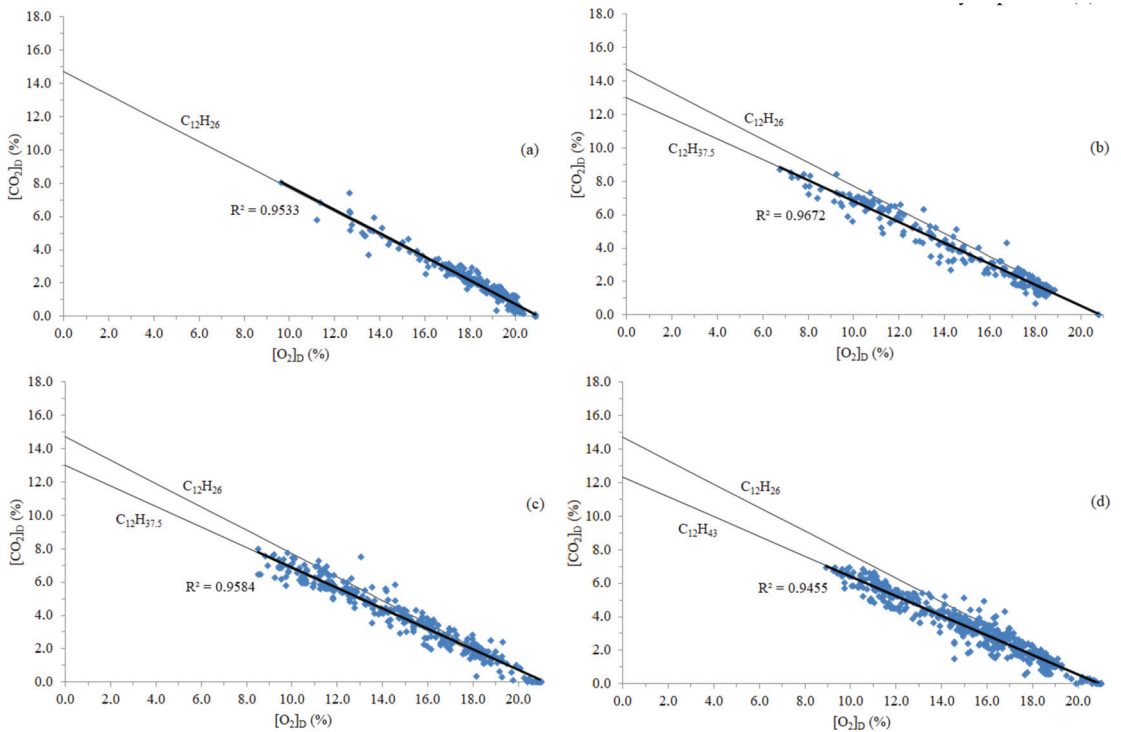


**Figure 4.** CO<sub>2</sub> concentration as function of O<sub>2</sub> concentration, both on a dry basis, for the combustion of diesel fuel in all trucks: #1 (a), #2 (b), #3 (c), and #4 (d).

It was observed that Truck #1 produced concentration results that fitted the diesel formulation, while the others presented carbon losses and, consequently, lower average CO<sub>2</sub> emission factors.

Table 4 presents the average carbon and energy losses for all the trucks. The results for Trucks #2 to #4 are a consequence of the very sooty emissions, such as that shown in Figure 1c.

**Table 4.** Average carbon and energy losses.

	Carbon Loss	Energy Loss
Truck #1	0.0%	0.0%
Truck #2	26.0%	19.8%
Truck #3	26.0%	19.8%
Truck #4	33.5%	25.5%

Table 5 presents the average emission factors for all the trucks. The reference value is given by ECC Canada [44], and the default value is given by IPCC [17]. It was observed that

each of the trucks burnt diesel fuel with different sets of maneuvers, in addition to possible differences between the trucks themselves and, therefore, different emission factors were obtained. The average EF of Truck #4 was 64.8% of the IPCC value, which led to a CO<sub>2</sub> emission 33.5% lower than that which was obtained by computing it with the default EF for the diesel fuel considered here. The emissions factors that were obtained by Li et al. [35] are presented in the same table.

A lower emission factor does not mean that the corresponding unit will emit less CO<sub>2</sub>; in fact, it will require larger quantities of diesel fuel to meet its energy requirements. Suppose that a truck is very well maintained and regulated, so that it emits a negligible amount of particles, being  $m$  the mass of fuel that is consumed to perform a determined task. Now, suppose a truck in a second situation, working with the characteristics of Truck #4, performing the same task, which can be estimated to require the same amount of energy. Taking the energy loss given in Table 4 for Truck #4 (25.5%), the mass of fuel that is required to perform the same task will be  $1/0.745 \cdot m = 1.342 m$ , and this is considering that the calorific value of the fuel does not decrease under the second situation.

Applying the factor 1.342 the emission factor of Truck #4 becomes 2.771. Comparing our results with those that were obtained by Li et al. [35], it is noticed that only the Truck#1 presents an emissions factor similar to that by Li et al. [35]. On the other hand, the Trucks #2, #3, and #4 presented lower emission factors. This is related to the fact that during the operation of Trucks #2, #3, and #4, the particulate matter emissions were higher than those for Truck #1. Therefore, the method that is presented in this article allows the identification of significant losses in the form of particulate matter, which manifest when the emission factor is lower than that which is determined by Equation (7).

It can be argued that the average emission factor that was calculated by the procedure developed here does not represent the real CO<sub>2</sub> emission of the unit, since much higher amounts of fuel are burned during movement, especially during acceleration, in comparison with operation in idle. The effect of operation under lower O<sub>2</sub> and higher CO<sub>2</sub> concentrations, characteristics of movement, was examined. The objective of doing this is to analyze the operation intervals for which the O<sub>2</sub> and CO<sub>2</sub> concentrations were lower and higher, respectively. These intervals represent a regime of operation of the engines. Other periods were not selected because they did not comply with this condition.

First, some portions of Figure 3b,c were deliberately cut to observe changes in the emission factor. These cuts, made to take into account operation at lower excess of air, were the following:

- Truck #2: the original 350 points, corresponding to 0–3490 s, were substituted by 86 points, corresponding to 1260–2110 s;
- Truck #3: the original 460 points, corresponding to 0–4590 s, were substituted by 85 points, corresponding to 990–1830 s.

The results of such cuts are presented in Figure 5. It is noted that the R<sup>2</sup> coefficient remains practically unchanged.

The main results that were obtained from Figure 5 indicate changes between the overall and selected periods of operation, according to:

- Truck #2: average EF of 2.298 kg CO<sub>2</sub>/kg diesel becomes 2.401 kg CO<sub>2</sub>/kg diesel (4.5% change, 75.4% of IPCC default value); average carbon loss of 26.0% becomes 22.7% (3.3% difference);
- Truck #3: average EF of 2.298 kg CO<sub>2</sub>/kg diesel becomes 2.547 kg CO<sub>2</sub>/kg diesel (10.8% change, 79.9% of IPCC default value); average carbon loss of 26.0% becomes 18.0% (8.0% difference).

**Table 5.** The average emission factors.

Source	Emission Factor (kg CO <sub>2</sub> /kg Diesel)	% Default Value (IPCC [17])
Laboratory [42]	3.197	100.3%
Laboratory [40]	3.106	97.5%
Truck #1	3.106	97.5%
Truck #2	2.298	72.1%
Truck #3	2.298	72.1%
Truck #4	2.065	64.8%
Li et al. (Truck) [35]	3.157	99.1%
Li et al. (Truck) [35]	3.183	99.9%
ECC Canada [44]	3.212 <sup>a</sup>	100.8%
IPCC [17]	3.186 <sup>b</sup>	100.0%

<sup>a</sup> For an average density of 0.85 kg/L; <sup>b</sup> 74100 kg CO<sub>2</sub>/TJ; Net Calorific Value = 43.0 TJ/Gg.

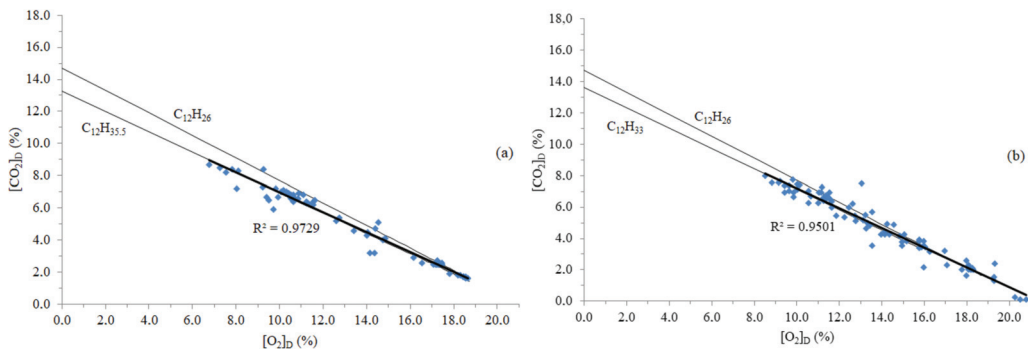


**Figure 5.** The CO<sub>2</sub> concentration as a function of O<sub>2</sub> concentration, both on a dry basis, for the combustion of diesel fuel in Trucks #2 and #3 at selected periods of operation; #2: 1260–2110 s (a); #3: 990–1830 s (b).

Next, some portions of Figure 3d were also deliberately cut to observe changes in the emission factor, but the approach was somewhat different:

- Truck #4: the original 655 points were substituted by 329 points, corresponding to operation under [O<sub>2</sub>]<sub>D</sub> < 17%;
- Truck #4: the original 655 points were substituted by 138 points, corresponding to operation under [O<sub>2</sub>]<sub>D</sub> < 13%.

The time variation of O<sub>2</sub> and CO<sub>2</sub> concentrations with time (in a continuous basis), for the above-described situations, is presented in Figure 6. As the O<sub>2</sub> concentration is limited to a certain value, the graph represents operation at richer conditions and consistent with higher mass flow rates of fuel. Figure 7 presents the CO<sub>2</sub> concentration as function of O<sub>2</sub> concentration, also for the above-described situations. A steep reduction of the R<sup>2</sup> coefficient is observed; however, the emission factor and the carbon loss remained practically the same as those that were calculated for overall average conditions.

Figures 6 and 7 are examples of how sampling can be divided into specific maneuver periods or conditions so that they can be assessed individually. The difference between the squared correlation coefficients happens because for the low air excess regime, there are fewer data than for high air excess.

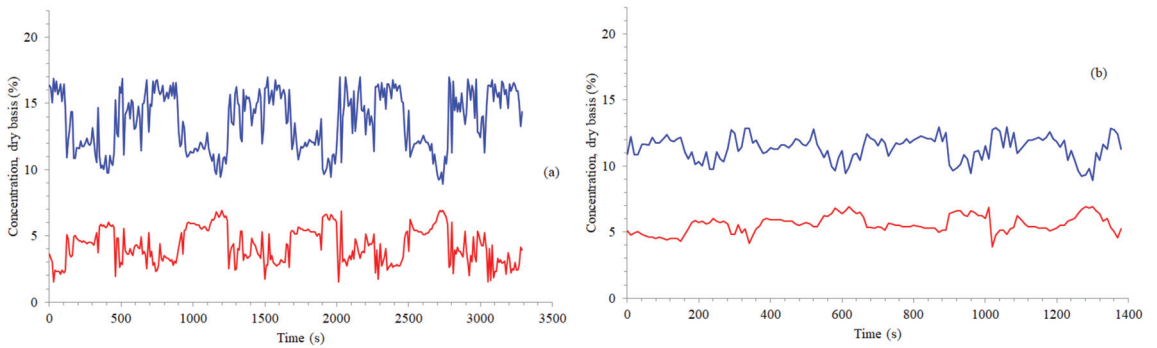


**Figure 6.** The O<sub>2</sub> and CO<sub>2</sub> concentrations as functions of time for Truck #4: for [O<sub>2</sub>]<sub>D</sub> < 17% (a), for [O<sub>2</sub>]<sub>D</sub> < 13% (b).

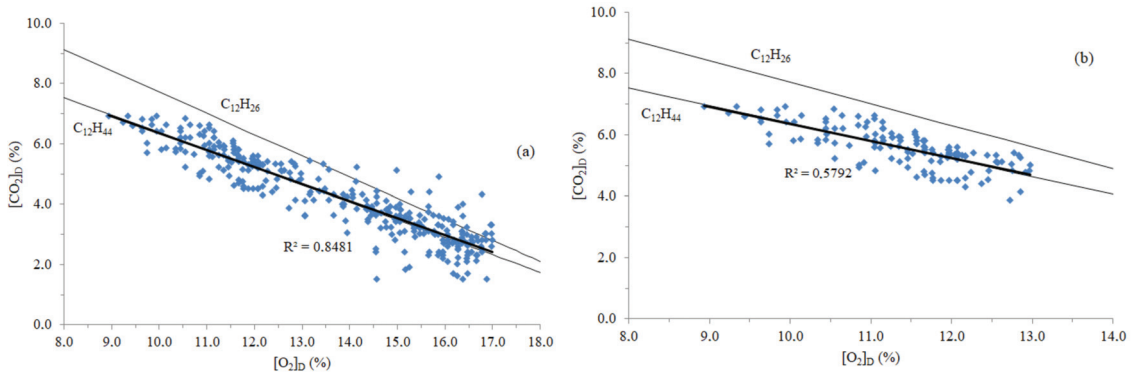


**Figure 7.** The CO<sub>2</sub> concentration as a function of O<sub>2</sub> concentration, both on a dry basis, for the combustion of diesel fuel in Truck #4: for [O<sub>2</sub>]<sub>D</sub> < 17% (a), for [O<sub>2</sub>]<sub>D</sub> < 13% (b).

3.2. Error Estimates

The resolutions of the O<sub>2</sub> and CO<sub>2</sub> sensors were 0.1% and 0.01%, respectively, as shown in Table 1. The errors were estimated by carrying out the same procedure that was used to obtain Figure 4, but adding and subtracting 0.1% and 0.01% to the measured concentrations of O<sub>2</sub> and CO<sub>2</sub>, respectively.

Table 6 presents the results. In the column named “Action”, ++ represents +0.1% and +0.01%, and so on. It is observed that, under the conditions of the unpredictable maneuvers that were performed by the trucks during the data collection of this work, the maximum estimated error was 5.9%, which occurred for Truck #1.

**Table 6.** The results for the error in relation to the calculated emission factor.

Truck	Action	Fuel Formula	Emission Factor Error <sup>a</sup>
#1	++	C <sub>12</sub> H <sub>24.3</sub>	5.9%
	+−	C <sub>12</sub> H <sub>24.3</sub>	5.9%
	−−	C <sub>12</sub> H <sub>26.1</sub>	−0.3%
	−+	C <sub>12</sub> H <sub>26.1</sub>	−0.3%
#2	++	C <sub>12</sub> H <sub>36.4</sub>	2.4%
	+−	C <sub>12</sub> H <sub>36.4</sub>	2.4%
	−−	C <sub>12</sub> H <sub>37.8</sub>	−0.6%
	−+	C <sub>12</sub> H <sub>37.5</sub>	0.0%



Table 6. Cont.

Truck	Action	Fuel Formula	Emission Factor Error <sup>a</sup>
#3	++	C <sub>12</sub> H <sub>35.9</sub>	3.5%
	+−	C <sub>12</sub> H <sub>36.0</sub>	3.3%
	−−	C <sub>12</sub> H <sub>37.6</sub>	−0.2%
	−+	C <sub>12</sub> H <sub>37.6</sub>	−0.2%
#4	++	C <sub>12</sub> H <sub>43.2</sub>	−0.4%
	+−	C <sub>12</sub> H <sub>43.1</sub>	−0.2%
	−−	C <sub>12</sub> H <sub>43</sub>	0.0%
	−+	C <sub>12</sub> H <sub>43.1</sub>	−0.2%

<sup>a</sup> In relation to the value that was calculated in the respective graph.

#### 4. Conclusions

A simple and novel method for determining CO<sub>2</sub> emission rates and carbon losses for heavy-duty vehicles was developed.

A series of four off-road heavy-duty trucks used to transport iron ore were analyzed for their CO<sub>2</sub> emission rates and carbon losses. The importance of gas concentration measurements in inferring instantaneous fuel composition, which can vary depending on the maneuver being performed and truck parameters such as age, maintenance records, type, etc., was demonstrated.

It has been shown that each of the four off-road trucks consumes diesel fuel with different efficiency and, therefore, each of them has a different average emission factor. The results for Truck #4 show that the average CO<sub>2</sub> emission factors can be as low as 64.8% of the IPCC default value for diesel fuel. On the other hand, even for Truck #4, losses can reach 33.5% in terms of carbon and 25.5% in terms of energy.

A limitation of the present study was the fact that it used the diesel oil formulation that was obtained in the laboratory for locomotives. The fuel had to be analyzed in the mining area before being used in the trucks, which was not possible. Another limitation was the difficulty in providing a valid error analysis for all situations in an unpredictable set of general truck characteristics and maneuvers. However, these do not invalidate the method that was developed here.

A similar line of thought has been applied in the past by two of the authors to: (a) detect and quantify leakage from coke ovens to combustion chambers in a conventional coke plant, and (b) detect and estimate scale formation in slab reheating furnaces. This work is available in the form of consulting reports. In the first case, carbon particles infiltrated the combustion chamber where coke oven gas (COG) was burned; the effective fuel was replaced by a mixture of COG and carbon particles. In the second case, oxygen was removed from the combustion products of natural gas by scale formation; the effective fuel was replaced by a mixture of natural gas and iron.

In future work, the authors intend to test the method with a portable emissions measurement system in order to develop a tool that be used to estimate the emissions factors in real time, during the normal operation of a heavy-duty vehicle.

The authors believe that the procedure that was outlined in this article, if carried out with proper error analysis, can be useful in problems involving energy losses in industrial combustion processes.

**Author Contributions:** Conceptualization, J.A.d.C.J.; methodology, J.A.d.C.J.; formal analysis, J.A.d.C.J., G.H.B. and P.A.d.S.J.; resources, P.A.d.S.J.; data acquisition, A.d.C.; writing—original draft preparation, J.A.d.C.J. and A.Z.M.; writing—review and editing, J.A.d.C.J., G.H.B., P.A.d.S.J. and A.Z.M.; supervision, P.A.d.S.J.; project administration, P.A.d.S.J.; funding acquisition, P.A.d.S.J. All authors have read and agreed to the published version of the manuscript.

**Funding:** This research received no external funding.

**Institutional Review Board Statement:** Not applicable.

**Informed Consent Statement:** Not applicable.

**Data Availability Statement:** Not applicable.

**Acknowledgments:** The authors are grateful to ANP, FINEP, and MCTI, through the program PRH 34.1 FEG/UNESP, and to Vale Mining Company.

**Conflicts of Interest:** The authors declare no conflict of interest.

## Nomenclature

$\alpha$	Air in excess factor
a	Hypothetical number of atoms of hydrogen in diesel's empirical molecule
b	Hypothetical number of atoms of hydrogen in diesel's empirical molecule
CH <sub>4</sub>	Methane
CO <sub>2</sub>	Carbon dioxide
CO	Carbon monoxide
CO <sub>2eq</sub>	Carbon dioxide equivalent emissions
COG	Coke oven gas
C <sub>m</sub> H <sub>n</sub>	Unburned hydrocarbon with m carbon and n hydrogen atoms
H <sub>2</sub> O	Water
$\dot{m}_{C,xi}$	Mass flow rate of carbon related to ith species
N <sub>2</sub> O	Nitrous oxide
N <sub>2</sub>	Nitrogen
NO	Nitrogen monoxide
O <sub>2</sub>	Oxygen
SO <sub>2</sub>	Sulphur dioxide
x	Number of atoms of hydrogen in diesel's empirical molecule
x <sub>i</sub>	Number of moles of ith species in combustion products
y	Number of mols of oxygen in reactants, mol
Y <sub>C,fuel</sub>	Mass fraction of carbon in the fuel
[CO <sub>2</sub> ] <sub>D</sub>	Molar concentration of CO <sub>2</sub> in dry basis
[O <sub>2</sub> ] <sub>D</sub>	Molar concentration of O <sub>2</sub> in dry basis
[X] <sub>i,D</sub>	Molar concentration of ith species in combustion products

## Abbreviations

ECC	Environment and Climate Change
EF	Emission factor
GHG	Greenhouse gases
IET	International Emissions Trading
IPCC	Intergovernmental Panel for Climate Change
NDIR	Infrared Non-dispersive System
PEMS	Portable Emissions Measurement Systems
UHC	Unburned hydrocarbons

## References

- Barrett, S. Political economy of the kyoto protocol. *Clim. Chang.* **2017**, *14*, 465–484. [\[CrossRef\]](#)
- Springer, U. The market for tradable GHG permits under the Kyoto Protocol: A survey of model studies. *Energy Econ.* **2003**, *25*, 527–551. [\[CrossRef\]](#)
- Johnson, E.; Heinen, R. Carbon trading: Time for industry involvement. *Environ. Int.* **2004**, *30*, 279–288. [\[CrossRef\]](#) [\[PubMed\]](#)
- Karpf, A.; Mandel, A.; Battiston, S. Price and network dynamics in the European carbon market. *J. Econ. Behav. Organ.* **2018**, *153*, 103–122. [\[CrossRef\]](#)
- Watson, F. *Global Carbon Market Grows 20% to \$272 Billion in 2020: Refinitiv*; S&P Glob Patts: London, UK, 2021.
- Aldhous, P. China's Burning Ambition. *Nature* **2005**, *435*, 1152–1156. [\[CrossRef\]](#) [\[PubMed\]](#)
- Hopke, P.K. Contemporary threats and air pollution. *Atmos. Environ.* **2009**, *43*, 87–93. [\[CrossRef\]](#)
- Wang, R.; Liu, W.; Xiao, L.; Liu, J.; Kao, W. Path towards achieving of China's 2020 carbon emission reduction target-A discussion of low-carbon energy policies at province level. *Energy Policy* **2011**, *39*, 2740–2747. [\[CrossRef\]](#)
- Auffhammer, M.; Carson, R.T. Forecasting the path of China's CO<sub>2</sub> emissions using province-level information. *J. Environ. Econ. Manag.* **2008**, *55*, 229–247. [\[CrossRef\]](#)

10. Ouyang, X.; Fang, X.; Cao, Y.; Sun, C. Factors behind CO<sub>2</sub> emission reduction in Chinese heavy industries: Do environmental regulations matter? *Energy Policy* **2020**, *145*, 111765. [CrossRef]
11. Gerlagh, R.; Lise, W. Carbon taxes: A drop in the ocean, or a drop that erodes the stone? The effect of carbon taxes on technological change. *Ecol. Econ.* **2005**, *54*, 241–260. [CrossRef]
12. Michaelowa, A.; Stronzik, M.; Eckermann, F.; Hunt, A. Transaction costs of the kyoto mechanisms. *Clim. Policy* **2003**, *3*, 261–278. [CrossRef]
13. Nagase, K. “Carbon-Money Exchange” to contain global warming and deforestation. *Energy Policy* **2005**, *33*, 1233–1238. [CrossRef]
14. ISO 14064-1:2018; Greenhouse Gases—Part 1: Specification with Guidance at the Organization Level for Quantification and Reporting of Greenhouse Gas Emissions and Removals. ISO: Geneva, Switzerland, 2019.
15. Friedl, B.; Getzner, M. Determinants of CO<sub>2</sub> emissions in a small open economy. *Ecol. Econ.* **2003**, *45*, 133–148. [CrossRef]
16. Katta, A.K.; Davis, M.; Kumar, A. Assessment of greenhouse gas mitigation options for the iron, gold, and potash mining sectors. *J. Clean. Prod.* **2020**, *245*, 118718. [CrossRef]
17. Inventories TF on NGG. *2019 Refinement to the 2006 IPCC Guidelines for National Greenhouse Gas Inventories—General Guidance and Reporting*; IPCC, United Nations: Geneva, Switzerland, 2019; Volume 1.
18. Benajes, J.; García, A.; Monsalve-Serrano, J.; Martínez-Boggio, S. Potential of using OMEx as substitute of diesel in the dual-fuel combustion mode to reduce the global CO<sub>2</sub> emissions. *Transp. Eng.* **2020**, *1*, 100001. [CrossRef]
19. Song, H.; Ou, X.; Yuan, J.; Yu, M.; Wang, C. Energy consumption and greenhouse gas emissions of diesel/LNG heavy-duty vehicle fleets in China based on a bottom-up model analysis. *Energy* **2017**, *140*, 966–978. [CrossRef]
20. Lao, J.; Song, H.; Wang, C.; Zhou, Y.; Wang, J. Beijing- Reducing atmospheric pollutant and greenhouse gas emissions of heavy duty trucks by substituting diesel with hydrogen in Tianjin-Hebei-Shandong region, China. *Int. J. Hydrogen Energy* **2021**, *46*, 18137–18152. [CrossRef]
21. Xing, Y.; Song, H.; Yu, M.; Wang, C.; Zhou, Y.; Liu, G.; Du, L. The Characteristics of Greenhouse Gas Emissions from Heavy-Duty Trucks in the Beijing-Tianjin-Hebei (BTH) Region in China. *Atmosphere* **2016**, *7*, 121. [CrossRef]
22. González, R.M.; Marrero, G.; Rodríguez-López, J.; Marrero, A.S. Analyzing CO<sub>2</sub> emissions from passenger cars in Europe: A dynamic panel data approach. *Energy Policy* **2019**, *129*, 1271–1281. [CrossRef]
23. Li, X.; Yu, B. Peaking CO<sub>2</sub> emissions for China’s urban passenger transport sector. *Energy Policy* **2019**, *133*, 110913. [CrossRef]
24. Breed, A.; Speth, D.; Plötz, P. CO<sub>2</sub> fleet regulation and the future market diffusion of zero-emission trucks in Europe. *Energy Policy* **2021**, *159*, 112640. [CrossRef]
25. Anderhofstadt, B.; Spinler, S. Preferences for autonomous and alternative fuel-powered heavy-duty trucks in Germany. *Transp. Res. Part D Transp. Environ.* **2020**, *79*, 102232. [CrossRef]
26. Quiros, D.; Smith, J.; Thiruvengadam, A.; Huai, T.; Hu, S. Greenhouse gas emissions from heavy-duty natural gas, hybrid, and conventional diesel on-road trucks during freight transport. *Atmos. Environ.* **2017**, *168*, 36–45. [CrossRef]
27. Tietge, U.; Mock, P.; Franco, V.; Zacharof, N. From laboratory to road: Modeling the divergence between official and real-world fuel consumption and CO<sub>2</sub> emission values in the German passenger car market for the years 2001–2014. *Energy Policy* **2017**, *103*, 212–232. [CrossRef]
28. Brizuela, E. A novel presentation of Ostwald’s combustion. *Ind. Comb. J. Int. Flame Res. Found.* **2015**. Available online: <https://ifrf.net/research/archive/a-novel-presentation-of-ostwalds-combustion/> (accessed on 15 January 2022).
29. Clairotte, M.; Suarez-Bertoa, R.; Zardini, A.; Giechaskiel, B.; Pavlovic, J.; Valverde, V.; Ciuffo, B.; Astorga, C. Exhaust emissions factors of greenhouse gases (GHGs) from European road vehicles. *Environ. Sci. Eur.* **2020**, *32*, 125–145. [CrossRef]
30. Wang, H.; Wu, Y.; Zhang, K.; Zhang, S.; Baldauf, R.; Snow, R.; Deshmukh, P.; Zheng, X.; He, L.; Hao, J. Evaluating mobile monitoring of on-road emission factors by comparing concurrent PEMS measurements. *Sci. Total Environ.* **2020**, *736*, 139507–139517. [CrossRef]
31. Liu, Y.; Tan, J. Green traffic-oriented heavy-duty vehicle emissions characteristics of China VI based on portable emission measurement systems. *IEEE Access* **2020**, *8*, 106639–106647. [CrossRef]
32. He, L.; Zhang, S.; Hu, J.; Li, Z.; Zheng, X.; Cao, Y.; Xu, G.; Yan, M.; Wu, Y. On-road emission measurements of reactive nitrogen compounds from heavy-duty diesel trucks in China. *Environ. Pollut.* **2020**, *262*, 114280–114290. [CrossRef]
33. Anable, J.; Brand, C.; Tran, M.; Eyre, N. Modelling transport energy demand: A socio-technical approach. *Energy Policy* **2012**, *41*, 125–138. [CrossRef]
34. Linton, C.; Grant-Muller, S.; Gale, W. Approaches and techniques for modelling CO<sub>2</sub> emissions from road transport. *Transp. Rev.* **2015**, *35*, 533–553. [CrossRef]
35. Li, X.; Ai, Y.; Ge, Y.; Qi, J.; Feng, Q.; Hu, J.; Porter, W.; Miao, Y.; Mao, H.; Jin, T. Integrated effects of SCR, velocity, and air-fuel ratio on gaseous pollutants and CO<sub>2</sub> emissions from China V and VI heavy-duty diesel vehicles. *Sci. Total Environ.* **2022**, *811*, 152311–152319. [CrossRef]
36. Nguyen, X.; Hoang, A.; Olçer, A.; Huynh, T. Record decline in global CO<sub>2</sub> emissions prompted by COVID-19 pandemic and its implications on future climate changes policies. *Energy Sources Part A* **2021**. [CrossRef]
37. Hoang, T.; Nizetic, S.; Olcer, A.; Ong, H.; Chen, W.; Chong, C.; Thomas, S.; Bandh, S.; Nguyen, X. Impacts of COVID-19 on the global energy system and shift progress to renewable energy: Opportunities, challenges and policy implications. *Energy Policy* **2021**, *154*, 112322. [CrossRef]

38. Nguyen, H.; Hoang, A.; Nizetic, S.; Nguyen, X.; Le, A.; Luong, C.; Chi, V.; Pham, V. The electric propulsion system as a green solution for management strategy of CO<sub>2</sub> emissions in ocean shipping: A comprehensive review. *Int. Trans. Electr. Energy Syst.* **2021**, *31*, e12580. [[CrossRef](#)]
39. Hoang, A.; Pham, V.; Nguyen, X. Integrating renewable sources into energy system for smart city as a sagacious strategy towards clean and sustainable process. *J. Clean. Prod.* **2021**, *305*, 127161. [[CrossRef](#)]
40. Portela, P.; Coelho, F.; Vale Mining Company. Personal Communication, 2007.
41. Borman, G.; Ragland, K. *Combustion Engineering*; McGraw-Hill: New York, NY, USA, 1998; pp. 125–126.
42. Paz, E. Substitution of Diesel Fuel by Ethyl Alcohol in Industrial Burners. Ph.D. Thesis, Universidade Estadual Paulista Julio de Mesquita Filho, Guaratinguetá, Brazil, 2007. (In Portuguese).
43. Garcia, R. Fuels and Industrial Combustion. Interciência: Rio de Janeiro, Brazil, 2002. (In Portuguese)
44. ECC Canada. *Environment and Climate Change Canada. Greenhouse Gas Emissions—Canadian Environmental Sustainability Indicators*; ECC Canada: Gatineau, QC, Canada, 2020; Volume 4.





Article

# The Cause of China's Haze Pollution: City Level Evidence Based on the Extended STIRPAT Model

Jingyuan Li <sup>1</sup>, Jinhua Cheng <sup>1</sup>, Yang Wen <sup>2,3</sup>, Jingyu Cheng <sup>4</sup>, Zhong Ma <sup>5</sup>, Peiqi Hu <sup>5,6,\*</sup> and Shurui Jiang <sup>5,\*</sup>

<sup>1</sup> School of Economics and Management, China University of Geosciences, Wuhan 430074, China; ljy420@cug.edu.cn (J.L.); chengjinhua100@126.com (J.C.)

<sup>2</sup> Chinese Academy of Macroeconomic Research, Beijing 100038, China; wenyangcywj@163.com

<sup>3</sup> Institute of Spatial Planning & Regional Economy, National Development and Reform Commission, Beijing 100038, China

<sup>4</sup> School of Physical Education, China University of Geosciences, Wuhan 430074, China; cjl@cug.edu.cn

<sup>5</sup> School of Environment and Natural Resources, Renmin University of China, Beijing 100872, China; zhongma@vip.sina.com

<sup>6</sup> Department of Forest and Conservation Science, University of British Columbia, Vancouver, BC V6T 1Z4, Canada

\* Correspondence: hupeiqi@ruc.edu.cn (P.H.); jiangshurui@ruc.edu.cn (S.J.)

**Abstract:** Based on the extended STIRPAT model, this paper examines social and economic factors regarding PM<sub>2.5</sub> concentration intensity in 255 Chinese cities from 2007 to 2016, and includes quantile regressions to analyze the different effects of these factors among cities of various sizes. The results indicate that: (1) during 2007–2016, urban PM<sub>2.5</sub> concentration exhibited declining trends in fluctuations concerning the development of the urban economy, accompanied by uncertainty under different city types; (2) population size has a significant effect on propelling PM<sub>2.5</sub> concentration; (3) the effect of structure reformation on PM<sub>2.5</sub> concentration is evident among cities with different populations and levels of economic development; and (4) foreign investment and scientific technology can significantly reduce PM<sub>2.5</sub> emission concentration in cities. Accordingly, local governments not only endeavor to further control population size, but should implement a recycling economy, and devise a viable urban industrial structure. The city governance policies for PM<sub>2.5</sub> concentration reduction require re-classification according to different population scales. Cities with large populations (i.e., over 10 million) should consider reducing their energy consumption. Medium population-sized cities (between 1 million and 10 million) should indeed implement effective population (density) control policies, while cities with small populations (less than 1 million) should focus on promoting sustainable urban development to stop environmental pollution from secondary industry sources.

**Keywords:** PM<sub>2.5</sub>; influencing factors; STIRPAT model; quantile regression

**Citation:** Li, J.; Cheng, J.; Wen, Y.; Cheng, J.; Ma, Z.; Hu, P.; Jiang, S. The Cause of China's Haze Pollution: City Level Evidence Based on the Extended STIRPAT Model. *Int. J. Environ. Res. Public Health* **2022**, *19*, 4597. <https://doi.org/10.3390/ijerph19084597>

Academic Editors: Roberto Alonso González Lezcano, Francesco Nocera and Rosa Giuseppina Caponetto

Received: 12 January 2022

Accepted: 7 April 2022

Published: 11 April 2022

**Publisher's Note:** MDPI stays neutral with regard to jurisdictional claims in published maps and institutional affiliations.



**Copyright:** © 2022 by the authors. Licensee MDPI, Basel, Switzerland. This article is an open access article distributed under the terms and conditions of the Creative Commons Attribution (CC BY) license (<https://creativecommons.org/licenses/by/4.0/>).

## 1. Introduction

With the rapid changes occurring in industrialization and urbanization, China's economic development has been expanding in recent decades. Consequently, massive haze pollution has been generated from such rapid economic development and it can no longer be ignored. In response to the frequent and widespread haze pollution problem, the Chinese government is now paying much greater attention to it. The Action Plan for the Prevention and Control of Air Pollution was issued in 2013, aiming to reduce the concentration of fine particles. PM<sub>2.5</sub> is one of the most widespread pollutants among fine particles. The Ministry of Environmental Protection adopted the Ambient Air Quality Standards (GB3095-2012) in 2012. It stipulates the annual average concentration limit of PM<sub>2.5</sub>, with the primary limit standard of 15 µg/m<sup>3</sup> and the secondary limit standard of 35 µg/m<sup>3</sup>. As seen in Figure 1, the proportion of PM<sub>2.5</sub> annual average concentration below the secondary concentration limit experienced an increase from 26.27% in 2007 to 36.86% in 2012, followed by a sharp

decline from 31.32% in 2013, and a steady increase up to 47.06% in 2016. The proportion of PM<sub>2.5</sub> annual average concentration is higher than 55 µg/m<sup>3</sup> but did decline gradually to 36.86% in 2007, then 18.43% in 2016 after a slight rebound in 2010 (31.76%) and 2013 (33.21%). The national average of PM<sub>2.5</sub> concentration was 47 µg/m<sup>3</sup> in 2016, with a 29% decrease compared to 2013.

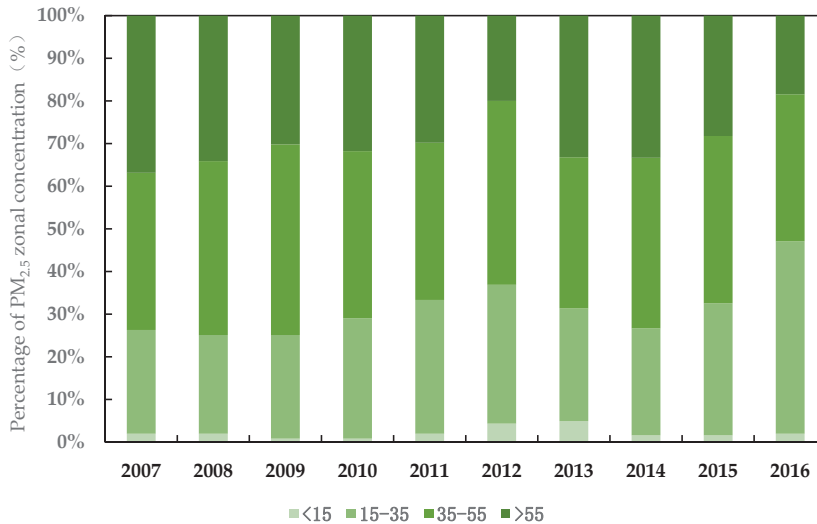


**Figure 1.** The trend regarding PM<sub>2.5</sub> concentration in China's 255 cities, 2007–2016 (µg/m<sup>3</sup>).

Most current studies in China have stated the main pollutants of air pollution such as: carbon dioxide (CO<sub>2</sub>), nitrogen oxide (NO<sub>x</sub>), sulfur dioxide (SO<sub>2</sub>) and fine particulate matter (PM<sub>2.5</sub>) [1–4]. Dong et al. examined key impact factors, specifically the CO<sub>2</sub> emissions of 128 countries from 1990 to 2014. The results indicate that causality varies among the variables across regions [5]. Diao et al. studied the industrial NO<sub>x</sub> emissions in China's provinces, and pointed out that the government must develop appropriate regulatory policies to combat regional pollution [6]. Miao et al. focused on the key factors of dust and SO<sub>2</sub> emissions and found that pollutant emissions are correlated across regions [7]. Yang and Shan also investigated regional industrial SO<sub>2</sub> emissions in the Jiangsu Province and its south, middle and north regions during 2004–2016 [8]. Meanwhile Weng et al. explored the urban environmental effect driven by multi-factors, such as industrial SO<sub>2</sub>, wastewater and dust emission intensity in prefecture-level cities [9]. PM<sub>2.5</sub> is one of the main particulate matters found in haze, which is evidenced as the main contributor of air pollution [10]. Wang et al. and Chen et al. also pointed out that PM<sub>2.5</sub> can in fact seriously affect ambient air quality [11,12].

Most Chinese scholars utilize certain variables to measure population density [13], urbanization [14] and FDI [15] when discussing the driving factor of PM<sub>2.5</sub> concentration at the city level. Furthermore, energy-related indicators also play an important role in PM<sub>2.5</sub> concentration but the effects are rarely examined due to the lack of data captured and in cities [16], which has led to the omitted variable bias. This study uses electricity consumption to measure the level of energy consumption mainly based on the following two considerations. Firstly, electricity consumption has been widely used by scholars as an indicator since it highly correlates with urban energy consumption. Secondly, data accuracy and availability of this indicator reduces the bias of omitted variables, thus improving the reliability of results [17,18].

Scholars have used different research methods, such as exploratory spatial data analysis (ESDA) [19], factor analysis [20], the Stochastic Impacts by Regression on Population,

Affluence and Technology (STIRPAT) model [21], GeogDetector [22,23] and spatial econometric model to explore the main factors affecting PM<sub>2.5</sub> concentration [4]. Zhang et al. used spatial regression to mainly discuss the direct and indirect influences which several factors make on PM<sub>2.5</sub> concentration. The study finds that environmental regulations not only have a direct impact on haze pollution, but also affect haze pollution indirectly through coal consumption, as it relates to foreign direct investment (FDI), and industrial structure and technological innovation [24]. Lu et al. employed both linear regression and grey system correlation analysis methods to analyze the spatial and temporal patterns, variation trends and the main factors influencing PM<sub>2.5</sub> concentration in China from 1998 to 2014. The results conclude that high PM<sub>2.5</sub> concentration in the northwest of China were mainly caused by natural factors (sand and dust), while in the eastern region mainly resulted from human activities. Low PM<sub>2.5</sub> concentration areas were mainly located in the less developed regions [25]. Yang et al. applied the GeogDetector method to quantify nonlinear associations between PM<sub>2.5</sub> concentration and potential factors. Both natural and socioeconomic factors and their interactive impacts on PM<sub>2.5</sub> pollution are considered [22]. Wang et al. employed multi-temporal and statistical analysis to show the temporal and spatial characteristics of PM<sub>2.5</sub> concentration in 338 Chinese cities during 2014–2017, and further used structural equation modeling (SEM) to quantify the socio-economic driving factors of PM<sub>2.5</sub> concentration changes. This concluded that urban population density contributes most significantly [26]. Zhou et al. verified that population scale yields a significantly positive effect on PM<sub>2.5</sub> concentration in 199 cities of China [27].

Few scholars evaluated the determinants of PM<sub>2.5</sub> concentration among various population scales. The factors causing the problem of PM<sub>2.5</sub> concentration vary in regions with different population sizes. Although previous scholars studied PM<sub>2.5</sub> concentration mainly at the national level, it has gradually expanded to provide research into the regions and regional or cross-regional levels, such as the Yangtze River Delta region, Beijing-Tianjin-Hebei region and various provinces of China [28–30]. For instance, Luo et al. employed an extended STIRPAT model to identify the socioeconomic determinants of PM<sub>2.5</sub> concentration for 12 different regions in China, and ranked the influencing factors on PM<sub>2.5</sub> concentration in descending order of importance [31]. Cheng et al. used the epsilon-based measure (EBM) meta-frontier Malmquist model to measure the meta-frontier Malmquist total factor productivity index (MMPI) in 10 city groups [32]. According to the above studies, most research focused on the differentiated determinants of PM<sub>2.5</sub> concentration in various geographic regions.

To differentiate the diverse effects of population sizes on PM<sub>2.5</sub> concentration, the quantile regression method is implemented. The ordinary least squares (OLS) method only analyzes the expected value of the effect of each explanatory variable. It cannot ascertain the influence of each factor on the distribution patterns alone of PM<sub>2.5</sub> concentration and distinguish the different results from one factor using such varied types. Quantile regression as proposed by Koenker and Bassett (1978), however, can perhaps solve this problem [33]. The quantile regression method assumes the quantile of the conditional distribution of the dependent variable as a linear function, and thus establishes a quantile regression of the dependent variable. It can obtain the quantile effect of the independent variable on the dependent variable, which gives a more detailed picture of the conditions of distribution and a more comprehensive set of results. It can avoid the shortcomings of OLS regression in analyzing the outliers and heteroskedasticity of the dependent variable [34,35]. Consequently, it is essential to consider population scale in our research by using the quantile regression model.

The Environmental Kuznets Curve (EKC) theory is another important issue widely discussed in current literatures. The inverted U-shaped curve relationship between the level of environmental pollution and income level implies that environmental degradation increases with output during the early stages of economic growth. However, it declines with output after reaching a specified threshold. Some scholars further studied the EKC hypothesis and found that haze pollution and economic development not only have an



inverted U-shaped curve relationship [36,37], but also have a U-shaped [38], N-shaped or inverted N-shaped relationship [39,40]. While some regions could not confirm the EKC hypothesis [41,42]. Apergis et al. postulated that the EKC hypothesis holds in only 10 states, while the remaining 38 states do not find the EKC hypothesis, which should prevent environmental degradation but not at the expense of economic growth [43]. Current studies such as those above have analyzed the driving factor of PM<sub>2.5</sub> concentration using various models to support the existence of EKC in PM<sub>2.5</sub> concentration. As referred to previously, a few scholars have combined the influential elements on PM<sub>2.5</sub> concentration and the EKC of the economy and PM<sub>2.5</sub> concentration, which is worth investigating further.

In summary, three aspects contribute to this research field. Firstly, instead of only considering the geological differences, cities in China are categorized into four types to explore the differentiated effect of variables on PM<sub>2.5</sub> concentration classified by population scale. Secondly, the urban scale and EKC effect are both taken into account. This paper constructs the STIRPAT model of PM<sub>2.5</sub> concentration in 255 cities and combines the EKC hypothesis to measure the determinants of haze pollution more comprehensively. Thirdly, total electricity consumption as a critical proxy of energy consumption is also involved in the model to measure the influence of energy consumption on PM<sub>2.5</sub> concentration, which enriches the model with more variables.

The following is further discussed. Section 2 presents the methodology, variables and data sources. Section 3 represents the results of the STIRPAT model and quantile regression. Section 4 proposes further discussion. The corresponding conclusions are articulated in Section 5.

## 2. Materials and Methods

### 2.1. Methodology

In 1971, Ehrlich and Holden first proposed the “*I = PAT*” model [44] to study the relationship between population and environment. Dietz later proposed the Stochastic Impacts by Regression on Population, Affluence and Technology (STIRPAT) model which takes the general form:

$$I = \alpha P^b A^c T^d \tag{1}$$

where *I* refers to environmental impact, *P* denotes population size, *A* represents affluence, *T* denotes technology level and *e* denotes random disturbance term. Both sides of the equation are taken logarithmically as:

$$\ln(I) = \alpha + b\ln(P) + c\ln A + d\ln T + e \tag{2}$$

To measure the influence of energy on urban PM<sub>2.5</sub> concentration, an extended STIRPAT-based model is implemented to empirically analyze the influencing factors of PM<sub>2.5</sub> concentration in 255 cities in China. The EKC curve between PM<sub>2.5</sub> emission intensity and economic development is also investigated. The equation in the form of logarithm is as follows:

$$\ln(PM_{2.5it}) = \alpha_0 + \alpha_1 \ln(PD_{it}) + \alpha_2 \ln(GDP_{it}) + \alpha_3 \ln(GDP_{it})^2 + \alpha_4 \ln(GDP_{it})^3 + \alpha_5 \ln(SE_{it}) + \alpha_6 \ln(TEC_{it}) + \alpha_7 \ln(FI_{it}) + \alpha_8 \ln(PSP_{it}) + \mu_{it} \tag{3}$$

where *i* represents region, *t* stands for time, PM<sub>2.5</sub> is PM<sub>2.5</sub> concentration in region *i* at time *t*, *PD* denotes population density, *GDP* denotes gross domestic product, *SE* refers to science expenditure, *TEC* denotes total electricity consumption, *FI* indicates actual foreign investment amount, *PSP* denotes the proportion of secondary industry in GDP and  $\mu_{it}$  denotes the disturbance term.

In order to investigate the influence of PM<sub>2.5</sub> concentration in cities with different population sizes at different quartiles, the following quantile regression model is developed.

$$Quant_{\theta}((\ln(PM_{2.5it}))|X_{it}) = \beta^{\theta} X_{it} \tag{4}$$

In Equation (4),  $X_{it}$  is the independent variable;  $\beta^\theta$  is the coefficient vector; and  $Quant_\theta((\ln(PM_{2.5it}))|X_{it})$  denotes the conditional quantile of  $PM_{2.5}$  concentration corresponding to the quantile  $\theta$  ( $0 < \theta < 1$ ) for a given  $X$ . The coefficient vector  $\beta^\theta$  corresponding to  $\theta$  is achieved by minimizing the absolute deviation (LAD):

$$\beta^\theta = \operatorname{argmin} \left\{ \sum_{i,t, (\ln(PM_{2.5it})) \geq X_{it}\beta} \theta |(\ln(PM_{2.5it})) - X_{it}\beta| + \sum_{i,t, (\ln(PM_{2.5it})) < X_{it}\beta} (1 - \theta) |(\ln(PM_{2.5it})) - X_{it}\beta| \right\} \tag{5}$$

The bootstraps intensive algorithm technique is applied to estimate the quantile regression coefficients  $\beta^\theta$ , which means that the confidence interval of the sample is obtained by continuously having a put-back sampling process.

2.2. Variable and Data

Integrating domestic and foreign studies,  $PM_{2.5}$  concentration is adopted as the proxy variable of air pollution, which can directly represent the extent of haze pollution. Six explanatory variables are selected in this paper based on the STIRPAT model. The main explanatory variables in STIRPAT model include: (1) Population density (*PD*) is the number of people in per unit area. (2) Gross domestic product (*GDP*) measures the level of urban output. This paper uses 2007 as the base period to do the treatment of the invariant price. (3) Science expenditure (*SE*) represents the intensity of government R&D investment. The control variables are selected according to the existing literature using extended STIRPAT model. They include: (1) total electricity consumption (*TEC*) used to measure the degree of energy consumption [45]; (2) actual foreign investment (*FI*) calculated to measure the degree of openness to the world [46]; and (3) the share of secondary industry in GDP (*PSP*) used to measure the effect of industrial structure on  $PM_{2.5}$  concentration [47].

In addition, two effects are considered in this paper due to the complexity of  $PM_{2.5}$  emission concentration impacts:

(1) Urban scale effect. Population is a crucial indicator of city characteristics, which not only reflects the level of urban development, but also is one of the main factors affecting  $PM_{2.5}$  concentration. Therefore, this paper adopts the variable of population as the classification criterion and divides 255 cities into four categories of cities, i.e., four groups of dummy variables, according to the Notice of the State Council on Adjusting the Criteria of City Size Classification issued by the State Council in 2014. Of these, cities with a population size of more than 10 million are Type I cities (Type I cities are the reference group), cities with populations between 5 million and 10 million are Type II cities, cities with populations between 1 million and 5 million are Type III cities, and cities with populations less than 1 million are Type IV cities. In the following analysis, the influence of each four city categories on  $PM_{2.5}$  concentration will be reported. The definitions and descriptive statistics of all the above variables are shown in Table 1.

Table 1. Data sources and definition of variables and descriptive statistics.

Variable	Definition	Units of Measurement	Mean	Median	Standard Deviation	Minimum	Maximum
$PM_{2.5}$	$PM_{2.5}$ emissions concentration	$\mu\text{g}/\text{m}^3$	45.71	43.02	18.09	8.70	104.30
<i>PD</i>	Population density	Per person/ $\text{km}^2$	459.15	393.21	332.59	4.82	2648.11
<i>GDP</i>	Per capita gross domestic product	10,000 Yuan	1786.00	991.03	2722.38	66.13	71,340.28
<i>SE</i>	Scientific expenditures	10,000 Yuan	70,652.13	18,797.00	238,982.50	469	4,035,240.00
<i>TEC</i>	Total electricity consumption	Billion kWh	156.41	102.59	175.52	2.25	1486.02
<i>FI</i>	Foreign investment	10,000 Dollars	84,956.71	22,596	196,498.10	16.00	3,082,563.00
<i>PSP</i>	Ratio of secondary industry to GDP	%	49.86	50.16	9.67	18.57	85.08

(2) EKC effect. The EKC effect is taken into consideration to verify the relationship between haze pollution and GDP. Before applying it, most studies based on a particular sample of data do not examine the random characteristics of the data and determine their suitability for the model. This brings about the deviation in the curve from the sample points within the sample interval [47]. We also introduce the secondary and tertiary terms of GDP into the model. The shape of the EKC curve is judged according to the coefficients  $\alpha_2$ ,  $\alpha_3$  and  $\alpha_4$  of Equation (3).

In order to explore the factors influencing PM<sub>2.5</sub> concentration in cities in China, 255 sample cities were selected for the period 2007–2016. To ensure that the logarithm value is positive, all ratios are calculated as percentages. The presence of large differences among variables makes the use of logarithms rational. Data sources are as follows. The PM<sub>2.5</sub> concentration data of each prefecture-level city were obtained from the global raster data based on satellite monitoring published by the Center for Socioeconomic Data and Applications of Columbia University. Other data were obtained from China Urban Statistical Yearbook (2008–2017), China Environmental Statistical Yearbook (2008–2017) and the provincial statistical yearbooks in (2008–2017).

### 3. Results

#### 3.1. Stationarity Test

To avoid the problem of pseudo-regressions and invalid *t*-tests, the Levin–Lin–Chu (LLC) test [48] and Fisher-ADF test [49] assess the stationarity of the variables (see Table 2). Except *lnPD* for horizontal series, all the results in Table 2 passed the significance test with a *p*-value less of than 0.01. Moreover, all variables for first-difference series are stationary at the 1% significance level.

Table 2. Unit root tests of variables.

Unit Root Tests	Variable	LLC	Fish-ADF
Horizontal Sequence	<i>lnPM<sub>2.5</sub></i>	−15.4620 ***	13.4164 ***
	<i>lnPD</i>	−3.3360 ***	−1.2033
	<i>lnGDP</i>	−49.3459 ***	47.0489 ***
	<i>lnSE</i>	−18.9008 ***	6.3799 ***
	<i>lnTEC</i>	−20.5336 ***	5.1772 ***
	<i>lnFI</i>	−12.8356 ***	5.6464 ***
	<i>lnPSP</i>	−3.7413 ***	2.9823 ***
First difference	<i>lnPM<sub>2.5</sub></i>	−2.0958 ***	5.2782 ***
	<i>lnPD</i>	−15.2374 ***	9.6203 ***
	<i>lnGDP</i>	−38.8361 ***	16.4137 ***
	<i>lnSE</i>	−31.7062 ***	13.7043 ***
	<i>lnTEC</i>	−82.8749 ***	59.3129 ***
	<i>lnFI</i>	−60.2082 ***	30.7214 ***
	<i>lnPSP</i>	4.9806 ***	9.6083 ***

Notes: \*\*\*, \*\* and \* represent significance at the 1%, 5% and 10% levels, respectively.

According to the co-integration theory, if all variables are single integers of the same order, co-integration relationships may exist between variables. Based on the Eangle and Granger two-step method, the Kao co-integration test of homogeneity and Pedroni co-integration test of heterogeneity are used [50–52]. Table 3 shows the results of different statistics in the Kao test and Pedroni test, which all passed the significance test with *p*-value less than 0.01. Hence, long-term stable equilibrium relationships exist among PM<sub>2.5</sub> concentration, foreign direct investment, electricity consumption, GDP, population density, share of secondary industry and science expenditure. A mixed OLS regression is illustrated in Table 2.

**Table 3.** Co-integration tests of variables.

Test Method	Statistics	Statistics Value
Kao test	ADF	−18.9077 ***
Pedroni test	Panel PP	−57.0751 ***
	Panel ADF	−42.8427 ***

Notes: \*\*\*, \*\* and \* represent significance at the 1%, 5% and 10% levels, respectively.

**3.2. Extended STIRPAT Model of 255 Cities**

Based on the panel data of 255 cities in China from 2007–2016, a mixed OLS regression is conducted. Both the random effect and the fixed effect are considered in panel data analysis. A Hausman test is adopted for modeling selection (See in Table 4). The result of the Hausman test shows significance, which shows evidence for the fixed effects model being more applicable than the random effects model. In addition, the F-test results of the fixed effects model demonstrate that the fixed effects model is better than the OLS regression, strongly suggesting that it is more appropriate to use fixed effects in the econometric regression.

**Table 4.** Regression results of factors influencing urban PM<sub>2.5</sub> concentration.

Variable	OLS	Fixed Effects	Random Effects
(1)	(2)	(3)	(4)
<i>lnPD</i>	0.220 *** (0.025)	0.172 *** (0.048)	0.164 *** (0.029)
<i>lnGDP</i>	0.523 ** (0.264)	0.558 ** (0.226)	0.563 ** (0.262)
$(lnGDP)^2$	−0.075 ** (0.036)	−0.080 ** (0.036)	−0.081 ** (0.036)
$(lnGDP)^3$	0.003 * (0.0016)	0.003 * (0.002)	0.003 ** (0.002)
<i>lnSE</i>	−0.051 *** (0.006)	−0.048 *** (0.004)	−0.047 *** (0.006)
<i>lnTEC</i>	0.013 (0.009)	0.011 * (0.006)	0.011 (0.009)
<i>lnFI</i>	0.012 *** (0.003)	0.011 *** (0.001)	0.011 *** (0.003)
<i>lnPSP</i>	−0.059 ** (0.026)	−0.058 ** (0.026)	−0.060 ** (0.026)
<i>lsize2</i>		0.487 *** (0.013)	0.491 *** (0.185)
<i>lsize3</i>		0.668 *** (0.045)	0.678 *** (0.190)
<i>lsize4</i>		0.872 *** (0.064)	0.886 *** (0.213)
<i>cons</i>	1.973 *** (0.656)	1.622 ** (0.570)	1.667 ** (0.670)
<i>Hausman test</i>		46.07 *** (Prob > chi = 0.000)	
<i>The shape of EKC</i>		N-shaped	

Notes: \*\*\*, \*\* and \* represent significance at the 1%, 5% and 10% levels, respectively.

Column 3 in Table 4 shows the fixed effect of ordinary least squares regression. For the main explanatory variables in the expanded STIRPAT model, *lnPD* (coefficient 0.172) passes the significance test at the 1% level, which means that for every 1% rise in the population density, PM<sub>2.5</sub> concentration increases by 0.172%. The coefficients of *lnGDP* and  $(lnGDP)^3$  are 0.558 and 0.003, respectively, statistically significant at the 5% and 10% levels. Furthermore, the coefficient of  $(lnGDP)^2$  is −0.08 at the 10% significance level. It indicates an inverted N-shaped relationship between PM<sub>2.5</sub> concentration and GDP, confirming the

existence of the Kuznets curve. Based on the trends of PM<sub>2.5</sub> concentration in 255 cities from 2007 to 2016, the inflection points of PM<sub>2.5</sub> concentration in each city will occur when economic progress is made. The coefficient of *lnSE* is  $-0.048$  at the 1% significance level, illustrating that the PM<sub>2.5</sub> concentration will increase by 0.048% when the scientific expenditure decreases by 1%. As for the control variables, the coefficients of *lnTEC* (0.011) and *lnFI* (0.011) are, respectively, statistically significant at the 10%, and 1% levels, which means that both total electricity consumption and foreign direct investment function to promote PM<sub>2.5</sub> concentration in 255 Chinese cities. The PM<sub>2.5</sub> concentration rises by 0.011% when total electricity consumption and actual use of foreign direct investment expands by 1%. On the contrary, *lnPSP* (coefficient  $-0.058$ ) is negative at the 5% level, which shows that the share of secondary production will lead to a decline in PM<sub>2.5</sub> concentration.

### 3.3. Quantile Regression by Different Population Size

The estimated coefficients in the expanded STIRPAT model can reflect the overall situation for all cities. Considering substantial city samples and long observation times in this paper, the overall OLS regression is not able to reflect the heterogeneity of the influential factors in various city categories based on population scale. A quantile regression is carried out to distinguish the differential effects of influential indicators on the PM<sub>2.5</sub> concentration for cities by various population-size categories and different quantile of city-size categories in every city size. The quantile regression model is an essential reference for the formulation and piloting implement of PM<sub>2.5</sub> concentration control policies in different cities. It is regressed that based on the conditional quantile of the dependent variable, the conditional quantile describes the variation of each indicator on PM<sub>2.5</sub> concentration more accurately. The 25%, 50% and 75% quantile represent the different PM<sub>2.5</sub> concentration from low to high in the same type cities. For example, the 25%, 50% and 75% quantile in type I mean the lower, middle and higher PM<sub>2.5</sub> concentration cities in this type, respectively.

Table 5 shows the results of the quantile regression in four city-size categories. Figures 2–5 show the changes in the variables’ coefficients in four types of cities’ quantile regressions. In Type I cities (population larger than 10 million), the coefficient of *lnPD* (0.141) is only significant at 10% significance when tested by the 50% quantile regression. This illustrates that population density worsens air pollution only for the middle PM<sub>2.5</sub> concentration cities. *lnGDP*,  $(lnGDP)^2$  and  $(lnGDP)^3$  are significant at 25%, or 50% quantile regression, the coefficients of which are positive, negative and positive at the 1% significance level. It indicates an inverted N-type Kuznets curve in cities with low and medium PM<sub>2.5</sub> concentration. This is consistent with the national situation. The coefficients of *lnTEC* are 0.557, 0.363 and 0.166, respectively, at 25%, 50% and 75% quantile regression. However, only coefficients at 25%, or 50% quantile pass the 1% significance level. This indicates that in Type I cities, the effect of energy consumption on air pollution is weakening as the PM<sub>2.5</sub> concentration rises. The coefficients of *lnFI* and *lnPSP* at 25% quantile regression are 0.087 and  $-0.549$ , which pass the significance test at 10% and 1%, respectively. It indicates that for every 1% increase in foreign direct investment, haze pollution is raised by 0.087%. Otherwise, PM<sub>2.5</sub> concentration rather declines by 0.549% as the share of secondary production advances every 1%.

**Table 5.** Quantile regression results of factors influencing urban PM<sub>2.5</sub> concentration.

Variable	Type I	Type II	Type III	Type IV
(1)	(2)	(3)	(4)	(5)
QR_25				
<i>lnPD</i>	0.064 (0.059)	0.353 *** (0.072)	0.343 *** (0.022)	$-1.184$ (2.066)
<i>lnGDP</i>	36.893 *** (12.299)	$-0.508$ (5.852)	3.766 ** (1.806)	$-132.832$ (187.802)

Table 5. Cont.

Variable	Type I	Type II	Type III	Type IV
$(\ln GDP)^2$	−4.319 *** (1.412)	−0.031 (0.772)	−0.524 * (0.279)	24.446 (34.582)
$(\ln GDP)^3$	0.164 *** (0.054)	0.004 (0.034)	0.025 * (0.014)	−1.499 (2.124)
$\ln SE$	−0.035 (0.058)	0.091 *** (0.031)	−0.068 *** (0.014)	0.050 (0.459)
$\ln TEC$	0.557 *** (0.112)	−0.032 (0.054)	−0.007 (0.018)	0.808 (0.482)
$\ln FI$	0.087 * (0.050)	0.096 *** (0.024)	−0.019 ** (0.008)	0.088 (0.190)
$\ln PSP$	−0.549 *** (0.186)	−0.203 (0.160)	0.421 *** (0.090)	0.637 (0.599)
_cons	−100.563 *** (35.434)	4.447 (14.793)	−8.302 ** (3.936)	243.430 (342.007)
QR_50				
$\ln PD$	0.141 * (0.078)	0.428 *** (0.032)	0.333 *** (0.013)	−0.824 (1.343)
$\ln GDP$	32.408 *** (11.645)	0.333 (3.207)	4.885 (3.304)	−113.113 (108.114)
$(\ln GDP)^2$	−3.818 *** (1.355)	−0.036 (0.427)	−0.705 (0.483)	20.916 (19.736)
$(\ln GDP)^3$	0.146 *** (0.052)	0.001 (0.019)	0.034 (0.023)	−1.287 (1.201)
$\ln SE$	0.078 (0.065)	−0.033 (0.028)	−0.056 *** (0.011)	−0.007 (0.295)
$\ln TEC$	0.363 *** (0.110)	−0.005 (0.023)	−0.034 *** (0.012)	0.295 (0.289)
$\ln FI$	0.068 (0.043)	−0.025 * (0.014)	−0.013 ** (0.006)	0.070 (0.152)
$\ln PSP$	−0.214 (0.153)	0.254 *** (0.088)	0.319 *** (0.057)	0.876 ** (0.334)
_cons	−88.946 *** (33.277)	0.104 (7.979)	−9.985 (7.455)	206.373 (198.116)
QR_75				
$\ln PD$	−0.052 (0.130)	0.451 *** (0.027)	0.289 *** (0.021)	−0.390 (0.910)
$\ln GDP$	20.410 (12.892)	−0.174 (3.215)	−0.567 (3.391)	−67.150 (81.754)
$(\ln GDP)^2$	−2.412 (1.515)	0.058 (0.432)	0.050 (0.498)	12.531 (14.908)
$(\ln GDP)^3$	0.092 (1.515)	−0.004 (0.432)	−0.000 (0.498)	−0.778 (14.908)
$\ln SE$	0.096 (0.080)	−0.057 *** (0.017)	−0.052 *** (0.014)	−0.093 (0.209)
$\ln TEC$	0.166 (0.188)	−0.014 (0.016)	−0.032 (0.021)	0.309 (0.231)
$\ln FI$	0.054 (0.043)	−0.056 *** (0.014)	−0.007 (0.009)	0.104 (0.126)
$\ln PSP$	0.111 (0.197)	0.234 ** (0.092)	0.279 *** (0.057)	0.939 *** (0.219)
_cons	−54.477 (36.651)	1.314 (7.956)	3.475 (7.660)	120.487 (149.651)

Notes: \*\*\*, \*\* and \* represent significance at the 1%, 5% and 10% levels, respectively. <sup>2</sup> and <sup>3</sup> represent the quadratic and cubic power of  $\ln GDP$  respectively.

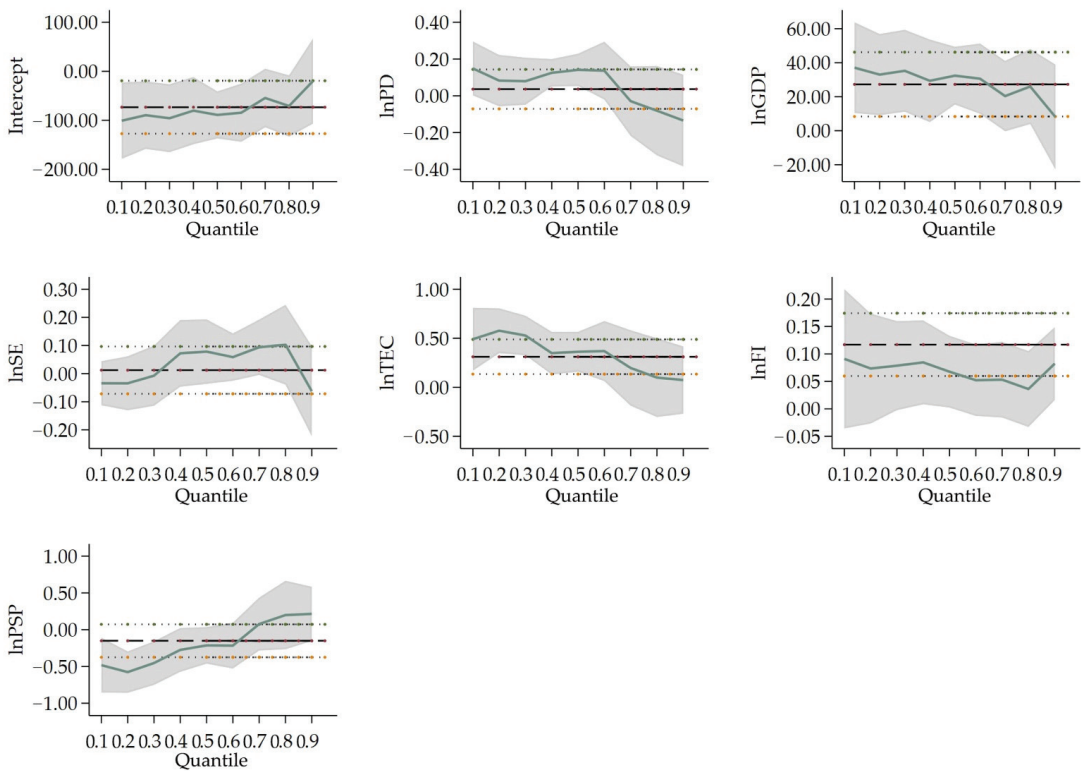


**Figure 2.** Change in variables' coefficients in Type I cities' quantile regression. Notes: The thicker dashed lines indicate the OLS regression estimates for the independent variables; the area which is parallel with thinner dashed lines is the confidence interval (95% confidence level) for the regression coefficients; The solid lines are the quantile regression coefficients of the respective variables, and the shaded area is the confidence interval (95% confidence level) of the quantile regression analysis estimates. The horizontal axis is the quantile of the dependent variable; the vertical axis is the regression estimate of the independent variable.

In Type II cities (population size between 5 million and 10 million), *lnPD* passes the significance test at 1% level, the coefficients of which are 0.353, 0.428 and 0.451 at 25%, 50% and 75% quantile regression, respectively. Such results illustrate that the enhanced population density does accelerate  $PM_{2.5}$  concentration in Type II cities. For instance, the higher the  $PM_{2.5}$  concentration is, the stronger the effect of population density on haze pollution is. The coefficient of *lnSE* is significantly negative at 25% and 75% quantile, which is 0.091 and  $-0.057$ , respectively. *lnFI* are significant at 25%, 50% and 75% quantile regression. The coefficient at 25% quantile is positive (0.096), while the coefficients at 50% and 75% quantile are both negative ( $-0.025$  and  $-0.056$ , respectively). It indicates that in Type II cities, the science expenditure and foreign direct investment will accelerate  $PM_{2.5}$  concentration at lower  $PM_{2.5}$  concentration cities, but hinder the  $PM_{2.5}$  concentration at higher  $PM_{2.5}$  concentration cities. *lnPSP* are significant at 1% and 5% level, respectively, the coefficients of which are  $-0.254$  at 50% quantile and  $-0.234$  at 75% quantile. These results indicate that the share of secondary production will exert a negative influence on air pollution at middle and higher  $PM_{2.5}$  concentration cities in Type II.

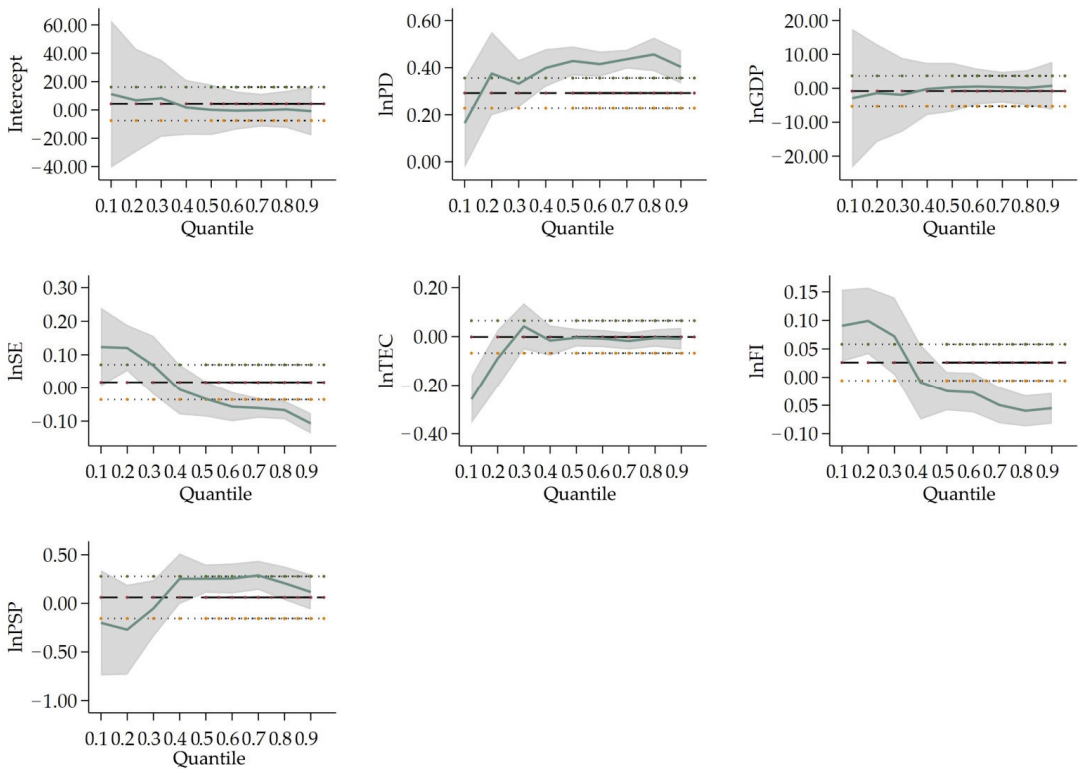


**Figure 3.** Change in variables' coefficients in Type II cities' quantile regression. Notes: the labels for all lines, the horizontal and vertical axis are the same as above.

In Type III cities (population between 1 million and 5 million), the coefficients of *lnPD* all pass the significance test at the 1% level, which are 0.343, 0.333 and 0.289 at 25%, 50% and 75% quantile regression, respectively. These results illustrate that population density will increase  $PM_{2.5}$  concentration in Type III cities. However, the higher the  $PM_{2.5}$  concentration is, the weaker the effect of population density on haze pollution. *lnGDP*,  $(lnGDP)^2$  and  $(lnGDP)^3$  are significant at 25% quantile regression, and the coefficients of which are 3.766,  $-0.524$  and  $0.025$ , in fact indicate the existence of a N-type Kuznets curve in cities with lower  $PM_{2.5}$  concentration. The coefficients of *lnSE* are  $-0.068$ ,  $-0.056$  and  $-0.052$ , which all pass the significance test at the 1% level. Expenditure on science will encourage technological innovation, which helps to improve the end-treatment measures and reduce polluting emissions and can to some extent improve air quality. Only *lnTEC* at 50% quantile regression passes the significance test in Type III. Total electricity consumption can alleviate air pollution only at middle  $PM_{2.5}$  concentration cities. The coefficients of *lnFI* are  $-0.019$  and  $-0.013$  at 25%, 50% quantile regression, respectively, which pass the 5% significance level.  $PM_{2.5}$  concentration will abate by 0.019% when foreign direct investment falls by 1% in cities with lower  $PM_{2.5}$  concentration. For middle  $PM_{2.5}$  concentration cities,  $PM_{2.5}$  concentration drops by 0.013% when foreign direct investment decreases by 1%. This indicates that in Type III cities, increases in foreign direct investment will restrict air pollution. The coefficients of *lnPSP* are 0.421, 0.319 and 0.279, all passing the significance test at the 1% level. The share of secondary production does exacerbate haze pollution, and the influence will grow as the  $PM_{2.5}$  concentration becomes higher in Type III cities.



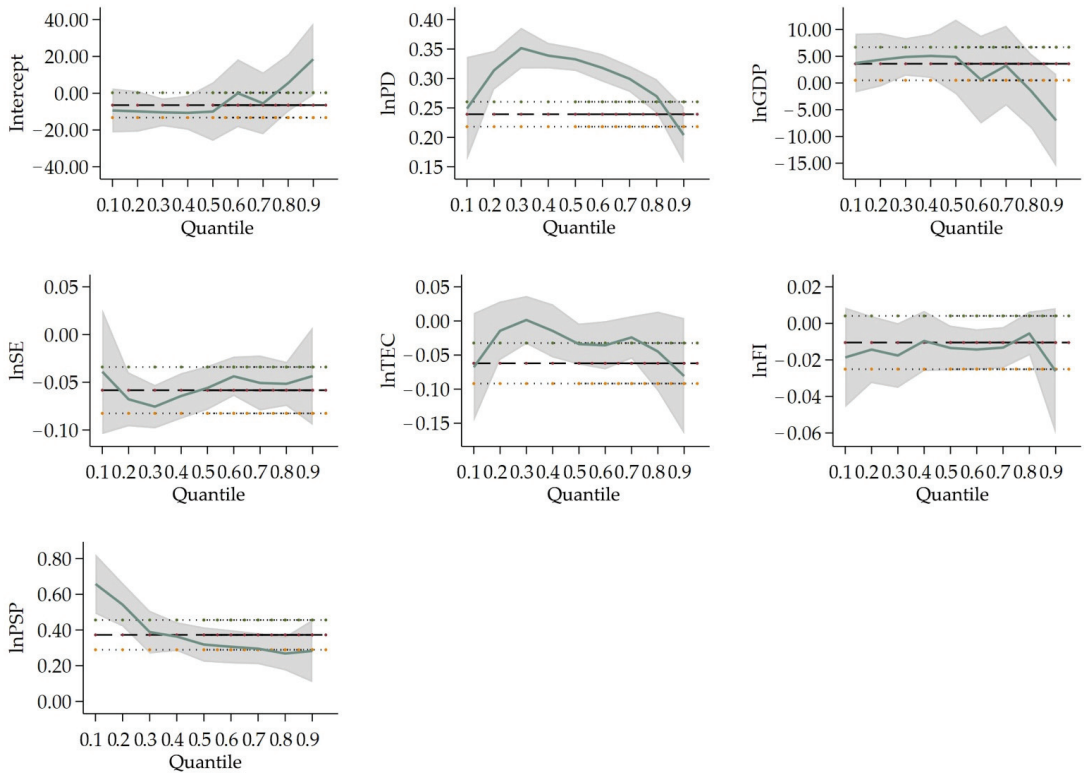


**Figure 4.** Change in variables' coefficients in Type III cities' quantile regression. Notes: the labels of all lines, the horizontal and vertical axis are the same as above.

In Type IV cities (population size less than 1 million), only the coefficient of *lnPSP* (0.876) at 50% quantile is significant, which means that the secondary production will exacerbate air pollution in cities with small population size.

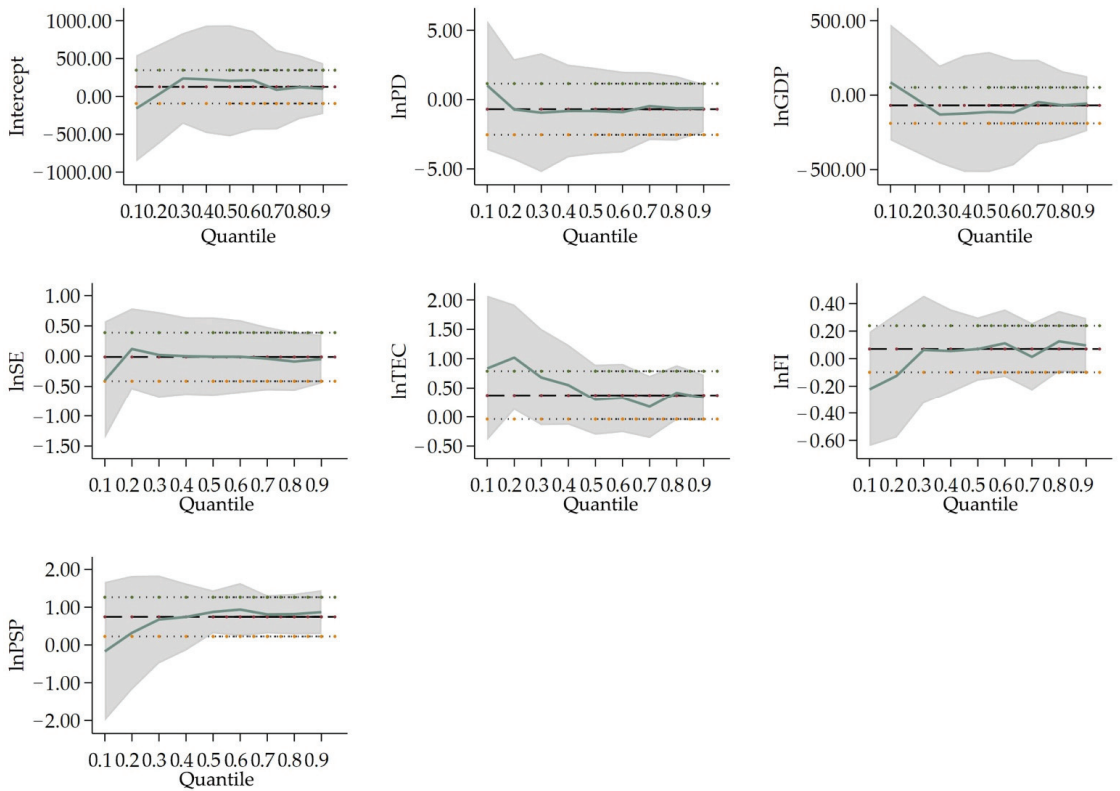


**Figure 5.** Change in variables’ coefficients in Type IV cities’ quantile regression. Notes: the labels for all lines, the horizontal and vertical axis are the same as above.

#### 4. Discussion

##### 4.1. The Discussion of Expanded STIRPAT Model Results

On a national scale, population density exerts the greatest positive influence on PM<sub>2.5</sub> concentration. During urbanization, having a much larger and concentrated population is one of the important manifestations. The relationship between PM<sub>2.5</sub> concentration and population density is shown in Figure 6. Along with the increase in urban population density, the GDP of cities also rises, which brings about the increment in PM<sub>2.5</sub> concentration. Cities with different urban population scales have significant diverse effects on PM<sub>2.5</sub> concentration. PM<sub>2.5</sub> concentration in Type I (cities over 10 million people), Type II (cities between 5 million and 10 million individuals) and Type III cities (cities between 1 million and 5 million people) are significantly higher compared to Type IV (cities less than 1 million people) cities, as can be seen in Table 3.

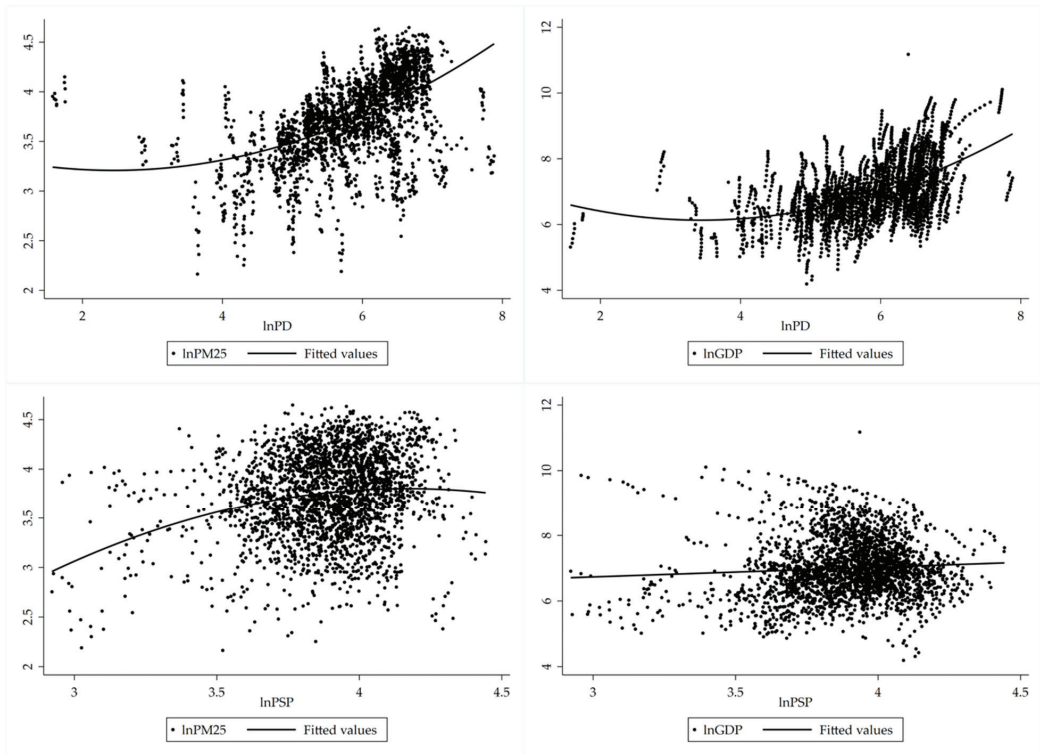


**Figure 6.** The relationship between PM<sub>2.5</sub> concentration and population density and secondary industry.

Social economic activities in cities with larger populations are more frequent, thus the PM<sub>2.5</sub> concentration are correspondently higher. The economic growth has an inverted N-shaped EKC curve with air pollution, which indicates the following experiences in Chineses cities. First, urban economic progress is accompanied by a reduction in haze pollution. Then, the higher economic expansion jeopardizes the environment and increases emissions. Finally, the air pollution gradually declines again when further economic development is accomplished. Expenditure on science has a significant effect on PM<sub>2.5</sub> concentration reduction. Research into pollution reduction technology and on haze emission reductions to improve industries can effectively mitigate urban PM<sub>2.5</sub> concentration.

Meanwhile, the coefficient of *lnTEC* (0.011) means that electricity consumption surges by every 1% when PM<sub>2.5</sub> concentration rises by 0.011%, due to the high correlation between society-wide electricity consumption and energy consumption. Foreign direct investment exerts a significant positive effect on PM<sub>2.5</sub> concentration, i.e., the PM<sub>2.5</sub> concentration rises by 0.011% when the actual utilization of foreign direct investment expands by 1%. This shows that foreign direct investment will accelerate haze pollution emissions, indicating that FDI inflow contributed to air pollution and the “pollution shelter” hypothesis was established in China. From the perspective of industrial distribution in foreign direct investment in 2015, the secondary industry accounts for the most of it, mainly the manufacturing (31.32%) and real estate (22.96%) industries. The unabated expansion of these industries and their current polluting processes will certainly compromise the quality of urban air.

On the contrary, the ratio of secondary industry to the regional GDP has a significant negative effect on PM<sub>2.5</sub> concentration for the following reasons. At the outset, the proportion of secondary industry is closely related to the level of urban economic development. When cities’ secondary industry expands, urban economic development increases. Secondly, as the latter increases (see Figure 2), cities with a comparatively high level of

economic sophistication will gradually eliminate backward production methods and move high-polluted and energy-consuming industries to less developed vicinities. Greener and more intensive and sustainable industries will take their place. Thus, the pollution generated by these cities will be transferred to underdeveloped areas.

#### 4.2. The Differences between Driving Indicators on Cities according to Different Population Sizes

When it comes to the effect of two main variables (population density ( $\ln PD$ ) and GDP ( $\ln GDP$ ,  $(\ln GDP)^2$ ,  $(\ln GDP)^3$ ) on different population sizes, the population density of Type I cities only influences  $PM_{2.5}$  concentration at the 50% quantile, indicating that in megacities with more than 10 million people, the population density does not show a significant effect on  $PM_{2.5}$  concentration. On the other hand, this indeed enhances  $PM_{2.5}$  concentration in Type II and III cities, for the reason that the regression coefficients of population density are all significantly positive at 25%, 50% and 75% quantile in these two types. In the middle-sized cities, the influx of residents accelerates urbanization and the consumption of private cars and houses, resulting in the rise of  $PM_{2.5}$  concentration. The coefficients of economic development are significant at the 25% and 50% quantile in Type I cities. In Type I cities, there is an inverted N-type Kuznets curve in cities with lower and medium  $PM_{2.5}$  concentration cities. In general, population density plays a more important role on  $PM_{2.5}$  concentration in Type II and III cities, while economic development has a more crucial effect on  $PM_{2.5}$  concentration in Type I cities comparatively.

Considering the perspective of industrial structure and energy consumption, in Type I cities,  $PM_{2.5}$  concentration is influenced more by energy consumption than other types of cities. It is shown that the coefficients of total electricity consumption are significant at the 25% and 50% quantile regression in Type I cities. Meanwhile, the coefficients of total electricity consumption are not significant in Type II and illustrate being negative for Type III.  $PM_{2.5}$  concentration enlarges as energy consumption increases in low and medium emission cities in Type I cities. Meanwhile, the proportion of the secondary industry can make a positive impact on  $PM_{2.5}$  concentration for Type II and III cities. Secondary industry expands accompanied by a surge in resource consumption of cities with permanent residents between 1 million to 10 million, which brings about the increment of  $PM_{2.5}$  concentration. In Type IV cities, the coefficient of industrial structure in the 75% quantile is the only significant variable. Cities with comparatively higher emissions in this type are influenced more by the secondary industry. Pollution will continue once the related manufacturing develops for those cities with a small scale of population.

Furthermore, foreign direct investment and science expenditure have different effects on  $PM_{2.5}$  concentration both in different types of cities and at different quantile regressions. In Type I cities, the foreign direct investment only boosts the  $PM_{2.5}$  concentration forming the 25% quantile at 10% significance level. As for Type II cities, the coefficients of foreign direct investment are 0.096,  $-0.025$  and  $-0.056$  at 25%, 50% and 75% quartile, while those of science expenditure are 0.091,  $-0.033$  and  $-0.057$  at 25%, 50% and 75% quartile. As the  $PM_{2.5}$  concentration increases in Type II cities, the effect of both foreign direct investment and science expenditure on  $PM_{2.5}$  concentration are moving from positive to negative with less populated cities to higher  $PM_{2.5}$  concentration cities. Type II cities with more than 5 million permanent residents tend to gradually transfer pollutants from higher  $PM_{2.5}$  concentration cities to lower  $PM_{2.5}$  concentration cities. This indicates that pollution is transferred to the lower  $PM_{2.5}$  concentration cities along with the transfer of foreign investment in most Chinese cities. Concerning Type III cities, both foreign direct investment and science expenditure have negative effects on  $PM_{2.5}$  concentration, but their effectiveness is much slighter compared to the strong rise in  $PM_{2.5}$  concentration from population density and the secondary industry. Foreign direct investment and science expenditure are required for Type III cities which aim to improve production equipment and processes, and abate pollutant emissions.

## 5. Conclusions

This paper analyzes the driving factors of PM<sub>2.5</sub> concentration in China's 255 prefecture-level cities from 2007 to 2016 based on the expanded STIRPAT model. The differences of each influencing factor across city categories are compared, while the differences of various influencing factors within each city category are compared using the quantile regression.

The main conclusions of this paper are as follows. On the whole, an inverted N-shaped Kuznets curve between economic development and PM<sub>2.5</sub> concentration exists in China. The phenomena of "pollution shelter" have been revealed in 255 of China's cities, and the progress of technology will improve the air quality. Meanwhile, the effects of driving factors on air pollution vary between cities with different population scales. Population density plays a more dominant role in PM<sub>2.5</sub> concentration in Type II and III cities (medium population between 1 million and 10 million), and energy consumption has a more crucial effect on PM<sub>2.5</sub> concentration in Type I cities (large populations over 10 million) comparatively. The secondary industry will enhance the PM<sub>2.5</sub> concentration in most Type IV cities (small population less than 1 million).

The above research conclusion provides policy recommendations for air pollution abatement in cities as follows. Firstly, policymakers should treat the relationship between environmental emission reduction and economic development rationally. From a national aspect, an EKC relationship exists between GDP and the environment; however, from the perspective of cities of different sizes, the EKC curve does not really exist between GDP and the environment. The relationship between economic development and air pollution in megacities is in line with the law of the Kuznets curve, and at the peak of the haze pollution. The medium and large population-sized cities coexist with the scale effect and technology effect, and the peak of haze pollution is not yet ascertained. The pollution in medium and large population-sized cities is influenced by changes in population size, so medium cities are in fact considered as diseconomies of scale caused by the expansion of population size when economic progress occurs. Consequently, policymakers should help balance the population size of cities with economic development, and pay more attention to the environment, technological improvement and better use of local natural resources.

Secondly, the proportion of the secondary industry has a great influence on urban PM<sub>2.5</sub> concentration, it is necessary to reasonably determine the scale of urban development and city size, promote industrial transformation and upgrade small and medium-sized cities synergistically in order to promote their functioning, state of industry and the environment, and promote the green economy and circular economy. Energy consumption has a more significant impact on the air quality of megacities; thus, policymakers should improve the concept of green consumption by enterprises and residents.

Thirdly, government should emphasize science and technology instead of focusing on better targeted investment. This is especially the case when introducing green capital to improve the situation of "pollution shelter" and increase investment in research on how to reduce pollution and improve remediation strategies.

**Author Contributions:** Conceptualization, J.C. (Jinhua Cheng), J.C. (Jingyu Cheng), Z.M. and P.H.; methodology, P.H.; software, J.L. and S.J.; validation, P.H.; formal analysis, J.L., P.H. and S.J.; investigation, J.L.; resources, S.J., J.L. and P.H.; writing—original draft preparation, J.L.; writing—review and editing, J.L., S.J., P.H., J.L., Y.W. and J.C. (Jinhua Cheng); visualization, S.J.; supervision, P.H., J.C. (Jingyu Cheng), Z.M., S.J. and J.L.; project administration, Y.W.; funding acquisition, P.H. and Y.W. All authors have read and agreed to the published version of the manuscript.

**Funding:** This research was supported by the National Social Science Foundation of China (No. 17BJY063).

**Institutional Review Board Statement:** Not applicable.

**Informed Consent Statement:** Not applicable.

**Data Availability Statement:** The basic data used in the research can be found on the website of the National Bureau of Statistics, China Statistical Yearbook and other databases.

**Conflicts of Interest:** The authors declare no conflict of interest.

## References

1. Li, H.; Mu, H.; Zhang, M.; Li, N. Analysis on Influence Factors of China's CO<sub>2</sub> Emissions Based on Path-STIRPAT Model. *Energy Policy* **2011**, *39*, 6906–6911. [CrossRef]
2. Zhao, D.; Chen, H.; Li, X.; Ma, X. Air Pollution and Its Influential Factors in China's Hot Spots. *J. Clean. Prod.* **2018**, *185*, 619–627. [CrossRef]
3. Hering, L.; Poncet, S. Environmental Policy and Exports: Evidence from Chinese Cities. *J. Environ. Econ.* **2014**, *68*, 296–318. [CrossRef]
4. Hao, Y.; Liu, Y. The Influential Factors of Urban PM<sub>2.5</sub> Concentrations in China: A Spatial Econometric Analysis. *J. Clean. Prod.* **2016**, *112*, 1443–1453. [CrossRef]
5. Dong, K.; Dong, X.; Dong, C. Determinants of the Global and Regional CO<sub>2</sub> Emissions: What Causes What and Where? *Appl. Econ.* **2019**, *51*, 5031–5044. [CrossRef]
6. Diao, B.; Zeng, K.; Su, P.; Ding, L.; Liu, C. Temporal-Spatial Distribution Characteristics of Provincial Industrial NO<sub>x</sub> Emissions and Driving Factors in China from 2006 to 2013. *Resour. Sci.* **2016**, *38*, 12. [CrossRef]
7. Miao, Z.; Baležentis, T.; Shao, S.; Chang, D. Energy Use, Industrial Soot and Vehicle Exhaust Pollution—China's Regional Air Pollution Recognition, Performance Decomposition and Governance. *Energy Econ.* **2019**, *83*, 501–514. [CrossRef]
8. Yang, J.; Shan, H. Identifying Driving Factors of Jiangsu's Regional Sulfur Dioxide Emissions: A Generalized Divisia Index Method. *Int. J. Environ. Res. Public Health* **2019**, *16*, 4004. [CrossRef]
9. Weng, Z.; Ma, Z.; Ge, C.; Cheng, C. Analysis on Urban Environmental Effect Driven by Multi-Factors of China: Based on Panel Data of 285 Prefecture Level Cities. *China Popul. Resour. Environ.* **2017**, *27*, 11. [CrossRef]
10. Lelieveld, J.; Evans, J.S.; Fnais, M.; Giannadaki, D.; Pozzer, A. The Contribution of Outdoor Air Pollution Sources to Premature Mortality on a Global Scale. *Nature* **2015**, *525*, 367–371. [CrossRef]
11. Wang, S.; Zhou, C.; Wang, Z.; Feng, K.; Hubacek, K. The Characteristics and Drivers of Fine Particulate Matter (PM<sub>2.5</sub>) Distribution in China. *J. Clean. Prod.* **2017**, *142*, 1800–1809. [CrossRef]
12. Chen, X.; Li, F.; Zhang, J.; Zhou, W.; Wang, X.; Fu, H. Spatiotemporal Mapping and Multiple Driving Forces Identifying of PM<sub>2.5</sub> Variation and Its Joint Management Strategies across China. *J. Clean. Prod.* **2020**, *250*, 119534. [CrossRef]
13. Liu, Q.; Wang, S.; Zhang, W.; Li, J.; Dong, G. The Effect of Natural and Anthropogenic Factors on PM<sub>2.5</sub>: Empirical Evidence from Chinese Cities with Different Income Levels. *Sci. Total Environ.* **2019**, *653*, 157–167. [CrossRef]
14. Yang, Y.; Li, J.; Zhu, G.; Guan, X.; Zhu, W. The Impact of Multi-Dimensional Urbanization on PM<sub>2.5</sub> Concentrations in 261 Cities of China. *IEEE Access* **2020**, *8*, 96199–96209. [CrossRef]
15. Yan, D.; Ren, X.; Kong, Y.; Ye, B.; Liao, Z. The Heterogeneous Effects of Socioeconomic Determinants on PM<sub>2.5</sub> Concentrations Using a Two-Step Panel Quantile Regression. *Appl. Energy* **2020**, *272*, 115246. [CrossRef]
16. Liang, X.; Li, S.; Zhang, S.; Huang, H.; Chen, S.X. PM<sub>2.5</sub> Data Reliability, Consistency, and Air Quality Assessment in Five Chinese Cities. *J. Geophys. Res. Atmos.* **2016**, *121*, 10–220. [CrossRef]
17. Lin, B.; Jiang, Z. Environmental Kuznets Curve Prediction and Influencing Factors of CO<sub>2</sub> in China. *Manag. World* **2009**, *4*, 27–36. [CrossRef]
18. Hao, Y.; Liao, H.; Wei, Y. Environmental Kuznets Curve of Energy Consumption and Electricity Consumption in China Based on Spatial Econometric Modeling of Panel Data. *China Soft Sci. Mag.* **2014**, *1*, 134–141.
19. Li, L.; Liu, X.; Ge, J.; Chu, X.; Wang, J. Regional Differences in Spatial Spillover and Hysteresis Effects: A Theoretical and Empirical Study of Environmental Regulations on Haze Pollution in China. *J. Clean. Prod.* **2019**, *230*, 1096–1110. [CrossRef]
20. Wu, W.; Zhang, M.; Ding, Y. Exploring the Effect of Economic and Environment Factors on PM<sub>2.5</sub> Concentration: A Case Study of the Beijing-Tianjin-Hebei Region. *J. Environ. Manag.* **2020**, *268*, 110703. [CrossRef]
21. Huang, W.; Wang, H.; Zhao, H.; Wei, Y. Temporal-Spatial Characteristics and Key Influence Factors of PM<sub>2.5</sub> Concentrations in China Based on STIRPAT Model and Kuznets Curve. *Environ. Eng. Manag. J.* **2019**, *18*, 2587–2604. [CrossRef]
22. Yang, D.; Wang, X.; Xu, J.; Xu, C.; Lu, D.; Ye, C.; Wang, Z.; Bai, L. Quantifying the Influence of Natural and Socioeconomic Factors and Their Interactive Impact on PM<sub>2.5</sub> Pollution in China. *Environ. Pollut.* **2018**, *241*, 475–483. [CrossRef] [PubMed]
23. Wang, Y.; Liu, C.; Wang, Q.; Qin, Q.; Ren, H.; Cao, J. Impacts of Natural and Socioeconomic Factors on PM<sub>2.5</sub> from 2014 to 2017. *J. Environ. Manag.* **2021**, *284*, 112071. [CrossRef] [PubMed]
24. Zhang, M.; Sun, X.; Wang, W. Study on the Effect of Environmental Regulations and Industrial Structure on Haze Pollution in China from the Dual Perspective of Independence and Linkage. *J. Clean. Prod.* **2020**, *256*, 120748. [CrossRef]
25. Lu, D.; Xu, J.; Yang, D.; Zhao, J. Spatio-Temporal Variation and Influence Factors of PM<sub>2.5</sub> Concentrations in China from 1998 to 2014. *Atmos. Pollut. Res.* **2017**, *8*, 1151–1159. [CrossRef]
26. Wang, Y.; Duan, X.; Wang, L. Spatial-Temporal Evolution of PM<sub>2.5</sub> Concentration and Its Socioeconomic Influence Factors in Chinese Cities in 2014–2017. *Int. J. Environ. Res. Public Health* **2019**, *16*, 985. [CrossRef]
27. Zhou, C.; Chen, J.; Wang, S. Examining the Effects of Socioeconomic Development on Fine Particulate Matter (PM<sub>2.5</sub>) in China's Cities Using Spatial Regression and the Geographical Detector Technique. *Sci. Total Environ.* **2018**, *619*, 436–445. [CrossRef]
28. Yan, D.; Lei, Y.; Shi, Y.; Zhu, Q.; Li, L.; Zhang, Z. Evolution of the Spatiotemporal Pattern of PM<sub>2.5</sub> Concentrations in China—A Case Study from the Beijing-Tianjin-Hebei Region. *Atmos. Environ.* **2018**, *183*, 225–233. [CrossRef]

29. Yan, J.; Tao, F.; Zhang, S.-Q.; Lin, S.; Zhou, T. Spatiotemporal Distribution Characteristics and Driving Forces of PM<sub>2.5</sub> in Three Urban Agglomerations of the Yangtze River Economic Belt. *Int. J. Environ. Res. Public Health* **2021**, *18*, 2222. [[CrossRef](#)]
30. Nagashima, F. Critical Structural Paths of Residential PM<sub>2.5</sub> Emissions within the Chinese Provinces. *Energy Econ.* **2018**, *70*, 465–471. [[CrossRef](#)]
31. Luo, K.; Li, G.; Fang, C.; Sun, S. PM<sub>2.5</sub> Mitigation in China: Socioeconomic Determinants of Concentrations and Differential Control Policies. *J. Environ. Manag.* **2018**, *213*, 47–55. [[CrossRef](#)]
32. Cheng, S.; Xie, J.; Xiao, D.; Zhang, Y. Measuring the Environmental Efficiency and Technology Gap of PM<sub>2.5</sub> in China's Ten City Groups: An Empirical Analysis Using the EBM Meta-Frontier Model. *Int. J. Environ. Res. Public Health* **2019**, *16*, 675. [[CrossRef](#)] [[PubMed](#)]
33. Koenker, R.; Bassett, G., Jr. Regression Quantiles. *Econometrica* **1978**, *46*, 33–50. [[CrossRef](#)]
34. Furno, M.; Vistocco, D. *Quantile Regression: Estimation and Simulation*; John Wiley & Sons: Hoboken, NJ, USA, 2018; Volume 216.
35. Lew, A.A.; Ng, P.T. Using Quantile Regression to Understand Visitor Spending. *J. Travel Res.* **2012**, *51*, 278–288. [[CrossRef](#)]
36. Ma, D.; Li, G.; He, F. Exploring PM<sub>2.5</sub> Environmental Efficiency and Its Influencing Factors in China. *Int. J. Environ. Res. Public Health* **2021**, *18*, 12218. [[CrossRef](#)] [[PubMed](#)]
37. Kiliç, C.; Balan, F. Is There an Environmental Kuznets Inverted-U Shaped Curve? *Panoeconomicus* **2018**, *65*, 79–94. [[CrossRef](#)]
38. Feng, Y.; Wang, X. Effects of Urban Sprawl on Haze Pollution in China Based on Dynamic Spatial Durbin Model during 2003–2016. *J. Clean. Prod.* **2020**, *242*, 118368. [[CrossRef](#)]
39. Du, G.; Liu, S.; Lei, N.; Huang, Y. A Test of Environmental Kuznets Curve for Haze Pollution in China: Evidence from the Penal Data of 27 Capital Cities. *J. Clean. Prod.* **2018**, *205*, 821–827. [[CrossRef](#)]
40. Ding, Y.; Zhang, M.; Chen, S.; Wang, W.; Nie, R. The Environmental Kuznets Curve for PM<sub>2.5</sub> Pollution in Beijing-Tianjin-Hebei Region of China: A Spatial Panel Data Approach. *J. Clean. Prod.* **2019**, *220*, 984–994. [[CrossRef](#)]
41. Azam, M. Does Environmental Degradation Shackle Economic Growth? A Panel Data Investigation on 11 Asian Countries. *Renew. Sust. Energ. Rev.* **2016**, *65*, 175–182. [[CrossRef](#)]
42. Azam, M.; Khan, A.Q. Testing the Environmental Kuznets Curve Hypothesis: A Comparative Empirical Study for Low, Lower Middle, Upper Middle and High Income Countries. *Renew. Sust. Energ. Rev.* **2016**, *63*, 556–567. [[CrossRef](#)]
43. Apergis, N.; Christou, C.; Gupta, R. Are There Environmental Kuznets Curves for US State-Level CO<sub>2</sub> Emissions? *Renew. Sust. Energ. Rev.* **2017**, *69*, 551–558. [[CrossRef](#)]
44. Ehrlich, P.R.; Holdren, J.P. Impact of Population Growth. *Science* **1971**, *171*, 1212–1217. [[CrossRef](#)] [[PubMed](#)]
45. Wang, P.; Wu, W.; Zhu, B.; Wei, Y. Examining the Impact Factors of Energy-Related CO<sub>2</sub> Emissions Using the STIRPAT Model in Guangdong Province, China. *Appl. Energy* **2013**, *106*, 65–71. [[CrossRef](#)]
46. Li, S.; Wang, S. Examining the Effects of Socioeconomic Development on China's Carbon Productivity: A Panel Data Analysis. *Sci. Total Environ.* **2019**, *659*, 681–690. [[CrossRef](#)]
47. Stern, D.I. The Rise and Fall of the Environmental Kuznets Curve. *World Dev.* **2004**, *32*, 1419–1439. [[CrossRef](#)]
48. Levin, A.; Lin, C.-F.; Chu, C.-S.J. Unit Root Tests in Panel Data: Asymptotic and Finite-Sample Properties. *J. Econom.* **2002**, *108*, 1–24. [[CrossRef](#)]
49. Maddala, G.S.; Wu, S. A Comparative Study of Unit Root Tests with Panel Data and a New Simple Test. *Oxford. B Econ. Stat.* **1999**, *61*, 631–652. [[CrossRef](#)]
50. Kao, C. Spurious Regression and Residual-Based Tests for Cointegration in Panel Data. *J. Econom.* **1999**, *90*, 1–44. [[CrossRef](#)]
51. Pedroni, P. Critical Values for Cointegration Tests in Heterogeneous Panels with Multiple Regressors. *Oxf. Bull. Econ. Stat.* **1999**, *61*, 653–670. [[CrossRef](#)]
52. Pedroni, P. Panel Cointegration: Asymptotic and Finite Sample Properties of Pooled Time Series Tests with an Application to the PPP Hypothesis. *Econom. Theory* **2004**, *20*, 597–625. [[CrossRef](#)]

## Article

# Investigation of the Thermal Performance of Lightweight Assembled Exterior Wall Panel (LAEWP) with Stud Connections

Tianzhen Li <sup>1</sup>, Jun Xia <sup>1,2</sup>, Chee Seong Chin <sup>1,2,\*</sup> and Pei Song <sup>3</sup>

<sup>1</sup> Department of Civil Engineering, Xi'an Jiaotong-Liverpool University, 111 Ren'ai Road, Suzhou 215123, China; tianzhen.li18@student.xjtlu.edu.cn (T.L.); jun.xia@xjtlu.edu.cn (J.X.)

<sup>2</sup> Institute for Sustainable Materials and Environment, Xi'an Jiaotong-Liverpool University, 111 Ren'ai Road, Suzhou 215123, China

<sup>3</sup> Shanghai Jun Dao Residential Industry Co., Ltd., 438 Jinwei Road, Baoshan District, Shanghai 201901, China; p.song@jundaozhugong.com

\* Correspondence: chee.chin@xjtlu.edu.cn

**Abstract:** One of the most effective ways to improve building energy efficiency and consumption is to increase the thermal insulation of the building envelope and reduce the heat loss through walls. A new type of thermal insulation wall panel, consisting of a lightweight assembled exterior wall panel, was investigated in this research through experimental and numerical analyses. The feasibility of achieving the anticipated thermal performance through finite element modeling using ABAQUS<sup>®</sup> was verified. Good agreement between numerical simulation and experimental measurement was found, and the accuracy is 98.8%. To further reduce the heat transfer coefficient (U-value) of the panel to improve its thermal performance, parametric analyses were conducted utilizing the validated finite element model. The simulation shows that changing the insulation material is the best option, and the U-value reduction percentage reached 13.2%. Moreover, the combination of reducing the number of steel studs, decreasing the size of steel studs, implementing the opening of the light-gauge steel, and improving the insulation material led to a 23.7% reduction in the U-value at  $0.695 \text{ W}\cdot\text{m}^{-2}\cdot\text{K}^{-1}$ .

**Keywords:** finite element analysis; heat transfer coefficient; light-gauge steel; parametric study

**Citation:** Li, T.; Xia, J.; Chin, C.S.; Song, P. Investigation of the Thermal Performance of Lightweight Assembled Exterior Wall Panel (LAEWP) with Stud Connections. *Buildings* **2022**, *12*, 473. <https://doi.org/10.3390/buildings12040473>

Academic Editors: Francesco Nocera, Roberto Alonso González Lezcano and Rosa Giuseppina Caponetto

Received: 9 March 2022

Accepted: 7 April 2022

Published: 12 April 2022

**Publisher's Note:** MDPI stays neutral with regard to jurisdictional claims in published maps and institutional affiliations.



**Copyright:** © 2022 by the authors. Licensee MDPI, Basel, Switzerland. This article is an open access article distributed under the terms and conditions of the Creative Commons Attribution (CC BY) license (<https://creativecommons.org/licenses/by/4.0/>).

## 1. Introduction

Enhancement of energy efficiency in the construction industry has become China's national priority [1] due to the increased weighting of building energy consumption in the past decades [2–4]. To achieve sustainable development goals, building energy conservation shall be achieved through the improvement of building design, construction, and usage. The exterior wall is one of the main components of a building, and its structure and materials directly affect the building's energy consumption. It has been estimated that 34% of the energy consumption of residential buildings is attributed to the exterior walls [5]. Therefore, to improve building energy efficiency and reduce energy consumption, the most effective way is to increase the thermal performance of the exterior building walls to reduce heat loss [6]. Lightweight assembled exterior wall panel (LAEWP), a new type of lightweight thermal insulation wall, usually consists of light-gauge steel, exterior slabs such as stone soundboard or oriented strand board, and interior insulation materials such as rock wool or thermal insulation mortar. Usually, the light-gauge steel frames serve as the main structural component. LAEWP is proposed to accelerate construction by reducing onsite work and was proved to be structurally sound [5]. However, its thermal performance is in doubt due to the light-gauge steel frame and steel studs as connectors.

Light-gauge steel has great mechanical properties, high strength, secure processing, and better connection. For the reason that the thermal conductivity of light-gauge steel is around  $50 \text{ W}\cdot\text{m}^{-1}\cdot\text{K}^{-1}$ , which is much higher than that of thermal insulation material



(thermal conductivity of rock wool is usually less than  $0.05 \text{ W}\cdot\text{m}^{-1}\cdot\text{K}^{-1}$ ), the thermal bridge will form and thus dramatically increase building energy consumption [7,8]. Condensation due to temperature differences will cause mildew and dripping off the wall, which would also deteriorate the thermal insulation performance of the insulation material and affect the everyday use of the wall panels. Therefore, thermal performance is a crucial factor for the implementation of LAEWP in addition to structural requirements.

In recent years, numerous studies have been focused on the thermal insulation performance of the assembled wall. Gorrell stated that condensation is the major problem in prefabricated composite building walls [9]. The main reasons identified were, for example, exfiltration of warm, moist indoor air, water vapor diffusion, and inadequate separation and/or insulation [9]. Fantozzi et al. conducted a detailed analysis and discussion on the dynamic thermal performance of the lightweight wall. They found that the thermal insulation performance of prefabricated exterior wall panels can be significantly improved through the lumped parameter method [10]. By comparing the conventional plate, Song et al. adopted the heat insulation bracket and improved aluminum die to reduce the phenomenon of the thermal bridge on the thermal performance of the metal curtain wall system [8]. Bamonte et al. analyzed the influence of the thermal performance of the wall panel with phase change material using the finite element method (FEM), and the wall panels with phase change materials led to a 20% reduction in the energy required for the indoor physical environment in the hot season [11]. Pekdogan and Basaran pointed out that more heat loss can be decreased in different climates and directions by adding the thermal insulation of the sandwich wall. The heat loss can also be dramatically reduced by 65% [12]. Hachim and Abed introduced a new design method of a sandwich wallboard designed by adding layers of insulation material to the wall, which can effectively save electricity [13].

Chu et al. analyzed the condensation problem of precast concrete sandwich insulation exterior wall panels and they found that all types of precast concrete sandwich insulation wall panels have condensation inside though the area was small [14]. Pan et al. used the infrared thermal imaging method to test the exterior envelope structure of the assembled building. The results showed that the defect of the envelope structure of the assembled building is more minor, which is beneficial for the building energy saving [15]. Bu et al. investigated the thermal insulation performance of the expanded polystyrene (EPS) modular shear wall structure system, and it was found that the insulation layer thickness on both sides of the EPS module system is 60 mm and the heat transfer coefficient is only  $0.27 \text{ W}\cdot\text{m}^{-2}\cdot\text{K}^{-1}$ , which shows that the system has excellent thermal insulation performance [16]. Li et al. analyzed the thermal insulation performance of sandwich ventilation walls. Compared with the heat transfer coefficient with a non-thermal insulation cover, the thermal insulation performance of the sandwich wall can be further improved by 12.3% [17]. Wang et al. stated that the polystyrene particle insulation mortar could adequately compensate for the shortcomings of the high thermal conductivity of steel bars and effectively reduce the thermal bridge effect and maintain the indoor temperature stability [18]. To decrease the heat transfer coefficient of the wall, Jin et al. put forward a reasonable web openings parameter and spacing, which provided design suggestions for engineering practice [19]. According to the simulation results presented by Li et al., it was found that when the number of web openings is five, the proportion of web opening is 50%, the height of the keel cross section is 200 mm, and more layers of gypsum board are added, the thermal insulation effect is better [20].

The LAEWP investigated in this research utilized a new type of high-strength concrete to reduce the thickness of the exterior concrete layer and, therefore, the self-weight of the pane was decreased. The decrease in panel weight will reduce the transportation cost and simplify the installation process. Although the panel is structurally adequate, the thermal performance is affected by adopting a 50 mm thick exterior concrete layer and steel head studs connecting the concrete slab and supporting light-gauge steel. The primary focus of

the research was to determine an improved insulation solution for the proposed LAEWP, for which a combined approach will be presented.

## 2. LAEWP Configuration

The configuration of the proposed LAEWP can be seen in Figure 1. The overall dimension of the panel is 1400 mm × 1400 mm × 200 mm and includes seven components, as shown in the figure legends. The dimensions are consistent with the thermal performance experiment, while the stud and light-gauge steel frame configuration is equivalent to the full-size panel. The exterior layer adopted high-strength concrete with compressive strength of over 140 MPa. The concrete layer was connected to the light-gauge steel by steel-headed studs whose diameter and length are 10 mm and 40 mm, respectively. A 10 mm thick air layer was maintained between the concrete and light-gauge steel by adjusting the embedment depth of the steel studs. Two types of light-gauge steel members, namely, the C-shape and U-shape, were used in the panel. The dimension of the C-shape and U-shape light-gauge steel members are 120 mm × 50 mm × 15 mm × 2 mm and 120 mm × 50 mm × 2 mm, respectively. The whole thickness of high-strength concrete is 50 mm. The 20 mm thick fibrous concrete board was utilized as the back panel, while sprayed EPS insulation material or polystyrene particle mortar with 120 mm thickness was used to fill the space between the front and back concrete panel and the space between the light-gauge steel frames. The fully prepared LAEWP specimen is shown in Figure 2.

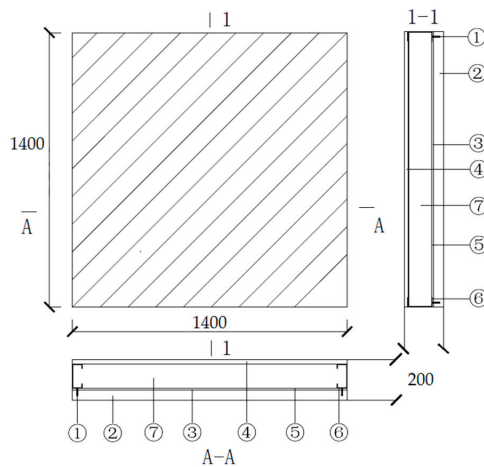


**Figure 1.** Configuration of LAEWP (unit: mm). ① steel stud, ② high strength concrete, ③ U-shape light-gauge steel, ④ fiber concrete board, ⑤ air layer, ⑥ C-shape light-gauge steel, and ⑦ EPS insulation layer.

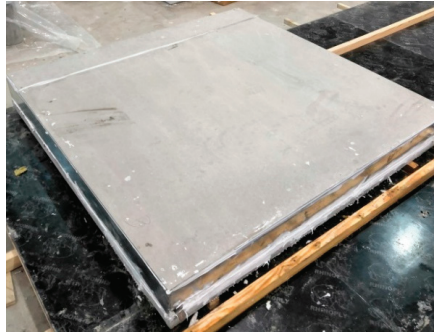


**Figure 2.** LAEWP specimen.

### 3. Thermal Performance Testing

The heat transfer coefficient of the LAEWP was measured according to BS EN ISO 8990:1996 [21] by a certified third party testing service provider. The heat flow due to moisture transfer or redistribution was prevented in the experiment by controlling the moisture in the testing environment and maintaining an initial dry condition of the specimen. The measured heat transfer coefficient for the two panels with polystyrene particle mortar and EPS foam are shown in Table 1. The heat transfer coefficient of the panel with EPS foam ( $0.9 \text{ W}\cdot\text{m}^{-2}\cdot\text{K}^{-1}$ ) was smaller than that of the panel with polystyrene particle mortar ( $1.15 \text{ W}\cdot\text{m}^{-2}\cdot\text{K}^{-1}$ ). Because the experiment is expensive and time-consuming, numerical simulation was adopted to assess the various improvement approaches and further optimization.

**Table 1.** Two different test results of the exterior wall panel.

Items	Insulation Material	Heat Transfer Coefficient ( $\text{W}\cdot\text{m}^{-2}\cdot\text{K}^{-1}$ )
1	Polystyrene particle mortar	1.15
2	EPS foam	0.90

### 4. Thermal Performance Simulation

#### 4.1. Method Verification

Thermal simulation results from previous research [22] were used to verify the simulation method used in the paper. It is stated that the steady-state heat transfer of the wall can be approximated as a one-dimensional steady-state heat transfer problem [23]. Therefore, a 3D model was created in ABAQUS<sup>®</sup> using 3D BH240 elements to simulate the masonry unit. The XY plane geometric dimensions of the new 3D BH240 model were acquired based on the geometry of 2D BH240 model in reference [22] and the length of the model in the Z direction is set as 190 mm, where the thickness of the air layer is 40 mm. All the boundary conditions, thermal conductivity of different materials, and simulation parameters of the new 3D BH240 model were obtained according to reference [22]. The third boundary condition of the steady-state heat conduction was used as the boundary condition of finite element analysis. Furthermore, a tie constraint was used for all contacts between components. The thermal conductivity of different materials and air interlayers in the FEM model are shown in Table 2. The indoor and outdoor ambient temperatures and surface conditions were obtained as shown in Table 3.

**Table 2.** Thermal conductivity values.

Items	Thermal Conductivity (W·m <sup>-1</sup> ·K <sup>-1</sup> )
Concrete	1.5100
Masonry mortar	0.9300
Air interlayer—40 mm	0.0845

**Table 3.** Simulation parameter values.

Items	Value
Indoor ambient temperature (°C)	18.0
Outdoor ambient temperature (°C)	0.0
Indoor surface film condition (W·m <sup>-2</sup> ·K <sup>-1</sup> )	8.7
Outdoor surface film condition (W·m <sup>-2</sup> ·K <sup>-1</sup> )	23.3

Through steady-state heat transfer analyses in ABAQUS®, the maximum and minimum temperature values of the hot and cold sides of the model were 15.050 °C and 0.953 °C, respectively. The maximum and minimum heat flux values of the model were 114.50 W·m<sup>-2</sup> and 6.20 W·m<sup>-2</sup>, respectively. The temperature distribution and heat flux distribution of the 3D model were similar to those in the literature, as shown in Figure 3a.

The heat transfer coefficient equals the heat of the unit area of the wall in a unit time when the temperature difference between the two sides of the wall is 1 °C. In the steady-state heat transfer process, the total heat flux of each layer of heat transfer surface in the vertical direction is equal. Therefore, the heat transfer coefficient of the wall can be calculated by the average temperature difference between the two sides of the wall and the average heat flux density of any section perpendicular to the heat flow direction. The calculation formula is shown in Equation (1):

$$K = \frac{q}{\Delta T} \quad (1)$$

$q$  is the average heat flux of the heat transfer layer in the vertical direction of heat flow;  $\Delta T$  is the average temperature difference on both sides of the wall. Based on the results of ABAQUS®, the average temperature difference is 14.097 K, so the heat transfer coefficient of the model can be obtained only by knowing the average heat flux. Because the heat flux distribution is the same along the thickness direction in any section perpendicular to the heat flow direction. The heat flow distribution on the section can be represented by any heat flow distribution path along the Y direction. Therefore, two different paths were created in the model, and then heat flux data of all nodes can be obtained in each path. Therefore, the average heat flux can be calculated through the average left and right heat flux values. Each path and the heat flux of each node can be shown in Figures 3 and 4.

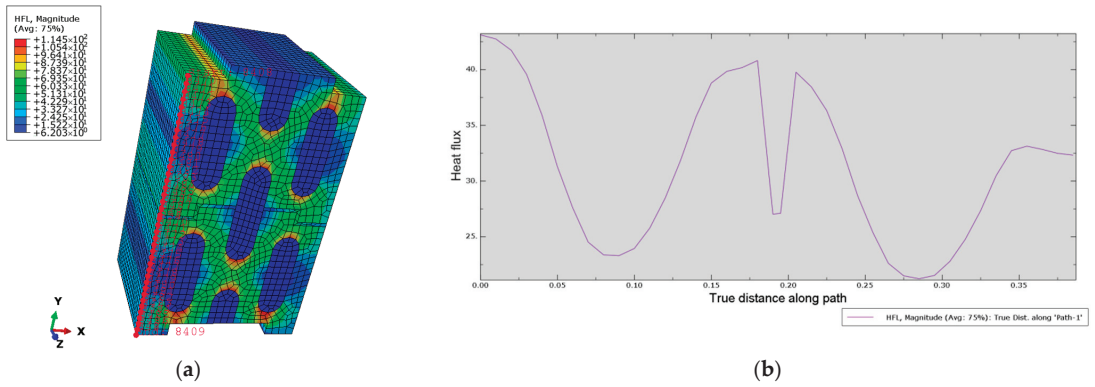


**Figure 3.** (a) Left calculation path in the 3D model; (b) heat flux ( $W \cdot m^{-2}$ ) of each node in the left path.

The average heat flux values of the left and the right path in the 3D model are  $31.25 W \cdot m^{-2}$  and  $32.09 W \cdot m^{-2}$ , respectively, so the average surface heat flux is  $31.67 W \cdot m^{-2}$ . Therefore, the heat transfer coefficient between the FEM model and the reference can be shown in Table 4, and the difference is only 1.5%. Thus, the method for obtaining the heat transfer coefficient was verified based on the 3D BH240 model and will be used to calculate the heat transfer coefficient.

**Table 4.** Heat transfer coefficient between the model and reference.

Items	Average Heat Flux ( $W \cdot m^{-2}$ )	Average Temp. Difference (K)	Heat Transfer Coefficient ( $W \cdot m^{-2} \cdot K^{-1}$ )
3D model	31.67	14.097	2.247
Reference [22]	31.90	13.979	2.282

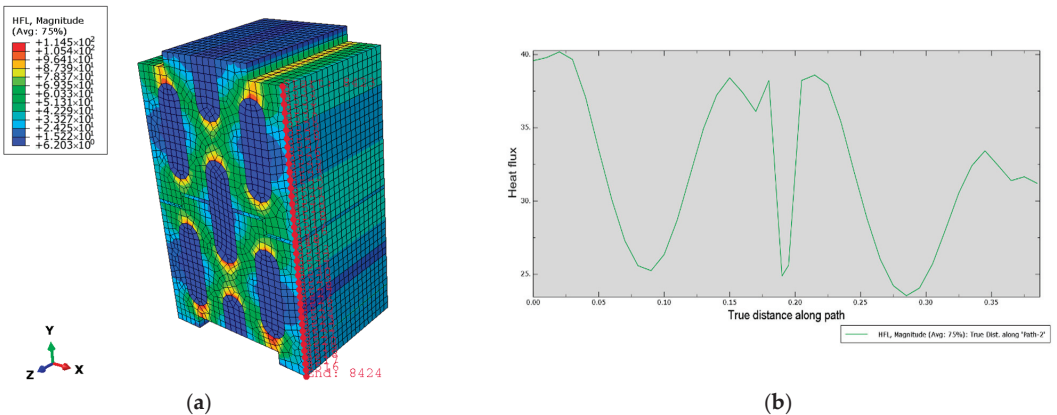


**Figure 4.** (a) Right calculation path in the 3D model; (b) heat flux ( $W \cdot m^{-2}$ ) of each node in the right path.

#### 4.2. FEM Model of the LAEWP

The FEM models of the LAEWP and each component are shown in Figure 5. All elements were considered as homogeneous solids, and the element type selected was the DC3D8 linear thermal analysis element. In practice, because light-gauge steel and concrete

are connected by studs, it is necessary to accurately simulate the stud holes in concrete in the ABAQUS® modeling process. Due to the occurrence of an air layer in the actual model, the heat flow cannot be transferred typically if the air layer model is not established in ABAQUS®. Therefore, it is necessary to establish the air layer according to the arrangement of studs.

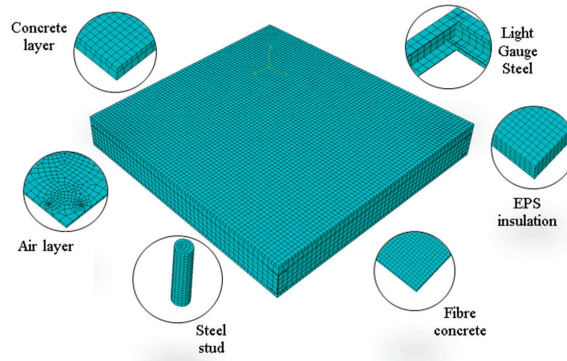


**Figure 5.** Mesh of the LAEWP and each component.

#### 4.3. Material Property

The thermal conductivity of concrete is estimated to be  $1.62 \text{ W}\cdot\text{m}^{-1}\cdot\text{K}^{-1}$  [24]. According to EN ISO 6946: 2017 [25], when the thickness of the air layer  $d$  was 10 mm, the thermal resistance  $R_T$  equals  $0.15 \text{ m}^2\cdot\text{K}^{-1}\cdot\text{W}^{-1}$ . Therefore, the thermal conductivity of the air layer  $\lambda$  can be calculated using Equation (2), which equals  $0.067 \text{ W}\cdot\text{m}^{-1}\cdot\text{K}^{-1}$ .

$$R_T = \frac{d}{\lambda} \quad (2)$$

Based on the results obtained from the literature, the thermal conductivity of the EPS insulation material and light-gauge steel were  $0.036 \text{ W}\cdot\text{m}^{-1}\cdot\text{K}^{-1}$  and  $50 \text{ W}\cdot\text{m}^{-1}\cdot\text{K}^{-1}$ , respectively [26]. The thermal properties of the steel stud were the same as that of light-gauge steel. As per GB 50176-2016 [27], the thermal conductivity of fiber concrete was  $0.85 \text{ W}\cdot\text{m}^{-1}\cdot\text{K}^{-1}$ . The thermal conductivity of different materials adopted for the LAEWP is summarized in Table 5.

**Table 5.** Thermal property of different materials of the LAEWP.

Items	Thermal Conductivity ( $\text{W}\cdot\text{m}^{-1}\cdot\text{K}^{-1}$ )	Density ( $\text{kg}\cdot\text{m}^{-3}$ )	Specific Heat ( $\text{kJ}\cdot\text{kg}^{-1}\cdot\text{K}^{-1}$ )
Concrete [24]	1.620	2500.00	0.92
Air layer [25]	0.067	1.29	1.00
EPS [26]	0.036	20.00	2.41
Steel stud [26]	50.000	7850.00	0.48
Light-gauge steel [26]	50.000	7850.00	0.48
Fiber concrete [27]	0.850	1500.00	1.05

#### 4.4. Boundary Conditions

The external and internal temperatures were set equal to  $-20 \text{ }^\circ\text{C}$  and  $20 \text{ }^\circ\text{C}$ , respectively. According to EN ISO 6946: 2017 [25], for horizontal heat flow, the convective surface heat transfer coefficient for the external and internal environment  $h_e$  and  $h_i$  can be set as  $25 \text{ W}\cdot\text{m}^{-2}\cdot\text{K}^{-1}$  and equals  $7.69 \text{ W}\cdot\text{m}^{-2}\cdot\text{K}^{-1}$ , respectively. The tie constraint was used for all contacts between components, and steady-state heat transfer analyses were conducted based on heat conduction.

#### 4.5. Results and Analysis

The distribution of temperature (NT11) and heat flux (HFL) of the LAEWP and different components are shown in Figure 6, and the extreme values of temperature and heat flux are summarized in Table 6. The maximum heat flow occurs at the connection between the steel stud and the light-gauge steel because the thermal conductivities of both materials are much higher than those of others, and there is a large amount of heat flow transfer when they are in contact. The minimum heat flow occurs around the EPS insulation layer because the thermal conductivity of EPS is the lowest, and a large amount of heat flow is transferred through the light-gauge steel.

**Table 6.** Extreme values of temperature and heat flux.

Items	Maximum	Minimum
Temperature (°C)	18.60	−19.57
Heat flux ( $W \cdot m^{-2}$ )	$1.730 \times 10^4$	1.608

According to Equation (1), to obtain the heat transfer coefficient of the LAEWP, the average heat flux  $q$  and the corresponding temperature difference  $\Delta T$  need to be calculated. Because the total heat flow at any section perpendicular to the direction of heat flow is equal, the value of HFL3 will be taken as the actual heat flow rather than the HFL magnitude. The integration point algorithm will be numerically carried out to obtain the average heat flux in this process. Then, the average heat flux of concrete and fiber concrete were obtained from the numerical model as shown in Figures 7 and 8, which equal  $30.8465827 W \cdot m^{-2}$  and  $30.8465868 W \cdot m^{-2}$ , respectively. The temperature difference  $\Delta T$  was also be calculated based on the average temperature of all nodes of concrete and fiber concrete, which equal  $-18.505 K$  and  $15.373 K$ , respectively. With an average heat flux of  $30.847 W \cdot m^{-2}$  and a temperature difference of  $33.878 K$ , the heat transfer coefficient of the LAEWP equals  $0.911 W \cdot m^{-2} \cdot K^{-1}$ , which is in good agreement with the experimental result of  $0.9 W \cdot m^{-2} \cdot K^{-1}$  and the accuracy is 98.8%. The numerical result is sufficient to serve as the benchmark for further optimization work. The potential reasons for the overestimation can be inaccurate thermal conductivities and partial heat loss in the practical test. Furthermore, in the actual specimen construction process, due to the filling of EPS insulation materials, the thickness of the air layer may have decreased. However, in the numerical simulation model, an air layer of 10 mm was set, and the thermal conductivity of the air layer is almost twice that of EPS, which will also lead to an increase in the  $U$  value in the numerical simulation and have an impact on the insulation performance of the panel. Therefore, this is also an optimization factor that we need to consider in the later optimization process.

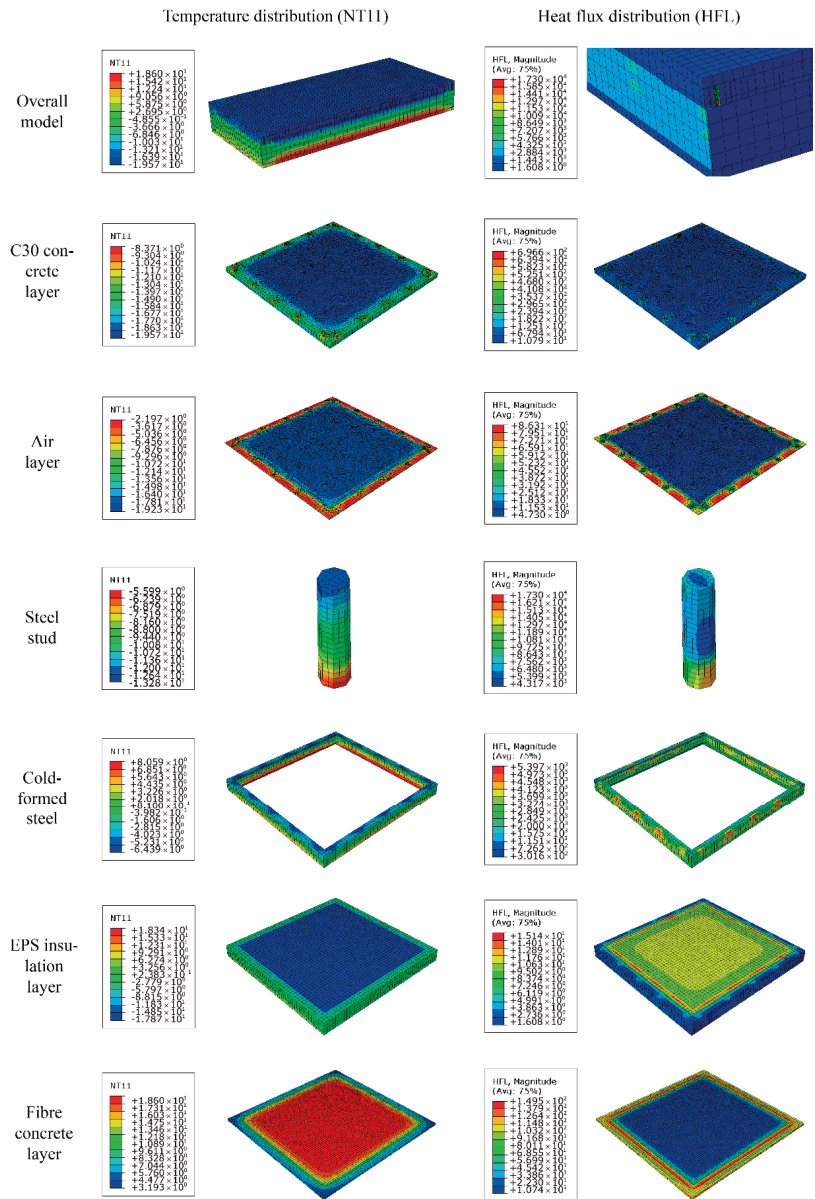


Figure 6. Temperature ( $^{\circ}\text{C}$ ) and heat flux ( $\text{W}\cdot\text{m}^{-2}$ ) distribution of NT11 and HFL of the LAEWP and all parts.





Figure 7. Heat flux ( $W \cdot m^{-2}$ ) of each node of concrete.

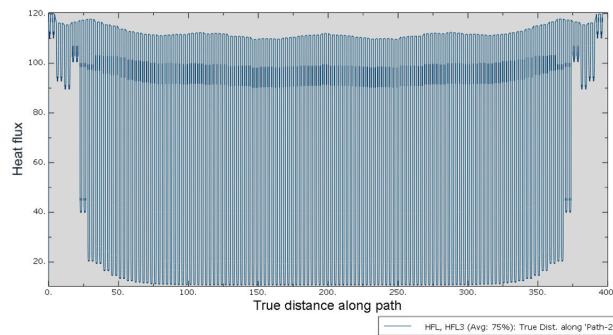


Figure 8. Heat flux ( $W \cdot m^{-2}$ ) of each node of fiber concrete.

## 5. Improvement of the LAEWP

### 5.1. Univariate Improvement Approaches

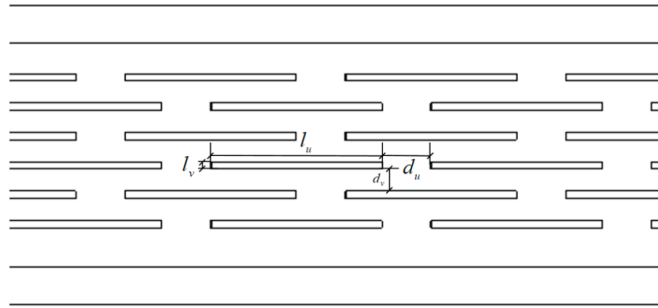
To further improve the thermal performance of the LAEWP, several improvement approaches were proposed, such as reducing the stud size, reducing the stud number, application of web openings, and enhancing the thermal conductivity of various insulation materials. The effectiveness of several of those approaches was evaluated through the FEM model. Details of the models are explained, as shown in Table 7.

Table 7. Description of Improvement Approaches.

Label	Approaches	Details
1 (SSR)	Stud size reduction	The diameter and length of studs reduced from 10 mm and 40 mm to 8 mm and 30 mm, respectively
2 (SNR)	Stud number reduction	The number of studs on each edge frame reduced from 5 to 4
3 (TCL)	Thicker concrete layer	The thickness of concrete/fiber concrete changed from 50 mm/20 mm to 60 mm/30 mm
4 (AAL)	Avoid air layer	The material property of the air layer ( $0.067 W \cdot m^{-1} \cdot K^{-1}$ ) changed to EPS ( $0.036 W \cdot m^{-1} \cdot K^{-1}$ )
5 (FWO)	Frame web opening	See Figure 9 and corresponding explanation
6 (IME)	Insulation material enhancement	The thermal conductivity changed to $0.02 W \cdot m^{-1} \cdot K^{-1}$ , which is an average number for aerogel insulation material

Web openings of light-gauge steel were introduced to extend the heat transfer path and decrease the equivalent thermal conductivity. The LAEWP is a non-bearing struc-

ture, so according to the reference [19,28], the dimension of the web openings can be  $70 \text{ mm} \times 3 \text{ mm} \times 20 \text{ mm} \times 9 \text{ mm}$  (length  $l_u \times$  height  $l_v \times$  horizontal spacing  $d_u \times$  vertical spacing  $d_v$ ). The ratio of web opening is set as 50%, and the end distance of the web opening is recommended to be 0 mm, as shown in Figure 9.



**Figure 9.** The layout of web openings of C light-gauge steel.

The extreme values of temperature and heat flux of the LAEWP under different improvement scenarios are summarized in Table 8. All six improvement approaches have limited influence on the extreme temperature values of the LAEWP. Only three improvement approaches, SNR, TCL, and FWO, can reduce the thermal bridge effect of the LAEWP to some extent.

**Table 8.** Description of Improvement Approaches.

Label	Temperature T (°C)		Heat Flux q (W·m <sup>-2</sup> )	
	Maximum	Minimum	Maximum	Minimum
1 (SSR)	18.60	−19.57	$1.934 \times 10^4$	1.556
2 (SNR)	18.60	−19.57	$1.601 \times 10^4$	1.334
3 (TCL)	18.60	−19.57	$1.696 \times 10^4$	1.572
4 (AAL)	18.64	−19.58	$2.079 \times 10^4$	1.349
5 (FWO)	18.60	−19.57	$1.532 \times 10^4$	0.567
6 (IME)	19.18	−19.99	$1.743 \times 10^4$	0.892
Benchmark	18.60	−19.57	$1.730 \times 10^4$	1.608

The heat transfer coefficient and the performance of different improvement methods can be obtained, as shown in Table 9. From the improvement approach labeled AAL, it was found that the final U value is decreased to  $0.829 \text{ W}\cdot\text{m}^{-2}\cdot\text{K}^{-1}$  when the air layer was replaced entirely by EPS material. The final U value was smaller than the experimental result,  $0.9 \text{ W}\cdot\text{m}^{-2}\cdot\text{K}^{-1}$ , which also validates the estimation in Section 4.5. From Table 9, all six improvement approaches can reduce the heat transfer coefficient of the LAEWP and improve its thermal insulation performance. However, the first three (SSR, SNR, and TCL) have less impact when compared with the rest of the approaches (AAL, FWO, and IME). The minimal heat transfer coefficient of all six models is  $0.791 \text{ W}\cdot\text{m}^{-2}\cdot\text{K}^{-1}$ , which indicates that the improvement of the insulation material has the greatest impact on the insulation performance of the LAEWP.

## 5.2. Multivariate Improvement Approaches

As can be seen from the above, several univariate improvement approaches can effectively improve the insulation performance of the LAEWP to some extent. To further improve the thermal performance of the panel, the combination of several improvement approaches were investigated. The combination cases and results can be found in Table 10. From the point of view of optimizing cost and facilitating panel installation, the multivariate

improvement approach labeled SSR + SNR + FWO was firstly carried out compared with other approaches because the labeled TCL will lead to the change of panel size and weight and bring construction difficulties. The labeled AAL and IME will lead to the increase in optimization cost, respectively. The result of the labeled SSR + SNR + FWO was below expectation, so the labeled AAL and IME can be respectively considered based on the result of the labeled SSR + SNR + FWO. All three multivariate improvement approaches can decrease the heat transfer coefficient of the LAEWP and better optimize the experimental result, where the approach labeled SSR + SNR + FWO + IME has been shown to give the best reduction percentage of the U-value by 23.7%. The heat transfer coefficient is  $0.695 \text{ W}\cdot\text{m}^{-2}\cdot\text{K}^{-1}$ .

**Table 9.** Heat transfer coefficient of univariate improvement approaches.

Label	$\bar{q}$ of LAEWP ( $\text{W}\cdot\text{m}^{-2}$ )	$\Delta T$ (K)	Heat Transfer Coefficient K ( $\text{W}\cdot\text{m}^{-2}\cdot\text{K}^{-1}$ )	Reduction (%)
Benchmark	30.847	33.878	0.911	-
1 (SSR)	30.160	33.921	0.889	2.4%
2 (SNR)	30.279	33.998	0.891	2.2%
3 (TCL)	30.446	33.703	0.903	0.9%
4 (AAL)	28.488	34.351	0.829	9.0%
5 (FWO)	28.890	34.270	0.843	7.5%
6 (IME)	27.318	34.528	0.791	13.2%

**Table 10.** Heat transfer coefficient of univariate improvement approaches.

Label	$\bar{q}$ of LAEWP ( $\text{W}\cdot\text{m}^{-2}$ )	$\Delta T$ (K)	Heat Transfer Coefficient K ( $\text{W}\cdot\text{m}^{-2}\cdot\text{K}^{-1}$ )
SSR + SNR + FWO	27.945	34.376	0.813
SSR + SNR + FWO + AAL	25.431	34.892	0.729
SSR + SNR + FWO + IME	24.369	35.046	0.695

## 6. Conclusions

To increase building energy efficiency, a new thermal insulation wall panel, consisting of a lightweight assembled exterior wall panel, was introduced to achieve sustainable development and decrease building energy consumption. Experimental and numerical analyses were carried out to study the thermal insulation performance of the LAEWP. The main conclusions can be summarized as follows:

1. The thermal insulation of the LAEWP with EPS foam ( $0.9 \text{ W}\cdot\text{m}^{-2}\cdot\text{K}^{-1}$ ) was found to have better performance than that of the LAEWP with polystyrene particle mortar ( $1.15 \text{ W}\cdot\text{m}^{-2}\cdot\text{K}^{-1}$ );
2. The heat transfer coefficient of LAEWP found numerically was  $0.911 \text{ W}\cdot\text{m}^{-2}\cdot\text{K}^{-1}$ , which is in good agreement with the experimental result and the accuracy is 98.8%. Therefore, the FEM result is close enough to serve as the benchmark to evaluate the effectiveness of various improvement approaches. Reasonable overestimation of the heat transfer coefficient was also validated in the later improvement stage;
3. All six improvement approaches analyzed led to a reduction in the heat transfer coefficient of the LAEWP, ranging from 0.9% to 13.2%. The relative effectiveness methods are enhancement of insulation material and air layer, as well as the implementation of a web opening;
4. The multivariate improvement approach labeled SSR + SNR + FWO + IME was found to have the best insulation performance. The best reduction percentage of the U-value is 23.7%, and the heat transfer coefficient of LAEWP was recorded as  $0.695 \text{ W}\cdot\text{m}^{-2}\cdot\text{K}^{-1}$ .

The paper presents the 3D FEM simulation tool that was verified to be as effective and accurate as the 2D FEM model. The 3D simulation model on LAEWP was further validated through the comparison with experimental results. Thus, the effectiveness of various optimization methods can be preliminarily assessed. The proposed tool provides a novel investigation method for the future optimization of the panel, which saves the time and effort of repeating the physical tests. However, it shall be noted that the actual performance of the panel may also be subject to its working environment, for example, the indoor and outdoor moisture contents and the moisture content in the specimen itself. Although prior research concluded that change in humidity mainly affects the radiation between air layers and has little effect on heat conduction and convection for the composite wall [29], the thermal performance of LAEWP is worth further investigation, especially its performance in the actual application through onsite monitoring.

**Author Contributions:** Conceptualization, P.S.; methodology, P.S.; validation, J.X.; formal analysis, T.L.; investigation, T.L.; resources, P.S.; writing—original draft preparation, T.L.; writing—review and editing, J.X., C.S.C. and P.S.; visualization, T.L.; supervision, J.X. and C.S.C.; project administration, J.X.; funding acquisition, C.S.C. All authors have read and agreed to the published version of the manuscript.

**Funding:** The authors acknowledge the financial support from Xi’an Jiaotong-Liverpool University and Shanghai Jun Dao Residential Industry Co., Ltd. under Grant Number RDS10120170090.

**Institutional Review Board Statement:** Not applicable.

**Informed Consent Statement:** Not applicable.

**Data Availability Statement:** The data presented in this study are available on request from the corresponding author.

**Conflicts of Interest:** The authors declare no conflict of interest.

## References

1. Wang, J.; Li, L. Sustainable energy development scenario forecasting and energy saving policy analysis of China. *Renew. Sustain. Energy Rev.* **2016**, *58*, 718–724. [[CrossRef](#)]
2. Nagy, B.; Stocker, G. Numerical Analysis of Thermal and Moisture Bridges in Insulation Filled Masonry Walls and Corner Joints. *Period. Polytech. Civ. Eng.* **2019**, *63*, 446–455. [[CrossRef](#)]
3. Yükses, I. The Evaluation of Building Materials in Terms of Energy Efficiency. *Period. Polytech. Civ. Eng.* **2015**, *59*, 45–58. [[CrossRef](#)]
4. Zhang, Y.; He, C.-Q.; Tang, B.-J.; Wei, Y.-M. China’s energy consumption in the building sector: A life cycle approach. *Energy Build.* **2015**, *94*, 240–251. [[CrossRef](#)]
5. Ye, Z. The Development Status and Trend of Prefabricated Composite Wallboard of Industrialization of Construction Industry. *Fujian Constr. Sci. Technol.* **2016**, *1*, 28–30. [[CrossRef](#)]
6. Cao, S. New Technologies of Building Energy Efficiency in Contemporary. *Sci. Technol. Inf.* **2012**, 15–16. [[CrossRef](#)]
7. Song, J.-H.; Lim, J.-H.; Song, S.-Y. Evaluation of alternatives for reducing thermal bridges in metal panel curtain wall systems. *Energy Build.* **2016**, *127*, 138–158. [[CrossRef](#)]
8. Song, J.-H.; Lim, J.-H.; Kim, Y.-I.; Song, S.-Y. Thermal Insulation Performance of Metal-exterior Curtain Wall Panel Systems with Thermal Bridges in Winter. *Procedia Eng.* **2016**, *146*, 8–16. [[CrossRef](#)]
9. Gorrell, T.A.; Kaskel, B.S.; Kudder, R.J.; Mitchell, M.R.; Link, R.E. Condensation Problems in Precast Concrete Cladding Systems in Cold Climates. *J. Test. Eval.* **2011**, *39*. [[CrossRef](#)]
10. Fantozzi, F.; Galbiati, P.; Leccese, F.; Salvadori, G.; Rocca, M. Thermal analysis of the building envelope of lightweight temporary housing. *J. Phys. Conf. Ser.* **2014**, *547*, 012011. [[CrossRef](#)]
11. Bamonte, P.; Caverzan, A.; Kalaba, N.; Tornaghi, M.L. Lightweight Concrete Containing Phase Change Materials (PCMs): A Numerical Investigation on the Thermal Behaviour of Cladding Panels. *Buildings* **2017**, *7*, 35. Available online: <http://www.mdpi.com/2075-5309/7/2/35> (accessed on 2 September 2019). [[CrossRef](#)]
12. Pekdogan, T.; Basaran, T. Thermal performance of different exterior wall structures based on wall orientation. *Appl. Therm. Eng.* **2017**, *112*, 15–24. [[CrossRef](#)]
13. Hachim, D.M.; Abed, Q.A. Thermal Analysis of Light Weight Wall Made from Sandwich Panels in The Aspect of Thermal Insulation Design for Sustainable. In Proceedings of the 6-th International Conference on Thermal Equipment, Renewable Energy and Rural Development TE-RE-RD, Moieciu de Sus, Romania, 8–10 June 2017.

14. Chu, H.; Wu, Z.; Pu, H.; Zhu, Q.; Li, C. Study on Internal Condensation of Assembled Concrete Sandwich Insulation Exterior Wall Panel. *China Concr. Cem. Prod.* **2017**, *60*–63. [[CrossRef](#)]
15. Pan, Z.; Yu, S.; Feng, G.; Li, H.; Zheng, S.; Ding, H. Analysis of The Influence of Insulation Capacity on Energy Conservation of Prefabricated Buildings. *Energy Conserv.* **2015**, *4*, 51–55. [[CrossRef](#)]
16. Bu, Y.; Ci, Q. Rural Housing with EPS Module Concrete Shear Wall Structure System. *Archit. Eng. Technol. Des.* **2015**, *11*, 1706–1708. [[CrossRef](#)]
17. Li, R.; Wei, X.; Li, H.; Zhu, J. Experimental Study on Ventilation and Thermal Performance of Exterior Sandwich Wall Based on Hot Box Method. *Procedia Eng.* **2017**, *205*, 2771–2778. [[CrossRef](#)]
18. Wang, L.; Sun, J.; Fu, S. Numerical Simulation Analysis of Temperature Effects of a New Type of Insulation Sandwich Panel. *Build. Sci.* **2017**, *33*, 103–109. [[CrossRef](#)]
19. Jin, X.; Yang, H.; Li, M.; Sun, P.; Sun, J.; Yan, Y. Key Parameters of Heat Transfer Performance of Light Steel Wall with Web Openings. *Low Temp. Archit. Technol.* **2014**, *10*, 4–6. [[CrossRef](#)]
20. Li, M.; Wang, Y.; Sun, Y.; Sun, P. Numerical Simulation Analysis of Thermal Distribution of Slotted Light-gauge Steel Stud Walls Exposed to Fire. *J. Archit. Civ. Eng.* **2015**, *32*, 89–95. [[CrossRef](#)]
21. *BS EN ISO 8990:1996*; Thermal Insulation—Determination of Steady-State Thermal Transmission Properties—Calibrated and Guarded Hot Box. BSI Standards: London, UK.
22. Yang, Z. Study on the Thermal Performance of Cross-Hole Interlocking Concrete Block Wall. *China Concr. Cem. Prod.* **2019**, *7*, 71–74. [[CrossRef](#)]
23. Wei, L.; Xiao, T. Effect of Masonry Method on Thermal Performance of Concrete Hollow Blocks. *China Concr. Cem. Prod.* **2014**, *12*, 70–74. [[CrossRef](#)]
24. Zhang, F.; Xiao, J.; Song, Z. The Prediction Models of Thermal Conductivity of Concrete and Their Application. *Ready-Mixed Concr.* **2009**, *2*, 23–26.
25. *EN ISO 6946:2017*; Building Components and Building Elements-Thermal Resistance and Thermal Transmittance-Calculation Method. European Committee for Standardization: Brussels, Belgium, 2017.
26. Roque, E.; Santos, P.; Pereira, A.C. Thermal and Sound Insulation of Lightweight Steel-Framed Façade Walls. *Sci. Technol. Built Environ.* **2019**, *25*, 156–176. [[CrossRef](#)]
27. *GB 50176-2016*; Code for Thermal Design of Civil Building. MOHURD: Beijing, China, 2016.
28. Liu, F.; Fu, F.; Wang, Y.; Liu, Q. Fire performance of non-load-bearing light-gauge slotted steel stud walls. *J. Constr. Steel Res.* **2017**, *137*, 228–241. [[CrossRef](#)]
29. Fang, W. Research on Air Humidity Affecting Heat Transfer of Thin Air Layer of Thermal Insulation Wall of Building. Master's Thesis, Anhui Jianzhu University, Hefei, China, April 2015.



Article

# Economic Development, Fiscal Ecological Compensation, and Ecological Environment Quality

Hongjie Cao <sup>1</sup>, Meina Li <sup>1</sup>, Fengqin Qin <sup>2,\*</sup>, Yankun Xu <sup>3</sup>, Li Zhang <sup>1</sup> and Zhifeng Zhang <sup>1,\*</sup>

<sup>1</sup> School of Economics, Qingdao University, Qingdao 266071, China; jaytsoo@qdu.edu.cn (H.C.); 2021020068@qdu.edu.cn (M.L.); 202130274@mail.sdu.edu.cn (L.Z.)

<sup>2</sup> Chinese Academy of Fiscal Sciences, Beijing 100142, China

<sup>3</sup> School of Economics, South-Central Minzu University, Wuhan 430074, China; 2019035@mail.scuec.edu.cn

\* Correspondence: qinfengqin@chineseafs.org (F.Q.); sasha\_china@hotmail.com (Z.Z.)

**Abstract:** Focusing on the exploration of the important role of fiscal ecological compensation in green development, this paper incorporates fiscal ecological compensation into the analytical framework of green development. Based on samples of data from county areas in China in 2017 and 2018, this paper empirically examines the shape of the green development routes in county areas in China. On this basis, this paper explores the impact and mechanism of fiscal ecological compensation on the green development path in China. The empirical results show that there is a nonlinear, N-shaped relationship between economic development and the ecological environment in China within the range of the sample examined. Fiscal ecological compensation has a direct governance effect on the ecological environment of deterring ecological damage and providing financial compensation. Fiscal ecological compensation has an indirect impact on the ecological management of different regions by influencing economic development. Therefore, while focusing on transforming the economic development model, local governments should adopt policy instruments such as expanding the coverage of financial ecological compensation, deepening the design of the financial ecological compensation system, and systematically evaluating the effects of financial ecological compensation policies. The government should further improve and optimize the fiscal eco-compensation system in order to help China's green and high-quality development.

**Keywords:** economic development; fiscal ecological compensation; ecological environment; N-shaped nonlinear relationship

**Citation:** Cao, H.; Li, M.; Qin, F.; Xu, Y.; Zhang, L.; Zhang, Z. Economic Development, Fiscal Ecological Compensation, and Ecological Environment Quality. *Int. J. Environ. Res. Public Health* **2022**, *19*, 4725. <https://doi.org/10.3390/ijerph19084725>

Academic Editors: Roberto Alonso González Lezcano, Francesco Nocera and Rosa Giuseppina Caponetto

Received: 19 March 2022

Accepted: 12 April 2022

Published: 13 April 2022

**Publisher's Note:** MDPI stays neutral with regard to jurisdictional claims in published maps and institutional affiliations.



**Copyright:** © 2022 by the authors. Licensee MDPI, Basel, Switzerland. This article is an open access article distributed under the terms and conditions of the Creative Commons Attribution (CC BY) license (<https://creativecommons.org/licenses/by/4.0/>).

## 1. Introduction

Since the reform and opening in 1978, Chinese economy has experienced rapid growth, and its development targets have been achieved. Past practice shows that excessive consumption of resources and environmental degradation are the main problems facing countries at the stage of rapid economic development. Many studies have revealed that there may be a non-linear relationship between economic growth and the ecological environment [1–5]. Among them, the EKC (Environmental Kuznets curve: Panayotou first called this relationship between environmental quality and per capita income the Environmental Kuznets Curve (EKC) in 1993, based on the Kuznets curve proposed by American economist Simon Smith Kuznets in 1955. When a country has a low level of economic development, the level of environmental pollution is less. However, as per capita income increases, environmental pollution tends to increase from low to high, and environmental degradation increases with economic growth. When economic development reaches a certain level, that is, after reaching a certain critical point or “inflection point”, with the further increase in per capita income, environmental pollution tends to decrease from high to low, and the degree of environmental pollution gradually slows down, and the quality of the environment gradually improves. On this basis, this paper further incorporates

ecology-related indicators into the core explanatory variables to give a more comprehensive response to the whole picture of ecological environment. In order to reflect the difference caused by this expansion, we define it as the ecological pants Nietzsche curve. However, this definition needs to be further studied and deepened.) theory illustrates that environmental pollution initially shows an upward and downward trend with economic development. Currently, rapid “broad” economic growth has exacerbated resource consumption and the deterioration of the ecological environment, limiting the sustainable development of the Chinese economy and society. Consequently, it is urgent to look for a method of green development.

The three-dimensional co-management framework, “government-corporate-individual”, is considered an ideal model to achieve green development. However, due to the externals of the ecological environment and the limitations of the stage of social development, society and individuals have failed to play an effective role in China’s existing ecological and environmental governance system. The government serves as the most important role in the current eco-environmental governance system. The government directly addresses the ecological environment through energy conservation and environmental protection expenditure and environmental protection taxes on both the fiscal and revenue sides. At the same time, the government also regulates ecological harm administratively through a series of legal systems. In addition, government policies also indirectly impact environmental management by influencing economic development.

Among the many ecological and environmental management measures taken by the government, financial ecological compensation, which regulates the main body of ecological and environmental relations by economic means, has been favored by the government. Fiscal ecological compensation focuses on the ecosystem itself with corresponding fiscal instruments, such as transfers and subsidies. It compensates ecological providers by paying for the additional protection, associated construction costs, and the opportunity costs of development foregone for this purpose. In addition, this policy tool internalizes the externality involved from the standpoint of the royalties of the beneficiaries in order to promote green development. The tax-sharing system based on Ecological Value-Added Tax and Service Tax, first established by the Parana State in Brazil in 1992, can be regarded as the specific application of fiscal ecological compensation in practice. Similarly, the transfer payment system for national key ecological functional areas that China began to pilot in 2008 is also the most important attempt of vertical fiscal ecological compensation in China’s reality. By 2022, more than 800 counties in China will have received ecological transfer payments, with the total size of the transfer payments exceeding CNY 600 billion. According to the corresponding county ecological and environmental governance assessments, national transfer payments to key ecological function areas have had a significant impact on China’s ecological and environmental governance and economic and social development [6].

This paper is based on the background of excessive consumption of resources and a certain degree of deterioration of ecological environment that China has faced along with the rapid economic growth since the reform and opening up. This paper combines the possible non-linear relationship between economic growth and ecological environment found in numerous studies. Under the requirement of green development, how to realize the coordinated and sustainable development of economic growth and ecological environment in the new normal remains an important research theme with distinctive contemporary significance. Accordingly, this paper focuses on the exploration of the important role of fiscal ecological compensation in green development. This paper seeks to analyze the direct and indirect impacts of fiscal ecological compensation systems on ecological governance based on the recognition of the relationship between economic development and the ecological environment.

Firstly, this article complements and tests the fundamental theory of green development. Fiscal ecological compensation is an innovative governance tool that combines market and government means. It is not limited to previous research on the incentive effect and mechanism of fiscal ecological compensation. This paper integrates economic devel-

opment and the environmental environment under the same analytical framework [5,6]. On this basis, this paper incorporates fiscal eco-compensation factors into the analytical framework to explore the direct and indirect impacts of fiscal eco-compensation on China's green development. This paper extends somewhat on the theoretical basis, impact, and mechanism of action of theories related to ecological fiscal compensation to promote the path of achievement of green development.

Second, based on a summary of the evolution of China's green development and fiscal eco-compensation system, this paper examines the relationship between economic and social development and eco-environmental governance and the green development effects of fiscal eco-compensation. The direct and indirect impacts of fiscal eco-compensation on green development are analyzed. The institutional barriers involved are analyzed in order to provide a benchmark for the construction of an eco-compensation system with institutional regulation, efficient incentives, and coordinated development and indirect effects; analyze the existing system and mechanism obstacles; and provide reference for the construction of a fiscal ecological compensation system with institutional norms, incentives, and coordinated development. With appropriate extensions, the research in this paper has important empirical implications for understanding green development in developing countries.

Third, rather than limiting research to parts of China or above the county level, this paper focuses on the county level, which is the foundation of China's overall economic and social governance. This paper seeks to specifically and precisely measure the relationship between economic development and the ecological environment and to explore the impact of fiscal ecological compensation on China's green development pathway.

The rest of this paper is arranged as follows: The Section 2 is literature review; Section 3 is empirical design; Section 4 is empirical analysis; and Section 5 is research conclusions and policy suggestions.

## 2. Literature Review

### 2.1. Economic Development and Ecological Environment

The study of the relationship between economic development and environmental sustainability began with Grossman and Krueger. Grossman and Krueger discovered that there is an inverse U-shaped relationship between SO<sub>2</sub> and soot emissions and economic growth [1]. Panayotou performed a detailed analysis of the inverse U-relationship between economic development and environmental pollution. Then, Panayotou suggested naming the inverted U-curve between the two as "Kuznets Environmental Curve" [2]. Subsequently, studies using different types of pollution discharge indicators, such as air pollution, water pollution, and solid waste pollution, as proxy variables of environmental pollution confirmed the nonlinear relationship between the two [3,4]. Grossman and Krueger presented the mechanism for the impact of economic development on the quality of the environment in terms of scale, technology, and structure [5].

Rapid economic development has led to excessive consumption of natural resources, and predatory exploitation of resources has put severe strain on the ecological environment [7,8]. Based on the research of Grossman and Krueger [1], the (inverted) U-shaped relationship between economic development and resources and ecology is supported by some studies, that is, in line with the traditional EKC hypothesis [9–11]. For instance, Madhusudan and Michael used the deforestation rate as a measure of the ecological environment, confirming that there is a strong EKC relationship between the income rate and the deforestation rate [9]. Based on the ecological footprint data of 22 European countries, Saqib and Benhmad empirically tested the quadratic relationship between income growth and ecological footprint [11]; that is, the hypothesis of ecological EKC is supported. At the same time, a large body of literature has found that the relationship between economic development and the ecological environment is not a simple quadratic one. Economic development and ecological environment show a cubic (inverse) N-shaped correlation [12–16]. For example, research results from Zhou et al. show a non-linear, N-shaped relationship



between economic development and environmental pollution [13,14]. The empirical results of Kang et al. demonstrate a non-linear, inverted N-shaped relationship between economic development and carbon dioxide emissions [15]. Moreover, some studies do not think that there is a non-linear relationship between the two [17]. Different empirical results may be linked to differences in sample time intervals, substitution variables, and selection of econometric models [18].

## 2.2. Influencing Factors of Nonlinear Relationship Changes

Economic and social factors are major shocks to the relationship between economic development and the ecological environment. Firstly, energy consumption patterns can alter the relationship between economic development and the ecological environment. With the development of the economy, the level of energy consumption of the population will change, initially increasing and then decreasing. When the level of economic development improves, people become more interested in the current and future environmental conditions. In addition, people are more willing to sacrifice energy consumption in return for a high-quality environmental environment. It shifts the inflection point of the non-linear curve between economic development and the ecological environment earlier and mitigates the negative impact of economic development on the ecological environment [19,20]. Secondly, financial development policies such as credit expansion have not only increased consumer demand for energy-intensive products but have also led to more environmental degradation. This in turn shifts the inverted U-shaped curve between economic development and the ecological environment [21,22]. Finally, the economic structure also affects the non-linear relationship between economic development and environmental protection. The modernization of the economic structure will change the “extensive” pattern of development of high pollution, high energy consumption, and high emissions at an early stage of economic development. This will reduce the pressure on the ecosystem caused by economic development and shift the EKC curve to the left [23].

The government’s environment policy is a factor that cannot be ignored to change the curve. Panayotou stressed that improving environmental quality depends primarily on government policies, social systems, and market integrity and functioning rules [24]. When the government has enough information, it can set higher ecological standards and stricter environmental laws and regulations. At the same time, the market uses more technologically advanced technology to produce its products. The second inflection point of the N-shaped curve means that the quality of the ecological environment will improve. The objective of regulating the relationship between economic development and the ecological environment could be achieved through commercial means. For example, carbon trading could reconcile supply and demand between those with a surplus of carbon credits and those with a shortage of carbon credits through market forces. This reduces the distance between the inflection points of the original N-type EKC curve and contributes significantly to the reduction of CO<sub>2</sub> emissions. A series of pollution-control policies developed by the government will also affect the relationship between economic development and the ecological environment [23]. In general, the use of coercive administrative regulation by the government can also shift the relationship between economic development and the ecological environment in a direction that is conducive to improving the ecological environment. For example, environmental regulations may have a significant impact on the peak and position of the EKC, which causes the EKC to move down to the left. However, the direction of government regulation of the relationship between economic development and the ecological environment through economic instruments such as green fiscal revenues and expenditures is uncertain. There are both positive and negative impacts. For example, green fiscal revenues and expenditures have a negative effect on carbon emissions. The cumulative effect of green finance on environmental protection has yet to be published, with China only recently involved in the economic sphere. In addition, there is a problem of moral hazard due to information asymmetry between enterprises and government. This has led some enterprises to increase their pollution emissions after obtaining green fiscal

support. This ultimately leads to green budget receipts and expenditures that inhibit the role of economic development in improving the environmental environment [25]. On the contrary, the government will not only increase the cost of enterprises through green fiscal revenue and constrain enterprises' pollutant-discharge behavior but also encourage enterprises to invest in environmental protection and improve technology through green fiscal expenditure measures. As a result, reducing pollution emissions and making the EKC inflection point could come earlier [22,26].

### 2.3. Eco-Environmental Effects of Fiscal Ecological Compensation

Ecological compensation is an institutional arrangement that adjusts the interest relationship between ecological beneficiaries and ecological protectors through a market-oriented mechanism to realize the internalization of ecological protection externalities [27]. At present, due to the absence of relevant legal systems and property rights arrangements, government-led vertical financial transfers have become an important means of ecological compensation. In other words, fiscal ecological compensation is the most important expression of ecological compensation [6].

The policy practice of fiscal eco-compensation could be traced back to the value-added tax-based tax-sharing system of the Brazilian State of Parana in 1992. This scheme has a positive effect on the ecological protection of the State of Parana [28]. Since then, Ecological Value-Added Tax and Service Tax has been used as a benchmark by other regions and countries and has created a positive incentive for environmental governance [29]. China's fiscal ecological compensation system can be traced back to the returning farmland to the forest system in the 1990s. However, the formal fiscal ecological compensation system is the national key ecological function area transfer payment system, which was piloted and implemented in 2008. Similarly, due to the unclear subjects responsible for ecological environmental governance in China and the immature market mechanism, vertical ecological transfer payments that incorporate ecological protection indicators into the intergovernmental financial redistribution standards have become the main means of ecological compensation [6]. In Chinese practice, fiscal ecological compensation has played an important positive role in boosting the governance behavior of the local government's ecological environment through the effect of financial compensation. It also significantly improves the local ecological environment and the level of supply of public services for the livelihoods of populations [30–34].

According to the above research, ecological financial compensation has become an important means for the government to coordinate environmental governance among regions. However, the above studies not only fail to reach a consensus on China's green development path but also have not yet clarified the theoretical basis, influence, and mechanism of the realization path of ecological financial compensation to promote green development. In this respect, this paper attempts to complement the inadequacy of the above research by incorporating economic development and the ecological environment into the same analytical framework.

## 3. Empirical Design

### 3.1. Data Sources

Geographical data, such as topographic reliefs, were calculated based on Feng et al. [35]. Currently, there are two kinds of time-series luminous remote sensing data commonly used: Defense Meteorological Satellite Program (DMSP)/Operational Linescan System (OLS) and Visible Infrared Imaging Radiometer Suite (NPP)/VIIRS (Visible Infrared Imaging Radiometer Suite). The first kind was adopted by us. Other data came from The Bulletin on China's Ecological and Environmental Conditions and the Statistical Yearbook of Chinese Cities, and the authors have carried on the corresponding manual statistical collation.

The data used in this paper come from the dataset of county-level regions in China in 2017 and 2018. Among them, the ecological environment status index and its five sub-indicators are the main explained variables, and the data come from the 2017 and

2018 “China Ecological Environment Status Bulletin”. The transfer payment data for the national key ecological function areas are obtained by applying to the Ministry of Finance for disclosure. Economic, social, and geographic data, such as Gross Domestic Product (GDP) per capita, number of industrial enterprises above designated size, population density, proportion of secondary industry, administrative area, average altitude, etc., are derived from public statistics such as the “China Urban Statistical Yearbook” in 2018 and 2019. Geographic data, such as terrain relief, are calculated according to the research of Feng et al. [35]. Light-intensity data includes the DMSP/OLS radiometric calibrated nighttime light data products for 2017 and 2018 as well as the stable light data products.

### 3.2. Variable Description

#### 3.2.1. Explained Variables

Ecological index (*EI*) is the explained variable in this paper, and its value represents the overall ecological environment quality: the larger the *EI*, the better the ecological environment quality; the smaller the *EI*, the worse the ecological environment quality. The specific calculation formula of *EI* is as follows:

$$EI = 0.25 \times BAI + 0.2 \times VCI + 0.2 \times WNDI + 0.2 \times LSI + 0.15 \times PLI$$

Among them, *BAI* refers to biological abundance index. *VCI* refers to vegetation coverage index. *WNDI* refers to water network density index. *LSI* refers to land stress index. *PLI* refers to the pollution load index. Indicators are selected from the Environmental Protection Department of the People’s Republic of China issued by the state environmental protection standards in 2015. The calculation method for ecological environment in it is to weight these five indicators accordingly. This method was also adopted in this paper. Combined with the availability of data in each county and district, these five items were selected in this study as the explanatory variables for the indicators of ecological environment status.

In the empirical research, in order to test the robustness of the empirical results and analyze the similarities and differences between different ecological environment indicators, this paper uses the ecological environment status index and its five sub-indicators to conduct subsequent empirical research.

#### 3.2.2. Core Explanatory Variables

Per capita GDP is one of the core explanatory variables of this paper, which is used to represent the current level of economic development. At the same time, in order to truly reflect the economic conditions of the evaluated regions, this paper deflates nominal GDP using 2017 as the base period to avoid the impact of rising price indices.

The national key ecological function area transfer payment (hereinafter referred to as ecological transfer payment) is another core explanatory variable of this paper. As it is not possible to obtain specific information on the size of ecological transfer funds received by each county-level region, this paper uses the list of county-level regions receiving ecological transfers to set dummy variables. Specifically, the county-level region that has obtained ecological transfer payment takes the value of 1, and otherwise, it is 0.

#### 3.2.3. Control Variables

The ecological environment of an area at county level is affected not only by the level of economic development but also by other economic, social, and geographic factors [6,19]. Therefore, in order to control for problems caused by omitted variables, this paper introduces control variables into the empirical model to control for the effects of other factors on the state of the ecosystem. This includes the number of industrial enterprise units above a certain size, population density, the proportion of secondary industry, the area of the administrative area, the average altitude and the topographic relief. Among them, the number of industrial enterprises above designated size is represented by the number of large-scale enterprises in the

county-level area. Population density is expressed in terms of population per square kilometer. The descriptive statistics of the above variables are shown in Table 1.

**Table 1.** Descriptive statistics of each variable.

Variables	Sign	Unit	Obs	Average	Standard Deviation	Min	Max
Ecological Condition Index	<i>EI</i>	%	2894	61.31	15.58	16.00	91.20
Biological Abundance Index	<i>BAI</i>	%	2894	44.19	21.58	3.20	96.80
Vegetation Cover Index	<i>VCI</i>	%	2894	81.36	17.10	8.30	100.00
Water Network Density Index	<i>WNDI</i>	%	2894	35.30	22.72	0.60	100.00
Land Stress Index	<i>LSI</i>	%	2894	14.99	16.75	0.20	100.00
Pollution Load Index	<i>PLI</i>	%	2894	98.35	3.79	49.90	100.00
Whether Receiving an Ecological Transfer	<i>fec</i>	-	2894	0.228	0.419	0	1
GDP Per Capita	<i>pcgdp</i>	CNY	2894	45,000	42,000	5245	450,000
Number of Industrial Enterprise Units above Scale	<i>nied</i>		2836	140	211	1	2499
Share of Secondary Sector	<i>Ind2</i>	%	2894	41.34	13.85	4.84	86.44
Population Density	<i>pd</i>	million people/km <sup>2</sup>	2894	0.04	0.03	0	0.44
Administrative Area	<i>area</i>	km <sup>2</sup>	2894	3189.83	6803.10	59.00	110,000
Elevation Mean	<i>altitude</i>	m	2894	712.10	906.67	−0.97	5113.84
Terrain Undulation	<i>slope</i>	m	2894	0.93	1.15	0	6.44
Light Intensity	<i>li</i>	10,000	2894	0.77	1.67	0	26.55

### 3.3. Model Building

#### 3.3.1. The Relationship between Economic Development and Ecological Environment

As stated earlier, there may be a non-linear relationship between economic development and the ecological environment. However, the specific form of the non-linear relationship is not clear. Different forms of non-linear relationships may be associated with differences in the selection of sample data and proxy variables. There is a lack of research at the county level, which is the basis of overall economic and social governance in China, and in particular, the possible impact and mechanisms of action of fiscal eco-compensation are not clear. Therefore, based on the data from county-level regions in China, this paper first examines the relationship between economic development and the ecological environment.

Referring to the research of Wu et al. [36], this paper uses the stepwise regression method to first test the relationship between economic development and ecological environment and then test the validity of the EKC hypothesis. The model is set as follows:

$$\ln EI_i = \alpha_0 + \beta_1 \ln pcgdp_i + \beta_2 (\ln pcgdp_i)^2 + \beta_3 (\ln pcgdp_i)^3 + \beta_4 fec_i + \lambda' X_i + \varepsilon_i \tag{1}$$

Among them, *EI<sub>i</sub>* represents the ecological environment status index of county-level region; *i*. *pcgdp<sub>i</sub>* represents the per capita GDP of county-level region; and *i*. *fec<sub>i</sub>* is the dummy variable of whether county-level region *i* has obtained the transfer payment for national key ecological function zones. If the transfer payment is obtained, then *fec<sub>i</sub>* = 1; otherwise, *fec<sub>i</sub>* = 0. *X<sub>i</sub>* represents a column vector composed of a series of other control variables.  $\varepsilon_i$  is a random disturbance term. *pcgdp<sub>i</sub>* is one of the important variables affecting the ecological environment. As already mentioned in Section 1, there may be a nonlinear relationship between the economic growth and ecological environment. The specific form of the nonlinear relationship is uncertain. Therefore, the variables in model (1) are set to the first-power, second-power, and third-power items of *pcgdp<sub>i</sub>*, respectively. Among them,  $\beta_1$ – $\beta_3$  are the core explanatory variable parameters concerned in this paper, and the validity of the ecological EKC hypothesis can be identified by the positive, negative, and significance of its coefficients. Firstly, when  $\beta_1$ – $\beta_3$  are not significant, economic development is not related to the ecological environment. Secondly, when  $\beta_2$ – $\beta_3$  is not significant, but  $\beta_1$  is significant and greater than zero, economic development and ecological environment are

positively correlated. In the contrast, when  $\beta_1$  is significant and less than zero, the two are negatively correlated. Thirdly, when  $\beta_3$  is not significant, but  $\beta_2$  is significant and greater than zero, the two are in a positive U-shaped relationship consistent with the ecological EKC hypothesis. On the contrary, when  $\beta_2$  is significant and less than zero, the two have an inverted U-shaped relationship. Finally, when  $\beta_3$  is significant and greater than zero, the two have an N-shaped relationship. Conversely, when  $\beta_3$  is significant and less than zero, the two are in an inverted N-shaped relationship.

### 3.3.2. The Impact of Fiscal Ecological Compensation

In order to further analyze the impact of fiscal ecological compensation on economic green development, referring to the research of He and Wang, and Antweiler [23,37], this paper further adds the interaction term of the product term of  $fec_i$  and  $pcgdp_i$  on the basis of model (1). The specific form of the model (2) is as follows:

$$\ln EI_i = \alpha_0 + \beta_1 \ln pcgdp_i + \beta_2 (\ln pcgdp_i)^2 + \beta_3 (\ln pcgdp_i)^3 + \beta_4 fec_i + \gamma \ln pcgdp_i \times fec_i + \lambda' X_i + \varepsilon_i \tag{2}$$

Among them, this paper uses the significance, magnitude, and direction of  $\beta_1$ – $\beta_3$  and  $\lambda$  to judge the impact of fiscal ecological compensation on the green development path. Based on the meaning, magnitude, and direction of  $\gamma$ , we judge whether the impact of  $pcgdp_i$  and  $fec_i$  on the green development path is the same. Further, we determine whether the impact of national key ecological function area transfer payment on  $pcgdp_i$  is inhibited or promoted.

## 4. Empirical Analysis

### 4.1. Basic Regression

This paper uses the least squares method to estimate model (1) and controls the annual trend and the fixed effects of county-level regions. At the same time, it also adopts robust heteroscedasticity as a standard error to control the heteroscedasticity problem. Table 2 illustrates the empirical results of the basic regression.

On the basis of stepwise regression testing the relationship between economic development and ecological environment, model (5) is the estimation for the whole sample. Models (6) and (7) were estimated for the 2017 and 2018 subsamples, respectively, with the aim of testing whether there are temporal differences in the ecological EKC assumptions. Without adding any control variables, from the estimation results of model (1) to model (3),  $R^2$  gradually increases, and the fitting degree of the model gradually improves. Among them, the coefficient of the cubic term of per capita GDP in model (3) is significant at the 1% significance level, and the model has a higher degree of fit. Therefore, this paper retains the cubic term of per capita GDP in model (4) on the basis of added ecological transfer payment. Model (4) demonstrates that the ecological transfer payment has a positive effect on the ecological environment at the 1% significance level. In order to accurately estimate the parameters of the model and avoid the problem of estimation bias caused by missing variables, model (5) further adds other control variables on the basis of model (4). From the regression results of model (5), the fitting degree of the model is further improved. The coefficient of the cubic term of per capita GDP is positive at the 1% significance level, indicating that there is an N-shaped nonlinear relationship between economic development and the ecological environment. The inflection points of the curve are CNY 23,195 and CNY 276,952 respectively.

The critical point calculation formula of N-shaped curve is as follows:

$$\frac{\partial \ln EI_i}{\partial \ln pcgdp_i} = \beta_1 + 2\beta_2 \ln pcgdp_i + 3\beta_3 (\ln pcgdp_i)^2$$

$$\text{Set it to zero: } \beta_1 + 2\beta_2 \ln pcgdp_i + 3\beta_3 (\ln pcgdp_i)^2 = 0.$$

To solve this equation:  $\ln pcgdp_i = \frac{-2\beta_2 \pm \sqrt{4\beta_2^2 - 12\beta_1\beta_3}}{6\beta_3}$ . Finally, the value of  $pcgdp_i$  was inversely solved by  $\ln pcgdp_i$ .

This means that when GDP per capita is between CNY 23,195 and CNY 276,952, economic development will gradually deteriorate the ecological environment; when GDP per capita is higher than CNY 276,952, economic development will bring about ecological improvement. The dummy variable coefficient of ecological transfer payment is positive at the 1% significance level, indicating that fiscal ecological compensation may significantly improve the ecological environment. As in the Brazil and India studies, the increase of fiscal ecological compensation has a significant positive effect on environmental improvement [28,29]. The regression results of the two subsamples in 2017 and 2018 show that the coefficients of the cubic terms of per capita GDP are all positive at the 1% significance level, which is consistent with the estimation results of the full sample. This means the N-shaped non-linear relationship between economic development and the ecological environment persists. The inflection points of the sample nonlinear relationship in 2017 were CNY 22,663 and CNY 299,628, and the inflection points of the nonlinear relationship in 2018 were CNY 21,498 and CNY 299,659, respectively. The conclusions of the sub-sample study are basically the same as that of the whole-sample study. Taking the 1444 samples in 2018 as an example, there are 304 counties with per capita GDP below CNY 21,498, accounting for 21.05% of the total sample. This shows that this region is in the first stage of an N-shaped nonlinear relationship, and economic development will bring ecological environmental improvement. Furthermore, there are 1135 counties with per capita GDP between CNY 21,498 and CNY 299,659, accounting for 78.60% of the total sample. That is, the region is in the second stage of the N-shaped nonlinear relationship, and economic development will gradually deteriorate the ecological environment. Furthermore, the only counties with per capita GDP higher than CNY 299,659 are Otuoque Banner, Wushen Banner, Yijinhuoluo Banner, Kunshan City, and Yiwu County, accounting for only 0.35% of the total sample. That is, the regions enter the third stage of the N-shaped non-linear relationship, where economic development will improve the ecological situation.

The N-shaped nonlinear relationship between economic development and ecological environment shows that, along with economic development, the ecological environment goes through three stages of improvement, deterioration, and improvement in turn. In the first stage, due to the relatively slow economic development, the speed of ecological environment governance and restoration is greater than the speed of consumption and destruction brought about by economic development. However, at the second stage, economic development has reached a certain scale. The “Extensive” development model has enabled China to achieve economic development only through increased consumption of factors of production, including natural resources, resulting in a rate of resource consumption that far exceeds the rate of resource regeneration. As a result, the negative impact of economic development on the ecological environment becomes apparent. In addition, the industrial shift from the east to the central and western parts of the country in recent years has also led to a continuous decline in environmental conditions, so there is a negative correlation with it [38,39]. Studies have shown that ultimately improving the environmental environment depends on public demand for a high-quality environmental environment in a highly developed economy [7,23,24]. A positive correlation between ecological environment quality and income level exists only when per capita income exceeds a certain level. In other words, people’s demand for ecological environment quality will increase with the increase of income. The objective conditions for a change in the pattern of economic development are also in place. Inflection point in the N-shaped non-linear relationship between economic development and ecology emerges. Society has entered a phase where economic growth and ecological environment are in harmony.

With respect to control variables, the empirical results of this article are essentially consistent with existing studies [7,21]. Specifically, the number of industrial enterprises above designated size, population density, and terrain fluctuation have a positive impact on the ecological environment at the significance level of 10%, 5%, and 1%, respectively.

Altitude has a negative impact on the ecological environment at the 10%, 1%, and 1% significance levels, respectively.

**Table 2.** Basic regression empirical results of the relationship between economic development and ecological environment.

	(1)	(2)	(3)	(4)	(5)	(6)	(7)
<i>lnpcgdp</i>	−0.0560 *** (−6.39)	0.9803 *** (6.26)	7.0480 *** (3.44)	7.4185 *** (3.63)	10.5810 *** (5.65)	10.8884 *** (4.04)	10.3028 *** (3.96)
<i>(lnpcgdp)<sup>2</sup></i>		−0.0486 *** (−6.62)	−0.6173 *** (−3.21)	−0.6472 *** (−3.38)	−0.9485 *** (−5.40)	−0.9746 *** (−3.86)	−0.9249 *** (−3.79)
<i>(lnpcgdp)<sup>3</sup></i>			0.0177 *** (2.95)	0.0185 *** (3.10)	0.0280 *** (5.12)	0.0287 *** (3.65)	0.0273 *** (3.59)
<i>fec</i>				0.0929 *** (6.47)	0.0504 *** (3.69)	0.0504 ** (2.52)	0.0506 *** (2.70)
<i>lnnied</i>					0.0200 * (1.95)	0.0176 (1.21)	0.0222 (1.53)
<i>lnpd</i>					0.0311 ** (2.09)	0.0345 (1.62)	0.0278 (1.33)
<i>lnInd2</i>					−0.0016 *** (−3.28)	−0.0018 *** (−2.59)	−0.0014 ** (−2.04)
<i>lnarea</i>					−0.0251 * (−1.84)	−0.0207 (−1.08)	−0.0293 (−1.51)
<i>lnaltitude</i>					−0.5060 *** (−17.02)	−0.5118 *** (−12.04)	−0.5001 *** (−11.98)
<i>lnslope</i>					0.5191 *** (19.27)	0.5234 *** (13.58)	0.5147 *** (13.61)
<i>cons</i>	−14.9847 (−0.69)	−19.0095 (−0.89)	−40.4708 * (−1.78)	−36.8851 (−1.64)	−44.6904 ** (−2.30)	−32.3585 *** (−3.41)	−30.1173 *** (−3.30)
Annual Trends	YES	YES	YES	YES	YES	NO	NO
District Fixed Effects	YES	YES	YES	YES	YES	YES	YES
<i>N</i>	2894	2894	2894	2894	2832	1427	1405
<i>F</i>	25.5942	29.8285	24.8436	28.1095	110.3445	59.4002	59.9515
<i>R<sup>2</sup><sub>adj</sub></i>	0.0465	0.0583	0.0601	0.0759	0.3326	0.3248	0.3356
<i>inflection point</i>	-	-	-	-	CNY 23,195	CNY 22,663	CNY 21,498
	-	-	-	-	CNY 276,952	CNY 299,629	CNY 299,659

Notes: *T*-statistics are in parentheses. \*\*\*, \*\*, and \* indicate significance at the 1%, 5%, and 10% levels, respectively.

#### 4.2. Analysis of Sub-Indicators of Ecological Environment Condition Index

According to the reliability of the test results, this paper uses the five sub-indices of the ecological environment condition index to replace the ecological environment condition index as the explained variables to test the robustness. The corresponding empirical results are shown in the model in Table 3 (1)–(5).

As shown in Table 3, for different sub-indices of the ecological environment condition index, there is a certain difference in the nonlinear relationship between it and per capita GDP. That is, there are different forms of non-linear relationships between the different sub-indices of the economic development and ecological status index. Specifically, the cubic coefficient of per capita GDP of the biological abundance index in model (1) is positive at the 1% significance level. It is showed that there is an N-shaped nonlinear relationship between the biological abundance index and economic development. The quadratic coefficients of GDP per capita for the vegetation cover index and the water network density index in models (2) and (3) are both negative at the 1% significance level. It is illustrated that an inverted U-shaped non-linear relationship exists between vegetation cover index and water network density index and economic development. The coefficient of the cubic term of GDP per capita for the land stress index in model (4) is negative at the 1% significance level.

This means there is an inverted N relationship between the land stress index and economic development. The quadratic coefficient of per capita GDP of the pollution load index in model (5) is negative at the 1% significance level. This means there is an inverted U-shaped nonlinear relationship between the pollution load index and economic development. The above findings are consistent with traditional EKC theory [7,23].

On the whole, there is an intricate relationship between economic development and the ecological environment. The nonlinear relationship between the two verified in this paper may be real. Since the meanings of the various sub-indicators differ, there are differences in their non-linear forms in the sample interval.

**Table 3.** The empirical results of the relationship between economic development and the sub-indicators of the ecological environment condition index.

	(1) BAI	(2) VCI	(3) WNDI	(4) LSI	(5) PLI
<i>lnpcgdp</i>	11.1273 *** (3.23)	1.4550 *** (8.31)	1.8587 *** (5.34)	−51.9992 *** (−8.80)	0.0803 * (1.93)
$(\lnpcgdp)^2$	−0.9571 *** (−2.94)	−0.0726 *** (−8.89)	−0.0820 *** (−5.03)	4.5749 *** (8.29)	−0.0049 ** (−2.42)
$(\lnpcgdp)^3$	0.0271 *** (2.65)			−0.1323 *** (−7.71)	
<i>fec</i>	0.1655 *** (7.06)	0.0696 *** (4.87)	0.1494 *** (5.80)	−0.0419 (−0.79)	−0.0034 * (−1.95)
<i>cons</i>	−19.3189 (−0.58)	−16.3955 (−0.92)	19.7236 (0.54)	152.3289 ** (2.18)	1.7395 (0.55)
Control	YES	YES	YES	YES	YES
Annual Trends	YES	YES	YES	YES	YES
District Fixed Effects	YES	YES	YES	YES	YES
<i>N</i>	2832	2832	2832	2832	2832
<i>F</i>	212.9734	63.6005	187.3018	57.4357	18.2326
<i>R<sup>2</sup><sub>adj</sub></i>	0.4257	0.4107	0.5692	0.1781	0.1478

Notes: *T*-statistics are in parentheses. \*\*\*, \*\*, and \* indicate significance at the 1%, 5%, and 10% levels, respectively.

### 4.3. Endogenous Analysis

In order to solve the endogenous problem caused by the two-way causal relationship between economic development and ecological environment, this paper attempts to use the instrumental variable method to discuss this endogenous problem in the model. In this paper, the nighttime light intensity (DMSP/OLS) and the per capita GDP (*L.lnpcgdp*) of the county-level area are used as instrumental variables. The 2SLS method is adopted for empirical research. The empirical results are shown in Table 4. When only the light intensity at night is used as an instrumental variable, the *F*-value of the first-stage regression is greater than 10, indicating that there is no weak instrumental variable problem. At the same time, the cubic coefficient of per capita GDP is positive at the 1% significance level. This means the N-shaped nonlinear relationship between economic development and ecological environment still exists significantly, and the basic regression results are more credible. Finally, when using only lagged one-period GDP per capita as an instrumental variable and taking the two variables as instrumental variables into the estimation equation, the latter fails to pass the over-identification test. Therefore, the *F* values of the above two equations in the one-stage regression are all greater than 10, and it could be observed that there is an N-shaped nonlinear relationship between the level of economic development and the ecological environment. This result further confirms the credibility of the aforementioned basic regression results.



**Table 4.** Empirical results of endogenous analysis of the relationship between economic development and ecological environment.

	<i>DMSP/OLS</i>	<i>L.lnpcgdp</i>	<i>DMSP/OLS and L.lnpcgdp</i>
<i>lnpcgdp</i>	97.4864 *** (2.85)	11.1606 *** (5.63)	11.5878 *** (5.80)
$(\lnpcgdp)^2$	-9.1336 *** (-2.91)	-1.0010 *** (-5.40)	-1.0429 *** (-5.58)
$(\lnpcgdp)^3$	0.2832 *** (2.95)	0.0296 *** (5.13)	0.0309 *** (5.32)
<i>fec</i>	0.0386 * (1.73)	0.0501 *** (3.65)	0.0491 *** (3.59)
<i>cons</i>	-381.4152 *** (-3.31)	-45.9006 ** (-2.33)	-48.5020 ** (-2.46)
Control	YES	YES	YES
Annual Trends	YES	YES	YES
District Fixed Effects	YES	YES	YES
<i>N</i>	2832	2805	2805
<i>R<sup>2</sup><sub>adj</sub></i>	-	0.3344	0.3342

Notes: *T*-statistics are in parentheses. \*\*\*, \*\*, and \* indicate significance at the 1%, 5%, and 10% levels, respectively.

#### 4.4. The Impact of Fiscal Ecological Compensation

Table 5 shows the effect of the model’s fiscal ecological compensation (2) on the relationship between economic development and the ecological environment. Among them, model (1) uses the ecological environmental condition index as a dependent variable to explore the impact of fiscal ecological compensation. At the same time, in order to ensure the robustness of the research results, the models (2)–(6) are, respectively, based on the biological abundance index, vegetation coverage index, water network density index, land stress index, and pollution load index, which are the five sub-indices of the ecological environment condition index. Indicators are used as dependent variables to explore the impact of fiscal ecological compensation. It could be seen from Table 5 that after adding the interaction term to the basic model, the nonlinear correlation between various ecological environment indicators and economic development is still significant, which is consistent with the nonlinear correlation obtained by the basic regression. In models (1)–(4), the coefficients of fiscal ecological compensation are all significantly positive. It is indicated that fiscal ecological compensation can directly improve the ecological environment. The coefficient of interaction between economic development variables and fiscal ecological compensation variables is significant. As a result, it could be inferred that fiscal ecological compensation could affect the relationship between economic development and ecological environment, thereby indirectly affecting the ecological environment.

To visualize the indirect effects of fiscal ecological compensation on the relationship between economic development and ecological environment, Figure 1 shows the economic development and ecological environment in areas without fiscal ecological compensation (*fec* = 0) and with fiscal ecological compensation (*fec* = 1). Figure 1a presents the impact of fiscal eco-compensation on the relationship between the ecosystem condition index and economic development. It could be seen that fiscal ecological compensation has led to a change in the non-linear relationship between economic development and the ecological status index. The specific performance is as follows: Fiscal ecological compensation shifts the non-linear curve between economic development and the index of ecological status upwards in the interval of GDP per capita below CNY 58,747. However, when the per capita GDP is higher than CNY 58,747, the fiscal ecological compensation makes the nonlinear curve between the economic development and the ecological environment condition index move downward. It could be indicated that the fiscal ecological compensation has changed the impact of economic development on the ecological environment condition index. In the full sample, approximately 79.68% of the counties are in the interval where GDP per capita

is below CNY 58,747, i.e., to the left of the intersection of the curves. The reason for this may be that in the early stages of economic development, fiscal ecological compensation can fully compensate for the opportunity costs of development that regions sacrifice by forgoing economic development. Therefore, local governments focus on protecting the ecological environment. However, with economic development, fiscal ecological compensation is gradually insufficient to make up for the development opportunity cost sacrificed by local governments for giving up economic development. In this case, local governments prefer to sacrifice the ecological environment in exchange for “extensive” economic development. According to the existing research, whether fiscal ecological compensation can encourage local governments to protect the environment depends on whether they can increase local financial expenditure to improve ecological and environmental conditions under China’s environmental governance [40].

**Table 5.** The regression results of the impact of fiscal ecological compensation.

	(1) EI	(W) BAI	(E) VCI	(4) WNDI	(5) LSI	(5) PLI
<i>lnpcgdp</i>	11.8659 *** (6.01)	13.1744 *** (3.57)	1.6611 *** (8.36)	2.0811 *** (5.48)	−53.7592 *** (−8.44)	0.0825 * (1.82)
<i>(lnpcgdp)<sup>2</sup></i>	−1.0586 *** (−5.76)	−1.1326 *** (−3.29)	−0.0818 *** (−8.88)	−0.0919 *** (−5.20)	4.7258 *** (8.01)	−0.0050 ** (−2.29)
<i>(lnpcgdp)<sup>3</sup></i>	0.0311 *** (5.47)	0.0321 *** (2.99)			−0.1366 *** (−7.51)	
<i>lnpcgdp × fec</i>	−0.0686 *** (−2.73)	−0.1094 ** (−2.28)	−0.0686 ** (−2.44)	−0.0740 * (−1.83)	0.0940 (1.02)	−0.0007 (−0.16)
<i>fec</i>	0.7533 *** (2.96)	1.2854 *** (2.63)	0.7717 *** (2.71)	0.9067 ** (2.21)	−1.0047 (−1.06)	0.0042 (0.09)
<i>cons</i>	−50.3490 ** (−2.57)	−28.3344 (−0.85)	−18.2660 (−1.03)	17.7061 (0.49)	160.0797 ** (2.26)	1.7193 (0.54)
Control Variables	YES	YES	YES	YES	YES	YES
Year Trend	YES	YES	YES	YES	YES	YES
County Effect	YES	YES	YES	YES	YES	YES
<i>N</i>	2832	2832	2832	2832	2832	2832
<i>F</i>	103.5556	198.7717	59.8273	175.1312	53.1909	18.3424
<i>R<sup>2</sup><sub>adj</sub></i>	0.3350	0.4276	0.4131	0.5695	0.1783	0.1475

Notes: *T*-statistics are in parentheses. \*\*\*, \*\*, and \* indicate significance at the 1%, 5%, and 10% levels, respectively.

The regression results for the sub-indices of the ecological environment condition index further prove the robustness of this result. Figure 1b illustrates the impact of fiscal ecological compensation on the relationship between the organic abundance index and economic development. It can be seen that fiscal ecological compensation changes the non-linear relationship between biological abundance index and economic development, which is embodied as follows: When GDP per capita is below CNY 126,696, fiscal ecological compensation shifts the nonlinear curve between the biological abundance index and economic development upward. When GDP per capita is higher than CNY 126,696, fiscal ecological compensation shifts the nonlinear curve between the index of biological abundance and economic development downward. Clearly, the results conform to Figure 1a, which confirms the economic logic of Figure 1a. Figure 1c presents the impact of fiscal ecological compensation on the relationship between vegetation cover index and economic development. In the range where the per capita GDP is lower than CNY 76,826, the fiscal ecological compensation makes the nonlinear relationship between economic development and the vegetation cover index move upward. When GDP per capita is higher than CNY 76,826, fiscal ecological compensation then shifts the curve of the non-linear relationship between economic development and vegetation cover index downwards. Figure 1d shows how fiscal ecological compensation affects the relationship between the water system density index and economic development. Similarly, in the interval where GDP per capita is below

CNY 209,546, fiscal ecological compensation shifts the curve of the non-linear relationship between economic development and the water network density index upwards. On the contrast, when GDP per capita is higher than CNY 209,546, fiscal ecological compensation shifts the curve of the non-linear relationship between economic development and the water network density index downwards. Figure 1c,d both present the same results. At low levels of economic development, fiscal eco-compensation can significantly improve the ecological environment. However, as the level of economic development increases, fiscal eco-compensation exacerbates the negative impact of economic development on the ecological environment. This result is different from the specific conclusions in Figure 1a,b. The reason for this may lie in the difference between the initial non-linear relationship between economic development and the vegetation cover index and the water network density index and the initial non-linear relationship between economic development and the ecological condition index and the biological abundance index. However, the following consistent results can still be drawn. When the level of economic development is low, fiscal ecological compensation could significantly improve the degree of improvement of the ecological environment caused by economic development. However, as the level of economic development increases, fiscal ecological compensation has a negative impact on the relationship between economic development and the ecological environment. Figure 1e presents the impact of fiscal ecological compensation on the relationship between land stress index and economic development. When the per capita GDP is lower than CNY 43,840, the fiscal ecological compensation makes the nonlinear relationship between economic development and the land coercion index move downward. When GDP per capita is higher than CNY 43,840, fiscal ecological compensation shifts the non-linear relationship between economic development and the land stress index upwards. While this outcome differs from Figure 1a,b, the reason may be that the meanings of specific environmental indicators are different. One possible reason is the contradiction between the unlimited demand for rapid economic growth and the limitation of land supply. Although this result is not significant, the result is still consistent with the previous analysis. Figure 1f presents the impact of fiscal ecological compensation on the relationship between the pollution load index and economic development. It could be seen that with economic development, fiscal ecological compensation will slow down the adverse impact of economic development on the ecological environment. However, this negative effect is found not to be statistically significant and there is only a slight economic difference (only  $-0.0007$ ).

Overall, fiscal ecological compensation has changed the nonlinear correlation between economic development and ecological environment. Fiscal ecological compensation can be directly used to improve the ecological environment. On the other hand, fiscal ecological compensation can fully compensate for the development opportunity cost sacrificed by the region because of giving up economic development. This policy may therefore encourage the government to pay greater attention to improving the ecological environment. Fiscal ecological compensation can significantly improve the degree of improvement of the ecological environment caused by economic development when the level of economic development is low. The robustness of this result is further proved from the test of the five sub-indices of the ecological environment condition index.

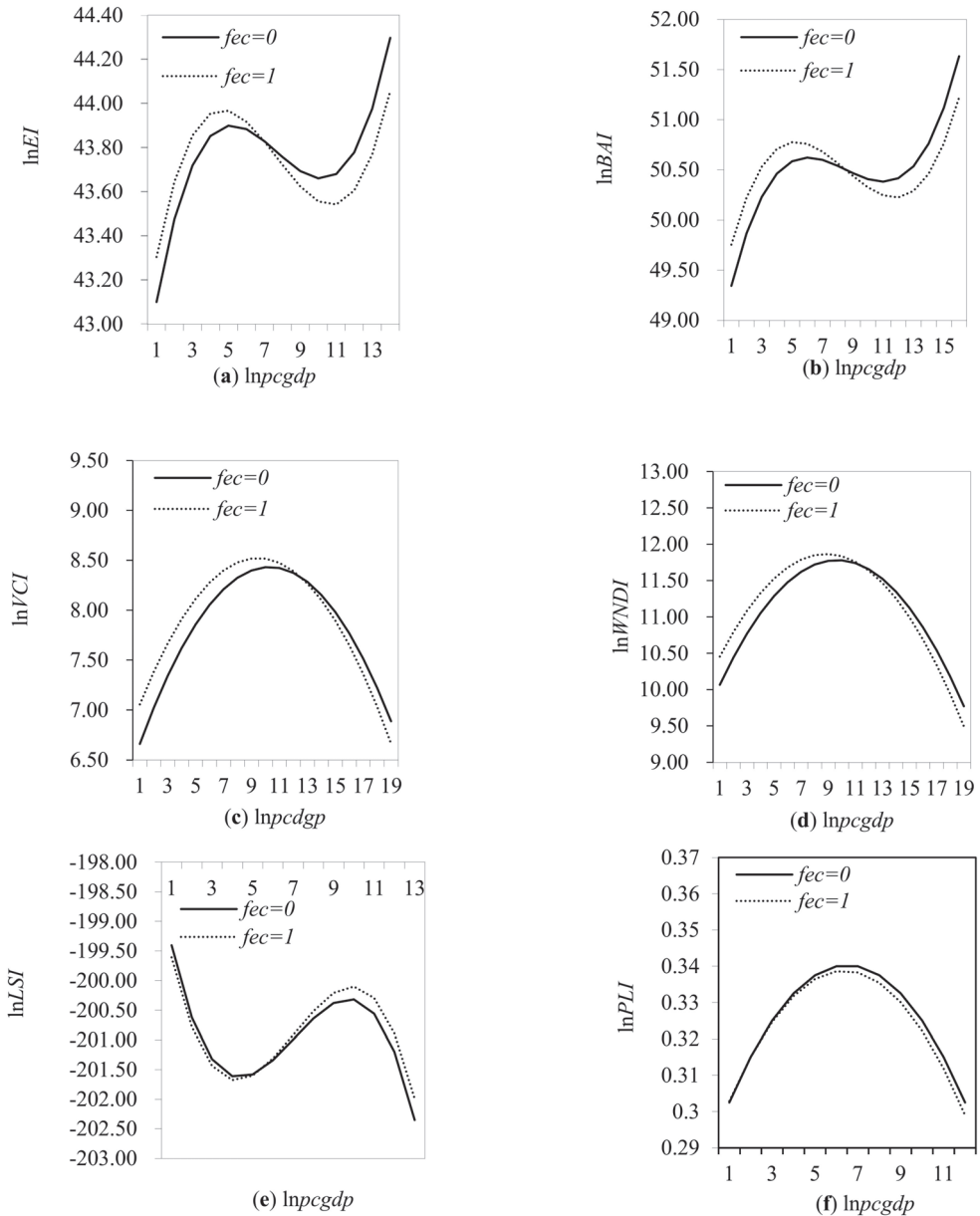


Figure 1. Impact of financial eco-compensation.

## 5. Research Conclusions and Policy Recommendations

### 5.1. Research Conclusions

In the context of green development, this paper uses the data of China’s county-level regions in 2017 and 2018 to construct an econometric model to analyze the impact of fiscal ecological compensation on China’s green development path. The main conclusions of this study are as follows:

Firstly, there is an N-shaped, nonlinear correlation between China’s economic development and the ecological environment. This means that, in parallel with economic

development, the ecological environment goes through the three stages of improvement, degradation, and improvement. In the first stage, due to the relatively slow economic development, the speed of ecological environment governance and restoration is greater than the speed of consumption and destruction brought about by economic development. However, under the “extensive” development model, China could only achieve economic growth by increasing the consumption of production factors, including natural resources, resulting in the speed of resource consumption far exceeding the speed of resource regeneration. As a result, the first inflection point appears. This means that the detrimental effects of economic development on the ecological environment arise. Only when per capita income exceeds a certain level, people’s demand for eco-environmental quality will increase with the growth of income. The objective conditions for a change in the pattern of economic development are also in place. Inflection point in the N-shaped non-linear relationship between economic development and ecology emerges. Society has entered a phase where economic growth and ecological environment are in harmony.

Secondly, fiscal ecological compensation has a direct positive impact on ecological environment governance. On the one hand, fiscal ecological compensation has curbed the ecological environment damage caused by the “extensive” development model of areas with important ecological functions, such as key ecological counties, prohibited development areas, and national ecological civilization experimental areas. On the other hand, fiscal ecological compensation provides direct public financial support for the above-mentioned areas to protect the ecological environment and provide basic public services, which could significantly improve the local ecological environment.

Finally, fiscal ecological compensation has an indirect impact on ecological environment governance by affecting economic development. For regions with a low level of economic development, fiscal ecological compensation may essentially offset the development opportunity cost because of policy requirements. For this reason, the regions benefiting from this policy are at an earlier stage of the coordinated development of economic development and the ecological environment. For areas with a high level of economic development, fiscal ecological compensation will limit the economic development of the area and place the area in a stage of negative correlation between economic development and ecological environment. The reason is that the opportunity cost for local governments to give up development due to the protection of the ecological environment is high. Due to insufficient fiscal ecological compensation, local governments still adopt an “extensive” development model to some extent.

## 5.2. Policy Recommendations

Firstly, transforming the economic development model and delivering high-quality economic development is a high priority. At present, about 78.60% of county-level areas in China are in the “green development trap” stage. In order to get rid of the shackles of the “green development trap” and achieve high-quality economic development, the most fundamental thing is to start from economic development itself and change the existing “extensive” economic development model. The high-quality development of the economy requires that the output of economic activities should be increased under the condition that the input scale of production factors is certain. This means the output efficiency of economic activities should be improved. In this way, the excessive consumption of natural resources by economic development under the “rough and tumble” development model could be transformed, and green economic development could ultimately be achieved.

Secondly, we recommend expanding the coverage of fiscal ecological compensation and deepening the design of the fiscal ecological compensation system. Fiscal ecological compensation can directly affect the governance of the ecological environment. However, according to the current situation in China, the coverage of fiscal ecological compensation is small, which makes it unable to give full play to its due ecological environment governance effect. Therefore, in order to give full play to the ecological environment governance effect of fiscal ecological compensation, the government may consider the following suggestions.

On the one hand, the government should appropriately expand the coverage of fiscal ecological compensation. This means the government should gradually include more counties in the fiscal eco-compensation policy, with an aim to bring to bear the positive impact of fiscal eco-compensation in eco-environmental management on a national scale. On the other hand, the government should continuously optimize the institutional design of financial eco-compensation to provide stable and continuous public funding support for it. Thereby, this is conducive to deepening the ecological governance effect of fiscal ecological compensation and helping to achieve green development.

Thirdly, focus should be placed on systematic evaluation of the policy effects of fiscal ecological compensation. Fiscal ecological compensation policy could significantly improve the ecological environment in areas with low economic development level in the short term. However, in the long term, this will hinder the economic transformation and development of regions with a high level of economic development. Fiscal ecological compensation should implement differentiated fund scale allocation on the basis of fully considering the level of local economic development. In addition to “adjusting measures to local conditions”, fiscal ecological compensation should also be “growing right crop for right time”. Therefore, the government should systematically evaluate the policy effects of fiscal ecological compensation. It should not only pay attention to the improvement role of fiscal ecological compensation in green development in the short and medium term but also pay attention to its impact on local economic development. This avoids disrupting the economic development model in such a way that the negative effects become apparent in the long term, making it difficult to achieve green development at a local level.

There is the possibility and necessity of further research on the research topic of this paper. For example, how to incorporate the spillover effect between regions into the analysis framework will be a very interesting research topic. Solving this problem will be definitely help coordinate the green and sustainable development among jurisdictions. Therefore, the positive impact of fiscal ecological compensation will be further released.

**Author Contributions:** Under supervision by F.Q. and Z.Z.; L.Z. performed empirical model design and data analysis; M.L. performed data processing and data collection; H.C. wrote conclusions and recommendations; F.Q., Y.X. and Z.Z. performed reviewing and editing. Furthermore, H.C. performed paper framework design and empirical conclusions. All authors have read and agreed to the published version of the manuscript.

**Funding:** This work was funded by Shandong Provincial Social Science Planning Project (21DJJJ01).

**Data Availability Statement:** Not applicable.

**Conflicts of Interest:** The authors declare no conflict of interest.

## References

1. Grossman, G.; Krueger, A. *Environmental Impacts of a North American Free Trade Agreement*; National Bureau of Economic Research Working Paper, No. 3914; National Bureau of Economic Research: Cambridge, MA, USA, 1991.
2. Panayotou, T. *Empirical Tests and Policy Analysis of Environmental Degradation at Different Stages of Economic Development*; ILO World Employment Programme Research Working Papers, No. 238; International Labour Organization: Geneva, Switzerland, 1993.
3. Li, Y.; Li, Y.; Zhou, Y.; Shi, Y.; Zhu, X. Investigation of a Coupling Model of Coordination between Urbanization and the Environment. *J. Environ. Manag.* **2012**, *98*, 127–133. [[CrossRef](#)] [[PubMed](#)]
4. Bekun, F. Mitigating Emissions in India: Accounting for the Role of Real Income, Renewable Energy Consumption and Investment in Energy. *Int. J. Energy Econ. Policy* **2022**, *12*, 188–192. [[CrossRef](#)]
5. Grossman, G.; Krueger, A. Economic Growth and the Environment. *Q. J. Econ.* **1995**, *110*, 353–377. [[CrossRef](#)]
6. Cao, H.; Qi, Y.; Chen, J.; Shao, S.; Lin, S. Incentive and Coordination: Ecological Fiscal Transfers’ Effects on Eco-environmental Quality. *Environ. Impact Assess. Rev.* **2021**, *87*, 106518. [[CrossRef](#)]
7. Zhang, Z.; Xu, H.; Shan, S.; Liu, Q.; Lu, Y. Whether the Agricultural Insurance Policy Achieves Green Income Growth-Evidence from the Implementation of China’s Total Cost Insurance Pilot Program. *Int. J. Environ. Res. Public Health* **2022**, *19*, 852. [[CrossRef](#)]
8. Chien, F.; Hsu, C.C.; Ozturk, I.; Sharif, A.; Sadiq, M. The role of renewable energy and urbanization towards greenhouse gas emission in top Asian countries: Evidence from advance panel estimations. *Renew. Energy* **2022**, *186*, 207–216. [[CrossRef](#)]
9. Madhusudan, B.; Michael, H. Institutions and the Environmental Kuznets Curve for Deforestation: A Crosscountry Analysis for Latin America, Africa and Asia. *World Dev.* **2001**, *29*, 995–1010.

10. Caravaggio, N. Economic Growth and the Forest Development Path: A Theoretical Re-assessment of the Environmental Kuznets Curve for Deforestation. *For. Policy Econ.* **2020**, *119*, 102282. [[CrossRef](#)]
11. Saqib, M.; Benhmad, F. Does Ecological Footprint Matter for the Shape of the Environmental Kuznets Curve? Evidence from European Countries. *Environ. Sci. Pollut. Res.* **2021**, *28*, 13634–13648. [[CrossRef](#)]
12. Bekun, F.V.; Adedoyin, F.F.; Lorente, D.B.; Driha, O.M. Designing Policy Framework for Sustainable Development in Next-5 Largest Economies Amidst Energy Consumption and Key Macroeconomic Indicators. *Environ. Sci. Pollut. Res.* **2022**, *29*, 16653–16666. [[CrossRef](#)]
13. Zhou, Q. The Effects of China's Regional Economic Growth on the Environmental Quality: Based on the Empirical Study of Eastern, Central and Western Kuznets Curve. *Stat. Inf. Forum* **2011**, *26*, 45–51. (In Chinese)
14. Farooq, S.; Ozturk, I.; Majeed, M.T.; Akram, R. Globalization and CO2 emissions in the presence of EKC: A global panel data analysis. *Gondwana Res.* **2022**, *106*, 367–378. [[CrossRef](#)]
15. Kang, Y.; Zhao, T.; Yang, Y. Environmental Kuznets Curve for CO2 Emissions in China: A Spatial Panel Data Approach. *Ecol. Indic.* **2016**, *63*, 231–239. [[CrossRef](#)]
16. Rashdan, M.O.J.; Faisal, F.; Tursoy, T.; Pervaiz, R. Investigating the N-shape EKC Using Capture Fisheries as a Biodiversity Indicator: Empirical Evidence from Selected 14 Emerging Countries. *Environ. Sci. Pollut. Res.* **2021**, *28*, 36344–36353. [[CrossRef](#)] [[PubMed](#)]
17. Bagliani, M.; Bravo, G.; Dalmazzone, S. A Consumption-based Approach to Environmental Kuznets Curves Using the Ecological Footprint Indicator. *Ecol. Econ.* **2008**, *65*, 650–661. [[CrossRef](#)]
18. Chowdhury, R.; Moran, E. Turning the Curve: A Critical Review of Kuznets Approaches. *Appl. Geogr.* **2012**, *32*, 3–11. [[CrossRef](#)]
19. Shahbaz, M.; Shafiullah, M.; Khalid, U.; Song, M. A Nonparametric Analysis of Energy Environmental Kuznets Curve in Chinese Provinces. *Energy Econ.* **2020**, *89*, 104814. [[CrossRef](#)]
20. Zhang, H.; Shi, X.; Wang, K.; Xue, J.; Song, L.; Sun, Y. Intertemporal Lifestyle Changes and Carbon Emissions: Evidence from a China Household Survey. *Energy Econ.* **2020**, *86*, 104655. [[CrossRef](#)]
21. Li, X.; Yu, Z.; Salman, A.; Ali, Q.; Hafeez, M.; Aslam, M.S. The Role of Financial Development Indicators in Sustainable Development-Environmental Degradation Nexus. *Environ. Sci. Pollut. Res.* **2021**, *28*, 33707–33718. [[CrossRef](#)]
22. Zhang, Z.; Duan, H.; Shan, S.; Liu, Q.; Geng, W. The Impact of Green Credit on the Green Innovation Level of Heavy-Polluting Enterprises—Evidence from China. *Int. J. Environ. Res. Public Health* **2022**, *19*, 650. [[CrossRef](#)]
23. He, J.; Wang, H. Economic Structure, Development Policy and Environmental Quality: An Empirical Analysis of Environmental Kuznets Curves with Chinese Municipal Data. *Ecol. Econ.* **2012**, *76*, 49–59. [[CrossRef](#)]
24. Panayotou, T. Demystifying the Environmental Kuznets Curve: Turning a black box into a policy tool. *Environ. Dev. Econ.* **1997**, *2*, 465–484. [[CrossRef](#)]
25. Ma, A.; He, Y.; Tang, P. Understanding the Impact of Land Resource Misallocation on Carbon Emissions in China. *Land* **2021**, *10*, 1188. [[CrossRef](#)]
26. Ma, J.; Hu, Q.; Shen, W.; Wei, X. Does the Low-Carbon City Pilot Policy Promote Green Technology Innovation? Based on Green Patent Data of Chinese A-Share Listed Companies. *Int. J. Environ. Res. Public Health* **2021**, *18*, 3695.
27. Busch, J.; Ring, I.; Akullo, M.; Amarjargal, O.; Borie, M.; Cassola, R.S.; Cruz-Trinidad, A.; Droste, N.; Haryanto, J.T.; Kasymov, U.; et al. A global review of ecological fiscal transfers. *Nat. Sustain.* **2021**, *4*, 756–765. [[CrossRef](#)]
28. Ring, I. Integrating Local Ecological Services into Intergovernmental Fiscal Transfers: The Case of the Ecological ICMS in Brazil. *Land Use Policy* **2008**, *25*, 485–497. [[CrossRef](#)]
29. Droste, N.; Ring, I.; Santos, R.; Kettunen, M. Ecological Fiscal Transfers in Europe—Evidence-Based Design Options for a Transnational Scheme. *Ecol. Econ.* **2018**, *147*, 373–382. [[CrossRef](#)]
30. Xu, H.; Zhang, W. Study on the Ecological Protection Effect of the Transfer Payment of National Key Ecological Function Areas: An Empirical Study Based on Shaanxi Data. *China Popul. Resour. Environ.* **2017**, *27*, 141–148. (In Chinese)
31. Qi, Y.; Chen, J.W.; Li, W.X.; Song, P.F. Ecological Environment Management, Economic Development and Public Service Supply-Quasi-Experimental Evidence from the National Key Ecological Functional Areas and Their Transfer Payments. *J. Manag. World* **2019**, *35*, 115–134, 227–228. (In Chinese)
32. Miao, X.; Zhao, Y. Impact of Transfer Payment in Eco-Functional Areas on Eco-Environmental Improvement: Capital Compensation or Institutional Incentives? *Public Financ. Res.* **2019**, *435*, 17–32. (In Chinese)
33. Pan, X.; Xu, L.; Yang, Z.; Yu, B. Payments for ecosystem services in China: Policy, practice, and progress. *J. Clean. Prod.* **2017**, *158*, 200–208. [[CrossRef](#)]
34. Gong, C.; Zhang, J.; Liu, H. Do industrial pollution activities in China respond to ecological fiscal transfers? Evidence from payments to national key ecological function zones. *J. Environ. Plan. Manag.* **2020**, *64*, 1184–1203.
35. Feng, Z.; Tang, Y.; Yang, Y.; Zhang, D. The Relief Degree of Land Surface in China and Its Correlation with Population Distribution. *Acta Geogr. Sin.* **2007**, *62*, 1073–1082. (In Chinese)
36. Wu, J.; Zheng, H.; Zhe, F.; Xie, W.; Song, J. Study on the relationship between urbanization and fine particulate matter (PM2.5) concentration and its implication in China. *J. Clean. Prod.* **2018**, *182*, 872–882.
37. Antweiler, W.; Copeland, B.; Taylor, M. Is Free Trade Good for the Environment? *Am. Econ. Rev.* **2001**, *91*, 877–908. [[CrossRef](#)]
38. Du, L.; Wang, H.; Xu, H. Analysis of spatial-temporal association and Factors Influencing Environmental Pollution Incidents in China. *Environ. Impact Assess. Rev.* **2020**, *82*, 106384. [[CrossRef](#)]

39. Liu, T.; Pan, S.; Hou, H.; Xu, H. Analyzing the Environmental and economic impact of Industrial Transfer Based on an Improved CGE Model: Taking the Beijing–Tianjin–Hebei Region as an Example. *Environ. Impact Assess. Rev.* **2020**, *83*, 106386. [[CrossRef](#)]
40. Postula, M.; Radecka-Moroz, K. Fiscal Policy Instruments in Environmental Protection. *Environ. Impact Assess. Rev.* **2020**, *84*, 106435. [[CrossRef](#)]







Article

# An Innovation Perspective to Explore the Ecology and Social Welfare Efficiencies of Countries

Z-John Liu <sup>1</sup>, Minh-Hieu Le <sup>2</sup> and Wen-Min Lu <sup>3,\*</sup>

<sup>1</sup> Department of Business Administration, Ling Tung University, No. 1, Ling Tung Rd., Taichung 408213, Taiwan; liuzjohn@gmail.com

<sup>2</sup> Faculty of Business Administration, Ton Duc Thang University, No. 19 Nguyen Huu Tho Street, Tan Phong Ward, District 7, Ho Chi Minh City 700000, Vietnam; leminhhieu@tdtu.edu.vn

<sup>3</sup> Department of International Business Administration, Chinese Culture University, No. 55, Hwa-Kang Road, Shilin District, Taipei 114, Taiwan

\* Correspondence: wenmin.lu@gmail.com

**Abstract:** This study aims to measure the ability of 29 countries in producing competitive products and services that fulfill individual needs and improve the level of welfare with less utilization of natural resources. We build a two-stage network production process model to investigate the ecology efficiency and social welfare efficiency of the countries and then further discriminate the efficient countries in post-analysis. The two-stage network directional distance function is applied to assess the efficiencies of countries, and the network-based ranking approach is used to further discriminate the efficient countries following the panel data between the years 2013 and 2016. Results show that Poland and Spain are strongly referenced by other countries in the ecology stage, whereas Bulgaria, the United States, and Sweden are leaders in the social welfare stage. A remarkable observation is an absence of countries' efficiency in both ecology and social welfare efficiencies. Most of the 29 countries have lower efficiency in the social welfare stage than in the ecology stage. This study suggests the strengths and highlights the weaknesses of the countries to help the governments efficiently improve and operate their countries.

**Keywords:** data envelopment analysis; network-based approach; directional distance function; ecology efficiency; social welfare efficiency

**Citation:** Liu, Z.-J.; Le, M.-H.; Lu, W.-M. An Innovation Perspective to Explore the Ecology and Social Welfare Efficiencies of Countries. *Int. J. Environ. Res. Public Health* **2022**, *19*, 5113. <https://doi.org/10.3390/ijerph19095113>

Academic Editors: Francesco Nocera, Roberto Alonso González Lezcano and Rosa Giuseppina Caponetto

Received: 2 April 2022

Accepted: 20 April 2022

Published: 22 April 2022

**Publisher's Note:** MDPI stays neutral with regard to jurisdictional claims in published maps and institutional affiliations.



**Copyright:** © 2022 by the authors. Licensee MDPI, Basel, Switzerland. This article is an open access article distributed under the terms and conditions of the Creative Commons Attribution (CC BY) license (<https://creativecommons.org/licenses/by/4.0/>).

## 1. Introduction

Over the last few decades, we have seen a participatory tendency in both environmental governance and knowledge production [1]. Environmental awareness is an essential component of both public and private decision-making [2]. Capturing the most economic gains while utilizing the fewest resources and resulting in the least damage to the environment is a critical issue for social development [3]. As society becomes ever more developed, units from different levels, that is, human beings, companies, and government, all are starting to pay attention to the importance of the environment and social welfare. Many cities throughout the world have set climate change mitigation targets, but activities to implement these targets have proven ineffective thus far. There may be confusion about who is accountable for acting, how to connect with a diverse variety of stakeholders, how to define goals, and how to measure performance [4]. Recently, Jones, Donaldson [5] vigorously encourage researchers related to management to consider social welfare in their empirical research. The idea of ecology efficiency and social welfare efficiency offers a comprehensive view for policymakers and government to achieve better national performance with the sustainable development goal [3]. The study of ecology efficiency has been previously performed on a national scale [6–9]. Moraes, Wanke [10] have recently studied social welfare and labor efficiency at a regional level. Remarkably, Lefebvre, Perelman [11] assess the overall welfare state performance of the 28 European Union countries based

on eight-year (2005–2012) period data. Although efficiency measurement in the public sector is traditionally long, and there is an immense number of researchers who publish the results of productivity comparisons of countries, it is not easy to identify and correctly evaluate the outcomes [11]. Balancing ecology efficiency and social welfare efficiency can better attain equilibrium and sustainable development [12]. Whereas ecology efficiency refers to the ability of countries to produce goods and services with less effect on the environment and lower levels of natural resources consumption [13], social welfare efficiency refers to poverty reduction and inequality alleviation, and protection against disease, unemployment, and ignorance [11].

Management performance evaluation is a difficult task because it involves multiple inputs and outputs [14]. Designing, evaluating, and monitoring activities, programs, and policies aimed at improving countries' growth at both the national and international levels is a difficult process that necessitates the use of a range of instruments. The requirement to measure economic, social, and environmental dimensions adds to the complexity of progress assessment [15]. Measurements of ecology efficiency and social welfare efficiency have been performed by many previous authors using the ratio approach, stochastic frontier analysis (SFA), or data envelopment analysis (DEA) [3,6,7,11,12,16–19]. Robaina-Alves, Moutinho [16] measured the environmental and resource efficiency of European countries by using data from two separate periods that can perceive the difference in the efficiency level before and after the achievement of the Kyoto protocol in 2005. Robaina-Alves, Moutinho [16] used the stochastic frontier approach in their study. However, DEA seems to be the most widely applied method because of the advantages of processing multiple inputs and outputs. Moreover, the previous studies measured the efficiency of countries without considering and analyzing the intermediate products and linking activities [8,12,13]. Unlike traditional DEA, which treats a system as a "black box," network DEA considers its underlying structure to get more insightful conclusions [20]. Quality development is not the objective pursued by economic development, but an instrument to accomplish sustainable economic and social development [12]. A multi-stage DEA model that links the ecology efficiency and social welfare efficiency to measure the overall efficiency of a country is suggested, as the overall efficiency can be obtained only when all subsequent processes work well [21,22]. For the conventional DEA model, if decision-making units (DMUs) are simultaneously effective, no differentiation exists for efficient leaders [23]. As noted in [16], a suggestion for future research is to uncover factors that are the reasons for efficient or inefficient countries. To further measure and explore the merits of efficient leaders, previous authors have applied different ranking methods including the super-efficiency DEA model [12], cross efficiency evaluation method [24,25], TOPSIS technique [26], rough set approach [27], and network-based ranking approach [28,29]. Especially, Liu, Lu [30] have suggested a network-based ranking approach as a useful and powerful efficiency ranking tool to distinguish the benchmark and highlight the strengths and weaknesses of DMUs (Liu et al. 2009).

Perceived from the current literature review, this study aims to measure the capacity of the countries to produce competitive products and services that satisfy individual needs and improve the level of well-being with less use of natural resources. We explore the ecology efficiency and social welfare efficiency of countries as two subsequent processes of a network production process structure to determine the best nation for benchmarking by applying a directional distance function (DDF) based model for efficiency measurement in two-stage network DEA. Inefficient countries may learn from pioneers to improve their efficiency. In addition, this study combines a network-based ranking approach [28–30] to further distinguish the benchmark countries. At a macro level for the countries, the findings are of great relevance to help policymakers set policies and plan budgets to implement these policies and achieve better performance. In summary, the current study contributes to the related literature review as follows:

First, a novel network production process framework in two-stage network DEA is produced for measuring the ecology efficiency and social welfare efficiency of countries by using DDF based model with consideration of undesirable outputs.

Second, this study is the first to use a network-based approach, which is a unique and powerful method, to further discriminate the benchmark countries in the context of ecology efficiency and social welfare efficiency. The results suggest the strengths and highlight the weaknesses of the countries that help the government efficiently improve and operate their countries.

## 2. Literature Review

Climate change is one of the most difficult issues confronting the globe today, and it is critical to have effective policies in place to handle its consequences [31,32]. Countries in the world are seriously dealing with the challenges and pressures from creating waste and pollution by many firms [9]. The governments need to consider integrating the economic, environmental, and social dimensions in their policy-making process to reach sustainable development, which requires minimizing the environmental concerns and maximizing economic and social indicators [9,33]. Economic efficiency together with environmental efficiency create ecological efficiency [7].

Tena Medialdea, Prieto Ruiz [34] recognized the requirement for ecological studies that address the role of humans as ecosystem members. Ecological efficiency (abbreviated eco-efficiency) has aroused increasing attention from the government, practitioners, and scholars in recent years [3,6,9,16,35]. Schaltegger and Sturm [36] proposed the concept of “eco-efficiency” as “a business link to sustainable development,” and the World Business Council revealed the term in 1992 as the index of economic and environmental efficiency, namely as a management strategy that links financial and environmental performance to create more value with less ecological impact [37]. According to Dyckhoff and Allen [38], the best-known definition of eco-efficiency is from World Business Council for Sustainable Development (WBCSD) “Eco-efficiency is achieved by the delivery of competitively priced goods and services that satisfy human needs and bring the quality of life, while progressively reducing ecological impact and resource intensity throughout the life-cycle to a level at least in line with the Earth’s estimated carrying capacity”. Zhou, Ang [39] provide a non-radial DDF approach to evaluate the energy and CO<sub>2</sub> performance of electricity production by using data in 2005 from 126 countries. In terms of CO<sub>2</sub> performance, OECD countries surpassed non-OECD countries, and OECD countries were equivalent to non-OECD countries in terms of energy performance [39]. Robaina-Alves, Moutinho [16] measured the eco-efficiency of European countries by applying the stochastic frontier approach using data in two separate periods including before (2000–2004) and after (2005–2011) the Kyoto Protocol. The efficiency levels of European countries between two periods before and after the creation of environmental targets are compared in the study [16]. Liu and Liu [40] measured the low carbon economy efficiency with a three-stage model to compare the largest 20 CO<sub>2</sub> emitting nations from 2000 to 2012. First, they applied DEA, using energy consumption, capital stock, and labor force as input factors, and GDP and CO<sub>2</sub> emissions as (undesirable) output factors, to get efficiency for each nation and compute the slack at the input and output, then applied SFA to remove the influence of external environmental variables on the slack. Finally, they recalculated the efficiency using updated input and output components to reflect the government’s ability to establish a low-carbon economy. According to their results, during the studied period, the performance was getting worse in these low carbon economies. Wu, Yin [41] used a two-stage DEA model to assess environmental efficiency for China’s 30 provinces and eight regions, with the production subsystem as the first stage and the pollution treatment subsystem as the second. Interestingly, both of the papers included undesirable outputs in their models. The recently published article that is related to ecology efficiency of Yang and Zhang [6] suggested an extended DEA approach, which incorporates global benchmark technology, DDF, and a bootstrapping method to explore the dynamic trends of Chinese regional eco-efficiency in the 2003–2014 period.

Pais-Magalhães, Moutinho [17] applied the DEA approach to measure the eco-efficiency of 15 European countries by using data in the 2001–2015 period. The countries, including Belgium, Luxembourg, Sweden, the Netherlands, and the United Kingdom, show better ecology performance in comparison with the other European countries.

The connection between ecology and human social welfare have gained visibility in the past few years [5,10,12,17]. It is important to put emphasis on human welfare at the social level and integrate social and economic objectives in the research [42]. However, the context of social welfare is rather complex. The satisfaction of basic and secondary needs experienced by individuals in a community is referred to as social welfare [43]. Social welfare is a normative term that various persons or social groups use to reflect on the ends—the “greater good”—that public policy should pursue to better society’s status quo. Importantly, when it comes to many issues of public policy, people mean different things based on their self- and other-regarding preferences, as well as socio-demographic variables such as education, income, wealth, and influence [44]. As noted in the research work of Hall, Giovannini [45], the ecosystem is equally important as the human well-being system, as the resources and services of human activities are provided by the ecosystem. Nissi and Sarra [46] based their research work on Hall, Giovannini [45], and address the measure of well-being in the context of Italian urban areas using an integrated DEA-entropy approach. Their findings show significant dualism between northern and southern cities, revealing significant variations in many facets of human and ecological well-being. Lefebvre, Perelman [11] provide a definition and a technique to evaluate the efficiency of the public sector. The authors then measure the efficiency of European welfare countries and their development over time by applying the DEA approach. Wang and Feng [12] used super-efficiency DEA and Malmquist index approach to measure the ecology welfare efficiency of China in the 2006–2018 period. Recently, Moraes, Wanke [10] reveal the endogeneity between labor efficiency and social welfare by applying a two-stage network DEA approach using data from 2013 to 2016 in Brazil.

### 3. Research Design

#### 3.1. Two-Stage Production Process of Countries

This article studies the ecology efficiency and social welfare efficiency of 29 countries in the 2013–2016 period. The data were collected from British Petroleum (BP), International Monetary Fund (IMF), Organization for Economic Cooperation and Development (OECD), and World Bank (WB). These databases are commonly used sources for research. Details are shown in Table 1. The selection of input, intermediate, and output variables is based on the related research listed in the social science citation index (SSCI). The initial selection of the variables is explained as follows. For the first stage, ecology efficiency, a nation requires land, capital, and labor and will consume energy to generate gross domestic product (GDP) and undesirable gas emissions (i.e., CO<sub>2</sub>). For the second stage, social welfare efficiency, government expenditure on general public services, economic affairs, health, and education along with the first stage output, GDP, as intermediate to generate outputs including employment population, population age above 65, and tertiary school enrollment population. Figure 1 shows the two different stages to examine the internal structure, namely, ecology efficiency and social welfare efficiency stages. The operational definition of each of the variables is shown in Table 1.

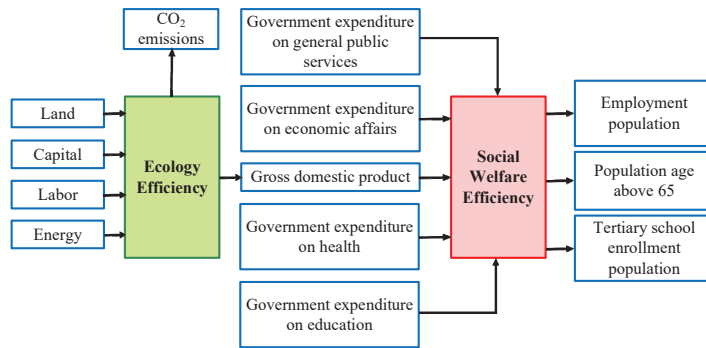


Figure 1. Two-stage production process of countries.

Table 1. Definitions of variables.

Variables	Definitions	Units	Sources
<i>Inputs for stage 1</i>			
Land	Land area is the overall area of a country, excluding inland water bodies, national claims to the continental shelf, and exclusive economic zones. In most situations, significant rivers and lakes are included in the concept of inland water bodies.	Square kilometer	WB
Capital	The cost of new fixed assets plus the net change in inventories.	Million USD	WB and IMF
Labor	All groupings of people aged 15 and up who fit the International Labor Organization’s (ILO) definition of economically active population.	People	WB and IMF
Energy consumption	The total amount of recycled and non-renewable energy consumed.	Million tons	BP
<i>Intermediate</i>			
GDP	A measure of a country’s economic position, the market price of all final goods and services produced in the country during the year.	Million USD	WB and IMF
<i>Output for stage 1</i>			
CO <sub>2</sub> emission (undesirable)	Greenhouse gases emitted by the combustion of fossil fuels.	Million tons	BP
<i>Additional input for stage 2</i>			
Government expenditure on general public services	Government spending on executive and legislative bodies, financial and fiscal affairs, external affairs, public debt transactions, general services, foreign economic aid, R&D, basic research, general public services, and transfers of a general nature between different levels of government.	Million USD	IMF
Government expenditure on economic affairs	Government spending covers general economic, commercial, and labor affairs, agriculture, forestry, fishing and hunting, fuel and energy, mining, manufacturing and construction, transportation, communication, other industries, R&D economic affairs, and economic affairs.	Million USD	IMF
Government expenditure on health	Medical products, appliances, and equipment, outpatient services, hospital services, public health services, R&D health, and health are all examples of government spending.	Million USD	IMF
Government expenditure on education	Total general (local, regional, and national) government education spending (current, capital, and transfers), expressed as a percentage of GDP. It includes government spending funded by transfers from international sources.	Million USD	IMF

Table 1. Cont.

Variables	Definitions	Units	Sources
<i>Outputs for stage 2</i>			
Employment population	The employment to population ratio denotes the percentage of a country’s population that is employed. Employment is defined as persons of working age who were engaged in any activity to produce goods or provide services for pay or profit during a short reference period, whether at work during the reference period (i.e., who worked in a job for at least one hour) or not at work due to temporary absence from a job or working-time arrangements. Working-age people are generally considered to be those aged 15 and up.	People	WB
Population age above 65	A country’s population aged 65 and up. The population is calculated using the de facto definition, which includes all residents regardless of legal status or citizenship.	People	WB
Tertiary school enrollment population	Total population of higher school students, regardless of age.	People	OECD

Note: WB is World Bank; OECD is Organization for Economic Co-operation and Development; IMF is International Monetary Fund; BP is British Petroleum.

Table 2 present the descriptive statistics for the variables of 29 countries. The variables have a positive connection (Table 3), which followed the isotonic condition employed to determine the efficient level. Table 2 indicates that most of the variables have a non-normal distribution (Kolmogorov-Smirnov test significant). This finding shows that using the DEA technique is the right option because the method requires no assumption of normality for data [47].

Table 2. Descriptive statistics of input/intermediate/output factors for DEA analysis.

Factors	Units	Mean	Minimum	Maximum	Std.Dev.	K-S Test <sup>a</sup>
Land	Square kilometer	827,475.00	20,141.10	9,388,211.00	2,345,481.00	$p < 0.01$
Capital	Million USD	423,543.00	6289.40	4,866,509.00	1,077,108.00	$p < 0.01$
Labor	People	42,108,745.00	684,412.80	786,639,089.00	146,348,397.00	$p < 0.01$
Energy	Million tons	152.00	2.90	1709.00	406.00	$p < 0.01$
GDP	Million USD	1,622,478.00	24,316.70	17,707,452.00	3,713,023.00	$p < 0.01$
CO <sub>2</sub> emission	Million tons	581.00	13.30	7864.00	1698.00	$p < 0.01$
Government expenditure on general public services	Million USD	84,903.00	975.40	1,016,089.00	193,448.00	$p < 0.01$
Government expenditure on economic affairs	Million USD	76,921.00	1127.90	862,939.00	187,640.00	$p < 0.01$
Government expenditure on health	Million USD	106,239.00	1272.90	1,594,631.00	295,824.00	$p < 0.01$
Government expenditure on education	Million USD	82,605.00	1439.80	1,088,363.00	209,487.00	$p < 0.01$
Employment population	People	48,204,755.00	755,646.10	911,642,187.00	169,726,118.00	$p < 0.01$
Population age above 65	People	9,559,414.00	246,012.60	130,420,422.00	24,963,669.00	$p < 0.01$
Tertiary school enrollment population	People	2,784,949.00	51,473.60	37,472,107.00	7,595,033.00	$p < 0.01$

Note: <sup>a</sup> Kolmogorov–Smirnov test.

Table 3. Correlation coefficients for input/intermediate/output factors.

Factors	X1	X2	X3	X4	Z1	UEY1	EX1	EX2	EX3	EX4	Y1	Y2	Y3
X1	1.000												
X2	0.979 **	1.000											
X3	0.826 **	0.900 **	1.000										
X4	0.993 **	0.994 **	0.858 **	1.000									

Table 3. Cont.

Factors	X1	X2	X3	X4	Z1	UEY1	EX1	EX2	EX3	EX4	Y1	Y2	Y3
Z1	0.938 **	0.907 **	0.635 **	0.937 **	1.000								
UEY1	0.977 **	0.996 **	0.921 **	0.990 **	0.879 **	1.000							
EX1	0.813 **	0.753 **	0.395 *	0.804 **	0.959 **	0.712 **	1.000						
EX2	0.972 **	0.999 **	0.908 **	0.990 **	0.896 **	0.993 **	0.740 **	1.000					
EX3	0.741 **	0.657 **	0.264	0.719 **	0.912 **	0.614 **	0.986 **	0.639 **	1.000				
EX4	0.874 **	0.812 **	0.479 **	0.859 **	0.980 **	0.779 **	0.989 **	0.798 **	0.972 **	1.000			
Y1	0.813 **	0.889 **	0.999 **	0.846 **	0.615 **	0.912 **	0.372 *	0.898 **	0.240	0.457 *	1.000		
Y2	0.885 **	0.952 **	0.985 **	0.919 **	0.744 **	0.962 **	0.534 **	0.959 **	0.406 *	0.601 **	0.980 **	1.000	
Y3	0.945 **	0.978 **	0.956 **	0.961 **	0.815 **	0.986 **	0.624 **	0.978 **	0.513 **	0.696 **	0.948 **	0.980 **	1.000

Notes: \*\*, \* correlations are significant at level 0.05, 0.01, respectively. X1 is land; X2 is capital; X3 is labor; X4 is energy; Z1 is GDP; UEY1 is CO<sub>2</sub> emission; EX1 is government expenditure on general public services; EX2 is government expenditure on economic affairs; EX3 is government expenditure on health; EX4 is government expenditure on education; Y1 is employment population; Y2 is population age above 65; Y3 is tertiary school enrollment population.

### 3.2. Research Method

This article uses the multivariate evaluation approach that simultaneously measures various dimensions of countries' efficiency to overcome the single-dimension shortcoming of the traditional approach. This article uses the two-stage network DDF in evaluating the internal network production structures to understand the countries' ecology and social welfare efficiencies [13,35]. To examine the merits of each country under different circumstances, this article incorporates multiple DEA specifications and a social network approach to determine the strengths and weaknesses of the countries [30]. The linear programming issues are shown below.

Let us consider a set of  $n$  countries ( $k = 1, \dots, m$ ). For a decision-making unit  $k$ ,  $m$  inputs  $x_{ak}$  ( $a = 1, \dots, m$ ) are used to produce  $z_{bk}$  ( $b = 1, \dots, l$ ), intermediate outputs in the first stage, and then  $z_{bk}$  plus a new set of factors  $z_{ck}$  ( $c = 1, \dots, g$ ) produce  $h$  outputs in the second stage ( $y_{dk}$ ,  $d = 1, \dots, h$ ).

Assume that the set of production possibilities for both inputs and outcomes is convex. The DDF two-stage network is defined as follows:

$$DDF(x, z, y; g_x, g_y) = \text{Max} \{ \delta + \beta : (x - \delta g_x, z, y + \beta g_y) \in T(x, z, y) \}. \tag{1}$$

The following is a definition of the technology set:

$T(x, z, y): x_{ak}$  can produce the intermediate outputs  $z_{bk}$  in the first process;  $z_{bk}$  and  $z_{ck}$  can produce the final  $y_{dk}$  in the second process.

According to Fried, Lovell [48], the direction vector  $g = (g_x, g_y)$  should be chosen by the researcher before evaluating the DDF. In this paper, we consider the direction to be  $g = (g_x = x, g_y = y)$ . As a result, the following linear programs can describe the inefficiency measure of the target country of the technology set under convex constraints:

$$\begin{aligned} \overline{DDF} &= \text{Max } \delta_o + \beta_o \\ \sum_{k=1}^n \lambda_{ko} x_{ak} &\leq x_{ao} - \delta_o g_{aox}, \quad a = 1, \dots, m, \\ \sum_{k=1}^n \lambda_{ko} z_{bk} &\geq z_{bo}, \quad b = 1, \dots, l, \\ \sum_{k=1}^n \mu_{ko} z_{bk} &\leq z_{bo}, \quad b = 1, \dots, l, \\ \sum_{k=1}^n \mu_{ko} z_{ck} &\leq z_{co}, \quad c = 1, \dots, g, \\ \sum_{k=1}^n \mu_{ko} y_{dk} &\geq y_{do} + \beta_o g_{do}, \quad d = 1, \dots, h, \\ \sum_{k=1}^n \lambda_{ko} &= 1, \\ \sum_{k=1}^n \mu_{ko} &= 1, \\ \lambda_k, \mu_k &\geq 0, \end{aligned} \tag{2}$$

where  $\lambda_{ko}$  and  $\mu_{ko}$  are the intensity variables corresponding to the first and second processes for a given country. The best solution  $\lambda_{ko}^*$  for an observed country demonstrates if a country



$k$  serves as a role model for the observed country in the first stage. The optimal solution  $\mu_{ko}^*$  is the same definition in the second stage. As a result, the first stage's production efficiency,  $EE_o = 1 - \delta_o$ , which is ecology efficiency. Ecology efficiency ranges between 0 and 1. The efficiency of the second stage in these sets is defined as  $SE_o = 1/(1 + \beta_o)$ , which is the social welfare efficiency. The social welfare efficiency is between 0 and 1. These variables indicate that the target country is efficient in the first and second stages if the  $EE_o$  and  $SE_o$  are equal to unity.

The concept of the reference-share measure is introduced below. With high probability, many DEA specifications are used in the efficiency evaluation. Using a variety of DEA specifications allows for examining the merits of each DMU under different situations, thus laying the foundation for further differentiation. For any DEA specification  $t$ , the linear programming problem (2) is represented as follows:

$$\begin{aligned}
 \overrightarrow{DDF}^t &= \text{Max } \delta_o^t + \beta_o^t \\
 \sum_{k=1}^n \lambda_{ko}^t x_{ak}^t &\leq x_{ao} - \delta_o^t g_{aox}, \quad a = 1, \dots, m, \\
 \sum_{k=1}^n \lambda_{ko}^t z_{bk}^t &\geq z_{bo}, \quad b = 1, \dots, l, \\
 \sum_{k=1}^n \mu_{ko}^t z_{bk}^t &\leq z_{bo}, \quad b = 1, \dots, l, \\
 \sum_{k=1}^n \mu_{ko}^t z_{ck}^t &\leq z_{co}, \quad c = 1, \dots, g, \\
 \sum_{k=1}^n \mu_{ko}^t y_{dk}^t &\geq y_{do} + \beta_o^t g_{doy}, \quad d = 1, \dots, h, \\
 \sum_{k=1}^n \lambda_{ko}^t &= 1, \\
 \sum_{k=1}^n \mu_{ko}^t &= 1, \\
 \lambda_k^t, \mu_k^t &\geq 0,
 \end{aligned} \tag{3}$$

Each specification  $t$  can be thought of as a competition game round. As a result, the initial DEA issue has been expanded from a one-round competition to a multi-round competition as a result of this action. Because the efficiency score is tied in the first round of this competition, extra game rounds may be requested to allow each DMU to demonstrate its worth in a variety of conditions. The champion is then determined based on the cumulative results. The efficiency calculation accounts for all conceivable input/output combinations.

The values of  $\lambda_{ko}^{t*}$  and  $\mu_{ko}^{t*}$  denote the optimal solution in Model 3. In the DEA setting, small efficient countries with lower input/output levels are likely to achieve higher  $\lambda_{ko}^{t*}$  and  $\mu_{ko}^{t*}$  than large efficient countries. Normalizing the  $\lambda_{ko}^{t*}$  and  $\mu_{ko}^{t*}$  could remove the effect of country size and render the approach applicable to both the constant and variable returns to scale models.

Let  $E_t$  be the index set for the observed country's reference set. Under DEA specification  $t$ , the contribution of the  $k$ th country's  $a$ th input to the  $o$ th country in the reference set is specified as

$$Ix_{ako}^t = \lambda_{ko}^{t*} x_{ak}^t / \sum_{k \in E_t} \lambda_{ko}^{t*} x_{ak}^t, \quad 0 < Ix_{ako}^t \leq 1, \quad a = 1, \dots, m. \tag{4}$$

Similarly, with DEA specification  $t$ , the contribution of the  $k$ th country's  $b$ th intermediate to the  $o$ th country in the reference set is defined as

$$MIz_{bko}^t = \frac{1}{2} \left( \lambda_{ko}^{t*} z_{bk}^t / \sum_{k \in E_t} \lambda_{ko}^{t*} z_{bk}^t \right) + \frac{1}{2} \left( \mu_{ko}^{t*} z_{bk}^t / \sum_{k \in E_t} \mu_{ko}^{t*} z_{bk}^t \right), \quad 0 < MIz_{bko}^t \leq 1, \quad b = 1, \dots, l. \tag{5}$$

Under DEA specification  $t$ , the contribution of the  $k$ th country's  $c$ th additional input to the  $o$ th country in the reference set is specified as

$$Iz_{cko}^t = \mu_{ko}^{t*} z_{ck}^t / \sum_{k \in E_t} \mu_{ko}^{t*} z_{ck}^t, \quad 0 < Iz_{cko}^t \leq 1, \quad c = 1, \dots, g. \tag{6}$$

Under DEA specification  $t$ , the contribution of the  $k$ th country's  $d$ th output to the  $o$ th country in the reference set is defined as

$$Oy_{dko}^t = \mu_{ko}^{t*} y_{dk}^t / \sum_{k \in E_t} \mu_{ko}^{t*} y_{dk}^t, 0 < Oy_{dko}^t \leq 1, d = 1, \dots, h. \tag{7}$$

The total of the input and output components of a normalized reference weight is obtained by averaging them out.

$$IMO1_{ko}^t = \frac{1}{m+l} \left[ \sum_{a=1}^m Ix_{ako}^t + \sum_{b=1}^l MIz_{bko}^t \right] \tag{8}$$

$$IMO2_{ko}^t = \frac{1}{l+g+h} \left[ \sum_{b=1}^l MIz_{bko}^t + \sum_{c=1}^g Iz_{cko}^t + \sum_{d=1}^h Oy_{dko}^t \right] \tag{9}$$

$$A1 = \left[ \sum_{t=1}^T IMO1_{ko}^t \right] \text{ and } A2 = \left[ \sum_{t=1}^T IMO2_{ko}^t \right] \tag{10}$$

The value  $T = (2^m - 1)(2^l - 1)(2^g - 1)(2^h - 1)$  is the number of combinations tested by the DEA model, whereas  $A1$  and  $A2$  are square matrices of size  $n \times n$ . Matrix elements  $A1$  and  $A2$  represent the combined power of the  $o$ th unit supporting the  $k$ th unit or the cumulative effect of the  $o$ th unit endorsing the  $k$ th unit.

We observe that  $A1$  and  $A2$  can be viewed as adjacency matrices of a directed and weighted network, where nodes are DMUs, and links express the amount of endorsement from one unit to the other. Bonacich and Lloyd [49] proposed alpha-centrality, an eigenvector-like metric, to distinguish the significance of nodes in a directed network. The significance of each node is embedded in the following formulation's solutions  $I1$  and  $I2$ :

$$I1 = \alpha A1 \cdot I1 + e \text{ and } I2 = \alpha A2 \cdot I2 + e \tag{11}$$

where  $e$  is a unit vector and  $\alpha$  is an arbitrary constant indicating the relevance of endogenous versus exogenous influences. Each vector element,  $I1_k$  and  $I2_k$ , provides the scores used to distinguish the efficient units in the first and second stages, respectively.

The efficient units for each I/M/O factor can also be differentiated. When Formula (10) is rearranged, the result is

$$A1 = \frac{1}{m+l} \left[ \sum_{a=1}^m A1I_a + \sum_{b=1}^l A1M_b \right] \tag{12}$$

$$A2 = \frac{1}{l+g+h} \left[ \sum_{b=1}^l A2M_b + \sum_{c=1}^g A2I_c + \sum_{d=1}^h A2O_d \right] \tag{13}$$

$$\begin{aligned} A1I_a &= \left[ \sum_{t=1}^T Ix_{ako}^t \right], a = 1, \dots, m; \\ A1M_b &= \left[ \sum_{t=1}^T MIz_{bko}^t \right], b = 1, \dots, l; \\ A2M_b &= \left[ \sum_{t=1}^T MIz_{bko}^t \right], b = 1, \dots, l; \\ A2I_c &= \left[ \sum_{t=1}^T Iz_{cko}^t \right], c = 1, \dots, g; \\ A2O_d &= \left[ \sum_{t=1}^T Oy_{dko}^t \right], d = 1, \dots, h. \end{aligned} \tag{14}$$

It is worth noting that  $A1I_a, A1M_b, A2I_c, A2O_d$  are square matrices of order  $n$ . Given that  $A1M_b$  and  $A2M_b$  are the aggregated reference matrices for the same intermediate factors in the first and second stages, the actual contribution of each intermediate component should be averaged. One can define

$$AM_b = \frac{1}{2}(A1M_b + A2M_b) = \left[ \sum_{t=1}^T MIz_{bko}^t \right]. \tag{15}$$

The matrices  $A1I_a, AM_b, A2I_c, A2O_d$  are thus the reference matrices for each I/M/O. Each matrix member indicates the aggregated endorsement of an observed unit to the  $k$ th unit in the reference set via a specific I/M/O factor. When the alpha centrality notion is applied to these matrices, the following results are obtained:

$$\begin{aligned} I1I_a &= \alpha A1I_a \cdot I1I_a + e \\ IM_b &= \alpha AM_b \cdot IM_b + e \\ I2I_c &= \alpha A2I_c \cdot I2I_c + e \\ I2O_d &= \alpha A2O_d \cdot I2O_d + e \end{aligned} \tag{16}$$

where the column vectors  $I1I_a, IM_b, I2I_c$  and  $I2O_d$  hold the centrality scores of each unit since each I/M/O factor is regarded as the standard for that specific factor among all units.

Internally, the unit strength of these I/M/O factors can also be compared. The sum of each row element of the matrices  $A1I_a, AM_b, A2I_c, A2O_d$  indicates the overall endorsement a unit obtains from its peers as a result of the contribution of a specific I/M/O factor. As a result, the endorsement from all other units' overall specifications to an efficient unit  $k$  via a specified I/M/O factor  $w$  equals

$$IMOS_k^w = \begin{cases} \sum_{o=1}^n \sum_{t=1}^T Ix_{ako}^t, & a = 1, \dots, m \text{ for } w = 1, \dots, m, \text{ and} \\ \sum_{o=1}^n \sum_{t=1}^T MIz_{bko}^t, & b = 1, \dots, l \text{ for } w = m + 1, \dots, m + l, \text{ and} \\ \sum_{o=1}^n \sum_{t=1}^T Iz_{cko}^t, & c = 1, \dots, g \text{ for } w = m + l + 1, \dots, m + l + g, \text{ and} \\ \sum_{o=1}^n \sum_{t=1}^w Oy_{dko}^t, & d = 1, \dots, h \text{ for } w = m + l + g + 1, \dots, m + l + g + h. \end{cases} \tag{17}$$

where  $w$  is a combined I/M/O factor index in this case. For an efficient unit  $k$ , the higher the  $IMOS_k^w$  larger the contribution of the  $w$ th factor to the unit's efficiency. To simplify comparison, the relative intensity of an I/M/O factor  $w$  defined in formula (17) is magnified using the formula:

$$IMO_k^w = \frac{(IMOS_k^w)^2}{\sum_{w=1}^{m+l+g+h} (IMOS_k^w)^2}. \tag{18}$$

As a result,  $IMO_k^w$  denotes the relative strength of an I/M/O factor  $w$  among all factors within an efficient unit  $k$ .

#### 4. Empirical Analysis

##### 4.1. Ecology Efficiency and Social Welfare Efficiency for Countries

Initially, this study conducts a preliminary analysis of the ecology efficiency and social welfare efficiency for countries by running on full specifications including inputs/intermediate/undesirable output/additional inputs/outputs. Table 4 shows the efficiencies of each country at each stage.

**Table 4.** Ecology efficiency and social welfare efficiency for each country.

Countries	Ecology Efficiency	Ranking	Social Welfare Efficiency	Ranking
Austria	0.8491	(15)	0.2003	(27)
Belgium	0.9716	(9)	0.1926	(28)
Bulgaria	0.736	(22)	1	(1)
China	0.7932	(20)	0.6329	(8)
Croatia	0.6216	(26)	0.4554	(14)
Czech Republic	1	(1)	0.2758	(22)
Denmark	0.6241	(25)	0.6452	(7)
Estonia	0.9097	(13)	0.2443	(23)
Finland	0.8522	(14)	0.2109	(25)
France	0.9263	(10)	0.4044	(16)
Germany	0.7105	(23)	0.5329	(11)
Hungary	0.9235	(11)	0.2875	(21)
Ireland	0.9983	(7)	0.5633	(9)
Israel	0.9828	(8)	0.3779	(18)
Italy	0.8019	(19)	1	(1)
Lithuania	0.8026	(18)	0.5199	(12)
New Zealand	1	(1)	0.1426	(29)
Norway	0.7708	(21)	0.7555	(6)
Poland	1	(1)	0.5056	(13)
Portugal	0.6168	(27)	0.9165	(5)
Romania	0.8332	(17)	0.3724	(19)
Slovak	0.835	(16)	0.3994	(17)
Slovenia	0.9191	(12)	0.2438	(24)
Spain	1	(1)	0.2046	(26)
Sweden	0.573	(28)	1	(1)
Switzerland	1	(1)	0.421	(15)
Turkey	1	(1)	0.3035	(20)
United Kingdom	0.7053	(24)	0.5448	(10)
United States	0.3555	(29)	1	(1)
Average	0.8315		0.4949	
Total efficient countries	6		4	

There is a total of six efficient countries at the ecology efficiency stage (Czech Republic, New Zealand, Poland, Spain, Switzerland, and Turkey) and four at the social welfare efficiency stage (Bulgaria, Italy, Sweden, United States). No country is efficient at both stages, and 19 countries are inefficient in two stages. As shown in Table 4, the average values of efficiency scores are 0.8315 and 0.4949 for ecology efficiency and social welfare efficiency, respectively, which emphasize a potential improvement of the social welfare efficiency for the countries. These preliminary results present an overview of the efficiencies of each country, but further differentiation is required to determine the best performer.

4.2. Analysis of Benchmarking of Production Factors

Next, this study used a network-based ranking approach to discover the most efficient country in each stage and each factor (inputs, intermediate, undesirable output, additional inputs, and outputs). The strengths of each country are also confirmed. Figures 2–4 show the analysis results are aggregated from a total of 1575 DEA runs. In Figure 2, the ecology efficiency of countries is visibly presented by the accrued reference networks. The endorsing connections are identified by the thickness and the darkness of the lines in the figure. Typically, if a country delegated by a node in the figure has more lines approach, its ranking is higher. Poland and Spain (Bulgaria, United States, and Sweden) are strongly referenced by other countries in the ecology stage (social welfare stage) (Figures 2 and 3). Our findings are different from the findings of [16], which considers the ecology efficiency in two distinct periods (2000–2004 and 2005–2011). However, the switch in the position of countries in terms of ecology efficiency due to the considered period in our study is

different from the study of Robaina-Alves, Moutinho [16]. Our study is conducted using data when Kyoto Protocol was adopted for a second commitment period, whereas the study of Robaina-Alves, Moutinho [16] was performed using data in periods of the first commitment (2005–2011) and before Kyoto Protocol entered into force (2000–2004). These findings show that there is an evolution of the ecology efficiency ranking of some European countries among periods. One example of such awareness is the adoption of the Kyoto Protocol. Kutlu [50] demonstrated that the Kyoto Protocol’s adoption and implementation aided the environment by reducing GHG emissions relative to (real) GDP. Therefore, it can be explained that the Kyoto Protocol helped in improving the ecology efficiency of the European countries [50]. Similarly, top benchmarks for overall efficiency are assigned to Bulgaria, the United States, and Sweden (Figure 4).

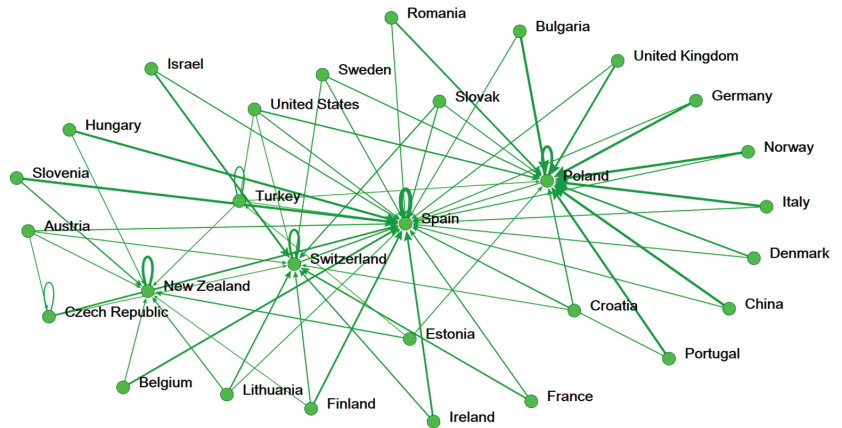


Figure 2. Reference network of 29 nations in the ecology efficiency stage.

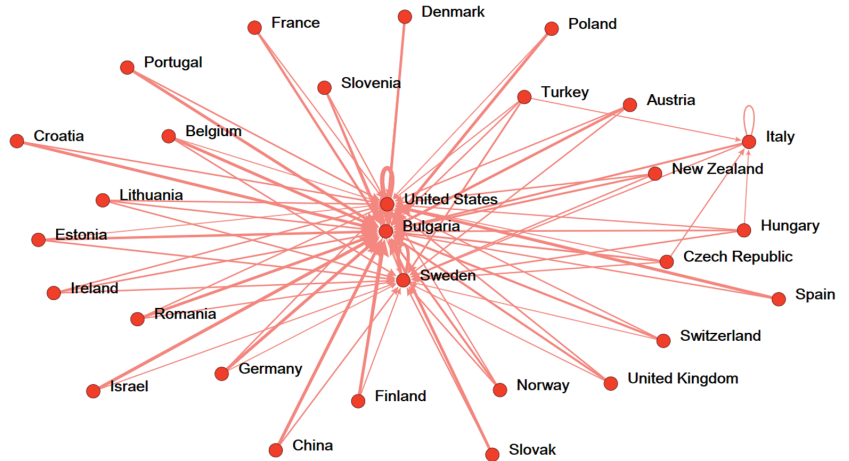


Figure 3. Reference network of 29 nations in social welfare efficiency.

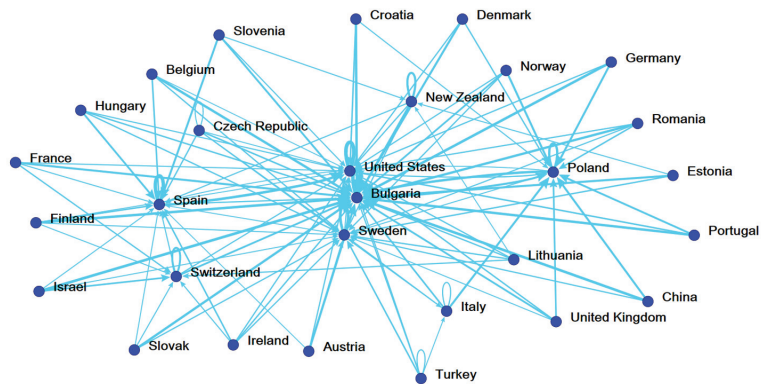


Figure 4. Reference network of 29 nations in overall efficiency.

Furthermore, Tables 5–8 reveal the calculated strength indices of input/undesirable output/intermediate/additional inputs/output factors for each country. In terms of input (land, capital, labor, and energy) and undesirable (CO<sub>2</sub>) factors at the ecology stage, 14 countries in Europe (Bulgaria, Croatia, Czech Republic, Estonia, Finland, Hungary, Ireland, Israel, Lithuania, New Zealand, Romania, Slovenia, Spain, Slovak Republic, and Austria) and Israel are in the top list (Tables 5 and 6).

Table 5. Rankings of a nation’s sensitivity to each input factor at the ecology stage.

Input Factors							
Land		Capital		Labor		Energy	
Country	Eigenvector Centrality	Country	Eigenvector Centrality	Country	Eigenvector Centrality	Country	Eigenvector Centrality
Bulgaria	0.223316 (1)	Bulgaria	0.223575 (1)	Bulgaria	0.223195 (1)	Bulgaria	0.223435 (1)
Croatia	0.223316 (1)	Croatia	0.223575 (1)	Croatia	0.223195 (1)	Croatia	0.223435 (1)
Czech Republic	0.223316 (1)	Czech Republic	0.223575 (1)	Czech Republic	0.223195 (1)	Czech Republic	0.223435 (1)
Estonia	0.223316 (1)	Estonia	0.223575 (1)	Estonia	0.223195 (1)	Estonia	0.223435 (1)
Finland	0.223316 (1)	Finland	0.223575 (1)	Finland	0.223195 (1)	Finland	0.223435 (1)
Hungary	0.223316 (1)	Hungary	0.223575 (1)	Hungary	0.223195 (1)	Hungary	0.223435 (1)
Ireland	0.223316 (1)	Ireland	0.223575 (1)	Ireland	0.223195 (1)	Ireland	0.223435 (1)
Israel	0.223316 (1)	Israel	0.223575 (1)	Israel	0.223195 (1)	Israel	0.223435 (1)
Lithuania	0.223316 (1)	Lithuania	0.223575 (1)	Lithuania	0.223195 (1)	Lithuania	0.223435 (1)
New Zealand	0.223316 (1)	New Zealand	0.223575 (1)	New Zealand	0.223195 (1)	New Zealand	0.223435 (1)
Romania	0.223316 (1)	Romania	0.223575 (1)	Romania	0.223195 (1)	Romania	0.223435 (1)
Slovenia	0.223316 (1)	Slovenia	0.223575 (1)	Slovenia	0.223195 (1)	Slovenia	0.223435 (1)
Spain	0.223316 (1)	Spain	0.223575 (1)	Spain	0.223195 (1)	Spain	0.223435 (1)
Slovak Republic	0.223316 (1)	Slovak Republic	0.223575 (1)	Slovak Republic	0.223195 (1)	Slovak Republic	0.223435 (1)
Austria	0.205360 (15)	Austria	0.205614 (15)	Austria	0.205250 (15)	Austria	0.205524 (15)

Notes: As there are 29 nations in our sample, this table presents only the top 15 nations. Numbers in parentheses are nations’ ranks for input factors at the ecology stage.

In terms of energy and CO<sub>2</sub> factors, our study confirms the results of the authors [39] in which China and the United States are found to have low performance. In their research [39], the authors explained the relatively poor electric power generation efficiency and the coal-dominated fuel input in electric power generation of these large countries [39]. Our results show that the inefficient countries in energy and CO<sub>2</sub> factors have enormous potential to decrease consumption of energy and CO<sub>2</sub> emission. Finland, New Zealand, and Spain are the best performers in the intermediate factor of GDP (Table 6).

**Table 6.** Rankings of a nation’s sensitivity to each intermediate/undesirable output factor at the ecology stage.

Intermediate			Undesirable Output		
GDP			CO <sub>2</sub> Emissions		
Country	Eigenvector Centrality		Country	Eigenvector Centrality	
Finland	0.257666	(1)	Bulgaria	0.223299	(1)
New Zealand	0.257666	(1)	Croatia	0.223299	(1)
Spain	0.257666	(1)	Czech Republic	0.223299	(1)
Romania	0.254200	(4)	Estonia	0.223299	(1)
Estonia	0.250589	(5)	Finland	0.223299	(1)
Czech Republic	0.248091	(6)	Hungary	0.223299	(1)
Slovak Republic	0.247188	(7)	Ireland	0.223299	(1)
Ireland	0.247185	(8)	Israel	0.223299	(1)
Hungary	0.236101	(9)	Lithuania	0.223299	(1)
Austria	0.234099	(10)	New Zealand	0.223299	(1)
Belgium	0.229228	(11)	Romania	0.223299	(1)
Slovenia	0.219672	(12)	Slovenia	0.223299	(1)
Germany	0.198977	(13)	Spain	0.223299	(1)
Poland	0.196221	(14)	Slovak Republic	0.223299	(1)
Sweden	0.189684	(15)	Austria	0.205371	(15)

Notes: As there are 29 nations in our sample, this table presents only the top 15 nations. Numbers in parentheses are nations’ ranks for intermediate/undesirable output factors at the ecology stage.

**Table 7.** Rankings of a nation’s sensitivity to each additional input factor at the social welfare stage.

Input Factors											
Government Expenditure on General Public Services			Government Expenditure on Economic Affairs			Government Expenditure on Health		Government Expenditure on Education			
Country	Eigenvector Centrality		Country	Eigenvector Centrality		Country	Eigenvector Centrality	Country	Eigenvector Centrality		
Belgium	0.218450	(1)	Belgium	0.218398	(1)	Belgium	0.218170	(1)	Belgium	0.218552	(1)
Finland	0.218450	(1)	Finland	0.218398	(1)	Finland	0.218170	(1)	Finland	0.218552	(1)
France	0.218450	(1)	France	0.218398	(1)	France	0.218170	(1)	France	0.218552	(1)
New Zealand	0.218450	(1)	New Zealand	0.218398	(1)	New Zealand	0.218170	(1)	New Zealand	0.218552	(1)
Norway	0.218450	(1)	Norway	0.218398	(1)	Norway	0.218170	(1)	Norway	0.218552	(1)
Poland	0.218450	(1)	Poland	0.218398	(1)	Poland	0.218170	(1)	Poland	0.218552	(1)
Spain	0.218450	(1)	Spain	0.218398	(1)	Spain	0.218170	(1)	Spain	0.218552	(1)
Sweden	0.218450	(1)	Sweden	0.218398	(1)	Sweden	0.218170	(1)	Sweden	0.218552	(1)
United Kingdom	0.218450	(1)	United Kingdom	0.218398	(1)	United Kingdom	0.218170	(1)	United Kingdom	0.218552	(1)
Romania	0.216727	(10)	Romania	0.215053	(10)	Romania	0.217085	(10)	Romania	0.216275	(10)
Switzerland	0.216690	(11)	Switzerland	0.215020	(11)	Switzerland	0.217062	(11)	Switzerland	0.216250	(11)
Slovak Republic	0.210317	(12)	Slovak Republic	0.210327	(12)	Slovak Republic	0.210022	(12)	Slovak Republic	0.210432	(12)
Ireland	0.210312	(13)	Ireland	0.210324	(13)	Ireland	0.210017	(13)	Ireland	0.210430	(13)
Austria	0.209197	(14)	Austria	0.209141	(14)	Austria	0.208929	(14)	Austria	0.209291	(14)
Estonia	0.200968	(15)	Estonia	0.201529	(15)	Estonia	0.200584	(15)	Estonia	0.200968	(15)

Notes: As there are 29 nations in our sample, this table presents only the top 15 nations. Numbers in parentheses are nations’ ranks for additional input factors at the social welfare stage.

**Table 8.** Rankings of a nation’s sensitivity to each output factor at the social welfare stage.

Output Factors								
Employment Population			Population Age above 65			Tertiary School Enrollment Population		
Country	Eigenvector Centrality		Country	Eigenvector Centrality		Country	Eigenvector Centrality	
Belgium	0.218366	(1)	Belgium	0.217690	(1)	Belgium	0.218349	(1)
Finland	0.218366	(1)	Finland	0.217690	(1)	Finland	0.218349	(1)
France	0.218366	(1)	France	0.217690	(1)	France	0.218349	(1)
New Zealand	0.218366	(1)	New Zealand	0.217690	(1)	New Zealand	0.218349	(1)

Table 8. Cont.

Output Factors					
Employment Population		Population Age above 65		Tertiary School Enrollment Population	
Country	Eigenvector Centrality	Country	Eigenvector Centrality	Country	Eigenvector Centrality
Norway	0.218366 (1)	Norway	0.217690 (1)	Norway	0.218349 (1)
Poland	0.218366 (1)	Poland	0.217690 (1)	Poland	0.218349 (1)
Spain	0.218366 (1)	Spain	0.217690 (1)	Spain	0.218349 (1)
Sweden	0.218366 (1)	Sweden	0.217690 (1)	Sweden	0.218349 (1)
United Kingdom	0.218366 (1)	United Kingdom	0.217690 (1)	United Kingdom	0.218349 (1)
Romania	0.214503 (10)	Romania	0.215933 (10)	Romania	0.216508 (10)
Switzerland	0.214475 (11)	Switzerland	0.215902 (11)	Switzerland	0.216489 (11)
Slovak Republic	0.210314 (12)	Slovak Republic	0.209581 (12)	Slovak Republic	0.210222 (12)
Ireland	0.210312 (13)	Ireland	0.209579 (13)	Ireland	0.210220 (13)
Austria	0.209108 (14)	Austria	0.208465 (14)	Austria	0.209100 (14)
Estonia	0.201508 (15)	Estonia	0.200674 (15)	Estonia	0.201343 (15)

Notes: As there are 29 nations in our sample, this table presents only the top 15 nations. Numbers in parentheses are nations' ranks for output factors at the social welfare stage.

At the social welfare stage, nine countries, including Belgium, Finland, France, New Zealand, Norway, Poland, Spain, Sweden, and the United Kingdom are the leaders in the input and output factors of government expenditure on general public services, government expenditure on economic affairs, government expenditure on health, government expenditure on education and population age above 65, employment population, tertiary school enrollment population, respectively (Tables 7 and 8).

### 5. Conclusions

Ecology efficiency and social welfare efficiency improvement are the the most important policy options for countries. This study aims to measure the ability of the 29 countries in producing competitive products and services that fulfill individual needs and improve the level of welfare with less utilization of natural resources. This study builds a two-stage network production process model to investigate the ecology efficiency and social welfare efficiency of the countries.

At the preliminary analysis of efficiencies, efficiency scores obtained from the two-stage network DDF function show six efficient countries at the ecology stage and four efficient countries at the social welfare stage. No country is efficient at both stages. The findings also demonstrate that most of the 29 countries have lower efficiency in the social welfare stage than in the ecology stage. The empirical results provide policymakers with a better awareness of the ecology efficiency and social welfare efficiency of the countries.

Furthermore, we examine efficient countries and confirm leading countries for learners. The findings suggest the strengths and highlight the weaknesses of the countries in terms of input/undesirable output/intermediate/additional input/output factors that assist the governments to improve and operate their country efficiently. It may be argued that nations producing large unfavorable outputs may not function eco-efficiently and hence have a great possibility to save the maximum amount of energy. Furthermore, nations with low energy consumption may be more eco-efficient and have a lower capacity to minimize undesired outputs. For example, countries such as Norway, Switzerland, China, the United States, Italy, and the United Kingdom have considerable opportunities for reducing energy usage and CO<sub>2</sub> emissions. Norway, the United States, Lithuania, Turkey, and China still have enormous potential to increase GDP. At the social welfare stage, countries including Turkey, Lithuania, China, Bulgaria, and Denmark have room to improve their social welfare efficiency by reducing the quantity of government expenditure on general public services, government expenditure on economic affairs, government expenditure on health, government expenditure on education while increasing population age above 65, employment population, and tertiary school enrollment population. From a macro



perspective, both the ecology efficiency and social welfare efficiency determine a country's overall efficiency level. According to the empirical findings, policy makers' varying degrees of interest preference affect the ecology efficiency and social welfare efficiency.

Following the limitations of this study, we suggest helpful guidance for future research. First, this study takes the data from various sources, although cross-database is our contribution in this study, our sample focuses on countries from different regions. Future research may consider studying the countries in the same region. Second, although this study uses panel data to investigate the ecology efficiency and social welfare efficiency of the countries, this does not allow us to compare the efficiency levels of countries in different distinct periods. Future research may consider dividing into distinctive periods (i.e., before the Kyoto Protocol entered into force period, the first commitment of the Kyoto Protocol period, and the second commitment of the Kyoto Protocol period).

**Author Contributions:** Conceptualization, Z.-J.L.; methodology, W.-M.L.; software, M.-H.L.; validation, Z.-J.L.; formal analysis, Z.-J.L.; investigation, Z.-J.L.; resources, M.-H.L.; data curation, M.-H.L.; writing—original draft preparation, Z.-J.L.; writing—review and editing, Z.-J.L.; visualization, M.-H.L.; supervision, Z.-J.L.; project administration, W.-M.L.; funding acquisition, Z.-J.L. All authors have read and agreed to the published version of the manuscript.

**Funding:** This research received no external funding.

**Institutional Review Board Statement:** Not applicable.

**Informed Consent Statement:** Not applicable.

**Data Availability Statement:** The data that support the findings of this study are available from the corresponding author, upon reasonable request.

**Conflicts of Interest:** The authors declare no conflict of interest.

## References

1. Turnhout, E.; Metz, T.A.P.; Wyborn, C.; Klenk, N.; Louder, E. The politics of co-production: Participation, power, and transformation. *Current Opinion in Environmental Sustainability*. *Wageningen* **2020**, *42*, 15–21.
2. Dewulf, A.; Klenk, N.; Wyborn, C.; Lemos, M.C. Usable environmental knowledge from the perspective of decision-making: The logics of consequentiality, appropriateness, and meaningfulness. *Curr. Opin. Environ. Sustain.* **2020**, *42*, 1–6. [[CrossRef](#)]
3. Zhu, W.; Xu, L.; Tang, L.; Xiang, X. Eco-efficiency of the Western Taiwan Straits Economic Zone: An evaluation based on a novel eco-efficiency model and empirical analysis of influencing factors. *J. Clean. Prod.* **2019**, *234*, 638–652. [[CrossRef](#)]
4. Freeman, R.; Yearworth, M. Climate change and cities: Problem structuring methods and critical perspectives on low-carbon districts. *Energy Res. Soc. Sci.* **2017**, *25*, 48–64. [[CrossRef](#)]
5. Jones, T.M.; Donaldson, T.; Freeman, R.E.; Harrison, J.S.; Leana, C.; Mahoney, J.T.; Pearce, J.L. Management Theory and Social Welfare: Contributions and Challenges. *Acad. Manag. Rev.* **2016**, *41*, 216–228. [[CrossRef](#)]
6. Yang, L.; Zhang, X. Assessing regional eco-efficiency from the perspective of resource, environmental and economic performance in China: A bootstrapping approach in global data envelopment analysis. *J. Clean. Prod.* **2018**, *173*, 100–111. [[CrossRef](#)]
7. Wursthorn, S.; Pogonietz, W.-R.; Schebek, L. Economic–environmental monitoring indicators for European countries: A disaggregated sector-based approach for monitoring eco-efficiency. *Ecol. Econ.* **2011**, *70*, 487–496. [[CrossRef](#)]
8. Moutinho, V.; Fuinhas, J.A.; Marques, A.C.; Santiago, R. Assessing eco-efficiency through the DEA analysis and decoupling index in the Latin America countries. *J. Clean. Prod.* **2018**, *205*, 512–524. [[CrossRef](#)]
9. Mavi, R.K.; Saen, R.F.; Goh, M. Joint analysis of eco-efficiency and eco-innovation with common weights in two-stage network DEA: A big data approach. *Technol. Forecast. Soc. Chang.* **2019**, *144*, 553–562. [[CrossRef](#)]
10. Moraes, R.K.; Wanke, P.F.; Faria, J.R. Unveiling the endogeneity between social-welfare and labor efficiency: Two-stage NDEA neural network approach. *Socio-Econ. Plan. Sci.* **2021**, *77*, 101026. [[CrossRef](#)]
11. Lefebvre, M.; Perelman, S.; Pestieau, P. *Productivity and Performance in the Public Sector*; LIDAM Discussion Papers CORE 2015052; Université catholique de Louvain, Center for Operations Research and Econometrics (CORE): Ottignies-Louvain-la-Neuve, Belgium, 2015.
12. Wang, R.; Feng, Y. Research on China's Ecological Welfare Performance Evaluation and Improvement Path from the Perspective of High-Quality Development. *Math. Probl. Eng.* **2020**, *2020*, 5476089. [[CrossRef](#)]
13. Picazo-Tadeo, A.J.; Beltrán-Estevé, M.; Gómez-Limón, J.A. Assessing eco-efficiency with directional distance functions. *Eur. J. Oper. Res.* **2012**, *220*, 798–809. [[CrossRef](#)]
14. Chiang, C.-Y.; Lin, B. An integration of balanced scorecards and data envelopment analysis for firm's benchmarking management. *Total Qual. Manag. Bus. Excell.* **2009**, *20*, 1153–1172. [[CrossRef](#)]

15. Sporchia, F.; Paneni, A.; Pulselli, F.M.; Caro, D. Investigating environment-society-economy relations in time series in Europe using a synthetic input-state-output framework. *Environ. Sci. Policy* **2021**, *125*, 54–65. [[CrossRef](#)]
16. Robaina-Alves, M.; Moutinho, V.; Macedo, P. A new frontier approach to model the eco-efficiency in European countries. *J. Clean. Prod.* **2015**, *103*, 562–573. [[CrossRef](#)]
17. Pais-Magalhães, V.; Moutinho, V.; Marques, A.C. Scoring method of eco-efficiency using the DEA approach: Evidence from European waste sectors. *Environ. Dev. Sustain.* **2020**, *23*, 9726–9748. [[CrossRef](#)]
18. Yu, C.; Shi, L.; Wang, Y.; Chang, Y.; Cheng, B. The eco-efficiency of pulp and paper industry in China: An assessment based on slacks-based measure and Malmquist–Luenberger index. *J. Clean. Prod.* **2016**, *127*, 511–521. [[CrossRef](#)]
19. Yu, Y.; Chen, D.; Zhu, B.; Hu, S. Eco-efficiency trends in China, 1978–2010: Decoupling environmental pressure from economic growth. *Ecol. Indic.* **2013**, *24*, 177–184. [[CrossRef](#)]
20. Pereira, M.A.; Ferreira, D.C.; Figueira, J.R.; Marques, R.C. Measuring the efficiency of the Portuguese public hospitals: A value modelled network data envelopment analysis with simulation. *Expert Syst. Appl.* **2021**, *181*, 115169. [[CrossRef](#)]
21. Guan, J.; Chen, K. Measuring the innovation production process: A cross-region empirical study of China’s high-tech innovations. *Technovation* **2010**, *30*, 348–358. [[CrossRef](#)]
22. Kao, C.; Hwang, S.-N. Efficiency decomposition in two-stage data envelopment analysis: An application to non-life insurance companies in Taiwan. *Eur. J. Oper. Res.* **2008**, *185*, 418–429. [[CrossRef](#)]
23. Rakhshan, S.A. Efficiency ranking of decision making units in data envelopment analysis by using TOPSIS-DEA method. *J. Oper. Res. Soc.* **2017**, *68*, 906–918. [[CrossRef](#)]
24. Liu, S.-T. A DEA ranking method based on cross-efficiency intervals and signal-to-noise ratio. *Ann. Oper. Res.* **2018**, *261*, 207–232. [[CrossRef](#)]
25. Wu, J.; Liang, L.; Yang, F. Achievement and benchmarking of countries at the Summer Olympics using cross efficiency evaluation method. *Eur. J. Oper. Res.* **2009**, *197*, 722–730. [[CrossRef](#)]
26. Vavrek, R.; Chovancová, J. Assessment of economic and environmental energy performance of EU countries using CV-TOPSIS technique. *Ecol. Indic.* **2019**, *106*, 105519. [[CrossRef](#)]
27. Lu, W.-M.; Kweh, Q.L.; Wang, C.-W. Integration and application of rough sets and data envelopment analysis for assessments of the investment trusts industry. *Ann. Oper. Res.* **2019**, *296*, 163–194. [[CrossRef](#)]
28. Liu, J.S.; Lu, W.-M. DEA and ranking with the network-based approach: A case of R&D performance. *Omega* **2010**, *38*, 453–464.
29. Liu, J.S.; Lu, W.-M.; Ho, M.H.-C. National characteristics: Innovation systems from the process efficiency perspective. *R&D Manag.* **2015**, *45*, 317–338.
30. Liu, J.S.; Lu, W.-M.; Yang, C.; Chuang, M. A network-based approach for increasing discrimination in data envelopment analysis. *J. Oper. Res. Soc.* **2009**, *60*, 1502–1510. [[CrossRef](#)]
31. Hao, F.; Liu, X.; Michaels, J.L. Social Capital, carbon dependency, and public response to climate change in 22 European countries. *Environ. Sci. Policy* **2020**, *114*, 64–72. [[CrossRef](#)]
32. Wegener, M.; Amin, G.R. Minimizing greenhouse gas emissions using inverse DEA with an application in oil and gas. *Expert Syst. Appl.* **2018**, *122*, 369–375. [[CrossRef](#)]
33. Rashidi, K.; Farzipoor Saen, R. Measuring eco-efficiency based on green indicators and potentials in energy saving and undesirable output abatement. *Energy Econ.* **2015**, *50*, 18–26. [[CrossRef](#)]
34. Medialdea, J.T.; Ruiz, J.A.P.; García, C.F.; Capilla, A.C.; Martorell, J.C.; Rodenas, J.B. Potential of science to address the hunger issue: Ecology, biotechnology, cattle breeding and the large pantry of the sea. *J. Innov. Knowl.* **2018**, *3*, 82–89. [[CrossRef](#)]
35. Chen, C.C. Measuring departmental and overall regional performance: Applying the multi-activity DEA model to Taiwan’s cities/counties. *Omega* **2017**, *67*, 60–80. [[CrossRef](#)]
36. Schaltegger, S.; Sturm, A. Ökologische Rationalität: Ansatzpunkte zur Ausgestaltung von ökologieorientierten Managementinstrumenten. *Die Unternehmung* **1990**, *44*, 273–290.
37. Pastorok, R.A.; Resit, A.; Helen, R.; Scott, F.; Steven, M.B. Role of Ecological Modeling in Risk Assessment. *Hum. Ecol. Risk Assess. Int. J.* **2003**, *9*, 939–972. [[CrossRef](#)]
38. Dyckhoff, H.; Allen, K. Measuring ecological efficiency with data envelopment analysis (DEA). *Eur. J. Oper. Res.* **2001**, *132*, 312–325. [[CrossRef](#)]
39. Zhou, P.; Ang, B.W.; Wang, H. Energy and CO<sub>2</sub> emission performance in electricity generation: A non-radial directional distance function approach. *Eur. J. Oper. Res.* **2012**, *221*, 625–635. [[CrossRef](#)]
40. Liu, X.; Liu, J. Measurement of Low Carbon Economy Efficiency with a Three-Stage Data Envelopment Analysis: A Comparison of the Largest Twenty CO<sub>2</sub> Emitting Countries. *Int. J. Environ. Res. Public Health* **2016**, *13*, 1116. [[CrossRef](#)]
41. Wu, J.; Yin, P.; Sun, J.; Chu, J.; Liang, L. Evaluating the environmental efficiency of a two-stage system with undesired outputs by a DEA approach: An interest preference perspective. *Eur. J. Oper. Res.* **2016**, *254*, 1047–1062. [[CrossRef](#)]
42. Walsh, J.P.; Weber, K.; Margolis, J.D. Social Issues and Management: Our Lost Cause Found. *J. Manag.* **2003**, *29*, 859–881.
43. Giménez, V.; Ayvar-Campos, F.J.; Navarro-Chávez, J.C.L. Efficiency in the generation of social welfare in Mexico: A proposal in the presence of bad outputs. *Omega* **2017**, *69*, 43–52. [[CrossRef](#)]
44. Marti, E.; Scherer, A.G. Financial Regulation And Social Welfare: The Critical Contribution Of Management Theory. *Acad. Manag. Rev.* **2016**, *41*, 298–323. [[CrossRef](#)]

45. Giovannini, E.; Hall, J.; Morrone, A.; Ranuzzi, G. A Framework to measure the progress of societies. *OECD Stat. Work. Pap.* **2011**, *121*, 93–118. [[CrossRef](#)]
46. Nissi, E.; Sarra, A. A Measure of Well-Being Across the Italian Urban Areas: An Integrated DEA-Entropy Approach. *Soc. Indic. Res.* **2018**, *136*, 1183–1209. [[CrossRef](#)]
47. Lin, F.; Lin, S.-W.; Lu, W.-M. Dynamic eco-efficiency evaluation of the semiconductor industry: A sustainable development perspective. *Environ. Monit. Assess.* **2019**, *191*, 435. [[CrossRef](#)]
48. Fried, H.O.; Lovell, C.K.; Schmidt, S.S. *The Measurement of Productive Efficiency Productivity Growth*; Oxford University Press, Inc.: New York, NY, USA, 2008.
49. Bonacich, P.; Lloyd, P. Eigenvector-like measures of centrality for asymmetric relations. *Soc. Netw.* **2001**, *23*, 191–201. [[CrossRef](#)]
50. Kutlu, L. Greenhouse Gas Emission Efficiencies of World Countries. *Int. J. Environ. Res. Public Health* **2020**, *17*, 8771. [[CrossRef](#)]



Article

# Does Intensive Land Use Contribute to Energy Efficiency?—Evidence Based on a Spatial Durbin Model

Haiqian Ke <sup>1</sup>, Bo Yang <sup>2</sup> and Shangze Dai <sup>2,\*</sup>

<sup>1</sup> Fanli Business School, Nanyang Institute of Technology, Nanyang 473000, China; kehaiqian@whu.edu.cn

<sup>2</sup> Institute of Central China Development, Wuhan University, Wuhan 430072, China; ycloud@whu.edu.cn

\* Correspondence: daishangze@whu.edu.cn

**Abstract:** In order to ensure the safety of cultivated land and promote urban productivity, the Chinese government began to promote intensive land use at the legislative level from 2014. At the same time, China faces problems of carbon emissions and energy, so we need to improve energy efficiency. Therefore, this paper aims to verify the spatial effects of intensive land use on energy efficiency of China from 2009 to 2018. We further use an index system to quantify intensive land use and use chain DEA (data envelope analysis) to quantify energy efficiency. This paper finds that: (1) intensive land use can significantly improve energy efficiency. A 1% increase in the level of intensive land use will increase energy efficiency by 1.3%. (2) The intensive use of land in one city will have a negative impact on the energy efficiency of surrounding cities. The reason is that the intensive use of land in a single city may lead to the transfer of energy-consuming industries to surrounding cities. (3) The impact of intensive land use on the energy efficiency of surrounding cities has negative threshold characteristics, and the negative impact will be weakened as the level of integration of the city increases.

**Keywords:** intensive land use; spatial durbin model; energy efficiency; carbon emissions

**Citation:** Ke, H.; Yang, B.; Dai, S. Does Intensive Land Use Contribute to Energy Efficiency?—Evidence Based on a Spatial Durbin Model. *Int. J. Environ. Res. Public Health* **2022**, *19*, 5130. <https://doi.org/10.3390/ijerph19095130>

Academic Editor: Paul B. Tchounwou

Received: 13 March 2022

Accepted: 20 April 2022

Published: 22 April 2022

**Publisher's Note:** MDPI stays neutral with regard to jurisdictional claims in published maps and institutional affiliations.



**Copyright:** © 2022 by the authors. Licensee MDPI, Basel, Switzerland. This article is an open access article distributed under the terms and conditions of the Creative Commons Attribution (CC BY) license (<https://creativecommons.org/licenses/by/4.0/>).

## 1. Introduction

The widespread, severe negative impacts of human activities on Earth's ecosystems over the past few decades have highlighted the importance of continuous and up-to-date monitoring of ecosystems health [1]. In the context of the "green revolution" sweeping the world and the prevalence of international green trade barriers, only the harmonious coexistence of economic development, energy consumption and the ecological environment can support sustainable development and maintain a competitive advantage. As China has reached crossroads of economic transformation and upgrading, it needs to transform its economic development mode and transform its economic growth momentum. Therefore, under the severe situation of the environmental carrying capacity reaching its upper limit, it is necessary to promote the transformation of the industrial economic growth mode to resource-saving and eco-environmental protection and promote the formation of a development model with higher eco-efficiency [2,3].

In addition, in December 2020, the Chinese government announced a series of new measures for China's National Independent Contributions, including that carbon dioxide emissions per unit of GDP before 2030 will drop by more than 65% compared to 2005, the proportion of primary energy consumption of non-fossil energy stations will reach about 25%, and forest storage will increase by 6 billion cubic meters compared with 2005, etc. China will strive to reach carbon peak by 2030 and achieve carbon neutrality by 2060. As of 2019, 46 countries and regions around the world have achieved carbon peaks, mainly developed countries. As the world's largest developing country, China has substantial carbon emissions, accounting for about 28% of the world's total, and its energy structure is dominated by coal. In 2019, coal accounted for 57.7% of total energy consumption. China's

economic development is still in the stage of stock accumulation, and it still needs to rely on capital stock driven by production investment and infrastructure investment, which, in turn, leads to carbon emissions; energy resource endowments are not abundant enough, and it is difficult to build a diversified and green energy structure. Raising awareness of environmental protection, encouraging green consumption, raising the level of green technology innovation and improving energy efficiency are all ways to mitigate the growth of carbon emissions. Among them, energy efficiency refers to obtaining a higher output under the same energy input, so the improvement of energy efficiency can effectively save the total energy use, thereby reducing related carbon emissions [4]. Improving energy efficiency means that comprehensive innovation and exploration are required to promote a new round of industrial energy revolution. Improving energy efficiency also requires substantial improvements in existing energy production and consumption methods. It is then conducive to promoting new industries, creating new growth points, and realizing a low-carbon transformation of economic development in the process.

Human economic activities use land as the primary bearing space, and a large amount of agricultural land is gradually transformed into non-agricultural land, which has gradually become one of the main factors for the rapid rise of carbon dioxide emissions. Additionally, the change of land use is the second most significant factor behind the increase in global atmospheric carbon dioxide content after the burning of fossil fuels [5]. The main reason is that the intensive use of land is through the increase in labor, capital, technology and other inputs to achieve a high-efficiency use of resources and achieve economic development, while also inevitably increasing the total amount of carbon emissions. In addition, China's increasingly limited land resources have increasingly restricted the direction and speed of urban development and have threatened food security and ecological security. When the cultivation process of the introduced planted food species is complex, the requirements for the living environment are relatively high, so a large amount of land is needed as a test field. At the same time, the development of the renewable green low-carbon energy industry requires large-scale engineering construction as a platform to support it, so it can be widely promoted and applied [6]. Therefore, as a non-renewable resource, land is an important support for economic development and an essential part of the coordinated and sustainable development of China's economy, society, and ecology. In the process of reducing carbon emissions, China needs strong support from land resources. The Chinese government has also successively issued a series of policies that emphasize the need to promote the formation of a new pattern of high-quality development and protection of land and space. It is proposed to continuously improve the land-saving and intensive-use system, alleviate the contradiction between human and land, reduce the phenomenon of land waste, and form favorable supporting conditions for the realization of sustainable development [7].

## 2. Literature Review and Theoretical Hypotheses

### 2.1. Energy Efficiency

Energy efficiency, or full-factor energy efficiency, has been the focus of research in the field of population, resource and environmental economics in recent years. As early as 1995, the World Energy Commission gave an explanation of the concept of energy efficiency. Energy efficiency can be defined as: "reducing energy input to provide equivalent energy services." From an economic point of view, Patterson (1996) defines energy efficiency based on the concept of energy consumption per unit of output: energy efficiency refers to the use of less energy to provide the same service or produce the same effective output. Patterson believes that the improvement of energy efficiency should be based on ensuring economic growth, rather than reducing investment [8]. Kilponen (2003) added the concept of environment to the goal of energy efficiency on the basis of predecessors, further enriching the concept of energy efficiency [9]. From early energy efficiency research, the measurement of energy efficiency comes from the ratio of energy consumption to GDP, which belongs to single-factor energy efficiency. As a method to measure factor input and output, single-

factor energy efficiency has the characteristics of good data openness, simple calculation, and clear economic significance. However, it ignores the substitution between factors, and in the actual production process, the inputs of production factors can replace each other to a certain extent, and the substitution rate can be expressed by the marginal substitution rate; single-factor energy efficiency does not take into account the externality of energy consumption, and in the process of energy consumption, waste water, waste gas and solid waste will inevitably be generated. Therefore, energy efficiency will be overestimated if single-factor energy efficiency is used [10].

Based on the shortcomings of single-factor energy efficiency, scholars began to look for better indicators to describe the relationship between energy consumption and output. Hu and Wang (2006) made a breakthrough study on the concept of energy efficiency, and they also combined data envelopment analysis to measure total factor productivity [11]. The addition of labor and capital to the input factors changed the analytical framework of previous studies that only considered energy factors, and at the same time introduced the concept of marginal substitution of factors. This method of calculation has also been widely used by later scholars. On the basis that the output remains unchanged, the ratio of the optimal energy input to the actual input can better present the connotation of efficiency because the coordination of different input elements is considered.

### *2.2. Intensive Land Use*

The concept of intensive use of land was first proposed by the classical economist David Ricardo in the theory of land rent, and it mainly refers to the increase in capital, labor and other factors input on the land to obtain higher output [12]. However, the input and output of capital and labor in the land is not an eternal, single positive correlation. After the input exceeds a certain range, the output will decrease as the input increases. Therefore, the increase in intensive land use is limited; when the continuous investment of capital and labor in land reaches the point of diminishing economic returns, that is, when the marginal revenue equals the marginal output, the operator will not add additional input. This critical point is the intensive boundary of land use. Land use that reaches the intensive boundary is called intensive land use. Conversely, land use that does not reach the intensive boundary is called extensive use.

Under these constraints, by changing the investment intensity and utilization intensity, the utilization efficiency can be maximized [13]. It emphasizes the sustainable development of intensive land use under the constraints of resource environmental protection. Technological progress and green policy system support are generally considered to be important ways to improve energy efficiency. This is because green emission reduction policies adjust industrial and energy structures to eliminate outdated production capacity and jointly achieve the goal of reducing carbon emissions [14]; technological progress can improve energy efficiency, save energy and increase the development and utilization of clean energy. It is worth noting that the intensive use of land at the urban level can help increase density, cause creative destruction, environmental regulation, and ultimately increase energy efficiency [15].

### *2.3. Intensive Land Use and Energy Efficiency*

However, the intensive use of land may have a spatial effect on energy efficiency, that is, the level of intensive use of land in a certain city will have an impact on the energy efficiency of surrounding cities. Existing research on pollution transfer issues from the perspectives of environmental regulation, foreign direct investment, foreign trade, economic growth, etc., verify the existence of a “polluted paradise” or “pollution refuge” [16]. China is a large developing country. For a long time, due to the huge differences in geographical conditions and resource endowments between regions, there has been a long-term large imbalance in the level of regional economic development. For areas with high levels of development, in order to improve the quality of local economic development and realize the upgrading of the industrial structure, those industries with high pollution intensity and obvious negative

externalities of production may be transferred out [17]. However, low-level development areas may have undertaken this part of the industrial transfer due to their economic growth as their primary goal. Therefore, for regions with low development levels, integration into large economic zones or urban agglomerations may face greater ecological environmental challenges while gaining industrial transfer and economic division of labor dividends.

Theoretically, the “Pollution Haven Hypothesis” (PHH) from the international division of labor indicates that, in the process of advancing international economic integration, regions with low levels of development may face the threat of pollution transfer from regions with high levels of development [18]. In other words, when there is a clear gap in the level of economic development between regions, the transfer of industries may be selective due to the inconsistent preference for economic growth and environmental pollution. Those late-developing areas with lower environmental requirements may become “pollution refuges” for pollution-intensive industries [19]. This pollution transfer effect caused by the difference in the level of economic development has been supported by many documents between developed and developing regions [20]. Therefore, the implementation of the intensive use of land in a certain city may lead to the transfer of industries from that city to surrounding cities, thereby improving the energy efficiency of the city and reducing the energy efficiency of surrounding cities.

However, this effect can be reduced to a certain extent. Regional integration effectively reduces the administrative barriers to the flow of factors and commodities, promotes the spatial allocation and integration of industrial resources and plays an important role in coordinating regional economic development and tapping the potential for economic growth through government cooperation between localities (regional integration in this article refers to economic integration, that is, the elimination of artificial factors that hinder the effective operation of the economy). Through mutual cooperation and unification, multiple separate economies are integrated into a large economy, so that goods and factors tend to flow freely in this large economy [21]. In recent years, with the implementation of the new urbanization development strategy, government cooperation within urban agglomerations has continued to deepen, and the integrated construction of urban agglomerations as a space carrier has attracted more and more attention from scholars [22]. This article suggests that spatial integration could be used to explore the inhibitory effect of intensive land use on the energy efficiency of surrounding cities for the following reasons: first, the spatial integration will to a large extent produce the coordinated development of governance capabilities within the spatial scope, which will lead to the coordinated governance of pollution across regions. By jointly carrying out the analysis and assessment of differences in current environmental protection standards, and orderly formulating and revising unified environmental protection standards in the fields of air, water, soil, hazardous waste, noise, etc., the spillover effects of pollution can be greatly reduced; secondly, the overall level of green innovation will be improved through integration, including the construction of a green industry system [23], for instance, jointly build a green technology innovation center and a green engineering research center, implement major green technology research and development and demonstration projects, encourage the National Green Development Fund to increase investment in the twin city economic circle; advocate a green lifestyle, co-build a standardized technical support platform for green cities, improve a unified green building standard and certification system, accelerate the promotion of garbage classification and jointly build a regional integrated garbage classification and recycling network system; carry out green development experiments and demonstrations, etc. [24]. In summary, the question is whether there is a relationship between intensive land use and energy efficiency and whether this relationship shows spatial characteristics. At present, there are few studies focusing on these questions, so this paper will explore the answers to these questions in depth, thereby enriching the research about land intensive use and energy efficiency.

### 3. Data and Methods

#### 3.1. Data

##### 3.1.1. Data Selection

To figure out the relationship between intensive land use and energy efficiency, the following variables are selected in this paper:

(1) Explained variable (energy efficiency, *Ene*): Referring to Patterson (1996) and Fan et al. (2020) [25], the input variables selected in this article are labor (unit is thousands, measured by the number of employees), capital (unit is RMB million, estimated according to the method of Lu Fei et al. [26] and energy (unit is thousand tons of standard coal); the output variable is GDP (unit is one hundred million yuan). This study uses the chain network DEA to quantify energy efficiency [27,28], so each city above the prefecture level is a decision-making unit  $DMU_i$ , assuming that there are  $s$  ( $s = 1, 2, \dots, S$ ) stages in the whole process, the input variables and output variables of each stage are  $I_i^s$  and  $O_i^s$ , respectively, and satisfy  $I_i^s \in R_+^{\alpha s}$  and  $O_i^s \in R_+^{\beta s}$ ; the intermediate variable of the  $s$  stage and the  $s + 1$  stage is set to  $P_i^{(s,s+1)}$ , and it satisfies  $P_i^{(s,s+1)} \in R_+^{\gamma(s,s+1)}$ , where  $\alpha, \beta$  and  $\gamma$  represent the number of input variables, output variables and intermediate variables, respectively,  $\alpha = 1, 2, \dots, x, \beta = 1, 2, \dots, y, \gamma = 1, 2, \dots, z$ .  $\lambda^s$  is the model weight,  $w^s$  is the weight variable of the  $s_{th}$  order in the whole process, and  $\lambda^S \in R_+^n, \mu^{s-}$  and  $\mu^{s+}$  are the slack variables of the input variable and the output variable [29,30], respectively; the goal of the network envelope analysis model can be expressed as  $\theta$ :

$$\theta = \min \frac{\sum_{s=1}^S \omega^s [1 - \frac{1}{\alpha} (\sum_{x=1}^{\alpha} \frac{\mu_x^{s-}}{I_{x0}^s})]}{\sum_{s=1}^S \omega^s [1 + \frac{1}{\beta} (\sum_{y=1}^{\beta} \frac{\mu_y^{s+}}{O_{y0}^s})]} \tag{1}$$

The constraints are:

$$\begin{aligned} I_0^s &= \sum_{i=1}^n \lambda_i^s I_i^s + \mu^{s-} \\ O_0^s &= \sum_{i=1}^n \lambda_i^s O_i^s + \mu^{s+} \\ P^{(s,s+1)} \lambda^{s+1} &= P^{(s,s+1)} \lambda^s \\ \sum_{i=1}^N \lambda_i^s &= \sum_{s=1}^S \omega^s = 1 \\ \lambda^S, \mu^{s-}, \mu^{s+}, w^s &\geq 0 \end{aligned}$$

The efficiency of stage  $s$  can be expressed as:

$$\theta_s = \frac{1 - \frac{1}{\alpha} (\sum_{x=1}^{\alpha} \frac{\mu_x^{s-*}}{I_{x0}^s})}{1 + \frac{1}{\beta} (\sum_{y=1}^{\beta} \frac{\mu_y^{s+*}}{O_{y0}^s})} \tag{2}$$

(2) Explanatory variable (intensive land utilization, *Liu*): China currently divides regional land into construction land and non-construction land. The former can be understood as the land that serves productive labor and capital factors and where various factors of production can play a role; the latter refers to other land, which does not have the nature of production. Because (positive) intensive land use refers to the investment of more production factors per unit area of land and the agglomeration of urban internal space, this article selects GDP density, population density, electricity consumption density, employment density, local fiscal expenditure density, and the inverse numbers of urban patch density (the inverse number of indicators that measure the degree of urban decentralization). The calculation method of density is the ratio of the total amount of economic indicators to the area of construction land. The ratio of the total amount to the total urban area is not adopted because many cities have large tracts of land without economic activities, and only the area of construction land is engaged in economic activities. The weighting is divided into subjective and objective methods. This article selects the



EVM (entropy value method), that is: first adopt the normalization method for the data  $(x_i - x_{min}) / (x_{max} - x_{min})$ , then suppose there are  $m$  indexes that have been normalized, and each index has  $n$  data, then the entropy value of the  $j_{th}$  item is:

$$-\frac{1}{Ln(n)} * \sum_{j=1}^m \frac{x_{ij}}{\sum_{i=1}^n x_{ij}} * Ln(\frac{x_{ij}}{\sum_{i=1}^n x_{ij}}) \tag{3}$$

Information redundancy  $d_j$  is the sum of the opposite of entropy and 1, and the weight of the indicator  $wA_j$  can be written as:  $\frac{d_j}{\sum_{j=1}^m d_j}$

$$d_j = 1 + \frac{1}{Ln(n)} * \sum_{j=1}^m \frac{x_{ij}}{\sum_{i=1}^n x_{ij}} * Ln(\frac{x_{ij}}{\sum_{i=1}^n x_{ij}}) \tag{4}$$

Following the EVM method above, the final weights given to the above indicators in this article are: 0.1322, 0.2462, 0.1896, 0.1308, 0.2404 and 0.0606. Because, under this index system, the intensive land use index has both positive and negative values, in order to facilitate the analysis of the quadratic term in the heterogeneity analysis part, in this paper, the value obtained under the index system is summed with 1 to obtain an index to measure the level of intensive land use.

We draw maps as Figures 1 and 2 to reflect the distribution of the energy efficiency and the intensive land use of Chinese cities from 2009 to 2018. Due to the data availability, the below maps are based on the majority of Chinese cities.

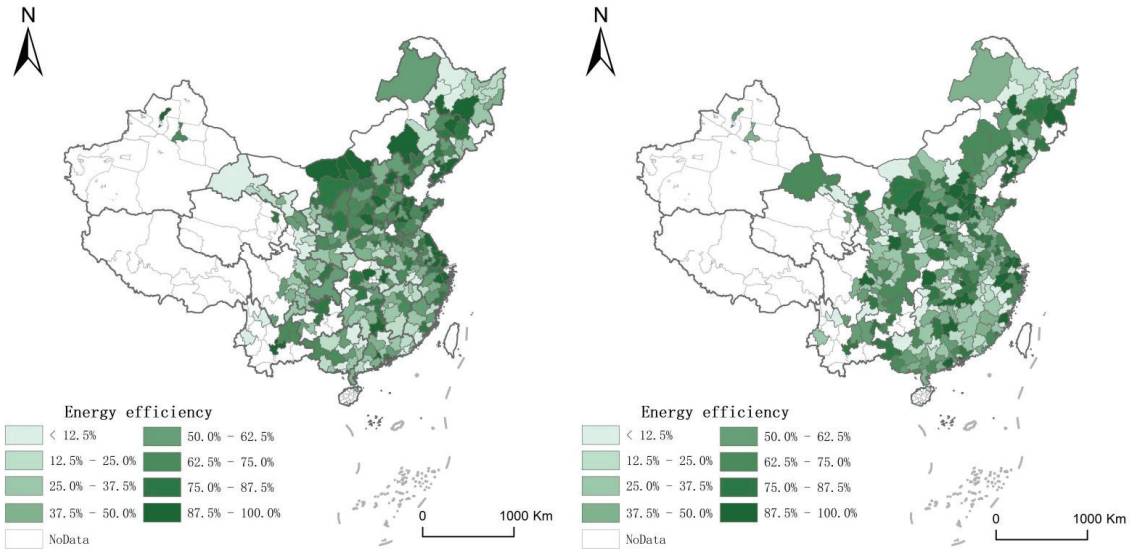
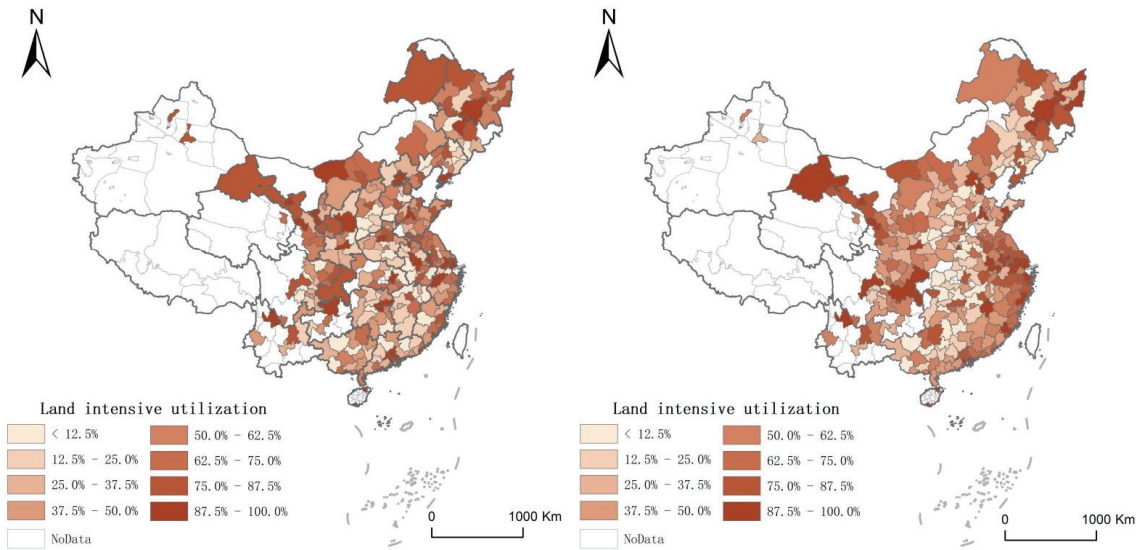


Figure 1. The distribution of the energy efficiency of China in 2009 and 2018.

(3) Threshold variables (spatial integration, *Spa*): the existing literature does not have a method to quantify spatial integration, so this article proposes the level of urban construction integration to measure it. The specific method is to use night light data to connect the geometric center of a certain city with the geometric centers of all neighboring cities. The night light brightness of all county-level administrative units passing through the connection is averaged and normalized for the measurement of spatial integration. If the value is larger, it means that even between the two city centers, the brightness value of the night lights is still very large, which, to a certain extent, indicates that the construction of the city is connected together, and this reduces the cost of transporting goods and

commuting people and represents a great deal of spatial integration (two regions can be “surrounding areas” if they border each other).



**Figure 2.** The distribution of land intensive use of China in 2009 and 2018.

(4) Control variables: In order to control the impact of other variables on energy intensity, this article selects four control variables: economic development, industrial structure, opening to the outside world and technological innovation. (1) Economic development. Faster economic development leads to more energy consumption, but the development of new technologies and upgrading industries will also lead to improved energy efficiency, thereby saving energy. Therefore, this article uses the logarithm of GDP (*Gdp*) and GDP per capita (*Gpp*) as the control variables [31,32]. (2) Industrial structure. Areas with a higher proportion of the secondary industry may have more carbon emissions. The reason is that industrial production consumes a lot of energy and reduces energy efficiency. Therefore, this article chooses the secondary industry (*Ssr*) and tertiary industry (*Tsr*) as the control variables as the proportion of GDP. (3) Opening up to the outside world. Under normal circumstances, the pace of regional opening up in order to attract foreign investment may cause cities to pay more attention to energy and environmental issues, and the higher the degree of opening up, the more likely it is to introduce clean technologies, which may have a positive effect on energy efficiency [33]. Therefore, this paper chooses the actual utilization of foreign capital as a control variable as the proportion of GDP (*Fdi*) [34–36]. (4) Technological innovation: Under normal circumstances, cities with higher technological innovation levels will also show more green technological innovations, which will help save energy and reduce emissions [37], thereby improving energy efficiency factors. This article selects the logarithm of the number of patent applications (*Pat*) and innovation efficiency (*Ine*) of the city as the control variables, and the quantitative method of the latter refers to Ke et al. (2021) [38], and all the variables’ descriptions are listed in Table 1.

**Table 1.** Variables explanation.

Variables	Name	Explanation	Data Source	
dependent variable	energy efficiency ( <i>Ene</i> )	this study uses the chain network DEA to quantify energy efficiency.	Yearbooks of various provincial administrative units, and “China Energy Statistical Yearbook”	
independent variable	intensive land utilization ( <i>Liu</i> )	we select GDP density, population density, electricity consumption density, employment density, local fiscal expenditure density, and the inverse numbers of urban patch density, using EVM method to give weights.	“China Statistical Yearbook”, “China City Statistical Yearbook”, Chinese Basic GIS data.	
threshold variable	spatial integration ( <i>Spa</i> )	the specific method is to use night light data to connect the geometric center of a certain city with the geometric centers of all neighboring cities. The night light brightness of all county-level administrative units passing through the connection is averaged and normalized for the measurement of spatial integration.	Visible Light Imaging Linear Scanning Service System (DMSP/OLS) in the U.S. Defense Weather Satellite and Visible Near Infrared Imaging Radiometer (NPP/VIIRS) from the National Polar Orbit Satellite	
control variables	GDP ( <i>Gdp</i> )	gross domestic product	“China Statistical Yearbook”, “China City Statistical Yearbook”	
	GDP per capita ( <i>Gpp</i> )	gross domestic product per capita		
	secondary industry ratio ( <i>Ssr</i> )	the proportion of secondary industry in total GDP.		
	tertiary industry ratio ( <i>Tsr</i> )	the proportion of tertiary industry in total GDP.		
	opening up ( <i>Fdi</i> )	the proportion of actual utilization of foreign capital in total GDP.		
	patent applications ( <i>Pat</i> )	logarithm of the number of patent applications		China national knowledge infrastructure
	innovation efficiency ( <i>Ine</i> )	quantitative method o refers to Ke et al. (2021)		China national knowledge infrastructure, “China Statistical Yearbook”, “China City Statistical Yearbook”

3.1.2. Data Source

The quantity of patent applications in this article was manually compiled on the CNKI platform. The rest of the data come from the “China Statistical Yearbook”, “China City Statistical Yearbook”, Statistical Yearbooks of Various Provincial Administrative Units, and “China Energy Statistical Yearbook”. The night light data are from the Visible Light Imaging Linear Scanning Service System (DMSP/OLS) in the U.S. Defense Weather Satellite and Visible Near Infrared Imaging Radiometer (NPP/VIIRS) from the National Polar Orbit Satellite. The sample selected in this paper is 280 cities as the data availability, and the time period is from 2009 to 2018. The missing data are filled in by the difference method (if a city has a missing year, we use the temporal trend of the variable to make it up).

3.2. Methods: Regression Model

3.2.1. Benchmark Regression

This paper establishes a panel least squares regression model:

$$y_{it} = \beta_1 x_{it} + \beta \text{Control}_{it} + I + t + \varepsilon_{it} \tag{5}$$

Among them, *y* is the explained variable, which is energy efficiency (*Ene*) in this article, *x* is the explanatory variable (*Liu*), which is the level of intensive land use in this article, and

*Control* is the control variable. After Hausman's test, this article adopts a two-way fixed effects model. Therefore, this article adds dummy variables for year  $t$  and individual  $i$ .

### 3.2.2. Spatial Regression

This article adopts spatial econometric regression. The spatial measurement model is divided into three types: spatial lag model, spatial error model and spatial Durbin model [38]. The spatial lag model adds the spatial lag term of the explained variable to the general panel data model, indicating that the explanatory variable on a certain spatial unit is affected by the explanatory variable of the adjacent spatial unit; the spatial error model adds spatially related error terms, that is, the error term of a certain spatial unit model is considered to be affected by the adjacent spatial unit model error term; the spatial Durbin model integrates the characteristics of the spatial lag model and the spatial error model. This intensity of the influence of adjacent spatial units is represented by a spatial weight matrix. The spatial lag model, the spatial error model and the spatial Durbin model are as follows:

$$y_{it} = \delta \sum_{j=1}^N W_{ij} y_{jt} + \varphi + \beta x_{it} + C_i + \alpha_t + \varepsilon_{it} \quad (6)$$

$$y_{it} = \varphi + \beta x_{it} + C_i + \alpha_t + u_{it}, u_{it} = \rho \sum_{j=1}^N W_{ij} u_{jt} + \varepsilon_{it} \quad (7)$$

$$y_{it} = \delta \sum_{j=1}^N W_{ij} y_{jt} + \varphi + \beta x_{it} + \delta \sum_{j=1}^N W_{ij} y_{ijt} \theta + C_i + \alpha_t + \varepsilon_{it} \quad (8)$$

where:  $\delta$  is the spatial regression coefficient, which represents the influence of the explained variable  $y$  of the adjacent spatial unit on the explained variable  $y$  of this spatial unit ( $y$  is the explained variable, which is energy efficiency "Ene"). If it is significantly positive, it means that the explained variable has obvious spatial overflow. That is, the increase in the variable by one spatial unit within the research scope corresponds to the increase in the variable in other spatial units;  $u_{it}$  is the spatial autoregressive error term;  $\rho$  is the spatial error coefficient, which represents the influence of the adjacent spatial unit error term  $u$  on the spatial unit error term  $u$ ;  $\theta$  is the spatial lag term coefficient of the explanatory variable, which indicates the influence of the explanatory variable  $x$  of the adjacent space unit on the explanatory variable  $y$  of this space unit;  $N$  is the number of spatial units, and  $W$  is the spatial weight matrix. First, use the LM test to determine whether the spatial lag effect and the spatial error effect are significant, then use Wald or LR test to judge whether the spatial Durbin model can be simplified into a spatial lag model or a spatial error model. Assumption 1:  $\theta = 0$ ; assumption 2:  $\theta + \lambda\beta = 0$ . If assumption 1 passes the significance test, it is considered that the spatial Durbin model can be reduced to a spatial lag model. If assumption 2 passes the significance test, it is considered that the spatial Durbin model can be reduced to a spatial error model [34]. After testing, assumption 1 and assumption 2 are not true, so this article chooses the spatial Durbin model.

### 3.2.3. Spatial Threshold Regression

Additionally, threshold regression is to test whether the parameters of the sample group divided according to the threshold value are significantly different, and it is often used to study the heterogeneity of the interaction between variables. The threshold regression model developed by Hansen (1999) [39] can endogenously divide the data interval according to the characteristics of the data itself, avoiding the randomness of artificially dividing the sample interval. The relationship between each city level and innovation performance may be nonlinear. Traditional linear regression cannot explain the relationship between the two. The threshold model regression is closer to reality. Therefore, this paper adopts the threshold regression model of Hansen (1999), which is different from the traditional threshold model. The spatial threshold model adopted in this paper adds the spatial

lag of explanatory variables and explained variables. First, the following single threshold regression model is set:

$$y_{it} = \lambda_0 + \lambda_1 w \times D_{it} \cdot I(thre_{it} \leq r_1) + \lambda_2 w \times D_{it} \cdot I(thre_{it} > r_1) + \lambda_3 X_{it} + \gamma \cdot t + \varepsilon_{it} \quad (9)$$

Among them,  $I(\cdot)$  represents an indicative function, and the value is 1 when the expression in the brackets is true and 0 when it is false.  $D_{it}$  is the core explanatory variable, where  $w \times D_{it}$  refers to the spatial lag term of the explained variable,  $Urbs_{it}$  is the threshold variable,  $X_{it}$  represents the control variable, and  $\varepsilon_{it}$  is the random disturbance term. When  $Urbs_{it} \leq r_1$ , the core explanatory variable  $D_{it}$  coefficient is  $\lambda_1$ ; when  $Urbs_{it} > r_1$ , the core explanatory variable  $D_{it}$  coefficient is  $\lambda_2$ .  $t$  is the time effect,  $\lambda_0$  is a constant term and  $\varepsilon_{it} \sim (0, \sigma)$  is a random interference term. Additionally, Equation (9) only assumes that there is one threshold, but there may be two or more thresholds. Due to space limitations, the double and more threshold tests will not be repeated.

To estimate these variables we mentioned above, we used software named STATA 15. This software is a general-purpose statistical software package developed by StataCorp for data manipulation, visualization, statistics and automated reporting.

## 4. Results

### 4.1. Benchmark Regression Results

Based on Equation (5), Table 2 shows the results of the benchmark regression. The first column is the OLS (ordinary least squares) regression before adding the control variables; the second column is the regression result using the two-way fixed effects model; the third column is the regression result of replacing the T test with D-K (Driscoll–Kraay) standard error, and the purpose is to eliminate the influence of heteroscedasticity and cross-sectional correlation on the regression result; the fourth column is the regression result using the system GMM (Generalized Method of Moment), with two-period lag and three-period lag as instrumental variables. The core of the system GMM model is to use the difference equation and the level equation as an equation system, so that the difference variable and the level variable are mutually instrumental variables for system estimation, so that the parameter estimation is more effective; the fifth column is to remove the extreme value. We remove the samples of the highest 5% and the lowest 5% of carbon emissions and perform regression again, which can eliminate the adverse effects of abnormal values on the results; the sixth column is the use of two-stage least squares regression; we choose the urban topographic undulation as an instrumental variable. The reason is that the higher the terrain undulation, the less the land area that can be used for production and living, and the higher the level of intensive land use. However, the terrain undulation may not directly impact energy efficiency.

In summary, during the study period, it can be found that every unit increase in the level of intensive land use will lead to a corresponding increase in energy efficiency by 1.3 units. Therefore, the intensive use of land is an inevitable requirement for developing a circular economy and a conservation-minded society and an essential guarantee for achieving carbon neutrality and improving energy efficiency. As the concept of sustainable development has become more and more widely accepted by people, the ideology of urban planning has also undergone tremendous changes. Sustainable land resource management has also been promoted to the strategic height of the country by countries worldwide. Especially since the 1990s, this kind of change has been clearly manifested, and some new urban planning ideas and urban land use ideas have appeared. For example, the United States of America is facing the social, economic, and political problems caused by land use. Thus, the USA tries to improve land management, especially reforming planning regulations. It is hoped that the legal function of planning as a weapon to deal with land development issues has become an issue that academia and government are concerned about.

Table 2. Benchmark regression results.

Variables	(1) OLS	(2) FE	(3) D-K	(4) GMM	(5) Drop Extremum	(6) 2SLS
<i>Liu</i>	1.209 *** (−3.61)	1.321 *** (4.34)	1.514 *** (5.17)	1.412 *** (3.84)	1.732 *** (4.70)	1.318 *** (4.68)
<i>GDP</i>		0.183 *** (6.45)	0.246 *** (6.54)	0.287 *** (9.73)	0.203 *** (8.08)	0.262 *** (9.76)
<i>Gpp</i>		0.230 *** (4.09)	0.322 *** (4.26)	0.166 *** (5.52)	0.241 *** (5.38)	0.231 *** (4.90)
<i>Ssr</i>		−2.152 *** (−6.54)	−2.733 *** (−6.29)	−2.249 *** (−6.16)	−1.875 *** (−5.27)	−2.522 *** (−6.34)
<i>Tsr</i>		3.367 *** (10.62)	3.268 *** (11.53)	2.339 *** (9.42)	3.385 *** (8.33)	2.670 *** (9.68)
<i>Fdi</i>		−0.211 (−1.09)	−0.308 (−1.17)	−0.084 (−1.20)	−0.107 (−0.99)	−0.151 *** (−1.19)
<i>Pat</i>		−0.130 (−0.49)	−0.087 (−0.50)	−0.084 (−0.49)	−0.116 (−0.33)	−0.074 (−0.44)
<i>Ine</i>		0.122 *** (6.16)	0.122 *** (5.86)	0.103 *** (4.93)	0.094 *** (5.09)	0.116 *** (4.49)
<i>Time × Individual fixed effect</i>	Control	Control	Control	Control	Control	Control
<i>Constant</i>	1.215 *** (11.04)	1.192 *** (3.83)	1.052 *** (3.41)	0.656 *** (3.68)	1.248 *** (−3.13)	1.319 *** (−4.21)
<i>R<sup>2</sup></i>	0.2638	0.7942	0.7942	0.7181	0.5654	0.8013
<i>Sample size</i>	2800	2800	2800	1960	2520	2800

Note: \*, \*\*, and \*\*\* represent significant at the 10%, 5%, and 1% levels, respectively, and the hypothesis test statistics are in parentheses.

For the control variables, it can be found that: (1) the increase in GDP and GDP per capita can significantly improve energy efficiency, and the reason is that with the growth of the economy, people’s demand for energy saving, emission reduction and a green and low-carbon lifestyle is increasing. In addition, the industrial structure has been shifting to cleaner production with economic growth, which has caused an increase in energy efficiency. (2) The increase in the proportion of the tertiary industry will help improve energy efficiency, and the decline in the proportion of agriculture will also help improve energy efficiency. Therefore, we can find that, based on paying attention to the carbon emissions caused by industry, we should pay attention to the impact of agriculture on carbon emissions and the impact of reduced energy efficiency. (3) The increase in the degree of opening up will not affect energy efficiency. The reason is that although opening up to the outside world can help green technology progress, developed countries may transfer backward, and energy-intensive industries may transfer to China, which is not conducive to energy efficiency. (4) Innovation efficiency significantly enhances energy efficiency, which is similar to the results of Ke et al. (2021) that innovation efficiency can reduce the ecological footprint, so this article will not repeat it.

Based on Equation (5), Table 3 shows the regression based on the eastern, central, western and northeastern regions. China’s eastern, central and western regions have different levels of economic development and ecological civilization construction, and the development goals of green finance should also be formulated from different angles. The eastern region has a more developed economy, a more mature capital operation, and a more complete policy environment. Green finance projects choose to invest and operate in the eastern region. Under the action of mature systems and mechanisms, they can achieve results in a short period of time. With the help of regional economic power, they can give full play to the role of production factors. These advantages cannot be highlighted in the central and western regions. For the eastern region, the improvement of the level of intensive land use has a greater degree of promotion of energy efficiency than other sectors. The reason is that the eastern region is the top priority of China’s economic development, so it carries a large number of economic activities and industrial development. Therefore,

it is necessary to strengthen land use regulation in the eastern region to avoid disorderly expansion of land [40].

**Table 3.** Benchmark regression results of four regions in China.

Variables	(1) Easter	(2) Middle	(3) West	(4) Northeast
<i>Liu</i>	1.81 *** (4.40)	1.78 *** (4.27)	1.75 *** (3.30)	1.42 *** (3.39)
<i>GDP</i>	0.22 *** (−6.43)	0.19 *** (6.68)	0.22 *** (−9.62)	0.18 *** (−8.53)
<i>Gpp</i>	0.15 *** (−5.12)	0.17 *** (4.97)	0.22 *** (−5.40)	0.18 *** (−5.68)
<i>Ssr</i>	−2.01 *** (−4.48)	−1.761 *** (−4.69)	−2.20 *** (−5.77)	−2.00 *** (−5.83)
<i>Tsr</i>	2.46 *** (11.63)	2.429 *** (8.75)	2.41 *** (9.99)	2.04 *** (8.29)
<i>Fdi</i>	−0.09 (−1.10)	−0.09 (−1.19)	−0.10 (−1.22)	−0.11 (−1.21)
<i>Pat</i>	−0.08 (−0.48)	−0.09 (−0.45)	−0.08 (−0.50)	−0.10 (−0.44)
<i>Ine</i>	−0.12 *** (−5.90)	−0.10 *** (−6.27)	−0.09 *** (−6.71)	−0.09 *** (−6.03)
<i>Time × Individual fixed effect</i>	Control	Control	Control	Control
<i>Constant</i>	0.807 *** (4.64)	1.122 *** (3.29)	1.121 *** (4.50)	1.076 *** (4.73)
<i>R<sup>2</sup></i>	0.6438	0.7017	0.8056	0.8321
<i>Sample size</i>	900	910	570	420

Note: \*, \*\*, and \*\*\* represent significant at the 10%, 5%, and 1% levels, respectively, and the hypothesis test statistics are in parentheses.

The difference in regression results between the sections may be related to the differences in the degree of industrialization in different regions. The contradiction between economic growth, scarcity of resources, and environmental damage will exist for a long time, which will be particularly prominent in the stage of rapid industrialization and urbanization. This result is the predicament of rapid economic growth and a manifestation of the underdevelopment of industrial technology. Of course, this has a lot to do with improper development. Resource and environmental problems are definitely not obstacles that cannot be overcome in economic development. Resource and environmental problems encountered in development cannot be solved by stopping development but can only be solved in development.

#### 4.2. Spatial Regression Results

Table 4 shows the regression results of the spatial model. In order to reduce the endogenous problems caused by the omitted variables, this paper adopts the spatial dynamic Durbin model. Based on the research results of LeSage and Pace in 2009 [41,42], the total effect represents the average impact of X on all regions, the direct effect represents the average impact of X on Y in this region, and the indirect effect represents the average impact of X on Y in other regions.

It can be found that although the intensive use of land can positively promote the energy efficiency of the region, it will lead to a decline in the energy efficiency of the surrounding areas. The reason is that the intensive use of land in a particular city may cause industries to shift to the surrounding areas. Therefore, when the intensity of environmental regulations increases, the market can guide different regions to make decisions that suit them. For each region, economic incentive-based environmental regulations have flexibility and incentives, which can more effectively mobilize enterprises' subjective initiative and enthusiasm. At the same time, it should be noted that different regions can flexibly

choose the most suitable type of environmental regulation according to their own specific conditions so as to achieve the purpose of protecting the environment while pursuing the maximization of the company’s own interests. For other control variables, it can be found that the signs of their direct effects and indirect effects are similar. Therefore, the impact on the local area and the surrounding area are similar, and it is similar to the benchmark regression part, so we will not repeat it in this article.

**Table 4.** Spatial regression results.

Variables	Durbin Model			Dynamic Durbin Model		
	Direct Effect	Indirect Effect	Total Effect	Direct Effect	Indirect Effect	Total Effect
<i>Liu</i>	2.125 *** (3.22)	−1.242 *** (−4.73)	0.883 *** (2.94)	2.784 *** (4.96)	−1.723 *** (−4.95)	1.061 *** (3.52)
<i>GDP</i>	0.272 *** (−6.63)	0.183 *** (−9.06)	0.455 *** (−3.92)	0.193 *** (−9.46)	0.231 *** (−6.13)	0.416 *** (−9.29)
<i>Gpp</i>	0.226 *** (−4.47)	0.211 *** (−4.60)	0.437 *** (−4.96)	0.147 *** (−5.57)	0.221 *** (−3.74)	0.368 *** (−3.32)
<i>Ssr</i>	−1.942 ** (−5.76)	−2.182 *** (−4.88)	−4.124 *** (−2.64)	−2.536 *** (−4.69)	−1.632 *** (−5.89)	−4.168 *** (−4.55)
<i>Tsr</i>	3.011 *** (7.48)	2.453 *** (11.55)	5.464 * (1.91)	3.088 (1.40)	2.760 (1.21)	5.848 ** (2.61)
<i>Fdi</i>	−0.125 (−1.04)	−0.094 (−1.24)	−0.219 ** (−2.27)	−0.082 (−0.81)	−0.133 (−1.06)	−0.215 (−1.87)
<i>Pat</i>	−0.082 (−0.44)	−0.083 (−0.44)	−0.165 (−0.89)	−0.103 (−0.51)	−0.082 (−0.39)	−0.175 (−0.90)
<i>Ine</i>	−0.113 *** (−4.30)	−0.114 *** (−6.57)	−0.227 *** (−5.38)	−0.123 *** (−6.26)	−0.121 *** (−5.34)	−0.244 (−11.60)
<i>Rho</i>		10.76 *** (5.61)			8.78 *** (3.63)	
<i>R<sup>2</sup></i>		0.7804			0.7676	
<i>likelihood ratio</i>		1308.272			1295.620	

Note: \*, \*\*, and \*\*\* represent significant at the 10%, 5%, and 1% levels, respectively, and the hypothesis test statistics are in parentheses.

### 4.3. Spatial Threshold Regression Results

We incorporated the spatial lag of intensive land use level into the threshold model. Table 4 shows the threshold effect test. It can be found in Table 5 that whether it is a single threshold model, a double threshold model, or a three-threshold model, they all exist significantly. Therefore, this paper uses the above three threshold models to verify the impact of intensive land use on energy efficiency under different spatial integration levels [43,44].

**Table 5.** Threshold effect test.

	F-Value	p-Value	1% Critical Value	5% Critical Value	10% Critical Value
Single threshold	18.937 ***	0.003	15.303	7.955	5.922
Double threshold	40.923 ***	0.007	34.044	18.871	11.045
Third thresholds	−11.530 *	0.090	11.707	−6.286	−12.327

Note: \*, \*\*, and \*\*\* represent significant at the 10%, 5%, and 1% levels, respectively, and the hypothesis test statistics are in parentheses.

The regression results of the spatial threshold model are shown in Table 6. It can be found that with the improvement of the integration level, the impact of the intensive use of land in a particular city on the surrounding areas has changed from a negative value to a positive value. Only at the level of integration of the space will the intensive use of land cause a decline in energy efficiency in the surrounding areas. Based on this, the state and local governments should pay attention to the sharing of resources, technology, and information in the region to realize the coordinated development of the regional economy and strengthen joint prevention and control in the region. In turn, it will realize the benign interaction and coordinated development of the region, give full play to the scale effect,



synergy effect and agglomeration effect of the region, and effectively promote the coordinated governance in the region. When implementing differentiated environmental policy combinations in different regions of our country, governments at all levels should be guided by economic means and market regulation, pay attention to encouraging governments and enterprises to use economic incentive-type environmental regulation policies, and guide different types of industrial enterprises to achieve clean and green development based on the characteristics of economic incentive environmental policies. At the same time, different regions use economic incentives and stimulus measures to promote the transformation and upgrading of different types of industrial enterprises as soon as possible.

**Table 6.** Spatial threshold effect results.

	(1) Single Threshold	(2) Double Threshold	(3) Third Thresholds
<i>Threshold variable</i>	−0.654 **	−1.125 **	−1.432 *
<i>&lt; δ1</i>	(−2.30)	(−2.02)	(−1.83)
<i>δ1 ≤ Threshold</i>	1.744 ***	−1.201 *	−1.532
<i>variable &lt; δ2</i>	(4.40)	(−1.92)	(−1.39)
<i>δ2 ≤ Threshold</i>	—	3.601 ***	2.565 ***
<i>variable &lt; δ3</i>	—	(7.61)	(3.07)
<i>δ3 &lt; Threshold</i>	—	—	2.278 **
			(2.19)
<i>GDP</i>	0.272 ***	0.252 ***	0.233 ***
	(−9.63)	(−9.11)	(−6.82)
<i>Gpp</i>	0.183 ***	0.147 ***	0.215 ***
	(−5.37)	(−5.70)	(−4.10)
<i>Ssr</i>	−1.895 ***	−2.348 ***	−2.394 ***
	(−4.46)	(−5.14)	(−6.65)
<i>Tsr</i>	3.273 ***	2.127 ***	2.034 ***
	(8.81)	(11.87)	(7.88)
<i>Fdi</i>	−0.712	−0.096	−0.115
	(−1.09)	(−1.04)	(−1.20)
<i>Pat</i>	−0.170	−0.047	−0.130
	(−0.37)	(−0.34)	(−0.54)
<i>Ine</i>	−0.11 ***	−0.09 ***	−0.10 ***
	(−5.05)	(−6.65)	(−6.43)
<i>Time fixed</i>	Control	Control	Control
<i>Individual fixed</i>	Control	Control	Control
<i>Constant</i>	0.692 ***	0.781 ***	0.882 ***
	(3.98)	(6.04)	(5.72)
<i>R<sup>2</sup></i>	0.7348	0.7725	0.7803
<i>Sample size</i>	3800	3800	3800
<i>δ1</i>	0.1304	0.1475	0.1477
<i>δ2</i>	—	0.2843	0.2628
<i>δ3</i>	—	—	0.3891

Note: \*, \*\*, and \*\*\* represent significant at the 10%, 5%, and 1% levels, respectively, and the hypothesis test statistics are in parentheses.

Spatial integration is conducive to improving the marketization of resources and environmental factors and the allocation efficiency of resources and environmental factors. For example, the trading market of pollution emission rights will form incentives for enterprises to reduce emissions. Market integration can reduce the transaction cost of environmental protection technology, facilitate the promotion and application of various energy saving and emission reduction technologies, promote the spillover of production technology between regions, narrow the gap of environmental protection technology between regions, and narrow the gap of regional pollution emissions. The integration of infrastructure and public services will improve the sharing and efficiency of public resources and reduce energy consumption and emissions.

### 5. Discussions

As the land use change has been the second largest factor contributing to the increase in global atmospheric carbon dioxide, more and more scholars are considering the need to emphasize ecological and environmental protection or the coordinated development of the

two in the process of intensive land use. In the meanwhile, energy efficiency, which plays a vital role in sustainable development of economy, has been the hot topic of research in the relevant field. On this basis, the relationship between land use and energy efficiency has also been concerned recently.

Existing studies have mostly focused on the economic effects brought about by intensive land use and its impact on the environment, and few have directly explored the relationship between intensive land use and energy efficiency from a spatial perspective [45–48]. However, this paper takes prefecture-level and city-level data from 2009 to 2018 as the research object and examines the complex impact of intensive land use on energy efficiency from a spatial perspective, which will help China realize the development of a larger-scale urban green economy, and has certain research value and application significance. Additionally, this paper has the following limitations, which can be improved in further study: first, this paper studies the impact of intensive land use on energy efficiency based on urban data in China. However, whether this proposition is also applicable in other countries deserves further robustness test. Secondly, this paper uses the DEA method to quantify energy efficiency, which can be quantified in a variety of ways in the future to improve the credibility of the proposition. Thirdly, although the improvement in energy efficiency mitigated the trend of carbon emission growth to some extent, it did not reduce the trend of total increase in carbon emission scale. To what extent the contribution of land intensive use to energy efficiency can continuously reduce carbon emissions is a direction we can study in the future. Finally, this paper does not attempt to use a general equilibrium framework for analysis, so it can be attempted in future studies.

## 6. Conclusions

In order to examine the relationship between intensive land use and urban energy efficiency, contributing to the sustainable development of economy, based on the panel data from 2009–2018, this paper first uses the least squares regression model to examine whether intensive land use contributes to energy efficiency, and then the spatial Durbin model and the spatial threshold model are used to empirically examine the spatial effects of intensive land use on energy efficiency and the changes that occur with the process of spatial integration. The results of our research show that: (1) the intensive use of land can contribute to the energy efficiency positively, as each percentage point increase in the level of intensive land use will increase energy efficiency by 1.3 percentage points. (2) Although the intensive use of land can improve the local energy efficiency of the region, it will have a negative effect on energy efficiency of the surrounding areas because of the transfer of energy-intensive industries to the surrounding areas. Space integration can solve this problem to a large extent. (3) The negative impact of intensive use of land on the energy efficiency of surrounding cities will be weakened when the level of integration of the city and its surrounding areas raises.

**Author Contributions:** Data curation, H.K.; Formal analysis, H.K.; Funding acquisition, H.K.; Investigation, B.Y.; Methodology, B.Y.; Project administration, S.D.; Resources, S.D.; Software, S.D.; Supervision, S.D. All authors have read and agreed to the published version of the manuscript.

**Funding:** This research received no external funding.

**Institutional Review Board Statement:** Not applicable.

**Informed Consent Statement:** Not applicable.

**Data Availability Statement:** Due to the confidentiality and privacy of the data, they will only be provided upon reasonable request.

**Conflicts of Interest:** The authors declare no conflict of interest.

## References

1. Tehrani, N.A.; Shafri, H.Z.M.; Salehi, S.; Chanusot, J.; Janalipour, M. Remotely-Sensed Ecosystem Health Assessment (RSEHA) model for assessing the changes of ecosystem health of Lake Urmia Basin. *Int. J. Image Data Fusion* **2021**, *1*–26. [\[CrossRef\]](#)
2. Ke, H.; Dai, S.; Yu, H. Effect of green innovation efficiency on ecological footprint in 283 Chinese Cities from 2008 to 2018. *Environ. Dev. Sustain.* **2021**, *24*, 2841–2860. [\[CrossRef\]](#)
3. Fan, F.; Dai, S.Z.; Zhang, K.K. Innovation agglomeration and urban hierarchy: Evidence from Chinese cities. *Appl. Econ.* **2021**, *53*, 6300–6318. [\[CrossRef\]](#)
4. Baldoni, E.; Coderoni, S.; Giuseppe, E.D.; Esposti, R.; Maracchini, G. A software tool for a stochastic life cycle assessment and costing of buildings energy efficiency measures. *Sustainability* **2021**, *13*, 7975. [\[CrossRef\]](#)
5. Zhao, R.Q.; Liu, Y.; Hao, S.L.; Ding, M.L. Research on the Low-carbon Land Use Pattern. *Res. Soil Water Conserv.* **2010**, *17*, 190–194.
6. Qi, G.Y.; Shen, L.Y.; Zeng, S.X.; Jorge, O.J. The drivers for contractors' green innovation: An industry perspective. *J. Clean. Prod.* **2010**, *18*, 1358–1365. [\[CrossRef\]](#)
7. Svirejeva-Hopkins, A.; Schellnhuber, H.J. Modelling carbon dynamics from urban land conversion: Fundamental model of city in relation to a local carbon cycle. *Carbon Balance Manag.* **2006**, *1*, 8. [\[CrossRef\]](#)
8. Patterson, M.G. What is energy efficiency? Concepts, indicators and methodological issues. *Energy Policy* **1996**, *24*, 377–390. [\[CrossRef\]](#)
9. Kilponen, L. Energy Efficiency Indicators-Concepts, Methodological issues, and Connection to Pulp and Paper Industry. Ph.D. Thesis, Helsinki University of Technology, Espoo, Finland, 2003.
10. Wu, H.; Hao, Y.; Ren, S.; Yang, X.; Xie, G. Does internet development improve green total factor energy efficiency? *Evid. China. Energy Policy* **2021**, *153*, 112247. [\[CrossRef\]](#)
11. Hu, J.L.; Wang, S.C. Total-factor Energy Efficiency of Regions in China. *Energy Policy* **2006**, *34*, 3206–3217. [\[CrossRef\]](#)
12. Ricardo, D. *The Principles of Political Economy and Taxation*; David Ricardo, J.M., Ed.; Dent & Sons Ltd.: London, UK, 1965; pp. 81–82.
13. Wolch, J.R.; Byrne, J.A.; Newell, J.P. Urban green space, public health, and environmental justice: The challenge of making cities 'just green enough'. *Landsc. Urban Plan.* **2021**, *125*, 234–244. [\[CrossRef\]](#)
14. Fischer, C. Environmental protection for sale: Strategic green industrial policy and climate finance. *Environ. Resour. Econ.* **2017**, *66*, 553–575. [\[CrossRef\]](#)
15. Aghion, P.; Antonin, C.; Bunel, S. *The Power of Creative Destruction: Economic Upheaval and the Wealth of Nations*; Harvard University Press: Cambridge, MA, USA; London, UK, 2021. [\[CrossRef\]](#)
16. Ke, H.Q.; Yang, W.Y.; Liu, X.Y. Does Innovation Efficiency Suppress the Ecological Footprint? Empirical Evidence from 280 Chinese Cities. *Int. J. Environ. Res. Public Health* **2020**, *17*, 6826. [\[CrossRef\]](#) [\[PubMed\]](#)
17. Zhao, S.F.; Huang, X.J.; Chen, Y.; Chen, Z.G. Research Progress in Urban Land Intensive Use. *J. Nat. Resour.* **2010**, *25*, 1979–1996.
18. Liu, S.; Fan, F.; Zhang, J.Q. Are Small Cities More Environmentally Friendly? An Empirical Study from China. *Int. J. Environ. Res. Public Health* **2019**, *16*, 727. [\[CrossRef\]](#)
19. Zhang, J.Q.; Chen, T.T. Empirical Research on Time-Varying Characteristics and Efficiency of the Chinese Economy and Monetary Policy: Evidence from the MI-TVP-VAR Model. *Appl. Econ.* **2018**, *50*, 3596–3613. [\[CrossRef\]](#)
20. Sun, C.Z.; Yan, X.D.; Zhao, L.S. Coupling efficiency measurement and spatial correlation characteristic of water-energy-food nexus in China. *Resour. Conserv. Recycl.* **2021**, *164*, 105151. [\[CrossRef\]](#)
21. Xiao, Z.L.; Du, X.Y. Convergence in China's high-tech industry development performance: A spatial panel model. *Appl. Econ.* **2017**, *49*, 5296–5308.
22. Wu, Y.; Chau, K.W.; Lu, W.; Shen, L.; Shuai, C.; Chen, J. Decoupling relationship between economic output and carbon emission in the Chinese construction industry. *Environ. Impact Assess. Rev.* **2018**, *71*, 60–69. [\[CrossRef\]](#)
23. Wang, X.L.; Wang, L.; Wang, S. Marketisation as a channel of international technology diffusion and green total factor productivity: Research on the spillover effect from China's first-tier cities. *Technol. Anal. Strateg. Manag.* **2021**, *33*, 491–504. [\[CrossRef\]](#)
24. Wang, Z.; Zong, Y.; Dan, Y.; Jiang, S.J. Country risk and international trade: Evidence from the China-B & R coun-tries. *Appl. Econ. Lett.* **2021**, *28*, 1784–1788.
25. Fan, F.; Lian, H.; Wang, S. Can regional collaborative innovation improve innovation efficiency? An empirical study of Chinese cities. *Growth Chang.* **2020**, *51*, 440–463. [\[CrossRef\]](#)
26. Lu, F.; Liu, M.H.; Sun, Y.Y. Trade Openness, Industrial Geography and Green Development-the Perspective of Agglomeration and Industrial Heterogeneity. *Econ. Theory Bus. Manag.* **2018**, *9*, 34–47.
27. Wu, J.; Xiong, B.; An, Q.; Sun, J.; Wu, H. Total-factor energy efficiency evaluation of Chinese industry by using two-stage DEA model with shared inputs. *Ann. Oper. Res.* **2015**, *255*, 257–276. [\[CrossRef\]](#)
28. Liu, Y.; Wang, K. Energy efficiency of China's industry sector: An adjusted network DEA (data envelopment analysis)-based decomposition analysis. *Energy* **2015**, *93*, 1328–1337. [\[CrossRef\]](#)
29. Wang, S.; Wang, X.L.; Lu, F. The impact of collaborative innovation on ecological efficiency—empirical research based on China's regions. *Technol. Anal. Strateg. Manag.* **2020**, *32*, 242–256. [\[CrossRef\]](#)
30. Yang, W.Y.; Fan, F.; Wang, X.L. Knowledge innovation network externalities in the Guangdong-Hong Kong-Macao Greater Bay Area: Borrowing size or agglomeration shadow? *Technol. Anal. Strateg. Manag.* **2021**, *33*, 1940922. [\[CrossRef\]](#)

31. Yu, H.C.; Liu, Y.; Liu, C.L. Spatiotemporal Variation and Inequality in China's Economic Resilience across Cities and Urban Agglomerations. *Sustainability* **2018**, *10*, 4754. [[CrossRef](#)]
32. Tang, H.Y.; Zhang, J.Q. High-speed rail, urban form, and regional innovation: A time-varying difference-in-differences approach. *Technol. Anal. Strateg. Manag.* **2022**, *34*, 2026322. [[CrossRef](#)]
33. Fan, F.; Zhang, K.K.; Dai, S.Z. Decoupling analysis and rebound effect between China's urban innovation capability and resource consumption. *Technol. Anal. Strateg. Manag.* **2021**, *33*, 1979204. [[CrossRef](#)]
34. Fan, F.; Zhang, X.R.; Yang, W.Y. Spatiotemporal Evolution of China's ports in the International Container Transport Network under Upgraded Industrial Structure. *Transp. J.* **2021**, *60*, 43–69. [[CrossRef](#)]
35. Zhu, Q.Y.; Sun, C.Z.; Zhao, L.S. Effect of the marine system on the pressure of the food–energy–water nexus in the coastal regions of China. *J. Clean. Prod.* **2021**, *319*, 128753. [[CrossRef](#)]
36. Liu, N.; Fan, F. Threshold effect of international technology spillovers on China's regional economic growth. *Technol. Anal. Strateg. Manag.* **2020**, *32*, 923–935. [[CrossRef](#)]
37. Fan, F.; Du, D.B. The Measure and the Characteristics of Temporal-spatial Evolution of China Science and Technology Resource Allocation Efficiency. *J. Geogr. Sci.* **2014**, *24*, 492–508. [[CrossRef](#)]
38. Ke, H.; Dai, S.; Yu, H. Spatial effect of innovation efficiency on ecological footprint: City-level empirical evidence from China. *Environ. Technol. Innov.* **2021**, *22*, 101536. [[CrossRef](#)]
39. Hansen, B. Threshold effects in non-dynamic panels: Estimation, testing, and inference. *J. Econom.* **1999**, *93*, 345–368. [[CrossRef](#)]
40. Geng, G.; Xiao, Q.; Zheng, Y.; Tong, D.; Zhang, Y.; Zhang, X.; Zhang, Q.; He, K.; Liu, Y. Impact of China's Air Pollution Prevention and Control Action Plan on PM2.5 chemical composition over eastern China. *Sci. China Earth Sci.* **2019**, *62*, 1872–1884. [[CrossRef](#)]
41. LeSage, J.; Pace, R.K. *Introduction to Spatial Econometrics*; CRC Press: New York, NY, USA, 2009.
42. Elhorst, J.P. *Dynamic Spatial Panels: Models, Methods and Inferences*; Springer: Berlin/Heidelberg, Germany, 2014.
43. Panwar, N.L.; Kaushik, S.C.; Kothari, S. Role of renewable energy sources in environmental protection: A review. *Renew. Sustain. Energy Rev.* **2011**, *15*, 1513–1524. [[CrossRef](#)]
44. Yu, H.C.; Zhang, J.Q.; Zhang, M.Q. Cross-national knowledge transfer, absorptive capacity, and total factor productivity: The intermediary effect test of international technology spillover. *Technol. Anal. Strat. Manag.* **2021**, *33*, 1915476. [[CrossRef](#)]
45. Liu, L.; Zong, H.; Zhao, E.; Chen, C.; Wang, J. Can China realize its carbon emission reduction goal in 2020: From the perspective of thermal power development. *Appl. Energy* **2014**, *124*, 199–212. [[CrossRef](#)]
46. Yin, R.; Siebert, J.; Eisenhauer, N.; Schdler, M. Climate change and intensive land use reduce soil animal biomass through dissimilar pathways. *elife* **2020**, *9*, e54749. [[CrossRef](#)] [[PubMed](#)]
47. Liu, Q.F.; Buyantuev, A.; Wu, J.; Niu, J.; Yu, D.; Zhang, Q. Intensive land-use drives regional-scale homogenization of plant communities. *Sci. Total Environ.* **2018**, *9*, 806–814. [[CrossRef](#)] [[PubMed](#)]
48. Buhk, C.; Alt, M.; Steinbauer, M.J.; Beierkuhnlein, C.; Warren, S.D.; Jentsch, A. Homogenizing and diversifying effects of intensive agricultural land-use on plant species beta diversity in central europe—A call to adapt our conservation measures. *Sci. Total Environ.* **2017**, *576*, 225–233. [[CrossRef](#)] [[PubMed](#)]





Article

# Pareidolia in a Built Environment as a Complex Phenomenological Ambiguous Stimuli

Chen Wang <sup>1</sup>, Liangcheng Yu <sup>1</sup>, Yiyi Mo <sup>2,\*</sup>, Lincoln C. Wood <sup>3</sup> and Carry Goon <sup>2</sup>

<sup>1</sup> Intelligence and Automation in Construction Fujian Province Higher-Educational Engineering Research Centre, College of Civil Engineering, Huaqiao University, Xiamen 361021, China; wch@hqu.edu.cn (C.W.); 20014086044@stu.hqu.edu.cn (L.Y.)

<sup>2</sup> College of Civil Engineering, Huaqiao University, Xiamen 361021, China; gooncarry@hotmail.com

<sup>3</sup> Department of Management, University of Otago, Dunedin 9054, New Zealand; lincoln.wood@otago.ac.nz

\* Correspondence: myy\_11@hotmail.com

**Abstract:** Pareidolia is a kind of misperception caused by meaningless, ambiguous stimuli perceived with meaning. Pareidolia in a built environment may trigger the emotions of residents, and the most frequently observed pareidolian images are human faces. Through a pilot experiment and an in-depth questionnaire survey, this research aims to compare built environmental pareidolian phenomena at different time points (6 a.m., 12 p.m., 2 a.m.) and to determine people's sensitivity and reactions towards pareidolia in the built environment. Our findings indicate that the differences in stress level do not influence the sensitivity and reactions towards pareidolia in the built environment; however, age does, and the age of 40 seems to be a watershed. Females are more likely to identify pareidolian faces than males. Smokers, toppers, and long-term medicine users are more sensitive to pareidolian images in the built environment. An unexpected finding is that most pareidolian images in built environments are much more easily detected in the early morning and at midnight but remain much less able to be perceived at midday. The results help architects better understand people's reactions to pareidolia in the built environment, thus allowing them to decide whether to incorporate it appropriately or avoid it consciously in building design.

**Keywords:** pareidolia; illusion; misperception; ambiguous stimuli; built environment

**Citation:** Wang, C.; Yu, L.; Mo, Y.; Wood, L.C.; Goon, C. Pareidolia in a Built Environment as a Complex Phenomenological Ambiguous Stimuli. *Int. J. Environ. Res. Public Health* **2022**, *19*, 5163. <https://doi.org/10.3390/ijerph19095163>

Academic Editor: Paul B. Tchounwou

Received: 30 March 2022

Accepted: 22 April 2022

Published: 24 April 2022

**Publisher's Note:** MDPI stays neutral with regard to jurisdictional claims in published maps and institutional affiliations.



**Copyright:** © 2022 by the authors. Licensee MDPI, Basel, Switzerland. This article is an open access article distributed under the terms and conditions of the Creative Commons Attribution (CC BY) license (<https://creativecommons.org/licenses/by/4.0/>).

## 1. Introduction

Pareidolia is an illusion caused by ambiguous stimuli [1], and the ambiguous forms are perceived as visual objects with meaning. Pareidolia is very common and phenomenological, for example, the visual illusions in dementia with Lewy bodies (DLB) [2]. Pareidolia is a phenomenon where an observer can feel significance from a vague and random stimulus [3]. Many different subjects may appear as pareidolia, but based on previous studies, the most frequent subjects that appear as pareidolia are human faces [4,5]. A newborn baby can recognize faces and human expressions, which means that the human brain may be sensitive enough to detect face-like patterns at birth. Some well-known examples of pareidolia include: seeing the face of Jesus Christ on a potato chip, a cinnamon bun with the face of Mother Teresa, the surface of a grilled sandwich showing the face of the Virgin Mary [6], Satan appearing in the smoke of 9/11, and a devil seen in the Queen's hair of a 1954 Canadian banknote [7]. The existence of pareidolia could be because of many reasons. In psychology, pareidolia is a partial illusion, and it happens in the condition of low luminance [8,9]. While in neuropathology, the existence of pareidolia is unintentional, and it is a random phenomenon [10]. Normally the pareidolian images received by the human brain are incomplete, but then the brain automatically uses built-in knowledge and the data gathered from previous experiences to fill in the missing parts, generating a complete interpretation that produces a coherent picture [11,12]. From the religious

perspective, paranormal believers are more likely to perceive the ambiguous stimuli as face-like patterns due to the sacralization of mythological characters [13].

Pareidolia frequently occurs in the architectural design of house envelopes and facades [14]. In the history of architecture from different cultures, faces frequently occur as decorative. The rock face is one natural formation that often seems to contain a human face [15]. Observers have emotional responses towards those house envelopes they perceive as having face-like patterns [14]. Human faces are the most frequent subject of visual illusion and pareidolia, according to previous studies such as [4]. Some house envelopes consist of a leading and outstanding pattern that can be justified as a human face. Pareidolia phenomena in the built environment may trigger emotional reactions such as happiness, scariness, anxiety, and depression. Therefore, there is a need for building designers to identify those key elements causing pareidolia to prevent negative impact.

Pareidolia is a term that originated from Greek [14]. Basically, the term “pareidolia” is the combination of “para” (para = beside or beyond) and “eidosis” (images, appearance, looks), which describes the tendency of the human visual system to extract patterns from noise [8]. In 1885, the Russian psychiatrist Victor Kandinsky (1849–1889) introduced the terms “Pareidolie” and “Nebenbildwahrnehmung” to express a partial visual illusion in which given objects are perceived as different objects, or human faces are precisely and consistently perceived as someone else’s, such as intermetamorphosis syndrome [8].

Pareidolic illusion is another term for pareidolia because it differs from ordinary illusion. Ordinary illusion is a lack of perceptual clarity provoked by intense emotions. When a common illusion becomes more complex and detailed, it will increase the intensity of the pareidolic illusion [10]. Pareidolia is also a form of apophenia, which was first described in terms of psychosis but now is regarded as a tendency in healthy people and could explain or inspire associated visual effects in arts and graphics [14]. According to Dyer [16], the observer’s ability to perceive any random and vague stimuli such as a face is considered pareidolia. Moreover, pareidolia is the illusory perception of a well-known structure such as an animal or a human face, even though no human face or animal exists [17]. There are many examples of pareidolia in various aspects. One example of pareidolia in planetary landforms is the man on the moon or faces and animals in the clouds. An example of pareidolia in a terrestrial object is a face in a tumor ultrasound [17]. Human faces are the most frequently observed subject of visual illusion because of the social importance of faces and our delicate ability to process them [18].

### 1.1. Pareidolia in Psychology and Neuropsychology

Pareidolia is a psychological phenomenon that perceives a dedifferentiated sensory stimulus as indicating a familiar object or structure such as a face [17]. Pareidolia causes misperceptions of unreal and unrelated patterns when receiving the vague stimulus, while the stimulus can exist as a glimpse at an unstructured background [18]. There is a consensus that people who display pareidolia have mental insight into the phenomenon, but he or she knows that it is not real [10]. Pareidolic illusion is differentiated from the regular illusion due to the inner impulse. The inner abnormality is not enough for its occurrence of illusion, and an exterior impulse needs to be added, which is why pareidolia is only a partial illusion [8]. Normally, illusion frequently occurs in high luminance, but pareidolia occurs in an opposite condition [9]. In sensory deceptions, the neuropsychological substrate of pareidolia is apophenia. Nowadays, the term apophenia is used in a looser sense, related to perception or psychiatric disease and an excess of perceptual or heuristic sensitivity leading to the judgment of patterns or random connections [8].

In psychopathology, pareidolia is the image seen from shape. It is argued whether the pareidolia phenomenon is non-diseased, voluntary, playful, diseased, unintentional, or distressing [10]. Pareidolia is an automatic phenomenon that occurs rapidly, insensibly, compulsorily, and free of capacity; therefore, humans cannot realize that the perception is misled by pareidolia [11]. However, Liu et al. [18] argued that pareidolia is not merely imaginary because it has a physical reality basis. Since a pareidolian image actually does

not contain faces, it needs the interpretive power of the human brain as a substantial tool to detect and connect the faded face-like features to match with the internal face representation [18]. Human experiences are normally filtered through notoriously unreliable senses, so it is impossible for us to really know the truth about the world around us [19].

For the objects containing patterns of two dots and a line segment, the chance for humans to see faces is high because the two dots and line segments appear to the pattern of a human face with eyes and a mouth, which is the most common pareidolia [14]. However, neuropsychological and psychiatric conditions can have a negative impact on the ability to identify facial expressions of sensation [14]. Human eyes can distinguish brightness differences in a range of 1–100, which means human eyes' dynamic contrast is high. The human eye is a brilliant detecting system that will undergo both physical and chemical processes from the view and send it to the brain. Though the outcome of the brain–eye system is perception, the brain does not always expound the information of the object seen in the real perception [11]. The most suspect human perceptual apparatus is sight because human eyes do not see a centralized field, while the saccadic movement of the eyes stores the image from detail to detail and is perhaps used later for data recall by forming a whole image [19]. The rhizome structure in the brain has many chemical reaction saccades for the first time of seeing, and it will leave many impressions unprocessed, disordered, and unknown. Since the human brain is a complex structure, the percipient information received in real-time will be eliminated, expanded, rearranged, and codified to form a common and logical layout of the external world. According to Wertheimer and Riezler [20], the Gestalt theory states that visual perception is the effect of the relationship among the objects observed instead of the simple add-up of the elements seen. As a result, the misperception of the shape and color of an object may be caused by the complicated and fast processing work of the brain and lead to illusion and pareidolia.

The brain is the most complex part of the human body, and one of the brain components in charge of face perception is the fusiform gyri [21]. Fusiform gyri shows higher activation when a facial expression is shown on the subject [22]. The face-sensitive neurons in nonhuman primates' inferior temporal cortex show the same selectivity for face-like object configurations [23]. Even a newborn baby can undergo face recognition and perform across view change [24]. According to Hoback [3], a 3-month-old baby already starts learning to identify the mother's face, while when the baby grows to four to nine months, the baby can distinguish several facial expressions such as happiness, fear, anger, surprise, or sadness. Moreover, detecting faces from the environment was the survival intuition of humans to ensure vigilance towards danger in the surrounding area [25].

### 1.2. Pareidolia in Religion

A German neurologist and psychiatrist, Klaus Conrad (1905–1961), promoted that pareidolia has a bearing on an even wider range of illusory phenomena, including the discernment of religious themes such as the faces of the Virgin Mary and Jesus [8]. Paranormal believers frequently have perceptual illusions in ambiguous visual stimuli [1]. Even though both paranormal believers and non-believers have the same ability to detect face perception, non-paranormal believers have less liberal response bias than paranormal believers [26], which is probably because paranormal believers perceive ambiguous stimuli as face-like patterns more easily. There is an interrelationship between illusory agency detection and paranormal belief in the studies regarding schizotypy and schizophrenia [13].

Both schizotypy and schizophrenia can cause pareidolia. The schizotypal personality sometimes comes with delusional beliefs, abnormal perceptual experiences, and magical thoughts [27]. According to Galdos et al. [28], a person with a schizotypal personality can sense meaningful patterns in random meaningless noise, while a person with schizophrenia is more able to link unrelated events. By using the moving triangle task, the person with schizotypal can gain meaning from geometrical images that move randomly [13]. Furthermore, some natural landscape elements are sacralized in the three mythological characters: Pan-Gu, Fu-Xi, and Shen-Nong. All these three mythological characters be-



long to the Chinese culture's formative period. The three humanized mountains were sacralized to identify these three outstanding Pareidolian Images in their origin. In the case of the commercial aircraft that destroyed New York City's World Trade Center on 9/11/01, many protestants saw demons and devil faces in the smoke, and they believed that the crisis destroyed the current seat of power of Satan living in the American financial institutions [29]. Pareidolia extends the illusionary connections between landscape and the mythological characters.

### 1.3. Present Study

Pareidolia exists in the built environment, such as landscapes, buildings, and furniture. Many pareidolian faces occur as ornaments or adornments in the architectural history of different cultures [14]. Some house envelopes consist of a leading pattern that can be justified as a human face. The facial expressions perceived in houses can trigger an emotional reaction; thus, the techniques of using pareidolia to produce positive emotions are applied in house design [3]. Experimental studies on the perception of illusory agency discovered that the tendency to sense human faces among random noise is high, which is more than 40%, especially in low information content [17]. There are interrelationships between pareidolian faces and aesthetic value [30]. Though there are many kinds of stimuli able to trigger the emotion of observers, a human face is the most effective one [5]. Examples of pareidolia in the landscape are faces in trees, faces on mountains, faces on stones, the man on the moon, and faces in clouds [18]. Pareidolia sometimes appears on house facades, windows of buildings, doors of buildings, electrical outlets, cupboards, and chairs [14]. Previous research validated the relationship between demographics and delusional disorder using questionnaire surveys and pilot experiments [3,14]. Mental anomalies may be the source causes of many tragedies and incidents [31]. In addition to job pressures, lifestyles and other aspects may affect the mental state to varying degrees. In fact, everyone will be in different mental states at different times of normal life. In general, people are in blurred thinking status when they wake up, while high brain activity during the day will leave people exhausted at night, and the brain activity time is negatively correlated with the human spirit [32]. Negative spirit status increases the possibility of pareidolia [33]. Therefore, this research compares built environmental pareidolian phenomena at different spirit state time points (6 a.m., 12 p.m., and 2 a.m.) with the purpose of determining people's sensitivity and reactions towards pareidolia in a built environment.

## 2. Materials and Methods

We applied a mix of qualitative and quantitative approaches in this study. We combined a pilot experiment and a questionnaire survey to triangulate the data collected in this study. The pilot experiment is an explanatory and descriptive method to categorize the phenomena of pareidolia in the built environment, which was then used to structure the questionnaire survey and provide readers with a better understanding of pareidolia. The qualitative approach relies on evidence rather than frequency to illuminate issues and uncover possible explanations.

### 2.1. Participants

#### 2.1.1. Pilot Experiment

According to Liu [18], 20 participants (10 females and 10 males, aged from 18 to 60) were randomly recruited from society for the pilot experiment and were offered financial remuneration for participation. The participants mainly consisted of five age groups: 11–20, 21–30, 31–40, 41–50, and 51–60. Four participants per age group. All participants had normal or corrected vision.

#### 2.1.2. Questionnaire Survey

The anonymous questionnaire survey was distributed to 500 people ranging from 11 to 60 years old through the post. In this study, the power was set to 0.8, and the threshold

for significance ( $\alpha$ ) was set to 0.05. According to the power analysis, if we wanted an 80% probability of correctly rejecting the null hypothesis, we needed a sample size of at least 217. A total of 228 valid forms were returned and assessed, representing a 45.6% response rate. The demographic details of the respondents are shown in Table 1. The percentage of females at 59.6% was slightly higher than that of males at 40.4%. The questionnaire survey targeted five age groups: 11–20 years old (6.6%), 21–30 years old (75.4%), 31–40 years old (6.6%), 51–60 years old (6.1%), and 41–50 years old (5.3%). Approximately 72.8% of respondents had a bachelor's degree, followed by 10.1% with secondary education, 9.2% with a diploma/advanced diploma, 5.3% with primary education, 2.2% with postgraduate degree/professional level, and 0.4% without formal education. In total, 49.6% of respondents considered their current job stressful, and 50.4% did not. There were 62.7% single respondents and 37.3% married. Moreover, 55.7% of respondents normally went to bed after 12 a.m., and 34.6% of respondents did not have any habits such as smoking, alcohol abuse, staying up late, or chronic diseases.

**Table 1.** Demographic details of respondents.

Demographic Categories	Category Breakdown	Frequency	Percent (%)	Cumulative Percent (%)
Gender	Male	92	40.4	40.4
	Female	136	59.6	100
Age Group	11–20	15	6.6	6.6
	21–30	172	75.4	82
	31–40	15	6.6	88.6
	41–50	12	5.3	93.9
	51–60	14	6.1	100
Education Level	No formal education	1	0.4	0.4
	Primary education	12	5.3	5.7
	Secondary education	23	10.1	15.8
	Certificate/diploma/advanced diploma level	21	9.2	25
	Degree level	166	72.8	97.8
	Postgraduate degree/professional level	5	2.2	100
Current Job Stress Level	Not stressful	113	49.6	49.6
	Stressful	115	50.4	100
Current Status	Single	143	62.7	62.7
	Married	85	37.3	100
Lifestyle	Smoking	8	3.5	3.5
	Alcohol abuse	7	3.1	6.6
	Sleep after 12 a.m.	127	55.7	62.3
	Long-term medicine user	7	3.1	65.4
	None of above	79	34.6	100

## 2.2. Stimuli

In total, 26 pareidolian images were used for this pilot experiment. The images were obtained from building photos taken on-site and were presented on paper with a picture size of 7.5 × 7.5 cm (H × W). A pareidolian face consists of a facial outline, left and right eyes, and a mouth [30]; thus, the images used in the experiment had similar characteristics.

## 2.3. Experimental Setup and Procedure

### 2.3.1. Pilot Experiment

In the pilot experiment, 20 participants were required to observe the 26 images provided by the researcher during the morning, midday, and midnight and share their feedback. Each image was observed as an individual experiment by 20 participants. Their feedback was then analyzed using content analysis and structured through tabulation.

2.3.2. Questionnaire Survey

Sensitivity in this study refers to a change in pareidolia’s likelihood when one factor changes. The questionnaire survey determined sensitivity and reactions towards pareidolia in a built environment. There were 69 questions in the questionnaire form. Section A focused on the respondents’ background, such as age, gender, occupation status, education level, lifestyle, and stress level (“Gender”: male, female; “Age group”: 11–20, 21–30, 31–40, 41–50, 51–60; “Educational Level”: no formal education, primary education, secondary education, certificate/diploma/advanced diploma level, degree, post-graduate degree/professional level; “Current job stress level”: stressful, not stressful; “Current status”: single, married; “Lifestyle”: smoking, alcohol abuse, sleep after 12 a.m., long-term medicine user). Section B focused on their sensitivity and reactions towards pareidolia in different spaces in the building. The questions offered a 5-point Likert-type scale for respondents to rank. First, they decided whether the displayed stimuli was a face (“Can you identify a face in Figure?”: yes, no), then they evaluated their sensitivity to face identification (“Can you easily identify a human face in the Figure?”: 5-very highly likely, 4-highly likely, 3-likely, 2-unlikely, 1-denote) and emotions when a face had identified (“What is your reaction when you see Figure?”: scared, depressed, funny, happy, no reaction). Investigating people’s emotional feedback determines what type of architectural design is more likely to be acceptable rather than radical when people generate pareidolia. The specific content of the questionnaire is presented in the Appendix A.

Two software were applied in the analysis: Statistical Package for the Social Sciences (SPSS) Version 22 and Smart PLS 2.0. Structural Equation Modeling (SEM) was used to test the theoretically supported model.

3. Results and Discussion

3.1. Findings in Pilot Experiments

Data collected from the pilot experiments were used to compare the participants’ sensitivity and reactions toward pareidolian images at different time points (6 a.m., 12 p.m., and 2 a.m.). There were 26 experiments conducted among the 20 participants, and the results are tabulated in Table 2. In general, the participants had very similar sensitivity and reactions towards these pareidolian images. Most participants could identify human faces at 6:00 a.m. in the morning and 2:00 a.m. at night, but not at 12:00 p.m. midday. Most participants felt scared when looking at the pareidolian images at 2 a.m.

Table 2. Tabulation of experiments results.





Pareidolian Image	Phenomenon			Reaction		
	6 a.m.	12 p.m.	2 a.m.	6 a.m.	12 p.m.	2 a.m.
	Face is detected	Normal building	Face is detected	Depress and sad	Neutral	Creepy and scary
	Looked like a blue monster	Normal building	Eyes are detected	Scary	Neutral	Creepy
	Cartoon-like face is detected	Fish mouth and eyes are detected	Fierce face is detected	Funny	Neutral	Creepy
	Face is detected	Normal building	Face is detected	Scary	Neutral	Scary

Table 2. Cont.










Pareidolian Image	Phenomenon			Reaction		
	6 a.m.	12 p.m.	2 a.m.	6 a.m.	12 p.m.	2 a.m.
	The face is not really obvious	Face is detected	Normal building	Neutral	Happy and cute	Neutral
	Face is detected	Normal building	Fierce face is detected	Scary	Scary	Creepy
	The face is not really obvious	Normal building	Normal building	Neutral	Neutral	Neutral
	Face is detected	Normal building	Fierce face is detected	Neutral	Neutral	Creepy
	Face is detected	Face is detected	Face is detected	Neutral	Neutral	Neutral
	Face is detected	Face is detected	Face is detected	Funny	Funny	Scary
	Face is detected	The face is not really obvious	Face is detected	Funny	Funny	Scary
	Face is detected	Face is detected	Face is detected	Scary	Funny	Scary
	Face is detected	Face is detected	Fierce face is detected	Funny	Funny	Scary
	Face is detected	The face is not really obvious	Fierce face is detected	Neutral	Neutral	Scary
	Face is detected	Face is detected	Fierce face is detected	Scary	Scary	Scary
	The face is not really obvious	The face is not really obvious	The face is not really obvious	Neutral	Neutral	Neutral
	The face is not really obvious	The face is not really obvious	The face is not really obvious	Neutral	Neutral	Neutral
	The face is not really obvious	The face is not really obvious	Face is detected	Neutral	Neutral	Scary
	The face is not really obvious	The face is not really obvious	Face is detected	Funny	Funny	Funny

Table 2. Cont.

Pareidolian Image	Phenomenon			Reaction		
	6 a.m.	12 p.m.	2 a.m.	6 a.m.	12 p.m.	2 a.m.
	Face is detected	Face is detected	Face is detected	Scary	Funny	Scary
	Face is detected	Face is detected	Face is detected	Neutral	Neutral	Neutral
	Face is detected	Face is detected	Fierce face is detected	Scary	Scary	Scary
	Face is detected	Face is detected	Face is detected	Funny	Funny	Funny
	Face is detected	Face is detected	Face is detected	Scary	Funny	Scary
	Face is detected	The face is not really obvious	Face is detected	Neutral	Neutral	Neutral
	The face is not really obvious	The face is not really obvious	Fierce face is detected	Scary	Neutral	Scary

According to the feedback from pilot experiments, face identification in the built environments was easier at midnight and in the morning. Especially at midnight, many participants described the faces as scared, whereas they only considered those images as normal pareidolian faces at other time points (6:00 a.m. and 12:00 p.m.). Therefore, the results suggested that pareidolia was more likely to occur when people were exhausted. In other words, when people are fatigued, it will be easier to identify pareidolian faces. Face identification was not significant at 12 p.m., probably because of a higher level of relaxation in brain activity; thus, it did not reach exhaustion at that time. Results from partial images' feedback showed people reacted differently between morning and midnight when identifying a face in Pareidolian Image 2, 10, 11, and 13. The people's reactions to images oscillated from "Funny" in the morning to "Scary" at midnight. The majority of pareidolian images reactions were "Scary", "Neutral", and "Creepy". As a result, the pilot experiments revealed that people were more likely to identify pareidolian faces at midnight and in the morning than at midday, and people reacted more negatively to pareidolian images at night.

3.2. Results of Questionnaire Survey

The Cronbach's Alpha of the questionnaire survey was 0.899, showing a high internal consistency and high reliability. In the study, factor analysis was first used to screen the images and eliminate the image results that could not be well classified by factors. The factor analysis' eigenvalue was set at 0.9, and the factor loadings of the original 21 images with an absolute value greater than 0.3 were considered acceptable. There were two criteria for screening images: first, one image had a large loading on two or more factors (factor loading > 0.4), and the difference between the absolute value of the factor loading was

less than 0.3; and second, only one image under a factor had factor loading. Only one image could be removed per screening and required reanalysis. The purpose of factor analysis is to integrate highly correlated factors to form new factors. The final KMO value was 0.938 (KMO value > 0.6), and the significance of the Bartlett sphericity test was 0.000 ( $p < 0.05$ ), indicating that the final questionnaire had excellent validity, and the last retained image was suitable for factor analysis. We used factor analysis to remove pareidolian images 1, 4, 5, 6, 7, 8, 9, 11, 13 and 21; the purpose of each image was to examine the effect of demographic information on pareidolia; thus, we could integrate the deleted images into one factor through factor analysis. The final new factor extracted the results from the majority of the images; thus, it could well represent the overall results of the returned questionnaire. We named this factor the pareidolia questionnaire result and used it for multivariate analysis. The image factor loadings in the pareidolia questionnaire result are shown in Table 3.

**Table 3.** The image factor loadings in the pareidolia questionnaire result.

Image Number	2	3	10	12	14	15	16	17	18	19	20
Factor Loading	0.838	0.782	0.906	0.736	0.771	0.788	0.891	0.581	0.595	0.932	0.894

Table 4 show the results of effect analysis between the demographic information in the pareidolia questionnaire results. Among them, age, gender, and lifestyle as a single factor showed a significant impact on pareidolia. Many two-factor between-subject effects also significantly influenced pareidolia identification, including Age\*Gender ( $p = 0.036 < 0.05$ ), Age\*Lifestyle ( $p = 0.000 < 0.05$ ), Gender\*Lifestyle ( $p = 0.000 < 0.05$ ) and Job Stress\*Lifestyle ( $p = 0.000 < 0.05$ ). It was worth noting that the three-factor and four-factor interaction effects did not show a significant influence on pareidolia identification.

**Table 4.** Tests of Between-Subjects Effects.

Source	Type III Sum of Squares	df	Mean Square	F	Sig.
Age	65.413	4	16.353	233.348	0.000
Gender	0.307	1	0.307	4.383	0.038
Job Stress	0.211	1	0.211	3.017	0.084
Lifestyle	1.156	4	0.289	4.124	0.003
Age*Gender	0.609	3	0.203	2.898	0.036
Age*Job Stress	0.010	2	0.005	0.068	0.934
Age*Lifestyle	3.134	7	0.448	6.388	0.000
Gender*Job Stress	0.002	1	0.002	0.025	0.874
Gender*Lifestyle	2.577	3	0.859	12.259	0.000
Job Stress*Lifestyle	3.020	2	1.510	21.544	0.000
Age*Gender*Job Stress	0.001	1	0.001	0.018	0.892
Age* Gender*Lifestyle	0.019	1	0.019	0.268	0.605
Age*Job Stress*Lifestyle	0.025	1	0.025	0.360	0.549
Age*Job Stress*Lifestyle	0.023	1	0.023	0.325	0.569
Age*Gender*Job Stress*Lifestyle	0.059	1	0.059	0.837	0.362

Figure 1 show the effect of significant two-factor between-subject effects on pareidolia identification. Two-factor estimated marginal means can not only show between-subject effects but also reflect the influence of a single factor on pareidolia. Figure 1a show the differences in pareidolia identification between males and females in different age groups. From the overall trend, females were more likely than males to identify pareidolian faces. Especially in the 21–40 age group, females performed much better than males in pareidolian face identification. However, gender had no significant influence on face identification in the 41–60 age group. Compared with gender, age had a significant impact on pareidolia.

The performance of pareidolia face identification improved with increasing age. It seemed that 40 years old was a watershed since the 41–50 age group displayed a significant difference from the 31–40 age group. When the age exceeded 40 years old, the performance of pareidolia face identification showed a steady trend.

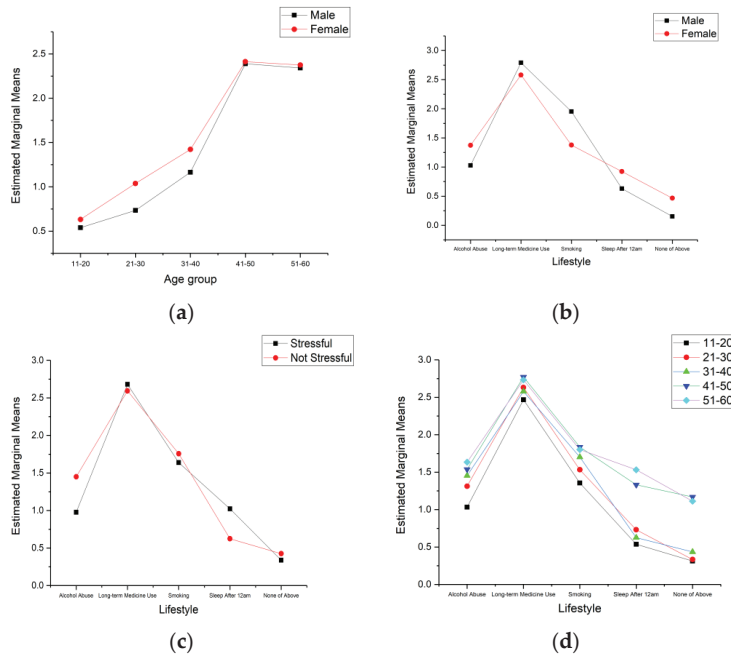


**Figure 1.** Two-factor Estimated Marginal Means of pareidolia questionnaire result. (a) Gender and age group; (b) Gender and lifestyle; (c) Job stress and lifestyle; (d) Age group and lifestyle.

Figure 1b show the differences in pareidolia identification between males and females with different lifestyles. Lifestyle significantly influenced pareidolia identification. The two-factor between-subject effects of lifestyle with age, gender, and job stress all demonstrated significant influence. Figure 1b,c both showed that long-term medicine users were more likely to identify pareidolia. Topers and smokers behaved similarly, but both influenced pareidolia identification to a large extent. Sleeping late had little influence on pareidolia recognition. However, people without these lifestyles seemed to be less prone to pareidolia. Figure 1b show the differences in pareidolia between males and females with different lifestyles. Male smokers and long-term medicine users were more likely to identify human faces than females. However, females who abused alcohol, slept late and did not have these lifestyles were more likely to identify human faces than males. This also confirmed that females were more likely to identify human faces than males in daily life. Figure 1c show the between-subject effects between job stress and lifestyle. There was little difference in pareidolia identification between long-term medicine users, smokers, and people without these lifestyles, whether they had job stress. Among late sleepers, people with job stress were more likely to identify human faces. Conversely, topers without job stress appeared to easily identify human faces.

Age and lifestyle were two factors that significantly affected pareidolia; the between-subject effect remained significant for pareidolia identification. From Figure 1d, people in the 41–60 age group had significantly higher pareidolia identification between different lifestyles than those in the 11–30 age group. Other lifestyle differences were revealed to not be significant in the 41–60 age group, except for long-term medicine users. However, in the 11–40 age group, long-term medicine users had a significant impact on pareidolia. Topers

and smokers had a large degree of sensitivity to identifying human faces in images. Other lifestyles did not show a significant influence on pareidolia.

### 3.3. PLS–SEM Analysis

This study used the PLS–SEM model to investigate the causal relationships between pareidolian images, pareidolia sensitivity, demographics, and pareidolian reactions. Since PLS modeling focuses on prediction and makes no assumptions regarding data distribution, residuals, or parameters of the observable variables, only generic linear regression requirements must be met. PLS modeling is more reliable than LISREL in analyzing the causal relationship between pareidolia factors. Figure 2 show the initial PLS–SEM model of this study.

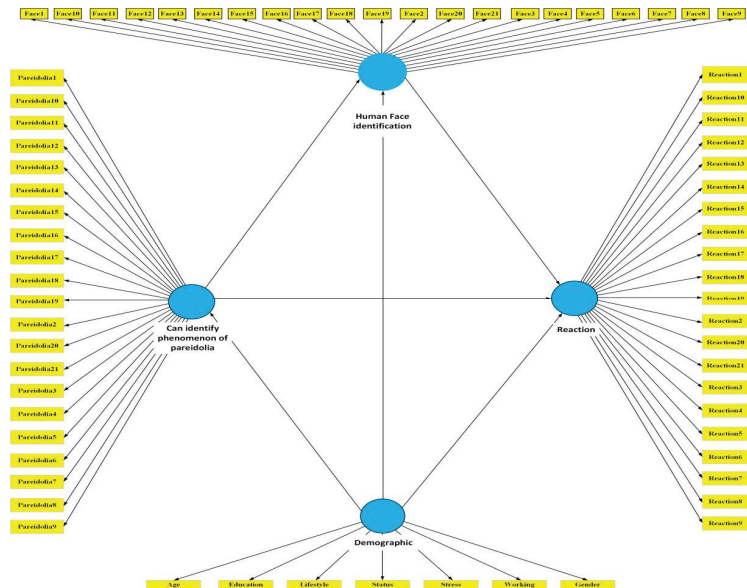


Figure 2. Initial PLS–SEM model of demographic data and sensitivity to pareidolia in the built environment.

To verify the rationality of the observed variables among the four latent variables, we conducted a reliability analysis on the latent variables. The reliability test was regarded passed if the Cronbach’s Alpha value and CR value in the internal consistency reliability test were both greater than 0.70. Table 5 show the initial latent variable reliability test results. The CR values of “Demographic” and “Can identify phenomenon of pareidolia” were both greater than 0.7, but the Cronbach’s Alpha value failed the test, indicating that the observed variables need to be modified or removed. Observed variables with variable loadings less than 0.5 were considered to lack correlation; thus, we removed “Working” and “Education” from “Demographic” and “Pareidolia 2” and “Pareidolia 21” from “Can identify the phenomenon of pareidolia”, respectively. The reliability test and correlation test of the revised PLS–SEM model both met the standard, indicating that the selected data had good reliability. Table 6 show the convergent validity test results of the PLS–SEM model. The AVE values of revised models were all greater than 0.5, suggesting that the revised model had better construct validity.

According to the PLS–SEM model path analysis in Figure 3, “Human face identification” (0.675), “Can identify phenomenon of pareidolia” (0.271), and “Demographics” (0.374) all had a direct impact on “Reaction”, and “Human face identification” (0.675) witnessed the most significant influence on “Reaction”; this may infer that people found it easier to identify pareidolian faces in the built environment, resulting in stronger emotional



reactions. “Demographics” showed no significant influence on both “Human face identification” (0.163) and “Can identify the phenomenon of pareidolia” (0.256). As demographic factors such as age and lifestyle changed, “Human face identification” and “Can identify the phenomenon of pareidolia” also experienced some variations. “Can identify the phenomenon of pareidolia” had a moderate impact on “Human face identification”; this may indicate that people were more likely to identify human faces in a built environment under an illusion. As a result, “Human face identification” was the most significant factor in influencing people’s reactions to the built environment. In addition, “Can identify the phenomenon of pareidolia” and “Demographics” both had a greater influence on pareidolian reaction through the indirect influence of “Human face identification”.

Table 5. Initial latent variable reliability test results.

Structural Reliability	Demographic	Can Identify Phenomenon of Pareidolia	Human Face Identification	Reaction
Cronbach’s Alpha	0.639	0.673	0.819	0.771
CR	0.767	0.716	0.849	0.733

Table 6. Convergent validity test results of revised model.

Convergent Validity	Demographic	Can identify Phenomenon of Pareidolia	Human Face Identification	Reaction
AVE	0.718	0.633	0.762	0.629

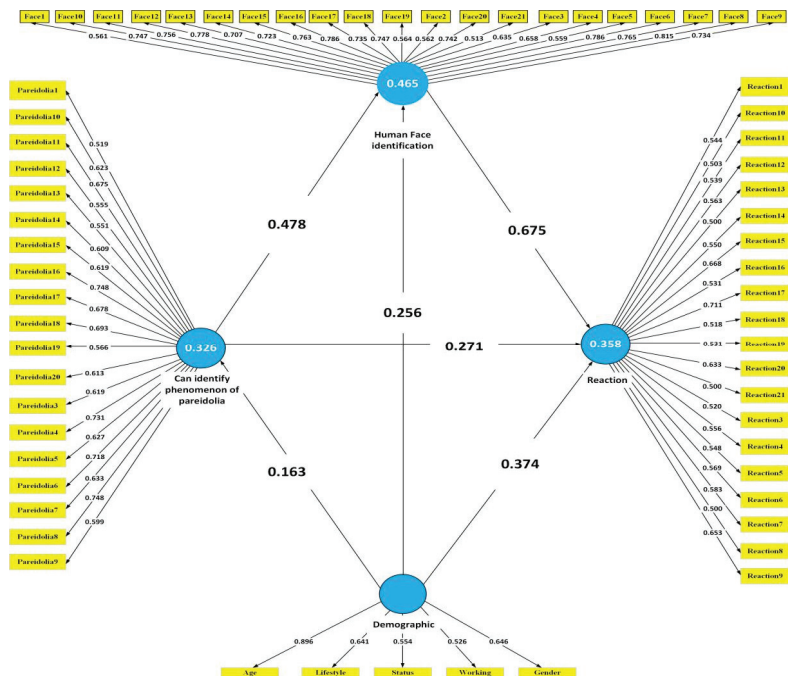


Figure 3. SEM tests between demographic data and sensitivity to pareidolia in the built environment.

### 3.4. Discussions

Consistent with the results of many studies, gender influenced the sensitivity and reactions towards pareidolia in a built environment, which might be explained by Pavlova et al. [34], who claimed that females are more likely to detect faces in arrangements of food on a plate. Age had a significant influence on pareidolia sensitivity. According to the single factor analysis, respondents' sensitivity to identify faces increased with age in the 11–40 age group, and they were more likely to have pareidolia than those over 40. This might indicate that the age of 40 is a watershed for pareidolia. However, there were significant differences between males and females in the 21–40 age group but non-significant differences in other age groups. Job stress seemed to have no significant impact on sensitivity to pareidolia in the built environment, which was not fully in line with [11]. Although the between-subject effects between job stress and lifestyle demonstrated a significant influence on pareidolia identification, the experimental results revealed that this influence mainly relied on the lifestyle factor. This is probably because pareidolia is an automatic phenomenon that occurs rapidly, insensibly, and compulsorily, and people do not realize their perception is misled by pareidolia [30]. Different lifestyles had some impact on the sensitivity and reactions towards pareidolia. This could be explained by Chalup et al. [14], who claimed that neuropathological and psychiatric conditions could affect the sensitivity and reactions to identify facial expressions of sensation. In the current research, smokers, toppers, and long-term medicine users tended to be more sensitive to pareidolian images in the built environment. Combining gender factors, long-term medicine users and smokers in males were more sensitive than females in face identification. Additionally, females who abused alcohol, slept late, and did not have these lifestyles were more likely to identify faces than males. This finding was consistent with previous findings that females are more likely to identify faces in pareidolian images [34] since sleeping late and having none of these lifestyles is common of most people nowadays. In addition, the between-subject effects of age and lifestyle both showed a significant influence on pareidolia. The 41–60 age group were more likely to identify faces than those in the 11–40 year age group with different lifestyles. However, long-term medicine users in different age groups were more likely to identify faces in pareidolian images. Among the respondents who slept late and did not have these lifestyles, the 41–60 age group differed significantly from those in the 31–40 age group in pareidolian face identification.

Through the path analysis of the PLS-SEM model, "Human face identification" significantly influenced people's reactions to pareidolia in the built environment, and demographic information also showed a moderate influence on pareidolian reactions. Pareidolian human faces appearing in buildings may cause positive or negative effects on human life. Some may lead to happiness and relaxation, but more lead to feelings of creepiness and depression. The facial expressions perceived in house designs through pareidolia can trigger emotional reactions based on the time of day [3].

### 4. Conclusions

We can categorize Pareidolia in a built environment into unintentional and intentional. The sensitivity and reactions towards pareidolia in a built environment are spontaneous and influenced by the age, gender, and lifestyles of observers. The majority of the respondents chose to change the design layout when they detected pareidolia in the built environment, including those living in the built environment with intentional pareidolian design elements. Residents rarely like any pareidolian faces in buildings, whether intentionally or unintentionally. The difference in gender influences the sensitivity and reactions towards pareidolia in a built environment because females have a stronger capability in face identification. The age of the respondents has a significant influence on pareidolia, and the age of 40 seems to be a watershed. Job stress has little impact on sensitivity to pareidolia in a built environment, but the between-subject effects of job stress and lifestyle have a considerable impact on pareidolia due to the dominance of lifestyle. The sensitivity to pareidolia varies depending on one's lifestyle. Smokers, toppers, and long-term medicine users are more sensitive to pareidolian images in the built environment. Similar results are

observed even when gender and age factors are taken into account. The identification of the pareidolian face in the built environment significantly influences pareidolian reactions and sensitivity. In addition, the pareidolian human faces appearing in buildings may cause positive or negative effects on human life. Some may lead to happiness and relaxation, but more lead to creepiness and depression. The facial expressions perceived in house design through pareidolia can evoke the emotion of the observers. As a limitation, a finding that remained unexpected is that most of the pareidolian images in the built environment are much more easily detected during early morning and at midnight but remain much less able to be perceived at midday. As a result, further and more in-depth studies are required, especially multi-disciplinary studies, to address this issue satisfactorily.

**Author Contributions:** Conceptualization, C.W. and Y.M.; data analysis, L.Y.; resources, L.C.W. and C.G.; writing—original draft preparation, C.W.; writing—review and editing, Y.M. All authors have read and agreed to the published version of the manuscript.

**Funding:** This research was funded by [Fujian Provincial Department of Science and Technology] grant number [2018J05121], [Fujian Provincial Department of Science and Technology] grant number [2021I0014], [Quanzhou Government] grant number [605-50X17234], [Huaqiao University] grant number [17BS201], and [Huaqiao University] grant number [605-50Y14007]. The APC was funded by [Fujian Provincial Department of Science and Technology].

**Institutional Review Board Statement:** Not applicable.

**Informed Consent Statement:** Informed consent was obtained from all subjects involved in the study.

**Data Availability Statement:** All data, models, and code generated or used during the study appear in the submitted article.

**Conflicts of Interest:** The authors declare no conflict of interest.

### Appendix A. Pareidolia Questionnaire Survey

You are invited to participate in a study examining the sensitiveness and reactions to pareidolia in a built environment. Pareidolia is a phenomenon of seeing faces in the environment, buildings and objects that surround us. Participation in this study is completely voluntary, your response will be completely confidential and only used for research purpose. In return for helping us with this, we would be very happy to give you the copies of the results of the study. For questions regarding this study, please contact Liangcheng YU at 20014086044@stu.hqu.edu.cn.

#### Appendix A.1. Background Information

Please TICK the following items that most closely correspond to your background.

<b>Gender</b>
A. Male
B. Female
<b>Age group</b>
A. 11–20
B. 21–30
C. 31–40
D. 41–50
E. 51–60
<b>Educational Level</b>
A. No formal education
B. Primary education
C. Secondary education
D. Certificate/Diploma/Advanced Diploma Level
E. Degree level
F. Postgraduate Degree/Professional Level

<b>Current job stress level</b>
A. Stressful
B. Not stressful
<b>Current status</b>
A. Single
B. Married
<b>Lifestyle</b>
A. Smoking
B. Alcohol abuse
C. Sleep after 12am
D. Long term medicine user
E. None of above

*Appendix A.2. Response to Pareidolia in the Built Environment*

This section is designed to ask you about your sensitiveness and reactions toward pareidolia in a built environment. There are no right or wrong answers, hence, you don't need to spend too long on each question, just go with your first impulse. Please TICK the item that that best describes your feeling and reactions.



 <p style="text-align: center;"><b>Figure A1</b></p>	<b>Can you identify a face in the Figure A1?</b>
	A. Yes
	B. No
	<b>Can you easily identify a human face in the Figure A1?</b>
	A. Very highly likely
B. Highly likely	
C. Likely	
D. Unlikely	
E. Denote	
<b>What is your reaction when you see Figure A1?</b>	
A. Scared	
B. Depressed	
C. Funny	
D. Happy	
E. No reaction	
 <p style="text-align: center;"><b>Figure A2</b></p>	<b>Can you identify a face in the Figure A2?</b>
	A. Yes
	B. No
	<b>Can you easily identify a human face in the Figure A2?</b>
	A. Very highly likely
B. Highly likely	
C. Likely	
D. Unlikely	
E. Denote	
<b>What is your reaction when you see Figure A2?</b>	
A. Scared	
B. Depressed	
C. Funny	
D. Happy	
E. No reaction	



Figure A3

Can you identify a face in the Figure A3?

- A. Yes
- B. No

Can you easily identify a human face in the Figure A3?

- A. Very highly likely
- B. Highly likely
- C. Likely
- D. Unlikely
- E. Denote

What is your reaction when you see Figure A3?

- A. Scared
- B. Depressed
- C. Funny
- D. Happy
- E. No reaction



Figure A4

Can you identify a face in the Figure A4?

- A. Yes
- B. No

Can you easily identify a human face in the Figure A4?

- A. Very highly likely
- B. Highly likely
- C. Likely
- D. Unlikely
- E. Denote

What is your reaction when you see Figure A4?

- A. Scared
- B. Depressed
- C. Funny
- D. Happy
- E. No reaction



Figure A5

Can you identify a face in the Figure A5?

- A. Yes
- B. No

Can you easily identify a human face in the Figure A5?

- A. Very highly likely
- B. Highly likely
- C. Likely
- D. Unlikely
- E. Denote

What is your reaction when you see Figure A5?

- A. Scared
- B. Depressed
- C. Funny
- D. Happy
- E. No reaction




 <p style="text-align: center;"><b>Figure A6</b></p>	<p><b>Can you identify a face in the Figure A6?</b></p> <p>A. Yes B. No</p> <p><b>Can you easily identify a human face in the Figure A6?</b></p> <p>A. Very highly likely B. Highly likely C. Likely D. Unlikely E. Denote</p> <p><b>What is your reaction when you see Figure A6?</b></p> <p>A. Scared B. Depressed C. Funny D. Happy E. No reaction</p>
 <p style="text-align: center;"><b>Figure A7</b></p>	<p><b>Can you identify a face in the Figure A7?</b></p> <p>A. Yes B. No</p> <p><b>Can you easily identify a human face in the Figure A7?</b></p> <p>A. Very highly likely B. Highly likely C. Likely D. Unlikely E. Denote</p> <p><b>What is your reaction when you see Figure A7?</b></p> <p>A. Scared B. Depressed C. Funny D. Happy E. No reaction</p>
 <p style="text-align: center;"><b>Figure A8</b></p>	<p><b>Can you identify a face in the Figure A8?</b></p> <p>A. Yes B. No</p> <p><b>Can you easily identify a human face in the Figure A8?</b></p> <p>A. Very highly likely B. Highly likely C. Likely D. Unlikely E. Denote</p> <p><b>What is your reaction when you see Figure A8?</b></p> <p>A. Scared B. Depressed C. Funny D. Happy E. No reaction</p>



Figure A9

Can you identify a face in the Figure A9?

- A. Yes
- B. No

Can you easily identify a human face in the Figure A9?

- A. Very highly likely
- B. Highly likely
- C. Likely
- D. Unlikely
- E. Denote

What is your reaction when you see Figure A9?

- A. Scared
- B. Depressed
- C. Funny
- D. Happy
- E. No reaction



Figure A10

Can you identify a face in the Figure A10?

- A. Yes
- B. No

Can you easily identify a human face in the Figure A10?

- A. Very highly likely
- B. Highly likely
- C. Likely
- D. Unlikely
- E. Denote

What is your reaction when you see Figure A10?

- A. Scared
- B. Depressed
- C. Funny
- D. Happy
- E. No reaction



Figure A11

Can you identify a face in the Figure A11?




- A. Yes
- B. No

Can you easily identify a human face in the Figure A11?

- A. Very highly likely
- B. Highly likely
- C. Likely
- D. Unlikely
- E. Denote

What is your reaction when you see Figure A11?

- A. Scared
- B. Depressed
- C. Funny
- D. Happy
- E. No reaction

	<p><b>Can you identify a face in the Figure A12?</b></p> <p>A. Yes B. No</p> <p><b>Can you easily identify a human face in the Figure A12?</b></p> <p>A. Very highly likely B. Highly likely C. Likely D. Unlikely E. Denote</p> <p><b>What is your reaction when you see Figure A12?</b></p> <p>A. Scared B. Depressed C. Funny D. Happy E. No reaction</p>	
<p><b>Figure A12</b></p>		<p><b>Can you identify a face in the Figure A13?</b></p> <p>A. Yes B. No</p> <p><b>Can you easily identify a human face in the Figure A13?</b></p> <p>A. Very highly likely B. Highly likely C. Likely D. Unlikely E. Denote</p> <p><b>What is your reaction when you see Figure A13?</b></p> <p>A. Scared B. Depressed C. Funny D. Happy E. No reaction</p>
<p><b>Figure A13</b></p>		<p><b>Can you identify a face in the Figure A14?</b></p> <p>A. Yes B. No</p> <p><b>Can you easily identify a human face in the Figure A14?</b></p> <p>A. Very highly likely B. Highly likely C. Likely D. Unlikely E. Denote</p> <p><b>What is your reaction when you see Figure A14?</b></p> <p>A. Scared B. Depressed C. Funny D. Happy E. No reaction</p>
<p><b>Figure A14</b></p>		






 <p style="text-align: center;"><b>Figure A15</b></p>	<p><b>Can you identify a face in the Figure A15?</b></p> <p>A. Yes B. No</p> <p><b>Can you easily identify a human face in the Figure A15?</b></p> <p>A. Very highly likely B. Highly likely C. Likely D. Unlikely E. Denote</p> <p><b>What is your reaction when you see Figure A15?</b></p> <p>A. Scared B. Depressed C. Funny D. Happy E. No reaction</p>
 <p style="text-align: center;"><b>Figure A16</b></p>	<p><b>Can you identify a face in the Figure A16?</b></p> <p>A. Yes B. No</p> <p><b>Can you easily identify a human face in the Figure A16?</b></p> <p>A. Very highly likely B. Highly likely C. Likely D. Unlikely E. Denote</p> <p><b>What is your reaction when you see Figure A16?</b></p> <p>A. Scared B. Depressed C. Funny D. Happy E. No reaction</p>
 <p style="text-align: center;"><b>Figure A17</b></p>	<p><b>Can you identify a face in the Figure A17?</b></p> <p>A. Yes B. No</p> <p><b>Can you easily identify a human face in the Figure A17?</b></p> <p>A. Very highly likely B. Highly likely C. Likely D. Unlikely E. Denote</p> <p><b>What is your reaction when you see Figure A17?</b></p> <p>A. Scared B. Depressed C. Funny D. Happy E. No reaction</p>



Figure A18

Can you identify a face in the Figure A18?

- A. Yes
- B. No

Can you easily identify a human face in the Figure A18?

- A. Very highly likely
- B. Highly likely
- C. Likely
- D. Unlikely
- E. Denote

What is your reaction when you see Figure A18?

- A. Scared
- B. Depressed
- C. Funny
- D. Happy
- E. No reaction



Figure A19

Can you identify a face in the Figure A19?

- A. Yes
- B. No

Can you easily identify a human face in the Figure A19?

- A. Very highly likely
- B. Highly likely
- C. Likely
- D. Unlikely
- E. Denote

What is your reaction when you see Figure A19?

- A. Scared
- B. Depressed
- C. Funny
- D. Happy
- E. No reaction



Figure A20

Can you identify a face in the Figure A20?

- A. Yes
- B. No

Can you easily identify a human face in the Figure A20?

- A. Very highly likely
- B. Highly likely
- C. Likely
- D. Unlikely
- E. Denote

What is your reaction when you see Figure A20?

- A. Scared
- B. Depressed
- C. Funny
- D. Happy
- E. No reaction


	<b>Can you identify a face in the Figure A21?</b>
	A. Yes
	B. No
	<b>Can you easily identify a human face in the Figure A21?</b>
	A. Very highly likely
B. Highly likely	
C. Likely	
D. Unlikely	
E. Denote	
<b>What is your reaction when you see Figure A21?</b>	
A. Scared	
B. Depressed	
C. Funny	
D. Happy	
E. No reaction	

Figure A21

Thank You for Your Participation.

## References

1. Nees, M.A.; Phillips, C. Auditory Pareidolia: Effects of Contextual Priming on Perceptions of Purportedly Paranormal and Ambiguous Auditory Stimuli. *Appl. Cogn. Psychol.* **2014**, *29*, 129–134. [[CrossRef](#)]
2. Yokoi, K.; Nishio, Y.; Uchiyama, M.; Shimomura, T.; Iizuka, O.; Mori, E. Hallucinators Find Meaning in Noises: Pareidolic Illusions in Dementia with Lewy Bodies. *Neuropsychologia* **2014**, *56*, 245–254. [[CrossRef](#)] [[PubMed](#)]
3. Hoback, A.S. Relationships between aggressive driving behaviors, demographics and pareidolia. *Transp. Res. Interdiscip. Perspect.* **2019**, *2*, 100037. [[CrossRef](#)]
4. Martínez-Horta, S.; Horta-Barba, A.; Perez-Perez, J.; Antoran, M.; Kulisevsky, J. Impaired face-like object recognition in premanifest Huntington’s disease. *Cortex* **2020**, *123*, 162–172. [[CrossRef](#)] [[PubMed](#)]
5. Uchiyama, M.; Nishio, Y.; Yokoi, K.; Hirayama, K.; Imamura, T.; Shimomura, T.; Mori, E. Pareidolias: Complex visual illusions in dementia with Lewy bodies. *Brain* **2012**, *135*, 2458–2469. [[CrossRef](#)] [[PubMed](#)]
6. Wiseman, R. Wired for Weird. *Sci. Am. Mind* **2012**, *22*, 52–57. [[CrossRef](#)]
7. Martínez-Conde, S.; Macknik, S.L. A Faithful Resemblance. *Sci. Am.* **2013**, *22*, 18–21. [[CrossRef](#)]
8. Blom, J.D. *A Dictionary of Hallucinations*; Springer: New York, NY, USA, 2010.
9. Iaria, G.; Fox, C.J.; Scheel, M.; Stowe, R.M.; Barton, J.J.S. A Case of Persistent Visual Hallucinations of Faces following LSD Abuse: A Functional Magnetic Resonance Imaging Study. *Neurocase* **2010**, *16*, 106–118. [[CrossRef](#)]
10. Fontenelle, L.F. Pareidolias in Obsessive-Compulsive Disorder: Neglected Symptoms That May Respond to Serotonin Reuptake Inhibitors. *Neurocase* **2008**, *14*, 414–418. [[CrossRef](#)]
11. Taubert, J.; Wardle, S.G.; Flessert, M.; Leopold, D.A.; Ungerleider, L.G. Face Pareidolia in the Rhesus Monkey. *Curr. Biol.* **2017**, *27*, 2505–2509. [[CrossRef](#)]
12. Kanizsa, G. Subjective contours. *Sci. Am.* **1976**, *234*, 48–52. [[CrossRef](#)] [[PubMed](#)]
13. Van Elk, M. Paranormal Believers Are More Prone to Illusory Agency Detection Than Skeptics. *Conscious. Cogn.* **2013**, *22*, 1041–1046. [[CrossRef](#)] [[PubMed](#)]
14. Chalup, S.; Hong, K.; Ostwald, M. Simulating Pareidolia of Faces for Architectural Pareidolian Image Analysis. *Int. J. Comput. Inf. Syst. Ind. Manag. Appl.* **2010**, *2*, 262–278.
15. Melcher, D.; Bacci, F. The Visual System as A Constraint on the Survival and Success of Specific Artworks. *Spat. Vis.* **2008**, *21*, 347–362.
16. Dyer, R. The Cat Behind the Wall. *Third Text* **2011**, *25*, 635–639. [[CrossRef](#)]
17. Rieth, C.A.; Lee, K.; Lui, J.; Tian, J.; Huber, D.E. Faces in the mist: Illusory face and letter detection. *I-Perception* **2011**, *2*, 458–459. [[CrossRef](#)]
18. Liu, J.; Li, J.; Feng, L.; Li, L.; Tian, J.; Lee, K. Seeing Jesus in Toast: Neural and Behavioral Correlates of Face Pareidolia. *Cortex* **2014**, *53*, 60–77. [[CrossRef](#)]
19. Marsching, J.D. Orbs, Blobs, and Glows: Astronauts, UFOs, and Photography. *Art J.* **2014**, *62*, 56–65. [[CrossRef](#)]
20. Wertheimer, M.; Riezler, K. Gestalt theory. *Soc. Res.* **1944**, *11*, 78–99.
21. Pelphrey, K.A.; Singerman, J.D.; Allison, T.; McCarthy, G. Brain activation evoked by perception of gaze shifts: The influence of context. *Neuropsychologia* **2003**, *41*, 156–170. [[CrossRef](#)]
22. Engell, A.D.; Haxby, J.V. Facial expression and gaze-direction in human superior temporal sulcus. *Neuropsychologia* **2007**, *45*, 3234–3241. [[CrossRef](#)] [[PubMed](#)]
23. Perrett, D.I.; Rolls, E.T.; Caan, W. Visual neurones responsive to faces in the monkey temporal cortex. *Exp. Brain Res.* **1982**, *47*, 329–342. [[CrossRef](#)] [[PubMed](#)]

24. Carbon, C.C.; Grüter, M.; Grüter, T. Age-Dependent Face Detection and Face Categorization Performance. *PLoS ONE* **2013**, *8*, e79164. [[CrossRef](#)] [[PubMed](#)]
25. Pfeiffer, K. *Pareidolia: A Photographic Exploration of Multistable Perception*; Published Art and Art History Honors Theses; Trinity University Press: San Antonio, TX, USA, 2013.
26. Riekkki, T.; Lindeman, M.; Aleneff, M.; Halme, A.; Nuortimo, A. Paranormal and Religious Believers Are More Prone to Illusory Face Perception than Skeptics and Non-believers. *Appl. Cogn. Psychol.* **2013**, *27*, 150–155. [[CrossRef](#)]
27. Brugger, P.; Mohr, C. The Paranormal Mind: How the Study of Anomalous Experiences and Beliefs May Inform Cognitive Neuroscience. *Cortex* **2008**, *44*, 1291–1298. [[CrossRef](#)]
28. Galdos, M.; Simons, C.; Fernandez-Rivas, A.; Wichers, M.; Peralta, C.; Lataster, T.; van Os, J.; Amer, G.; Myin-Germeys, I.; Allardyce, J.; et al. Affectively salient meaning in random noise: A task sensitive to psychosis liability. *Schizophr. Bull.* **2011**, *37*, 1179–1186. [[CrossRef](#)]
29. Gunn, J. The Rhetoric of Exorcism: George W. Bush and the Return of Political Demonology. *West. J. Commun.* **2004**, *68*, 1–23. [[CrossRef](#)]
30. Takahshi, K.; Watanabe, K. Face Is Beautiful: Aesthetic Evaluation of Pareidolian Faces. In Proceedings of the 2014 6th International Conference on Knowledge and Smart Technology (KST), Chonburi, Thailand, 30–31 January 2014; pp. 108–111.
31. Stuart, H. Violence and mental illness: An overview. *World Psychiatry* **2003**, *2*, 121–124.
32. Li, G.; Huang, S.; Xu, W.; Jiao, W.; Jiang, Y.; Gao, Z.; Zhang, Z. The impact of mental fatigue on brain activity: A comparative study both in resting state and task state using EEG. *BMC Neurosci* **2020**, *21*, 20. [[CrossRef](#)]
33. Watanabe, H.; Nishio, Y.; Mamiya, Y.; Narita, W.; Iizuka, O.; Baba, T.; Takeda, A.; Shimomura, T.; Mori, E. Negative mood invites psychotic false perception in dementia. *PLoS ONE* **2018**, *13*, e0197968. [[CrossRef](#)]
34. Pavlova, M.A.; Scheffler, K.; Sokolov, A.N. Face-n-food: Gender differences in tuning to faces. *PLoS ONE* **2015**, *10*, e0130363. [[CrossRef](#)] [[PubMed](#)]





Article

# Co-Movement between Carbon Prices and Energy Prices in Time and Frequency Domains: A Wavelet-Based Analysis for Beijing Carbon Emission Trading System

Rundong Luo, Yan Li \*, Zhicheng Wang and Mengjiao Sun

Business School, Shandong University, Weihai 264209, China; luorundong@sdu.edu.cn (R.L.); 201916299@mail.sdu.edu.cn (Z.W.); 202117202@mail.sdu.edu.cn (M.S.)

\* Correspondence: liyan5@sdu.edu.cn

**Abstract:** This study aims to investigate the co-movement and lead–lag relationship between carbon prices and energy prices in the time–frequency domain in the carbon emission trading system (ETS) of Beijing. Based on wavelet analysis method, this study examines the weekly data on oil and natural gas prices and carbon prices in Beijing ETS from its establishment in November 2013 to April 2019. Empirical results show the following important findings: (1) Carbon and natural gas prices are mainly negatively correlated, with natural gas prices occupying a leading position in the 12–20 weeks frequency band, indicating that the increase (decrease) of natural gas price will lead to the decrease (increase) of carbon price; (2) carbon and oil prices show an unstable dependence relationship, and their leadership position in the market constantly changes. The partial wavelet coherency and partial phase differences vary greatly in different time–frequency domains, indicating that there is no stable coherency between oil prices and carbon prices. The estimation results prove the existence of coherency between the carbon and energy prices in the Beijing ETS. The research findings of this paper provide quantifiable references for investors to achieve risk control in asset allocation and investment portfolio in the ETS market.

**Keywords:** Beijing carbon emission trading system; energy prices; wavelet analysis; time–frequency domain

**Citation:** Luo, R.; Li, Y.; Wang, Z.; Sun, M. Co-Movement between Carbon Prices and Energy Prices in Time and Frequency Domains: A Wavelet-Based Analysis for Beijing Carbon Emission Trading System. *Int. J. Environ. Res. Public Health* **2022**, *19*, 5217. <https://doi.org/10.3390/ijerph19095217>

Academic Editors: Francesco Nocera, Roberto Alonso González Lezcano and Rosa Giuseppina Caponetto

Received: 28 March 2022

Accepted: 24 April 2022

Published: 25 April 2022

**Publisher's Note:** MDPI stays neutral with regard to jurisdictional claims in published maps and institutional affiliations.



**Copyright:** © 2022 by the authors. Licensee MDPI, Basel, Switzerland. This article is an open access article distributed under the terms and conditions of the Creative Commons Attribution (CC BY) license (<https://creativecommons.org/licenses/by/4.0/>).

## 1. Introduction

Climate change should be addressed through coordination and consummation of energy policies in the global society [1,2]. The Kyoto Protocol, which was adopted in December 1997, stipulates that by 2008–2012, total emissions of major greenhouse gases in developed countries should have been reduced by 5.2% relative to the baseline in 1990. Since the Kyoto Protocol came into effect, a carbon emission trading system (ETS) has been implemented by a growing number of countries and regions [3]. The global carbon market has emerged since the implementation of the European Union's ETS in 2005, with both carbon trading volume and turnover increasing rapidly [4].

The rationale for ETS is theoretically straightforward: Operating the carbon market encourages enterprises with low emission-reduction costs to exceed their emission reductions and sell their remaining carbon quotas or greenhouse gas emission reductions to companies with high emission-reduction costs through trading. Such a method helps companies with high emission-reduction costs to achieve the set emission-reduction targets and effectively reduces emission-reduction costs.

In the carbon market, greenhouse gas emission credits have become a tradable commodity that can be traded between regions and countries [5]. Carbon prices are jointly formed by the supply-and-demand relationship of greenhouse gas emission quotas in the carbon market [6]. The ETS embraces multiple attributes of environment, market, finance, and policy [7]. The price level itself can have varying degrees of effects on im-

proving environmental quality, reducing energy demand, and promoting macroeconomic growth [8].

China has committed to reducing its carbon emissions from peak levels by 2030, and seven pilot carbon ETSs in Beijing, Tianjin, Shanghai, Chongqing, Hubei Province, Guangdong Province, and Shenzhen have been launched [9]. The objective is to compel companies to carry out low-carbon technology innovation through market-oriented means so that low-cost emission reduction can be achieved. The carbon reduction in each pilot has achieved initial results since the pilot initiation of the Chinese ETS. *China's Policies and Actions for Addressing Climate Change (2019)* states that the country has fulfilled its international commitment to reducing carbon emissions intensity by 40% to 45% by 2020 compared with the levels in 2005. However, China's carbon market remains troubled by inadequate development and a complex policy environment for energy saving and emission reduction [10]. In this context, improving the operating efficiency of the ETS and using market means to achieve carbon dioxide emission reduction has become a centrally important research question [11].

In this study, carbon and energy prices are dynamically analyzed by using wavelet analysis method based on the data in the Beijing carbon ETS from November 2013 to April 2019. Results reveal the coherency between the carbon and energy prices. The lead–lag relationship between the carbon and energy prices is analyzed through the lag effect of the response between changes in the carbon and energy prices.

The innovation of this study lies in the following aspects: (1) wavelet analysis, which can deal with nonstationarity in economic time series, is adopted for accurate analysis of the structural changes in carbon and energy prices in a nonstationary time series; (2) local coherency analysis is performed from different frequency scales (short and long term), and then the dynamic coherency between carbon and energy prices is studied; and (3) wavelet partial phase difference is used to analyze the lead–lag relationship amongst changes in carbon prices, natural gas prices, and oil prices.

This study adds quantifiable evidence on the relationship between carbon and energy prices in China's ETS and contributes to deep understanding of the influencing factors of carbon prices and the interaction between China's ETS and energy markets. Thus, this study provides a valuable reference for investors in asset allocation and investment portfolio for risk control.

The rest of this paper is organized as follows: Section 2 describes Beijing's carbon market, Section 3 reviews the literature, Section 4 introduces the methodology and data, Section 5 discusses empirical results, and Section 6 presents the conclusion and recommendations.

## 2. Beijing Carbon Market

The Beijing carbon ETS was established on 28 November 2013. According to data provided by the Beijing Carbon Exchange, by the end of 2018, the total amount of Beijing's carbon market quota reached 51 million tons, the total exchange volume was 29.07 million tons, the total trading turnover reached CNY 1.049 billion, and the average annual exchange price fluctuated around CNY 50/ton. Among the pilot carbon markets in China, the Beijing carbon market ranks first in volume, turnover, and trading activity. According to the *Beijing Municipal Commission of Development and Reform and the Beijing Environment Exchange (2018)*, the Beijing carbon market covers approximately 1000 companies, including electric power, heat, cement, petrochemicals, other industrial companies, service industries, urban rail transit, and public electric passenger cars.

The experience of carbon ETS pilots, as pioneers, plays an important role in establishing a national carbon emission market [12,13]. As one of the pilot regions of China's carbon market, Beijing ETS has achieved good performance and results in reducing emissions. According to the *Annual Report of Beijing Carbon Market 2018*, from 2013 to 2018, the energy consumption per CNY 10,000 of GDP and carbon dioxide emissions in Beijing dropped by 22.5% and 28.2%, respectively, while the city's energy efficiency ranks first in China. This finding indicates that initial results have been achieved in Beijing through the adoption

of the market means to promote energy conservation and emission reduction. In terms of market construction, a relatively complete policy and regulation system of “1 + 1 + N” has formed in the Beijing carbon exchange market. Specifically, the policies include the legislation set forth during the Beijing Municipal People’s Congress on 27 December 2013 (1), local government regulations presented on 28 May 2014 (1), and the specific rules and regulations (N) of the Municipal Commission of Development and Reform and relevant departments in recent years. Meanwhile, a market supervision system based on the maximum position limit and price warning has been formed, which can be an important reference and inspiration for the construction of the national carbon market. The establishment of China’s carbon market is a major impetus to further strengthen the country’s ecological development and promote energy conservation and emission reduction measures.

Beijing ETS was chosen for this study for three main reasons. Firstly, the Beijing carbon market is more active, with trading entities actively trading in the market, its turnover is increasing, and the trading system is operating safely and stably [14]. The price of carbon allowances in Beijing has become an important reference for other pilot cities [15]. Secondly, Beijing carbon market information is disclosed more timely, the market carbon price can reflect market information in a more timely manner, and the construction of the carbon market system is at the forefront of the pilot carbon market [16]. Finally, Beijing’s energy use efficiency is among the highest of all Chinese provinces and cities, indicating that the use of market instruments to promote energy conservation and emission reduction has begun to bear fruit in Beijing [17]. Based on these considerations, this study selects the Beijing carbon market, which has performed well in the carbon market pilots, as the subject of this study.

### 3. Literature Review

A growing body of literature has begun to examine carbon price fluctuations and their influencing factors [18]. The contributing factors of the carbon market can be grouped into internal factors and external ones. The internal factors mainly include the market trading behavior, the adjustment of carbon trading policy, and the uncertainty about economic policy. For example, Wang et al. [19] studied the impact of different types of trading behaviors in the EU ETS on the carbon market. It was found that “compliant transactions” and the inventories of the financial intermediaries have an impact on carbon price trends, while “non-compliant transactions” have an impact on carbon price volatility. Other researchers have confirmed that the EU and China’s carbon trading policies will have an impact on the carbon market [20,21]. Li et al. [22] found that trade policy uncertainty and monetary policy uncertainty will have a positive impact on China’s carbon market prices, while exchange rate policy uncertainty has a negative impact. External factors mainly refer to macroeconomic and weather variables. For example, Bento and Gianfrate [23] proved that macro-level determinants, such as gross domestic product (GDP), the presence of a national carbon price mechanism, and industry attributes, are correlated with the carbon market, and that countries with higher per-capita GDP are usually subject to higher carbon market price levels. Hintermann [24] found that in the EU carbon market, temperature and precipitation affect ETS quota prices in a nonlinear manner. In addition, some studies argue that the performance of financial market, energy market, and foreign exchange market also exert a significant effect on the volatility of carbon prices [25–27]. Sun et al. [28] studied the causal relationship between China’s carbon price and the four major energy-intensive stock indexes and found that there is a weak two-way causal relationship between China’s carbon market and the stock market.

Research on the coherency between the carbon market and the energy market has motivated an in-depth study of the influencing factors and effects to form a theoretical underpinning for the development and improvement of the carbon market and its efficiency [29–31]. Adekoya [32] found that the prices of energy sources such as crude oil, natural gas, and coal can help investors predict the price of carbon allowances in Europe. Energy prices, such as those of oil and natural gas, are considered amongst the important



influencing factors of the carbon price [33]. Zhang and Sun [34] proved that a one-way and time-varying spillover effect exists between the European ETS and the coal and natural gas markets, and no significant spillover effect can be observed between the European carbon market and the crude oil market. However, Ji et al. [35] studied the coherency between the returns and volatility of the carbon energy system under the EU carbon emissions exchange system. Their findings show that Brent crude oil prices play an important role in affecting carbon price fluctuation and risks. Wu, Wang, and Tian [29] proved that the volatility spillover between the coal and carbon emission markets is the strongest by using the recursive graph method and recursive quantitative analysis method. Hammoudeh et al. [36] studied the effect of changes in United States crude oil, natural gas, and other energy prices on carbon prices. Jiang and Chen [37] found that the outbreak of COVID-19 will expand the spillover effect between carbon and energy markets. To sum up, there has been growing evidence of the coherency between the carbon market and the energy market.

For China's carbon market, few studies have focused on its coherency with the energy markets. Zeng, Nan, Liu, and Chen [15] studied the dynamic relationship between carbon prices in the Beijing carbon market and economic development and energy prices through the structural vector autoregression (SVAR) model. Applying the adaptive lasso method, Guo [38] found that the carbon price in the Shenzhen ETS was mainly affected by the EUR exchange rate and domestic oil prices. Wang et al. [39] simulated the changes in China's energy system and the trend of carbon emissions by establishing a hybrid energy model to minimize costs. Dong et al. [40] studied the relationship between China's regional carbon emission intensity and energy structure by using a static spatial econometric model and a panel co-integration model. Wagner et al. [41] investigated the relationship between renewable energy costs and carbon prices in China. Using the vector error correction model, Zhou and Li [42] studied the dynamic relationship amongst energy prices, macroeconomic indicators, air quality, and carbon prices in the Hubei carbon ETS. By using a multi-time series model and an ARCH model, Li and Lei [43] found that the industrial revenue, energy prices, government intervention, and number of participating companies in the carbon ETS in Hubei affected carbon prices considerably.

Although the above studies shed light on our research, they still have shortcomings. In terms of research perspective, although the coherency between carbon and energy prices in the Chinese carbon market has been investigated, studies are mostly conducted from a static perspective without reflecting the dynamic coherency and leader–follower (lead–lag) relationship between variables in different time and frequency domains. In terms of research method, empirical research on the relationship between carbon and energy prices is mainly conducted by using geographically weighted regression, SVAR, Bayesian SVAR, and other traditional approaches [15,44,45]. These research methods have certain weakness and difficulty in accurately identifying the effective information of carbon prices and energy prices from the perspective of time and frequency domains. Multivariate wavelet analysis can effectively compensate for the inadequacies of traditional methods [46]. Wavelet analysis tools can reflect the changes in variables in the time domain and the short-term and long-term coherency between variables in the frequency domain [47]. Wavelet analysis has been used in research on carbon emissions and carbon assets [48–50]. Therefore, a wavelet analysis tool is a powerful alternative to confirm the coherency between carbon prices and energy prices in various time and frequency domains. Based on this, we use the wavelet analysis method to conduct dynamic analysis of carbon price and energy price and explore the correlation between carbon price and energy price. At the same time, the lead–lag relationship between the carbon and energy prices is analyzed through the lag effect of the response between changes in the carbon and energy prices.

## 4. Methods and Data

### 4.1. Research Methods

Wavelet analysis is a mathematical analysis method that was gradually developed in the middle and late 1980s. This method inherits the localized idea of Fourier transformation

and overcomes its shortcomings in that the window size is not changed along with frequency [51]. Wavelet theory has become one of the most commonly used tools in the field of signal processing [52]. Its advantages are the following: (1) Analysis is conducted by combining the windows with different frequency fluctuations and different time scales, that is, combining time and frequency domains [53,54]. (2) The method has good localization properties and can find information about structural characteristics hidden in the data that cannot be recognized by other signal methods. (3) Nonstationary time series can be handled and analyzed well. (4) In the long wavelength band, the wavenumber resolution of the overall spectrum of the wavelet transform is higher and the error is lower [55]. On the basis of these excellent characteristics, wavelet analysis is widely used in signal processing, physics, geography, and other fields, and it began to be used in the economic and financial fields in the 1990s [56]. Continuous wavelet transform and wavelet analysis tools, such as wavelet power spectrum, wavelet coherence coefficient, and wavelet phase difference, are introduced in the present paper. In accordance with the research needs of this study, wavelet analysis tools can be extended to cases with three time variables.

#### 4.1.1. Continuous Wavelet Transform

Given a time series  $x(t)$ , the expression of its continuous wavelet transform function is

$$W_x(\tau, s) = \int_{-\infty}^{\infty} x(t) \bar{\psi}_{\tau, s}(t) dt. \tag{1}$$

In Equation (1),  $\bar{\psi}_{\tau, s}(t)$  indicates a complex conjugation function of the daughter wavelet function  $\psi_{\tau, s}$ ,

Where  $\psi_{\tau, s}(t)$  is a sequence of functions obtained after scaling and translation of mother wavelet function  $\psi(t)$  [55,57], which can be shown as

$$\psi_{\tau, s}(t) = \frac{1}{\sqrt{|s|}} \psi\left(\frac{t - \tau}{s}\right), s, \tau \in R, s \neq 0. \tag{2}$$

where  $s$  and  $\tau$  are the scaling and translation parameters, respectively. When  $|s| > 1$ , the mother wavelet is stretched and transformed to obtain a high-frequency part with a short duration in the sample time series. When  $|s| < 1$ , the mother wavelet is compressed and transformed to obtain a low-frequency part with a long duration in the sample time series. The translation transformation is the movement of the mother wavelet function on the time axis. Different values of  $\tau$  represent different window positions.

The mother wavelet function  $\psi(t)$  needs to satisfy the following conditions, which means that the function fluctuates up and down around the time axis:

$$0 < \int_{-\infty}^{+\infty} \frac{\psi(\omega)}{|\omega|} d\omega < \infty. \tag{3}$$

$$\int_{-\infty}^{+\infty} \psi(t) dt = 0. \tag{4}$$

$$\int_{-\infty}^{+\infty} \psi^2(t) dt = 0. \tag{5}$$

The mother wavelet function has numerous forms. In this study, Morlet wavelet is used as the mother wavelet function because it is more commonly used in the analysis of financial and economic time series. The Morlet wavelet is expressed as follows:

$$\psi_{\omega_0}(t) = \pi^{-\frac{1}{4}} e^{i\omega_0 t} e^{-\frac{t^2}{2}}. \tag{6}$$

The value of  $\omega_0$  deserves special attention. A high value leads to poor localization property of the Morlet wavelet in the time domain, while a small value leads to the poor

localization property of the Morlet wavelet in the frequency domain. To effectively balance the effect of these two aspects,  $\omega_0 = 6$  is usually considered.

#### 4.1.2. Wavelet Power Spectrum

When the wavelet power spectrum is expressed as the volatility of a single time series under the time and frequency domains, it is called the self-wavelet power spectrum and is defined as  $|W_x(\tau, s)|^2$ . The volatility in the self-wavelet power spectrum can be indicated by the warm and cool colours in the picture (Figures 1–3). The blue part corresponds to the low-power region, indicating that the volatility is low at this time and frequency domain; the red part represents the high-power region, indicating that the volatility is high at this time and frequency domain.

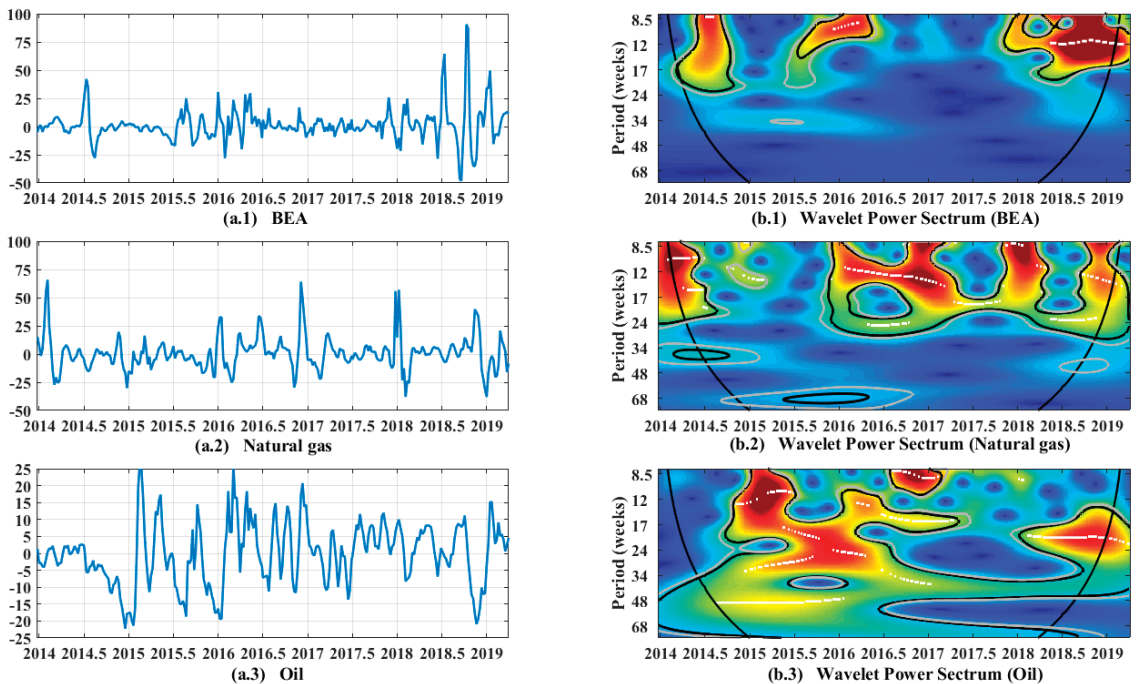


**Figure 1.** Monthly rate of return and self-wavelet power spectrum. **Note:** (a.1–a.3) indicates monthly return chart for each time series, and (b.1–b.3) shows self-wavelet power spectrum.

When the wavelet power spectrum is expressed as the coherency of two time series in the time and frequency domains, it is called cross-wavelet power spectrum and defined as  $|W_{xy}(\tau, s)|^2 = |W_x(\tau, s)|^2 |W_y(\tau, s)|^2$ . Similarly, the strength of the coherency between the two time series can be indicated by the warm and cool colours in the cross-wavelet power spectrum. The blue part corresponds to the low-power region, indicating that the correlation of two time series is low at this time and frequency domain. The red part represents the high-power region, indicating that the coherency of two time series is high at this time and frequency domain.

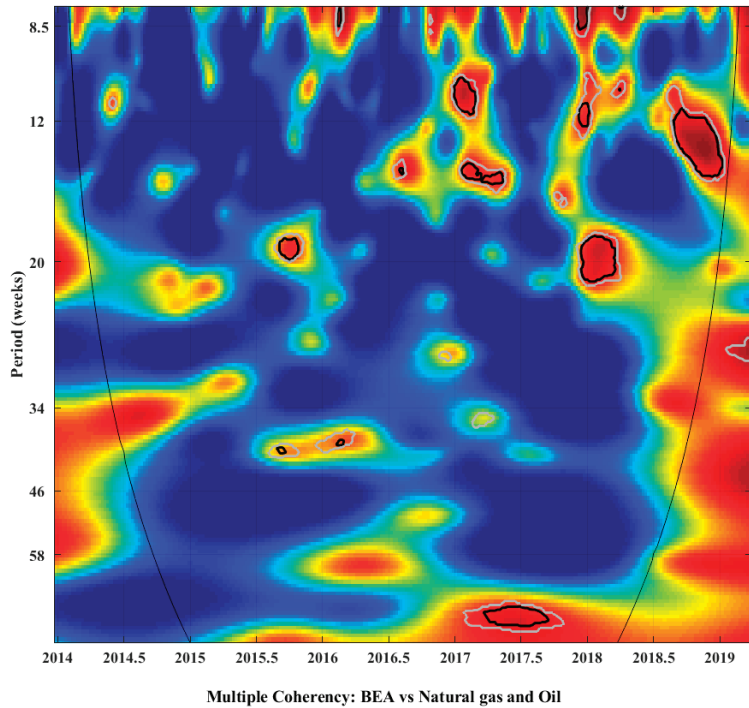


**Figure 2.** Multiple-wavelet power spectrum between Beijing carbon price and energy (natural gas and oil) prices.

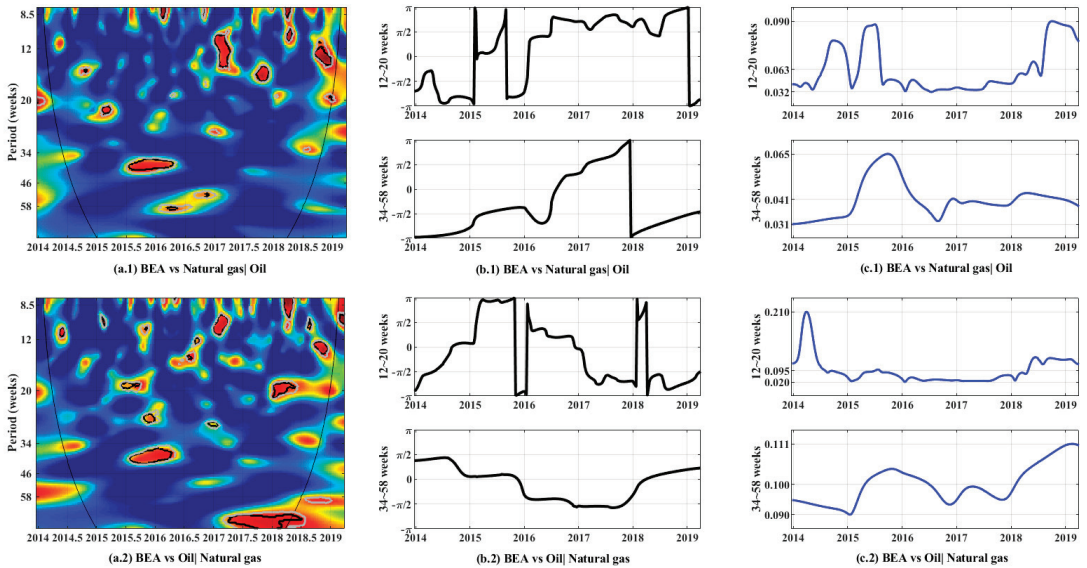


**Figure 3.** Partial wavelet coherency, phase difference, and wavelet gain. **Note:** (a) partial wavelet coherency between Beijing carbon price and natural gas price (a.1) or oil price (a.2); (b) partial wavelet phase difference between Beijing carbon price and natural gas price (b.1) or oil price (b.2); and (c) partial wavelet gain between Beijing carbon price and natural gas price (c.1) or oil price (c.2).

#### 4.1.3. Wavelet Coherency Coefficient and Wavelet Phase Difference

Although the cross-wavelet power spectrum can obtain the correlation between the two time series in the time and frequency domain, knowing which sequence plays a leading role is difficult, that is, the lead–lag relationship between the two time series is unclear. Therefore, the introduction of wavelet coherency coefficients and wavelet phase differences is required.

The wavelet coherency coefficient, which can measure the coherency and size of two time series, is defined as

$$R_{xy} = \frac{|s(W_{xy})|}{[s(|W_x|^2)s(|W_y|^2)]^{1/2}}. \tag{7}$$

In Equation (7),  $s$  is the smoothing operator achieved by convolution in both time and scale. To further obtain the lead–lag relationship of the time series, we define the wavelet phase difference as

$$\phi_{yx} = \tan^{-1} \left( \frac{\Im(W_{xy})}{\Re(W_{xy})} \right). \tag{8}$$

In Equation (8),  $\Re(W_{xy})$  and  $\Im(W_{xy})$  represent the real and imaginary parts of cross-wavelet power spectrum  $W_{xy}$ . The different values of wavelet phase difference represent the lead–lag relationship between two time series in specific time and frequency domains. If  $\phi_{yx} = 0$ , then  $x(t)$  and  $y(t)$  of the time series are completely positively correlated. If  $\phi_{yx} = \pm\pi$ , then the time series are completely negatively correlated. If  $\phi_{yx}$  ranges between 0 and  $\pi/2$ , then the series are positively correlated and  $y(t)$  occupies a leading position compared with  $x(t)$ . If  $\phi_{yx}$  ranges between  $-\pi/2$  and 0, then the series are negatively correlated and  $x(t)$  occupies a leading position compared with  $y(t)$ . If  $\phi_{yx}$  ranges between  $\pi/2$  and  $\pi$ , then the series are negatively correlated and  $x(t)$  occupies a leading position compared with  $y(t)$ . If  $\phi_{yx}$  ranges between  $-\pi$  and  $-\pi/2$ , then the series are negatively correlated and  $y(t)$  occupies a leading position compared with  $x(t)$ .

Wavelet analysis can be extended to cases with multiple time series. This study focuses on three time series. The corresponding wavelet power spectrum is called multiple-wavelet power spectrum, which can be used to analyze the coherency between multiple time series. The warm and cool colors indicate the coherency between the series. Corresponding partial wavelet coherency and partial phase difference indicate research on the coherency and lead–lag relationship between the other two time series, with one time series controlled. Due to the limited space, the paper of Aguiar can be referred to for the specific content of multiple time series [58].

#### 4.2. Data

Three variables are considered in the estimation model: carbon exchange price in the Beijing carbon ETS (BEA), natural gas price, and oil price. Carbon dioxide gas emissions originate mainly from the combustion of fossil energy. Different enterprises have different needs for various types of fossil energy as a result of changes in fossil energy prices. When the price of fossil energy is low, a company increasingly uses fossil energy. This condition leads to greater carbon dioxide emissions, which raises the demand for carbon subsidies and further increases carbon prices, and vice versa. Therefore, oil and gas prices are selected as two variables that affect carbon prices. The present study uses weekly data. Carbon price is the transaction price data on the Beijing carbon market from its establishment until 11 April 2019; these data are obtained from the China Carbon Emissions Exchange Network. Due to the high correlation between the Chinese energy market and the international energy market [59] and the lack of relevant data in China, natural gas prices adopt the natural gas spot price of Port Henry, Louisiana, and the oil price adopts the Russian ESPO crude oil spot price.

## 5. Empirical Results

### 5.1. Empirical Findings of Self-Wavelet Power Spectrum

Self-wavelet power spectrums of carbon price, natural gas price, and oil price in the Beijing carbon market are given in the following. A preliminary analysis on the characteristics of the three time series for carbon price, natural gas price, and oil price from the perspective of volatility shows the actual oscillations of each time series. On the left side of Figure 1, the monthly rate of return of the BEA price and trend chart of the monthly increase rate of natural gas and oil prices are plotted. On the right side of Figure 1, the self-wavelet power spectrum is plotted, with a time span from the end of 2013 to the 14th week of 2019.

In terms of the energy spectrum, the abscissa represents time and the ordinate represents frequency, which is represented by a time period in weeks. Frequency and period can be converted by using the following formula:  $\text{frequency} = 1/\text{period}$ . At each time and frequency, the color of the wavelet power spectrum shows the fluctuation degree of the time series. The color ranges from dark blue to deep red. The deep blue color indicates weaker volatility, while the deep red color indicates stronger volatility. The part inside the red area, that is, the part indicated by the white line, is the time–frequency domain with the most volatility. The black and grey circles represent significance levels of 5% and 10%, respectively. The black conic line indicates the cone of influence, which identifies the wavelet power spectrum region and existence of edge effects. Aguiar’s wavelets toolkit [58] allows current research using wavelet analysis to proceed smoothly. The toolkit can be run with MATLAB, which facilitates the research work of scholars. We thank them for their development and sharing of wavelets tools.

The results of self-wavelet power spectrum are presented in Figure 1, which helps identify the volatility of carbon prices and natural gas and oil prices in the Beijing carbon market under different timescales. Figure 1a.1 shows that the carbon price in the Beijing carbon ETS exhibits a relatively stable fluctuation overall, while strong fluctuations occurred in several areas, which is consistent with the red region in the power spectrum in Figure 1b.1. Days with strong fluctuations are usually concentrated from mid-2014, mid-2015 to mid-2016, and from early 2018 to 2019, which represents the high-frequency domain (less than 17 weeks). In general, the carbon price in the Beijing carbon ETS has been relatively stable. The local fluctuations may be due to the following reasons: in mid-2014, the Beijing carbon ETS conducted its first annual compliance work since its establishment. During this period, emission-controlling companies that have limited knowledge of the carbon market decided to participate so that they could complete the year’s emission-reduction tasks. Furthermore, the secondary market relaxed the conditions for institutional investor participation and introduced the participation of individual investors, making carbon trading active at this stage and thereby leading to large fluctuations in carbon prices. From mid-2015 to mid-2016, the Beijing carbon ETS had more abundant exchange products and initially exerted its central market function, which resulted in considerable activity. In 2018, the Beijing carbon ETS committed to promoting the formation of a multilevel carbon financial market system that coordinates onsite and offsite co-movement, which makes the carbon market active and prices volatile.

The price of natural gas always exhibits obvious cyclical fluctuations, and large fluctuations occur in the fourth quarter of each year. This condition occurs mainly because the increased heating demand, inventory data, and cold air lead to fluctuations in gas prices as the weather gradually cools down [60]. This condition corresponds to the time interval in which the red region appears in the power spectrum, and volatility is higher under the high-frequency domain (periods under 17 weeks), as shown in Figure 1b.2.

In comparison, oil prices are more susceptible to political and economic factors [61]; thus, the oil price is more volatile. Figure 1a.3 shows that the oil price was on a downward trend before 2015, whereas it rapidly increased after 2015. Since then, the price continuously declined and increased at a great amplitude. In terms of oil prices, the more volatile dates are mainly from 2015 to 2017, which are high-frequency domain with a period less than

24 weeks. This condition may have occurred because of the recovery of the world economy in 2015, which effectively promoted the recovery of the global crude oil market. The oil price increased sharply and then fluctuated sharply in the next two years. Oil prices are susceptible to demand and competition, trade prospects, and politics [62], which are also important reasons for oil price fluctuations.

### 5.2. Empirical Findings of Multiple-Wavelet Power Spectrum

Multiple-wavelet power spectrum is helpful in identifying the coherency of multiple time series. Figure 2 shows an estimate of the multiple coherency between the carbon price and the other two time series (natural gas price and oil price), indicating the time and frequency domains when the coherency is the strongest.

Figure 2 shows that from the latter half of 2015 to the end of 2018, the carbon ETS is related to the natural gas and oil markets. In addition, the span of each black circle line is less than half a year, which indicates that no significant long-term coherency exists between the carbon and energy markets. Furthermore, in the high-frequency domain (12–20 weeks), the carbon price and the natural gas and oil price in the Beijing carbon ETS in the two periods of the first half of 2017 and 2018 exerted a significant coherency. This coherency can be reflected in the red area distribution of the multiple power spectrum. In the low-frequency domain (34–58 weeks), two circles exist at the same time point. In general, the relationship between the carbon price and the natural gas and oil price in Beijing's carbon ETS is hardly affected by long-term and continuous changes, whereas it is more affected by short-term price shocks. The influence on carbon prices and natural gas and oil prices intensifies over time, as proven by the fact that the significantly coherent time–frequency domains in 2017 and 2018 are more concentrated.

Multiple-wavelet coherency presents evidence of coherency between carbon and energy prices (natural gas and oil) at different frequency and time domains, illustrating the importance of the relationship between carbon and energy prices (natural gas and oil). However, the relationship between the two variables cannot be distinguished by this information alone. Therefore, further analysis should be based on the partial wavelet coherency and partial phase difference.

### 5.3. Empirical Results of Partial Wavelet Coherency and Partial Phase Differences

This study employed partial wavelet coherency and partial phase difference to identify the lead–lag relationship of carbon and natural gas and oil prices in the Beijing carbon ETS as well as evaluate the dynamic relationship between these prices in the time–frequency domain.

Figure 3 describes partial wavelet coherency, partial wavelet phase difference, and partial wavelet gain between carbon price and each energy price (after another energy price is controlled), thereby reflecting the effect of one variable on another. The middle and right sides of Figure 3 are selected to display the wavelet phase difference and wavelet gain of two frequency bands, which are, respectively, 12–20 and 34–58 weeks, to intuitively reflect the coherency information. This finding is consistent with the coherent and statistically significant frequency bands in Figure 2.

In some partial wavelet coherency diagrams, the coherency color ranges from blue (low coherency) to red (high coherency). For wavelet phase difference, the horizontal axis represents the time scale and the vertical axis represents the phase difference, ranging from  $-\pi$  to  $+\pi$ . The research results prove several findings.

Firstly, the partial coherency (Figure 3a.1) and phase difference (Figure 3b.1) results between the carbon and natural gas prices are obtained from the top part of Figure 3. Three important regions with high coherency overlapped with the highly coherent regions estimated in Figure 2. In the low-frequency domain (34–58 weeks) from the second half of 2015 to the first quarter of 2016, the phase difference ranges between  $-\pi/2$  and 0, indicating that carbon and natural gas prices have a positive coherency. Fluctuations in natural gas prices lead to fluctuations in carbon prices, that is, natural gas is in a leading

position. Another two regions are in the high-frequency domain (12–20 weeks), including the first half of 2017 and the second half of 2018. The phase difference ranges between  $\pi/2$  and  $\pi$ , indicating that carbon and natural gas prices have a negative coherency. An increase in natural gas prices lead to a decrease in carbon prices. The preceding research results indicate the following: (1) In the short term, as in the first half of 2017 and the second half of 2018, the carbon price of the Beijing carbon ETS is negatively related to the price of natural gas, and changes in natural gas prices lead to changes in carbon prices. (2) Over time, the dependence between carbon and natural gas prices intensifies due to the continuous improvement of the carbon price formation mechanism of the Beijing carbon ETS. Partial wavelet gain also shows that, compared with the first half of 2017, the price gains fluctuated more in the second half of 2018, indicating that natural gas and carbon prices are greatly affected by external shocks. Prior to this, the relationship between carbon prices and natural gas prices has also been studied. Duan et al. [63] found that natural gas prices can have an opposite effect on carbon prices through two channels, the aggregated carbon demand effect and the fuel switching mechanism. Hammoudeh, Nguyen, and Sousa [45] also demonstrated that an increase in the price of natural gas reduces the purchase demand of firms and reduces carbon emissions, thus causing the price of carbon to fall. However, Batten et al. [64] show that the effect of natural gas prices on carbon prices is not significant. Our findings confirm the conclusions of the first two studies.

Secondly, the partial coherency (Figure 3a.2) and phase difference (Figure 3b.2) results between the carbon and oil prices are obtained from the bottom part of Figure 3. The regional distribution of this coherency is scattered, indicating that only a short-term co-movement exists between the carbon and oil markets. Therefore, the co-movement relationship between the two is more affected by short-term shocks than by long-term persistence. To further explain the relationship between carbon prices and oil prices, three important regions are selected for further analysis in the high-frequency (period of 12–20 weeks) and low-frequency (period of 34–58 weeks) domains. These three regions have a high coherency at 10% significance level, as shown in Figures 2 and 3. The first region lies in the low-frequency domain from the fourth quarter of 2015 to the first quarter of 2016, whose phase difference ranges between  $-\pi/2$  and 0. This result indicates that carbon and natural gas prices have a positive coherency. Oil is in a leading position in that fluctuations in oil prices lead to fluctuations in carbon prices. In the first quarter of 2018, the second region lies in the high-frequency domain, where the phase difference ranges between  $\pi/2$  and  $\pi$ . This result indicates that carbon and natural gas prices have a positive coherency. Oil is in a leading position in that fluctuations in oil prices lead to fluctuations in carbon prices. In the fourth quarter of 2018, the third region lies in the high-frequency domain, where phase difference ranges between  $-\pi$  and  $-\pi/2$ . This finding indicates that carbon and oil prices have a negative coherency. Carbon is in a leading position in that fluctuations in carbon prices lead to fluctuations in oil prices. The analysis results based on the aforementioned three highly coherent regions show that the carbon and oil prices have an unstable dependence relationship, and their leadership position in the market constantly changes. This result is consistent with the complexity of oil price changes and the fact that the carbon price formation mechanism of the Beijing ETS is incomplete. In addition, partial wavelet gain graph shows that partial gain is stable in both frequency bands, and the value is close to 0.1, which is approximately twice the partial gain between carbon and natural gas prices. The relationship between oil and carbon prices has also been explored by previous researchers. Duan, Ren, Shi, Mishra, and Yan [63] found that oil prices can positively affect the price of natural gas through aggregated carbon demand effects. Hammoudeh, Nguyen, and Sousa [45] found that an increase in crude oil price promotes carbon price in the short run but suppresses it in the long run. In the short run, our findings are consistent with previous studies. However, in the longer term, we believe that the dominant relationship between the price of carbon and the price of oil is changing and there is no clear relationship.



## 6. Conclusions and Policy Recommendations

Understanding the influencing factors of carbon price changes is crucial for studying carbon market prices. In this study, empirical analysis of the coherency and lead–lag relationship between carbon prices and energy prices (natural gas and oil) of the Beijing carbon ETS in the time and frequency domains is performed by using wavelet analysis tools, including partial wavelet coherency and partial phase difference. The conclusions help carbon market participants make appropriate investment and portfolio decisions based on the relationship between the carbon and energy markets. Moreover, the conclusions also have important policy implications for market regulators. For example, risk control and management of market exchanges should be strengthened, and reasonable exchange rules, such as price restrictions and risk reserves, should be formulated to ensure the security and stability of market transactions.

The analysis reveals the following: (1) Multiple-wavelet coherency results show that the carbon price and energy price series are in the high-frequency domain around 2017 and from 2018 to early 2019 (less than 20 weeks), indicating a significantly strong coherency. However, the low-frequency domain (more than 34 weeks) shows a significant coherency in the local period from the second half of 2015 to the middle of 2016. Therefore, the coherency between carbon prices and energy price series has strong coherency in the short term and weak coherency in the long term. The estimation results indicate the correlation between the carbon market and the energy market, especially in the short term. (2) Partial wavelet coherency results of carbon and natural gas prices reflect that these prices have a significantly high coherency in the short term (specifically, the first half of 2017 and the second half of 2018). In the high-frequency band, the phase difference ranges between  $\pi/2$  and  $\pi$  more than half the time, indicating that carbon and natural gas prices have a negative coherency, in that changes in natural gas prices lead to changes in carbon prices. (3) The results of partial coherency and partial phase difference between the carbon price and the oil price series vary greatly in different time–frequency domains. The lead–lag relationship between the two in the high-frequency and low-frequency bands also changes constantly. Therefore, the carbon and oil prices show an unstable dependence relationship. In conclusion, these prices in the Beijing carbon market have a close relationship.

Based on the research results, the following recommendations are presented:

- (1) Investors in the carbon market should pay close attention to energy markets that are strongly coherent with the carbon market. Our findings suggest that the relationship between carbon prices in the Beijing carbon market and the natural gas and oil markets is more influenced by short-term shocks than by long-term persistent factors. In the short term, gas prices and carbon market prices are negatively correlated. Moreover, natural gas prices move earlier than carbon market prices. Although oil price movements are positively correlated with carbon market price movements in the short term, the leadership of the two prices is not certain. This suggests that investors should take full account of the sources of carbon price changes and trends in energy market influences when making long- and short-term investment decisions about the carbon market. Investors can not only use price changes in natural gas to predict carbon price changes in the carbon market, but they can also hedge their risk by investing in the natural gas market for risk control purposes.
- (2) Companies should adjust their energy consumption structure to achieve the optimal carbon emission reduction strategy based on the coherency and fluctuation mechanism between the carbon and energy markets. Our findings suggest that in the short term, the carbon price in the carbon market is negatively correlated with the price of natural gas and positively correlated with the price of oil. Therefore, companies may consider reducing their carbon emissions by increasing the proportion of natural gas in their energy consumption to compress costs when the carbon price rises.
- (3) Regulatory institutions should pay close attention to the possible negative effects of the carbon market bubble. Our findings show that although the trend of carbon price volatility in the Beijing carbon market has been relatively stable overall, strong local

fluctuations have emerged. Therefore, regulators should carry out effective risk control by establishing a sound market supervision mechanism so that the carbon emissions trading market can effectively achieve energy saving and emission reduction.

- (4) Governments need to ensure price stability and secure supply of energy. Our findings show that energy markets are closely linked to carbon markets, and that stability in energy markets helps to ensure the effective functioning of carbon markets. Therefore, in order to fulfil the role of carbon markets in environmental sustainability, it is necessary to ensure a stable and secure supply of energy and to continue to promote the use of renewable energy.

Future research can be further explored in terms of both the research object and the factors influencing the carbon market. In terms of the research object, the official opening of China's national carbon emissions trading market was in July 2021. The relationship between the national carbon market price and the energy price can be further explored by taking the national carbon market as the research object. In terms of carbon market influencing factors, researchers could also consider the linkages between other energy markets and the carbon market, such as the renewable energy market. This could provide more reference for government policy-making and investors' investment decisions.

**Author Contributions:** Conceptualization, R.L. and Y.L.; methodology, R.L., Y.L. and Z.W.; software, Z.W. and M.S.; validation, Z.W. and M.S.; writing—original draft, Z.W. and M.S.; writing—review and editing, Y.L. All authors have read and agreed to the published version of the manuscript.

**Funding:** This research was funded by the National Science Foundation of China (NO. 71904009), Beijing Social Science Fund NO. 20GLC054, MOE (Ministry of Education in China) Project of Humanities and Social Sciences (NO. 18YJC840041), the Postdoctoral Science Foundation of China NO. 2019M652415, Young Scholars Program of Shandong University at Weihai, and Scientific Research Fund for Graduate Students of Business School of Shandong University.

**Institutional Review Board Statement:** Not applicable.

**Informed Consent Statement:** Not applicable.

**Data Availability Statement:** Not applicable.

**Acknowledgments:** Thank Sun Zuoren for the polishing service provided during the modification process.

**Conflicts of Interest:** The authors declare no conflict of interest.

## References

1. Wang, H.; Chen, W. Modeling of energy transformation pathways under current policies, NDCs and enhanced NDCs to achieve 2-degree target. *Appl. Energy* **2019**, *250*, 549–557. [[CrossRef](#)]
2. Cabel, R.; Dechezlepretre, A. Environmental Policy and Directed Technological Change: Evidence from the European Carbon Market. *Rev. Econ. Stat.* **2016**, *98*, 173–191. [[CrossRef](#)]
3. Li, M.Y.; Weng, Y.Y.; Duan, M.S. Emissions, energy and economic impacts of linking China's national ETS with the EU ETS. *Appl. Energy* **2019**, *235*, 1235–1244. [[CrossRef](#)]
4. Ellerman, A.D.; Marcantonini, C.; Zaklan, A. The European Union Emissions Trading System: Ten Years and Counting. *Rev. Environ. Econ. Policy* **2015**, *10*, 89–107. [[CrossRef](#)]
5. McAfee, K. Green economy and carbon markets for conservation and development: A critical view. *Int. Environ. Agreem. Politics Law Econ.* **2016**, *16*, 333–353. [[CrossRef](#)]
6. Wang, C.; Wang, W.; Huang, R. Supply chain enterprise operations and government carbon tax decisions considering carbon emissions. *J. Clean. Prod.* **2017**, *152*, 271–280. [[CrossRef](#)]
7. Yi, L.; Li, Z.P.; Yang, L.; Liu, J.; Liu, Y.R. Comprehensive evaluation on the “maturity” of China's carbon markets. *J. Clean. Prod.* **2018**, *198*, 1336–1344. [[CrossRef](#)]
8. Li, W.; Lu, C. The research on setting a unified interval of carbon price benchmark in the national carbon trading market of China. *Appl. Energy* **2015**, *155*, 728–739. [[CrossRef](#)]
9. Jiang, J.; Xie, D.; Ye, B.; Shen, B.; Chen, Z. Research on China's cap-and-trade carbon emission trading scheme: Overview and outlook. *Appl. Energy* **2016**, *178*, 902–917. [[CrossRef](#)]
10. Mo, J.-L.; Agnolucci, P.; Jiang, M.-R.; Fan, Y. The impact of Chinese carbon emission trading scheme (ETS) on low carbon energy (LCE) investment. *Energy Policy* **2016**, *89*, 271–283. [[CrossRef](#)]

11. Wang, Q.; Chen, X. Energy policies for managing China's carbon emission. *Renew. Sustain. Energy Rev.* **2015**, *50*, 470–479. [CrossRef]
12. Nai, P.; Luo, Y.; Yang, G. The establishment of carbon trading market in People's Republic of China: A legislation and policy perspective. *Int. J. Clim. Change Strateg. Manag.* **2017**, *9*, 138–150. [CrossRef]
13. Chang, C.-L.; Mai, T.-K.; McAleer, M. Establishing national carbon emission prices for China. *Renew. Sustain. Energy Rev.* **2019**, *106*, 1–16. [CrossRef]
14. Lu, M.; Wang, X.; Speeckaert, R. Price bubbles in Beijing carbon market and environmental policy announcement. *Commun. Stat.-Simul. Comput.* **2021**, 1–15. [CrossRef]
15. Zeng, S.; Nan, X.; Liu, C.; Chen, J. The response of the Beijing carbon emissions allowance price (BJC) to macroeconomic and energy price indices. *Energy Policy* **2017**, *106*, 111–121. [CrossRef]
16. Zhang, N.; Liu, Z.; Zheng, X.; Xue, J. Carbon footprint of China's belt and road. *Science* **2017**, *357*, 1107. [CrossRef] [PubMed]
17. Huang, R.; Zhang, S.; Wang, P. Key areas and pathways for carbon emissions reduction in Beijing for the "Dual Carbon" targets. *Energy Policy* **2022**, *164*, 112873. [CrossRef]
18. Zhu, B.; Ye, S.; Han, D.; Wang, P.; He, K.; Wei, Y.-M.; Xie, R. A multiscale analysis for carbon price drivers. *Energy Econ.* **2019**, *78*, 202–216. [CrossRef]
19. Wang, J.; Gu, F.; Liu, Y.; Fan, Y.; Guo, J. Bidirectional interactions between trading behaviors and carbon prices in European Union emission trading scheme. *J. Clean. Prod.* **2019**, *224*, 435–443. [CrossRef]
20. Fan, Y.; Jia, J.-J.; Wang, X.; Xu, J.-H. What policy adjustments in the EU ETS truly affected the carbon prices? *Energy Policy* **2017**, *103*, 145–164. [CrossRef]
21. Song, Y.; Liang, D.; Liu, T.; Song, X. How China's current carbon trading policy affects carbon price? An investigation of the Shanghai Emission Trading Scheme pilot. *J. Clean. Prod.* **2018**, *181*, 374–384. [CrossRef]
22. Li, X.; Li, Z.; Su, C.-W.; Umar, M.; Shao, X. Exploring the asymmetric impact of economic policy uncertainty on China's carbon emissions trading market price: Do different types of uncertainty matter? *Technol. Forecast. Soc. Chang.* **2022**, *178*, 121601. [CrossRef]
23. Bento, N.; Gianfrate, G. Determinants of internal carbon pricing. *Energy Policy* **2020**, *143*, 111499. [CrossRef]
24. Hintermann, B. Allowance price drivers in the first phase of the EU ETS. *J. Environ. Econ. Manag.* **2010**, *59*, 43–56. [CrossRef]
25. Tan, X.; Sirichand, K.; Vivian, A.; Wang, X. How connected is the carbon market to energy and financial markets? A systematic analysis of spillovers and dynamics. *Energy Econ.* **2020**, *90*, 104870. [CrossRef]
26. Yu, J.; Mallory, M.L. Exchange rate effect on carbon credit price via energy markets. *J. Int. Money Financ.* **2014**, *47*, 145–161. [CrossRef]
27. Adekoya, O.B.; Oliyide, J.A.; Noman, A. The volatility connectedness of the EU carbon market with commodity and financial markets in time-and frequency-domain: The role of the US economic policy uncertainty. *Resour. Policy* **2021**, *74*, 102252. [CrossRef]
28. Sun, X.; Fang, W.; Gao, X.; An, H.; Liu, S.; Wu, T. Complex causalities between the carbon market and the stock markets for energy intensive industries in China. *Int. Rev. Econ. Financ.* **2022**, *78*, 404–417. [CrossRef]
29. Wu, Q.; Wang, M.; Tian, L. The market-linkage of the volatility spillover between traditional energy price and carbon price on the realization of carbon value of emission reduction behavior. *J. Clean. Prod.* **2019**, *245*, 118682. [CrossRef]
30. Asl, M.G.; Adekoya, O.B.; Oliyide, J.A. Carbon market and the conventional and Islamic equity markets: Where lays the environmental cleanliness of their utilities, energy, and ESG sectoral stocks? *J. Clean. Prod.* **2022**, *351*, 131523. [CrossRef]
31. Moutinho, V.; Oliveira, H.; Mota, J. Examining the long term relationships between energy commodities prices and carbon prices on electricity prices using Markov Switching Regression. *Energy Rep.* **2022**, *8*, 589–594. [CrossRef]
32. Adekoya, O.B. Predicting carbon allowance prices with energy prices: A new approach. *J. Clean. Prod.* **2021**, *282*, 124519. [CrossRef]
33. Cao, G.; Xu, W. Nonlinear structure analysis of carbon and energy markets with MFDDCA based on maximum overlap wavelet transform. *Phys. A Stat. Mech. Appl.* **2016**, *444*, 505–523. [CrossRef]
34. Zhang, Y.J.; Sun, Y.F. The dynamic volatility spillover between European carbon trading market and fossil energy market. *J. Clean. Prod.* **2016**, *112*, 2654–2663. [CrossRef]
35. Ji, Q.; Zhang, D.Y.; Geng, J.B. Information linkage, dynamic spillovers in prices and volatility between the carbon and energy markets. *J. Clean. Prod.* **2018**, *198*, 972–978. [CrossRef]
36. Hammoudeh, S.; Lahiani, A.; Nguyen, D.K.; Sousa, R.M. An empirical analysis of energy cost pass-through to CO<sub>2</sub> emission prices. *Energy Econ.* **2015**, *49*, 149–156. [CrossRef]
37. Jiang, W.; Chen, Y. The time-Frequency connectedness among carbon, traditional/new energy and material markets of China in pre-and post-COVID-19 outbreak periods. *Energy* **2022**, *246*, 123320. [CrossRef]
38. Guo, W. Factors impacting on the price of China's regional carbon emissions based on adaptive Lasso method. *China Popul. Resour. Environ.* **2015**, *S1*. Available online: [http://en.cnki.com.cn/Article\\_en/CJFDTotal-ZGRZ2015S1077.htm](http://en.cnki.com.cn/Article_en/CJFDTotal-ZGRZ2015S1077.htm) (accessed on 20 January 2021).
39. Wang, Z.; Zhu, Y.; Zhu, Y.; Shi, Y. Energy structure change and carbon emission trends in China. *Energy* **2016**, *115*, 369–377. [CrossRef]
40. Dong, F.; Long, R.; Li, Z.; Dai, Y. Analysis of carbon emission intensity, urbanization and energy mix: Evidence from China. *Nat. Hazards* **2016**, *82*, 1375–1391. [CrossRef]

41. Wagner, G.; Kåberger, T.; Olai, S.; Oppenheimer, M.; Rittenhouse, K.; Sterner, T. Energy policy: Push renewables to spur carbon pricing. *Nature* **2015**, *525*, 27–29. [[CrossRef](#)]
42. Zhou, K.; Li, Y. An Empirical Analysis of Carbon Emission Price in China. *Energy Procedia* **2018**, *152*, 823–828. [[CrossRef](#)]
43. Li, H.; Lei, M. The influencing factors of China carbon price: A study based on carbon trading market in Hubei Province. In *IOP Conference Series: Earth and Environmental Science*; IOP Publishing: Bristol, UK, 2018; p. 052073.
44. Li, W.; Sun, W.; Li, G.; Jin, B.; Wu, W.; Cui, P.; Zhao, G. Transmission mechanism between energy prices and carbon emissions using geographically weighted regression. *Energy Policy* **2018**, *115*, 434–442. [[CrossRef](#)]
45. Hammoudeh, S.; Nguyen, D.K.; Sousa, R.M. What explain the short-term dynamics of the prices of CO<sub>2</sub> emissions? *Energy Econ.* **2014**, *46*, 122–135. [[CrossRef](#)]
46. Sousa, R.; Aguiar-Conraria, L.; Soares, M.J. Carbon financial markets: A time–Frequency analysis of CO<sub>2</sub> prices. *Phys. A Stat. Mech. Appl.* **2014**, *414*, 118–127. [[CrossRef](#)]
47. Vacha, L.; Barunik, J. Co-movement of energy commodities revisited: Evidence from wavelet coherence analysis. *Energy Econ.* **2012**, *34*, 241–247. [[CrossRef](#)]
48. Ortas, E.; Álvarez, I. The efficacy of the European Union Emissions Trading Scheme: Depicting the co-movement of carbon assets and energy commodities through wavelet decomposition. *J. Clean. Prod.* **2016**, *116*, 40–49. [[CrossRef](#)]
49. Bilgili, F.; Öztürk, İ.; Koçak, E.; Bulut, Ü.; Pamuk, Y.; Muğaloğlu, E.; Bağlıtaş, H.H. The influence of biomass energy consumption on CO<sub>2</sub> emissions: A wavelet coherence approach. *Environ. Sci. Pollut. Res.* **2016**, *23*, 19043–19061. [[CrossRef](#)] [[PubMed](#)]
50. Kamdem, J.S.; Nsouadi, A.; Terraza, M. Time-Frequency Analysis of the Relationship between EUA and CER Carbon Markets. *Environ. Model. Assess.* **2016**, *21*, 279–289. [[CrossRef](#)]
51. Daubechies, I. The wavelet transform, time–frequency localization and signal analysis. *IEEE Trans. Inf. Theory* **1990**, *36*, 961–1005. [[CrossRef](#)]
52. Khanna, N.; Kaushik, S.; Jarrah, A. Wavelet packets: Uniform approximation and numerical integration. *Int. J. Wavelets Multiresolut. Inf. Process.* **2020**, *18*, 2050004. [[CrossRef](#)]
53. Zhang, D. Wavelet transform. In *Fundamentals of Image Data Mining*; Springer: Berlin/Heidelberg, Germany, 2019; pp. 35–44.
54. Khanna, N.; Kumar, V.; Kaushik, S. Wavelet packet approximation. *Integral Transform. Spec. Funct.* **2016**, *27*, 698–714. [[CrossRef](#)]
55. Kirby, J.; Swain, C. Power spectral estimates using two-dimensional Morlet-fan wavelets with emphasis on the long wavelengths: Jackknife errors, bandwidth resolution and orthogonality properties. *Geophys. J. Int.* **2013**, *194*, 78–99. [[CrossRef](#)]
56. Addison, P.S. *The Illustrated Wavelet Transform Handbook: Introductory Theory and Applications in Science, Engineering, Medicine and Finance*; CRC Press: Boca Raton, FL, USA, 2017.
57. Mallat, S. *A Wavelet Tour of Signal Processing*; Academic Press: New York, NY, USA, 1998.
58. Aguiar-Conraria, L.; Soares, M.J.; Sousa, R. California’s Carbon Market and Energy Prices: A Wavelet Analysis. *Philos. Trans. R. Soc. A Math. Phys. Eng. Sci.* **2018**, *376*, 20170256. [[CrossRef](#)]
59. He, Y.; Wang, B.; Wang, J.; Xiong, W.; Xia, T. Correlation between Chinese and international energy prices based on a HP filter and time difference analysis. *Energy Policy* **2013**, *62*, 898–909. [[CrossRef](#)]
60. Mu, X. Weather, storage, and natural gas price dynamics: Fundamentals and volatility. *Energy Econ.* **2007**, *29*, 46–63. [[CrossRef](#)]
61. Reboledo, J.C.; Rivera-Castro, M.A.; Ugolini, A. Wavelet-based test of co-movement and causality between oil and renewable energy stock prices. *Energy Econ.* **2017**, *61*, 241–252. [[CrossRef](#)]
62. Baumeister, C.; Kilian, L. Forty years of oil price fluctuations: Why the price of oil may still surprise us. *J. Econ. Perspect.* **2016**, *30*, 139–160. [[CrossRef](#)]
63. Duan, K.; Ren, X.; Shi, Y.; Mishra, T.; Yan, C. The marginal impacts of energy prices on carbon price variations: Evidence from a quantile-on-quantile approach. *Energy Econ.* **2021**, *95*, 105131. [[CrossRef](#)]
64. Batten, J.A.; Maddox, G.E.; Young, M.R. Does weather, or energy prices, affect carbon prices? *Energy Econ.* **2021**, *96*, 105016. [[CrossRef](#)]





Article

# Health-Related Quality of Life According to Sociodemographic Characteristics in the South Korean Population

Chan-Hee Park <sup>1,†</sup>, Eunhee Park <sup>2,3,†</sup>, Hyun-Min Oh <sup>1</sup>, Su-Jin Lee <sup>2</sup>, Sun-Hee Park <sup>4</sup> and Tae-Du Jung <sup>2,3,\*</sup>

<sup>1</sup> Department of Rehabilitation Medicine, Kyungpook National University Hospital, Daegu 41944, Korea; chany9090@gmail.com (C.-H.P.); ohm0105@gmail.com (H.-M.O.)

<sup>2</sup> Department of Rehabilitation Medicine, Kyungpook National University Chilgok Hospital, Daegu 41404, Korea; ehmdpark@knu.ac.kr (E.P.); sujin89898@gmail.com (S.-J.L.)

<sup>3</sup> Department of Rehabilitation Medicine, School of Medicine, Kyungpook National University, Daegu 41944, Korea

<sup>4</sup> Division of Nephrology, Department of Internal Medicine, School of Medicine, Kyungpook National University, Daegu 41944, Korea; 00sum@hanmail.net

\* Correspondence: teeed0522@knu.ac.kr

† These authors contributed equally to this work.

**Abstract:** Health-related quality of life (HRQoL) concerns satisfaction with life and happiness with regard to physical, mental, and social factors. RAND-36 is a publicly available, self-administered questionnaire that examines eight health dimensions. This study evaluated the HRQoL of the South Korean population using the RAND-36 questionnaire and compared HRQoL across sociodemographic characteristics. From May 2015 to May 2019, South Koreans who visited public places aged 19–80 years were recruited and the RAND-36 questionnaire was administered. Overall, 1002 participants were recruited (mean age 45.34 years, 52% men). Men scored better than women in both physical and mental health ( $p < 0.05$ ). There were significant differences in bodily pain ( $p < 0.05$ ), general health perception ( $p < 0.05$ ), and energy / fatigue ( $p < 0.05$ ) dimensions according to the participants' health condition. The HRQoL of South Koreans was lower than average in most dimensions compared with other countries. As the first study to assess this, its data can be used in future studies that apply RAND-36 to evaluate the HRQoL of diseased individuals, as they can compare their findings with those of our study population.

**Keywords:** health-related quality of life; RAND-36; South Korea

**Citation:** Park, C.-H.; Park, E.; Oh, H.-M.; Lee, S.-J.; Park, S.-H.; Jung, T.-D. Health-Related Quality of Life According to Sociodemographic Characteristics in the South Korean Population. *Int. J. Environ. Res. Public Health* **2022**, *19*, 5223. <https://doi.org/10.3390/ijerph19095223>

Academic Editors: Roberto Alonso González Lezcano, Francesco Nocera and Rosa Giuseppina Caponetto

Received: 22 March 2022

Accepted: 24 April 2022

Published: 25 April 2022

**Publisher's Note:** MDPI stays neutral with regard to jurisdictional claims in published maps and institutional affiliations.



**Copyright:** © 2022 by the authors. Licensee MDPI, Basel, Switzerland. This article is an open access article distributed under the terms and conditions of the Creative Commons Attribution (CC BY) license (<https://creativecommons.org/licenses/by/4.0/>).

## 1. Introduction

The concept of health continues to change as medicine and the medical sciences develop. Health is defined as a dynamic state of human welfare characterized by physical, mental, and social potential that meets life-related needs as well as the absence of illness or infirmity. Health-related quality of life (HRQoL) relates to individuals' life satisfaction or happiness with regard to their health status and social and cultural context [1]. This HRQoL mainly addresses public health issues in high-income and rapidly aging countries. HRQoL is typically measured using generic or disease-specific tools [2]. The decision to use a generic or disease-specific tool is determined by several factors, such as the reason for the measurement, the efficiency of the applicable tools, and the population in question. Generic measures are not specific to any disease, age, or treatment group and can be used to compare patients in different situations and with the general population [2,3].

General population data play an important role in determining whether groups or individuals' scores are higher or lower than the average based on country of residence, age, and sex. Published general population data are available for several countries around the world, including the United States [4], Sweden [5], China [1,6], Hong Kong [7], Taiwan [8], and Japan [9]. However, to our knowledge, although HRQoL data of the general population

are very important, there are no suitable general population data on HRQoL in South Korea. In particular, in a revolutionary dynamic situation such as the coronavirus pandemic period, there is a need for research on the HRQoL of the general population to compare between general populations and coronavirus survivors, or to confirm the change in HRQoL before and after coronavirus treatments. It is hoped that this study may be helpful for follow-up studies by presenting results prior to the coronavirus pandemic period, which will be the subject of comparison for future studies.

Many generic questionnaires have been developed to evaluate HRQoL; one of the most widely used instruments is the Short Form-36 Health Survey (SF-36) [1]. The SF-36 was created in the Medical Outcome Study (MOS), a four-year study that specifically focused on outcomes of care [10]. Since its creation, many variations and derivatives of the SF-36 have been developed. In particular, working with the RAND Corporation in 1992, Ware and Sherbourne published their version of SF-36, known as Ware-36, which focuses on eight health domains [11,12]. In 1993, Hays, Sherbourne, and Mazel released the RAND-36 [13]. Unlike Ware-36, the RAND-36 questionnaire and scoring methods are publicly available on the RAND Corporation's website. A longitudinal study performed by MOS showed that the difference in scores between the Ware-36 and RAND-36 scales was subtle, without any significant differences [13]. Specifically, the two surveys differed only in terms of bodily pain and general health dimension subscales. However, according to Hays et al., bodily pain and general health dimension scores had a correlation coefficient of 0.99 [13].

Considering this, we aimed to obtain HRQoL-related data for South Korea using the RAND-36 survey and identify the sociodemographic factors that influence HRQoL.

## 2. Material and Methods

### 2.1. Data Collection

This retrospective cross-sectional study was conducted in South Korea to evaluate HRQoL in five urban and suburban areas. A total of 1002 South Korean citizens aged 19–80 years were recruited to visit public places where areas had foot traffic, including community centers and train stations that attract large populations. This study used a face-to-face questionnaire in Korean. Informed consent was obtained from all of the participants involved in this study. The inclusion criteria were those 19 years of age or older who are capable of independent daily living. From May 2015 to May 2019, a total of 1002 South Koreans were recruited. The participants were asked to fill out a questionnaire that included the RAND-36 health survey and items designed to obtain their general information, such as age, sex, region of residence, education status, occupational status, and marital status. In addition, respondents were asked whether they had been diagnosed with the following diseases: hypertension, angina, myocardial infarction (MI), diabetes mellitus (DM), or cancer and whether they had any of the following health problems: allergies, back pain, visual impairment, skin problems, chronic lung problems, hearing problems, functional impairment in a leg or arm, or joint pain.

Responses to items concerning diseases and current health problems were classified into four categories: (1) no diseases and current health problems, (2) past or current diseases only, (3) current health problems only, and (4) diseases and current health problems [14]. The respondents took approximately 10–15 min to complete the questionnaire, immediately checked the questionnaire after completion, and if data were missing, they were asked to enter the data in question. If there were missing data even after this, the questionnaires were excluded from the statistical analysis. Ethical approval was obtained from the Institutional Review Board of Kyungpook National University Chilgok Hospital (KNUCH IRB no. 2018-11-020).

### 2.2. RAND-36

The RAND-36 is a standardized questionnaire, perhaps the most widely used health-related quality of life (HRQoL) survey tool in the world today [15]. It includes eight health dimensions: physical function (PF), role limitations due to physical health problems (RP),

bodily pain (BP), general health perception (GHP), energy/fatigue (EF), social function (SF), role limitations due to emotional problems (RE), and emotional well-being (EWB). According to the instructions provided on the RAND Corporation website, the eight health dimensions were calculated using 36 items ([https://www.rand.org/health-care/surveys\\_tools/mos/36-item-short-form.html](https://www.rand.org/health-care/surveys_tools/mos/36-item-short-form.html), accessed on 5 May 2015).

The items evaluating role limitations (physical and emotional) are answered using “yes” or “no” responses, whereas the other items are scored using scales ranging from 3 to 6 points. According to RAND-36 scoring algorithms, the raw scores for each item should be summed and converted to a 0–100 scale, with 100 representing the best possible health state [13]. The RAND-36 dimensions can be classified into two categories: physical health composites (PHCs), which relate to physical function, and mental health composites (MHCs), which relate to mental and emotional well-being. PHCs were obtained by summing the scores for the PF, RP, BP, and GHP dimensions, whereas MHC was determined by summing the scores for the EF, SF, RE, and EWB dimensions [13].

### 2.3. Statistical Analysis

Descriptive statistics are presented as mean values and standard deviations (SDs) and included percentages for absolute counts regarding age, sex, education level, marital status, and health condition. The internal consistency of the RAND-36 questionnaire was evaluated using Cronbach’s  $\alpha$  coefficient; a Cronbach’s  $\alpha$  of 0.7 or greater is generally considered to indicate adequate internal consistency [16]. In addition, construct validity was evaluated using correlation analysis, and factor loadings greater than 0.50 were considered to indicate validity [17]. Finally, analysis of covariance was used to assess the independent effects of education, marital status, and health condition on the RAND-36 scale by controlling for age and sex effects. The data were processed and analyzed using a statistical software program (IBM SPSS Statistics 25.0, IBM, New York, NY, USA).

## 3. Results

### 3.1. Sample Characteristic

A questionnaire survey was administered between May 2015 and May 2019. Data from 1002 participants (525 men and 477 women) were analyzed. All subjects were aged between 19 and 80 years, with an average age of  $45.34 \pm 12.00$  years. Respondents’ characteristics are listed in Table 1.

**Table 1.** The demographic characteristics of the respondents (n = 1002).

Sociodemographic Factors		n (%)
Age	29 or less (years)	122 (12%)
	30–39	197 (20%)
	40–49	302 (30%)
	50–59	264 (26%)
	60 or more	117 (12%)
Gender	Male	525(52%)
	Female	477(48%)
Education level	Elementary school education	45 (4%)
	Middle school education	47 (5%)
	High school education	330 (33%)
	University education	580 (58%)
Marital status	Single	184 (18%)
	Married/Cohabitant	792 (79%)
	Widows/Widowers	15 (1%)
	Divorced/Separated	11 (1%)
Health condition	No disease and current health problem	525 (52%)
	Past or current disease only	180 (19%)
	Current health problem only	224 (22%)
	Disease and current health problem	73 (7%)



Of the 1002 subjects, 26% had a past or current disease, with hypertension being the most common (160; 63%), followed by MI (16; 6%), angina (10; 4%), DM (65; 26%), and cancer (61; 24%). Approximately 30% had a current health problem, with chronic back pain (115; 39%) and chronic allergies (89; 30%) being the most common.

### 3.2. Data Quality

The internal reliability of the RAND-36 was assessed using Cronbach’s  $\alpha$  coefficient. This indicated that six of the eight dimensions had good internal consistency, with the exception of EF and EWB. Overall, of the eight dimensions, the lowest Cronbach’s  $\alpha$  coefficient was found for the EWB (0.366), whereas the SF scored the highest (0.989; Table 2).

**Table 2.** Reliability estimates (Cronbach’s  $\alpha$ ) and correlation for the RAND-36 dimensions.

Dimension	No. of Items	Reliability		Correlation	
		Cronbach’s $\alpha$	Correlations between Dimensions and Items	PHC	MHC
PF	3, 4, 5, 6, 7, 8, 9, 10, 11, 12	0.875	0.299–0.756	0.577	0.380
RP	13, 14, 15, 16	0.904	0.812–0.869	0.707	0.452
BP	21, 22	0.774	0.820–0.945	0.648	0.397
GHP	1, 33, 34, 35, 36	0.785	0.612–0.808	0.710	0.570
EF	23, 27, 29, 31	0.369	0.618–0.711	0.488	0.757
SF	20, 32	0.989	0.761–0.909	0.538	0.737
RE	17, 18, 19	0.878	0.865–0.882	0.548	0.580
EWB	24, 25, 26, 28, 30	0.366	0.604–0.740	0.459	0.875

PF, physical functioning; RP, role limitation, physical; BP, bodily pain; GHP, general health perception; EF, energy/fatigue; SF, social function; RE, role limitation, emotional; EWB, emotional well-being; PHC, physical health composites; MHC, mental health composites.

Spearman’s correlation analysis was used to analyze the correlation between the dimensions and items. PF, RP, BP, and GHP were more closely related to the PHC scale, whereas EF, SF, RE, and EWB were more closely related to MHC. Moreover, the correlation between PHC and its constituent dimensions ranged from 0.577 (PF) to 0.710 (GHP), whereas the correlation between MHC and its component dimensions ranged from 0.580 (RE) to 0.875 (EWB; Table 2).

### 3.3. HRQoL Data

The HRQoL data stratified by age and sex are presented in Table 3. For each dimension, when all age groups’ scores were considered cumulatively, men scored higher than women ( $p < 0.05$ ). In this regard, the difference in the RE dimension was greatest at 4.35, and the difference in the EWB dimension was smallest at 1.96 points on a scale ranging from 0 to 100. Comparing specific age groups across sexes, females had lower scores than males in almost all dimensions. Here, the exceptions were PF, SF, and RE for females aged 30–39 years, GHP and SF for females aged 19–29 years, and EWB for females aged 50–59 years.

Among males, subjects aged 50–59 years showed the lowest scores in PF, GHP, and EWB, and those aged 40–49 years showed the lowest scores in RP, BP, and RE. In EF and SF, subjects aged 30–39 years had the lowest scores, whereas, in the PHC scales, subjects aged 60 years or older had the highest scores, and subjects aged 50–59 years had the lowest scores.

Among females, subjects over 60 years old returned the lowest scores in PF, RP, BP, GHP, and EF, whereas subjects aged 20–29 years showed the lowest scores in the EWB dimension. For the MHC scale, subjects aged 30–39 years returned the highest scores, whereas subjects aged 40–49 years showed the lowest scores. For the PHC scales, the lowest scores were provided by participants over 60 years of age; the higher the age, the lower the score.

**Table 3.** Mean RAND-36 dimensions scores (SD) by gender and age groups (higher scores indicate better health).

	Age Group											
	≤29 Years		30–39 Years		40–49 Years		50–59 Years		≥60 Years		ALL	
	M (n = 49)	F (n = 73)	M (n = 100)	F (n = 97)	M (n = 152)	F (n = 150)	M (n = 152)	F (n = 112)	M (n = 72)	F (n = 45)	M (n = 525)	F (n = 477)
PF	92.55 (10.01)	92.12 (12.27)	90.10 (15.06)	90.67 (11.03)	91.12 (14.84)	88.83 (12.56)	88.62 (18.22)	85.80 (16.50)	91.88 (13.01)	78.22 (21.32)	90.44 (15.36)	88.00 (14.72)
RP	86.73 (33.50)	79.79 (36.48)	84.50 (32.33)	83.76 (30.63)	75.33 (40.07)	74.67 (35.12)	79.61 (35.98)	75.00 (35.36)	82.64 (36.25)	62.78 (44.79)	80.38 (36.46)	76.26 (35.85)
BP	84.63 (16.95)	84.05 (18.06)	84.04 (19.06)	79.39 (19.08)	82.69 (19.65)	78.93 (21.73)	82.74 (20.64)	80.21 (21.37)	86.58 (16.53)	73.27 (24.25)	83.68 (19.18)	79.58 (20.94)
GHP	62.00 (16.02)	62.56 (20.40)	62.19 (17.99)	61.40 (18.32)	62.84 (15.60)	59.03 (17.32)	61.43 (15.91)	60.21 (16.62)	65.97 (17.48)	57.27 (20.82)	62.66 (16.47)	60.16 (18.20)
EF	57.96 (12.45)	53.49 (15.76)	56.25 (13.36)	54.28 (14.98)	58.16 (13.41)	54.53 (13.56)	57.14 (13.32)	54.78 (14.48)	59.58 (13.76)	53.33 (17.58)	57.68 (13.32)	54.27 (14.77)
SF	84.95 (16.33)	86.13 (20.15)	84.13 (20.09)	86.08 (18.56)	85.53 (18.32)	78.75 (19.90)	85.12 (19.34)	83.48 (19.29)	89.24 (15.60)	80.00 (19.84)	85.60 (18.45)	82.60 (19.70)
RE	85.03 (31.23)	78.54 (37.42)	83.33 (34.33)	84.19 (30.84)	77.85 (38.92)	71.78 (40.27)	82.89 (33.88)	78.27 (35.71)	82.87 (38.35)	77.04 (41.33)	81.71 (35.85)	77.36 (37.23)
EWB	62.69 (11.06)	60.33 (15.34)	63.20 (13.59)	62.47 (13.95)	64.08 (13.91)	61.01 (13.54)	62.66 (13.26)	62.71 (14.61)	66.17 (14.30)	62.04 (14.11)	63.66 (13.47)	61.70 (14.19)
PHC	52.55 (5.10)	51.83 (7.19)	52.01 (6.68)	51.34 (6.36)	51.15 (6.98)	49.86 (6.97)	51.10 (7.10)	49.86 (7.48)	52.84 (6.00)	46.57 (9.50)	51.66 (6.69)	50.15 (7.39)
MHC	47.35 (6.13)	45.93 (8.46)	47.02 (7.66)	46.85 (7.33)	47.43 (7.22)	44.90 (7.70)	47.13 (7.42)	46.33 (7.73)	48.91 (6.90)	45.42 (8.10)	47.46 (7.23)	45.84 (7.80)

PF, physical functioning; RP, role limitation, physical; BP, bodily pain; GHP, general health perception; EF, energy/fatigue; SF, social function; RE, role limitation, emotional; EWB, emotional well-being; PHC, physical health composites; MHC, mental health composites.

When age and sex were adjusted for, marital status was found to have no significant effect on any dimension (Table 4). However, when comparing raw scores, widow/widower subjects (15; 1%) showed the highest scores in all dimensions except for PF, in which divorced/separated subjects (11; 1%) showed the highest score. However, divorced/separated participants had the lowest scores in all dimensions except PF, RP, and EWB. Education level had no significant effect on any of the dimensions. In all dimensions, subjects who only had elementary school education (45; 4%) showed the lowest scores; however, there was no corresponding pattern among subjects with high education levels (i.e., they did not return the highest scores in all dimensions).

For BP, GHP, and EF, after controlling for the effects of age and sex, we found statistical differences in health conditions (Table 4). As expected, subjects without diseases and current health problems had the highest scores, whereas respondents with no diseases but current health problems returned the lowest scores. Health conditions had no significant effect on the MHC scale but had a significant effect on the PHC scale, which seems to reflect the results for BP and GHP.

**Table 4.** RAND-36 dimensions scores in relation to marital status, education level, and health condition (raw scores and controlled for age and gender by ANCOVAs (=in bold)).

	PF	RP	BP	GHP	EF	SF	RE	EWB	PHC	MHC
Marital status										
<i>p</i> -Value	0.862	0.118	0.387	0.467	0.051	0.517	0.189	0.739	0.277	0.261
Single	91.58	82.75	83.81	62.37	55.76	83.83	83.15	62.02	52.00	46.61
Married/Cohabitant	<b>89.75</b>	<b>79.76</b>	<b>83.16</b>	<b>62.12</b>	<b>56.02</b>	<b>83.05</b>	<b>82.92</b>	<b>62.35</b>	<b>51.39</b>	<b>46.61</b>
Widows/Widowers	88.84	77.05	81.33	61.20	56.08	84.22	78.54	62.80	50.67	46.66
Divorced/Separated	<b>89.19</b>	<b>77.62</b>	<b>81.43</b>	<b>61.23</b>	<b>56.01</b>	<b>84.36</b>	<b>78.56</b>	<b>62.73</b>	<b>50.79</b>	<b>46.65</b>
University education	83.33	93.33	82.93	66.53	63.33	88.33	93.33	66.40	52.57	49.94
High school education	<b>86.65</b>	<b>98.99</b>	<b>85.23</b>	<b>67.77</b>	<b>64.17</b>	<b>90.46</b>	<b>95.24</b>	<b>66.63</b>	<b>53.95</b>	<b>50.51</b>
Middle school education	90.46	84.09	73.73	59.18	49.09	80.68	81.82	64.00	50.38	45.61
Elementary school education	<b>91.18</b>	<b>85.27</b>	<b>73.93</b>	<b>59.24</b>	<b>48.92</b>	<b>80.96</b>	<b>81.83</b>	<b>63.83</b>	<b>50.61</b>	<b>45.58</b>
Education level										
<i>p</i> -Value	0.504	0.659	0.232	0.747	0.679	0.663	0.285	0.123	0.548	0.355
Elementary school education	83.22	67.22	77.58	60.02	55.22	80.56	68.89	61.78	48.46	45.29
Middle school education	<b>86.40</b>	<b>71.34</b>	<b>78.99</b>	<b>61.19</b>	<b>55.07</b>	<b>81.74</b>	<b>69.68</b>	<b>60.78</b>	<b>49.55</b>	<b>45.22</b>
High school education	89.04	75.53	81.13	63.81	57.02	86.17	82.98	62.30	50.88	47.17
University education	<b>91.01</b>	<b>77.93</b>	<b>81.54</b>	<b>64.25</b>	<b>56.35</b>	<b>86.55</b>	<b>82.91</b>	<b>61.27</b>	<b>51.45</b>	<b>46.86</b>
Past or Current disease only	89.08	78.18	79.78	61.26	55.21	84.21	78.69	61.52	50.64	46.22
Current health problem only	<b>89.51</b>	<b>78.79</b>	<b>80.10</b>	<b>61.50</b>	<b>55.35</b>	<b>84.46</b>	<b>78.95</b>	<b>61.50</b>	<b>50.82</b>	<b>46.29</b>
Disease and Current health problem	89.88	79.66	83.20	61.52	56.52	84.27	80.75	63.73	51.31	47.02
Health condition	<b>89.22</b>	<b>78.80</b>	<b>82.87</b>	<b>61.25</b>	<b>56.51</b>	<b>84.00</b>	<b>80.54</b>	<b>63.69</b>	<b>51.08</b>	<b>47.02</b>
Health condition										
<i>p</i> -Value	0.101	0.858	<b>0.001 *</b>	<b>0.040 *</b>	<b>0.034 *</b>	0.659	0.680	0.479	<b>0.018 *</b>	0.337
No disease and Current health problem	90.62	79.52	84.06	62.89	57.13	84.38	80.63	63.17	51.67	47.04
Past or Current disease only	<b>90.30</b>	<b>78.99</b>	<b>83.98</b>	<b>62.91</b>	<b>57.32</b>	<b>84.31</b>	<b>80.60</b>	<b>63.31</b>	<b>51.58</b>	<b>47.09</b>
Current health problem only	86.86	76.94	80.94	60.98	55.27	85.07	77.04	63.02	50.36	46.63
Disease and Current health problem	<b>87.14</b>	<b>77.44</b>	<b>80.71</b>	<b>60.72</b>	<b>54.67</b>	<b>84.93</b>	<b>76.70</b>	<b>62.63</b>	<b>50.38</b>	<b>46.41</b>
Health condition	88.50	76.90	77.14	58.92	54.55	82.65	79.17	61.46	49.81	45.92
No disease and Current health problem	<b>88.69</b>	<b>77.19</b>	<b>77.42</b>	<b>59.10</b>	<b>54.81</b>	<b>82.85</b>	<b>79.50</b>	<b>61.61</b>	<b>49.92</b>	<b>46.04</b>
Past or Current disease only	87.95	78.77	80.95	60.34	54.80	85.10	80.37	62.69	50.58	46.65
Current health problem only	<b>88.97</b>	<b>80.50</b>	<b>81.16</b>	<b>60.24</b>	<b>54.14</b>	<b>85.30</b>	<b>80.46</b>	<b>62.20</b>	<b>50.88</b>	<b>46.47</b>
Disease and Current health problem										

PF, physical functioning; RP, role limitation, physical; BP, bodily pain; GHP, general health perception; EF, energy/fatigue; SF, social function; RE, role limitation, emotional; EWB, emotional well-being; PHC, physical health composites; MHC, mental health composites. \* *p*-Value < 0.05, *p*-Value apply for adjusted scores for age and gender.

#### 4. Discussion

This study observed HRQoL-related data for South Korea using the RAND-36 health questionnaire. Such data can provide a basis for future studies seeking to analyze and evaluate the quality of life of South Koreans with regard to age and sex. Additionally, the HRQoL data can be used as comparative data for future studies that seek to use RAND-36 to evaluate the HRQoL of patients with specific diseases.

To perform this, internal consistency was evaluated using Cronbach’s  $\alpha$  coefficient, and we consequently determined that six of RAND-36’s eight dimensions had good internal consistency, with EF and EWB being the exceptions. Specifically, the Cronbach’s  $\alpha$  coefficients for the EWB and EF were 0.366 and 0.369, respectively. This low coefficient can be attributed to the characteristics of South Koreans. Traditionally, South Koreans are reluctant to reveal the state of their mental health [18,19]. For example, among South Koreans, many mental health patients choose to keep their treatment and condition secret. Socially, the country has a culture that regards the diagnoses of mental illnesses as different from those of physical illnesses. For items 24, 25, and 28, which are part of the EWB dimension and concern the negative aspects of mental health, the respondents may have selected responses that portrayed their mental health more positively, regardless of their actual condition. In contrast, for items with positive content, such as items 26 and 30, the respondents may have selected responses reflecting their reality. For EF, participants may have given more positive responses to items 29 and 31 and may have answered positive items, such as 23 and 27, more accurately. This should be understood as a characteristic of regions with significant differences in the diagnosis rate of depression, including East Asia, or regions, such as South Korea, with low access to mental health services for various

reasons (social awareness, institutional disadvantage, treatment costs, drug side effects). These characteristics should be considered when interpreting the study results.

Our results showed that the RAND-36 questionnaire has reliable construct validity, which is consistent with the findings of previous surveys [20]. Our correlation analysis indicated that each of the eight dimensions was highly correlated with the related composite scale. Specifically, we found that PF, RP, BP, and GHP had higher correlations with PHC, whereas EF, SF, RE, and EWB had higher correlations with MHC, which is consistent with previous studies [11,13,20]. Thus, using RAND-36 to evaluate the HRQoL of the general South Korean population was determined to be reasonable.

Previous studies have shown that men generally scored higher than women in terms of quality of life index by age group. In particular, the higher the age group, the larger the gap, which shows that there are time and economic reasons behind the decline in quality of life as people age [21,22]. It turns out that time factors are at play in middle age and economic factors are at play in old age.

In this study, quality of life was divided into PHC and MHC groups. For the PHC dimensions, male respondents scored higher than female respondents. For females, physical scores tended to decrease with age, which can be attributed to age-related biological changes, and there was no change in their physical role or position despite being older. In males, physical scores decreased up to the 50–59 years age group and then increased, with better health status observed among older individuals. This may be due to sociological changes that occur in men when they retire in their early 60s. At that time, they can pay more attention to their health because of the economic and time allowance.

Regarding MHC dimensions, as with the PHC scales, males scored higher than females. Men had the poorest mental health at 30–39 years, when they were likely to be in the most stressful situations. At this age, they must find jobs and struggle to survive in employment. They also establish new homes and support themselves, both economically and mentally. The finding that older individuals had the best mental health was attributed to the above-mentioned sociological changes that occur at retirement. Sprangers and Schwartz [23] suggested that men over 60 years of age scored higher on the PHC and MHC scales as a result of the theoretical model of response shift. Unlike males, females aged 40–49 years had the lowest scores on the mental scale. At this age, middle-aged women may have a very poor quality of life, not only because of family problems but also because of children's educational problems.

Education level and marital status had no significant effects on any dimension. In South Korea, education up to middle school is compulsory, but South Koreans are generally zealous about educating their children, with a high school enrollment rate of 99% and university enrollment rate of 69.76%, which is the highest among OECD countries [24,25]. Among the participants in this survey, 91% had graduated from high school. The fact that marital status did not have a significant effect was attributed to the Confucian culture that persists in South Korea. In South Korea, divorce and separation are considered sinful and worthy of social punishments. In addition, there are many cases where couples refrain from divorce or separation to avoid negatively affecting their children. Reflecting on these Confucian characteristics, 97% of the respondents in this study were single or married/cohabitant. These social and cultural characteristics significantly affected education level and marital status.

This study had some limitations. First of all, we did not conduct sampling before recruiting our study population. Random sampling is the best method for evaluating the quality of life in participants. However, this was not done in our study, and there is a possibility of sampling bias. Second, we recruited participants and interviewed them face-to-face in the foot traffic areas that attract large populations, so it took a long time, namely four years. This could cause a source of bias. Third, among the total respondents, the number of respondents in the widow/widower and divorced/separated groups in terms of marital status was very small, and the number of respondents in the elementary and middle school education groups in terms of education level was very small. This

was due to socioeconomic and cultural differences, which may have affected the statistical analysis. To recruit respondents from various areas, questionnaires were distributed to public and commercial service organizations, community centers, and train stations that attract large populations. Among the respondents recruited, some lived in suburban areas; however, as most of the areas were located downtown, we may have recruited more urban-based than suburban-based people, which may have affected the results. Although the interviewers who instructed the participants to complete the questionnaire received identical instructions, there could have been differences in the explanations provided by the interviewers, which might have influenced the results. It is difficult to evaluate this quantitatively; however, it can still be considered a limitation of this study.

## 5. Conclusions

In conclusion, the HRQoL data for the South Korean population showed that the scores were somewhat lower than those of other countries or cities. In particular, South Korea's EF and EWB dimensions, which are part of the MHC, were the sixth lowest among the countries and cities analyzed. There were no significant differences in HRQoL scores with regard to education level and marital status in South Korea, but there were significant differences in BP, GHP, and EF with regard to health conditions. These HRQoL data for our study population can be used in future studies that seek to use the RAND-36 questionnaire to evaluate the HRQoL of patients with specific diseases and compare the results with those of our study population. In addition, this is a kind of preliminary study in a study targeting a general population that has been subjected to appropriate random sampling in the future, and it is expected that it will be helpful in interpreting the results.

**Author Contributions:** Conceptualization, S.-H.P. and T.-D.J.; methodology, S.-J.L.; formal analysis, H.-M.O.; investigation, S.-J.L.; writing—original draft preparation, E.P.; writing—review and editing, C.-H.P.; supervision, S.-H.P. and T.-D.J. All authors have read and agreed to the published version of the manuscript.

**Funding:** There is no funding to report for this submission.

**Institutional Review Board Statement:** The study was conducted in accordance with the Declaration of Helsinki, and approved by the Institutional Review Board of Kyungpook National University Chilgok Hospital (No. 2018-11-020).

**Informed Consent Statement:** Informed consent was obtained from all subjects involved in the study.

**Data Availability Statement:** Available upon reasonable request.

**Acknowledgments:** We thank all the study respondents for their participation in our survey. We thank the anonymous reviewer for their helpful comments, which improved our manuscript.

**Conflicts of Interest:** There are no conflict of interest for any of the authors.

## References

1. Wang, R.; Wu, C.; Zhao, Y.; Yan, X.; Ma, X.; Wu, M.; Liu, W.; Gu, Z.; Zhao, J.; He, J. Health related quality of life measured by SF-36: A population-based study in Shanghai, China. *BMC Public Health* **2008**, *8*, 1–8. [[CrossRef](#)] [[PubMed](#)]
2. Bell, M.J.; Bombardier, C.; Tugwell, P. Measurement of functional status, quality of life, and utility in rheumatoid arthritis. *Arthritis Rheum.* **1990**, *33*, 591–601. [[CrossRef](#)] [[PubMed](#)]
3. McKenna, S. Book Review: Quality of Life and Pharmacoeconomics in Clinical Trials.(1996). B. Spilker (Ed.). Lippincott-Raven, Philadelphia. Pp xlv+ 1259.£ 114.50. ISBN 0-7817-0332-8 (hardback). *J. Community Appl. Soc. Psychol.* **1997**, *7*, 425–428. [[CrossRef](#)]
4. Ware, J.E. SF-36 health survey: Manual and interpretation guide. *Health Inst.* **1993**, *10*, 16–17.
5. Ohlsson-Nevo, E.; Hiyoshi, A.; Norén, P.; Möller, M.; Karlsson, J. The Swedish RAND-36: Psychometric characteristics and reference data from the Mid-Swed Health Survey. *J. Patient-Rep. Outcomes* **2021**, *5*, 1–11. [[CrossRef](#)]
6. Li, L.; Wang, H.; Shen, Y. Chinese SF-36 Health Survey: Translation, cultural adaptation, validation, and normalisation. *J. Epidemiol. Community Health* **2003**, *57*, 259–263. [[CrossRef](#)]
7. Lam, C.; Lauder, I.; Lam, T.; Gandek, B. Population based norming of the Chinese (HK) version of the SF-36 health survey. *Hong Kong Pract.* **1999**, *1*, 1–9.
8. Tseng, H.-M.; Lu, J.-f.R.; Gandek, B. Cultural issues in using the SF-36 Health Survey in Asia: Results from Taiwan. *Health Qual. Life Outcomes* **2003**, *1*, 1–9. [[CrossRef](#)]

9. Fukuhara, S.; Ware, J.E., Jr.; Kosinski, M.; Wada, S.; Gandek, B. Psychometric and clinical tests of validity of the Japanese SF-36 Health Survey. *J. Clin. Epidemiol.* **1998**, *51*, 1045–1053. [[CrossRef](#)]
10. Tarlov, A.R.; Ware, J.E.; Greenfield, S.; Nelson, E.C.; Perrin, E.; Zubkoff, M. The Medical Outcomes Study: An application of methods for monitoring the results of medical care. *JAMA* **1989**, *262*, 925–930. [[CrossRef](#)]
11. Ware, J.E., Jr.; Sherbourne, C.D. The MOS 36-item short-form health survey (SF-36): I. Conceptual framework and item selection. *Med. Care* **1992**, *30*, 473–483. [[CrossRef](#)]
12. Ware, J.E., Jr. SF-36 health survey update. *Spine* **2000**, *25*, 3130–3139. [[CrossRef](#)] [[PubMed](#)]
13. Hays, R.D.; Sherbourne, C.D.; Mazel, R.M. The rand 36-item health survey 1.0. *Health Econ.* **1993**, *2*, 217–227. [[CrossRef](#)] [[PubMed](#)]
14. HÅvard Loge, J.; Kaasa, S. Short form 36 (SF-36) health survey: Normative data from the general Norwegian population. *Scand. J. Soc. Med.* **1998**, *26*, 250–258. [[CrossRef](#)]
15. Hays, R.D.; Morales, L.S. The RAND-36 measure of health-related quality of life. *Ann. Med.* **2001**, *33*, 350–357. [[CrossRef](#)]
16. Tavakol, M.; Dennick, R. Making sense of Cronbach’s alpha. *Int. J. Med. Educ.* **2011**, *2*, 53. [[CrossRef](#)] [[PubMed](#)]
17. Fang, J.-Q. *Handbook of Medical Statistics*; World Scientific Publishing Co. Pte. Ltd.: Singapore, 2017.
18. Jin-Ah, J.; Min-Kyung, J.; Nang-Hee, K.; Park, J.; Yong-Ju, L.; Yun, S.; Yoo, H.-Y.; Bo-Eun, K. *A Study on Strategies to Strengthen Access to Mental Health Services Centered on Consumers*; 8968276560; Korea Institute for Health and Social Affairs: Sejong City, Korea, 2019.
19. Ferrari, A.J.; Charlson, F.J.; Norman, R.E.; Patten, S.B.; Freedman, G.; Murray, C.J.; Vos, T.; Whiteford, H.A. Burden of depressive disorders by country, sex, age, and year: Findings from the global burden of disease study 2010. *PLoS Med.* **2013**, *10*, e1001547. [[CrossRef](#)]
20. Han, C.-W.; Lee, E.-J.; Iwaya, T.; Kataoka, H.; Kohzuki, M. Development of the Korean version of Short-Form 36-Item Health Survey: Health related QOL of healthy elderly people and elderly patients in Korea. *Tohoku J. Exp. Med.* **2004**, *203*, 189–194. [[CrossRef](#)]
21. Cherepanov, D.; Palta, M.; Fryback, D.G.; Robert, S.A. Gender differences in health-related quality-of-life are partly explained by sociodemographic and socioeconomic variation between adult men and women in the US: Evidence from four US nationally representative data sets. *Qual. Life Res.* **2010**, *19*, 1115–1124. [[CrossRef](#)]
22. Orfila, F.; Ferrer, M.; Lamarca, R.; Tebe, C.; Domingo-Salvany, A.; Alonso, J. Gender differences in health-related quality of life among the elderly: The role of objective functional capacity and chronic conditions. *Soc. Sci. Med.* **2006**, *63*, 2367–2380. [[CrossRef](#)]
23. Sprangers, M.A.; Schwartz, C.E. Integrating response shift into health-related quality of life research: A theoretical model. *Soc. Sci. Med.* **1999**, *48*, 1507–1515. [[CrossRef](#)]
24. Byung-young, P. 2017 *Brief Statistics on Korean Education (SM2017-02-02)*; [KEDI] Research Report; KEDI: Seoul, Korea, 2017; pp. 1–63.
25. OECD. *Health at a Glance 2017: OECD Indicators*; OECD: Paris, France, 2017.





Article

# An Analysis of the Colony Structure of Prokaryotes in the Jialing River Waters in Chongqing

Maolan Zhang <sup>1,†</sup>, Guoming Zeng <sup>1,†</sup>, Dong Liang <sup>1</sup>, Yiran Xu <sup>1</sup>, Yan Li <sup>2</sup>, Xin Huang <sup>1</sup>, Yonggang Ma <sup>2</sup>, Fei Wang <sup>1</sup>, Chenhui Liao <sup>1</sup>, Cheng Tang <sup>1</sup>, Hong Li <sup>3,\*</sup>, Yunzhu Pan <sup>4,\*</sup> and Da Sun <sup>5,\*</sup>

- <sup>1</sup> Chongqing Engineering Laboratory of Nano/Micro Biological Medicine Detection Technology, School of Architecture and Engineering, Chongqing University of Science and Technology, Chongqing 401331, China; 2019016@cqust.edu.cn (M.Z.); 2017015@cqust.edu.cn (G.Z.); 1632413306@163.com (D.L.); x8532105@163.com (Y.X.); 2019443106@cqust.edu.cn (X.H.); 2021206106@cqust.edu.cn (F.W.); 2021206103@cqust.edu.cn (C.L.); 2021206010@cqust.edu.cn (C.T.)
- <sup>2</sup> School of Pharmacy, Taizhou Polytechnic College, Taizhou 225300, China; 20066954@cqu.edu.cn (Y.L.); zml@cqu.edu.cn (Y.M.)
- <sup>3</sup> Key Laboratory of Eco-Environment of Three Gorges Region, Ministry of Education, Chongqing University, Chongqing 400044, China
- <sup>4</sup> School of Chemical Engineering, Sichuan University of Science and Engineering, Zigong 643000, China
- <sup>5</sup> Institute of Life Sciences and Biomedical Collaborative Innovation Center of Zhejiang Province, Wenzhou University, Wenzhou 325035, China
- \* Correspondence: hongli@cqu.edu.cn (H.L.); panyuzhu19870506@163.com (Y.P.); sunday@wzu.edu.cn (D.S.); Tel./Fax: +86-173-6586-6501 (D.S.)
- † These two authors contributed equally to this work.

**Citation:** Zhang, M.; Zeng, G.; Liang, D.; Xu, Y.; Li, Y.; Huang, X.; Ma, Y.; Wang, F.; Liao, C.; Tang, C.; et al. An Analysis of the Colony Structure of Prokaryotes in the Jialing River Waters in Chongqing. *Int. J. Environ. Res. Public Health* **2022**, *19*, 5525. <https://doi.org/10.3390/ijerph19095525>

Academic Editors: Roberto Alonso González Lezcano, Francesco Nocera, Rosa Giuseppina Caponetto and Paul B. Tchounwou

Received: 29 March 2022

Accepted: 29 April 2022

Published: 2 May 2022

**Publisher's Note:** MDPI stays neutral with regard to jurisdictional claims in published maps and institutional affiliations.



**Copyright:** © 2022 by the authors. Licensee MDPI, Basel, Switzerland. This article is an open access article distributed under the terms and conditions of the Creative Commons Attribution (CC BY) license (<https://creativecommons.org/licenses/by/4.0/>).

**Abstract:** At present, research on the influence of human activities (especially urbanization) on the microbial diversity, structural composition, and spatial distribution of rivers is limited. In this paper, to explore the prokaryotic community structure and the relationship between the community and environmental factors in the Jialing River Basin of Chongqing, so as to provide a basis for monitoring microorganisms in the watershed. The V3–V4 region of the 16 S rRNA gene was analyzed by high-throughput sequencing and the microbial community of the waters of the Jialing River was analyzed for the diversity and composition of the prokaryotic community as well as the species difference of four samples and correlations with environmental factors. The main results of this study were as follows: (1) The diversity index showed that there were significant differences in the biodiversity among the four regions. At the genus level, *Limnohabitans*, *unclassified\_f\_Comamonadaceae*, and *Hgcl\_clade* were the main dominant flora with a high abundance and evenness. (2) A Kruskal–Wallis H test was used to analyze the differences of species composition among the communities and the following conclusions were drawn: each group contained a relatively high abundance of *Limnohabitans*; the Shapingba District had a higher abundance of *Limnohabitans*, the Hechuan District had a wide range of *unclassified\_f\_Comamonadaceae*, and the Beibei District had a higher *Hgcl\_clade*. (3) Through the determination of the physical and chemical indicators of the water—namely, total nitrogen, total phosphorus, chemical oxygen demand, chlorophyll A, and an analysis by an RDA diagram, the results demonstrated that the distribution of microbial colonies was significantly affected by the environmental factors of the water. Chemical oxygen demand and ammonia nitrogen had a significant influence on the distribution of the colonies. Different biological colonies were also affected by different environmental factors.

**Keywords:** prokaryotes; high throughput sequencing; biological information analysis; community structure

## 1. Introduction

Microbial communities in aquatic ecosystems play an important role in degrading organic matter and participating in nutrient cycling, but they are sensitive to the external



environment [1,2]. At present, the research on bacterial community diversity and its relationship with environmental factors is growing [3]. However, most studies focus on coastal areas, lakes, and oceans [4,5], and there are few studies on rivers. Due to the increasingly serious pollution of urban rivers, the response of aquatic biota in urban rivers has gradually attracted researcher's attention.

Rivers are an important part of the global water cycle and one of the important water sources for human industrial and agricultural production as well as for life; they can provide an early warning to the overall quality of the water environment [6]. The Jialing River Basin in Chongqing is an ecological security barrier in the southwest of the country. The Jialing River is an important water source for industrial and agricultural production as well as domestic water and fishery in the urban area of Chongqing. It is also an important water source conservation area in the upper reaches of the Yangtze River. The water quality of the Jialing River affects the economic and social development of Chongqing [7]. Therefore, it is significant to study the characteristics of flora in the Jialing River Basin.

Microorganisms are an important part of ecosystems and are highly adaptable and prone to variation. Their structures and functions follow the changes of environmental factors. Microorganisms can maintain the overall stability of the ecosystem [8,9] and play a vital role in water quality control [10]. They have significant ecological functions in nutrient cycling, pollution reduction, soil protection, climate regulation, and water conservation [11]. As a key part of the composition of the biosphere, bacteria play an extraordinary role in the flow of matter and energy. The compositional diversity, distribution characteristics and inter-community structure of bacterial communities in lake ecosystems are the basis and prerequisite for understanding the structure and maintenance mechanism of lake ecosystems, and provide an important basis for basic theoretical research and environmental monitoring of lake microbial ecology.

In this paper, the research method based on high-throughput sequencing was used to conduct sampling at four sampling points in the Jialing River Basin, the Hechuan District, the Beibei District, the Shapingba District, and the Jiangbei District. The total microbial DNA was extracted from the samples, a PCR library was constructed, and the V3–V4 of the fragment 16S rDNA fragment was used as the research object. The structural diversity of bacterial flora in Jialing River water was analyzed by high-throughput sequencing, their relationship with environmental factors was analyzed by redundancy analysis (RDA) [12], and the biological community was analyzed by bioinformatics and metagenomics methods. To explore the prokaryotic community structure and the relationship between the community and environmental factors in the upper, middle, and lower reaches of the Jialing River Basin, so as to provide a theoretical basis for microbial monitoring in the entire river basin in Chongqing.

## 2. Materials and Methods

### 2.1. Experimental Materials

A bacterial genomic DNA extraction kit (Baimaike Biotechnology Co., Ltd., Beijing, China) and a PCR kit (Baimaike Biotechnology Co., Ltd., Beijing, China) were used in addition to sulfuric acid, nitric acid, potassium persulfate, phenolphthalein, potassium dihydrogen phosphate, sodium hydroxide, potassium iodide, potassium dichromate, potassium dihydrogen phosphate, and acetone (Meiji Biotechnology Co., Ltd., Shanghai, China). All chemical reagents of absolute ethanol, boric acid, hydrochloric acid, and potassium phthalate (Meiji Biotechnology Co., Ltd., Shanghai, China) are of analytical grade. A vertical pressure steam sterilizer (YXQ-LS-50A), UV-Vis spectrophotometer (TU-1901, T68), and small Benchtop Refrigerated Centrifuge (Centrifuge 5418R) were also used in the experiments.

### 2.2. Sample Collection

The sample collection took place between July–September 2020, as this was the high-water season of the Jialing River. To analyze the characteristics of microbial colonies in the Chongqing area of the Jialing River, four sampling points (as shown in Figure 1) were

selected for sampling. The four sampling points were the Nanping Bridge of the Jialing River in the Hechuan District (upstream, indicated as H), the Beibei Jialing River Bridge (upper and middle reaches, indicated as B), the Shapingba Shimen Bridge (middle and lower reaches, indicated as S), and the Jiangbei QianSimen Bridge (downstream, indicated as J). Each sampling point is divided into upper, middle, and lower vertical levels. Due to the large variation in the river water depth, the upper sampling depth (height from the river water surface) was approximately 0.5 m, the middle layer was approximately 3–5 m, and the lower layer was approximately 5–10 m. The tertiary water was then mixed and repeated three times for each sampling point. A total of 1 L of the water sample was filtered through a 0.22  $\mu\text{m}$  microporous membrane and stored at  $-80\text{ }^{\circ}\text{C}$ . This was then sent to a sequencing company for 16S rDNA transcriptome sequencing.

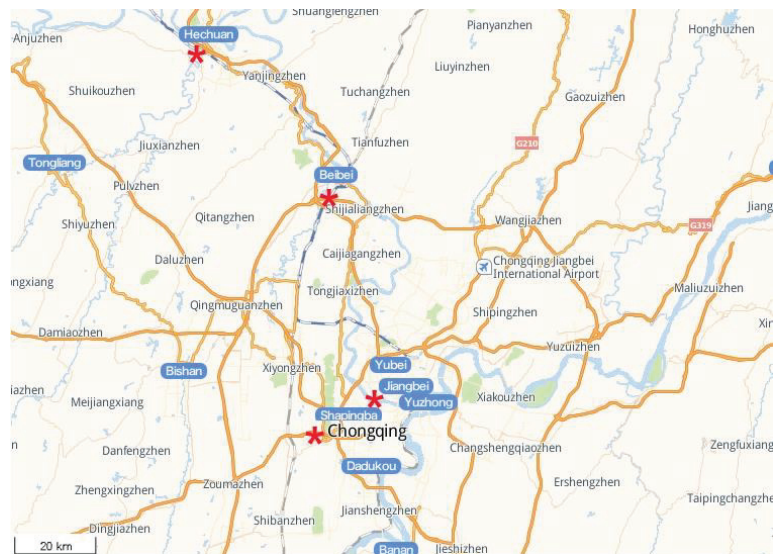


**Figure 1.** Sample collection site, 1:100,000.

### 2.3. Determination of Physical and Chemical Indicators of Water Bodies

Four sampling points were in the Jialing River Basin, the Hechuan District, the Beibei District, the Shapingba District, and the Jiangbei District. The reason for choosing Shapingba District and Jiangbei District is that they belong to the upper end of the Jialing River and have a large population base. Beibei District belongs to the middle section of the Jiangling River and has a medium population. Hechuan District belongs to the lower end of the Jialing River, which is a suburb and has a small population. The determination of physical and chemical indicators of the samples obtained, water quality total nitrogen (GB-11894-1989), total phosphorus (GB-11893-1989), ammonia nitrogen (GB-7479-87), chemical oxygen demand (GB-11914-1989), and chlorophyll A (HJ-897-2017) were performed in accordance with the national standards.

### 2.4. Bacterial Genomic DNA Extraction

The total bacterial DNA extraction was performed according to the Bacterial Genomic DNA Extraction Kit Manual in Table 1. Electrophoresis of 1% agarose gel was then used to detect the amount of DNA extracted, and NanoDrop2000 (micro-ultraviolet spectrophotometer) was used to determine the concentration and purity of DNA. A total of 100  $\mu\text{L}$  of buffer B1 was added to 0.5 mL of a bacterial solution, and then 100  $\mu\text{L}$  of buffer B2 were added. This mixture was well-shaken, placed in a centrifuge, and centrifuged at

12,000 rpm/min for 2 min. After centrifugation, 100 µL of the supernatant were pipetted into another clean centrifuge tube for use as a template.

**Table 1.** DNA extraction kit product content.

Product Composition	KG203-02 (50 Preps)	KG203-03 (200 Preps)
Buffer B1	6 mL	24 mL
Buffer B2	6 mL	24 mL
2 × Det PCR MasterMix	500 µL	2 × 1 mL
Grinding Pesties	10 ↑	20 ↑

### 2.5. PCR Amplification

Bacterial 16S rDNA PCR operation steps, establishment of a PCR reaction system, and 20 µL system in Table 2. After adding TransStart FastPfu buffer, dNTPs, upstream primers, downstream primers, TransStart FastPfu DNA polymerase, and template DNA were added to produce a 20 µL mixture. All reagents were collected at the bottom of the tube by brief centrifugation. The 16S rRNA gene V3-V4 variable region was PCR amplified using 338F(5'-ACTCCTACGGGAGGCAGCAG-3') and 806R (5'-GGACTACHVGGGTWTCTAAT-3') in triplicate per sample.

**Table 2.** PCR reaction system.

Product Composition	Volume
5 × TransStart FastPfu Buffer	4 µL
2.5 mL dNTPs	2 µL
upstream primer (5 uL)	0.8 µL
downstream primer (5 uL)	0.8 µL
TransStart FastPfu DNA polymerase	0.4 µL
Template DNA	10 µL

### 2.6. Data Statistical Analysis

The bases were filtered with a tail quality value below 20 of the reads, a 50 bp window was set, and the reads were filtered below 50 bp after quality control. The reads containing N bases were then removed, according to the overlap relationship between the PE reads. The paired reads were then merged into one sequence; the minimum overlap length was 10 bp, and the maximum mismatch ratio allowed in the overlap region of the spliced sequence was 0.2. The samples were distinguished according to the barcodes and primers at the beginning and end of the sequence, and the sequence direction was adjusted. The number of mismatches allowed by a barcode was 0, and the maximum number of primer mismatches was 2. Using UPARSE software (version 7.1) [13], the sequences were OTU clustered with a similarity of 97% [14,15], and chimeras were eliminated. The RDP classifier (version 2.2) [13] was used to classify and annotate each sequence, and then compared with the Silva 16S rRNA database (v138) with an alignment threshold of 70%. Solexa was then used, which is sequencing-by-synthesis (SBS) technology that uses DNA clustering, bridge PCR, and reversible blocking methods to read the base sequences in DNA in turn. Optical equipment is used to read and record the fluorescent signal; finally, the computer converts the analysis results into sequencing information.

The data obtained in the experiment were analyzed and processed using the Origin 8.0 software, OriginLab, (OriginLab, Redmond, WA, USA) processing system, and Windows Excel and Word (2003, 2010 editions) office software, (Microsoft, OriginLab, Redmond, WA, USA.) All determinations were carried out in triplicate, and the mean values were presented. The data are reported as the averages of three separate experiments ± SD ( $n = 3$ ).

### 3. Results and Discussion

#### 3.1. Water Quality Measurement Results

As important freshwater habitats for microorganisms, urban rivers are mainly affected by the terrestrial environment and human activities. When pollutants flow into the river, basic parameters such as pH, temperature, dissolved oxygen, salinity, and nitrogen and phosphorus content in the water body change, which is of great significance for regulating the complex microbial community and further reshapes the bacterial community structure [16–18]. For the microbial community structure at the water–sediment interface found in the Chaka Salt Lake (China) study, the apparent changes in the lake water salinity were associated with a decrease in lake water [19]; studies in the Ebro River (Iberian Peninsula, Spain) revealed that electrical conductivity, temperature, and dissolved inorganic nitrogen are the main environmental factors affecting the composition of phytoplankton communities [20]. The water quality indicators of the sampled water bodies were measured; the results are shown in Table 3. The sampling areas had obvious differences, particularly the Hechuan District, which had a high ammonia nitrogen content, a high total nitrogen content, and a low chemical oxygen demand. Furthermore, by monitoring the water quality of the four sampling points, it was found that the water quality of the four points was polluted to a certain extent. The indicators of nitrogen and phosphorus exceeded the normal values of the water body; in particular, the indicators of algae and chlorophyll *a* exceeded the average value of the river body. Therefore, it is speculated that the four sampling points are prone to the risk of water eutrophication in summer and autumn. Changes in the river environment can affect the balance between alien bacteria introduced by surface runoff and indigenous communities, predation or competition in the food chain, and directly or indirectly affect the function of bacterial communities [21]. Therefore, understanding river bacterial community diversity and spatial distribution has profound implications for monitoring ecosystem health.

**Table 3.** Measurement results of water quality indicators.

Sample Collection Place	Ammonia Nitrogen mg/L	Chemical Oxygen Demand mg/L	Total Phosphorus mg/L	Total Nitrogen mg/L	Chlorophylla $\mu\text{g/L}$
Shapingba	0.033	24	0.15	0.52	4.1
Hechuan	0.094	7	0.30	1.06	4.2
Jiangbei	0.035	18	0.27	0.51	5.4
Beibei	0.035	12	0.21	0.55	3.9

#### 3.2. Alpha/Beta Diversity Analysis

Alpha analysis is a composition analysis—the similarity of the species composition of each sample or group could be reflected. Determining bacterial metabolic potential through river bacterial diversity is an extremely important but under-recognized scientific issue. Changes in the bacterial structure of rivers can further lead to changes in metabolic and environmental information processing pathways [22,23]. From the upper to the lower reaches of the Danube, the relative abundance of its typical freshwater flora gradually increased due to a decrease in microbial richness and evenness [24]. The microbial diversity of the Yenisei peaked in the middle section, which may be associated with high flow and rapid turbulence [25]. As seen in Figure 2, the Shannon indices of the samples were all between 3.2 and 4.5 and the species composition richness and diversity of the four groups were relatively high. PCA analysis showed that the four groups could clearly be distinguished, indicating that the four groups had significant differences in the composition of the biological community. The R value was relatively close to 1, indicating that the difference between the groups was slightly greater than the difference within the group. There were obvious differences in the community composition structure of the four groups and the community composition in the different regions was different. The reason for

this may be that Jiangbei District has the largest industrial area, agricultural area, and population, which has a greater impact on water bodies, so the diversity of bacterial species is the highest; Beibei District and Hechuan District are rich in ecological communities, so the microorganisms in the riparian zone may be due to rainwater washed into the lake, so the microbial community is relatively rich, while the Shapingba area has the weakest community diversity because the industrial area, agricultural area, and ecological community zone are relatively less than the above-mentioned sampling points. Therefore, identifying the bacterial diversity of rivers can help to determine the impact of the metabolic potential of river bacterial communities.

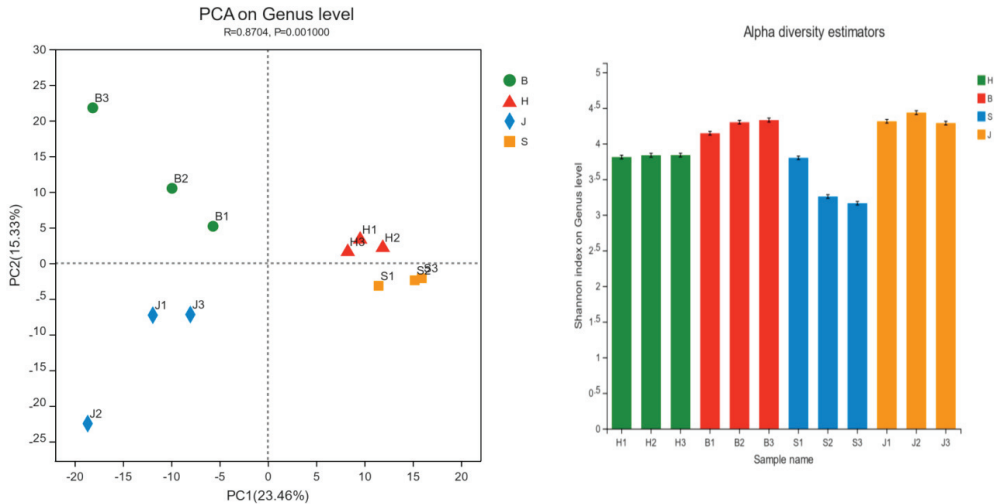


**Figure 2.** Alpha Shannon index diagram/PCA analysis diagram. (H represents the Hechuan District, S represents the Shapingba District, J represents the Jiangbei District, and B represents the Beibei District).

### 3.3. Community Composition Analysis

#### 3.3.1. Venn Diagram Analysis

A Venn diagram permits a macroscopic reflection of the number of species in the community through an intersection, which can reflect the composition of species. As seen in Figure 3, the Hechuan District and Beibei District shared 308 species, the Hechuan District and Shapingba District shared 217 species, the Hechuan District and Jiangbei District shared 319 species, the Beibei District and Shapingba District shared 243 species, the Beibei District and Jiangbei District shared 232 species, and the Shapingba District and Jiangbei District share 248 species. The Beibei District had the greatest number of distinct species (109 species), and the Shapingba District had the smallest number of distinct species (9 species). This may be due to riparian influences leading to the proliferation of exotic bacteria (i.e., soil and groundwater) and indigenous flora (i.e., increased bacterial richness). For example, studies on the Mississippi River (US) [26], Thames River (UK) [27], and Amazon River [28] have found that the “heterologous input process” or “mass effect” in the riparian zone further indicates that the diffusion rate of organic matter exceeds the local bacterial extinction rate, making the exogenous input bacteria [29–31]. The diversity is much higher than the river itself.



Figure 3. Venn diagram analysis of community distribution.

### 3.3.2. Community Bar Chart Analysis

Through a bar chart analysis, it could be seen that the measured water samples had a significantly high bacterial diversity. Figure 4 showed the bar map at the phylum level. The community composition structure of the Beibei District and Jiangbei District were relatively similar. The higher relative abundance in the Hechuan District were *unclassified-f-Comamonadaceae* [32], *unclassified-f-Rhodobacteraceae* [33], and the *Hgcl\_clade* [34]. The dominant flora was the *Hgcl\_clade*, and its abundance in the three samples in this group was 12.35, 12.25, and 15.28%, respectively. The relatively high relative abundance levels in the Beibei District were *unclassified\_f\_Comamonadaceae*, the *Hgcl\_clade*, and *Acinetobacter*. The dominant flora was *Hgcl-clade*, whose abundances in the three samples were 12.98, 10.78, and 11.57%, respectively. In the Shapingba District, the relative abundances form *Limnohabitans*, *Acinetobacter*, and *Vogesella*. The dominant flora was *Limnohabitans*, whose abundances in the three samples were 13.17, 14.65, and 17.51%, respectively. The most abundant species in the Jiangbei area were *Limnohabitans*, *unclassified-f-Comamonadaceae*, and the *CL500-29-marine-group*. The dominant flora was *Limnohabitans*, whose abundances in the three samples were 11.18, 11.56, and 11.81%, respectively.

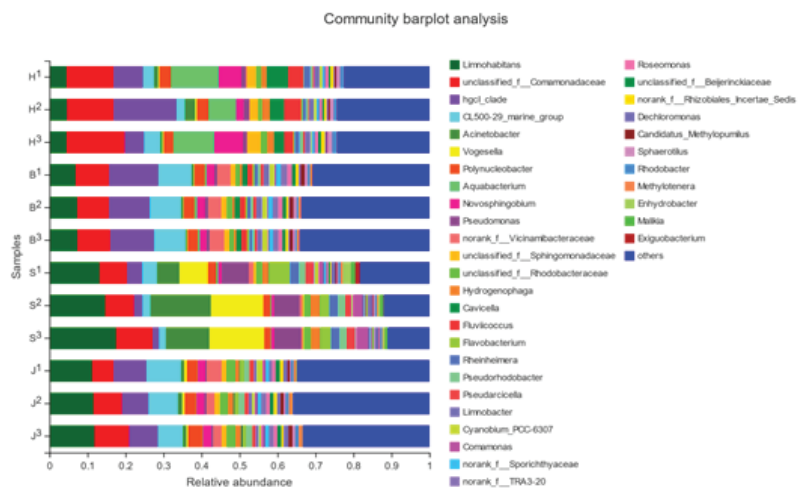
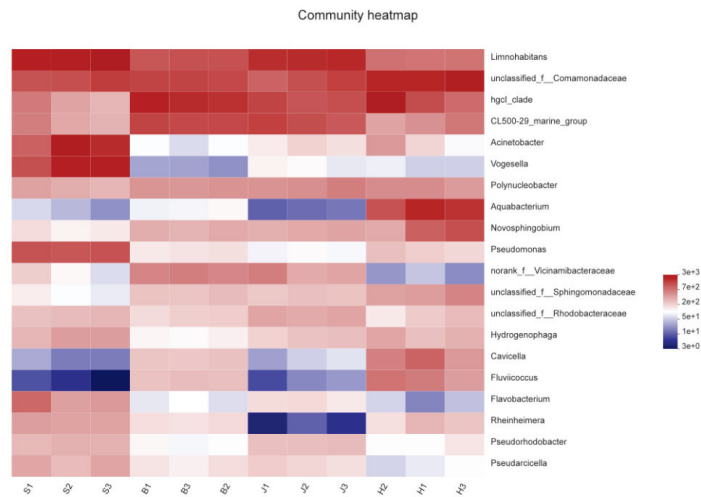


Figure 4. Analysis of the bacterial colony structure at the genus level of the four groups. (H represents the Hechuan District, S represents the Shapingba District, J represents the Jiangbei District, and B represents the Beibei District).

### 3.3.3. Heatmap Analysis of Community Composition

The heatmap displayed the species composition information of the community by reflecting the number of species through a color ladder. As can be seen in Figure 5, the community composition of the three samples collected from the Jiangbei District and the Beibei District was relatively uniform; one of the three samples collected from the Hechuan District and the Shapingba District had a few differences. The community composition of Hechuan and Beibei was the most similar. *Limnohabitans* [35], *comamonadaceae*, *hgcl\_clade*, and *CL500-29-marine-group* had a higher abundance in the four samples; in the Shapingba District, it also contained high levels of *Acinetobacter* and *Vogesella*, and Hechuan District also contains high levels of *Aquabacterium*. Bacilli are the predominant flora in urban river water and sediments, which are associated with the gut flora of many mammals and humans, and are effective fecal surrogate indicators. The higher abundance of bacilli in the downstream may be due to the high concentrations of nitrate, ammonia, feces, etc. in medical waste liquid and domestic wastewater [36]. The results of this study showed that the concentration of pollutants gradually increased along the flow direction of the river due to the discharge of domestic and industrial wastewater, which seriously affected the abundance changes of the bacterial community in the river.



**Figure 5.** Heatmap analysis.

### 3.3.4. Pie Chart

We statistically analyzed the species abundance of the samples at a certain taxonomic level and present the analysis results in the form of pie charts to present the composition of the species in different groups.

Figure 6a reflects the species composition of the Beibei District, which can clearly reflect that *unclassified\_f\_Comamonadaceae*, *Hgcl\_clade*, and the *CL500-29 marine group* were the dominant species in the Beibei District with a relatively high relative abundance that accounted for the total community of 28.8%. Figure 6b reflects the species composition of the Shapingba District, which clearly reflects that *Limnohabitans*, *Vogesella*, and *Acinetobacter* were the dominant species in the Shapingba District. The relative abundance of *Limnohabitans* was relatively high, accounting for 15.12% of the total community. Figure 6c reflects the species composition of the Jiangbei District, which clearly reflects that *Limnohabitans*, *unclassified\_f\_Comamonadaceae*, and the *CL500-29 marine group* were the dominant species in the Jiangbei District. The relative abundance of *Limnohabitans* was high, accounting for 11.52% of the total community. Figure 6d reflects the species composition of Hechuan District, which clearly reflect that *unclassified\_f\_Comamonadaceae*, the *Hgcl\_clade*, and the *CL500-29*

marine group were the dominant species in the Hechuan District. The relative abundance of *unclassified\_f\_Comamonadaceae* was high, accounting for 13.30% of the total community. Combining Venn diagrams, community Bar diagrams, Heatmap diagrams of community composition, and pie diagram test results can help us explore the species composition of the communities at the four sampling points, including the number of species and species abundance, by comparing samples or groups. The differences in species composition can reflect the composition information between them more clearly, and provide detailed parameters for monitoring and judging the pollution of the entire Jialing River.

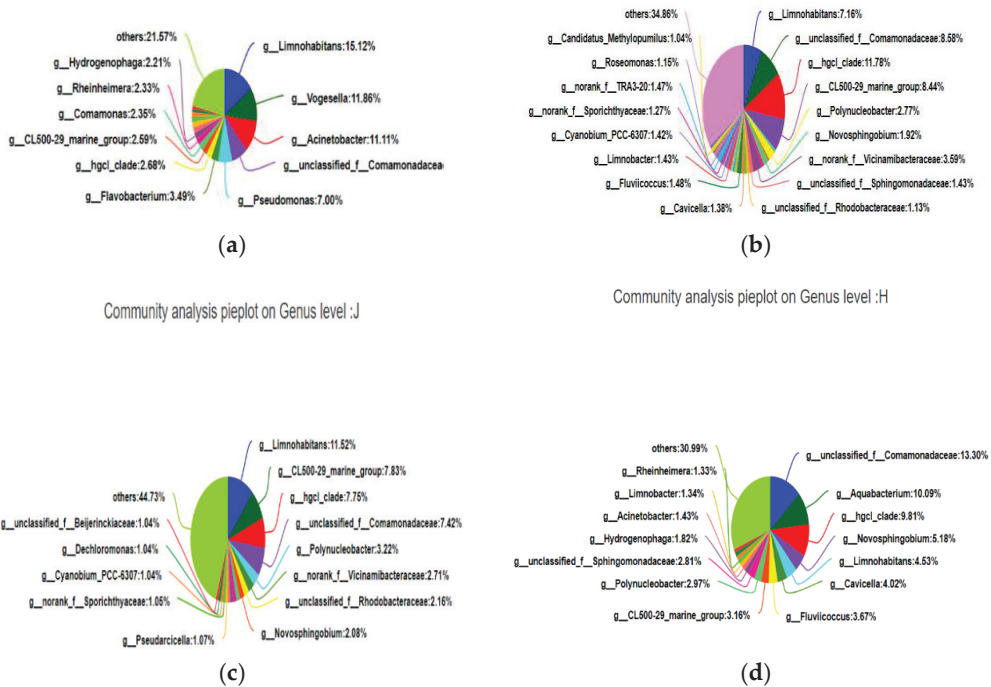


Figure 6. (a) Community composition analysis map of the Beibei District, (b) community composition analysis of the Shapingba District, (c) community composition analysis of the Jiangbei District, and (d) community composition analysis of the Hechuan District.

### 3.4. Analysis of Species Differences

#### 3.4.1. Kruskal–Wallis H Test Analysis

In this study, the Kruskal–Wallis H test was used to analyze the species difference of the samples. As seen in Figure 7, each group contained the genus *Limnohabitans*, the genus *unclassified\_f\_Comamonadaceae*, and the genus of the Hgcl\_clade with a relatively high relative abundance. Compared with other groups, the species with significant differences in the Shapingba District were *Acinetobacter* [37], *Vogesella*, and *Pseudomonas*, all of which had a higher relative abundance, whereas *Cavicella* had a lower relative abundance. The species with significant differences in the Hechuan District were *Aquabacterium*, *Novosphingobium*, and *Cavicella* with a higher relative abundance, whereas *norank\_Vicinamibacteraceae* had a lower relative abundance. The species with significant differences in the Beibei District had a higher relative abundance of *norank\_Vicinamibacteraceae* and a lower relative abundance of *Vogesella*. The species with significant differences in the Jiangbei District were *Acinetobacter*, *Vogesella*, and *Aquabacterium*; all of which had relatively low relative abundances.



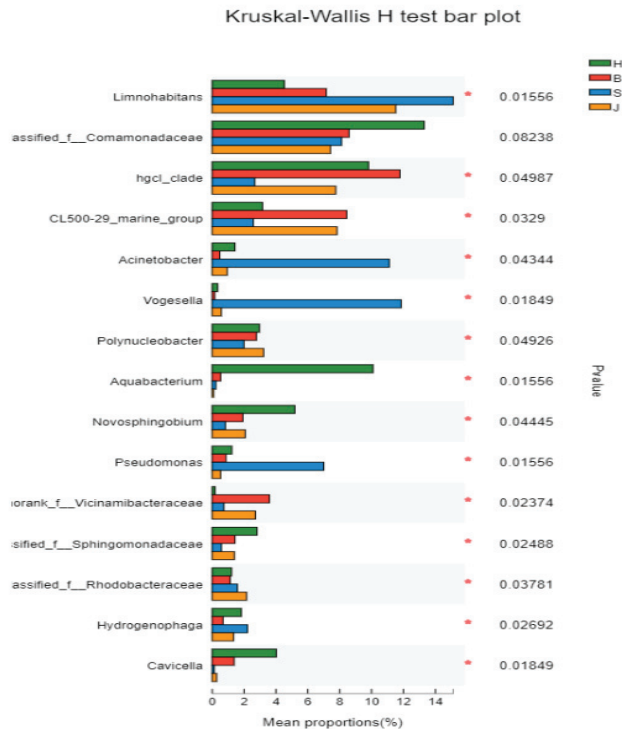


**Figure 7.** Kruskal–Wallis H test analysis results. (The left side of the vertical axis represents the species name and the right side is the *p*-value. The abscissa represents the relative abundance. H represents the Hechuan District, S represents the Shapingba District, J represents the Jiangbei District, and B represents the Beibei District).

### 3.4.2. LefSe Analysis

A LefSe analysis is used to analyze species with significant differences between samples or groups, reflecting each taxonomic level from high to low from inside to outside. As seen in Figure 8, among the four groups, the species with significant difference in the Beibei District is *Actinobacteriota* and its LDA value is 4.94825; the species with significant difference in the Shapingba District was *Gammaproteobacteria*, which had the greatest impact, and its LAD value was 4.857, The species with a significant difference in the Hechuan District was *Comamonadaceae*, whose LDA value was 4.857 and the species with a significant difference in the Jiangbei District was *Pseudomonadale*, whose LDA value is 4.975. In an ecosystem, there are always high-abundance and low-abundance species. By using Kruskal–Wallis H test analysis and LefSe analysis, it can help us find out the differences between the species at these four sampling points, and successfully construct the ASV set to obtain the differences in the species distribution of different microbial communities, and then to infer the species status of the entire Jialing River in Chongqing. To sum up, hospital waste liquid, agricultural sewage, and urban wastewater contain some antibacterial agents, drugs, and high-concentration pollutants. By exerting selective pressure, these substances promote the emergence of indigenous bacterial diversity, which in turn differentiates high-abundance bacteria in the watershed [38,39]. Therefore, as the main source of drinking water in cities, the discharge of sewage directly poses a threat to human health and the ecological security of the river basin.

Cladogram

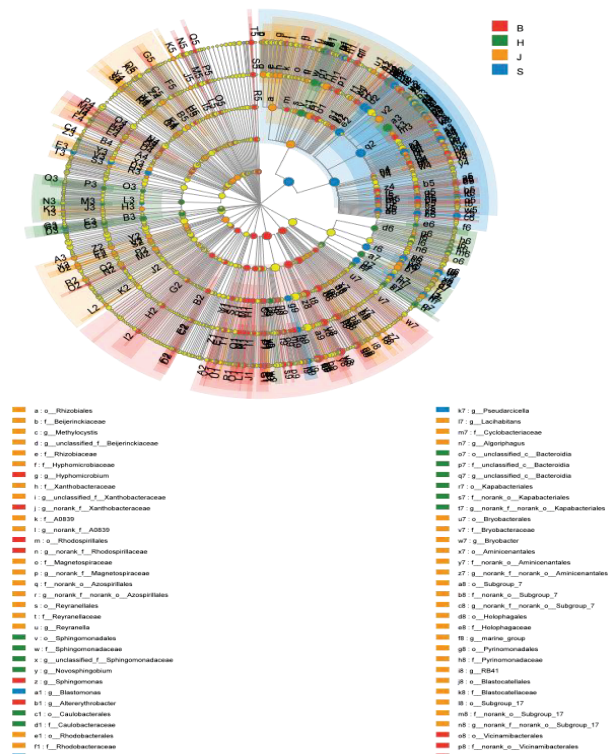


**Figure 8.** H represents the Hechuan District, S represents the Shapingba District, J represents the Jiangbei District, and B represents the Beibei District; the yellow nodes represent five significantly different species, the colored nodes represent species with significant differences, and the corresponding colors represent the corresponding regions.

3.5. RDA/CCA Analysis

Using the RDA map to analyze the relationship between the water environmental factors and the bacterial colonies, we could detect the relationship between the environment, the colony, and the sample as well as their inter-relationships. Studies have shown that pH, turbidity, and nutrients are the dominant factors leading to changes in bacterial community composition. Turbidity is an important driving force for biological metabolism in rivers, and has the greatest contribution to the changes of bacterial community composition in the river basin. Phosphorus and inorganic nitrogen concentrations are generally considered to be important drivers of biological metabolism in flowing water, and phosphorus was shown to be the most determinant factor significantly associated with changes in plankton bacterial communities [40,41]. As seen in Figure 9, ammonia nitrogen, the chemical oxygen demand, and total nitrogen all had significant effects on the distribution of bacterial colonies; among them, ammonia nitrogen had the greatest impact. Ammonia nitrogen had a greater impact on samples 1 and 2 and samples 3 and 2 in the Hechuan District. The influence of chlorophyll A on sample 1 and sample 3 as well as sample 2 and sample 3 in the Shapingba District was quite different; samples 1 and 2 and samples 1 and 3 in the Jiangbei District were significantly affected by the environmental factor of chlorophyll A. The figure shows the correlation between the five species and environmental factors. Among them, *Acinetobacter* was the most abundant and its distribution was most affected by chemical

oxygen demand. Its colony distribution was positively correlated with chemical oxygen demand, and the ammonia nitrogen, total phosphorus, and chlorophyll A were negatively correlated. The relative abundance of *unclassified\_f\_Comamonadaceae* was the smallest, and its distribution was most affected by the chemical oxygen demand. The distribution of the colony was positively correlated with ammonia nitrogen and total phosphorus content; it was negatively correlated with chlorophyll A and the chemical oxygen demand.

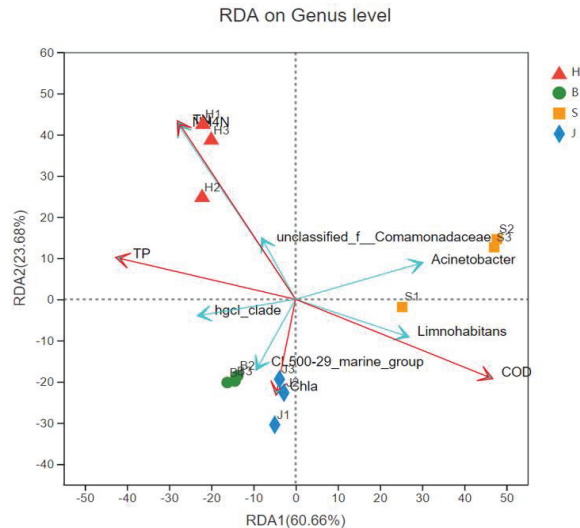


**Figure 9.** Correlation analysis between community structure and environmental factors. (H represents the Hechuan District, S represents the Shapingba District, J represents the Jiangbei District, and B represents the Beibei District. The longer the red arrow, the greater its influence and the longer the blue arrow, the greater its abundance, COD represents chemical oxygen demand, NH<sub>4</sub>N represents ammonia nitrogen, and Chla represents chlorophyll A.).

### 3.6. Evolutionary Analysis

An evolutionary analysis was comprehensively considered using the maximum likelihood method [42]. As seen in Figure 10, the evolutionary distance between *Methylothera* and *norank\_Methylophilaceae* was relatively close. The evolutionary distance between *unclassified\_Rhodobacteraceae* and *Pseudorhodobacter* as well as *Novosphingobium* and *unclassified\_Sphingomonadaceae* was also relatively close. *Dinghuibacter* and *Sediminibacterium* were relatively close; the *Hgcl\_clade* and *norank\_Sporichthyaceae* were also relatively close. By an ML maximum likelihood analysis, it was ascertained that the evolutionary distance between *Methylothera* and *norank\_Methylophilaceae* was relatively close. There was an unclassified evolutionary distance between *Rhodobacteraceae* and *Pseudorhodobacter*. *Novosphingobium* had a close evolutionary distance to *unclassified\_Sphingomonadaceae*. *Dinghuibacter* and *Sediminibacterium* had a close evolutionary distance and the evolutionary distance between the *Hgcl\_clade* and *norank\_Sporichthyaceae* was also close. Based on the above experimental results, the analysis of Heatmap and RDA shows that *Limnohabitans*, *unclassified\_f\_comamonadaceae* and *hgcl\_clade* are the dominant bacterial groups in the Jialing River waters in Chongqing during the wet season, indicating that the prokaryotic community in this watershed has high genetic diversity. Its distribution is greatly affected by ammonia nitrogen and chemical oxygen demand.

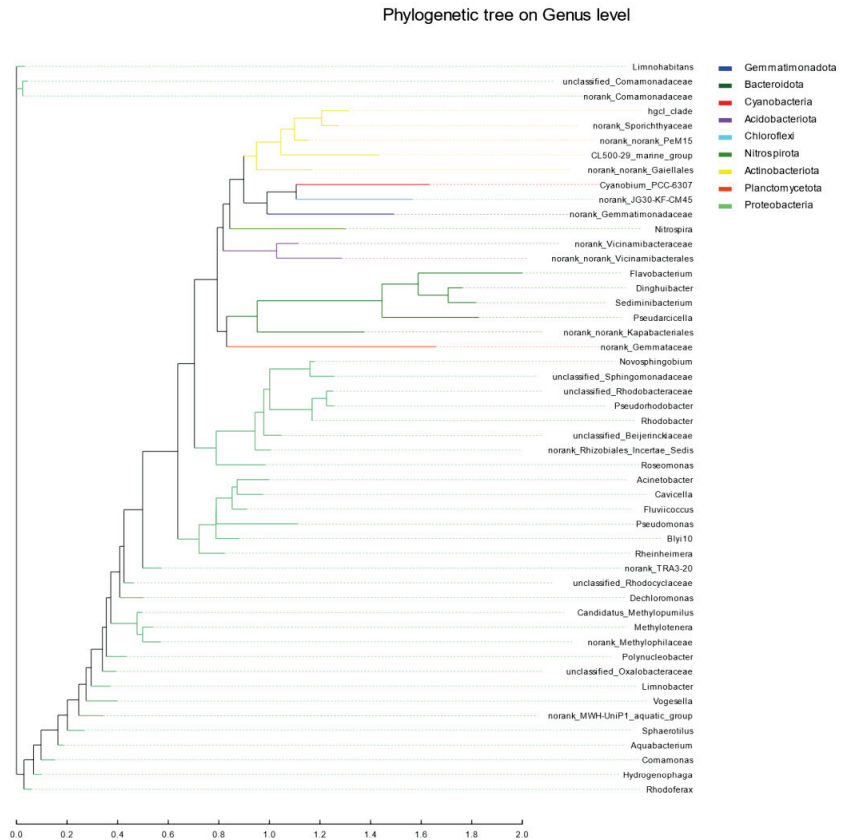


**Figure 10.** Phylogenetic tree analysis on genus level. (Each branch represents a species and the length of the branch represents the evolutionary distance.)

#### 4. Conclusions

In this paper, high-throughput sequencing was used to analyze the V3-V4 of 16srDNA, and the microbial community in the Jialing River waters in Chongqing was analyzed from the prokaryotic community diversity, community composition and species differences of the four samples, as well as the correlation analysis with environmental factors. The diversity index showed that there were obvious differences in the biodiversity of the four regions, with the highest biodiversity in Jiangbei District and the lowest in Shapingba. At the genus level, *Limnohabitans*, *unclass\_f\_comamonadaceae*, and *hgcl\_clade* were the main dominant flora with greater abundance and uniformity. The Kruskal–Wallis H test was used to analyze the differences in species composition among the communities. It was found that the Shapingba area has higher abundance of *Limnohabitans*, the Hechuan area has a wide range of *unclass\_f\_comamonadaceae*, and the Beibei area has higher *hgcl\_clade*. By measuring the physical and chemical indicators of the water body, namely total nitrogen, total phosphorus, chemical oxygen demand, and chlorophyll, and using the RDA chart to analyze, the results show that the distribution of microbial colonies is greatly affected by environmental factors in the water body, and the chemical oxygen demand and ammonia nitrogen have a greater impact on the distribution of colonies, and different biological colonies are affected by different environmental factors differently. This subject provides technical parameters for inferring the water quality of the Jialing River, and provides an important basis for the basic theoretical research and environmental monitoring of lake microbial ecology in China.

In the following research work, a long-term mechanism should be established for the monitoring of the watershed ecosystem. We should consider sampling in different seasons and years in terms of time, compare and analyze the interannual differences in microbial diversity and structure, and explore their laws, so as to provide a scientific theoretical basis for river water quality monitoring and water ecological changes.

**Author Contributions:** Conceptualization, G.Z. and M.Z.; methodology, D.S.; software, Y.X. and Y.P.; validation, F.W., C.L. and C.T.; formal analysis, Y.M.; investigation, X.H.; resources, G.Z.; data curation, Y.L.; writing—original draft preparation, M.Z.; writing—review and editing, M.Z. and H.L.; visualization, D.L.; supervision, D.S.; project administration, M.Z.; funding acquisition, D.S. All authors have read and agreed to the published version of the manuscript.

**Funding:** This research was funded by the National Natural Science Foundation of China: 52103156, 51901160; Chongqing Science and Technology Commission Project grant number: cstc2021jcyj-msxmX0663, cstc 2020jcyj-msxm X0928, cstc2021jcyj-msxmX0901, cstc2019jcyj-msxmX0562; Taizhou Science and Technology Support (Agriculture) Project: TN202012, SNY20210008; Basic scientific research project of Wenzhou: S2020005; Provincial and Ministerial Co-constructive of Collaborative Innovation Center for MSW Comprehensive Utilization: shljzyh2021-23; Chongqing Bayu Scholars Young Scholars Project: YS2021089; Chongqing University of Science and Technology Graduate Innovation Program Project. 2022 College Student Innovation and Entrepreneurship Training Program Cultivation Project [grant numbers 2021198, 202211551007].

**Institutional Review Board Statement:** Not applicable.

**Informed Consent Statement:** Not applicable.

**Data Availability Statement:** The data presented in this article are available on request from the corresponding authors.

**Acknowledgments:** All individuals included in this section have consented to the acknowledgement.

**Conflicts of Interest:** The authors declare no conflict of interest.

## References

1. Findlay, S. Stream Microbial Ecology in a Changing Environment. In *Stream Ecosystems in a Changing Environment*; Academic Press: Cambridge, MA, USA, 2016; pp. 135–150.
2. Jiang, J.G.; Shen, Y.F. Development of the microbial communities in lake donghu in relation to water quality. *Environ. Monit. Assess.* **2007**, *127*, 227–236. [[CrossRef](#)] [[PubMed](#)]
3. Laque, T.; Farjalla, V.F.; Rosado, A.S.; Esteves, F.A. Spatiotemporal Variation of Bacterial Community Composition and Possible Controlling Factors in Tropical Shallow Lagoons. *Microb. Ecol.* **2010**, *59*, 819–829. [[CrossRef](#)] [[PubMed](#)]
4. Simon, M.; Grossart, H.; Schweitzer, B.; Ploug, H. Microbial ecology of organic aggregates in aquatic ecosystems. *Aquat. Microb. Ecol.* **2002**, *28*, 175–211. [[CrossRef](#)]
5. Ping, X.; Leff, L.G. Longitudinal changes in the benthic bacterial community of the Mahoning River (Ohio, U.S.A.). *Hydrobiologia* **2004**, *522*, 329–335.
6. Herrera, E.C.; Nadaoka, K. Temporal dynamics and drivers of lake ecosystem metabolism using high resolution observations in a shallow, tropical, eutrophic lake (Laguna Lake, Philippines). *J. Great Lakes Res.* **2021**, *47*, 997–1020. [[CrossRef](#)]
7. Kosolapova, N.A.; Matveeva, L.G.; Nikitaeva, A.Y.; Molapisi, L. Modeling Resource Basis for Social and Economic Development Strategies: Water Resource Case. *J. Hydrol.* **2017**, *553*, 438–446. [[CrossRef](#)]
8. Yu, W.; Fei, Y.; Sheng, J.W.; Jia, P.W.; Jia, Y.; Kai, Q.X.; Yi, G.H. Biogeographic pattern of bacterioplanktonic community and potential function in the Yangtze River: Roles of abundant and rare taxa. *Sci. Total Environ.* **2020**, *747*, 141335.
9. Lemke, M.J.; Brown, B.J.; Leff, L.G. The Response of Three Bacterial Populations to Pollution in a Stream. *Microb. Ecol.* **1997**, *34*, 224–231. [[CrossRef](#)]
10. Ren Lijuan, H.D.; Xing, P.; Wang, M.Q.; Wu, Q.L. Research progress on bacterial diversity and ecological functions in lake waters. *Biodiversity* **2013**, *21*, 421–432.
11. Qian, L.; Hao, W.W.; Cong, H.; Hui, L.; Wei, L.; Xiu, F.Z.; Zhi, L.L.; Si, H.L. Microbial compositions, ecological networks, and metabolomics in sediments of black-odour water in Dongguan, China. *Environ. Res.* **2022**, *210*, 112918.
12. Jiang, T.; Sun, S.; Chen, Y.; Qian, Y.; An, D. Microbial diversity characteristics and the influence of environmental factors in a large drinking-water source. *Sci. Total Environ.* **2021**, *769*, 144698. [[CrossRef](#)] [[PubMed](#)]
13. Edgar, R.C. UPARSE: Highly accurate OTU sequences from microbial amplicon reads. *Nat. Methods* **2013**, *10*, 996–998. [[CrossRef](#)] [[PubMed](#)]

14. Wang, Q.; Garrity, G.M.; Tiedje, J.M.; Cole, J.R. Naïve Bayesian Classifier for Rapid Assignment of rRNA Sequences into the New Bacterial Taxonomy. *Appl. Environ. Microbiol.* **2007**, *73*, 5261. [[CrossRef](#)] [[PubMed](#)]
15. Vilo, C.; Dong, Q. Evaluation of the RDP Classifier Accuracy Using 16S rRNA Gene Variable Regions. *Metagenomics.* **2012**, *1*, a1–a5. [[CrossRef](#)]
16. Shade, A.; Jones, S.E.; McMahon, D. The influence of habitat heterogeneity on freshwater bacterial community composition and dynamics. *Nature* **2007**, *10*, 145–163. [[CrossRef](#)]
17. Liu, T.; Zhang, A.N.; Wang, J.W.; Liu, S.F.; Jiang, X.T.; Dang, C.Y.; Ma, T.; Liu, S.T.; Chen, Q.; Xie, S.G.; et al. Integrated biogeography of planktonic and sedimentary bacterial communities in the Yangtze River. *Microbiome* **2018**, *6*, 16. [[CrossRef](#)]
18. Kolmakova, O.V.; Gladyshev, M.I.; Rozanov, A.S.; Peltek, S.E.; Trusova, M.Y. Spatial biodiversity of bacteria along the largest Arctic river determined by next-generation sequencing. *FEMS Microbiol. Ecol.* **2014**, *89*, 442–450. [[CrossRef](#)]
19. Jiang, H.C.; Dong, H.L.; Zhang, G.X.; Yu, B.S.; Leah, R.C.; Matthew, W.F. Line Lake in Northwestern China. *Appl. Microbiol. Biot.* **2006**, *72*, 3832–3845.
20. Clara, R.G.; Juan, P.N.G.; Paul, A.D.G. Terrestrial origin of bacterial communities in complex boreal freshwater networks. *Ecol. Lett.* **2015**, *18*, 1198–1206.
21. Sujay, S.K.; Katie, D.N.; Stuarde, G.F.; Tamara, A.N.; Duan, S.W.; Michael, J.P.; Gwendolyn, M.S.; Ashley, M.S.R.; Mark, R.W.; Kenneth, T.B. Longitudinal patterns in carbon and nitrogen fluxes and stream metabolism along an urban watershed continuum. *Biogeochemistry* **2014**, *121*, 23–44.
22. Zhang, S.; Song, H.L.; Yang, X.L.; Huang, S.; Dai, Z.Q.; Li, H.; Zhang, Y.Y. Dynamics of antibiotic resistance genes in microbial fuel cell-coupled constructed wetlands treating antibiotic-polluted water. *Chemosphere* **2017**, *178*, 548–555. [[CrossRef](#)] [[PubMed](#)]
23. Nogales, B.; Lanfranchi, M.P.; Pina, V.J.M.; Bosch, R. Anthropogenic perturbations in marine microbial communities. *FEMSMicrobiol. Rev.* **2011**, *35*, 275–298. [[CrossRef](#)] [[PubMed](#)]
24. Fagervold, S.K.; Bourgeois, S.; Pruski, A.M.; Charles, F.; Kerherve, P.; Vétion, G.; Galand, P.E. River organic matter shapes microbial communities in the sediment of the Rhone prodelta. *ISME J.* **2014**, *8*, 2327–2338. [[CrossRef](#)]
25. Na, G.S.; Lu, Z.H.; Gao, H.; Zhang, L.X.; Li, Q.W.; Li, R.J.; Yang, F.; Huo, C.L.; Yao, Z.W. The effect of environmental factors dynamics on the prevalence of antibiotic-resistant *Escherichia* and migration coli in estuary environments. *Sci. Rep.* **2018**, *8*, 1663. [[CrossRef](#)]
26. Staley, C.; Unno, T.; Gould, T.J.; Jarvis, B.; Phillips, J.; Cotner, J.B.; Sadowsky, M.J. Application of Illumina next-generation sequencing to characterize the bacterial community of the Upper Mississippi River. *J. Appl. Microbiol.* **2013**, *115*, 1147–1158. [[CrossRef](#)]
27. Daniel, S.R.; Hyun, S.G.; Michael, J.B.; Lindsay, K.N.; Dawn, F.; Mark, J.B.; Robert, I.G. Catchment-scale biogeography of riverine bacterioplankton. *ISME J.* **2014**, *9*, 516–526.
28. Ghai, R.; Rodriguez-valera, F.; McMahon, K.D.; Toyama, D.; Rinke, R.; Oliveira, T.C.S.D.; Garcia, J.W.; Miranda, F.P.D.; Henriques-silva, F. Metagenomics of the Water Column in the Pristine Upper Course of the Metagenomics of the Water Column in the Pristine Upper Course of the Amazon River. *PLoS ONE* **2011**, *6*, e23785. [[CrossRef](#)] [[PubMed](#)]
29. Heino, J.; Schmera, D.; Eros, T. A macroecological perspective of trait patterns in stream communities. *Freshw. Biol.* **2013**, *58*, 1539–1555. [[CrossRef](#)]
30. Brandon, A.M.; Gao, S.H.; Tian, R.; Ning, D.; Yang, S.S.; Zhou, J.; Wu, W.M.; Criddle, C.S. Biodegradation of Polyethylene and Plastic Mixtures in Mealworms (Larvae of *Tenebrio molitor*) and Effects on the Gut Microbiome. *Environ. Sci. Technol.* **2018**, *52*, 6526–6533. [[CrossRef](#)]
31. Yang, Y.; Xu, C.; Cao, X.; Lin, H.; Wang, J. Antibiotic resistance genes in surface water of eutrophic urban lakes are related to heavy metals, antibiotics, lake morphology and anthropic impact. *Ecotoxicology* **2017**, *26*, 831–840. [[CrossRef](#)]
32. Devarajan, N.; Kohler, T.; Sivalingam, P.; Delden, C.V.; Mulaji, C.K.; Mpiana, P.T.; Ibelings, B.W.; Jonh, P. Antibiotic resistant *Pseudomonas* spp. in the aquatic environment: A prevalence study under tropical and temperate climate conditions. *Water Res.* **2017**, *115*, 256–265. [[CrossRef](#)] [[PubMed](#)]
33. Wuertz, S.; Okabe, S.; Hausner, M. Microbial communities and their interactions in biofilm systems: An overview. *Water Sci. Technol.* **2004**, *49*, 327. [[CrossRef](#)] [[PubMed](#)]
34. Qiu, Z.; Wang, R.; Zhang, Y.; Wu, Q.; Xie, B.; Yang, J.; Chen, J.; Sun, Z. Recent Progress in Studies of *Rhodococcus* and Its Application of in Biodegradation. *Food Sci.* **2016**, *37*, 254–258.
35. Wang, J.T.; Fan, H.B.; He, X.J.; Zhang, F.B.; Xiao, J.B.; Yan, Z.L.; Feng, J.J.; Li, R. Response of bacterial communities to variation in water quality and physicochemical conditions in a river-reservoir system. *Glob. Ecol. Conserv.* **2021**, *27*, e01541. [[CrossRef](#)]
36. Kasalický, V.; Jezbera, J.; Hahn, M.W.; Šimek, K. The Diversity of the Limnohabits Genus, an Important Group of Freshwater Bacterioplankton, by Characterization of 35 Isolated Strains. *PLoS ONE.* **2013**, *8*, e58209. [[CrossRef](#)]
37. Abdelhaleem, D. Mini Review—Acinetobacter: Environmental and biotechnological applications. *Afr. J. Biotechnol.* **2003**, *2*, 71–74.
38. Tamura, K.; Peterson, D.; Peterson, N.; Stecher, G.; Nei, M.; Kumar, S. MEGA5: Molecular Evolutionary Genetics Analysis Using Maximum Likelihood, Evolutionary Distance, and Maximum Parsimony Methods. *Mol. Biol. Evol.* **2011**, *28*, 2731–2739. [[CrossRef](#)]
39. Li, D.; Sharp, J.O.; Drewes, J.E. Influence of Wastewater Discharge on the Metabolic Potential of the Microbial Community in River Sediments. *Microb. Ecol.* **2016**, *71*, 78–86. [[CrossRef](#)]

40. Correll, D.L. The Role of Phosphorus in the Eutrophication of Receiving Waters: A Review. *J. Environ. Qual.* **1998**, *27*, 261. [[CrossRef](#)]
41. Wang, Q.; Zhang, L.M.; Shen, J.P.; Du, H.; Han, L.L.; He, J.Z. Nitrogen fertiliser-induced changes in N<sub>2</sub>O emissions are attributed more to ammonia-oxidising bacteria rather than archaea as revealed using 1-octyne and acetylene inhibitors in two arable soils. *Bio. Fert. Soils* **2016**, *52*, 1163–1171. [[CrossRef](#)]
42. Tram, N.H.; Gin, K.Y.H.; Ngo, H.H. Fecal pollution source tracking toolbox for identification, evaluation and characterization of fecal contamination in receiving urban surface waters and groundwater. *Sci. Total Environ.* **2015**, *538*, 38–57. [[CrossRef](#)] [[PubMed](#)]

## Article

# Positive Effects of Advanced Daylight Supply of Buildings on Schoolchildren—A Controlled, Single-Blinded, Longitudinal, Clinical Trial with Real Constructive Implementation

Marcel Neberich <sup>1,2,\*</sup>, Nathalie Gerner <sup>1,†</sup>, Carina Romodow <sup>1</sup>, Johanna Freidl <sup>1</sup>, Daniela Huber <sup>1</sup>, Renate Weisböck-Erdheim <sup>1</sup>, Christina Pichler <sup>1</sup> and Arnulf Hartl <sup>1</sup>

<sup>1</sup> Institute of Ecomedicine, Paracelsus Medical University, 5020 Salzburg, Austria; nathalie.gerner@pmu.ac.at (N.G.); carina.romodow@traunstein.bayern (C.R.); johanna.freidl@pmu.ac.at (J.F.); daniela.huber@pmu.ac.at (D.H.); rene.erdheim@pmu.ac.at (R.W.-E.); christina.pichler@pmu.ac.at (C.P.); arnulf.hartl@pmu.ac.at (A.H.)

<sup>2</sup> Distributed Energy Conversion and Storage, Technische Hochschule Nürnberg Georg Simon Ohm, 90429 Nuremberg, Germany

\* Correspondence: m.neberich@th-nuernberg.de; Tel.: +49-911-58803176

† These authors contributed equally to this work.

**Abstract:** Sunlight controls endogen hormone balances and numerous health effects. Therefore, it is important to provide building users, such as schoolchildren, with sufficient daylight. Too much of it, however, leads to overheating, which is why shading systems are used. Consequently, these systems improve energy balance, but might not have positive effects on present people's health. Within this study, shading systems were installed in classrooms of a middle school: common shading in two rooms, while two others were equipped with shading blades "Schlotterer RETROLux 80D" in an innovative design, reflecting more daylight indoors. The participating classes were divided between rooms with ordinary daylighting ( $n = 43$ ) and advanced daylighting ( $n = 42$ ). They spent, on average, 5 days weekly and 5–8 h daily in these classrooms. Saliva samples were collected during three semesters to detect hormonal changes. Questionnaires were collected to obtain more information about the mental alterations and, furthermore, to support the physiological results. A significant reduction in cortisol levels between 6:30 AM and 11:30 AM ( $p < 0.001$ ) was observed within the group that had advanced daylighting. Questionnaires show that both groups sleep less as study duration increases ( $p < 0.001$  time effect), but only the control group has a concurrent increase in daytime sleepiness according to relative treatment effects. The results show that increased daylight supply indoors leads to a significant greater reduction in cortisol levels of children and that those positive outcomes can be achieved by using innovative technologies for buildings.

**Citation:** Neberich, M.; Gerner, N.; Romodow, C.; Freidl, J.; Huber, D.; Weisböck-Erdheim, R.; Pichler, C.; Hartl, A. Positive Effects of Advanced Daylight Supply of Buildings on Schoolchildren—A Controlled, Single-Blinded, Longitudinal, Clinical Trial with Real Constructive Implementation. *Buildings* **2022**, *12*, 600. <https://doi.org/10.3390/buildings12050600>

Academic Editors: Francesco Nocera and Rosa Giuseppina Caponetto

Received: 4 April 2022

Accepted: 27 April 2022

Published: 5 May 2022

**Publisher's Note:** MDPI stays neutral with regard to jurisdictional claims in published maps and institutional affiliations.



**Copyright:** © 2022 by the authors. Licensee MDPI, Basel, Switzerland. This article is an open access article distributed under the terms and conditions of the Creative Commons Attribution (CC BY) license (<https://creativecommons.org/licenses/by/4.0/>).

**Keywords:** daylighting; circadian rhythm; indoor environmental quality; cortisol awakening response; daytime sleepiness

## 1. Introduction

By spending time inside buildings, people keep themselves away from natural stimuli, such as daylight, even though it is known that the specific rhythm of color, color temperature, and intensity of natural light has a direct impact on human health and well-being. The strong bluish illumination of sunlight during daytime inhibits the endogenously serotonin-derived hormone melatonin, which is produced by the pineal gland inside the epithalamus. By this process, the brain manages the body's sleep–wake rhythms [1]. Another endogenous hormone that underlies the circadian rhythm is cortisol, which is a stress hormone, produced by the adrenal cortex, that causes the body to adapt to particular daily strains and exposures [2]. Endogenous hormones, which are subject to such a rhythm, are controlled by external parameters. During the evolution of the human body, first c-opsin and r-opsin



receptors developed, which evolved into different highly specialized receptor cell types, each of which has specific hormonal and functional tasks. In terms of the visual interface of the body with its environment, these specialized set of cells consists of rods, cones, bipolar and horizontal cells, amacrine, and ganglion cells [3]. Sunlight changes over the day. The spectrum of light arriving on the ground is reddish at the beginning of the day, because it must pass through more atmospheric particles, bluish at midday, while it is taking the shortest way through the atmosphere, and reddish again as soon as the sun “sets” [4,5]. The stated receptors in the human eyes are reacting to these varying spectra. Wavelength ( $\lambda$ ) sensitivity of photoreceptors has been intensively researched for more than 20 years. Especially with regard to the sensitivity to bluish light sources of intrinsically photosensitive retinal ganglion cells (ipRGC), much effort has been invested in science, as these are mainly related to endogenous hormone control [6,7]. However, recent studies suggest that, in addition to ipRGC, receptors for visual perception, i.e., rods and cones, also play a role in hormone control, all of which have different wavelength sensitivities [8]. Most artificial light sources, though, were not developed to mimic the light spectrum of the sun. Their spectra are very dissimilar to that of daylight in most cases and there are several medical conditions related to the long-time exposure to those “wrong” spectra, e.g., there is a link between breast cancer and circadian disruption of melatonin [9] and cortisol [10]. Moreover, long time exposure to fluorescent artificial light results in degradation of dopaminergic neurons, which can be an indication of Parkinson’s disease later on [11]. The healthiest and highest quality of light, to which the internal processes of our body have adjusted, comes from the sun.

In Central Europe, however, 80–90% of our daily routine does not take place openly exposed to daylight, but indoors [12,13]. The indoor spaces where people spend time change over the course of the day. The most common places are the domestic stay, means of transport (bus, train, car), workplace (e.g., offices), schools, universities, etc. [12]. Additionally, modern cities are built in a more compact and dense way than the ones our ancestors used to live in. Dense development does not only have social and cultural advantages. The neighborhood’s carbon footprint is reduced by 42% for every doubling of its density [14]. However, the denser cities are built, the more nature is being suppressed and the less daylight (among many other natural parameters) reaches the inside of the buildings. Given the fact that natural environments keep humans healthy in the long run, the worldwide trend of urbanization makes specific shortcomings severe [13,15]. These facts have come to the attention of legislators in recent years. DIN EN 17037 “Daylight in buildings” is a European standard that was adopted in 2019 [16]. Countries such as Austria and Switzerland thus received a daylight-regulating standard for the first time.

Although sunlight is an important factor for healthy indoor environments, the supply of natural light needs to be managed. In winter times, glazing allows us to gather solar energy, which supports the building’s energy efficiency by heating up the interior, and, depending on fenestration, internal gains from the winter sun can be one of the most influential aspects to a building’s energy performance [17]. In summer times, though, large window sizes overheat the building. Therefore, modern buildings’ windows are being covered by interior or exterior shading systems, such as shading blades, shutters, or textiles.

Human eyes are not the only interface of the body with the rhythm of the sun. The occurrence of electromagnetic radiation (especially UV light) on the skin stimulates the production of pre-vitamin D<sub>3</sub>, which is then converted into pro-vitamin D<sub>3</sub> by nutrient uptake with the help of hormones from the liver, a.o. [18]. Therefore, vitamin D<sub>3</sub> production is also subject to wavelength sensitivity, which is also documented in DIN 5031-10 [19]. Psychological disorders, such as delayed sleep phase disorder, are very common for teenagers and young adults while their lifestyle is changing, leading to an intrinsic “free running” circadian rhythm and poor sleep hygiene (watching videos and using social media at night) [20]. Consequently, sleeping disorders such as these might lead to depression and have a negative impact on children’s and adolescents’ performance in school [20]. The logical assumption is that sunlight has a positive effect on all of these issues. Nevertheless,

children and adolescents spend a large part of their life indoors. This is confirmed by a study from the USA, in which almost 10,000 households were examined, e.g., depending on the age group, between 7 AM and 5 PM, more than 90% of young people spend their time in schools, while adults occupy offices or manufacturing workplaces [21]. Therefore, they are in special need of advanced (indoor) daylighting in related buildings.

There are more aspects of Indoor Environmental Quality (IEQ) apart from interior lighting. Visual comfort, acoustic comfort, indoor temperatures, air quality, and even more parameters affect the person that is using a building's interior at the same time. It is well known that indoor air pollution can lead to diverse unhealthy issues. Children are afflicted most frequently [22]. Rating models for thermal comfort currently only exist for adults, while comfort tables for children have only been proposed in research [23]. A study from Korea concluded from a survey of 119 kindergarten children that the thermal comfort range of children is 3 °C lower than that of adults. Thus, they are more sensitive to high temperatures [24]. This aspect is making the stated shading systems for windows even more important in schools and kindergarten buildings.

In a study in 2014, the overall indoor environmental quality of Finnish elementary schools was investigated. Some children suffered from the effects of poorly planned interiors. Within 4248 questionnaires, sleepiness topped the list of symptoms with 7.7% [25]. Furthermore, in most cases, the school's timetable contradicts with the "free running" circadian rhythm of adolescents, shortening the duration of weekly sleep patterns by as much as 120 min [26]. Making matters more aggravating, 18 out of 29 daily free-time activities of young adults typically take place indoors as well, which was discovered by a German research association through computer-assisted personal interviews with over 1000 children [27].

Other studies on lighting situations in school buildings can be found in the current literature, such as those that investigated the comfort and performance of preschool children in Greece in 2022 [28], the positive impact of lighting system upgrades on the energy performance of African school buildings in 2021 [29], or the holistic improvement of IEQ and related well-being of schoolchildren in Iran in 2018 [30]. The latter found in their study of 842 schoolchildren with building physics measurements and questionnaires a correlation between the degree of energy renovation of the school buildings and the overall IEQ assessment of the schoolchildren. The lighting situation played a major role in this study along with thermal and visual comfort. Nevertheless, a comparable study in which engineers and physicians worked hand in hand on the effects of daylighting on schoolchildren and could demonstrate measurable endogenous hormonal effects of cortisol levels, can hardly be found. This represents a knowledge gap where this study can help provide new information in the subject area. Since the structural situations of indoor spaces that need to be provided with daylight are invariably dissimilar, with countless parameters having an impact on the quality of light, studies that investigate the effects of real built environments are of particular importance to the scientific community.

To sum this up, experiencing sunlight is an important preventive intervention for many health issues for children and adults. Given the fact that humans spend more and more time inside buildings, optimizing a building's daylight supply is a strong reason for maintaining physical and mental health. All of this shows the risks of poor daylighting and indoor artificial lighting that is not of high quality. The presented controlled, single-blinded, longitudinal clinical trial (ISRCTN Registration number ISRCTN15982336) addresses this issue by implementing an innovative shading system that creates an improved supply of sunlight in classrooms. Throughout the study, psychological and physiological endpoints were observed, such as stress, sleepiness and sleep duration, and concentration.

## 2. Materials and Methods

### 2.1. Study Design and Setting

The present controlled, single-blinded, longitudinal intervention study investigated the effects of advanced daylighting on physiological and psychological parameters of

pupils. The allocation ratio for two groups (advanced daylighting and control) was set at comparable sample sizes. The intervention was conducted in the New Secondary School of Adnet (NSSA) (Salzburg, Austria) between March 2015 and June 2016. The study protocol was approved by the Ethics Committee of Salzburg (415-E/1857/2-2015) and was authorized by the State School Council of Salzburg (7151/0022-AP/2015). Due to the graduation of two classes in summer 2015, two new classes were added to the study population in autumn 2016. By doing so, the sample size was kept on a constant level. Therefore, the effects of advanced daylighting are reported for one semester and, subsequently, for two semesters of exposure.

## 2.2. Study Population

The study population consisted of pupils of the 3rd and 4th grade of the NSSA, which was also set as inclusion criteria. The pupils were aged between 10 and 12 years, e.g., to ensure sufficient reading comprehension. Before participants were finally enrolled in the study, children and their parents or legal guardians had to sign an informed consent form. School administrators and teachers of the enrolled classes gave their consent to the study as well.

## 2.3. Intervention

The school's building needed a modernization. Two classrooms were equipped with innovative sun shading systems that were made out of special shading blades, the "Schlotterer RETROLux 80D" (80D) (Figure 1), which reflects more daylight into the building than conventional systems do, while maintaining the protection of overheating in summer. As the control condition, the shading systems "Schlotterer 80R" (80R) (Figure 2) were installed in two rooms. The 80R shading blade was used as a control intervention, as this product represents one of the well-known and most commonly used modern shading devices to protect buildings from sunlight in summer months. The so-called external venetian blinds are the third most demanded external shading technology, after roller shutters and awnings [31]. Figure 3 shows a technical drawing from which it can be deduced how 80D was installed in the facade of the school. The 80R shading blades were installed at the classrooms of the control groups, who did not experience significantly less or more daylight than pupils in an ordinary school building would do. The 80D are folded in a way that direct sunlight in summer times cannot enter the building, whereas indirect light and direct sunlight in winter is reflected inside the room's ceiling. At the (white painted) ceiling, the light is reflected a second time in a more diffuse way, so it will not glare the building's users and gets distributed evenly in the entire room. By using the 80D shading blade, the manufacturer states that the daylight yield (light intensity in lux), in comparison to the common design of 80R, will be improved as follows [32]:

- 8% to 33% at the back of the room;
- −10% to 47% at the front of the room;
- 53% to 63% at the room's ceiling.

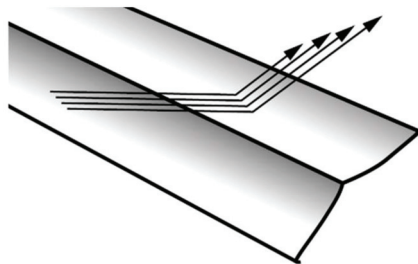


**Figure 1.** Schlotterer RETROLux 80D shading blade, reflecting sunlight direct in winter.

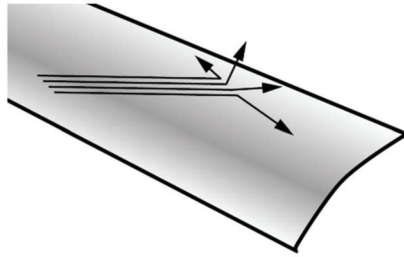


**Figure 2.** Schlotterer 80R shading blade design, reflecting sunlight diffuse at any time.

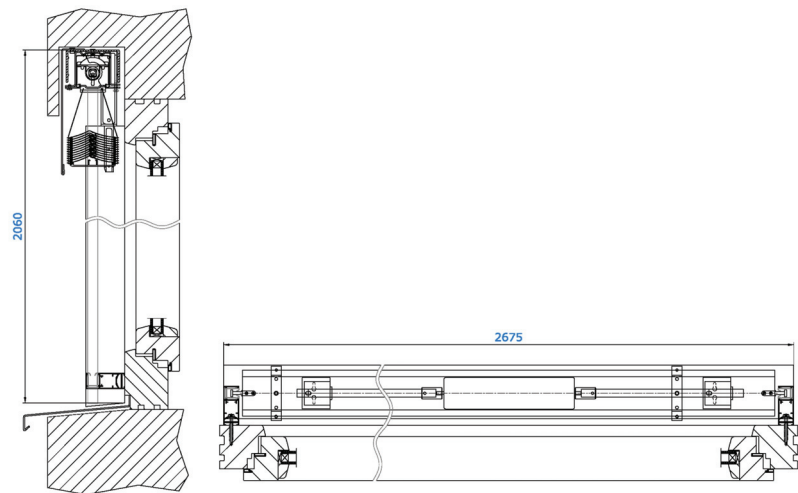


**Figure 3.** Structural design of the connection detail in the window reveal for the installation of the 80D shading system at NSSA. This is also standard procedure for installation in solid brickwork with external thermal insulation.

The number variation exists due to different solar altitudes and possible weather conditions. To sum this up, it can be assumed that schoolchildren in classrooms with 80D would be provided with more sunlight during the course of the day. The participating pupils of the NSSA spent 5 days per week and 5 to 8 h a day in their classrooms on average. During the intervention, all children lived at home, maintaining their usual lifestyle. Assessments were performed at the same time between March 2015 and June 2016 over a period of three semesters.

#### 2.4. Building Specifications

The building of the NSSA (GPS: 47°41'41.698" N 13°7'45.357" E, 484 m above sea level) is a four-level object, having classrooms facing south-south-east orientation. The four classrooms, which were examined in this study, are located in the third and fourth floor. All rooms have a floor space between 63 m<sup>2</sup> and 66 m<sup>2</sup>, their walls are painted in the same color, and the same furniture and teaching equipment (desks, chairs, blackboards) are available. The classrooms have three windows of equal size, with a totaled-up glazing surface of 14.0 m<sup>2</sup> (Figure 4). The artificial lighting system consists of eight luminaires per room that are equally distributed over the ceiling (Figure 5). The artificial light sources of the classrooms are fluorescent light tubes with an applied power of 18 W, which are installed in grid arrays on a suspended ceiling. The correlated color temperature (CCT), according to the manufacturer's data, corresponds to 4400 Kelvin. The calculated value

from the recorded spectral history data, following DIN 5033-7, results in 4330 Kelvin, and thus confirms the factory specification. Calculation outcomes illustrated in the false-color representations show that the technical lighting requirements specified in EN 12464-1 are closely fulfilled by using these luminaires. Illuminants of those lamps are fluorescent lamps, having a spectral power distribution (SPD) that vastly varies from daylight color rendering (Figure 6). The artificial light is not automated. Turning the lights on and off is left to the teacher. The quality and quantity of sunlight children can experience in this building depend on certain parameters, e.g., weather, external shading of the facade openings and wall thickness, shading system, window specifications (number of glass layers, UV-protective or IR-protective glass), window cleanliness, and position and orientation of the child's desk in the room. Most of these parameters did not change during the study or changed equally for every classroom. No major weather events were observed.

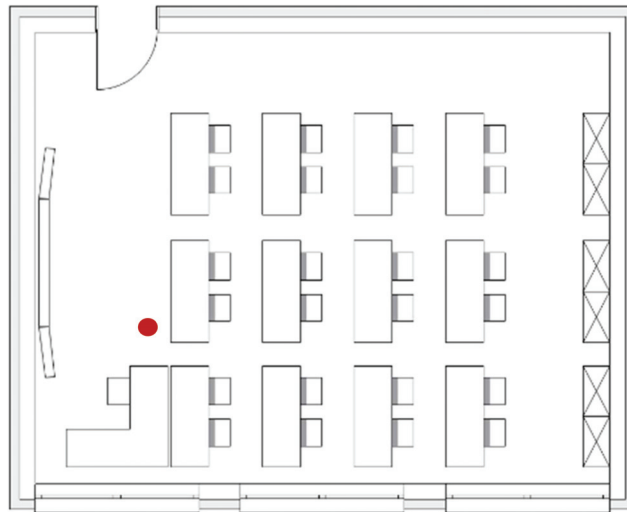


**Figure 4.** NSSA floor plan (oriented). Furnishing situation of each classroom consists of cabinets, a blackboard and teacher's workspace, and desks with two seats each for pupils. The door is located opposite the window side. All investigated classrooms have identical equipment. Red dot: measuring point for SPD.

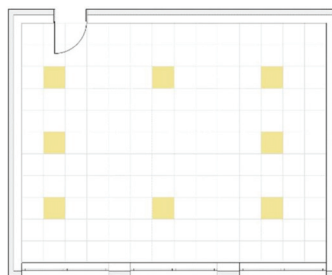


**Figure 5.** Reflected ceiling plan. Existing artificial lighting equipment in the investigated classrooms consists of fluorescent lamps in 60 cm by 60 cm grid arrays. There are eight lamps in total, which are distributed in a circular pattern for uniform illumination of the room.

The evaluation of the daylight and artificial light situation in a simulation shows that the daylight supply of the existing building is very high on the window side and decreases sharply on the opposite side of the room (Figure 7). The artificial light supply is

homogeneous (Figure 8). Daylight and artificial light combined ensure a sufficient supply of light at every workstation in the classroom (Figure 9).

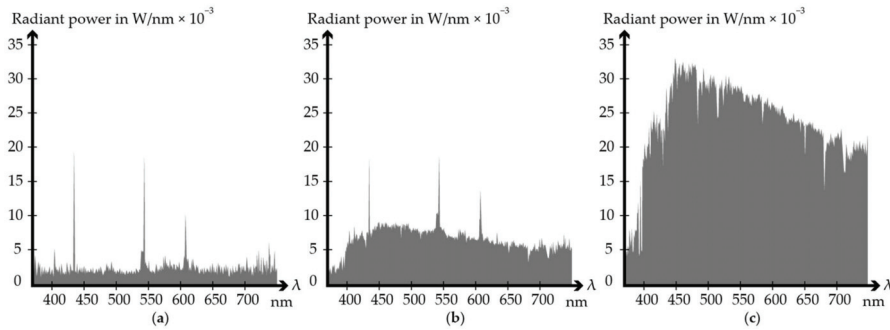


**Figure 6.** SPD of different light situations inside NSSA, measured in spectral radiant flux (electromagnetic radiation power) as a function of wavelength. (a): Measurement of mainly artificial lighting (fluorescent lamps in combination with activated conventional shading 80R) of visual wavelengths in order to demonstrate the characteristic spectrum. (b): Artificial light distribution of the visual spectrum indoors in combination with natural light (activated advanced daylighting 80D). (c): Natural light distribution of the visual spectrum exclusively inside NSSA (no shading system active).

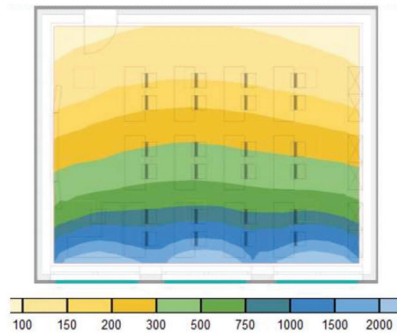


**Figure 7.** False-color representation of daylight illumination at NSSA. The intensity distribution of illumination varies from 100 lx (light yellow) along side of the door to 2000 lx (light blue) on the window side.

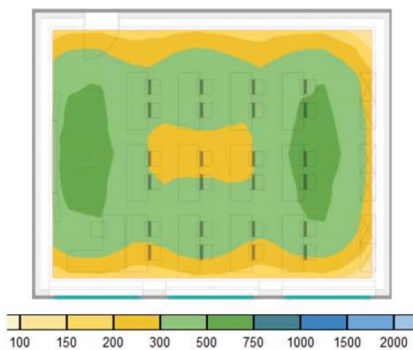


**Figure 8.** False-color representation of artificial light illumination at NSSA. The intensity distribution of illumination varies from 150 lx (yellow) at the far edge of the room to 750 lx (dark green).

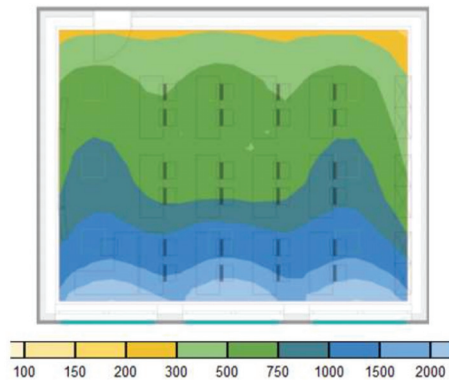


**Figure 9.** False-color representation of combined daylight and artificial light illumination at NSSA. Exemplary calculation for 21 March at 10 am.

### 2.5. Outcomes

All outcomes were collected at NSSA. Further examinations were performed in the lab of the Institute of Ecomedicine of Paracelsus Medical University in Salzburg. Data were anonymized by using four-digit IDs. Primary outcome was salivary cortisol levels. Sleep duration and daytime sleepiness measured by the Pediatric Daytime Sleepiness Scale [33], as well as concentration measured by d2-R scales [34] and inverted visual analogue scales (VAS) to investigate stress, sleepiness, and exhaustion were set as secondary outcomes.

Additionally, physical parameters, such as SPD for differentiation of daylight and artificial light usage, indoor air quality with regard to CO<sub>2</sub> concentration as described in DIN EN 13211 [35], room air temperature following VDI 2078 [36], and relative humidity, were monitored. These indoor air quality parameters were measured permanently in each of the four classrooms using air quality data loggers (TROTEC, BZ30) and saved every four minutes. This was performed to ensure that influencing variables deviating from standard conditions that might affect the physiological or psychological endpoints of the subjects could be identified. For the analysis of indoor air quality, only school days from 8 AM to 1 PM were included. Quality and intensity of artificial and natural light indoors were measured by using a Q-mini USB (RGB Photonics GmbH, Kelheim, Germany) spectral light meter. It is able to detect visual wavelengths from  $\lambda = 350$  nm to  $\lambda = 750$  nm and measures the illuminance in lux [37]. Light was measured every 4 min from 8 AM to 1 PM as well. Since the spectra of artificial light and sunlight are significantly dissimilar, this makes it easy to distinguish whether the shading blades and/or the artificial light sources were in use at a given time. It was, therefore, possible to document the artificial light shares the students experienced during the study period. For simulations, the software Relux by Relux Informatik AG, Münchenstein, Germany, in version 2022.1.3.0 was used.

#### 2.5.1. Data Collection

Assessments were performed at baseline (day 0, T1) (Figure 10), as well as before and after each semester (T2, T3, T4, T5), with the exception of VAS, which were carried out once a week. Saliva samples from the study participants were additionally collected starting at T3 to measure the stress-associated hormone cortisol, whose production and inhabitation is dependent on the supply of daylight [2]. The study timetable is presented in Figure 10, which also illustrates the timing of the assessments.

#### 2.5.2. Salivary Cortisol

Saliva samples were collected at T3–T5 immediately after waking up, and at 9 and 12 AM to determine the strength of cortisol reduction during the course of the morning and at midday. The samples were collected in 15 mL ultra-pure polypropylene tubes by

passive drool method. They were cooled within 30 min and stored at  $-80^{\circ}\text{C}$  within four hours of collection until analysis. Levels of active free cortisol in saliva were analyzed with the enzyme immunoassay Cortisol Saliva ELISA Free (Labor Diagnostika Nord GmbH & Co.KG, Lingen/Ems, Germany), following the manufacturer's instructions. Absorbance was read on a plate reader at  $450 \pm 10\text{ nm}$ . To reduce the dispersion of the data, responders were defined as  $>10, \leq 40\text{ ng/mL}$ .

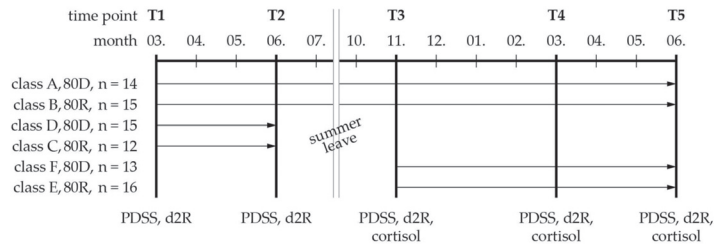


**Figure 10.** Study timetable: classes A and B participate during the whole period of time (T1 to T5), while classes C and D graduated after time point 2, which is why classes E and F joined the study at time point 3. VAS was performed once a week, regardless of the time points.

### 2.5.3. Sleepiness and Sleep Duration

The Pediatric Daytime Sleepiness Scale (PDSS) quantifies daytime sleepiness through self-reporting measures. The eight items of the questionnaire consist of daily sleep patterns, school achievement, mood, sleepiness, quality of life, and extracurricular activities. The answers are represented in the form of a Likert-scale ranging from “never” (0) to “always” (4).

### 2.5.4. Concentration

The d2-R attention and concentration assessment is an established test procedure to measure attention in three categories: concentration performance, work speed, and accuracy, while, in this study, only the subjects' concentration performance was analyzed. It is validated for the age range from 9 to 60 years. The test consists of 14 lines. Each participant has 20 s for each line to mark all symbols that look like the letter “d” with two dashes. There are many other symbols, such as the letters “d” and “p” with one to four dashes, to challenge the participant [38]. The whole duration of the test totals up to 4 min 40 s.

### 2.5.5. Visual Analogue Scales

Additionally, the pupils were asked to report sleepiness, stress, and exhaustion on single scales of an inverse visual analogue scale (VAS) on a weekly basis. The scales of 0 to 10 cm ranged from “very bad” to “very good”, whereby a higher value indicates a better clinical result. This unidimensional measuring instrument is widely used in research to examine anxiety [39], pain [40], and other outcomes in children.

### 2.6. Sample Size, Randomization, and Blinding

The comparable sample size per intervention and control group could be realized based on two approximately equally large class sizes. No sample size calculation was performed. At the beginning of the study, the four selected classes were randomly allocated to one of the two rooms with shading system 80D or one of the two rooms with shading system 80R (control). Since two of these classes graduated, the two additional classes were added and randomized. For the two classes that remained after summer leave, the already existing randomization was not changed. Recruitment and enrollment of eligible participants, as well as randomization, were performed by the same researcher. The allocation to the shading systems was blinded for teachers, schoolchildren, and their parents.



### 2.7. Statistical Methods

The data were collected in an excel-based database. The statistical analysis and interpretation took place at the Institute for Ecomedicine of the Paracelsus Medical University in Salzburg. All statistical analyses were implemented in the R-GNU software environment (General Public License, R Foundation for Statistical Computing, Vienna, Austria, version 4.0.2). Variables reported in tables are presented as means and their standard deviation, as far as not stated otherwise. The level of significance was set to alpha 0.05. Data were tested for normal distribution with the Shapiro–Wilk test. Longitudinal data analysis was performed with the nparLD package [41], which offers full nonparametric data analysis with ANOVA-type statistics [42]. F1-LD-F1 models were set up for group, time, and group\*time interaction effects. In the event of a significant main effect for time, post hoc analyses were used to compare the baseline for each particular time point with another F1-LD-F1 model. Multiple testing was compensated using Bonferroni–Holm corrections. To quantify the effect of the intervention, relative treatment effects (RTE) are reported. The RTE is a unitless value, which ranges between 0 and 1. An RTE of 0.5 indicates that no subgroup has a propensity to rank higher or lower. An RTE of 0.25 for a subgroup indicates that a randomly selected person from this subgroup has a 25% chance of scoring better than a randomly selected person from the overall dataset. On the other hand, it is predicted that a randomly selected person from this subgroup would score lower than a randomly selected person from the entire dataset by 75%.

For the statistical analysis of the cortisol decline, data from T3–T5 were pooled. An F1-LD-F1 model was used to test the hypothesis that the morning cortisol levels do not differ between T3 and T5. As this hypothesis could be confirmed, the pooled cortisol data were analyzed by another F1-LD-F1 model.

In addition to the text-based tables, the data are being represented via dot-and-whiskers diagrams, which include mean, median, and standard deviation values.

For the analysis of the data of the visual analogue scales for self-assessment, a Wilcoxon rank sum test was calculated, as well as *p*-values. The results are being compared in simple comparisons. The Wilcoxon test was compared by groups rather than by individual time points.

## 3. Results

### 3.1. Study Participants, Baseline Characteristics, and CONSORT Flow Diagram

The study population consisted of 85 schoolchildren. The pupils were 10 to 12 years old. The youngest group, on average, was the control group of the class, which participated for two semesters, starting at T3 ( $10.45 \pm 0.51$  years). Meanwhile, the averaged oldest group was the class with advanced daylighting, which took part for one semester, starting at T1 ( $10.83 \pm 0.66$  years). These schoolchildren were also among the group with the longest nighttime sleep duration at the beginning of the study ( $8.67 \pm 0.78$  h). The highest daytime sleepiness was found in the control group, which attended for one semester, starting at T1 ( $12.26 \pm 5.82$ ). A presentation of those and other baseline criteria is shown in Table 1. No children were excluded during the study (Figure 11).

**Table 1.** Baseline characteristics of the study population.

Participation	1 Semester Starting at T1		2 Semesters Starting at T3		Whole Study	
	80D	80R (Control)	80D	80R (Control)	80D	80R (Control)
Group						
Number	29	27	27	31	56	58
Sex—male	14	19	15	13	34	27
Sex—female	15	8	16	14	24	29
Age (years)	$10.83 \pm 0.66$	$10.63 \pm 0.63$	$10.59 \pm 0.57$	$10.45 \pm 0.51$	$10.71 \pm 0.62$	$10.53 \pm 0.57$
Cortisol * (ng/mL)	N/A	N/A	$12.07 \pm 6.5$	$9.75 \pm 6.23$	$13.6 \pm 6.67$	$9.76 \pm 5.68$
PDSS total score	$11.76 \pm 4.26$	$12.26 \pm 5.82$	$11.56 \pm 3.85$	$11.61 \pm 5.1$	$11.66 \pm 4.03$	$11.91 \pm 5.41$
Sleep duration (h)	$8.67 \pm 0.78$	$8.44 \pm 1.14$	$8.15 \pm 0.96$	$8.56 \pm 1.12$	$8.42 \pm 0.9$	$8.51 \pm 1.12$

Data are presented as the mean  $\pm$  SD; no significant baseline differences were found; 1 semester participation includes students from class A–D, two semester participation includes students from class A, B, E, and F, and whole study participation includes students from class A–F. \* Baseline levels at 6:30 AM.

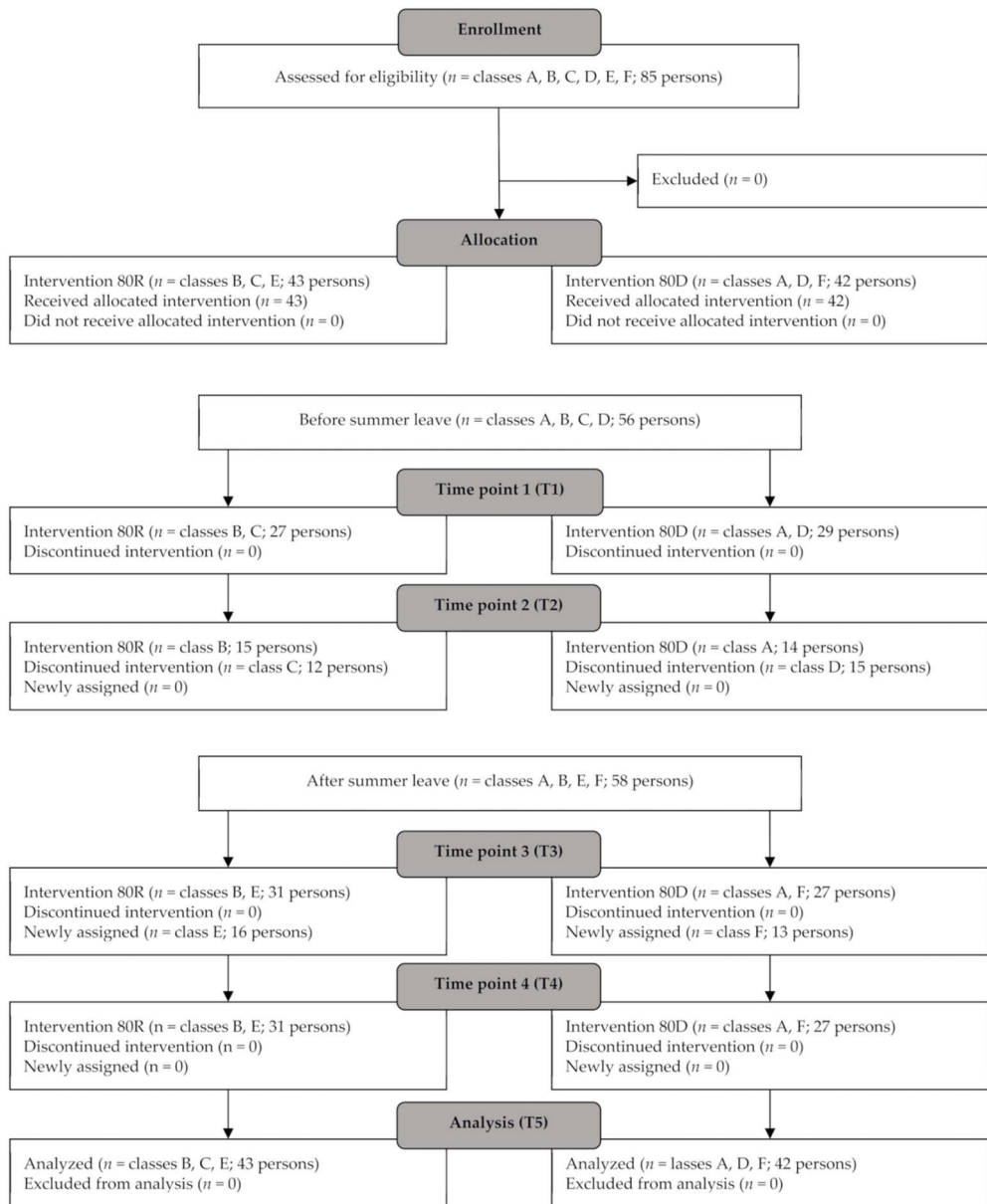


**Figure 11.** Study flowchart of schoolchildren included and excluded in the respective semesters presented by a CONSORT flow diagram. Due to the graduation of classes C and D, classes E and F were added after the summer leave.

### 3.2. Indoor Air Quality

CO<sub>2</sub> values were in a representative range throughout the year. Since windows are usually closed far more often during the winter months, the CO<sub>2</sub> content in the air increased slightly at this time to the highest values of  $1293.62 \pm 462.28$  ppm in the rooms with 80D and  $1070.96 \pm 466.21$  ppm in the other two rooms (cf. Table 2, CO<sub>2</sub> (ppm)). The results of the measurements of air humidity show an equally characteristic picture. In summer,

humidity increased to the highest proportion of  $44.68 \pm 3.16\%$  in rooms with 80D and to  $42.83 \pm 4.82\%$  in rooms with 80R (cf. Table 2, air humidity (%)). The highest measured mean indoor temperatures of  $26.66 \pm 1.12$  °C for 80D and  $25.39 \pm 1.80$  °C for 80R were documented in summer and the lowest mean temperatures of  $24.03 \pm 1.05$  °C for 80D and  $24.67 \pm 1.26$  °C for 80R occurred during wintertime (cf. Table 2, air temperature (°C)).

**Table 2.** Measured variables concerning indoor air quality, i.e., CO<sub>2</sub> (ppm), relative air humidity (%), air temperature (°C).

Months	Time Point	CO <sub>2</sub> (ppm)		Air Humidity (%)		Air Temperature (°C)	
		80D	80R (Control)	80D	80R (Control)	80D	80R (Control)
March–May	1	982.68 ± 424.77	896.54 ± 409.74	35.98 ± 5.92	36.97 ± 6.39	24.84 ± 1.42	24.82 ± 1.72
June	2	674.38 ± 278.43	839.91 ± 443.49	44.68 ± 3.16	42.83 ± 4.82	26.66 ± 1.12	25.39 ± 1.80
October–November	3	1066.52 ± 485.65	1054.97 ± 420.87	39.30 ± 5.24	36.09 ± 4.98	24.04 ± 1.02	24.21 ± 0.99
December–February	3	1293.62 ± 462.28	1070.96 ± 466.21	35.46 ± 5.10	37.06 ± 6.01	24.03 ± 1.05	24.67 ± 1.26
March–May	4	982.68 ± 424.77	896.54 ± 409.74	35.98 ± 5.92	36.97 ± 6.39	24.84 ± 1.42	24.82 ± 1.72
June	5	674.38 ± 278.43	839.91 ± 443.49	44.68 ± 3.16	42.83 ± 4.82	26.66 ± 1.12	25.39 ± 1.80

Data are presented as the mean ± SD.

### 3.3. Artificial lighting

Table 3 shows the shares of the total light supply in the respective classrooms, which were provided by artificial light, for the duration of the study (T1–T5). From the table, e.g., it can be noted that, as is common, daylight harvesting was much lower in the winter months (artificial light share  $55.27 \pm 27.66\%$  for 80D) than in summer (artificial light share  $26.08 \pm 32.88\%$  for 80D). Figure 6 aids to analyse which SPD can be expected during those times, respectively. Figure 6a represents a lighting supply yield by artificial light exclusively, while Figure 6c shows how the SPD representation looks whenever artificial light was turned off.

**Table 3.** Artificial light shares (%) measured near the teacher’s desk (Figure 4).

Months	Time Point	80D		80R (Control)	
		Mean ± SD	Median ± IQR	Mean ± SD	Median ± IQR
March–May	1	24.90 ± 31.15	0.00 ± 45.46	31.81 ± 32.47	28.57 ± 55.67
June	2	26.08 ± 32.88	0.00 ± 54.55	29.93 ± 32.15	10.00 ± 56.00
October–November	3	40.10 ± 29.89	41.88 ± 0.92	31.19 ± 30.80	30.95 ± 55.56
December–February	3	55.27 ± 27.66	59.17 ± 40.63	48.96 ± 34.37	55.05 ± 52.14
March–May	4	24.90 ± 31.15	0.00 ± 45.46	31.81 ± 32.47	28.57 ± 55.67
June	5	26.08 ± 32.88	0.00 ± 54.55	29.93 ± 32.15	10.00 ± 56.00

Data are presented as the mean ± SD.

The measurements with the spectrometers show a clear difference in the use of the two sun shading systems (Figure 6). During the activation of the conventional external venetian blind, the characteristic spectrum of daylight almost does not appear, whereas the wide full spectrum of sunlight is clearly shown in the diagram when using the advanced daylighting system.

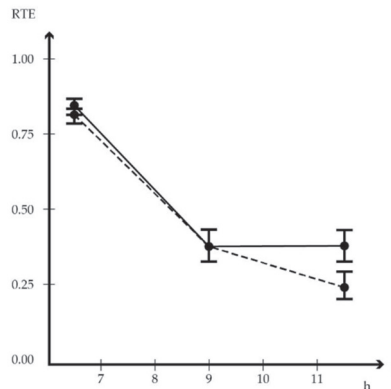
### 3.4. Cortisol

No significant difference was found among the morning cortisol levels between T3 and T5. Therefore, data from these time points were pooled for the analysis of salivary cortisol decrease (Table 4). The F1-LD-F1 model for the salivary cortisol decrease between 6:30 AM and 11:30 AM revealed significant treatment, time, and interaction effects. Salivary cortisol levels decrease in both groups. Although post hoc test reveals no further significant effects at the single time points, RTEs indicate lower salivary cortisol levels of the 80D group (RTE 0.24,  $2.68 \pm 1.54$  ng/mL) at midday in comparison to the control group (RTE 0.38,  $3.37 \pm 2.24$  ng/mL) as it is represented in Figure 12.

**Table 4.** Results from the F1-LD-F1 model, including relative treatment effects for salivary cortisol over the course of Semester 2–3.

		F1-LD-F1 Pretest for Equal Baseline Values			Relative Treatment Effects (RTE)				
		F	p-Value <sup>1</sup>		Time Point	80D		80R (Control)	
Cortisol at 6:30 AM Semester 2–3	Treatment	1.35 (1.00, ∞)	0.245	n.s.		80D	0.54	Control	0.47
	Time	1.68 (1.96, ∞)	0.188	n.s.	T3	80D × T3	0.49	80R × T3	0.48
	Treat. × Time	0.89 (1.96, ∞)	0.408	n.s.	T4	80D × T4	0.58	80R × T4	0.51
					T5	80D × T5	0.54	80R × T5	0.41
		F1-LD-F1 Model for Cortisol Decrease			Relative Treatment Effects (RTE)				
		F	p-Value <sup>1</sup>		Time of Day	80D		80R (Control)	
Cortisol decreases 6:30 AM–11:30 AM	Treatment	4.60 (1.00, ∞)	0.032	*		80D	0.48	Control	0.53
	Time	253.43 (1.91, ∞)	0.000	***	06:30	80D × 06:30	0.81	80R × 06:30	0.84
	Treat. × Time	3.91 (1.91, ∞)	0.022	*	09:00	80D × 09:00	0.37	80R × 09:00	0.38
					11:30	80D × 11:30	0.24	80R × 11:30	0.38
	Treat. × 09:00	0.96 (1.00, ∞)	0.353	n.s.	11:30	80D × 11:30	0.24	80R × 11:30	0.38
Treat. × 11:30	1.83 (1.00, ∞)	0.353	n.s.						

F1-LD-F1 model with time and treatment and the interaction of treatment and time (treat × time). No effect on the morning values over time or through the treatment was evaluated. All times from the school year 2015 and 2016 can be pooled for a common evaluation. <sup>1</sup> Significance level is indicated as \*\*\*  $p < 0.001$ ; \*  $p < 0.05$ ; n.s. (not significant).

**Figure 12.** Cortisol levels of the morning hours plotted over time (calculation of the combined results of one semester after summer leave), RTE of classes A, B, E, F; dashed line: 80D with advanced daylighting, solid line: 80R (control).

### 3.5. PDSS Pediatric Daytime Sleepiness Questionnaire, Sleep Duration, and d-2R Concentration

Table 5 contains daytime sleepiness and sleep duration results. Taking a look at daytime sleepiness during the course of one semester, the outcomes did not change noticeably between T1 (80D,  $11.759 \pm 4.257$ ; 80R,  $12.259 \pm 5.815$ ) and T2 (80D,  $11.621 \pm 4.570$ ; 80R  $11.963 \pm 5.768$ ), albeit sleep duration decreases significantly ( $p < 0.01$  time effect) in the group with 80D between T1 ( $8.672 \pm 0.782$  h) and T2 ( $7.922 \pm 1.223$  h). Therefore, the group with advanced daylighting sleeps less with the same level of daytime sleepiness. When looking at daytime sleepiness over two semesters, there is a trend in the main effect for time ( $p < 0.1$ ). Looking at corresponding RTEs, it becomes clear that the control group suffers from increased daytime sleepiness from T3 ( $11.613 \pm 5.103$ ) to T5 ( $13.581 \pm 5.904$ ), while the values of the 80D group did not increase in between T3 ( $11.556 \pm 3.846$ ) and T5 ( $10.889 \pm 3.945$ ). At the same time, sleep duration decreases significantly in both groups as well from T3 (80D,  $8.148 \pm 0.959$  h; 80R,  $8.565 \pm 1.124$  h) to T5 (80D,  $7.574 \pm 1.680$  h; 80R,  $7.306 \pm 1.662$  h).

**Table 5.** Results from the F1-LD-F1 models for daytime sleepiness, sleep duration, and concentration.

		F1-LD-F1 Model			Relative Treatment Effects (RTE)					
		F	p-Value <sup>1</sup>		Time Point		80D		80R (Control)	
Daytime sleepiness Semester 1	Treatment	0.244	0.622	n.s.			80D	0.483	Control	0.518
	Time	0.002	0.963	n.s.	T1	0.501	80D × T1	0.478	80R × T1	0.524
	Treat × Time	0.104	0.747	n.s.	T2	0.500	80D × T2	0.487	80R × T2	0.512
Daytime sleepiness Semester 2–3	Treatment	1.392	0.238	n.s.			80D	0.460	Control	0.535
	Time	2.468	0.085	.	T3	0.520	80D × T3	0.497	80R × T3	0.507
	Treat × Time	2.147	0.117	n.s.	T4	0.458	80D × T4	0.424	80R × T4	0.492
Sleep duration (h) Semester 1					T5	0.532	80D × T5	0.458	80R × T5	0.606
	Treatment	0.107	0.741	n.s.			80D	0.490	Control	0.510
	Time	5.564	0.018	*	T1	0.549	80D × T1	0.595	80R × T1	0.503
Sleep duration (h) Semester 2–3	Treat × Time	7.410	0.006	**	T2	0.452	80D × T2	0.385	80R × T2	0.518
	Treatment	0.012	0.913	n.s.			80D	0.497	Control	0.503
	Time	11.193	0.000	***	T3	0.595	80D × T3	0.544	80R × T3	0.647
d-2R concentration Semester 1	Treat × Time	1.869	0.158	n.s.	T4	0.514	80D × T4	0.533	80R × T4	0.495
					T5	0.391	80D × T5	0.414	80R × T5	0.367
	Treatment	0.020	0.887	n.s.			80D	0.505	Control	0.495
d-2R concentration Semester 2–3	Time	64.155	0.000	***	T1	0.396	80D × T1	0.423	80R × T1	0.369
	Treat × Time	2.965	0.085	.	T2	0.603	80D × T2	0.586	80R × T2	0.621
	Treatment	0.812	0.368	n.s.			80D	0.535	Control	0.470
d-2R concentration Semester 2–3	Time	23.970	0.000	***	T3	0.395	80D × T3	0.431	80R × T3	0.359
	Treat × Time	0.360	0.549	n.s.	T4	0.499	80D × T4	0.526	80R × T4	0.472
					T5	0.613	80D × T5	0.647	80R × T5	0.578

F1-LD-F1 model with time and treatment and the interaction of treatment and time (Treat × Time);<sup>1</sup> Significance level is indicated as \*\*\*  $p < 0.001$ ; \*\*  $p < 0.01$ ; \*  $p < 0.05$ ;  $p < 0.1$ ; n.s. (not significant).

Furthermore, Table 5 shows the results of the F1-LD-F1 model regarding the d-2R concentration tests. The test scores of both groups improved considerably during the study, over the course of one semester in between T1 (80D,  $104.345 \pm 22.502$ ; 80R,  $101.852 \pm 13.620$ ) and T2 (80D,  $109.897 \pm 16.205$ ; 80R  $114.704 \pm 13.958$ ), as well as over the course of two semesters starting at T3 (80D,  $107.296 \pm 12.776$ ; 80R  $104.355 \pm 14.190$ ) until T5 (80D,  $117.444 \pm 12.292$ ; 80R,  $114.419 \pm 11.372$ ).

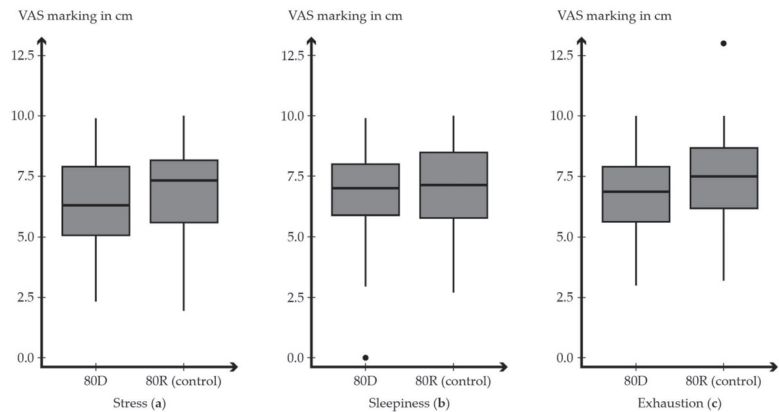
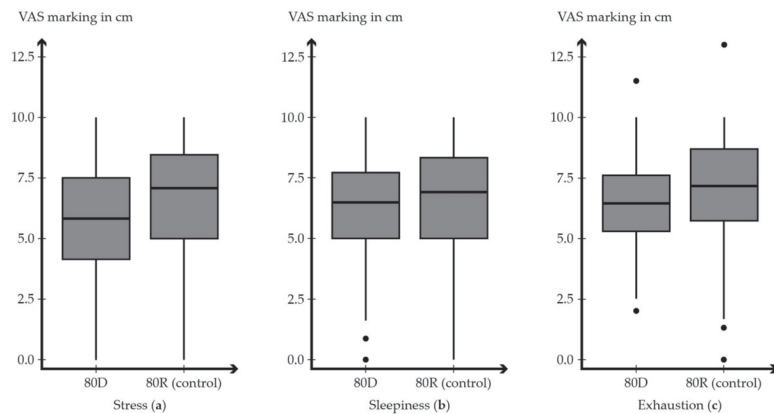
### 3.6. Visual Analogue Scales

The results of the self-assessment of the physiological and psychological condition by the schoolchildren themselves are summarized in Table 6, as well as in Figures 13 and 14. Over the one-semester course (T1–T2), the lowest score for psychological stress can be found in the 80D group ( $5.411 \pm 1.810$  cm), while the highest (best) value on average can be attributed to the control group ( $7.467 \pm 1.616$  cm). During the two-semester period (T3T5), a similar picture can be observed. Here, the lowest voting value is also attributable to the 80D group ( $5.064 \pm 2.229$  cm), while the highest value lies in the control group ( $7.290 \pm 2.188$  cm). In this observation, however, the calculations show a significant difference ( $p < 0.001$ ) in the simple comparison between 80D and 80R (control). Regarding sleepiness in the one-semester course, the control group has both the lowest ( $6.430 \pm 1.677$  cm) and the highest ( $7.828 \pm 1.872$  cm) average voting result. It is the same with sleepiness in the two-semester course. Exhaustion voting results for one semester have the same outcome as the ones of psychological stress. The lowest value is within the 80D group ( $6.193 \pm 1.594$  cm), while the highest (best) value is found in the control group ( $7.652 \pm 1.743$  cm). It is the same with exhaustion in the two-semester observation.

**Table 6.** Results from simple comparison models of visual analogue scales for self-assessed stress, sleepiness, and exhaustion levels over the course of the study.

VAS Scale	Time Point	Simple Comparison		
		Wilcoxon Rank Sum	$p$ -Value <sup>1</sup>	
Stress	T1–T2	7351	0.025	*
	T3–T5	33,607	0.000	***
Sleepiness	T1–T2	6927.5	0.171	n.s.
	T3–T5	28,178	0.333	n.s.
Exhaustion	T1–T2	7640.5	0.005	**
	T3–T5	30,312	0.014	*

<sup>1</sup> Significance level is indicated as \*\*\*  $p < 0.001$ ; \*\*  $p < 0.01$ ; \*  $p < 0.05$ ; n.s. (not significant).

**Figure 13.** Results of visual analogue scales for self-assessment over the course of 1 semester from T1 to T2 of stress (a) ( $p = 0.017$ ), sleepiness (b) ( $p = 0.061$ ), and exhaustion (c) ( $p = 0.002$ ) on a scale of 0 to 10 cm (one schoolchild voted out of scale). In this case, the Y-axis scale extends to 12.5 cm because the children voted off-scale in the questionnaire. The black dots represent outliers.**Figure 14.** Results of visual analogue scales for self-assessment over the course of 2 semester from T3 to T5 of stress (a) ( $p < 0.001$ ), sleepiness (b) ( $p = 0.590$ ), and exhaustion (c) ( $p = 0.024$ ) on a scale of 0 to 10 cm (some schoolchildren voted out of scale). In this case, the Y-axis scale extends to 12.5 cm because the children voted off-scale in the questionnaire. The black dots represent outliers.

#### 4. Discussion

In the field of IEQ, the relationship between (day-)lighting and user health has been intensively researched for decades. Research projects that confirm scientific findings with real constructive implementations in buildings are not very common in the current literature, which can be experienced by taking a look into current review papers [43–47]. Although it is known that the hormone is subject to a circadian rhythm and is associated with substantial medical inter-relationships, cortisol is rarely addressed in the field of human-centric lighting [10]. Unlike cortisol, the interface between the likewise endogenous hormone melatonin and the long-term health of building users is currently the focus of legislators in Germany and other countries, especially due to the years of development of DIN/TS 5031-100 [48]. Although the links were considered well-known, the melanopic effect of daylight and artificial light sources was significantly questioned in 2015 during the so-called Manchester workshop, as further evidence from *ex situ* studies emerged, such as that the opacity of the lens of the eye plays an important role in older age and that other photoreceptors besides ipRGC contribute to the melanopic effect. A summary of the workshop results can be viewed as a CIE standard [49]. Since the interface between the hormone cortisol and the lighting situation in buildings currently receives lesser attention from experts than the melanopic effect, it can be expected that findings from field studies will also play an important role in this field in the future. This study additionally addressed the question of how the operator of a building is able to achieve the stated health-promoting effects with the implementation of technology, which is why the results are likewise valuable for the scientific community as well as for professionals in practice and administration.

In this study, with the help of SPD measurement, it can be distinguished at which points in time the interior was supplied with artificial light in combination with sunlight, as the characteristic SPD of the installed energy saving lamps is easily recognizable (Figure 6a). Whenever the daylight supply is not sufficient, artificial light is switched on; this characteristic wavelength distribution is, therefore, shown in combination with daylight (Figure 6b). At time periods when there was enough daylight, the fluorescent lights remained switched off. At these times, the diagrams of the measurement results show a typical curve of a sunlight spectrum (Figure 6c). Just how often the teachers switched on the artificial light is shown in light shares in Table 3. When comparing the curves of SPD with and without switched-on artificial light, it becomes clear that schoolchildren experienced a much more intensive and complete spectrum of light once the total illuminance occurring in the room was provided by daylight only. In addition, the innovative shading blades increase the intensity of daylight indoors by the percentages mentioned in Section 2.3. Therefore, the measurements show that subjects in 80D classrooms were qualitatively and quantitatively exposed to more sunlight during the course of the study.

Initially, it is important to determine whether the psychological or physiological parameters of the subjects were influenced by any uncommon physical IEQ parameters besides lighting. This is why, in addition to the lighting situation, air quality and indoor temperature play an important role in this regard. CO<sub>2</sub> concentrations were at or below the benchmark of 1000 ppm at most times of the year. Values above 1400 ppm are categorized as IDA 4 (low indoor air quality) according to DIN EN 16798-3 [19]. In winter, the classrooms with advanced daylighting exceeded 1500 ppm ( $1293.621 \pm 462.284$  ppm) occasionally. The indoor air temperature averaged around 24 °C. According to the examples of design criteria for rooms in different types of buildings according to DIN EN ISO 7730, operative temperatures of  $23.5 \pm 1.0$  °C to  $23.5 \pm 2.5$  °C should be planned for kindergartens (schools are not listed) depending on the surface temperatures of surrounding building components [19]. Humidity levels in all classrooms were within a representative range of 40% or below throughout the duration of the study. The conclusions from that (cf. Section 3.2.) and the comparison with the dedicated standards and ordinances show that all influencing parameters are representative. Special attention was paid to the indoor temperature, since

80D is ultimately a shading system, protecting the building from the sun, that must function properly in addition to its supposed positive health effects.

An elevated cortisol level during a period of time that is opposite to the natural biological rhythm is an indicator of an unnecessary amount of psychological stress in the daily life of the studied subjects [50]. There is a highly significant stronger reduction in the pupils' cortisol level in the classrooms that were equipped with the innovative shading system during the course of the morning in comparison to the control group. The use of advanced daylighting technologies, such as 80D, have a significant stress reducing effect. Table 4 shows that the cortisol levels of pupils in rooms with advanced daylighting are significantly lower ( $p < 0.001$  time effect). Between time points T3 and T5 (October till June), the RTE values resulting from the cortisol saliva samples appeared quite equal after getting up (80D RTE = 0.81, control RTE = 0.84), then, shortly after the start of school day, the values decreased due to the natural circadian rhythm (80D RTE = 0.37, control RTE = 0.38), but, at midday, measurements of the supposed positive effect of the improved supply with daylight become very noticeable (80D RTE = 0.24, control RTE = 0.38). The progression is illustrated in Figure 12. Since this represents a significant difference in cortisol levels between the two groups at that time point of nearly 37%, it is likely that cortisol was reduced more quickly during the day due to the improved supply with natural light.

Supporting these results, it can be additionally observed that the RTEs calculated with the help of the PDSS questionnaire results indicate that the control group suffers more from daytime sleepiness, especially by taking a closer look at the last time point (80D RTE = 0.458, control RTE = 0.606). Overall sleep duration goes down for both groups over time (Table 5), but this means that only the control group suffers from a concurrent increase in daytime sleepiness. Since both positive effects are correlated and each occurs in the group of the classroom with advanced daylighting, it can be argued that 80D have a significant positive influence. The evaluation of the study shows that the installation of the innovative shading system that provides the building with advanced daylight supply leads to a better overnight sleep of the pupils.

The evaluation of the concentration tests shows a clear learning effect. Scales of both groups show a main effect for time in Table 5 ( $p < 0.001$  time effect). 80D, therefore, has no effect on the scales of the D2R when measured over one semester. A similar picture is found when evaluated over two semesters.

In the self-evaluation of schoolchildren by VAS, most of the entries are at a similar level. There were some outliers, especially because children marked outside the scale (higher than 10 mm), which was supposedly a sign to indicate that they were doing particularly well during this time. Trends and also significances in the results of stress and exhaustion can be recognized, which, however, describe mainly a positive situation in the control group. The indications of sleepiness and exhaustion, e.g., started higher in group 80D than in the control group in one semester observation (Table 6). At the end of this period of analysis, the group with advanced daylighting scored lower. None of the results are concerning. The imbalance at the end of the semester may also be due to the exam period.

The use of natural light for a building's lighting design provides a stronger connection to the daily routines of nature and helps the body to manage its circadian endocrine rhythms. The global trend of urbanization is creating a future situation in which most of the people will be living in dense cities, far away from "healthy" natural parameters. Which is why the handling of those effects, such as daylight, in urban buildings is becoming more and more important. Simply blocking the light from coming in will not be a solution for smart cities of the future. Sunlight needs to be controlled for the indoor environment to remain comfortable, rather than blocked by shading systems. Without shading, the summer sun would overheat the building and the winter sun will glare the building's user. Consequently, as this study shows, daylighting brings a plausible combination of medical and engineering benefits. In this project, scientists of the medical, engineering, and architectural fields worked together to change a built environment. This interdisciplinary effort made a longitudinal clinical trial possible, the specific results of which are giving



an inside perspective into the practical impacts of theoretical medical relations. The otherwise scarce level of information is likewise an important trigger for a change in the market and highlights the share of both healthy and sustainable methods in the creation of modern architecture.

### *Limitations*

Only one school was studied. Therefore, no conclusion can be drawn about the built and natural environment surrounding the school, e.g., in front of the south-south-east facade is a tree, which might influence the classrooms by shading them in different intensities over the year. To avoid a specific bias, both the 80D and the 80R were compared in the third and fourth floor. Shading from the tree, if any occurred, was comparable for both groups. Furthermore, most of the direct light is being blocked by the shading system anyway, which is why the tree shadow's impact is almost insignificant.

## 5. Conclusions

1. Advanced daylight supply can improve cortisol balance in schoolchildren.
2. Providing more natural light can lower daytime sleepiness, even if sleep duration decreases.
3. Indoors, the benefits of natural light can be obtained by utilizing innovative technology.

Different sources of artificial light and daylight differ considerably in their SPD. Thereby, qualities of light affect health maintenance of our body in a diverse manner. Exposure to school classrooms with advanced daylighting through the use of special sun protection shading blades, redirecting more natural light into the building than convenient blades, led to improved hormonal balance with respect to endogenous cortisol, as well as better sleep quality in schoolchildren during a three-semester clinical study, with reference to the baseline characteristics. Other physical environmental parameters were controlled and remained within a normative range. It is, therefore, very likely that the implementation of innovative daylighting technologies can be used to achieve the known health benefits of sunlight for building users. Studies that are based on specific building measures involve interdisciplinary collaboration between physicians, architects, or engineers. Only when investigating buildings in operation can all the inter-relationships and influencing variables really be considered. The study results attest to the importance of high-quality and nature-based IEQ, in this case, the visual components. The state of knowledge could be extended by further evidence, which shows that decisions in construction and operation of buildings regarding daylight and artificial light supply have a direct influence on the health of building users. Technologies that allow quality light with a full spectrum to reach people indoors, while taking into account the avoidance of overheating the building, should therefore be given preference by operators and developers.

**Author Contributions:** The study was registered at ISRCTN15982336. Conceptualization, C.R. and A.H.; methodology, C.R., J.F. and A.H.; formal analysis, M.N., C.R., J.F. and D.H.; investigation, M.N., N.G., C.R., J.F., R.W.-E. and A.H.; writing—original draft preparation, M.N.; writing—review and editing, N.G., J.F., D.H., C.P., R.W.-E. and A.H.; visualization, M.N. and J.F.; supervision, A.H.; project administration, C.R. and A.H.; funding acquisition, C.R. and A.H. All authors have read and agreed to the published version of the manuscript.

**Funding:** This project was funded by the Federal State of Salzburg, Austria (funding scheme: Trans4Tech). Sponsors had no role in the design of the study; in the collection, analyses, or interpretation of data; in the writing of the manuscript, or in the decision to publish the results.

**Institutional Review Board Statement:** The study was conducted in accordance with the Declaration of Helsinki, and approved by the Ethics Committee of the Federal State of Salzburg, 5010 Salzburg, Austria (protocol code 415-E/1857/2-2015, 16 March 2015).

**Informed Consent Statement:** Informed consent was obtained from all subjects involved in the study, resp. their legal guardians.

**Data Availability Statement:** Not applicable.

**Acknowledgments:** We greatly appreciate the New Secondary School Adnet and all of our study participants that enabled the implementation of the study. We want to thank Erich Franek, NSSA school’s principal, and Wolfgang Auer, mayor of Adnet (Austria), for their important support. Many thanks to our industrial partners “Schlotterer Sonnenschutz Systeme GmbH—CEO Peter Gubisch and technician Michael Mayr, our research partners “Landesinnung BAU Salzburg” and the ITG—“Innovationservice für Salzburg” for the initialization of this project, as well as their invaluable support and collaboration.

**Conflicts of Interest:** The authors declare no competing interests.

## References

- Houser, K.; Boyce, P.; Zeitzer, J.; Herf, M. Human-centric lighting: Myth, Magic or Metaphor? *Lighting Res. Technol.* **2020**, *53*, 97–118. [[CrossRef](#)]
- Elverson, C.A.; Wilson, M.E. Cortisol: Circadian Rhythm and Response to a Stressor. *Newborn Infant Nurs. Rev.* **2005**, *5*, 159–169. [[CrossRef](#)]
- Arendt, D. Evolution of eyes and photoreceptor cell types. *Int. J. Dev. Biol.* **2003**, *47*, 563–571.
- Hernández-Andrés, J.; Romero, J.; Nieves, J.L.; Lee, R.L. Color and spectral analysis of daylight in southern Europe. *J. Opt. Soc. Am. A* **2001**, *18*, 1325. [[CrossRef](#)]
- Judd, D.B.; MacAdam, D.L.; Wyszecki, G.; Budde, H.W.; Condit, H.R.; Henderson, S.T.; Simonds, J.L. Spectral Distribution of Typical Daylight as a Function of Correlated Color Temperature. *J. Opt. Soc. Am.* **1964**, *54*, 1031. [[CrossRef](#)]
- Brainard, G.C.; Hanifin, J.P.; Greenson, J.M.; Byrne, B.; Glickman, G.; Gerner, E.; Rollag, M.D. Action Spectrum for Melatonin Regulation in Humans: Evidence for a Novel Circadian Photoreceptor. *J. Neurosci.* **2001**, *21*, 6405–6412. [[CrossRef](#)] [[PubMed](#)]
- Thapan, K.; Arendt, J.; Skene, D.J. An action spectrum for melatonin suppression: Evidence for a Novel Non-Rod, Non-Cone Photoreceptor System in Humans. *J. Physiol.* **2001**, *535*, 261–267. [[CrossRef](#)]
- Lucas, R.J.; Peirson, S.N.; Berson, D.M.; Brown, T.M.; Cooper, H.M.; Czeisler, C.A.; Figueiro, M.G.; Gamlin, P.D.; Lockley, S.W.; O’Hagan, J.B.; et al. Measuring and using light in the melatonin age. *Trends Neurosci.* **2014**, *37*, 1–9. [[CrossRef](#)] [[PubMed](#)]
- Stevens, R.G. Circadian Disruption and Breast Cancer: From Melatonin to Clock Genes. *Epidemiology* **2005**, *16*, 254–258. [[CrossRef](#)]
- Sephton, S.; Spiegel, D. Circadian disruption in cancer: A Neuroendocrine-Immune Pathway from Stress to Disease? *Brain Behav. Immun.* **2003**, *17*, 321–328. [[CrossRef](#)]
- Fasciani, I.; Petragnano, F.; Aloisi, G.; Marampon, F.; Rossi, M.; Coppolino, M.F.; Rossi, R.; Longoni, B.; Scarselli, M.; Maggio, R. A New Threat to Dopamine Neurons: The Downside of Artificial Light. *Neuroscience* **2020**, *432*, 216–228. [[CrossRef](#)] [[PubMed](#)]
- Moriske, H.-J. (Ed.) *Stellungnahme der Kommission Innenraumlufthygiene am Umweltbundesamt*; Umweltbundesamt: Dessau-Roßlau, Germany, 2020.
- al horr, Y.; Arif, M.; Kafatygiotou, M.; Mazroei, A.; Kaushik, A.; Elsarrag, E. Impact of indoor environmental quality on occupant well-being and comfort: A Review of the Literature. *Int. J. Sustain. Built Environ.* **2016**, *5*, 1–11. [[CrossRef](#)]
- Gudipudi, R.; Fluschnik, T.; Ros, A.G.C.; Walther, C.; Kropp, J.P. City density and CO<sub>2</sub> efficiency. *Energy Policy* **2016**, *91*, 352–361. [[CrossRef](#)]
- Maller, C.; Townsend, M.; Pryor, A.; Brown, P.; Leger, L.S. Healthy nature healthy people: ‘contact with nature’ as an upstream health promotion intervention for populations. *Health Promot. Int.* **2006**, *21*, 45–54. [[CrossRef](#)] [[PubMed](#)]
- DIN EN 17037:2019*; Daylight in Buildings. German Institute for Standardisation: Berlin, Germany, 2019.
- Gasparella, A.; Pernigotto, G.; Cappelletti, F.; Romagnoni, P.; Baggio, P. Analysis and modelling of window and glazing systems energy performance for a well insulated residential building. *Energy Build.* **2011**, *43*, 1030–1037. [[CrossRef](#)]
- Wacker, M.; Holick, M.F. Sunlight and Vitamin D: A Global Perspective for Health. *Derm. Endocrinol.* **2013**, *5*, 51–108. [[CrossRef](#)]
- DIN EN ISO 7730:2006*; Ergonomics of the Thermal Environment—Analytical Determination and Interpretation of Thermal Comfort Using Calculation of the PMV and PPD Indices and Local Thermal Comfort Criteria. German Institute for Standardisation: Berlin, Germany, 2006.
- Bartlett, D.J.; Biggs, S.N.; Armstrong, S.M. Circadian rhythm disorders among adolescents: Assessment and Treatment Options. *Med. J. Aust.* **2013**, *199*, S16–S20. [[CrossRef](#)]
- Klepeis, N.E.; Nelson, W.C.; Ott, W.R.; Robinson, J.P.; Tsang, A.M.; Switzer, P.; Behar, J.V.; Hern, S.C.; Engelmann, W.H. The National Human Activity Pattern Survey (NHAPS): A Resource for Assessing Exposure to Environmental Pollutants. *J. Expo Sci. Environ. Epidemiol.* **2001**, *11*, 231–252. [[CrossRef](#)]
- Committee on Environmental Health. Ambient Air Pollution: Health Hazards to Children. *Pediatrics* **2004**, *114*, 1699–1707. [[CrossRef](#)]
- Mors, S.T.; Hensen, J.L.M.; Loomans, M.G.L.C.; Boerstra, A.C. Adaptive thermal comfort in primary school classrooms: Creating and Validating PMV-Based Comfort Charts. *Built. Environ.* **2011**, *46*, 2454–2461. [[CrossRef](#)]
- Yun, H.; Nam, I.; Kim, J.; Yang, J.; Lee, K.; Sohn, J. A field study of thermal comfort for kindergarten children in Korea: An Assessment of Existing Models and Preferences of Children. *Built. Environ.* **2014**, *75*, 182–189. [[CrossRef](#)]
- Turunen, M.; Toyinbo, O.; Putus, T.; Nevalainen, A.; Shaughnessy, R.; Haverinen-Shaughnessy, U. Indoor environmental quality in school buildings, and the health and wellbeing of students. *Int. J. Hyg. Environ. Health* **2014**, *217*, 733–739. [[CrossRef](#)] [[PubMed](#)]

26. Hansen, M. The Impact of School Daily Schedule on Adolescent Sleep. *Pediatrics* **2005**, *115*, 1555–1561. [CrossRef] [PubMed]
27. mpfs, Welche Freizeitaktivitäten übst Du Täglich oder Wöchentlich Aus? 2019. Available online: <https://de.statista.com/statistik/daten/studie/29982/umfrage/regelmaessige-freizeitaktivitaeten-von-kindern/> (accessed on 23 November 2020).
28. Samiou, A.I.; Doulos, L.T.; Zerefos, S. Daylighting and artificial lighting criteria that promote performance and optical comfort in preschool classrooms. *Energy Build.* **2022**, *258*, 111819. [CrossRef]
29. Booyesen, M.J.; Samuels, J.A.; Grobbelaar, S.S. LED there be light: The Impact of Replacing Lights at Schools in South Africa. *Energy Build.* **2021**, *235*, 110736. [CrossRef]
30. Tahsildoost, M.; Zomorodian, Z.S. Indoor environment quality assessment in classrooms: An Integrated Approach. *J. Build. Phys.* **2018**, *42*, 336–362. [CrossRef]
31. World Bank; UN DESA. Urbanisierungsgrad: Anteil der Stadtbewohner an der Gesamtbevölkerung in Deutschland in den Jahren von 2000 bis 2019. Statista. 2020. Available online: <https://de.statista.com/statistik/daten/studie/662560/umfrage/urbanisierung-in-deutschland/> (accessed on 25 June 2021).
32. RETROLux 80D Tageslichtlenkung. 2020. Available online: [www.schlotterer.com/de/produkte/retrolux-80d](http://www.schlotterer.com/de/produkte/retrolux-80d) (accessed on 12 April 2021).
33. Meyer, C.; Junior, G.J.F.; Barbosa, D.G.; Andrade, R.D.; Pelegrini, A.; Felden, É.P.G. Analysis of daytime sleepiness in adolescents by the Pediatric daytime sleepiness scale: A Systematic Review. *Rev. Paul. De Pediatr.* **2017**, *35*, 351–360. [CrossRef]
34. Brickenkamp, R. *d2-Aufmerksamkeits-Belastungstest*; Hogrefe: Göttingen, Germany, 2002.
35. DIN German Institute for Standardization, DIN EN 13211 Air Quality—Stationary Source Emissions—Manual Method of Determination of the Concentration of Total Mercury; German Version EN 13211:2001. 2001. Available online: <https://www.perinorm.com/document.aspx?hitnr=0&q=AC:DE45757898> (accessed on 26 April 2021).
36. Association of Engineers, VDI 2078 Calculation of Thermal Loads and Room Temperatures (Design Cooling Load and Annual Simulation). 2015. Available online: <https://www.perinorm.com/document.aspx?hitnr=0&q=AC:DE88185767> (accessed on 26 April 2021).
37. rgb Photonics User Manual. 2020. Available online: [https://www.rgb-photonics.com/fileadmin/user\\_upload/downloads/manuals/Qmini\\_1\\_Spectrometer.pdf](https://www.rgb-photonics.com/fileadmin/user_upload/downloads/manuals/Qmini_1_Spectrometer.pdf) (accessed on 14 October 2021).
38. Brickenkamp, R.; Schmidt-Atzert, L.; Liepmann, D. *d2-R-Aufmerksamkeits-und Konzentrationstest*; Hogrefe Verlag: Göttingen, Germany, 2010.
39. Lazor, T.; Tigelaar, L.; Pole, J.D.; de Souza, C.; Tomlinson, D.; Sung, L. Instruments to measure anxiety in children, adolescents, and young adults with cancer: A Systematic Review. *Support. Care Cancer* **2017**, *25*, 2921–2931. [CrossRef]
40. von Baeyer, C.L. Children’s Self-Reports of Pain Intensity: Scale Selection, Limitations and Interpretation. *Pain Res. Manag.* **2006**, *11*, 157–162. [CrossRef]
41. Noguchi, K.; Gel, Y.R.; Brunner, E.; Konietzschke, F. nparLD: An R Software Package for the Nonparametric Analysis of Longitudinal Data in Factorial Experiments. *J. Stat. Softw.* **2012**, *50*, 1–23. [CrossRef]
42. Weinfurt, K.P. Repeated measures analysis: Anova, Manova, and Hlm. In *Reading and Understanding More Multivariate Statistics*; American Psychological Association: Washington, DC, USA, 2000; pp. 317–361.
43. Zeitzer, J.M. When is a proxy not a proxy? The foibles of studying non-image forming light. *J. Physiol.* **2018**, *596*, 2029–2030. [CrossRef] [PubMed]
44. Vetter, C.; Pattison, P.M.; Houser, K.; Herf, M.; Phillips, A.J.K.; Wright, K.P.; Skene, D.J.; Brainard, G.C.; Boivin, D.B.; Glickman, G. A Review of Human Physiological Responses to Light: Implications for the Development of Integrative Lighting Solutions. *Leukos* **2021**, *18*, 1–28. [CrossRef]
45. Vetter, C. Circadian disruption: What Do We Actually Mean? *Eur. J. Neurosci.* **2020**, *51*, 531–550. [CrossRef] [PubMed]
46. Rossi, M. Conclusions and Possible Guidelines for Circadian Lighting Design. In *Circadian Lighting Design in the LED Era*; Springer International Publishing: Cham, Switzerland, 2019; pp. 257–277. [CrossRef]
47. Safranek, S.; Collier, J.M.; Wilkerson, A.; Davis, R.G. Energy impact of human health and wellness lighting recommendations for office and classroom applications. *Energy Build.* **2020**, *226*, 110365. [CrossRef]
48. *DIN/TS 5031-100:2021*; Optical Radiation Physics and Illuminating Engineering—Melanopic Effects of Ocular Light on Human Beings—Quantities, Symbols and Action Spectra. German Institute for Standardisation: Berlin, Germany, 2021.
49. *CIE TN 003:2015*; Report on the First International Workshop on Circadian and Neurophysiological Photometry. International Commission on Illumination: Vienna, Austria, 2015.
50. Hellhammer, D.H.; Wüst, S.; Kudielka, B.M. Salivary cortisol as a biomarker in stress research. *Psychoneuroendocrinology* **2009**, *34*, 163–171. [CrossRef]



Article

# Public Expenditure and Green Total Factor Productivity: Evidence from Chinese Prefecture-Level Cities

Weixiang Zhao<sup>1</sup> and Yankun Xu<sup>2,\*</sup>

<sup>1</sup> School of Public Finance and Taxation, Zhongnan University of Economics and Law, Wuhan 430074, China; zhaoweixiang@stu.zuel.edu.cn

<sup>2</sup> School of Economics, South-Central Minzu University, Wuhan 430074, China

\* Correspondence: 2019035@mail.scuec.edu.cn

**Abstract:** Whilst effective public expenditure policies are essential for transforming the traditional factor-driven economy into a green and innovation-driven economy, the impacts of public expenditure's size and composition on green economic development have not been comprehensively investigated. This paper attempts to fill this research gap. Based on the data of Chinese prefecture-level cities from 2010 to 2018, we first measure green total factor productivity (GTFP), the proxy variable for green development, and briefly analyze its spatial-temporal trends. Then, using the dynamic panel models, dynamic panel mediation models, and dynamic panel threshold models, we evaluate how public expenditure affects GTFP. The main findings are fourfold: (1) there is a significant inverted U-shaped relationship between the expenditure size and GTFP. (2) The expansion of social expenditures and science and technology (S&T) and environmental protection expenditures play an important role in stimulating green growth, while economic expenditures and administrative expenditures have adverse effects. (3) Public expenditure mainly promotes green development through four channels: human capital accumulation, technological innovation, environmental quality improvement, and labor productivity increase. (4) The expenditure composition influences the turning point of the inverted U-shaped relationship. Based on these findings, we propose some targeted policy suggestions to promote green development.

**Keywords:** public finance; expenditure size and composition; green total factor productivity; China

**Citation:** Zhao, W.; Xu, Y. Public Expenditure and Green Total Factor Productivity: Evidence from Chinese Prefecture-Level Cities. *Int. J. Environ. Res. Public Health* **2022**, *19*, 5755.

<https://doi.org/10.3390/ijerph19095755>

Academic Editors: Roberto Alonso González Lezcano, Francesco Nocera and Rosa Giuseppina Caponetto

Received: 7 April 2022

Accepted: 5 May 2022

Published: 9 May 2022

**Publisher's Note:** MDPI stays neutral with regard to jurisdictional claims in published maps and institutional affiliations.



**Copyright:** © 2022 by the authors. Licensee MDPI, Basel, Switzerland. This article is an open access article distributed under the terms and conditions of the Creative Commons Attribution (CC BY) license (<https://creativecommons.org/licenses/by/4.0/>).

## 1. Introduction

Pollutant emissions from industrial and rapidly industrializing economies directly lead to worldwide environmental issues such as pollution and climate change, posing severe threats to public health [1,2]. In order to reconcile the conflicting relationship between human economic activities and the environment, more and more countries have been attempting to pursue green economic development, which deviates from the traditional extensive growth strategy and aims at improving welfare and social equity while significantly reducing environmental risk and ecological scarcity [3,4]. The realization of green development requires the participation of micro-market players and social subjects, such as enterprises increasing technological innovation and residents greening their consumption and investments [5,6]. However, considering that green behavior has obvious positive externalities, various participants' green behavior may not show incentive compatibility, which may lower the efficiency and the subjects' willingness to promote the transition towards a greener economy. In this case, relying on the guidance, regulation, and financial compensation of public expenditures financed by taxation to achieve the goal of overall green development transformation is reasonable, legitimate, and inevitable.

The impacts of public expenditures on green development are multidimensional and double-edged. In the economic growth model, public expenditures have significant positive externalities and knowledge-spillover effects. Expenditures on education and

healthcare help to promote economic growth from being physical capital-driven to human capital and technology-driven. Environmental protection expenditures help to internalize the environmental externalities associated with production activities and provide greater incentives for green behavior. Finally, expenditures on science and technology (S&T) promote innovation, particularly green innovation. However, the size and composition of public expenditure can also have negative consequences for green development. Excessive government expenditures will crowd out effective social resources, which is not conducive to the overall efficiency of society. For example, a large scale of economic spending may lead to excessive government intervention in the private sector and weaken the fundamental driving force of economic development. Too-high administrative expenditures may indicate that the government is inefficient and will reduce economic efficiency. Therefore, an appropriate size and reasonable composition of government expenditure are of great significance to promoting green transformation and development.

To date, a few studies have focused on the impacts of fiscal behavior, especially public expenditure, on green growth. Lopez et al. [7] were the first to analyze the environmental effects of public expenditure. Their theoretical analysis found that increasing the size of public expenditure was conducive to a reduction in air and water pollutants, while this positive impact turns neutral when the proportion of public expenditure to private expenditure remains unchanged. Halkos and Paizanos [8] used a dataset containing 77 countries or regions to study the impacts of government spending on air pollution and found that government expenditures had a significant negative impact on dioxide emissions per capita, especially in low-income countries. Hua et al. [9] constructed an Optimal Control model and described a negative relationship between education expenditure, S&T expenditure, and air pollution, which showed a decreasing trend from coastal to inland areas. Using the panel data of Chinese cities, Lin and Zhu [10] applied a non-radial distance function in constructing a green economic growth index. They conducted a system GMM estimation and derived that the education expenditure and R&D expenditure can promote green economic growth. Postula and Radecka-Moroz [11] took the European Union as an example to analyze the role of fiscal tools in environmental protection and found that public expenditure only had a long-term effect.

Nevertheless, these existing studies are relatively limited. They mainly support a linear relationship between public spending size and environmental pollution or green development, while the crowding out effect of excessive government spending is little explored. From the perspective of the composition of public expenditure, environmental economists have analyzed the environmental effects of education and S&T expenditures, and little attention has been paid to the impacts of economic expenditures, environmental expenditures, and administrative expenditures. In addition, almost all current literature focuses on the impact of fiscal spending on pollution emissions, and the research on the impact on green development performance remains insufficient. Given that public expenditures have multiple environmental and economic effects, the question of how to promote the coordination of environment and economic development has become a fundamental goal of green transformation. While considering the environmental and economic development goals, this paper tries to fill the aforementioned literature gaps by comprehensively analyzing the impacts of public expenditure size and composition on green development performance using city-level panel data from China.

The paper most similar to ours is Lin and Zhu [10], which focused on the impact of education expenditure and R&D expenditure on the green economic growth index. By comparison, our work mainly expands on three aspects. First, we elucidate the stages of China's green development transition and public-expenditure policies. Afterward, we reveal that the impact of public expenditures on green development is mainly conducted in two dimensions, which are the expenditure size and structure. Second, we measure green total factor productivity (GTFP) as a proxy variable for green development using a global non-angle, non-radial DEA-SBM model combined with the GML (Global Malmquist–Luenberger) index. We briefly analyze the trends, structure, and regional distribution of GTFP. Third, we

construct dynamic panel models, dynamic panel mediation models, and dynamic threshold panel models to examine the impact of public expenditure on GTFP in detail. Specifically, we find that the size of public expenditure and GTFP show a clear inverted U-shaped relationship, and there are significant differences in the impact of various categories of public expenditure on GTFP, namely, economic expenditures, social expenditures, administrative expenditures, S&T, and environmental protection expenditures. Among them, social expenditures and expenditures on S&T and environmental protection significantly promote green transformation and development. Our results also show that the impact of public expenditures on GTFP is mainly transmitted through four channels, namely, human capital accumulation, science and technology innovation, environmental quality improvement, and labor productivity increase. Social expenditures positively affect GTFP by promoting human capital accumulation, technological innovation, and increasing labor productivity. S&T and environmental protection spending positively affect GTFP through all four channels. Last but not least, we find that changes in the spending composition affect the inverted U-shaped relationship between expenditure size and GTFP. When the proportion of social expenditures and S&T and environmental protection expenditures and administrative expenditures reach their respective threshold values, the value of the turning point of the inverted U-shaped relationship between public expenditure size and GTFP will be increased, creating more room for the expansion of public spending to promote green development.

This paper contributes to the literature in the following ways. We comprehensively study the impacts of public expenditures on green development. The existing research mainly focuses on how pollution emissions, energy consumption, and ecological conservation can be affected by public expenditures. Only a small amount of attention has been paid to the impact of public spending on green development. This paper fills this literature gap by explaining and evaluating the impacts of the size and composition of public expenditure on GTFP. Additionally, our research reveals and verifies the underlying mechanisms of public expenditure's impacts from an empirical perspective. In particular, considering the impacts of different types of public expenditures on green development performance and the impacts of different types of public expenditures on different mediation variables helps in more accurately understanding the complex relationship between public expenditure and green development. Finally, our research has important implications for developing countries, especially for transitional countries in the process of green transformation and development, in the design of public expenditure policies. Public expenditure policy should take into account not only appropriate size but also structural optimization, and the policymaker should accurately recognize the stages and driving forces of the green development transformation and design policies with these in mind.

The rest of this study is organized as follows. Section 2 reviews the background and characteristics of public expenditure policies and green development transformation in China and analyzes the mechanisms of public expenditures' impact on green development along the dimensions of size and composition. Section 3 introduces a global non-angle and non-radial DEA-SBM model combined with the GML index to measure GTFP and analyze the distribution of GTFP from spatial and temporal perspectives. Section 4, mainly for the preparation of empirical analysis, provides the details of empirical models, methods, and data used in this paper. Section 5 includes an empirical analysis examining the impact of public expenditure on GTFP and its mechanisms and interpreting the results. Section 6 concludes with some targeted policy suggestions.

## 2. Institutional Background and Theoretical Mechanism Analysis

### 2.1. The Green Development Strategy and Public Expenditure Policies in China

China's green development strategy, which is the core content of its "national strategy of ecological civilisation", was developed in the context of attempting to change China's extensive economic growth since the reform and opening up. Since it became a national strategy in 2012, China has issued a number of national action plans regarding air, water,

soil, solid waste, ecological resources, etc., with the aim of reversing the current trend of the rapid deterioration of ecological and environmental quality. At the same time, ecological and environmental considerations have also begun to be integrated into other economic and social policies, including fiscal policy, monetary policy, industrial policy, land policy, judicial policy, and social security policy. This rapid “greening” of China’s public policies provides a useful context for us to study the progress of green development and its driving mechanisms.

The fiscal system has a special status and importance in China. The establishment of a modern fiscal system has been clearly established as the foundation, and an important pillar, of the country’s national governance capacity and the modernization of its systems. Fiscal policy has also been widely used in ecological and environmental governance. In 2007, environmental expenditure became an independent expenditure item in China’s public budget, alongside education, medical care, social security, and other listed expenditure items. From the government budget perspective, China’s public expenditure includes four main types: general public budget expenditure, budgetary expenditures of government-managed funds, social security budget expenditure, and state-owned capital budget expenditure. While the latter three types of expenditure are mainly arranged for specific fields and purposes, the general public budget expenditure has the characteristics of universality, extensiveness, and transparency. In this paper, therefore, we mainly focus on China’s general public budget expenditure.

In 2007, China carried out a reform regarding the classification of budgetary revenues and expenditures, which is still in effect today. Public expenditure is classified into 18 types of specific components. Based on the economic property of each component, they can be further divided into several categories [12,13]. Referring to Jia et al. [14] and Wu et al. [15], we classify public expenditures into four types in this paper, namely, social expenditures, economic expenditures, science and technology (S&T) and environmental protection expenditures, and administrative expenditures. Social expenditures include education expenditure, cultural, sports and media expenditure, social security and employment expenditure, medical and health and family planning expenditure, urban and rural community expenditure, and housing security expenditure. Economic expenditures comprise expenditures on agriculture, forestry, water, and transportation. S&T and environmental protection expenditures are composed of scientific and technological innovation expenditure and energy conservation and environmental protection expenditure, while administrative expenditures consist of public service expenditure and public security expenditure. Table 1 shows the changes in the size and structure of China’s local government fiscal spending from 2010 to 2018. As a whole, the largest expenditure category for local governments in China was social expenditures, which accounted for 54.88% of total expenditure in 2018. In the same year, the proportions of economic expenditures, administrative expenditures, and environmental protection and S&T expenditures in total public spending were in descending order. During the sample period, social expenditures and S&T and environmental protection expenditures showed a steady upward trend, while administrative expenditures presented a downward trend. Economic expenditures have a tendency of first rising and then falling within a given period.

**Table 1.** Size and proportion of various types of public expenditure in Chinese local governments.

Year	Social Expenditures		Economic Expenditures		S&T and Environmental Protection Expenditures		Administrative Expenditures	
	Size	Proportion	Size	Proportion	Size	Proportion	Size	Proportion
	100 Million yuan	%	100 Million yuan	%	100 Million yuan	%	100 Million yuan	%
2010	34,600.26	46.83	11,740.58	15.89	3961.38	5.36	13,142.24	17.79
2011	45,268.83	48.82	16,687.68	18.00	4452.67	4.80	15,352.03	16.55
2012	54,515.73	50.86	18,803.96	17.54	5142.01	4.80	17,630.27	16.45
2013	60,510.30	50.53	21,448.47	17.91	6050.20	5.05	19,243.42	16.07
2014	67,192.69	52.00	23,303.42	18.03	6348.69	4.91	19,096.54	14.78
2015	79,154.02	52.65	28,144.98	18.72	7786.66	5.18	20,288.28	13.50
2016	88,022.30	54.89	27,494.88	17.15	8317.19	5.19	22,871.44	14.26
2017	96,372.77	55.63	27,897.81	16.10	9706.79	5.60	25,851.23	14.92
2018	103,273.08	54.88	30,462.34	16.19	11,076.43	5.89	28,610.98	15.20

Data source: China Statistical Yearbook (2011–2019).

### 2.2. Mechanisms of the Impact of Public Expenditure on Green Development

Public expenditure mainly affects green development by influencing the ecological and environmental quality and economic growth [10]. Public expenditure is largely financed through taxes, which per se are an important channel to internalize negative externalities and, to a certain extent, consider the cost of energy and environmental and ecological consumption. Neutral tax policies help to promote economic growth and productivity. Public expenditure is mainly used to supply public goods, which have strong positive externalities. By providing public goods, public spending can help to increase the marginal productivity of various production factors that promote economic growth. The increase in productivity itself implies an increase in the efficiency of resources and energy consumption and a decline in pollutant emissions. Moreover, expenditure can help to compensate, guide, and support actions with strong externalities, such as clean energy, pollution-reduction technologies, and ecological environment governance.

Theoretically speaking, a certain size of public expenditure can act on green development through taxation and public products to promote green transformation and development. However, excessive public expenditure may inhibit green growth, mainly in the form of a crowding-out effect. Disproportionate allocation of resources to the public sector can crowd out factor resources required by the private sector’s production activities, which may raise the private sector’s production costs, such as credit costs and human costs. This, in turn, is not conducive to the improvement of production efficiency. Moreover, in China, although public resources can be partially transferred to the private sector through subsidies and tax incentives, these resources are usually disproportionately allocated to state-owned enterprises. The fund-leakage phenomenon for the private sector is evident, particularly affecting green innovation behaviors that rely more on external subsidies and tax incentives [16]. Meanwhile, Baumol’s cost disease exists in the public sector. Excessive resource allocation to the public sector is not conducive to the improvement of public sector efficiency, and low public efficiency can further drag down the efficiency of the private sector [17]. Therefore, there may be an inverted U-shaped relationship between public expenditure and green development.

In this paper, taking differences in the types of public expenditure into account, we further divide the total expenditure into four categories, namely, social expenditures, economic expenditures, S&T and environmental protection expenditures, and administrative expenditures, which can cover most expenditure types [10,14]. Considering the different purposes and economic properties of each category of expenditure, they may have heterogeneous effects on green development. Social expenditures, mainly used in the areas of education, healthcare, health, and social security, are an important way of accumulating



and enhancing human capital, especially for developing countries and countries in transition. Public sector investment in social spending can compensate for the negative impact of insufficient private investment. Human capital is also considered to be an essential way to induce innovation and an important channel for increasing labor productivity and total factor productivity [9,10]. Along with the increase in the level of human capital, the demand for clean products will further increase, which will force the production of polluting products to be reduced and improve the overall efficiency of clean production. Meanwhile, an increase in the level of human capital will also help to improve the overall resource allocation and management capabilities of society. Overall, social spending with human capital improvement as the core could contribute to green development.

Economic spending is mainly directed at improving the efficiency of resource allocation and maintaining economic stability in areas of market failure. However, since market failure is not a necessary and sufficient condition for government intervention, the government also faces the risk of failure under market conditions. In the early stage of economic development, a certain amount of economic expenditures can help compensate for the lack of private investment. For the middle and late stages of economic development, economic spending tends to have crowding-out effects on private investment and consumption behavior, raising the cost of private economic behavior and inhibiting economic efficiency [18]. Meanwhile, compared with non-economic expenditures, economic expenditures mainly belong to physical capital investment and industrial investment. Investment in capital-intensive industries often causes considerable energy consumption and pollution emission. Therefore, the increase in economic expenditures may hinder green development.

S&T and environmental protection expenditures mainly involve public expenditures for technological innovation, energy conservation, and environmental protection activities. S&T expenditure can help promote R&D and technology spillover effects, encourage cleaner production behaviors, and improve total factor productivity [19,20]. Most environmental protection expenditure is used to compensate and subsidize ecological, environmental governance, and resource and energy conservation and provide incentive and guidance for positive external private-sector environmental behaviors. Moreover, environmental protection expenditures are primarily oriented toward green innovations, energy-saving technologies, and ecological protection and have direct green production attributes [21–26]. In brief, S&T and environmental protection expenditure can boost the green development of the economy.

Administrative expenditures are the basis for the regular operation of the government. They are purely expendable and do not directly contribute to economic growth and ecology. Given the limited public funds, excessive administrative expenditure is detrimental to overall economic growth and green development [7,14]. Because administrative expenditures are mainly used for staff salaries and benefits and the functioning of the state apparatus, excessive administrative spending is an essential indication of inefficient and costly government operations, which is detrimental to overall green transformation and development.

This section detailedly analyzes the theoretical impacts of the size and composition of public expenditure on green development. It is relatively evident that human capital accumulation, scientific and technological innovation, environmental quality, and labor productivity are the main channels through which public expenditure affects green development. Thus, we regard them as mediation variables in our empirical analysis to analyze the mechanisms of the green effect of public expenditure. In addition, there may be an inverted U-shaped relationship between public expenditure and green development. The curve's turning point may indicate room for the expansion of public expenditure to enhance green development. We will verify the existence of this possible inverted U-shaped relationship in an empirical analysis and examine whether changes in the proportion of each category of public expenditure alter the impact of public spending's expansion on green development.

### 3. The Construction of GTFP and Its Distribution

#### 3.1. The Calculation Method

After years of rapid development, China’s economic dynamism has been greatly improved. However, China’s extensive growth, characterized by the high consumption of resources and energy and high pollutant emissions, has brought side effects, namely, “unbalanced, uncoordinated and unsustainable development”. Therefore, increasing green total factor productivity (GTFP), which is an essential indicator to measure the level of green and high-quality development [27], has become a fundamental way to promote green economic transformation and achieve environmentally friendly and sustainable development.

In this paper, we treated city-level GTFP as the proxy variable to measure China’s green development. We used the non-radial, non-angle slack-based measure (SBM) proposed by Tone [28], which is able to cover non-desired output variables in the production process and supports slack improvement, to accurately evaluate urban environmental efficiency. We took the prefecture-level cities in China as decision-making units ( $DMU_i^t, i = 1, \dots, I; t = 1, \dots, T$ ) to construct production frontiers. The number of input factors  $x$  for each decision unit is  $n$ , including labor (L), capital stock (K), water supply (W), and electricity consumption (E) (it is worth noting that most scholars choose “coal consumption” or “oil consumption” to measure energy inputs in national and provincial level studies. However, data on coal and oil at the city level are currently not available, and data on gas and LPG are missing, so this paper adopts social electricity consumption as a proxy for urban energy input [10,29,30]). The decision unit uses input factors to produce  $m$  desired outputs  $y$ , including gross domestic product (GDP) and greening coverage (G) of each region, and  $j$  non-desired outputs  $b$ , including industrial wastewater (IW), sulfur dioxide emission (SDE), and soot emission (SE). The data needed to measure each variable are obtained from the China Urban Statistical Yearbook, and the definitions are shown in Table 2. In summary, the production possibility set can be described as:

$$P^t(x^t, y^t, b^t) = \{(y^t, b^t) | x^t \text{ can produce } (y^t, b^t)\} \tag{1}$$

**Table 2.** The definitions and descriptive statistics of the input and output indicators for GTFP’s calculation.

Indicators	Definition	Unit	Mean	SD	Min	Max	
Inputs	Workforce (L)	Persons employed in urban units at year-end calculated through the perpetual inventory method	Person	51.15	56.80	5.01	613.50
	Capital Stock (K)		Billion Yuan	491.13	481.03	26.44	3382.64
	Water Supply (W)	-	Million tons	140.46	240.56	2.020	2288.50
	Electricity Supply (E)	-	Million kwh	10,771.95	14,081.44	97.54	156,248.97
Desirable outputs	GDP	Gross Regional Product (base period 2000)	Billion Yuan	1238	1399	68.78	12,870
	Green Coverage (G)	Green-covered area as % of built-up area	Percentage	38.55	8.06	0.36	95.25
	Industrial Waste (IW)	Volume of industrial waste water discharged	Ten thousand tons	6323	7589	7	93,814
Undesirable outputs	Sulfur Dioxide Emissions (SDE)	Volume of Industrial sulfur dioxide emission	Ton	42,978	43,836	0	496,377
	Soot Emission (SE)	Volume of industrial soot (dust) emission	Ton	35,191	151,948	34	5,168,812

In Equation (1),  $P^t(x^t, y^t, b^t)$  contains the input–output conditions of all prefecture-level cities in period  $t$ . Combining Equation (1) with the directional distance function,

we can calculate the GTFP change index for each prefecture-level city at each period. However, the results obtained using this classical algorithm are not cyclic and have the drawback of being unsolvable by linear programming [31]. Therefore, we calculated the GML (Global Malmquist–Luenberger) index constructed by Oh [32] that simultaneously scales the production frontier for all periods to address the above issues. The global production possibility set can be expressed as:  $PG = P^1 \cup P^2 \cup \dots \cup P^T$ . According to Li [33], the SBM-DDF model with constant payoffs to scale when applying the global production possibility set is shown in the following equation:

$$\begin{aligned} \hat{P}G_i^t(X_i^t, Y_i^t, B_i^t) &= \max[w_n^x \sum_{n=1}^N \frac{\hat{\beta}_{n,i}^{X-t}}{N} + w_m^y \sum_{m=1}^M \frac{\hat{\beta}_{M,i}^{Y-t}}{M} + w_j^b \sum_{j=1}^J \frac{\hat{\beta}_{j,i}^{B-t}}{J}] \\ \text{s.t. } \sum_{t=1}^T \sum_{i=1}^I \theta_i^t X_{in}^t &\leq (1 - \hat{\beta}_{in}^{X-t}) X_{in}^t, \forall n; \\ \sum_{t=1}^T \sum_{i=1}^I \theta_i^t Y_{im}^t &\geq (1 - \hat{\beta}_{im}^{Y-t}) Y_{im}^t, \forall m; \\ \sum_{t=1}^T \sum_{i=1}^I \theta_i^t B_{ij}^t &= (1 - \hat{\beta}_{ij}^{B-t}) B_{ij}^t, \forall j; \\ \theta_i^t &\geq 0, i = 1, \dots, I; t = 1, \dots, T; n = 1, \dots, N; m = 1, \dots, M; j = 1, \dots, J \end{aligned} \tag{2}$$

where the constant returns to scale assumption removes the differences in results from input- and output-oriented calculation of the GML index;  $w_n^x, w_m^y, w_j^b$  denote the weight vectors of inputs, desired outputs, and undesired outputs, respectively. Under the general assumption that the inputs and outputs are equally important, the weights for them are  $\frac{N}{N+M+J}, \frac{M}{N+M+J}, \frac{J}{N+M+J}$ , respectively. The scale vector  $\hat{\beta}_i^t$  is represented using the optimal solution of  $\hat{\beta}_i^t = (\hat{\beta}_{n,i}^{X-t}, \hat{\beta}_{M,i}^{Y-t}, \hat{\beta}_{j,i}^{B-t})$ , which can ensure that both the input and undesired output scale reduction and the desired output scale expansion of the decision unit are maximized.  $\theta_i^t$  is the intensity variable of  $DMU_i$  at  $t$ , which is a constant vector of  $I \times 1$ . Combining all the constraints above, Equation (2) is able to find the optimal state where the minimum amount of resources is invested, and the maximum desired output and the minimum undesired output can be achieved, i.e., the global production frontier. We refer to Oh [32] and express the GML index under the assumption of constant returns to scale as follows:

$$GML^{t,t+1}(x^{t+1}, y^{t+1}, b^{t+1}, x^t, y^t, c^t) = \frac{1 - PG^{t+1}(x^{t+1}, y^{t+1}, b^{t+1}|C)}{1 - PG^t(x^t, y^t, b^t|C)} \tag{3}$$

A greater than one  $GML^{t,t+1}$  index of a city means an increase in GTFP for this city from  $t$  to  $t + 1$  and vice versa. The GML index can be further decomposed as follows:

$$\begin{aligned} GML^{t,t+1} &= \left[ \frac{1 - PG^{t+1}(x^{t+1}, y^{t+1}, b^{t+1}|C)}{1 - PG^{t+1}(x^{t+1}, y^{t+1}, b^{t+1}|V)} \right] \times \left[ \frac{1 - PG^t(x^t, y^t, b^t|C)}{1 - PG^t(x^t, y^t, b^t|V)} \right] \\ &= GTPCH^{t,t+1} \times GPECH^{t,t+1} \times GSECH^{t,t+1} \end{aligned} \tag{4}$$

where  $C$  denotes constant returns to scale, and  $V$  denotes variable returns to scale.  $GTPCH^{t,t+1}, GPECH^{t,t+1},$  and  $GSECH^{t,t+1}$  represents the technological progress index, pure technical efficiency index, and scale efficiency index, respectively. The three indices greater than, equal to, or less than 1 indicate that the level of technology, level of pure technical efficiency, and level of scale efficiency of a prefecture-level city increase, remain unchanged, and decrease from period  $t$  to period  $t + 1$ , respectively.

3.2. The spatial-Temporal Patterns of GTFP and Its Composition

3.2.1. Overall Analysis

O'Donnell [34] points out that the GML index is not the total factor of productivity. Drawing on Li and Wu [35], we calculated green total factor productivity (GTFP) and technological progress (GTECH), pure technical efficiency (PGEFFCH), and scale efficiency (SGEFFCH) for each prefecture-level city of each period using the following formulas:

$$\begin{aligned}
 GTFP^t &= 1 \times GML^1 \times \dots \times GML^t \\
 GTECH^t &= 1 \times GTPCH^1 \times \dots \times GTPCH^t \\
 PGEFFCH^t &= 1 \times \dots \times GPECH^t \\
 SGEFFCH^t &= 1 \times \dots \times GSECH^t
 \end{aligned}
 \tag{5}$$

We present the main results in Tables 3 and 4. We can see from Table 3 that the average values of GTFP in China increased from 1.070 in 2010 to 1.147 in 2018, indicating that China in general achieved green development during the sample period selected for this paper. Specifically, green total factor productivity at the prefecture-level city level in China showed a trend of oscillating growth, consistent with the results in Chen et al. [36]. Moreover, we present the calculation results of GTFP from 2010, 2015, and 2018 in the form of topographic maps to intuitively reflect the regional differences and dynamic changes of the GTFP (these three periods are selected because 2010 and 2018 are the starting and ending years of our sample period, and 2015 is the last year that the overall GTFP incurs a decrease. Therefore, we believe that choosing these three periods can help us better understand the dynamics of China's green development).

Table 3. National average values of GTFP and its composition.

Year	National Average			
	GTFP	GTECH	PGEFFCH	SGEFFCH
2010	1.070	1.009	1.062	1.020
2011	1.025	0.944	1.104	1.019
2012	1.024	0.961	1.085	1.017
2013	1.007	0.872	1.166	1.024
2014	0.940	0.884	1.088	1.008
2015	0.928	0.839	1.153	0.998
2016	1.036	0.946	1.090	1.031
2017	1.083	0.860	1.232	1.051
2018	1.147	0.931	1.213	1.057

Table 4. Regional average values of GTFP and its composition.

Year	Northeast China Average				East China Average			
	GTFP	GTECH	PGEFFCH	SGEFFCH	GTFP	GTECH	PGEFFCH	SGEFFCH
2010	1.079	0.971	1.093	1.031	1.078	1.098	1.026	0.979
2011	1.069	0.909	1.174	1.047	0.994	1.035	1.005	0.971
2012	1.056	0.937	1.127	1.046	0.986	1.038	1.017	0.950
2013	1.158	0.863	1.285	1.086	0.955	0.943	1.094	0.955
2014	0.935	0.858	1.109	1.029	0.898	0.932	1.027	0.963
2015	0.911	0.811	1.163	1.012	0.904	0.889	1.103	0.951
2016	0.998	0.907	1.107	1.039	1.016	1.009	1.030	0.999
2017	1.129	0.820	1.315	1.071	1.080	0.936	1.155	1.015
2018	1.150	0.849	1.305	1.065	1.128	1.067	1.069	1.036

Table 4. Cont.

Year	Central China Average				West China Average			
	GTFP	GTECH	PGEFFCH	SGEFFCH	GTFP	GTECH	PGEFFCH	SGEFFCH
2010	1.011	0.969	1.059	1.008	1.114	0.999	1.071	1.063
2011	0.978	0.919	1.124	0.985	1.061	0.915	1.114	1.074
2012	0.988	0.936	1.101	1.002	1.066	0.934	1.096	1.070
2013	0.924	0.840	1.130	1.006	0.989	0.842	1.158	1.049
2014	0.920	0.882	1.049	1.009	1.007	0.864	1.167	1.029
2015	0.891	0.828	1.144	0.980	1.006	0.827	1.202	1.047
2016	1.031	0.937	1.082	1.027	1.098	0.931	1.141	1.061
2017	1.070	0.841	1.265	1.024	1.053	0.841	1.195	1.092
2018	1.184	0.900	1.279	1.048	1.127	0.908	1.200	1.079

Comparing the three maps (as shown in Figure 1), we can see that the number of red and orange areas on the map increased from 2010 to 2015, reflecting a reduction in the level of green total factor productivity in China’s cities, which is consistent with Xia and Xu [37]. This is due to the “after-effects” of China’s four-trillion investment plan in 2008 to stabilize the economy in response to the US’s subprime mortgage crisis that became gradually apparent between 2010 and 2015. The investment plan was effective in stimulating economic growth, but the huge amount of capital generated was largely invested in heavy industries such as steel and coal, and mining, which led to an increase in problems such as overcapacity and environmental pollution, seriously affecting the quality of China’s economic development.

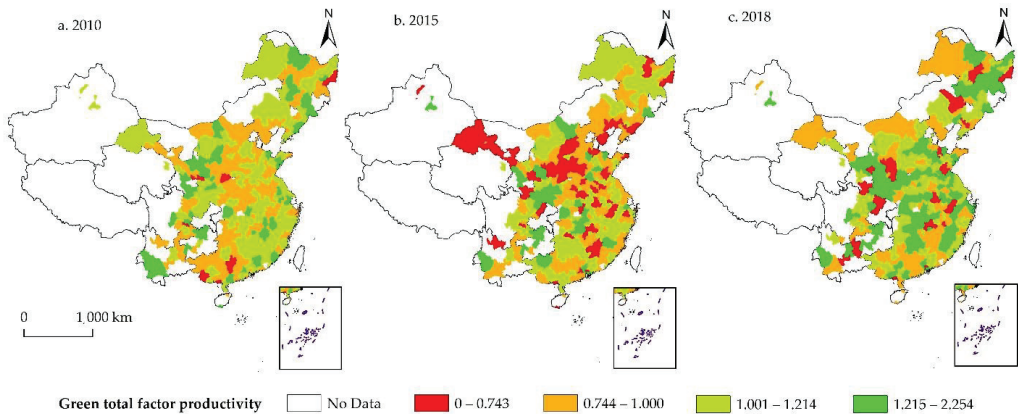


Figure 1. Spatial-temporal pattern of GTFP in China during 2010–2018.

The 2018 map shows a significant increase in green areas compared to 2010 and 2015 and a considerable decrease in orange and red areas, implying an improvement in China’s economic development quality (specifically, 167 cities saw their GTFP improve in 2018 compared to 2010, while 227 cities saw their GTFP improve compared to 2015). China’s GTFP has gradually improved since 2016, mainly due to the country’s focus on building an ecological civilization and combating pollution since the 18th National Congress and the 13th Five-Year Plan. Furthermore, Chinese central and local governments continued to encourage economic restructuring and industrial upgrading, contributing to high-quality economic growth and improved resource efficiency.

We also present how the components of GTFP changed on average at the national level over time in Table 3. The table shows that Chinese cities as a whole have witnessed a downward trend in their GTECH, indicating that they may have suffered a significant

decline in the level of technology (technological progress indicates an outward shift in the global production frontier. The production frontier is shifted outwards when and only when the input–output ratio of the city on the production frontier decreases, which indicates an improvement in technology and vice versa). Technological regression seems to be contrary to reality [38,39]. However, regions in China generally faced increasing input–output ratios since the scale of factors of production was expanding faster than the scale of the desired output. Such changes would undoubtedly lead to a year-on-year inversion of the production frontier and consequently to a technological regression. This phenomenon does not imply a real decline in the level of production technology.

The results in Table 3 also indicate that improvements in pure technical efficiency (PG-EFFCG) and scale efficiency (SGEFFCH) were the main engines of green and high-quality economic growth in China over the sample period. The increase in pure technical efficiency implies a significant improvement in the ability of cities to allocate productive resources appropriately and use them efficiently. The improvement in scale efficiency suggests that cities focus on exploiting the economies of scale brought about by the increased scale of production resources. The results of this paper also indicate that pure technical efficiency played a more significant role in China’s green development process than scale efficiency.

### 3.2.2. Regional analysis

The level of regional green development varies from region to region in China due to differences in regional development strategies (for example, China implemented the “Eastern Coastal Opening” strategy in 1978, the “Western Development” strategy in 2000, the “Revitalisation of the Old Northeast Industrial Base” strategy in 2003, and the “Rise of Central China” strategy in 2006) and resource-endowment conditions. We divide China into eastern, northeastern, central, and western regions (the eastern region comprises ten provinces, including Beijing, Tianjin, Hebei, Shanghai, Jiangsu, Zhejiang, Fujian, Shandong, Guangdong, and Hainan province. The central region includes Shanxi, Anhui, Jiangxi, Henan, Hubei, and Hunan. The western region includes Inner Mongolia, Guangxi, Chongqing, Sichuan, Guizhou, Yunnan, Shanxi, Gansu, Qinghai, Ningxia, and Xinjiang. The northeast region includes Liaoning, Jilin, and Heilongjiang) in order to analyze the GTFP and its composition in each region to reflect these differences.

Table 4 shows that GTFP in all four major regions of China improved over the sample period. At the time of 2018, the central region had the highest level of green development, followed by the northeastern, eastern, and western regions. As a result of actively improving the coordination among production factors and learning management techniques, both pure technical efficiency and scale efficiency in the Northeast region increased highly over time, leading to improved green development in the Northeast region. However, the rate of technological progress in Northeast China was the lowest among the four major regions during the sample period. This indicates that its development strategy, which focused on labor- and pollution-intensive industries, only yielded relatively low positive output and high undesired output after investing in production resources. Similarly, China’s central and western regions also achieved green growth over the sample period and showed relatively significant increases in pure technical efficiency and technical efficiency at scale. Finally, we find that the green growth pattern in the eastern region differs from the other areas. It relied primarily on improvements in technology levels to drive green and high-quality economic development. Local governments in the eastern region actively encouraged enterprises to develop green production technologies and pollutant treatment and reuse technologies to achieve green, high-quality production [40]. In addition, the abundant human capital in the eastern region helped to promote the further transformation of the industrial structure towards a more specialized, advanced, and high-quality one, which also indirectly reduced energy consumption per unit of GDP. As Färe et al. [41] stated, improving production technologies and pollution treatment technologies can reduce pollution emissions and energy consumption and ultimately increase GTFP.

#### 4. Econometric Methodology

##### 4.1. Dynamic Panel Model

###### 4.1.1. The Impacts of Fiscal Expenditure Size on GTFP

Improving GTFP is essential in achieving green growth. Changes in the size of fiscal spending, which represents an important method of government intervention in the economy, will inevitably have an impact on GTFP. Therefore, we use the GTFP of Chinese cities calculated by Equations (4) and (5) as the dependent variables and establish a regression model to explore the effect of the size of public expenditure on green, high-quality growth. The specific model is as follows:

$$GTFP_{it} = \alpha_0 + \alpha_1 wperexp_{it} + \alpha_2 wperexp_{it}^2 + \theta X_{it} + \mu_i + \tau_t + \varepsilon_{it} \quad (6)$$

where  $wperexp_{i,t}$  denotes the size of fiscal expenditure. Drawing on the existing studies, this paper selects per capita fiscal expenditure as a measure of expenditure size [29,42,43].  $X_{it}$  represents the set of control variables used in all regression models in this paper.  $\alpha$ ,  $\theta$  are parameters to be estimated.  $\mu_i$  and  $\tau_t$  represent the city-level and time-level fixed effects.  $\varepsilon_{it}$  is the standard error term. In this paper, all error terms are clustered at the city level.

Based on the theoretical analysis, we add a quadratic term of fiscal expenditure size in Equation (6) to analyze the possible nonlinear relationship between the expenditure size and GTFP. Considering that the GTFP used in the paper is a continuous cumulative process over time and there may be correlations between its current and earlier periods, the lagging one-stage variable  $GTFP_{it-1}$  is added to the Equation (6) [10,15,44]. This leads to the following model:

$$GTFP_{it} = \alpha_0 + \alpha_1 GTFP_{it-1} + \alpha_2 wperexp_{it} + \alpha_3 wperexp_{it}^2 + \theta X_{it} + \mu_i + \tau_t + \varepsilon_{it} \quad (7)$$

###### 4.1.2. The Impacts of Fiscal Expenditure Composition on GTFP

Different categories of public expenditures serve different purposes (for example, social expenditures are mainly used to provide basic public services such as education, health care, and pensions, while administrative expenditures are mainly used to maintain the operation of the government). According to the analysis in the previous section, the increase in the proportion of social expenditure and science and technology (S&T) and environmental protection expenditure helps to promote green development, while economic expenditure and administrative expenditure are unfavorable to it. Therefore, we construct a regression model to analyze the relationship between fiscal expenditure composition and GTFP to provide empirical evidence for the results of the theoretical analysis. The specific model is as follows:

$$GTFP_{it} = \alpha_0 + \alpha_1 GTFP_{it-1} + \alpha_2 persco_{it} + \alpha_3 pereco_{it} + \alpha_4 perino_{it} + \alpha_5 pergov_{it} + \theta X_{it} + \mu_i + \tau_t + \varepsilon_{it} \quad (8)$$

where  $persco_{it}$  denotes the proportion of social expenditure to fiscal expenditure and  $pereco_{it}$ ,  $perino_{it}$  and  $pergov_{it}$  represent the proportion of economic expenditure, S&T and environmental protection expenditure, and administrative expenditure, respectively.

##### 4.2. Dynamic Panel Mediation Model

###### Mechanism Analysis of the Impact of Fiscal Expenditure on GTFP

The estimation results of Equations (7) and (8) can help clarify the direction and extent of the impact of changes in the size and composition of fiscal expenditures on GTFP. We further construct dynamic panel mediation models to elucidate the mechanisms of fiscal spending's impact on GTFP. According to the analysis in Section 2.2, we take human capital accumulation, science and technology innovation, environmental quality, and labor productivity as mediation variables. Human capital accumulation is represented by the number of university students per 10,000 people [45–47], and S&T innovation is proxied by the number of green patents granted per 10,000 people [6], environmental quality uses PM2.5 level as a proxy variable [48,49], and labor productivity is expressed as the local GDP

divided by the number of local employees [50]. We estimate the following equation using the mediation effects test procedure developed by [51], which mainly referred to the causal steps approach proposed by Baron and Kenny [52]. The specific models are as follows:

$$GTFP_{it} = \alpha_0 + \alpha_1 GTFP_{it-1} + \alpha_2 persco_{it} + \alpha_3 pereco_{it} + \alpha_4 perino_{it} + \alpha_5 pergov_{it} + \theta X_{it} + \mu_i + \tau_t + \varepsilon_{it} \tag{9}$$

$$mediator_{it} = \alpha_0 + \alpha_1 persco_{it} + \alpha_2 pereco_{it} + \alpha_3 perino_{it} + \alpha_4 pergov_{it} + \theta X_{it} + \mu_i + \tau_t + \varepsilon_{it} \tag{10}$$

$$GTFP_{it} = \alpha_0 + \alpha_1 GTFP_{it-1} + \alpha_2 mediator_{it} + \alpha_3 persco_{it} + \alpha_4 pereco_{it} + \alpha_5 perino_{it} + \alpha_6 pergov_{it} + \theta X_{it} + \mu_i + \tau_t + \varepsilon_{it} \tag{11}$$

where Equation (9) is the same as Equation (8), and *mediator<sub>it</sub>* represents the four mediation variables mentioned above.

Equations (7)–(11) all contain lagged terms of the explanatory variables, which represents that these equations are dynamic panel regression models [10]. Since the lagged terms of the explanatory variables may be correlated with the random error terms of the regression models, and there may also be interactions between fiscal expenditure size and structural variables and GTFP, there may be endogeneity among the variables. The estimation results obtained from the traditional static estimation methods may be biased because of the potential endogeneity problems. Therefore, we adopt the generalized method of moments (GMM), which not only alleviates the endogeneity problem of dynamic panel data models but also eliminates the effect of fixed effects and avoids small sample errors (for one thing, system GMM can utilize more information than difference GMM. It can also estimate variables that do not vary with time, and the accuracy of the estimation results is higher. For another thing, two-step GMM is more robust and efficient than a one-stage estimate. However, the two-step estimate is prone to a severe underestimation of the standard errors of the estimated coefficients when the sample is small. In this paper, the standard error estimates are corrected using the method proposed by Windmeijer [53]). To be more specific, this paper uses a two-stage system GMM. Considering that the key to obtaining consistently estimated coefficients for two-step system GMM is the selection of valid instrumental variables and the absence of second-order autocorrelation in the residual terms, we use the Hansen test to determine the validity of the selected instrumental variables and the AR test to determine whether there is autocorrelation in the random error term after the first-order difference. In addition, to ensure the consistency of the estimation method, we also use a two-step system GMM model for the estimation of Equation (10).

#### 4.3. Dynamic Threshold Panel Model

##### The Impact of Fiscal Expenditure Composition on the Relationship between Fiscal Expenditure and GTFP

Changes in the proportion of a particular type of fiscal expenditure may affect the relationship between the fiscal expenditure size and GTFP (for example, if the Chinese government expands fiscal spending while maintaining a high proportion of social spending, the resulting impact on GTFP may be different from the impact of fiscal spending expansion with a relatively low share of social spending). Therefore, we develop a dynamic threshold panel model to analyze the effect of changes in the proportion of each category of public expenditure on the green growth effect of the fiscal expenditure size's expansion. The specific model is as follows:

$$GTFP_{it} = \alpha_0 + \alpha_1 GTFP_{it-1} + \alpha_2 wperexp_{it} + \alpha_3 wperexp2_{it} \cdot Q(Z_j \leq \gamma_j) + \alpha_4 wperexp2_{it} \cdot Q(Z_j > \gamma_j) + \theta X_{it} + \mu_i + \tau_t + \varepsilon_{it} \tag{12}$$

where  $Q(\cdot)$  is an indicator function,  $Z_j(j = 1, 2, 3, 4)$  denotes the regime-switching variables, including the fiscal expenditure composition variables, i.e., *persco<sub>it</sub>*, *pereco<sub>it</sub>*, *perino<sub>it</sub>*, and *pergov<sub>it</sub>*.  $\gamma_j(j = 1, 2, 3, 4)$  represents the threshold parameter. The estimation results of dynamic threshold panel models obtained from static methods are biased. Therefore, we refer to the method proposed by Dang et al. [54] and improved by Wu et al. [55] (this



method uses a grid search algorithm over the range between the 15th and 85th percentiles of the regime-switching variable to calculate the threshold value. Then, the Wald statistic, whose gradual distribution can be obtained through the bootstrap method, is used to determine whether the threshold effect is significant or not. The smaller the corresponding probability is, the more significant the threshold effect. Finally, the two-step system GMM is used to estimate the coefficients of each variable) to estimate Equation (12), which can endogenously determine the threshold values based on the characteristics of the regime-switching variables and solve the potential endogeneity problem.

4.4. Data Source

We include the same set of explanatory variables in all regression models to reduce model specification errors and to capture city-level characteristics. Drawing on existing studies [6,10,20], we choose the level of infrastructure (road), the level of financial development (mon), the degree of opening up (fdi), the level of economic development (pgdp), the industrial structure (sec), and the degree of fiscal decentralization (gov) as explanatory variables. The sample period of this paper ranges from 2010 to 2018, and, due to the lack of data in some cities, the data of each period contain 275 China’s prefecture-level cities. We present the definitions, measures, and descriptive statistics of the dependent variables, core independent variables, and control variables in Table 5. Data for these variables are from the China Urban Statistical Yearbook, China Urban Construction Statistical Yearbook, the EPS database, economic and social development reports of each city, and the statistical yearbooks published on the official websites of each city’s statistical bureaus.

Table 5. Variables used in the empirical analysis and their definitions.

Variable	Mean	SD	Min	Max	N
Green total factor productivity, gtfp	1.021	0.262	0.362	2.311	2475
Fiscal expenditure per capita, wperexp, 10 thousand yuan	0.648	0.944	0.023	13.303	2456
The square of wperexp, wperexp2	1.311	7.488	0.001	176.958	2456
The number of university students per 10,000 people, pouni	1.836	2.431	0.006	13.112	2426
The number of green patents granted per 10,000 people, pogreenino	0.477	1.058	0.000	18.396	2473
PM2.5, pm25, $\mu\text{g}/\text{m}^3$	42.814	19.514	4.134	110.121	2475
The local GDP divided by the number of local employees, labor	24.583	10.322	0.633	140	2473
The proportion of social expenditure in total fiscal expenditure, persco	0.501	0.072	0.045	0.958	2444
The proportion of economic expenditure in total fiscal expenditure, pereco	0.162	0.052	0.013	0.691	2425
The proportion of environmental protection and S&T expenditure in total fiscal expenditure, perino	0.045	0.023	0.002	0.263	2437
The proportion of administrative expenditure, pergov	0.157	0.037	0.034	0.402	2375
Area of city paved roads per capita at year-end, road, 10,000 sq.m	6.351	11.710	0.102	162.383	2416
The proportion of loans of national banking system at year-end in GDP, mon	0.907	0.549	0.118	7.450	2473
The proportion of foreign capital actually utilized in GDP, fdi	0.018	0.0177	0.000	0.210	2348
GDP per capita, pgdp, 10,000 yuan	2.812	1.796	0.352	17.059	2468
The proportion of employees in the secondary industry to all employees, sec	0.453	0.142	0.045	0.844	2473

5. Empirical Results

5.1. The Results of the Dynamic Models Estimation

5.1.1. The Impacts of Fiscal Expenditure Size on GTFP

We present the results of Equation (7) using the two-step system of GMM in column (4) of Table 6. The Hansen test as well as AR(2) test cannot be rejected at the 10% significance level, indicating that the instrumental variables we selected are valid and that there is no autocorrelation in the first difference of the random error terms [56,57].

Table 6. Estimation results of public expenditure scale on GTFP.

	OLS	Fixed Effect	Two-Step SYS-GMM	Two-Step SYS-GMM	Two-Step SYS-GMM	Two-Step SYS-GMM
VARIABLES	(1) GTFP	(2) GTFP	(3) GTFP	(4) GTFP	(5) GTFP	(6) GTFP
L. GTFP				0.339 *** (0.004)	0.303 *** (0.004)	0.286 *** (0.002)
wperexp	0.023 * (0.094)	0.099 ** (0.015)	0.149 *** (0.000)	0.103 *** (0.010)	0.056 *** (0.008)	
wperexp2	−0.004 *** (0.005)	−0.008 *** (0.002)	−0.009 *** (0.000)	−0.007 *** (0.009)		
expgdp						2.414 *** (0.008)
Expgdp2						−4.664 *** (0.005)
road	0.001 (0.135)	−0.000 (0.972)	−0.005 ** (0.026)	−0.003 * (0.060)	−0.002 * (0.062)	0.001 (0.326)
mon	−0.033 *** (0.001)	−0.026 (0.208)	−0.029 (0.125)	−0.033 ** (0.038)	−0.030 ** (0.049)	−0.018 (0.181)
fdi	−0.209 (0.482)	1.124 ** (0.011)	−0.095 (0.916)	0.048 (0.901)	0.096 (0.808)	−0.325 (0.624)
pgdp	0.041 *** (0.000)	0.060 *** (0.001)	0.041 *** (0.001)	0.037 *** (0.000)	0.040 *** (0.000)	0.040 *** (0.000)
sec	−0.286 *** (0.000)	−0.453 *** (0.000)	−0.230 ** (0.011)	−0.461 ** (0.011)	−0.404 ** (0.029)	−0.001 (0.239)
gov	0.001 (0.863)	0.020 (0.110)	−0.027 (0.192)	0.025** (0.013)	−0.001 (0.940)	−0.002 (0.825)
Constant	1.086 *** (0.000)	1.048 *** (0.000)	1.088 *** (0.000)	0.735 *** (0.000)	0.766 *** (0.000)	0.506 *** (0.003)
Observations	2.268	2.268	1.978	2.008	2.008	1.978
Adjusted R <sup>2</sup>	0.132	0.218				
City FE	NO	YES	YES	YES	YES	YES
Time FE	YES	YES	YES	YES	YES	YES
AR(2)			−1.231 [0.218]	1.059 [0.290]	1.003 [0.316]	0.848 [0.396]
Hansen test			8.868 [0.354]	14.654 [0.686]	9.259 [0.753]	4.468 [0.614]
Number of cities	270	270	269	270	270	269

Note: Robust and cluster standard errors in parentheses and *p*-value in brackets. \*\*\* *p* < 0.01, \*\* *p* < 0.05, \* *p* < 0.1.

The results in Table 6 indicate that the estimated coefficient for the fiscal expenditure size is positive, and the coefficient for its squared term is negative, both of which are significant at the 1% level. This suggests an inverted U-shaped relationship between fiscal expenditure and GTFP, which is consistent with the analysis in the second section and with the findings of Armye [58] and Chen and Lee [59]. In other words, all else being equal, there may be an optimal size of fiscal expenditure that results in the highest level of GTFP in China. Until this size is reached, expanding fiscal expenditure size will be beneficial to improving GTFP. However, this positive effect decreases at the margin as the expenditure size increases, eventually declining to zero when the optimal expenditure size is reached. We draw on Wu et al. [60] to use the OLS model, FE model, and two-step system GMM to repeat the estimation of Equation (6) to ensure the robustness of the inverted U-shaped relationship. The estimation results in columns (1) to (3) indicate that the significance and sign of the coefficients of the fiscal expenditure size and its squared term are almost the same using different estimation methods, demonstrating the robustness of the inverted U-shaped relationship.

We use estimated coefficients in column (4) to calculate the turning point of the inverted U-shaped relationship between fiscal expenditure size and GTFP, which is 75,000 yuan

per capita. The only two cities, Lanzhou and Nantong, exceeded this point in 2018. This phenomenon suggests that the vast majority of prefecture-level cities in China can improve GTFP and promote green economic development by expanding the fiscal expenditure size. It also suggests that the Chinese government's expansionary fiscal spending preferences are somewhat justified. Moreover, we estimated Equation (7) without the squared term. The results in column (5) show that the coefficient of the fiscal expenditure size is significantly positive at the 1% level, which empirically proves the robustness of this finding.

To ensure that the nonlinear relationship between expenditure size and GTFP is robust to different specifications of public spending size, we further constructed another variable, which is  $expdp_{it}$ , measured as the size of fiscal spending divided by local GDP, and re-estimated Equation (7). Column (6) indicates that the sign and significance of the coefficients of alternative measurements of expenditure size and its quadratic term remain unchanged, proving that the inverted U-shaped relationship is robust. In addition, the coefficients of the first-order lagged terms of GTFP in columns (3) to (6) are all significantly positive, indicating that the increase in GTFP in the previous period is conducive to the improvement in the economic growth quality in the current period. This suggests that China's green and high-quality development has strong inertia, consistent with conclusions obtained from the analysis in Section 3.2 above and the findings in Wu et al. [15].

#### 5.1.2. The Impacts of Fiscal Expenditure Composition on GTFP

We drew on the approach used in Jia et al. [14] when estimating Equation (8). Specifically, we first estimated this equation using the two-step system of GMM. Afterward, we validated the robustness of the regression results by placing each expenditure composition variable in four regression equations for estimation. Table 7 shows that the estimated coefficients of the expenditure composition variables and other explanatory variables in columns (2) to (5) are very close to those in column (1), which indicates that the estimation results in this section are robust. We also conducted sensitive analysis by constructing alternative measurements of public expenditure composition, namely, using each category of public expenditure scaled by local GDP as independent variables. The estimation results shown in column (6) are consistent with those in column (1). In addition, all six regression models pass the second-order autocorrelation test. The results of the Hansen test also show that the original hypothesis of the validity of the instrumental variables cannot be rejected. Therefore, the whole model is reasonably set up, and the instrumental variables chosen are valid.

We regard column (1) as the benchmark result, which shows that an increase in the proportion of social expenditure and the proportion of expenditure on science and technology (S&T) and environmental protection can improve GTFP. On the contrary, an increase in the share of economic expenditure or administrative expenditure is not beneficial to GTFP, provided that the public expenditure size remains unchanged. These results are consistent with the previous analysis.

At present, China has entered the stage of high-quality economic development [10]. The limitations of the previous high-consumption, high-pollution economic development strategy gradually became apparent. Therefore, an increase in the proportion of economic expenditure will not be conducive to GTFP. In order to achieve sustained high-quality growth, the Chinese government needs to promote a shift from a factor-driven to an innovation-driven economic growth and focus on improving the quality of people's lives and ecological environment. Social expenditure and expenditure on S&T and environmental protection are more in line with the connotation of high-quality economic development than economic expenditure, and increasing the proportion of these two types of expenditure is conducive to the rise of GTFP. In addition, administrative expenditure does not directly contribute to economic development and ecological quality improvement. Excessive administrative expenditure means that government operations are inefficient and costly, which may obstruct green and high-quality economic development [14]. Therefore, increasing the proportion of administrative expenditure will not be conducive to improving GTFP.

**Table 7.** Estimation results of the impact of public expenditure composition on GTFP.

	(1)	(2)	(3)	(4)	(5)	(6)
VARIABLES	GTFP	GTFP	GTFP	GTFP	GTFP	GTFP
L. GTFP	0.630 *** (0.000)	0.238 ** (0.045)	0.277 ** (0.017)	0.647 *** (0.000)	0.620 *** (0.000)	0.610 *** (0.000)
persco	0.852 ** (0.023)	1.129 *** (0.009)				
pereco	−0.408 ** (0.027)		−0.914 ** (0.048)			
perino	1.397 *** (0.005)			0.917 ** (0.010)		
pergov	−1.100 ** (0.014)				−0.776 ** (0.048)	
scogdp						0.483 * (0.078)
ecogdp						−1.090 * (0.079)
inogdp						1.548 ** (0.025)
govgdp						−1.109 * (0.089)
road	−0.000 (0.860)	0.001 (0.215)	0.000 (0.650)	−0.001 (0.525)	−0.002 (0.349)	0.001 (0.495)
mon	−0.084 *** (0.008)	−0.063 *** (0.009)	−0.073 ** (0.022)	−0.034 * (0.066)	−0.087 *** (0.005)	−0.088 *** (0.005)
fdi	1.286* (0.087)	1.250 (0.193)	1.058 (0.240)	−0.178 (0.554)	−0.190 (0.570)	0.774 (0.202)
pgdp	0.005 (0.684)	0.034 *** (0.000)	0.032 *** (0.001)	0.040 *** (0.007)	0.065 ** (0.036)	0.022 *** (0.008)
sec	−0.215 *** (0.001)	−0.276 *** (0.001)	−0.355 *** (0.000)	−0.272 *** (0.001)	−0.318 ** (0.015)	−0.003 *** (0.000)
gov	−0.031 (0.690)	0.006 (0.878)	−0.133 * (0.075)	0.004 (0.744)	−0.003 (0.534)	−0.053 (0.448)
Constant	0.336 (0.195)	0.302 (0.220)	1.154 *** (0.000)	0.413 *** (0.000)	0.601 *** (0.000)	0.638 *** (0.000)
Observations	1.927	1.944	1.956	1.991	1.958	1.929
City FE	YES	YES	YES	YES	YES	YES
Time FE	YES	YES	YES	YES	YES	YES
AR(2)	1.463 [0.144]	0.402 [0.687]	1.142 [0.254]	1.617 [0.106]	1.579 [0.114]	1.630 [0.103]
Hansen test	34.427 [0.154]	17.354 [0.363]	19.632 [0.354]	10.942 [0.205]	7.239 [0.299]	38.170 [0.209]
Number of cities	269	268	269	270	269	269

Note: Robust and cluster standard errors in parentheses and p-value in brackets. \*\*\*  $p < 0.01$ , \*\*  $p < 0.05$ , \*  $p < 0.1$ .

### 5.2. The Results of the Dynamic Panel Mediation Models' Estimation

#### Mechanism Analysis of the Impact of Fiscal Expenditure on GTFP

The results in Table 7 reveal that the impacts of changes in the proportion of different types of fiscal expenditures on GTFP are different. However, the results do not reflect the mechanism of these heterogeneous impacts. Therefore, we further construct dynamic panel mediation models to clarify the paths through which the composition of fiscal expenditure affects GTFP. We estimated Equations (9)–(11) using the two-step system GMM and present the results in Table 8. The results in all columns pass the Hansen test and AR(2) test, which proves that the models we set are reasonable and valid. The existence of the mediation effects requires the following four conditions to be satisfied [51]:

1. Before including the mediation variables in the regression model, the effect of the core independent variables on the dependent variables is statistically significant.

2. The effects of independent variables on the mediation variables are statistically significant.
3. After including the mediation variables, the effects of these variables on the dependent variables are statistically significant.
4. After including the mediation variables, the effects of the core independent variables on the independent variables weaken.

The estimated results of the four sets of mediation models we obtained fully satisfy the above four conditions. Next, we interpret the results one by one.

Columns (1)–(3) in part a of Table 8 present the estimated results of the regression model with human capital accumulation as the mediation variable. Column (1) shows that an increase in the level of human capital can significantly improve GTFP. Human capital accumulation is fundamental to technological progress. Moreover, an increase in human capital helps improve society’s overall resource allocation and management capacity. Therefore, improving the human capital level can enhance GTFP [10].

**Table 8.** (a) Estimation results of the dynamic panel mediation models. (b) Estimation results of the dynamic panel mediation models.

(a)						
MEDIATORS VARIABLES	Human Capital Accumulation			Technological Innovation		
	GTFP	Pouni	GTFP	GTFP	Pogreenino	GTFP
L. GTFP	0.660 *** (0.000)		0.305 *** (0.003)	0.655 *** (0.000)		0.307 *** (0.000)
pouni	0.018 * (0.085)		0.024 *** (0.002)			
pogreenino				0.037 * (0.096)		0.048 ** (0.013)
persco	0.842 * (0.093)	8.787 *** (0.000)		0.768 ** (0.020)	2.405 *** (0.001)	
pereco	−0.279 * (0.072)	−12.712 *** (0.001)		−0.323 ** (0.039)	−2.798 ** (0.034)	
perino	0.882 *** (0.007)	10.259 * (0.059)		1.384 *** (0.002)	5.927 *** (0.007)	
pergov	−1.384 *** (0.002)	11.610 ** (0.016)		−1.025 ** (0.031)	−2.088 * (0.093)	
road	−0.001 (0.509)	0.029 (0.115)	−0.002 (0.162)	−0.001 (0.144)	0.055 ** (0.017)	0.001 (0.279)
mon	−0.065 *** (0.005)	1.862 *** (0.000)	−0.085 *** (0.003)	−0.071 ** (0.013)	−0.213 (0.153)	−0.060 ** (0.014)
fdi	0.015 (0.966)	9.001 ** (0.013)	−0.223 (0.523)	2.707 *** (0.007)	−8.464 ** (0.039)	0.053 (0.873)
pgdp	0.001 (0.966)	0.695 *** (0.001)	0.028 *** (0.001)	−0.009 (0.587)	0.513 *** (0.000)	0.015 (0.110)
sec	−0.053 (0.485)	−5.236 *** (0.000)	−0.187 *** (0.009)	−0.193 *** (0.005)	−0.941 (0.147)	−0.250 *** (0.001)
gov	−0.012 (0.876)	−0.001 (0.982)	−0.005 (0.578)	−0.007 (0.569)	−0.001 (0.974)	0.015 * (0.093)
Constant	0.277 (0.328)	−5.023 *** (0.002)	0.874 *** (0.000)	0.191 (0.332)	−1.125 ** (0.037)	0.835 *** (0.000)
Observations	1.898	1.889	1.980	1.925	1.906	2.004
City FE	YES	YES	YES	YES	YES	YES
Time FE	YES	YES	YES	YES	YES	YES
AR(2)	1.455	−1.131	0.902	1.491	1.188	0.928
ar2p	[0.146]	[0.258]	[0.367]	[0.136]	[0.235]	[0.353]
Hansen test	23.685	202.741	2.453	14.519	116.950	28.279
hansenp	[0.128]	[0.375]	[0.293]	[0.338]	[0.903]	[0.450]
Number of cities	269	268	270	269	268	270

Table 8. Cont.

(b)						
MEDIATORS VARIABLES	(7)	(8)	(9)	(10)	(11)	(12)
	Environmental Quality			Labor Productivity		
	GTFP	pm25	GTFP	GTFP	Labor	GTFP
L. GTFP	0.660 *** (0.000)		0.661 *** (0.000)	0.634 *** (0.000)		0.315 *** (0.003)
pm25	−0.001 ** (0.041)		−0.005 *** (0.000)			
labor				0.003 ** (0.017)		0.004 *** (0.007)
persco	0.946 ** (0.022)	131.439 *** (0.000)		0.802 ** (0.047)	4.392 ** (0.041)	
pereco	−0.436 ** (0.035)	−111.041 *** (0.000)		−0.264 ** (0.044)	−26.657 ** (0.010)	
perino	1.355 ** (0.023)	−113.727 ** (0.036)		0.695 ** (0.019)	43.247 ** (0.043)	
pergov	−0.970 ** (0.027)	146.621 *** (0.000)		−1.041 ** (0.014)	−40.247 *** (0.002)	
road	0.002 (0.247)	0.319 *** (0.000)	0.002 ** (0.027)	0.002 * (0.091)	−0.078 ** (0.033)	−0.001 (0.496)
mon	−0.084 ** (0.016)	−6.012 *** (0.007)	−0.056 *** (0.006)	−0.046 (0.121)	−6.179 *** (0.000)	−0.013 (0.480)
fdi	0.525 (0.189)	300.989 *** (0.000)	1.040 ** (0.033)	0.100 (0.737)	−23.967 (0.408)	0.103 (0.761)
pgdp	0.019 (0.191)	−5.691 *** (0.000)	0.026 ** (0.024)	0.003 (0.639)	4.461 *** (0.000)	0.024 ** (0.023)
sec	−0.293 * (0.093)	41.663 *** (0.000)	−0.549 * (0.076)	−0.099 (0.164)	−60.135 *** (0.000)	−0.136 * (0.081)
gov	−0.066 (0.308)	−2.093 * (0.072)	−0.004 (0.698)	0.020 ** (0.018)	0.436 (0.540)	−0.036 * (0.060)
Constant	0.267 (0.303)	−27.809 * (0.065)	0.793 *** (0.000)	0.180 (0.459)	51.511 *** (0.000)	0.703 *** (0.000)
Observations	1.926	2.170	2.008	1.907	2.170	2.008
City FE	YES	YES	YES	YES	YES	YES
Time FE	YES	YES	YES	YES	YES	YES
AR(2)	1.453	1.339	1.522	1.521	−1.333	1.277
ar2p	[0.146]	[0.181]	[0.128]	[0.128]	[0.183]	[0.202]
Hansen test	51.691	240.532	4.898	24.585	99.054	2.335
hansenp	[0.102]	[0.112]	[0.298]	[0.266]	[0.241]	[0.311]
Number of cities	269	269	270	269	269	270

Note: Robust and cluster standard errors in parentheses and *p*-value in brackets. \*\*\* *p* < 0.01, \*\* *p* < 0.05, \* *p* < 0.1.

In column (2) of part a of Table 8, we can see that the increase in the proportion of social expenditure can significantly raise the number of college students per 100 people, which suggests that the government’s educational spending can effectively motivate individuals to receive high-level education, thus promoting human capital accumulation [10]. Compared with the social expenditure, an increase in the proportion of S&T and environmental expenditure has a higher positive effect. This may be due to the fact that S&T expenditure can significantly increase the overall level of scientific and technological knowledge stock in society, which can more directly stimulate the increase in human capital level. Our results also indicated that the expansion of administrative expenditure could also increase the level of human capital, which seems to be inconsistent with our theoretical analysis. We argue that this is reasonable as the government can remove institutional barriers to human resource allocation by increasing general public service expenditure [61], which in turn can optimize the human capital allocation structure. The increase in the share of economic expenditure has a significant inhibitory effect on human capital. The primary function of

economic expenditures is to compensate for market failures and maintain market resource allocation, and expanding the share of economic expenditures has a crowd-out effect on other public spendings [18].

Columns (4)–(6) present the estimation results of the regression model with science and technology innovation (STI) as the mediating variable. According to column (4), STI has a significant positive effect on GTFP. For one thing, firms improve the input–output ratio and reduce the pollution emissions of economic activities mainly by developing and applying new technologies. For another thing, STI implies technological progress, which is one of the components of GTFP [35]. Therefore, the increase in the STI level can improve GTFP.

The results in column (5) suggest that an increase in the share of social expenditures can promote STI. This is because social spending has a significant human capital accumulation effect, and human capital is considered to be an important way to incur STI. The positive impact of expanding the proportion of S&T and environmental expenditures on GTFP is more significant than that of social expenditures. This may indicate that government spending on S&T can directly support economy-wide R&D spending and innovation compared to social spending [19]. Expenditures on energy conservation and environmental protection can directly compensate for green innovation, energy-saving technologies, and ecological protection, which have strong green development attributes [23,25]. Economic and administrative expenditures do not directly support innovation in science and technology. Increasing the proportion of both will crowd out social and environmental expenditures, so increasing the proportion of both will inhibit GTFP's rise.

Columns (7) to (9) present the estimation results of the model with environmental quality as the mediation variable. The results in column (7) indicate that the deterioration of environmental quality significantly impairs GTFP. Green development requires a balance between economic growth, resource conservation, and environmental friendliness, and the development strategy at the cost of environmental quality is contrary to the connotation of green development [62]. Therefore, the damage to the environment and ecology will directly reduce GTFP.

Column (8) shows that increasing social expenditures is not conducive to environmental quality improvement. Social expenditure can influence STI by promoting human capital accumulation. Technologies related to cleaner production and energy conservation are mainly applied by firms to improve environmental quality. However, this indirect impact on environmental quality may have a certain lag [63], resulting in an insignificant green effect of social spending. In contrast, S&T expenditure can directly stimulate green innovation [26]. Energy conservation and environmental protection spending can also compensate for ecological and environmental management behaviors more straightforwardly than social expenditure. Therefore, expanding the proportion of S&T and environmental protection expenditure can significantly improve environmental quality.

An increase in economic spending at the 1% level is beneficial to environmental quality, which seems like a counterintuitive conclusion. One reason for this may be that the Chinese government has been optimizing the composition and direction of its fiscal expenditure on agriculture, forestry, and water affairs in recent years to promote a low-carbon transition in agriculture [14]. Chinese agriculture has been characterized by high consumption, high emissions, and high pollution for quite a long time [64]. In recent years, the Chinese government has actively promoted economical and environmentally friendly agricultural technologies and increased the efficiency of energy use and the proportion of clean energy in agriculture. With unremitting efforts, the growth rate of China's agricultural carbon emissions has gradually slowed down and tended to reach its peak [65]. Therefore, the expansion of economic expenditures can improve the environmental quality to some extent. Finally, the increase in the share of administrative expenditure is not conducive to environmental quality improvement due to the strong crowding-out effect of administrative expenditure on scientific and environmental expenditures and economic expenditures.

Columns (10)–(12) present the estimation results with labor productivity as a mediation variable. According to column (10), an increase in labor productivity can significantly improve GTFP. Increasing labor productivity implies that more output can be obtained per unit of time for the same labor, i.e., reaching a higher input–output ratio. Moreover, from the perspective of the calculation process of GTFP, a higher input–output ratio symbolizes a higher GTFP.

We can see from column (11) in part b of Table 8 that social expenditure can significantly improve labor productivity. Social spending can promote the diffusion of advanced production technologies, improve practitioners’ knowledge and operational proficiency, provide high-quality labor for economic activities, and increase labor productivity [9]. The positive effect of increasing the share of expenditure on S&T and environmental protection on labor productivity is greater than that of social expenditure, which indicates that the innovation of production technology is the fundamental driving force to production efficiency improvement. In addition, moderately reducing economic and administrative expenditures may be another essential way to improve labor productivity.

We clarify in this section the paths through which fiscal expenditure affects GTFP. Specifically, social spending positively affects GTFP through promoting human capital accumulation, scientific and technological innovation, and increasing labor productivity. Economic expenditure mainly improves GTFP by improving environmental quality. Scientific and environmental expenditure has positive effects on GTFP through all four channels. Administrative expenditure can improve GTFP by increasing the level of human capital. These results can be regarded as an essential complement to the current literature where the influencing channels of public expenditure composition have been explored less.

5.3. The Results of the Dynamic Threshold Panel Models’ Estimation

The Impact of Fiscal Expenditure Composition on the Relationship between Fiscal Expenditure and GTFP

We have explored in detail the impacts of fiscal expenditure on GTFP and revealed the possible mechanisms of these impacts. In analyzing how changes in the composition of fiscal expenditure affect GTFP, we assumed a constant size of expenditure. Therefore, the results obtained in the previous section can be referred to as static effects of public expenditure composition. In this section, we construct a dynamic threshold panel model with four categories of fiscal expenditure as regime-switching variables to analyze the dynamic effects of public spending composition, i.e., how changes in spending composition affect the “inverted U-shaped” relationship between expenditure size and GTFP. Similar evaluation is still lacking among the existing studies. Specifically, we estimate Equation (12) by drawing on the methodology used in Dang et al. [54] and Wu et al. [55] and present the results in Tables 9 and 10, respectively.

Table 9. The threshold value of four regime-switching variables and its confidence interval.

Threshold Variable	Dynamic Threshold Model	Threshold Value	Wald Statistics	p-Value	Number of Bootstrapping	95% Confidence Interval	
						Lower	Higher
persco	SYS-GMM	0.525	0.027 ***	0.000	1000	0.391	0.598
pereco	SYS-GMM	0.132	0.682 ***	0.000	1000	0.087	0.243
perino	SYS-GMM	0.035	5.204 ***	0.000	1000	0.015	0.085
pergov	SYS-GMM	0.134	2.283 ***	0.000	1000	0.101	0.224

Note: \*\*\* indicates significance at the 1% level.



**Table 10.** Estimation results of the dynamic threshold panel model.

	(1)	(2)	(3)	(4)
Threshold Variables	Persco	Pereco	Perino	Pergov
Dependent Variables	GTFP			
L. GTFP	0.371 ** (0.033)	0.429 *** (0.000)	0.338 *** (0.003)	0.421 *** (0.000)
wperexp2×I(tvar < c)	−0.007 *** (0.000)	−0.006 *** (0.002)	−0.013 *** (0.002)	−0.016 *** (0.000)
wperexp2×I(tvar ≥ c)	−0.005 ** (0.047)	−0.012 ** (0.043)	−0.006 *** (0.002)	−0.006 *** (0.001)
Turning Point (Yuan)				
Below the threshold value	81,000	73,000	41,000	35,000
Above the threshold value	109,000	38,000	84,000	85,000
Percentage change (%)				
wperexp	34.6% 0.107 *** (0.000)	−48.0% 0.090 ** (0.015)	51.2% 0.103 *** (0.001)	58.8% 0.109 *** (0.000)
road	−0.003 *** (0.008)	−0.002 (0.157)	−0.003 ** (0.031)	−0.004 ** (0.011)
mon	−0.020 (0.122)	−0.016 (0.209)	−0.021 (0.109)	−0.016 (0.174)
fdi	−0.128 (0.717)	0.123 (0.685)	−0.090 (0.795)	0.071 (0.817)
pgdp	0.000 ** (0.013)	0.000 *** (0.005)	0.000 *** (0.001)	0.000 *** (0.003)
sec	−0.162 ** (0.035)	−0.144 ** (0.025)	−0.168 ** (0.014)	−0.154 ** (0.015)
gov	0.001 (0.821)	0.000 (0.961)	0.001 (0.927)	0.000 (0.972)
Constant	0.669 *** (0.000)	0.638 *** (0.000)	0.740 *** (0.000)	0.616 *** (0.000)
Observations	2.008	2.008	2.008	2.008
City FE	YES	YES	YES	YES
Time FE	YES	YES	YES	YES
AR(2)	1.450 [0.147]	1.313 [0.189]	1.173 [0.241]	1.457 [0.145]
Hansen test	2.203 [0.332]	16.89 [0.531]	9.268 [0.507]	8.181 [0.225]
Number of cities	270	270	270	270

Note: Robust and cluster standard errors in parentheses and *p*-value in brackets. \*\*\* *p* < 0.01 and \*\* *p* < 0.05.

Table 9 shows the threshold values and confidence intervals for the four types of public expenditure composition variables. The *p*-values of Wald statistics indicate that all the threshold effects are significant at the 1% significance level. Therefore, we can conclude that changes in the share of different fiscal expenditures can affect the inverted U-shaped relationship between the size of fiscal expenditures and GTFP.

The results of the Hansen test, as well as the AR(2) test in Table 10 columns (1)–(4), are not rejected at the 10% significance level, indicating that the instrumental variables we selected are valid and the first difference of the random error terms is not second-order autocorrelated. The results in column (1) show that when the share of social expenditures reaches the threshold (*c* = 52.5%), the regression coefficient of the squared term of fiscal expenditure size changes, indicating variation in the inverted U-shaped relationship between fiscal expenditure size and GTFP. Specifically, when the share of social expenditure is less than the threshold, the positive effect of fiscal expenditure expansion on GTFP disappears after per capita fiscal expenditure reaching 81,000 yuan. However, when the percentage of social spending exceeds the threshold, the turning point increases from 81,000 yuan to 109,000 yuan, with a percentage of 34.6%, implying a more extensive scope for fiscal

spending to improve GTFP. Based on the empirical results in the previous sections, it is clear that social spending can promote human capital accumulation, technological R&D innovation, and labor productivity. Therefore, it is more beneficial for the government to expand its fiscal expenditure while maintaining a high proportion of social expenditure for China's long-term green development.

Column (2) results suggest that the government should pay attention to controlling the proportion of economic expenditure when expanding the size of expenditure. Appropriate economic spending can compensate for market failures, maintain the allocation of market resources and adjust the operation of the national economy, which has a significant boosting effect on GTFP. However, as economic spending is inclined to factor inputs to drive economic development, the expansion of fiscal spending with economic spending exceeding the threshold value ( $c = 13.2\%$ ) is not conducive to China's long-term development goal of green transformation [18].

The results in column (3) show that the expansion of public expenditure after the share of S&T and environmental protection expenditure reaches the threshold ( $c = 3.5\%$ ) has a more lasting boost to GTFP than when the threshold is not reached. S&T spending can facilitate the shift in China's economic growth model from factor-driven to innovation-driven. Moreover, spending on energy efficiency and environmental protection can compensate for ecological and environmental management and promote environmentally friendly production technologies [21,25]. Therefore, the government should ensure a higher share of S&T and environmental expenditure when expanding the size of fiscal expenditure, which is more beneficial to China's long-term green development. Moreover, when the share of spending on S&T and environmental protection is below the threshold, the turning point of the "inverted U-shaped" relationship between fiscal expenditure and green total factor productivity is relatively low. This phenomenon confirms that the old path of relying on factor inputs to drive economic growth is not sustainable.

The results in column (4) are interesting, which show that the positive effect of fiscal expenditure on GTFP is limited when the share of administrative expenditure is below the threshold ( $c = 13.4\%$ ). However, when it is above the threshold, the contribution of fiscal expenditure to green development is extended, which may be contradictory to current studies, such as those of Lopez et al. [7] and Jia et al. [14]. One possible explanation for this is that the increase in expenditure on defense and public security provides a strong material basis for securing national territory and sovereignty as well as social stability. Moreover, it is only when the country is stable and socially stable that people's livelihoods improve and the country's economic development is guaranteed. In addition, an appropriate size of public service expenditure can improve the wages and benefits of public servants, increase their motivation and improve the efficiency of government operations, and optimize the allocation of human capital to a certain extent [9]. This result, in fact, suggests something to the Chinese government, namely, not to over-compress administrative expenditure and that an appropriate proportion of administrative expenditure is more conducive to China's long-term green development.

## 6. Conclusions and Policy Implications

In this paper, we elaborate on the theoretical mechanism by which public expenditure size and composition affect green development. Afterward, urban green total factor productivity is measured using data from 275 prefecture-level cities in China from 2010 to 2018. We treat it as a proxy variable for green development in China and perform the two-stage GMM system on dynamic panel models to examine the impact of the size and composition of public spending on green growth. In order to disclose the possible mechanisms through which public expenditure affects GTFP, dynamic panel mediation models are further constructed and estimated. Finally, we used dynamic threshold panel models to analyze the impacts of changes in public expenditure composition on the inverted U-shaped relationship between fiscal expenditure size and GTFP.

The main findings of this paper are as follows: (1) China achieved green development between 2010 and 2018, with GTFP showing an oscillating growth trend of rising, then falling, then rising again. The four main economic regions in China have also achieved green development. The eastern region mainly relied on technological progress to promote green growth, while the northeast, central, and western regions were driven by pure technical efficiency and scale efficiency. (2) Currently, the expansion of fiscal spending by the Chinese government continues to promote green growth. At the same time, there is a clear, inverted U-shaped relationship between fiscal expenditure and GTFP. (3) There are significant differences in the impacts of different types of fiscal expenditures on GTFP, with social and S&T and environmental protection expenditures having a particularly significant boost to GTFP. In contrast, economic and administrative expenditures inhibit the improvement of GTFP. (4) Human capital accumulation, technological innovation, environmental quality, and labor productivity are essential mediators of fiscal expenditure's green effect. (5) The turning point of the inverted U-shaped relationship between fiscal expenditure size and GTFP can be influenced by fiscal expenditure composition. When social spending reaches its threshold value, i.e., when the share of social spending exceeds 52.5% of total public spending, the turning point of the inverted U-shaped curve expands from 81,000 yuan to 109,000 yuan per capita, which is an increase of 34.6%, indicating that fiscal spending has more room for expansion to promote green development. S&T and environmental protection expenditures and administrative expenditures have similar effects when they exceed their respective thresholds, i.e., 3.5% and 13.4%. However, when the proportion of economic expenditure surpasses 13.2%, the turning point narrows significantly, from 73,000 yuan to 38,000 yuan per capita, which is a decrease of 48.0%, also indicating that a large proportion of economic expenditures is not conducive to expanding the green effect of fiscal expenditure.

Based on these findings, the following relevant and straightforward policy implications can be derived: (1) there is an optimal size of public expenditure with tax financing as the main source. For developing countries with a high overall tax burden, the contribution of fiscal expenditure to GTFP may be close to a critical value. In other words, relying solely on the expansion of fiscal expenditure size to promote green and high-quality transformational development is feasible but not sustainable, as it may impose a heavy burden on economic growth and environmental governance. (2) Optimizing fiscal expenditure composition may be the preferred strategy for promoting green development compared to expanding the size of fiscal expenditure. Specifically, for developing countries, which are mostly developmental governments, increasing the proportion of social spending and spending on environmental protection and science and technology may better accelerate their transformation towards green and innovation-driven economies. Moreover, improving the expenditure structure can also increase the marginal benefits of the expansion of public expenditure size. Meanwhile, the transformation of government governance concepts and functions, the correct handling of the relationship between government and the market, and the gradual withdrawal of government from competitive areas, as well as increased supervision and restraint of government, are essential guarantees of the effectiveness of expenditure structure optimization. (3) Economic and administrative expenditures generally cannot promote green development, but governments can amplify their effects on human capital accumulation, environmental quality improvement, technological innovation, and labor productivity enhancement. These are the four main channels of fiscal expenditure promoting green economic development.

This paper extends the existing research, helping to understand the relationship between public spending and green development from a more comprehensive perspective. At the same time, there are limitations and room for further extension of this paper. For example, the DEA-SBM model and GML index used in this paper to measure GTFP are typical non-parametric methods. The parametric methods, such as the Stochastic Frontier Model, can also be used for the calculation of the level of green growth. Moreover, we regard electricity consumption as city-level energy inputs, while using specific energy data

such as oil, natural gas, and petroleum consumption in GTFP's evaluation may derive more accurate results. There is also room for improvement of the public expenditure measurement, as the implicit fiscal expenditure and quasi-fiscal expenditure commonly exist in developing countries, including China, which may need further expansion in subsequent studies. Moreover, how to consider the spatial relationship between fiscal expenditure and green development remains a complex problem, and the findings may be more affluent after analyzing it.

**Author Contributions:** Conceptualization, Y.X. and W.Z.; Methodology, Y.X. and W.Z.; Software, W.Z.; Validation, Y.X. and W.Z.; Formal Analysis, W.Z.; Investigation, Y.X. and W.Z.; Resources, Y.X. and W.Z.; Data Curation, W.Z.; Writing—Original draft preparation, Y.X. and W.Z.; Writing—review and editing, Y.X. and W.Z.; Visualization, W.Z.; Supervision, Y.X.; Project Administration, Y.X.; Funding Acquisition, Y.X. All authors have read and agreed to the published version of the manuscript.

**Funding:** This work was funded by the National Natural Science Foundation of China (No. 72103208); The Fundamental Research Funds for the Central Universities, South-Central Minzu University (CPT22007); Key Research Project of Philosophy and Social Science of Ministry of Education of China (21JZD028).

**Institutional Review Board Statement:** Not applicable.

**Informed Consent Statement:** Not applicable.

**Data Availability Statement:** The data used in this paper comes from the China Urban Statistical Yearbook, the China Urban Construction Statistical Yearbook, the EPS database, economic and social development reports of each city, and the statistical yearbooks published on the official websites of each city's statistical bureaus.

**Conflicts of Interest:** The authors declare no conflict of interest.

## References

1. Adams, B. *Green Development: Environment; Sustainability in A Developing World*; Routledge: London, UK, 2019.
2. Giglio, S.; Kelly, B.; Stroebel, J. Climate finance. *Annu. Rev. Financ. Econ.* **2021**, *13*, 15–36. [[CrossRef](#)]
3. Liu, S. *Ten Years Outlook for China's Economic Growth (2020–2029): War Epidemic Growth Model*; CITIC Publishing House Books Genuine Books; CITIC Publishing Group: Beijing, China, 2020.
4. UNEP. *As We Reboot the Global Economy, A Sustainable Pathway Is the Only Road Ahead*; UNEP Policy Research Report; UNEP: Nairobi, Kenya, 2020.
5. Amore, M.D.; Bennedsen, M. Corporate governance; green innovation. *J. Environ. Econ. Manag.* **2016**, *75*, 54–72. [[CrossRef](#)]
6. Wang, Q.; Zhou, B.; Zhang, C.; Zhou, D. Do energy subsidies reduce fiscal; household non-energy expenditures? A regional heterogeneity assessment on coal-to-gas program in China. *Energy Policy* **2021**, *155*, 112341. [[CrossRef](#)]
7. López, R.; Galinato, G.I.; Islam, A. Fiscal spending; the environment: Theory; empirics. *J. Environ. Econ. Manag.* **2011**, *62*, 180–198. [[CrossRef](#)]
8. Halkos, G.E.; Paizanos, E.A. The channels of the effect of government expenditure on the environment: Evidence using dynamic panel data. *J. Environ. Plan. Manag.* **2017**, *60*, 135–157. [[CrossRef](#)]
9. Hua, Y.; Xie, R.; Su, Y. Fiscal spending; air pollution in Chinese cities: Identifying composition; technique effects. *China Econ. Rev.* **2018**, *47*, 156–169. [[CrossRef](#)]
10. Lin, B.; Zhu, J. Fiscal spending; green economic growth: Evidence from China. *Energy Econ.* **2019**, *83*, 264–271. [[CrossRef](#)]
11. Postula, M.; Radecka-Moroz, K. Fiscal policy instruments in environmental protection. *Environ. Impact Assess. Rev.* **2020**, *84*, 106435. [[CrossRef](#)]
12. Barro, R.J. Government Spending in a Simple Model of Endogeneous Growth. *J. Political Econ.* **1990**, *98*, S103–S125. [[CrossRef](#)]
13. Devarajan, S.; Swaroop, V.; Zou, H.-F. The composition of public expenditure; economic growth. *J. Monet. Econ.* **1996**, *37*, 313–344. [[CrossRef](#)]
14. Jia, J.; Guo, Q.; Zhang, J. Fiscal decentralization; local expenditure policy in China. *China Econ. Rev.* **2014**, *28*, 107–122. [[CrossRef](#)]
15. Wu, S.; Li, B.; Nie, Q.; Chen, C. Government expenditure, corruption; total factor productivity. *J. Clean. Prod.* **2017**, *168*, 279–289. [[CrossRef](#)]
16. Zhou, M.; Wang, B.; Chen, Z. Has the anti-corruption campaign decreased air pollution in China? *Energy Econ.* **2020**, *91*, 104878. [[CrossRef](#)]
17. Baumol, W.J. Macroeconomics of Unbalanced Growth: The Anatomy of Urban Crisis. *Am. Econ. Rev.* **1967**, *57*, 415–426.
18. Huang, Y.I.; Pagano, M.; Panizza, U.G.O. Local Crowding-Out in China. *J. Financ.* **2020**, *75*, 2855–2898. [[CrossRef](#)]
19. Sung, B. Do government subsidies promote firm-level innovation? Evidence from the Korean renewable energy technology industry. *Energy Policy* **2019**, *132*, 1333–1344. [[CrossRef](#)]

20. Song, Q.; Qin, M.; Wang, R.; Qi, Y. How does the nested structure affect policy innovation?: Empirical research on China's low carbon pilot cities. *Energy Policy* **2020**, *144*, 111695. [CrossRef]
21. Porter, M.E. America's green strategy. *Sci. Am.* **1991**, *264*, 168. [CrossRef]
22. Warhurst, A. Future roles of business in society: The expanding boundaries of corporate responsibility; a compelling case for partnership. *Futures* **2005**, *37*, 151–168. [CrossRef]
23. Sauquet, A.; Marchand, S.; Féres, J.G. Protected areas, local governments,; strategic interactions: The case of the ICMS-Ecológico in the Brazilian state of Paraná. *Ecol. Econ.* **2014**, *107*, 249–258. [CrossRef]
24. Droste, N.; Lima, G.R.; May, P.H.; Ring, I. Municipal Responses to Ecological Fiscal Transfers in Brazil: A microeconomic panel data approach: Municipal Responses to Ecological Fiscal Transfers. *Environ. Policy Gov.* **2017**, *27*, 378–393. [CrossRef]
25. Droste, N.; Ring, I.; Santos, R.; Kettunen, M. Ecological Fiscal Transfers in Europe—Evidence-Based Design Options for a Transnational Scheme. *Ecol. Econ.* **2018**, *147*, 373–382. [CrossRef]
26. Cui, J.; Liu, X.; Sun, Y.; Yu, H. Can CDM projects trigger host countries' innovation in renewable energy? Evidence of firm-level dataset from China. *Energy Policy* **2020**, *139*, 111349. [CrossRef]
27. Chow, G.C.; Li, K.-W. China's Economic Growth: 1952–2010. *Econ. Dev. Cult. Ch.* **2002**, *51*, 247–256. [CrossRef]
28. Tone, K. A slacks-based measure of efficiency in data envelopment analysis. *Eur. J. Oper. Res.* **2001**, *130*, 498–509. [CrossRef]
29. Lu, H.; Yu, J.; Zhang, N. Vertical Administrative Governance Structure; Local Government Expenditure Size. *J. Financ. Res.* **2017**, *10*, 35–51.
30. Jiang, H.; Jiang, P.; Wang, D.; Wu, J. Can smart city construction facilitate green total factor productivity? A quasi-natural experiment based on China's pilot smart city. *Sustain. Cities Soc.* **2021**, *69*, 102809. [CrossRef]
31. Pastor, J.T.; Lovell, C.K. A global Malmquist productivity index. *Econ. Lett.* **2005**, *88*, 266–271. [CrossRef]
32. Oh, D.-H. A global Malmquist-Luenberger productivity index. *J. Product. Anal.* **2010**, *34*, 183–197. [CrossRef]
33. Li, H.-L.; Zhu, X.-H.; Chen, J.-Y.; Jiang, F.-T. Environmental regulations, environmental governance efficiency; the green transformation of China's iron steel enterprises. *Ecol. Econ.* **2019**, *165*, 106397. [CrossRef]
34. O'Donnell, C.J. An aggregate quantity framework for measuring and decomposing productivity change. *J. Product. Anal.* **2012**, *38*, 255–272. [CrossRef]
35. Li, B.; Wu, S. Effects of local; civil environmental regulation on green total factor productivity in China: A spatial Durbin econometric analysis. *J. Clean. Prod.* **2017**, *153*, 342–353. [CrossRef]
36. Chen, H.; Liu, P.; Xu, P. The study on the evolution mechanism of urban green total factor productivity. *China Popul. Resour. Environ.* **2020**, *30*, 93–105.
37. Xia, F.; Xu, J. Green total factor productivity: A re-examination of quality of growth for provinces in China. *China Econ. Rev.* **2020**, *62*, 101454. [CrossRef]
38. Lin, Y.; Liu, P. The Effects of Development Strategy on Capital Accumulation and Technological Progress: An Empirical Analysis of Chinese Experience. *Soc. Sci. China* **2003**, *4*, 13–32.
39. Henderson, D.J.; Russell, R.R. Human Capital and Convergence: A Production-Frontier Approach. *Int. Econ. Rev.* **2005**, *46*, 1167–1205. [CrossRef]
40. Ma, L.; Long, H.; Chen, K.; Tu, S.; Zhang, Y.; Liao, L. Green growth efficiency of Chinese cities; its spatio-temporal pattern. *Resour. Conserv. Recycl.* **2019**, *146*, 441–451. [CrossRef]
41. Färe, R.; Grosskopf, S.; Pasurka, J.C.A. Accounting for Air Pollution Emissions in Measures of State Manufacturing Productivity Growth. *J. Reg. Sci.* **2001**, *41*, 381–409. [CrossRef]
42. Reingewertz, Y. Do municipal amalgamations work? Evidence from municipalities in Israel. *J. Urban Econ.* **2012**, *72*, 240–251. [CrossRef]
43. Blesse, S.; Baskaran, T. Do municipal mergers reduce costs? Evidence from a German federal state. *Reg. Sci. Urban Econ.* **2016**, *59*, 54–74. [CrossRef]
44. Hao, Y.; Gai, Z.; Wu, H. How do resource misallocation; government corruption affect green total factor energy efficiency? Evidence from China. *Energy Policy* **2020**, *143*, 111562. [CrossRef]
45. Moretti, E. Chapter 51—Human Capital Externalities in Cities. In *Handbook of Regional; Urban Economics*; Henderson, J.V., Thisse, J.-F., Eds.; Elsevier: Amsterdam, The Netherlands, 2004; Volume 4, pp. 2243–2291.
46. Berry, C.R.; Glaeser, E.L. The divergence of human capital levels across cities. *Pap. Reg. Sci.* **2005**, *84*, 407–444. [CrossRef]
47. Diamond, R.; Persson, P. The Long-term Consequences of Teacher Discretion in Grading of High-Stakes Tests. 2016. Available online: <https://EconPapers.repec.org/RePEc:nbr:nberwo:22207> (accessed on 6 May 2022).
48. Romero-Lankao, P.; Qin, H.; Borbor-Cordova, M. Exploration of health risks related to air pollution; temperature in three Latin American cities. *Soc. Sci. Med.* **2013**, *83*, 110–118. [CrossRef] [PubMed]
49. Voorhees, A.S.; Wang, J.; Wang, C.; Zhao, B.; Wang, S.; Kan, H. Public health benefits of reducing air pollution in Shanghai: A proof-of-concept methodology with application to BenMAP. *Sci. Total Environ.* **2014**, *485–486*, 396–405. [CrossRef] [PubMed]
50. Alam, M.S.; Miah, M.D.; Hammoudeh, S.; Tiwari, A.K. The nexus between access to electricity; labour productivity in developing countries. *Energy Policy* **2018**, *122*, 715–726. [CrossRef]
51. Wen, Z.; Ye, B. Analyses of Mediating Effects: The Development of Methods; Models. *Adv. Psychol. Sci.* **2014**, *22*, 731–745. [CrossRef]

52. Baron, R.M.; Kenny, D.A. The Moderator-Mediator Variable Distinction in Social Psychological Research: Conceptual, Strategic, Statistical Considerations. *J. Personal. Soc. Psychol.* **1986**, *51*, 1173–1182. [[CrossRef](#)]
53. Windmeijer, F. A finite sample correction for the variance of linear efficient two-step GMM estimators. *J. Econom.* **2005**, *126*, 25–51. [[CrossRef](#)]
54. Dang, V.A.; Kim, M.; Shin, Y. Asymmetric capital structure adjustments: New evidence from dynamic panel threshold models. *J. Empir. Financ.* **2012**, *19*, 465–482. [[CrossRef](#)]
55. Wu, H.; Hao, Y.; Weng, J.-H. How does energy consumption affect China's urbanization? New evidence from dynamic threshold panel models. *Energy Policy* **2019**, *127*, 24–38. [[CrossRef](#)]
56. Arellano, M.; Bond, S. Some Tests of Specification for Panel Data: Monte Carlo Evidence; an Application to Employment Equations. *Rev. Econ. Stud.* **1991**, *58*, 277–297. [[CrossRef](#)]
57. Arellano, M.; Bover, O. Another look at the instrumental variable estimation of error-components models. *J. Econom.* **1995**, *68*, 29–51. [[CrossRef](#)]
58. Armev, D. *The freedom Revolution: The New Republican House Majority Leader Tells Why Big Government Failed, Why Freedom Works, How We Will Rebuild America*; Regnery Publishing: Washington, DC, USA, 1995.
59. Chen, S.-T.; Lee, C.-C. Government size; economic growth in Taiwan: A threshold regression approach. *J. Policy Modeling* **2005**, *27*, 1051–1066. [[CrossRef](#)]
60. Wu, H.; Hao, Y.; Ren, S. How do environmental regulation; environmental decentralization affect green total factor energy efficiency: Evidence from China. *Energy Econ.* **2020**, *91*, 104880. [[CrossRef](#)]
61. Curristine, T.; Lonti, Z.; Joumard, I. Improving Public Sector Efficiency: Challenges and Opportunities. *OECD J. Budgeting.* **2007**, *7*. [[CrossRef](#)]
62. Liu, Z.; Hanley, N.; Campbell, D. Linking urban air pollution with residents' willingness to pay for greenspace: A choice experiment study in Beijing. *J. Environ. Econ. Manag.* **2020**, *104*, 102383. [[CrossRef](#)]
63. Lora, E.; Olivera, M. Public debt; social expenditure: Friends or foes? *Emerg. Mark. Rev.* **2007**, *8*, 299–310. [[CrossRef](#)]
64. Chen, Y.-H.; Wen, X.-W.; Wang, B.; Nie, P.-Y. Agricultural pollution; regulation: How to subsidize agriculture? *J. Clean Prod.* **2017**, *164*, 258–264. [[CrossRef](#)]
65. Chen, X.; Shuai, C.; Wu, Y.; Zhang, Y. Analysis on the carbon emission peaks of China's industrial, building, transport, agricultural sectors. *Sci. Total Environ.* **2020**, *709*, 135768. [[CrossRef](#)]





Article

# Sensitivity to Different Reanalysis Data on WRF Dynamic Downscaling for South China Sea Wind Resource Estimations

Anandh Thankaswamy <sup>1</sup>, Tao Xian <sup>1,2,\*</sup>, Yong-Feng Ma <sup>1,2</sup> and Lian-Ping Wang <sup>2,3,\*</sup>

- <sup>1</sup> Southern Marine Science and Engineering Guangdong Laboratory (Guangzhou), 1119 Haibin Road, Nansha District, Guangzhou 511458, China; anandhts4u@gmail.com (A.T.); mayf3@sustech.edu.cn (Y.-F.M.)
- <sup>2</sup> Guangdong Provincial Key Laboratory of Turbulence Research and Applications, Center for Complex Flows and Soft Matter Research and Department of Mechanics and Aerospace Engineering, Southern University of Science and Technology, Shenzhen 518055, China
- <sup>3</sup> Guangdong-Hong Kong-Macao Joint Laboratory for Data-Driven Fluid Mechanics and Engineering Applications, Southern University of Science and Technology, Shenzhen 518055, China
- \* Correspondence: xiant@sustech.edu.cn (T.X.); wanglp@sustech.edu.cn (L.-P.W.)

**Abstract:** As the world is moving toward greener forms of energy, to mitigate the effects of global warming due to greenhouse gas emissions, wind energy has risen as the most invested-in renewable energy. China, as the largest consumer of world energy, has started investing heavily in wind energy resources. Most of the wind farms in China are located in Northern China, and they possess the disadvantage of being far away from the energy load. To mitigate this, recently, offshore wind farms are being proposed and invested in. As an initial step in the wind farm setting, a thorough knowledge of the wind energy potential of the candidate region is required. Here, we conduct numerical experiments with Weather Research and Forecasting (WRF) model forced by analysis (NCEP-FNL) and reanalysis (ERA-Interim and NCEP-CFSv2) to find the best choice in terms of initial and boundary data for downscale in the South China Sea. The simulations are validated by observation and several analyses. Specific locations along China’s coast are analyzed and validated for their wind speed, surface temperature, and energy production. The analysis shows that the model forced with ERA-Interim data provides the best simulation of surface wind speed characteristics in the South China Sea, yet the other models are not too far behind. Moreover, the analysis indicates that the Taiwan Strait along the coastal regions of China is an excellent region to set up wind farms due to possessing the highest wind speeds along the coast.

**Citation:** Thankaswamy, A.; Xian, T.; Ma, Y.-F.; Wang, L.-P. Sensitivity to Different Reanalysis Data on WRF Dynamic Downscaling for South China Sea Wind Resource Estimations. *Atmosphere* **2022**, *13*, 771. <https://doi.org/10.3390/atmos13050771>

Academic Editors: Roberto Alonso González Lezcano, Francesco Nocera and Rosa Giuseppina Caponetto

Received: 18 April 2022

Accepted: 5 May 2022

Published: 10 May 2022

**Publisher’s Note:** MDPI stays neutral with regard to jurisdictional claims in published maps and institutional affiliations.



**Copyright:** © 2022 by the authors. Licensee MDPI, Basel, Switzerland. This article is an open access article distributed under the terms and conditions of the Creative Commons Attribution (CC BY) license (<https://creativecommons.org/licenses/by/4.0/>).

**Keywords:** South China Sea; wind energy; WRF modeling; sensitivity test

## 1. Introduction

The development of any nation in our world is dependent on the energy it consumes. As the world is industrializing more, the world’s energy requirement has been increasing significantly in recent decades. To meet the energy demands, global nations have been using thermal power stations based on fossil fuels, nuclear power, and hydroelectric power. The world energy production in the year 2019 was about 31% from oil, 26% from coal, 23% from natural gas, 10% from electric power, 10% from biomass, and the rest from other sources [1]. Of this world production, 24.5% of global energy is consumed by China, 16.1% by the USA, with India coming third at 6% [1]. The countries, which were mainly dependent on fossil fuels for their energy sources, have been asked to reduce their emissions and their contributions to the global climate crisis in the last decade. In 2019, China’s dependence on nonrenewable energy sources is about 73% and it is trying to shift most of its energy production to renewable energy from wind and solar radiation. On the renewable energy front, the majority of the energy comes from hydroelectric followed by wind energy. Preliminary analysis of the first half of 2020 has shown that China’s energy production from renewable has increased up to 40% [2]. Even though hydroelectric is



renewable, its environmental impact and feasibility have made wind energy the most investable source of future renewable energy investment. China has more than doubled its construction of wind and solar power plants in the year 2020 [2].

China's wind energy farming is mainly focused on wind resources in the mountainous Northern China where the power load is minimum. Meanwhile, most of China's power grids are located in Southeastern China along the coastal region [3,4]. Hence, most of the onshore wind energy potential of China is underutilized, as they are expensive to connect to the grid. Recently, there has been an incentive to increase the power production along the offshore region where the population and demand coexist. Offshore wind energy farms can be set up in the coastal region where the average depth of the ocean is less than 50 m. Eastern and Southeastern China have a coastal region that satisfies these criteria [5].

Wind energy production along the South China Sea has a significant seasonal variability, with most of the wind energy in the fall and winter seasons [6–8]. To maximize energy production, it is necessary to have a thorough understanding of the energy available for higher spatial–temporal resolution along the coastal regions of southern China. Data sources from satellites, in situ observations, and numerical weather forecast models pave our initial mode of analysis. Previous studies found that the South China Sea has been identified as having an excellent wind energy source. Figure 1 shows the terrain and bathymetry of the South China Sea and the surrounding region. Along the southern coast of China (Figure 1b), the continental shelf extends up to 100 km away from the coastal region with vast shallow coasts. With the lack of in situ data for offshore conditions, satellite data are used for wind energy analysis along the South China Sea [9–12]. With the onset of satellite data, Taiwan Strait along the South China Sea has been found to have the highest wind speed in the winter season (above  $600 \text{ Wm}^{-2}$ ) [13,14]. Satellite records steady wind speed during the fall and winter seasons (above  $6 \text{ m s}^{-1}$ ) in the central and northern parts of the South China Sea [15]. The satellite data is limited by temporal resolution, cloud cover, and constricted only to the surface. Data from global models, which have been accumulating for the past 25 years, can be used but they are not consistent or high resolution to analyze the recent variations [16]. Numerical weather prediction models are an excellent tool for analyzing the regional wind resources in a hindcast and forecast manner for understanding the resources at any location. Global wind atlases from numerical models are available which provides monthly climatology of wind speed across the globe at high resolutions, but they are not tailored for a particular region. In numerical weather prediction, the selection of initial and boundary conditions plays an important role in the model outcomes. These initial and boundary conditions are obtained mostly from global models which are run at a low resolution. Since there are many global models to obtain these data, we here analyze the performance of downscaling three widely used global reanalysis to simulate the wind conditions over the South China Sea and the surrounding region.

The numerical model, especially the Weather Research and Forecasting (WRF-ARW) model, was developed to provide high resolution temporal and spatial atmospheric data and is being used by many researchers for wind energy estimations [17–19]. Hasager et al. [20] analyzed the South China Sea wind energy using WRF, forced with ERA-Interim reanalysis. Wang et al. [21] analyzed the South China Sea wind spatial distribution using WRF forced by NCEP/NCAR reanalysis. They emphasized that the maximum wind occurs along coastal Southern China. Several more numerical modeling analyses have been conducted over China and surrounding regions as well [22–24].

In the field of regional-scale atmospheric modeling, researchers use mainly three different reanalysis data, namely (i) National Centers for Environmental Predictions Final Analysis (NCEP-FNL) [25], (ii) European Centre for Medium-Range Weather Forecasts Reanalysis project (ERA-Interim) [26], and (iii) the National Centers for Environmental Prediction Climate Forecast System version 2 (NCEP-CFSv2) [27]. The selection of the reanalysis data for wind speed estimations depends on the performance of each of these over any particular region. For example, ERA-Interim data are found to be the best for downscaling among five other reanalysis data (NCEP-R2, NCEP-CFSR, NASA-MERRA,

NCEP-FNL, and NCEP-GFS) over the Iberian Peninsula [28]. ERA-Interim is also used in the downscaling along the North Sea [29,30], along the Chilean coast [31], along Poland [32], and over Tibetan Plateau [33]. NCEP-FNL data is also widely used by researchers in their regional modeling. For example, NCEP-FNL data is used for atmosphere modelling along Caribbean Islands [34], Timor Leste islands [35], and the Indian coastal region [36,37]. NCEP-FNL data is found to outperform ERA-Interim data in a long-term downscaling study across the world [38]. NCEP-CFSv2 data is also used in modeling works across the world. Notably, NCEP-CFSv2 is used in monsoon studies across India [39,40], extratropical cyclones over the Atlantic region [41], wind energy estimations along the Black Sea [42], and extreme events over Korea [43]. The objective of this work is to study the impact of different reanalysis data on the long term WRF dynamic downscaling of the South China Sea and the surrounding region, and the seasonal variability of wind resources along the South China Sea coast.

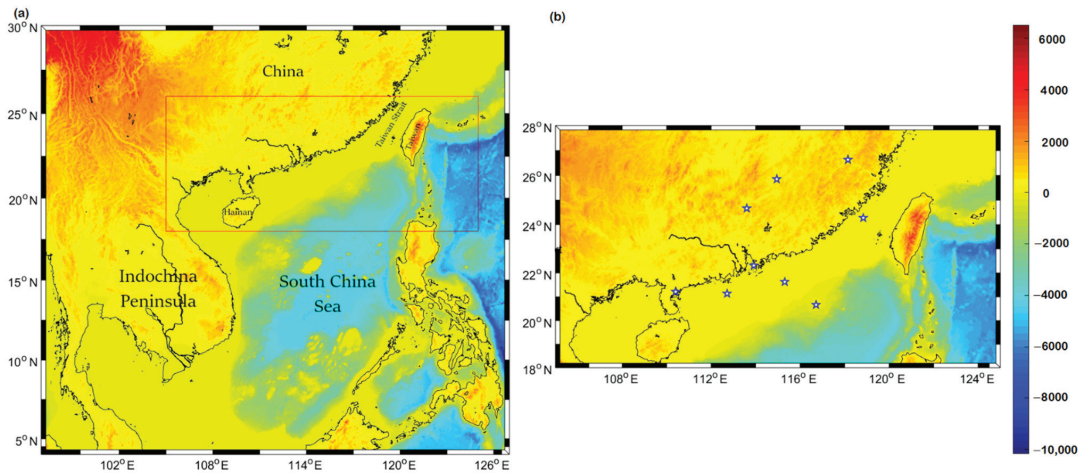


**Figure 1.** (a) Terrain and Bathymetry (m) of South China Sea and surrounding region from ETOPO2 data. (b) Southern China coast showing the shallow bathymetry. The point locations used in the following analysis are shown as blue stars.

## 2. Materials and Methods

### 2.1. Data

To analyze the impact of different initial and forcing boundary conditions, we used three datasets: (i) NCEP-FNL data, (ii) ERA-Interim, data and (iii) NCEP-CFSv2 data. The NCEP-FNL data are analysis data while the other two are reanalysis data. The NCEP-FNL data has a spatial resolution of  $1^\circ$ , ERA-Interim has  $0.75^\circ$ , and NCEP-CFS2 has  $0.5^\circ$ . All the models have high number of vertical levels with 52 levels in NCEP-FNL, 60 in ERA-Interim, and 64 in NCEP-CFS2. The simulations are conducted over the years 2015–2018.

For the model validations, the following datasets are used as well. Satellite-derived data include surface temperature and oceanic surface winds from the Modern-Era Retrospective analysis for Research and Applications (MERRA-2) which is created from Goddard Earth Observing System Data Assimilation System Version 5 (GEOS-5) [44] and Advanced Scatterometer (ASCAT) [45]. The MERRA data is extracted for the period 2015–2018 with  $\sim 0.5^\circ$  resolution. The MERRA data have been validated by many researchers [46,47] and hence are used as observational data for the locations where in situ data are not available in our comparisons. For analysis over a location (in Section 3.1), the data are extracted through the nearest neighbor method. The in situ global hourly integrated surface data from National Centers for Environmental Information (NCEI), National Oceanic Atmospheric Administration (NOAA) [48] are also used for model validations. These data are

available near international airports with a high temporal resolution. The topography for the study region is obtained from ETOPO2 data [49]. For seasonal comparison, the near-surface winds over monthly scales are estimated from ECMWF-ERA5 [50] with  $\sim 2.5^\circ$  resolution, NCEP 2 reanalysis data [51] with  $\sim 2^\circ$  resolution, and QuikScat data [52] with  $\sim 0.25^\circ$  resolution.

## 2.2. Model Description

The advanced WRF model (version 4.0) [53] used for this study consists of a dynamics solver together with physics schemes, initialization routines, and a data assimilation system (the assimilation system is not used here). WRF is a fully compressible, Euler non-hydrostatic model, using terrain-following hydrostatic pressure vertical coordinate, with the vertical grid stretching such that the vertical levels are closer together near the surface and more spread out aloft. The horizontal grid is an Arakawa C grid. For integrating the equations, a third-order Runge Kutta scheme with a smaller time step is used for acoustic and gravity wave modes.

In terms of model physics, the WRF model utilizes the rapid and accurate radiative transfer scheme [54] for the estimation of longwave radiation and the Dudhia scheme [55] for the estimation of shortwave radiation. For the calculations of the planetary boundary layer, the MYNN scheme [56] is used as it is recommended by many in the estimation of wind at the wind turbine height level. NOAA land surface physics model and Kain-Fritsch cumulus convections scheme [57] are used. Morrison 2-moment scheme [58] is used for estimating cloud microphysics.

The WRF model was initiated every eighth day (including the initial one grace day for spin-up) for a period of four years. The model simulations are considered apt for analysis after 24 h of initialization and the next seven days are validated for their wind profiles at the selected stations, seasonal wind estimations, surface temperature, and wind energy estimations at 100 m height. The model domains are two-way nested to have an innermost resolution of 4 km and the region extends from  $90^\circ$  E to  $135^\circ$  E and  $2^\circ$  N to  $35^\circ$  N covering Southern China and the whole South China Sea (Figure 2). The top of the atmospheric domain is at the 50 mb pressure level.

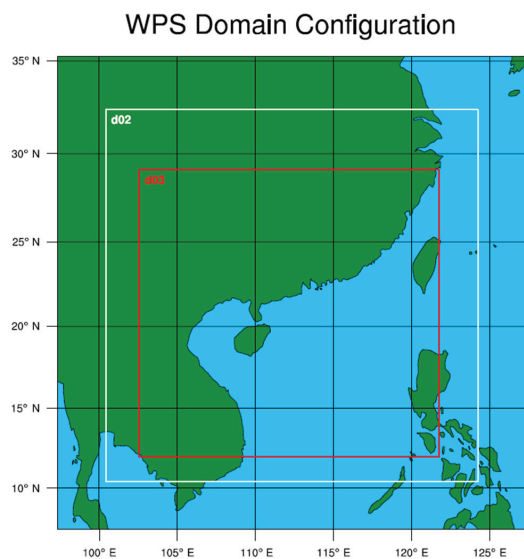


**Figure 2.** WRF preprocessing system (WPS) domains of this study, with the innermost domain covering entire South China Sea.

### 2.3. Methodology

The simulation results are validated by comparing the satellite and in situ datasets. For the analysis purposes, we have obtained long-term temporal resolution data from nine locations (six offshore and three onshore) along the Southern China coast, with the information listed in Table 1 and denoted in Figure 1b. For those offshore locations, three sites along the Southern China coast and the other three sites further interior to the ocean are considered. For onshore locations, three sites at the airports were analyzed. The correlation, root mean square error (RMSE), and the standard deviation were analyzed with the Taylor diagram [59] between different datasets and model simulations. Taylor diagrams bring these statistical parameters together to evaluate the model performance.

**Table 1.** Coordinates of the locations used in the analysis.

No	Coordinates	Locations	Category
1	24.667° N → 113.60° E	SHAOGUAN	Onshore
2	26.633° N → 118.15° E	NANPING	Onshore
3	25.850° N → 114.95° E	GANZHOU	Onshore
4	24.775° N → 118.84° E	100 km away from QUANZHOU	Offshore
5	22.627° N → 115.31° E	100 km away from SHANWEI	Offshore
6	21.137° N → 110.71° E	100 km away from NANSAN	Offshore
7	20.667° N → 116.72° E	DONGSHA	Offshore island
8	21.217° N → 110.40° E	ZHANJIANG	Coastal
9	22.309° N → 113.91° E	HONGKONG	Coastal

The interannual variability (*I**AV*) is estimated by the coefficient of variability [60] which is defined as the ratio between interannual standard deviation ( $\sigma = (x_i - \mu)$ , *i* is in years) at any location to the interannual mean ( $\mu$ ).

$$I\text{AV} = \frac{\sigma}{\mu} * 100\% \tag{1}$$

We also analyzed the wind power density (*W**PD*), which gives the measure of how much energy is available at any location that can be extracted through a wind turbine [61]

$$W\text{PD} = 0.5 \rho A v^3 \tag{2}$$

where  $\rho$  is the air density ( $\text{kg m}^{-3}$ ), *A* is the cross-sectional area of the wind turbine ( $\text{m}^2$ ) and *v* is the velocity ( $\text{m s}^{-1}$ ) measured at the height of wind turbine (i.e., 100 m here). Having  $\rho$  and *A* as constant, we can write Equation (2) as

$$W\text{PD} \propto v^3 \tag{3}$$

It should be noted that the maximum available wind energy that can be extracted by wind turbines is governed by Betz's law [62] and it is about 59.3% of the *W**PD*.

## 3. Results

### 3.1. Comparison of Surface Winds

The hourly 10 m simulated wind speeds are extracted from the WRF simulations. The 10 m constrain is placed because of available long-term hourly data from the observation. The simulated results are then averaged over a day and used for the analysis. Figure 3 compares the daily average from model results with NOAA integrated surface data for the land and MERRA data for interior oceans. When comparing the simulation results, WRF simulations forced with NCEP-FNL data are represented by WRF-N, WRF simulations forced by ERA-Interim models are represented by WRF-E, and WRF simulations forced with CF5v2 models are represented by WRF-C. In this section, we have taken three locations, one along the onshore (Nanping), one along the coastal China (Hong Kong), and one at

100 km offshore of Quanzhou. Additional locations and their analysis are provided in the Appendix A (Figures A1–A3). The results in the Appendix A are equally valid. The model output daily averaged wind speed shows a good correlation with the observational data with narrow deviation from the diagonal favoring higher wind speed derived from the simulations. The maximum wind speeds occur in the offshore region (including sites in Appendix A Figures A1–A3) with overall wind speed ranging from 5 to 20 m s<sup>-1</sup>. For coastal and interior China, the wind speed is lower with a range from 2 to 10 m s<sup>-1</sup>. Along the coastal region, WRF-E has lower deviations from the one-to-one line, while WRF-N and WRF-C simulations have a significant positive bias.

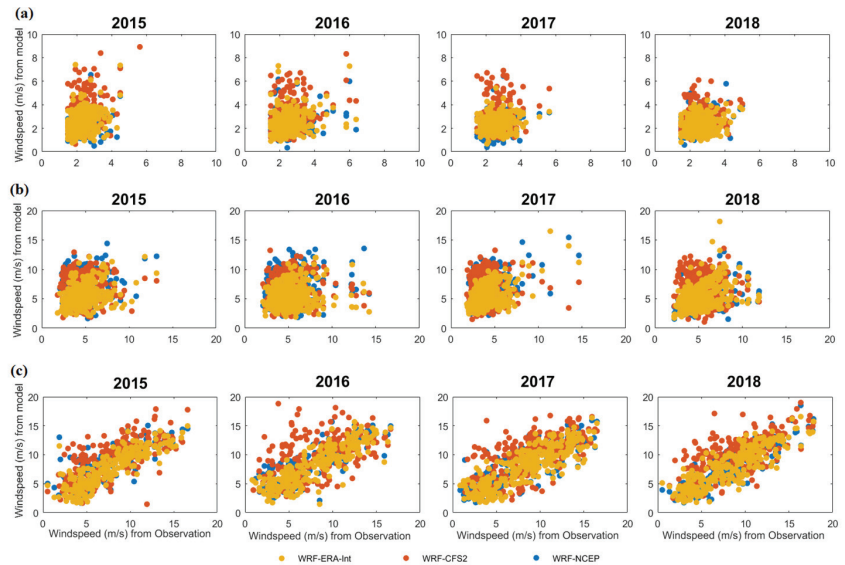


**Figure 3.** Daily average wind speed in m s<sup>-1</sup> from the models and observations at the locations (a) Nanping, (b) Hong Kong, and (c) offshore Quanzhou.

The RMSE and correlation for the daily wind speed for the entire simulation period at different locations are listed in Table 2 and compared in Figure 4 using Taylor diagrams. In the Taylor diagrams, data from the NOAA surface data are considered as the observation and the simulated results are validated against it. When compared with in situ observation, WRF-E simulations show a better correlation and lower RMSE along the onshore region. For the higher wind speed situations, the WRF-E has 0.5 m s<sup>-1</sup> lower RMSE than WRF-N simulations. In most of the locations, WRF-E simulations generally show a better correlation with lower standard deviation and RMSE when compared to the other simulations. Taylor diagrams for additional locations are given in .

Figure 5 compares the monthly mean observed wind speed for different sites with simulations forced by three different initial and boundary conditions. Here, it is noted that the models perform well in simulating the onshore and offshore winds (Figure 5a,b) very well, but at the coastal sea, the models are inefficient in simulating the monthly winds. The monthly variations in the wind speeds are absent in the interior and far-off China but register highly in the coastal regions. The offshore region records the maximum winds in the fall and winter seasons (from October to February), while the remaining months have relatively low wind speeds. In the coastal region, the WRF-E can be seen closely matching the available observational data than the other models. Additional locations are provided in the , Figures A6 and A7.

Table 2. Statistics of wind speed at different locations.

No	Locations	RMSE			Std Deviation			Correlation Coefficient		
		WRF-E	WRF-N	WRF-C	WRF-E	WRF-N	WRF-C	WRF-E	WRF-N	WRF-C
1	SHAOGUAN	0.413	0.507	0.298	0.503	0.809	0.666	0.755	0.613	0.627
2	NANPING	0.291	0.280	0.393	0.278	0.288	0.404	0.778	0.676	0.693
3	GANZHOU	0.434	0.372	0.383	0.437	0.452	0.290	0.895	0.819	0.890
4	Offshore QUANZHOU	0.692	1.043	0.898	1.990	1.910	2.220	0.962	0.899	0.924
5	Offshore SHANWEI	1.178	1.630	1.222	0.598	1.053	0.982	0.886	0.792	0.816
6	Offshore NANSAN	1.121	1.446	1.183	0.898	1.324	1.338	0.902	0.812	0.837
7	DONGSHA	2.298	2.285	2.379	1.037	1.071	0.938	0.918	0.912	0.933
8	ZHANJIANG	0.552	0.728	0.817	0.765	0.642	0.683	0.707	0.712	0.687
9	HONGKONG	0.520	0.879	0.957	0.832	1.064	0.957	0.819	0.707	0.536

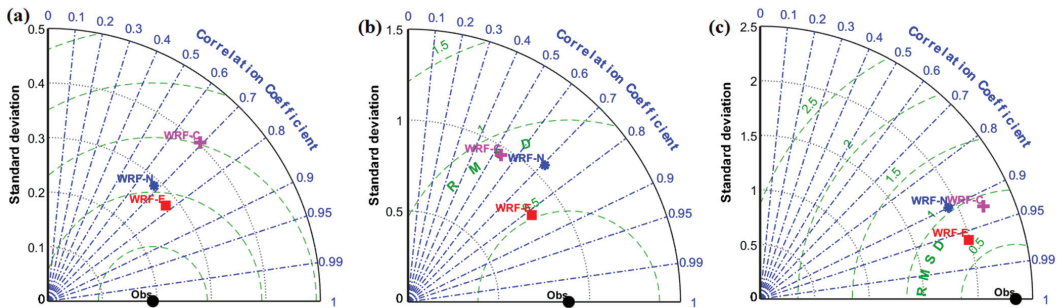


Figure 4. Taylor diagram for wind speed in  $m s^{-1}$  from the models and observations at the locations (a) Nanping, (b) Hong Kong, and (c) offshore Quanzhou.

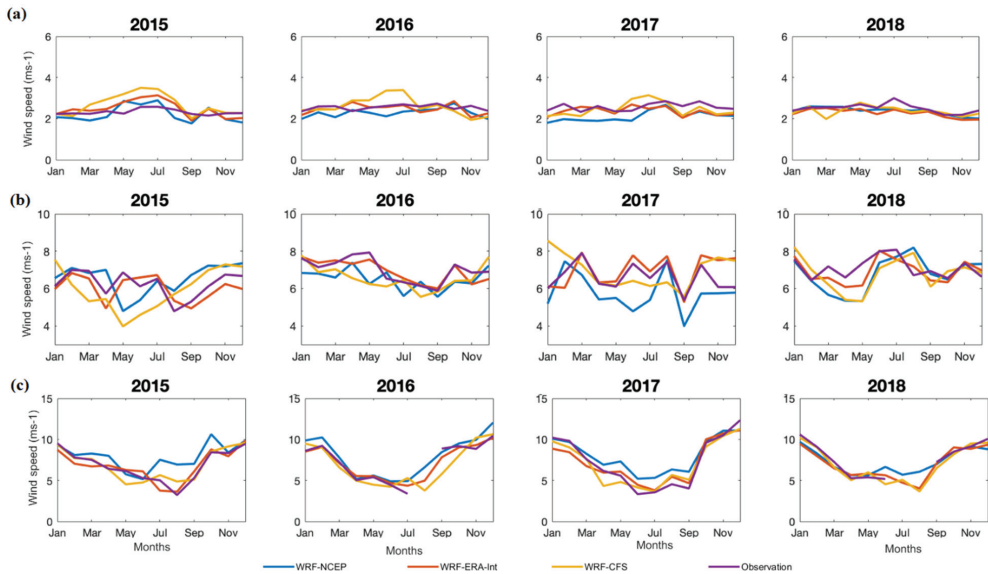
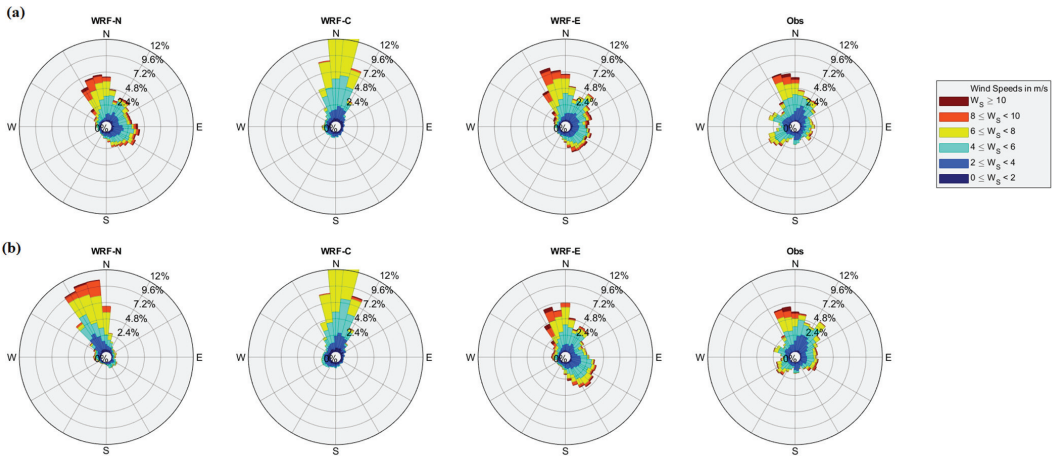


Figure 5. Monthly averaged wind speed in  $m s^{-1}$  from the models and observations at the locations (a) Nanping, (b) Hong Kong, and (c) offshore Quanzhou.

### 3.2. Comparison of Wind Direction

The simulated 10 m level wind direction in Hong Kong is compared with the in situ observation for the years 2015 and 2016 (Figure 6). The WRF-N and WRF-E models estimate that most of the strong winds are north and northward, which agrees well with the observation. In 2015, the models also reproduce weak eastward wind while observation shows weak eastward and westward winds. In 2016, the WRF-N model reproduces predominantly northward winds, while the WRF-E shows northward predominant and southeastward mild winds. The observed winds are seen predominantly northwards with the low frequent east and west winds. During these two years, the WRF-C simulation fails to reproduce the direction and wind speed and it shows winds are only in the northward direction. The similar analysis for Dongsha island for the years 2015 and 2016 is shown in Figure 7. The simulations are also able to reproduce the observed northeastward winds. The low frequent southwestwards winds are reproduced in WRF-N and WRF-E simulations but absent in WRF-C simulations for both years. Additional analysis through wind rose diagrams for different years are available in and Figure A9.



**Figure 6.** Wind rose diagram from the models and observations for the years (a) 2015 and (b) 2016 in Hong Kong.

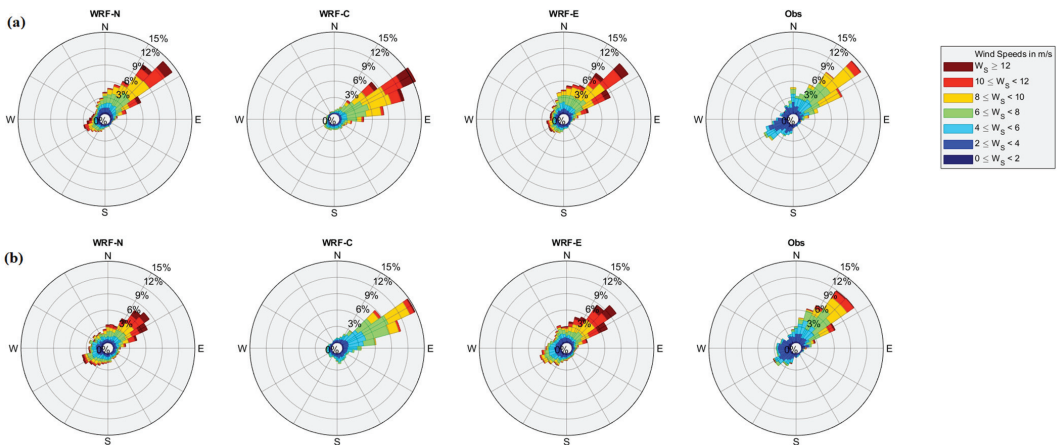


**Figure 7.** Wind rose diagram on an hourly timescale from the models and observations for the years (a) 2015 and (b) 2016 in Dongsha Island.

### 3.3. Comparison of Surface Temperature

For the verification in simulating the surface temperature, we compared the model results to that from MERRA reanalysis datasets for the temperature at the 2 m level, as shown in Figure 8. The WRF-C simulation overestimates the surface temperature while the WRF-N underestimates the same. Figure 8 shows that the simulations are able to capture the temperature variations, with a bias of about 0.5 K for the WRF-E simulations. More scatter plot analyses for temperature are added in Appendix A Figures A10–A12.

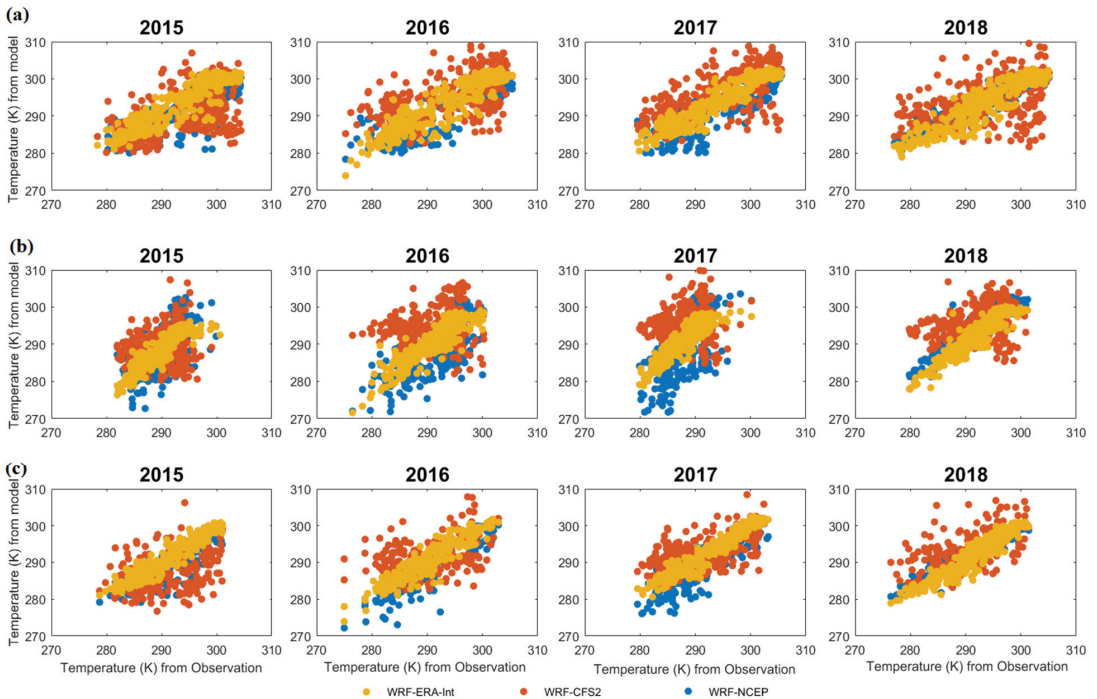


**Figure 8.** Daily average temperature in (unit: K) from the models and observations at the locations (a) Nanping, (b) Hong Kong, and (c) offshore Quanzhou.

The RMSE and correlation for the daily average surface temperature for the entire simulation period at different locations are listed in Table 3 and three locations (Nanping, Hong Kong, and offshore Quanzhou) are compared in Figure 9 using Taylor diagrams (additional locations are available in Appendix A Figure A13). WRF-E simulations have higher correlations and smaller standard deviations. It is again noted that the models perform well in interior and offshore China but have lower accuracy in the coastal region. The RMSE of the model simulated temperature is found to be  $\sim 1$  K in WRF-E model simulations and  $\sim 1.5$  K in the WRF-N model simulations and the largest in the WRF-C simulations. The correlation between observation and the WRF-N model simulations is 0.7, while that for WRF-E simulations is 0.9 for the Hong Kong region. The WRF-C model overestimates the temperature, the WRF-N underestimates, and WRF-E falls in a good range.



Table 3. Statistics of temperature at different locations.

No	Locations	RMSE			Std Deviation			Correlation Coefficient		
		WRF-E	WRF-N	WRF-C	WRF-E	WRF-N	WRF-C	WRF-E	WRF-N	WRF-C
1	SHAOGUAN	0.574	2.331	2.586	6.635	6.377	5.554	0.997	0.952	0.915
2	NANPING	1.407	2.404	2.609	5.954	5.814	4.271	0.978	0.929	0.737
3	GANZHOU	2.101	2.803	3.662	5.351	6.046	7.500	0.958	0.871	0.875
4	Offshore QUANZHOU	0.660	2.150	3.510	5.850	6.010	3.740	0.994	0.936	0.609
5	Offshore SHANWEI	0.416	2.448	2.594	4.894	6.165	4.146	0.997	0.923	0.828
6	Offshore NANSAN	0.429	2.951	2.781	5.002	6.073	3.669	0.998	0.880	0.872
7	DONGSHA	1.137	1.148	1.913	2.909	2.877	1.277	0.932	0.930	0.917
8	ZHANJIANG	0.909	1.154	2.267	2.316	2.930	2.599	0.991	0.972	0.883
9	HONGKONG	2.050	3.320	3.250	2.270	3.320	3.330	0.902	0.739	0.587

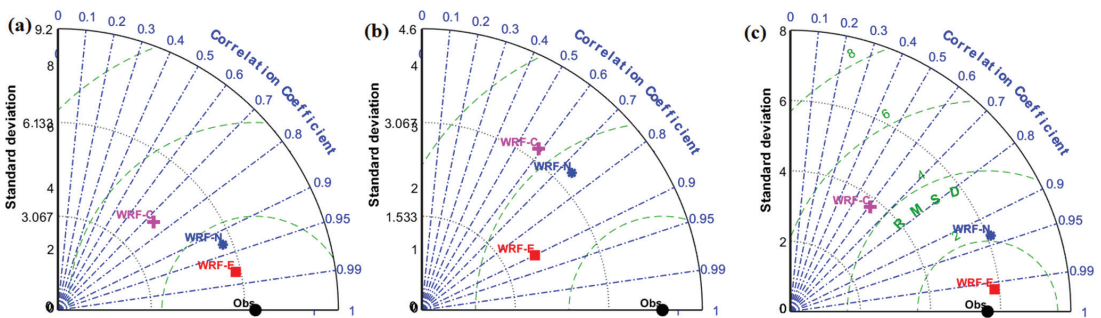
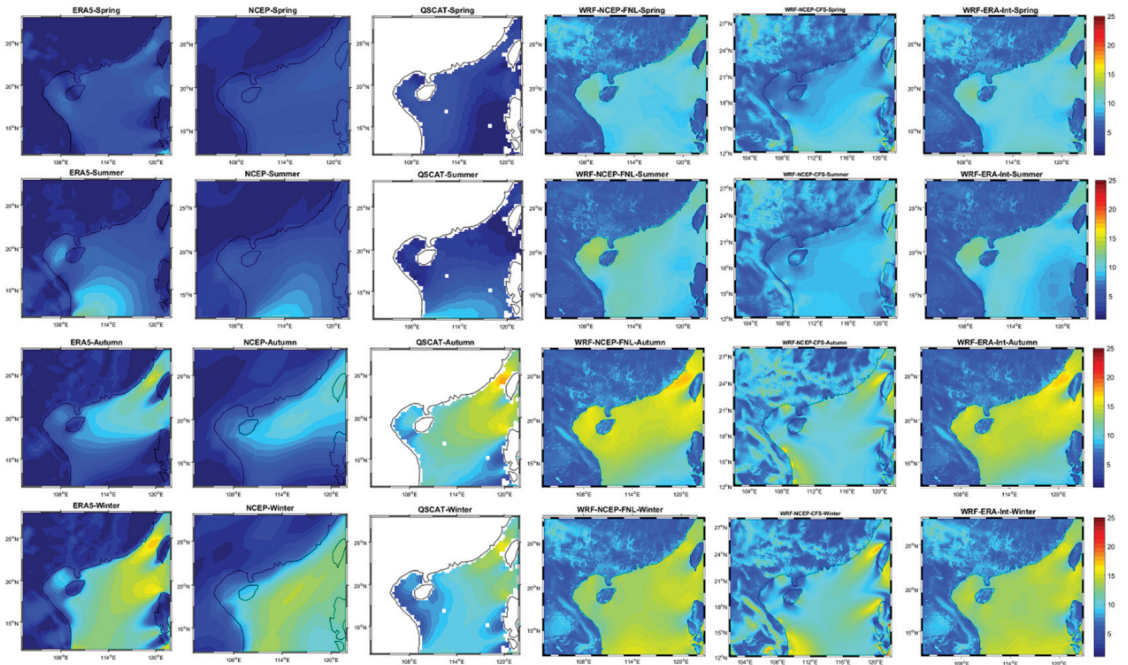


Figure 9. Taylor diagram for temperature in K from the models and observations at the locations (a) Nanping, (b) Hong Kong, and (c) offshore Quanzhou.

3.4. Comparison of Seasonal Winds

For the South China Sea, the seasons are defined as follows: summer comprises June–August, autumn in September–November, winter in December–February, followed by spring in March–May. The seasonal variability in wind speed over the South China Sea and the surrounding regions are mainly influenced by the Asian monsoon and the orography of the region. Figure 10 compares the seasonal wind speeds from the models with those from satellite QuikSCAT observation and other reanalysis datasets. The winds are calm during the summer monsoon while they reach their maximum during the winter monsoonal period. Both the WRF-N and WRF-E simulations are able to reproduce the seasonal wind pattern with maximum winds occurring along the Taiwan Strait. The southern coast of China receives the strongest winds with the persistent high reaching above  $15 \text{ m s}^{-1}$  in winter. These winds start at the end of summer and continue till the end of winter. The coastal region between Hainan and Taiwan are excellent locations for wind farm settings due to the rich wind resource and shallow bathymetry.



**Figure 10.** Average seasonal wind speed in  $\text{m s}^{-1}$  from the models and observations for all the seasons along the study area. Spring is shown in first row, summer in second row, autumn in third row and winter in fourth row. The first column represents ERA5 data, second column from NCEP Reanalysis 2, third column from QuikScat, fourth column from WRF-N simulations, fifth from WRF-C simulations and sixth from WRF-E simulations.

### 3.5. Interannual Variations and Wind Power Density

To optimize the windfarm setting, the interannual variations (IAV) of the wind speed and the average wind power density in terms of cubic windspeed using Equation (3) are examined. Since the WRF-E simulation has a better performance in reproducing the wind field characteristics, the following analysis will be mainly based on the WRF-E results. Figure 11a shows that the IAVs along the coastal region are low (<2%) and hence these regions act as an excellent region for long-term offshore wind energy investments. The open ocean has the highest interannual variations. Along the coastal regions, Taiwan Strait has the maximum average wind power density and minimum interannual variations. This region acts as an excellent region to obtain wind energy in the South China Sea. This region is also identified as one of the best regions over the globe to extract wind energy in the range higher than  $600 \text{ W m}^{-2}$  [63,64]. Followed by the Taiwan strait, the regions around Guangdong province and the Hunan province also share some of the highest wind power density amidst lower interannual variations in the South China Sea.

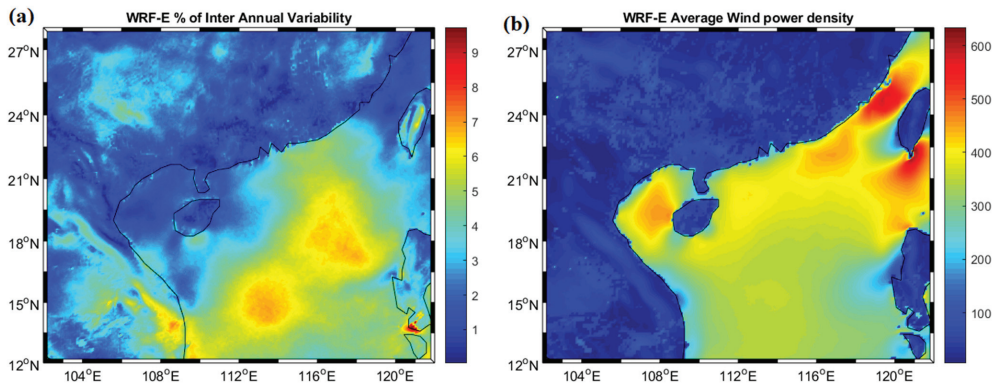


**Figure 11.** (a) Interannual variability and (b) average wind power density ( $\text{m}^3 \text{s}^{-3}$ ) for the year 2015–2018 from WRF-E simulations.

#### 4. Discussions

The main difference between analysis (NCEP-FNL) and reanalysis (ERA-Interim and NCEP-CFSv2) data is the amount of observational data that enters in the data assimilation step. For example, the analysis data are created very quickly while reanalysis data takes more than 3–4 days. Therefore, biases are corrected, and more satellite data enters the creation of reanalysis data [28]. Reanalysis data is dependent on the underlying forecast models, data input sources, and assimilation systems [65]. The main advantage of the ERA-Interim data is the inclusion of a four-dimensional variational analysis (4D-Var) assimilation system of observed data, while the other reanalysis data have the 3D-Var assimilation system. The 4D-Var assimilation system reduces the various biases in the model output. The boundary conditions used by these reanalyses are different. For example, SSTs for the NCEP-CFSv2 model are generated by an atmosphere–ocean coupling model, while the ERA-Interim is run with observed SSTs [66].

Among the three reanalysis datasets used to simulate the wind resources along South China Sea, ERA-Interim forced models produced the best results. However, along the coastal regions, even ERA-Interim forced data could not reproduce the wind speed and its evolution well. This mainly happens because the interactions between ocean and atmosphere near coastal regions are complex and a standalone atmosphere model will not be able to capture them. In future, this modeling approach can be extended with coupled numerical models, where there exists constant interchange of data between atmosphere and oceans, can be used to improve the wind resource estimations. Further, the innermost domain of the current study is in the range of 4 km which is considered coarser for wind farms as they require sub-kilometer scale wind resource estimations. With this study as the base, more studies can be built by selecting the region of interest and performing higher resolution modeling in a sub-kilometer scale.

With ERA-Interim data providing the best wind resource estimations over South China Sea, the sensitivity of WRF model can be further analyzed by varying different parameterization schemes for planetary boundary layer and land surface models. The parameterization schemes for this study are chosen based on the literatures but different combination of the schemes can provide different and improved results which can be further explored.

#### 5. Summary and Conclusions

In this study, the high-resolution WRF simulations over the South China Sea and surrounding regions are conducted to study the sensitivity of various initial and boundary conditions in simulating the near-surface wind and temperature fields. Three state-of-the-art reanalysis datasets (NCEP-FNL, ERA-Interim, and NCEP CFSv2) are used as the forcing

data for the numerical simulations between 2015 and 2018. The model results are analyzed and compared with various observed datasets.

ERA-Interim-forced simulations performed well in comparison with other datasets. The error from the simulations is lowest in the WRF-E models followed by WRF-N and WRF-C simulations when comparing daily wind speeds. Over most of the locations considered, WRF-E has a better correlation and lower RMSE among the three. The monthly variations are also captured by the simulations along the coastal region but not for the open ocean.

The simulations are also able to reproduce the wind directions along the coastal China, with WRF-E and WRF-N simulations performing better followed by WRF-C. In a seasonal characteristics of wind speed, WRF-E and WRF-N performed well while WRF-C could not reproduce high wind speeds in the open ocean. The near-surface temperature simulations show that the models are able to capture the variations with small deviation from the observation data. Of all the models, the WRF-E simulations outputs are good when compared with other simulations for temperature. The WRF-N has a negative temperature bias, while the WRF-C has a positive bias in some regions. Seasonal variations show that autumn and winter provide excellent conditions to extract wind energy along the South China Sea. Furthermore, interannual variability of windspeed shows that the wind energy near the onshore and coastal region is stable, with the coastal regions registering maximum wind power density over the South China Sea. These coastal regions are excellent grounds for future wind power investments as they have low interannual variability. Overall, WRF forced with ERA-Interim data provided the best simulations followed by NCEP Final analysis and CFSv2 data for the South China Sea, which indicates that the ERA-Interim data can be used as the best initial and boundary data for further numerical modeling in this region.

**Author Contributions:** Conceptualization, T.X. and Y.-F.M.; numerical modeling, visualization, and original draft preparation, A.T.; writing—review and editing, T.X., Y.-F.M. and L.-P.W.; funding acquisition, L.-P.W. All authors have read and agreed to the published version of the manuscript.

**Funding:** This work has been supported by the Southern Marine Science and Engineering Guangdong Laboratory (Guangzhou) (GML2019ZD0103), the National Natural Science Foundation of China (91852205, 91741101, 11961131006, 42075071, and 42075078), NSFC Basic Science Center Program (11988102), Guangdong Provincial Key Laboratory of Turbulence Research and Applications (2019B21203001), Guangdong-Hong Kong-Macao Joint Laboratory for Data-Driven Fluid Mechanics and Engineering Applications (2020B1212030001), and Shenzhen Science and Technology Program (KQTD20180411143441009).

**Institutional Review Board Statement:** Not applicable.

**Informed Consent Statement:** Not applicable.

**Data Availability Statement:** The data used in this manuscript are downloaded from the following open websites: ERA-Interim: <https://rda.ucar.edu/datasets/ds627.0>, accessed on 25 May 2021. NCEP-FNL: <https://rda.ucar.edu/datasets/ds083.2>, accessed on 25 May 2021. NCEP-CFSv2: <https://rda.ucar.edu/datasets/ds094.0>, accessed on 25 May 2021. ETOPO2: <https://rda.ucar.edu/datasets/ds759.3>, accessed on 25 October 2020. MERRA: <https://gmao.gsfc.nasa.gov/reanalysis/MERRA-2/>, accessed on 20 October 2020. NOAA: <https://www.ncei.noaa.gov/products/land-based-station/integrated-surface-database>, accessed on 20 October 2020. ECMWF-ERA5: <https://cds.climate.copernicus.eu/cdsapp#!/dataset/reanalysis-era5-pressure-levels-monthlymeans?tab=overview>, accessed on 15 January 2021. NCEP Reanalysis2: <https://psl.noaa.gov/data/gridded/data.ncep.reanalysis2.gaussian.html>, accessed on 13 February 2021. QuikScat: <https://www.remss.com>, accessed on 15 January 2021. Computing resources are provided by the Center for Computational Science and Engineering of Southern University of Science and Technology.

**Acknowledgments:** We would like to acknowledge the high-performance computing support from “TaiYi” provided by SUSTech Center for Computational Science & Engineering.

**Conflicts of Interest:** The authors declare no conflict of interest.

Appendix A

This appendix provides additional figures to the validation of model results.



Figure A1. Daily average wind speed in  $\text{m s}^{-1}$  from the models and observations at the onshore locations (a) Shaoguan, (b) Nanping, and (c) Ganzhou.

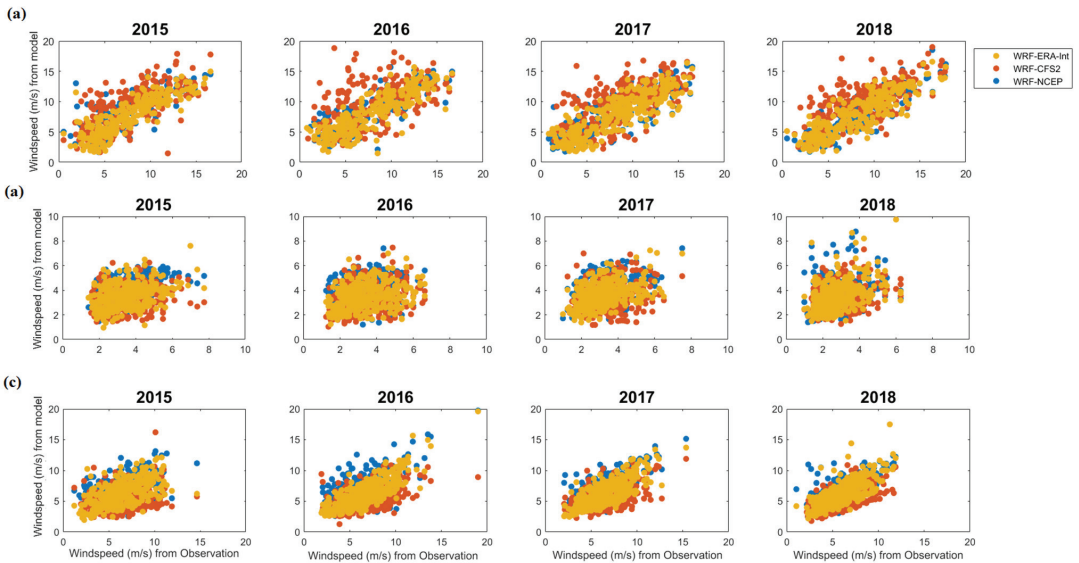


Figure A2. Daily average wind speed in  $\text{m s}^{-1}$  from the models and observations at the offshore locations (a) Quanzhou, (b) Shanwei, and (c) Nansan.

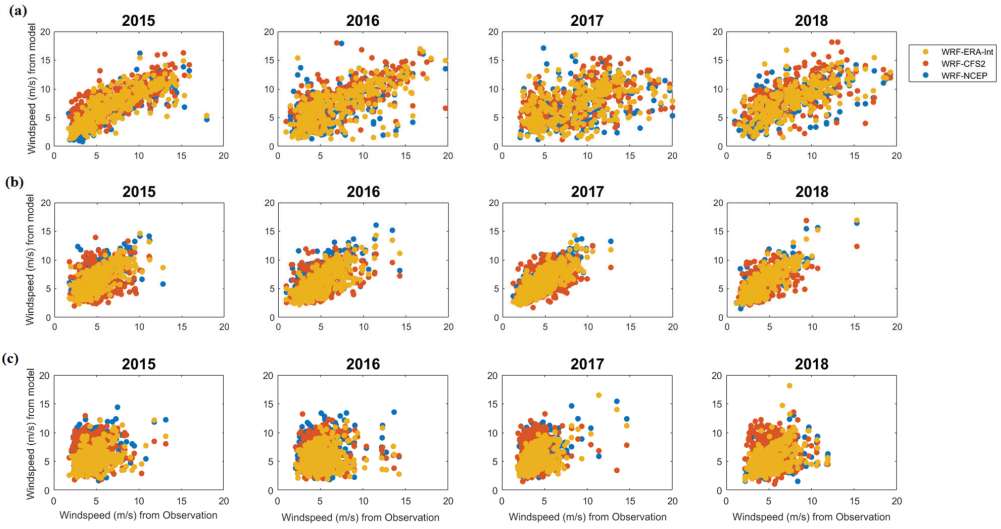


Figure A3. Daily average wind speed in  $m\ s^{-1}$  from the models and observations at the locations (a) Dongsha, (b) Zhanjiang, and (c) Hong Kong.

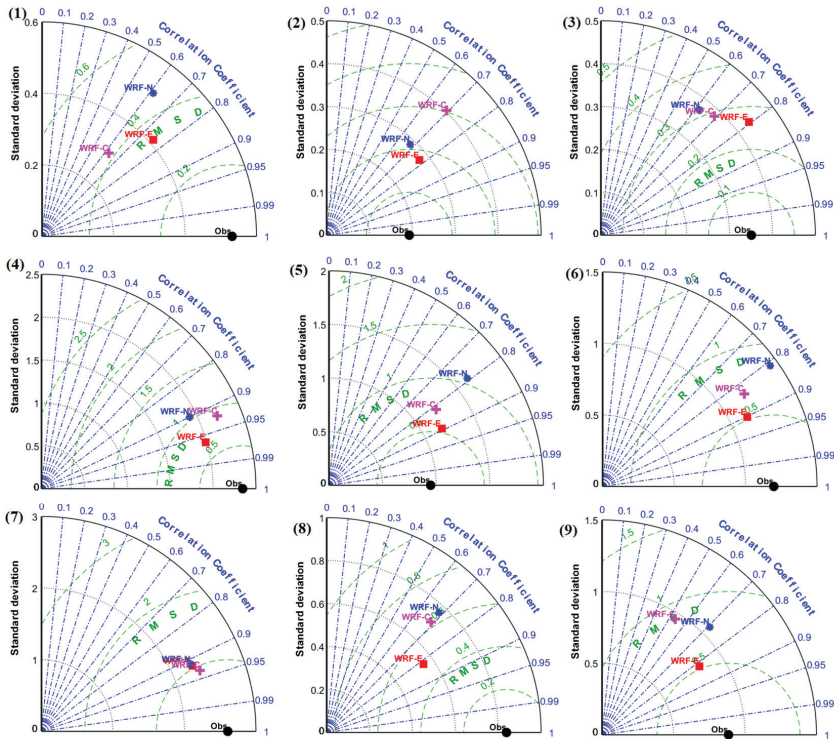
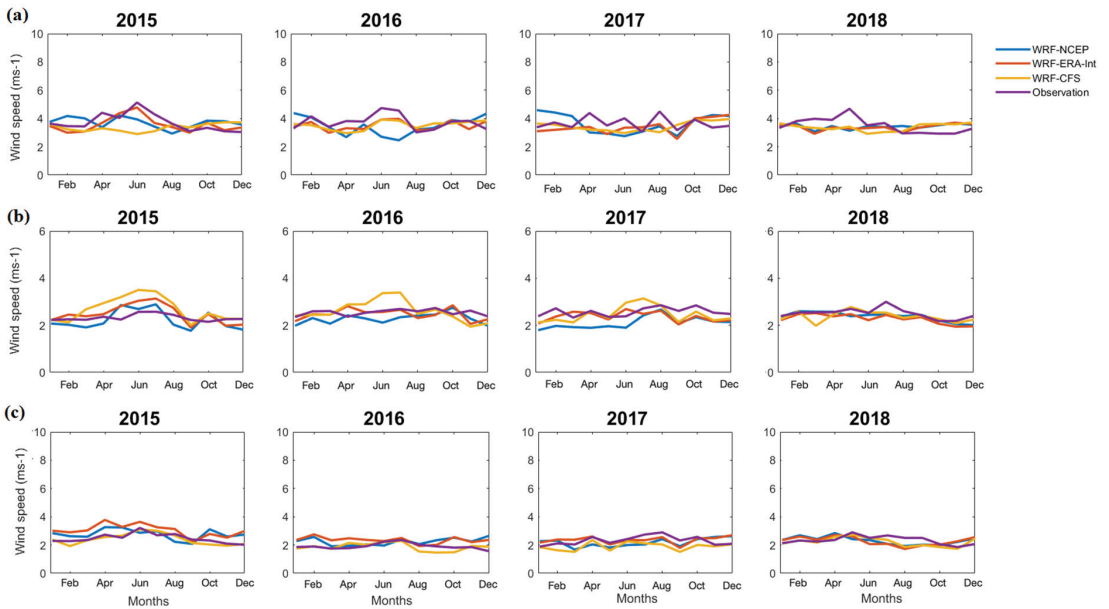
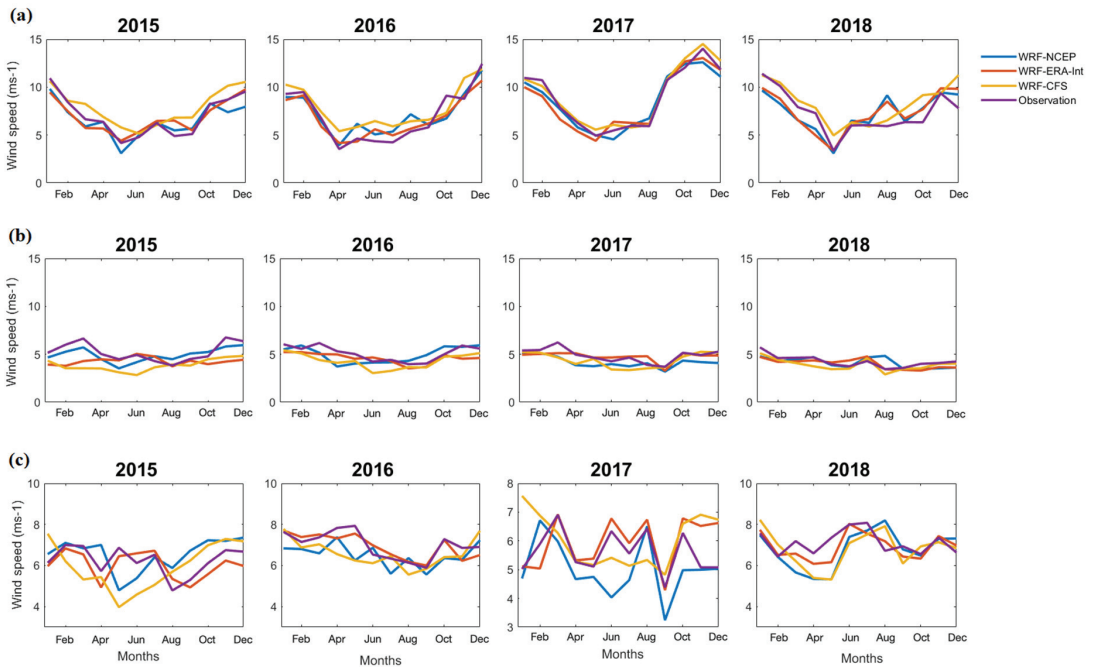


Figure A4. Taylor diagram for wind speed in  $m\ s^{-1}$  from the models and observations at the locations (1) Shaoguan, (2) Nanping, (3) Ganzhou, (4) Offshore Quanzhou, (5) Offshore Shanwei, (6) Offshore Nansan, (7) Dongsha, (8) Zhanjiang and (9) Hong Kong.



**Figure A5.** Monthly averaged wind speed in  $\text{m s}^{-1}$  from the models and observations at the onshore locations (a) Shaoguan, (b) Nanping, and (c) Ganzhou.



**Figure A6.** Monthly averaged wind speed in  $\text{m s}^{-1}$  from the models and observations at the offshore locations (a) Quanzhou, (b) Shanwei, and (c) Nanshan.

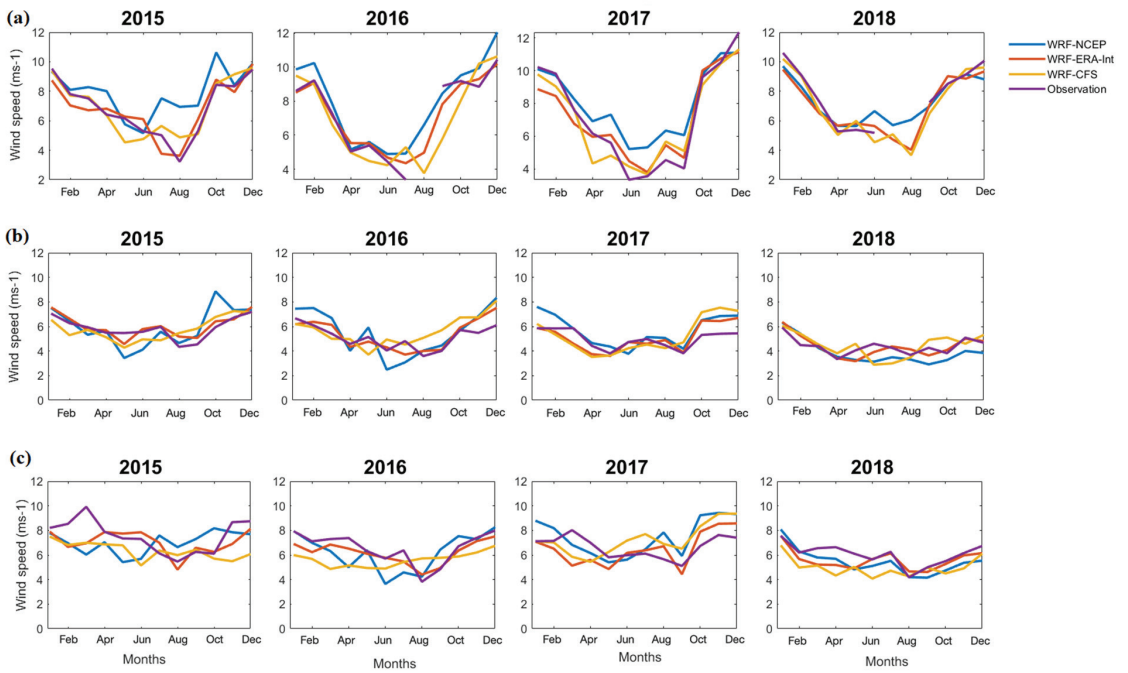


**Figure A7.** Monthly averaged wind speed in  $\text{m s}^{-1}$  from the models and observations at the locations (a) Dongsha, (b) Zhanjiang, and (c) Hong Kong.

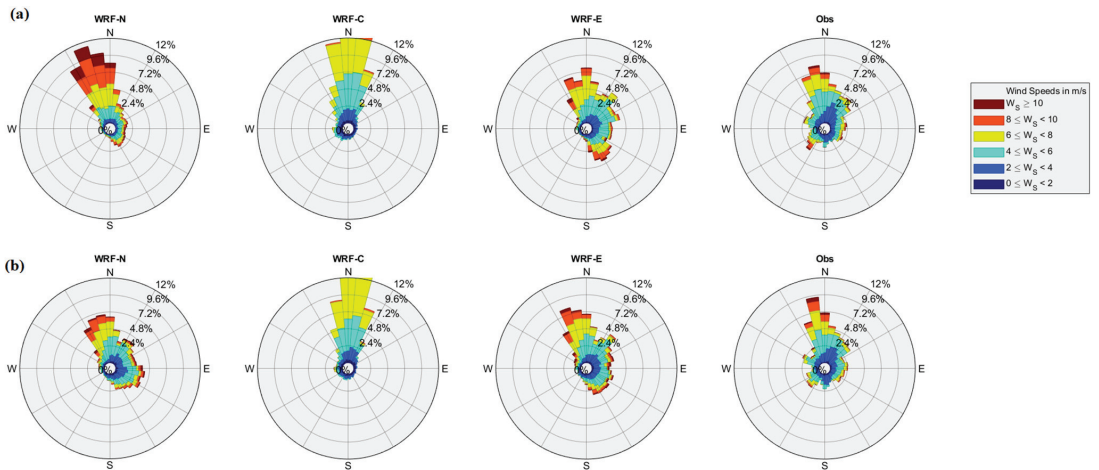


**Figure A8.** Wind rose diagram on an hourly timescale from the models and observations for the years (a) 2017 (top) and (b) 2018 (bottom) at Hong Kong.



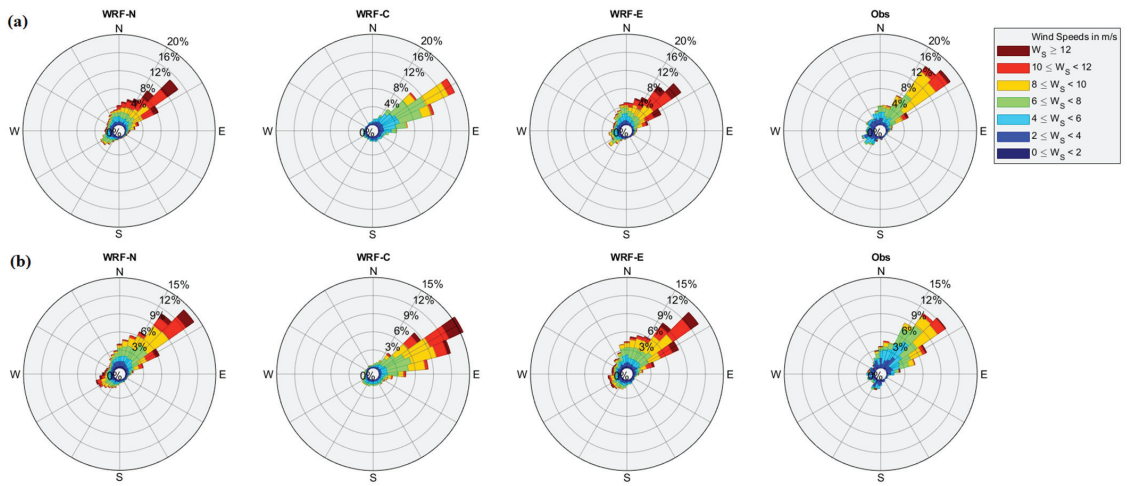


Figure A9. Wind rose diagram on an hourly timescale from the models and observations for the years (a) 2017 (top) and (b) 2018 (bottom) at Dongsha Dao.

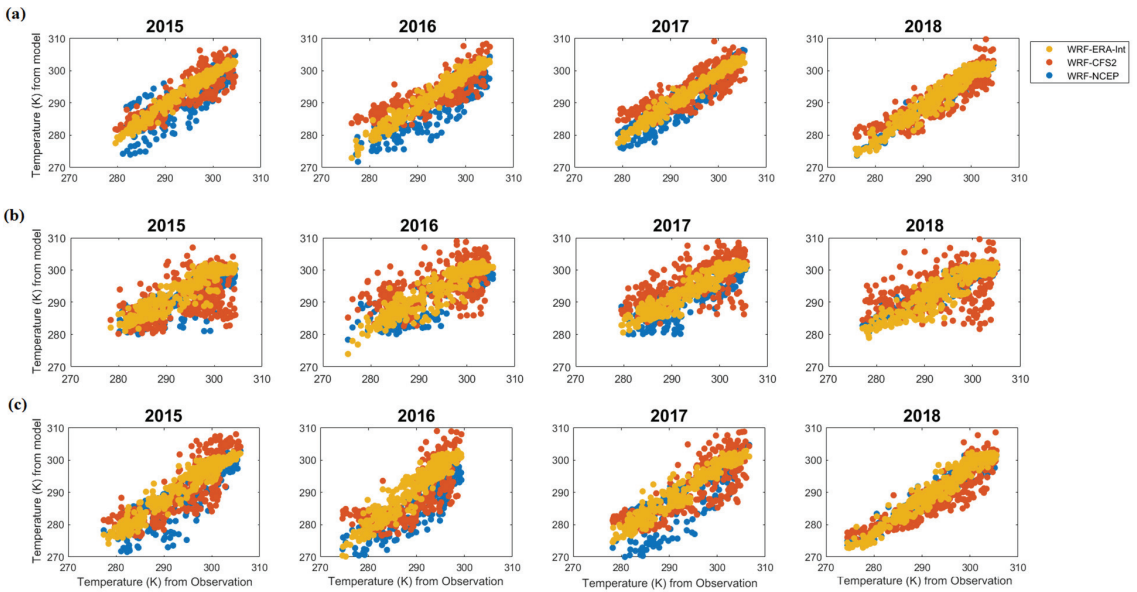
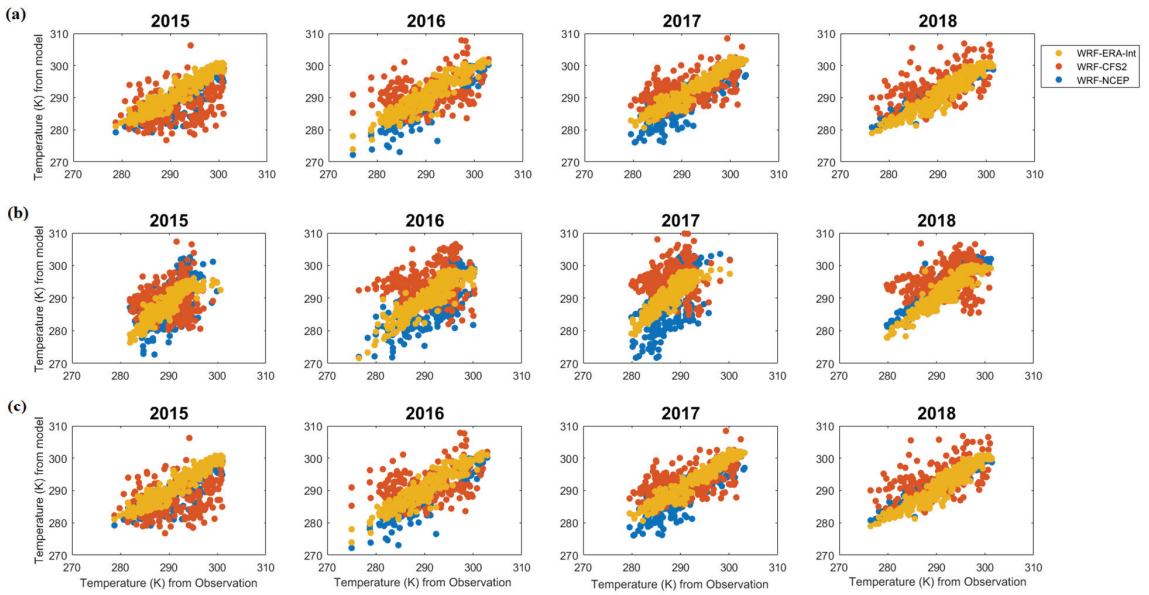
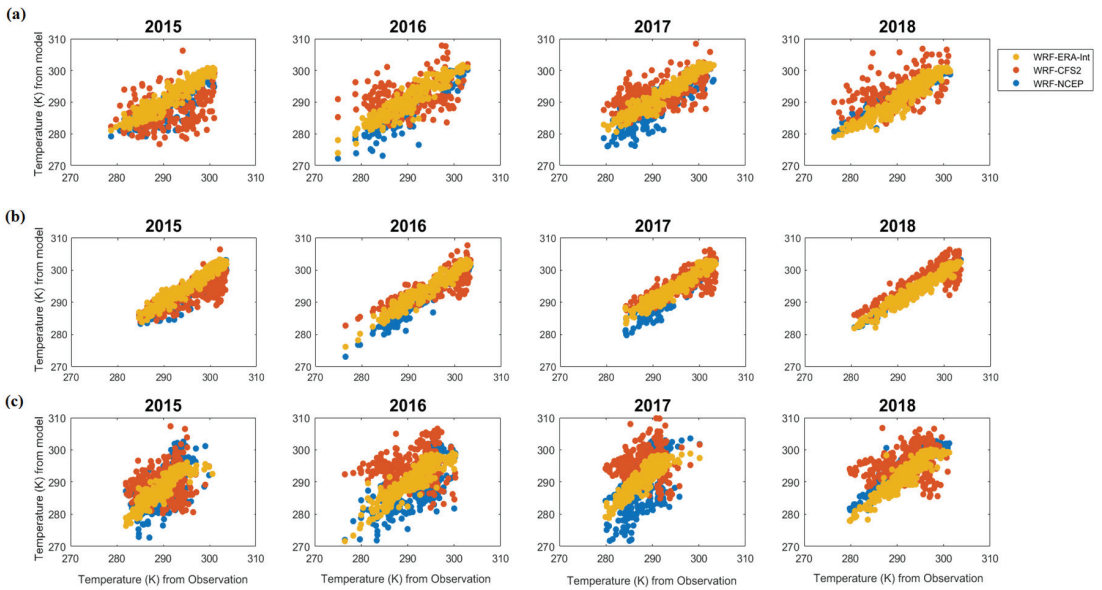


Figure A10. Daily average temperature in K from the models and observations at the onshore locations (a) Shaoguan, (b) Nanping, and (c) Ganzhou.



**Figure A11.** Daily average temperature in K from the models and observations at the offshore locations (a) Quanzhou, (b) Shanwei, and (c) Nansan.



**Figure A12.** Daily average temperature in K from the models and observations at the locations (a) Dongsha, (b) Zhanjiang, and (c) Hong Kong.



12. Nezhad, M.M.; Neshat, M.; Heydari, A.; Razmjoo, A.; Piras, G.; Garcia, D.A. A new methodology for offshore wind speed assessment integrating Sentinel-1, ERA-Interim and in-situ measurement. *Renew. Energy* **2021**, *172*, 1301–1313. [[CrossRef](#)]
13. Chen, X.; Pan, D.; He, X.; Bai, Y.; Wang, Y.; Zhu, Q. Seasonal and interannual variability of sea surface wind over the China seas and its adjacent ocean from QuikSCAT and ASCAT data during 2000–2011. In *Remote Sensing of the Ocean, Sea Ice, Coastal Waters, and Large Water Regions, Proceedings of the SPIE Remote Sensing, 2012, Edinburgh, UK, 24–27 September 2012*; SPIE: Bellingham, WA, USA, 2012; Volume 8532, p. 853214. [[CrossRef](#)]
14. Jiang, D.; Zhuang, D.; Huang, Y.; Wang, J.; Fu, J. Evaluating the spatio-temporal variation of China's offshore wind resources based on remotely sensed wind field data. *Renew. Sustain. Energy Rev.* **2013**, *24*, 142–148. [[CrossRef](#)]
15. Sun, S.; Fang, Y.; Zu, Y.; Liu, B.; Samah, A.A. Seasonal characteristics of mesoscale coupling between the sea surface temperature and wind speed in the South China Sea. *J. Clim.* **2020**, *33*, 625–638. [[CrossRef](#)]
16. Larsén, X.G.; Mann, J. Extreme winds from the NCEP/NCAR Reanalysis Data. *Wind. Energy* **2009**, *12*, 556–573. [[CrossRef](#)]
17. Gallego, C.; Pinson, P.; Madsen, H.; Costa, A.; Cuerva, A. Influence of local wind speed and direction on wind power dynamics—Application to offshore very short-term forecasting. *Appl. Energy* **2011**, *88*, 4087–4096. [[CrossRef](#)]
18. Jiménez, B.; Durante, F.; Lange, B.; Kreutzer, T.; Tambke, J. Offshore wind resource assessment with WASP and MM5: Comparative study for the German Bight. *Wind Energy* **2007**, *10*, 121–134. [[CrossRef](#)]
19. Wallcraft, A.J.; Kara, A.B.; Barron, C.N.; Metzger, E.J.; Pauley, R.L.; Bourassa, M.A. Comparisons of monthly mean 10 m wind speeds from satellites and NWP products over the global ocean. *J. Geophys. Res.* **2009**, *114*, 16109–16114. [[CrossRef](#)]
20. Hasager, C.B.; Astrup, P.; Zhu, R.; Chang, R.; Badger, M.; Hahmann, A.N. Quarter-century offshore winds from SSM/I and WRF in the North Sea and South China Sea. *Remote Sens.* **2016**, *8*, 769. [[CrossRef](#)]
21. Wang, Z.; Duan, C.; Dong, S. Long-term wind and wave energy resource assessment in the South China sea based on 30-year hindcast data. *Ocean. Eng.* **2018**, *163*, 58–75. [[CrossRef](#)]
22. Huang, Y.; Liu, Y.; Liu, Y.; Li, H.; Knierel, J.C. Mechanisms for a record-breaking rainfall in the coastal metropolitan city of Guangzhou, China: Observation analysis and nested very large eddy simulation with the WRF model. *J. Geophys. Res. Atmos.* **2019**, *124*, 1370–1391. [[CrossRef](#)]
23. Pan, L.; Liu, Y.; Roux, G.; Cheng, W.; Liu, Y.; Hu, J.; Jin, S.; Feng, S.; Du, J.; Peng, L. Seasonal variation of the surface wind forecast performance of the high-resolution WRF-RTFDDA system over China. *Atmos. Res.* **2021**, *259*, 105673. [[CrossRef](#)]
24. Zhang, C.; He, J.; Lai, X.; Liu, Y.; Che, H.; Gong, S. The impact of the variation in weather and weason on WRF dynamical downscaling in the Pearl River Delta region. *Atmosphere* **2021**, *12*, 409. [[CrossRef](#)]
25. National Centers for Environmental Prediction/National Weather Service/NOAA/U.S. Department of Commerce. 2000, Updated Daily. NCEP FNL Operational Model Global Tropospheric Analyses, continuing from July 1999. Research Data Archive at the National Center for Atmospheric Research, Computational and Information Systems Laboratory. Available online: <https://rda.ucar.edu/datasets/ds083.2/> (accessed on 25 May 2021). [[CrossRef](#)]
26. European Centre for Medium-Range Weather Forecasts. 2009, Updated Monthly. ERA-Interim Project. Research Data Archive at the National Center for Atmospheric Research, Computational and Information Systems Laboratory. Available online: <https://rda.ucar.edu/datasets/ds627.0/> (accessed on 25 May 2021). [[CrossRef](#)]
27. Saha, S.; Moorthi, S.; Wu, X.; Wang, J.; Nadiga, S. NCEP Climate Forecast System Version 2 (CFSv2) 6-Hourly Products. Research Data Archive at the National Center for Atmospheric Research, Computational and Information Systems Laboratory. 2011. Available online: <https://rda.ucar.edu/datasets/ds094.0/> (accessed on 25 May 2021). [[CrossRef](#)]
28. Carvalho, D.; Rocha, A.; Gómez-Gesteira, M.; Santos, C.S. Offshore wind energy resource simulation forced by different reanalyses: Comparison with observed data in the Iberian Peninsula. *Appl. Energy* **2014**, *134*, 57–64. [[CrossRef](#)]
29. Giannakopoulou, E.M.; Nhili, R. WRF model methodology for offshore wind energy applications. *Adv. Meteorol.* **2014**, *2014*, 319819. [[CrossRef](#)]
30. Lorenz, T.; Barstad, I. A dynamical downscaling of ERA-Interim in the North Sea using WRF with a 3 km grid—For wind resource applications. *Wind Energy* **2016**, *19*, 1945–1959. [[CrossRef](#)]
31. Mattar, C.; Borvarán, D. Offshore wind power simulation by using WRF in the central coast of Chile. *Renew. Energy* **2016**, *94*, 22–31. [[CrossRef](#)]
32. Kryza, M.; Wałaszek, K.; Ojrzyńska, H.; Szymanowski, M.; Werner, M.; Dore, A.J. High-resolution dynamical downscaling of ERA-interim using the WRF regional climate model for the area of Poland. Part 1: Model configuration and statistical evaluation for the 1981–2010 Period. *Pure Appl. Geophys.* **2017**, *174*, 511–526. [[CrossRef](#)]
33. Li, X.; Gao, Y.; Pan, Y.; Xu, Y. Evaluation of near-surface wind speed simulations over the Tibetan Plateau from three dynamical downscalings based on WRF model. *Theor. Appl. Climatol.* **2018**, *134*, 1399–1411. [[CrossRef](#)]
34. Chadee, X.T.; Seegobin, N.R.; Clarke, R.M. Optimizing the Weather Research and Forecasting (WRF) model for mapping the near-surface wind resources over the Southernmost Caribbean Islands of Trinidad and Tobago. *Energies* **2017**, *10*, 931. [[CrossRef](#)]
35. De Araujo, J.M.S. WRF wind speed simulation and SAM wind energy estimation: A case study in Dili Timor Leste. *IEEE Access* **2019**, *7*, 35382–35393. [[CrossRef](#)]
36. Lakshmi, D.D.; Murty, P.L.N.; Bhaskaran, P.K.; Sahoo, B.; Kumar, T.S.; Shenoi, S.S.C.; Srikanth, A.S. Performance of WRF-ARW winds on computed storm surge using hydodynamic model for Phailin and Hudhud cyclones. *Ocean. Eng.* **2017**, *131*, 135–148. [[CrossRef](#)]

37. Anandh, T.S.; Das, B.K.; Kuttippurath, J.; Chakraborty, A. A coupled model analyses on the interaction between oceanic eddies and tropical cyclones over the Bay of Bengal. *Ocean. Dyn.* **2020**, *70*, 327–337. [[CrossRef](#)]
38. Chen, C.; Sasa, K.; Ohsawa, T.; Kashiwagi, M.; Prpić-Oršić, J.; Mizojiri, T. Comparative assessment of NCEP and ECMWF global datasets and numerical approaches on rough sea ship navigation based on numerical simulation and shipboard measurements. *Appl. Ocean. Res.* **2020**, *101*, 102219. [[CrossRef](#)]
39. Devanand, A.; Roxy, M.K.; Ghosh, S. Coupled land-atmosphere regional model reduces dry bias in Indian Summer Monsoon rainfall simulated by CFSv2. *Geophys. Res. Lett.* **2018**, *45*, 2476–2486. [[CrossRef](#)]
40. Diaz, L.R.; Mollmann, R.A.; Muchow, G.B.; Käfer, P.S.; Rocha, N.S.; Kaiser, E.A.; Costa, S.T.L.; Hallal, G.P.; Alves, R.C.M.; Rolim, S.B.A. Analysis of an extratropical cyclone in the Southwest Atlantic: WRF model boundary conditions sensitivity. In Proceedings of the International Archives of the Photogrammetry, Remote Sensing and Spatial Information Sciences, Santiago, Chile, 22–26 March 2020; XLII-3/W12-2020. pp. 107–112. [[CrossRef](#)]
41. Gippius, F.N.; Myslenkov, S.A. Black Sea wind wave climate with a focus on coastal regions. *Ocean. Eng.* **2020**, *218*, 108199. [[CrossRef](#)]
42. Im, E.S.; Ha, S.; Qiu, L.; Hur, J.; Jo, S.; Shim, K.M. An evaluation of temperature-based agricultural indices over Korea from the high-resolution WRF simulation. *Front. Earth Sci.* **2021**, *9*, 357. [[CrossRef](#)]
43. Samanta, D.; Hameed, S.N.; Jin, D.; Thilakan, V.; Ganai, M.; Rao, S.A.; Deshpande, M. Impact of a narrow coastal Bay of Bengal Sea surface temperature front on an Indian summer monsoon simulation. *Sci. Rep.* **2018**, *8*, 17694. [[CrossRef](#)]
44. Rienecker, M.M.; Suarez, M.J.; Gelaro, R.; Todling, R.; Bacmeister, J.; Liu, E.; Bosilovich, M.G.; Schubert, S.D.; Takacs, L.; Kim, G.; et al. MERRA: NASA's Modern-Era Retrospective Analysis for Research and Applications. *J. Clim.* **2011**, *24*, 3624–3648. [[CrossRef](#)]
45. Bentamy, A.; Fillon, D.C. Gridded surface wind fields from Metop/ASCAT measurements. *Int. J. Remote Sens.* **2012**, *33*, 1729–1754. [[CrossRef](#)]
46. Gruber, K.; Regner, P.; Wehrle, S.; Zeyringer, M.; Schmidt, J. Towards global validation of wind power simulations: A multi-country assessment of wind power simulation from MERRA-2 and ERA-5 reanalyses bias-corrected with the global wind atlas. *Energy* **2022**, *238*, 121520. [[CrossRef](#)]
47. Olauson, J.; Bergkvist, M. Modelling the Swedish wind power production using MERRA reanalysis data. *Renew. Energy* **2015**, *76*, 717–725. [[CrossRef](#)]
48. Global Surface Hourly [Integrated Surface Dataset]. NOAA National Centers for Environmental Information, 2011. Available online: [https://journals.ametsoc.org/view/journals/bams/92/6/2011bams3015\\_1.xml](https://journals.ametsoc.org/view/journals/bams/92/6/2011bams3015_1.xml) (accessed on 20 October 2020). [[CrossRef](#)]
49. National Geophysical Data Center/NESDIS/NOAA/U.S. Department of Commerce. ETOPO2, Global 2 Arc-minute Ocean Depth and Land Elevation from the US National Geophysical Data Center (NGDC). Research Data Archive at the National Center for Atmospheric Research, Computational and Information Systems Laboratory, 2001. Available online: <https://rda.ucar.edu/datasets/ds759.3/> (accessed on 25 October 2020). [[CrossRef](#)]
50. Copernicus Climate Change Service (C3S): ERA5: Fifth Generation of ECMWF Atmospheric Reanalyses of the Global Climate. Copernicus Climate Change Service Climate Data Store (CDS), 2017. Available online: <https://cds.climate.copernicus.eu/cdsapp> (accessed on 15 January 2021).
51. Kanamitsu, M.; Ebisuzaki, W.; Woollen, J.; Yang, S.K.; Hnilo, J.J.; Fiorino, M.; Potter, G.L. NCEP-DOE AMIP-II Reanalysis (R-2). *Bull. Am. Meteorol. Soc.* **2002**, *83*, 1631–1643. [[CrossRef](#)]
52. Risien, C.M.; Chelton, D.B. A global climatology of surface wind and wind stress fields from eight years of QuikSCAT scatterometer data. *J. Phys. Oceanogr.* **2008**, *38*, 2379–2413. [[CrossRef](#)]
53. Skamarock, W.C.; Klemp, J.B.; Dudhia, J.; Gill, D.O.; Liu, Z.; Berner, J.; Wang, W.; Powers, J.G.; Duda, M.G.; Barker, D.M.; et al. *A Description of the Advanced Research WRF Model Version 4*; National Center for Atmospheric Research: Boulder, CO, USA, 2019; p. 145.
54. Mlawer, E.J.; Taubman, S.J.; Brown, P.D.; Iacono, M.J.; Clough, S.A. Radiative transfer for inhomogeneous atmospheres: RRTM, a validated correlated-k model for the longwave. *J. Geophys. Res.* **1997**, *102*, 16663–16682. [[CrossRef](#)]
55. Dudhia, J. Numerical study of convection observed during the winter monsoon experiment using a mesoscale two-dimensional model. *J. Atmos. Sci.* **1989**, *46*, 3077–3107. [[CrossRef](#)]
56. Nakanishi, M.; Niino, H. An Improved Mellor–Yamada Level-3 Model: Its Numerical Stability and Application to a Regional Prediction of Advection Fog. *Bound.-Layer Meteorol.* **2006**, *119*, 397–407. [[CrossRef](#)]
57. Kain, J.S. The Kain–Fritsch convective parameterization: An update. *J. Appl. Meteorol.* **2004**, *43*, 170–181. [[CrossRef](#)]
58. Morrison, H.; Thompson, G.; Tatarskii, V. Impact of cloud microphysics on the development of trailing stratiform precipitation in a simulated squall line: Comparison of one-and two-moment schemes. *Mon. Weather. Rev.* **2009**, *137*, 991–1007. [[CrossRef](#)]
59. Taylor, K.E. Summarizing multiple aspects of model performance in a single diagram. *J. Geophys. Res. Atmos.* **2001**, *106*, 7183–7192. [[CrossRef](#)]
60. Brower, M.C. *Wind Resource assessment: A Practical Guide to Developing a Wind Project*; John Wiley & Sons, Inc.: Hoboken, NJ, USA, 2012; p. 280. ISBN 9781118249864.
61. Manwell, J.F.; McGowan, J.G.; Rogers, A.L. *Wind Energy Explained: Theory, Design and Application*, 2nd ed.; John Wiley & Sons, Inc.: Washington, DC, USA, 2010; p. 689. ISBN 978-0470015001.
62. Betz, A. *Introduction to the Theory of Flow Machines*; Pergamon Press: Oxford, UK, 1966; ISBN 9781483180908.

63. Zheng, C.W.; Li, X.Y.; Luo, X.; Chen, X.; Qian, Y.H.; Zhang, Z.H.; Gao, Z.S.; Du, Z.B.; Gao, Y.B.; Chen, Y.G. Projection of future global offshore wind energy resources using CMIP data. *Atmos.-Ocean* **2019**, *57*, 134–148. [[CrossRef](#)]
64. Soares, P.M.; Lima, D.C.; Nogueira, M. Global offshore wind energy resources using the new ERA-5 reanalysis. *Environ. Res. Lett.* **2020**, *15*, 1040a2. [[CrossRef](#)]
65. Xian, T.; Homeyer, C.R. Global tropopause altitudes in radiosondes and reanalyses. *Atmos. Chem. Phys.* **2019**, *19*, 5661–5678. [[CrossRef](#)]
66. Fujiwara, M.; Wright, J.S.; Manney, G.L.; Gray, L.J.; Anstey, J.; Birner, T.; Davis, S.; Gerber, E.P.; Harvey, V.L.; Heggin, M.I.; et al. Introduction to the SPARC Reanalysis Intercomparison Project (S-RIP) and overview of the reanalysis systems. *Atmos. Chem. Phys.* **2017**, *17*, 1417–1452. [[CrossRef](#)]





Article

# Does Subjective Well-Being Promote Pro-Environmental Behaviors? Evidence from Rural Residents in China

Xi Ouyang<sup>1</sup>, Wen'e Qi<sup>2,\*</sup>, Donghui Song<sup>1</sup> and Jianjun Zhou<sup>3</sup>

<sup>1</sup> National School of Agricultural Institution and Development, South China Agricultural University, Guangzhou 510642, China; ouyangxi@stu.scau.edu.cn (X.O.); dhsong@stu.scau.edu.cn (D.S.)

<sup>2</sup> College of Economics and Management, South China Agricultural University, Guangzhou 510642, China

<sup>3</sup> School of Economics, Central University of Finance and Economics, Beijing 100081, China; 2018110098@email.cufe.edu.cn

\* Correspondence: qiwene@scau.edu.cn

**Abstract:** The spontaneous pro-environmental behavior (PEB) of rural residents is essential for rural environmental governance. Existing studies have primarily focused on the impact of objective factors on individual PEB, while less attention has been paid to the role of subjective factors, such as rural residents' subjective well-being, in shaping such behaviors. Based on the Chinese General Social Survey (CGSS) data, this study evaluates the impact of subjective well-being on the PEB of rural residents. The results show that subjective well-being significantly promoted the PEB in both the private sphere with reciprocity and the public sphere with altruistic attributes. Subjective well-being affected PEB mainly by enhancing rural residents' social interaction and reciprocity with others and raising their fraternity and altruism. Moreover, the positive effect was mainly driven by women and individuals with more environmental knowledge. Therefore, enhancing rural residents' subjective well-being is not only an important development goal, but also the starting point and foothold of solving the contradiction between economic development and environmental protection and promoting social harmony.

**Keywords:** subjective well-being; pro-environmental behavior; reciprocal; altruism; rural residents

**Citation:** Ouyang, X.; Qi, W.; Song, D.; Zhou, J. Does Subjective Well-Being Promote Pro-Environmental Behaviors? Evidence from Rural Residents in China. *Int. J. Environ. Res. Public Health* **2022**, *19*, 5992. <https://doi.org/10.3390/ijerph19105992>

Academic Editors: Francesco Nocera, Roberto Alonso González Lezcano and Rosa Giuseppina Caponetto

Received: 31 March 2022

Accepted: 11 May 2022

Published: 14 May 2022

**Publisher's Note:** MDPI stays neutral with regard to jurisdictional claims in published maps and institutional affiliations.



**Copyright:** © 2022 by the authors. Licensee MDPI, Basel, Switzerland. This article is an open access article distributed under the terms and conditions of the Creative Commons Attribution (CC BY) license (<https://creativecommons.org/licenses/by/4.0/>).

## 1. Introduction

Soil, water and air pollution, ecosystem deterioration and other environmental problems have become increasingly prominent in rural areas. These environmental concerns have caused irreparable losses to production and human health [1,2]. However, it is extremely difficult to ease the pressure on the rural environment. Rural environmental issues are even more challenging to address than urban ones because the former is confronted with not only the ineffectiveness of public goods, but also the slow development of the rural environmental market with its own specificity. Therefore, given the ineffective rural environmental governance, either government-led or private-sector-initiated, it is vital to promote the proactive participation of rural residents in pro-environmental behavior (PEB). PEB is considered a social cooperation that requires individuals to sacrifice part of their interests for the greater collective good [3]. In this case, a rational self-interested economic person is usually reluctant to spontaneously take this cooperative action, PEB [4]. Nevertheless, researchers have provided a wealth of empirical evidence on the influencing factors of individuals' PEB. Most of these studied factors are objective ones [5–7], including individual objective factors and social objective factors, while subjective factors are scarcely explored. With the rise of behavioral economics, researchers have increasingly recognized that subjective factors, such as emotions, play an essential role in individual's behavioral decision making [8,9]. Moreover, it has been argued that subjective factors are more likely than objective factors to promote individuals' pro-social behavior in terms of enhancing social cooperation, and the behavioral change driven by subjective factors is stable in



long term [10]. Studies have shown that subjective factors also play an important role in promoting environmental sustainability [11,12]. Therefore, it is necessary to focus on subjective factors when motivating rural residents to develop PEB voluntarily.

Subjective well-being is the comprehensive state of an individual's emotions and satisfaction based on the individual's conditions and has a high marginal utility for the individual [13]. With the quiet rise of happiness economics, economists have realized that subjective well-being or happiness is a more justified proxy than income to measure people's level of well-being [14]. Numerous studies have shown that subjective well-being plays a non-negligible role in promoting pro-social behavior [15,16]. Subjective well-being helps to motivate individuals' goodwill, enhance altruism and promote individuals to treat others in a more friendly way [17–19]. This assertion has been supported by extensive research. For example, individuals with higher subjective well-being show less hostility towards others, higher social adaptation and communication skills, and more cooperative behaviors [20,21]. To sum up, subjective well-being has become a key factor for individuals participating in social cooperation [15,20].

PEB, a type of pro-social behavior, requires individuals to voluntarily participate in social cooperation to benefit the communities or other individuals. Theoretically, subjective well-being should have a positive impact on PEB. However, empirical evidence on the relationship between subjective well-being and PEB is still scarce. Most previous literature on the relationship, based on emotion-inducing experiments, found that positive emotions (subjective well-being) help individuals to participate in PEB [22,23]. However, the existing literature has not explored the influencing mechanism of subjective well-being on PEB, which requires further systematic research [24]. Meanwhile, the existing literature also ignores the impact of subjective well-being on PEB in specific rural contexts. It is worth noting that the rural environment system is distinct from the urban one. Urban environmental protection issues are mainly purely public issues, that is, the beneficiary of environmental protection is the entire urban society. However, rural environmental issues contain certain private interest attributes in addition to the public interest attributes. For example, garbage in the village only affects the villagers' personal impression or feeling, though the application of chemical fertilizers with a peculiar smell or the discharge of livestock manure affect the air and water quality of the whole village. The environmental protection behavior of rural residents is not as merely altruistic as that of urban residents; instead, it may represent self-interest and reciprocity to a certain degree. Therefore, it is necessary to specifically analyze how subjective well-being affects the PEB of rural residents.

Based on the 2013 Chinese General Social Survey (CGSS2013) data, this study systematically examines the influence of subjective well-being on the PEB of rural residents and explores the mechanism of such influence. Following Stern's [25] classification of behavior, this study divides PEB into two types, namely, the private-sphere PEB and the public-sphere PEB. The private-sphere PEB refers to environmental protection actions that individuals take to benefit themselves or their families and are closely related to daily life, such as not littering; the public-sphere PEB refers to individuals' voluntary participation in environmental protection or active participation in addressing environmental problems, such as donating money to environmental protection and participating in collective afforestation. Therefore, concerning the beneficiaries of PEB, the private-sphere one mainly concentrates on individuals' families or the communities they live in, whereas the public-sphere one benefits broad groups, going beyond oneself, neighbors and friends to cover even strangers. In this regard, despite individuals' PEB being generally regarded as pro-social altruistic [26,27], it should be understood from two perspectives: the public-sphere one is more altruistic, while the private-sphere one is more reciprocal.

This study found that subjective well-being significantly and positively impacts both the private-sphere PEB with reciprocity and private-sphere PEB with altruistic properties. This result is robust to various internal validity checks. To verify the mechanism underlying the relationship between subjective well-being and PEB, this study examines the moderating effects of reciprocity and altruism on the relationship, using individuals' social

frequency and environmental knowledge to represent reciprocity and altruism, respectively. Our empirical results suggest that subjective well-being influences rural residents' PEB based on reciprocal and altruistic motivations. In other words, subjective well-being promotes PEB by enhancing social reciprocity between rural residents and others and increasing their fraternity and altruism. Since the effect of subjective well-being on PEB may vary across different groups, this study adopted a microscopic heterogeneity analysis. We found that the positive effect of subjective well-being on the PEB of rural residents is more driven by women than by men. Additionally, environmental knowledge moderates the relationship between rural residents' subjective well-being and PEB. The higher the level of rural residents' environmental knowledge, the stronger the effect of subjective well-being on PEB.

This study contributes to the existing literature in several ways. First, it theoretically explains and empirically tests whether PEB is affected by subjective well-being in rural contexts, which has been largely ignored in previous studies. As mentioned above, the PEB of rural residents has unique characteristics. Second, this study contributes to a better understanding of the mechanism underlying the influence of rural residents' subjective well-being on PEB. Previous research on the relationship primarily treats PEB as a whole without distinguishing between different types. This study emphasizes that the private-sphere PEB and public-sphere PEB have different attributes and empirically examines PEB in the two spheres. The mechanistic analysis further validates that subjective well-being promotes PEB based on reciprocity and altruistic motivation. Finally, few studies have paid attention to the heterogeneous influence of subjective well-being on PEB among different groups; this study fills the gap by identifying the heterogeneity caused by gender and environmental knowledge.

The rest of this paper is arranged as follows. Section 2 reviews the literature and proposes the conceptual hypotheses. Section 3 presents the research design, including data description, model assumptions and descriptive statistics. Section 4 demonstrates the empirical research results of the influence of subjective well-being on the PEB of rural residents by conducting benchmark regression, robustness testing, mechanism analysis and heterogeneity analysis. Section 5 concludes the study.

## 2. Literature Review

### 2.1. The Influence of Subjective Well-Being on the PEB of Rural Residents

Individuals' positive psychological emotions, such as being more caring, more sympathetic and happier, can promote pro-social and pro-environmental behaviors [28]. Subjective well-being is particularly important for individual behavioral decision making [29]. Previous experimental economics studies have confirmed that subjective well-being can inhibit retaliatory behaviors and improve pro-social behaviors [30,31]. Game experiments also have shown that the happier the individuals, the higher their tolerance for others' selfish behaviors and the greater their interest in cooperation [32,33]. In terms of environmental resources, studies have also confirmed the importance of positive psychological factors, such as subjective well-being in reducing resource consumption and maintaining environmental sustainability [34–36]. On this basis, other studies have shown that subjective well-being, longevity and sustainable behavior are positively correlated [37]. In other words, individuals with higher subjective well-being have greater environmental awareness, health awareness and care for future generations, so they are willing to improve their quality of life by engaging more in sustainable behaviors.

In rural areas where the unified environmental management service provided by the government is lacking, whether the local environment is clean primarily affects rural residents themselves. Therefore, it is believed that rural residents' subjective well-being influences not only their public-sphere PEB with pure altruism, but also the private-sphere PEB with self-interest and reciprocity.

## 2.2. Mechanisms: Reciprocity and Altruism

Subjective well-being can affect the PEB of rural residents in two ways: reciprocity and altruism.

First, an important mechanism by which subjective well-being influences rural residents' PEB is to shape the reciprocity level of rural residents in the region. The happier the individuals, the more positive emotions they have, and thus the more frequently they participate in social gatherings to enhance their social capital [38,39] that can effectively promote individual participation in collective cooperation, such as PEB [40]. Social capital is particularly important for rural residents. Compared with cities, a rural society is a more traditional "acquaintance society" with strong shared memories and close personal relationships based on kinship and geographic proximity. People establish connections through these personal relationships and gradually form a relationship network. For example, in China's rural "acquaintance society", the relationship between people is a network that maintains *renqing* (personal feelings) and interpersonal communications. In this context, high levels of social capital are conducive to promoting cooperation by enhancing information sharing and reducing cooperation risks to achieve mutual benefits [41]. Therefore, a higher subjective well-being helps rural residents to achieve reciprocity with others and thus promote PEB.

Secondly, subjective well-being, a positive subjective feeling, can also increase rural residents' fraternity and altruism. Psychological studies have found that happiness is positively related to individuals' good characteristics, such as benevolence and justice [42]. Compared with sad emotions, positive and optimistic emotions are more conducive for individuals to help others and develop pro-social behaviors [43]. Extending to environmental issues, a more philanthropic and altruistic individual is shown to have a higher level of environmental attention, which is often used as a direct or indirect measure of PEB [44,45]. A person with more subjective well-being may be more willing to sacrifice income to protect the environment because they are more generous [46]. In a nutshell, the more positive the rural residents' subjective feelings, the higher their benevolence and environmental awareness level and the stronger their willingness to adopt PEB.

## 2.3. Moderators: Gender and Environmental Knowledge

Some factors are expected to moderate the relationship between subjective well-being and PEB.

One of these factors is gender. Studies have shown that women generally show higher levels of attention to and engagement in family-oriented PEB, while men are likely to pay more attention to and participate more frequently in economic behaviors [47,48]. This is related to the traditional theory of gender socialization and the resulting division of gender roles [49,50]. According to this theory, socialization in early childhood predisposes women to the role of "caregiver". Relative to men, women display a worldview that is more concerned with life, health and relationships and empathy for the feelings and needs of others. In this sense, the behavior of women with a "maternal mindset" is more susceptible to emotional influence. Therefore, compared with men, when women's subjective well-being is higher, they are more likely to stimulate their fraternity and altruism, and then engage in more PEB.

Second, environmental knowledge may also moderate between subjective well-being and PEB. Increased environmental knowledge can deepen individuals' understanding of environmental issues and thus promote their environmental concern and responsibility [51,52] and PEB [53]. Moreover, it has been found that environment knowledge can promote the relationship between intrinsic perception, such as the perceived green value, and environmental intentions [54]. Therefore, we believe that the promotion effect of subjective well-being on rural residents is stronger when the individual's environmental knowledge level is higher.

#### 2.4. Theoretical Framework

Based on the above analysis, the theoretical framework of this paper was constructed (Figure 1). This framework explains how rural residents' subjective well-being affects their PEB. Specifically, subjective well-being promotes PEB, both the private-sphere PEB and public-sphere PEB, mainly through reciprocal and altruistic mechanisms. In addition, gender and environmental knowledge moderate the relationship between rural residents' subjective well-being and PEB. Specifically, the effect of subjective well-being on PEB is mainly driven by women and individuals with higher environmental knowledge.

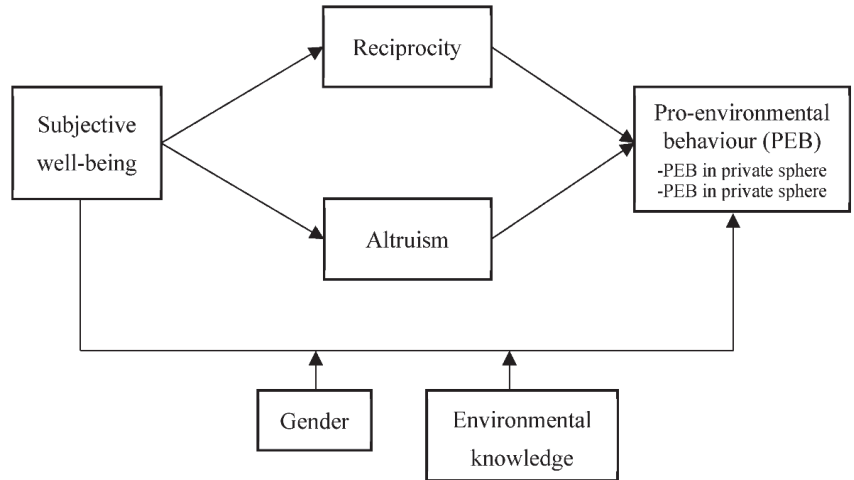


**Figure 1.** The theoretical framework.

### 3. Data Sources and Research Methods

#### 3.1. Data Sources

This study was based on the 2013 Chinese General Social Survey (CGSS2013) data. CGSS2013 is China's first nationwide, comprehensive and continuous large-scale social survey data led by Renmin University of China (Beijing, China). It is the most comprehensive and up-to-date data covering both PEBs and subjective attitudes (e.g., individuals' perception of happiness) in China, which suits well the aim of the present study. The CGSS2013 data adopts a multi-stage random sampling method. The total sample size is 11,438, including 4217 rural samples, distributed across China's 100 counties (districts) and five major cities (Beijing, Shanghai, Tianjin, Guangzhou and Shenzhen).

#### 3.2. Variable Selection

##### 3.2.1. Dependent Variable: PEB

The dependent variable of this study was PEB. The CGSS2013 questionnaire contains ten questions about individuals' PEB. Following Stern [25], five classified types of environmental behavior were selected as the private-sphere PEB, including "sorting garbage", "discussing environmental protection with relatives and friends", "shopping with own bags or baskets", "reusing plastic packaging" and "paying attention to environmental issues and environmental information"; another five types were classified as the public-sphere PEB, including "participating in environmental protection activities organized by governments", "participating in environmental protection activities organized by non-governmental environmental protection organizations", "paying for the maintenance of forests or green spaces", "donating money to environmental protection" and "participating in complaints and appeals to resolve environmental issues". Those private-sphere PEBs may benefit rural residents themselves and their neighbors, that is, these behaviors may be motivated by

self-interest or reciprocity as long as altruism. However, the benefits of public sector PEBs are much larger and more altruistic driven.

Figure 2 illustrates the distribution of rural residents’ PEBs by behavior type. The PEBs are ranked in a descending order of participation frequency: reusing plastic packaging, shopping with own bags or baskets, paying attention to environmental issues and environmental information, discussing environmental protection with relatives and friends, sorting garbage, paying for the maintenance of forests or green spaces, participating in environmental protection activities organized by governments, participating in environmental protection activities organized by non-governmental environmental protection organizations, donating money to environmental protection, and participating in complaints and appeals to resolve environmental issues. Overall, rural residents obviously adopted more PEBs in the private sphere (ranking the top five) than in the public sphere (ranking the lowest five).

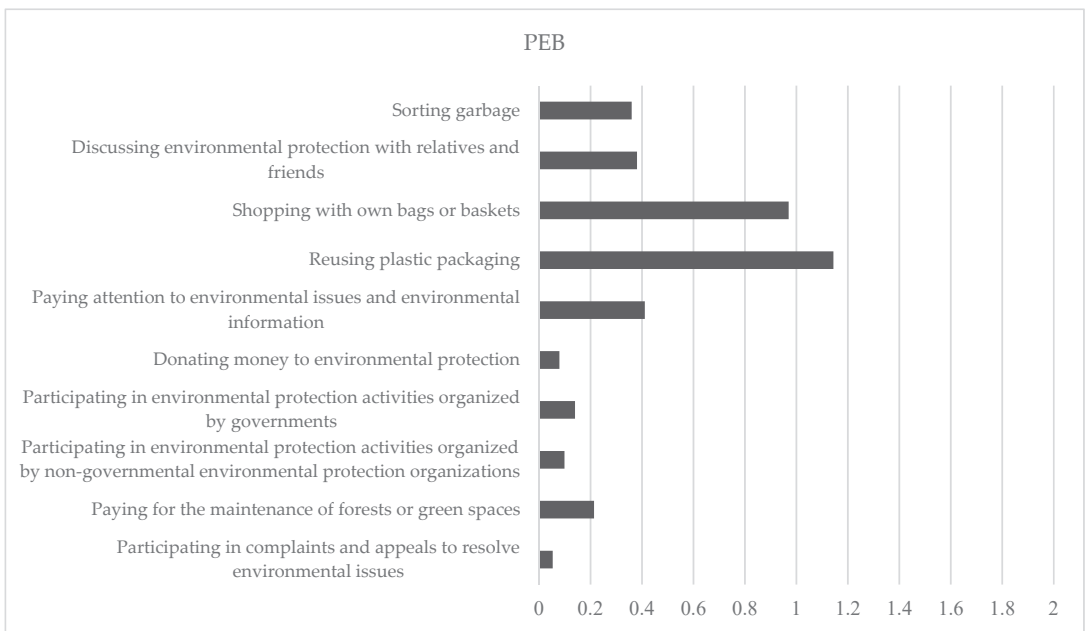


**Figure 2.** The pro-environmental behavior (PEB) of rural residents.

### 3.2.2. Key Independent Variable: Subjective Well-Being

According to the research on subjective well-being by Kahneman et al. [55] [43], the most frequently asked questions to measure subjective well-being are: “All things considered, how satisfied are you with your life as a whole?” and “In general, do you think you are happy these days?” This study used the question “In general, do you think your life is happy?” to represent the subjective well-being of rural residents, measured on a 5-point Likert scale ranging from 1 (very unhappy) to 5 (very happy). As shown in Figure 3, 12.96% of rural residents were very happy, 60.89% were happy, 15.99% were neither happy nor unhappy, 8.49% were unhappy, and 1.67% were very unhappy. In general, most rural residents showed a relatively high happiness index.

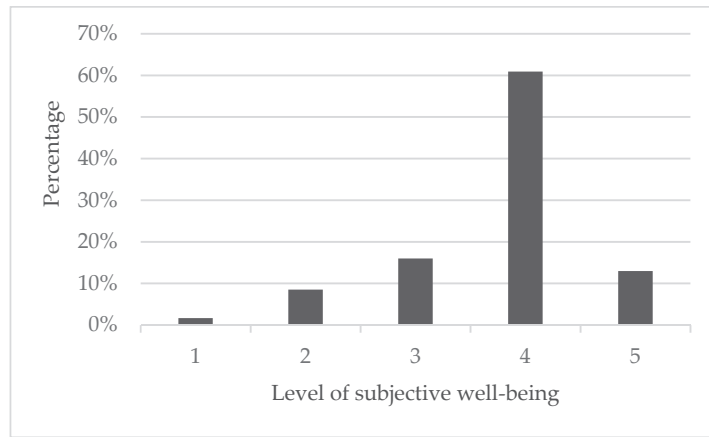


**Figure 3.** Subjective well-being of rural residents.

3.2.3. Mediating Variables: Reciprocity and Altruism

This paper used the closeness of contact between rural residents and their relatives and friends as a proxy variable to measure rural residents’ social interaction and reciprocity with others. The CGSS2013 questionnaire asks the following question to collect information on social interaction: “What is the closeness degree of contact and connection between you and your relatives and friends?” The answers are measured on a 5-point Likert scale.

In the study, the proxy variable for altruism was whether individuals are concerned about air pollution, water pollution, noise pollution, industrial waste pollution, domestic waste pollution, lack of green space, destruction of forest vegetation, degradation of cultivated land quality, shortage of freshwater resources, food pollution, desertification and reduction in wildlife. Individuals who are more concerned about environmental issues tend to have more fraternity and altruism.

3.2.4. Control Variables

According to the existing literature, environmental cognition, personal characteristics and family characteristics impact the PEB of rural residents. This study controlled the following variables: environmental cognitive variable (environmental knowledge), individual demographic characteristics (e.g., age, gender, health status, religious belief, political identity, education level, social network, social status and expectation of social class) and family characteristics variables (e.g., family income, marriage condition, number of children and number of properties). As is shown in Table 1, the above variables are discussed in detail.

**Table 1.** Descriptive statistics.

Variable	Definition	Mean	SD	Min	p50	Max
<b>Dependent variable</b>						
	Sorting garbage (1–3)	1.360	0.604	1.000	1.000	3.000
	Discuss environmental issues with relatives and friends (1–3)	1.381	0.551	1.000	1.000	3.000
Private-sphere PEB	Shopping with own bags or baskets (1–3)	1.970	0.790	1.000	2.000	3.000
	Reusing plastic packaging (1–3)	2.144	0.799	1.000	2.000	3.000
	Paying attention to environmental issues and environmental information (1–3)	1.411	0.607	1.000	1.000	3.000

Table 1. Cont.

Variable	Definition	Mean	SD	Min	p50	Max
Public-sphere PEB	Donating money to environmental protection (1–3)	1.079	0.286	1.000	1.000	2.000
	Participating in environmental protection activities organized by governments (1–3)	1.140	0.394	1.000	1.000	3.000
	Participating in environmental protection activities organized by non-governmental environmental protection organizations	1.099	0.338	1.000	1.000	3.000
	Paying for the maintenance of forests or green spaces (1–3)	1.214	0.516	1.000	1.000	3.000
	Participating in complaints and appeals that resolve environmental issues (1–3)	1.053	0.249	1.000	1.000	2.000
<b>Main independent variable</b>						
Subject well-being	Level of subjective well-being (1–5)	3.750	0.847	1.000	4.000	5.000
<b>Control variable</b>						
Environmental knowledge <sup>1</sup>	The level of understanding about environmental knowledge (0–1)	0.721	0.449	0.000	1.000	1.000
Age	Actual value (Year)	50.816	15.410	19.000	50.000	82.000
Gender	Male = 1, female = 0	0.497	0.500	0.000	0.000	1.000
Health	Self-perception of health status (1–5)	3.532	1.167	1.000	4.000	5.000
Political identity	CPC (Communist Party of China) member =1, non-CPC member =0	0.051	0.220	0.000	0.000	1.000
Education level	Never went to school = 1, primary school = 2, junior high school = 3, high school = 4, university and above = 5	2.347	1.004	1.000	2.000	5.000
Religion <sup>2</sup>	Have a religious belief = 1, have no religious belief = 0	0.116	0.320	0.000	0.000	1.000
Social network	Frequency of contact with relatives and friends (1–5)	3.422	0.865	1.000	4.000	5.000
Social class	Self-perception of social class (1–10, top = 10, bottom = 1)	4.080	1.686	1.000	4.000	9.000
Expectation of social class	Self-perception of the social class in 10 years (1–10, top = 10, bottom = 1)	5.099	2.026	1.000	5.000	10.000
Family income	Natural logarithm of family income for one year	8.789	3.365	0.000	9.904	11.918
Marriage	Married = 1, others = 0	0.940	0.237	0.000	1.000	1.000
Number of children	The number of children in the family	2.142	1.327	0.000	2.000	6.000
Number of properties	The number of real estate properties owned by the family (0–10)	1.111	0.441	0.000	1.000	3.000

<sup>1</sup> Answer an environmental knowledge question, correct = 1, wrong or do not know = 0. <sup>2</sup> Religious beliefs include Buddhism, Catholicism, Christianity, Islam and Judaism and so on: have any religious belief = 1, have no religious belief = 0.

### 3.3. Empirical Strategy

To investigate the influence of subjective well-being on the PEB of rural residents, this study employed a model with rural residents’ PEB as the dependent variable, their subjective well-being as the core explanatory variable and their environmental cognitive, individual and family characteristics as the control variables. Since the dependent variable is ordinal, this study adopted an ordered probit model as

$$PEB_i = a_0 + a_1Happy_i + \sum_{n=1} a_2D_{ni} + \varepsilon_i. \tag{1}$$

where  $PEB_i$  is the PEB of the  $i$ th rural resident, which is calculated by summing up the frequency of all the ten PEBs. Accordingly, private-sphere PEB and public-sphere PEB are calculated by summing up the frequency of the five private-sphere PEBs and five public-sphere PEBs, respectively.  $Happy_i$  is the subjective well-being of the  $i$ th rural resident.  $D_{ni}$  represents control variables, such as the individual, family and regional characteristics, of the  $i$ th rural resident and  $\varepsilon_i$  is an error term.

This identification strategy may suffer from two problems. The first one is an endogeneity problem that may lead to biased or even inconsistent parameter estimation, as reverse causality exists where subjective well-being affects the PEB of rural resident. On the one hand, the happier individuals may be more altruistic and thus participate more in PEB than the less happy ones; on the other hand, PEB may increase subjective well-being, with those who adopt PEB developing a happy mentality of “a little fragrance always clings to the hand that gives the roses”. To solve this endogeneity problem, this study further employed an instrumental variable (IV) analysis based on benchmark regression. The IVs should be related to the core explanatory variable, namely, subjective well-being, but not directly affect the dependent variable, namely, the PEB of rural residents. This study then chose the frequency of individuals’ recreational activities, such as listening to music in their spare time as an IV for subjective well-being. Recreational activities increase rural residents’ happiness, promoting subjective well-being, but they are not related to PEB. In this regard, the frequency of such recreational activities satisfies the instrumental variable selection criteria. The ERM model was selected for the estimation, referring to the practice of Roodman and Botezat [56,57]. The ERM model, which can effectively avoid the endogeneity problem, is suitable for both categorical and continuous endogenous explanatory variables. Specifically, since both the endogenous independent variable and dependent variable (i.e., PEB) are ordinal, this study used the extended oprobit (eoprobit) model for estimation.

The second problem is robustness issues, because the results we obtained from the above estimate cannot be considered reliable and credible unless the conclusion remains unchanged under changing conditions. In this study, several factors may affect the robustness of the empirical results. First, the measurement of the core explanatory variable subjective well-being may cause a robustness problem and thus the robustness analysis was conducted using a different measurement. Second, the robustness problem caused by the sample was tested mainly by using another sample. Finally, the robustness problem caused by the model estimation was tested mainly by adjusting the estimation method.

Next, to examine the mechanism (i.e., reciprocity and altruism) by which subjective well-being affects the PEB of rural residents, the mediating effect model was incorporated into Model (1), constructing the following Models:

$$Mediate_i = \beta_0 + \beta_1 Happy_i + \sum_{n=1} \beta_2 F_{ni} + \lambda_i \tag{2}$$

$$PEB_i = \gamma_0 + \gamma_1 Mediate_i + \gamma_2 Happy_i + \sum_{n=1} \gamma_3 G_{ni} + \mu_i \tag{3}$$

where  $Mediate_i$ , the mediating variable, represents the frequency of engaging in social interactions and altruism of the  $i$ th rural residents. This study examined the mediating effects of social interactions and altruism separately.  $PEB_i$ , the dependent variable, is the PEB of the  $i$ th rural residents.  $Happy_i$ , the independent variable, is the subjective well-being of the  $i$ th rural resident.  $F_{ni}$  and  $G_{ni}$  represent control variables, such as the environmental cognitive, individual, family and regional characteristics of the  $i$ th rural resident.  $\lambda_i$  and  $\mu_i$  are error terms. Specifically, in the case that  $a_1$  is significant, the mediating effect is established if  $\beta_1$  and  $\gamma_1$  are both significant at the same time. With the mediating effect established, significant  $\gamma_2$  and insignificant  $\gamma_2$  mean that  $Mediate_i$  is a partial mediating variable and a complete mediating variable, respectively.

In addition, we conducted a heterogeneity analysis to examine whether the effect of subjective well-being on PEB of rural residents differed across different groups. First, we used grouped regression to examine the impact of subjective well-being on the PEB of rural residents of different genders. Secondly, to examine the impact of subjective well-being on the PEB of rural residents with different levels of environmental knowledge, an interaction term was added into Model (1), constructing the following Model:

$$PEB_i = \delta_0 + \delta_1 Happy_i + \delta_2 Knowledge_i + \delta_3 Happy_i \times Knowledge_i + \sum_{n=1} \delta_4 H_{ni} + \tau_i \tag{4}$$



where  $Knowledge_i$  is the level of understanding about the environment of the  $i$ th rural residents.  $Happy_i \times Knowledge_i$  is the interaction term of subjective well-being and the level of environmental knowledge of the  $i$ th rural residents. The focus is on  $\delta_3$ , which is significantly positive if environmental knowledge can promote the effect of subjective well-being on the PEB of rural residents.

#### 4. Empirical Analysis

##### 4.1. The Influence of Subjective Well-Being on the PEB of Rural Residents

###### 4.1.1. Benchmark Regression

Table 2 shows that subjective well-being positively impacted the PEB of rural residents. In other words, the higher the subjective well-being of rural residents, the higher the frequency of their PEB. The PEB of rural residents were further divided into the private-sphere one and the public-sphere one. The oprobit regression results showed that both the private- and public-sphere PEBs of rural residents were significantly positively influenced by their subjective well-being. The private-sphere PEB is often self-interested and reciprocal. The higher the subjective well-being of rural residents, the more likely they adopt PEB in daily life. Moreover, increased subjective well-being helps to strengthen rural residents' "benevolence" and promote their PEB in the public sphere. Subjective well-being reflects the satisfaction and pleasure of rural residents in their daily life. Rural residents with higher subjective well-being are more satisfied with their living conditions and more willing to improve their life quality, and thus they are more intended to protect the environment to maintain or improve happiness.

**Table 2.** The influence of subject well-being on the PEB of rural residents.

	(1)	(2)	(3)
	Overall PEB	Private-Sphere PEB	Public-Sphere PEB
Subjective well-being	0.072 *** (0.021)	0.071 *** (0.021)	0.058 ** (0.028)
Environmental awareness			
Environmental knowledge	0.360 *** (0.038)	0.352 *** (0.038)	0.249 *** (0.052)
Demographics			
Age	−0.003 * (0.002)	−0.003 * (0.002)	−0.000 (0.002)
Male	−0.033 (0.036)	−0.077 ** (0.036)	0.106 ** (0.046)
Health	0.014 (0.016)	0.004 (0.017)	0.036 * (0.021)
CPC member	0.350 *** (0.083)	0.222 *** (0.078)	0.432 *** (0.089)
Education level (never went to school = control)			
Primary school	0.035 (0.045)	0.050 (0.045)	0.041 (0.066)
Junior high school	0.205 *** (0.053)	0.210 *** (0.053)	0.186 ** (0.073)
High school	0.381 *** (0.077)	0.341 *** (0.077)	0.462 *** (0.090)
University and above	0.786 *** (0.117)	0.705 *** (0.115)	0.767 *** (0.134)
Religion	0.203 *** (0.056)	0.174 *** (0.055)	0.165 ** (0.075)
Social network	0.068 *** (0.020)	0.055 *** (0.020)	0.096 *** (0.026)
Social class	−0.054 *** (0.015)	−0.050 *** (0.015)	−0.034 * (0.019)
Expectation of social class	0.063 *** (0.013)	0.062 *** (0.013)	0.033 ** (0.016)

Table 2. Cont.

	(1)	(2)	(3)
	Overall PEB	Private-Sphere PEB	Public-Sphere PEB
Family characteristics			
Family income	0.011 ** (0.006)	0.014 *** (0.005)	0.002 (0.007)
Marriage	0.005 (0.082)	−0.021 (0.081)	0.069 (0.097)
Number of children	−0.020 (0.016)	−0.011 (0.016)	−0.051 ** (0.022)
Number of properties	0.051 (0.037)	0.039 (0.038)	0.062 (0.046)
Region dummy variable	yes	yes	yes
Obs.	4055	4066	4068
Pseudo R <sup>2</sup>	0.034	0.032	0.066

Note: \*\*\*  $p < 0.01$ , \*\*  $p < 0.05$ , \*  $p < 0.10$ . Standard errors are in parenthesis.

Control variables that had significant impacts on rural residents’ PEB include environmental knowledge, social network, gender, education, political identity, health, social class, expectation of social class and the number of real estate properties.

#### 4.1.2. Endogenous Analysis

Given the endogeneity between subjective well-being and the PEB of rural residents, this study used the ERM model, and the results are shown in Table 3. The Durbin–Wu–Hausman statistic was significant, indicating an endogeneity problem. In addition, the F-value of the first-stage joint significance test was greater than 10, indicating that there was no problem of weak instrumental variables. Table 3 shows that after the introduction of IV, subjective well-being still positively influenced the PEB of rural residents in both the private and public spheres. These results are consistent with those of the benchmark regression shown in Table 2, thus indicating their reliability.

Table 3. The influence of subject well-being on PEB: endogeneity analysis.

	(1)	(2)	(3)
	Overall PEB	Private-Sphere PEB	Public-Sphere PEB
Subjective well-being	1.046 *** (0.042)	0.969 *** (0.059)	1.072 *** (0.037)
Control variables	yes	yes	yes
Region dummy variable	yes	yes	yes
DWH test	84.969 ***	66.952 ***	49.302 ***
F-stat.	13.583 ***	13.710 ***	14.010 ***
Under-identification test	13.882 ***	14.020 ***	14.290 ***
Obs.	3998	4009	4009

Note: \*\*\*  $p < 0.01$ . Standard errors are in parenthesis. “Yes” is added to indicate a series of control variables being controlled, such as environmental knowledge, age, gender, health status, political identity, education level, religion, social network, social class, expectation of social class, family income, marriage, number of children, number of properties and region dummy variable.

#### 4.1.3. Robustness Check

We then turned to the robustness analysis to test the reliability of the effect of subjective well-being on PEB. First, we re-defined subjective well-being. In Table 2, the answer to the question “In general, do you think your life is happy?” was used to describe individuals’ subjective well-being. This paper replaced the independent variable with a substitution one—individuals’ perception of a comfortable life. This substitution variable was derived

from the responses to the statement “I live a comfortable life, and there are not many things to worry about” in the CGSS2013 questionnaire. The answer was measured on a 4-point Likert scale, namely, “strongly disagree”, “disagree”, “agree” and “strongly agree”. Individuals’ perception of a comfortable life was then used to measure the individual subjective well-being, and estimate Model 1 again. Panel A in Table 4 shows that subjective well-being still had a significantly positive impact on the PEB of rural residents and the positive effect was identified in both private-sphere PEB and public-sphere PEB. This was generally consistent with the estimation results in Table 2. This means that the research results were still robust when the independent variable was changed.

**Table 4.** Robustness check.

	(1)	(2)	(3)
	Overall PEB	Private-Sphere PEB	Public-Sphere PEB
<i>Panel A: Substitution of the independent variable</i>			
Subjective well-being	0.105 *** (0.020)	0.101 *** (0.020)	0.081 *** (0.024)
Control variables	yes	yes	yes
Region dummy variable	yes	yes	yes
Obs.	4023	4034	4034
<i>Panel B: Change of sample</i>			
Subjective well-being	0.073 *** (0.022)	0.073 *** (0.022)	0.059 ** (0.029)
Control variables	yes	yes	yes
Region dummy variable	yes	yes	yes
Obs.	3807	3818	3819
<i>Panel C: Substitution of the estimation method</i>			
Nearest neighbour matching	0.585 ***	0.421 ***	0.136 **
Radius matching	0.501 ***	0.391 ***	0.107 **
Kernel Matching	0.494 ***	0.383 ***	0.105 **

Note: \*\*\*  $p < 0.01$ , \*\*  $p < 0.05$ . Standard errors are in parenthesis. “Yes” is added to indicate a series of control variables being controlled, such as environmental knowledge, age, gender, health status, political identity, education level, religion, social network, social class, expectation of social class, family income, marriage, number of children, number of properties and region dummy variable.

Secondly, we re-estimated Model 1 by changing the sample. A potential criticism is related to the sample of rural residents, as it includes those with rural *hukou* (registration of residence) and a small number of rural residents with urban *hukou* who may have different behavior patterns. To better understand the impact of subjective well-being on the PEB of genuine rural residents, that is, rural residents with rural *hukou*, this study re-estimated the findings in Table 2 using a sample that excludes those rural residents with urban *hukou*. As is shown in panel B, the results still showed that rural residents with a higher subjective well-being were more inclined to participate in PEB in both the private and public spheres, which was consistent with the results of the benchmark regression. The findings were therefore representative and robust.

Thirdly, the model estimation was tested by adjusting the estimation method. PEB is the self-selection behavior of rural residents, which may cause a self-selection bias-related endogeneity problem to previous models. The propensity score matching (PSM) method can effectively address this problem. Panel C shows the impact of subjective well-being on the PEB of rural residents under three different matching methods. Although a variety of matching methods were used, the influence direction and degree of subjective well-being on the PEB of rural residents were basically the same; the ATT value reflected the fact that rural residents with a higher subjective well-being adopted more PEBs. This was consistent with the estimation results in Table 2, which further confirmed the robustness of the estimation results.

4.2. The Mechanism by Which Subjective Well-Being Affects PEB

Theoretically, subjective well-being may affect individuals’ PEB through reciprocity and altruism. This study empirically verified the mechanism between subjective well-being and PEB.

Panel A in Table 5 shows the mediating effect of reciprocity in the relationship between subjective well-being and the PEB of rural residents. As shown in columns (1) and (2), subjective well-being had a significantly positive impact on the PEB of rural residents, under both the oprobit and eoprobit regression models. Additionally, the regression results of oprobit in column (3) and eoprobit in column (4) show that subjective well-being had a significantly positive impact on social interaction. In other words, subjective well-being helped to enhance the level of social interaction and reciprocity between rural residents and others. In addition, the oprobit regression results in column (5) and eoprobit results in column (6) both indicate that, after the introduction of the social interaction variable, subjective well-being still had a significantly positive impact on the PEB of rural residents, and social interaction per se significantly and positively influenced such behavior. According to the test process of the mediating effect constructed in the previous models (Equations (1)–(3)), it is reasonable to conclude that social interaction partially mediated the relationship between subjective well-being and the PEB of rural residents. To test the robustness of the results, this paper used the Sobel test and the generalized structural equation modelling (GSEM) to explore further the mediating effect of social interaction in the influence of subjective well-being on the PEB of rural residents. The Sobel test *p*-value was less than 0.05, and the mediating effect accounted for 24.99% of the total effect, confirming the mediating effect of social interaction. The results of GSEM show that the indirect effect was 0.080, a small coefficient but with a significant *p*-value, verifying the mediating effect; the total effect was 0.314, which was also significant; the mediating effect accounted for 25.48% of the total effect. Therefore, all the results indicate that reciprocity is indeed an essential mechanism by which rural residents’ high subjective well-being transforms into PEB.

**Table 5.** The test results of the mechanism (reciprocity) by which subjective well-being influences the PEB of rural residents.

	(1)	(2)	(3)	(4)	(5)	(6)
	PEB		Social Network		PEB	
	Oprobit	Eoprobit	Oprobit	Eoprobit	Oprobit	Eoprobit
<i>Panel A: reciprocity</i>						
Subjective well-being	0.081 *** (0.021)	1.057 *** (0.044)	0.163 *** (0.023)	0.573 *** (0.157)	0.073 *** (0.021)	1.051 *** (0.045)
Social interaction					0.067 *** (0.020)	0.032 *** (0.011)
Control variables	yes	yes	yes	yes	yes	yes
Region dummy variable	yes	yes	yes	yes	yes	yes
Obs.	4055	4055	4093	4093	4055	4055
<i>Panel B: altruism</i>						
Subjective well-being	0.081 *** (0.021)	1.057 *** (0.044)	0.077 *** (0.022)	0.871 *** (0.091)	0.069 *** (0.021)	1.034 *** (0.050)
Environmental awareness					0.059 *** (0.005)	0.031 *** (0.005)
Control variables	yes	yes	yes	yes	yes	yes
Region dummy variable	yes	yes	yes	yes	yes	yes
Obs.	4055	4055	4085	4085	4049	4049

Note: \*\*\* *p* < 0.01. Standard errors are in parenthesis. “Yes” is added to indicate a series of control variables being controlled, such as environmental knowledge, age, gender, health status, political identity, education level, religion, social network, social class, expectation of social class, family income, marriage, number of children, number of properties and region dummy variable.

Similarly, Panel B shows the mediating effect of altruism in the relationship between subjective well-being and the PEB of rural residents. It can be seen that environmental-related altruism partially mediated the relationship between subjective well-being and the PEB of rural residents. The Sobel test and the generalized structural equation modelling (GSEM) also verified the existence of the partial mediating effect of environmental-related altruism, and calculated that the mediating effect accounted for 25% of the total effect. In a nutshell, these results mean that altruism is also an essential mechanism by which rural residents' high subjective well-being transforms into PEB.

#### 4.3. A Further Analysis

Next, the heterogeneity of the empirical results was explored. The effect of subjective well-being on the PEB of rural residents may differ by gender and environmental knowledge. The discussion and analysis of the heterogeneity can more effectively clarify the mechanism that transforms subjective well-being to PEB, thus facilitating the formulation of well-targeted environmental policies.

##### 4.3.1. Heterogeneity Analysis by Gender

This study examined whether the influence of subjective well-being on the PEB of rural residents differs between genders. As shown in Table 6, the positive effect of subjective well-being on the PEB of rural residents was mainly driven by women. Specifically, such influence was much stronger in the female sample than in the male sample. This is because, as noted above, women are more compassionate and altruistic than men, and thus they are more willing to participate in PEB, which is altruistic and requires sacrificing individual interests for the collective good.

**Table 6.** The influence of subjective well-being on the PEB of rural residents by gender.

	(1)	(2)	(3)	(4)	(5)	(6)
	Male			Female		
	Overall PEB	Private-Sphere PEB	Public-Sphere PEB	Overall PEB	Private-Sphere PEB	Public-Sphere PEB
Subjective well-being	0.040 (0.031)	0.049 (0.031)	0.015 (0.038)	0.114 *** (0.029)	0.101 *** (0.029)	0.115 *** (0.041)
Control variables	yes	yes	yes	yes	yes	yes
Region dummy variable	yes	yes	yes	yes	yes	yes
Obs.	2021	2028	2029	2034	2038	2039
Pseudo R <sup>2</sup>	0.029	0.027	0.068	0.044	0.044	0.065

Note: \*\*\*  $p < 0.01$ . Standard errors are in parenthesis. "Yes" is added to indicate a series of control variables being controlled, such as environmental knowledge, age, gender, health status, political identity, education level, religion, social network, social class, expectation of social class, family income, marriage, number of children, number of properties and region dummy variable.

##### 4.3.2. Moderating Role of Environmental Knowledge

This study further explored whether environmental knowledge moderates the effect of subjective well-being on the PEB of rural residents by integrating an interaction variable "environmental knowledge  $\times$  subjective well-being". Environmental knowledge measures the individuals' mastery of environmental knowledge.

Table 7 shows that the moderating effect of the interaction between subjective well-being and environmental knowledge was positive, indicating that, when rural residents' environmental knowledge increased, the positive effect of subjective well-being on PEB significantly increased. Specifically, the positive moderating effect of environmental knowledge was identified in the private sphere.

**Table 7.** The influence of subjective well-being on the PEB of rural residents: the moderating role of environmental knowledge.

	(1)	(2)	(3)
	Overall PEB	Private-Sphere PEB	Public-Sphere PEB
Subjective well-being	0.008 (0.122)	−0.024 (0.125)	0.150 (0.184)
Subjective well-being × environmental knowledge	0.302 ** (0.141)	0.347 ** (0.143)	0.026 (0.207)
Environmental knowledge	0.399 *** (0.121)	0.348 *** (0.124)	0.448 ** (0.179)
Control variables	yes	yes	yes
Region dummy variable	yes	yes	yes
Obs.	4081	4092	4094
Pseudo R <sup>2</sup>	0.035	0.032	0.068

Note: \*\*\*  $p < 0.01$ , \*\*  $p < 0.05$ . Standard errors are in parenthesis. “Yes” is added to indicate a series of control variables being controlled, such as environmental knowledge, age, gender, health status, political identity, education level, religion, social network, social class, expectation of social class, family income, marriage, number of children, number of properties and region dummy variable.

## 5. Discussion

This paper focused on the impact of subjective well-being on the PEB of rural residents. The empirical results show that subjective well-being promoted PEB in both the public and private spheres. This means that subjective well-being reflects not only rural residents’ purely altruistic motives to participate in collective cooperation, but also their reciprocal motives. On this basis, this study further explored the mechanism by which subjective well-being influences the PEB of rural residents and found that subjective well-being influences their PEB by reciprocity and altruism. Individuals with a higher subjective well-being tend to have more reciprocity with others and more altruism and thus promoted their PEB. The heterogeneity analysis yielded two important results. First, the influence of subjective well-being on the PEB of rural residents was significantly positive in the female group, but it had no significant effect in the male group. This finding is consistent with the theory of gender socialization and the resulting division of gender roles [34,35]. Secondly, subjective well-being was more likely to promote PEB for individuals with a high environmental knowledge.

### 5.1. Theoretical Contributions

This study has made the following contributions. First, it complements the research on the influencing factors of individual PEB. Previous research has provided rich empirical evidence on the objective influencing factors of individual PEB, including socio-demographic characteristics (e.g., gender, age, location, education level and income) and social objective factors, such as social networks [5], government regulation [6] and social supervision [7]. However, few studies have focused on the subjective factors affecting PEB, the key factor motivating individuals’ spontaneous turn to PEB in the long run. Second, this study contributes to the literature on the effects of subjective well-being. The existing literature mainly focuses on the influencing factors of subjective well-being [58–60], but the literature on the effects of well-being has only slowly emerged in recent years [55], such as the influence of subjective well-being on economic growth [61], consumption and saving [62], investment and risk identification [63], immigration intentions [64], employment [65], democratic culture [66], personal income and productivity [67] and the reduction in excessive personal risk-taking [68]. This study adds knowledge to the literature by exploring the effects of subjective well-being on PEB.

### *5.2. Practical Implications*

The results of this study have important policy implications for rural environmental governance. Improving well-being is critical for the PEB of rural residents. Increasing rural residents' subjective well-being is not only an important development goal, but also the starting point and foothold of solving the contradiction between economic development and environmental protection in rural areas. Governments should strive to create a better economic and social environment, bestowing rural residents the expectation of a happy life and thus promoting their adoption of PEB. While cultivating rural residents' subjective well-being to promote PEB is a long-term task, the short-term instrumental coping strategy in the face of severe rural environmental problems is environmental protection propaganda. This study found that reciprocity and altruism are the mediating factors between subjective well-being and the PEB of rural residents. Additionally, subjective well-being plays a greater role in promoting the PEB of rural residents with a higher environmental knowledge. Therefore, extensive environmental protection publicity and environmental education will effectively promote the PEB of rural residents. In addition, the frequent interactions among rural residents are conducive to the spread and diffusion of information, knowledge and technology, and thus increase the likelihood of transforming subjective well-being into PEB. Therefore, environmental organizations can partially address rural environmental governance issues by enhancing the rural residents' social network (e.g., discussing with friends, neighbors and colleagues about what to do for the environment, how and why). Finally, given that the influence of subjective well-being on the PEB of rural residents is mainly driven by female groups, environmental protection organizations can give priority to those population groups when implementing environmental protection activities and policies, thus encouraging them to lead others to adopt PEB.

### *5.3. Limitations and Future Research*

Based on the CGSS2013 data, this study found that improving the subjective well-being of rural residents can help to promote their PEB. This result reveals that subjective factors, such as subjective well-being, play an unignorable role in promoting individual PEB in the face of environmental governance dilemmas. We call for more future research on the influence of subjective factors, such as the perception of fairness, trust and pursuit of reputation, on PEB and broader pro-social behavior. It seems to be an exciting and effective way to explore the issue of environmental governance from the perspective of subjective factors. Inevitably, this study suffers from some limitations. First, this study is embedded in the rural context, and thus the results may differ from those retrieved from the urban context. Future research can further examine the effect of urban residents' subjective well-being on their PEB and make urban-rural comparisons to deepen the understanding of this issue. Second, this study is based on the CGSS data in 2013. Although the CGSS data has been updated to 2017, it is a pity that the questionnaires after 2013 did not simultaneously collect information on PEB and subjective well-being. Therefore, while it is reasonable for this study to use CGSS2013 data, we call for future research to use updated data to validate the model results of this study. Third, this study explored the causal effect of subjective well-being on PEB, which inevitably suffers from an endogeneity problem. The effects of the endogeneity problem may not be completely excluded, though the instrumental variable method and a series of robustness tests were used to address endogeneity and verify the reliability of the results. Future studies can use longitudinal panel data to verify the results further.

## **6. Conclusions**

Given the importance of rural residents' spontaneous PEB and the positive role of subjective well-being in influencing individual behaviors, this study empirically examined the influence of rural residents' subjective well-being on their PEB and the mechanism underlying the influence based on CGSS data, which has been largely ignored by previous research. Borrowing the classification of Stern [13], this study divided PEB into two

categories, namely, the private-sphere PEB with reciprocal attributes and the public-sphere PEB with altruistic properties. Then, it revealed the different effects of subjective well-being on the two categories and their mechanisms. This study expanded existing research by examining the possible heterogeneous effects of subjective well-being on PEB among different groups.

This study found that subjective well-being promotes rural residents' participation in social cooperative PEB in both the private and public spheres. This result passed a series of robustness tests, indicating that the estimation results are reliable. The results also suggest that subjective well-being influences rural residents through not only reciprocal motives but also altruistic motives. Further mechanistic tests proved that subjective well-being promotes PEB by enhancing rural residents' interaction and reciprocity with others and altruism. In this sense, rural residents with higher levels of subjective well-being tend to have more connections with others for mutual benefit and have more good qualities, such as fraternity and altruism. Moreover, this study found that the effect of rural residents' subjective well-being on their PEB is more driven by women than by men. This conclusion is consistent with the theory of gender socialization and the resulting division of gender roles [49]. We also noticed that environmental knowledge could moderate the relationship between subjective well-being and PEB. The higher the level of the rural residents' environmental knowledge, the stronger the effect of subjective well-being on PEB, especially the private-sphere PEB.

**Author Contributions:** Conceptualization, X.O. and W.Q.; methodology, X.O. and J.Z.; validation, X.O., W.Q., D.S. and J.Z.; formal analysis, X.O.; resources, X.O. and W.Q.; data curation, X.O. and D.S.; writing—original draft preparation, X.O.; writing—review and editing, X.O., J.Z. and W.Q.; visualization, W.Q.; supervision, X.O. and W.Q.; project administration, W.Q.; funding acquisition, W.Q. All authors have read and agreed to the published version of the manuscript.

**Funding:** This research was funded by China Agriculture Research System of MOF and MARA (CARS-34-17).

**Institutional Review Board Statement:** Ethical review and approval were waived for this study due to the only data we used is publicly available. The data released by the CGSS project team has deleted the respondents' privacy, so applicants can directly apply to obtain the data without an ethical review.

**Informed Consent Statement:** Not applicable.

**Data Availability Statement:** The data is available in a publicly accessible repository: <http://www.cnsda.org/index.php?r=projects/view&id=93281139> (accessed on 25 January 2020).

**Acknowledgments:** The authors would like to extend a special thanks to Tong Zhang of the National School of Agricultural Institution and Development, South China Agricultural University and Qin Li of College of Economics and Management, South China Agricultural University for their guidance and help.

**Conflicts of Interest:** The authors declare no conflict of interest.

## References

1. Chen, M.; Chen, J.; Du, P. An inventory analysis of rural pollution loads in China. *Water Sci. Technol.* **2006**, *54*, 65–74. [[CrossRef](#)] [[PubMed](#)]
2. Karimyan, K.; Alimohammadi, M.; Maleki, A.; Yunesian, M.; Nodehi, R.N.; Foroushani, A.R. Human health and ecological risk assessment of heavy metal (loid)s in agricultural soils of rural areas: A case study in Kurdistan Province, Iran. *J. Environ. Health Sci. Eng.* **2020**, *18*, 469–481. [[CrossRef](#)] [[PubMed](#)]
3. Tam, K.P.; Chan, H.W. Generalized trust narrows the gap between environmental concern and pro-environmental behavior: Multilevel evidence. *Global Environ. Change* **2018**, *48*, 182–194. [[CrossRef](#)]
4. Cubitt, R.P.; Drouvelis, M.; Gächter, S. Framing and free riding: Emotional responses and punishment in social dilemma games. *Exp. Econ.* **2011**, *14*, 254–272. [[CrossRef](#)]
5. Videras, J.; Owen, A.L.; Conover, E.; Wu, S. The influence of social relationships on pro-environment behaviors. *J. Environ. Econ. Manag.* **2012**, *63*, 35–50. [[CrossRef](#)]
6. Zhang, R.; Zheng, H.; Zhang, H.; Hu, F. Study on the influence of social capital on farmers' participation in rural domestic sewage treatment in Nanjing, China. *Int. J. Environ. Res. Public Health* **2020**, *17*, 2479. [[CrossRef](#)]



7. Martinez, C.P.; Castaneda, M.G.; Marte, R.B.; Roxas, B. Effects of institutions on ecological attitudes and behaviour of consumers in a developing Asian country: The case of the Philippines. *Int. J. Consum. Stud.* **2015**, *39*, 575–585. [[CrossRef](#)]
8. Kahneman, D. Maps of bounded rationality: Psychology for behavioral economics. *Am. Econ. Rev.* **2003**, *93*, 1449–1475. [[CrossRef](#)]
9. Wei, X.; Yu, F. Envy and environmental decision making: The mediating role of self-control. *Int. J. Environ. Res. Public Health* **2022**, *19*, 639. [[CrossRef](#)]
10. Dedeurwaerdere, T.; Admiraal, J.; Beringer, A.; Bonaiuto, F.; Cicero, L.; Fernandez-Wulff, P.; Hagens, J.; Hiedanpää, J.; Knights, P.; Molinaro, E.; et al. Combining internal and external motivations in multi-actor governance arrangements for biodiversity and ecosystem services. *Environ. Sci. Policy* **2016**, *58*, 1–10. [[CrossRef](#)]
11. Kaida, N.; Kaida, K. Pro-environmental behavior correlates with present and future subjective well-being. *Environ. Dev. Sustain.* **2016**, *18*, 111–127. [[CrossRef](#)]
12. Zelenski, J.M.; Desrochers, J.E. Can positive and self-transcendent emotions promote pro-environmental behavior? *Curr. Opin. Psychol.* **2021**, *42*, 31–35. [[CrossRef](#)] [[PubMed](#)]
13. Glaeser, E.L.; Gottlieb, J.D.; Ziv, O. Unhappy cities. *J. Labor Econ.* **2016**, *34*, S129–S182. [[CrossRef](#)] [[PubMed](#)]
14. Quarona, F. Happiness and interpersonal relationships in economics: Theory and empirical analysis. *J. Cogn. Psychother.* **2010**, *30*, 60–72.
15. Aknin, L.B.; Van de Vondervoort, J.W.; Hamlin, J.K. Positive feelings reward and promote prosocial behavior. *Curr. Opin. Psychol.* **2018**, *20*, 55–59. [[CrossRef](#)]
16. Thoits, P.A.; Hewitt, L.N. Volunteer work and well-being. *J. Health Soc. Behav.* **2001**, *42*, 115–131. [[CrossRef](#)]
17. O'Malley, M.N.; Andrews, L. The effect of mood and incentives on helping: Are there some things money can't buy? *Motiv. Emot.* **1983**, *7*, 179–189. [[CrossRef](#)]
18. Aknin, L.B.; Dunn, E.W.; Norton, M.I. Happiness runs in a circular motion: Evidence for a positive feedback loop between prosocial spending and happiness. *J. Happiness Stud.* **2012**, *13*, 347–355. [[CrossRef](#)]
19. Isen, A.M.; Levin, P.F. Effect of feeling good on helping: Cookies and kindness. *J. Pers. Soc. Psychol.* **1972**, *21*, 384–388. [[CrossRef](#)]
20. Garaigordobil, M. Predictor variables of happiness and its connection with risk and protective factors for health. *Front. Psychol.* **2015**, *6*, 1176. [[CrossRef](#)]
21. Van Doorn, E.A.; Heerdink, M.W.; Van Kleef, G.A. Emotion and the construal of social situations: Inferences of cooperation versus competition from expressions of anger, happiness, and disappointment. *Cogn. Emot.* **2012**, *26*, 442–461. [[CrossRef](#)] [[PubMed](#)]
22. Chatelain, G.; Hille, S.L.; Sander, D.; Patel, M.; Hahnel UJ, J.; Brosch, T. Feel good, stay green: Positive affect promotes pro-environmental behaviors and mitigates compensatory “mental bookkeeping” effects. *J. Environ. Psychol.* **2018**, *56*, 3–11. [[CrossRef](#)]
23. Ibanez, L.; Moureau, N.; Roussel, S. How do incidental emotions impact pro-environmental behavior? Evidence from the dictator game. *J. Behav. Exp. Econ.* **2017**, *66*, 150–155. [[CrossRef](#)]
24. Lange, F.; Dewitte, S. Positive affect and pro-environmental behavior: A preregistered experiment. *J. Econ. Psychol.* **2020**, *80*, 102291. [[CrossRef](#)]
25. Stern, P. Toward a coherent theory of environmentally significant behavior. *J. Soc. Issues* **2000**, *56*, 407–424. [[CrossRef](#)]
26. Ramus, C.A.; Killmer, A.B.C. Corporate greening through prosocial extrarole behaviours—a conceptual framework for employee motivation. *Bus. Strategy Environ.* **2007**, *16*, 554–570. [[CrossRef](#)]
27. Sawitri, D.R.; Hadiyanto, H.; Hadi, S.P. Pro-environmental behavior from a socialcognitive theory perspective. *Procedia Environ. Sci.* **2015**, *23*, 27–33. [[CrossRef](#)]
28. Zubair, M.; Iqbal, S.; Usman, S.M.; Awais, M.; Wang, R.; Wang, X. Message framing and self-conscious emotions help to understand pro-environment consumer purchase intention: An ERP study. *Sci. Rep.* **2020**, *10*, 18304. [[CrossRef](#)]
29. Krause, A. Don't worry, be happy? Happiness and reemployment. *J. Econ. Behav. Organ.* **2013**, *96*, 1–20. [[CrossRef](#)]
30. Kirchsteiger, G.; Rigotti, L.; Rustichini, A. Your morals might be your moods. *J. Econ. Behav. Organ.* **2006**, *59*, 155–172. [[CrossRef](#)]
31. Hopfensitz, A.; Reuben, E. The importance of emotions for the effectiveness of social punishment. *Econ. J.* **2009**, *119*, 1534–1559. [[CrossRef](#)]
32. Drouvelis, M.; GROSSKOPF, B. The effects of induced emotions on pro-social behaviour. *J. Public Econ.* **2016**, *134*, 1–8. [[CrossRef](#)]
33. Drouvelis, M.; Powdthavee, N. Are happier people less judgmental of other people's selfish behaviors? Experimental survey evidence from trust and gift exchange games. *J. Behav. Exp. Econ.* **2015**, *58*, 111–123. [[CrossRef](#)] [[PubMed](#)]
34. Vlek, C.; Steg, L. Human behavior and environmental sustainability: Problems, driving forces, and research topics. *J. Soc. Issues* **2007**, *63*, 1–19. [[CrossRef](#)]
35. Corral-Verdugo, V.; Tapia, C.; García, F.; Varela, C.; Cuen, A.; Barrón, M. Validation of a scale assessing psychological restoration associated with sustainable behaviours. *Psychology* **2012**, *3*, 87–100. [[CrossRef](#)]
36. Gowdy, J. Toward a new welfare economics for sustainability. *Ecol. Econ.* **2005**, *53*, 211–222. [[CrossRef](#)]
37. Veenhoven, R. Well-being in nations and well-being of nations. *Soc. Indic. Res.* **2009**, *91*, 5–21. [[CrossRef](#)]
38. Tapia-Fonllem, C.; Corral-Verdugo, V.; Fraijo-Sing, B.; Durón-Ramos, M.F. Assessing sustainable behavior and its correlates: A measure of pro-ecological, frugal, altruistic and equitable actions. *Sustainability* **2013**, *5*, 711–723. [[CrossRef](#)]
39. Guven, C. Are happier people better citizens? *Kyklos* **2011**, *64*, 178–192. [[CrossRef](#)]
40. Zhou, Y.; Song, H.; Huang, X.; Chen, H.; Wei, W. How does social capital affect residents' waste-separation behavior? Evidence from China. *Int. J. Environ. Res. Public Health* **2022**, *19*, 3469. [[CrossRef](#)]

41. Zheng, J.; Yang, M.; Xu, M.; Zhao, C.; Shao, C. An empirical study of the impact of social interaction on public pro-environmental behavior. *Int. J. Environ. Res. Public Health* **2019**, *16*, 4405. [CrossRef] [PubMed]
42. Rick, S.; Loewenstein, G. The role of emotion in economic behavior. *Handb. Emot.* **2008**, *3*, 138–158. [CrossRef]
43. Baek, T.H.; Reid, L.N. The interplay of mood and regulatory focus in influencing altruistic behavior. *Psychol. Mark.* **2013**, *30*, 635–646. [CrossRef]
44. Oliver, D.M.; Zheng, Y.; Naylor, L.A.; Murtagh, M.; Waldron, S.; Peng, T. How does smallholder farming practice and environmental awareness vary across village communities in the karst terrain of southwest China? *Agric. Ecosyst. Environ.* **2020**, *288*, 106715. [CrossRef]
45. Salahodjaev, R. Is there a link between cognitive abilities and environmental awareness? Cross-national evidence. *Environ. Res.* **2018**, *166*, 86–90. [CrossRef]
46. Liu, W.; Aaker, J. The happiness of giving: The time-ask effect. *J. Consum. Res.* **2008**, *35*, 543–557. [CrossRef]
47. Hunter, L.M.; Hatch, A.; Johnson, A. Cross-national gender variation in environmental behaviors. *Soc. Sci. Q.* **2004**, *85*, 677–694. [CrossRef]
48. Tindall, D.B.; Davies, S.; Mauboules, C. Activism and conservation behavior in an environmental movement: The contradictory effects of gender. *Soc. Nat. Resour.* **2003**, *16*, 909–932. [CrossRef]
49. Davidson, D.J.; Freudenburg, W.R. Gender and environmental risk concerns: A review and analysis of available research. *Environ. Behav.* **1996**, *28*, 302–339. [CrossRef]
50. Zelezny, L.C.; Chua, P.P.; Aldrich, C. Elaborating on gender differences in environmentalism. *J. Soc. Issues* **2000**, *56*, 443–458. [CrossRef]
51. Liu, P.; Teng, M.; Han, C. How does environmental knowledge translate into pro-environmental behaviors? The mediating role of environmental attitudes and behavioral intentions. *Sci. Total Environ.* **2020**, *728*, 138126. [CrossRef] [PubMed]
52. Saari, U.A.; Damberg, S.; Frömling, L.; Ringle, C.M. Sustainable consumption behavior of Europeans: The influence of environmental knowledge and risk perception on environmental concern and behavioral intention. *Ecol. Econ.* **2021**, *189*, 107155. [CrossRef]
53. Cao, H.; Zhu, X.; Heijman, W.; Zhao, K. The impact of land transfer and farmers' knowledge of farmland protection policy on pro-environmental agricultural practices: The case of straw return to fields in Ningxia, China. *J. Clean. Prod.* **2020**, *277*, 123701. [CrossRef]
54. Hamzah, M.I.; Tanwir, N.S. Do pro-environmental factors lead to purchase intention of hybrid vehicles? The moderating effects of environmental knowledge. *J. Clean. Prod.* **2021**, *279*, 123643. [CrossRef]
55. Kahneman, D.; Krueger, A.B. Developments in the measurement of subjective well-being. *J. Econ. Perspect.* **2006**, *20*, 3–24. [CrossRef]
56. Roodman, D. Fitting fully observed recursive mixed-process models with cmp. *Stata J.* **2011**, *11*, 159–206. [CrossRef]
57. Botezat, A.; Pfeiffer, F. The Impact of Parents Migration on the Well-Being of Children Left Behind—Initial Evidence from Romania. ZEW—Centre for European Economic Research Discussion Paper No. 14-029. 2014. Available online: [https://papers.ssrn.com/sol3/papers.cfm?abstract\\_id=2432946](https://papers.ssrn.com/sol3/papers.cfm?abstract_id=2432946) (accessed on 10 January 2022).
58. Frey, B.S.; Stutzer, A. What can economists learn from happiness research? *J. Econ. Lit.* **2002**, *40*, 402–435. [CrossRef]
59. Wang, P.; Pan, J.; Luo, Z. The impact of income inequality on individual happiness: Evidence from China. *Soc. Indic. Res.* **2015**, *121*, 413–435. [CrossRef]
60. Huang, J.; Wu, S.; Deng, S. Relative income, relative assets, and happiness in urban China. *Soc. Indic. Res.* **2016**, *126*, 971–985. [CrossRef]
61. Kenny, C. Does growth cause happiness, or does happiness cause growth? *Kyklos* **1999**, *52*, 3–25. [CrossRef]
62. Guven, C. Reversing the question: Does happiness affect consumption and savings behavior? *J. Econ. Psychol.* **2012**, *33*, 701–717. [CrossRef]
63. Chuluun, T.; Graham, C. Local happiness and firm behavior: Do firms in happy places invest more? *J. Econ. Behav. Organ.* **2016**, *125*, 41–56. [CrossRef]
64. Akay, A.; Constant, A.; Giuliotti, C. The impact of immigration on the well-being of natives. *J. Econ. Behav. Organ.* **2014**, *103*, 72–92. [CrossRef]
65. Warr, P. Self-employment, personal values, and varieties of happiness—unhappiness. *J. Occup. Health Psychol.* **2018**, *23*, 388. [CrossRef]
66. Dorn, D.; Fischer, J.A.; Kirchgässner, G.; Sousa-Poza, A. Is it culture or democracy? The impact of democracy and culture on happiness. *Soc. Indic. Res.* **2007**, *82*, 505–526. [CrossRef]
67. De Neve, J.E.; Oswald, A.J. Estimating the influence of life satisfaction and positive affect on later income using sibling fixed effects. *Proc. Natl. Acad. Sci. USA* **2012**, *109*, 19953–19958. [CrossRef]
68. Goudie, R.J.; Mukherjee, S.; De Neve, J.E.; Oswald, A.J.; Wu, S. Happiness as a driver of risk-avoiding behaviour: Theory and an empirical study of seatbelt wearing and automobile accidents. *Economica* **2014**, *81*, 674–697. [CrossRef]



## Article

# Influence of Ventilation Operating Modes on Energy Efficiency

Jelena Tihana \*, Aleksandrs Zajacs, Dmitrijs Ivancovs and Baiba Gaujena

Department of Heat Engineering and Technology, Faculty of Civil Engineering, Riga Technical University, Kalku Street 1, LV-1658 Riga, Latvia; aleksandrs.zajacs@rtu.lv (A.Z.); dmitrijs@ivancovs.com (D.I.); baiba.gaujena@rtu.lv (B.G.)

\* Correspondence: jelena.tihana@rtu.lv; Tel.: +371-2648-1386

**Abstract:** The most significant increase in construction volumes in Latvia was registered in the time period from 2005 to the middle of 2008. Many large suburban areas around Riga were landscaped for building single-family-type houses. People have been using these properties for 12–15 years, and now, the challenge for the inhabitants is to find the most efficient way to maintain a high level of living comfort. Deteriorating systems require investments, so it is in the interest of owners to ensure that the benefits of such investments are maximized and that energy consumption is as low as possible. In this study, the authors simulated various scenarios where HVAC system parameters were changed, and the thermal performance of building structures was improved. Annual energy consumption, indoor quality and thermal comfort were analyzed. The importance of this work is justified by the need to realize and define the energy efficiency levels of existing single-family houses and demonstrate the amount of investment required to move closer to established energy efficiency targets.

**Keywords:** HVAC systems; energy consumption; thermal comfort

**Citation:** Tihana, J.; Zajacs, A.; Ivancovs, D.; Gaujena, B. Influence of Ventilation Operating Modes on Energy Efficiency. *Buildings* **2022**, *12*, 668. <https://doi.org/10.3390/buildings12050668>

Academic Editors: Roberto Alonso González-Lezcano, Francesco Nocera and Rosa Giuseppina Caponetto

Received: 9 April 2022  
Accepted: 11 May 2022  
Published: 17 May 2022

**Publisher's Note:** MDPI stays neutral with regard to jurisdictional claims in published maps and institutional affiliations.



**Copyright:** © 2022 by the authors. Licensee MDPI, Basel, Switzerland. This article is an open access article distributed under the terms and conditions of the Creative Commons Attribution (CC BY) license (<https://creativecommons.org/licenses/by/4.0/>).

## 1. Introduction

The Paris Agreement on Climate Change supports the attempts of the European Union to decarbonize the building sector and facilitate the transition from fossil fuels to renewable and locally available energy. The latest version of the Energy Performance of Buildings Directive 2018/844/EU requires the simultaneous integration of indoor environmental quality assessment with energy performance and cost-optimal requirements, without compromising comfort, wellbeing and healthy indoor climate conditions. For the promotion of energy performance in the building sector, the directive uses the common term “nearly zero-energy buildings”, which is applicable both for new buildings and buildings undergoing major renovations. In many European countries, the construction of nearly zero-energy buildings is encouraged on the national level, limiting the thermal energy consumption of buildings for heating purposes to 40–60 kWh/m<sup>2</sup> [1]. However, energy consumption for cooling buildings is not strictly regulated.

The Passive House (PH) standard provides a cost-efficient way of minimizing the energy demands of buildings in accordance with the global principle of sustainability [2,3]. The PH standard is a voluntary quality assurance standard focused upon maximizing the health and wellbeing of occupants while reducing the demand for space heating to a very low level, or 15 kWh/m<sup>2</sup>. Complementary synergistic technology approaches based on the same physics of thermal energy transfer and storage are implemented in the “net zero-energy building” approach, which means over the span of one year, a building does not use more energy than it generates.

The construction and operation of buildings is a complex process that requires an integrated approach at all stages in order to successfully meet the required energy consumption levels. When it comes to sustainable construction in particular, various certification tools are in place to help address different aspects. The best-known international certification systems are overviewed in [4], showing that all certification systems are aiming to award

buildings that ensure environmental protection, reduce energy consumption, encourage resource efficiency and strive for ambition and innovation.

During the last decade, the HVAC solutions available to the single-family house market have been significantly improved. A lot of smart solutions are available for controlling and operating systems in accordance with different IAQ parameters. Additionally, strategies for monitoring and adjusting ventilation are available, including using IoT monitoring systems and cloud computing [5]. However, not all possible contaminant sources are always realized and properly addressed. In most cases, the focus is on CO<sub>2</sub> and VOCs [6–10]. Retrofitting buildings in the area of Eastern Europe and changing from coal furnaces to gas heaters can cause the occurrence of significant CO problems [11].

When choosing suitable options for renovation, it is necessary to compare the advantages and disadvantages of applying different renovation scenarios and evaluate the comfort parameters for each of them. A unique performance and comfort optimization solution, validated by simulations built on real data acquisition, is described in [12,13].

In the case of renovation of existing buildings, careful economical evaluation and optimization methodology should be applied. Building strategies for low-energy buildings include a variety of methods and approaches. Different modeling, optimization and simulation strategies have been described in four studies, where the authors have emphasized the importance of careful calculation procedures before the implementation of energy-saving measures [14–17]. Cost-optimal analysis and indoor environmental quality assessment for nearly zero-energy buildings in temperate climates were presented by Tanasa et al. The cost-optimal analysis results show that among the investigated scenarios, the lowest global cost is achieved by a house that has a passive house envelope, mechanical ventilation with heat recovery, a heat pump and a solar collector [18].

Material selection is another issue when choosing different refurbishment solutions. The environmental impact and benefits of adding materials and technologies in order to reduce the energy consumption of a building by evaluating the embodied and operational energy were assessed by Kovacic et al. [19]. Another study provides an assessment of different materials in terms of CO<sub>2</sub>-eq savings. A careful selection of materials can reduce net CO<sub>2</sub>-eq savings by up to 68%, especially when using wood material [20]. Many studies have demonstrated that the thermal transmittance of envelope materials is not a valid parameter for the comparison and harmonization of envelope energy losses because countries set different transmittance values for each climate zone, which are then defined on the basis of different ranges of degree variations per day and calculated using different base temperatures [21–23]. Results from Albayyaa et al. show that the total energy required for heating during winter is reduced by 37% and 36% using passive solar and energy efficiency design strategies for constructing standard fibro and brick veneer houses, respectively. On the other hand, increasing the thermal mass (building materials with higher R values), utilizing different walls and flooring systems, replacing fibro houses with brick veneer houses and applying PSEEDS could reduce the total energy requirement by up to 58%. Thus, incorporating PSEEDS and higher thermal mass in the construction of residential buildings can yield significant savings in energy costs over the considered lifetime period of 50 years [24]. A study by Panão et al. shows the measured and modeled performance of the internal mass of a thermal energy battery for energy-flexible residential buildings [25]. Reda et al. propose to consider possible directions of further research in the low-energy building context, including interaction with utility networks. The general conclusion is that at northern latitudes, the energy generated onsite with conventional solar technologies is not enough to reach the net-zero energy target, and research should focus on innovative solutions, such as seasonal storage and advanced “building to urban energy networks” solutions to go even beyond the net-zero energy horizon and achieve positive energy buildings [26].

Air change rate is one of the key factors that shows the correlation between a building’s energy efficiency level and a healthy indoor environment. The proposed air change rates of 0.3–0.7 h<sup>−1</sup> represent the most commonly extracted values from the database of energy

performance certificates, which is available for practicing energy auditors. According to Blight et al., an air change (ACH) rate of  $0.3 \text{ h}^{-1}$  is recommended; otherwise, the air can become “stale” (excess  $\text{CO}_2$ , flushing of indoor air pollutants) and excessively dry (less than 40% humidity) [27]. Such low levels of air change imply the careful selection of interior finishes and furnishings, to minimize indoor air pollution from VOCs (e.g., formaldehyde). Such a low air exchange rate is very commonly applied to regular buildings without consideration of the careful selection of interior elements, as well as with the “assumption” that this air change rate will be provided by means of natural ventilation with window openings. This approach leads to the fact that many single-family homes suffer from “sick house” syndrome, and there are real complaints about the existing microclimate. In turn, the increase in air exchange entails a significant increase in energy consumption, which negatively affects the energy efficiency of the building and bills for consumed energy. Considering these factors, it is necessary to conduct a detailed analysis of building systems and propose possible solutions to improve the indoor microclimate and energy performance of buildings while reaching the goals set by the existing energy policy of the European Union.

## 2. Materials and Methods

Computational analyses were carried out using IDA Indoor Climate and Energy (IDA-ICE) 4.7 software. IDA-ICE is a tool for dynamic simulation of thermal comfort, indoor air quality and energy consumption in buildings. The accuracy of this simulation tool has been studied in several reports, which have conducted an empirical validation study of models in IDA-ICE related to the thermal behavior of buildings and HVAC equipment. A number of studies have been devoted to investigating methods of energy saving and thermal comfort with the help of simulation in IDA Indoor Climate and Energy software (IDA-ICE) [28–31]. These studies have shown the accuracy of the simulation results and their correlation with real measured parameters [32,33].

It was concluded that the agreement between the simulated and measured data was good, and disagreements were similar to the measurement uncertainty. IDA-ICE was validated according to prEN 13,791. The analyzed building model was created with Autodesk Revit software and transferred to the simulation software in IFC format.

The method proposed for the study is the analysis of the building model realized in the energy simulation software. Scenarios with different activities, such as changes in ventilation operation modes, improvement of building insulation or window change, were simulated and analyzed.

## 3. Results

### 3.1. Case Study

A two-story residential building situated in Mežares parish, Latvia, was designed as the simulation model. The thermal properties, hourly load for equipment, occupancy and lighting were set. The building is two floors high, with a balcony and a garage. A model is shown in Figure 1. The first floor consists of an entrance hall, living room and kitchen, while the bedrooms are located on the second floor, as seen in the plans in Figures 2 and 3. The locations chosen for evaluation are the living room with a kitchen zone on the first floor marked Nr. 7 on the Figure 2a plan and a bedroom on the second floor marked Nr. 12 on the Figure 2b plan.

The building has a strip foundation; the first floor is constructed as slab-on-ground. Light concrete block construction with mineral wool insulation is chosen as the typical local construction method. The wall envelope of the base project consists of several layers of mineral wool with a total thickness of 250 mm, and the total U-value of the wall is  $0.30 \text{ W}/(\text{m}^2 \times \text{K})$ . The roof envelope of the base project primarily consists of one layer of loose mineral wool with a total thickness of 650 mm that is blown into gaps between the roof wooden I-joists; it has a vapor barrier, and the finish is gypsum board on a wooden frame. Roof bituminous roll materials are installed on the OSB layer that rests on the I-joists.

The floor envelope of the base project primarily consists of a 250 mm base gravel layer, a 250 mm XPS 300 insulation layer, a vapor barrier, a 150 mm concrete slab and a parquet floor covering. The total U-value of the floor envelope is  $0.13 \text{ W}/(\text{m}^2 \times \text{K})$ .

The climate data and wind profile are used according to ASHRAE 2013. The building data used in the energy analysis are presented in Table 1. Calculations are taken from the American Society of Heating and Air-Conditioning Engineers (ASHRAE) hourly climate data for the whole year for Riga.

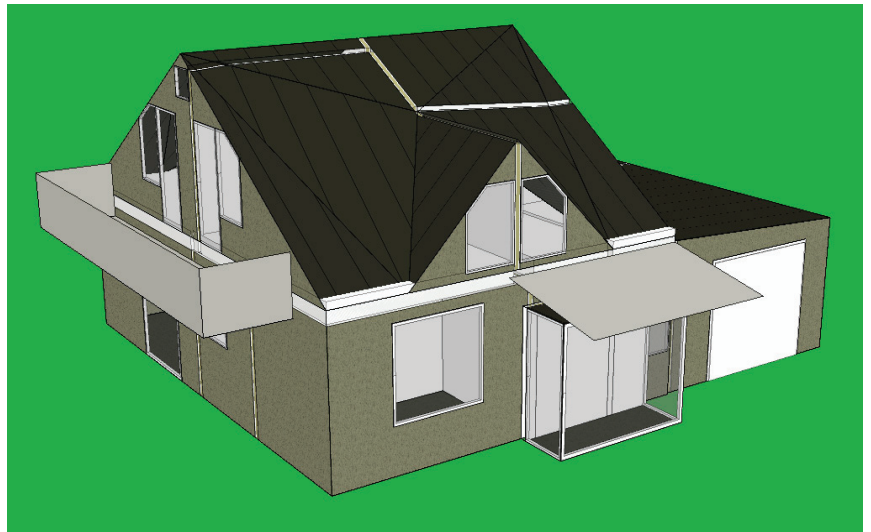


**Figure 1.** Single-family residential house building example model.

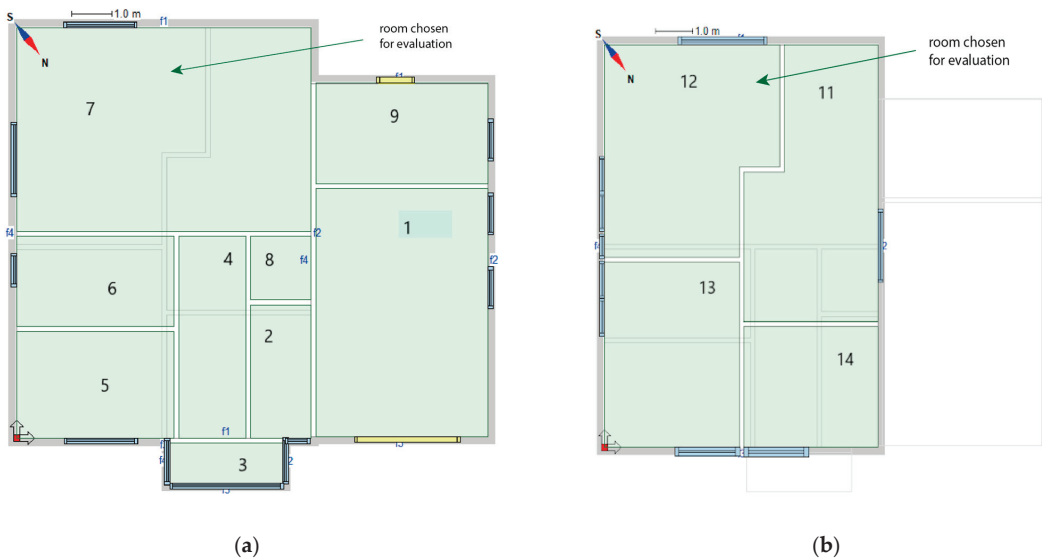
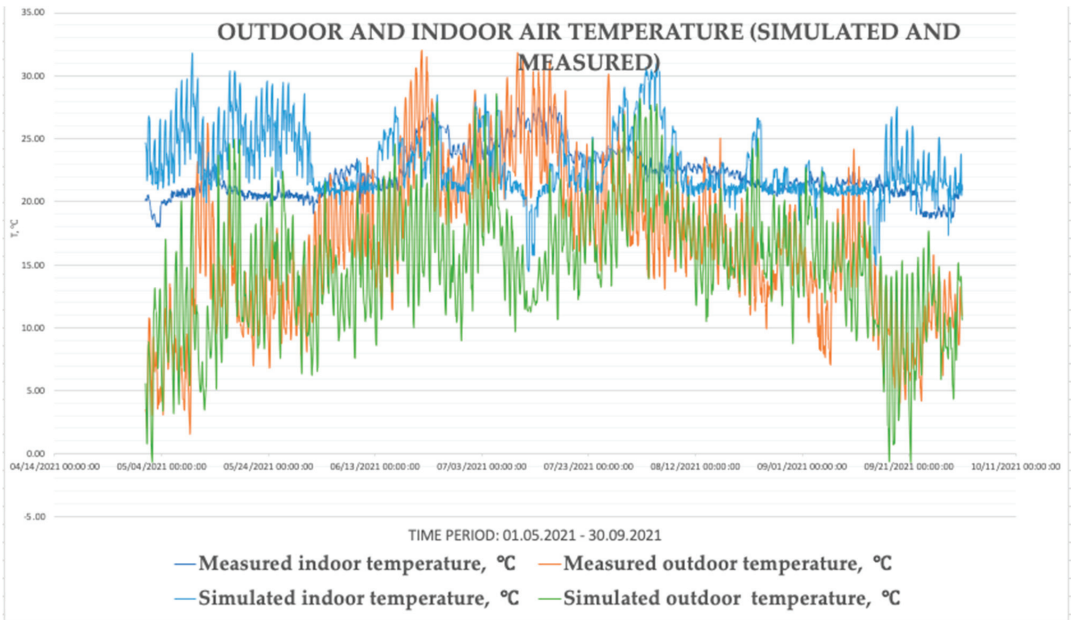
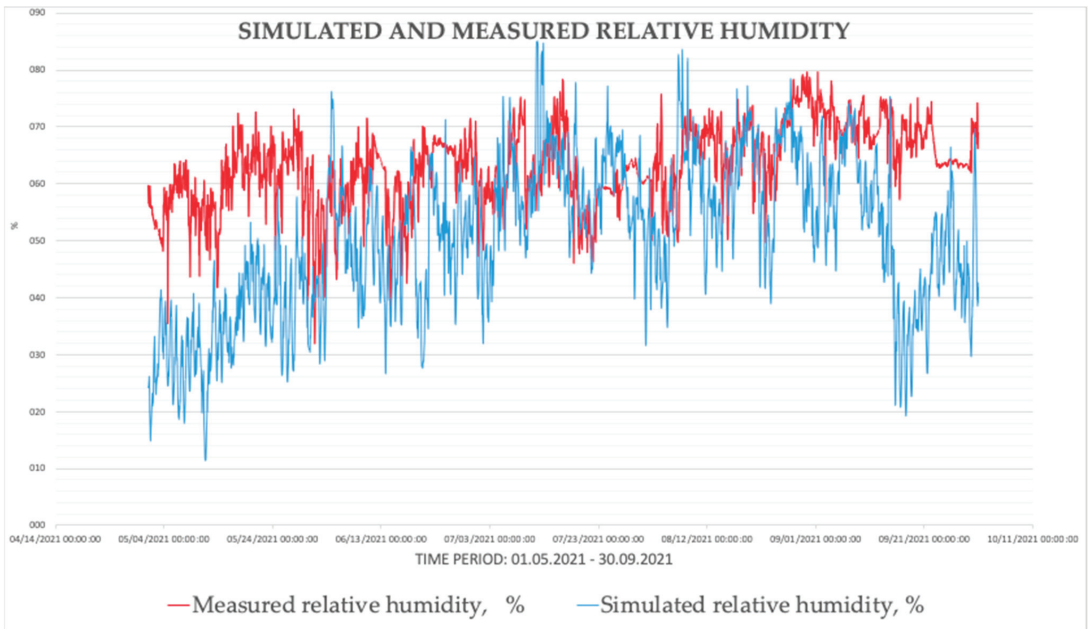


**Figure 2.** (a) First floor of single-family residential house building; (b) second floor of single-family residential house building.



(a)



(b)

Figure 3. (a) Outdoor and Indoor air temperature; (b) simulated and measured relative humidity.



**Table 1.** Outdoor average climate data for Riga (source: ASHRAE).

	Variables					
	Dry-Bulb Temperature	Rel. Humidity of Air, %	Direct Normal Rad, W/m <sup>2</sup>	Diffuse Rad. On Hor. Surf, W/m <sup>2</sup>	Wind Speed, x-Component, m/s	Wind Speed, y-Component, m/s
January	−0.1	87.6	41.3	14.2	1.9	1.3
February	−3.0	85.7	64.5	31.9	0.7	0.4
March	1.3	82.5	105.4	57.9	0.6	0.4
April	6.3	69.8	141.4	88.3	0.3	−1.2
May	12.2	65.7	183.2	116.3	0.8	−1.2
June	15.3	70.9	176.7	135	1.1	−0.9
July	17.2	78.3	162.6	126.6	1.7	0.1
August	18.1	76.6	143.8	103.8	1.4	0.2
September	12.3	77.1	104.0	71.9	−0.8	0.8
October	7.9	83.7	93.3	39	−0.2	1.9
November	2	81.5	59.3	18.6	1.3	0.1
December	−1.3	84.9	36.6	10.7	0.9	1.0

Seven different scenarios were simulated and selected for discussion in this paper. The selected scenarios are presented in Table 2 and summarize the most important parameters that were used for the comprehensive evaluation of the indoor microclimate and energy consumption of the building.

**Table 2.** Scenarios used during the simulation, their main description, ventilation system identification and heating used in each of the scenarios accordingly.

Case	Type of Ventilation System	Name of Ventilation System in IDA-ICE
“0”	Natural	Basic case
1A	Natural	Basic case + window opening night ventilation (time schedule, proportional–integral (PI) temperature control)
1B	Natural	Basic case + improved insulation
1C	Natural	Basic case + improved insulation + window change
1D	Mechanic	Basic case “0” + heat recovery
1E	Mechanic	Basic case + improved insulation + heat recovery
1F	Mechanic	Basic case + improved insulation + window change + heat recovery

For the basic scenario, Scenario “0”, natural air exchange was simulated (natural supply through windows or wall vents and mechanical exhaust in bathroom/kitchen). Windows were never opened in winter. Number of inhabitants: 4; heat source: district heating; lighting: 3 bulbs (60 W) in each room; heat gains from equipment: 3 W/m<sup>2</sup>; window opening only summer 25% from 1 of June to 15 of September, 08:00–20:00; occupant activity: 1MET (0.85 + −0.25 CLO; external wall U-value: 0.17 W/(m<sup>2</sup>×K) (fibro blocks 0.25 m + light insulation 0.15 m); window U-value: 1.46 W/(m<sup>2</sup>×K); external door U-value: 1.3 W/(m<sup>2</sup>×K); floor on ground U-value: 0.15 W/(m<sup>2</sup>×K); roof U-value: 0.15 W/(m<sup>2</sup>×K); air change rate: 0.3 h<sup>−1</sup>.

For Scenario “1A”, in addition to the scheduled conditions of the basic scenario, window opening was added, and every hour, the windows were opened for 10 min from 7:30 to 20:30 all year round (special realistic schedule based on window orientation).

For Scenario “1B”, in addition to the conditions of Scenario “1A”, the façade insulation was additionally simulated. The U-value of the external walls of 0.14 W/(m<sup>2</sup>×K) was improved by mounting polystyrene (0.2 m thick).

For Scenario “1C”, in addition to the conditions of Scenario “1B”, the installation of triple-glazed windows was simulated. The U-value of the window was 0.74 W/(m<sup>2</sup>×K).

For Scenario “1D”, in addition to the conditions of Scenario “0”, the installation of mechanical ventilation was simulated. The set indoor air temperature was +20 °C during wintertime and +22 °C during summertime (AHU 75%).

For Scenario “1E”, in addition to the conditions of Scenario “1D”, the façade insulation was additionally simulated. The U-value of the external walls of  $0.14 \text{ W}/(\text{m}^2 \times \text{K})$  was improved by mounting polystyrene (0.2 m thick).

For Scenario “1F”, in addition to the conditions of Scenario “1E”, the installation of triple glazed windows was simulated. The U-value of the window was  $0.74 \text{ W}/(\text{m}^2 \times \text{K})$ .

### 3.2. Validation of the Model

Analyzing the model, the problem of overheating in the summer period was highlighted, so the summer period from 1 May to 30 September was considered in detail. In the period from 10 May to 15 May, the measured temperature at certain moments is 15 degrees Celsius higher than the simulated temperature. Analyzing the data of the measured and simulated outdoor and indoor temperatures, the following observations can be noted: in the period from 4 June to 15 June, the measured temperature is on average  $5 \text{ }^\circ\text{C}$  higher than the simulated temperature; from 5 July to 20 July, the simulated temperature is  $10 \text{ }^\circ\text{C}$  below the measured temperature (Figure 3a).

Analyzing the relative humidity graph, the actual readings exceed the simulated readings by 20% in May and September (Figure 3b).

Considering the lethal period from 6 November to 20 December, we can make the following observations: the measured air temperature is on average  $1.5 \text{ }^\circ\text{C}$  higher than the simulated temperature. This factor can affect the total annual consumption. However, the measured outdoor temperature during the period from 5 to 15 November is  $10 \text{ }^\circ\text{C}$  higher than the simulated temperature, and during the period from 13 to 17 December, the measured temperature is  $15\text{--}20 \text{ }^\circ\text{C}$  higher than the simulated temperature (Figure 4a,b).

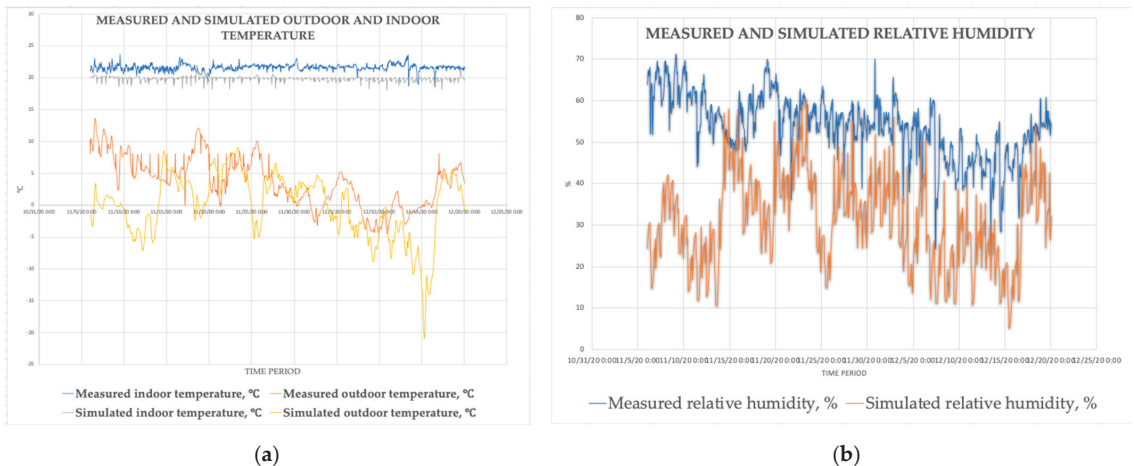


**Figure 4.** (a) Measured and simulated outdoor and indoor temperature; (b) measured and simulated relative humidity.

The measured and simulated  $\text{CO}_2$  readings show a significant difference of 55.82%. The simulated  $\text{CO}_2$  average is 773 PPM, and the measured average is 1386 PPM (Figure 5). According to EN 16798-1 “Indoor Environmental Quality Categories”, the indoor comfort quality levels have the following breakdown: QI—high, QII—medium, QIII—moderate and QIV—low. An average level of  $\text{CO}_2$  would be most applicable. The highest level can be chosen for areas where people with special needs are (children, the elderly, people with disabilities). Lower levels do not pose any health risk but may increase discomfort. The  $\text{CO}_2$  concentration limits are based on the indoor concentration of the substance, taking into account the outdoor concentration. In areas with comfort quality levels: QI— $\text{CO}_2$  delta 550—in the living room and 380 in the bedroom, QII— $\text{CO}_2$  delta 800—in the living

room and 550 in the bedroom, QIII—CO<sub>2</sub> delta 1350—in the living room and 950 in the bedroom and QIV—CO<sub>2</sub> delta 1350—in the living room and 950 in the bedroom.

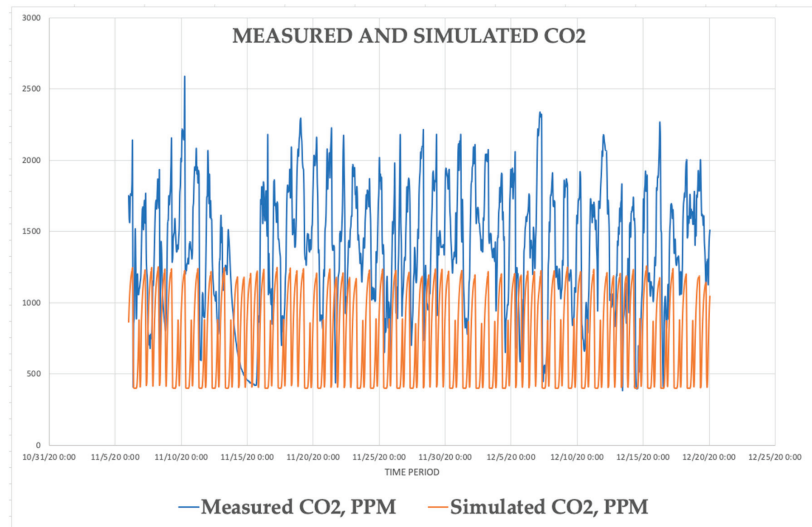


Figure 5. Measured and simulated CO<sub>2</sub>.

Differences in temperatures for all cases can be explained by the difference in outdoor temperature charts and do not influence the reliability of the results. Additionally, this can be confirmed by low deviations between the simulated and measured heat consumption data. However, the measured CO<sub>2</sub> data are significantly higher and can be explained by the location of the sensors in the area where CO<sub>2</sub> is exuded, while IDA ICE shows average CO<sub>2</sub> levels for the whole volume of the building. This parameter shows discrepancies, and simulated values cannot be used as a reliable source for evaluation of the IAQ.

The measured overall heat consumption in 2021 is 3.25% higher compared to 2020. According to the simulation program, the annual heat consumption does not change since the calculation is carried out according to the same temperature values (Figure 6a,b). The measured heat consumption is higher than the simulated heat consumption by 3.83%. The data in Table 3 show what investments need to be made according to different scenarios and the cost of energy per year, assuming that the price is 0.20 EUR/Kwh (price correlates with the actual situation during measurements in 2020–2021).

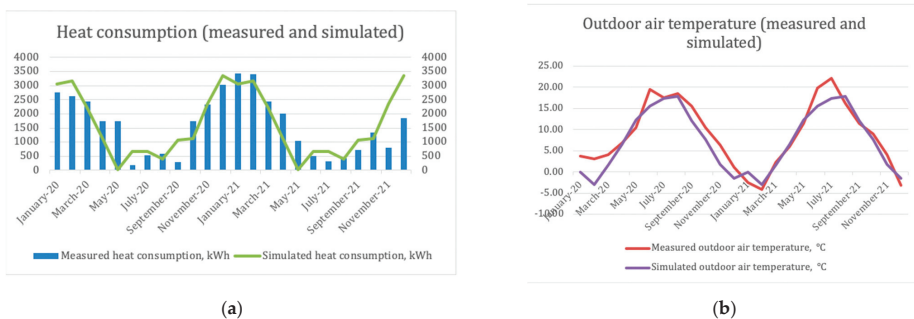


Figure 6. (a) Measured and simulated heat consumption for Scenario 1B; (b) measured and simulated outdoor air temperature.

Table 3. Energy consumption and costs for different scenarios.

Title 1	Energy Consumption, KWh/m <sup>2</sup>	Energy Consumption per Year, KWh (F = 120 m <sup>2</sup> )	Heating Costs, EUR/Year	Investments, EUR
O	52.74	6328.8	1266	
1A	120	14 400	2880	
1B	118.8	14 256	2851	4950
1C	108.6	13 032	2606	11,650
1D	111.6	13 392	2678	2500
1E	110.1	13 212	2642	7450
1E	99.54	11 944.8	2389	14,150

#### 4. Discussion

Scenario “0” is the basic case where energy consumption is quite low, but the problem of overheating occurs during the summer period. Analyzing operative temperature data for Room Nrs. 7 and 12, we can highlight the overheating temperature sector between 27 and 36 °C in the time period between 20 April and 1 June and between 15 September and 15 October. For Scenario “1A”, a window opening schedule is recorded daily throughout the period between 1 June 2020, and 15 September 2020, from 7:00 to 20:30. Opening the windows leads to a sharp increase in energy consumption from 52.74 kWh/m<sup>2</sup> to 120.3 kWh/m<sup>2</sup>, or an increase of 128% when comparing Scenarios “0” and “1A”. This action will improve the quality of indoor air. The PPM reduction is 8.3% from 12:00 to 11:00 for 6.5 months a year (period from 15 September to 15 March). It also creates additional expenses for energy, at 1614 EUR/year. Analyzing the operative temperature data for Room Nrs. 7 and 12, we can highlight the overheating temperature sector between 27 and 36 °C in the time period between 20 April and 1 June and between 15 September and 15 October. For Scenario “1B”, the U-value of the external walls is improved to 0.14 W/(m<sup>2</sup>×K), and the façade is installed by mounting polystyrene (0.2 m thick). Additional insulation of the façade ensures only 1.24% energy saving when comparing Scenarios “1A” and “1B”. The investment of EUR 4950 provides a negligible financial saving. It is not recommended to improve the insulation in this type of building for energy-saving reasons. It should only be performed in the case of insulation damage in particular areas. For Scenario “1C”, in addition to external wall insulation, installing windows with a U-value of 0.74 W/(m<sup>2</sup>×K) is planned. This ensures only 8.59% energy saving when comparing Scenarios “1B” and “1C”. However, the investment of EUR 11,650 does not pay off during the lifespan of the house. For Scenario “1D”, a mechanical ventilation system is added, resulting in a decline in energy consumption by 7% in comparison with Scenarios “1A” and “1D”. The main advantage of AHU installation is the PPM reduction is 51.7% from 12:00 to 5:50 for 6.5 months a year (period from 15 September to 15 March) and 50% from 11:00 to 5:50 for 6.5 months a year (period from 15 March to 15 September). The investment of EUR 2500 provides EUR 60 savings per year, and its payback period is about 55 years, though the indoor air quality has a positive impact and long-term nonmaterial effect on the quality of sleep, life and health of residents of the house. Analyzing the operative temperature data for Room Nrs. 7 and 12, we can highlight an overheating temperature sector between 27 and 36 °C in the time period between 20 April and 1 June and between 15 September and 15 October. This scenario is a recommended and guaranteed solution for overheating during summer periods and maintaining a healthy environment throughout the year. For Scenario “1E”, in addition to the mechanical ventilation system, the U-value of the external walls is improved to 0.14 W/(m<sup>2</sup>×K), and the façade is installed by mounting polystyrene (0.2 m thick). The additional insulation of the façade ensures only 0.9% negligible energy and financial saving in comparison to Scenarios “1D” and “1E”. The investment of EUR 4950 provides negligible financial savings. For Scenario “1F”, in addition to the AHU installation and external wall insulation, installing windows with a U-value of 0.74 W/(m<sup>2</sup>×K) is planned. This ensures 10.8% energy saving when comparing Scenarios “1F” and “1D”. However, the investment of EUR 14,150 does not pay off during the lifespan of the house.

## 5. Conclusions

Regularly opening windows (Scenario “1A”) daily throughout the period between 1 June and 15 September, 2020, leads to a PPM reduction of 8.3%, improves the quality of indoor air, but increases energy consumption sharply. The improvement of the insulation of external walls, described in Scenario “1B”, is not recommended for this type of building (a private house built 10–15 years ago) for energy-saving reasons and can be applicable in the case of insulation damage, in particular façade zones. The installation of a mechanical ventilation system, as described in Scenario “1D”, reduces energy consumption by 7% in comparison to Scenario “1A”. The main advantage of AHU installation is the PPM reduction of 50–51.7%. This scenario is a recommended and guaranteed solution for overheating during summer periods and maintaining a healthy environment throughout the year. The investment payback period is too long, though the indoor air quality has a positive impact and long-term nonmaterial effect on the quality of sleep, life and health of residents of the house.

Validation of the model demonstrates positive results, and differences in temperatures for all scenarios can be explained by the difference in outdoor temperature data.

The results of this work provide information to homeowners on how various combinations of building utility system improvements affect overall energy consumption.

**Author Contributions:** Conceptualization, A.Z.; methodology, J.T.; software, A.Z.; validation, J.T.; formal analysis, B.G. and D.I.; investigation, A.Z. and J.T.; resources, B.G., A.Z.; data curation, D.I.; writing—original draft preparation, A.Z. and J.T.; writing—review and editing, B.G. and D.I.; visualization, J.T.; supervision, D.I., Riga Technical University Doctoral Studies department; project administration, Riga Technical University Doctoral Studies Department. All authors have read and agreed to the published version of the manuscript.

**Funding:** This research was funded by post-doctoral research, Grant Number 1.1.1.2/VIAA/2/18/259 and “Efficiency of compact gas hybrid appliance in Latvian climate conditions”.



**Institutional Review Board Statement:** Not applicable.

**Informed Consent Statement:** Not applicable.

**Data Availability Statement:** Not applicable.

**Conflicts of Interest:** The authors declare no conflict of interest.

## References

1. Kalamees, T.; Lupišek, A.; Sojková, K.; Mørck, O.C.; Borodinecs, A.; Almeida, M.G.; Rovers, R.P.; Silva, S.M.; Op't Veld, P.; Kuusk, K.; et al. What kind of heat loss requirements NZEB and deep renovation sets for building envelope? In Proceedings of the CESB 2016—Central Europe Towards Sustainable Building 2016: Innovations for Sustainable Future, Prague, Czech Republic, 22–24 June; Grada Publishing: Prague, Czech Republic, 2016; pp. 137–144, ISBN 978-802710248-8.
2. Wang, Y.; Kuckelkorn, J.; Zhao, F.-Y.; Spliethoff, H.; Lang, W. A state of art of review on interactions between energy performance and indoor environment quality in Passive House buildings. *Renew. Sustain. Energy Rev.* **2017**, *72*, 1303–1319. [[CrossRef](#)]
3. Szczepanik, N.; Schnotale, J. CFD simulations and measurements of carbon dioxide transport in a passive house. In Proceedings of the 24th IIR International Congress of Refrigeration, Yokohama, Japan, 16–22 August; 2015.
4. Krizmane, M.; Slihte, S.; Borodinecs, A. Key Criteria Across Existing Sustainable Building Rating Tools. *Energy Proc.* **2016**, *96*, 94–99. [[CrossRef](#)]
5. Scislo, L.; Szczepanik-Scislo, N. Air Quality Sensor Data Collection and Analytics With IoT for an Apartment With Mechanical Ventilation. In Proceedings of the 11th IEEE International Conference on Intelligent Data Acquisition and Advanced Computing Systems: Technology and Applications (IDAACS), Cracow, Poland, 22–25 September; 2021; Volume 2, pp. 932–936. [[CrossRef](#)]
6. Staveckis, A.; Borodinecs, A. Impact of impinging jet ventilation on thermal comfort and indoor air quality in office buildings. *Energy Build.* **2021**, *235*, 110738. [[CrossRef](#)]
7. Zemitis, J.; Borodinecs, A.; Lauberts, A. Ventilation impact on VOC concentration caused by building materials. *Mag. Civ. Eng.* **2018**, *84*, 130–139. [[CrossRef](#)]

8. Bogdanovica, S.; Zemitis, J.; Bogdanovics, R. The Effect of CO<sub>2</sub> Concentration on Children's Well-Being during the Process of Learning. *Energies* **2020**, *13*, 6099. [[CrossRef](#)]
9. Zemitis, J.; Bogdanovics, R.; Bogdanovica, S. The Study of CO<sub>2</sub> Concentration in A Classroom During The COVID-19 Safety Measures. *E3S Web Conf.* **2021**, *246*, 01004. [[CrossRef](#)]
10. Zemitis, J.; Borodinecs, A.; Frolova, M. Measurements of moisture production caused by various sources. *Energy Build.* **2016**, *127*, 884–891. [[CrossRef](#)]
11. Johnston, D.; Siddall, M.; Ottinger, O.; Peper, S.; Feist, W. Are the energy savings of the passive house standard reliable? A review of the as-built thermal and space heating performance of passive house dwellings from 1990 to 2018. *Energy Effic.* **2020**, *13*, 1605–1631. [[CrossRef](#)]
12. De Vita, M.; Beccarelli, P.; Laurini, E.; De Berardinis, P. Performance analyses of temporary membrane structures: Energy saving and CO<sub>2</sub> reduction through dynamic simulations of textile envelopes. *Sustainability* **2018**, *10*, 2548. [[CrossRef](#)]
13. Prozuments, A.; Kim, A.A.; Borodinecs, A. Evaluation of the building stock thermal performance under various building code compliance scenarios: The case of Latvia. In Proceedings of the Construction Research Congress 2020: Infrastructure Systems and Sustainability—Selected Papers from the Construction Research Congress, Tempe, AZ, USA, 8–10 March; 2020.
14. Yuan, Y.; Shim, J.; Lee, S.; Song, D.; Kim, J. Prediction for Overheating Risk Based on Deep Learning in a Zero Energy Building. *Sustainability* **2020**, *12*, 8974. [[CrossRef](#)]
15. Wang, R.; Lu, S.; Feng, W. A three-stage optimization methodology for envelope design of passive house considering energy demand, thermal comfort and cost. *Energy* **2020**, *192*, 116723. [[CrossRef](#)]
16. Forde, J.; Hopfe, C.J.; McLeod, R.; Evins, R. Temporal optimization for affordable and resilient Passivhaus dwellings in the social housing sector. *Appl. Energy* **2020**, *261*, 114383. [[CrossRef](#)]
17. Niskanen, J.; Rohracher, H. Passive houses as affiliative objects: Investment calculations, energy modelling, and collaboration strategies of Swedish housing companies. *Energy Res. Soc. Sci.* **2020**, *70*, 101643. [[CrossRef](#)]
18. Tanasa, C.; Dan, D.; Becchio, C.; Corgnati, S.; Stoian, V. Cost-optimal and indoor environmental quality assessment for residential buildings towards EU long-term climate targets. *Energy Sustain. Dev.* **2020**, *59*, 49–61. [[CrossRef](#)]
19. Kovacic, I.; Reisinger, J.; Honic, M. Life Cycle Assessment of embodied and operational energy for a passive housing block in Austria. *Renew. Sustain. Energy Rev.* **2017**, *82*, 1774–1786. [[CrossRef](#)]
20. Piccardo, C.; Dodoo, A.; Gustavsson, L. Retrofitting a building to passive house level: A life cycle carbon balance. *Energy Build.* **2020**, *223*, 110135. [[CrossRef](#)]
21. Soria, B.R.; Hernández, J.D.; Pérez-Bella, J.M.; Diaz, J.J.D.C. Review of international regulations governing the thermal insulation requirements of residential buildings and the harmonization of envelope energy loss. *Renew. Sustain. Energy Rev.* **2014**, *34*, 78–90. [[CrossRef](#)]
22. Mihai, M.; Tanasiev, V.; Dinca, C.; Badea, A.; Vidu, R. Passive house analysis in terms of energy performance. *Energy Build.* **2017**, *144*, 74–86. [[CrossRef](#)]
23. Schnieders, J.; Eian, T.D.; Filippi, M.; Florez, J.; Kaufmann, B.; Pallantz, S.; Paulsen, M.; Reyes, E.; Wassouf, M.; Yeh, S.-C. Design and realisation of the Passive House concept in different climate zones. *Energy Effic.* **2020**, *13*, 1561–1604. [[CrossRef](#)]
24. Albayyaa, H.; Hagare, D.; Saha, S. Energy conservation in residential buildings by incorporating Passive Solar and Energy Efficiency Design Strategies and higher thermal mass. *Energy Build.* **2018**, *182*, 205–213. [[CrossRef](#)]
25. Panão, M.O.; Mateus, N.M.; Da Graça, G.C. Measured and modeled performance of internal mass as a thermal energy battery for energy flexible residential buildings. *Appl. Energy* **2019**, *239*, 252–267. [[CrossRef](#)]
26. Reda, F.; Fatima, Z. Northern European nearly zero energy building concepts for apartment buildings using integrated solar technologies and dynamic occupancy profile: Focus on Finland and other Northern European countries. *Appl. Energy* **2019**, *237*, 598–617. [[CrossRef](#)]
27. Blight, T.S.; Coley, D. Sensitivity analysis of the effect of occupant behaviour on the energy consumption of passive house dwellings. *Energy Build.* **2013**, *66*, 183–192. [[CrossRef](#)]
28. Luc, K.M.; Kotol, M.; Lading, T. Energy-efficient Building in Greenland: Investigation of the Energy Consumption and Indoor Climate. *Procedia Eng.* **2016**, *146*, 166–173. [[CrossRef](#)]
29. Ahmed, K.; Kurnitski, J.; Sormunen, P. Demand controlled ventilation indoor climate and energy performance in a high performance building with air flow rate controlled chilled beams. *Energy Build.* **2015**, *109*, 115–126. [[CrossRef](#)]
30. Hilliaho, K.; Lahdensivu, J.; Vinha, J. Glazed space thermal simulation with IDA-ICE 4.61 software—Suitability analysis with case study. *Energy Build.* **2015**, *89*, 132–141. [[CrossRef](#)]
31. Hilliaho, K.; Nordquist, B.; Wallentén, P.; Hamid, A.A.; Lahdensivu, J. Energy saving and indoor climate effects of an added glazed facade to a brick wall building: Case study. *J. Build. Eng.* **2016**, *7*, 246–262. [[CrossRef](#)]
32. Ryan, E.; Sanquist, T. Validation of building energy modeling to idealistic and realistic conditions. *Energy Build.* **2012**, *47*, 375–382. [[CrossRef](#)]
33. Verbai, Z.; Lakatos, Á.; Kalmár, F. Prediction of energy demand for heating of residential buildings using variable degree day. *Energy* **2014**, *76*, 780–787. [[CrossRef](#)]





Article

# Resident Willingness to Pay for Ecosystem Services in Hillside Forests

Wan-Jiun Chen <sup>1</sup>, Jih-Fa Jan <sup>2</sup>, Chih-Hsin Chung <sup>3</sup> and Shyue-Cherng Liaw <sup>4,\*</sup>

<sup>1</sup> Department of Economics, Chinese Culture University, No. 55, HawKang Rd., Taipei 111, Taiwan; cwj@ulive.pccu.edu.tw or chenwanjiun@gmail.com

<sup>2</sup> Department of Land Economics, National Chengchi University, No. 64, Section 2, Zhinan Rd., Taipei 116, Taiwan; jfjan@nccu.edu.tw

<sup>3</sup> Department of Forestry and Natural Resources, National Ilan University, No. 1, Section 1, Shennong Rd., Yilan City 260, Yilan County, Taiwan; chchung@ems.niu.edu.tw

<sup>4</sup> Department of Geography, National Taiwan Normal University, No. 162, Section 1, Heping E. Rd., Taipei 106, Taiwan

\* Correspondence: liaw@ntnu.edu.tw; Tel.: +886-7749-1649

**Abstract:** This study investigated the willingness of residents to pay for ecosystem services in a hillside forest in the Lanyang River Basin, which is among the most vulnerable watersheds in Taiwan. The economic value of provisioning, regulating, cultural, and supporting ecosystem services was evaluated. The Contingent Valuation Method (CVM) was applied for economic analysis of public welfare. The determinants of the economic values were identified. A total of 444 respondents completed the questionnaire. The results revealed that the four ecosystem services had high economic value, indicating that conserving hillside forests can ensure the welfare of nearby residents. The findings of this study can serve as reference for regional land planning and social and economic system development policies. In addition, this study addressed policy implementation from the perspective of ecological economics to contribute to an improved Anthropocene.

**Keywords:** forests; ecosystem services; local industries; economic value; organic farming; contingent valuation method

**Citation:** Chen, W.-J.; Jan, J.-F.; Chung, C.-H.; Liaw, S.-C. Resident Willingness to Pay for Ecosystem Services in Hillside Forests. *Int. J. Environ. Res. Public Health* **2022**, *19*, 6193. <https://doi.org/10.3390/ijerph19106193>

Academic Editors: Roberto Alonso González Lezcano, Francesco Nocera and Rosa Giuseppina Caponetto

Received: 5 May 2022  
Accepted: 18 May 2022  
Published: 19 May 2022

**Publisher's Note:** MDPI stays neutral with regard to jurisdictional claims in published maps and institutional affiliations.



**Copyright:** © 2022 by the authors. Licensee MDPI, Basel, Switzerland. This article is an open access article distributed under the terms and conditions of the Creative Commons Attribution (CC BY) license (<https://creativecommons.org/licenses/by/4.0/>).

## 1. Introduction

Our planet is an ecosystem. The successive evolution of our world has transformed from an empty world to a full world, as defined by ecological economists [1–5]. It is possible to conceive that our world is highly developed; however, the planetary ecosystem and resources are finite. Because the economic system is a subsystem in the planetary boundary [6,7], the finite nature of Earth's resources limits the economic growth.

Anthropocene is often used to represent the status quo of our current full world [8–11]. In previous studies, Bennett et al. [9] suggested the needs of initiatives that can lead to a better Anthropocene, and McPhearson et al. [11] also point out radical improvements are required for a better Anthropocene.

In philosophy, anthropocentrism refers to the belief that humans are the central or the most significant entity in the world. In accordance with the anthropocentric viewpoint, diverse functions performed under the circulation of the ecosystem directly or indirectly provide local residents with tangible or intangible benefits. The benefits obtained by individuals from the ecosystem refer to ecosystem services. The Millennium Ecosystem Assessment (MEA) was conducted by the United Nations to examine the effects of changes in the ecosystem on the well-being of humans. In the MEA, the relationship between ecosystem services and human well-being was determined by dividing ecosystem services into four aspects: provisioning, regulating, cultural, and supporting [12]. Provisioning services refer to material products that individuals obtain from the ecosystem, including food, fresh



water, and biofuels. Regulating services refer to benefits obtained from physical, chemical, and biological processes in nature, including natural disaster control, carbon storage, climate and water regulation, and pest and disease control. Cultural services are defined as intangible and nonmaterial benefits provided by the ecosystem to humans, including spiritual, aesthetic, educational, and recreational values and cultural diversity. Supporting services refer to indirect services provided by the biochemical cycles of ecosystems; these services are necessary for the production of provisioning, regulating, and cultural services, including fundamental processes that support soil formation, nutrient cycling, photosynthesis, biodiversity, hydrology, and nutrient cycling on which humans are highly dependent [12,13]. The multifaceted and critical functions of the ecosystem are highly valuable and closely related to the well-being of individuals living in that ecosystem [14]. Only parts of these services are traded in the market system.

Direct benefits obtained by individuals from commercialized goods that are produced from the ecosystem and traded services that are provided by the ecosystem can be clearly determined. Moreover, the price in the trading systems usually serve as determinants and the driving forces that guide people's decisions in our society. However, the price in the trading market system can only partially reflect the value of ecosystem services to humans. That the values in the market trading system cannot represent the full value of ecosystems to humans is proposed in the perspective of ecological economics [7].

In terms of environmental protection and conservation, if the value of each service provided by the ecosystem cannot be clearly identified and quantified, the intangible value that has not been quantified may be misunderstood and ignored in mainstream society, resulting in the loss of crucial ecosystem services as a result of lacking awareness. Therefore, scholars have clearly defined specific ecosystem services [12] and evaluated the value of ecosystem services [7].

Because of the complexity of ecosystem services, existing market prices cannot precisely quantify their value. In the long-term pursuit of economic growth, mainstream capitalized society has lost the balance between the natural society and human society, neglecting the coexistence of the ecological environment. From the transdisciplinary perspective of ecological economics, after economic development for a certain period, the world has transitioned from an empty world to a world full of humans and economic activities [1,2]. The space for human life and economic activities has expanded from relatively safe and flat land to hillside areas with extremely high environmental risks. Further reclamation or development can increase the multifaceted risks of hillsides, resulting in their increased sensitivity to extreme climate events such as heavy rainfall and floods. The prioritization of income growth by mainstream society has reduced the necessity and weakened the coercive and driving forces of environmental conservation and climate adaptation by the government and relevant private sectors. Assessment of the economic value of marketable and nonmarketable ecosystem services can help identify the value indicators of the four ecosystem services. Moreover, the findings of such assessment can guide the transformation of policies and strategies in the mainstream economy. On the basis of anthropocentric philosophy, the economic valuation techniques developed in the field of neoclassical economics. The assessment helps in guiding whether to conserve or exploit nature for human well-being is based on the benefit to human beings [15].

The boundary between human society and nature is the critical frontier requiring government intervention for mediation. Well-maintained forests in hillside areas enable local residents to reap benefits from ecosystem services. Hillslope lands are vulnerable to climate change and human activities [16,17]. Human disturbance can aggravate landslides and water and soil pollutions [18]. These problems are especially acute in mountainous areas in Taiwan.

Concerns regarding the conservation and protection of ecosystem services exist worldwide, and land-use changes might hinder optimal use of local ecosystem services [19]. Land-use zoning generally serves as the basis for ecological plans [20]. The Taiwanese government has planned land zoning on the basis of regional landscape characteristics in

Taiwan [21]. By using the Lanyang River Basin in Yilan County as the study site, this study evaluated the economic value of ecosystem services available in conserved low-altitude hillside forest areas, which are classified by government land classifications.

Residents were interviewed, using a questionnaire survey, to determine their opinions regarding the four ecosystem services (provisioning, regulating, cultural, and supporting) provided by the adjacent forest on the low-altitude hillside of the Lanyang River Basin. The benefits of the ecosystem services were determined using a five-point Likert scale, and the economic value of the ecosystem services was determined using the single-bounded dichotomous contingent valuation method.

The findings of this study can provide policy references for guiding the formulation and promotion of local economic development strategies, enhancing local resilience to future impacts, and reducing social and economic damage caused by inappropriate land use.

## 2. Materials and Methods

### 2.1. Study Site

The climate in Taiwan ranges from tropical to subtropical. Being surrounded by sea, Taiwan frequently experiences seasonal monsoons and severe typhoons in summer and autumn. Climate change has resulted in extreme rainfall, drought, and strong winds. In Taiwan, the mountains are high and steep, and the coastal plains, occupying a small area, are densely populated. The marginal land area is rich in natural resources. Prudent land classification and corresponding zoning to preserve forests and prevent disasters have resulted in the regulation of land use and protection of vulnerable hillside areas. Furthermore, the intervention of the government to limit the development of sloping land resources and protect steep slopes from large-scale disasters has improved the conservation of soil and water, the integrity of the overall ecosystem of the sloping land, and the protection of existing ecosystem services in hillside areas.

The impact of climate change has caused an increase in the frequency of extreme climate events and changes in the distribution patterns of high temperature and rainfall. The United Nations Intergovernmental Panel on Climate Change (IPCC) synthesized the latest research in various academic fields in the 2019 Special Report on Climate Change and Land [22], discussing climate change, land degradation, sustainable land management, food security, and greenhouse gas fluxes in terrestrial ecosystems. In the report, the IPCC indicated that more than a quarter of the world's land is facing the risk of degradation and that climate change continues to intensify; thus, strengthening the protection and restoration of forests is a key solution to prevent land degradation and disasters [22].

Extreme weather events resulting from climate change often cause substantial damage in many areas of Taiwan, especially land and rock disasters on slopes caused by high-intensity typhoon rainfall. Global warming has caused extreme climate uncertainty, changes in precipitation patterns, and drought and flood problems. Moreover, unusual weather caused by climate change is frequently reported in Taiwan and worldwide, breaking meteorological records and posing a considerable threat to a country's social economy, individuals, and property. Thus, responding to catastrophic weather has become a crucial problem in terms of national security. Uncertainty regarding climate such as uneven rainfall in the monsoon and typhoon seasons poses a particular challenge to Taiwan's slope land areas [23–26].

The gradual movement of some agricultural activities from plains to mountainous areas would exacerbate the fragmentation of the hillside landscape. Moreover, this situation would result in the hillside and its ecosystem being divided into scattered units, thus reducing the services of the ecosystem and increasing the complexity of hillside disasters. Therefore, determining the value of the ecosystem services that can be destroyed by natural disasters caused by climate change is essential, especially in the context of misleading policies or poor preparation for mitigating future climate change. However, low-altitude hillside areas, which are located at the critical interface between man and

nature, are directly affected by human activities. Because of climate change, fruits and vegetables are increasingly being cultivated in more temperate, cooler, and well-drained mountainous areas [27,28]. The optimal temperature for the growth of cabbage, which is widely cultivated in Taiwan, is approximately 20 °C. However, cabbage grows slowly and its taste is negatively affected during high temperatures in summer that exceed 30 °C. Unfavorable conditions resulting from climate change has forced the movement of agriculture to mountainous areas [27,28].

Against the backdrop of potential threats and crises, the sustainable management of the ecosystem in mountainous areas has become crucial. Determining the economic value of the ecosystem services provided by forests to residents can inform the development of policies to manage possible changes in the relationship between humans and nature in the future.

The Lanyang River Basin is located in Yilan County, northeastern Taiwan, and covers plains and high mountainous areas. This basin is rich in biodiversity and is a crucial area for agricultural production and recreational activities. The Lanyang River Basin frequently experiences strong winds, torrential rains, and typhoons, which adversely affect the ecosystem and environment. Climate change, extreme weather events, typhoons, and torrential rain may lead to the loss of soil and water resources and the destruction of sloping animal and plant habitats, posing a potential threat to the ecosystem services. In Taiwan, Yilan County is among the areas most affected by typhoons and is thus a suitable representative research area for investigating the impact of climate change on hillsides.

By using the Lanyang River Basin as the research area (Figure 1), this study analyzed the current economic value of the ecosystem services in low-altitude hillside areas to provide basic background knowledge for the management and adjustment of catchment areas.



**Figure 1.** Study site: Sanshing Township (SST), Yuangshan Township (YST), and Dongshan Township (DST) in Yilan County, Taiwan.

Three of Yilan County’s 12 townships are located at a lower altitude, a conjunct area between the Lanyang Plain and mountains, and residents live in the vicinity of the hillside. Two townships are located high on the watershed. The remaining townships are located close to the sea and have active economic activities.

In this study, the three townships located at low altitude were investigated: Sanshing Township (SST), Yuangshan Township (YST), and Dongshan Township (DST). These three townships are geographically located at the intersection of mountains and plains, with areas of 74.77, 133.69, and 78.02 km<sup>2</sup>, respectively, and population densities of 21,221, 32,177, and 52,954, respectively. In the following subsections, the basic characteristics of

these three townships are described on the basis of information provided by Yilan County Government, Taiwan [29].

#### 2.1.1. SST

SST is located to the west of the Lanyang Plain. This township contains many plains and river networks; the rocks and sand coming down from the fragile mountainous area are accumulated in riverbeds. The land SST is located on was formed following the creation of a large sandbar in the creek bed of the Lanyang River. In the past, SST was subject to frequent river flooding, and new residents arrived to reclaim the land. This township is characterized by frequent flood damage, and the principal crops were rice, peanuts, and sugarcane.

SST is prone to flooding due to its geographical location. Moreover, individuals of multiple ethnic groups reside in SST. Trade mainly occurs between individuals living in mountainous areas and individuals living on the plains. Thus, SST has been a crucial place for multiethnic and cultural fusion since ancient times and a place of ethnic and cultural conflicts and trade.

In recent decades, floods have become less frequent due to intervention by the government, and ethnic conflicts between aboriginal and Han people have been minimized following ethnic diffusion; however, the stagnation of social and economic development has prompted the exodus of many residents. Villages are now home mostly to older people and children. However, due to dedicated agricultural development in SST in the last two decades, it has attracted attention for its high-quality agricultural produce. The cultivation of green onion, garlic, silver willow, and pear has provided economic benefits to the residents and improved their lives.

#### 2.1.2. YST

YST is mostly a hilly area with a beautiful landscape. The sloping topography and climatic conditions of YST are suitable for the cultivation of various crops such as tangerines, pineapples, bamboo shoots, ginger, starfruit, leeks, guava, lotus mist, shallots, and pears. The green hills and fruit fields are particularly suitable for the promotion of agricultural recreational activities. Fruit picking services are provided during the ripening season.

#### 2.1.3. DST

DST is mostly a hilly area, and tea plants and fruits are mainly cultivated in this area. In DST, agriculture is actively transforming into precision farming to promote local agricultural recreational activities, including tea gardens, local food restaurants, and sight-seeing orchards. Tea is the most popular agricultural produce. With the efforts of local farmers' associations, the cultivation of local specialty products, such as tea, pears, pomelo, peach, and yam, is promoted. Agricultural recreational activities involve recreational forest trails in mountainous areas and visits to waterfalls, lakes, flood diversion weirs, and tree seedling nurseries.

### 2.2. Methodology

In Taiwan, because of high mountains with steep slopes, short rivers, rapid instream flow, and heavy rainstorms, dangerous hillsides and geologically fragile zones are challenging to exploit. However, long-term soil conservation practices have effectively protected hillside forest areas.

The hillside forest ecosystem provides ecosystem services for local residents, and the contingent valuation method based on consumption theory can be used to estimate the economic value of marketable and nonmarketable goods [30]. The economic value can be used as an indicator to reflect the economic value of the ecosystem services [31,32].

This study evaluated the economic value of the ecosystem services of the hillside areas of the Lanyang River Basin forest to local residents.

Ecosystem services provide both marketable and nonmarketable benefits, and their value cannot be fully and directly presented in the trading market. To determine the complete economic value of the four specific ecosystem services for residents, with the aim of facilitating government decision-making, this study used the single-bounded dichotomous contingent valuation method. This study established a hypothetical market in which respondents needed to indicate their willingness to pay a certain amount for a given service. The economic value of the ecosystem services was analyzed using the single-boundary dual-condition evaluation method. This quantitative analysis can help identify factors that affect the willingness to pay for services and the relevant amount; this information can be beneficial for formulating relevant policies.

### 2.2.1. Contingent Valuation Method

The contingent valuation method is an application of stated preference that involves (1) establishing a hypothetical market for target goods or services to be evaluated, (2) eliciting values by directly asking stakeholders, and (3) calculating the economic value of the target goods or services based on the theory of welfare economics. This method is used to evaluate various goods and services and is often used to examine nonmarketable goods and services. In the hypothetical market, various elicitation methods are used in the questionnaire. To simulate the real purchasing pattern in the exchange market, closed-ended questions are preferred over open-ended questions. Cameron and James [33] indicated that the single-bounded method with close-ended questions is efficient. The binary choice method is regarded as an ideal method. The estimation process for dichotomous choices is widely applied for evaluating environmental goods and services [34].

In binary selection, if a series of higher or lower bidding amounts remain after the first binary selection, the single-bounded dichotomous method is extended to make it double-bounded, triple-bounded, and so on. The aforementioned methods have been compared in various empirical studies [35–38]. Boyle et al. [39] used the single-bounded method, whereas Kumaraswamy [40], Sundar and Subbiah [41], Kanninen [42], Yoo and Yang [43], and Yoo and Kwak [44] have used the double-bounded method. Langford, Bateman, and Langford [45], Bateman et al. [46], and Carson and Hanemann [38] have used triple-bounded dichotomous questions. Moreover, studies have discussed the limitations and solutions of the use of these methods [47–49] in terms of bias during the survey and the respondent's psychological behaviors.

Although the increase in the bidding time in a questionnaire would shorten the interval used to estimate economic values, Hanemann et al. [50] theoretically verified that the estimation results of the double-bounded method were more statistically efficient than those of the single-bounded method. However, an increase in the bidding time would increase the complexity and difficulty in processes at both the stages of practically interviewing respondents and technically estimating the average willingness to pay. Increasing the number of the bidding inquiries involving binary choices would reduce the marginal efficiency of estimation [51].

The single-bounded dichotomous evaluation method has been employed to examine the economic value of ecosystem services in empirical studies [52–55] due to the simplicity and efficiency of the interview and analysis processes, despite considerable discussion of potential problems since its early use by Bishop, Heberlein, and Kealy [56]. Moreover, the evaluation has significance in the empirical application in ecology assessment [57–60]. Gould et al. [55] had indicated that the ecosystem services research and evaluations can advance ecological economics principles. Hence, the contingent valuation method remains useful for identifying environmental and ecological value indicators.

### 2.2.2. Residents and Respondents

In this study, local residents were regarded as critical stakeholders because they directly received the ecosystem services from the hillside forest. The residents' views on the economic value of the ecosystem services in the constructed hypothetical market

were explored in this study. The residents' willingness to pay for conserving the current ecosystem services generated from the forest present in the vicinity was evaluated.

### 2.2.3. Eliciting Process

A closed-ended questionnaire with a single-bounded dichotomous choice method was used to elicit the willingness of respondents to pay for the service. This method is similar to the ordinary trading behavior of individuals in the market, and the answering of questions is easier for respondents in this method. Respondents were required to simply indicate whether they were willing to pay the assigned amount provided in the questionnaire. The following question was asked to the respondent: "With the knowledge that the present ecosystem services will be destroyed one day, would you be willing to pay \$  $A_i^0$  to conserve your current ecosystem services now?" The dichotomous choices to be selected were "willing" or "unwilling" to pay. Such questions involving a binary response correspond to the single-bounded discontinuous contingent valuation method. If the  $i$ th response is "yes," the  $i$ -th respondent's real willingness to pay ( $A_i$ ) would be in the range ( $A_i^0, \infty$ ); if the response is "no,"  $A_i$  would be in the range of  $(0, A_i^0)$ .

### 2.2.4. Embedding Effect

The embedding effect occurs when parts of inseparable mosaics are estimated. This effect is observed when commodities are analyzed on the basis of their characteristics [61].

When the economic value of an individual service is analyzed, the embedded effect is likely to occur because the four ecosystem services are simultaneously generated from the ecosystem and are not independent commodities. The ecological circulating and functioning systems for the four ecosystem services classified by MEA [12] are not mutually exclusive. The provisioning, regulating, culture, and supporting ecosystem services cannot be separate.

Although these services can be estimated separately, the overall ecosystem value cannot be represented by the linear addition of estimated individual values because of the presence of unknown intangible and complex interconnections in the system and between them. The four ecosystem services are embedded in each other. Thus, this study analyzed the economic benefits of the four ecosystem services individually.

### 2.2.5. Payment Channel

A payment was asked for the ecosystem services to conserve the well-protected hillside forest. A well-designed payment method can promote and affect the willingness to pay and the estimated economic value of a service. In terms of payment methods, residents could use conservation funds from the local community. In addition, government taxations are usually regarded as a lump sum amount already paid for all general public services, and the inclusion of this payment channel in questionnaires tends to evoke protesting and invalid responses [62].

### 2.2.6. Estimation Procedure of the Single-Bounded Method

This study used the single-bounded method reported by Hanemann [30] to estimate the economic value. The economic value was estimated by fitting questionnaire data to the binary logit function. The logit function is as follows:

$$P(Y) = \left(1 + \exp^{-(\beta_0 + \beta_1 A + X\Phi) + e}\right)^{-1} \quad (1)$$

where  $P(Y)$  is the probability of the respondent saying "yes;"  $A$  is the bidding value;  $X$  is a vector of independent variables including the demographic characteristics of respondents;  $\beta_0$ ,  $\beta_1$ , and  $\Phi$  are parameters; and  $e$  is the random error. Estimation of the logistic model requires random errors, implying the presence of incomplete knowledge on respondents' preferences.

The point estimate of the economic value was calculated with reference to the studies of Cameron [34,63] and after performing logistic regression (1) and determining the estimated coefficient of the bidding variable  $\hat{\beta}_1$

$$E(WTP) = -1/\hat{\beta}_1 \tag{2}$$

2.2.7. Pilot, Bidding Values, and Survey

To collect information on residents’ opinions and willingness to pay for the four ecosystem services, an on-site questionnaire survey was performed during August 2021 in SST, YST, and DST. The survey interviews were performed at the township office, post office, train station, and farmers’ association of these townships. A total of 450 residents were randomly selected, of whom 90, 136, and 224 were from SST, YST, and DST, respectively; the number of the township residents depended on the total population of each township.

A total of 444 respondents completed the questionnaire, of whom 89, 136, and 219 were residents of SST, YST, and DST, respectively.

The overall bidding range and the seven bidding values were determined on the basis of WTP from the pilot by assuming that the population distribution of WTP could be reliably derived from the pilot survey. The five bidding values were 250, 500, 1000, 2000, and 3000 New Taiwan dollar (NTD), and they were randomly assigned to the respondents in the survey.

The bidding value was set at 250, 500, 1000, 2000, and 3000 NTD in accordance with the findings of the pilot survey conducted from July to August 2021. In the pilot survey, 50 residents were asked an open-ended question to determine their willingness to pay for conserving current ecosystem services in the hillside forest. The bidding values in the final survey represent the 20th, 30th, 50th, 70th, and 80th percentile (P20, P30, P50, P70, and P80, respectively) of the amount indicated in responses to the open-ended question in the pilot survey (Table 1).

Table 1. Means and percentiles of the pilot survey.

Ecosystem Services	Provision	Regulation	Culture	Support	
number of respondents	<i>n</i> = 50	<i>n</i> = 50	<i>n</i> = 50	<i>n</i> = 50	
mean	2269	2389	1927	2460	
percentile					
	P20	211	223	500	223
	P30	284	440	500	440
	P50	1000	1000	1000	1000
	P70	2000	2000	2000	2000
	P80	3000	3000	3000	3000

Unit: New Taiwan Dollar.

On the basis of the theoretical principle of welfare economics, utility occurs when an individual consumes a commodity or enjoys a service and is willing to exchange the benefit for a monetary amount. The welfare of the consumer can be calculated by following the principle of consumer theory. This study established a hypothetical market, and the residents were asked if they are willing to pay a bidding amount each year.

The bidding amounts of 250, 500, 1000, 2000, and 3000 NTD were randomly assigned to the questionnaire items. That is, the respondents simply responded to the value provided in the questionnaire item; they did not choose a specific bidding amount for each questionnaire item. The results of the survey, the statistics of responses to different bidding amounts, and the estimated economic value are reported in the next section.

3. Results

3.1. Residents’ Agreement with the Ecosystem Services

In the survey, the opinions of the residents regarding the ecosystem services provided by the nearby hillside forest were investigated. The interviewed residents exhibited high

agreement with statements regarding the hillside forest ecosystem’s ability to provide the provisioning, regulating, cultural, and supporting ecosystem services (Tables 2 and 3).

**Table 2.** Residents’ opinion regarding the ecosystem services provided by the hillside forest.

Likert Scale	5	4	3	2	1	Total
Ecosystem services						
provision	236 (53.15)	161 (36.26)	34 (7.66)	10 (2.25)	3 (0.68)	444 (100)
regulation	289 (65.09)	137 (30.86)	14 (3.15)	3 (0.68)	1 (0.23)	444 (100)
culture	247 (55.63)	164 (36.94)	25 (5.63)	8 (1.8)	0 (0.00)	444 (100)
support	254 (57.21)	161 (36.26)	26 (5.86)	2 (0.45)	1 (0.23)	444 (100)

Note: This table illustrates the number and percentage (in parentheses) for a total of 444 respondents. A 5-point Likert-type scale was used to measure the agreement of the residents with statements regarding the ecosystem services provided by the low-latitude forest in the vicinity. The responses for the 5-point scale were strongly agree, agree, neutral, disagree, and strongly disagree for the scores of 5, 4, 3, 2, and 1, respectively.

**Table 3.** Residents’ opinions regarding the ecosystem services (by township).

Township	SST (n = 89)					YST (n = 136)					DST (n = 219)					
	Likert Scale	5	4	3	2	1	5	4	3	2	1	5	4	3	2	1
Ecosystem services																
provision	55 (12.39)	29 (6.53)	5 (1.13)	0 (0.00)	0 (0.00)	79 (17.79)	50 (11.26)	5 (1.13)	1 (0.23)	1 (0.23)	102 (22.97)	82 (18.47)	24 (5.41)	9 (2.03)	2 (0.45)	
regulation	60 (13.51)	25 (5.63)	3 (0.68)	1 (0.23)	0 (0.00)	96 (21.62)	36 (8.11)	3 (0.68)	0 (0.00)	1 (0.23)	133 (29.95)	76 (17.12)	8 (1.80)	2 (0.45)	0 (0.00)	
culture	50 (11.26)	35 (7.88)	4 (0.90)	0 (0.00)	0 (0.00)	80 (18.02)	41 (9.23)	10 (2.25)	5 (1.13)	0 (0.00)	117 (26.35)	88 (19.82)	11 (2.48)	3 (0.68)	0 (0.00)	
support	56 (12.61)	27 (6.08)	5 (1.13)	0 (0.00)	1 (0.23)	80 (18.02)	52 (11.71)	4 (0.90)	0 (0.00)	0 (0.00)	118 (26.58)	82 (18.47)	17 (3.83)	2 (0.45)	0 (0.00)	

Note: This table illustrates the number and percentage for a total of 444 respondents.

### 3.2. Response Statistics of Different Bidding Amounts

The different bidding amounts were distributed evenly (Table 4).

**Table 4.** Even distribution of the bidding amount in the three townships.

Townships	SST		YST		DST		Total	
Bid	Number	%	Number	%	Number	%	Number	%
250	18	20.22	28	20.59	42	19.18	88	19.82
500	17	19.10	27	19.85	42	19.18	86	19.37
1000	18	20.22	27	19.85	45	20.55	90	20.27
2000	18	20.22	27	19.85	45	20.55	90	20.27
3000	18	20.22	27	19.85	45	20.55	90	20.27
sum	89	100.00	136	100.00	219	100.00	444	100.00

The interviewees were asked to indicate if they were willing to pay the assigned bidding amount. Respondents answered “yes” if their valuation of the ecosystem service was higher than the bidding amount and “no” if their valuation was lower than the amount asked. Table 5 presents the statistical data of the respondents’ responses; the number of positive responses slightly declined with the increase in the bidding amount in the three townships.



Table 5. Agreement to pay the corresponding bidding amount.

Bid	Provision			Regulation		Culture		Support	
	Number of Respondents	Number “Yes” Response	%	Number “Yes” Response	%	Number “Yes” Response	%	Number “Yes” Response	%
250	88	52	59.09	54	61.36	47	53.41	51	57.95
500	86	45	52.33	48	55.81	45	52.33	45	52.33
1000	90	47	52.22	47	52.22	44	48.89	46	51.11
2000	90	37	41.11	35	38.89	36	40.00	36	40.00
3000	90	32	35.56	32	35.56	29	32.22	32	35.56
Sum (%)	444	213 (47.97)		216 (48.65)		201 (45.27)		210 (47.30)	

The results indicated that 60.67%, 58.82%, and 55.71% of the residents of SST, YST, and DST were willing to pay. Most of the respondents strongly agreed with the value of the ecosystem services provided by the hillside forest in the Lanyang River Basin. Nearly half of the respondents expressed that they were willing to pay the bidding amount.

### 3.3. Determinants of Residents’ Willingness to Pay

This study performed logit regression to analyze the determinants of the residents’ willingness to pay for the randomly assigned bidding amount. On the basis of the estimates of logit regression, the economic value of the ecosystem services was calculated by following Cameron [34]. The dependent variable  $P(Y)$  was the binary responses of the residents in the single-bounded contingent valuation method and calculated as follows:

$$P(Y_i) = f\left(\text{BID}_i, \text{AGREE}_{EE_i}, \text{GENDER}_i, \text{OCCU}_{D_{\text{PUBLIC}}}_i, \text{STAY}_{HR}_i, \text{AGE}_{D60}_i * \text{INC}_{D30}_i, \text{INC}_{10T}_i, \text{DON}_{D_i}\right) + \mu_i \quad (3)$$

where  $\mu$  is the residual and subscript  $i$  represents the  $i$ th respondent. Table 6 presents the definitions of the variables included in this regression and their descriptive statistics. In addition to the bidding variables, demographic variables have high accessibility and are often used as regressors. Other variables, namely the individual agreement with the value of the ecosystem services offered by the forest, length of stay per visit to represent the personal interaction with the hillside forest, and history of monetary donation for environmental protection, were included in logistic regression. The degree of the agreement of the respondents with statements regarding the value of the four ecosystem services was measured using a five-point Likert scale. Because the five points used in the Likert scale were not equidistant, its arithmetic mean is not indicated in the statistics in Table 6. Monetary donation for environmental protection, which is an actual economic response action, was included as a regressor.

Table 7 lists the estimated results of logistic regression. The extrapolation and interpolation results indicated significant variables in logistic regression. The variables listed in Table 7 were examined using the chi-square test and Student’s  $t$  test, and high collinearity was not observed between the explanatory variables. The chi-square test was used to examine associations between categorical variables, and Student’s  $t$  test was used to determine correlations between continuous variables. The determinants were determined on the basis of the estimates in Table 7.

In the estimated logit regression model, the bidding amounts assigned to the respondents (variable BID) were significantly negatively correlated with the four ecosystem services. The willingness to pay tended to decrease with the increase in the bidding amount. However, the bidding amount was not the only significant variable.

The willingness to pay increased with agreement regarding the value offered by the hillside forest in terms of the four ecosystem services.

Table 6. Definitions of variables.

Variable	Definition	Mean (S.D.)			
		SST	YST	DST	Total
$P(Y)$	Binary dependent variable, used to represent the willingness to pay. In the survey, if the respondent indicated “yes”, $P(Y) = 1$ ; otherwise, it is 0.	-	-	-	-
C	Constant	-	-	-	-
BID	The bidding value (New Taiwan dollar, NTD)	-	-	-	-
AGREE <sub>EE</sub>	Agreement with the ecosystem services. *	-	-	-	-
GENDER	Gender dummy, 1, if female 0, if male	0.56 (0.50)	0.52 (0.50)	0.45 (0.50)	0.50 (0.50)
OCCU <sub>DPUBLIC</sub>	Occupation dummy, 1, those who do not directly depend on local resources for their livelihood, such as those in the military, civil service, and education sector; 0, otherwise.	0.11 (0.32)	0.10 (0.31)	0.09 (0.29)	0.10 (0.30)
STAY <sub>HR</sub>	Average length of stay per visit (hours)	1.76 (1.12)	1.78 (1.16)	1.79 (1.15)	1.78 (1.14)
AGE <sub>D60</sub> × INC <sub>D30</sub>	AGE <sub>D60</sub> × INC <sub>D30</sub> = 1 if older resident with low income; otherwise, the value is 0. #	0.15 (0.36)	0.14 (0.35)	0.12 (0.32)	0.13 (0.34)
INC <sub>10T</sub>	Yearly household income (10,000 NTD)	51.40 (33.95)	56.54 (37.56)	57.58 (32.82)	56.02 (34.56)
DON <sub>D</sub>	Donation dummy 1, history of donation for environmental protection; 0, otherwise.	0.21 (0.41)	0.29 (0.45)	0.20 (0.40)	0.23 (0.42)

Note: Standard deviations are indicated in parentheses. \* A typical 5-point Likert scale was used (5 = strongly agree, 4 = agree, 3 = neutral, 2 = disagree, and 1 = strongly disagree). # Two dummy variables were multiplied to create a variable (AGE<sub>D60</sub> × INC<sub>D30</sub>) representing older residents with low income. AGE<sub>D60</sub> = 1, if age > 60 years; otherwise, the value is 0. INC<sub>D3</sub> = 1 if the yearly household income is <300,000 NTD; otherwise, the value is 0.

Table 7. Estimation results of the logit model.

Aspects of Ecosystem Services	Provision		Regulation		Culture		Support				
	Coefficient	Prob.	Coefficient	Prob.	Coefficient	Prob.	Coefficient	Prob.			
C	-2.3566	**	0.0013	**	0.0016	-2.4930	**	0.0017	**	0.0017	
BID	-0.000372	***	0.0004	***	≤0.0001	-0.000388	***	0.0002	-0.000392	***	0.0002
AGREE <sub>EE</sub>	0.4985	***	0.0009	**	0.0014	0.4488	**	0.0062	0.5151	**	0.0023
GENDER	-0.3321		0.1157	*	0.0460	-0.2621		0.2130	-0.3379		0.1060
OCCU <sub>DPUBLIC</sub>	-1.1301	**	0.0017	**	0.0035	-1.0967	**	0.0028	-1.0541	**	0.0031
STAY <sub>HR</sub>	0.1631		0.0802	**	0.0355	0.2161	*	0.0196	0.2006	*	0.0294
AGE <sub>D60</sub> × INC <sub>D30</sub>	-1.0980	**	0.0025	**	0.0034	-0.8493	*	0.0161	-1.0427	**	0.0030
INC <sub>10T</sub>	0.0089	*	0.0109	**	0.0065	0.0100	**	0.0040	0.0087	**	0.0098
DON <sub>D</sub>	0.8491	**	0.0010	**	0.0025	0.8886	***	0.0005	0.6833	**	0.0068

Note:  $P(Y)$  is the dependent variable. Refer to Table 6 for variable definitions. \*, \*\*, and \*\*\* significant at the 10%, 5%, and 1% levels, respectively. Standard errors are in parentheses.

The willingness to pay for conserving the regulating, culture, and supporting ecosystem services exhibited a significant positive association with length of stay per visit. Length of stay per visit was included in this study as a variable to represent personal direct interaction with the hillside forest because the regulating, culture, and supporting ecosystem services necessitate on-site interaction between humans and nature.

An individual’s judgment regarding the affordability of a service is constrained by income. Household income positively affected the willingness to pay the bidding amount.

The residents who were employed in the military, civil service, or education sector tended to reject the payment. Moreover, those who did not directly depend on local resources for their livelihood declined to pay for conserving the ecosystem services. Those who had high reliance on forest resources for their livelihood assigned higher value to the ecosystem services.

An individual’s willingness to pay for conserving the ecosystem services offered by the forest was strongly influenced by a history of donations for environmental protection. The residents who had ever donated for environmental protection were more willing to pay.

The older residents with low income tended to decline paying the bidding amount because of their perception of affordability and local economic stagnation. Rampant urbanization in Taiwan has prompted the exodus of people from rural areas despite local social and economic development initiatives promoted by the government [64].

The women were more willing than men to pay for conserving the regulating ecosystem services; willingness to pay for the other services did not differ significantly between the sexes.

### 3.4. Economic Value of the Ecosystem Services

This study examined the economic value of the ecosystem services on the basis of the results of the single-bounded dichotomous contingent valuation method and regression analysis (Table 7).

The economic value of the forest ecosystem services to residents was determined by evaluating the residents’ willingness to pay for conserving the current ecosystem services that they received and enjoyed. Some respondents psychologically resisted paying for the ecosystem services they already had access to; these should be classified as protesting samples. Those who did not agree with the economic value received no benefits from the ecosystem services. The protesting residents were unwilling to pay the bidding amount, indicating that the economic value they assigned to the service was lower than the bidding amount.

The point estimates for the economic value of the provisioning, regulating, culture, and supporting ecosystem services were 2688.17, 2092.05, 2577.32, and 2551.02 NTD, respectively (Table 8).

**Table 8.** Point estimates of the economic value of the ecosystem services. Unit: NTD.

Aspects of Ecosystem Services	Provision	Regulation	Culture	Support
	2688.17	2092.05	2577.32	2551.02

Note: Cameron [34,63] indicated that the point estimates of the willingness to pay in the single-bounded contingent valuation method can be approximated using the formula  $E(WTP) = -1/\beta_1$ , and the  $\beta_1$  is the estimator of the bidding variable in logit regression.

## 4. Discussion

### 4.1. Land Zoning Policy and Government Intervention

Taiwan is located at the junction of the Eurasian plate and the Philippine plate and has high mountains and steep slopes. The Lanyang River Basin, located in northeast Taiwan, is the most vulnerable watershed on the island. The stream, only 73 km long, originates from more than 3000 m above sea level from the northern Nanhu Mountain, to rush into the sea. It flows through the entire Yilan County. The watershed covers an area of 978 km<sup>2</sup> [65]. In the middle- and high-altitude areas of the Lanyang River Basin (areas with an altitude of approximately 500 m above sea level), the mountains are high and steep, with limited human activities. Where the Lanyang River flows into the foothills in its downstream reaches, local residents are typically involved in agricultural activities. The river then enters the delta plain, which is metropolitan area with numerous human activities.

The land zoning plan implemented by the government calls for forest coverage in the foothills of the Lanyang River Basin, and local ecosystem services are relatively effective. However, the basin is affected by land-use patterns such as agricultural reclamation.

Because the entire water catchment area is located in the northeast of Taiwan and it is on the windward side of most typhoons striking the island, the land is highly vulnerable. Thus, this land has been the focus area of global environmental changes. The benefits and impacts of low-altitude piedmont forest ecosystems on local residents merit in-depth study and evaluation and are directly related to the current agricultural reclamation development and climate change adaptation. Further human exploitation would result in an increase in the risk of disasters.

The evidences provided in this study affirmed the need to conserve hillside forests as the residents have high agreements toward the four aspects of the ecosystem services (Tables 2 and 3).

Moreover, with the increasing threat of natural disasters due to climate change, information on the value of the ecosystem services can be used as a policy basis for the management of low-altitude sloping land disaster risk systems. The economic values of the ecosystem services the residents received are evidenced high as indicated in Table 8. This information can promote the establishment of disaster adaptation strategies for maintaining the hillside ecosystem and its services as well as facilitate the overall spatial planning for hillside areas under climate change.

#### *4.2. Better Governance of Our Full World at Current Anthropocene*

Based on the image of our current world—a full world, as it is called by Herman Dally [1]—it tends to be a world of anthropocentric Anthropocene, and humans are the primary benefactors and the receivers of ecosystem services [66,67]. Hence, the present study assessing for a relevant value indicator that can serve as an index for government interventions would help a better governance of our full world at current Anthropocene. The economic values of provisioning, regulating, cultural, and supporting ecosystem services enhance the feasibility of policy formation for land zoning at mountain frontiers in an ultimate use of the ecosystem services for the benefit of humans. It can also help to ensure long-term human well-being and sustainable development.

The difference in philosophy between anthropocentricity and biocentricity has led to a debate [15]. In terms of anthropocentric philosophy, the benefits that humans can derive from their activities are a major focal point. Anthropocentric philosophy tends to prioritize humanity and view other species only as exploitable resources. Exploitation or protection for human well-being is a primary choice and has attracted attention because of the self-interest of humans. Biocentricity seems an ideal, however. On behalf of sustainability, the evaluation conducted in the current research affirmed that conservation for hillside forests can ensure local residents' welfare and so leads to a better Anthropocene.

#### *4.3. Local Industries and Livelihood of Residents*

Yilan is an agricultural county and attaches considerable importance to environmental protection. Limited industrial activity takes place in the coastal area. The land is fertile, and water and soil resources are pure and abundant.

Agricultural recreational activities are popular in this area, and they can be combined with forest ecological resources in the foothills to promote ecotourism and leisure agriculture in the form of organic agriculture or ecological or environmentally friendly agriculture. Recreational, organic, or friendly farming all depend on a healthy ecosystem. Yilan County is an ideal area to promote these farming practices and is an appropriate area for Taiwan to construct a model of sustainable agriculture.

#### *4.4. Policy Implementation at the Mountain Frontier of Human Activities*

The livelihood and property of local residents rely substantially on nearby hillside forests [57]. In this study, the local residents exhibited high agreement with the value of the ecosystem services, thus highlighting the importance of maintaining slope forest ecosystems for the welfare of local residents. Disturbing slope forests would strongly affect the economic well-being of local residents in relation to ecosystem services; thus, the current

expansion of agriculture to hillside forest areas due to climate change is inappropriate. Local agriculture can be promoted through dedicated organic farming due to the availability of pristine water and soil and can be combined with the recreational or processing industry instead of advanced mechanized farming. Moreover, hillside ecotourism that can maintain the ecosystem services and sustain residents' livelihood should be promoted.

#### *4.5. Noncommodification of Nature: Economic Valuation from the Perspective of Ecological Economics*

Market exchange systems can only represent a part of the economic value of ecosystem services. In human society, trading is a mechanism for maintaining social order. Most ecosystem services are public goods with positive externalities and are neglected by the public. The value of nonmarketable services cannot be directly presented in the trading market. Thus, the nonmarketable value of ecosystem services is often omitted in society, leading to lack of focus on such services in relevant policies. The value of nonmarketable services should be considered to understand the true economic value of the ecosystem from the perspective of the interdisciplinary field of ecological economics.

The economic value of nonmarketable services should be estimated in order to increase the importance attached to the conservation of services offered by the natural environment. This would not be a valuation for subsequent sale in the human-centered misconception of the natural capital marketization and financialization. In the contingent valuation method, welfare is measured in terms of mainstream value reasoning in consumer theory. The value index can guide the conservation of the environment for public good and as a common asset; this valuation does not refer to a price for sale in the dynamic circulation of materials, energy, and services from the ecological economics perspective. In terms of geographical Anthropocene [68], humans are now overwhelming the great forces of nature. As aforementioned, conservation and protection of hillside forests in the mountain frontier is critical for a better Anthropocene.

## **5. Conclusions**

At the frontier of land development and the junction of nature and human society, the forest ecosystem provides nearby residents with provisioning, regulating, culture, and supporting ecosystem services and generates economic value. Most of the ecosystem services are nonmarketable, and only a few of the services are marketized. No market price can accurately quantify the direct benefits that nearby residents derive from these services. In contemporary society, specific price indicators generated in the trading market system are used as tools for economic and social decision-making. Thus, ecosystem services have not been provided reasonable attention in the process of overall social decision-making. This study investigated how ecosystem services benefit residents in a frontier area from the perspective of ecological economics.

The single-bounded dichotomous contingent valuation method was applied with logit regression. The results indicated that the forests in the low-latitude hillsides of the Lanyang River Basin currently provide the local residents with the provisioning, regulating, culture, and supporting ecosystem services. The economic value of the four ecosystem services was considerably high. The results of this study highlight the importance of the conservation and maintenance of the low-latitude hillside forest ecosystem and that disturbances in the hillside forest can affect the economic well-being associated with the ecosystem services enjoyed by local residents.

This study investigated the determinants of the value of these ecosystem services. Binary regression analysis was conducted to identify factors affecting the residents' willingness to pay specific bidding amounts for ecosystem services. The results indicated that the residents' willingness to pay increased with their agreement with the value of the ecosystem services and their income. The residents with experience in donating to environmental organizations tended to be willing to pay the amount asked. However, the

older individuals with low income in the area had lower willingness to pay due to their perceptions of affordability.

Ecosystem services refer to benefits that ecosystems provide to humans. Taiwan is mountainous and densely populated. Thus, the appropriate management of forest cover at the intersection of natural ecosystems and areas with widespread human activity is crucial. The forest ecosystem service at the junction of agricultural and residential areas is extremely sensitive to the surrounding land use and social and economic activities as well as changes in nearby land-use patterns. Moreover, the societal disturbances can affect ecosystem services. The results of this study have crucial policy implications. The conservation of hillside forests and the performance of ecosystem services are directly related to the survival, life, and livelihood of local residents. The forests and surrounding residents dynamically and continually interact with ecosystem services. Individuals who live nearby hillside forests benefit from the ecosystem services provided by these areas; residents who engage in occupations dependent on nature stand to benefit the most from such services. The life of nearby residents is closely integrated with the provisioning, regulating, culture, and supporting ecosystem services of the hillside forest. Relevant land planning policies should consider the interaction between humanity and nature. Current hillside forests that are well protected by government zoning regulation are better maintained. Viable local policy for vicinity residents' livelihood is suggested to promote ecotourism to maintain the ecosystem services of hillside forests and to integrate together with local recreational and organic agriculture.

**Author Contributions:** Conceptualization, methodology, investigation, software, validation, and formal analysis, writing, and editing: W.-J.C.; organizing research project, survey design, paper review, and paper submission: S.-C.L.; research project administration, W.-J.C., J.-F.J., C.-H.C. and S.-C.L. All authors have read and agreed to the published version of the manuscript.

**Funding:** This research was funded by Ministry of Science and Technology, Taiwan, grant number MOST 110-2321-B-004-001.

**Institutional Review Board Statement:** Not applicable.

**Informed Consent Statement:** Not applicable.

**Data Availability Statement:** Not applicable.

**Acknowledgments:** We gratefully acknowledge three reviewers for their helpful comments and suggestions. The interviewers of this in-person survey are: W.J.C., W.R.C., C.C.C., I.J.H., W.M.H. and S.C.L.

**Conflicts of Interest:** The authors declare no conflict of interest.

## References

1. Daly, H.E. Economics in a full world. *Sci. Am.* **2005**, *293*, 100–107. [[CrossRef](#)] [[PubMed](#)]
2. Boulding, K.E. The economics of the coming spaceship earth. In *The Earthscan Reader in Environmental Economics*; Taylor & Francis: New York, NY, USA, 1966; pp. 1–17. Available online: <http://www.ub.edu/prometheus21/articulos/obsprometheus/BOULDING.pdf> (accessed on 20 April 2022).
3. Goodland, R. The case that the world has reached limits: More precisely that current throughput growth in the global economy cannot be sustained. *Popul. Environ.* **1992**, *13*, 167–182. [[CrossRef](#)]
4. Goodland, R.J.; Daly, H.E.; El Serafy, S. *Population, Technology, and Lifestyle*; Island Press: London, UK, 1992.
5. Daly, H.E. From empty-world economics to full-world economics: Recognizing an historical turning point in economic development. In *Population, Technology, and Lifestyle: The Transition to Sustainability*; Goodland, R., Daly, H., El Serafy, S., Eds.; Island Press: Washington, DC, USA, 1992; 154p.
6. Running, S.W. A measurable planetary boundary for the biosphere. *Science* **2012**, *337*, 1458–1459. [[CrossRef](#)]
7. Costanza, R.; Cumberland, J.H.; Daly, H.; Goodland, R.; Norgaard, R.B. *An Introduction to Ecological Economics*, 2nd ed.; CRC Press: New York, NY, USA, 2014.
8. Yusoff, K. Anthropogenesis: Origins and endings in the Anthropocene. *Theory Cult. Soc.* **2016**, *33*, 3–28. [[CrossRef](#)]
9. Bennett, E.M.; Solan, M.; Biggs, R.; McPhearson, T.; Norström, A.V.; Olsson, P.; Pereira, L.; Peterson, G.D.; Raudsepp-Hearne, C.; Biermann, F.; et al. Bright spots: Seeds of a good Anthropocene. *Front. Ecol. Environ.* **2016**, *14*, 441–448. [[CrossRef](#)]
10. Creutzig, F. Limits to liberalism: Considerations for the Anthropocene. *Ecol. Econ.* **2020**, *177*, 106763. [[CrossRef](#)]

11. McPhearson, T.; M Raymond, C.; Gulsrud, N.; Albert, C.; Coles, N.; Fagerholm, N.; Nagatsu, M.; Olafsson, A.S.; Soininen, N.; Vierikko, K. Radical changes are needed for transformations to a good Anthropocene. *Npj Urban Sustain.* **2021**, *1*, 5. [CrossRef]
12. Millennium Ecosystem Assessment (MEA). Guide to the Millennium Assessment Reports. 2005. Available online: <https://www.millenniumassessment.org/en/index.html> (accessed on 17 October 2021).
13. Yang, H.; Gou, X.; Yin, D. Response of biodiversity, ecosystems, and ecosystem services to climate change in China: A Review. *Ecologies* **2021**, *2*, 18. [CrossRef]
14. Ma, L.; Qin, Y.; Zhang, H.; Zheng, J.; Hou, Y.; Wen, Y. Improving well-being of farmers using ecological awareness around protected areas: Evidence from Qinling region, China. *Int. J. Environ. Res. Public Health* **2021**, *18*, 9792. [CrossRef]
15. Morelli, F.; Tryjanowski, P.; Benedetti, Y. Differences between niches of anthropocentric and biocentric conservationists: Wearing old clothes to look modern? *J. Nat. Conserv.* **2016**, *34*, 101–106. [CrossRef]
16. Liu, J.E.; Wang, Z.; Li, Y. Efficacy of natural polymer derivatives on soil physical properties and erosion on an experimental loess hillslope. *Int. J. Environ. Res. Public Health* **2018**, *15*, 9. [CrossRef] [PubMed]
17. Zheng, J.; Chen, G.; Zhang, T.; Ding, M.; Liu, B.; Wang, H. Exploring Spatial Variations in the Relationships between Landscape Functions and Human Activities in Suburban Rural Communities: A Case Study in Jiangning District, China. *Int. J. Environ. Res. Public Health* **2021**, *18*, 9782. [CrossRef] [PubMed]
18. Chen, Q.; Huang, F.; Cai, A. Spatiotemporal Trends, Sources and Ecological Risks of Heavy Metals in the Surface Sediments of Weitou Bay, China. *Int. J. Environ. Res. Public Health* **2021**, *18*, 9562. [CrossRef] [PubMed]
19. Qu, Y.; Zong, H.; Su, D.; Ping, Z.; Guan, M. Land Use Change and Its Impact on Landscape Ecological Risk in Typical Areas of the Yellow River Basin in China. *Int. J. Environ. Res. Public Health* **2021**, *18*, 11301. [CrossRef]
20. Liu, L.; Song, W.; Zhang, Y.; Han, Z.; Li, H.; Yang, D.; Wang, Z.; Huang, Q. Zoning of Ecological Restoration in the Qilian Mountain Area, China. *Int. J. Environ. Res. Public Health* **2021**, *18*, 12417. [CrossRef]
21. Urban and Rural Development Branch, Construction and Planning Agency, Ministry of the Interior, Taiwan (URDB-CPA-MI-T). 2022. Available online: <https://ngis.tcd.gov.tw/> (accessed on 7 April 2022).
22. Intergovernmental Panel on Climate Change (IPCC). Special Report on Climate Change and Land. 2019. Available online: <https://www.ipcc.ch/srccl/> (accessed on 15 August 2021).
23. Hsu, C.L.; Son, P.S. The investigation and discussion on vulnerability of aboriginal township in Pingtung County after Typhoon Morakot. *J. Slopeland Hazard Prev.* **2011**, *10*, 1–9.
24. Yang, M.D.; Lin, J.Y.; Lin, W.J.; Huang, K.S.; Wu, D.Y. Disaster investigation in Chenyulan River Basin during Typhoon Morakot. *J. Chin. Soil Water Conserv.* **2009**, *40*, 345–358.
25. Lee, C.T.; Fei, L.Y. Potential landslide and debris flow hazard prediction in the Lanyang River Basin. *J. Adv. Technol. Manag.* **2011**, *1*, 67–83.
26. Sui, C. BBC News: Why Has Taiwan’s Water Shortage Attracted Worldwide Attention, and How Serious Is It This Time? 2021. Available online: <https://www.bbc.com/zhongwen/trad/chinese-news-56814382> (accessed on 5 April 2022).
27. Ahmadi, H.; Ghalhari, G.F.; Baaghdeh, M. Impacts of climate change on apple tree cultivation areas in Iran. *Clim. Change* **2019**, *153*, 91–103. [CrossRef]
28. Wang, R.H.; Sheu, S.J.; Lin, H.I. Estimating the Elasticity of Demand of Cabbage: An Application of Geographical Climate Information. *Taiwan Agric. Econ. Rev.* **2020**, *26*, 1–50.
29. Yilan County Government, Taiwan. Characteristics of Townships in Yilan County. 2022. Available online: <https://www.e-land.gov.tw/cp.aspx?n=9E1BEC13B38E00CE> (accessed on 3 April 2022).
30. Hanemann, W.M. Welfare evaluations in contingent valuation experiments with discrete responses. *Am. J. Agric. Econ.* **1984**, *66*, 332–341. [CrossRef]
31. Costanza, R.; d’Arge, R.; De Groot, R.; Farber, S.; Grasso, M.; Hannon, B.; Limburg, K.; Naeem, S.; O’Neill, R.V.; Paruelo, J.; et al. The value of the world’s ecosystem services and natural capital. *Nature* **1997**, *387*, 253–260. [CrossRef]
32. Costanza, R.; De Groot, R.; Sutton, P.; Van der Ploeg, S.; Anderson, S.J.; Kubiszewski, I.; Farber, S.; Turner, R.K. Changes in the global value of ecosystem services. *Glob. Environ. Change* **2014**, *26*, 152–158. [CrossRef]
33. Cameron, T.A.; James, M.D. Efficient estimation methods for “closed-ended” contingent valuation surveys. *Rev. Econ. Stat.* **1987**, *69*, 269–276. [CrossRef]
34. Cameron, T.A. Interval estimates of non-market resource values from referendum contingent valuation surveys. *Land Econ.* **1991**, *67*, 413–421. [CrossRef]
35. Fattahi Ardakani, A.; Alavi, C.; Arab, M. The comparison of discrete payment vehicle methods (dichotomous choice) in improving the quality of the environment. *Int. J. Environ. Sci. Technol.* **2017**, *14*, 1409–1418. [CrossRef]
36. Alberini, A. Optimal designs for discrete choice contingent valuation surveys: Single-bound, double-bound, and bivariate models. *J. Environ. Econ. Manag.* **1995**, *28*, 287–306. [CrossRef]
37. Venkatachalam, L. The contingent valuation method: A review. *Environ. Impact Assess. Rev.* **2004**, *24*, 89–124. [CrossRef]
38. Carson, R.T.; Hanemann, W.M. Contingent valuation. *Handb. Environ. Econ.* **2005**, *2*, 821–936.
39. Boyle, K.J.; MacDonald, H.F.; Cheng, H.T.; McCollum, D.W. Bid design and yea saying in single-bounded, dichotomous-choice questions. *Land Econ.* **1998**, *74*, 49–64. [CrossRef]
40. Kumaraswamy, P. A generalized probability density function for double-bounded random processes. *J. Hydrol.* **1980**, *46*, 79–88. [CrossRef]

41. Sundar, V.; Subbiah, K. Application of double bounded probability density function for analysis of ocean waves. *Ocean Eng.* **1989**, *16*, 193–200. [[CrossRef](#)]
42. Kanninen, B.J. Optimal experimental design for double-bounded dichotomous choice contingent valuation. *Land Econ.* **1993**, *69*, 138–146. [[CrossRef](#)]
43. Yoo, S.H.; Yang, H.J. Application of sample selection model to double-bounded dichotomous choice contingent valuation studies. *Environ. Resour. Econ.* **2001**, *20*, 147–163. [[CrossRef](#)]
44. Yoo, S.H.; Kwak, S.J. Using a spike model to deal with zero response data from double bounded dichotomous choice contingent valuation surveys. *Appl. Econ. Lett.* **2002**, *9*, 929–932. [[CrossRef](#)]
45. Langford, I.H.; Bateman, I.J.; Langford, H.D. A multilevel modelling approach to triple-bounded dichotomous choice contingent valuation. *Environ. Resour. Econ.* **1996**, *7*, 197–211.
46. Bateman, I.J.; Langford, I.H.; Jones, A.P.; Kerr, G.N. Bound and path effects in double and triple bounded dichotomous choice contingent valuation. *Resour. Energy Econ.* **2001**, *23*, 191–213. [[CrossRef](#)]
47. Carson, R.T.; Flores, N.E.; Meade, N.F. Contingent valuation: Controversies and evidence. *Environ. Resour. Econ.* **2001**, *19*, 173–210. [[CrossRef](#)]
48. Hausman, J.A. (Ed.) *Contingent Valuation: A Critical Assessment*; North-Holland: New York, NY, USA, 2012.
49. Weimer, D.L. *Behavioral Economics for Cost-Benefit Analysis: Benefit Validity when Sovereign Consumers Seem to Make Mistakes*; Cambridge University Press: Cambridge, UK, 2017.
50. Hanemann, M.; Loomis, J.; Kanninen, B. Statistical efficiency of double-bounded dichotomous choice contingent valuation. *Am. J. Agric. Econ.* **1991**, *73*, 1255–1263. [[CrossRef](#)]
51. Scarpa, R.; Bateman, I. Efficiency gains afforded by improved bid design versus follow-up valuation questions in discrete-choice CV studies. *Land Econ.* **2000**, *76*, 299–311. [[CrossRef](#)]
52. Nurin Fadhlina, M.H.; Matthew, N.K.; Shuib, A. Visitors' willingness to pay for entrance fee at Puncak Janing Forest Eco-Park, Kedah, Malaysia. *J. Trop. For. Sci.* **2021**, *33*, 49–57.
53. Pengwei, W.; Linsheng, Z. Tourist willingness to pay for protected area ecotourism resources and influencing factors at the Hulun Lake Protected Area. *J. Resour. Ecol.* **2018**, *9*, 174–180. [[CrossRef](#)]
54. Susilo, H.; Takahashi, Y.; Yabe, M. The opportunity cost of labor for valuing mangrove restoration in Mahakam Delta, Indonesia. *Sustainability* **2017**, *9*, 2169. [[CrossRef](#)]
55. Gould, R.K.; Ricketts, T.H.; Howarth, R.B.; Telle, S.; Gladkikh, T.; Posner, S.; Gourevitch, J.; Yoshida, Y. How ecosystem services research can advance ecological economics principles. In *Sustainable Wellbeing Futures: A Research and Action Agenda for Ecological Economics*; Costanza, R., Erickson, J.D., Farley, J., Kubiszewski, I., Eds.; Edward Elgar Publishing: Northampton, MA, USA, 2020.
56. Bishop, R.C.; Heberlein, T.A.; Kealy, M.J. Contingent valuation of environmental assets: Comparison with a stimulated market. *Nat. Resour. J.* **1983**, *23*, 619.
57. Carrión-Mero, P.; Montalván-Burbano, N.; Morante-Carballo, F.; Quesada-Román, A.; Apolo-Masache, B. Worldwide research trends in landslide science. *Int. J. Environ. Res. Public Health* **2021**, *18*, 9445.
58. Feng, D.; Liang, L.; Wu, W.; Li, C.; Wang, L.; Li, L.; Zhao, G. Factors influencing willingness to accept in the paddy land-to-dry land program based on contingent value method. *J. Clean. Prod.* **2018**, *183*, 392–402.
59. Ren, Y.; Lu, L.; Zhang, H.; Chen, H.; Zhu, D. Residents' willingness to pay for ecosystem services and its influencing factors: A study of the Xin'an River basin. *J. Clean. Prod.* **2020**, *268*, 122301.
60. Yu, B.; Xu, L.; Wang, X. Ecological compensation for hydropower resettlement in a reservoir wetland based on welfare change in Tibet, China. *Ecol. Eng.* **2016**, *96*, 128–136.
61. Dupont, D.P. CVM embedding effects when there are active, potentially active and passive users of environmental goods. *Environ. Resour. Econ.* **2003**, *25*, 319–341.
62. Chen, W.J.; Liaw, S.C. Analysis of Yilan County citizens' opinions on the management of the upper Lanyang River Watershed and evaluation for natural resources. *Q. J. Chin. For.* **2006**, *39*, 477–496.
63. Cameron, T.A. A new paradigm for valuing non-market goods using referendum data: Maximum likelihood estimation by censored logistic regression. *J. Environ. Econ. Manag.* **1988**, *25*, 355–379. [[CrossRef](#)]
64. National Development Council. Regional Revitalization. 2022. Available online: <https://www.twrr.ndc.gov.tw/index> (accessed on 4 April 2022).
65. Ministry of Culture of Taiwan. Encyclopedia of Taiwan, Lanyang River. 2022. Available online: <https://nrch.culture.tw/twpedia.aspx?id=1501> (accessed on 30 March 2022).
66. Pecl, G.; Araujo, M.B.; Bell, J.D.; Blanchard, J.; Bonebrake, T.C.; Chen, I. Biodiversity redistribution under climate change: Impacts on ecosystems and human well-being. *Science* **2017**, *355*, eaai9214. [[CrossRef](#)] [[PubMed](#)]
67. Liu, M.; Fan, J.; Wang, Y.; Hu, C. Study on Ecosystem Service Value (ESV) Spatial Transfer in the Central Plains Urban Agglomeration in the Yellow River Basin, China. *Int. J. Environ. Res. Public Health* **2021**, *18*, 9751. [[CrossRef](#)] [[PubMed](#)]
68. Lewis, S.L.; Maslin, M.A. Defining the Anthropocene. *Nature* **2015**, *519*, 171–180. [[CrossRef](#)]





MDPI  
St. Alban-Anlage 66  
4052 Basel  
Switzerland  
Tel. +41 61 683 77 34  
Fax +41 61 302 89 18  
[www.mdpi.com](http://www.mdpi.com)

MDPI Books Editorial Office  
E-mail: [books@mdpi.com](mailto:books@mdpi.com)  
[www.mdpi.com/books](http://www.mdpi.com/books)







Academic Open  
Access Publishing

[www.mdpi.com](http://www.mdpi.com)

ISBN 978-3-0365-8225-2